University of Brasilia
Faculty of Gama (FGA)/ Faculty of Tecnology (FT)

Part of

Proceedings of the Brazilian Conference on Composite Materials

Organized and edited by

**Sandra Maria da Luz
&
Carla Tatiana Mota Anflor**

Brasilia-DF
[Selo editorial da UnB]
2024

Edited as an initiative of: Universidade de Brasilia

Faculdade do Gama (FGA) / Faculdade de Tecnologia (FT)

Programas de Pós-Graduação em Integridade de Materiais da Engenharia and Ciências Mecânicas

Address:

Universidade de Brasilia, Campus do Gama

Área Especial de Indústria e Projeção– Setor Leste

Prédio UED (Unidade de Ensino e Docência) - 1º Andar

CEP: 72.444-240, Gama - DF, Brasil

Contact: WebSites: http://www.pgintegridade.unb.br/ and http://www.pcmec.unb.br/

E-mail anflor@unb.br; sandraluz@unb.br

Letter from editors

Dear Readers and Participants,

It is with great pleasure that we present the Proceedings of the 7th Brazilian Conference on Composite Materials, a compendium that gathers the papers, research, and discussions presented during this edition of the event. This conference has been a space for meeting, knowledge exchange, and the development of new ideas that will undoubtedly contribute significantly to the advancement of composite materials.

In this edition, the selected papers reflect the diversity and depth of current research in composite materials. The authors offer contributions that cover both theoretical aspects and practical applications, revealing the richness of the field and its ability to address contemporary challenges. The event brought together 160 participants, 18 speakers, 32 moderators, and about 15 visitors. In addition to Brazilian participants, the event welcomed researchers from various countries, including Argentina, the United States, Canada, Portugal, the United Kingdom, Sweden, Italy, and Pakistan.

We would like to express our gratitude to all the authors who submitted their work, as well as to the members of the scientific committee, whose rigorous reviews were essential to ensuring the quality of the publications. We also thank the speakers, who enriched the conference with their inspiring and thought-provoking presentations, stimulating debate and reflection among the participants.

The production of this volume of the Proceedings was a collaborative effort that involved not only the event organization but also the dedicated work of reviewers, editors, and the technical team. Everyone played a crucial role in making this document a valuable reference for researchers, professionals, and students interested in the field of composite materials. We hope that the Proceedings of the 7th Brazilian Conference on Composite Materials will be a source of inspiration and knowledge, promoting new research and strengthening collaborative networks among professionals in the field. May this material be consulted and used as a solid foundation for the continuous development of knowledge and practice in composite materials.

We wish you all a productive and stimulating reading experience.
Sincerely,

Sandra Maria da Luz & Carla Tatiana Mota Anflor
July 14–17, 2024, Brasília, DF, Brazil.

Acknowledgement to supporters of the 7th BCCM

The Organizing Committee of the 7th Brazilian Conference on Composite Materials would like to thank for the financial support provided by:

The Brazilian research agencies:

I. CNPq – National Council for Scientific and Technological Development (Conselho Nacional de Desenvolvimento Cientfico e Tecnológico) – Grant number 446281/2023-9.
II. FAPDF – Federal District Research Funding Foundation (Fundação de Amparo à Pesquisa do Distrito Federal) – Grant number 00193-00000442/-85.

The companies:

I. Instron
II. MTS Systems
III. Zwick Roell Group
IV. Waters[TM] TA Instruments

Hosted by

Organized by

Gold Sponsors

Silver Sponsors

Support

Committee

<u>Conference Chair</u>

Sandra Maria da Luz

<u>Conference Co-Chair</u>

Claudio Henrique Soares Del Menezzi

<u>Organising Committee</u>

Carla Tatiana Mota Anflor

Daniel Pasquini

Karoline Sales de Oliveira

Lays Furtado de Medeiros Souza Kataoka

Linconl Araujo Teixeira

Thiago de Carvalho Rodrigues Doca

Vilson Dalla Libera Junior

Nacional Scientific Committee

- Alcides Lopes Leão (UNESP)
- Alfredo Rocha de Faria (ITA)
- Ana Paula Cysne Barbosa (UFRN)
- Antonio Henrique Monteiro da Fonseca Thomé da Silva (UFF)
- Artem Andrianov (UnB)
- Derval dos Santos Rosa (UFABC)
- Edson Cocchieri Botelho (UNESP)
- Flamínio Levy Neto (UnB)
- Flávio de Andrade Silva (PUC-RJ)
- Gerson Marinucci (IPEN)
- João Marciano Laredo dos Reis (UFF)
- José Daniel Diniz Melo (UFRN)
- José Ricardo Tarpani (USP - São Carlos)
- José Roberto Moraes d'Almeida (PUC-RJ)
- Leonardo Fonseca Valadares (Embrapa)
- Luiz Cláudio Pardini (ITA)
- Maikson Luiz Passaia Tonatto (UFSM)
- Marcelo A. Trindade (USP)
- Marcelo Leite Ribeiro (USP - São Carlos)
- Marcílio Alves (USP)
- Maria Odila Hilário Cioffi (UNESP)
- Maurício Vicente Donadon (ITA)
- Michelle Leali Costa (UNESP)
- Paulo Henrique Ribeiro Borges (CEFET/MG)
- Rodrigo Teixeira Santos Freire (UFSJ)
- Samuel da Silva (UNESP)
- Sandro Campos Amico (UFRGS)
- Sérgio Henrique Pezzin (UDESC)
- Tulio Hallak Panzera (UFSJ)
- Volnei Tita (USP)

International Scientific Committee

- Antonio Miravete (University of Zaragoza - Spain)
- António Torres Marques (University of Porto - Portugal)
- Brian Wardle (MITUSA - USA)
- Carlos Thomas Garcia (University of Cantabria - Spain)
- Chiara Bisagni (Politecnico di Milano - Italy)
- Debashish Bhattacharjee (Tata Group - India)
- Dipa Roy (University of Edinburgh - United Kingdom)
- Fabrizio Scarpa (University of Bristol - United Kingdom)
- Giovanni Filippone (University of Naples Federico II - Italy)
- Javier Lorca (Polytechnic University of Madrid - Spain)
- Jiping Bai (University of South Wales - United Kingdom)
- João Paulo Davim (University of Aveiro - Portugal)
- Junuthula N Reddy (Texas A&M University - USA)
- Luc St-Pierre (Aalto University - Finland)
- Luís Miguel Durão (Porto School of Engineering - Portugal)
- Martina Salzano de Luna (University of Naples Federico II - Italy)
- Nicholas Fantuzzi (University of Bologna - Italy)
- Pascal Hubert (University of McGill - Canada)
- Pedro Camanho (University of Porto - Portugal)
- Per Wennhage (KTH Royal Institute of Tehcnology - Sweden)
- Piero Cerruti (Institute for Polymers, Composites and Biomaterials - Italy)
- Stephen W. Tsai (Stanford University - USA)
- Sung K. Há (Hanyang University - Korea)
- Tay Tong Earn (National University of Singapore)
- Veronica Ambrogi (University of Napoli - Italy)
- Vijay Kumar Thakur (Cranfield University - United Kingdom)

Invited Lectures

Prof. Anastasia Elias
University of Alberta - Canada

ResearchGate

Prof. Anastasia Elias joined the department of Chemical and Materials Engineering at the University of Alberta in 2008, and is currently a Professor. Her research focuses on multifunctional polymer-nanomaterial composites. In her main research area, she explores the processing, properties, stability and degradation of biopolymer composites. She holds a Ph.D. in Electrical Engineering (University of Alberta, 2007) and a B.Sc. in Engineering Physics (University of Alberta, 2002). During her graduate studies she was a visiting researcher at the Technische Universiteit Eindhoven (2003-2006), where she conducted research in the Department of Chemical Engineering and Chemistry. From 2007-2008 she was a postdoctoral fellow in the Materials and Interfacial Chemistry Group at the NRC National Institute for Nanotechnology (NINT) in Edmonton. From 2016-2017 she was a Humboldt Fellow at the Leibniz Institute of Polymer Research, Dresden, Germany. She has co-authored more than 50 scientific publications, and she holds 2 US patents. Dr. Elias has been serving as the Associate Dean (Research Strategy) in the Faculty of Engineering since 2021.

Prof. Leandro Nicolas Ludueña
National University of Mar del Plata, Argentina

ResearchGate

Dr. Leandro N. Ludueña is a materials engineer and a doctor in materials science who graduated from the National University of Mar del Plata Engineering Faculty. He is a researcher and professor of polymer processing at the engineering faculty of the National University of Mar del Plata, Argentina. He coordinates the Thermoplastic Composite Materials Group (CoMP) of Argentina's Institute for Materials Science and Technology (INTEMA). Since 2006, he has gained experience with processing and characterizing thermoplastic polymer composites and nanocomposites, confirmed by 42 publications in scientific journals and more than 50 papers at international conferences. He has been part of 26 research projects in thermoplastic polymer composites and nanocomposites and more than 50 projects involving academic-private consortiums.

Prof. Louis Laberge Lebel
Polytechnique Montreal - Canada

ResearchGate

Louis Laberge Lebel is a professor at Polytechnique Montreal and since 2014. He is leading the Advanced Composite and Fiber Structures Laboratory (ACFSlab). In 2021-22, he held a visiting professor position at Gifu University, Japan, as a Japanese Society for the Promotion of Science (JSPS) research fellow. Professor Laberge Lebel has also worked in

the aerospace industry as a materials and process engineer, researcher, and advanced designer for more than 3 years at Bombardier Aerospace and Pratt & Whitney Canada. Prior to that, he was a JSPS post-doctoral fellow at the Kyoto Institute of Technology. Prof Laberge Lebel has contributed 40 journal publications and 9 patent applications. His main research interests are textile composites, manufacturing, modelling, nano- and bio-composites.

Prof. Michael R. Wisnom
University of Bristol - United Kingdom

ResearchGate

Prof. Wisnom is Director of Bristol Composites Institute (ACCIS) at University of Bristol. His interests are mainly concerned with failure of composites and the application of finite element analysis to understand and predict the behaviour of materials and structures under load. He has co-authored more that 373 scientific publications and he is the Editor in Chief of Composites Part A: Applied Science and Manufacturing from Elsevier.

Prof. Nazanin Emami
Luleå University of Technology - Sweden

ResearchGate

Prof. Nazanin Emami, received her Ph.D. in Composite Materials from Luleå University of Technology, Sweden, in 2004. She is currently a Professor at the Department of Engineering Sciences and Mathematics of the Luleå University of Technology. Prof. Emami is Director of the studies for Sweedish Research School in Tribology, Participating universities: LTU, KTH, Uppsala University, Halmstad University. She is the recipient of the 2019 Royal Swedish Academy of Engineering Sciences (IVA) and the 2008 Award winner of "Royal Skytteanska Samfundet".

Prof. Pedro Camanho
University of Porto - Portugal

ResearchGate

Prof. Pedro Camanho, received his Ph.D. in Composite Materials from the Imperial College London, United Kingdom, in 1999. He is currently Full Professor at the Department of Mechanical Engineering of the University of Porto. Prof. Camanho is the President of the Associated Laboratory in Energy, Transportation and Aeronautics (LAETA), and member of the Editorial Board of multiple international journals. His main research interests are the mechanics of deformation and fracture of advanced polymer composite materials, and new concepts for lightweight composite materials and structures for aerospace applications such as hybrid, nano-structured, multi-functional, variable-stiffness, morphing, energy-storage and ultra-thin composites. He is the recipient of the 2006 NASA -H.J.E. Reid Award for Outstanding Scientific Paper. He also received the 2020 Excellence in Research Award of the University of Porto, and the Career Award from the Portuguese Society of Fatigue and Structural Integrity.

Keynotes

Dr. Sabrina Carroccio
Institute for Polymers, Composites and Biomaterials (IPCB), CNR, Italy

Prof. Giovanni Filippone
Department of Chemical, Materials and Production Engineering, University of Naples Federico II, Italy

Prof. Lina Bufalino
Universidade Federal Rural da Amazônia, Belém, PA, Brazil

Prof. Rafael Delucis
Universidade Federal de Pelotas, Pelotas, RS, Brazil

Prof. Sajid Hussain Siyal
Department of Metallurgy & Materials Engineering, University of Engineering and Technology, Karachi, Pakistan

Prof. Vijay Rangari
Department of Material Science and Engineering, Tuskegee University, Tuskegee, United States

Dr. Leonardo Fonseca Valadares
Embrapa Agroenergia, Brasilia, DF, Brazil

Note from the Organisers & Editors
of the 7th BCCM Proceedings Book

Organisers & Editors of this book are responsible for the editing, compilation, layout and publication. The authors of each article retain its copyright and are solely responsible for the content of the information and due credit to the references used.

This book has a browse resource by titles through bookmarks.

A u t h o r s h i p S t a t e m e n t – Organising & Editing

S.M. da Luz: (I) Management of submission and review processes of full manuscripts; C.T.M. Anflor: (I) Supervision of submission and review processes; (II) Template and editing of full manuscripts; (III) Supervision and review of book editing and layout; (IV) Resources; (V) Organisation, compilation, layout and publication of the book.

Note to article authors

We recommend that you use the ISSN as identifier to register your publication in platforms of bibliographic output (ORCID, Lattes CV, etc). If you wish to make your work available on an open access platform (ResearchGate, e.g.), please upload ONLY the pages of the book that correspond to your article. Check out this video (https://youtu.be/EEVRoa88FOA) on how to make your work available on ResearchGate. Check out this video (https://youtu.be/pR0ts2fTOVQ) on how to make your work available on Zenodo with a free DOI.

How to cite an article from this book

Name(s) of article author(s), using et al. if there are more than three (3) authors. "Article title". In Proceedings of the 7th Brazilian Conference on Composite Materials (Part of ISSN 2316-1337), Organised and Edited by S.M. da Luz & C.T.M. Anflor, 2024, pp. page interval.

Example:
T.F., Rodrigues, E.D.M, Santanna, C.T.M., Anflor, "Study of crack behavior and propagation using Finite Elements in polymer structures reinforced with carbon Fibers". In Proceedings of the 7th Brazilian Conference on Composite Materials (Part of ISSN 2316-1337), Organised and Edited by C.T.M. Anflor. & S.M. da Luz, 2024, pp. 402-408.

Brasilia, DF, Brazil

Chosen as a UNESCO World Heritage Site due to its modernist architecture, Brasilia is the capital of Brazil. The city was planned and developed by Lúcio Costa and Oscar Niemeyer in 1956 in order to move the capital from Rio de Janeiro to a more central location. The landscape architecture was designed by Roberto Burle Marx.

As a venue for music performances and movie festivals, Brasilia is a cosmopolitan city, with 124 embassies, a wide range of international and local restaurants, malls, theaters and a complete infrastructure ready to host any kind of event. Not surprisingly, the city stands out as an important business/tourism destination.

Brasilia international airport Juscelino Kubitschek receives direct flights from Lisbon (TAP), Paris (AirFrance), Atlanta (Delta Air lines) and Miami (American Airlines). Further, there are international flights running in a daily basis from all over the world to São Paulo and Rio de Janeiro. These cities are connected to Brasilia through direct domestic flights, offered nearly every hour. The main airlines operating in Brazil are: TAM, GOL and Azul.

University of Brasilia

The University of Brasilia offers free public education of excellence for Brazilian and foreign students, with a humanistic, embracive and plural perspective of citizens' rights. Our goals and our mission are to be a reference in teaching, research and community projects, contributing to global knowledge in an interconnected world.

- The University of Brasilia was created in 1962 following the joint vision of the anthropologist Darcy Ribeiro and the educator Anísio Teixeira.
- Its conception came from the same revolutionary spirit that gave rise to the federal capital, Brasilia: to renew the methods of learning and to teach towards the future.
- Dedicated to the promotion of free, inclusive and high-quality education, UnB is among the best universities in Brazil.
- Its institutional mission is to produce, integrate and disseminate knowledge, and to educate citizens to be committed to ethics, social responsibility and sustainable development.
- In 1995, the university was the first in the country to offer a three-stage entrance exam (Serial Evaluation Program – PAS), with tests for candidates at the end of each year of high school.
- In 2003, UnB was the first Brazilian federal university to approve affirmative action for black and indigenous applicants.

University of Brasilia, Campus Darcy Ribeiro

Summary

7   Composite structures

8   Delamination, damage and fracture

9   Design and application of composite structures

10 Durability of composite materials

11 Failure of composites

11.2   Mechanical characterization of carbon/epoxy laminates manufactured by filament winding

11.3   Short-beam strength of glass fiber-epoxy composites with healing agent

12   FRP in concrete, steel and composite steel/concrete structures

12.1   Machine learning with data augmentation for concrete constitutive modelling

12.2   Application of artificial neural network in predicting the mechanical performance of reinforced concrete columns confined with CFRP

13   Laminated composites

13.1   Fire behaviour of wood-glass and jute-glass hybrid laminates manufactured by vacuum infusion

13.2   Influence of hybridization on the mechanical properties of sisal/carbon and sisal/glass fiber metal laminates

13.3   Torsional test on glass/epoxy and sisal/epoxy tubular composites

13.4   Characterization of damage due to ballistic impact on thin-walled epoxy fiberglass laminates

13.5   Quasi static indentation tests to predict low velocity impact behaviour of aramid/s2-glass/epoxy hybrid laminates

14   Micromechanics

14.1   Micromechanical study of the behavior of unidirectional composites during hot pressing manufacturing

14.2   Failure envelope for unidirectional laminae subjected to transversal and out-of-plane shear loads

14.3   Abrasive wear of carbon nanostructures and epoxy composites

15   Modelling, simulation and testing of composites, sandwich and adaptive structures

15.1   Experimental radial compression analysis of variable-angle tow filament-wound composite cylinders with and without stress concentrators

15.2   Parametric optimization of composite beams with non-symmetric cross-section under four-point bending

15.3   Design and analysis of laminate lay-ups for composite pressure vessels for air storage

15.4   Experimental investigation of the uniaxial ratcheting behavior of polypropylene matrix

16   Multifunction composites

16.1   Evaluation of biosilicateâ® functionalization by RF plasma through solid maleic anhydride

17   Nanocomposites

17.1   Improvements in the mechanical properties of epoxy adhesives with plasma-functionalized carbon nanotubes

17.2   Investigation of the mechanical properties of a castor oil polyurethane foam reinforced with cellulose microfibrils

17.3   Obtaining and characterizing polyacrylonitrile (pan) mats reinforced with graphene

17.4   Thermal and mechanical analyses of a graphene acrylonitrile styrene acrylate composite for additive manufacturing use

17.5   Effect of nanodiamonds functionalization on thermo-mechanical behavior of bionanocomposites

17.6   Evaluating the dispersion methods of graphene oxide and their impact on the thermal and dynamic mechanical properties of epoxy nanocomposites

17.7   Sensor made of carbon nanotubes and carbon black in rubber matrix for monitoring bolted joints

17.8   The influence of plasticizers on the conductivity of nanocomposite films of regenerated cellulose and silver nanoparticles

17.9   Thermal characterization comparison between commercial pla and pla/graphene filaments The influence of plasticizers on the conductivity of nanocomposite films of regenerated cellulose and silver nanoparticles

18 Natural fiber composites

19 Non-destructive inspection techniques for composite materials and structures

1 Aeronautical composite materials and structures

Organized and edited by

Sandra Maria da Luz
&
Carla Tatiana Mota Anflor

PRODUCTION AND CHARACTERIZATION OF ZIRCONIA-TITANIA-LANTANIA CERAMIC MATRIX COMPOSITES FOR COATING THE ENGINE EXHAUST SYSTEM IN THE AEROSPACE SECTOR

Filipe Eliakine Patricio dos Santos[1*]; Bruna Amorim Advincula [1]; Gisele Macêdo de Araujo [1]; Renata Oliveira Domingues [1]; Ricardo Artur Sanguinetti Ferreira [1]; Yogendra Prasad Yadava [1]

(1) Student. Federal University of Pernambuco (Universidade Federal de Pernambuco (UFPE). Av. Prof. Moraes Rego, 1235, Cidade Universitária, Recife, CEP 50670-901, PE.)
* Corresponding author: filipe.eliakine@ufpe.br

(a) 0009-0003-7333-1606 (University of Pernambuco – Brazil)
(b) 0000-0003-1052-162X (University of Pernambuco – Brazil)
(c) 0009-0004-0121-8826 (University of Pernambuco – Brazil)
(d) 0009-000-0738-9549 (University of Pernambuco – Brazil)
(e) 0000-0002-4136-8421 (University of Pernambuco – Brazil)
(f) 0000-0001-7424-5682 (University of Pernambuco – Brazil)

* Corresponding author: filipe.eliakine@ufpe.br

Keywords: Composite; Thermal Barrier Coating; Gas Turbine

Abstract: The aerospace sector, comprised of the defense, aeronautics and space sectors, is an industrial branch that expresses considerable technological and financial value in its final product. The exhaust system of space vehicles, specifically the exhaust nozzle, has been the target of research aimed at improving its efficiency and useful life. They are made of titanium and aluminum superalloys resistant to oxidizing environments and high temperatures. However, they are not completely immune to these degrading effects that reduce their mechanical resistance and useful life. To protect the nozzles, zirconia-based ceramics have been used as thermal protection, avoiding thermal and mechanical stress on the substrate. However, like most ceramic materials, zirconia in its monoclinic phase is brittle and, to increase toughness, stabilizing oxides are added to zirconia to keep it in the tetragonal phase where toughness occurs through transformation. In this work, zirconia-titania-lanthania ceramic composites were produced by thermomechanical processes. The oxides were mixed in percentage by weight and the mixture was ground in a ball mill for twelve hours, compacted in a circular matrix under pressure of twelve tons per cm², for seven minutes. Subsequently, sintered at a temperature of 1350°C for twenty-four hours. The structure, microstructure and mechanical properties of the sintered discs were characterized by XRD, scanning electron microscopy and Vickers hardness, and the characterization results were applied to be applied as a ceramic coating in the exhaust system of turbines in the aerospace sector.

1. INTRODUCTION

The aerospace industry is responsible for carrying out research, design, manufacturing and operations of aircraft, sounding rockets and other air and space vehicles. This sector has a variety of activities involving the aeronautical, defense and space sectors. According to the Aerospace Industries Association (AIAB), the Brazilian aerospace industry is the largest in the Southern Hemisphere and continues to be a leader in several segments of this sector [1].

The gas turbine is responsible for the propulsion of aerospace vehicles, which justifies its wide and indispensable application. It is a thermal engine capable of generating greater powers than thermal engines of the same weight [2]. The field of aeronautical propulsion was the most impacted, as the gas turbine allowed the manufacture of more powerful and lighter aircraft [3].

In the development of the gas turbine, one of the main focuses is the study of metallurgical limitations. From a thermodynamic point of view, the higher the operating temperature of the equipment, the greater its performance. In other words, the efficiency of the turbine is closely linked to the materials that make it up.

In the case of rockets, during propulsion, gases from the combustion chamber flow with high temperature (2500 to 4100°C) and pressure at the entrance to the exhaust nozzle, which accelerates the gases producing thrust [4] and [5]. The purpose of the exhaust nozzle is to transform thermal energy into kinetic energy. The gases generated in the combustion chamber are accelerated by the nozzles, suffering a drop in pressure and temperature while the speed reaches high values (1800 to 4300m/s).

Due to the working conditions of the nozzles, such as high temperatures and gas velocities, the substrate tends to suffer oxidation, erosion, corrosion, among other degrading effects. With the aim of providing thermal protection to the substrate, coatings such as thermal barriers (TBCs – Thermal Barrier Coatings) have gained ground in the aerospace sector, due to their simple application technology and for providing a longer useful life to the nozzle [6].

Ceramic matrix composites have been the subject of research and interest in the aerospace sector regarding their application as TBCs, for coating hot exhaust parts. The refractory nature of ceramic materials attracts applications that require high heat flow. However, the relative high density of this class of materials, as well as the fragility, are still challenges to be overcome by engineering [7].

Among refractory materials, zirconia dioxide is a strong candidate for multiple engineering applications. High mechanical strength, chemical stability, wear resistance, fracture toughness and coefficient of thermal expansion close to that of iron and ferroalloys are inherent properties of this material [8]. However, fragility is also a characteristic that accompanies zirconium dioxide as it is a ceramic.

To reduce the brittleness of zirconia ($ZrO2$), oxides are added that act as reinforcements, improving the mechanical integrity of the ceramic. Important studies were carried out on the manufacture of composites such as $ZrO2$-yttria ($Y2O3$), $ZrO2$-ceria ($CeO2$), $ZrO2$-calcium (CaO) and $ZrO2$-$Y2O3$-magnesia (MgO) where the results were encouraging regarding their use as TBCs [9-12].

With the objective of providing greater useful life to the nozzles, reducing the weight of the vehicle generated by the nickel components, enabling operations at higher temperatures and powers, this work proposes to develop zirconia-lanthania-titania ceramic matrix composites for coating aerospace turbine nozzles.

2. MATERIALS AND METHODS

The ceramic composites were separated into two samples, both containing thirty grams and their own amounts of zirconia, lanthanum and titania, all defined by weight percentage. Table 1 displays the compositions.

Table 1 – Sample compositions.

	Sample 1	Sample 2
ZrO_2	85%	78%
La_2O_3	5%	5%
TiO2	10%	15%

Both samples were subjected to the same manufacturing processes: grinding and homogenization for 24 hours with 32 alumina spheres. To weigh the oxides, an analytical balance with four decimal places (Model MARCONI: FA2014N) was used. In the compaction stage, the powder was added to a 30 mm diameter metal matrix. The mass of powder inserted into the die was approximately 8.70 g to produce tablets with a thickness of 4 mm. Pressing was carried out in a hydraulic press applying pressure of 5 tons/cm2 for 2 minutes and then another 7 tons/cm2, totaling 7 minutes and 12 tons/cm2. To assist in demolding and avoid breaking the green compact, ethylene glycol was applied to the matrix, serving as a lubricant. The use of this did not change the chemical composition of the samples, as it evaporated easily. Sintering was carried out in a high temperature muffle furnace (model Jung 0614), at 1350°C for 24 hours. Subsequently, the ceramic plates were subjected to X-ray diffraction analysis (Bruker, model D8 Advanced Davinci) with Cu-Kα radiation (λ= 1.5406 Å). For the Vickres hardness test, the samples were prepared through a metallography process in which sandpaper with grain sizes between 220 and 1200 was used to facilitate visualization and measurement of indentation. At this stage, the equipment used was a microhardness meter (model HVS-5, nº 0021). In order to analyze the microstructure and chemical composition of each phase of the sintered samples, scanning electronic microstructure and energy dispersive spectroscopy techniques were used (model HITACHI – TM300 and Tescan Mira 3).

3. RESULTS AND DISCUSSION

X-ray Difraction (DRX)

The sintered tablets were analyzed by X-ray diffraction, with the aim of determining structural information. The diffractogram of composition 1 (Figure 1 a) shows the composite with the characteristic peaks for each constituent. No phases other than zirconia, lanthania and titania were detected. It is also possible to notice the greater number of peaks characteristic of tetragonal zirconia at room temperature. The diffractogram of composition 2 (Figure 1 b) shows a smaller number of tetragonal zirconia peaks, due to the decrease in the percentage of zirconium oxide in composition 2.

Figure 1 – Diffractograms of samples a) sample 1 and b) sample 2
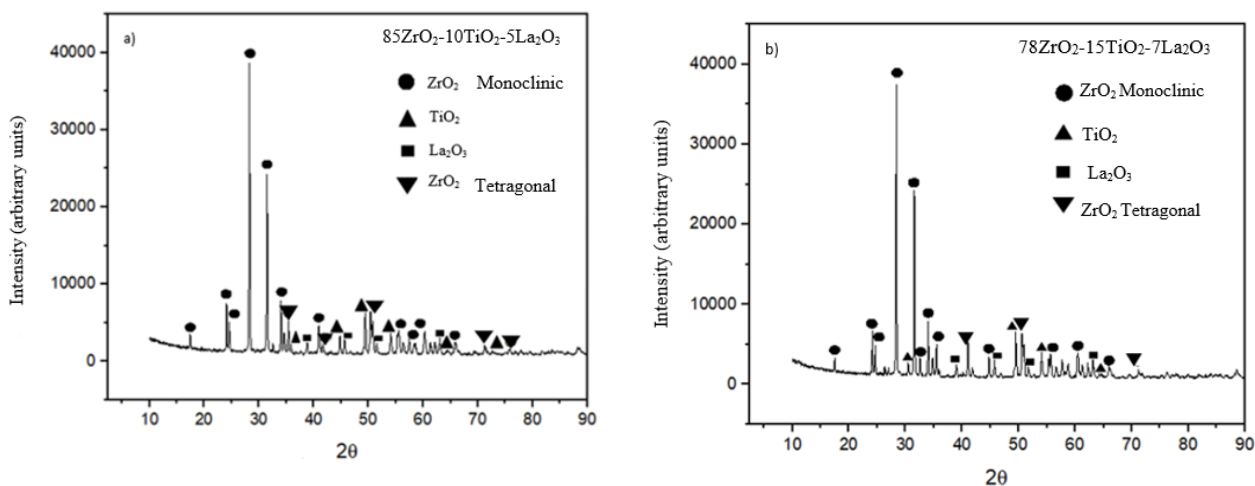
Scanning electron microscopy (SEM)

The sintered tablets were subjected to scanning electron microscopy. As these are insulating materials, for this analysis it was necessary to coat them with a thin layer of gold, in order to facilitate the conduction of electrons. Figure 2 shows the microstructure of sample 1. A microstructure with little homogeneity in terms of particle size and particle size distribution can be noted, as well as the presence of residual pores.

Figure 2 – Scanning electron microscopy of sample 1 (a) 1kx (b) 5kx (c) 10kx and (d) 20 kx.
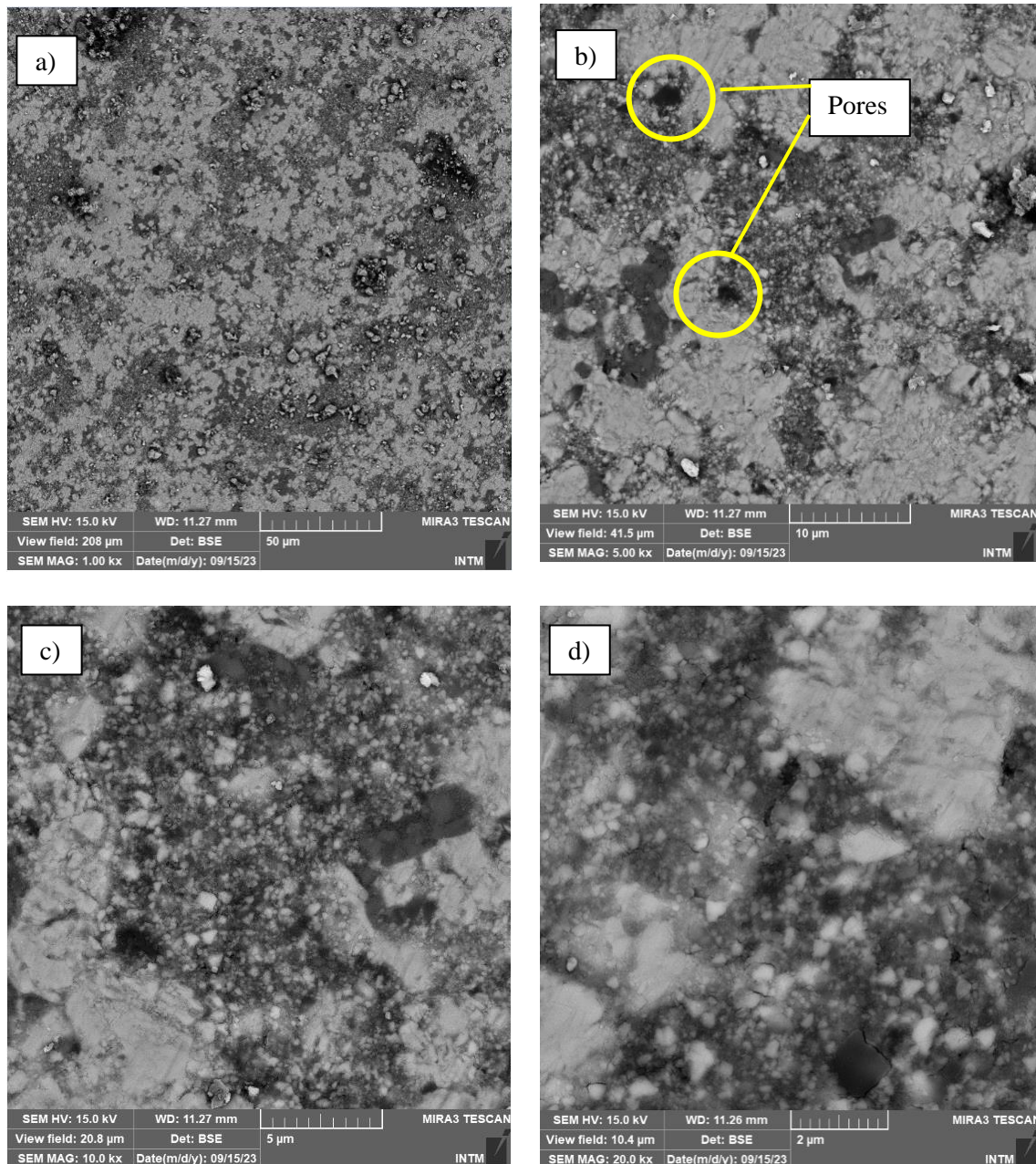
Figure 3, referring to sample 2, displays a more homogeneous microstructure in terms of particle size and particle size distribution. Such effects increased the average hardness of the material (137.17 Hv) and can be attributed to the higher percentage of titania and lanthanum (15% and 7% respectively).

Figure 3 – Scanning electron microscopy of sample 2 (a) 1kx (b) 5kx (c) 10kx and (d) 20 kx.
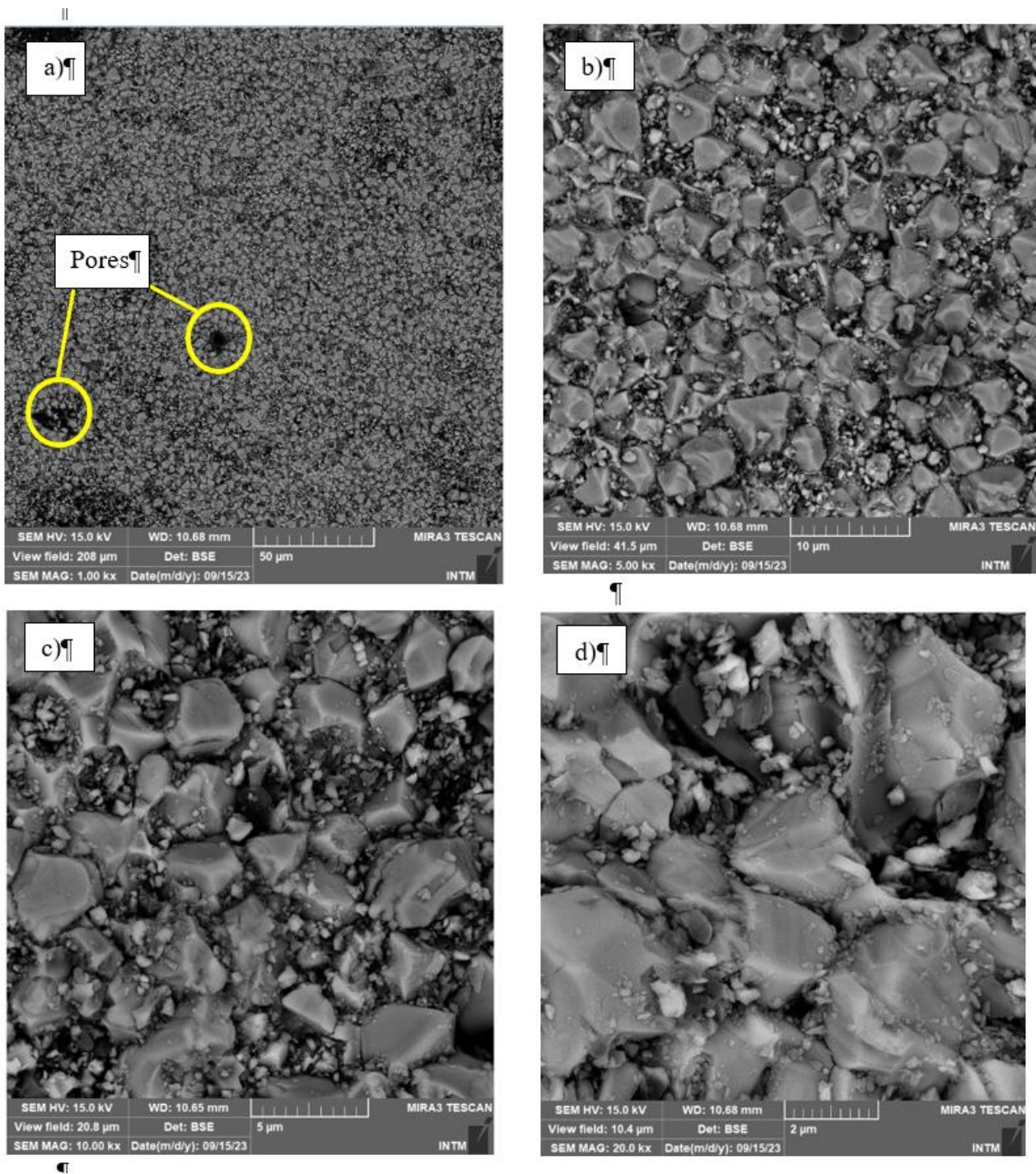
Energy dispersive Epectroscopy

In addition to the analysis of the microstructure of the tablets, carried out using SEM, the Energy Dispersive Spectroscopy (EDS) technique was performed, in order to obtain elementary microanalysis of the sample, that is, a qualitative and semiquantitative microanalysis of chemical elements present in the sample.

Figure 4 - Energy Dispersive Spectroscopy of sample 1
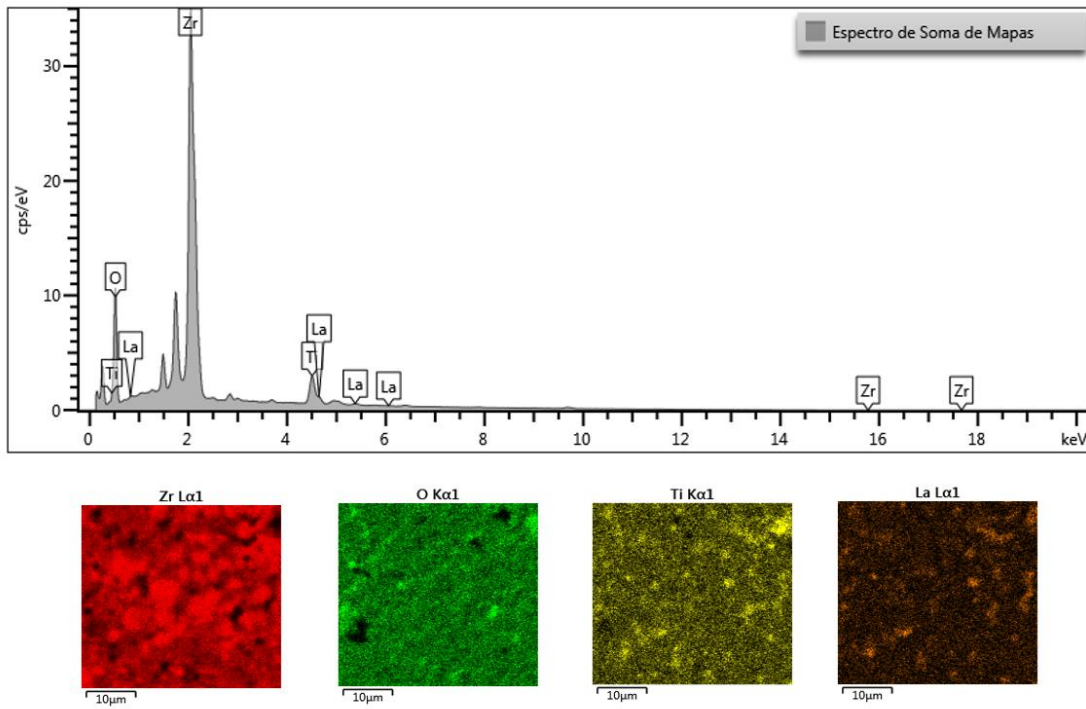
Figure 5 - Energy Dispersive Spectroscopy of sample 2
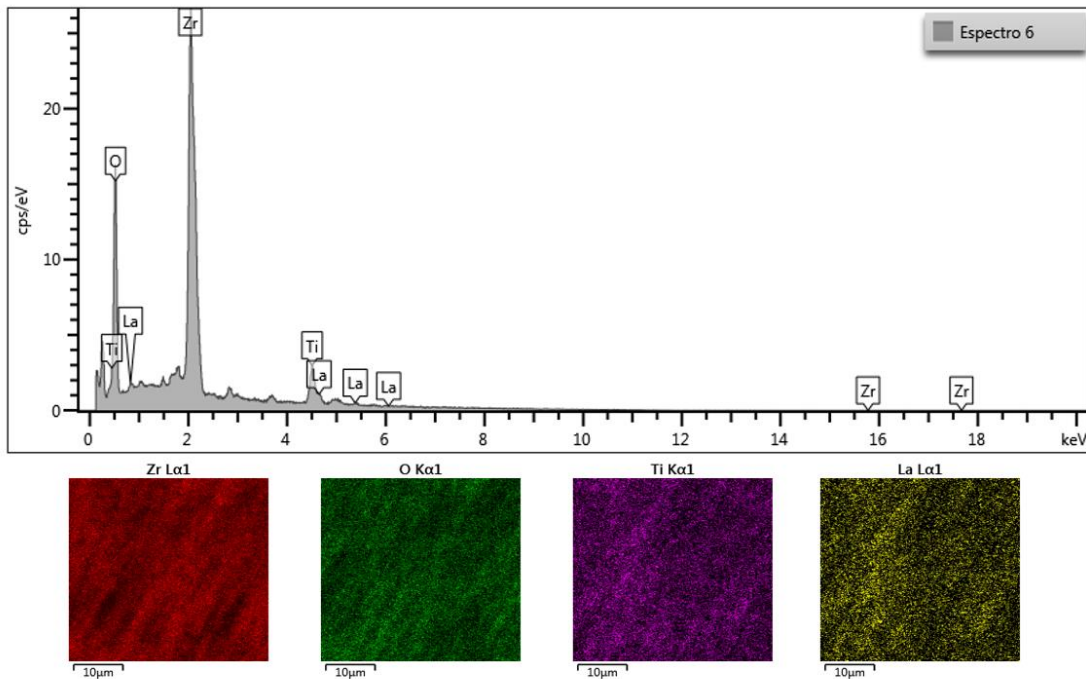
Analyzing the EDS of the ZrO2La2O3TiO2 ceramic composites only shows the presence of the expected elements. It can be stated that neither of the two samples suffered contamination during processing.

Vickers microhardness

The Vickers microhardness test on a material can be understood as the resistance of the test piece to the penetration of a pyramid-shaped diamond with a square base. In order to obtain the hardness of the samples, a Vickres microhardness tester was used, applying a load of 1kg, with 10x magnification for 10s. 15

indentations were made on each sample in different locations on the specimen. The two most outlier values were excluded when calculating the arithmetic mean. Table 2 displays the values obtained in the test as well as the respective means obtained. It can be seen that the increase in titania and lanthanum content provided an increase in hardness in composition 2.

Table 2 – Hardness measurements of the samples and their averages.

	Sample 1	Sample 2
	212,12	328,05
	219,4	214,38
	143,62	122,69
	71,65	86,47
	65,51	94,02
Microhardness Vickers(HV)	86,84	92,41
	161,5	128,84
	69,45	81,7
	163	130,87
	162,44	222,25
	84,87	94,15
	85,56	112,63
	115,23	74,78
Average (HV)	126,25	137,17

4. CONCLUSIONS

The diffractograms of the two samples proved that the sintering temperature (1350 °C) promoted the phase transformation from monoclinic to tetragonal zirconia. The latter remained stable at room temperature, coexisting with the monoclinic phase. Complementing the diffractograms, the microstructure obtained by SEM shows the formation of the composite where three phases can be noted by different colors: dark gray, light gray and white. Analysis of the results of X-ray diffraction, scanning electron microscopy and Vickres microhardness showed that sample 2 presented better performance to be used as a thermal barrier coating.

ACKNOWLEDGMENTS

REFERENCES

[1] ASSOCIAÇÃO DAS INSDÚSTRIAIS AEROESPACIAIS DO BRASIL. A indústria Aeroespacial Brasileira. Disponível em: http://www.aiab.org.br/indutria-aeroespacial.asp Acesso em: 16 jan. 2024.

[2] PEREIRA, L. X.; BENEGRA, M. Revestimentos Alternativos para palhetas de turbinas resistentes a oxidação. In: 5º Seminário de Iniciação Científica, 2011, Curitiba. 12º Caderno de Iniciação Científica. Curitiba: Associação Franciscana de Ensino Senhor Bom Jesus, 2011. v. 1. p. 359-378.

[3] COHEN, H.; ROGERS, G. F. C.; SARAVANAMUTTOO, H. I. H. Gas Turbine Theory. 4ª. ed. Harlow: Harlow: Longman Group, 1996.

[4] SUTTON, G. P., BIBLARZ, O. Rocket propulsion elements: an introduction to the engineering of rockets, 7thed, 2001.

[5] POLYAEV, V.M., BURKALTSEV, V. A. Liquid propellant rocket engines, Thermal to mechanical energy conversion: Engines and requirements – Vol.II, Department of rocket engines, Bauman Moscow State Technical university, Russia, 2002.

[6] SCHLOESSER, J., FEDOROVA, T., BÄKER, M. and RÖSLER, J. Thermal Barrier Coatings on Copper Substrates for Rocket Applications, Journal of Solid Mechanics and Materials Engineering, Vol.4, N° 2, pp.189-195, 2010.

[7] DICHIARA, A.R., BOEING, C.O. Ceramic tile, for launch vehicles, comprises oxide ceramic matrix composite comprising ceramic fiber, and cured metal oxide ceramic material impregnating ceramic fiber, where core material has surface(s) covered by ceramic matrix composite; Patent number us2005084665-a1, us6969546-b2, 2005.

[8] WU, Z. G.; ZHAO, Y. X.; LIU, D. S. The synthesis and characterization of mesoporous silica-zirconia aerogels. Microporous and Mesoporous Materials, v. 68, p. 127-132, 2004.

[9] FERREIRA, Y. C. Caracterização da microestrutura e das propriedades mecânicas de cerâmicas de zircônia parcialmente nanoestruturadas em função da quantidade de Nb2O5 para aplicações espaciais. São José dos Campos: INPE, 2010. 42 p. (Relatório científico).

[10] MARTINS, R. Implantes de zircônia reforçada com ítria (Y-TZP). Avaliação histomorfométrica. 2013. 175 p. Tese de doutorado - Faculdade de Odontologia de Bauru, Universidade de São Paulo. Bauru, 2013.

[11] SANTOS, A. A.; CHRISTIE, C. M.; MARUYAMA, N. H.; GENOVA, L. A. Relação entre variáveis de processo e as curvas de compactação e microestruturas obtidas. In: Congresso Brasileiro de Cerâmica, 55. Anais. Porto de Galinhas: 2011.

[12] RÊGO, S. A. B. C.; FERREIRA. R. A. S.; YADAVA. Y. P. Uso de óxidos de alumínio, titânio e cério na produção de compósitos cerâmicos para revestimento protetor de tanques de armazenamento e transporte de petróleo cru. 56° Congresso Brasileiro de Cerâmica, Curitiba-PR, 2012.

PARAMETRIC STUDY OF BONDED COMPOSITE JOINTS UNDER MIXED-MODE I+II

Jailto A.P. da Silva[a], Rafael Beck[b], Lucas F.M. da Silva[d],
Volnei Tita[e], Ricardo De Medeiros [c], *

(a) 0000-0002-7800-447X (University of São Paulo – Brazil)
(b) 0000-0002-1026-5059 (Santa Catarina State University – Brazil)
(c) 0000-0002-8055-3275 (Santa Catarina State University – Brazil)
(d) 0000-0003-3272-4591 (University of Porto – Portugal)
(e) 0000-0002-8199-1162 (University of São Paulo – Brazil)
* Corresponding author: ricardo.medeiros@udesc.br

Abstract: Composite aircraft structures have been undergone thoroughly examination concerning various loading combinations capable of inducing different failure modes. These failure modes, specifically the fracture energies associated with modes I and II, are influenced by geometric and material variables, contributing to both epistemic and intrinsic uncertainties. This work introduces a numerical methodology to simulate the Mixed Mode Bending (MMB) test conducted on specimens manufactured with carbon/epoxy adherents and a ductile-based epoxy adhesive. The methodology employs a 2D finite element model within Abaqus® software aided by a Python™ routine. To evaluate the impact of mechanical and geometric variables on the fracture strength responses under various mixed-mode ratios, the Compliance-Based Beam Method (CBBM) adapted for the MMB test is utilized following the ASTM D6671 standard. The numerical model incorporates a 4-node cohesive type element (COH2D4) for the adhesive and the 4-node plane strain element (CPE4R) for composite adherents. The loading mechanism representing the testing apparatus is modelling using a 2-node, two-dimensional, linear rigid link (R2D2). The adhesive response is evaluated using a triangular traction-separation law (TSL), allowing the validation of the numerical model based on experimental results obtained from the literature. The mixed-mode fracture energy ($G_{Tc, MMB}$) resulting from CBBM for various modes II to I ratios are used to compare, which allowed evaluating the methodology to be applied in the design of composite material joints.

1. INTRODUCTION

Applications involving the replacement of traditional metallic materials with composite materials play a significant role in introducing new attributes to aircraft structures and advancing technology in damage tolerance design and analysis [1-2]. The damage-tolerant design philosophy [3] is crucial in the designing composite aircraft structures because it involves assessing the allowable limits of loadings/strain, which aids in the development of these challenging designs. To achieve this, prior knowledge of the types of loads acting on composite structures provides valuable information for safety and failure analysis. Precursor crack initiation [2] must be assessed to ensure accurate localization. Complex loading combinations, such as mixed modes, are influenced by mixed-mode ratios, thereby affecting the failure modes in bonded composite joints [4]. This underscores the need for comprehensive inquiries and resolutions due to the limited studies on the impacts of mechanical and geometric variables on the fracture strength of composite bonded joints under the loading

conditions. These uncertainties are both epistemic and intrinsic [5-6], potentially leading to mechanisms such as intra/interlaminar failures, despite the application of certain surface treatment types [7] aimed at their enhancement.

Regarding the geometric influences on mixed-mode fracture energy (G_{Tc}) when applying the Asymmetric Single Leg Bending (ASLB) test, research conducted by Moreira et al. [8] and Oliveira et al. [9] has been significant. However, this bonded joint type necessitates distinct specimen geometries for each mixed-mode ratio [10], posing challenges when seeking a straightforward and expedient assessment of G_{Tc}. The Mixed-Mode Bending (MMB) test, utilized in studies by Koo and Kim [11], Floros, Tserpes, and Löbel [12], Leone, Girolamo, and Dávila [1], Fatolahi and Khoramishad [13], and Silva et al. [10], emerges as a more suitable option due to its unique geometry for estimating G_{Tc}. The proposed methodology leads to a more precise and comprehensive evaluation of fracture behaviour, fostering an improved comprehension of the performance of these joints under Mixed-Mode I+II loading conditions. Thus, this work presents a numerical methodology to simulate the Mixed Mode Bending (MMB) test conducted on specimens manufactured with carbon/epoxy adherents and a ductile-based epoxy adhesive.

2. METHODOLOGY

The MMB test involves carefully dimensioned equipment, typically made of metal, which applies loading via a yoke supported by a saddle to a roller attached to a lever, thus loading the mid-plane of the MMB specimen as per ASTM D6671 standard [15]. Considerations regarding loading decompositions are employed based on previously defined mixed-mode ratios, determined by their crack mode type, namely opening-mode I (P_I) and shear-mode II (P_{II}), relative to the original applied load (P). Figure 1 provides a schematic representation of the MMB test, illustrating its components and details of the test specimen. The saddle [14] minimizes the non-linearity of the load point (rollers attached to it) and generates mixed-mode loads based on the lever load length (c_{load}), which can be predefine according to [15] for desired mixed-mode ratio, facilitating the measurement of the corresponding mixed-mode fracture energy (G_{Tc}). The lever load (c_{load}) exerts varying degrees of influence depending on the mode type in G_{Tc}, with additional information including the lever weight (P_g) and the lever length weight (c_g) based on its centre of gravity.
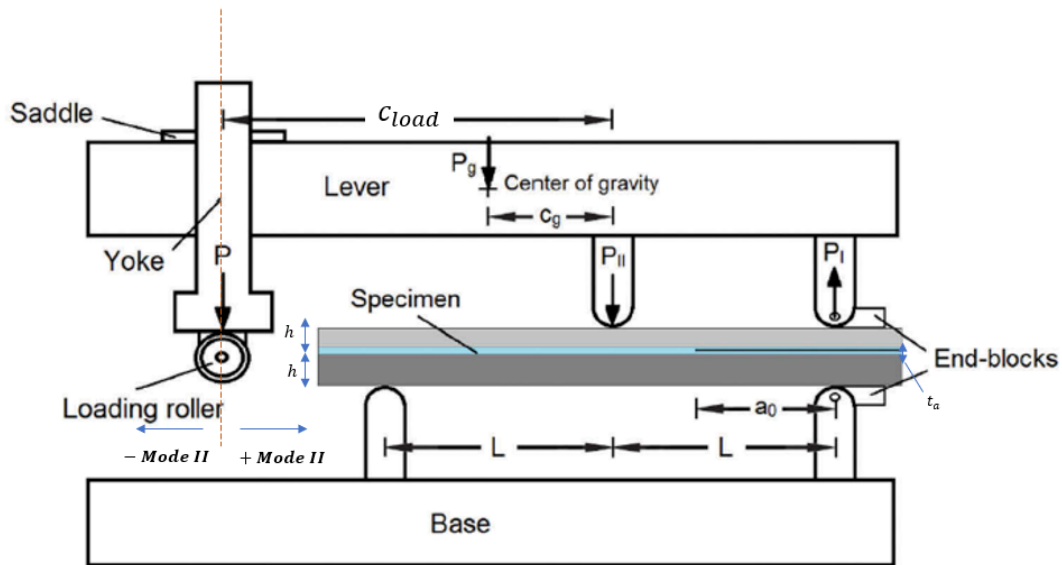
Figure 1. MMB test scheme containing the apparatus and test specimen [16].

In this study, numerical simulations were carried out using experimental results from [1] of MMB specimens manufactured with FM-300M adhesive and the TE-1 Grade 190 Type 35 Carbon/Epoxy CFRP laminate due to their known mechanical properties and MMB experimental take from [1]. The numerical analysis followed the study by Leone, Girolamo, and Dávila [1]. Figure 2 illustrates the geometry parameters analyzed by the model, covering two failure mode ratios. For the 25% and 50% failure mode ratios, parameters included a pre-crack length (a_0) of 30 mm, half-length of the adherent (L) of 70 mm, adherent width (B) of 25 mm, adherent thickness (h) of 1.50 mm, and adhesive thickness (t_A) of approximately 0.25 mm. For 60% and 75% mixed-mode ratios, a pre-crack length (a_0) of 45 mm, half-length adherent (L) of 100 mm, adherent width (B) of 25 mm, adherent thickness (h) of 2.50 mm, and adhesive thickness (t_A) of approximately 0.25 mm were

considered. Figure 2 also emphasizes the boundary conditions and the loads/displacements application point. The length of the adherent tips of the MMB specimens is defined as 15 mm (L_1) and 10 mm (L_2) for the left and right sides, respectively. For each MMB numerical model, $G_{T, MMB}$ values were estimated as being similarly to a real experiment that has implicit epistemic/intrinsic uncertainties.
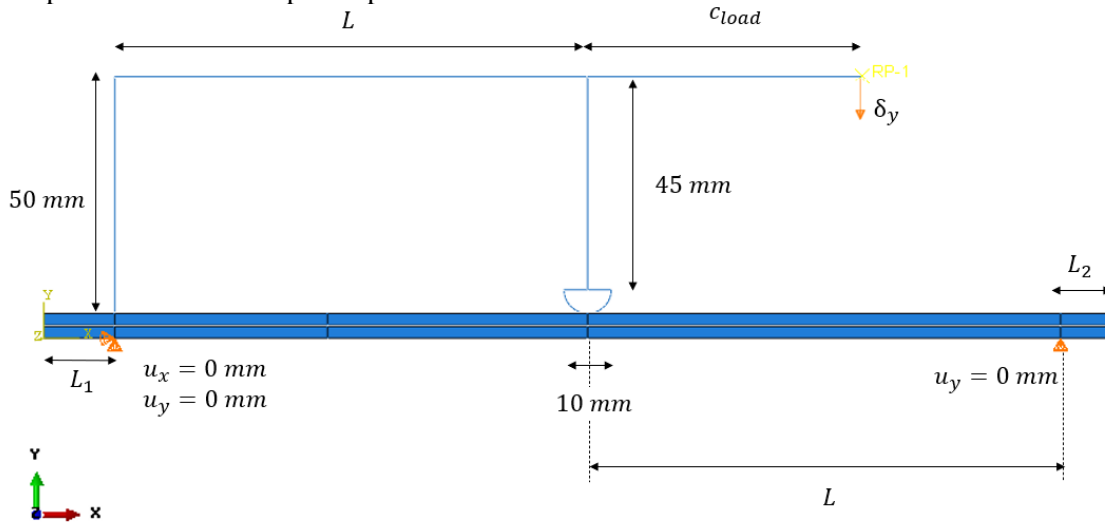
Figure 2. Abaqus® two-dimensional MMB model: boundary conditions and applied displacement.

The MMB test is simulated using a two-dimensional model via Abaqus® software, considering geometric non-linearities due to large displacement and rotation under increasing loads. The four-node, two-dimensional, cohesive element (COH2D4) modelled the adhesive thickness, and the four-node plane strain element (CPE4R) modelled the adherents. A two-node, two-dimensional linear rigid link (R2D2) modelled the MMB test, and adhesive degradation followed a linear traction-separation law (TSL).

A viscosity parameter of 10^{-3} was applied to cohesive finite elements for numeric convergence improvement in MMB model with 75% mixed-mode ratio, and 10^{-5} for MMB models with 60%, 50%, and 25% mixed-mode ratios. The loading mechanism was modelled using R2D2 elements of 1.00 mm, and Table 1 presents the number of link elements, along with the c_{load} length for the various mixed-mode ratios.

Table 1 – Number of R2D2 links in MMB equipment and lever load lengths based mixed-mode ratios used in each numerical modelling.

m (%)	c_{load} (mm)	Number of R2D2 elements (MMB equipment)
25	106.9586	298
50	58.3529	249
60	71.2660	292
75	58.0927	279

Following the ASTM D6671 standard [14], the effect of the lever weight was disregarded in MMB numerical modelling as it is less than 3% of the applied force. Contact behaviour between the upper and lower surface adherents of the MMB specimen was defined via Abaqus® software based on experimental results for different for different mixed-mode ratios, using an exponential contact model with pressure overclosure and clearance. Simulations were conducted to determine the appropriate parameter set, calibrated case-by-case for accurate estimation. It was considered the value of 0.01 for frictional coefficient of the tangential behaviour of the contact. Similar application was addressed to indenter and upper adherent for pressure closure from 600 to 0, and from 0 to 0.025 for clearance. Finally, mixed-mode fracture energy for Mixed-Mode Bending Test ($G_{Tc, MMB}$) resulting from CBBM for various modes II to I ratios were compared to experimental results following Fatolahi and Khoramishad's [13] methodology.

3. RESULTS AND DISCUSSION

Numerical simulations were conducted for each mixed-mode ratio based on the experimental results from [1], and Figure 3 presents these comparisons. It is evident that significant delamination effects are observed for 25% and 50% mixed-mode ratios, complicating the assessment of peak values in force vs displacement curves.
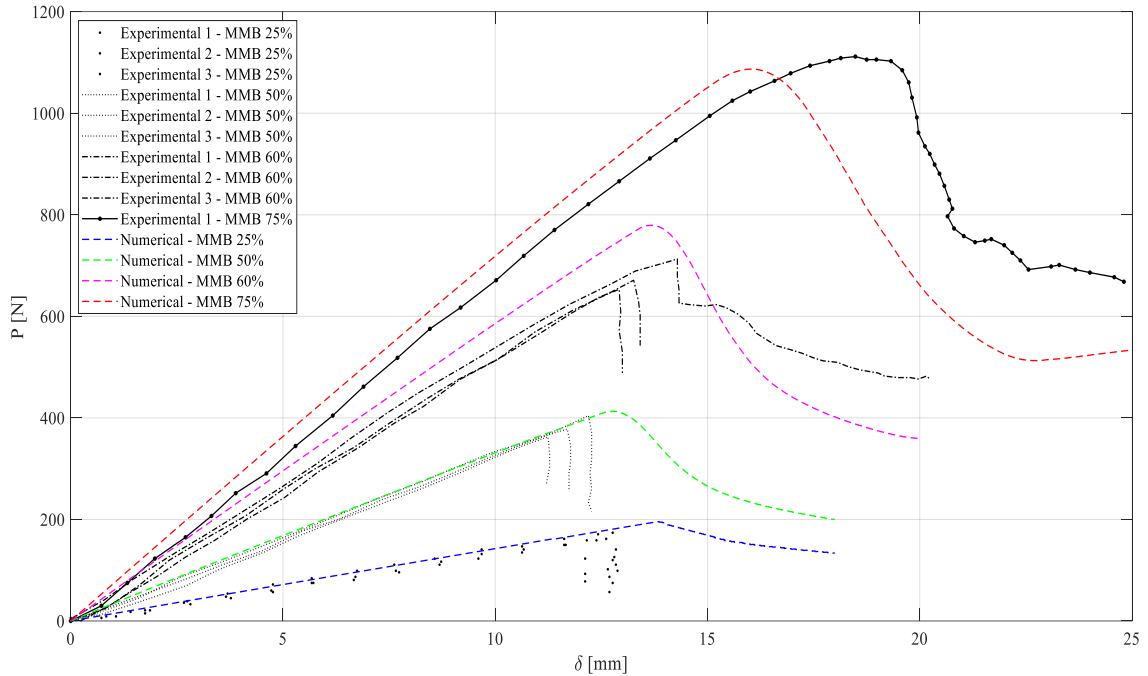
Figure 3. MMB experimental test based in [1] versus numerical analysis for MMB test for 25%, 50%, 60%, and 75% mixed-mode ratios.

To estimate $G_{Tc,MMB}$ in two-dimensional MMB numerical models, Python™ scripts were utilized following Fatolahi and Khoramishad's [13] methodology, which combines Compliance-Based Beam Method (CBBM) and ASTM D6671 standard [14]. This approach is based on equivalent crack length (a_{eq}) and accounts for the effects of root rotation and energy losses in the Fracture Process Zone (PFZ), which can be considerable in ductile adhesives. In other words, the dissipated energy in the PFZ is not considered in classical methods that takes into account the crack measurement.

Figure 4 presents the numerical and experimental results of $G_{Tc, MMB}$ fracture energy. It can be noted that the experimental results from [1] are lower than numerical results due to unaccounted dissipated energy from the PFZ. additionally, intrinsic and epistemic influences can impact their accurate assessments since deterministic approaches overlook these factors, potentialially leading to variations that complicate the analysis when using a simplistic approach.
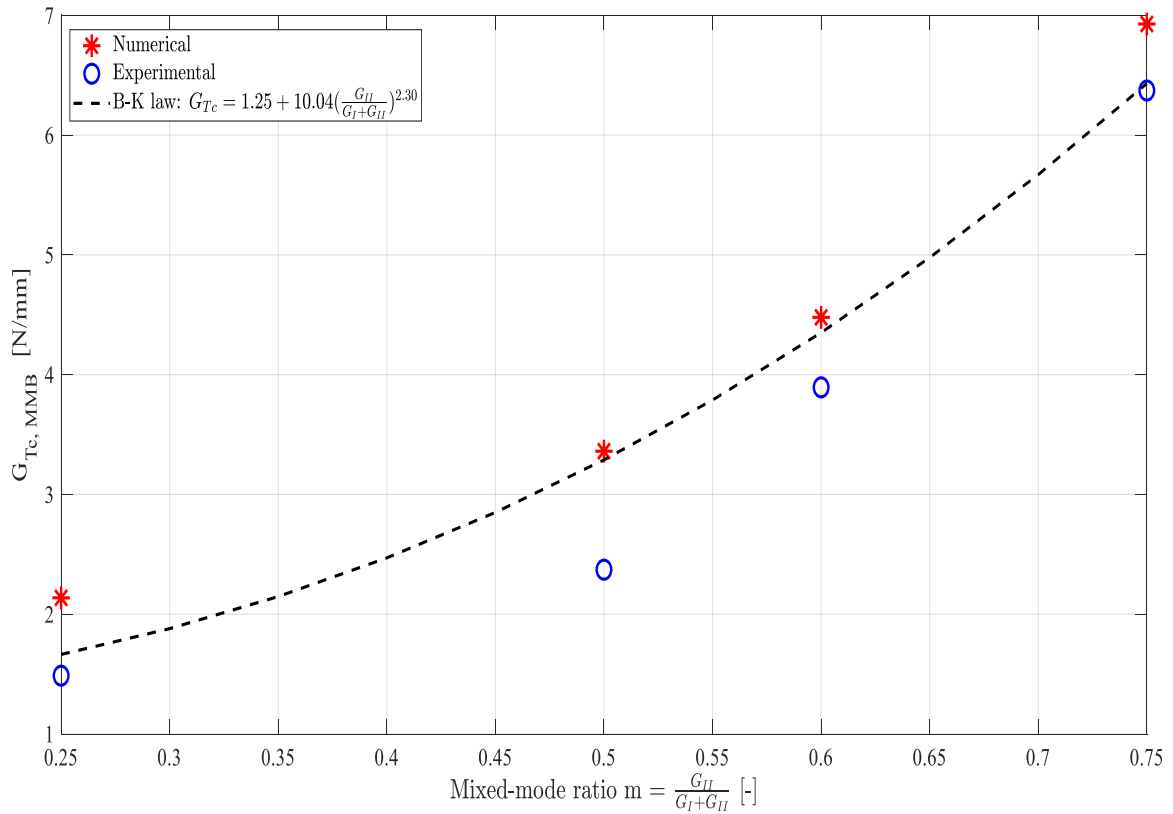
Figure 4. Experimental results based in [1] versus numerical analysis for fracture energy based in CBBM for mixed-mode ratio 25%, 50%, 60%, and 75%.

4. CONCLUSIONS

This study utilizes two-dimensional numerical Mixed-Mode models to estimate force vs displacement curves and their mixed-mode fracture energies. Following numerical calibration procedures, the numerical results were compared to experimental data. The ASTM 6671 standard was employed to estimate lever load lengths (c_{load}) and mixed-mode fracture energy for Mixed-Mode Bending Test (G$_{Tc, MMB}$) combined to Compliance-Based Beam Method (CBBM). Upon verifying the numerical and experimental results for both force vs displacement and G$_{Tc, MMB}$, it is evident that there are several critical issues that to be addressed.

One significant issue is the non-accounted of dissipated energy from PFZ. This unaccounted energy can lead to discrepancies between numerical predictions and experimental observations, especially in ductile adhesives where the energy losses in the FPZ can be important. Moreover, intrinsic and epistemic uncertainties must be considered in the current approach. These uncertainties arise from factors such as material properties, manufacturing variations, and testing conditions, which can significantly impact the accuracy of the results.

Therefore, it is imperative to incorporated statistical procedures as Design of Experiments (DoE) when dealing with bonded composite joints. DoE allows for systematic exploration of geometric and mechanical influences on the strength outcomes, providing a more comprehensive understanding of the joint behaviour. By considering these factors and employing an efficient statistical method, it can address the challenges posed by non-accounted energy losses and uncertainties, leading to more reliable and accurate assessments of the composite joint strength.

4.1. Acknowledgements

5. REFERENCES

[1] Leone, F. A.; Girolamo, D.; Dávila, C. G. Progressive Damage Analysis of Bonded Composite Joints. NASA/TM-2012-217790, 2012.

[2] Fan, X.L.; Sun, Q.; Kikuchi, M. Review of Damage Tolerant Analysis of Laminated Composites. Journal of Solid Mechanics Vol. 2, No. 3 (2010) pp. 275-289.

[3] Bogenfeld, R.; Freund, S.; Dähne, S.; Wunderlich, T.; Wille, T. Damage tolerance allowable calculation for the aircraft design with static ultimate load. Composite Structures 329 (2024) 117803.

[4] Silva, L.F.M.; Öchsner, A.; Adams, R. D., Ed. Handbook of Adhesion Technology, 2nded.; p. 1805. 2018.

[5] Omairey, S.; Jayasree, N.; Kazilas, M. Defect and Uncertainties of Adhesively Bonded Composite Joints. Sn. Appl. Sci. 2021, 3(9), 769.

[6] Melchers, R.E.; Beck, A. T. Structural Reliability Analysis and Prediction, 3rd; John Wiley & Sons: Southern Gate, Chichester, West Sussex, UK, 2018; p. 506.

[7] Naat, N.; Boutar, Y.; Naïmi, S.; Mezlini, S.; Silva, L. F. M. Effect of Surface Texture on the Mechanical Performance of Bonded Joints: A Review. J. Adhes. 2021, 99(2), 166–258.

[8] Moreira, R.D.F.; Moura, M.F.S.F.; Silva, F.G.A.; Ramírez, F. M. G.; Rodrigues, J. S. Mixed-mode I+II fracture characterisation of composite bonded joints. Journal of Adhesion Science and Technology, 2020.

[9] Oliveira, J.M.Q.; Moura, MF.S.F.; Morais, J.J.L. Application of the end loaded split and single-leg bending tests to the mixed-mode fracture characterization of wood. Holzforschung, vol. 63, pp. 597-602, 2009.

[10] Silva, L.F.M.; Esteves, V.H.C.; Chaves, F.J.P. Fracture toughness of a structural adhesive under mixed mode loadings. Mat. Wiss. u. Werkstofftech. 2011, 42, No. 5.

[11] Khoo, T.T.; Kim, H. Effect of Bondline Thickness on Mixed-Mode Fracture of Adhesively Bonded Joints. The Journal of Adhesion, 87:989–1019, 2011.

[12] I.S. Floros, K.I. Tserpes, T. Löbel. Mode-I, mode-II and mixed-mode I + II fracture behavior of composite bonded joints: Experimental characterization and numerical simulation. Composites Part B 78 (2015) 459-468.

[13] Fatolahi, A.R.; Khoramishad, H. A comprehensive study on the fracture behavior modeling of adhesively bonded composite joints using a compliance-based beam method. International Journal of Adhesion & Adhesives 129 (2024) 103585.

[14] AMERICAN SOCIETY FOR TESTING AND MATERIALS – ASTM. Test method for mixed mode I-mode II interlaminar fracture toughness of unidirectional fiber reinforced polymer matrix composites (ASTM D6671), 2001.

[15] Chen, J.H.; Sernow, R.; Schulz, E.; Hinrichsen, G. A modification of the mixed-mode bending test apparatus. Composites: Part A 30 (1999) 871–877.

[16] Arouche, M. M.; Wang, W.; Freitas, S. T.; Barros, S. Strain-based methodology for mixed-mode I+II fracture: A new partitioning method for bi-material adhesively bonded joints. The Journal of Adhesion 2019, vol. 95, nos. 5–7, 385–404.

DEVELOPMENT OF NANOTECHNOLOGICAL PRODUCTS, PARTICULARLY SILICA AEROGELS, HYBRIDIZED WITH POLYMERS, TO OBTAIN MATERIALS WITH HIGH IMPACT RESISTANCE FOR APPLICATIONS IN DRONES AND AEROSPACE STRUCTURES.

Paulo Aparecido Fernandes Bau [1]*; Arnaldo Carlos Morelli [2]

(1) Studant. Federal Institute of Education Science and Technology of São Paulo - Brazil (Estrada Municipal Paulo Eduardo de Almeida, CEP:, 13565-820 - Prado, São Carlos - SP, 13565-820)
(2) Professor. Federal Institute of Education Science and Technology of São Paulo - Brazil (Estrada Municipal Paulo Eduardo de Almeida, CEP:, 13565-820 - Prado, São Carlos - SP, 13565-820)
*Corresponding author: Bau.paulo@aluno.ifsp.edu.br

CODE: BCCM7-54

Abstract: Silica aerogels are nanoporous materials obtained through sol-gel technology with unusual properties, such as high surface area (500-1200 m²/g), high porosity (80-99.8%), and low density (~0.003 g/cm³) [1]. When hybridized with polymers, these materials can create new materials with enhanced physical and mechanical properties and low densities, which are of great interest to various segments of the aerospace industry. The objective of this work was to obtain aerogels with densities between 0.20 and 0.40 g/cm³, with mechanical compressive strength around 700 kPa, and hydrophobic properties. Our proposal involved the use of epoxy resins and network reinforcements in the gel structure, to significantly increase properties such as impact resistance and compressive strength, while controlling the conditions to maintain the initial physical characteristics, such as density and hydrophobicity, unchanged.

1. INTRODUCTION

New materials and technologies are continuously being developed worldwide, aiming to enhance existing products as well as explore new materials and processes that offer technological advantages in terms of physical and mechanical properties, as well as in terms of material costs and production processes efficiency, enabling the replacement of products used in various equipment. Our proposed work is directly linked to the above-mentioned criteria through the development of sol-gel technology, modified by the introduction of polymers into its porous network, resulting in new products derived from the technique, yielding new materials with vastly superior physical and mechanical characteristics than those that materials alone could not replicate. This technique is primarily focused on cross-linking and strengthening the porous network of the gel to reproduce a nanoporous structure forming a skeleton capable of resisting capillary pressures arising from drying processes, thus providing sufficient strength to maintain the structure coherent and united, forming a monolithic solid. The main advantage in terms of processing lies in the absence of additional modeling equipment, such as injectors, extruders, vacuum, among others, requiring only a final mold into which the material will be poured, acquiring the shape of the desired piece to be molded. Therefore, it can be observed that this type of process and the products derived from this technology could have applications in various fields of technology where lighter materials with improved physical and mechanical properties are needed.

Particularly in the aerospace segment, where we are situated, these materials could be used in the manufacture of drone structures, honeycomb-shaped structures, and even in parts of large aerospace structures.

2. METHODOLOGY

2.1 PRECURSOR PREPARATION

This research was aimed at the aerospace industry focusing on the production of lighter composite materials with enhanced hydrophobic properties and improved physical and mechanical resistances. The methodological steps included obtaining materials with densities between 0.15 – 0.50 g/cm³, using ambient pressure drying processes (APD) or similar processes.

Initially, aerogels were produced using the conventional method, employing gel preparation methods with a high-speed conventional propeller mixer to homogenize compositions. This was done using conventional precursors such as micrometric silica with characteristics described in Table 1, dissolved in alcohols like methanol or ethanol and solvents such as hexane, heptane, esters, among others.

TABLE 1. Characteristics of the micrometric silica used

Particle size (MalvernMasterasizer), μm	pH (5% aqueous suspension)	Loss at 1000°C (%)	Pore volume, ml/g	Surface area (BET), m²/g*	Whiteness (Harrison)
.6 - 8	2.5 - 4	7.0 max	1.5	360	93 min

2.2 DOPING

Immediately after obtaining the solution using sol-gel technology, the liquid-phase crosslinking process was initiated by adding crosslinking agents such as epoxy resins, acrylic phenolics, or isocyanates, aiming to modify the initial properties of the sol, with the goal of enhancing the physicochemical properties of the final gel.

2.3 AGING

OAging of the gel before drying was employed to strengthen the network and reduce the risk of fracture. In this phase, which we refer to as gel aging, the gel is placed in a hermetically sealed container and placed in an oven with controlled temperatures, left in this condition for potentially months to allow the completion of sililation reactions and crosslinking reactions to strengthen the network. Gel aging is necessary to produce a stabilized gel capable of withstanding the drying steps before forming it into an aerogel.
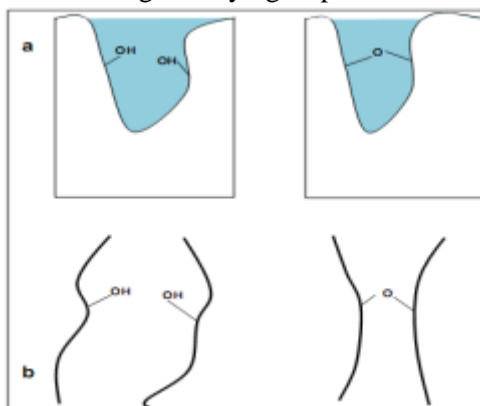
Figure 1: Syneresis scenarios: a) bonding between two neighboring molecules, resulting in retraction and relaxation of the new bond, b) two flexible chains can bond resulting in the limitation of flexibility extension and significant retraction. [4].

2.4 DRYING:

We opted for ambient pressure drying (APD) for the synthesis of aerogels instead of the supercritical process, aiming to avoid associated risks and high energy consumption. Obtaining silica aerogels at ambient pressure involves both modifying the surface of the pores in the gel and strengthening the network. This includes chemically modifying the surface inside the pore, for example, through sililation. The replacement of H in Si-OH groups with hydrolytically stable Si-R groups via oxygen bonding prevents water absorption and thus results in hydrophobic aerogels. Figure 4 illustrates a scheme of hydrogen substitution in Si-OH groups by Si-OR.
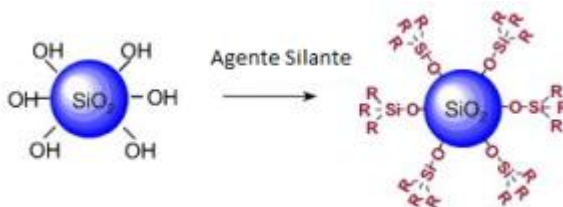
Figure 2: Silane agent in silica gel. After another solvent exchange, drying occurs by evaporation. Silica gel evaporation drying can be separated into three steps: [2].

.

2.5 CHARACTERIZATION:

We conducted measurements of physical properties, including density determination using the Archimedes method, and compression resistance tests according to ASTM D 695-10 standard. These analyses provided a comprehensive understanding of the mechanical characteristics of the materials obtained. This comprehensive and detailed methodology allowed us to obtain silica aerogels with desired properties for applications in the aerospace industry, demonstrating a significant advancement in the field of composite materials.

3. RESULTS AND DISCUSSION:

The samples obtained during this study demonstrated densities ranging from 0.20 to 0.35 g/cm³, accompanied by volumetric shrinkage of 7 to 11%. The strategic introduction of network crosslinkers played a significant role in improving the material structure, both in the gel phase and in the final product. This optimization was complemented by the presence of resin and basic catalyst during the manufacturing process, resulting in the development of desired hydrophobic characteristics as observed in Figure 4. Compression tests, conducted according to ASTM D 695-10 standards, revealed remarkable compression resistance values, as detailed in Table 2 and graphically visualized in Figure 3.

TABLE 2. General compression results obtained from the test specimens.

Tension Average Max Force(MPa)	Force Average(N)
0.6205	201.1
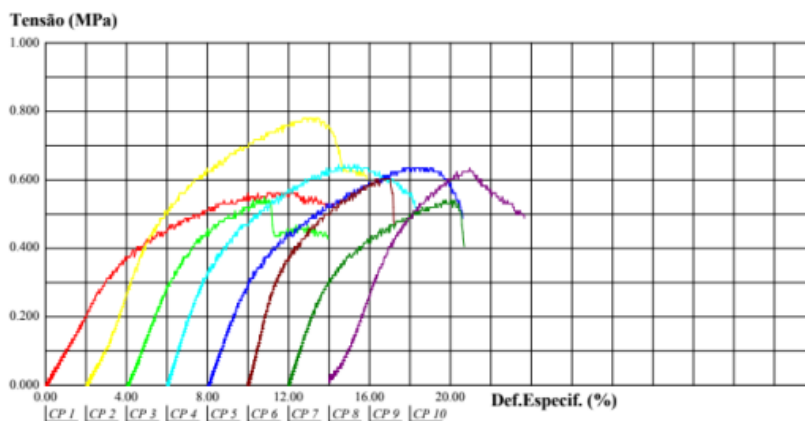
Figure 3: Compression test graph showing Stress (MPa) / Strain (%)

Figure 4: Aerogel obtained demonstrating its hydrophobic characteristic.

4. CONCLUSIONS

The impacts of this research are particularly significant in the domain of manufacturing structures for aerospace drones. The possibility of constructing both monolithic and segmented structures through the sol-gel process represents a considerable technological advancement in this sector. Additionally, these materials exhibit significantly lower densities than traditional thermosetting or thermoplastic materials, providing the produced structures with a competitive advantage in terms of weight.

We anticipate that the applications of these new materials will have implications beyond the aerospace drone sector, potentially influencing areas such as the design of structures for large aircraft, the automotive industry, naval industry, and others that require lighter materials with improved physical and mechanical properties. Furthermore, the expectation is that these materials can contribute to significant reductions in production costs and production processes, becoming an attractive option for a variety of industrial applications.

4.1. DECLARATION OF COMPETING INTEREST

The authors declare no conflict of interest.

4.2. ACKNOWLEDGMENTS

5. REFERENCES

[1]FRICKE, J.; EMMERLING, A. Aerogels - Recent Progress in Production Techniques and Novel Applications. Journal of Sol-Gel Science and Technology, 13(1-3), 299-303, 1999.

[2]BRINKER, C. J., & SCHERER, G. W. "Sol-gel science: The physics and chemistry of sol-gel processing". Boston: Academic Press, 1990.

[3]STROM, R. A., ET AL. "Strengthening and aging of wet silica gels for up-scaling of aerogel preparation". Journal of Sol-Gel Science and Technology, 41(3), 291-298, 2007.

[4]LOY, D. A., ET AL. "Evolution of porosity and morphology in alkylene-bridged polysilsesquioxane xerogels as a function of gel aging time". Boston, MA, 2005.

CHARPY IMPACT TEST OF EPOXY/SOYBEAN OIL COMPOSITES REINFORCED WITH PAPYRUS (*Cyperus papyrus*) FIBER

Mateus U. Nascimento[a],*, Paulo R.C. Marcelino [b], Felipe G.S. Araújo [c], Gabriel M.Valene[d], Roseméri B.S. Silva[e], Michel P. Oliveira[f]

(a) 0009-0008-3032-8134 (Federal University of Espírito Santo – Brazil)
(b) 0000-0001-8594-0920 (Federal University of Espírito Santo – Brazil)
(c) 0009-0000-7069-5408 (Federal University of Espírito Santo – Brazil)
(d) 0000-0002-2736-4440 (Federal University of Espírito Santo – Brazil)
(e) 0009-0004-6432-591X (Federal University of Espírito Santo – Brazil)
(f) 0000-0001-9241-0194 (Federal University of Espírito Santo – Brazil)
* Corresponding author: urbanomateus28@gmail.com

Abstract: Composite materials are widely employed in various applications. In this sense, understanding the mechanical properties of a composite is essential to ensure its performance, safety, efficiency, and durability. In this regard, the present study aims to assess the fracture toughness of epoxy/epoxidized soybean oil composite reinforced with papyrus fibers through the Charpy impact test. Test specimens were produced according to ASTM D6110 standard. The composites were produced from epoxy matrix incorporated with 20% (w/w) of epoxidized soybean oil and three different mass ratios of aligned fibers in the composites (10 and 20). The specimens were subjected to Charpy impact testing, and the fracture surface was analyzed by scanning electron microscopy (SEM). It was found that impact resistance was maximum for epoxy/epoxidized soybean oil matrix composites incorporated with 20% fiber, reaching a value of 6.79 KJ/m².

1. INTRODUCTION

No In the contemporary scenario of materials development, polymer composites reinforced with plant fibers are emerging as a promising alternative to conventional materials. This trend is driven by the quest for more sustainable and eco-friendly solutions in the industry, aiming to reduce dependence on non-renewable resources and mitigate environmental impacts. Polymer composites reinforced with plant fibers offer a range of advantages, such as reduced weight, good specific strength, biodegradability, and abundant availability of raw materials [1,2].

Different types of natural fibers have been widely studied for use in composites. Plant fibers are common in applications where strength and rigidity are essential. In this regard, the use of papyrus fibers as a reinforcement element in composites is a possibility, as they exhibit remarkable mechanical properties, with indications in the literature of improvements in the strength properties of polymer composites [3,4].

In addition to the use of plant fibers, petroleum-derived matrices can be partially replaced in their composition by renewable natural compounds. Among the substitutes, epoxidized soybean oil (ESO) has been explored to incorporate into epoxy resin matrices, which, being a vegetable oil, reduces the use of some synthetic components, thereby reducing health and environmental risks associated with them, leading to more environmentally sustainable materials [5].

From this perspective, to ensure the viability and safety of these materials in practical applications, it is crucial to perform a detailed characterization of their mechanical and microstructural properties. Therefore,

this work aims to evaluate the fracture toughness in epoxy/ESO composite reinforced with papyrus fibers through the Charpy impact test.

2. METHODOLOGY

2.1 Fiber Obtaining

The papyrus plant was collected from an agro-industrial effluent treatment lake. Only the plant's stem was used, cut into approximately 50 cm sections.

To extract the fibers, the epidermis of the papyrus stems was removed, exposing the fibers covered with mucilage, which was then removed through a mechanical brushing process with plastic bristle brushes. The fibers were then washed to remove mucilage residues, beaten to prevent fiber adhesion, and air-dried at room temperature. Finally, the fibers were further dried in a forced air circulation oven at 103°C for 24 hours and stored in plastic bags at room temperature.

2.2. Composite Production

Composites with 0, 10, and 20% fiber fractions by mass were produced. The composites were prepared in silicone molds with dimensions of the test specimens according to ASTM D6110 [6]. Polymer composites were made using epoxy resin 2004 and epoxy hardener 3154 in a 2:1 ratio, respectively, with the incorporation of 20% by mass of commercial epoxidized soybean oil. The resin composed of soybean oil and epoxy corresponds to the green epoxy resin. Table 1 outlines the other treatments and their proportions. The matrix components were homogenized, and the mixture was poured over the previously oriented fibers in the mold in the longitudinal direction. Five specimens were prepared for each of the four treatments. The composites were left in a fume hood at room temperature and pressure for 24 hours for curing.

Table 1. Composition of the test specimens.

Mass fraction			
Epoxy resin (%)	Green epoxy resin (%)	Fiber (%)	Sample
100	0	0	RE
0	100	0	RE20O
0	90	10	RE20O10
0	80	20	RE20O20

2.4. Charpy Impact Testing

Charpy impact tests were conducted using a Pantech Instruments testing machine (Gujarat, India) with an 11 J pendulum. Five specimens samples of each composition were tested, as listed in Table 1. Each specimen was notched with standard prismatic dimensions (127 x 12,7 x 12,7 mm), a depth of 2.54 mm, and a 45° angle using a manual notcher (CEAST, Notchvas model), following ASTM D6110 [6].

2.5. Scanning Electron Microscopy (SEM)

Samples of the fractured composites were morphologically analyzed on the fracture surface by scanning electron microscopy (SEM) in secondary electrons mode using a JEOL, JSMIT200 model. For analysis, the samples were first fixed on a metal stub and coated with gold to promote material electrical conductivity.

3. RESULTS AND DISCUSSION

Figure 1 presents the Charpy impact energy for treatments with different fractions of papyrus fibers and matrix type. From Figure 1, it is noted that with the incorporation of soybean oil into the epoxy resin, the toughness is doubled compared to unmodified resin. This is due to the addition of epoxidized soybean oil (ESO), which increases impact resistance by incorporating long chains into the matrix, resulting in a reduction of internal stress within the network structure [7,8]. Another factor is associated with good initial compatibility with epoxy, followed by phase separation induced in the epoxy matrix during curing, a condition necessary for improving toughness in modified thermosetting resin [9].

As ESO has intermediate miscibility, before curing it remains miscible with epoxy and undergoes phase separation induced during resin curing, leading to the formation of a biphasic microstructure, as previously reported. A portion of the ESO does not react and induces cavitation in the epoxy matrix, which will be seen in SEM images later, through which impact resistance increases through the shearing process, dissipating energy in each formed cavity and reducing crack propagation between them [10].
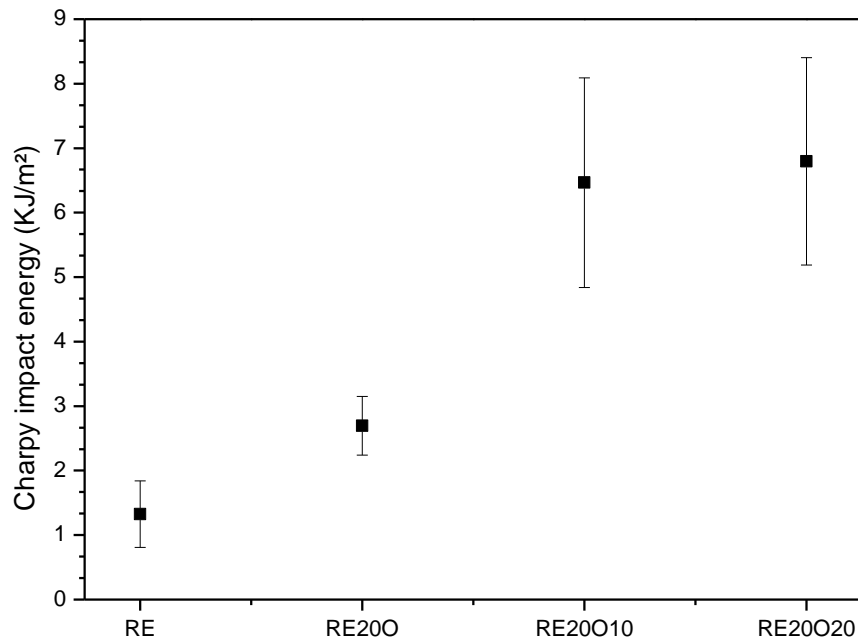
Figure 1. Impact strength comparison of the composites.

Similar results were found by Kumar et al. (2017) [11] and Sahoo, Mohanty, and Nayak (2015) [9], who evaluated the impact toughness of epoxy resins incorporated with 20% epoxidized soybean oil, achieving values of 65% and 60%, respectively, higher than the impact energy of virgin epoxy resin. In this sense, Sahoo, Mohanty, and Nayak (2015) [9] suggest that the incorporation of 20% ESO is ideal for achieving better impact energy results, with a reduction of this above 30%. According to the authors, higher oil contents in the resin cause phase inversion, resulting in separation between the oil and the matrix.

Regarding the epoxy:ESO ratios, Gupta, Ahmad, and Dev (2011) [12] observed a decrease in impact energy in resins with a higher volume of epoxy, which the authors attributed to an increase in cross-linking density, accompanied by lower energy dissipation in the internal structure.

It was observed that the impact energy increases with the increase in the percentage of fibers in the composite, reaching a maximum value with the addition of 20% fibers (6.79 KJ/m²). Sahoo, Mohanty, and Nayak (2018) [13] also observed an increase in impact energy in composites loaded with 16% fiber in epoxy resin incorporated with 20% ESO. According to Sahoo, Mohanty, and Nayak (2017) [14], who evaluated the addition of sisal fibers in the composition of epoxy/epoxidized soybean oil composites, the increase in fiber loading is accompanied by a progressive increase in impact energy. The higher the fiber loading, the greater the interactions existing in the crack path, thus more energy is required for fracture.

However, treatments with 10 and 20% fiber loading showed similar values, supposedly due to the lower fiber wettability due to the higher fiber loading in the composite. This causes the fiber-matrix interaction to be reduced, so the impact energy may not be efficiently transferred between the composite components, resulting in interfacial failures [15,16].

The toughness of fiber-reinforced composites is generally improved through the fiber-matrix interface, as strong interfacial bonding allows for better stress transfer from the matrix to the fiber, acting as reinforcement architecture to prevent crack propagation [13,17].

Complementing the results obtained by the Charpy impact test, the microscopic morphology of the fracture surface reveals SEM micrographs of the impact fracture surface presented in Figure 2.
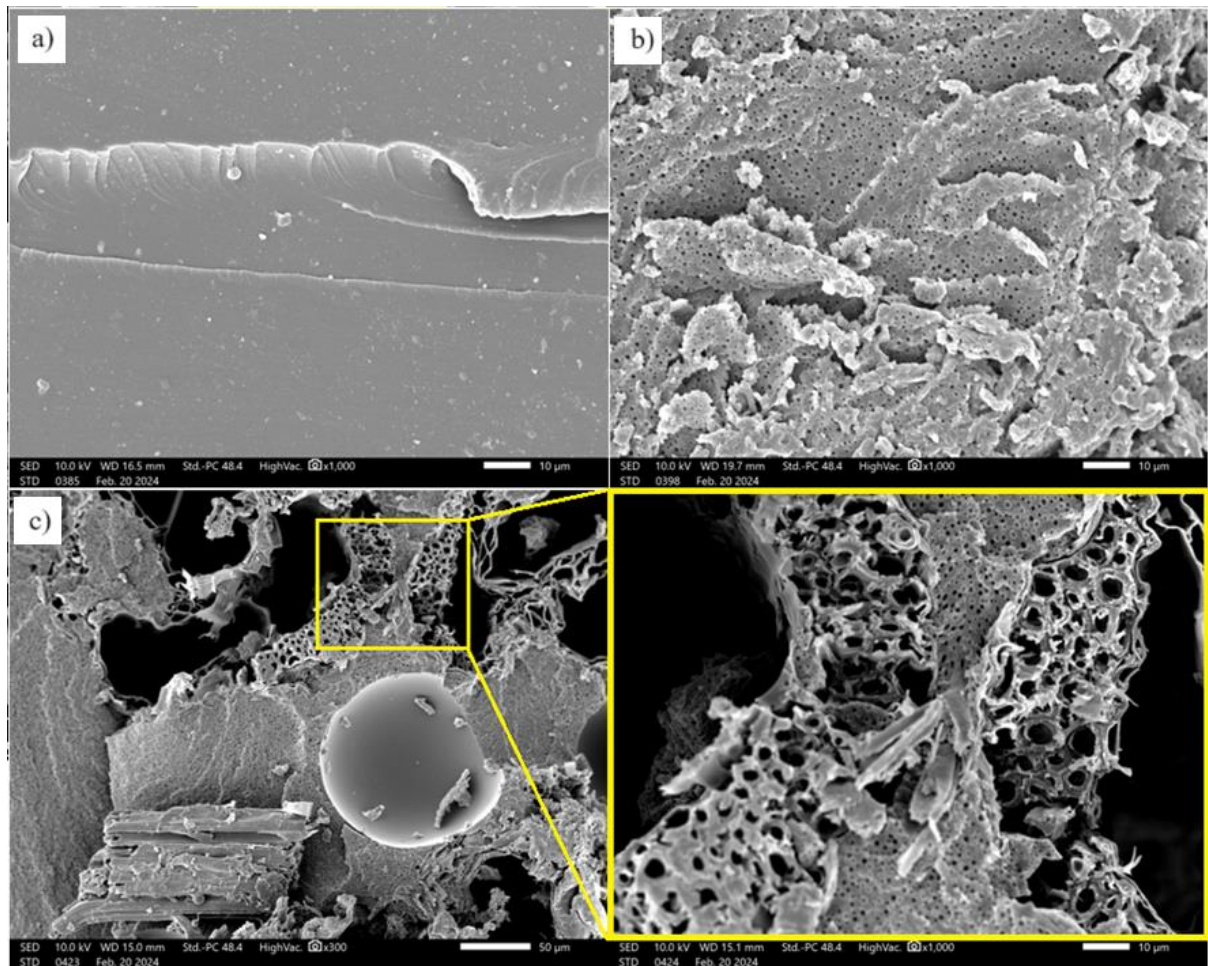
Figure 2. SEM micrographs of the impact fracture surface of (a) RE, (b) RE20O e (c) RE20O20.

The micrograph of the unmodified epoxy resin surface reveals long continuous lines, suggesting that cracks propagated easily, thus demonstrating a series of brittle fractures. In contrast, the fracture surface of RE20O presents roughness and small spherical domains distributed uniformly due to the dispersion of epoxidized oil in the matrix. The domains are evenly dispersed along the polymer surface, indicating the presence of a second phase. These dispersed domains in the matrix act as energy dissipation centers, increasing impact energy values [10].

From Figure 2, it is possible to verify few spaces between the matrix and the fiber, indicating good fiber-matrix interface, which increases the mechanical strength of fiber-reinforced composites and explains the growth of impact energy followed by the increase in fiber loading.
.

4. CONCLUSIONS

It was possible to increase the impact resistance of the epoxy resin by adding soybean oil and by increasing the content of plant fibers in the epoxy/epoxidized soybean oil matrix.

The impact resistance was maximum for composites with a matrix of epoxy/ESO incorporated with 20% fiber, reaching a value of 6.79 KJ/m², even though it is close to that observed for loads with 10% fiber, the higher concentration is desirable to reduce the amount of polymer matrix used.

4.1. Declaration of Competing Interest

The authors declare no conflict of interest.

4.2. Acknowledgements

5. REFERENCES

[1] SHARMA, A. K. et al. Polymer matrix composites: A state of art review. Materials Today: Proceedings, v. 57, p. 2330-2333, 2022. (https://doi.org/10.1016/j.matpr.2021.12.592).

[2] MYLSAMY, B., et al. **A review on natural fiber composites: Polymer matrices, fiber surface treatments, fabrication methods, properties, and applications**. Polymer Engineering & Science, 2024. (https://doi.org/10.1002/pen.26713).

[3] ALMAADEED, M. Al A.; PONNAMMA, D.; EL-SAMAK, A. A. **Polymers to improve the world and lifestyle: physical, mechanical, and chemical needs**. In: Polymer Science and Innovative Applications. Elsevier, 1-19, 2020. (http://dx.doi.org/10.1016/B978-0-12-816808-0.00001-9).

[4] BEMERW, B. et al. **Development of Papyrus Fiber Reinforced Natural Rubber Composite for Shoe Sole**. Journal of Natural Fibers, 1-11, 2021. (http://dx.doi.org/10.1080/15440478.2021.1875375)

[5] WILLEMS, F.; MOENS, P. **Green composites: properties, design, and life cycle assessment**. Nova Science Publishers, 1st Edition, Nova Science Publishers, 2010. (ISBN: 978-1-60741-301-1).

[6] ASTM D6110-18, **Standard Test Method for Determining the Charpy Impact Resistance of Notched Specimens of Plastics D6110**. ASTM International, 2018. (www.astm.org).

[7] CHEN, Y., et al. **Thermal and mechanical properties of epoxy resin toughened with epoxidized soybean oil**. Journal of thermal analysis and calorimetry, 2013, 113: 939-945. (https://doi.org/10.1007/s10973-012-2859-4).

[8] HU, F., et al. **Epoxidized soybean oil modified using fatty acids as tougheners for thermosetting epoxy resins:** Part 1. Journal of Applied Polymer Science, 2021, 138.24: 50570. (https://doi.org/10.1002/app.50570).

[9] SAHOO, S. K.; MOHANTY, S.; NAYAK, S. K**. Synthesis and characterization of bio-based epoxy blends from renewable resource based epoxidized soybean oil as reactive diluent**. Chinese Journal of Polymer Science, 2015, 33: 137-152. (https://doi.org/10.1007/s10118-015-1568-4).

[10] PARZUCHOWSKI, P. G., et al. **Epoxy resin modified with soybean oil containing cyclic carbonate groups**. Journal of Applied Polymer Science, 2006, 102.3: 2904-2914. (https://doi.org/10.1002/app.24795).

[11] KUMAR, S., et al. **Epoxidized soybean oil-based epoxy blend cured with anhydride-based cross-linker: thermal and mechanical characterization**. Industrial & Engineering Chemistry Research, 2017, 56.3: 687-698. (http://dx.doi.org/10.1021/acs.iecr.6b03879).

[12] GUPTA, A. P.; AHMAD, S.; DEV, A. **Modification of novel bio-based resin-epoxidized soybean oil by conventional epoxy resin**. Polymer Engineering & Science, 2011, 51.6: 1087-1091. (https://doi.org/10.1002/pen.21791).

[13] SAHOO, S. K.; MOHANTY, S.; NAYAK, S. K. **Mechanical, dynamic mechanical, and interfacial properties of sisal fiber-reinforced composite with epoxidized soybean oil-based epoxy matrix**. Polymer Composites, 2018, 39.6: 2065-2072. (https://doi.org/10.1002/pc.24168).

[14] SAHOO, S. K.; MOHANTY, S.; NAYAK, S. K. **Mechanical, thermal, and interfacial characterization of randomly oriented short sisal fibers reinforced epoxy composite modified with epoxidized soybean oil**. Journal of natural fibers, 2017, 14.3: 357-367. (http://dx.doi.org/10.1080/15440478.2016.1212757).

[15] EL-SHEKEIL, Y. A., et al. **Influence of fiber content on the mechanical and thermal properties of Kenaf fiber reinforced thermoplastic polyurethane composites**. *Materials & Design*, 2012, 40: 299-303. (http://dx.doi.org/10.1016/j.matdes.2012.04.003).

[16] ÖZTURK, Sultan. **Effect of fiber loading on the mechanical properties of kenaf and fiberfrax fiber-reinforced phenol-formaldehyde composites**. Journal of Composite Materials, 2010, 44.19: 2265-2288. (https://doi.org/10.1177/0021998310364265).

[17]   PRAJAPATI, A. R.; DAVE, H. K.; RAVAL, H. K**. Effect of fiber volume fraction on the impact strength of fiber reinforced polymer composites made by FDM process**. Materials Today: Proceedings, 2021, 44: 2102-2106.

DEVELOPMENT, CHARACTERIZATION AND SINTERING BEHAVIOR OF ZrO2-Al2O3 CERAMIC COMPOSITES REINFORCED WITH RARE EARTH OXIDES FOR APPLICATION AS THERMAL BARRIER COATING IN THE AEROSPACE SECTOR

Bruna A. L. A. da Rocha [(a)*]; Gisele M. de Araújo [(b)]; Filipe E. P. dos Santos [(c)]; Yogendra P. Yadava [(d)]

(a) 0000-0003-1052-162X (Federal University of Pernambuco – Brazil)
(b) 0009-0004-0121-8826 (Federal University of Pernambuco – Brazil)
(c) 0009-0003-7333-1606 Federal University of Pernambuco – Brazil)
(d) 0000-0001-7224-5682 (Federal University of Pernambuco – Brazil)
* Corresponding author: brunaadvincula@gmail.com

Abstract: Extreme temperatures are the operating conditions of the exhaust nozzles' gas turbines in the aerospace sector, leading to the premature failure of these equipment. Given the expensive nature of the industry and its influence in the global economy, many techniques and studies have been developed in order to increase the lifespan of such devices - one of the most important methods includes the use of pulverized ceramic composites as Thermal Barrier Coating (TBC). While exhaust nozzles are typically made of nickel and cobalt alloys, and, as metallic bonds, are good conductors of heat and electricity, ceramics are capable of withstanding high temperatures while reducing the need for air cooling, the reason as to why this method has been so successful. However, ceramics are inherently brittle and the incorporation of additives is necessary. Previous research findings have shown that zirconia and alumina exhibit enhanced fracture toughness, resistance to high temperatures, and chemical stability, and the addition of rare earth oxides improves even further the properties mentioned. In this study, ceramic composites of zirconia-alumina (ZrO_2- Al_2O_3) matrix with the incorporation of rare earth oxide (CeO_2 and Y_2O_3) were produced using thermomechanical processing and characterized. Two different sintering processes were applied in order to analyze the sintering behavior of the composites and determine their suitability to TBC applications in the aerospace sector

1. INTRODUCTION

Contemporary gas turbine engines require a continuous evolution in order to meet the demands of various industries and keep pace of rapidly evolving technological advancements to propel aircraft and to generate electricity. This evolution encompasses several aspects, such as engine design, combustion characteristics, and the materials involved [1].

These equipment are present in transportation, energy and defense sectors, and modern versions exhibit substantially higher gas temperatures than their predecessor – these devices operate according to the principles of Carnot cycles, where efficiency and core power are dependent on the gas temperature at the turbine inlet [2].

The consistent increase in the maximum gas temperature on turbine airfoils, and consequently of their performance, is a result of the combination of many advancements, most notably the development of viable coating technologies for depositing high-temperature thermal insulating coatings on turbine components [1].

This technology is commonly known as Thermal Barrier Coating (TBC). With an ever-growing demand for efficiency, the temperature of gases entering the turbine will continue to increase, relying on further improvements to existing TBCs [3]. Thermal barrier coatings refer to refractory-oxide ceramic coatings applied to the surfaces of metallic parts in the hottest sections of gas-turbine engines [2]. These devices, predominantly composed of nickel and cobalt superalloys, are highly efficient in absorbing heat and greatly benefit from the application of TBC systems, capable of reducing the metal temperatures by up to 140 ºC [4].

The TBC application involves the deposition of a thermal insulating layer between the metallic surface and the hot gases - this system typically comprises two layers: the bond coat, situated internally and in direct contact with the metal, and the top coat, positioned externally and in contact with the gases [5]. Materials selected for applications TBC must meet requirement such as: a high melting point, absence of phase transformation between room temperature and operation temperature, low thermal conductivity, chemical inertness, thermal expansion compatibility with the metallic substrate, good adherence to the metallic substrate and low sintering rate of the porous microstructure [6].

Studies ranging from various fields, including energy and dentistry, have consistently attested for the exceptional properties of the zirconium oxide (ZrO_2), or zirconia [7, 8] - these properties include fracture toughness and low thermal conductivity, among others. In its pure form, zirconia exhibits three crystalline phases at ambient pressure: monoclinic (m) up to 1170 ºC, tetragonal (t) from 1170 to 2370 ºC, and cubic (c) from 2370 to 2680 ºC [8]. However, due to the significant volume variation associated with the t-m transition, practical engineering applications for this material are limited. The addition of stabilizing oxides is essential to maintain the polymorphic phases at high temperatures at room temperature, most commonly, yttria (Y_2O_3). Recent studies have shown that a mixture of yttrium oxides and rare earth oxides (REO) are a strong alternative as a stabilizing agent of the tetragonal. Additives such as MgO and CaO allow the formation of partially or completely stabilized zirconia [9].

The aluminum oxide (Al_2O_3), also known as alumina, is a high-performance ceramic material, possessing many properties suitable for TBC applications, including high hardness, thermal stability, wear resistance, and chemical inertness. Furthermore, it is an abundant ceramic material of relatively low cost. Given the inherent fragility of ceramics, the development of hybrid ceramic/metal materials has been an alternative to enable the application of these materials in the aerospace sector [9].

In this study, zirconia-alumina ceramic composites (ZrO_2-Al_2O_3) were reinforced with different REO, ceria (CeO_2) and yttria (Y_2O_3), and produced through thermomechanical processing. These composites were subjected to two different sintering temperatures, 1350 ºC for 12 hours and 1150 ºC for 24 hours, and had their mechanical properties, structure and microstructure characterized by means of X-ray Diffraction, Scanning Electron Microscopy, Energy Dispersive Spectroscopy and Vickers microhardness, in order to determine the suitability of theses ceramic composites for application as a thermal barrier coating in the exhaust nozzles of gas turbines in the aerospace industry.

2. METHODOLOGY

The oxides used to form the composites were weighted in an analytical scale and mixed together according to the weight percentages listed in Table 1. The ceramic powders, both with a zirconia-alumina ceramic matrix, but each reinforced with a different rare earth oxide, have the same proportions of zirconia, alumina and rare earth oxides. Al_2O_3 was added in ZrO_2 in 5wt% ratios and the rare earth oxides were added at a 3wt%.

Table 1. Composition of the ceramic powders, in percentage per weight (wt%)

	ZrO2	Al2O3	CeO2	Y2O3
C.Ce	92	5	3	-
C.Y	92	5	-	3

After the ceramic powder was formed, each batch underwent the milling process through a ball mill (Equipments Marconi MA-50) in a stainless-steel milling chamber containing 36 alumina balls, for 6 hours. This mechanical process is intended to mix and homogenize the mixture by reducing particle size, consequently enhancing the reaction rate and improving the mechanical properties of the composites.

The ground and homogenized mixtures extracted from the ball mill were compressed utilizing a uniaxial press (Schiwing SIWA, modelo ART6500089). The powder was divided into 3g samples, that were placed in a metallic mold, fabricated from abrasion resistant AISI A2 steel (HRC 58), and compacted into discs under a load of 12 ton/cm3 for a total of 5 minutes, to ensure uniform pressure distribution during compaction. The compacted discs had a 20 mm diameter and a 5 mm thickness.

Afterwards, the samples were subjected to the conventional solid-state sintering process. For this step, they were separated in two categories: those sintered for 12 hours at 1350 °C (C.Ce.12 and C.Y.12) and those sintered for 24 hours at 1150 °C (C.Ce.24 and C.Y.24). The sintering process was conducted in high-purity alumina crucibles starting from ambient temperature to the desired sintering temperature, using a high-temperature muffle furnace (Jung 0614), followed by furnace cooling until the samples returned to their initial temperature. Proper sintering is essential to the process, as it leads to modifications in the ceramic, such as reduction in porosity and grain growth.

The sintered discs underwent metallographic processing, with sandpaper ranging from 200 to 1200 grit, followed by polishing with an electric rotary sander (Arotec, Aropol 2V) until a mirror-like surface was achieved. Structural characteristics and phase identification were analyzed using X-ray diffractometry (XRD) with a Shimadzu X-ray Diffractometer equipped with Cu-Kα radiation ($\lambda = 1.5406$ Å). Once composite formation was confirmed through XRD analyses, a study of the mechanical properties and microstructural features of the sintered ceramics was conducted.

Mechanical properties of the sintered ceramic composites were evaluated using a Vickers hardness indenter (model HVS-5, No 0021). Vickers micro-hardness was determined by making 12 indentations, with the two most disparate values excluded from the calculation of the arithmetic average and standard deviation. This process assessed the resistance of the ceramic composite surface to penetration by a pyramidal diamond. The microstructure of the sintered ceramic composites was examined using Scanning Electron Microscopy (SEM) with a scanning electron microscope (Oxford, X-act) and Energy Dispersive Spectroscopy (EDS) with a unit attached to the microscope (Tescan, Mira 3). As the composites are not electrical conductors, the samples were coated with a thin layer of gold using a sputtering coater (Quorum, SC7620).

3. RESULTS AND DISCUSSION

3.1. X-ray diffraction

The XRD data was processed to generate diffractograms, within defined angular ranges of 10 degrees to 80 degrees. To identify the peaks of the diffractograms, a qualitative analysis was applied, utilizing established parameters from the International Centre for Diffraction Data (ICDD).

The structural characteristics and phase identification conducted via XRD revealed the characteristic behavior of ZrO_2, Al_2O_3 and rare earth oxides (CeO_2 and Y_2O_3) - the absence of additional phases suggesting no reaction between constituent materials and confirming composite formation. The presence of rare earth oxide phases was subtly discernible in XRD patterns due to their low concentration within the compound.

The C.Ce.12 sample exhibits a more pronounced presence of tetragonal zirconia, albeit still showing characteristics of the monoclinic phase. The ceria sample sintered for a longer period of time, C.Ce.24, displays significantly fewer traces of monoclinic zirconia, predominantly consisting of tetragonal zirconia. Samples reinforced with yttria behave similarly, with C.Y.12 containing both tetragonal and monoclinic zirconia, whereas C.Y.24 consists primarily of tetragonal zirconia. It is known that the monoclinic phase remains stable only until 1170 °C.
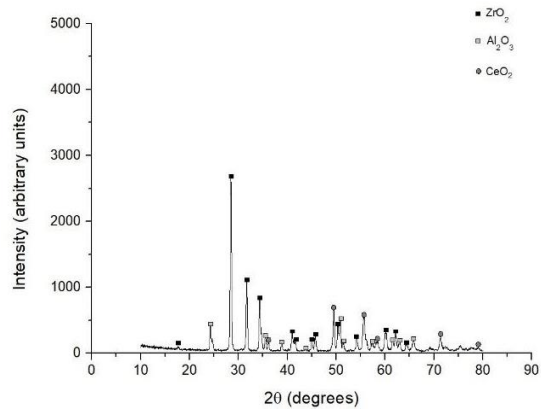
Figure 1. Diffractogram of the C.Ce.12 sample
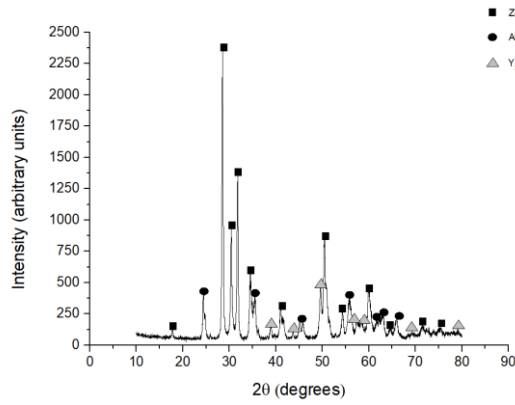
Figure 2. Diffractogram of the C.Y.12 sample
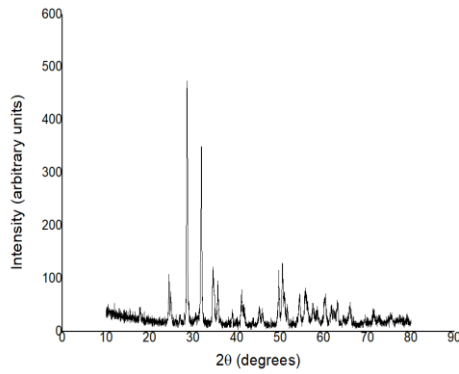
Figure 3. Diffractogram of the C.Ce.24 sample
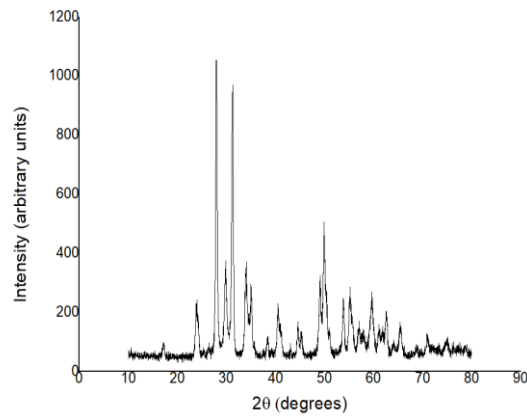
Figure 4. Diffractogram of the C.Y.24 sample

3.2. Scanning electron microscopy

The Scanning Electron Microscopy (SEM) technique was used to analyze the microstructure of the ceramic composites - in the images generated, the grain size and distribution is more explicit and the presence of the constituent phases can be studied as well. The SEM micrographs were taken using backscattering electron mode. The images show good homogeneity, and the composites reinforced with yttria (Figure 2c and 2d) have better grain refinement, as justified in the reference literature: rare earth oxides function as grain refinement agents, with yttria having superior effectiveness compared to ceria. Although the sintering process hasn't been fully successful, as evidenced by the absence of necking and grain constriction in the images, composite C.Y.24 exhibits more appropriate characteristics for the intended purposes.
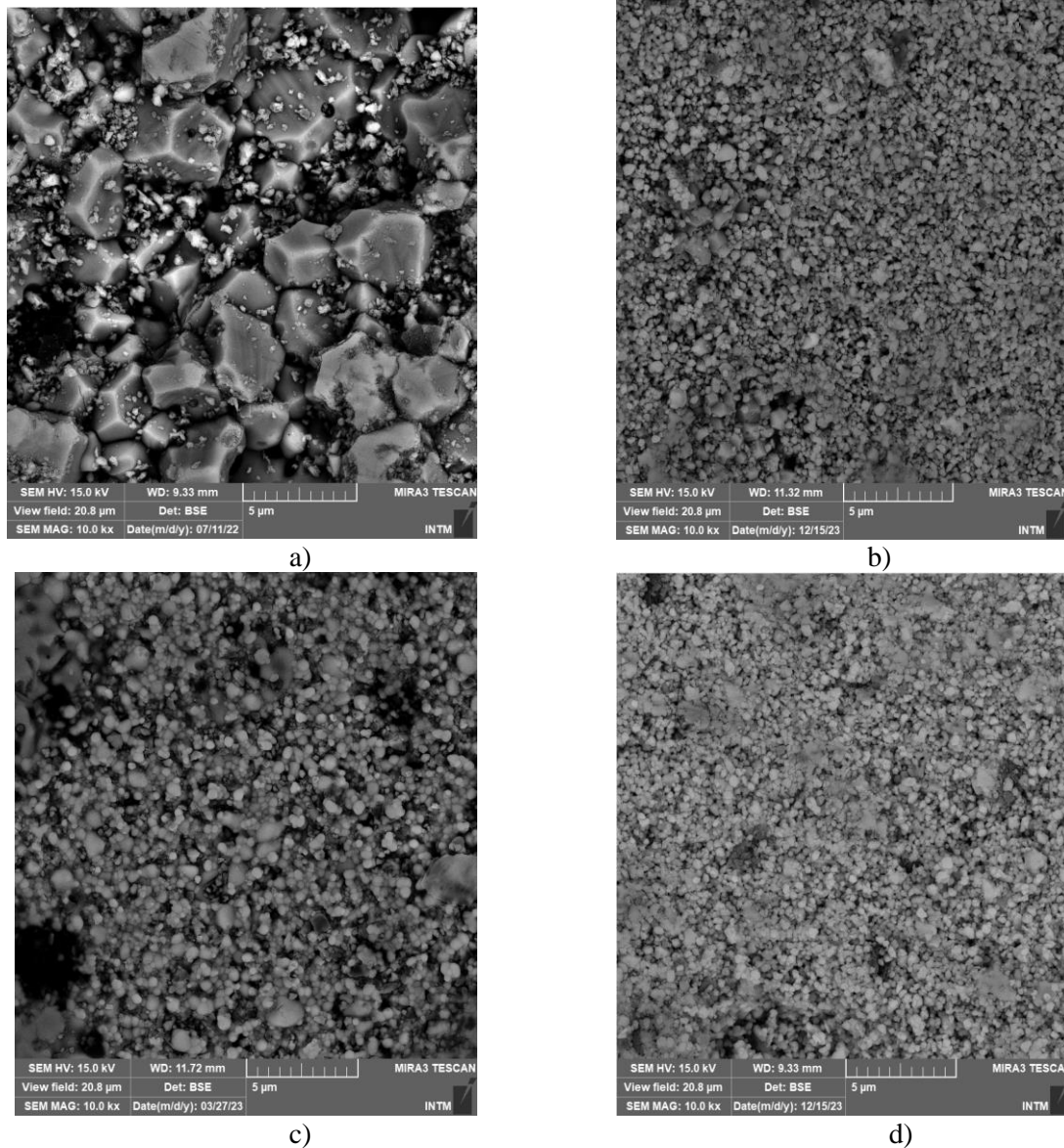
Figure 5. Microscopic image of the sintered composites. (a) C.Ce.12, (b) C.Ce.24, (c) C.Y.12 and (d) C.Y.24

3.3. Energy dispersive spectroscopy

The graphs generated by EDS indicate that the samples did not experience any form of contamination, as the elements identified in the analysis are consistent with the constituent elements of the composites. The

data depicted in the graphs represents a compilation of several "maps" - sections of the surface analyzed by the machine, demonstrating the homogeneity of the samples.
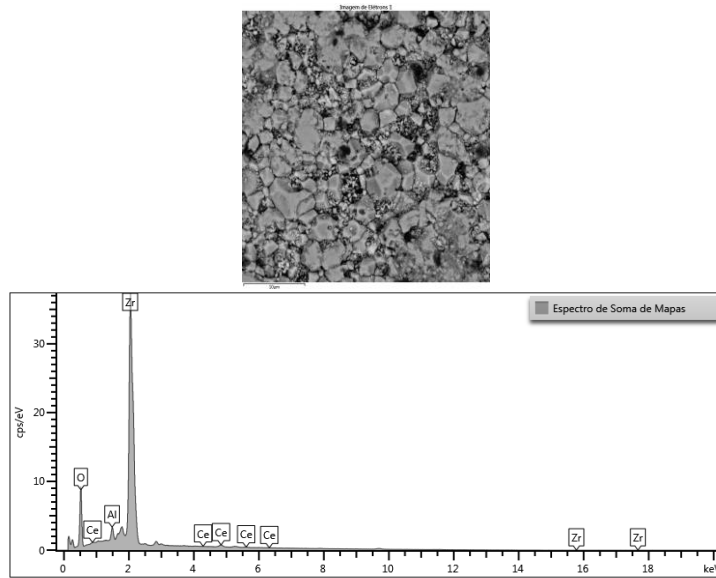
Figure 6. EDS results of C.Ce.12
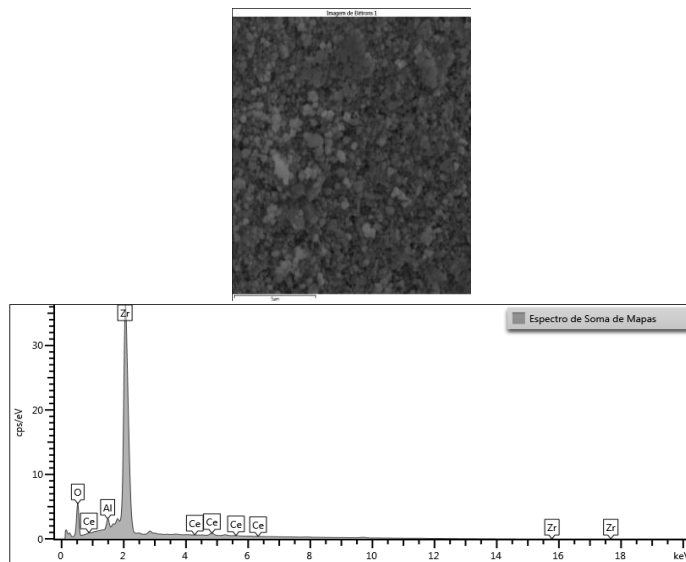
Figure 7. EDS results of C.Ce.24
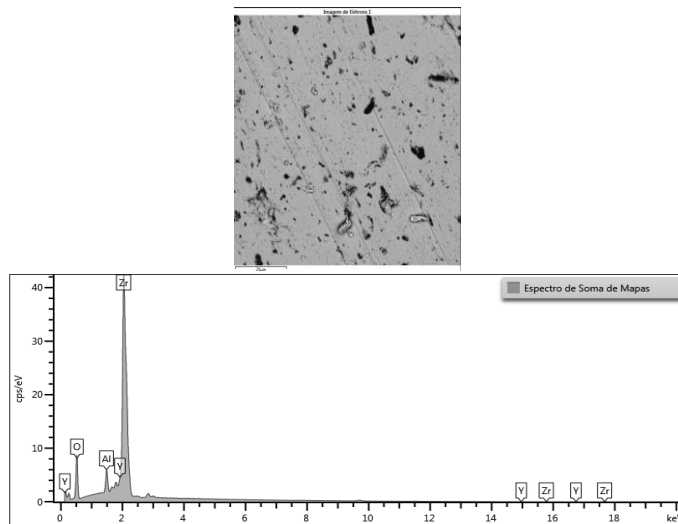
Figure 8. EDS results of C.Y.12
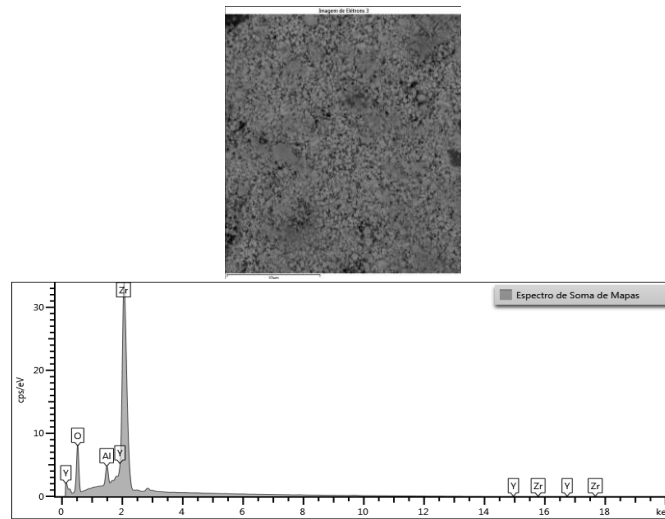
Figure 9. EDS results of C.Y.24

3.4. Vickers microhardness

The Vickers microhardness test presents the correlation between the presence of the rare earth oxides in the composites, their microstructure, and the sintering process they were subjected to. Table 2 displays the data obtained from this test, including the average and standard deviation.

Table 2. Composition of the ceramic powders, in percentage per weight (wt%)

Samples	C.Ce.12	C.Ce.24	C.Y.12	C.Y.24
	156,89	120,48	259,31	163,79
	145,47	119,64	255,34	156,43
	138,18	118,85	251,28	154,93
	136,55	118,32	250,91	154,04
Vickers microhardness (HV)	128,57	116,45	242,87	153,42
	127,90	111,86	232,15	152,55
	115,36	107,29	231,97	149,08
	111,76	99,25	223,93	137,17
	98,44	89,27	222,25	136,93
	93,02	88,05	221,35	123,82
Arithmetic average ± standard deviation (HV)	125,210 ± 20,440	108,946 ± 12,555	239,136 ± 14,539	148,216 ± 11,926

The hardness of the composites exhibited a significant decrease with prolonged sintering, even at lower temperatures. Composite C.Y.24 also displayed the smallest deviation, indicating the most homogeneous behavior across its surface.

4. CONCLUSIONS

The XRD results of all four composites revealed similar phase formations; however, SEM images suggest that the sintering process was most effective in the 92%ZrO_2-5%Al_2O_3-3%Y_2O_3 composites, particularly in the composite sintered at 1150 ºC for 24 hours. This composite also exhibits the most stable hardness across its surface and demonstrates homogeneous behavior, indicating its superior potential for application as a TBC in the aerospace industry.

4.1. Declaration of Competing Interest

The authors declare no conflict of interest.

4.2. Fundings

5. REFERENCES

[1]   C. R. C. Lima. Revestimentos para barreira térmica: evolução e perspectivas. *Soldagem & Inspeção*, Volume 19, 2014. (https://doi.org/10.1590/0104-9224/SI1904.11)

[2]   D. R. Clarke, M. Oechsner, N. P. Padture. Thermal-barrier coatings for more efficient gas-turbine engines. *MRS bulletin*, Volume 37, 2012. (https://doi.org/10.1557/mrs.2012.232)

[3]   B. Gleeson. Thermal Barrier Coatings for Aeroengine Applications. *Journal of Propulsion and Power*, Volume 22, 2006. (https://doi.org/10.2514/1.20734)

[4]   M. Peters, C. Leyens, U. Schulz, W. Kaysser. EB-PVD Thermal Barrier Coatings for Aeroengines and Gas Turbines. Advanced Engineering Materials, Volume 3, 2001. (https://doi.org/10.1002/1527-2648(200104)3:4<193::AID-ADEM193>3.0.CO;2-U)

[5]   Carlos R. C. Lima, Roseana E. Trevisan. *Aspersão Térmica: Fundamentos e Aplicações*. 2nd Edition, 2007. Art Liber. (ISBN: 8588098075)

[6]   X. Q. Cao, R. Vassen, D. Stoever. Ceramic materials for thermal barrier coatings. *Journal of the European Ceramic Society*, Volume 24, 2004. (https://doi.org/10.1016/S0955-2219(03)00129-8).

[7]   E. E. Daou. The zirconia ceramic: strengths and weaknesses. *The open dentistry journal*, Volume 8, 2014. (https://doi.org/10.2174/1874210601408010033)

[8]   C. Kuranaga, F. S. A. Ribeiro, M. Filgueira. Estudo da sinterização da zircônia dopada com óxidos de terras raras a 5 GPa de pressão. *Cerâmica*, Volume 51, 2005. (https://doi.org/10.1590/S0366-69132005000200015)

[9]   R. V. Camerini. Desenvolvimento de compósitos cerâmicos laminares à base de alumina e zircônia. 2013. Thesis (Materials Engineering Doctorate) - Universidade Federal do Rio Grande do Sul.

BUCKLING ANALYSIS OF A REINFORCED CFRP PANEL USING QUAD AND DOUBLE-DOUBLE LAMINATES

Roberto A. S. Cardoso [a], Leonardo P. S. Ferreira [b], Carlos A. Cimini Jr. [c]*

(a) 0009-0008-6779-2088 (Federal University of Minas Gerais – Brazil)
(b) 0000-0002-4963-8801 (FEMTO-ST – Université de Bourgogne Franche-Comté – France)
(c) 0000-0002-6612-0211 (Federal University of Minas Gerais – Brazil)
*Corresponding author: carlos.cimini@gmail.com

Abstract: The aeronautical industry relies on the QUAD quasi-isotropic laminate layup, basically using the combination of four angles and limited to symmetric and balanced laminates. Also, a minimum of 10% of plies for each angle is required. These rules restrict the potential that composite materials can offer. Recently, a new family of laminates was defined, composed of two angle-ply blocks arranged in a continuous stacking sequence. These laminates are called Double-Double, or simply DD. In this study, a CFRP (Carbon Fiber Reinforced Polymer) flat panel reinforced by longitudinal stringers is submitted to a compressive load for buckling analysis. The component is designed as a typical upper wing surface panel, considering the current QUAD design rules. A finite element model was developed to verify the critical buckling load. Then, an equivalent DD laminate was selected to match the QUAD design. Finally, an optimum DD was searched in the continuous angle-based design space to outperform the initial QUAD design. Results showed that an increase of up to 66% in the critical buckling load can be achieved with the optimum DD for the same weight as compared to the initial QUAD design. On the other hand, ply-drops in the DD layup could reduce the component mass by up to 16% for a buckling load still 3% higher than the QUAD.

1. INTRODUCTION

With the increasing number of aircraft structural components made of composite materials, the usage of more precise models and mathematical tools becomes continuously more important and necessary. Although composite laminates represent a change in the paradigms related to materials properties and aircraft manufacturing, they also impose new challenges within engineering projects. Due to their typical small thickness, bucking is a critical failure mode for aircraft composite reinforced panels. Comprehending the nature of the structural behaviour is crucial for modelling accordingly. Therefore, to validate numerical models, it is essential to compare computational and experimental results. In this matter, experimental data plays an important role related to the calibration of predictions not only for the critical buckling load but also for the post-buckling behaviour of the structural component. The success of a numerical model depends heavily on the appropriate application of forces and boundary conditions, which are fundamental in this kind of analysis.

Currently, QUAD quasi-isotropic laminate layups, based on collections of plies oriented at 0°, 90° and ±45°, are the most used configuration in the design of composite components for aeronautical applications. Due to strong restrictions and the reliability of well-known conservative methodologies, the aeronautical industry still imposes limitations to these laminates regarding their symmetry, balance, and ply angle ratio (minimum of 10% of the overall layup for each angle). However, limiting the possible configurations holds back the potential offered by composite materials when it comes to the maximization of design output

(stiffness, strength, damage tolerance, etc.). Thus, studies have been looking for new designs to overcome the decade-long era of QUAD laminates hegemony. Tsai [1] introduced, based on the theory of invariants, the concept of Double-Double (DD) laminates, composed of repeated blocks (sub-laminates) of four plies with two different angles, in the angle-ply configuration [±Φ/±Ψ]. These building blocks can be continuously added to the laminate according to the properties needed. The repetition of the sub-laminate in a process called homogenization leads to satisfactory symmetry and balance conditions, without the same restrictions faced when using QUAD quasi-isotropic layups. The effects of sub-laminate asymmetry are minimized by the increase in the number of blocks. Homogenization shows that the laminate normalized coupling matrix B^* tends to zero, and the laminate normalized in-plane stiffness and bending matrices approach to each other ($A^* = D^*$).

The aim of his work is to compare how QUAD and DD laminates perform for initial buckling analysis of a CFRP (Carbon Fiber Reinforced Polymer) flat panel reinforced with longitudinal stringers. The component, presented by Cabral et al. [2], was designed as a typical upper wing surface panel, considering the current QUAD design rules. A finite element analysis (FEA) for initial buckling was performed to verify the critical buckling load. Experimental results [2] were used for model correlation. Then a DD laminate was designed to be equivalent to the standard QUAD laminate for a comparative study. Finally, an optimum DD was searched in the continuous angle-based design space to outperform the previous designs.

2. METHODOLOGY

2.1. Software

For the FEA, the software platforms used for the was the for pre- and post-processing *HyperMesh*® [3] and the solver *NASTRAN*®[4], standard in the aerospace industry. Data acquisition and manipulation were later performed using *Microsoft Excel*®[5], useful for creating the graphs for the figures.

2.2. Finite element model

The finite element model used in this study was based on the reinforced panel presented by Cabral et al. [2] (Fig. 1a). Four-node-first-order composite shell elements were used together with similar boundary conditions. The model has four different group properties, purposefully separated to represent the correct orientation of plies in the building of the corresponding laminates (Fig. 1b). These laminate groups are based on the layup sequences for the stringers and for the skin, respectively [45/0/0/–45/0/0/–45/0/45/90]ₛ and [90/45/0/0/–45/0/0/45/90/90/45/0/–45/0/0/–45]ₛ. The connection between stringers and skin was considered as perfect bonding.

(a)   (b)
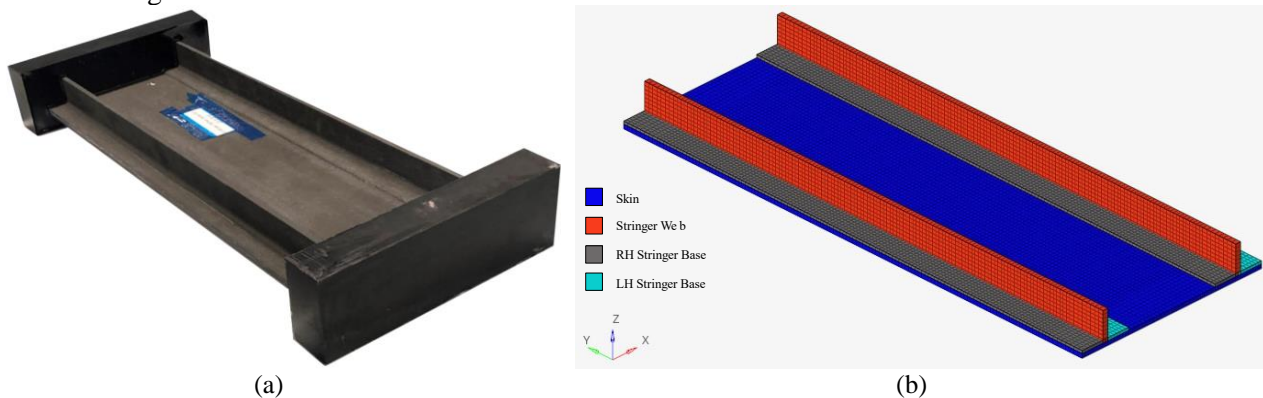
Figure 1. CFRP reinforced panel: (a) experimental structure (adapted from [1]), and (b) Finite element model.

The stacking sequence direction of the laminates was defined as shown in Fig. 2. Defining z1 as the first layer and z2 as the last layer, the normal-to-plane orientation for all laminates is depicted in this figure.
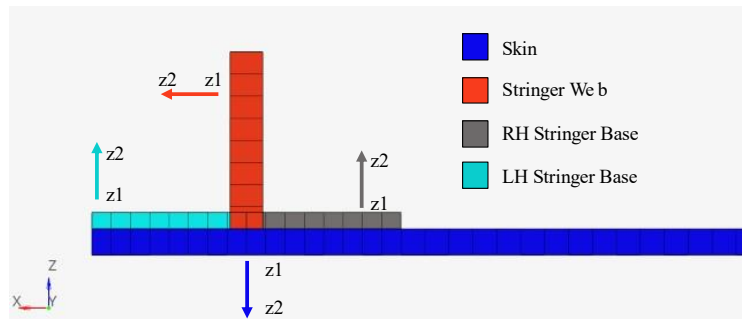
Figure 2. Stacking sequence orientation for all laminate groups.

Load was applied through a compressive force vector with magnitude of 720 kN (Fig. 4). Using rigid elements (RBE2), a compressive force was applied in the central node at the height of the neutral axis. The structural stability depends on the position of the applied force. The application of any force out of the neutral axis generates a destabilizing moment on the panel, which can result in divergences related to the maximum compression load. As for the boundary conditions, a full clamping is defined in the top and bottom faces of the resin blocks (lines marked in red in Fig. 4) and only out-of-plane displacements were restricted in the interface lines of the resin blocks and the panel (lines marked in red in Fig. 3).
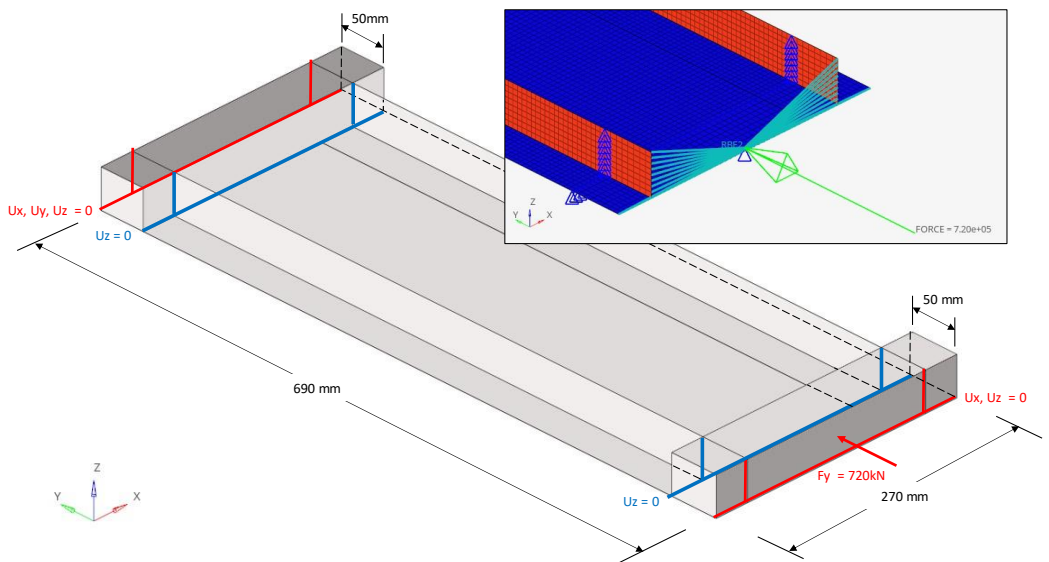
Figure 3. Load application.

The ply properties used in this study, corresponding to those from Cabral et al. [1], are displayed in Table 1.

Table 1. Ply properties [2].

Property	Value	Unit
E_1	119	GPa
E_2	9.8	GPa
ν_{12}	0.316	-
G_{12}	4.7	GPa
Ply thickness	0.186	mm

2.3. Optimization of the Double-Double laminate

The first stage (Case 1) of the panel optimization was performing FEA sweeping DD angles (Φ and Ψ) from 0° to 90°, in intervals of 10°, and generating the corresponding combination of critical buckling loads for the interval. Initially, both the skin and the stringers had the same configuration, i.e. the same DD angles Φ and Ψ. After defining smaller intervals with the highest critical buckling loads, results were refined analysing more closely only these intervals, with angle variation reduced to 1°. In the second stage (Case 2), the configurations of skin and stringers were studied separately. The layup of the stringers was assumed unidirectional (0°) and only the DD skin configuration was changed, obtaining the best skin DD laminate. Finally, for the third stage (Case 3), the fibers of the skin were maintained fixed at 0° with variations only for the DD layups of the stringers, leading to the verification of the ideal configuration for the stringers. For Cases 2 and 3, the same refinement process for the Case 1 was also performed.

In light of separate optimization of the layups for the skin and the stringers, it was possible to define an optimal configuration capable of withstanding the maximum buckling load.

2.4. Data analysis

The results obtained through *NASTRAN*® were exported to *MS Excel*®. One spreadsheet was created for each stage previously mentioned. The graphs were then plotted, and, based on them, it was possible to find the critical buckling load and the correspondent pair of angles [±Φ/±Ψ] for each condition. The final results were also organized on a separate table to allow a better comparison.

3. RESULTS AND DISCUSSION

Cabral et al. [2] experimental results were initially compared to the QUAD model FEA. The critical buckling load was experimentally measured as 739,4 kN. On the other hand, the simulation prediction for this condition was 694.0 kN, therefore 6% lower. This means that the FE model was 6% conservative in predicting the critical buckling load for the QUAD reinforced panel. However, for comparison reasons between QUAD and DD laminates, we will only consider the FEA predictions.

As described in section 2.3, the optimization for the DD laminates was divided in three stages: skin and stringers with the same configuration (Case 1), skin with DD varying configuration and stringers with fixed unidirectional [0] (Case 2), and stringers with DD varying configuration with skin fixed unidirectional [0] (Case 3).

For Case 1, both DD angles of the skin and of the stringers were varied between 0° and 90°, in 10° intervals. Fig. 5 shows the plot of the critical buckling loads as function of the DD laminate angles.
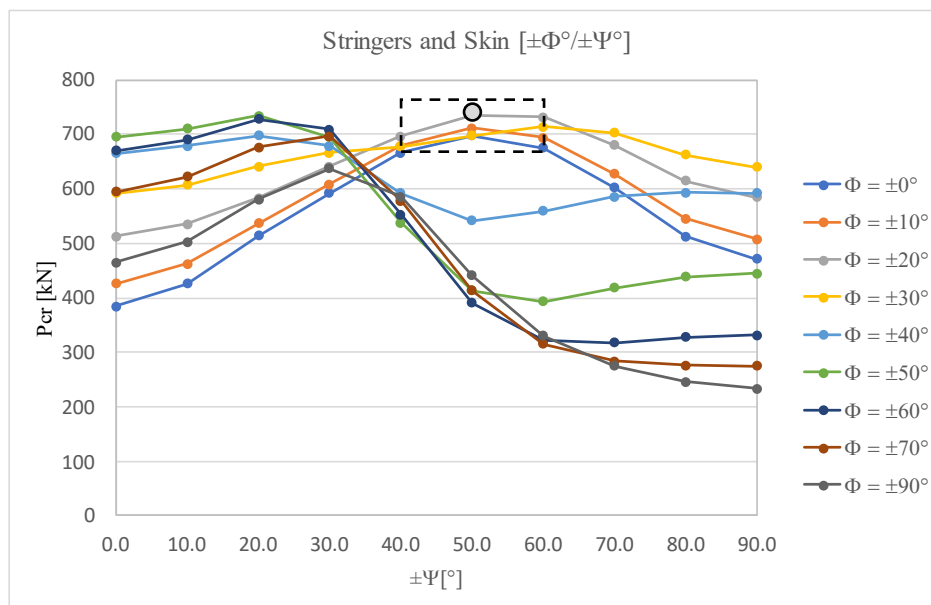
Figure 4. [±Φ/±Ψ] vs. critical buckling load (P_{cr}) – Case 1: same DD layup for skin and stringers.

It can be observed in Fig. 4 that the configuration which resulted in the maximum critical buckling load was [±20/±50], marked with a large dot. However, a more detailed analysis should be performed in the

region of interest, showed by the dashed box on Fig. 4, varying DD angles in smaller steps on the intervals $\pm 10 \leq \Phi \leq \pm 30$ and $\pm 40 \leq \Psi \leq \pm 60$, in order to find a better layup. The plot of this refinement is displayed in Fig. 5. Therefore, a more optimized DD laminate configuration $[\pm 23/\pm 56]$, marked with a large dot. This configuration refers to the whole component, that is, the skin and the stringers with the same DD layup.
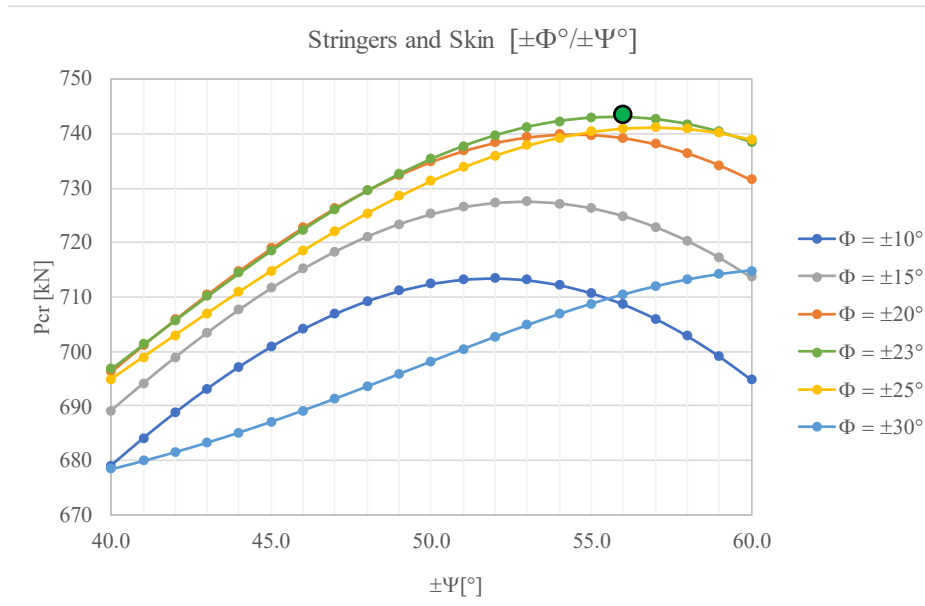
Figure 5. $[\pm\Phi/\pm\Psi]$ vs. critical buckling load (P_{cr}) – Case 1: refinement.

For Case 2, only the skin was optimized. The stringers were kept at a unidirectional configuration [0], while the skin was altered according to the DD layup $[\pm\Phi/\pm\Psi]$, varying both angles from 0° to 90°. The results are shown in Fig. 6.
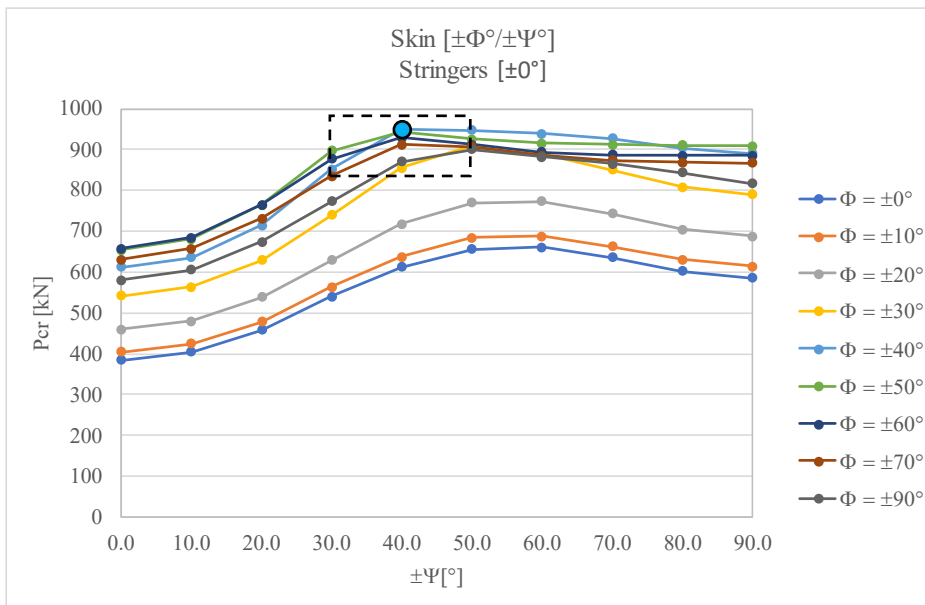
Figure 6. $[\pm\Phi/\pm\Psi]$ vs. critical buckling load (P_{cr}) – Case 2: Fixed 0° stringers and varying skin DD.

The configuration that resulted in the maximum critical buckling load was $[\pm 40/\pm 40]$, marked with a large dot. The region of interest for refinement was defined as $\pm 30 \leq \Phi \leq \pm 50$ to $\pm 30 \leq \Psi \leq \pm 50$. Again, the refinement results are displayed in Fig. 7. The optimized configuration for the skin of the reinforced panel, specifically, was found to be $[\pm 40/\pm 44]$, marked with a large dot, maintaining the stringers at unidirectional layup.
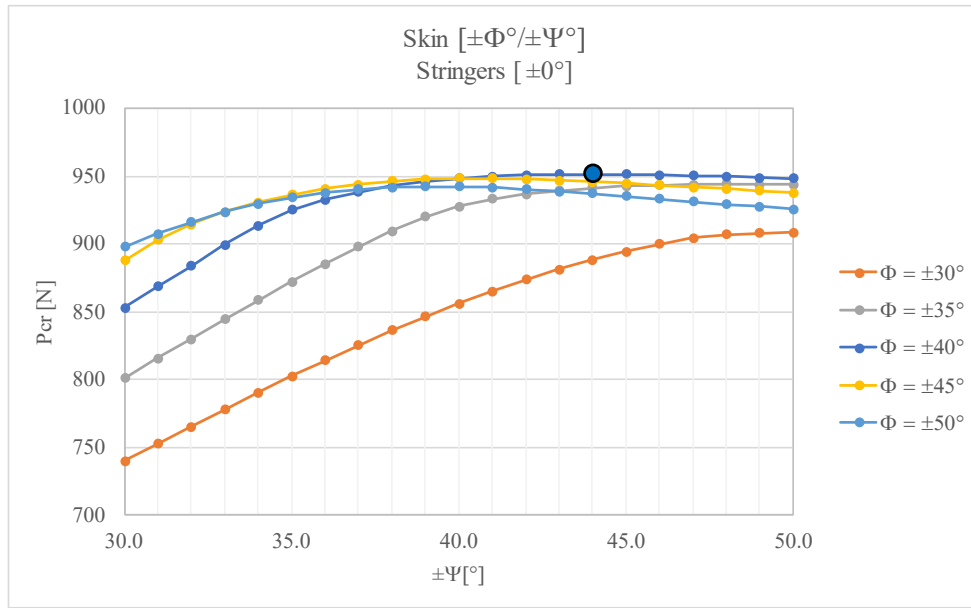
Figure 7. [±Φ/±Ψ] vs. critical buckling load (P_{cr}) – Case 2: refinement.

For Case 3, only the stringers were optimized, using the DD layup [±Φ/±Ψ], varying both angles from 0° to 90°. The skin layup was kept unidirectional [±0]. The results are shown in Fig. 8.
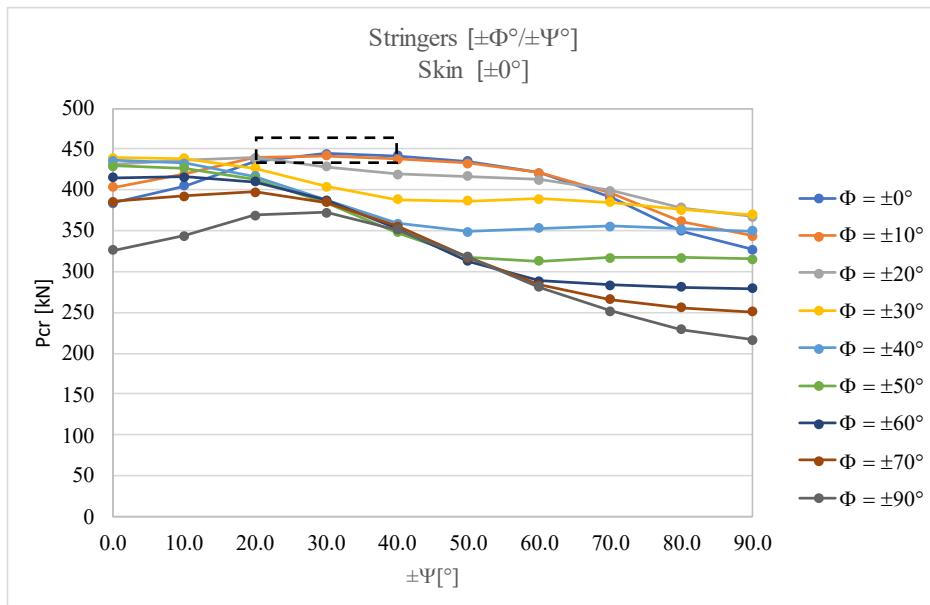
Figure 8. [±Φ/±Ψ] vs. critical buckling load – Case 3: Fixed 0° skin and varying stringers DD.

The configuration related to the maximum critical buckling load for the stringers was [±0/±30], marked with a large dot. The region of interest was defined as ±0 ≤ Φ ≤ ±10 to ±20 ≤ Ψ ≤ ±40. Once more, the refinement results are shown in Fig. 9. The optimized DD layup for the stringers according to the refinement kept the [±0/±30] DD layup as optimum, marked with a large dot.
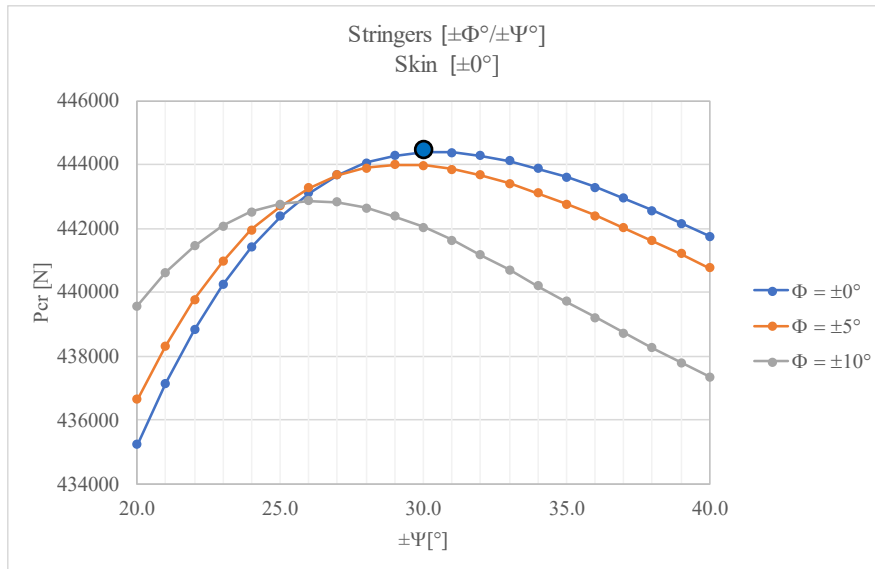
Figure 9. [±Φ/±Ψ] vs. critical buckling load (P_{cr}) – Case 3: refinement.

The results were then combined in different configurations:

(a) QUAD original configuration (baseline);
(b) DD general optimization (skin and stringers optimized together) – Case 1;
(c) DD optimized stringers based on their general results (Case 3) and optimized skin based on its general results (Case 2);
(d) DD optimized stringers (Case 3) and while skin layup was $[(\pm45°)_{16}]_s$ for maximum buckling load configuration of simply supported plate, corresponding to the DD $[\pm45/\pm45]_8$;
(e) DD optimized stringers based on their refined results (Case 3) and optimized skin based on its refined results (Case 2);
(f) DD optimized with ply-drops in both stringers and skin.

For the first five configurations, (a) to (e), the number of plies of the skin and stringers did not change, keeping 20 plies for the stringers and 32 plies for the skin. Then comparison in terms of critical buckling load increase could be performed in the same basis. On the other hand, the last configuration considered ply-drops of one DD building block for both stringers and skin, resulting in a lighter laminate with 16 plies for the stringers and 28 plies for the skin.

Table 2 summarize these six configurations. There, the baseline standard QUAD quasi-isotropic laminate is compared with different configurations for DD laminates in terms of critical buckling load. It was noticed that the number of blocks in the DD laminate could be reduced and the critical buckling load would still be higher than the one for the QUAD laminate. A reduction was made for the DD combination with the higher critical buckling load (combination 4). These results are also included in Table 2.

Table 2. Final results for each laminate configuration.

Config	P_{cr} [kN]	Laminate type	Load increase [%]	Layup Stringers	Layup Skin
(a)	694.0	QUAD	0	$[45/0/0/-45/0/0/$ $-45/0/45/90]_s$	$[90/45/0/0/-45/0/0/45/90/90/$ $45/0/-45/0/0/-45]_s$
(b)	743.0	DD	7	$[\pm23/\pm56]_5$	$[\pm23/\pm56]_8$
(c)	1114.7	DD	61	$[\pm0/\pm30]_5$	$[\pm40/\pm40]_8$
(d)	1139.9	DD	64	$[\pm0/\pm30]_5$	$[\pm45/\pm45]_8$
(e)	1152.2	DD	66	$[\pm0/\pm30]_5$	$[\pm40/\pm44]_8$
(f)	715.5	DD	3	$[\pm0/\pm30]_4$	$[\pm40/\pm44]_7$

From Table 2, it is possible to verify that for configuration (b) the equivalent DD increased the initial buckling load of the QUAD by 7% (Case 1). Optimization for QUADS, keeping the restrictions (symmetry, balance, 10% minimum of each angle, etc.) is not an easy task to do. However, the continuous nature of DD angles associated with the homogenization obtained by the [±Φ/±Ψ] building block repetition facilitates the optimization, as no symmetry is required. Once established the best [±Φ/±Ψ], one can simply drop plies in order to achieve the target buckling load, keeping the same laminate stiffness properties. Performing the optimization steps for Cases 2 and 3 combined, the performance of DD increased the initial buckling load by 61%, 64% and 66%, respectively for the configurations (d), (e) and (f). Moreover, using these same optimum layups of configuration (e), it is possible to drop one DD building block (4 plies) on both the stringers and skin layups and still have the initial buckling load 3% higher. For this case, due to the ply-drops, the total mass of the component is reduced by 16% as compared to the other layups, including the original QUAD.

4. CONCLUSIONS

In this work, finite element simulations were performed in a model of a CFRP reinforced with different layups. The analyses were carried out to compare the critical buckling load supported in each configuration, which included a standard QUAD quasi-isotropic baseline layup and different DD layups obtained for particular optimization cases.

It was possible to verify that DD alternatives proved to be more efficient in terms of buckling load capacity as compared to the QUAD baseline laminate. Consequently, a structural component using DD configuration could be designed using less material, thus reducing weight. The study concluded that, for the same mass (same number of plies for stringers and skin), the buckling load could be increased by up to 66% using DD instead of QUAD. On the other hand, a weight saving of up to 16%, related to one DD building block ply-drop for stringers and skin, could still result in a critical buckling load 3% higher, as compared to the QUAD laminate baseline.

This study highlights the potential of DD laminates for replacing standard QUAD quasi-isotropic laminates in terms of weight optimization for critical buckling load, beyond all other benefits that this design approach could facilitate in terms of design and manufacturing.

4.1. Declaration of Competing Interest
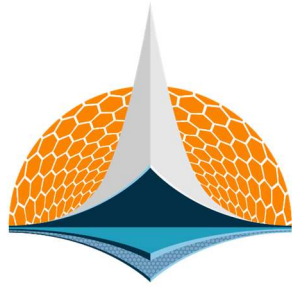
The authors declare no conflict of interest.

4.2. Acknowledgements

5. REFERENCES

[1] Tsai, SW. Double–Double: New family of composite laminates. *AIAA Journal*, 2021 29(15):4293-4305. (https://doi.org/10.2514/1.J060659).

[2] Cabral PH, Carrera E, dos Santos, HEAA, Galeb PHG, Pagani A, Peeters D, Prado AP. Experimental and numerical vibration correlation of pre-stressed laminated reinforced panel. *Mechanics of Advanced Materials and Structures*, 2020 29(15):1-11. (https://doi.org/10.1080/15376494.2020.1853285).

[3] Altair HyperMesh® 2019 [Computer software]. Altair®. (www.altair.com/hypermesh).

[4] NASTRAN® 2020 [Computer software]. Hexagon. (www.hexagon.com).

[5] Microsoft Excel® 2016 [Computer software]. Microsoft Inc. (www.microsoft.com).

2 Advanced numerical techniques

Organized and edited by

Sandra Maria da Luz
&
Carla Tatiana Mota Anflor

ANALYSIS OF ADHESIVE DEBONDING IN THE THREE POINT BENDING TEST USING THE BOUNDARY ELEMENT METHOD

Eder Lima de Albuquerque[(a),*], Lucas Silveira Campos [(b)] , Thiago Vasconcellos Birro [(c)] , Jairo Francisco Useche Vivero [(d)] , René Quispe Rodriguez [(e)] , Sergio Gustavo Ferreira Cordeiro [(f)]

(a) 0000-0002-7154-6946 (University of Brasília – Brazil)
(b) 0000-0002-9734-4613 (Federal University of Espirito Santo – Brazil)
(c) 0000-0001-7872-9342 (Capgemini Engineering – France)
(d) 0000-0002-9761-2067 (Universidad Tecnológica de Bolívar – Colombia)
(e) 0000-0002-1676-924X (Federal University of Santa Maria – Brazil)
(f) 0000-0002-6826-5457 (Aeronautics Institute of Technology – Brazil)

* Corresponding author: eder@unb.br

Abstract: In the realm of adhesive joint design and multi-material structures, numerous mechanical characterization tests are commonly employed to evaluate adhesive properties, with limited methodologies available for assessing interfacial properties. As an alternative, the standard ISO 14679:1997 includes a specific three-point bending test (3PBT) that has been useful in identifying critical forces and displacements associated with bond strength. However, this test only provides a qualitative assessment of the bond line. In recent years, a new quantitative methodology has been developed to determine critical stress and fracture toughness based on a coupled stress-energy criterion, also known as coupled criterion (CC). Nonetheless, evaluating these parameters requires a significant effort using semi-analytical or finite element analysis techniques. The Boundary Element Method (BEM) offers a compelling alternative to conventional approaches, eliminating the need for domain mesh elements. Unlike traditional methods, BEM utilizes fundamental solutions to directly calculate unknown field variables on the domain's boundary without requiring any information about the domain itself. This approach allows for modeling complex geometries and interface debonding problems with greater accuracy and efficiency, as the computational effort is focused only on the boundary and interfaces. The present study uses the CC and a cohesive interface boundary element method to investigate the interfacial properties of a 3PBT specimen between an aluminum alloy 2024-T3 and the DGEBA/DETA adhesive. An intrinsic mixed-mode cohesive model is applied to simulate debonding, introducing local cohesive stiffness matrices into the boundary element equations. The numerical results involve a 3PBT specimen, incorporating interface strength properties through an incremental energy release rate and critical stress. The boundary element method is validated through comparisons with experimental data and other numerical methods. The results confirm that the method is well-suited for analyzing adhesive joint interfaces, providing accurate stress-strain solutions that align with experimental findings. This study contributes valuable insights for the future design of multi-material structures.

1. INTRODUCTION

Over the past few years, a mechanical test called the three-point bending test (3PBT) has gained popularity to assess bond strength. This test involves bonding a thick adhesive stiffener with fixed dimensions to a substrate element of a specific thickness. During the test, a central displacement is applied to the specimen, which causes stress concentration near one of the inner edges of the adhesive-substrate interface. This leads to interface debonding, which is the primary failure mechanism. Figures 1 and 2 illustrate the setup and failure mechanism of the test, respectively.
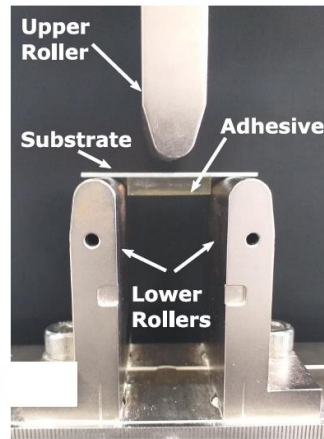
Figure 1. Set-up of the three-point bending according to ISO 14679-1997 [1].
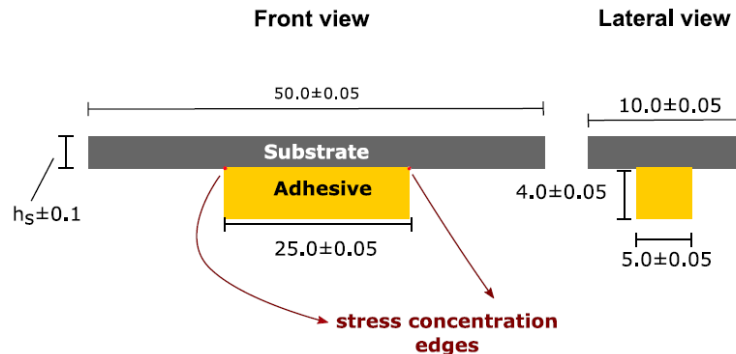
Figure 2. Dimensions of the 3PBT specimen according to ISO 14679-1997 (dimensions in mm) [1].

The test involves precise displacement control of the specimen by the upper roller at a 0.5 mm/min rate. Interfacial debonding occurs when the critical force (F_c) is reached, as shown in Figure 3 at Point B. Failure propagation happens along the overlap until debonding occurs (from point B to point C), and the substrate stiffness is observed at the end of the test (segment CE). The dissipated energy (W_c) is a common indicator of bond strength and is calculated by measuring the area between the unbroken and broken structural responses.
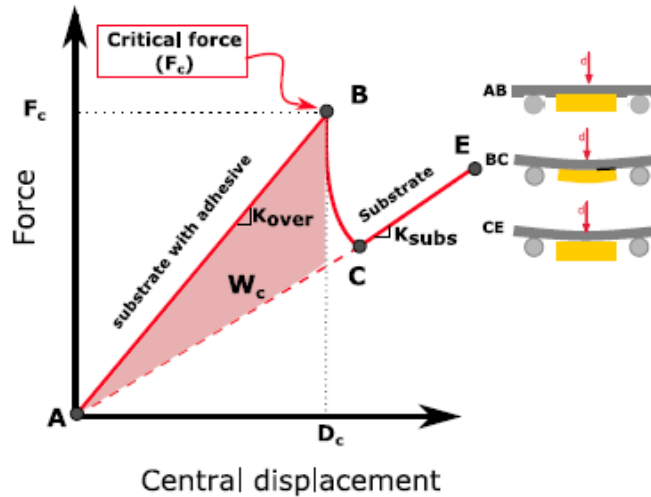
Figure 3. Typical curve of 3PBT: AB – specimen stiffness; B – instantaneous failure initiation; BC –Failure Propagation; CE –substrate stiffness.

Birro (2021) [2] has effectively utilized the coupled energy-stress criterion (CC) to assess the fracture toughness (G_c) and the critical stress (σ_c) for predicting the mechanical characteristics of the interface. The model assumes a weak interface model, where the interface is represented as an infinite spring layer in both peel (k_I) and shear (k_{II}) solicitation. To make this method work, interface stiffnesses k_I and k_{II} must be calibrated to match the numerical model's compliance with the experimental test. Additionally, Birro [2] assumed no mode differentiation, which means that the interface stiffness in shear is equal to the stiffness in peel solicitation ($k_I = k_{II}$). As a result, the CC method successfully predicted the failure initiation for different substrate configurations as a first attempt. Birro [2] employed the parameters estimated through CC for the estimation of crack interface debonding by using a progressive traction-separation law between the adhesive and the substrate. The analysis was conducted using a bilinear damage law. A rapid numerical simulation was able to estimate the macro-results (critical force and displacement) obtained through experimental testing.

Classical finite element analysis can be quite challenging when it comes to simulating this particular problem. However, the Boundary Element Method (BEM) [3] presents an intriguing alternative by eliminating the need for domain discretization. BEM utilizes fundamental solutions to directly calculate unknown displacements and tractions field variables on the boundary of the domain. This approach allows for more precise and efficient modeling of complex geometries and interface debonding problems. Concentrating the computational effort solely on the boundary and interface makes the resulting system much smaller, enhancing precision and efficiency.

Two approaches can be used for modeling the interface between different materials: weak interface modeling and strong interface modeling [3]. Strong interface modeling assumes perfect bonding, while weak interface modeling uses springs coupling the kinematics of the bonding surfaces. Weak interface modeling is typically associated with a thin adhesive layer or interphases between materials. Several authors have combined this model with appropriate fracture criteria to obtain analytical or semi-analytical solutions for structural joints under different geometries, materials, and loading parameters [2,4,5].

2. METHODOLOGY

2.1. LINEAR ELASTIC FRACTURE PROPAGATION CRITERION

An algorithm for modeling linear elastic fracture propagation (LEFP) was proposed in 2005 by [6]. The original algorithm was developed for an imposed force. In this work, the approach is slightly modified to adapt to an imposed displacement. The first Equation in (1) determines the overall stiffness of pre-cracked samples with different crack sizes, denoted by indexes *i*. The energy release produces the load drop from FS[i] to

FI[i+1] for a constant displacement. The second Equation can thus determine the value of displacement d[i] in (1):

$$
\begin{cases}
K_{over}^{[i]} = \dfrac{F_{max}^{[i]}}{d_{max}} \\
d^{[i]} = \sqrt{\dfrac{2W}{K_{over}^{[i]} - K_{over}^{[i-1]}}}
\end{cases}
$$

(1)

Finally, the lower and upper force values FI[i] and FS[i], respectively, are determined using Equation (2).

$$
\begin{cases}
FS^{[i-1]} = d^{[i]} \cdot K_{over}^{[i-1]} \\
FI^{[i]} = d^{[i]} \cdot K_{over}^{[i]}
\end{cases}
$$

(2)

The collection of all values of d[i] and FI[i] allows the construction of the response of the structural debonding problem.

2.2. TRACTION SEPARATION LAW

The concept of a traction separation law involves defining the relationship between tractions and displacement discontinuities along the surfaces of a fictitious crack representing an interface process zone. This is done through surface constitutive relationships. There are different shapes of models available in the literature. The model adopted in the present work was proposed by [8], which is described in Equation (3) and shown in Figure 3.

$$
\begin{cases}
T_n = (1 - \beta) \dfrac{u_n}{\delta_{0n}} \sigma_i^c \\
T_t = (1 - \beta) \dfrac{u_t}{\delta_{0t}} \tau_i^c
\end{cases}
$$

(3)

where T_n (T_t) denotes the normal (tangential) interfacial traction, u_n (u_t) denotes the normal (tangential) displacement discontinuities along the interface. The damage variable β is responsible for the degradation process. The surface parameters δ_{0n} (δ_{0t}) and σ_i^c (τ_i^c) denote, respectively, the normal (tangential) discontinuities values related to damage initiation and the normal (tangential) material strength. The softening law shown in Figure 3 has three phases: (i) the increase of stress until a critical value, corresponding to an undamaged part; (ii) the stress uncharged region and loss of the stiffness after the critical stress, corresponding to the development of the damaged variable; and finally (iii) the creation of a stress-free surface, after reaching the critical displacement jump.
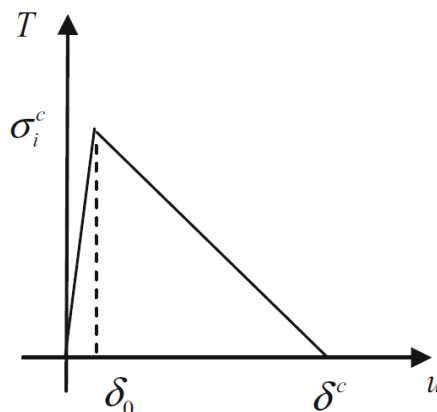
Figure 3. Bilinear Traction-separation law [6].

During the softening phase (ii), the damage variable β can be computed as:

$$\beta = \frac{\kappa}{\eta(1+\kappa)} \tag{4}$$

where

$$\eta = \left(1 - \frac{\delta_{0n}}{\delta_n^c}\right) = \left(1 - \frac{\delta_{0t}}{\delta_t^c}\right) \tag{5}$$

is another surface parameter, with δ_n^c (δ_t^c) representing the critical normal (tangential) displacement jumps and

$$\kappa = \sqrt{\left(\frac{u_n}{\delta_{0t}}\right)^2 + \left(\frac{u_t}{\delta_{0n}}\right)^2} - 1 \tag{6}$$

is an internal variable. As adopted in [8], no attempt was made here to distinguish mode I from mode II. This is achieved by setting $\sigma_i^c = \tau_i^c$, $\delta_{0n} = \delta_{0t}$ and $\delta_n^c = \delta_t^c$. This particular option suggests that the onset of damage at the interface is triggered by a stress-based criterion that is akin to the one employed by Birro [2].

2.3. BOUNDARY ELEMENT FORMULATION

This section presents a short overview of the boundary element formulation used in this work. A more detailed text can be found in Reference [9]. Compared to [9], the single-domain dual BEM formulation (see [8]) was replaced by the well-known multi-domain formulation (see [10]) and the PPR traction-separation was replaced by the progressive traction-separation law described in section 2.2. The governing linearized equilibrium equations of the solid can be represented in terms of BIE. Assuming nil body forces, the displacement (singular) BIE is written for a boundary source point **x's**:

$$\mathbf{c(x')u(x')} + \mathcal{C} \int_\Gamma \mathbf{t^*(x', x)u(x)}d\Gamma = \int_\Gamma \mathbf{u^*(x', x)t(x)}d\Gamma \tag{7}$$

where $\mathbf{x'}$ and $\mathbf{x}$ are the source and field points. $\mathbf{u(x')}$ indicates the displacement at the source point, $\mathbf{u(x)} = u_i$ $\mathbf{e}_i$ and $\mathbf{t(x)} = t_i$ $\mathbf{e}_i$ represent the displacement and traction boundary fields, $\mathbf{u^*(x',x)} = u^*_{ij}$ $(\mathbf{x',x})\mathbf{e}_i \otimes \mathbf{e}_j$ and $\mathbf{t^*(x',x)} = t^*_{ij}$ $(\mathbf{x',x})\mathbf{e}_i \otimes \mathbf{e}_j$ are the Kelvin fundamental solutions for displacements and tractions. After the discretization of the boundary into boundary elements and approximating displacements and tractions using linear boundary elements, it is possible to obtain a matrix equation given by:

$$\mathbf{HU = GT} \tag{8}$$

The dense square matrices **H** and **G** arise from the integration of the kernels, whereas the column matrices **U** and **T** collect the coefficients u_α^e and t_α^e from the displacements and tractions approximations over the boundary. Singular and hypersingular integrals are regularized by the subtraction singularity technique. Discontinuous boundary elements are adopted in regions of geometric or traction discontinuities and for crack boundary elements.

Regarding the position of the elements on the boundaries: Γ_u, Γ_t, Γ_{c+}, and Γ_{c-}, which represents Dirichlet, Neumann and sides + and - of the interface crack, Equation (8) can be split as

$$\lambda\mathbf{H}_u\overline{\mathbf{U}} + \mathbf{H}_t\mathbf{U}_t + \mathbf{H}_{c+}\mathbf{U}_{c+} + \mathbf{H}_{c-}\mathbf{U}_{c-} = \mathbf{G}_u\mathbf{T}_u + \lambda\mathbf{G}_t\overline{\mathbf{T}} + \mathbf{G}_{c+}\mathbf{T}_{c+} + \mathbf{G}_{c-}\mathbf{T}_{c-} \tag{9}$$

where **U** and **T** with superscript bars are prescribed displacement and traction patterns, and λ is a load factor. Defining the global displacement discontinuity $\Delta_c = \mathbf{U}_{c+} - \mathbf{U}_{c-}$, imposing the traction force balance $\mathbf{T}_{c+} + \mathbf{T}_{c-} = \mathbf{0}$, and imposing the intrinsic cohesive model at the interface crack $\mathbf{T}_{c+} = \mathbf{K}_c\Delta_c$ (see details in [7]), it is possible to obtain the final system of (nonlinear) equations of the problem

$$\mathbf{AX} - \lambda\overline{\mathbf{B}} = 0 \tag{10}$$

were the square matrix **A** and the column matrices **B** and **X** are:

$$\mathbf{A} = \left[\ \mathbf{H}_t \quad -\mathbf{G}_u \quad (\mathbf{H}_{c+} + \mathbf{H}_{c-}) \quad [\mathbf{H}_{c+} + (\mathbf{G}_{c-} - \mathbf{G}_{c+})\mathbf{K}_c] \ \right]$$

$$\overline{\mathbf{B}} = \mathbf{G}_t\overline{\mathbf{T}} - \mathbf{H}_u\overline{\mathbf{U}}$$

$$\mathbf{X} = \begin{bmatrix} \mathbf{U}_t^T & \mathbf{T}_u^T & \mathbf{U}_{c-}^T & \mathbf{\Delta}_c^T \end{bmatrix}^T \qquad (11)$$

in which

$$\mathbf{K}_c = \begin{bmatrix} \mathbf{k}_c^1 & & \\ & \ddots & \\ & & \mathbf{k}_c^{N_c} \end{bmatrix} \qquad (12)$$

is the global cohesive stiffness matrix and $\mathbf{k}_c^i$ the local cohesive stiffness matrices, as defined in [7]. To find the unknowns $\mathbf{X}$, it should be noticed that the activation of the damage variable β makes $\mathbf{K}_c = \mathbf{K}_c(\mathbf{\Delta}_c)$. Therefore, the solution of the system in Equation (10) demands the use of nonlinear solution techniques. Details regarding those techniques can be seen in [9].

3. RESULTS AND DISCUSSION

The three-point bending test (3PBT) illustrated in Figure 2 was analyzed, for a substrate thickness $h_s = 1.08$ mm, with BEM models by the discussed methodologies: (i) LEFP analysis (damage variable inactivated, i.e. $\beta=0$) with crack size increments of 0.1mm, and (ii) progressive damage cohesive analysis (damage variable β activated). The experimental test was conducted by [2], which also conducted a finite element analysis of the test. The geometry and boundary conditions adopted in the BEM analysis are illustrated in Figure 4. The adopted dimensions were: $L_{tot} = 35.9$ mm, $L_1 = 5.45$ mm, $b_s = 10$ mm, $b_a = 5$ mm.
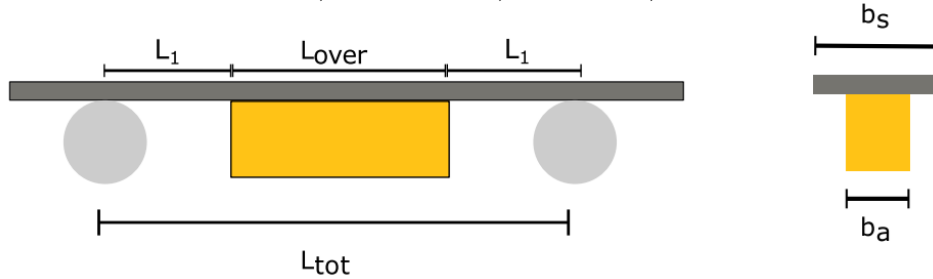
Figure 4. Geometry and boundary conditions for BEM analysis.

The elastic modulus and Poisson's ratio of the materials are $E_s = 68000$ MPa and $\nu_s = 0.33$ for the substrate and $E_a = 3000$ MPa and $\nu_a = 0.35$ for the adhesive. The problem was analyzed in plane stress with an equivalent substrate width $b_{s*} = b_a = 5$ mm and a new substrate Young's modulus $E_{s*} = b_s E_s/b_a$, as reported in [2]. The interface's initial stiffnesses were set as $k_I = k_{II} = 2000$ MPa.mm^{-1}, as suggested by [2]. For the progressive damage cohesive model, the required surface constitutive parameters were the interface strengths $\sigma_i^c = \tau_i^c = 48.9$ MPa and the interface fracture energy $G_I = G_{II} = 0.609$ N.mm^{-1}. The remaining surface parameters can be computed as: $\delta_{0n} = \sigma_i^c/k_I$, $\delta_{0t} = \tau_i^c/k_{II}$, $\delta_n = 2G_I/\sigma_i^c$ and $\delta_t = 2G_{II}/\tau_i^c$.

3.1. LINEAR ELASTIC FRACTURE PROPAGATION USING BEM ANALYSIS

For the Linear elastic fracture propagation analysis, the interface crack was incrementally advanced in 100 steps symmetrically at both sizes of the adhesive extremes, and multiple linear elastic BEM analyses were performed. For each linear elastic analysis, the upper roller's vertical displacement imposed in the substrate was $u_y = 0.57$ mm, corresponding to the ultimate load. The adopted BEM model consists of 722 linear elements, 406 to discretize the substrate´s boundaries and 316 to discretize the adhesive´s boundaries. The most refined boundaries were the interface boundaries of the substrate and adhesive, which were discretized with 10 elements per mm. The size of the crack increment was chosen as $\Delta a = 0.1$ mm, which is compatible with the adopted interface boundary element mesh. The values of the displacements d[i] and forces FI[i] were computed with the LEFP described in section 2.1 for each one of the 100 steps. The final crack sizes at both extremes of the interface were 10 mm. At the end of the analysis, from the original 25 mm of uncracked interface, only the central 5 mm remained uncracked. The load-displacement results of the analysis are presented.

3.2. PROGRESSIVE DAMAGE COHESIVE BEM ANALYSIS

For the progressive damage cohesive analysis, the vertical displacement imposed in the substrate by the upper roller was 1.6 mm, which was applied in 100 load steps for nonlinear analysis purposes. At each load step, the

same convergence criteria adopted in [9] were used. Four BEM models with different interface refinements (4, 8, 16, and 32 elements per mm) were analyzed. The four BEM models resulted, respectively, in 422, 622, 1022, and 1822 linear elements, with 256, 356, 556, and 956 to discretize the substrate´s boundaries and 166, 266, 466, and 866 to discretize the adhesive´s boundaries. The load-displacement results of the analysis are next presented together with snapshots of the deformed specimen configurations.

3.3. RESULTS

The load-displacement results are illustrated in Figure 5. In Fig. 5 (left), the load-displacement results obtained with the LEFP analysis and with the progressive damage cohesive analysis of the most refined model were compared with the reference response from [2]. Fig. 5 (right) shows the convergence of the load-displacement results for progressive damage cohesive analysis with respect to interface discretization refinements: 4, 8, 16, and 32 elements per mm.
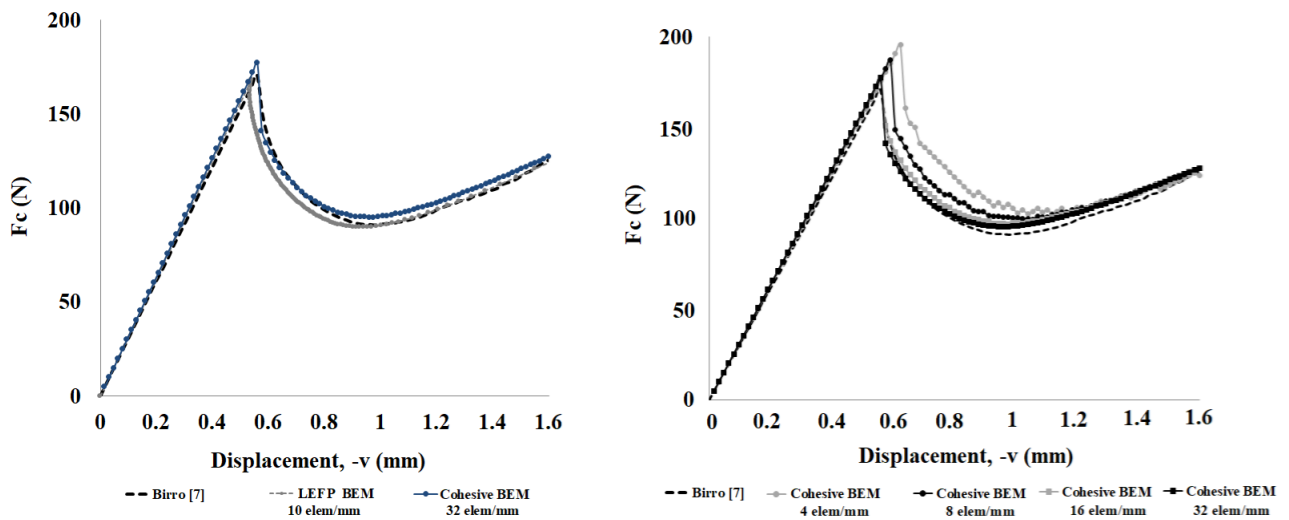
Figure 5. Load-displacement results obtained with the BEM analysis.

From Fig. 5 it is possible to observe that both the coupled energy stress criterion analysis and the progressive damage cohesive analysis were able to produce results with excellent agreement with respect to the results from [2]. As it is based on Linear Elastic Fracture Mechanics assumptions, the LEFP results are a lower bound for the structural response while the progressive damage cohesive results appear as an upper bound for the structural response (see Fig. 5 left). The upper bound convergence of the progressive damage cohesive results can be confirmed from Fig. 5 right.

4. CONCLUSIONS

This paper introduces a novel methodology for determining the load-displacement relationship of adhesive-adherent joints using a LEFP. Unlike traditional Finite Element Method (FEM) approaches, this methodology employs Boundary Element Method (BEM) for modeling a three-point bending test, offering several advantages such as the elimination of domain elements and improved accuracy in computing displacements and stresses. Load-displacement diagrams were obtained through two techniques: analysis based on the LEFP and progressive damage cohesive analysis, both evaluated with varying mesh refinements. Results demonstrate that the proposed methodology yields excellent agreement with existing literature, affirming its efficacy for analyzing failure in adhesive-adherent interfaces. Moreover, this method proves to be particularly suitable due to its ability to deliver precise results using simplified numerical models, surpassing conventional FEM-based approaches.

5. Declaration of Competing Interest

The authors declare no conflict of interest.

6. REFERENCES

[1]   ISO 14679:1997. ISO n.d. https://www.iso.org/standard/25226.html (accessed February 23, 2024).

[2]   Birro TV. Prediction of adhesive failure of metallic bonded joints. Thesis. Université de Toulouse, 2021.

[3]   Aliabadi MH. The boundary element method: Applications in solids and structures. John Wiley & Sons Inc, 2002.

[4]   P. Cornetti, V. Mantic, A. Carpinteri, Finite fracture mechanics at elastic interfaces, International Journal of Solids and Structures 49 (7) (2012) 1022 – 1032.

[5]   X. Wu, R. Jenson, Stress-function variational method for stress analysis of bonded joints under mechanical and thermal loads, International Journal of Engineering Science 49 (3) (2011) 279–294

[6]   Barros S. Modèle d'interface pour la simulation du comportement des assemblages collés. Thesis. Université de Versailles Saint-Quentin-en-Yvelines, 2005.

[7]   Alfano G, Crisfield MA. Finite element interface models for the delamination analysis of laminated composites: mechanical and computational issues. International Journal for Numerical Methods in Engineering 2001;50:1701–36. https://doi.org/10.1002/nme.93.

[8]   Martin E, Vandellos T, Leguillon D, Carrère N. Initiation of edge debonding: coupled criterion versus cohesive zone model. International Journal of Fracture 2016;199:157–68. https://doi.org/10.1007/s10704-016-0101-2.

[9]   Cordeiro SGF, Daumas GO, Monteiro FAC. A general DBEM for mixed-mode cohesive crack problems. Theoretical and Applied Fracture Mechanics 2024;130:104249. https://doi.org/10.1016/j.tafmec.2023.104249.

[10]   Blandford GE, Ingraffea RA, Liggett JA. Two-dimensional stress intensity factor computations using the boundary element method. International Journal for Numerical Methods in Engineering 1981;17:387-404. https://doi.org/10.1002/nme.1620170308.

ANALYSIS OF FRETTING PROBLEMS IN ANISOTROPIC MATERIALS USING THE BOUNDARY ELEMENT METHOD

Leonardo B. e Silva[(a), *], Eder L. de Albuquerque[(b)], Thiago de C. R. Doca[(c)], Lucas S. Campos[(d)]

(a) 0000-0002-9540-7932 (University of Brasília – Brazil)
(b) 0000-0002-7154-6946 (University of Brasília – Brazil)
(c) 0000-0001-5376-5590 (University of Brasília – Brazil)
(d) 0000-0002-9734-4613 (Federal University of Espírito Santo – Brazil)

* Corresponding author: leobsilvaa@gmail.com

Abstract: The primary aim of this research is to employ an algorithm enabling the assessment of frictional contact issues through the Boundary Element Method (BEM), particularly focusing on fretting conditions concerning anisotropic materials. To accomplish this objective, a boundary element formulation tailored for two-dimensional elastic bodies was devised, considering the displacement constraints and force equilibrium to model the mechanical interaction between contacting bodies. This entails tackling a nonlinear problem, as the initial contact area is unknown and evolves during loading. The approach was validated by solving a flat specimen problem, and the numerical findings were juxtaposed against analytical solutions, revealing satisfactory agreement between them. A known fretting problem with isotropic materials was also solved in order to assess the ability to tackle problems with cyclic loads.

1. INTRODUCTION

Fretting fatigue by [1] is a failure process observed in contact surfaces under cyclical loading. It is regarded as the main cause of failure in several mechanical systems (i.e., dovetail joints, wire cables, threaded pipe connections, bolted and riveted joints) and can represent a considerable cost in terms of a country's GNP by [2]. Moreover, high strength aluminium and titanium are often the material of choice in components susceptible to fretting fatigue. They are costly and difficult to machine. Therefore, cost-efficient methods for the life estimation of components are paramount.

Although finite elements are the most used numerical method for the analysis of fretting problems, Boundary Element based approaches have some interesting features that should be taken into account. An analysis using BEM requires less cost associated with the discretization of the problem. Although the contact problem is a non-linear problem, this non-linearity is due to the lack of prior knowledge of the boundary conditions, thus not being an impediment to obtaining fundamental solutions, a necessary step in the development of the BEM formulations.

The anisotropic behaviour of materials increases the number of variables in structural analysis. Due to this, analytical solutions are limited to simple problems. Numerical methods are necessary for the analysis of complex structures.

The use of BEM for the solution of problems with anisotropic materials has become more common in recent years. As anisotropy increases the number of material elastic constants, difficulties in modelling arise in the development of the numerical formulations. Particularly, in the boundary element formulation, the larger number of variables means far more difficulty in deriving fundamental solutions. This aspect is evident in the

literature. The number of references in which the boundary element method is applied to anisotropic structure is significantly smaller than the number for isotropic structures.

It is necessary to highlight some of the advantages of using the Boundary Element Method (BEM) to evaluate contact systems, in relation to other numerical techniques, such as the Finite Element Method (FEM). The main advantages that should be highlighted is the decrease in an order the dimension of the proposed problem, being possible to notice that there is a decrease in the amount of input data, in the processing time and in the storage of processed information, guaranteeing less computational effort.

2. METHODOLOGY

2.1. Boundary element method formulation for 2D anisotropic elasticity

The boundary integral equation for 2-D anisotropic problem is given by [3]:

$$c_{ij}(\mathbf{z_o})u_i(\mathbf{z_o}) + \oint_G T_{ij}(\mathbf{z},\mathbf{z_o})u_j(\mathbf{z})d G(\mathbf{z}) = \oint_G U_{ij}(\mathbf{z},\mathbf{z_o})t_j(\mathbf{z})d G(\mathbf{z}) \quad " \ z \ \grave{o} \ G \tag{1}$$

where the coefficient $c_{ij}(\mathbf{z_o})$ is given by $d_{ij} + A_{ij}(\mathbf{z_0})$, in which d_{ij} is the Kronecker's delta. At a smooth boundary point, $c_{ij}(z_o) = d_{ij} / 2$, at an internal point, $c_{ij}(z_o) = 1$. Fundamental solutions for displacement $U_{ij}(\mathbf{z},\mathbf{z_o})$ and traction $T_{ij}(\mathbf{z},\mathbf{z_o})$ are:

$$U_{ij}(\mathbf{z},\mathbf{z_o}) = 2\hat{A}[q_{i1}A_{j1}\log(z_{o_1} - z_1) + q_{i2}A_{j2}\log(z_{o_2} - z_2)] \tag{2}$$

and,

$$T_{ij}(\mathbf{z},\mathbf{z_o}) = 2\hat{A}\left[\frac{g_{j1}(m_1 n_1 - n_2)A_{i1}}{(z_{o_1} - z_1)} + \frac{g_{i2}(m_2 n_1 - n_2)A_{j2}}{(z_{o_2} - z_2)}\right] \tag{3}$$

where the terms q_{ij}, g_{ji} and A_{ij} are complex material constants, $\hat{A}$ stands for the real part of a complex number and $\log$ is the natural logarithm. Constants m_k are complex numbers that are the roots of a characteristic polynomial as given by [3,4]. The field point $\mathbf{z}$ and the source point $\mathbf{z_o}$ are written in complex form as:

$$\mathbf{z} = \begin{Bmatrix} z_1 \\ z_2 \end{Bmatrix} = \begin{Bmatrix} x_1 + m_1 x_2 \\ x_1 + m_2 x_2 \end{Bmatrix} \tag{4}$$

and,

$$\mathbf{z}_o = \begin{Bmatrix} z_{o_1} \\ z_{o_2} \end{Bmatrix} = \begin{Bmatrix} x_{o_1} + m_1 x_{o_2} \\ x_{o_1} + m_2 x_{o_2} \end{Bmatrix} \tag{5}$$

2.2. Contact formulation

A classical depiction of a contact process is given in Figure 1. It encompasses two basic stages: 1) the evaluation of the normal gap, g, between the contacting surfaces; and 2) the calculation of the contact pressure, l_n, whenever the normal gap is closed.
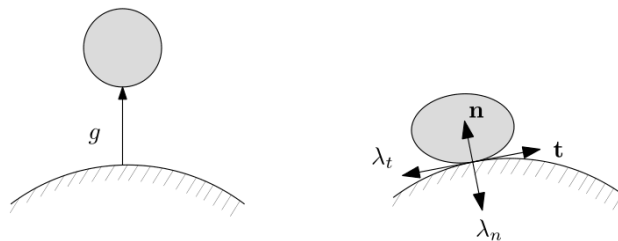
Figure 1. Bodies separated by an initial gap (left) and establishment of a contact condition (right) [5].

This relationship is often denoted as the Kuhn-Karush-Tucker condition:

$$
\begin{aligned}
g &\geq 0, \\
l_n &\leq 0, \\
l_n g &= 0.
\end{aligned}
\tag{6}
$$

Moreover, the contact conditions can be thought as constraints that must be satisfied for each node-pair within the contact zone. Therefore, they can be defined into three states: separated, stick and slip.

Table 1. lists the relationships that represent the three modes of contact previously stated, where t_n and t_t are the normal and tangential tractions, u_n and u_t are the normal and tangential displacements (expressed in local coordinates), respectively.

Table 1. Set of traction/displacement relations for the contact conditions.

Separated	Stick	Slip
$t_t^a - t_t^b = 0$	$t_t^a - t_t^b = 0$	$t_t^a - t_t^b = 0$
$t_n^a - t_n^b = 0$	$t_n^a - t_n^b = 0$	$t_n^a - t_n^b = 0$
$t_t^a = 0$	$u_t^a - u_t^b = 0$	$t_t^a \pm m t_n^a = 0$
$t_n^a = 0$	$u_n^a - u_n^b = g^{ab}$	$u_n^a - u_n^b = g^{ab}$

It is important to remark that state of the node-pairs is continuously updated within the iterative procedure. The proposed formulation addresses frictional contact in a two-dimensional setting. The solids are regarded as homogeneous isotropic linear elastic bodies. For instance, let us consider the bodies A and B so that their deformations can be described by two coupled integral equations, one for each body, as follows,

$$
\begin{aligned}
c_{ij}^A u_j^A + \sum_{n=1}^{N_A} H_{ij}^A u_j^A &= \sum_{n=1}^{NA} G_{ij}^A t_j^A \\
c_{ij}^B u_j^B + \sum_{n=1}^{N_B} H_{ij}^B u_j^B &= \sum_{n=1}^{NB} G_{ij}^B t_j^B
\end{aligned}
\tag{7}
$$

where N_A and N_B are the number of collocation points of bodies A and B, respectively. Therefore, two sets of linear equations are obtained and their matrix form, can be written such that,

$$
[H]\{u\}^g = [G]\{t\}^g , g = A, B
\tag{8}
$$

3. NUMERICAL APPLICATION

A depiction of the loading scheme is shown in Figure 2. Firstly, a normal load is applied. Then, this load is maintained constant while a tangential load is cyclically applied. In Figure 2, point A is when the normal load P reaches its final value, whereas point B is the moment when the maximum tangential load is applied. Afterwards, tangential load starts to decrease, passing through zero at point C and decreasing further. Point D is when the tangential load is in its minimum value and, finally, point E is when the tangential load reaches zero again.
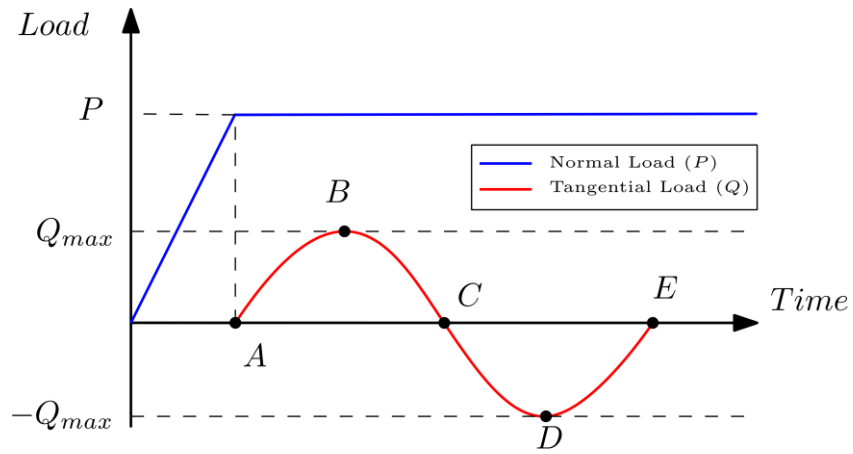
Figure 2. Loading scheme containing five steps (A-E) [5].

3.1. Bulk stress problem using isotropic material

In this section, a numerical application of the developed formulation will be presented. An isotropic material was used for validation. The bulk stress problem geometry is shown in Figure 3. In this problem, tangential and bulk loads are in phase with each other. Geometry, material and load properties are in Table 2.

Table 2. Bulk stress problem – geometric and material properties.

Property	Symbol	Value
Radius	R	70 mm
Width	w	6.5 mm
Young's Modulus	E	73.4 GPa
Poisson's ratio	n	0.33
Friction coefficient	f	0.3
Pressure	P	100 N/mm
Tangential load	Q	15 N/mm
Bulk load	B	15 N/mm
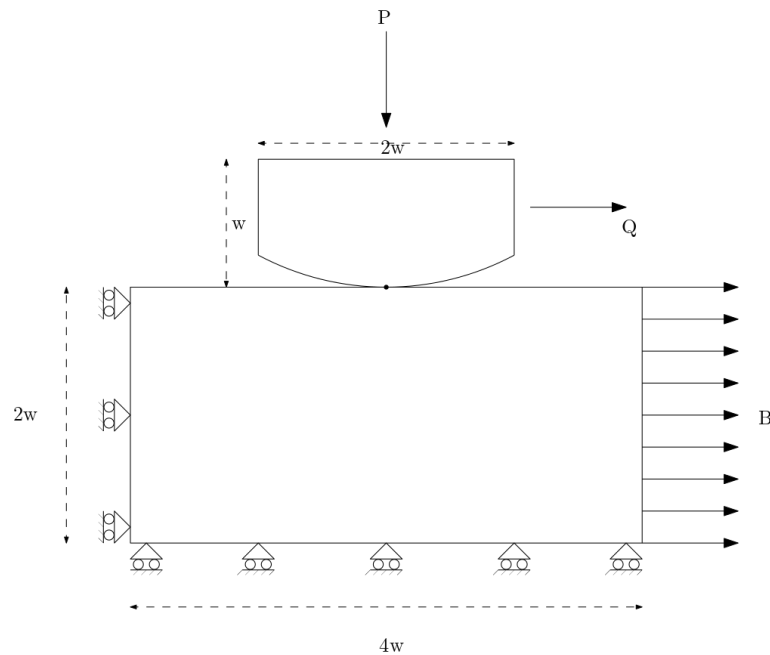
Figure 3. Bulk stress problem geometry [5].

This configuration has been chosen because it is commonly used for fretting fatigue experiments, according to by [5]. Figure 4 shows the pressure distribution profile on the surface of contact for the condition where there is only the presence of normal traction. In Figure 5 presents the result of a shear traction distribution in presence of the Bulk load.
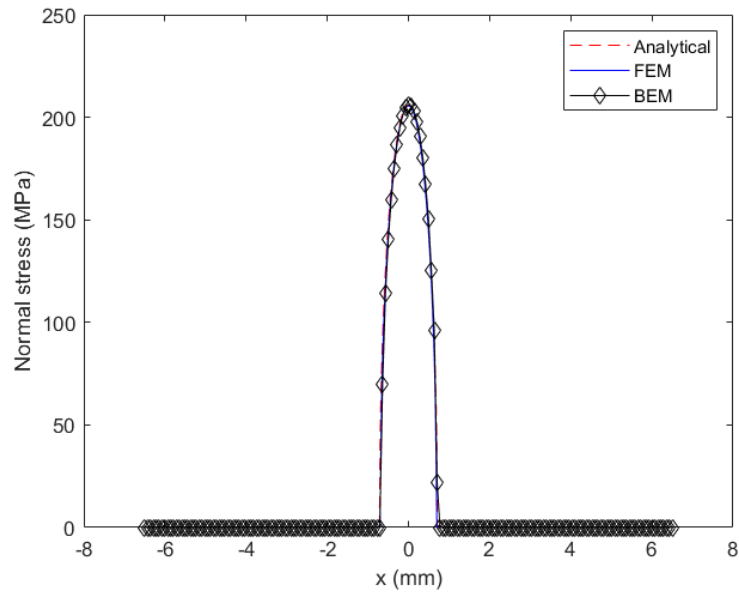
Figure 4. Contact pressure distribution.
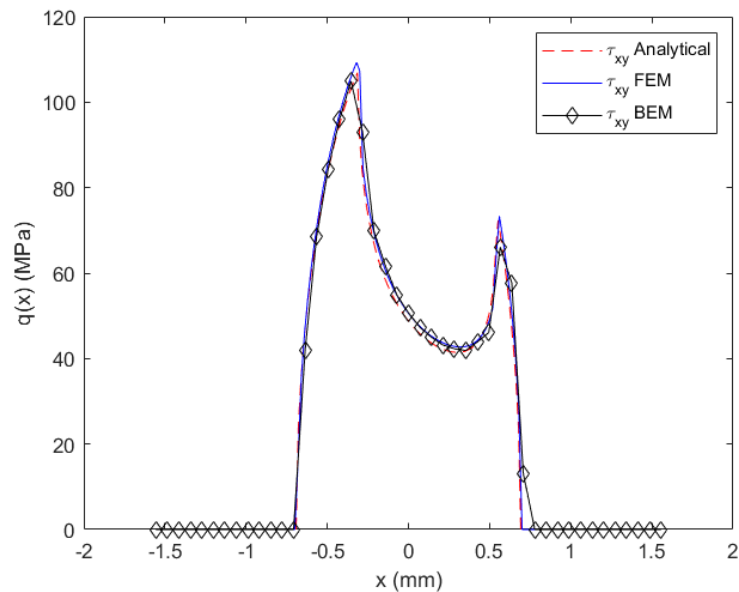
Figure 5. Shear traction distribution in presence of the Bulk load.

A comparison was made between the analytical and numerical (BEM, FEM). It was possible to show that there was good agreement in the results.

3.2. Contact problem of orthotropic material

In this section, the article [6] was used as validation for contact problem using BEM. The example used is a flat-ended punch in contact with an elastic foundation, using the same geometry and loading.

Both geometries are made up of an orthotropic material whose properties, expressed by the elastic stiffness C_{ij}, are defined as:

$$C_{11} = 147.34\,GPa,\ C_{22} = C_{33} = 10.78\,GPa,\ C_{23} = 3.32\,GPa,$$
$$C_{12} = C_{13} = 4.23\,GPa,\ C_{44} = C_{55} = C_{66} = 4.1\,GPa. \tag{9}$$

In Figure 6, we compare the normalized tangential tension τ_{nt} and the normalized normal tension σ_n for different friction conditions μ.
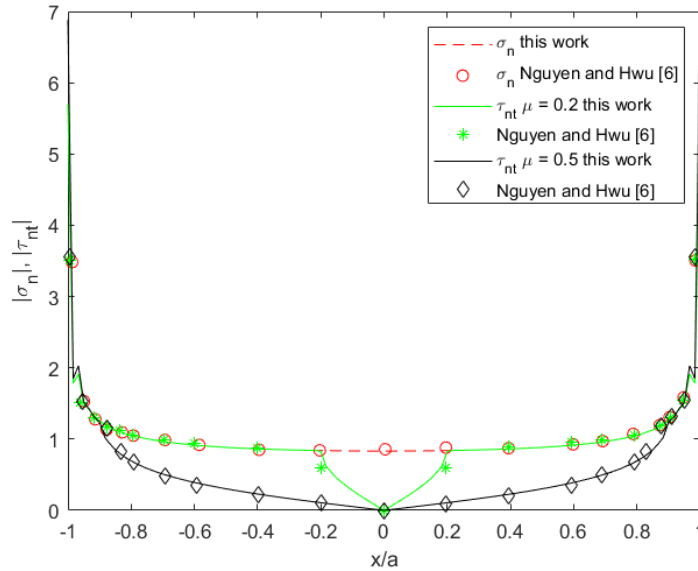
Figure 6. Validation tractions under the flat-ended elastic punch.

With the results obtained, it is possible to observe that when the friction coefficient increases, the stick zone increases and slip zone decreases. The results obtained showed good agreement with the data from the article [6].

4. CONCLUSIONS

In this paper, BEM and FEM are compared in elastic contact problems, these methods are compared with analytical solution when available.

In the example using isotropic material, it was possible to compare both methods and the analytical solution. With this, we validated the simulation for this material, showing good agreement.

In the following example, the results were validated using orthotropic material through comparison with the article [6].

In conclusion, BEM is fitting for modelling elastic contact problems and fretting fatigue. This method proved to be an interesting alternative to commercial finite element software. Therefore, the next step is to use an anisotropic material and refine the meshes to obtain comparison of both methods.

4.1. Declaration of Competing Interest

The authors declare that they have no known competing financial interests or personal relationships that could have appeared to influence the work reported in this paper.

4.2. Acknowledgements

5. REFERENCES

[1]   Mohammad Sheikh and Miller {K J} and Brown, {M W} and Fernando, {U S}. Fretting Fatigue. United Kingdom: Professional Engineering Publishing; 1994.
[2]   Reed, RP. The Economic Effects of Fracture in the United States. U.S. Dept. of Commerce. 1983.

[3]   Sollero P, Aliabadi MH. Fracture mechanics analysis of anisotropic plates by the boundary element method. Int J Fract 1993;64:269–84. https://doi.org/10.1007/BF00017845.

[4]   S. G. Lekhnitskii. Theory of Elasticity of an Anisotropic Body. 1981.

[5]   Loyola FM de, Doca T, Campos LS, Trevelyan J, Albuquerque ÉL de. Analysis of 2D contact problems under cyclic loads using IGABEM with Bézier decomposition. Eng Anal Bound Elem 2022;139:246–63. https://doi.org/10.1016/j.enganabound.2022.03.017.

[6]   Nguyen VT, Hwu C. Boundary element method for two-dimensional frictional contact problems of anisotropic elastic solids. Eng Anal Bound Elem 2019;108:49–59. https://doi.org/10.1016/j.enganabound.2019.08.010.

3 Analysis of wood and natural fiber composites

Organized and edited by

Sandra Maria da Luz
&
Carla Tatiana Mota Anflor

TURNING FOREST WASTE INTO DURABLE MATERIALS: DEVELOPMENT AND EVALUATION OF WOOD-PLASTIC COMPOSITES

Paula G. Dornelles[(a)], Rossana C. da Rosa[(b)], Annie K.L Cavalcante [(c)], Bento B. Viana [(d)], Cláudio H.S. Del Menezzi [(e)]

(a) 0009-0002-1767-504X (University of Brasília – Brazil)
(b) 0000-0002-5754-7918 (University of Brasília – Brazil)
(c) 0000-0002-1838-1054 (University of Brasília – Brazil)
(d) 0000-0003-2719-5373 (University of Brasília – Brazil)
(e) 0000-0003-3369-2392 (University of Brasília – Brazil)
*Corresponding author: paulagdornelles@gmail.com

Abstract: Only a small fraction of plastics produced worldwide are recycled, resulting in several negative environmental impacts. A promising solution is the production of wood-plastic composites, which consist of a combination of natural fiber waste and a thermoplastic polymer matrix. This study explores the manufacture of these composites using Pine waste and polypropylene as a polymeric matrix. Analyses were performed to evaluate the properties such as longitudinal density profile and rheological information such as conservation modulus (E'), loss modulus (E"), and damping factor (tan d) of the composites. The findings showed that as more lignocellulosic material was added, the composite became denser and stiffer, exhibiting higher viscosity and reduced elasticity. In conclusion, WPCs offer a promising sustainable material alternative by reducing waste, conserving natural resources, and enhancing production sustainability. This study provides key insights into material development across applications and advances knowledge in the field.

1. INTRODUCTION

Wood-plastic composites (WPC) are an innovative class of composites that employ wood and a thermoplastic polymer matrix. These composites are manufactured through processes such as extrusion, injection molding, or through compression molding, which combine thermoplastic polymers and natural fibers [1–3]. WPCs have gained popularity in recent years due to their high durability, low maintenance requirements, and environmental compatibility compared with traditional wood products [5]. A significant factor in the growing demand for wood-plastic composites is the need to reuse waste generated by the wood industry [3,6,7].

The thermoplastic polymer component in WPCs provides hardness, while the wood component acts as a reinforcement to enhance the resistance and rigidity of the composite [4]. The moldability of plastics allows WPCs to be used in different areas, such as internal and external construction materials, pallets, decks, fences, and even in automotive components such as door coverings or seat backs [6]. In addition to these uses, this material can also be used in the furniture industry for decorative purposes or for small objects such as food containers [8–10].

Multicomponent WPCs are influenced by several factors that affect their service life. Among these, thermal stability during processing and usage is a crucial factor. The thermal properties of WPCs encompass various heat- and temperature-related characteristics [11]. Understanding the kinetics of thermal degradation can be a valuable tool in the selection of materials of natural origin to be used as reinforcement in conventional polymers. It is important to highlight that both synthetic and natural materials are often subject to fires, therefore, information on thermal degradation kinetics can provide more accurate data on the thermal stability

of different materials [12].

The use of forestry waste as a raw material in WPCs offers the potential to reuse low-value waste into high-quality products, preserve natural resources, and improve the sustainability of the production process. In view of the above, the objective of this study is to produce and characterize wood-plastic composites produced from pine wood waste and polypropylene (PP) polymer matrix.

2. METHODOLOGY

To manufacture the composites, pine waste and a polypropylene (PP) polymer matrix were used. Pine residue with a particle size of 40 mesh and an average moisture content of 5.77% was used. WPCs were produced with two compositions: (i) 25% waste + 75% polypropylene (WPP – 25/75) and (ii) 60% waste + 40% polypropylene (WPP – 60/40).

The production of composites occurred in three stages (Figure 1). In the first stage, pellets of plastic with a length of 0.5 mm were produced and then mixed with the waste. In the second stage, the plastic waste mixture was extruded using a co-rotating twin-screw extruder (Thermo Scientific™ Process 11 Parallel Twin-Screw Extruder). Extrusion of the composite was performed at a temperature of 195 °C in all heating zones, a screw speed of 100 RPM, and a casting pressure of 9 bar. The third stage was the preparation of the test specimens using an injection molding machine with a piston molding system (HAAKE™ MiniJet Pro) at 250 °C and 200 bar injection pressure.
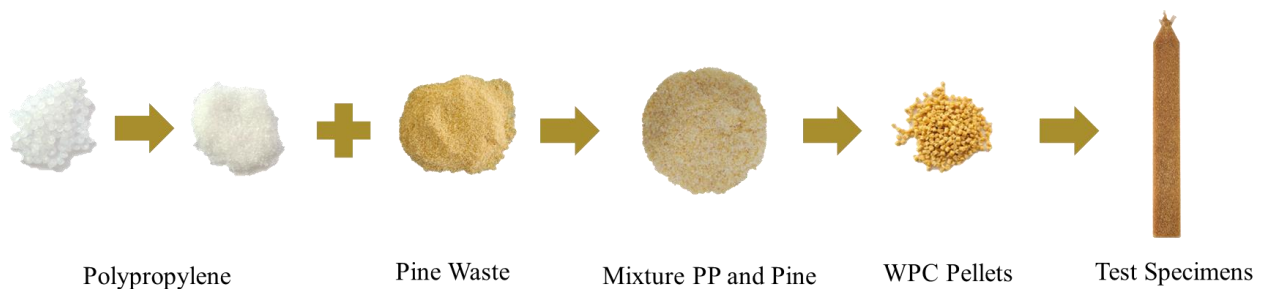
Figure 1. Composites manufacture steps.

To determine the longitudinal density profile, samples measuring 35 x 10 x 3 mm were used. An X-ray microdensitometer (Grecon Dax 6000) was used for the analysis.

The rheological properties of the composites were determined by dynamic mechanical analysis using DMA 242 E Netzsch equipment. The conservation modulus (E'), loss modulus (E"), and damping factor (tan d) were determined under two conditions: (i) isothermal with a temperature of 30 °C for 30 min and (ii) with temperature variation from 30 °C to 130 °C for 45 min.

3. RESULTS AND DISCUSSION

3.1. Longitudinal Density Profile

Figure 2 shows the longitudinal density profiles of each composite. The longitudinal density profile was used depending on the dimensions of the samples used for the test. The average density of the composite profiles varied between 968 kg/m^3 for the WPP-25/75 composite and 1071 kg/m^3 for the WPP-60/40. The analysis demonstrated that there were no significant variations in density along the length of the composites, indicating good homogenization between the residue and the polypropylene matrix.
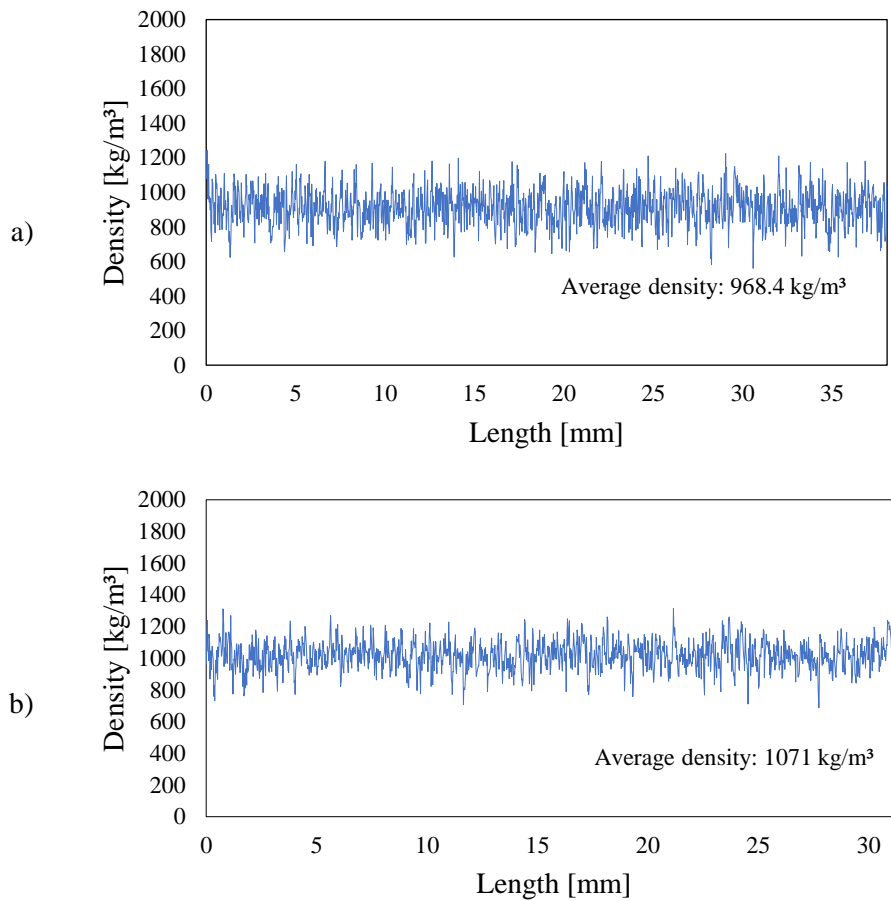
Figure 2. Longitudinal microdensity of plastic-waste composites: a) WPP – 25/75; b) WPP – 60/40

3.2.   Dynamic Mechanical Analysis

3.2.1.   Isothermal

The conservation modulus (E') is a measure of the elasticity of the material, indicating its ability to withstand the applied load. The loss modulus or viscous modulus (E") expresses the energy lost due to internal friction. The damping factor (tan d) is given by the ratio between loss and conservation modulus, which is an indicator of the efficiency with which the material loses energy due to molecular rearrangements and internal friction [13]. Figure 3 shows the viscoelastic response of the two composites to sinusoidal loading at 1 Hz.
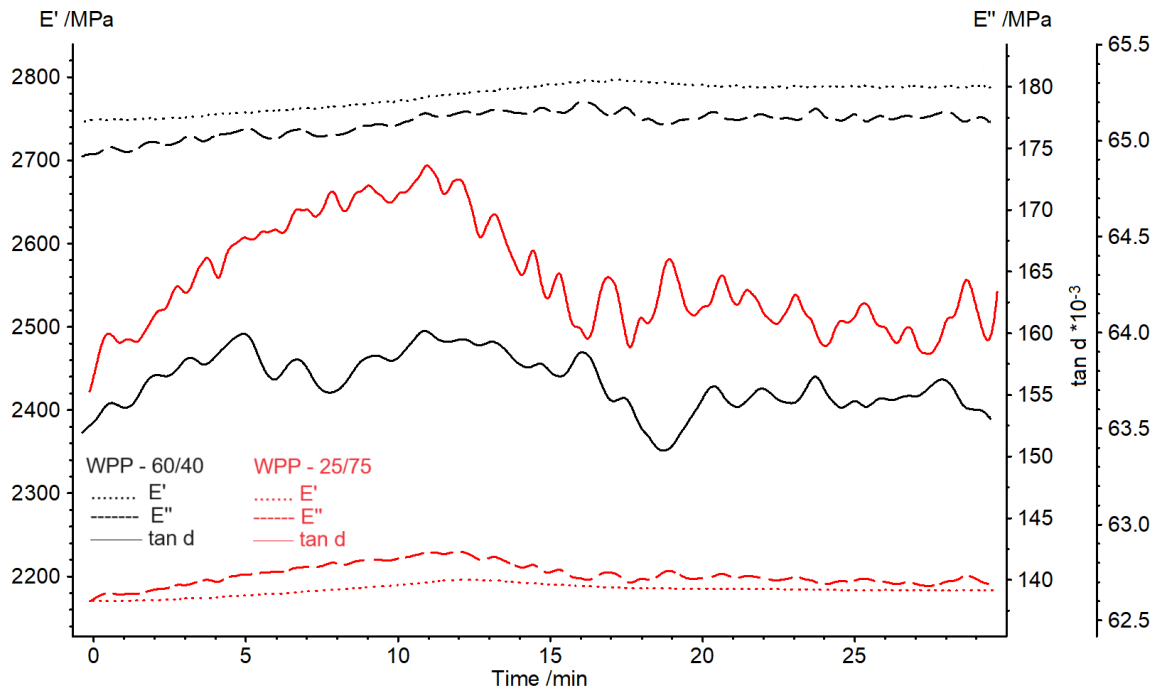
Figure 3. Variation of the conservation modulus (E'), Loss modulus (E”), and damping factor (tan d) in a dynamic test of three-point bending under isothermal conditions of 30°C for 30 min with a loading frequency of 1 Hz.

The conservation modulus of WPP-60/40 (2740 – 2780 MPa) was approximately 21% higher than that of WPP-25/75 (≈2160 MPa), indicating that the addition of wood residue to the composite provides a stiffer and more rigid material with greater ability to recover its original shape after removing the load. A similar behavior was observed for loss values (E”), the WPP-60/40 composite presented a loss modulus of 175 MPa while the WPP-25/75 composite values were around 140 MPa, indicating that the addition of wood in the composite implies a more viscous material compared to a composite with lower wood content in its composition. The damping factor is an expression of the energy dissipation of a material under cyclic loading, which is influenced by the interface and adhesion between the fibers and the polymer matrix [14]. In relation to tan d, the WPP-25/75 composite showed an increasing behavior in the first 10 min of testing, starting at 0.0637 with a peak at 0.0648 around 10 min into the test and stabilizing at around 0.0640 during the final 15 min of testing. The WPP-60/40 composite presented constant values of approximately 0.0635.

3.2.2. Dynamic

Figure 4 shows the results of the composites subjected to temperature variations from 30 °C to 130 °C. It is possible to observe that the resistance of the composites is affected by temperature variation. The WPP-60/40 composite at the beginning of the test (T = 31ºC) presents E' values of 3112 MPa, whereas the WPP-25/75 composite has a conservation modulus of 1732 MPa. At the end of the test (T = 130 °C), the composites showed E' values of 700 MPa (WPP-60/40) and 291 MPa (WPP-25/75), respectively, a reduction of approximately 77% and 83%. The reduction in the conservation modulus due to the increase in temperature is the result of the increase in the mobility of the polypropylene segmental chains generated by heat [15,16]. This increase in stiffness due to the increase in the percentage of lignocellulosic waste was observed in a dynamic test [15].
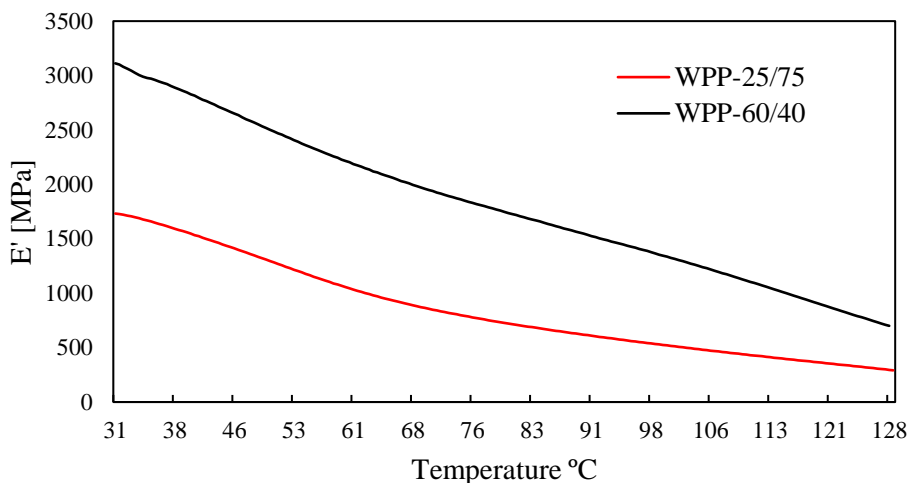
Figure 4. Preservation modulus (E') of the dynamic test.

Figure 5 presents the tan d curves of wood-plastic composites. The highest tan d values were found at 130ºC, being 0.20 for the WPP-60/40 composite and 0.13 for the WPP-25/75. The addition of wood waste increased the tan d value by approximately 54%. According to Ambrósio et al. [17], the increase in tan d may be related to friction between particles in agglomerates within the composite and/or friction between the wood and the polymeric matrix when there is no interfacial adhesion. The lower the tan, the more elastic the material, and therefore less viscous.
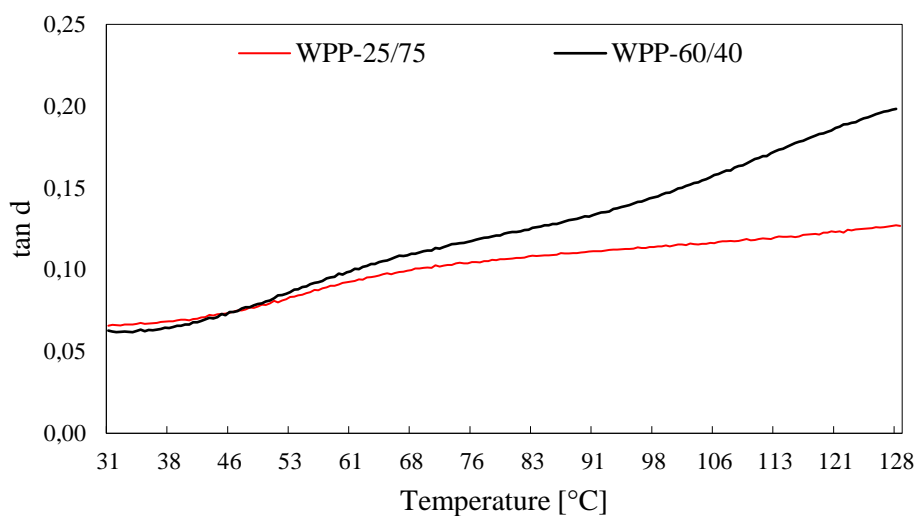
Figure 5. Tan d curves of wood-plastic composites

4. CONCLUSIONS

Wood-plastic composites are a class of materials developed to meet the need for more sustainable, environmentally friendly, and durable materials. They are made from a combination of wood fibers and thermoplastic polymers, resulting in a material that has both the natural appearance of wood and the durability and ease of use of plastic.

The findings revealed a direct correlation: as the proportion of lignocellulosic material increased, so did the density and rigidity of the composite, along with heightened viscosity and decreased elasticity. Using waste wood and polypropylene as composite constituents presents an opportunity to reduce waste volume, preserve natural resources, and enhance the sustainability of the manufacturing process.

This study will contribute to the growing body of knowledge on the production and properties of composites made from waste, providing valuable information for the development of sustainable materials.

4.1. Declaration of Competing Interest

The authors declare no conflict of interest.

4.2. Acknowledgements

5. REFERENCES

[1]   Chan CM, Vandi L-J, Pratt S, Halley P, Richardson D, Werker A, et al. Composites of Wood and Biodegradable Thermoplastics: A Review. Polymer Reviews 2018; 58:444–94. https://doi.org/10.1080/15583724.2017.1380039.

[2]   Correa CA, Fonseca CNP, Neves S, Razzino CA, Hage, Jr. E. Compósitos termoplásticos com madeira. Polímeros 2003; 13:154–65. https://doi.org/10.1590/S0104-14282003000300005.

[3]   Flores-Hernández MÁ, Torres-Rendón JG, Jiménez-Amezcua RM, Lomelí-Ramírez MG, Fuentes-Talavera FJ, Silva-Guzmán JA, et al. Studies on Mechanical Performance of Wood-Plastic Composites: Polystyrene-Eucalyptus globulus Labill. Bioresources 2017; 12:6392–404. https://doi.org/10.15376/biores.12.3.6392-6404.

[4]   Keskisaari A, Kärki T. The use of waste materials in wood-plastic composites and their impact on the profitability of the product. Resour Conserv Recycl 2018; 134:257–61. https://doi.org/10.1016/j.resconrec.2018.03.023.

[5]   Basalp D, Tihminlioglu F, Sofuoglu SC, Inal F, Sofuoglu A. Utilization of Municipal Plastic and Wood Waste in Industrial Manufacturing of Wood Plastic Composites. Waste Biomass Valorization 2020; 11:5419–30. https://doi.org/10.1007/s12649-020-00986-7.

[6]   Wechsler A, Hiziroglu S. Some of the properties of wood-plastic composites. Build Environ 2007; 42:2637–44. https://doi.org/10.1016/j.buildenv.2006.06.018.

[7]   Chowdhury FI, Islam J, Haldar SS, Zabed HM. Recycled wood plastic biocomposites and development of new materials. Recycled Plastic Biocomposites, Elsevier; 2022, p. 119–45. https://doi.org/10.1016/B978-0-323-88653-6.00011-0.

[8]   Chaharmahali M, Mirbagheri J, Tajvidi M, Najafi SK, Mirbagheri Y. Mechanical and physical properties of wood-plastic composite panels. Journal of Reinforced Plastics and Composites 2010; 29:310–9. https://doi.org/10.1177/0731684408093877.

[9]   Moritzer E, Hopp M. Bonding of wood-plastic composites (WPC)—material and surface modification for special applications. Welding in the World 2017; 61:1029–38. https://doi.org/10.1007/s40194-017-0487-0.

[10]   Feng L, Xie W. Analysis of factors affecting creep of wood– plastic composites. Forests 2021;12. https://doi.org/10.3390/f12091146.

[11]   Guo Y, Zhu S, Chen Y, Li D. Thermal Properties of Wood-Plastic Composites with Different Compositions. Materials 2019; 12:881. https://doi.org/10.3390/ma12060881.

[12]   Bianchi O, Dal Castel C, Oliveira RVB, Bertuoli PT, Hillig E. Avaliação da degradação não-isotérmica de madeira através de termogravimetria-TGA. Polímeros 2010; 20:395–400. https://doi.org/10.1590/S0104-14282010005000060.

[13]   Menard   KP.   Dynamic   Mechanical   Analysis.   CRC   Press;   2008. https://doi.org/10.1201/9781420053135.

[14]   Stanciu MD, Teodorescu Draghicescu H, Tamas F, Terciu OM. Mechanical and Rheological Behaviour of Composites Reinforced with Natural Fibres. Polymers (Basel) 2020; 12:1402. https://doi.org/10.3390/polym12061402.

[15]   Shaikh H, Alothman OY, Alshammari BA, Jawaid M. Dynamic and thermo-mechanical properties of polypropylene reinforced with date palm nano filler. J King Saud Univ Sci 2023; 35:102561. https://doi.org/10.1016/j.jksus.2023.102561.

[16]   Núñez-Decap M, Wechsler-Pizarro A, Vidal-Vega M. Mechanical, physical, thermal and morphological properties of polypropylene composite materials developed with particles of peach and cherry stones.   Sustainable   Materials   and   Technologies   2021;   29:e00300. https://doi.org/10.1016/j.susmat.2021.e00300.

[17]   Ambrósio JD, Sônego M, Staffa LH, Chinelatto MA, Costa LC. Characterization of flexible Poly (vinyl   butyral)/wood   flour   composites.   Compos   B   Eng   2019;   175:107118. https://doi.org/10.1016/j.compositesb.2019.107118.

EVALUATION OF BIODEGRADABLE SANDWICH COMPOSITES WITH HONEYCOMB MADE ON A 3D PRINTER

G Garcia del Pino[a]*, A Bezazi[b], H Boumediri[c], AC Kieling[d], JCM Neto[e], AR Torres[f], MD dos Santos[g], SD Garcia[h], DL Dantas[i], CG Costa[j], TH Panzera[k]

[a] 0000-0003-0754-2390 (State University of Amazonas - Brazil)
[b] 0000-0002-4461-6689 (Universty of Guelma - Algeria)
[c] 0000-0002-9578-0948 (Universty of Guelma - Algeria)
[d] 0000-0002-0552-954X (State University of Amazonas - Brazil)
[e] 0000-0003-1155-0027 (State University of Amazonas - Brazil)
[f] 0000-0001-5138-2932 (State University of Amazonas - Brazil)
[g] 0000-0002-4356-491X (State University of Amazonas - Brazil)
[h] 0000-0002-8316-0012 (State University of Amazonas - Brazil)
[I] 0009-0005-8330-0301 (State University of Amazonas - Brazil)
[J] 0009-0001-4503-5800 (State University of Amazonas - Brazil)
[K] 0000-0001-7091-456X (Federal University of São João del-Rei – Brazil)
* Corresponding author: gpino@uea.edu.br

Abstract: In modern society, polymer composites are widely used due to their high strength/weight ratio, among other properties. In recent times due to environmental issues and higher costs, most industries and engineering sectors are trying to reduce the use of synthetic fibers by using natural fibers or lignocellulosic fibers. New composite materials using renewable materials and additive manufacturing enable better development of high-performance materials for various sectors. The objective of the work was to determine the behavior of a fully biodegradable sandwich composite using sheets of Sisal fibers in a Castor Oil Polyurethane Matrix and 3D printed PLA honeycomb.

Firstly, a study was carried out to determine the best alkaline treatment for the Sisal fibers within sheets are made. The best alkaline treatment found was the concentration of 10% sodium hydroxide and 4 hours of immersion of the fiber in dissolution. To check treatment effectiveness, fibers were also observed by SEM and DRX. Subsequently, the sandwich composites were manufactured, in which sheets are produced with Castor Oil Polyurethane resin and treated sisal fibers, also using a 10% w of fibers, and cores are made of PLA and PETG filaments with honeycomb structure for comparison. Bending tests demonstrated that the sandwich composites performed better with PETG. In all tests, PETG was more resistant, generally 21% to 32% more resistant than PLA. But the specific resistances are similar, with PLA composites having a core density of 13.8% lower than PETG cores. The results obtained in the work coincide with previously published results from other authors.

1. INTRODUCTION

Vegetable fibers are increasingly explored as promising reinforcements in the composition of composite materials. This awakening of interest is attributed to their low environmental impact, affordable cost, wide availability, versatile applications (construction, packaging, furniture, transportation), low energy

consumption and minimal health risks [1-2]. Furthermore, the biodegradability of these fibers presents a solution to mitigate environmental pollution. [3-4].

Among the wide variety of natural fibers, sisal fibers are increasingly cultivated around the world, minimizing their transportation needs and, ultimately, carbon dioxide gas emissions. Sisal fibers are considered a viable source of natural fiber due to their high strength and biodegradability [5], it is adapted for better abrasion and fungus resistance, high strength, better thermal stability and economical and biodegradable reasons [6, 7].

The sisal plant belongs to the *Agave sisalama* family and the fiber is extracted from the leaves and can reach up to 2 m in length. The number of fiber bundles per leaf depends on the age and origin of the plant, with length varying from 60 to 120 mm, has 1.45 g/cm³ density resulting in a porosity of around 17%. This fiber is hydrophilic and can absorb up to 11% moisture in an environment where relative humidity reaches 65%. The chemical composition mainly includes cellulose (50–78%), hemicellulose (10–20%), lignin (8–12%) and waxes (about 2%). In terms of mechanical properties, the tensile strength varies from 300 to 430 MPa, the Young's modulus varies from 5 to 15 GPa and the elongation at break varies from 5 to 14%. [2]

The problem in polymer composites with vegetable fibers is the incompatibility between the vegetable fibers and the polymer matrix due to the fact that the fibers are hydrophilic in nature and the polymer matrix is hydrophobic. As direct consequences of this fact, there is a weak interfacial adhesion between the polar and hydrophilic fiber and the non-polar and hydrophobic matrix and mixing difficulties due to the low wettability of the fiber by the matrix, which leads to a weak interface of these composites, reducing the mechanical resistance of the composite. [8]. Therefore, the fibers must be appropriately modified through physical or chemical treatments with the aim of improving adhesion between them and thus improving the mechanical resistance of the composite, one of the most used being treatment with sodium hydroxide (NaOH). [9]

Sandwich panels are types of structural composites whose core is made of a less dense material than the faces. They are designed to be low-weight beams with high rigidity. It consists of 2 faces joined to a core using an adhesive [10]. One of the most used cores is with a Honeycomb structure. Honeycombs are part of the class of cellular materials, formed by "voids" separated by solid walls, which stand out for having a low relative density. [11]. One of the processes that can be used to manufacture honeycombs is additive manufacturing through FDM (Fused Deposition Modeling) 3D printing.

In this work, the study of a composite sandwich structure was carried out using sisal fiber composite faces in a castor oil polyurethane matrix and a honeycomb structural core 3D printed in PETG (Polyethylene Terephthalate Glycol) and PLA (Polylactic Acid), with emphasis on the mechanical behavior of the composite in relation to the dimensions of the core and the materials used. The work comprises two parts, the first to determine the best chemical treatment of Sisal fiber to obtain the best mechanical properties based on tensile stress and the second part to analyze the sandwich composites applying the best treatment obtained.

2. METHODOLOGY

2.1. Chemical Treatment

To obtain better adhesion of the sisal fiber in the matrix, a study was conducted to determine the best chemical treatment for the fibers by varying the concentrations of sodium hydroxide and the immersion time of the fibers in the dissolution, with which specimens of epoxy resin matrix composites were subsequently manufactured to determine the highest tensile strength of all specimens and thus the best treatment.

Sisal fibers are supplied by FIBRAEX Company (Brazil); sodium hydroxide is provided by the Chemistry Lab of Amazon State University (UEA/EST), and castor oil polyurethane supplied by Azevedo Oil Industry and Commerce Ltda (Brazil). An anti-bubble additive is also used. [12]

To eliminate impurities fibers are washed in running water and dried at room temperature for 24 hours. Four different concentrations of sodium hydroxide are applied: 2.5, 5, 7.5 and 10 (% by weight) corresponding to 20 g, 40 g, 60 g and 80 g of sodium hydroxide respectively in 800 ml of distilled water as can be seen in Fig. 1a, maintaining a ratio of 3/8 (fiber dissolution in all cases) [13].

The immersion time of the fibers in dissolution was 1, 4, 8 and 12 hours [14]. After finishing the immersion time for each treatment, the fibers were washed several times in running water and then in distilled water to stabilize the pH and left to dry at room temperature for 24 hours and then in an oven at 60°C for 8 hours.

To manufacture specimens, a metallic mold with internal dimensions of 225 mm x 155 mm x 3.2 mm is used. Before the process start fibers are placed in an oven at a temperature of 100 °C for one hour to complete eliminate moisture and a release wax is applied to the internal surface of the mold to facilitate the extraction.

Specimens are manufactured by mixing the resin and 4% of the anti-bubble agent manually for 15 minutes in a beaker, according to the manufacturer's recommendation. A first part of the resin is placed in the mold, then the fibers as shown in Fig. 1b and finally the rest of the resin content. Before closing the mold with the lid, isopropyl alcohol is sprayed on the surface to help eliminate possible bubbles [12].The mold is closed and *cold* pressure is applied to the upper lid.

The mold stays closed under pressure for 24 hours in a first curing process, then the composite sheet is removed from the mold (Fig. 1c) and placed in the oven for 8 hours at temperature of 80 ^{0}C, to complete the process curing and increase the strength of the composite. After curing, the sheet is laser cut according to the dimensions of the tensile test standard [15] (Fig. 1d). All specimens had the same amount of fiber (20% by weight) to be able to study the effect of the chemical treatment.
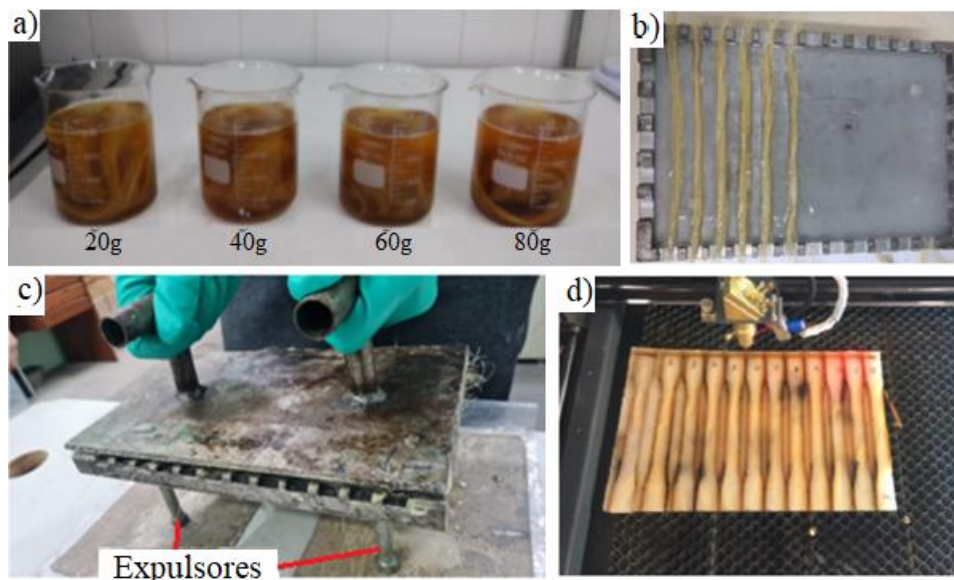
Figure 1: Manufacturing sheets process: a) chemical treatment of the fibers, b) fibers and resin placement inside mold, c) closing the mold, d) specimens laser cutting.

2.2. Tensile Tests

Tensile tests are carried out with a 150 KN load cell and a standard speed of 5 mm/min, as presented in Fig. 2a and 2b. The combination of sodium hydroxide concentration types (4) and different immersion times (4) provided a total of 16 specimens. As 4 replications of each case were carried out to take the average values, the total number of specimens was 64.

The best treatment in relation to the highest average value of tensile effort corresponded to the treatment with 10% by weight of sodium hydroxide concentration and 4 hours of immersion of the fibers in dissolution, which corresponds to results obtained in the literature [13, 14, 16, 17], Fig. 2c presents the graph with the stress-deformation curves generated by the machine corresponding to the chemical treatment that caused the greatest tensile effort (best treatment).
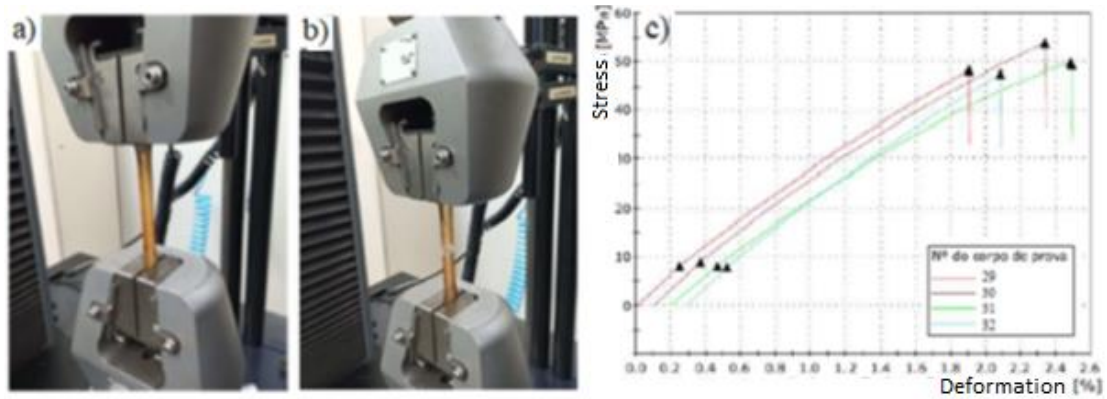
Figure 2: Tensile tests: a) beginning of load application, b) moment of rupture, c) stress-deformation graphs for the 4 replicas of the best results.

2.3. Sandwich Composites Manufacturing

Sandwich composites are fabricated by sheets made of sisal fibers treated, as shown in Fig. 3a, with the best treatment found (10% by weight of NaOH and 4 hours immersed) and epoxy resin matrix. Sheets are manufactured similar to the process described previously, but composite must be 2 mm thick, so a 1 mm thick metal plate is placed in the mold cavity to obtain such dimension, , as can be seen in Fig. 3b. After the curing process sheets are cut on a laser cutting machine with dimensions of 200 mm x 70 mm, as figures 3d and 3e demonstrates. In total, 8 faces are cut to compose the 4 sandwich composites.

Cores are 3D printed in a honeycomb structure, as shown in Figure 4. To define the dimensions of the cores, 3 criteria are applied: Smallest possible layer thickness, 2 types of height in the cores and same size of the hexagons for all cores. The wall thickness was 0.3mm ± 0.05mm, considering the horizontal expansion of the filament.

Two different core heights are defined, 10 mm and 15 mm, based on the honeycomb cores that are currently commercialized [19]. Two different materials are used, PLA and PETG filaments, resulting in a total of four cores. Honeycomb cores are glued to the sisal composite faces with a resin matrix. After pouring the resin over the faces, the core was placed centrally (see Fig. 4b) and then a weight was placed on the cores. The process is repeated after 48 hours, to glue the upper face [20].
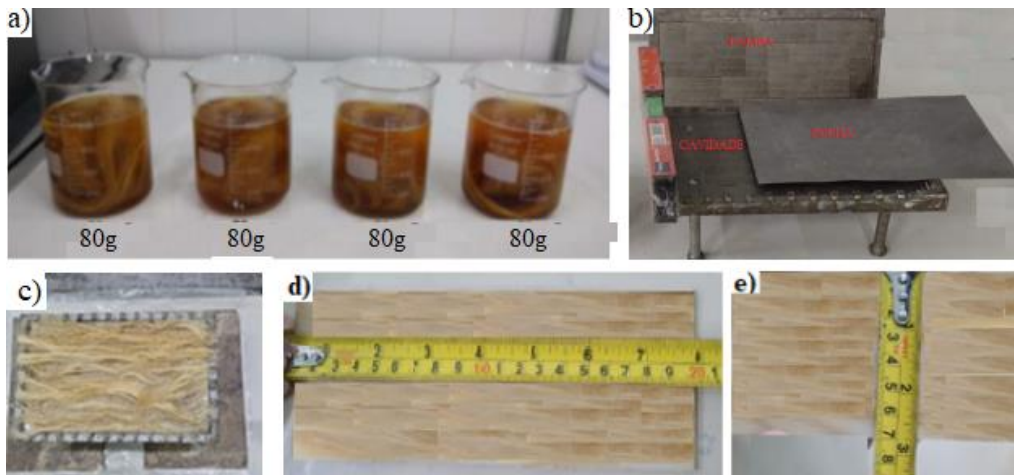
Figure 3: Sandwich faces fabrication: a) alkaline treatment, b) face mold, c) placement of the fibers and resin inside the mold, d) face length, e) face width.
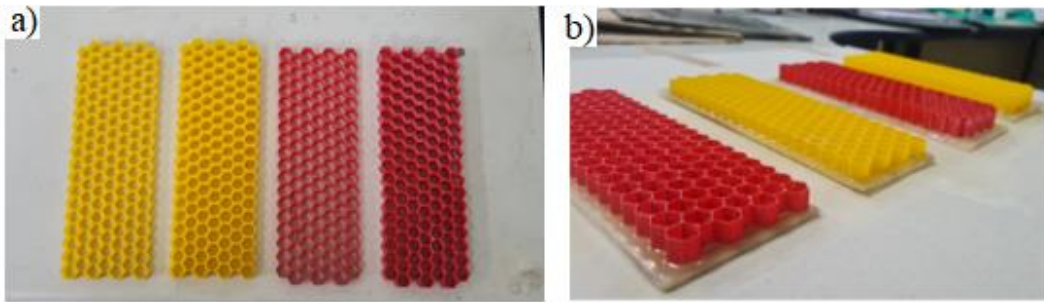
Figure 4: a) Honeycombs printed, b) honeycombs glued to first sheet

2.4. Bending Tests

Bending tests are carried out at three points of the sandwich composites. The tests are conducted on the INSTRON 5984 model machine from EST/UEA, in the R&D Materials laboratory. All specimens have dimensions of 200mm x 70mm, with two sides 2 mm thick. The tests followed the ASTM standard [21, 22] for three-point bending test, the test speed was 2 mm/min. The distance between lower points was 100mm.

3. RESULTS AND DISCUSSION

Results of the three-point bending test on sandwich panels are presented in Table 1. As can be seen in Fig. 5 and 6, there was no rupture on the faces, but there was detachment of the core, which may have influenced the results. With the results obtained from the tests, it was possible to analyze and compare the tension and deformation of the test specimens. The results obtained coincide with other previously published works [23, 24]. Analyzing the results in relation to height, we see that the composites with a 15 mm core supported 3.3 to 3.6 times more load than the 10 mm cores.

Table 1: Results of three-point bending tests for all specimens

Test body	Core Material	Core Height [mm]	Maximum load [N]	Flexural Stress at Maximum Load [MPa]	Flexural Deformation [%]	Modulus of elasticity [Gpa]
1	PLA	10	396,13	3,18	13,32	0,023
2	PETG	10	525,1	4,38	9,68	0,043
3	PLA	15	1443,91	6,73	2,41	0,280
4	PETG	15	1744,62	8,13	3,00	0,342

Figure 5: Three-point bending test of specimen 1

Figure 6: Three-point bending test of specimen 2

In all tests, PETG was more resistant, generally 21% to 32% more resistant than PLA (see Fig. 7 and 8). Although there was no rupture in the specimens, the PETG cores deformed 0.5% to 3.6% less than PLA. The PLA composites were lighter, due to the core density being 13.8% lower than the PETG cores.
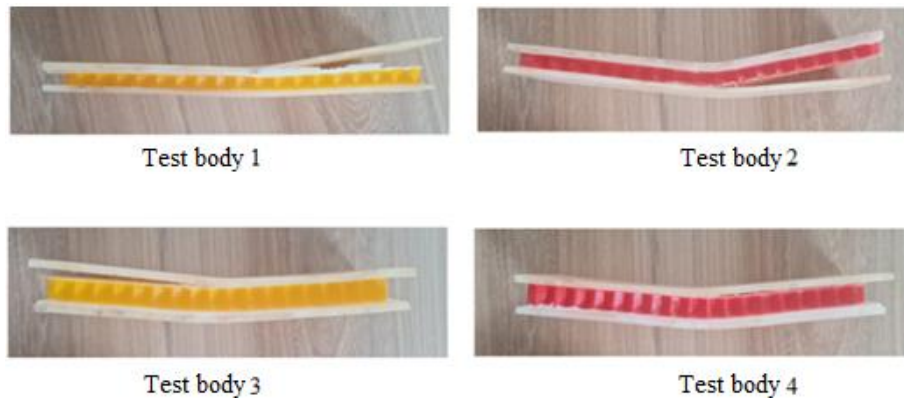
Figure 7: Specimens (1-4) after flexural tests
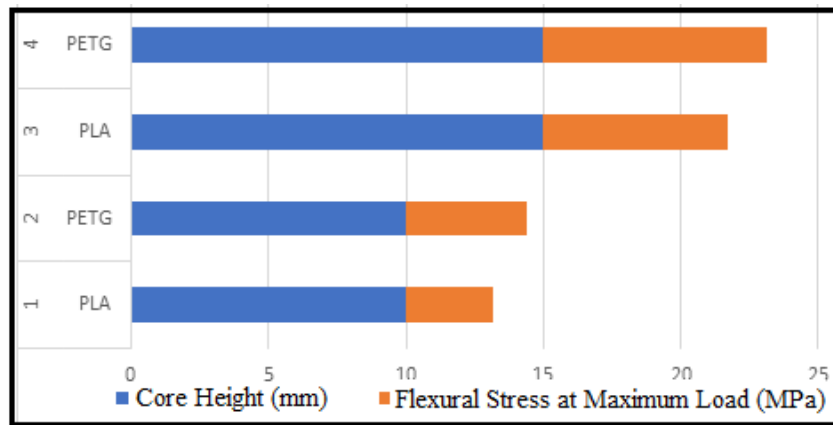
Fig. 8: Influence of honeycomb material and height on maximum bending stress

4. CONCLUSIONS

The main objective of the work was to create a sandwich composite with a honeycomb core made using a 3D printer, with PLA and PETG. Sisal fibers contribute to the income of small producers, research related to plant fibers helps the technological growth of composite materials, even enabling their use in industry. Analyzing the results in relation to height, we see that the composites with a 15mm core supported 3.3 to 3.6 times more load than the 10mm cores.

The materials used in the cores were chosen for their ease of printing and for having ecological origins. PLA, as it is biodegradable and compostable, can be manufactured using corn, beetroot and cassava, as they are rich in starch. PETG can be obtained through recycling PET bottles, reducing the impacts caused by pollution.

In all tests, PETG was more resistant, generally 21% to 32% more resistant than PLA. Although there was no rupture in the specimens, the PETG cores deformed 0.5% to 3.6% less than PLA. The PLA composites were lighter, due to the core density being 13.8% lower than the PETG cores. In general, it can be concluded that the PETG cores were better, preferably the 15mm high cores. The results were similar to other previous works in the bibliography. Honeycomb proved to be a very resistant, low-density structural arrangement, occupying only 5.4% of the available volume between the faces, which allows it to be used in applications that may require the passage of other internal materials, such as pipes and cables. Furthermore, they can be used in applications that require low density, such as the aeronautical and naval industries.

4.1. Declaration of Competing Interest

The authors declare no conflict of interest.

5. REFERENCES

[1] Achille Désiré Betené Omgba et al. Effect of extension speed on the mechanical performance of sisal and coir fiber bundles. International Journal of Polymer Analysis and Characterization, 2024, doi:10.1080/1023666X.2024.2316966.

[2] Zwane, P. E., T. Ndlovu, T. T. Mkhonta, M. T. Masarirambi, and J. M. Thwala. 2019. Effects of enzymatic treatment of sisal fibres on tensile strength and morphology. Sci. Afr. 6: e00136. doi:10.1016/j.sciaf.2019.e00136.

[3] Venkatesh R, Raguvaran R, Murugan A et al (2023) Evaluation of thermal adsorption and mechanical behaviour of intralaminar jute/sisal/e-glass fibre-bonded epoxy hybrid composite as an insulator. Adsorp Sci Technol 2023. https:// doi.o rg/ 10.1 155/2023/9 2225 62

[4] Veigas, M. G., M. Najimi, and B. Shafei. 2022. Cementitious composites made with natural fibers: investigation of uncoated and coated sisal fibers. Case Stud. Constr. Mater. 16:e00788. doi:10.1016/j.cscm.2021.e00788.

[5] Kumar MD, Jayasrinivasan S, Ashwin S (2021) Study on static and dynamic behavior of jute/sisal fiber reinforced epoxy composites. Mater Today Proceed 46(19):9425–9428

[6] Kumar SS, Raja VM, Chakravarthy CN, Muthalagu R (2021) Determination of mechanical properties and characterization of alkali-treated sugarcane bagasse, pineapple leaf and sisal fibers reinforced hybrid polyester composites for various applications. Fiber Polym 22:1675–1683

[7] Nagappan S, Subramani SP, Palaniappan SK, Mylsamy B (2022) Impact of alkali treatment and fiber length on mechanical properties of new agro waste *Lagenaria siceraria* fiber reinforced epoxy composites. J Natural Fibers 19(13):6853–7664

[8] Sreenivasan, V.S.; Ravindran, D; Manikanda, V.; Narayanasamy, R. Influence of fiber treatments on mechanical properties pf short Sansevieria cylindrica / polyester composites. Materials & Design, v.37, p111–21, 2012

[9] Pandey, J.K.; Ahn,S.H.; Lee, C.S.; Mohanty, A.K.; Misra, M. Recent Advances in the Application of Natural Fiber Based Composites. Macromolecular Materials and Engineering, v295, n.11, p.975–89, 2010

[10] Callister JR., W.D. Ciência E Engenharia De Materiais: Uma Introdução, 7ª edição. Rio de Janeiro, 2008.

[11] YAMASHITA, M.; GOTOH, M. Impact Behavior Of Honeycomb Structures With Various Cell Specifications—Numerical Simulation And Experiment. International Journal of Impact Engineering, v. 32, n. 1, p. 618–630, 2005.

[12] REDELEASE. Resina Epóxi Transparente com endurecedor 01 kg. 2024. Disponível em https://www.redelease.com.br/resina–epoxi–transparente–com–endurecedor–01–kg.html.html. Acesso em: 20 de janeiro de 2024.

[13] Garcia del Pino, G. et al. Optimal tensile properties of biocomposites made of treated Amazonian curauá fibres using Taguchi Method. Materials Research, v.24, 2021. doi.org/10.1590/1980-5373-MR-2021-0326

[14] Garcia del Pino, G. et al. Hybrid polyester composites reinforced with curauá fibres and nanoclays, Fibers and Polymers. v 21, 2020. doi.org/10.1007/s12221-020-9506-7

[15] ASTM D638-14. Standard test method for tensile properties of plastics. West Conshohocken, PA: ASTM International, 2014.

[16] Bezazi, A. et al. Alkali treatment effect on physicochemical and tensile properties of date palm rachis fibers. Journal of Natural Fibers 2020. doi.org/10.1080/15440478.2020.1848726

[17] 28- Khelifa H. et al. Mechanical characterization of mortar reinforced by date palm mesh fibers: Experimental and statistical analysis. Construction and Building Materials, v.300, 2021. doi.org/10.1016/j.conbuildmat.2021.124067

[18] Almeida, M. I. Comportamento estrutural de painéis sanduíche compósitos para aplicações na indústria da construção. Instituto Superior Técnico, 2009.

[19] E–COMPOSITES. Núcleo Honeycomb de Aramida. 2023. Disponível em: https://www.e–composites.com.br/honeycomb_aramida/p. Acesso em: 15 de fevereiro de 2023.

[20] Oliveira PR, Silva LJ, Panzera TH, Garcia G del Pino and F Scarpa, Transverse fastening reinforcement of sandwich panels with upcycled bottle caps core, Journal of Composite Materials 0(0) 1–9, 2020, DOI: 10.1177/0021998320960522

[21] ASTM INTERNATIONAL. Standard Test Method for Flexural Properties of Polymer Matrix Composite Materials. 2016

[22] ASTM INTERNATIONAL. Standard Test Method for Flexural Properties of Sandwich Constructions. 2016

[23] Oliveira PR, Silva LJ, Panzera TH, Garcia G del Pino and F Scarpa, Transverse fastening reinforcement of sandwich panels with upcycled bottle caps core, Journal of Composite Materials 0(0) 1–9, 2020, DOI: 10.1177/0021998320960522

[24] GIordano, C. M.; Zancul, E. S.; Rodrigues, V. P. Análise Dos Custos Da Produção Por Manufatura Aditiva Em Comparação A Métodos Convencionais. Revista Produção Online. v. 16, n. 2, p. 499–523, 2016.

UTILIZATION OF RESIDUES FROM THE CAPIXABA FURNITURE INDUSTRY IN THE PRODUCTION OF WOOD-PLASTIC COMPOSITES

Gilson Mendonça de Miranda Júnior [(a)], Rejane Costa Alves[(b) *], Glaucinei Rodrigues Corrêa [(c)]

(a) 🆔 0000-0002-9312-156X (Federal University of Espírito Santo - Brazil) – gilsonmmjunior@gmail.com
(b) 🆔 0000-0003-4059-3974 (Federal University of Espírito Santo – Brazil) - * rejanealvesufes@gmail.com
(c) 🆔 0000-0002-4311-5444 (Federal University of Minas Gerais – Brazil) – glaucinei.correa@gmail.com

Abstract: The Brazilian timber industry generates large quantities of wood waste, necessitating sustainable solutions for its reuse. This study focuses on the production and characterization of wood-plastic composites (WPCs) using *Eucalyptus spp*. residues (ER) and poly(vinyl acetate) (PVA). The ER were combined with PVA in different proportions (70%, 60%, and 40%) and particle sizes of 60 mesh, with the composites being prepared by thermoforming. For the characterization of the composite, static bending tests and dynamic ultrasonic wave propagation tests were conducted, following ASTM D790-17 and NBR 5800 (1995) standards. From the tests performed, it was confirmed that the non-destructive ultrasonic wave propagation test showed similar behavior to the static test, thus being an efficient tool for determining the modulus of elasticity in the studied composites. The results revealed that the proportion of ER and the concentration of PVA significantly influence the properties of the WPCs. The WPCs with 60% ER and 40% PVA showed the best overall performance, combining high flexural strength and dynamic modulus of elasticity (MOE). This optimized proportion offers a balance of desirable properties for various applications, such as in the furniture industry, design, and other potential productions.

1. INTRODUCTION

The timber industry, based on managed planted forests, plays a vital role in the economy of the State of Espírito Santo. Standing out for the production of mechanically processed wood, it recorded a gross production value of R$ 26.8 billion in 2022, representing 5.8% of the national total [1]. However, the processes of the furniture industry's production chain generate considerable amounts of wood waste, not always adequately disposed of, contributing to Brazil's position as a major generator of wood processing waste [2].

The main waste generated by the furniture industry includes sanding dust, sawdust, scraps, wood residues, solvents, and water from the painting booth [3]. Among these, wood scraps and residues stand out as the most significant proportions in furniture industries. According to NBR 10004 (ABNT, 2004), these residues present specific characteristics such as combustibility and biodegradability [4].

In this context, the production of wood-plastic composites (WPC) emerges as a promising alternative for the reuse of waste from the timber industry in Espírito Santo. This study aims to evaluate the mechanical properties of these composites, using residues of Eucalyptus spp (EW) and poly(vinyl acetate) (PVA). In addition to reducing the waste of natural resources, the goal is to develop materials with potential for controlled environmental degradation.

Mechanical characterization plays a crucial role in assessing the quality and controlling the manufacturing processes of composite materials. To determine the mechanical properties of the material, three-point bending tests were performed according to ASTM D790. This type of test is widely used for brittle or high-hardness materials since their low ductility hinders or prevents the application of other mechanical testing methods [5]. Additionally, ultrasonic tests were conducted using the FAKOPP Ultrasonic Timer equipment.

Conducting ultrasonic tests alongside had the purpose of comparing the results obtained by a destructive method (bending strength test) with a non-destructive method (ultrasonic), providing a comprehensive analysis of the material properties.

2. METHODOLOGY

The selected matrix was vinyl acetate homopolymer, an aqueous emulsion adhesive based on polyvinyl acetate (PVA), with a concentration ranging from 45% to 47%. This material appears as a yellowish viscous liquid, with a solids content of 45.41% and a specific weight between 1.060 and 1.100 g/cm³ [6]. The reinforcement in the composite preparation consists of untreated Eucalyptus spp. wood residues, sourced from virgin materials.

The wood residues (ER) were collected from a sawmill located in the municipality of Alegre, Espírito Santo, and subjected to a drying process in an oven at 100°C for 24 hours before being ground in a knife mill (steps I and II in Figure 2). After grinding, the residues were sieved using an automatic sieve with meshes of 20, 35, and 60 mesh, opting to work with the particle size fractions retained on the 60 mesh screens (steps III, IV, and V in Figure 2).

The wood-plastic composite was produced at the Laboratory of Three-Dimensional Experimentation (LET) of the School of Architecture and Design at the Federal University of Minas Gerais, using a Bovenau hydraulic press (model P30000, with a capacity of 30 tons). The closed mold has electric resistances distributed in two on the upper mold and two on the lower mold, ensuring thermal stability. A digital controller adjusts the temperature according to the needs of each material. The force exerted by the hydraulic jack reaches approximately 30 tons. The mold used has an area of 289 cm², resulting in plates with dimensions of 170x170x6 millimeters (width, length, and thickness).

The plates were manufactured with various proportions of eucalyptus residues (70%, 60%, and 40%) in 60 mesh particle sizes (T1, T2, and T3, respectively), totaling 3 distinct treatments. These proportions were arranged to investigate the effects of different concentrations of eucalyptus residues on the properties of the plates.

The procedures for manufacturing the plates followed the following steps:

VI) Precise dosing: Weighing of the eucalyptus residue and the polymeric matrix to achieve the target density of 650 kg/m³;

VII) Mixing homogeneity: The mixture was thoroughly homogenized to ensure uniform distribution of the components;

VIII) Application of release agent: Chem Trend's PURA 28014W release agent was used on the upper and lower molds to prevent material adhesion, followed by the deposition of the mixture into the molds;

IX) Two-stage pressing:

a) Initial pressing

Air removal: An initial force of 8 to 10 tons was applied at a temperature of 150°C, repeating the procedure until complete air removal.

b) Final pressing

Compaction: A final force of 20 tons was applied at a temperature of 150°C for 5 minutes to consolidate the material and ensure proper compaction of the plates.

X) Plate Removal: The plates were carefully removed from the molds for further analysis;

XI) Random Sample Preparation: The specimens for ultrasonic and flexural tests were randomly prepared in the Wood Machining Laboratory (Carpentry) at the Department of Forestry and Wood Sciences - UFES. The randomness in the preparation sequence aimed to minimize the influence of external factors and ensure more precise results. Figure 1 illustrates the process of cutting and preparing the specimens;

Figure 1. Representation of cross-sections of the test specimens.

XII) Conducting the tests:
a) Non-Destructive Testing: Ultrasonic
b) Mechanical Testing: Static Flexion
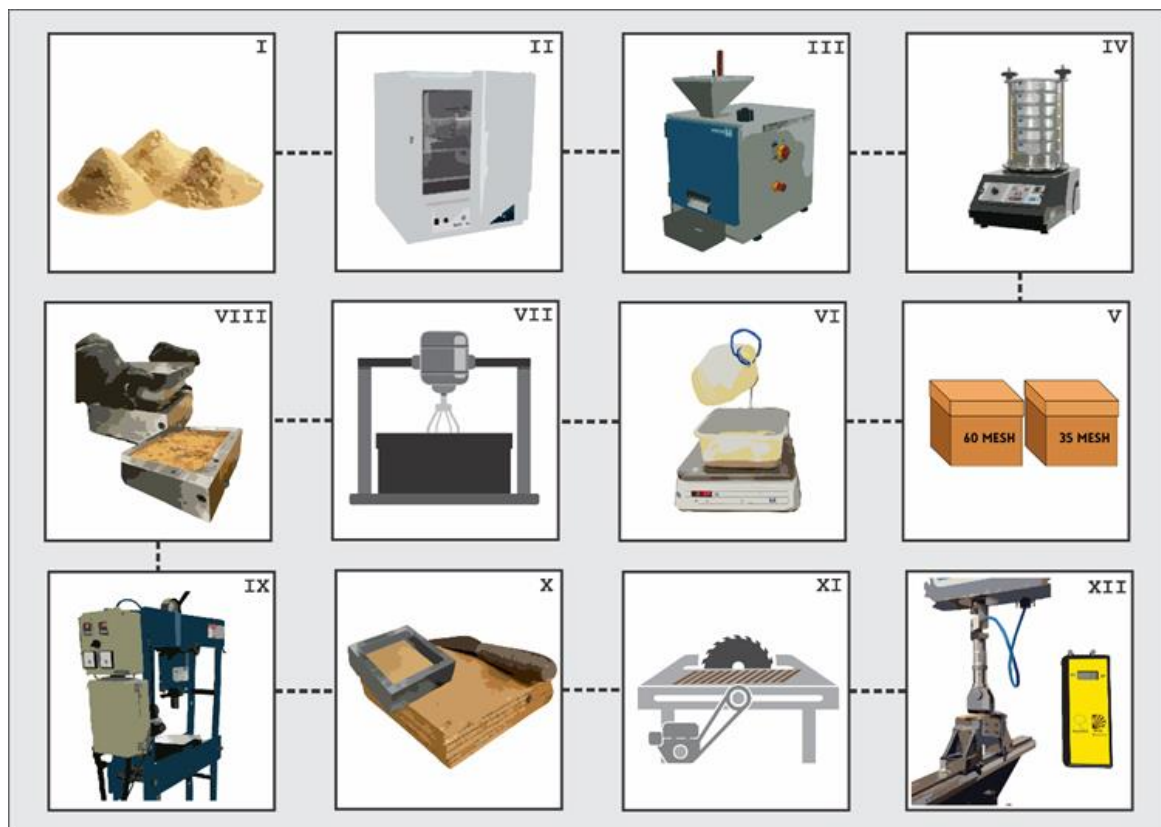
Figure 2. Flowchart of the Plastic-Wood Composite (WPC) Manufacturing Process

2.1. Non-Destructive Testing – Ultrasonic

The ultrasound tests were conducted using the FAKOPP Ultrasonic Timer equipment, employing two identical piezoelectric transducers (SD 33) with a frequency of 90 kHz (Figure 3). In accordance with the NBR 58000 (1995) standard, these tests were conducted on specimens with dimensions of 170x30x6 mm (length, width, and thickness) [7]. These tests enable the detection of flaws or discontinuities in the internal structure of the plates, providing crucial information about their integrity and quality.
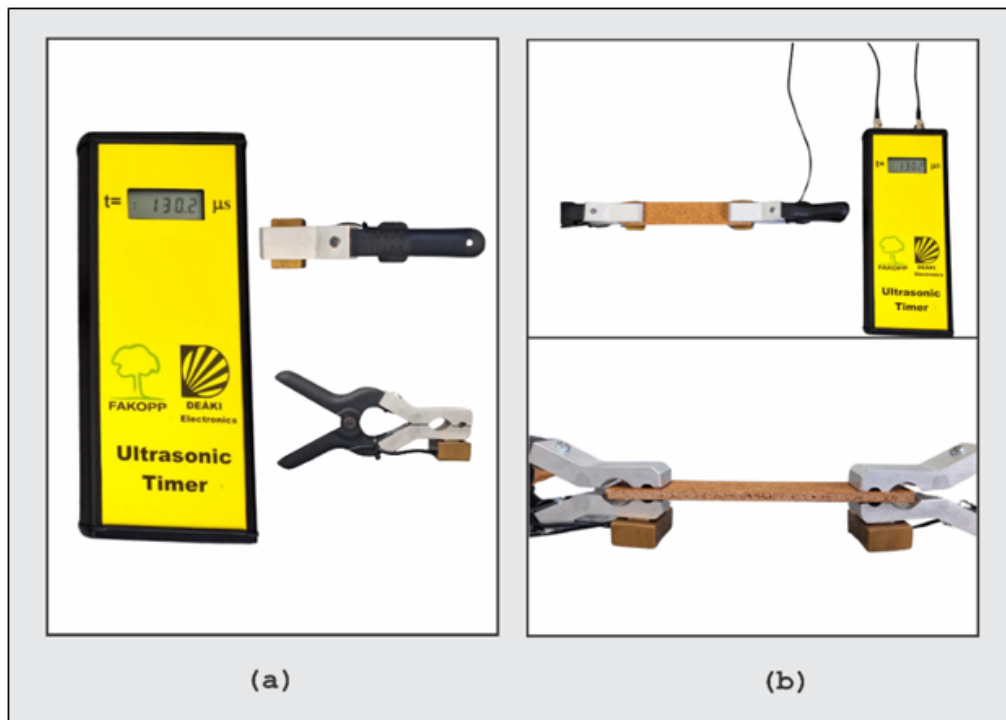
Figure 3. Ultrasonic Test: (a) Ultrasonic Timer Equipment; (b) Ultrasonic test procedure.

2.2. Mechanical Testing - Static Flexural

The flexural test was conducted on the EMIC universal testing machine (DL 10000 - maximum capacity 100 kN, Jerônimo Monteiro, Brazil). The test followed ASTM D790-17 (2017) standard, using specimens with "Procedure A" geometry, a load cell of 450 kgf, and a deformation rate of 4 mm/min. This technique provides information about the material's strength and stiffness [8].

Figure 4. Flexural Test: (a) EMIC DL 10000 Equipment in use; (b) Flexural test procedure.

The data was obtained through ultrasonic and flexural tests. With these values, descriptive parameters of the analyzed composite were calculated, including flexural strength and modulus of elasticity for both tests.

3. RESULTS AND DISCUSSION

The average values and grouping information obtained in the bending (static) and ultrasound (dynamic) tests for the wood-plastic composites, using the Tukey method with a 95% confidence interval, are presented in Table 1.

Table 1. Average Values and Groupings of Bending and Ultrasound Tests for Wood-Plastic Composites (Tukey Method, 95% CI)

Dynamic Ultrasound						
Factor	N°	Mean	Standard Deviation	95% CL	Grouping	
Treatment 2	10	4604,4	270,6	(4611,6; 4874,4)	A	
Treatment 1	10	4743	190,7	(4473,0; 4735,7)	A	
Treatment 3	10	3157,1	116	(3025,7; 3288,5)		B
Static Flexion						
Factor	N°	Mean	Standard Deviation	95% CL	Grouping	
Treatment 2	10	3279	552	(2919; 3638)	A	
Treatment 1	10	2545	782	(2186; 2905)		B
Treatment 3	10	1760,4	56	(1401,3; 2119,5)		C

The results presented in Table 1 reveal significant differences in the performance of wood-plastic composites in terms of static flexion and dynamic ultrasound, as determined by the Tukey method with a 95% confidence interval. In the dynamic ultrasound test, Treatment 2 exhibited the highest Dynamic Modulus of Elasticity (MOE), followed by Treatment 1, both in the same grouping, indicating that their differences are not statistically significant. In contrast, Treatment 3 showed a significantly lower MOE, highlighting the negative impact of a higher amount of PVA on the dynamic stiffness of the composite.

In static flexion, Treatment 2 again demonstrated the best strength, classified in group A, while Treatments 1 and 3 were classified in groups B and C, respectively, with Treatment 3 showing the lowest strength. These results suggest that the proportion of PVA and eucalyptus residues significantly influences the mechanical properties of the composites, with Treatment 2, which has a balanced ratio of components, providing better results in both tests. Additionally, means that do not share the same letter in the groupings are significantly different from each other, reinforcing the conclusion that the excess of PVA in Treatment 3 compromises the stiffness and strength of the material.
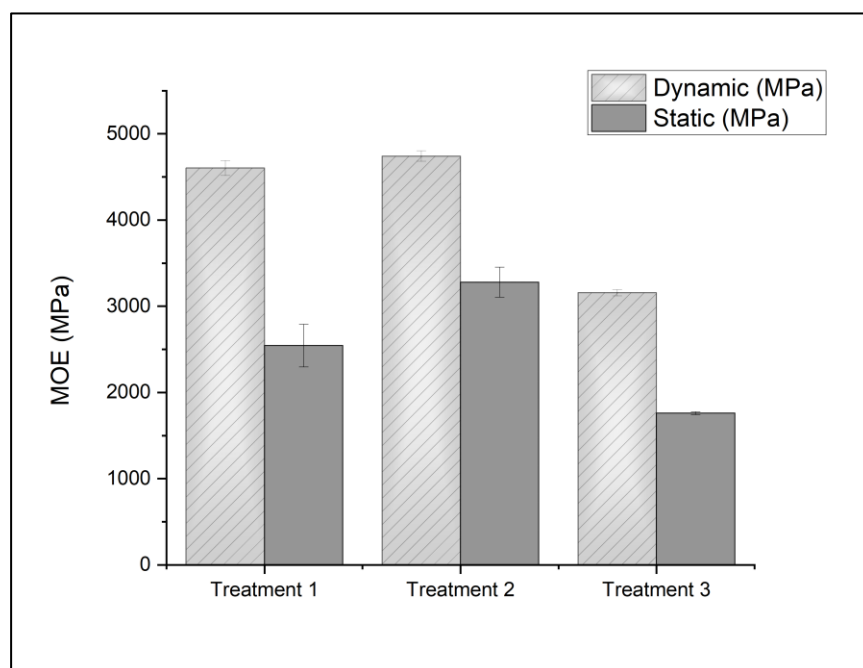
Figure 5. Average values in bending and ultrasound tests.

The results of the three-point bending tests reveal a subtle trend of increasing flexural strength with the reduction of the proportion of eucalyptus residues in the mixture. This trend is observed when comparing Treatments T1 and T2, where the flexural strength of T2 is slightly higher than that of T1. However, this relationship does not remain consistent in the comparison between T2 and T3, as the flexural strength of T3 is lower than that of T2. On the other hand, the results indicate that treatments with higher PVA content (T3) exhibit lower static flexural strength compared to treatments with lower PVA content (T1 and T2). This difference can be attributed to the lower stiffness of PVA compared to eucalyptus residues, suggesting that the addition of PVA to the mixture may have reduced its stiffness and, consequently, its flexural strength.

The values from the ultrasound test show a significant increase in the Dynamic Modulus of Elasticity (MOE) when comparing Treatments T1 and T2, while the average MOE of Treatment T3 is lower than that of Treatment T2. This suggests that the proportion of residues and PVA impacts the quality of the mixture, indicating that the addition of PVA in small quantities can increase the modulus of the composite, while larger quantities have the opposite effect, interfering with wave propagation.
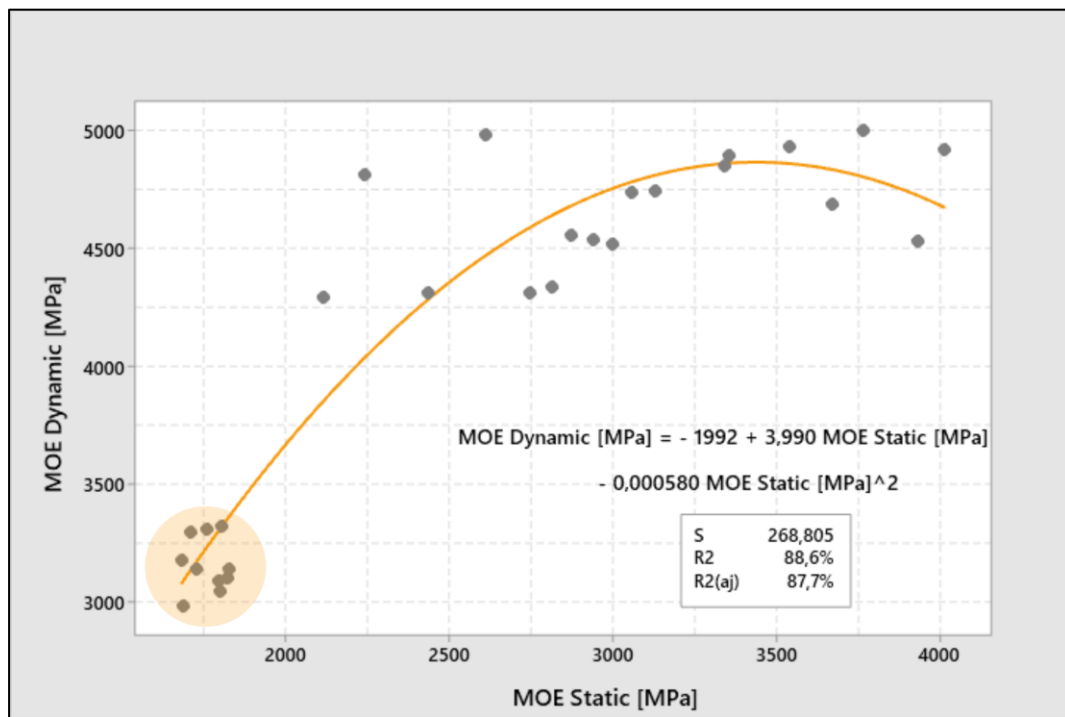
Figure 6. Polynomial Regression Analysis: Dynamic MOE vs. Static MOE.

The polynomial regression analysis revealed a significant relationship between the Dynamic Modulus of Elasticity (MOE) and the Static MOE, with a coefficient of determination (R^2) of 88.6%, indicating that the model explains a large portion of the variation in dynamic MOE as a function of static MOE. This result highlights the predictive capability of dynamic MOE from static MOE using a second-degree polynomial model, which may have relevant implications in areas such as materials engineering, wood science, biomechanics, and composites. This approach offers an effective and accessible alternative to estimate the elastic properties of materials without the need for complex and destructive dynamic tests.

The line traversing the graph in Figure 6 reveals a positive linear trend between Dynamic MOE and Static MOE. This implies that as Static MOE increases, Dynamic MOE also increases, indicating a direct relationship between these variables. This relationship is confirmed by the high coefficient of determination (R^2), indicating that the line fits the data well, confirming a strong correlation between the variables. However, it can be observed that the data points cluster in distinct regions, each with a different slope from the line. The highlighted region accommodates points with relatively low values of both Static and Dynamic MOE, corresponding to Treatment 3, indicating that the higher proportion of PVA influences its mechanical properties.
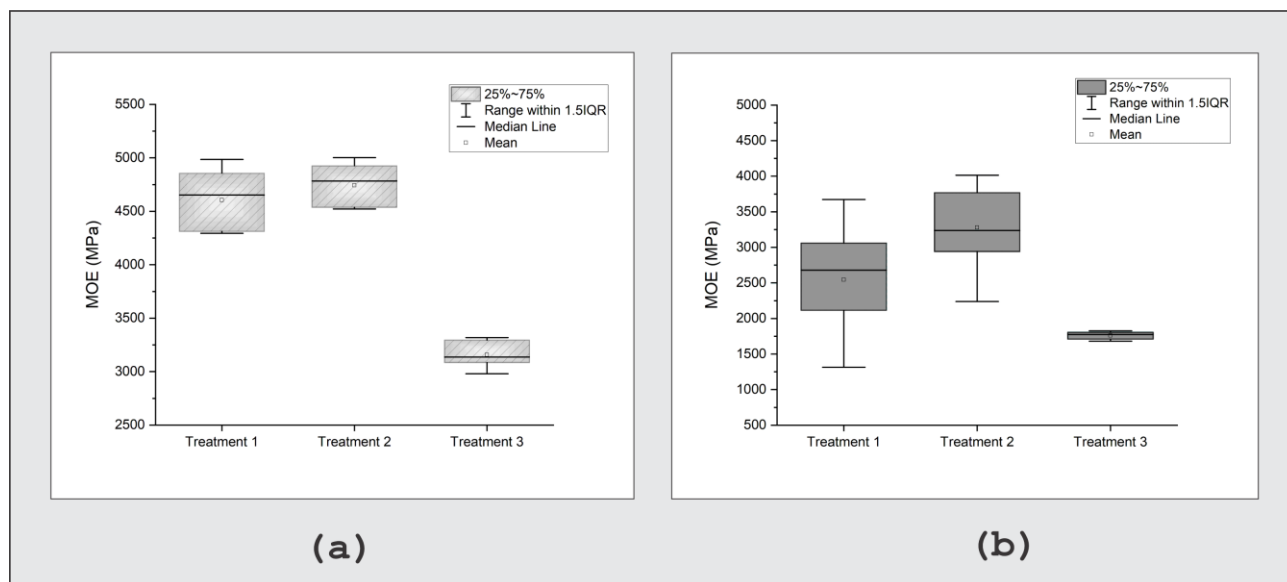
Figure 7. Boxplot: (a) Ultrasonic; (b) Static Flexion.

When assessing the homogeneity of result dispersion, it's equally essential to consider the heterogeneity of treatments. Notably, Treatment 3 exhibits relative homogeneity, with more uniform results compared to Treatments 1 and 2, which show considerable dispersion. This finding suggests that lower concentrations of residues may contribute to better uniformity in results, as indicated by the lower standard deviation observed in Treatment 3.

Additionally, when comparing the results of ultrasound and static bending tests, it's observed that treatments composed of 60% residues and 40% PVA present the highest values in both tests, indicating an appropriate proportion compared to other treatments. On the other hand, treatments with 70% residues exhibit higher modules in both analyses compared to those composed of 40% residues, which record the lowest MOE values. However, it's worth noting that treatments with 40% residues stand out for greater homogeneity in both analyses, pointing to a complex relationship between material composition and performance uniformity.

4. CONCLUSIONS

This study investigated the mechanical properties of wood-plastic composites (WPCs) produced with Eucalyptus spp residues (ER) and poly(vinyl acetate) (PVA) as a sustainable solution to reuse waste from the timber industry in Espírito Santo. By combining Eucalyptus spp residues (ER) and poly(vinyl acetate) (PVA) in different proportions, we identified that the composition of these materials plays a crucial role in their properties.

The analysis of the results indicates that the proportion of PVA and eucalyptus residues has a significant impact on the mechanical properties of wood-plastic composites. Treatment 2, with a balanced proportion, provides better results in both static flexion and dynamic ultrasound. Conversely, Treatment 3, with a higher content of PVA, shows inferior performance, suggesting that excess PVA may compromise the mechanical properties of the composite. Furthermore, regression analysis revealed a significant relationship between dynamic and static MOE, allowing accurate predictions of composite performance.

Thus, this study not only promotes the development of sustainable materials but also deepens our understanding of the relationships between composition, properties, and performance of WPCs, paving the way for more effective and environmentally responsible applications in the industry.

4.1. Declaration of Competing Interest

The authors declare no conflict of interest.

4.2. Fundings

4.3. Acknowledgements

We would like to thank the Three-Dimensional Experimentation Laboratory (LET) of the School of Architecture and Design at the Federal University of Minas Gerais (UFMG) for generously providing their facilities and equipment for the fabrication of the plastic-wood composite (WPC) panels in this study.

5. REFERENCES

[1] ABIMCI, Brazilian Association of Mechanically Processed WOOD Industry. Sectoral Study 2022: 2021 base year, p. 1-172, 2022.

[2] ALMEIDA Jr. et al. Contribution of ecodesign to the furniture sector: analysis of residues from the furniture pole of Ubá. Mediação. N 09.2019, 2019. (https://revista.uemg.br/index.php/mediacao/article/view/4334).

[3] TRANSRESIND. *The residues of the furniture industry*. September, 2021. (https://transresind.com.br/os-residuos-da-industria-moveleira/).

[4] BRAZILIAN ASSOCIATION OF TECHNICAL STANDARDS. ABNT NBR 10004: Solid Waste - Classification. Rio de Janeiro-RJ, 2004.

[5] John, G. P. Teles, et al. Flexural Properties of Composites Reinforced with Bamboo and Sisal Fibers. In: Proceedings of the 67th ABM International Congress, p. 772-782, 2012. (https://doi.org/ 10.5151/2594-5327-20973).

[6] FISPQ, Chemical Product Safety Information Sheet. 2021. Eurocryl 5300. 9p. Euroamerican do Brasil, Jandira, São Paulo, 2021.

[7] BRAZILIAN ASSOCIATION OF TECHNICAL STANDARDS. NBR 58000: Information and documentation: citations in documents. Rio de Janeiro. 2007. [Online] Available: [https://abnt.org.br/]

[8] ASTM D790-17, Standard Test Methods for Flexural Properties of Unreinforced and Reinforced Plastics and Electrical Insulating Materials. ASTM International, 2017 (www.astm.org).

[9] Minitab® 2019 [Computer software] (www.minitab.com).

4 Applications of composites

Organized and edited by

Sandra Maria da Luz
&
Carla Tatiana Mota Anflor

HOW ADDING ABS TO A PC MATRIX INFLUENCES THE BLEND'S PERFORMANCE: A THERMAL ANALYSIS ATTEMPT TO EXPLAIN ABNORMAL MECHANICAL BEHAVIOR

T. Pandim [(a), *], S. M. da Luz [(b)], T. Doca [(c)]

(a) Thiago Pandim Barbosa Machado (University of Brasília – Brazil)
(b) Sandra Maria da Luz (University of Brasília – Brazil)
(c) Thiago de Carvalho Rodrigues Doca (University of Brasília – Brazil)
* Corresponding author: 21006692@aluno.unb.br

Abstract: Polymer blending has gained prominence as a strategy to optimize material properties for diverse applications, requiring a careful consideration of interactions between its constituents. Polymer blends can be used on their own or as matrices for composite materials, e.g. glass fiber reinforced polymer composites (GFRP) or carbon fiber reinforced polymer composites (CFRP), which may use epoxy resins mixed with other polymer like polyether to tailor the resulting material's properties. Polycarbonate/acrylonitrile-butadiene-styrene (PC/ABS) is a polymer blend widely used in various industries, from housings of consumer electronics to parts of aerospace vehicles. Its mechanical behavior varies considerably with the weight ratios of each component, in a non-linear manner. Recent studies pointed to an elusive optimal blend of composition around 60:40 – 65:35, but no clear explanation has been given to account for its remarkable behavior. Herein, we study the mechanical behavior of configurations with PC to ABS weight ratios of 100:0, 80:20, 65:35 and 0:100 by employing analysis techniques, including Thermogravimetric Analysis (TGA) and Differential Scanning Calorimetry (DSC). TGA revealed 65:35 to behave very similarly to pure PC, whereas the blend 80:20 displayed similar results to those of pure ABS. Moreover, 65:35 exhibits an early start in thermal degradation, but degrades over a wider temperature range than the other compositions. Regarding glass transition temperatures, the results indicate that the amount of ABS in the blend results in very minor changes in the values of T_g. Therefore, the notable mechanical resistance of 65:35, as reported in the literature does not seem to have a direct correlation with that thermodynamical parameter. This works provides valuable insight and specific data regarding commercial PC/ABS blends with widespread use.

1. INTRODUCTION

Polymeric materials have been used for decades in industrial settings, with their market size reaching more than USD 700 billion in 2021 and growing in a compound rate of about 4.69 % from 2022 to 2030 [1]. With this ever-growing usage, experimental research of polymers has also increased substantially. These materials have been extensively tested in traditional ways under both monotonic (e.g. tensile, compression, bending and hardness tests, etc [2-5], impact [6,7] and dynamic loads (e.g. fatigue and wear tests) [8-12]. This enables researchers to better understand the behavior of polymers and help design engineers select more suitable materials for industrial applications. With the growing usage of polymers and polymer-based materials, it is essential to investigate how different blends of certain polymers behave under determined conditions.

Polymer blending, a process that combines two or more polymers with distinct properties, offers the advantage of tailoring materials with a unique set of characteristics. The resulting polymeric blend exhibits a combination of the individual polymer components' features, thereby enabling to an array of applications spanning from packaging materials to medical devices. How the properties of each constituent will combine

in the finished blend depends on many factors, such as the constituents themselves, the manufacturing of the blend and the usage of additives. Sometimes it might be the case that a few properties from each component are lost after blending, while new properties arise. Other times, the combination of the constituents' properties might be almost additive, in the sense that the blend ends up with all the desirable properties of each component. This seems to be the case for polycarbonate/acrylonitrile-butadiene-styrene (PC/ABS), as reported in [13]. The design of such blends demands meticulous consideration of not only the constituent polymers but also the interactions between them.

PC/ABS is a thermoplastic composed of two amorphous constituents, extensively utilized in various applications due to its accessibility, cost-efficiency, notable impact resistance, and high mechanical strength. Originating in the 1960s, this composite material has witnessed significant market expansion since its inception. PC/ABS blends are often employed in frames of electronic devices, household items and protective coatings. In industrial applications they are subjected to harsh loading conditions and experiment failure mechanisms such as wear, creep and fatigue. The weight ratio of each constituent directly affects the polymer's overall behavior, including its mechanical strength, toughness and impact resistance [13, 14]. Vast literature can be found regarding the mechanical properties of PC/ABS. For instance, common mechanical and thermal properties of PC/ABS blends have been addressed in [13, 15-17] while the friction and wear responses under usual contact configurations are detailed in [18,19].

It is known that the way through which macromolecules intertwine in a polymer can profoundly affect the material's behavior. Geiss [20], for instance, stablishes the following as the dominant parameters influencing the mechanical properties of polymeric materials: average molecular weight, statistical distribution, the presence of secondary bonds between adjacent chains and the degree of entanglement and cross-linking by side chains. That also seems to apply to polymer blends such as PC/ABS. Indeed, Krache *et al.* [14] hypothesized that for PC/ABS blends with either ABS or PC contents between 0% and 40%, the morphology of the mix is such that the main component would form a matrix over which the other constituent would be disperse. For compositions around 50:50, they suspected the phases would be closely connected in a co-continuous structure.

Other studies seemed to confirm the discrepancy in performance of such blends with weight ratios in the aforementioned range. For instance, Pandim *et al.* [9] observed that PC/ABS 60:40 displayed a remarkable resistance to torsional fretting wear under severe loads, making it a suitable candidate for coating applications in hostile environments. More recently, Pandim *et al.* [21] subjected PC/ABS blend with ratios 100:0, 80:20, 65:35 and 0:100 to the same tests as before, and also to pure compressive creep. They found that, indeed, the 65:35 composition was by far the most resistant to those failure mechanisms, with notably low indentation and wear damage. These findings point to an optimal PC/ABS blend regarding mechanical resistance, probably around the ratios of PC to ABS around 65:35 and 60:40. Moreover, it is reasonable to assume that such remarkable behavior is probably associated with the inner structure of the blend and how its constituents interact with each other depending on their weight ratios. One way to get insight on how the blend's constituents actually interact in different compositions is through thermal analysis.

Thermal analysis assumes a critical role in comprehending the dynamics of polymers and polymer blends, providing important information about their thermal stability, degradation kinetics, and phase transitions. Among these methodologies, Differential Scanning Calorimetry (DSC) stands as a fundamental approach for detailing thermal occurrences in polymers. This technique finds diverse applications, including the determination of the glass-transition temperature, T_g, of a polymeric material, evident as a discontinuity in the baseline of the DSC curve [22]. Additionally, it facilitates the rapid identification of phase transitions. The integration of DSC with thermogravimetric analysis (TGA) allows for the differentiation between degradation events and phase transitions. For instance, the manifestation of an endothermic event in DSC, indicating heat absorption by the material from the machine, without a significant weight drop in TGA, strongly suggests a physical phase transition, such as fusion.

Even though PC/ABS has a wide-spread and increasing usage in various industries and the data points to a possibly groundbreaking composition to resist complex wear and compressive loads, little research is found on the thermal properties or molecular structures of such blends for different weight ratios. Yin *et al.* [23], for instance, conducted dynamic-mechanical analysis (DMA) on PC/ABS samples with weight ratios of 100:0, 80:20, 60:40, 50:50, 40:60, 0:100 and estimated the T_g of each composition from two different data sources. Chinnadurai *et al.* [24] studied the thermo-mechanical behavior of ultrasonically welded PC/ABS 60:40 and found that, before welding, the blend exhibited only one value of T_g due to good miscibility at around 131 °C. Devi *et al.* [25] investigated the effects of compatibilizers in different PC/ABS blends with ratios of 100:0, 60:40, 50:50, 40:60 and 0:100 through DMA and found that 40:60 was the only one to display a single T_g value of 110 °C, closer to that of ABS (114 °C). All the other compositions showed two different

values of T_g, which would become closer to either PC's (154 ℃) or ABS's as the amount of the respective constituent was greater. Thus, they inferred that in 40:60 a possible molecular interaction between PC and ABS took place, leading to partial miscibility. Finally, Yazdi *et al.* [26] studied how different methods of measuring T_g would affect the results. Namely, they assessed PC/ABS's 75:25 T_g through a thermomechanical analyzer (TMA), found two different peaks as expected and compared the values to those found on the literature measured by DSC and DMA. They reported a considerable difference in the values depending on the methodology, which is to show the high complexity and difficulty of measuring such properties.

Considering the relevance of the topic, the same materials used by the author [21] have been inspected in this study using TG and DSC techniques, in order to further understand the materials' thermal behavior and hopefully give some insight on their inner structure. That would possibly help to explain the mechanical properties previously measured by the author.

2. METHODOLOGY

In this study, various PC/ABS were tested in a thermal analyzer which can perform simultaneous TG and DSC analyzes. The specific equipment used was TA Instrument's SDT Q600 model. The materials used, as well as their melt temperature ranges (withdrawn from the manufacturer's data sheets) used for injection molding the samples are shown in Table 1.

Table 1. Composition of the materials used.

Material	Manufacturer	Commercial name	PC content [% wt]	ABS content [% wt]	Melt Temperature [℃]
Pure PC	SABIC	LEXAN 243R	100	0	295 - 315
PC/ABS 80:20	INEOS	Novodur Ultra 4140PG	80	20	240 - 260
PC/ABS 65:35	Ravago	Mablex 451	65	35	210 - 230
Pure ABS	INEOS	Terluran GP-35	0	100	220 - 260

The procedure is visually summarized in Fig. 1 and will be detailed in the following sections.

2.1. Sample Preparation

The materials were initially supplied in injection molded prismatic shapes with 25 x 25 x 5 mm dimensions, as seen in Fig. 1. In order to ensure optimal results from the TGA and DSC runs, each material was manually grated, generating small ribbon-like elongated pieces of materials in the order of 1 – 2 mm long and 0.5 mm wide. To avoid cross contamination between the compositions, all materials was manipulated using sterile gloves and the grated particles fell directly on separate and clean plastic containers. Before grating the next composition, the grater was thoroughly cleaned, left to dry on air for one hour and the gloves were changed to a new pair each time.

Then, the grated samples were heated in a micro processed drying oven from Quimis, model 0317M-22 at 80 ℃ for 3 hours. Immediately after removing them from the oven, the samples were stored in a desiccator, which contained a drying agent to remove any moisture that might be present.
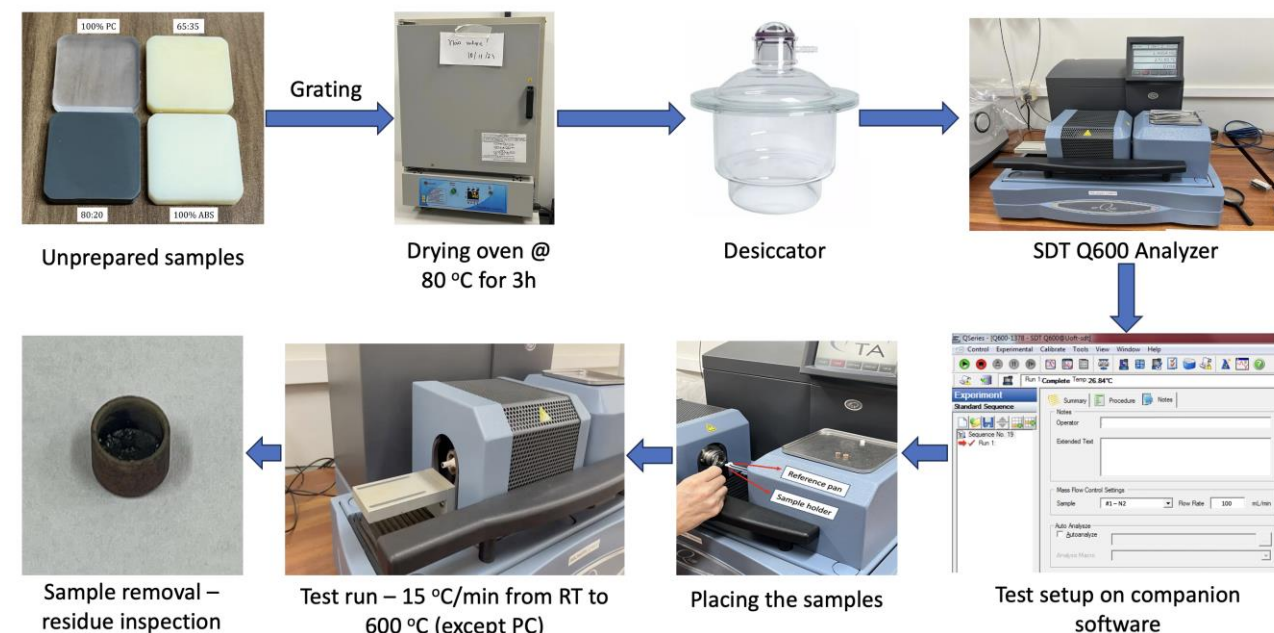
Figure 1. Flowchart of experimental procedure.

2.2. Thermogravimetric Analysis and Differential Scanning Calorimetry

The following is a detailed step-by-step description of the testing procedures employed in this research, so as to enable replication of the results herein presented.

Before removing the samples from the desiccator, the complete test setup was done on the machine. First, the analyzer was turned on and the restriction valve on the compressed fluid line was opened to allow for the flow of the desired gas, which in this case was N_2. The configuration parameters for all tests were the same and are shown in Table 2. The only exception was pure PC, which was heated up to 1000 ºC, since it did not show complete degradation at 600 ºC, in contrast with the other compositions. The companion software used was QSERIES-1600-1180-SDT Q600.

Table 2. Software configuration parameters for TGA and DSC.

Software Tab	Section	Subsection	Value
Summary	**Mode**	-	SDT Standard
	Test	-	Custom
	Sample Information	**Pan Type**	Alumina
		Sample Name	PC/ABS X-Y (where X and Y are the %wt of PC and ABS, respectively)
		Commentary	PC/ABS X-Y, N2, 15 oC
		Data file name	PCABSX-Y
Procedure	**Test**	-	Custom
	Method	-	Dynamic
		Ramp	15 oC/min
			600 oC
Note	**Operator/Extended text**	-	optional
	Mass Flow Controle Settings	**Sample**	#1 (N2)
		Flow rate	100 ml/min
		Auto Analyze	unchecked

After setting the test up on the machine's software, the furnace was opened, and both the reference and the sample pan were carefully placed on their respective pads. The furnace was then closed, and the scale was tared. With the furnace reopened, the sample material was gradually placed in the appropriate pan, until the scale reached around 10 mg. After reclosing the furnace, the test was run.

Upon reaching 600 °C, the analyzer stopped the test. Then, the machine was left to cool by its own cooler until around 500 °C. After that threshold, an air compressor connected to the analyzer was turned on, so as to accelerate the cooling process down to room temperature. The sample was then removed, had its residue visually inspected and the data was extracted from the companion's software.

It should be mentioned that new pans were used for each composition, the pans and all utensils were cleaned with lab-graded acetone before each test and the handling of every component, instrument, tool and material was done using sterile gloves.

Finally, it is worth noting that the methodology employed in this research has been applied to various composite materials which utilize polymers or polymer blends as matrices. For instance, DSC and TGA have been used to analyze carbon fiber reinforced polymers (CFRP), glass fiber reinforced polymers (GFRP) [30, 31] and other composite materials, such as carbon fiber/ polyether ether ketone (PEEK) [32]. Therefore, the aforementioned methods are widely applicable to both polymeric and composite materials.

3. RESULTS AND DISCUSSION

The results of this study will be reported in two different sections. First, the data attained from the TGA and DSC experiments are directly analyzed. Then, a discussion is presented on the thermal parameters estimated by the tests, focusing specifically on the Glass Transition Temperature, T_g, of the materials studied.

3.1. Thermogravimetric Analysis (TGA) and Differential Scanning Calorimetry (DSC)

The weight loss curves obtained from the TG and DSC data are shown for all materials in Fig. 2.

a)

b)
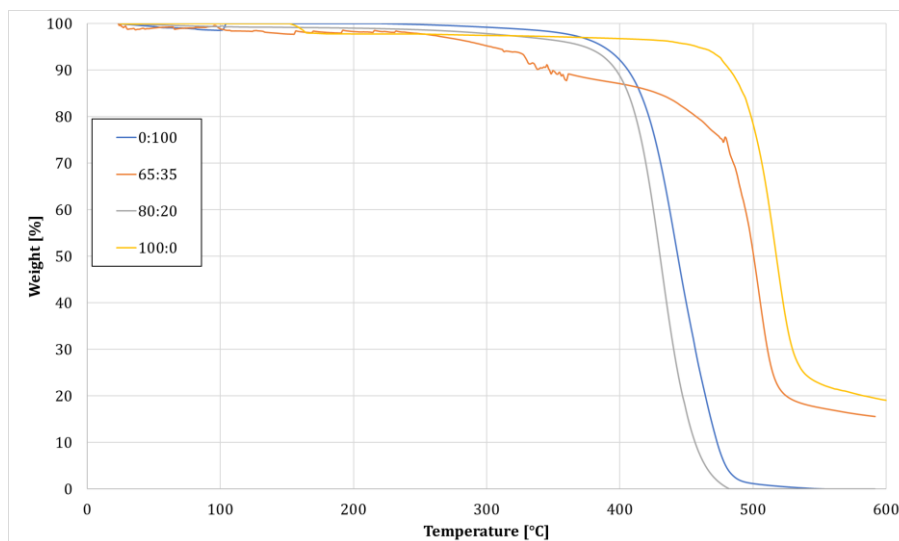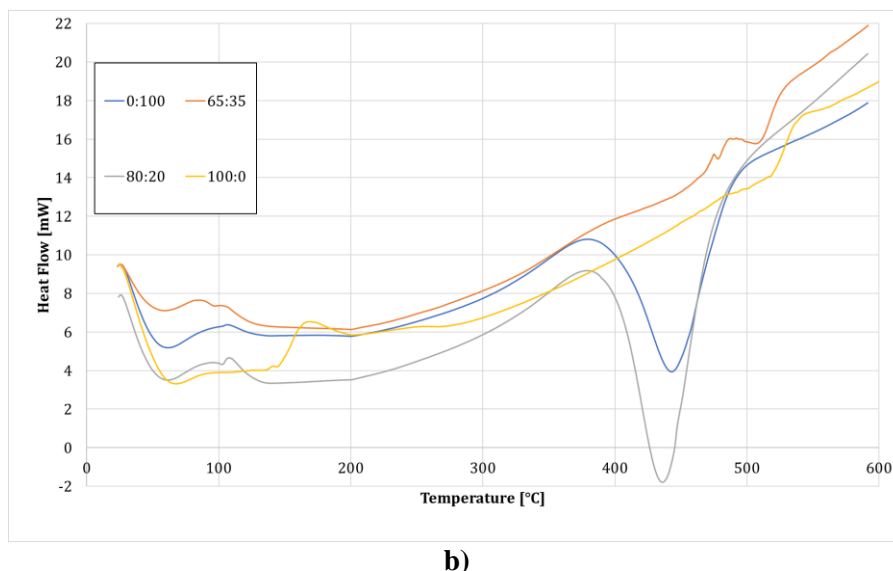
Figure 2. TGA (a) and DSC (b) curves of the blends.

A quick glance at. Fig. 2a shows that pure ABS and 80:20 are the least thermally stable compositions, whereas 65:35 is almost as stable as pure PC. Moreover, pure ABS and 80:20 displayed no residue at 600 ºC, in contrast with pure PC and 65:35, which kept around 20% of residue at that temperature. A possible explanation for that in pure PC is inorganic compounds either formed during the heating or were there in the first place in the form of additives. It is intriguing that 65:35 also showed that residue, which could only be explained by the presence of additives or other unidentified compounds in the blend, considering the manufacturers of both are different.

Nevertheless, it is remarkable how similar PC/ABS 65:35 behaves in comparison to pure PC. It is as though replacing 35% in weight of PC to ABS almost didn't change the material's thermal stability, whereas increasing only 20% changed it completely. In Fig. 2b, one can also promptly see these similarities. 80:20 and pure ABS present distinct valleys around 450 ºC, where there is a massive degradation (as shown in Fig. 2a). However, that is not the case for 65:35 and pure PC. For those compositions, the degradation is considerably less severe, leading to slight fluctuations in the DSC curve.

Another interesting feature of 65:35 is that it starts to degrade at around 300 ºC, while pure ABS and 80:20 start at around 400 ºC and pure PC at more than 450 ºC, but that blend's degradation is spread over a wider temperature range than the others and shows a few bumps on the curve. That is suggestive of complex reactions taking place during the heating process, and possibly breaking or weakening some of the bonds formed between the macromolecules that would account for its notable mechanical behavior, as seen in the literature [9, 14, 21].

Moreover, the similarity between 80:20 and pure ABS is also easily noticeable in Fig. 2. One could argue that might be due to both compositions having been supplied by the same manufacturer, i.e., INEOS. Indeed, it is known that different polymer blend manufacturers use different mixing compounds and additives in various concentrations. Thus, it would be reasonable to assume that 80:20 and pure ABS thermal degradation curves are alike because the materials come from the same manufacturer. Even though that might play a reasonably important role in the development of the peaks shown in the curves and the overall aspect of the curves, it doesn't seem to be the main cause for the aforementioned similarity for a few reasons.

Firstly, the fact that 65:35 and pure PC behave in similar fashions, even though the former is made by Ravago and the latter by SABIC, already suggests that additives and other compounds supposably inserted into the mixture are not solely responsible for the thermal behavior of these blends. Secondly, and perhaps more importantly, as it will be discussed further, the similarities arise not only in the thermal degradation tests, but also in the mechanical responses of these materials to complex and severe loading schemes [21]. In other words, 80:20 mechanically behaves more closely to pure ABS, whereas 65:35 is more alike pure PC under severe loads, which could not be attributed to the presence of additives or other mixing compounds.

Therefore, when analysing the results herein discussed, one should take into account the fact that two of the compositions are supplied by the same manufacturer, but that doesn´t seem to be the main cause of the similarity between their thermal and mechanical behavior.

3.2. Glass transition temperature (T$_g$)

The glass transition temperature, T$_g$, is a critical thermodynamical parameter that characterizes the transition in a material between a more solid and rigid (glassy) state to a more viscous and flexible (rubbery) one. It is known that T$_g$ is influenced not only by the material's chemical composition, but also by how its components are interconnected and by the presence of additives. In the case of polymer blends, it is not generally trivial to calculate the T$_g$, since there might be more than one value measured by the usual experimental methods (such as DSC, for instance) and there is general way to combine those different values. While some studies simply take the mean of those values and attribute them to the blend, others take more complex approaches, such as all-atomistic molecular dynamics simulations, neural networks, genetic algorithms, and lattice fluid models [27, 28].

That phenomenon has been seen in PC/ABS. Yin *et al.* [23], for instance, identified two distinct points for each PC/ABS blend tested in DMA. However, the blends herein studied apparently displayed a single value for T$_g$. For an easier visualization, the TG and DSC curves for each composition are show in a single plot in Fig. 3.
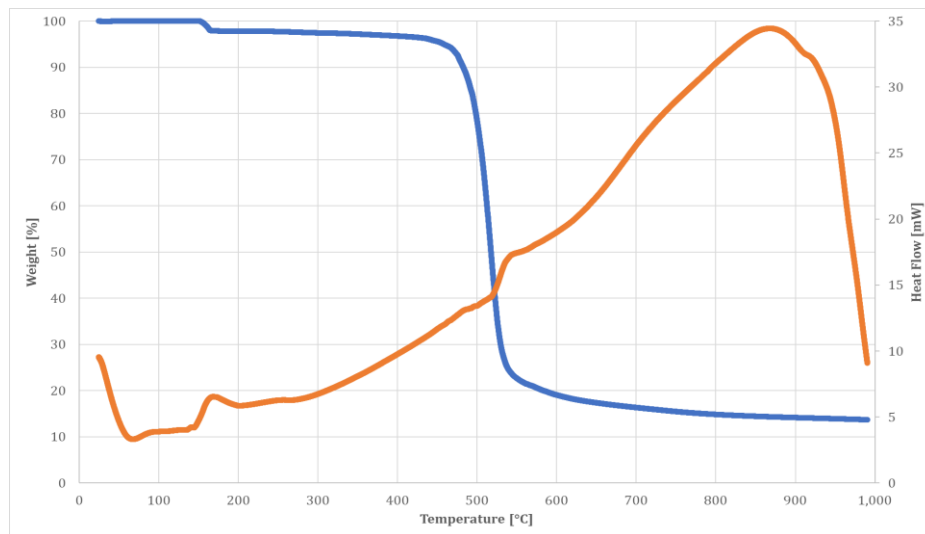
a)
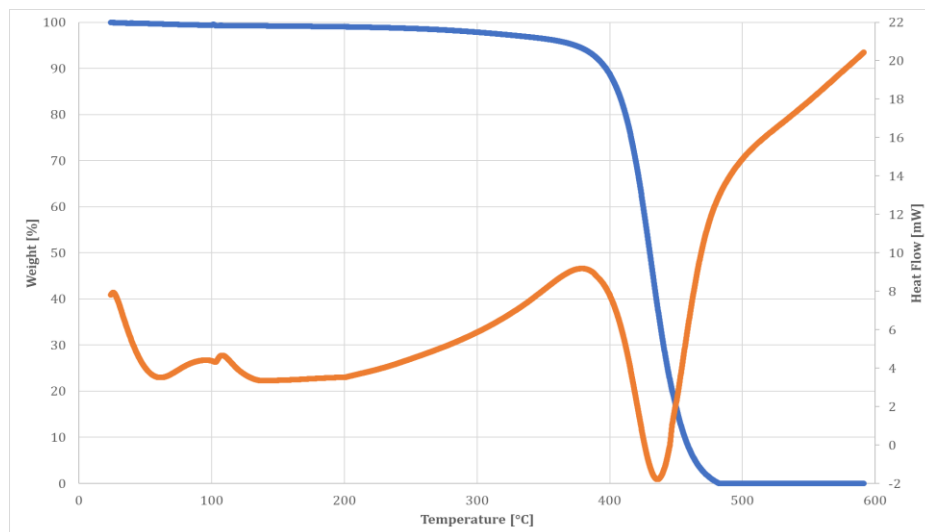
b)
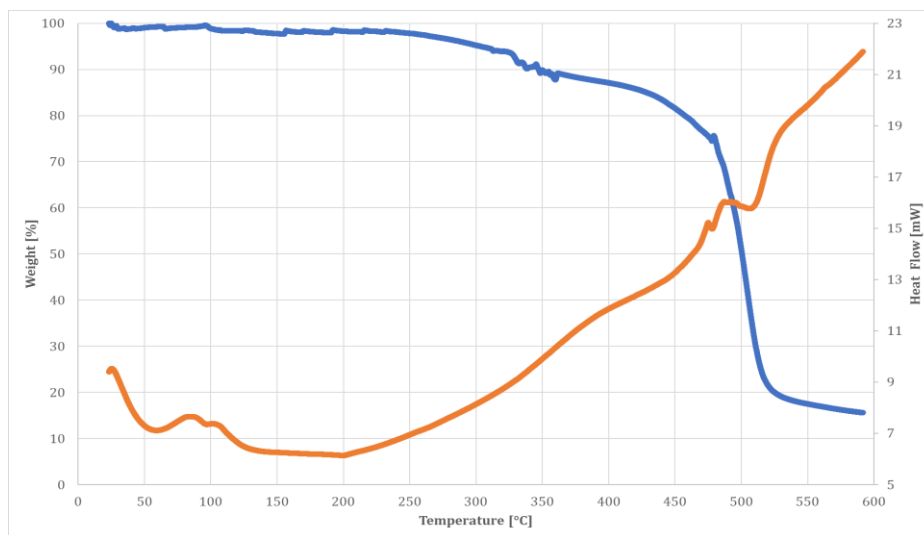
c)
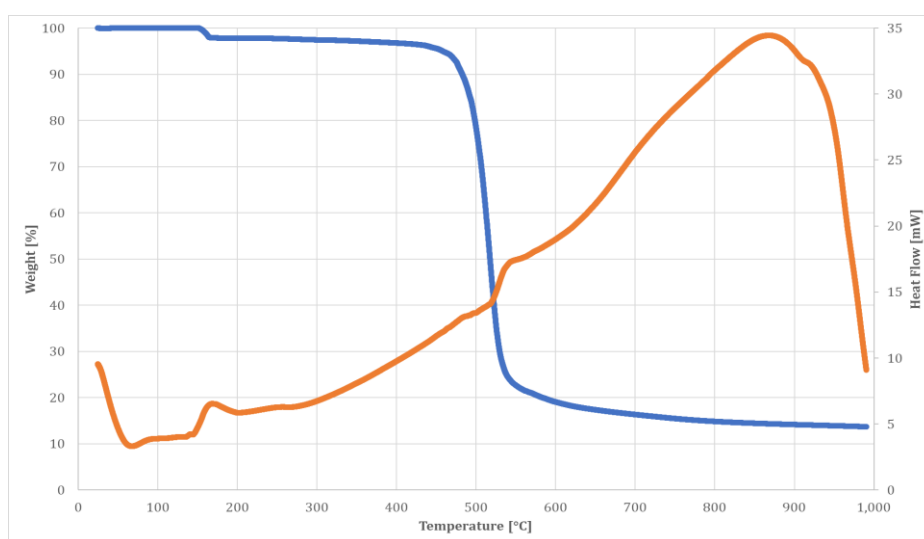
d)

Figure 3. Plots of both DSC and TGA curves for each material: a) Pure PC, b) PC/ABS 80:20, c) PC/ABS 65:35, d) Pure ABS. Note: the curves for pure PC are shown up to 1,000 ºC.

The values of T_g for each blend, measured using the companion's software, are shown in Table 3, as well as the enthalpy associated with the degradation and the melting temperature, T_m.

Table 3. Thermal parameters measured for each blend.

Material	PC content [% wt]	ABS content [% wt]	T_g [ºC]	$\Delta H_{degradation}$ [J/g]	T_m [ºC]
Pure PC	100	-	143.90	16.16	518.04
PC/ABS 80:20	80	20	111.26	364.8	436.92
PC/ABS 65:35	65	35	108.20	20.46	509.73
Pure ABS	0	100	110.81	262.4	444.03

The data in Table 3 corroborates the previously analysis, in the sense that is noticeable how similar 80:20 is to pure ABS and 65:35 to pure PC, in terms of thermal stability. Indeed, one can promptly see that both pure PC and 65:35 show a very low degradation enthalpy, which, in association with the fact that the weight loss in these materials is considerably lower than the other compositions, suggest that partial degradation took place. In other words, it is possible that this specific amount of ABS (35%) protected the blend from degradation, making it behave like PC. However, a distinct difference between those two materials is that their glass transition temperatures vary considerably. PC/ABS 65:35 displayed a similar T_g to all the

other compositions, at around 108 – 110 °C, whereas pure PC displayed a much higher value, at around 144 °C. That means ABS does influence the blend's behavior, resulting in a glass transition similar to that of pure ABS, which could account for the desired characteristic of PC/ABS blends in terms of malleability and easy processing. That is coherence with previous results found in the literature [23].

It is known that when polymers are partially miscible, the T_g of mixed amorphous phases will fluctuate between those of the pure components [29]. In other words, PC/ABS's T_g should vary between the glass transition temperature of ABS, i.e., 110 °C and that of pure PC, i.e., 144 °C. The variation is expected to follow the proportion of each component in the blend. Thus, blends with higher contents of ABS should have a T_g closer to that of pure ABS and vice-versa. However, once again the 65:35 behaved differently, displaying the lowest value of T_g, despite not having the lowest amount of ABS.

No consistent explanation was found on the literature that explained this interesting characteristic. Nevertheless, the fact is that blends with ratios around 60:40 and 65:35 seem to behave notably better under mechanical loads [9, 21], and apparently under thermal degradation as well. In a previous study, this author investigated the resistance of the same PC/ABS blends herein analyzed under complex compressive loads. More specifically, the resistance to compression (indentation and compressive creep) as well as torsional fretting wear was measured by the total volume and total depth of the damage marks left on prismatic samples (shown in Fig. 1) after applying the compressive loads with a naval-graded steel hemispherical indenter. The findings were promising for industrial applications, but they lacked a deeper explanation as to why 65:35 is so much more resistant than the other blends.

Given the results of the present study, as an attempt to correlate the values of T_g to some parameters measured in the aforementioned papers, Fig. 4 was created. It shows that there is no direct correlation between the blend's T_g and the mechanical properties therein measured. That suggests the reason for such remarkable behavior of PC/ABS 65:35 lies not specifically on the glass transition phase, but perhaps in other aspects of the blend. For further details on the mechanical tests conducted, the reader is referred to [21].

Considering the results discussed above, it seems as though the elusive optimal blend for mechanical resistance under compressive loads hypothesized by Pandim *et al* [21] is indeed in the ratio range of 60:40 – 65:35 and the reasons for their distinctly good results might have to do with thermal characteristics, but not directly with the glass transition of the blend.

Therefore, more research is required in the specific composition of the commercial blend used, perhaps through more sophisticated techniques, such as Fourier-transform infrared spectroscopy (FTIR) and a chemical analysis of the possible reactions taking place when considering those ratios of components.
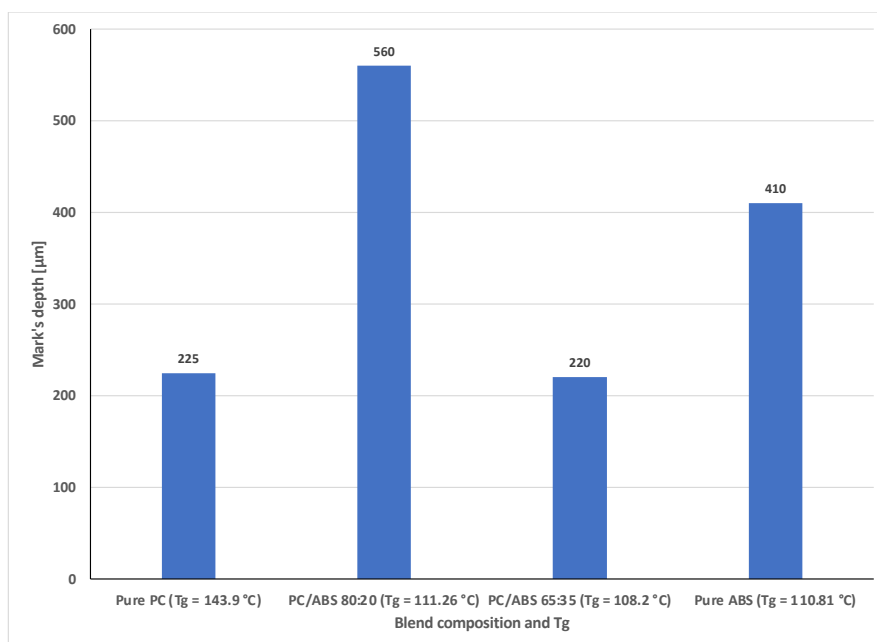
a)
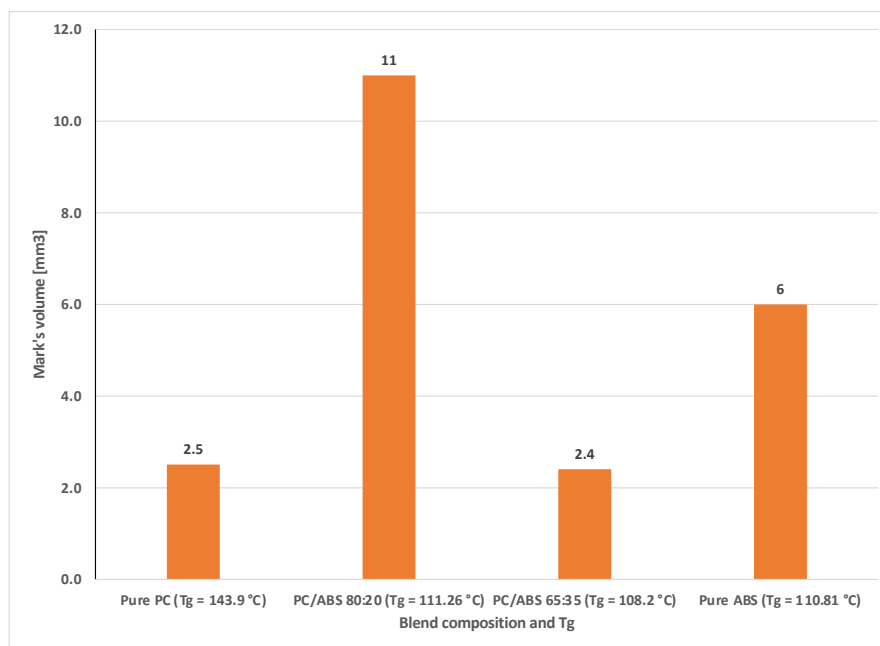
b)

Figure 4. Comparison of total mark depth (a) and total mark volume (b) for all blends. Data combined with [21].

4. CONCLUSIONS

This work intended to analyze samples of PC/ABS with weight ratios of 100:0 (pure PC), 80:20, 65:35 and 0:100 (pure ABS). That was done by conducting simultaneously TG and DSC tests using a TA Instruments' SDT Q600 thermal analyzer. All samples were heated from room temperature up to 600 ºC at a heating reate of 15 ºC/min, except pure PC (which was heated at the same rate, but up to 1000 ºC). The main conclusions of this work can be summarized as follows:

- Thermogravimetric Analysis (TGA) revealed that pure ABS and 80:20 are the least thermally stable compositions, whereas 65:35 is almost as stable as pure PC. The behaviors 65:35 and pure PC are remarkably similar, also with respect to the residue left, which suggests that 65:35 may either have an additive in its composition or undergo some reaction during manufacturing that results in a very resistant inorganic compound.

- Moreover, PC/ABS 65:35 starts to degrade earlier than the other compositions, but does it over a wider temperature range and only undergoes considerable weight loss at temperatures higher than those of PC/ABS 80:20, once again suggesting that not only the ABS content in a PC matrix defines the blend's thermal stability.

- Differential Scanning Calorimetry (DSC) supported the TGA findings, indicating the similar behavior between 65:35 and pure PC, and also between pure ABS and 80:20.

- Regarding glass transition temperatures, the results indicate that the amount of ABS in the blend results in very minor changes in the values of T_g. Therefore, the notable mechanical resistance of 65:35, as reported in the literature [21] does not seem to have a direct correlation with that thermodynamical parameter.

- More research is needed to investigate the precise chemical composition of the blends herein studied, as well as their morphology in a molecular level, by means of FTIR and advanced microscopy techniques.

4.1. Declaration of Competing Interest

The author declares no conflict of interest.

5. REFERENCES

[1] P. Research. Polymers Market Size to hit around USD 1078.5 Billion by 2030. Precedence Research, available on: https://www.precedenceresearch.com/polymers-market. Accessed at 09.20.2023.

[2] M. Ziaie *et al.* Numerical and experimental study on mechanical properties of glass fiber-reinforced polymer sandwich structure with polyurethane foam-filled M-shaped core. *Polymer Composites*. Volume 44, 2022.

[3] M. Maghsoudlou *et al.* Effect of interphase, curvature and agglomeration of SWCNTs on mechanical properties of polymer-based nanocomposites: Experimental and numerical investigations. *Composites Part B: Engineering*. Volume 175, 2019.

[4] J. Zhou *et al.* Experimental investigation of size effect on mechanical properties of carbon fiber reinforced polymer (CFRP) confined concrete circular specimens. *Construction and Building Materials*. Volume 127, 2016.

[5] H. Vinay *et al.* Experimental Study on Mechanical Properties of Polymer Based Hybrid Composite. *Materials Today: Proceedings*. Volume 4, 2017.

[6] H. Veenstra *et al.* On the mechanical properties of co-continuous polymer blends: experimental and modelling. *Polymer.* Volume 41, 2000.

[7] Y. Liao *et al.* An Experimental Study on the Dynamic Mechanical Properties of Epoxy Polymer Concrete under Ultraviolet Aging. *Materials*. Volume 14, 2021.

[8] K. Chandran. Mechanical fatigue of polymers: A new approach to characterize the SN behavior on the basis of macroscopic crack growth mechanism. *Polymer*. Volume 91, 2016.

[9] T. Pandim *et al.* Torsional fretting wear experimental analysis of a R3 offshore steel against a PC/ABS blend. *Tribology International.* Volume 143, 2020.

[10] Q. Wang *et al*. Experimental investigation on tribological behavior of several polymer materials under reciprocating sliding and fretting wear conditions. *Tribology International.* Volume 104, 2016.

[11] S. Terekhina *et al.* Contact fatigue and wear behaviour of bismaleimide polymer subjected to fretting loading under various temperature conditions. *Tribology International*. Volume 44, 2011.

[12] X. Gao *et al.* Effects of Different Forms of Polytetrafluoroethylene Microparticles on Fretting Wear Resistance and Mechanical Properties of Polycarbonate/Acrylonitrile Butadiene Styrene Composites. *Journal of Materials Engineering and Performance*. Volume 31, 2022.

[13] L. Utracki. Commercial Polymer Blends. *Springer-Science+Business Media B.V.* 1988.

[14] R. Krache, I. Debbah. Some mechanical properties and Thermal Properties of PC/ABS Blends. *Materials Science and Applications*. Volume 2, 2011.

[15] J. Hund *et al.* An experimental and constitutive modeling study on the large strain deformation and fracture behavior of PC/ABS blends. Mechanics of Materials. Volume 124, 2018.

[16] M. Ishikawa. Stability of plastic deformation and toughness of polycarbonate blended with poly(acrylonitrile-butadiene-styrene) copolymer. *Polymer.* Volume 36, 1994.

[17] K. N. Win, E. Liu. Thermal, mechanical and tribological properties of polycarbonate/acrylonitrile-butadiene-styrene blends. *Journal of Polymer Engineering*. Volume 33, 2013.

[18] J. W. M. Mens *et al.* Friction and wear behaviour of 18 polymers in contact with steel in environments of air and water. *Wear*. Volume 149, 1991.

[19] A. L. Zaitscv. Mechanisms of hard alloy wear in frictional processes with polymers and composite materials. *Wear*. Volume 162, 1993.

[20] P. L. Geiss. Creep Load Conditions. In: *Handbook of Adhesion Technology*. Berlin, 2011.

[21] T. Pandim *et al.* Indentation, creep and axial-torsioanl fretting wear analysis of PC/ABS blends. *Tribology International*. Volume 188, 2023.

[22] M. E. Brown. Introduction to Thermal Analysis – Techniques and Applications. *Kluwer Academic Publishers*. 2004.

[23] Yin *et al.* Experimental investigation of the viscoelastic deformation of PC, ABS and PC/ABS alloys. *Materials Letters*. Volume 62, 2008.

[24] T. Chinnandurai *et al.* Experimental studies on Thermo-Mechanical Behavior of Ultrasonically Welded PC/ABS Polymer Blends. *Silicon.* Volume 10, 2018.

[25] S. Devi. Effect of compositions and compatibilizer on the viscoelastic behavior of polycarbonate/acrylonitrile butadiene styrene blends. In: *AIP Proceedings*, 2021.

[26] M. Yazdi, P. Lee-Sullivan. Determination of Dual Glass Transition Temperatures of a PC/ABS blend using two TMA modes. *Journal of Thermal Analysis and Calorimetry*. Volume 96, 2009.

[27] C. Wu. A multiscale scheme for simulating polymer Tg. *Journal of Molecular Modeling.* Volume 24, 2018.

[28] N. Roy *et al.* Designing Polymer Blends Using Neural Networks, Genetic Algorithms, and Markov Chains. *Applied Intelligence.* Volume 20, 2004.

[29] N. Romanova *et al*. Thermal properties of products based on ABS/PC. In: *MATEC Web of Conferences, ICMTMTE 2019*. Volume 298, 2019.

[30] A. Ghani, J. Mahmud. Shear deformation behavior of hybrid composite (GFRP/CFRP). *Materialwissenschaft Werkst*. Volume 48, 2017.

[31] Y. Kim *et al*. Thermo-gravimetric analysis method to determine the fiber volume fraction for PAN-based CFRP considering oxidation of carbon fiber and matrix. *Composites Part A: Applied Science and Manufacturing.* Volume 102, 2017.

[32] M. Giżyński, B. Romelczyk-Baishya. Investigation of carbon fiber–reinforced thermoplastic polymers using thermogravimetric analysis. *Journal of Thermoplastic Composite Materials.* Volume 34, 2019.

INVESTIGATING THE IMPACT OF HYGROTHERMAL AGING ON MODE II INTERLAMINAR FRACTURE TOUGHNESS IN EPOXY-BONDED COMPOSITE JOINTS

Carlos Eduardo Moraes[a]*, Luis Felipe de Paula Santos[b], Michelle Leali Costa[c], Edson Cocchieri Botelho[d]

(a) 0000-0001-7095-1029 (UNESP - São Paulo State University – Brazil)
(b) 0000-0002-5089-1089 (Laboratório de Estruturas Leves – LEL/IPT – Brazil; UNESP - São Paulo State University – Brazil)
(c) 0000-0001-9492-8544 (UNESP - São Paulo State University – Brazil; Forza Composites- Brazil)
(d) 0000-0001-8338-4879 (UNESP - São Paulo State University – Brazil)
* Corresponding author: eduardo.moraes@unesp.br

Abstract: Technological advancements in composite materials are crucial across industries like oil and gas, addressing challenges in engineering for lighter and more durable structures. Adhesive techniques offer solutions, mitigating issues such as sparks during welding and delamination caused by mechanical fasteners. This study assesses interlaminar fracture toughness (G_{IIC}) using the end-notched flexure (ENF) test on carbon fiber/epoxy composites and epoxy-based adhesive. The effects of humidity on this property are examined. Three surface preparations (manual sanding, solvent cleaning, peel ply (fuseply) application) and adhesive thickness variations (0.5 and 1.0 mm) are applied to analyze the adhesive-adherend interaction and thickness impact on shear behavior. Results show that isopropyl alcohol cleaning effectively generates a strong adhesive bond, reducing costs in oil and gas industries by eliminating unnecessary preparation steps. Samples with 1.0 mm thickness exhibit superior energy dissipation, confirmed by scanning electron microscopy. Hygrothermal aging reduces G_{IIC} values by approximately 45%, indicating humidity's adverse effects on adhesive performance.

1. INTRODUCTION

In the oil and gas industry, where extreme environments and severe operating conditions are common, the choice of fastening materials for various structures is crucial to ensure the safety, efficiency, and durability of these joints [1-2]. Currently, welding is still a structural joining technique widely used on offshore platforms, for example, but it brings with it safety risks such as the sparks generated by this process, which can come into contact with gases and other petroleum products that are highly volatile and cause explosions [3]. In this sense, structural adhesives appear as an alternative that is capable of mitigating these risks, in addition to presenting other advantages about mechanical fasteners such as screws and rivets [4]. When it comes to joining composite materials, screws, and rivets need to pierce the surface of these materials, which can cause stress concentration, fiber breakage, and even delamination [4]. However, the application of structural adhesives in aggressive environments (high UV radiation, high levels of humidity and salinity, high-temperature variations, among others) is not so simple [5]. Therefore, the study of the behavior of these materials in such conditions and especially the effects caused in structural adhesive joints are of crucial importance. This study, therefore, involves the evaluation of adhesive joints using the End Notched Flexure (ENF) test, in carbon fiber/epoxy composites and epoxy-based structural adhesive. The influences of the exposure of these joints to hygrothermal

aging are also evaluated, focusing on the effects caused by the interlaminar fracture toughness property in mode II (G_{IIC}). Furthermore, three different surface treatments of the adherent material are evaluated, namely: cleaning with isopropyl alcohol, sanding with an abrasive sponge, and application of peel ply (fuseply), to understand the impact of these surface preparations on the interface region. of the adhesive joint. The study also evaluates the influence of two adhesive layer thicknesses, 0.5 and 1.0 mm, to verify how the thickness of the adhesive influences the mechanical property evaluated.

2. METHODOLOGY

2.1. Materials

For this study, the epoxy-based structural adhesive used was AeroPaste X1003 supplied by Solvay. It is a two-component (epoxy resin and hardener) with a mixing ratio of 2:1, respectively. The adherend material consisted of a carbon fiber/epoxy laminate (AS4 8552) supplied by Embraer.

2.2. Composite surface treatments and adhesive layer

Three different surface treatments were conducted to verify the levels of adhesion achieved in each case. The first one was solvent cleaning, which consisted of cleaning the adherend surface with isopropyl alcohol for decontamination. The second one was manual sanding with an abrasive sponge, followed by a solvent cleaning to avoid recontamination from the particulates that originated in the sanding process. The last surface treatment was the peel ply (fuseply) application. In this case, a fabric base on polyamide-6 was applied before the curing cycle and, before the bonding process, the fabric was removed leaving a woven impression on the adherend surface. Regarding the thickness of the adhesive layer, two different thicknesses were tested, 0.5 and 1.0 mm.

2.3. EFN Test

According to the ASTM D7905 standard, the ENF test consists of testing specimens without pre-crack (NPC) and with pre-crack (PC), determining the interlaminar fracture toughness values G_{IIC}_NPC and G_{IIC}_PC. The first test (NPC condition) was carried out for crack lengths (a_0) of 12mm, 24mm, and 18 mm, following this order, with a distance between the supports of 100 mm. When the load (P) reaches a pre-determined value, which does not initiate delamination, the test is terminated and the test specimen is removed and repositioned in the device to the next position a_0. In the last position of a_0 (18mm), the test is carried out until the test piece begins to delaminate. The test is then stopped when the load value P reaches its maximum value. After completing the NPC fracture test, which creates a shear pre-crack, the specimen is removed from the testing machine and reused to conduct the test in the PC condition with the crack length measurement being the new tip location. of delamination. The PC tests were conducted using the same procedure as the NPC test, with the crack induced in the last NPC test being the reference for the a_0 markings. Using equation 1, the coefficients A (intercept) and m (angular coefficient of the straight line) are determined from the linear regression data of the compliance curve (mm/N) versus a03 (mm³)

$$C = A + m \times a_0^3 \tag{1}$$

Mode II interlaminar fracture toughness (GIIC) was calculated using equation 2:

$$G_{IIc} = \frac{3 \times m \times P_{max}^2}{2 \times B} \tag{2}$$

Where P_{max} is the maximum delamination load and B is the sample width.

2.4. Hygrothermal aging

To assess the effects of the conditioning in the adhesive bond, the specimens prepared with fuseply as adherend surface treatment and 0.5 mm of adhesive layer were immersed in deionized water at 80ºC for 115 days. The choice of the fuseply as surface treatment and 0.5 mm of adhesive layer thickness as well as the water temperature, were due to some requirements of the oil and gas industry.

3. RESULTS AND DISCUSSION

3.1. Pre-conditioning ENF test

Figure 1 presents the load (N) versus displacement (mm) curves for all evaluated conditions of surface treatment and adhesive layer thickness.
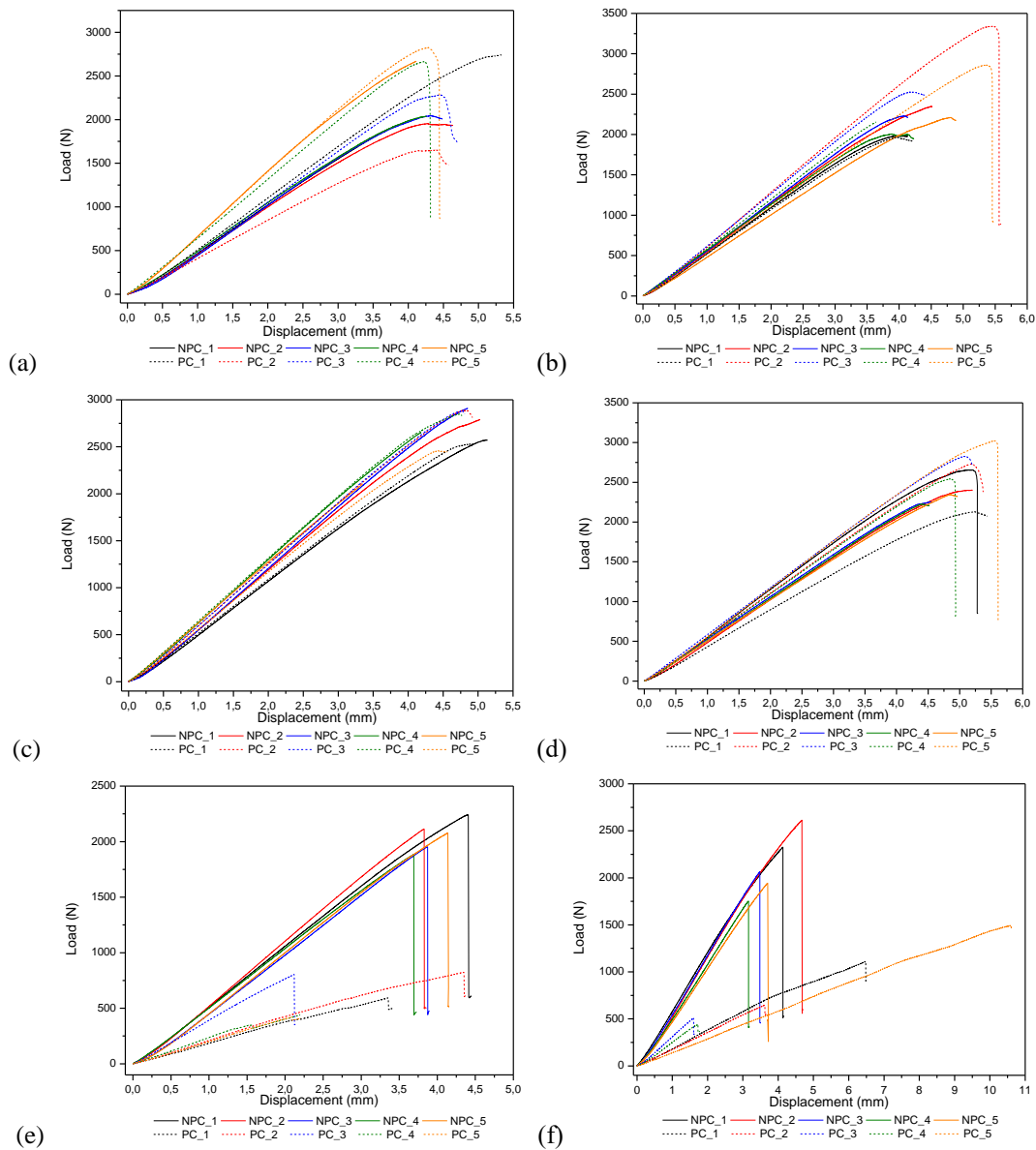
Figure 1. Load (N) versus displacement (mm) curves for the following conditions: (a) solvent cleaning – 0.5 mm; (b) solvent cleaning – 1.0 mm; (c) manual sanding – 0.5 mm; (d) manual sanding – 1.0 mm; (e) fuseply – 0.5 mm; (f) fuseply – 1.0 mm

Figure 1 shows a very similar behavior of the load versus displacement curves in the solvent cleaning condition in both thicknesses (Figure 1a and Figure 1b) and manual sanding condition, also in both thicknesses (Figure 1c and Figure 1d). It starts with a linear increase in load up to the point where it reaches a maximum value and the crack propagates by shear. It is noted that the curves of the NPC and PC test also showed a certain degree of similarity, which suggests good adhesion between the components of the adhesive joint, resulting in the action of cohesive forces in the adhesive/adhesive interface region [6]. What reinforces this hypothesis is the behavior seen in samples that use fuseply as a surface treatment (Figure 1e and Figure 1f). In both thicknesses, there was a significant drop in the load versus displacement curve between the NPC and PC conditions, indicating low adhesion and, consequently, a low level of action of cohesive forces in the interface region. Tables 1 and 2 show a summary of G_{IIC} values for NPC and PC conditions, respectively, for all analyzed combinations of surface treatment and adhesive layer thickness.

Table 1. Summary of G_{IIC} values calculated for each NPC condition of each surface treatment and adhesive layer thickness analyzed.

Sample	Fuseply 0.5 mm	Fuseply 1.0 mm	Manual sanding 0.5 mm	Manual sanding 1.0 mm	Solvent cleaning 0.5 mm	Solvent cleaning 1.0 mm
	Interlaminar fracture toughness in mode II (G_{IIC}) - NPC (J/m²)					
1	159.88	150.23	201.30	201.80	105.79	113.92
2	126.13	186.35	201.56	178.79	123.99	154.07
3	121.40	109.73	214.22	151.46	149.49	130.12
4	112.63	88.32	171.31	159.60	121.52	124.42
5	145.74	106.68	119.29	189.10	164.39	152.88
Average	133.16 ± 19.24	128.26 ± 39.56	181.54 ± 38.21	176.15 ± 20.71	133.04 ± 23.51	135.08 ± 17.77

Table 2. Summary of G_{IIC} values calculated for each PC condition of each surface treatment and adhesive layer thickness analyzed.

Sample	Fuseply 0.5 mm	Fuseply 1.0 mm	Manual sanding 0.5 mm	Manual sanding 1.0 mm	Solvent cleaning 0.5 mm	Solvent cleaning 1.0 mm
	Interlaminar fracture toughness in mode II (G_{IIC}) - NPC (J/m²)					
1	22.92	79.67	194.61	164.49	235.72	119.86
2	38.15	24.51	200.73	246.62	98.07	311.64
3	20.55	9.11	210.21	223.59	166.62	155.78
4	11.18	8.56	197.97	196.72	168.85	144.84
5	10.16	102.88	174.54	295.13	169.59	255.24
Average	20.59 ± 11.30	44.95 ± 43.55	195.61 ± 13.13	225.31 ± 49.62	167.77 ± 48.69	197.47 ± 82.01

Analyzing the tables, the reduction in cohesive adhesion forces in the condition using fuseply as surface treatment becomes even clearer, while the other treatments maintained relatively close fracture toughness values in mode II in the NPC and PC conditions. In fact, in all other surface treatments, there was an increase in the average values obtained for G_{IIC} between the NPC and PC conditions, which highlights the good adhesion of these conditions in comparison to the fuseply treatment. The increase in thickness from 0.5 mm to 1.0 mm generated an increase in the average values obtained for G_{IIC}, especially in the PC condition, for all surface treatments analyzed, a fact that can be explained by the size of the plastic region formed in the tip of the crack. The increase in the thickness of the adhesive layer means that the adhesive can generate larger plastic regions before fracture, being able to dissipate greater levels of energy [7-8].

The results from ANOVA statistical analysis for the NPC condition are shown in Table 3 and for the PC condition, in Table 4. One can observe that, for both conditions of test (NPC and PC) the p-value of the surface condition was less than 0.05 and, therefore, is a significant variable. Conversely, the thickness of the adhesive layer resulted in a p-value greater than 0.05, therefore being a non-significant variable. This suggests that, at a statistical level, the surface treatment of the adherend had a greater influence on the interlaminar fracture toughness than the thickness of the adhesive layer. Logically, this result has a very significant influence on the surface preparation using fuseply, as it was what generated G_{IIC} values with higher levels of discrepancy compared to the others.

Table 3. ANOVA results for the NPC condition.

Variable source	DF	SQ	QM	F_{value}	p-value
Surface treatment	2	12561.8	6280.92	8.36	0.002
Thickness	2	142.6	71.28	0.09	0.910
Error	25	18772.2	750.89	-	-
Total	29	33360.5	-	-	-

Table 4. ANOVA results for the NPC condition.

Variable source	DF	SQ	QM	Fvalue	p-value
Surface treatment	2	170.028	85414.1	38.78	0.000
Thickness	2	5858	2928.8	1.33	0.283
Error	24	55.058	2202.3	-	-
Total	29	243599	-	-	-

Figure 3 shows the micrographs obtained via SEM for the fracture surfaces that use fuseply as a surface treatment for the adherend. In the condition with 0.5 mm thickness of the adhesive layer (Figure 3a), it is possible to observe the presence of some points of rupture of the adherend fibers (yellow arrows) indicating that, despite the adhesive failure, there were points where the failure occurred on the surface of the adherent. It is also possible to observe a few points of resin debris (orange arrows), which indicates the presence of energy dissipation mechanisms even in the condition that presented the lowest results about G_{IIC} values. The increase in thickness (Figure 3b) made it possible to observe the presence of the same mechanisms described previously, in addition to the presence of small points where the adhesive becomes visible on the adherent (green arrow), which indicates the low adhesion of the adhesive on this surface compared to the other preparations carried out.

Figure 4 presents the micrographs obtained via SEM for the fracture surfaces that use manual sanding as surface treatment of the adherend. In the condition with 0.5 mm thickness of the adhesive layer (Figure 4a), the presence of fiber marks (yellow arrows), fractured fibers (green arrows), cusps (purple arrows), and deformation of the adhesive layer (red arrow) were observed. Many fracture micromechanisms make it clear that this surface treatment condition was the most effective in dissipating energy, reaching higher G_{IIC} values compared to the other treatments carried out. In addition to observing the same fracture micromechanisms, the increase in thickness (Figure 4b) also made it possible to observe river marks (orange arrow), formed by several pairs of unequal crack planes, which are directed towards a single crack plane during fault propagation [9].

Figure 5 shows the micrographs obtained via SEM for the fracture surfaces that use solvent cleaning as a surface treatment of the adherent. In the condition with an adhesive layer thickness of 0.5 mm (Figure 5a), it is possible to observe the presence of fiber marks (blue arrows), cusps (purple arrows), and fractured fibers (green arrows). Fracture micromechanisms indicate the dissipation of high levels of energy, as in the manual sanding condition. However, the solvent cleaning condition resulted in lower mean G_{IIC} values compared to the sanded condition. The increase in thickness (Figure 5b) also made it possible to observe the presence of the same fracture micromechanisms, in addition to the scarps (yellow arrows), which indicate the direction of crack propagation. In all surface preparations, increasing thickness proved to be efficient in dissipating higher levels of energy due to the adhesive's larger plastic area, generating the same fracture micromechanisms as the thinner condition and new micromechanisms.

(a)　(b)
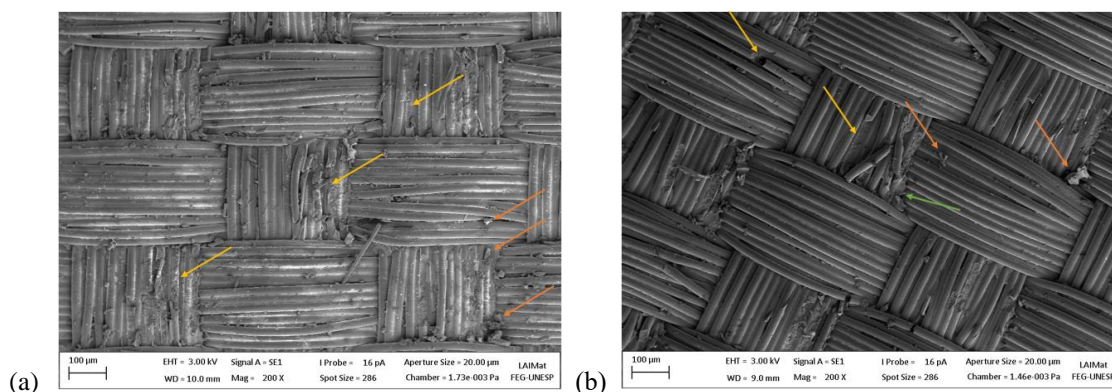
Figure 3. Micrographs obtained via SEM of the fracture surfaces under conditions using fuseply and adhesive layer thickness of (a) 0.5 mm and (b) 1.0 mm.
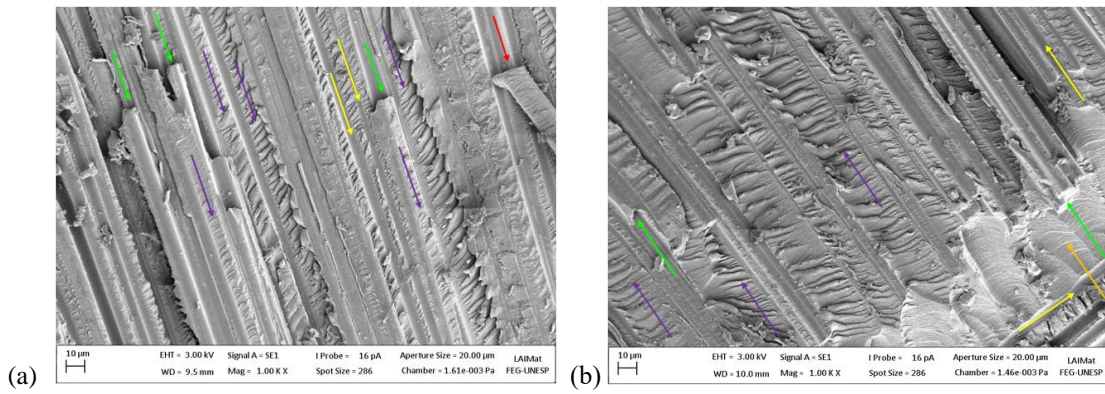
Figure 4. Micrographs obtained via SEM of the fracture surfaces under conditions using manual sanding and adhesive layer thickness of (a) 0.5 mm and (b) 1.0 mm.
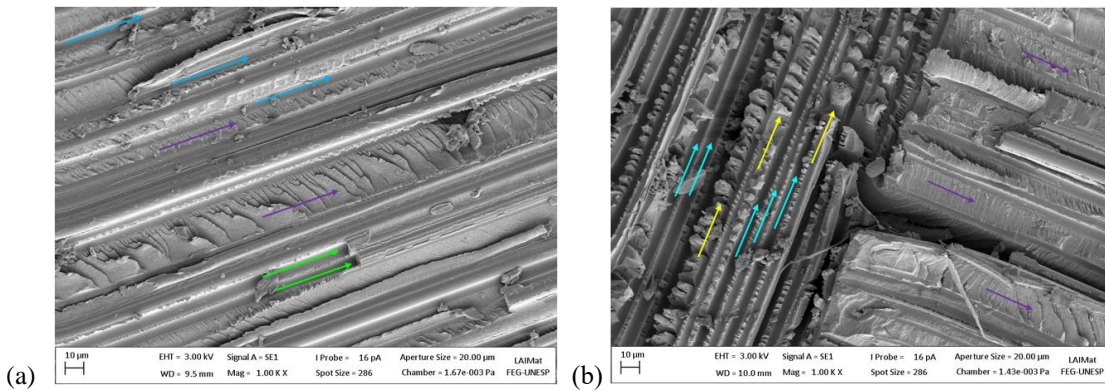
Figure 5. Micrographs obtained via SEM of the fracture surfaces under conditions using solvent cleaning and adhesive layer thickness of (a) 0.5 mm and (b) 1.0 mm.

3.2. Post hygrothermal aging ENF test

Figure 6 presents the load versus displacement curves for the 6 specimens evaluated after hygrothermal aging. In all specimens, the behavior observed in this same combination of surface treatment and adhesive layer thickness before the aging process was maintained. In both the NPC and PC conditions, what can be observed is a significant decrease in G_{IIC} values. What is observed is a significant reduction in loads, generally increasing the average compliance values obtained when compared to the same non-aged situation. According to reference [5], the drop in cohesive forces in adhesive joints exposed to a high humidity environment is the result of a series of interconnected factors, such as, for example, swelling of the adhesive due to water sorption, splitting of the adhesive's polymer chains, the drop in T_g and consequent plasticization of the material.
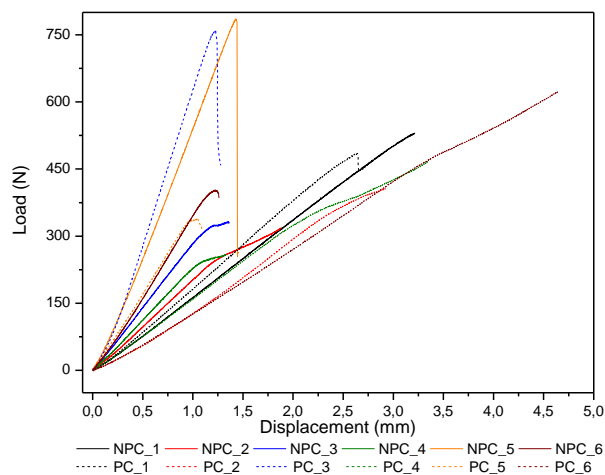
Figure 6. Load (N) versus Displacement (mm) curves for aged samples.

Table 5 shows a comparison highlighting the effects of hygrothermal aging on the final G_{IIC} values. In the NPC condition, the reduction in average fracture toughness values was around 93%, while in the PC condition, the reduction was around 45%. The load versus displacement curves of the samples without pre-cracking show an increasing linear behavior, although not very accentuated, indicating that the tests carried out at the $a_0 = 12$ mm and $a_0 = 24$ mm markings may have accentuated the weakening of the adhesive joint before carrying out the test at the last marking ($a_0 = 18$ mm). In the PC condition, there is the possibility that the innermost portions of the adhesive layer were less affected by humidity than the regions closer to the edge and, therefore, the reduction in the average G_{IIC} values was less significant than in comparison to the NPC condition.

Table 5. Comparison of GIIC values of samples before and after hygrothermal conditioning.

Samples	Interlaminar fracture toughness in mode II (G_{IIC}) – J/m²			
	NPC (Pre aging)	PC (Pre aging)	NPC (Post aging)	PC (Post aging)
1	159.88	22.92	14.89	9.21
2	126.13	38.15	6.91	7.93
3	121.40	20.55	5.36	13.98
4	112.63	11.18	3.86	12.13
5	145.74	10.16	17.87	4.64
6	-	-	6.93	20.39
Average	133.16 ± 19.24	20.59 ± 11.30	9.30 ± 5.68	11.38 ± 5.49
Percentage change			-93.0%	-44.7%

In Figure 7, one can observe the micrograph obtained via SEM of the joint failure region, where it is possible to observe the presence of debris (orange arrows) and fractured adherent fibers (green arrows), repeating exactly what was seen of fracture micromechanisms in unaged samples. It is also possible to observe a few points where the adhesive is visible on the adherent surface (blue arrows), indicating that adhesion was not effective in this surface preparation.
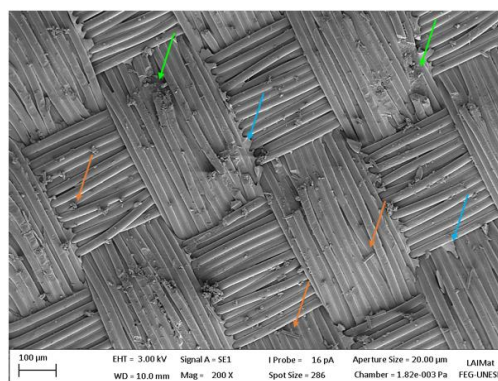
Figure 7. Micrograph obtained via SEM of the failure region.

4. CONCLUSIONS

G_{IIC} results alongside the ANOVA analysis indicated that beyond the adherend surface cleaning with isopropyl alcohol before the bonding process, none of the other surface treatments tested in this paper is

significant to obtain a well-consolidated adhesive bond. Thus, reducing the number of processes for surface preparation before bonding is an advantage for the oil and gas industry, making it possible to reduce costs and also save manufacturing time. Regarding the thickness of the adhesive joint, results indicate the 1.0 mm thick adhesive was more efficient in dissipating energy due to the larger plastic regions, although ANOVA showed that this variable was not statistically significant. Hygrothermal aging affected G_{IIC} results especially in the NPC condition, contributing to a reduction of about 93%. For the PC condition, the reduction in G_{IIC} was also significant, around 44%. Humidity caused swelling of the adhesive, increasing the volume of voids that caused the increase in volume of sorbed water. The water caused the breakdown of the adhesive's molecular chains and consequent leaching, which further contributed to the increase in the void region and the consequent increase in the amount of water sorbed.

4.1. Declaration of Competing Interest

The authors declare no conflict of interest.

4.2. Acknowledgments

5. REFERENCES

[1] Freitas, S. T. et al. Interface adhesion assessment of composites to metal bonded joints under salt spray conditions using peel tests. *Composite Structures*, Volume 164, 2017. (https://doi.org/10.1016/j.compstruct.2016.12.058).

[2] Setvati, M. R. et al. A review on composite materials for offshore structures. In: *Proceedings of the 33rd International Conference on Ocean, Offshore and Arctic Engineering*, p.1-8, 2014. (https://doi.org/10.1115/OMAE2014-23542).

[3] Hayashibara, H. et al. Degradation of structural adhesive bonding joints on ship exposure decks. *Journal of Marine Science Technology*, Volume 25, 2020. (https://doi.org/10.1007/s00773-019-00657-w).

[4] Srivastava, V.K. et al. Fracture behavior of adhesively bonded carbon fabric composite plates with nanomaterials filled polymer matrix under DCB, ENF, and SLS tests. *Engineering Fracture Mechanics*, Volume 202, 2018. (https://doi.org/10.1016/j.engfracmech.2018.09.030).

[5] Tauheed, M.; Datla, N. Characterization and prediction of hygrothermally aged CFRP adhesive joint subjected to mode II load. *Composites Part C: Open Access*, Volume 11, 2023. (https://doi.org/10.1016/j.jcomc.2023.100357).

[6] Moreira, R.D.F. et al. Mode II fracture toughness of carbon–epoxy bonded joints with femtosecond laser-treated surfaces. *International Journal of Mechanical Sciences*, Volume 148, 2018. (https://doi.org/10.1016/j.ijmecsci.2018.09.029).

[7] Kinloch, A.J. *Adhesion and Adhesives: Science and Technology*, 1st Edition, 1987. Chapman and Hall. (ISBN: 978-90-481-4003-9).

[8] Banea, M.D.; Silva, L.F.M.; Campilho, R. The Effect of Adhesive Thickness on the Mechanical Behavior of a Structural Polyurethane Adhesive. *Journal of Adhesion*, Volume 91, 2014. (https://doi.org/10.1080/00218464.2014.903802).

[9] Barbosa, L.C.M.; Bortoluzzi, D.B.; Ancelotti Jr, A.C. Analysis of fracture toughness in mode II and fractographic study of composites based on Elium® 150 thermoplastic matrix. *Composites Part B*, Volume 175, 2019. (https://doi.org/10.1016/j.compositesb.2019.107082).

DEVELOPMENT OF A NOVEL CEMENTITIOUS COMPOSITE FOR AIR RESTRICTORS IN AEROSTATIC THRUST BEARINGS

Fábio Assunção Rosa [a*]; Pâmela Maria da Costa Deveza [b]; Júlio César dos Santos [c]; Leandro José da Silva [d]; Pabllo Miguel Maia Pires [e]; Túlio Hallk Panzera [f]

(a) 0000-0003-3324-7643 (Federal University of São João del Rei - UFSJ – Brazil)
(b) 0009-0005-0424-0209 (Federal University of São João del Rei - UFSJ – Brazil)
(c) 0000-0002-7485-491X (Federal University of São João del Rei - UFSJ – Brazil)
(d) 0000-0002-4606-3483 (Federal University of São João del Rei - UFSJ – Brazil)
(e) 0000-0003-0592-3587 (Federal University of São João del Rei - UFSJ – Brazil)
(f) 0000-0001-7091-456X (Federal University of São João del Rei - UFSJ – Brazil)
* Corresponding author: fabiorosa@ufsj.edu.br

Abstract: Aerostatic thrust bearings utilise air as a lubricant to support loads and minimise friction and wear. The flow of air in these bearings is regulated by a restrictor, which can be made from various materials, including porous materials. The choice of porous material for the restrictor depends especially on factors such as permeability, stiffness, and stability. In the context of air restrictors for aerostatic thrust bearings, compacted cementitious materials have been developed. This study presents a novel cementitious composite comprising silicon carbide particles and Portland cement. The composite is manufactured through cold pressing at a pressure of 10 MPa and a low water-to-cement ratio of 0.30. To understand the impact of SiC particle size (30.8 and 10.2 μm) and weight fraction (50 and 67%) on the physical and mechanical properties of the composites, a statistical design is conducted. It is observed that incorporating smaller SiC particles with a higher weight fraction resulted in a general reduction in density, strength, and elastic modulus. On the other hand, a higher amount of smaller particles leads to significant increases in porosity and oxygen permeability. This configuration shows promise as an air restrictor for porous bearings.

1. INTRODUCTION

Bearings are machine elements designed to facilitate relative motion between two surfaces. Aerostatic bearings utilize a pressurized air film, typically with a micrometre thickness ranging from 5 to 20 micrometres, to support moving parts and withstand external loads [1]. The use of high-pressure air as a lubricant results in significantly lower friction coefficients, leading to substantial performance enhancements in terms of motion precision, speed, and reduced pollution compared to precision bearings with rolling elements [2]

The lubricating film is generated between the moving parts through the airflow, facilitated by the bearing component known as the restrictor. This can be achieved by machining small diameter and shaped holes on the stationary surface of the bearing. However, restrictors manufactured through this method produce a heterogeneous pressure distribution in the air film, with a peak in the central hole region [3]. Consequently, to enhance pressure distribution, machining multiple holes becomes necessary, making restrictor production more challenging.

An alternative for achieving a more uniform pressure distribution is to fabricate the restrictor using porous materials, which contain a multitude of pores (or holes) that compose the element. This enhanced pressure distribution contributes to improved bearing performance in terms of load capacity, stiffness, and

damping characteristics. Additionally, manufacturing bearings with porous restrictors is simpler compared to traditional bearings with holes [2].

The current limitations on the use of aerostatic bearings stem from the scarcity of porous materials possessing suitable characteristics for gas fluid flow [2]. To be suitable for restrictor manufacturing, a material must exhibit a uniform structure of open pores, with a porosity level between 20 and 35%, and a permeability coefficient ranging from $6.5 \times 10^{-16} m^2$ to 8.4×10^{-14} m². Additionally, the ideal restrictor should be lightweight for dynamic applications with high accelerations, possess high mechanical flexural strength (around 35 MPa), a high elasticity modulus to withstand working pressures with minimal deformation, a low thermal expansion coefficient to endure temperature gradients, and chemical stability [3].

Ceramic materials typically display a low coefficient of thermal expansion and perform admirably at high temperatures; nevertheless, they often demonstrate a predisposition to brittle fracture [4]. The inclusion of particles, fibres, or whiskers as reinforcing phases in ceramic matrix composites can lead to substantial enhancements in tensile strength, fracture toughness, and modulus of elasticity [5]. The dispersed phase in ceramic composites effectively impedes the propagation of cracks in the matrix, thereby enhancing the mechanical performance of the ceramic material [6].

In recent years, researchers have explored various porous media to produce restrictors used in aerostatic bearings. The most extensively studied materials include sintered ceramics such as alumina [4, 7, 9] and graphite [10], silicon carbide composites (matrix and carbide fibres) [6], and cementitious composites reinforced with particles (silica and silicon carbide) [2, 11, 12], carbon nanotubes [2], and carbon microfibers [12]. Unlike sintered ceramics, which require high temperatures to solidify, cementitious composites rely solely on a chemical hydration process to form solid phases and cement microstructure [6]. Consequently, Portland cement-based composites have recently garnered attention for the production of porous restrictors for aerostatic bearings. Additionally, these materials are cost-effective and easy to process, and their physic-mechanical properties can be tailored for this specific application [2, 11, 12].

Silicon carbide-based cementitious composites, manufactured with low water-to-cement ratio and uniaxial compacting pressures of 10, 20, and 30 MPa, were studied for application as aerostatic bearings [13]. The weight fraction of SiC used as reinforcement was set at 20 and 30 wt% relative to the cement weight. Results indicated that both physical and mechanical properties were significantly influenced by the factors of compacting pressure and weight fraction. Composites manufactured with higher compacting pressure, particularly those with 20 and 30 wt% of SiC, demonstrated greater flexural strength. However, these composites exhibited an apparent porosity of less than 15%, suggesting potential limitations for their use as porous restrictors in aerostatic bearings [11].

In other work [12], silicon carbide particles (10-20 μm) were utilized in the production of cementitious composites through cold uniaxial pressing at 30 MPa. A SiC-to-cement ratio of 0.67 was employed, along with varying water-to-cement ratios of 0.28, 0.30, 0.33, and 0.35. The findings indicated that the composite manufactured with a water-to-cement ratio of 0.30 exhibited superior results for restrictor manufacturing, demonstrating appropriate levels of porosity and permeability, as well as increased structural stiffness in compression and bending. The restrictor created with the silicon carbide-reinforced composite displayed promising behaviour, maintaining stability under applied loads exceeding 15 N, with a minimum air film thickness of 60 and 80 μm for working pressures of 1 bar and 2 bars, respectively.

Continuing the studies of SiC-based cementitious composite for application as a porous restrictor for aerostatic bearings, this work aims to mitigate the severe reduction in porosity, a reduced uniaxial compacting pressure of 10 MPa and a water-to-cement ratio of 0.30 was considered. Effects of higher weight fractions of SiC (50 and 67 wt%), and different particle sizes (~10.2 μm and ~30.8 μm) are evaluated by a statistical design (22 factorial design) on the physic-mechanical properties of composites.

2. METHODOLOGY

2.1. Materials

Portland cement (CPV ARI Plus, from Holcim-Brazil) and silicon carbide powder from FIVEN NORGE AS are utilised in the production of cementitious composites. The silicon carbide (SiC) particles are assessed in two different particle size ranges: 360s (average size of 30.8 μm) and 1200s (average size of 10.2 μm). These particles exhibit densities of 1.33 g/cm³ and 1.00 g/cm³, respectively. The weight fractions of SiC are 50 and 67 wt% to the weight of the cement. A full factorial design of 2^2 is established to explore the combination of the experimental factors, resulting in 4 experimental conditions as shown in Table 1.

Table 1. Design of experiment – 2^2

Experimental condition	Particle size	Weight fraction (wt%)
1	360s	50
2	360s	67
3	1200s	50
4	1200s	67

2.2. Manufacturing

The composites are produced by manually mixing the components, beginning with a dry mixing of cement and silicon carbide, followed by the addition of water. A water-to-cement ratio of 30 wt% is maintained under all experimental conditions. The wet mortar is then placed into a metallic mould with a geometry suitable for compression tests, as depicted in Fig. 1. Subsequently, the mortar undergoes cold pressing using a low-speed electric pressing device, applying a pressure of 10 MPa. For compression test specimens, the mortar is inserted into a PVC tube to facilitate easy removal from the mould after pressing. After a curing period of 28 days, the test specimens are extracted from the tubes. During the curing process, the specimens are encased in PVC film to prevent water loss to the environment. Following this period, the specimens are readied for physical and mechanical tests.

Figure 1. The geometry of the mould used in compression tests.

To validate the estimation of experimental error and establish a reliable foundation for result inference, each experimental condition is replicated three times. The manufacturing and characterisation procedures are carried out randomly to minimize the impact of uncontrollable conditions, thus enabling experiment reproducibility.

2.3. Response Variables

The response variables include bulk density (ρ_v), apparent porosity (P_{ap}), coefficient of oxygen permeability (φ), compressive strength (σ_C), and compressive modulus of elasticity (E_c). The physical and mechanical properties are analysed using analysis of variance (ANOVA), at a significance level of 0.05 (5%) with Minitab® software version 19.

The principle of Archimedes is applied to determine the bulk density and apparent porosity, following the guidelines of ISO 10545-3 [14], which involve calculating the mass of the sample under three conditions: m_1 – dry mass, m_2 – mass saturated with water, and m_3 – mass of the sample saturated and suspended in water. The oxygen permeability test utilises the Hagen-Poiseuille equation, modified by Cabrera and Lynsdale (1998) [15] for the use of oxygen as a compressible fluid. This equation, when solved for the permeability coefficient (φ), yields Eq. 1 [2], where the dynamic viscosity of oxygen at a temperature of 20°C assumed as 2.02×10^{-5} N.s/m².

$$\varphi = \frac{2 \cdot Va \cdot Ps \cdot L \cdot 2.02 \times 10^{-16}}{Ac(P^2 - Ps^2)} \tag{1}$$

Where: φ is the permeability coefficient ($\times 10^{-16}$ m²), Va is the fluid flow rate (m³/s), Ps is the assumed outlet pressure during the test as the atmospheric pressure (N/m²), Ac is the cross-sectional area of the sample (m²), and Pa is the inlet pressure (absolute) (N/m²).

The compression test is performed at a rate of 2 mm/min, following BS EN 12390-05 [16]. An Instron universal testing machine equipped with a 50 kN load cell is used.

3. RESULTS AND DISCUSSION

Table 2 presents the mean values and standard deviation, based on three replicates, for the physical and mechanical properties of the cementitious composites.

Table 2. Results for the physical and mechanical properties of the cementitious composites.

	Replicate	ρ_v(g/cm^3)	P_{ap} (%)	φ ($\times 10^{-16}$m²)	σ_C (MPa)	E_c (GPa)
	R1	2.19 ± 0.31	5.64 ± 0.02	37.89 ± 14.03	29.53 ± 11.10	3.65 ± 1.19
C1	R2	2.18 ± 0.01	6.60 ± 0.11	33.62 ± 8.10	26.77 ± 6.05	2.99 ± 0.42
	R3	2.20 ± 0.02	4.69 ± 0.11	29.98 ± 3.38	28.15 ± 6.09	4.09 ± 0.83
	R1	2.14 ± 0.29	8.48 ± 0.23	93.48 ± 5.28	21.86 ± 5.83	2.77 ± 0.16
C2	R2	2.13 ± 0.01	9.84 ± 0.82	54.41 ± 16.62	25.60 ± 6.49	2.81 ± 0.26
	R3	2.15 ± 0.01	7.12 ± 0.41	44.71 ± 7.19	25.64 ± 5.35	2.85 ± 0.38
	R1	1.90 ± 0.03	18.69 ± 1.50	260.79 ± 16.55	17.23 ± 4.48	2.45 ± 1.04
C3	R2	1.92 ± 0.01	17.03 ± 0.25	252.18 ± 11.13	19.71 ± 3.41	2.68 ± 0.31
	R3	1.90 ± 0.01	16.54 ± 0.22	245.92 ± 10.90	19.36 ± 1.66	2.93 ± 0.63
	R1	1.85 ± 0.01	22.20 ± 0.70	456.56 ± 11.95	12.73 ± 1.91	1.83 ± 0.24
C4	R2	1.84 ± 0.04	23.78 ± 2.02	479.20 ± 13.09	13.13 ± 1.77	2.04 ± 0.27
	R3	1.83 ± 0.01	20.88 ± 0.47	468.82 ± 14.22	11.42 ± 1.39	1.36 ± 0.43

Table 3 shows the results (p-value) from the ANOVA for the investigated experimental factors (particle size and weight fraction of SiC). Additionally, it includes the p-values for the Anderson-Darling normality test and the coefficient of determination (R² adjusted) for all response variables. Significant effects of individual or interaction factors on the response variables are indicated in Table 3 (p-value < 0.05) [17]. Furthermore, all response variables demonstrate a tendency to follow a normal probability distribution based on the Anderson-Darling test (p-value > 0.05), validating the ANOVA model used. The adjusted R² values range from 78.02% to 99.48%, indicating a satisfactory fit of the model to the response variable data.

Table 3. Results from ANOVA model.

	Response variables				
	ρ_v	P_{ap}	φ	σ_C	Ec
Individual or interaction factors	*p-values ≤ 0.05*				
Particle size	0.000	0.000	0.000	0.000	0.001
Weight fraction	0.000	0.001	0.000	0.000	0.003
Particle size*weight fraction	0.346	0.193	0.000	0.183	0.671
Normality test	*p-values ≥ 0.05*				
Anderson-Darling test	0.522	0.297	0.561	0.139	0.534
Coefficient of determination	*(%)*				
R² (adjusted)	99.48	96.93	99.35	94.24	78.02

In addition to ANOVA, the Tukey test is performed to determine which particle size and weight fraction of SiC yield statistically different results from the others. These results are represented by letters (A, B, C) directly on the interaction plots of the experimental factors. Similar letters denote statistically equivalent means, whereas different letters indicate differences between the results.

3.1. Bulk density and apparent porosity

The bulk density data of the SiC-based cementitious composites vary from 1.83 to 2.20 g/cm³, while the apparent porosity ranges from 4.69 to 23.78%. As indicated in Table 3, both individual factors significantly influence the physical responses, with p-values below 0.05. Moreover, there is no interaction between these factors for either response variable (p-values > 0.05). Main effects plots displaying the mean values of bulk density and apparent porosity are presented in Fig. 2a and 2b, respectively.
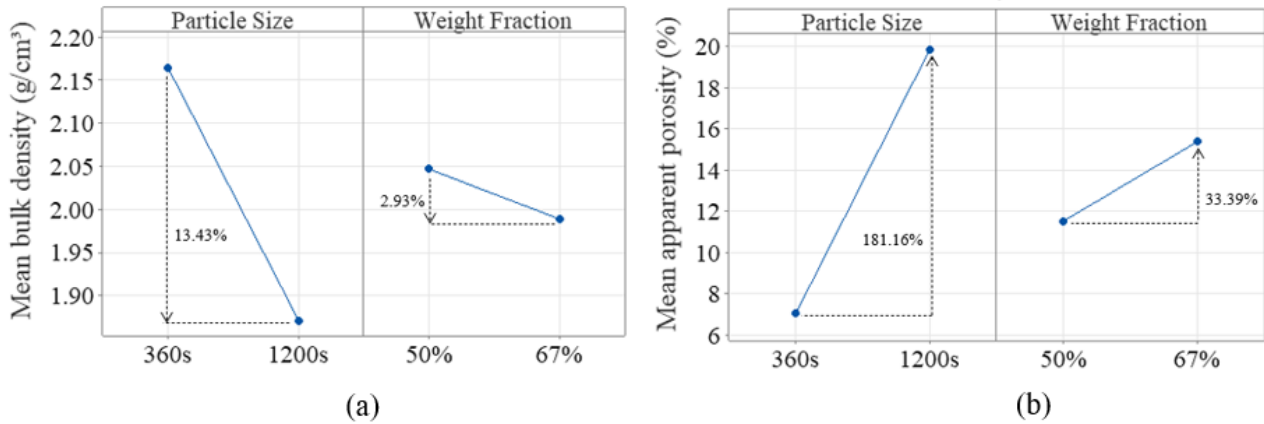
Figure 2. Main effect plots for the mean (a) bulk density and (b) apparent porosity.

The use of smaller particles (1200s) of SiC leads to a 13.43% decrease in bulk density and an 181.16% increase in apparent porosity. The variation in bulk density due to the monomodal particle size of SiC aligns with findings reported in the literature [11, 18]. A similar trend is observed for the impact of weight fraction, wherein an increase from 50 to 67 wt% of SiC results in a slight 2.93% reduction in bulk density and a significant 33.39% increase in apparent porosity.

The formation of porous structures in cementitious composites occurs in two distinct stages [18]. The first stage is determined by the compaction pressure and mixture composition, while the second stage is heavily influenced by the hydration process. Larger particles have a smaller surface area, which promotes the utilization of water content in the mixture, potentially leading to increased hydration products and, consequently, a reduction in porosity.

According to [3], the ideal range for apparent porosity is typically between 20% and 35%, allowing the material to be utilized in porous bearings. Therefore, cementitious composites produced with 67 wt% of 1200s SiC (condition C4) fall within this desired porosity range.

3.2. Oxygen Permeability

The coefficient of oxygen permeability for the SiC-based cementitious composites ranges from 3×10^{-15} m² to 4.79×10^{-14} m². The ANOVA results in Table 3 demonstrate that the main factors and their interaction significantly impact the permeability response (p-value = 0.000). The interaction effect plot for the mean permeability data is presented in Figure 3, along with the Tukey test (group of letters).

In Figure 3, it is evident that the interaction between the factors is reflected in the similar results obtained for composites manufactured with 360s SiC (indicated by the same letters) and the significant difference in those made with 1200s SiC (denoted by different letters). The use of smaller particles (1200s) results in substantial increases in the mean oxygen permeability, with values such as 647.77% and 629.27% for 50 wt% and 67 wt% levels, respectively. Furthermore, a notable 85% increase in permeability is achieved with the higher content (67%) of 1200s SiC. Overall, the observed increase in the coefficient of oxygen permeability can be attributed to the rise in the apparent porosity of the SiC-based cementitious composites.

In agreement with the trends in bulk density and apparent porosity, condition C4, composed of 67 wt% of 1200s SiC, exhibits a higher coefficient of oxygen permeability, showcasing promising potential for application in porous restrictors for aerostatic bearings.
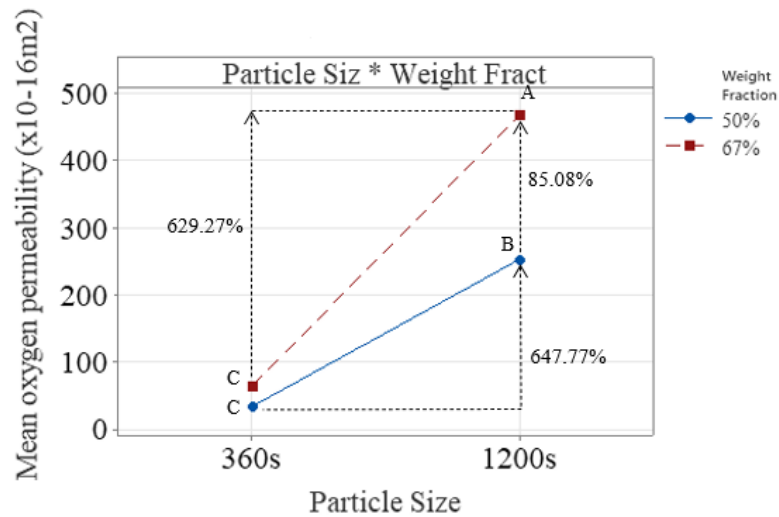
Figure 3. Interaction effect plot of particle size and weight fraction on the oxygen permeability of cementitious composites.

3.3. Compressive Strength and Modulus of Elasticity

The compressive strength and modulus data range from 11.42 to 29.53 MPa and from 1.36 to 4.09 GPa, respectively. Similar to the physical properties, there are significant individual effects and no interaction effect for both compressive strength and modulus (refer to the p-values in Table 3). Figure 4 presents the main effect plots for the mean values of compressive strength (Fig. 4a) and compressive modulus (Figure 4b).

(a)   (b)
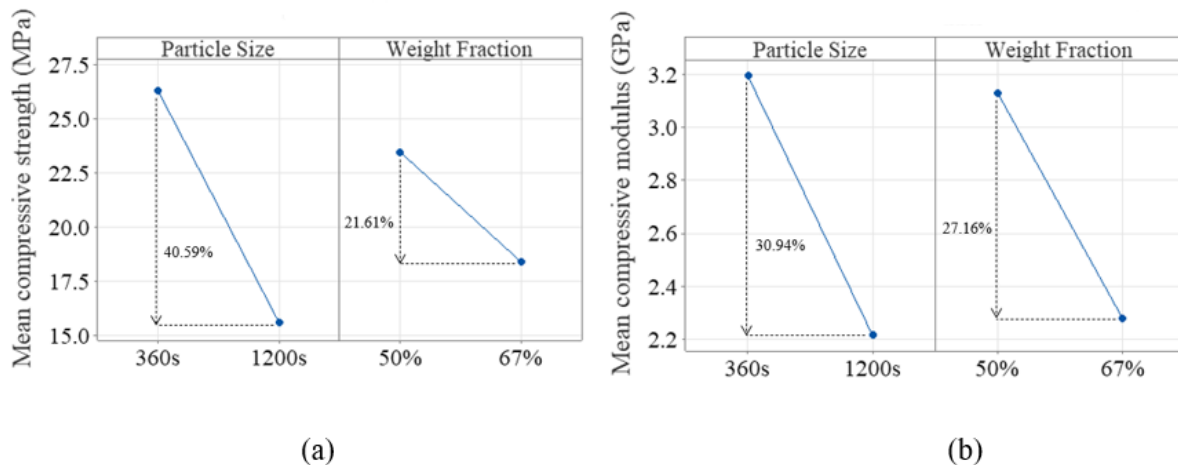
Figure 4. Main effect plots for compressive strength (a) and modulus of elasticity (b) of the cementitious composites.

As depicted in Fig. 4a and 4b, the utilization of smaller SiC particles (1200s) results in decreases of 40.59% and 30.94% in the mean compressive strength and modulus of the composites, respectively. Similarly, an increase in the weight fraction of SiC from 50 to 67 wt% leads to reductions of 21.61% (strength) and 27.16% (elastic modulus) in the mechanical properties when a higher SiC content (67 wt%) is considered. These trends align with the effects observed for bulk density; specifically, an increase in apparent porosity implies a decrease in bulk density, consequently leading to an increase in mechanical properties [19].

The highest mechanical property values are attained when a low content of larger SiC particles is utilized in composite production. This is attributed to the smaller surface area of larger particles, which promotes a favourable water-to-cement ratio during the cementitious paste hydration process, leading to increased hydration products [18, 19]. Additionally, a lower particle surface area can result in a weaker interface between the cement paste and SiC particles. Therefore, lower mechanical strength is not solely linked to the presence of more pore formation but also to lower hydration products and a larger area of weaker interface. An in-depth investigation of the composites' microstructure will be the focus of future research.

The development of a porous restrictor for aerostatic bearings necessitates a balance between porosity (volume of open pores), permeability, and mechanical strength of the material. As per reference [3], a material

intended for restrictor manufacturing should feature a uniform structure of open pores, with a porosity level between 20 and 35%, and a permeability coefficient ranging from 6.5×10^{-16} m² to 8.4×10^{-14} m². In this context, the C4 condition achieved higher mean values of porosity and oxygen permeability, while exhibiting lower mean values of mechanical properties. Nonetheless, this condition shows promise for porous aerostatic bearings, as the strategic design of the porous restrictor thickness could enhance structural performance. Subsequent investigations will involve testing this material in porous bearing bench tests to validate its suitability as an air restrictor.

4. CONCLUSION

This study conducted a Design of Experiments (DoE) investigation to examine the impacts of particle size and weight fraction of SiC on the physical and mechanical behaviour of cold-pressed SiC-based cementitious composites. The experimental factors demonstrated significant effects on the response variables, including bulk density, apparent porosity, oxygen permeability, compressive strength, and modulus. Overall, higher content of smaller SiC led to significant reductions in density, compressive strength, and modulus, while yielding significant increases in porosity and oxygen permeability. From a holistic viewpoint, it can be concluded that the developed material showcases promising characteristics for the application of porous restrictors for aerostatic bearings. Particularly in terms of apparent porosity and oxygen permeability, the composite manufactured with 67 wt% of smaller SiC particles (~10 μm) met the desired requirements for such an application.

4.1. Declaration of Competing Interest

The authors declare no conflict of interest.

4.2. Acknowledgements

5. REFERENCES

1. Q. Gao et al. Aerostatic bearings design and analysis with the application to precision engineering: State-of-the-art and future perspectives. Tribology International, v. 135, p. 1-17, 2019.

2. Silva, L. J. Mancais aerostáticos porosos fabricados em compósito cimentício reforçado com nanotubos de carbono. 2015. 207p. Tese. Escola de engenharia da Universidade federal de Minas gerais. [S.l.], 2015.

3. Kwan, Y. B. P. Processing and fluid flow characteristics of hot isostatically pressed porous alumina for aerostatic bearing applications. 1996. Cranfield, Ph.D. Thesis, Cranfield Institute of Technology, 1996.

4. Herakovich, C. T. Mechanics of fibrous composites. New York: John Wiley & Sons, 1998.

5. E. Uhlmann, C. Neumann. Air bearings based on porous ceramic composites. Intelligent Production Machines and Systems, v.8, p. 211-216, 2006.

6. Callister, Jr., W. D. Ciência e Engenharia de Materiais: Uma introdução. 10ª ed. Rio de Janeiro: LTC, 2021.

7. Z. C. Silveira et al. Ceramic Matrices Applied to Aerostatic Porous Journal Bearings: Material Characterization and Bearing Modeling. Cerâmica, v. 56, p. 201-211, 2010.

8. R. Nicoletti, B. M. Purquerio, Z. C. Silveira. The Effect of Permeability Distribution on the Numerical Analysis of Aerostatic Ceramic Porous Bearings. Lubrication Science, v. 25, p. 185–194, 2013.

9. I. S. Durazo-Cardenas, J. Corbett, J. D. Stephenson. Permeability and Dynamic Elastic Moduli of Controlled Porosity Ultra-precision Aerostatic Structures. Ceramics International, v. 40, p. 3041–3051, 2014.

10. W. Ding-Zhu, T. Ji-Zhong. Analysis on the Static Performance of Porous Graphite Aerostatic Thrust Bearings. In: 2nd International Conference on Computer Engineering and Technology, p. 112-115, 2010.

11. T.H. Panzera et al. Microstructural design of materials for aerostatic bearings, Cem. Concr. Compos. 30/7 (2008) 649–660.

12. Z. M. V. Missagia et al. Assessment of compacted-cementitious composites as porous restrictors for aerostatic bearings. Proceedins of the Institution of Mechanical Engineers, Part L: Journal of Materials: Design and Applications. V. 234 (1) p. 79-89. 2020.

13. H. C. Melo, J. L. Silva. Material compósito de matriz cimentícia reforçado com partículas de carbeto de silício para aplicação como restritor poroso em mancais aerostáticos. In: IX COEN - Congresso de Engenharias da UFSJ. P. 1-14, 2019.

14. BS EN ISO 10545-3. Ceramic tiles—part 3: determination of water absorption, apparent porosity, apparent relative density and bulk density, 1997.

15. CABRERA JG and LYNSDALE CJ. A new gas permeameter for measuring the permeability of mortar and concrete. Mag Concr Res, v.40, n,3, p.177-182, 1988.

16. BS EN 12390-05. Testing hardened concrete – Part 3: compressive strength of test specimens. London: British Standards Institution, 2001, pp.1–15.

17. DRUMOND, F. B. et al. Metodologia de otimização de processos. 1993. Departamento de Estatística da UFMG, Departamento de Tecnologia Mineral do CDTN/CNEM, Belo Horizonte, Minas Gerais, 1993.

18. JAMBOR, J. Pore structure and strength development of cement composites. Cement and Concrete Research, v. 20, p. 948-954, 1990.

19. PANDOLFELLI, V. C. et al. Dispersão e empacotamento de partículas. São Paulo: Fazendo Arte, 2000.

THERMAL CHARACTERIZATION AND OPEN-HOLE COMPRESSION PROPERTIES OF SNAP CURE RESIN COMPOSITES

JVPN Gomes [a], JB de Oliveira [b], VA Silva [c], CPN Silva [d], RBC de Lima [e], TPFG Leal [f], MMP Zaia [g], RF Gouvêa[h], BMF Marques [i], LFP Santos [j], ML Costa[k]

(a) 0000-0002-6825-7238 (Laboratório de Estruturas Leves (LEL/IPT) - Brazil)
(b) 0000-0003-2460-2930 (Laboratório de Estruturas Leves (LEL/IPT) - Brazil)
(c) 0000-0002-7192-3094 (Laboratório de Estruturas Leves (LEL/IPT) - Brazil)
(d) 0000-0002-2869-2411 (Laboratório de Estruturas Leves (LEL/IPT) - Brazil)
(e) 0009-0002-3487-7196 (Maxion Structural Components – Brazil)
(f) 0000-0001-7695-4298 (EMBRAER S.A. – Brazil)
(g) 0009-0002-9200-8829 (EMBRAER S. A. – Brazil)
(h) 0009-0005-1953-8294 (Laboratório de Estruturas Leves (LEL/IPT) - Brazil)
(i) 0000-0002-2367-9410 (Federal Institute of Education, Science and Technology of São Paulo / Laboratório de Estruturas Leves (LEL/IPT) - Brazil)
(j) 0000-0002-5089-1089 (UNESP - São Paulo State University / Laboratório de Estruturas Leves (LEL/IPT) - Brazil)
(k) 0000-0001-9492-8544 (UNESP - São Paulo State University / Forza Composites - Brazil)
* Corresponding author: joaogomes@ipt.br / jv.passosng@gmail.com

CODE: BCCM7-72

Keywords: snapcure prepreg, thermal properties, open-hole compression strength (OHC).

Abstract: Fiber-reinforced polymer composites (FRPC) have been the subject of studies and applications in various industrial sectors, including mobility and, consequently, the automotive and aeronautic sectors. There is a growing demand for polymer composites in these sectors. The substitution of steel with CFRP in automotive component production causes a 30% increase in fuel efficiency and reduces carbon dioxide (CO_2) emissions by 20%. The use of snap, or fast, cure prepregs has proven to be a promising alternative for enhancing the production speed of components, reducing manufacturing costs associated with the long curing cycles of conventional thermosets, and allowing the production of components with high thickness (approximately 5 to 7mm) without the need for autoclaves, through hot compression moulding, since they have the property of curing within a time interval, usually between 0.5 and 30 minutes. Thus, these materials appear in the composite market as a new technology capable of impacting thermoset composite processing in general. This study aims to investigate the thermal properties of snap cure prepregs and laminates produced, enhancing the understanding of these materials compared to traditional prepreg properties and evaluating the open-hole compression strength (OHC) of the laminates. Initially, a differential scanning calorimetry (DSC) analysis was performed in dynamic and isothermal condition on the snap-cure prepreg to identify the cure temperature and cure time of the resin, respectively. The laminates were processed using the hot compression molding from a stack of 24 layers of snapcure prepreg, T2700 from Toray. The material degradation was evaluated through thermogravimetric analysis (TGA), and the glass transition temperature (T_g) and viscoelastic properties were obtained by dynamic mechanical analysis (DMA). Finally, OHC was performed according to ASTM D6484-20. The curing process started at 118°Cand the curing time at 150°C was 10 minutes proving the ability to cure in short periods. The laminate degradation started around 235°C, showing at least 3 degradation stages. Storage modulus at 30°C was approximately 3.85×10^{10} Pa, and T_g was 181°C. The average open-hole compression

strength reached (335.87 ± 5.17) MPa. The results demonstrate the properties of snap cure prepregs closely align with those conventional prepregs, thereby supporting the applications of these materials.

1. INTRODUCTION

The growth in the applicability of new products necessitates reassessing the development of innovative components for use with new materials and processes. Various material combinations can optimize component design for specific applications. The desired properties of a polymer composite are achieved through the deliberate combination of a polymer matrix and fiber reinforcement (fiber-reinforced polymer composites - FRPC), indicating the versatile and growing potential of these materials [1].

Enhancing the manufacturing capacity of composite materials is essential to maintaining ongoing interest in these applications within the automotive sector. This entails increasing production rates while simultaneously reducing defects and rejected parts. It is important to note that the concern extends beyond weight reduction; it also encompasses passenger comfort and safety, overall vehicle quality, noise and vibration minimization, and processing cost efficiency [2]. In this context, the use of snapcure or fastcure prepregs presents a viable alternative, as it accelerates production rates, reduces manufacturing costs associated with the long curing cycles of conventional thermosets, and enables the production of components with high thicknesses (~5 to 7 mm) without the need for autoclaves, utilizing hot compression molding. Therefore, this new material shows significant promise and warrants further study and evaluation for potential application in the market [3].

Although introducing holes is expected in the final assembly of various components, it significantly impacts the properties of polymeric composites. Holes can induce delamination, microcracks, and fiber tearing, leading to reduced performance. In polymer composites reinforced with carbon fiber, the presence of a hole can decrease the compressive strength of the laminate by up to 47% to 50%, thereby diminishing the advantages associated with these materials. Consequently, studying the resistance of laminates under such conditions becomes essential for ensuring the structural integrity of components with holes, which are prevalent in sets and joints of parts, particularly in the mobility sector [4]. In this context, the open-hole compression (OHC) test proves valuable for determining the compressive strength of laminates under hole conditions [5]. This test evaluates the resistance to interlaminar compression and can be conducted in static or dynamic conditions.

Therefore, this study is dedicated to the thermal characterization of a fast-curing prepreg available on the market. It aims to evaluate its thermal properties using techniques such as differential scanning calorimetry (DSC), thermogravimetric analysis (TGA), and dynamic mechanical analysis (DMA). These analyses will determine the prepreg's curing cycle, thermal stability and glass transition temperature (Tg). The mechanical property of OHC will also be studied. This comprehensive analysis intends to contribute to understanding snapcure prepreg technology as a viable alternative. This technology can operate at a high cadence in both the automotive and aeronautical industries. Meeting rigorous production and quality control requirements can bring the industry closer to this manufacturing technology, thereby introducing significant innovation in this segment.

2. METHODOLOGY

2.1 Composites' processing

For DSC analyses and the production of laminates, a snapcure prepreg T2700 (Toray) reinforced with 12k carbon fibers and a plain weave arrangement was used. The laminates were processed by hot compression containing ten layers (resulting in approximately 4 mm thickness). The curing cycle used was 5 min at 150°C with a pressure of 1 MPa, parameters provided by the manufacturer and confirmed by thermal analyses. Furthermore, it should be noted that the material was only inserted into the press once the tooling reached a temperature of 150°C. Subsequently, the laminate was cut to the appropriate dimensions to carry out the other analyses proposed in the work (TGA, DMA and OHC).

2.2 Thermal characterization

DSC analyses were conducted based on ASTM E2160 [6] on TA Instruments equipment, model Q20. The analyses were carried out in 3 stages, as shown below:

1) Dynamic test to determine the curing temperature: temperature range from 25 ºC to 250 ºC, with a heating rate of 10 ºC.min^{-1}, mass of approximately 5 mg, hermetic aluminum sample holder and nitrogen atmosphere with flow 40 mL.min^{-1};

2) Isothermal test to determine curing time: initial temperature of 150 ºC and time of 20 min. The mass was approximately 5 mg, with a hermetic aluminum sample holder and nitrogen atmosphere with a flow of 40 mL.min^{-1};

3) Dynamic test to evaluate the material's behavior after curing, determination of the glass transition temperature (T_g): temperature range from 25 ºC to 250 ºC, with a heating rate of 20 ºC.min^{-1}, sample mass was approximately 5 mg, hermetic aluminum sample holder and nitrogen atmosphere with a flow of 40 mL.min^{-1}. This analysis was carried out after the isothermal test.

The TGA tests followed the ASTM E2550 standard [7] on the laminates produced on equipment from SII Nanotechnology – SEIKO, model TGA/DTA 6200. The following parameters were used: temperature range from 25 ºC to 1000 ºC, heating rate temperature of 10 ºC.min^{-1}, synthetic air atmosphere with flow of 100 mL.min^{-1}, and approximate mass of 20 mg.

DMA analysis on the laminates followed the ASTM D7028 standard [8], which aims to evaluate the viscoelastic behavior of the material and the glass transition temperature (T_g). The following parameters were used: dual cantilever mode, temperature range from 25 ºC to 250 ºC, heating rate of 3 ºC.min^{-1}, nitrogen atmosphere with flow of 100 mL.min^{-1}, frequency of 1 Hz, amplitude of 10 µm, force of 2000 mN and sample dimensions of approximately (55 x 10 x 3) mm.

2.3 Mechanical characterization

The open-hole compression (OHC) test was conducted following ASTM D 6484 [9] guidelines to assess the impact of drilling on compressive strength. Standardized specimens measuring (300 x 36 x 4) mm were prepared. OHC test was performed using an MTS universal mechanical testing machine, model 370.25, equipped with a 250 kN load cell and operated at a 2 mm/min test speed.

3. RESULTS AND DISCUSSION

3.1 Thermal characterization

Figure 1 shows the dynamic DSC curve of the T2700 prepreg. It can be observed that the polymer curing (exothermic peak observed in the curve) in the material begins at a temperature of 117°C, with two curing peaks observed at 143°C and 162°C, a final temperature of 228°C, and an enthalpy change (ΔH) of -232 J/g.
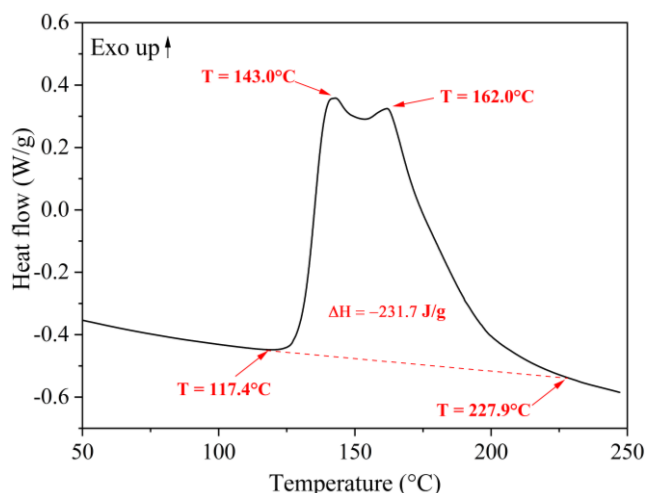
Figure 1. DSC curve (dynamic mode) of T2700 prepreg [Author].

According to the presented results, two shoulders are observed in the peaks of the DSC curves, suggesting that more than one kinetic process is occurring during the resin reaction. Due to the possible existence of different epoxy groups, the collision between molecules (pre-exponential factor) increases with the temperature rise, making the curing reaction increasingly complex, releasing more energy, and

consequently, the exothermic enthalpy increases [10]. Typically, if more than one thermal process occurs during the curing process, two or more exothermic peaks or even shoulders can be easily observed [11]. The onset of the epoxy resin curing reaction requires the opening of the epoxy groups through bonding with the amine catalysed by temperature. The curing reaction of epoxy resin with amine hardeners leads to the formation of two main reactions: secondary amine formation and tertiary amine formation. The hydroxyl groups generated during the reaction or by the addition of solvents or other catalysts, or by the presence of impurities and even moisture, significantly accelerate the reaction between the glycidyl ether and the amine. However, in all cases, the hydroxyl groups behave only as reaction catalysts and not as consumers of epoxy groups in competition with the amine group [12].

Figure 2 (a) presents the result of the DSC curve in the isothermal mode of the material at 150°C for 20 minutes. As observed, the exothermic event is associated with the curing of the prepreg, which according to the graph occurs in 10 minutes.

The curve obtained in DSC dynamic mode of the material after the DSC analysis in isothermal mode is presented in Figure 2 (b). An exothermic peak can be observed in the material between 175°C and 250°C, which may be associated with residual curing of the material or specific behaviour of this fast-curing polymer, additionally it is not possible to verify the material's Tg, which may be associated with the equipment's sensitivity. A summary of the main values obtained in the DSC tests is presented in Table 1.
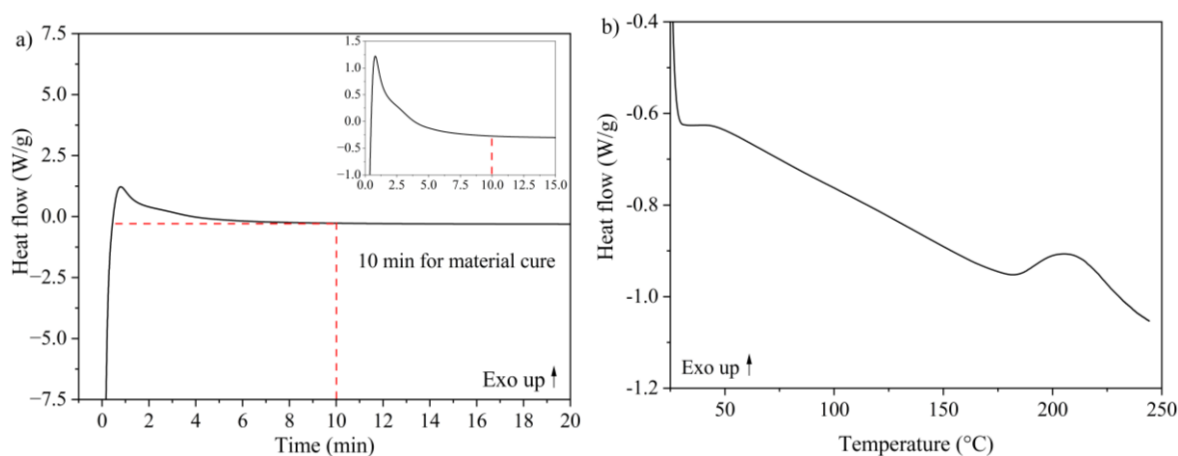
Figure 2. DSC curve (a) isothermal mode at 150°C (b) dynamic mode post-isothermal mode analysis of T2700 prepreg [Author].

The curves obtained from the TGA analysis, in a synthetic air atmosphere, for the T2700 laminate sample are presented in Figure 3 (a). The material exhibits at least 3 degradation stages, separated by a dashed black line, with start and end temperatures identified by red arrows with respective mass values in percentage. Additionally, for the mass rate curve (dashed black), the peak temperatures of each event were also indicated by red arrows.

The degradation behavior of the laminate presents a traditional profile of carbon fiber epoxy composites, that is, at least 3 main stages in a synthetic air (tthermal-oxidative) atmosphere [13]. Firstly, there is the breaking of epoxy resin chain bonds and char formation; in the second stage, there is oxidation of the non-volatile residues formed in the first stage (char); the first two stages consist of resin decomposition, and finally, above 630°C, carbon fiber degradation [14]. The start of the first event occurs at 234°C, so the laminate will begin its degradation process at the mentioned temperatures, requiring that the material does not reach the analyzed temperatures during its application.
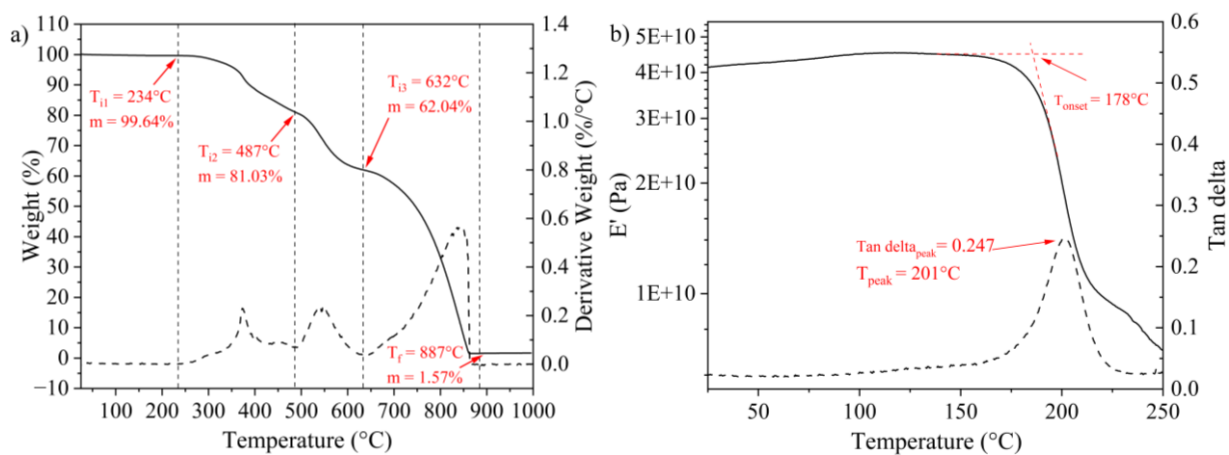
Figure 3. (a) TGA and mass rate curve (b) DMA curve (E' and tan delta) of T2700 laminate [Author].

The curves obtained through DMA analysis, in a nitrogen atmosphere, of the T2700 laminate are presented in Figure 3 (b). The viscoelastic behavior of the laminates is observed; the left Y-axis displays the storage modulus (E') in Pascal (Pa), representing the material's elastic response to applied cyclic load, and the right Y-axis displays the loss tangent or tangent delta (tan δ), representing the phase angle between the elastic and viscous behavior of the material when subjected to a sinusoidal cyclic load. Additionally, the red arrows indicate the Tonset on the E' curve, which in this case represents the material's Tg, and indicate on the Tan δ curve the peak temperature and tangent value.

In general, only the most pronounced transition, called α, was observed, which characterizes the glass transition temperature (Tg), where the E' modulus shows a significant decrease in its values due to the increased mobility of the main polymeric chains within a certain temperature range. The transitions called "sub-Tg", representing movements in side chains or secondary relaxations were not observed.

Thus, the values of E' (at 30°C) were 4.17×10^{10} Pa, and the Tg found, according to ASTM D7028-07 standard, was 178°C. It is worth noting that the Tg value, in thermosetting matrices, helps determine the material's maximum application temperature because once this temperature is reached, the polymer begins to exhibit a decrease in mechanical properties due to increased mobility of the polymeric chains [15]. The main results obtained in the TGA and DMA analyses are contained in Table 1.

Table 1. Summary of principals' results obtained in this work [Author].

Analysis	Standard	Property	T2700
TGA	ASTM E2250	Initial of total degradation temperature	234°C
		Final of total degradation temperature	886°C
		Residue at 1000°C	1.57 %
DSC dynamic	ASTM E2160	Initial cure temperature	117 °C
		Final cure temperature	228 °C
DMA	ASTM D7028	Storage modulus (E') at 30°C	$4.17.10^{10}$ Pa
		Glass transition temperature (Tg)	178 °C
OHC	ASTM D6484	OHC Strength	(335.87 ± 5.17) MPa

3.2 Open-Hole Compression Strength (OHC)

The laminates sample used in the OHC test is shown in Figure 4 (a). Regarding the OHC results, repeatability among the samples was observed, indicated by the low standard deviation value in 8 samples, suggesting homogeneity and effective processing. Based on the obtained data, the compression strength with holes was calculated and the value obtained was 335.87 ± 5.17 MPa (Table 1). These values are close to those provided by the respective manufacturers, which is 315 MPa. Even though materials with different fibers and layups were used, the OHC results obtained were similar in magnitude to those found in the literature [4, 16].

Another observed characteristic is that for both materials, the sample failure occurs in the central region of the hole and propagates laterally toward the edges. This failure mode is initiated by twisting and buckling the layers within the laminate, as demonstrated in Figure 4 (b). It is possible to indicate that the sample failure presents a similar aspect to those obtained in literature [4], which suggests that the failure occurs due to fiber compression and delamination on the lateral view.
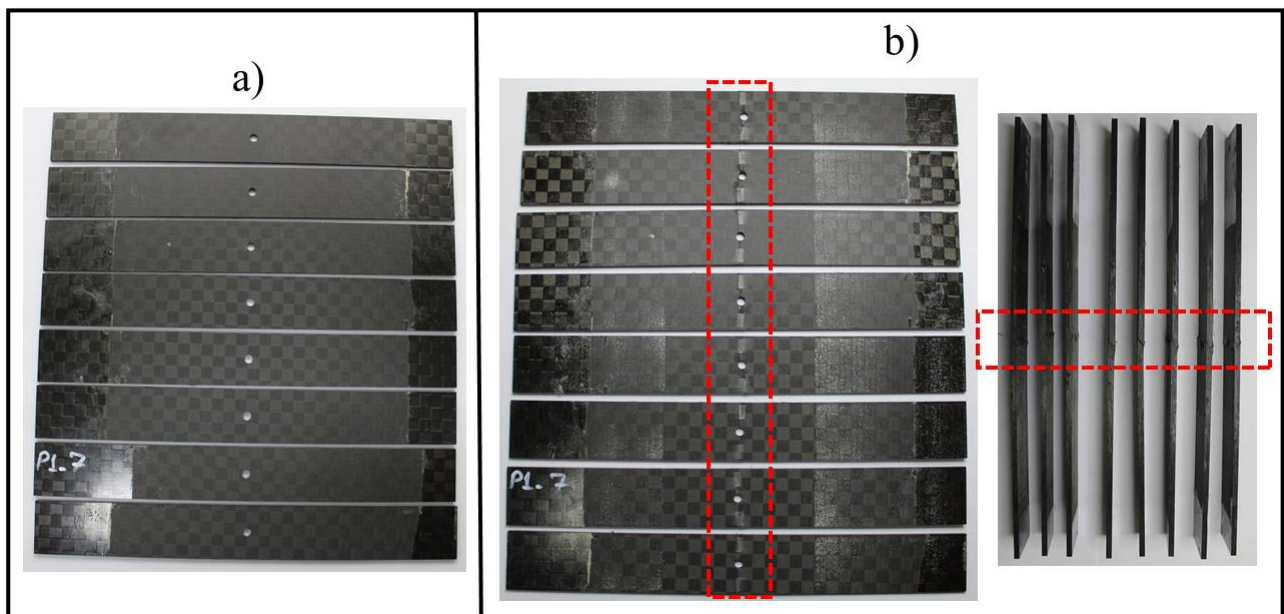
Figure 4. Samples of T2700 laminates (a) before and (b) after the OHC test [Author].

4. CONCLUSIONS

The demand for FRPC (Fiber-Reinforced Polymer Composites) in applications requiring high performance and weight reduction is growing every day in the automotive and aerospace sectors. However, production throughput remains a limiting factor. This challenge is being overcome through the use of rapid-cure prepregs. Therefore, based on the study conducted, the potential of these composites for applications in the mentioned sectors is demonstrated. Among the results obtained, the following stand out:

From dynamic DSC, it was observed that the prepreg curing begins at approximately 117°C and ends around 230°C. On the other hand, thermal analyses performed with the Toray laminate (T2700), using TGA, yielded an average initial degradation temperature of 237°C; final degradation temperature around 887°C; and residue at 1000°C in the range of 1.57%. Finally, DMA revealed a glass transition temperature of 178°C.

From the OHC test, the homogeneity and repeatability of the processed and drilled samples were verified. Additionally, the compression strength values with holes were found to be close to the material's datasheet values, i.e., (335.87 ± 5.17) MPa for the T2700.

4.1. Declaration of Competing Interest

The authors declare no conflict of interest.

4.2. Acknowledgements

5. REFERENCES

[1] R. Stanik et al. Experimental-numerical validation of the curing reaction of snap-cure polymer systems for component families of small batch sizes and high diversity. MATEC Web of Conference, Volume 349, 2021. (https://doi.org/10.1051/matecconf/202134904012).

[2] K. Rouf et al. Effect of Strain Rate on the Transverse Tension and Compression Behavior of a Unidirectional Non-Crimp Fabric Carbon Fiber/Snap-Cure Epoxy Composite. Materials, Volume 14, 2021. (https://doi.org/10.3390/ma14237314).

[3] C. Netzel et al. An experimental study of defect evolution in corners by autoclave processing of prepreg material. Composites Part A: Applied Science and Manufacturing, Volume 144, 2021. (https://doi.org/10.1016/j.compositesa.2021.106348).

[4] D. Zhang et al. A comparative study on failure mechanisms of open-hole and filled-hole composite laminates: Experiment and numerical simulation. Thin-Walled Structures, Volume 198, 2024. (https://doi.org/10.1016/j.tws.2024.111730).

[5] R. Higuchi et al. Experimental and numerical study on progressive damage and failure in composite laminates during open-hole compression tests. Composites Part A: Applied Science and Manufacturing, Volume 145, 2021. (https://doi.org/10.1016/j.compositesa.2021.106300).

[6] ASTM E2160-04(2018), Standard Test Method for Heat of Reaction of Thermally Reactive Materials by Differential Scanning Calorimetry. ASTM International, 2018. (www.astm.org).

[7] ASTM E2550-21, Standard Test Method for Thermal Stability by Thermogravimetry. ASTM International, 2021. (www.astm.org).

[8] ASTM E7028-07 (2015), Standard Test Method for Glass Transition Temperature (DMA Tg) of Polymer Matrix Composites by Dynamic Mechanical Analysis (DMA). ASTM International, 2015. (www.astm.org).

[9] ASTM D6484/D6484M-20, Standard Test Method for Open-Hole Compressive Strength of Polymer Matrix Composite Laminates. ASTM International, 2020. (www.astm.org).

[10] R. Lin et al. Study on Curing Kinetics of Fatty Amine/Epoxy Resin Using Non-Isothermal DSC Method. IOP Conference Series: Earth and Environmental Science, Volume 252, 2019. (10.1088/1755-1315/252/2/022048).

[11] Elias George K., A. Mathiazhagan. Evaluation of Reaction Kinetics and Properties of Epoxy Resin with Two Hardeners. International Journal of Science and Research (IJSR), Volume 10, 2021. (10.21275/SR21505171635).

[12] S. M. Silva et al. Studies of curing cycle of carbon fiber/epoxy resins (8552® and M21®) prepregs based on thermal and rheological analyses. Eclética Química Journal, Volume 47, 2022. (http://dx.doi.org/10.26850/1678-4618eqj.v47.2SI.2022.p83-99).

[13] D. Quang Dao et al. Determination of characteristic parameters for thermal decomposition of epoxy resin/carbon fibre composites in cone calorimeter. International Journal of Hydrogen Energy, Volume 38, 2013. (http://dx.doi.org/10.1016/j.ijhydene.2012.05.116).

[14] C. Branca et al. Thermal and kinetic characterization of a toughened epoxy resin reinforced with carbon fibers. Thermochimica Acta, Volume 517, 2011. (doi:10.1016/j.tca.2011.01.034).

[15] L. F. de P. Santos et al. The influence of carbon nanotube buckypaper/poly (ether imide) mats on the thermal properties of poly (ether imide) and poly (aryl ether ketone)/carbon fiber laminates. Diamond and Related Materials, Volume 116, 2021. (https://doi.org/10.1016/j.diamond.2021.108421).

[16] Su Yu, J. S. Colton. A compact open-hole compression test fixture for composite materials. Composites Part B, Volume 223, 2021. (https://doi.org/10.1016/j.compositesb.2021.109126).

APPLICATION OF NANOCELLULOSE/MODIFIED GRAPHITE COMPOSITE AIRGELS AS HETEROGENEOUS CATALYST FOR BIODIESEL PRODUCTION BY ESTERIFICATION

Érica Rost [a] *, Daniel Pasquini [b]

(a) 0000-0001-7441-5143 (Federal University of Uberlândia – Brazil)

(b) 0000-0002-2850-8610 (Federal University of Uberlândia – Brazil)

* Corresponding author: erica.rost@ufu.br

Abstract: The efficiency of heterogeneous acid catalysis for biodiesel production can be affected by surface area and polarity of the catalyst. The airgel derived from cellulose nanofibers (NFC)/modified graphite has high porosity and hydrophobicity, which are desired properties. This study aims to apply heterogeneous acidic catalysts for biodiesel production. These catalysts are composites in the form of an airgel, produced by mixing NFC with sulfonated graphite with sulfanilic acid. To the sulfonation step were employed pure graphite and oxidized graphite. The efficiency of the catalysts were evaluated by esterification reactions carried out employing a molar ratio of methanol:oleic acid 10:1, catalyst amount of 5% (m/m) with respect to the mass of oleic acid. The variables studied were: time (10 and 120 min); catalyst particle size (original airgel or milled airgel); and temperature (100°C and 150°C). The efficiency of the reactions were evaluated by FTIR and gas chromatography. Among the variations in esterification conditions, temperature was the most significant. Increasing the contact surface (milled airgel) did not significantly increase conversions of oleic acid to ester. The highest conversion was obtained in the condition of time of 2 h and temperature of 150°C, reaching 70%.

1. INTRODUCTION

Heterogeneous catalysis has some characteristics that are advantageous, such as ease of separation, purification and reuse, in addition to stability [1,2]. However, present some difficulties like the need for a greater catalyst load, high temperature, excess alcohol, and slower reaction rates, due to the steric hindrance caused by the separation between the solid catalyst and the reactants. The increase in temperature is important, as it provides additional kinetic energy to the molecules, increasing their average speed and facilitating their diffusion to the functional sites of the catalyst. Also, excess alcohol helps increase the probability that more alcohol molecules will react with the carboxylic acid molecules on the catalyst surface [2-4].

It is important to highligth that when the catalyst is immobilized on a support it facilitates its separation and reuse [5]. Thus, the use of graphite, in addition to helping with immobilization, could contribute to increasing corrosion resistance, mechanical resistance, as well as thermal stability and, consequently, its useful life. Within the reasoning of immobilizing the catalyst on a support, the use of cellulose nanofibers, a nanometric cellulose textile material $(C_6H_{10}O_5)n$, is interesting, as it has characteristics of low cost, ease of catalytic coating, high availability, biocompatibility, renewability , biodegradability, high rigidity, good mechanical, thermal and traction resistance, in addition to low density [6].

In the form of airgel, a solid material characterized by being highly porous, nanocellulose has the characteristics of high surface area, good flexibility, high porosity, low thermal conductivity and sorption of liquids in large quantities. In this sense, it is believed that a catalyst support in the form of an airgel, developed

from cellulose nanofibers, presents advantages of high sorption and porosity, as these are characteristics that could benefit esterification reactions, in addition to good thermal and mechanical resistance.

Thus, this work studied the application of heterogeneous acid catalysts in the form of composites of NFC airgel with sulfonated pure graphite (GPS) and sulfonated oxidized graphite (GOS) for esterification reactions of oleic acid.

2. METHODOLOGY

2.1. Oxidation of graphite

The production of oxidized graphite (GO), mediated by the TEMPO (2,2,6,6- Tetramethylpiperidine 1-oxyl free radical), was carried out according to Araki and Hida [7]. In this study, TEMPO and sodium bromide (NaBr) were added to 100 mL of water containing 1 g of pure graphite (GP) in a mass ratio of Graphite:NaBr:TEMPO = 1.0:0.5:0.2. An aqueous solution of sodium hypochlorite (NaClO) (NaClO:Graphite = 1:1, m/m) was added to initiate the oxidation of graphite and the obtained mixture was stirred for 4 h at room temperature. The pH of the system was maintained between 10 and 11 by careful addition of 2 M aqueous NaOH solution. Oxidation was terminated by the addition of 0.5 mL of ethanol, which resulted in complete consumption of NaClO. Finally, the material was subjected to the washing and filtering process by aqueous dialysis, using a commercial polymeric dialysis membrane, made of cellulose acetate, for 3 days. Subsequently, sonication was performed for 5 min. The solid was separated by centrifugation at 20°C, 5000 rpm, for 15 min. At the end of the reaction, the sample obtained was dried at 90° C in an oven for 12 h. The suspensions obtained were adjusted to 1.5% solid content.

2.2. Graphite sulfonation

The sulfonation procedure was carried out using the adapted methodology, according to Lim *et al.* [8], in which 15 g of sulfanilic acid ($C_6H_7NO_3S$) were dispersed, with continuous stirring, in 300 mL of 1 M HCl aqueous solution. maintained at 5 ºC. Subsequently, 90 mL of 1 M aqueous sodium nitrite (NaNO$_2$) solution was added dropwise. After all the 1 M NaNO$_2$ was added, a clear solution was obtained and the mixture was stirred for another 1 h, maintaining the temperature at 5° C. Then, the mixture was allowed to settle and the white precipitate of 4-Benzenediazonium sulfonate (4-BDS) formed was filtered through dialysis to remove impurities. The 4-BDS obtained was mixed with 200 mL of aqueous solution containing GP or GO (1.5% concentration, i.e., 3 g of GP or GO) and 60 mL of ethanol. The temperature was maintained between 3 and 5 ºC with an ice bath. Subsequently, 100 mL of 30 wt% hypophosphorous acid (H$_3$PO$_2$) was added and left to stir for 30 min. Then, another 50 mL of H$_3$PO$_2$ was added and left stirring for another 1 h. The resulting sulfonated graphite was washed and filtered with aqueous dialysis for 3 days, then washed and centrifuged at 20°C, until reach neutral pH. Subsequently, it was subjected to an ultrasonic bath for 5 min. Finally, it was dried in an oven for 12 h, at 60 ° C. The samples obtained at the end of the sulfonation with sulfanilic acid were called GPS and GOS, for the pure graphite and oxidized graphite respectively.

2.3. Preparation of aerogels

The NFC (supplied by Suzano S.A.) were used as received, in aqueous solutions, which have a concentration of 3.0% by mass of nanofibers. To prepare the aerogels, 20.00 g of the NFC suspension (containing 0.6 g of dry nanofibers) was weighed and 0.3 g of the graphite samples (GP, GO, GPS or GOS) were added to it, slowly, under mechanical stirring, for 3 min, until the graphite samples were visible dispersed. Then, the mixture was subjected to the lyophilization process (Terroni benchtop lyophilizer, model LS3000) to obtain the aerogels and, finally, these were dried in an oven at 60°C, for 2 days, to ensure drying [9]. The airgel samples prepared with different graphite samples were named NFC-GP, NFC-GO, NFC-GPS and NFC-GOS.

2.4. Esterification with oleic acid

The methyl oleic acid esterification reactions were carried out with the catalyst, in a Parr bench reactor (Parr Instrument Company, model 4848) with a heating and temperature regulation system. The methodology was used, according to de Lima [10], which used a molar ratio of methanol:oleic acid 10:1, catalyst loading of 5% (m/m) in relation to the mass of oleic acid. The temperature studied were 100°C and 150°C, and the times were 10 min and 120 min. The catalyst were employed also in the milled form with particle sizes of

approximately 1.7 mm, obtained after milling in a in a Marconi micro knife mill, model MA048, and sieved through a 10 mesh sieve. The catalyst samples and respective reaction conditions for the analyzes are presented in Table 1.

Table 3. Conversion for esterification reactions with different reaction conditions

Sample	Reaction Temperature (°C)	Reaction Time (min)
NFC-GPS	100	10
NFC- GOS	100	10
NFC-GPS	100	120
NFC-GOS	100	120
NFC-GPS Milled	100	120
NFC-GOS Milled	100	120
NFC-GPS	150	120
NFC-GOS	150	120

At the end of the esterification reactions, the products (methyl oleate, water and methanol) were filtered to separate the catalyst. The liquid product went through the rotary evaporation process for 30 minutes to remove methanol. Heating was done in a water bath at 70°C, with rotation speed 100 rpm. Finally, the material obtained was decanted into a decantation funnel to separate the biodiesel from the possible remaining residues, with the upper less dense phase corresponding to biodiesel.

2.5. Fourier Transform Infrared Spectroscopy (FTIR)

For the FTIR analysis of biodiesel samples, a Shimadzu spectrophotometer, model IR Prestige-21, was used. All spectra were analyzed in the range of 4000 to 500 cm^{-1}. Pure KBr pellets were prepared and the liquid (biodiesel) was brushed on the surface of the KBr pellet. In sequence, 32 scans were performed for each sample. From the change from the peaks at 1710 cm^{-1} (C=O bond of carboxylic acids) and 1742 cm^{-1} (C=O bond of esters), it is possible to observe whether there is a higher percentage of oleic acid or ester. Like this, it becomes feasible to calculate the percentage of conversion of oleic acid to methyl oleate (ester). This assessment takes into account the height of the peaks, when drawing a baseline under the peaks of interest and determining their intensity, the relationship between them is made using a rule of three, with the sum of the intensities being equivalent to 100% [10].

2.6. Gas chromatography with flame ionization detector (CG-FID)

The products resulting from the oleic acid esterification reactions were subjected to analysis by a gas chromatograph, carried out by the Laboratório de Pesquisas em Materiais de Separação e Cromatografia (Cromat). The gas chromatograph was equipped with a flame ionization detector, from the brand Thermo, model Focus GC. Initially, to prepare the samples for analysis on the Gas Chromatograph, a solution of the sample in n-heptane was prepared by diluting 50 µL of the sample in 950 µL of n-heptane. Then, 50 µL of this solution was added to 450 µL of methyl heptadecanoate solution (internal standard) at 500 mg L-1. Next, to construct the analytical curve for methyl oleate, a stock solution of methyl oleate (OM) at 100 µL mL-1 in n-heptane was initially prepared with the ester standard (methyl oleate). To construct the analytical curve, standard solutions of methyl oleate were prepared by adding known volumes of the stock solution to the methyl heptadecanoate solution (internal standard, PI) at 500 mg L-1. Analysis conditions included a constant column oven temperature of 190°C, split injection with a flow split of 1:50 and temperature of 250°C, flame ionization detection with the detector held at 250°C. Sample injection was 1 µL, and the total analysis time for each sample was 5 min. The column used was a capillary column with poly(ethylene glycol) stationary phase from Carbowax, measuring 30 m in length, 0.32 mm in internal diameter and 0.25 µm in film thickness.

3. RESULTS AND DISCUSSION

Figure 1 shows the images of the prepared aerogels and also the scanning electron microscopy images of the respective aerogels.
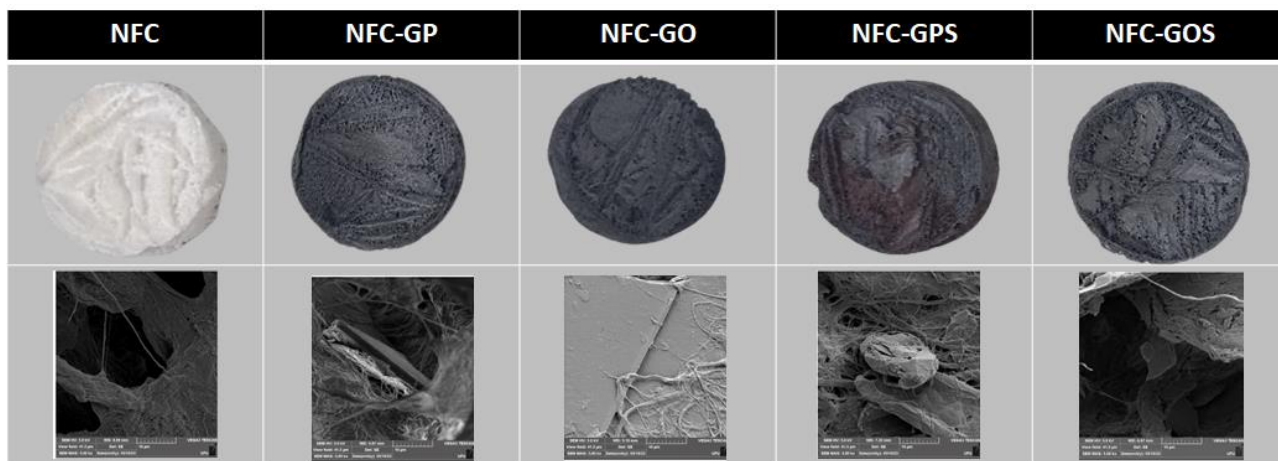
Figure 1. Photos of the prepared aerogels (top) and their respective scanning electron microscopy images (bottom) at 5,000x magnification.

From the images in Figure 1, it is possible to verify that the aerogels present good dispersion of graphite particles in the cellulose nanofibers, forming a homogeneous material. It is also possible to verify that the structure of the aerogels has preserved pores even with the insertion of graphite particles, whose porosity is important to increase the region of contact with the reagents during the synthesis of biodiesel.

To verify the existence of impurities in oleic acid and the effect of oleic acid autocatalysis, a reaction was carried out with only oleic acid and methanol without catalyst (blank experiment). Then, the same experiment were carried out with the catalysts to compare the conversions. Initially, the conditions for esterification followed the methodology used according to de Lima [10], which used a molar ratio of methanol:oleic acid 10:1, catalyst loading of 5% (m/m) in relation to the mass of oleic acid, temperature 100°C and time of 10 min. For these conditions, quantitative analyzes of the conversions of oleic acid to methyl oleate were carried out by GC - FID, without replicates, and the results are presented in Table 2.

Table 2. Results obtained from CG-FID analysis for the conversion of oleic acid to methyl oleate

Sample	% Conversion to Methyl Oleate (m/m)
Oleic acid	0
Blank	5.3
NFC-GP	1.9
NFC-GO	1.7
NFC-GPS	25.3
NFC-GOS	14.1

From the GC - FID analysis, it was demonstrated that the biodiesel samples obtained with NFC-GPS and NFC-GOS aerogels achieved the highest conversions (25.3 and 14.1% respectively) when compared to the other samples, and this is consequence of the presence of sulfonated groups inserted in the graphite during the funcionalization with sulfanilic acid. The sample obtained in the blank experiment showed a conversion of 5.3%, and this conversion is due to the autocatalytic effect of oleic acid, which is an acid and can also catalyze the esterification reaction under study. Although the sulfonated samples showed higher conversions as expected, due to the effect of the presence of sulfonic groups, the conversions were still low. According to de Lima [10], which carried out esterification experiments in similar experimental conditions for the porous membrane catalyst made of polysulfone and sulfonated polystyrene polymers, the low conversion, in addition to inadequate reaction conditions (low reaction time, low temperatura etc.), may be also due to the reversal of the reaction, which would form oleic acid by hydrolysis of the ester.

Due to the low conversion obtained in this first step, and the mild reactional conditions employed, it was decided to investigate the variation of some conditions of the esterification reaction, such as time, catalyst particle size and temperature. As demonstrated in the first step the need for sulfonic groups for greater

efficiency in the reaction, the studies of the following steps were carried out only with catalysts containing sulfonated graphite (NFC-GPS and NFC-GOS). In this way, it was carried out experiments with reaction times of 120 minutes, 150 °C of temperture and employing milled aerogel. In Figure 3, are presented the FTIR spectra relating to the reaction with different experimental conditions explored. Based on the constructed FTIR spectra, the amount of conversion of biodiesel esters was calculated considering the intensities of the C=O peaks for acid (1710 cm^{-1}) and ester (1740 cm^{-1}), as described in the experimental section. The results obtained are reported in Table 3.

In the first analysis of the effect of reaction time, comparing the NFC-GPS and NFC-GOS samples at a temperature of 100 °C and reaction times of 10 and 120 min, it is evident that with increasing time, both samples had a small increase in its ester conversion. Statistical analyzes have not yet been carried out, as this study is an exploratory study area. According to Ilgen [11] which developed studies on the esterification reaction with oleic acid, using a methanol:oleic acid ratio of 3:1, temperature of 100 °C, time of 2 h and loading of 15% solid catalyst sulfonated divinylbenzene/copolymer, it was observed that the reaction is fast in the first 120 min and then becomes slower. In their results, varying the time from 60 min to 120 min, there is an increase in conversion from 56.3% to 85.7%, respectively. By increasing the time to 360 min and 480 min, conversions of 96.8% and 99% were achieved.

(A) Biodiesel samples with time variation of 10 min and 120 min

(B) Biodiesel samples with variation in contact surface

(C) Biodiesel samples with temperature variation of 100°C and 150°C
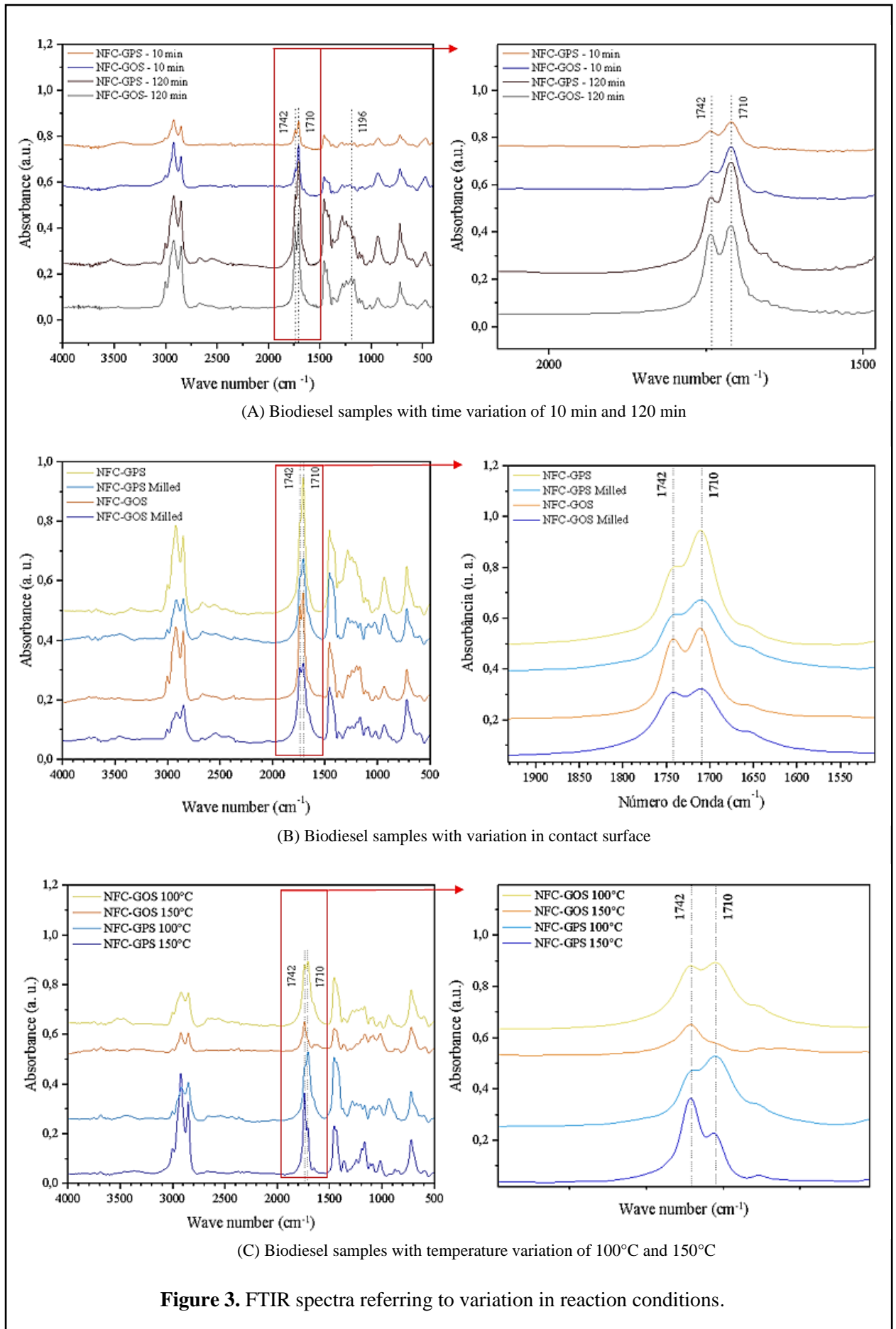
Figure 3. FTIR spectra referring to variation in reaction conditions.

Table 3. Conversion for esterification reactions with different reaction conditions

Sample	Reaction Temperature (°C)	Reaction Time (min)	Itensity of the peak at 1710 cm^{-1} (C=O of carboxylic acids)	Itensity of the peak at 1740 cm^{-1} (C=O of esters)	Sum of peak intensities	Oleic acid (%)	Methyl Oleate (%)
NFC-GPS	100	10	0.1162	0.075	0.1912	61	39
NFC-GOS	100	10	0.2031	0.0897	0.2928	69	31
NFC-GPS	100	120	0.4615	0.3119	0.7734	60	40
NFC-GOS	100	120	0.3708	0.33999	0.71079	52	48
NFC-GPS Milled	100	120	0.2755	0.2163	0.4918	56	44
NFC-GOS Milled	100	120	0.2605	0.248	0.5085	51	49
NFC-GPS	150	120	0.1885	0.3279	0.5164	37	63
NFC-GOS	150	120	0.0524	0.1235	0.1759	30	70

Regarding the effect of particle sizes, comparing samples obtained at temperatures of 100 °C, reaction times of 120 minutes, milled and unmilled, no change was observed in the conversion of oleic acid to methyl oleate. The increase in the contact surface of the catalyst (by reducing the particle size) with the mixture of oleic acid and methanol was thought to increase the exposure of the catalyst surface to the reaction mixture, meaning a greater quantity of active sites available. However, this was not observed in this study, most likely due to the fact that aerogels are porous in nature and their grinding did not affect the surface area present in the material without grinding, and therefore, grinding in this case did not generate changes in the catalytic sites and reactions yields.

Evaluating the effect of the temperture, It is noticeable that this variable is the most significant for the esterification reaction. Comparing the results obtained in samples obtained with 120 minutes of reaction, but increasing the temperatures from 100 to 150 °C, it was observed a considerably increased the conversion of oleic acid to methyl oleate, obtaining values of 63% for biodiesel produced with NFC-GPS and 70% for the sample esterified with NFC-GOS. It is understood that increasing the temperature provides an improvement in the conversion into biodiesel, caused by kinetic favoring, as the molecules have more kinetic energy and collide more frequently and with greater energy, which increases the probability of a reaction. Also, it is understood that the increase in temperature thermodynamically favors the reaction, due to the displacement of the reaction equilibrium towards the products [11].

4. CONCLUSIONS

It appears that the work carried out achieved the objective of verifying the potential of acid catalysts in the form of airgel composites of cellulose nanofiber and sulfonated graphite for the esterification reaction of oleic acid. Regarding the conversions of methyl oleate, it was noticed that among the variation of the conditions studied, temperature was the most significant, due to the reaction being kinetically and thermodynamically favored. The esterification reaction carried out for 10 min and 100° C, without catalyst (blank experiment), demonstrated by CG-FID the conversion of 5.3% into methyl oleate, indicating the autocatalysis of the reaction mediated by carboxylic acid, in this case the acid oleic itself. The highest conversions involve the conditions of molar ratio methanol: oleic acid 10:1 (m/m), catalyst loading of 5% (m/m) in relation to the mass of oleic acid, time of 2 h and temperature of 150°C, reaching 63% for biodiesel produced with NFC-GPS and 70% for the sample obtained with NFC-GOS airgel. Thus, the work contributed scientifically to developing an acid catalyst to be used in the production of biodiesel. Therefore, to achieve process efficiency with its use, the need to optimize reaction conditions to achieve higher yields in biodiesel production is evident.

4.1. Declaration of Competing Interest

The authors declare no conflict of interest.

4.2. Fundings

4.3. Acknowledgements

5. REFERENCES

[1] M. K. Lam; K. T. Lee; A. R. Mohamed. Homogeneous, heterogeneous, and enzymatic catalysis for transesterification of high free fatty acid oil (waste cooking oil) to biodiesel: A review. *Biotechnology Advances*, Volume 28, 2010. (https://doi.org/10.1016/j.biotechadv.2010.03.002).

[2] T. S. Cardoso et al. A review of the use of heterogeneous catalysts for the production of biodiesel. *Brazilian Applied Science Review*, Volume 4, Number 1, 2020. (https://doi.org/10.34115/basrv4n1-016).

[3] D. W. Lee; K. Y. Lee. Heterogeneous solid acid catalysts for esterification of free fatty acids. *Catalysis Surveys from Asia,* Volume 18, 2014. (https://doi.org/ 10.1007/s10563-014-9166-y).

[4] I. M. R. Fattah et al. State of the art of catalysts for biodiesel production. *Frontiers in Energy Research*, Volume 8, 2020. (https://doi.org/ 10.3389/fenrg.2020.00101).

[5] C. Godard; C. Claver; A. C. Albéniz. Supported Catalysts. *European Journal of Inorganic Chemistry*, Volume 5, 2022. (https://doi.org/10.1002/ejic.202101024).

[6] M. Zanini. *Aerogéis Hidrofóbicos de nanofibras de celulose*. 2016. Dissertation (Master's) – Postgraduate Program in Process Engineering and Technologies, University of Process Engineering, (https://repositorio.ucs.br/xmlui/handle/11338/1199), accessed 17 February 2022.

[7] J. Araki; Y. Hida. Comparison of methods for quantitative determination of silver content in cellulose nanowhisker/silver nanoparticle hybrids. *Original Paper*, Volume 25, 2018. (https://doi.org/10.1007/s10570-017-1640-z).

[8] S. Lim et al. Biodiesel synthesis from oil palm empty fruit bunch biochar derived heterogeneous solid catalyst using 4 -benzenediazonium sulfonate. *Journal of Hazardous Materials*, Volume 390, 2020. (https://doi.org/10.1016/j.jhazmat.2019.121532).

[9] P. Zhu et al. Electrostatic self-assembly enabled flexible paper-based humidity sensor with high sensitivity and superior durability. *Chemical Engineering Journal*, Volume 404, Number 127105, 2021. (https://doi.org/10.1016/j.cej.2020.127105).

[10] A. P. de Lima. *Desenvolvimento, caracterização e aplicação de novos catalisadores poliméricos heterogêneos baseados em poliestireno sulfonado e polissulfona para produção de biodiesel metílico a partir do ácido oleico*. 2018. Thesis (Doctorate) - Postgraduate Program in Biofuels, Federal University of Uberlândia, (https://repositorio.ufu.br/bitstream/123456789/21299/1/DesenvolvimentoCaracteriza%C3%A7%C3%A3oAplica%C3%A7%C3%A3o.pdf), accessed 10 January 2022.

[11] O. Ilgen. Investigation of reaction parameters, kinetics and mechanism of oleic acid esterification with methanol by using Amberlyst 46 as a catalyst. *Fuel Processing Technology*, Volume 124, 2014. (https://doi.org/10.1016/j.fuproc.2014.02.023).

REPLACEMENT OF A STEEL COMPONENTE WITH A GLASS-FIBER REINFORCED INJECTED COMPONENT, USING NUMERICAL SIMULATION AND EXPERIMENTAL TESTS FOR VALIDATION

Gabriel I. Pistorello[1] *, Lusardo E. dos Santos [1], Guilherme D. Erlo [1], Felipe Biondo [1], Alexsandro Sordi [1]

(1) Research. Marcopolo S.A. (Rio Branco Avenue, 4889, CEP 95060-145, Caxias do Sul, RS, Brazil)
* Corresponding author: gabriel.pistorello@marcopolo.com.br

CODE: BCCM7-176

Abstract: This study presents the successful replacement of a traditional steel component with a polymer component in industrial applications. The increasing demand for lighter, more durable, and cost-effective materials has driven the research for alternatives to metallic in various industries. Our research aimed to assess the technical and economic feasibility of the replacement, considering factors such as strength, durability, cost, and environmental impact. The component is question, called as emergency lever, is used for extracting bus windows in risky situations. Initially made of steel, it was redesigned using composite materials, employing tools like topological optimization and structural simulation to define the ideal materials and geometry. Subsequently, the model was prototyped in polycarbonate for initial testing and numerical correlation. Finally, the component was produced by injection molding, using blend of composite material with short fiber as the matrix material. The results demonstrate that the polymer component meets the required strength and durability for its application while offering additional benefits, including reduced weight, corrosion resistance, and fewer final components. Moreover, cost analysis reveals significant financial savings and a reduction in environmental impact over the product's lifecycle. This study contributes to the advancement of materials engineering by highlighting the advantages of replacing metallic components with polymers in industrial applications, providing valuable insights for innovation and sustainable development in the industry.

1. INTRODUCTION

The replacement of metallic components with polymers in industrial applications has been a growing trend, driven by the demand for lighter, more durable, and cost-effective materials. This trend is particularly relevant in sectors such as automotive, aerospace, and transportation, where weight reduction and increased efficiency are essential. The use of polymer composites has been increasingly explored due to their excellent mechanical properties and the ability to customize the material properties.

Composite materials have been widely adopted to combine high performance with low weight. As defined by ASTM D3878 (2007), composite materials refer to the fusion of two or more materials that are not miscible with each other, with the purpose of creating a new material with characteristics that are not individually achieved by the original materials.

According to Freitas (2016), composite materials are on the rise due to their lightness and practicality, which are not possible with conventional materials. Schöntag (2009) highlights that the most relevant properties of composite materials include high resistance to corrosion, moisture, heat, and fatigue. Batista (2017) adds that one of the advantages of composite materials is the ability to adjust their desired properties through the selection of the involved materials, which directly influences the mechanical characteristics of the

resulting composite. Due to the versatility of these materials, the automotive industry has shown increasing interest in their application.

In this context, the main objective of this study is to evaluate the feasibility of replacing a steel component with a polymer composite obtained through the injection process. The component under analysis is the emergency mechanism used to extract bus windows in risk situations. Initially manufactured in steel, the replacement with a polymer material can offer significant benefits in terms of weight reduction, mechanical strength, corrosion resistance, durability, ergonomics, and production costs.

2. CURRENT SCENARIO

Passenger safety is a priority in any mode of transportation, including buses, where in an emergency situation, such as accidents or fires, the rapid evacuation of passengers is critical. Emergency windows play a crucial role in these moments, providing essential escape routes. In cases of fire or accident, quick and safe accessibility to these routes can make the difference in saving lives. Therefore, the reliability and performance of the components involved in evacuation become extremely important for user safety. Hence, these systems must ensure the effectiveness of these operations during emergencies.

In Brazil, the Brazilian Association of Technical Standards, through ABNT NBR 15570:2021, is the regulation that defines standards and requirements for the manufacture of accessible vehicles with urban characteristics. It also establishes procedures and test methods that these vehicles must follow. Specifically regarding emergency mechanisms, ABNT NBR 15570:2021 requires that these devices be located near emergency exits, in visible, easily accessible locations, and within reach of passengers. It also stipulates that a unit must be installed at each end of the emergency window, which must be operable and require a maximum force of 300 N for activation.

Figure 1 illustrates in (a) the distribution of the mechanism along the emergency windows and (b) shows the assembly of the steel emergency mechanism currently in use.

(a)   (b)

Figure 1: (a) Positioning of emergency windows; (b) Steel emergency mechanism

Currently, throughout the company, there are more than 10 types of emergency levers to address different types of situations and applications. Therefore, one of the premises for the development of this new component, in addition to meeting legislation requirements, is to have a lighter, interchangeable part that facilitates window extraction, is economically viable, and aligns with the goal of standardizing components and simplifying assembly.

3. METHODOLOGY

The methodology used to develop the mechanism was based on a structured process as detailed in Table 1.

Table 1. Steps mapped for development of the new mechanism

Item	Phases
1.1	Map requirements, legislation, standards, and company criteria.
1.2	Brainstorm ideas, materials, and processes.
1.3	Design using previously conducted studies.
1.3	Perform numerical validation (structural, ergonomic, efforts) using CAE tools.
1.4	Carry out experimental characterization tests (according to ABNT NBR 15570/2021).
1.5	Perform virtual topology optimization analyses.
1.6	Manufacture the component via additive manufacturing.
1.7	Perform experimental tests, in accordance with ABNT NBR 15570/2021, with prototype parts and parts produced via additive manufacturing.
1.8	Create definitive tooling.
1.9	Validate experimentally in accordance with ABNT NBR 15570/2021.
2.0	Implement the project.

The project began with an in-depth mapping of all the standards and regulations related to the design of emergency levers. It was verified that the standard ABNT NBR 15570:2021 applies to all bus models, and if the requirements specified in the standard are met, the component will be approved. Figure 2 shows the current steel system mounted on a device for conducting an experimental test to obtain the forces required for window extraction. Figure 3 presents the test results after its execution, with approval results according to the ABNT NBR 15570:2021 standard.

Figure 2. The current system tested experimentally for obtaining applicable loads

Figure 3. Validation of the mechanism according to ABNT NBR 15570:2021 standard

"Subsequently, the functional and performance requirements of the new mechanism were established, considering aspects such as fire resistance, ease of assembly, and enhancement of ergonomics for opening.

Based on the established requirements, various designs were studied, evaluating their feasibility and functionality through finite element analysis. Considering that the standard stipulates a maximum window extraction force of 300 N, a simplified model of the mechanism was simulated, applying a force of 500 N, using a safety coefficient in relation to the nominal value. The numerical model was developed to simulate the extraction of an emergency window. For the numerical simulations, the HyperMesh and HyperView software from Altair were used as pre-processing and post-processing tools, respectively, and OptiStruct as the solver for the calculations. **Figure 4** shows the initial model with boundary conditions.
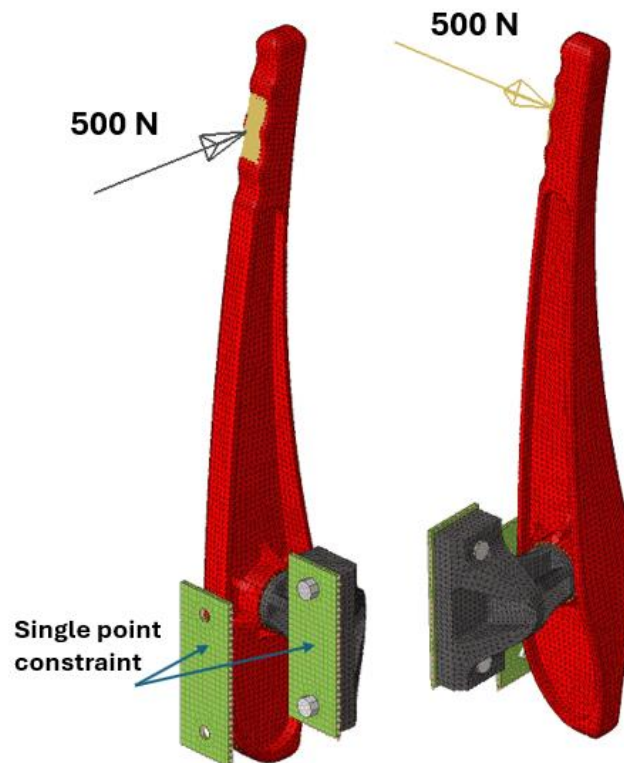
Figure 4. Numerical model for concept validation

The complete numerical model consisted of a total of 99,849 elements, including 2D and 3D elements. The main components of the system, consisting of the lever and the bearing, were modeled using second-order tetrahedral elements. Hexahedral elements were employed for the bearing fixation screws, while the plates representing the constraints were modeled with shell elements.

For the emergency lever and its bearing, a polymeric composite with the properties listed in **Table 2**, were used:

Table 2 – Properties of the polymeric compound

	Material 1
Density	1.12 g/cm³
Maximum traction strength	48.87 MPa
Maximum compression strength	100 MPa
Elongation at Break	2.3 %

4. RESULTS AND DISCUSSION

As detailed in **Table 1**, the 3D design of the final part underwent the process of topological optimization, a technique that studies load paths and guides the design to consider these efforts in predicting the ideal geometry. Topological optimization allows for determining the best material distribution within a given space, maximizing structural efficiency, and minimizing weight. Based on this analysis, the part was designed to be produced by the plastic injection molding process, which provided great geometric freedom in the design conception. **Figure 5** show all the stages of numerical validation of designs originated from topological optimization analyses to the definition of the final concept.
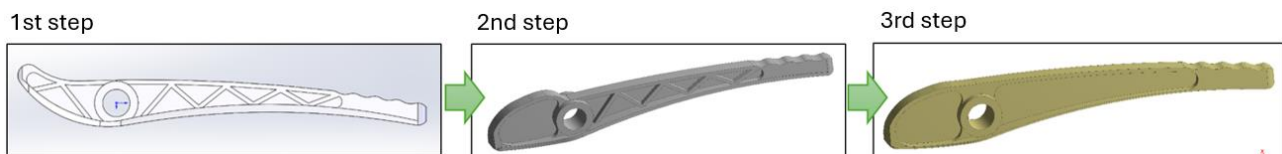
Figure 5. Evolution of topological optimization

After selecting and validating the most promising concept through structural analyses via the finite element method, experimental tests were conducted to verify the functionality of the proposed geometry and the window extraction force. As illustrated in **Figure 6**, the results obtained were satisfactory, meeting the requirements of the ABNT NBR 15570:2021 standard.

Figure 6. First prototype tested experimentally after a loop of virtual analyses (functional verification of geometry and window extraction force

The cam developed to perform the window extraction demonstrated a performance that meets the requirements of the standard, as demonstrated by the maximum force value measured for window removal, as presented in **Table 3**.

Table 3 – Experimental results of maximum force

Sample	Maximum force applied [N]	Maximum force applied [kgf]
Conceptual project	**236.7**	**24.14**

After concluding the first cycle of prototype testing, the mechanism underwent refinement based on the results obtained. This systematic and structured process ensured the development of a reliable and efficient emergency window mechanism, meeting the highest safety standards for passengers who use the bus as their daily mode of transportation. Following the iterations of topological optimization, a final injected piece concept was reached, and with this concept, numerical validation analyses of the component were performed.

With the final concept defined after numerical validations, a set was manufactured via additive manufacturing to test and validate the final geometry. **Figure 7** shows the piece with the final geometry printed using additive manufacturing.

Figure 7. Printed Part

As the printed piece did not consider the material of the final part, a failure occurred in the bearing where the lever exerted greater force, thus requiring the use of a steel bearing to validate the final geometry. **Figure 8** shows the results of the experiment, where (A) and (B) present the piece with the bearing printed using additive manufacturing, and (C) and (D) show the piece with the modification of the bearing to steel. It was found that the new emergency mechanism was able to extract the window with a force of 216 N, thus being approved according to the normative requirements.
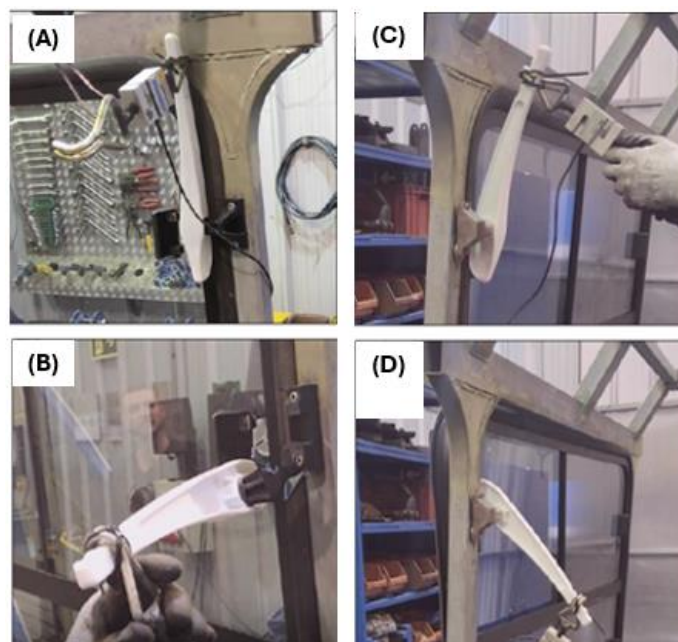
Figure 8. Validation of the printed part geometry

To evaluate the results of the finite element model, the Christensen failure criterion was used. This criterion is a material failure theory for isotropic materials that attempts to cover the range of ductile to brittle materials and takes into account the ultimate tensile and compressive strengths, as per Christensen (2016).

For evaluation, one must consider not only the tensile (T) and compressive (C) strength of the material but also the resulting maximum principal stresses $(\sigma_1, \sigma_2, \sigma_3)$ from the loading case, as shown in Equation 1 below. If the result is less than or equal to 1, it is considered acceptable.

Equation 1 – Christensen failure criterion

$$\left(\frac{1}{T} - \frac{1}{C}\right)(\sigma_1 + \sigma_2 + \sigma_3) + \frac{1}{2TC}\left[(\sigma_1 - \sigma_2)^2 + (\sigma_1 - \sigma_3)^2 + (\sigma_3 - \sigma_1)^2\right] \leq 1$$

The maximum displacement found was 81 mm in the upper region of the emergency lever, as shown in **Figure 9**.
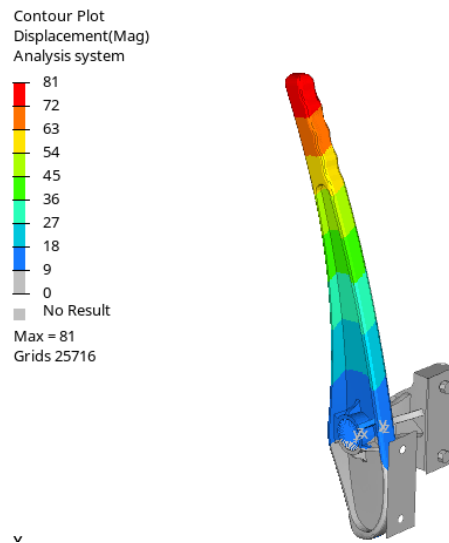
Figure 9. Displacement results

According to the Christensen failure criterion, the proposed material with the mechanical properties listed in Table 2 meets the criterion. As shown in Figure 10, the points closest to the limit of the criterion were in the bearing, indicating that the results correspond to the previously conducted test for geometric concept validation.
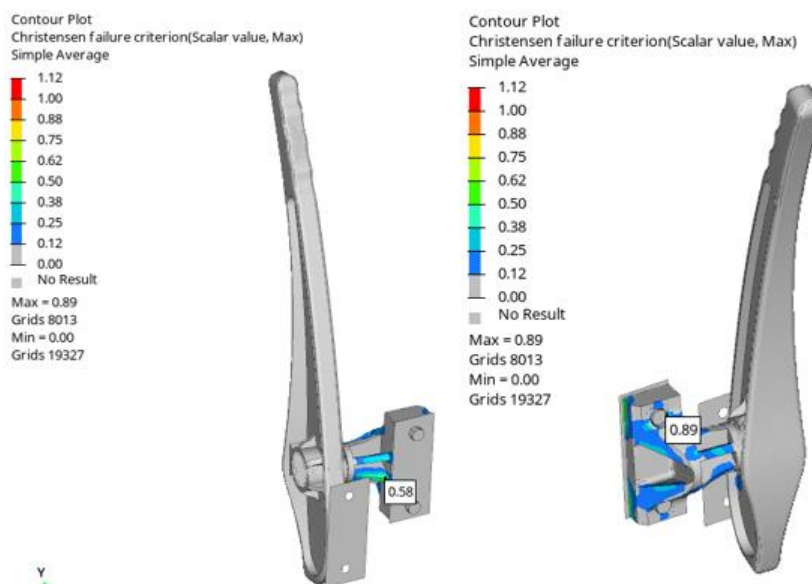
Figure 10. Christensen failure criterion results

After geometric, functional and mechanical resistance validations, the tooling was then created with the final part and implemented in the vehicles. Figure 11 shows the applications of the final product. In (A) the final concept of the part and its assembly located close to the emergency windows are shown, and in (B) the application in a complete vehicle.
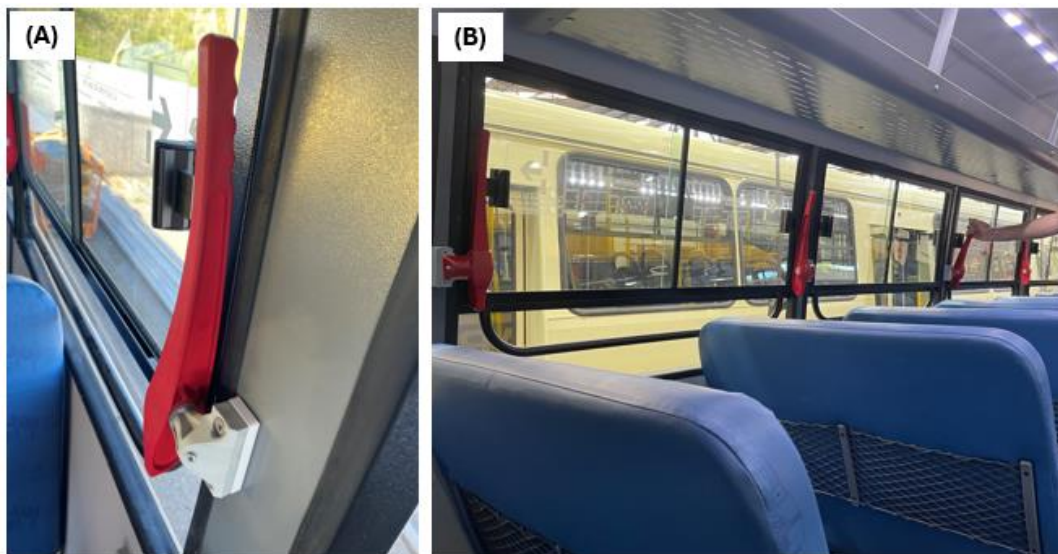
Figure 11. Application of the mechanism in a complete vehicle

5. CONCLUSIONS

Based on the presented results, it is possible to conclude that various applications using traditional materials and processes can be replaced by composite components, provided they are studied in detail and with well-defined requirements. This project produced several benefits as listed below:

- The force result for window extraction, according to ABNT NBR 15570:2021 is 30 kgf, this new design improve in approximately 27% efficiency of this component, complying with all regulatory requirements.
- The weight of each emergency mechanism reduced by 76%.
- The unitary cost of each piece reduced by 65%.
- Due to its geometry, it was possible to standardize left-side and right-side pieces and various models, reducing the number of part numbers by 80%.

Additionally, the project provided a significant increase in the team's knowledge of new applications of composite materials, stimulating the search for innovative solutions using this type of material.

5.1. Declaration of Competing Interest

The authors declare that there is no conflict of interest.

6. REFERENCES

[1] AMERICAN SOCIETY FOR TESTING AND MATERIALS. ASTM D3878: Standard terminology of high-modulus reinforcing fibers and their composites. Estados Unidos, 2007. 5 p.

[2] FREITAS, V. J. G. Resposta ao impacto longitudinal e transversal de laminados de vidro/epóxi. 2016. 62 f. Dissertação (Mestrado em Engenharia Mecânica) - Programa de Pós-Graduação em Engenharia Mecânica, Universidade de Coimbra, Portugal, 2016.

[3] SCHÖNTAG, J. M. Caracterização da profundidade de defeitos em materiais compósitos utilizando shearografia com carregamento vibracional. 2009. 107 f. Dissertação (Mestrado em Metrologia Cientifica e Industrial) - Programa de Pós-Graduação em Metrologia Cientifica e Industrial, Universidade Federal de Santa Catarina, Santa Catarina, 2009.

[4] BATISTA, Ana Claudia de M. C. Comportamento mecânico de compósitos poliméricos híbridos: estudos experimentais, analíticos e numéricos. 2017. Tese (Doutorado em engenharia mecânica) - Universidade Federal Do Rio Grande Do Norte, Natal.

[5] ASSOCIAÇÃO BRASILEIRA DE NORMAS TÉCNICAS. NBR 15570: Transporte - Especificações técnicas para fabricação de veículos de características urbanas para transporte coletivo de passageiros. Rio de Janeiro: ABNT, 2011.

[6] CHRISTENSEN, Richard M. The theoretical measure of the ductility of failure for all isotropic materials in all states of stress. Journal of Applied Mechanics, v. 83, n. 6, p. 061001, 2016.

MAGNESIUM METAL MATRIX COMPOSITES WITH SILICON CARBIDE PARTICULATES (MMMC/SiCp) PRODUCED BY SHAKE CASTING FOR APPLICATION IN THE AUTOMOTIVE SECTOR

Wellington Bruno Silva de Jesus [(a)]*; Hellen Karina Pereira Alkimim [(b)]; Marcella Cândido Velloso [(c)]; Jeremias Ismael Nunes Fortini [(d)]; Maria Adrina Paixão de Souza da Silva [(e)]; Eduardo de Sousa Lima [(f)]

(a) 0000-0002-8176-8980 (Military Institute of Engineering – Brazil)
(b) 0000-0002-5055-9254 (Military Institute of Engineering – Brazil)
(c) 0000-0002-9006-6411 (Military Institute of Engineering – Brazil)
(d) 0000-0003-3098-0102 (Military Institute of Engineering – Brazil)
(e) 0000-0002-7202-4541 (Federal University of Pará – Brazil)
(f) 0000-0001-6795-9927 (Military Institute of Engineering – Brazil)

* Corresponding author: wellington.bruno@ime.eb.br

CODE: BCCM7-211

Abstract: Metal matrix composites (MMCs), particularly magnesium-based MMCs reinforced with silicon carbide particulates (SiCp), have gained significant attention in the automotive sector for weight reduction and enhanced performance. This literature review explores the potential applications of MMMC/SiCp, focusing on the impact of SiC content on mechanical properties as hardness, tensile strength, and compressive strength. By investigating the advantages of utilizing MMMC/SiCp for weight reduction and improved performance in automotive applications, this study sheds light on the innovative solutions offered by magnesium-based composites with SiC reinforcement.

1. INTRODUCTION

Magnesium metal matrix composites with silicon carbide particulates (MMMC/SiCp) have aroused great interest due to their unique properties and significant advantages. Magnesium is known to be one of the lightest structural metals, offering an excellent strength-to-weight ratio, which is crucial for reducing vehicle weight and improving energy efficiency. However, pure magnesium has some limitations in terms of mechanical strength and wear resistance.

The addition of silicon carbide particulates (SiCp) as reinforcement in these magnesium composites helps overcome these limitations. Silicon carbide is an extremely hard ceramic material with high wear resistance and thermal stability, which contributes to increasing the strength and durability of Mg/SiC composites. In addition, SiCp can also improve mechanical properties such as modulus of elasticity and tensile strength, making composites more suitable for demanding structural applications. The stirring casting technique is one of the techniques used these composites, involving the intimate mixing of molten magnesium with SiCp followed by solidification. This process allows for an even distribution of the reinforcing particles within the magnesium matrix, resulting in a refined microstructure and improved mechanical properties. Stir casting also offers advantages in terms of scalability and cost, making it an efficient approach to large-scale manufacturing of these with high-performance composites.

Studies such as that of M. AMIR, according to reference [1], demonstrate the potential of the use of SiC particulate reinforcements in magnesium metal matrix composites. The research evaluated the mechanical

properties of pure Mg/SiCp composites and observed a significant increase in the values of hardness, tensile strength and yield strength due to the addition of SiC to the base matrix. Similarly, L. Xi et al, [2] also presented satisfactory results of the mechanical properties of Mg/SiC composites produced. The study provides a new strategy to overcome the trade-off between strength and toughness in metal matrix nanocomposites.

This review underscores the potential of MMMC/SiCp to replace conventional materials like aluminum and steel alloys in automotive components, thereby contributing to weight reduction, enhanced performance, and improved safety and durability. By offering a unique blend of properties, magnesium-based composites with silicon carbide reinforcement represent an innovative solution poised to drive the evolution of more efficient, safer, and sustainable vehicles in the automotive industry.

2. LITERATURE REVIEW

Magnesium is the element in the periodic table whose chemical symbol is Mg and its atomic number is 12. This element belongs to the group of alkali-earth metals and has a silvery tone in its natural state. Contact with air tends to oxidize and take on a greyish hue, due to the formation of an oxide layer (MgO), which protects it from corrosion [3].

As a metal, pure magnesium has interesting mechanical properties such as low density, low melting point, and relative mechanical strength, among others. Magnesium has good castability, high specific strength, and good damping capacity. The wear resistance of magnesium is comparatively low, which limits its future applications, but this resistance of magnesium and magnesium alloys can be remarkably increased by the addition of SiC, B_4C, TiC, steering grey, Al_2O_3, etc [4].

Magnesium alloy is one of the promising light metals for structural applications. Due to its hexagonal crystal structure with insufficient sliding systems, its formality at low temperatures is not as satisfactory. In addition, its resistance is also low due to the easy activation of basal slippage. Currently, most commercial components produced from magnesium alloys are manufactured by die casting, while the use of forged magnesium alloys is very small, with less than 10% [5].

In recent years, a series of studies have been developed on the possibilities of improving the mechanical properties of Mg alloys and composites, to further expand their applications in the automotive and aerospace industries. Based on the previous investigations, the researchers developed new Mg alloys with high strength by modifying existing commercial alloy systems or by developing new alloy systems, taking full advantage of the strengthening of grain refinement [5].

Silicon carbide (SiC) is the only binary compound of silicon and carbon present in the solid phase under normal conditions. Since 1824, when Jöns Jakob Berzelius first suggested the possibility of a chemical bond between silicon and carbon, interest in this compound has grown. Although rare on Earth, silicon carbide is abundant in the universe, often being found in meteorites [6].

SiC is classified as an advanced ceramic due to its several advantageous characteristics such as excellent chemical stability in corrosive environments, its ability to withstand high temperatures without deformation or deterioration, and its low density compared to other ceramic materials. These properties make SiC a highly versatile material suitable for a wide range of industrial and technological applications, including protective coatings, high-power electronic components, advanced cooling systems, shielding, and the aerospace industry [7].

Recently, there has been a significant increase in the demand for materials that can replace or complement traditional materials. In this sense, composites have stood out as a viable alternative, due to their ability to integrate distinct properties of different materials, offering versatile and adaptable solutions. This trend reflects the search for more efficient, durable, and ecologically sustainable materials, driving advancements in industries such as engineering, construction, and technology [8].

Magnesium-based metal matrix composites (MMCs) have aroused considerable interest due to their advantageous characteristics such as a superior strength-to-weight ratio, improved thermal conductivity, and remarkable wear resistance. These attributes position as a primary choice for advanced applications in a variety of industries, including automotive, aerospace, and electronics. However, magnesium-based MMCs face challenges related to limited strength and ductility, especially in applications that require high mechanical strength and toughness. The strategic incorporation of reinforcing particles, such as silicon carbide (SiC), can significantly improve these essential properties, offering an effective solution to expand the use of MMCs in technologically advanced applications [9].

Particle size plays a critical role in the formation of the microstructure and consequently influences the properties of particle-reinforced magnesium matrix composites (PRMMCs). Recent studies indicate that micrometer-sized ceramic particles can reduce ductility, while nanometer reinforcements can increase the

strength and ductility of Mg composites. Despite promising results, achieving a uniform density distribution in compacted green parts during consolidation remains a challenge, as the inhomogeneous density distribution can result in uneven shrinkage or distortion during subsequent sintering or heat treatment processes. This issue is crucial for effective development, and consistent and reliable performance [9].

The increase in the hardness of the composite with the increase in the strengthened SiC content is due to the rigid and tough nature of silicon carbide (SiC). When incorporated into the Mg matrix, SiC strengthens the structure of the composite, making it more resistant to deformation and wear. However, this increase in hardness and density can also affect other material properties, such as toughness and machinability, depending on the specific applications of the composite. [10]. The efficacy of SiC particles and their impact on the mechanical properties of the composite depend significantly on their uniform distribution in the matrix. However, due to the small size and large specific surface area of these particles, it is extremely challenging to incorporate, distribute, and disperse them uniformly in the magnesium matrix [11].

Particle-reinforced composites have been produced using a variety of methods: stirring casting, disintegrated melt deposition, powder metallurgy, etc. However, the casting method is preferred over other techniques due to its ability to produce complex shapes with a high production rate and low costs. Stirring casting is a manufacturing technique that involves applying motion or stirring to molten metal during solidification [12].

This method is used to improve the quality of the molten material, control the microstructure, and reduce defects such as gas inclusions and segregation. The benefits of shaking casting include the production of parts with improved mechanical properties, a more uniform microstructure, and a reduction in the formation of porosity and segregation in the molten material [12].

In this process, the metal is usually weighed and placed in a furnace until it melts. Simultaneously, the booster particles are preheated to remove moisture. The preheating of the particles is carried out in a muffle furnace on average at a given one hour. The crucible and mold are also preheated in the same furnace for thirty-two minutes to prevent thermal shock. After the preheating process, the reinforcement particles are added to the molten metals and then stirred for 1 minute to obtain a homogeneous mixture. Then, the molten composite is poured into the crucible and transferred to the preheated mold. The mold is opened after the composite solidifies [13].

3. RESULTS AND DISCUSSION

Currently, a series of research is underway focused on SiC particle-reinforced metal matrix composites (MMCs), which are a new type of structural material known for their high strength, hardness, and thermal stability. The potential applications of this composite in the aerospace, automotive, electronics, and specialized mechanical equipment industries are of great relevance to the scientific community to understand the main advantages and disadvantages of this material, exploring the relationship between the mechanical properties and the microstructure of these composites [14].

There are several approaches to studies focused on Mg/SiC composites, as in M. Gandhi, et al. (2023) according to the reference [15], In his work, he conducts an experimental investigation focused on the analysis of the influence of SiC reinforcement on the mechanical and machinability of hybrid magnesium composites in wire electrical discharge machining (WEDM). For manufacturing, 5 and 10% by weight of silicon carbide and 5% by weight of boron carbide to AZ31 alloy were used through the process of stirring casting under a controlled atmosphere.

From the analysis of the micrograph (Figure 1. a, b, and c) obtained by optical microscopy, it is possible to visualize the grains in the magnesium composite. The presence of the reinforcements is observed, with a notable increase in their presence evidenced in Figures 1b and c when 10% of SiC is added to the composite. Regardless of the amount of reinforcement, the microstructural study revealed a decrease in the average grain size in the hybrid composites compared to the unreinforced material. The mechanical properties, such as tensile strength and hardness of the fabricated metal matrix composite, were also evaluated, and the results are presented in Figure 2, along with the percentage of elongation of the material.
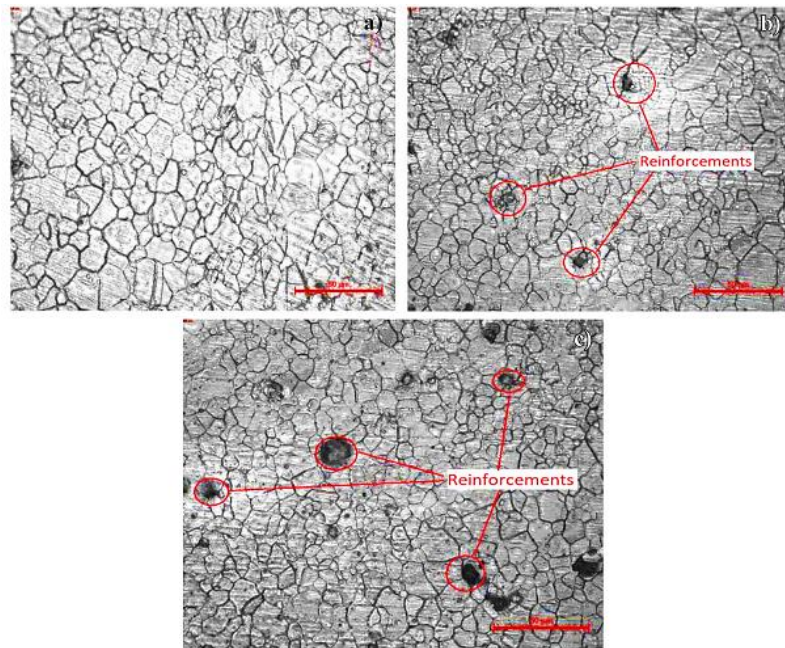
Figure 1. Optical micrograph of (a) Mg AZ31, Hybrid Composites with (b) 5% and (c) 10% SiC [15].

The combined effects of grain size reduction and strengthening effects caused by impeding the movement of dislocations, a large increase in hardness and tensile properties can be observed, as illustrated in Figure 2. In addition, reinforcement has a significant impact on hardening and load transfer. The thermal mismatch between the components of the composites also contributes significantly to the generation of dislocation density.
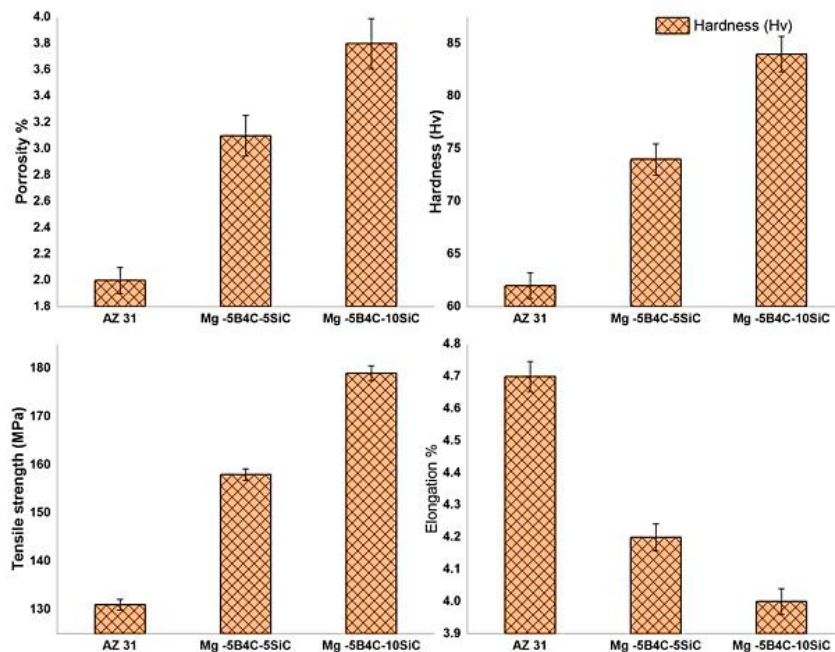
Figure 2. Mechanical Properties of Fabricated Materials [13].

In another study, the mechanical properties of magnesium metal matrix composites were investigated by E. Mohsen et al. (2016) according to reference [16], where AM50 and AZ91D matrix composites reinforced with oxidized and non-oxidized SiC particles were produced, as a complex system to the formation of various types of intermetallic particles that can form during solidification in SiC-reinforced Mg alloys.

Figure 3 shows the hardness variations of AM50 and AZ91 alloys and metal matrix composites (MMCs). MMCs have become harder than base alloys. The use of HCS 59N reinforcement (SiC particles in the size range 0.1 and 1.9 μm) resulted in maximum hardness, increasing from approximately 50 to 73 in the

AM50 alloy and from 64 to 76 in the AZ91D alloy. HCS 400 (larger SiC particles in the size range of 4-28 μm) provided a lower hardness than HCS 59N, but still higher than unreinforced AM50 and AZ91D alloys. Unlike the amount of reinforcement in MMCs, a reduction in content did not result in greater hardness. However, this reduction may have contributed to a lower dispersion in the hardness results of CMMs produced with HCS 400, using a content of 40% compared to other CMMs.
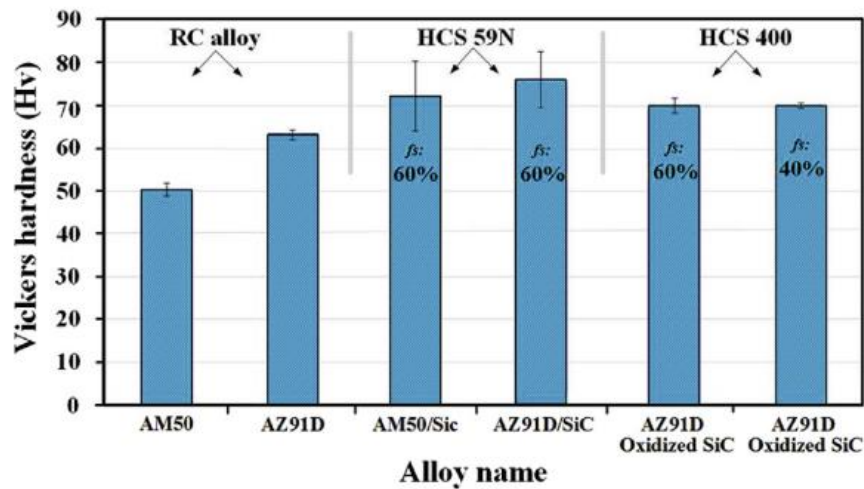
Figure 3. The hardness of RC alloys and MMCs produced by the two types of SiC particles and values [16].

These composites represent an option for the automotive industry, which in recent decades has constantly sought to improve and develop new materials for the manufacture of automotive components. This effort is mainly aimed at reducing the weight of components, which directly impacts fuel consumption, performance, sustainability, and, consequently, competitiveness in the market. In addition, this search for new materials is in line with the new guidelines of the automotive sector, increasing the interest in these composites.

The influence of SiC content on the mechanical properties of Mg/SiC composites is notorious. These composites are presented as an option for the automotive industry, which in recent decades has been constantly improving and developing new materials for the manufacture of automotive components concerning reducing the weight of components, directly reflecting on the requirements of fuel consumption, performance, sustainability and, consequently, on its competitiveness in the market, in addition to meeting the new industry guidelines, increasing interest in this material [17].

The correlation between microstructure and mechanical properties can also be observed in the work developed by P. Kowit. et al. (2023), according to reference [18], when manufacturing AZ91D alloy composites reinforced with various weight fractions (0.0, 1.0, 1.5, and 2.0% by weight) of SiC nanoparticles and evaluating their microstructural characteristics and mechanical properties. Figure 4 shows the graph of the variation in the mean grain size of α-Mg as a function of the weight fraction of SiC, together with the error bar indicating the standard deviation. As can be seen, the average size of the primary α-Mg grains in the unreinforced AZ91D alloy was approximately 154 (±19) μm. The addition of 1.0 wt% of SiC nanoparticles to the AZ91D matrix alloy led to a significant reduction of approximately 51% in the average α-Mg grain size, from 154 (±19) to 76 (±14) μm. With further increases in SiC concentration to 1.5 and 2.0% by weight, the mean α-Mg grain sizes were 67 (±12) and 48 (±9) μm, respectively, indicating a reduction of 57% and 69%.
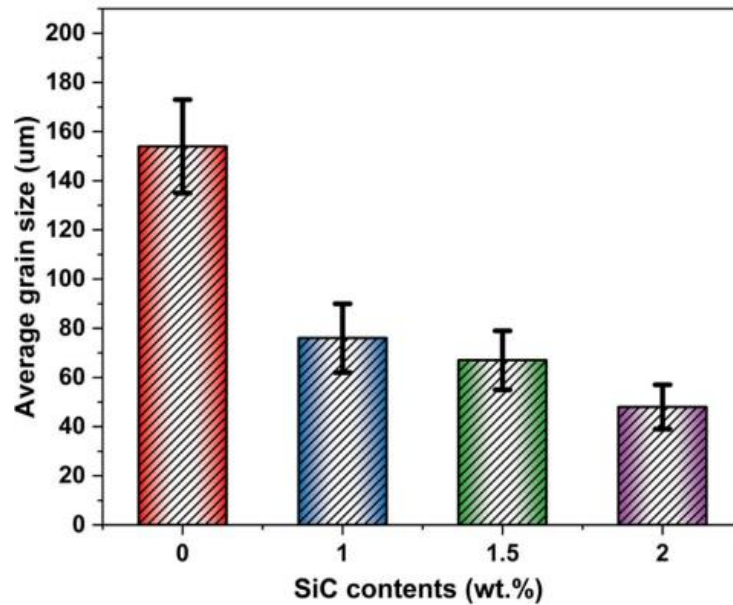
Figure 4. Variation in average grain size α-Mg in AZ91D/ nanocomposites
SiC as a function of SiC content [18].

Next, it is possible to observe the influence of grain size on the average values of hardness by microindentation of the alloy reinforced with varying amounts of SiC nanoparticles and not reinforced (Figure 5), with the error bars representing the standard deviation obtained from one hundred indentation points. The results indicated that the microhardness of all AZ91/SiC nanocomposites surpassed that of the unreinforced AZ91D alloy. In addition, an increase in SiC percentage by weight exhibited a linear correlation with the increase in microhardness for AZ91D/SiC [18].
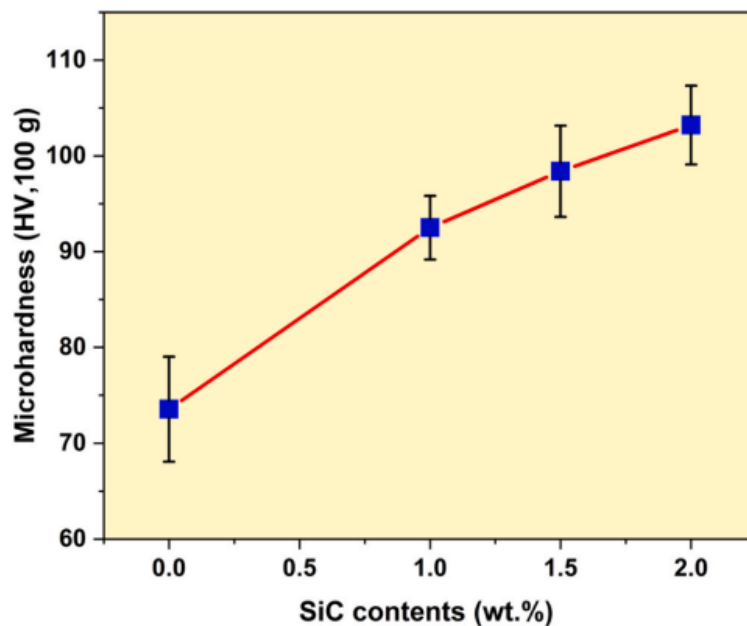
Figure 5. Microhardness variation of AZ91D/SiC nanocomposites as a consequence
of different weight fractions of SiC [18].

The addition of SiC reinforcement particles showed significant effects on the improvements of the microstructural and mechanical properties of the Mg/SiC composites. These attributes make them especially suitable for applications that require materials that are lightweight, resistant, and able to withstand severe temperature and wear conditions, such as materials used in structural components that require high strength and rigidity or can be used in vehicle parts.

4. CONCLUSIONS

This study provides a review of SiC particle-reinforced metal matrix composites (MMCs), which are a new type of structural material known for its high strength, hardness, and thermal stability and its potential for applications in the aerospace industry and especially automotive, addressing preparation technology, microstructure, and mechanical properties.

The stirring casting process is simple and easy to operate so that a uniform mixture of the single reinforcement with the die material is obtained. This process offers an efficient and cost-effective route to manufacturing these composites, allowing for customization of material properties according to the specific requirements of each automotive application. In any case, it is possible to improve the preparation process and the level of research on composites, always focusing on the effectiveness and cost of the materials that are directly influenced by the form of preparation.

Therefore, the results of this study are extremely relevant for the development and understanding of the production and characterization of the Mg/SiC composite. With more research and development in this area, MMMC/SiCp is expected to play an important role in the technological evolution and innovation of the automotive sector, driving the creation of more efficient, safer, and more sustainable vehicles.

4.1. Declaration of Competing Interest

The authors state that they have no competing financial interests or known personal relationships that may have influenced the work reported in this article.

4.2. Acknowledgments

5. REFERENCES

[1] K. B. Nie et al. Microstructures and mechanical properties of SiCp/AZ91 magnesium matrix nanocomposites processed by multidirectional forging. Journal of Alloys and Compounds, Volume 622, 2015. (https://doi.org/10.1016/j.jallcom.2014.11.045).

[2] L. Xi et al. Deformation and failure behavior of heterogeneous Mg/SiC nanocomposite under compression. Journal of Magnesium and Alloys, Volume 10, 2022. (https://doi.org/10.1016/j.jma.2021.04.008)

[3] M. K. Kulekci. Magnésio e suas ligas aplicações na indústria automotiva. International Journal of Advanced Manufacturing Technology, Volume 39, 2008. (https://doi.org/10.1007/s00170-007-1279-2).

[4] B. Ram et al. Effect of hot extrusion on microstructure and tribological behavior of Mg and Mg/SiC metal matrix composite produced by stir casting route. Materials Research Express, Volume 6, 2019. (https://doi.org/10.1088/2053-1591/ab07d8).

[5] S. You et al. Recent research and developments on wrought magnesium alloys. Journal of Magnesium and Alloys, Volume 5, 2017. (https://doi.org/10.1016/j.jma.2017.09.001)

[6] S. Kukushkin. Silicon Carbide: From Fundamentals to Applications. Materials, Volume 14, 2021. (https://doi.org/10.3390/ma14051081).

[7] G.T. Saleiro et al. Mechanical behavior of sic additivated with Al_2O_3 e Y_2O_3 produced by synthesis by auto combustion sustained at high temperature/comportamento mecânico do sic aditivado com Al_2O_3 e Y_2O_3 produzidos pela síntese por combustão autossustentável à alta temperatura. Tecnologia em Metalurgia, Materiais e Mineração, Volume 15, 2018. (http://dx.doi.org/10.4322/2176-1523.1573).

[8] H. B. S. Lima et al. Análise das propriedades de flexão e flamabilidade em compósitos poliméricos com incorporação do resíduo de lama vermelha. Peer Review, Volume 5, 2023. (https://doi.org/10.53660/1201.prw2710).

[9] F. R. Mehr. et al. M. Desempenho Ótimo de Nanocompósito de Mg-SiC: Desvendando a Influência do Tamanho de Partículas de Reforço na Compactação e Densificação em Materiais Processados via Moagem Mecânica e Prensagem Isostática a Frio. Ciências Aplicadas, Volume 13, 2023. (https://doi.org/10.3390/app13158909).

[10] K. Balamurugan et al. Estudos de erosão por jato de ar em compósito mg/SiC. Silício, Volume 12, 2020. (https://doi.org/10.1007/s12633-019-00148-y)

[11] D. Penther et al. Efeito de nanopartículas de SiC no processo de fabricação, microestrutura e dureza de nanocompósitos de Mg-SiC produzidos por moagem mecânica e extrusão a quente. Ciência e Engenharia de Materiais, Volume 738, 2018. (https://doi.org/10.1016/j.msea.2018.09.106).

[12] A. Matin et al. Microstructure and mechanical properties of Mg/SiC and AZ80/SiC nano-composites fabricated through stir casting method. Materials Science and Engineering, Volume 625, 2015. (http://dx.doi.org/10.1016/j.msea.2014.11.050).

[13] A. Z. SyahriaL; N. D. Hannan. The effect of variation of nano sic reinforcement particle addition to mechanical properties of Mg/Nano SiC composite by stir casting method. In: IOP Conference Series. Materials Science and Engineering. p. 012021, 2019. (doi:10.1088/1757-899X/547/1/012021).

[14] Y. Wang; T. Monetta. Systematic study of preparation technology, microstructure characteristics and mechanical behaviors for SiC particle-reinforced metal matrix composites. Journal of Materials Research and Technology, Volume 25, 2023. (https://doi.org/10.1016/j.jmrt.2023.07.145)

[15] M. Gandhi et al. Effect of SiC reinforcement on mechanical and machinability characteristics of Mg/SiC/B4C hybrid composite developed through stir casting. Silicon, Volume 15, 2023. (https://doi.org/10.1007/s12633-023-02444-0)

[16] E. Mohsen et al. A new semi-solid casting technique for fabricating SiC-reinforced Mg alloys matrix composites. Composites Part B: Engineering, Volume 94, 2016. (http://dx.doi.org/10.1016/j.compositesb.2016.02.019)

[17] Z. Zeng et al. Ligas de extrusão de magnésio: uma revisão dos desenvolvimentos e perspectivas. Revisões Internacionais de Materiais, Volume 64, 2018. (https://doi.org/10.1080/09506608.2017.1421439).

[18] K. Ponhan; D. Weston; K. Tassenberg. Influence of SiC nanoparticle contents on microstructural evolution and mechanical behavior of AZ91D magnesium matrix composites synthesized through a combination of a master pellet feeding technique and stir casting assisted by ultrasonic vibration. Materials Today Communications, Volume 36, 2023. (https://doi.org/10.1016/j.mtcomm.2023.106785).

5 Beam, plate and shell theories and computational models for laminated composites

Organized and edited by

Sandra Maria da Luz
&
Carla Tatiana Mota Anflor

STABILITY AND STRESS ANALYSIS OF CARBON/EPOXY CYLINDERS UNDER AXIAL COMPRESSION

E.L. Albuquerque[(a)] *, F. Levy Neto [(b)]

(a) 0000-0002-7154-6946 (University of Brasília – Brazil)
(b) 0000-0001-7327-6575 (University of Brasília – Brazil)
* Corresponding author: eder@unb.br

CODE: BCCM7-11

Keywords: composite cylinders, stress analysis, stability

Abstract: This work is mainly concerned with an numerical and experimental study on the stability and stress analysis of 47 carbon/epoxy cylinders, subjected to axial compression. Such composite structures present excellent corrosion resistance in marine environment, as well as low weight combined with high strength and stiffness, and are widely used in submersible as well as aerospace structures. The purpose of this study was to evaluate the failure loads of cylinders with internal diameter (D) of 40 mm, and thickness (t) ranging from 0.2 and 0.6 mm. The experimental results were compared with those obtained using the finite elements programs Nastran and Compshell. The failure of specimens with length (L) varying from 100 to 300 mm, and t=0.6 mm was controlled mainly by material failure. In particular, first ply failure (FPF), according with the failure criteria of Hoffman and Maximum Strain. Whereas for those with L= 450 mm and t= 0.2 mm by bifurcation buckling (BB).

1. INTRODUCTION

Axisymmetric composite shells have been used in marine, chemical, petroleum and aerospace industries. Mainly due to the fact that they present: high stiffness and mechanical strength ratios per weight; and corrosion resistance in marine environment [1]. Some typical applications of such structures are: cylindrical pipes and pressure vessels, subjected to internal ou external pressure. In particular, when these components are subjected to external loads, the shell wall has to withstand compressive stresses. The main objective of this work is to present experimental as well as numerical results of carbon/epoxy cylinders subjected to axial compressive loads.

When a laminated composite cylinder is under the action of an axial compressive load different mechanisms of failure can take place: (i) bifurcation buckling (BB) with the formation of local waves or a reticulated buckling pattern; (ii) axisymmetric collapse (AC) with the formation of a ring in the cross section; (iii) material failure (fracture) in which the failure of the first ply (*first ply failure*, FPF) determines the total failure of the laminate; and (iv) material failure with residual strength after FPF occurs, implicating in the rupture of successive plies of the laminate (last ply failure, LPF), before the component looses its mechanical strength totally [2]. The predominance of one among these four failure mechanisms depends on factors such as: the ratios of diameter over thickness (D/t) and length over diameter (L/D) of the carbon/epoxy cylinder; the orientation of the fibers; as well as the volume fraction and mechanical properties of the laminate constituents.

The main purpose of this study was to investigate, experimentally and numerically, the mechanical behavior, including stiffness, strength and failure modes of carbon/epoxy cylinder fully clamped at both ends, under the action of compressive axial loads.

2. EXPERIMENTAL METHODOLOGY

Forty seven cylinders, with internal diameter D = 40 mm, were manufactured using unidirectional carbon/epoxy prepregs (Hexcel Advanced Composites tapes CMS 91010) with nominal thickness 0.10 mm. Its physical, elastic and strength properties are presented at Table 1.

Table 1. Properties of the unidirectional carbon/epoxy plies.

Physical, Elastic and Strength Properties	
Density, ρ (g/cm^3)	1.57
Longitudinal Elasticity Modulus, E_{11} (GPa)	170
Transverse Elasticity Modulus, E_{22} (GPa)	12.4
Shear Modulus, S_{12} (GPa)	7.0
Major Poisson Ratio, ν_{12}	0.27
Minor Poisson Ratio, ν_{21}	0.02
Tensile Longitudinal Strength, X_{1T} (MPa)	1009
Tensile Transverse Strength, X_{2T} (MPa)	16
Compressive Longitudinal Strength, X_{1C} (MPa)	661
Compressive Transverse Strength, X_{2C} (MPa)	126
In plane Shear Strength, S_{12} (MPa)	40
Longitudinal Maximum Tensile Strain, ε_{1T} %	0.594
Transverse Maximum Tensile Strain, ε_{2T} %	0.129
Longitudinal Maximum Compressive Strain, ε_{1C} %	0.388
Transverse Maximum Compressive Strain, ε_{2T} %	1.020
Maximum Shear Strain, γ_{12}	0.571

The specimens, depending on the length, L, of the cylinders and the stacking sequence of the fibers were organized in four groups: I, II, III and IV, as shown in Table 2. The orientation of the fibers refers to the angle, in degrees, they form relatively to the longitudinal direction (meridian) of the cylinders.

Table 2. Characteristics of the four groups of specimens.

Orientation of the fibres [*]	Identification of specimens	D external Average (mm)	L (mm)	Number of Specimens
[0º]$_6$	I-1	41.24	100	5
[0º]$_6$	I-2	41.27	200	5
[0º]$_6$	I-3	41.28	300	5
[0º/ ± 45º]$_S$	II-1	41.31	100	5
[0º/ ± 45º]$_S$	II-2	41.31	200	5
[0º/ ± 45º]$_S$	II-3	41.28	300	5
[0º/ ± 60º]$_S$	III-1	4131	100	5
[0º/ ± 60º]$_S$	III-2	41.30	200	5
[0º/ ± 60º]$_S$	III-3	41.28	300	5
[± 45º]$_T$	IV	40.41	450	2

(*) the subscript $_S$ means symmetric about the middle surface and $_T$ total number of layers

The cylinders of groups I, II and III had six layers of carbon/epoxy tapes and nominal D/t ratios of ~67, whereas those of group IV only two layers, and D/t = 200. All the specimens were fabricating using a male mould of 6061 aluminium alloy and vacuum bag. The cure of the resin was carried out in two stages. The first stage at the temperature of 80 ℃, for 30 minutes, and the second at 120 ℃ for 90 minutes.

After the fabrication the specimens were clamped inside disks of SAE 4340 endowed with circular grooves, witch were filled with epoxy resin LY553/HY951 (Ciba-Geigy). Each cylinder was instrumented with strain gauges to record the deformations during the destructive compression tests in the Otto Wolpert machine, as showed in Fig. 1.
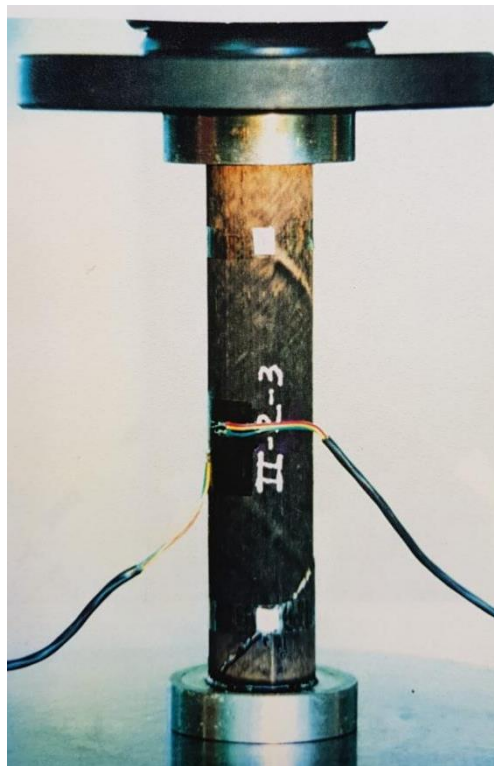
Figure 1. Fracture of fibers, cylinder II-2-2 with staking sequence of fibers **[0º/ ± 45º]$_S$** .

3. THEORETICAL ANALYSIS

The finite element approximations for the displacements of the shell wall are represented by linear variations of the meridional *u* and circumferential *v* displacement components with respect to the meridional distance. The normal displacement *w* is assumed to vary as a cubic function. Each element comprises two end nodal rings, each having four degrees of freedom per node: the three displacement components and rotation β about the circumferential vector.

Strains and changes in curvature of the wall are defined in terms of the assumed displacements using Novozhilov's non-linear strain-displacement relationship [3]. The membrane forces and bending moments of the wall are determined by relating the strain and

curvature functions through elastic constitutive equations. Detailed descriptions of these functions can be found in Bushnell [4] and Mitry [5].

Let σ and ε denote the stress and strain resultants of the shell wall, respectively. The total potential energy of a shell segment is:

$$\Phi = \tfrac{1}{2} \int_A \{\sigma\}^\top \{\varepsilon\} r \ d\theta ds - W \qquad (1)$$

where A is the total area of the shell segment, r, θ, and s are radial, circumferential and meridional coordinates of the shell, respectively, and W is the potential of the (external) applied pressure and axial (compression) loading of the shell. The superscript T denotes transpose of the matrix quantities throughout. The finite element equations are formulated by examining the variation of Φ under pre-buckling and post-buckling conditions at the point of bifurcation from the initial loading path. Under pre-buckling conditions, the deformation of the shell segment is axisymmetric (with circumferential wave number n=0, and the equilibrium equations are expressed through the variation of Φ.

$$\delta\Phi = 0 \qquad (2)$$

where the Q are generalised nodal forces and the q_0 are generalised nodal displacements. $[S_0]$ is a square stiffness matrix. The strain-displacement functions employed in the derivation of the stiffness matrix involve second-order terms of large displacements, and as a result $[S_0]$ is not a constant matrix. Hence, it is necessary to use Newton-Raphson iterations or similar techniques to solve the non-linear algebraic equations.

$$\{Q\}=[S_0]\{q_0\} \qquad (3)$$

On the other hand, the buckling conditions of the shell can be established by considering the variation of the second-order total potential (Φ_2) in terms of the virtual post-buckling displacements δq.

$$\delta\Phi_2 = 0 \qquad (4)$$

The post-buckling path at the bifurcation point may follow a nonaxisymmetric deformation route with displacement components corresponding to a general circumferential wave number n. It follows that:

$$[S_n]\{\delta q\} = \{0\} \qquad (5)$$

where $[S_n]$ is the stability matrix of the shell and it depends on the pre-buckling stresses and wave number n. At the bifurcation point, the stability matrix is singular. The buckling load is found by a step-by-step search of the singular stability matrix starting from a zero load for a range of circumferential wave numbers. The critical buckling load is the lowest load in the range of n selected. The shell may experience material failure before reaching buckling conditions. To detect the initial occurrence of failure, known as first-ply failure (FPF), a check

is conducted at each load step. A computer program, developed based on the aforementioned theory, utilizes seven different criteria to predict FPF. These criteria include:

(a) Maximum stress

(b) Maximum strain

(c) Tsai-Hill

(d) Hoffman

(e) Tsai-Wu Stress

(f) Tsai-Wu Strain

(g) Owen

The program is written in FORTRAN77. Tests have been performed to evaluate the convergence of the numerical results. In this article only Maximum Strain and Hoffman criteria were used.

4. RESULTS AND DISCUSSION

In the forty seven destructive tests under compression load carried out in the Otto Wolpert universal machine, the experimental failure stresses were obtained dividing the maximum load by the cross section areas of the cylinders, $\pi.(D^2_{ext} - D^2_{int})/4$. So far four modes of failure were observed:
(i) Rupture of the fibers controlled by first ply failure (FPF) with significant emission of noise at the moment of the failure. This mode of failure occurred for the specimens type II, with symmetric stacking sequence of fibers at **0º/ ± 45º**, presenting fracture at 45º, as showed in Fig. 1, as well as type III, with symmetric fibers at **0º/ ± 60º**, and rupture at the cross section of the cylinders (i.e. transverse plane at 90º, relatively to the longitudinal direction), as presented at Fig. 2. Although the length of the specimens varied from 100 mm to 300 mm for both types of cylinders, the theoretical FPF stresses did not vary, and the experimental failure stresses varied only slightly, as presented in Table 3.
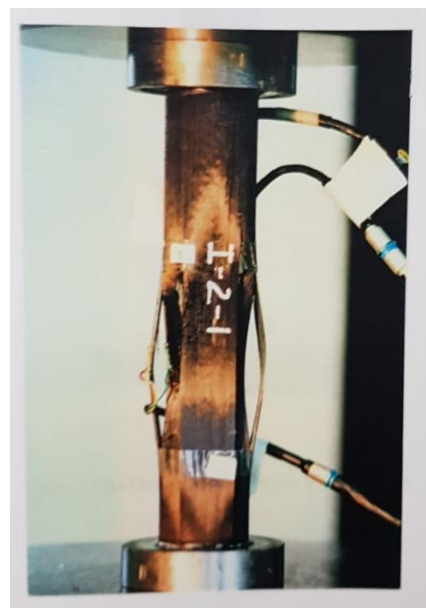
Figure 2. Fracture of fibers, cylinder III-2-3 with staking sequence of fibers **[0º/ ± 60º]s** .

Figure 3. Local buckling and matrix longitudinal split, cylinder I-2-1with [0º]₆.

Table 3. Numerical (FPF and buckling) and experimental results

Identification and Orientation of the fibres [*]	FPF Failure Stress (MPa)		Buckling Stress (MPa)	Experimental Failure Stress (MPa)
	Hoffman	Max. Deformation		
I-1 **[0º]₆**	580	585	568	217
I-2 **[0º]₆**	580	523	558	231
I-1 **[0º]₆**	578	504	556	206
II-1 **[0º/ ± 45º]s**	144	131	963	227
II-2 **[0º/ ± 45º]s**	144	131	757	214
II-3 **[0º/ ± 45º]s**	144	131	599	210
III-1 **[0º/ ± 60º]s**	240	205	970	245
III-2 **[0º/ ± 60º]s**	240	206	812	232
III-3 **[0º/ ± 60º]s**	240	206	676	198
IV **[± 45º]т**	149	140	162	40

(ii) Local buckling combined with fracture of the epoxy matrix in the transverse direction of the cylinders. This failure mode, shown in Fig. 3 and presented in Table 4, took place only for the specimens type I, with all the fibers at 0° (i.e. longitudinal). For all the cylinders of this group, with lengths form 100 mm to 300 mm, the experimental and numerical results (FPF and buckling) varied only slightly. The experimental results were much lower than the numerical predictions. This failure mode was characterized by a significant increase in the radius of the cylinders close to their middle sections and the split of the epoxy matrix along the longitudinal direction. Apparently the fibers did not break. The fracture was observed only in the epoxy matrix, according to Fig. 3.

(iii) Elastic bifurcation buckling. This mode of failure, shown in Fig. 4 and presented in Table 3, took place only with cylinders type IV. And, as soon as the load was released the specimens returned to their original geometry. These cylinders were reinforced with only two layers of carbon/epoxy, at ± **45º**.

Figure 4. Bifurcation buckling, cylinder IV-4-2 with staking sequence of fibers **[± 45º]$_T$** .

5. CONCLUSIONS

For the cylinders in which the failure was controlled either by local buckling (type I) or bifurcation bucking (type IV) the experimental loads were well below the numerical predictions. By a factor greater than two for cylinders type I, reinforced with six layers, and close to four for cylinders type IV, reinforced with only two layers.

The failure of cylinders type IV was a typical elastic buckling since the specimens returned to their initial geometry after the load was released.

The failure of the specimens types II and III were controlled by FPF. For the cylinders of type II (symmetric fibers at **0º/ ± 45º**) the material failure predicted using the criteria of Hoffman and Maximum Strain were more conservative the experimental results. For those of type III (symmetric fibers at **0º/ ± 45º**) the experimental failure were close to the predictions using the criteria of Hoffman and maximum Strain.

For specimens type II and III, the variation in length of cylinders, from 100mm to 300 mm, keeping the same radius, R, and thickness, t, did not affect the FPF predictions

5.1. Declaration of Competing Interest

The authors declare no conflict of interest.

5.2. Acknowledgements

6. REFERENCES

[1] F. Levy Neto and L.C. Pardini, *Compósitos Estruturais - Ciência e Tecnologia*. 2a Edição, 2016, Editora Edgard Blucher, São Paulo.

[2] A. Gonçalves, *Análise Experimental da estabilidade e resistência de cilindros de carbono/epóxi submetidos a cargas compressivas uniaxiais*. Dissertação de Mestrado, ITA, 1997.

[3] Novozhilov, V. V., Foundation of the Non-linear Theory of Elasticity. Graylock Press, Rochester, New York, 1953.

[4] Bushnell, D., Computerized analysis of shells - governing equations. Computers & Structures, 18 (3) (1984) 471-536.

[5] J. Mistry. Theoretical investigation into the effect of the winding angle of the fibres on the strength of filament wound GRP pipes subjected to combined external pressure and axial compression. Composite Structures 20 (1992) 83-90.

DAMAGE DETECTION IN FIBER-LAMINATED COMPOSITE MATERIAL CONSIDERING NUMERICAL ANALYSIS VIA GENETIC ALGORITHM

Sabrina M. J. Moreira [a] *, Maurício M. Nilton [b], *

(a) ⓘ xxxx-xxxx-xxxx-xxxx (Federal University of São João del-Rei – Brazil)
(b) ⓘ xxxx-xxxx-xxxx-xxxx (Federal University of São João del-Rei – Brazil)
* Corresponding author: sabrinamoura744@gmail.com

CODE: BCCM7-17

Abstract: In this study, a computational numerical analysis of an approach for damage detection applied to a composite material plate was conducted. To achieve this, the composite plate was modeled using the finite element method, employing a specific type of plate element in conjunction with the First Order Shear Deformation Theory (FSDT), aiming to obtain information about the mechanical response of the plate. Damage modeling was performed by reducing the stiffness in the numerical model representing the mechanical behavior of the fiber-reinforced laminated composite material. The characteristics of the material response studied were the displacements of the nodes, enabling the development of a damage detection methodology using a genetic algorithm, which proved effective in the detection process.

1. INTRODUCTION

Technological advances are driving the use of composite materials in various industries. Consequently, the search for techniques and methods for modelling composites has become increasingly important, as it allows for predicting their behaviour without the need to conduct tests on prototypes, which would be financially unfeasible (SOUZA et al., 2017).

One numerical method that has received a lot of attention is the finite element method (FEM). Its central approach involves dividing a continuous system into smaller parts, on discretizing it into what are called finite elements, which are connected by points called nodal points. Each element has a mathematical representation, consisting of a set of functions known as shape functions. This technique allows for detailed analysis of complex structures, making it easier to comprehend their mechanical behaviour.

Where analytical theories are unable to deal with the complexity of a system, the finite element method can predict the behaviour of a variety of systems, even when the equations become very complex, or the boundary conditions are difficult to define. Additionally, there are several software programs based on FEM, such as Ansys®, Nastran®, Abacus®, among others. Another application would be the mathematical combination with FEM in a programming environment such as Matlab® to accurately predict the behaviour of systems.

Since composite materials are expensive and difficult to obtain for experimental tests, a viable strategy is to model their behaviour using FEM.

It is widely recognised that the use of composite materials has been increasing, as Callister Jr. (2016) suggests, due to the need for materials with properties distinct from those of conventional ones such as metals, ceramics, and polymers. This trend is largely driven by the specific requirements of high-tech industries.

There are several theories that describe the mechanical behavior of composite structures. Two of them stand out: the first-order shear deformation theory - FSDT and the higher-order shear deformation theory - HSDT. In FSDT, it is assumed that the transverse shear strain changes linearly through the thickness of the material, making it very useful for evaluating global mechanical characteristics such as buckling loads, natural frequencies, and deflections. HSDT, on the other hand, takes a more elaborate approach, considering both

transverse and normal shear strains, as well as stress distributions through the thickness. These theories are essential for accurately predicting the static and dynamic behaviour of composite structures (REDDY, 1997).

Although visual inspection is a simple way to identify damage to materials, it does not always provide a complete structural assessment and usually only gives qualitative results. For this reason, modern techniques such as X-rays, ultrasound, laser beams and eddy currents have been increasingly used to achieve a more comprehensive assessment of structural integrity. However, these techniques may have limitations in their application due to the access conditions in many structures (GADÉA,2005).

As pointed out by Lopes (2007), genetic algorithms (GA's) are a category of global optimization techniques, which means that they are more likely to find the best global solution for a given system. According to experts, GA's can be successfully applied to the problem of damage detection.

In this type of problem, which can be seen as a form of system identification or an inverse problem, various techniques can be employed to determine the unknown damage parameters. These include methods such as neural networks and Kalman filters. Optimization techniques, such as GA's, aim to minimize or maximize a specific function, seeking to find the best solution within a set of possible alternatives (LOPES,2010).

Damage to a structure, such as a hole or a crack, is caused by externa factors that alter the structure's stiffness, impacting its behaviour and functioning compared to the expected operating state. This understanding is crucial for the accurate detection and analysis of structural damage (DIACENCO, 2016)

In this context, this study focuses on the detection of damage in composite material laminates with fibers, allowing for numerical analysis using the Matlab® programming environment and employing genetic algorithms.

1.1. Objective

The main objective of this project is to develop and apply a methodology based numerical analysis using a genetic algorithm for the accurate and efficient detection of damage in composite materials laminated with fibers.

2. METHODOLOGY

2.1. Finite Element Modelling of Fiber Reinforced Composite Board

The finite element method is a common approach to modelling damage in composite materials. To apply it, it is crucial to establish the initial state of the structure before any damage occurs. This model requires consideration of parameters that experience significant changes when damage is present.

To increase the probability of detecting damage, the process involves three distinct steps. Initially, an analysis is conducted without considering the presence of damage, focusing on elastic studies based on displacements and deformations, as well as dynamic analyses using natural frequencies and modal damping factors. In the second stage, the focus shifts to identifying irregularities in the structure, which indicate the presence of damage. Finally, in the third step, the objective is to maximize the probability of effectively detecting the identified damages.

This project uses the Finite Element Method (FEM) to describe the mechanical behaviour of a composite structure laminated with fibers. This approach allows for the determination of key parameters in the structure's initial state, using values derived from the mass matrix, stiffness, and displacements. The modelling of damage in the composite plate based on changes in its structural rigidity, as rigidity is a fundamental characteristic of materials, and any reduction in it is interpreted as damage. Therefore, in this project, the damage is represented by a decrease in stiffness.

2.2. FSDR Theory associated with Finite Elements

The FSDT displacement fields, according to Reddy (1997), are represented by the following set of equations,

$$u(x, y, z, t) = u_0 (x, y, t) + z\psi_x(x, y, t), \tag{1}$$
$$v(x, y, z, t) = v_0 (x, y, t) + z\psi_y(x, y, t), \tag{2}$$
$$w(x, y, z, t) = w_0 (x, y, t), \tag{3}$$

where ψ_x and ψ_y represents the rotations of the segments normal to the reference surface around the x and y axes respectively in addition to that u_0, v_0 and w_0 represents a spatial and temporal distribution.

The above equations can be rewritten matriliny as shown below.

$$U(x, y, z, t) = [u(x, y, z, t)v(x, y, z, t)w(x, y, z, t)]^T, \tag{4}$$

$$A(z) = \begin{bmatrix} 1 & 0 & 0 & z & 0 \\ 0 & 1 & 0 & 0 & z \\ 0 & 0 & 1 & 0 & 0 \end{bmatrix} \tag{5}$$

$$U(x, y, z, t) = [u_0(x, y, z, t)v_0(x, y, z, t)w_0(x, y, z, t)\psi_x(x, y, z, t)\psi_y(x, y, z, t)]^T, \tag{6}$$

Mechanical deformations are established through different forms than mechanical displacements, as shown in the equation below.

$$\varepsilon_{xx} = \frac{\partial u}{\partial x}, \varepsilon_{yy} = \frac{\partial v}{\partial y}, \varepsilon_{zz} = \frac{\partial w}{\partial z}, \gamma_{xy} = \frac{\partial u}{\partial y} + \frac{\partial v}{\partial x}, \gamma_{xz} = \frac{\partial u}{\partial z} + \frac{\partial w}{\partial y}, \gamma_{yz} = \frac{\partial v}{\partial z} + \frac{\partial w}{\partial y}, \tag{7}$$

With the displacement-deformation relationship, represented in equation 7, it is possible to obtain the operator matrix, substituting expressions 1 in 4, resulting in the deformations represented by equations 4 and 5, it is possible to compose the mass and stiffness matrices of the finite element model.

$$\varepsilon_b(x, y, z, t) = [D_{b0} + zD_b]u(x, y, t) = D_b(z)u(x, y, t), \tag{8}$$

$$\varepsilon_s(x, y, z, t) = [D_{s0}]u(x, y, t) = D_su(x, y, t), \tag{9}$$

Through equations 1 and 3 it is possible to determine the displacement matrices by the degrees of freedom exposed by the theory, represented by equation 6. Corresponding to the overall behaviour of a fiber reinforced laminated composite board.

$$D_b = \begin{bmatrix} \frac{\partial}{\partial x} & 0 & 0 & z\left(\frac{\partial}{\partial x}\right) & 0 \\ 0 & \frac{\partial}{\partial y} & 0 & 0 & z\left(\frac{\partial}{\partial y}\right) \\ \left(\frac{\partial}{\partial x}\right) & \left(\frac{\partial}{\partial y}\right) & 0 & z\left(\frac{\partial}{\partial y}\right) & z\left(\frac{\partial}{\partial y}\right) \end{bmatrix} \tag{10}$$

$$D_b = \begin{bmatrix} 0 & 0 & \frac{\partial}{\partial x} & 1 & 0 \\ 0 & 0 & \frac{\partial}{\partial y} & 0 & 1 \end{bmatrix} \tag{11}$$

2.3. Serendipity Element

Serendipity elements have a rectangular geometry and consist of eight nodal points, also known as nodes. This type of finite element is used in the project because it is widely referenced in the literature, allowing for the comparison of results obtained through the developed method.
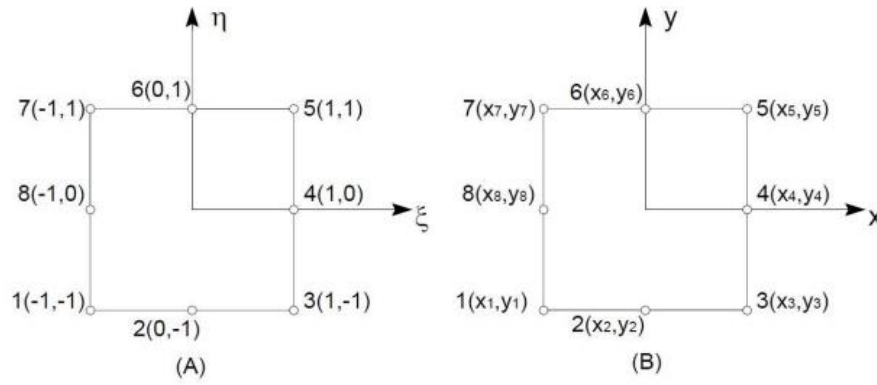
Figure 1. – Representation of the serendipity element used in the formulation by finite elements (a) local coordinates; (b) global coordinates. Available at Faria [2006, p.67].

The equations below are given by the relationship between global and local coordinates.

$$\xi = \frac{(2x - x_8 - x_4)}{x_8 - x_4}, \tag{12}$$

$$X = \frac{1}{2}[\xi(x_8 - x_4) + x_8 + x_4, \tag{13}$$

$$\eta = \frac{(2y - y_6 - y_2)}{y_6 - y_2}, \tag{14}$$

$$Y = \frac{1}{2}[\eta(y_6 - y_2) + y_6 + y_2, \tag{15}$$

The square matrix of the equation 16 is the Jacobian matrix that relates the derivative of the shape functions is equation 12,13,14 and 15 with respect to global coordinates with the derivative of the shape functions with respect to local coordinates and is expressed according to Roddy (1997) in the form:

$$[J] = \begin{bmatrix} \dfrac{\partial x}{\partial \xi} & \dfrac{\partial y}{\partial \xi} \\ \dfrac{\partial x}{\partial \eta} & \dfrac{\partial y}{\partial \eta} \end{bmatrix} = \frac{1}{2}\begin{bmatrix} (x_8 - x_4) & 0 \\ 0 & (y_6 - y_2) \end{bmatrix} \tag{16}$$

The determinant of the Jacobian matrix is the Jacobian, seen below.

$$J = \frac{\partial x}{\partial \xi}\frac{\partial y}{\partial \eta} - \frac{\partial x}{\partial \eta}\frac{\partial y}{\partial \xi} = \frac{(y_6 - y_2)(x_8 - x_4)}{4} \tag{17}$$

Serendipity element used for finite element modelling has shape functions that relate the displacements at any point with the displacements at nodal points. The shape functions are:

$$N_1(\xi, \eta) = -\frac{1}{4}(1 - \xi)(1 - \eta)(1 + \xi + \eta), \tag{18}$$

$$N_2(\xi, \eta) = \frac{1}{2}(1 - \xi)(1 + \xi)(1 - \eta), \tag{19}$$

$$N_3(\xi, \eta) = -\frac{1}{4}(1 + \xi)(1 - \eta)(1 - \xi + \eta), \tag{20}$$

$$N_4(\xi, \eta) = \frac{1}{2}(1 + \xi)(1 + \eta)(1 - \eta), \tag{21}$$

$$N_5(\xi,\eta) = -\frac{1}{4}(1+\xi)(1+\eta)(1-\xi-\eta), \tag{22}$$

$$N_6(\xi,\eta) = \frac{1}{2}(1-\xi)(1+\xi)(1-\eta)(1+\eta). \tag{23}$$

$$N_7(\xi,\eta) = \frac{1}{4}(1-\xi)(1+\eta)(1+\xi-\eta), \tag{24}$$

$$N_8(\xi,\eta) = \frac{1}{2}(1-\xi)(1+\eta)(1-\eta), \tag{25}$$

Having these equations, discretize the operator matrices according to what was represented in equations 18 to 23 and uses the form of the Serendipity elements obtaining:

$$U(x,y,z,t) = A(z)N(\xi,\eta)u(t) \tag{26}$$

$$\varepsilon_b(x,y,z,t) = D_b(z)N(\xi,\eta)u(t) = B_b(\xi,\eta)u(t) \tag{27}$$

$$\varepsilon_s(x,y,z,t) = D_s(z)N(\xi,\eta)u(t) = B_s(\xi,\eta)u(t) \tag{28}$$

It $N(\xi,\eta)$ represents the matrix of shape functions of dimension 5x40 and is shown below:

$$\begin{bmatrix} \begin{bmatrix} N_1 & 0 & 0 & 0 & \cdots & N_2 & 0 & 0 & N_8 & 0 \\ & \vdots & & & \ddots & & & \vdots & & \\ 0 & & 0 & & \cdots & 0 & & & 0 & N_8 \end{bmatrix} \end{bmatrix} \tag{29}$$

2.4. Obtaining mass and stiffness matrices

According to finite element theory for a plate element, the elementary mass and stiffness matrices can be determined according to the equation below:

$$M^{(e)} = \sum_{k=1}^{n} \int_{z=Z_R}^{z_{k+1}} \int_{\xi=-1}^{\xi=+1} \int_{\eta=-1}^{\eta=+1} \rho_k N^t(\xi,\eta)A^T(z)A(z)N(\xi,\eta)\det(J)\,d\eta d\xi dz \tag{30}$$

Where ρ is the density, $N\,T\,(\xi,\eta)$ é is the transposed matrix of the shape functions of the Serendipity element, $A\,T$ is the transposed matrix of the A matrix, and J is the Jacobian.

According to Reddy (1997), it is necessary to change the coordinate system of the matrix of elastic coefficients from local to global, through a rotation of an angle around the z axis. The elementary matrices are calculated for each element of the finite element mesh and the global equations of motion are developed considering the connectivity of the nodal points, employing standard finite element assembly mechanisms (DIACENO, 2010).

The global equation of motion in the time domain can be represented by the equation:

$$M\ddot{q}(t) + Kq(t) = f(t) \tag{31}$$

This equation can be placed in the frequency domain, being represented by:

$$[K(\omega) - \omega 2M]Q(\omega) = F(\omega) \tag{32}$$

3. RESULTS AND DISCUSSION

3.1. Damage Modelling

The formulation of the damage detection problem occurs after collecting the modal information from the composite plate, for which the developed finite element methodology aims to provide data.

Damage was modelled considering a reduction in the stiffness of the plate, which can be applied to one or more finite elements. The reduction in stiffness leads to a change in natural frequencies, and this s information can be used to formulate the damage detection problem. The solution to the problem can then bedwith the help of Genetic Algorithms (GAs).

The unknown damage parameters were developed by modelling the direct problem, generating the mass and stiffness matrices to solve the eigenvector and eigenvalue problem. This reduction was simulated by multiplying the stiffness value of the undamaged system by a factor, as illustrated in the following equation,

$$K_d^e = (1 - \alpha)K_{nd}^e , \tag{33}$$

where K_d^e represents the elementary stiffness of the damaged element, K_{nd}^e represents the elementary stiffness of the undamaged element, and α represents the stiffness reduction factor, $(0 \leq \alpha \leq 1)$.

Damage detection requires consideration of neighbouring elements to the one selected for stiffness reduction, as these elements are also affected. Consequently, there is an impact around the node chosen for modelling the damage, which helps define the affected region, as illustrated in Figure 2. This process is further explained by Diacenco (2016).
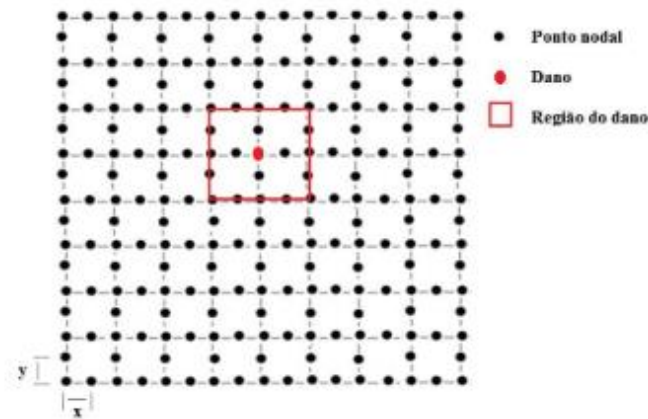
Figure 2. – Representation of damage modelling. Available at Diacenco [2006, p.53].

Figure 2 represents the discretization of the plate using finite elements, where it has eight nodal points, a given Serendipity element, the distance between the nodal points is in the same x and y direction. The stiffness reduction created at the nodal point also affects the region around it, so it must be considered that this region corresponds to the damage, where the implemented algorithm aims to find this region.

According to Diacenco (2016), the reduction of this region makes it possible to increase the probability of success, but it can also increase the probability of failure, that is, it may be possible to identify an element that is not damaged or even not be able to identify one. element that is damaged.

After the rigidity reduction, the problem was once again resolved to manage a new set of frequencies that will be used to formulate the AG's. Nodal displacements were used to compose the population of genetic algorithms.

3.2. Numerical Application Using Genetic Algorithm

3.2.1.Problem Formulation

The analysis of the damage detection methodology was conducted using a composite plate, represented by Figure 3, comprising a unidirectional layer with a thickness of 0.004 m and dimensions Lx =0.20 m and Ly =0.20 m, illustrated by Figure 3(a). Additionally, the finite element discretization is represented by Figure 3(b) where the plate contains 64 elements, the fiber orientation was set at 45 degrees.

| (a) | (b) |
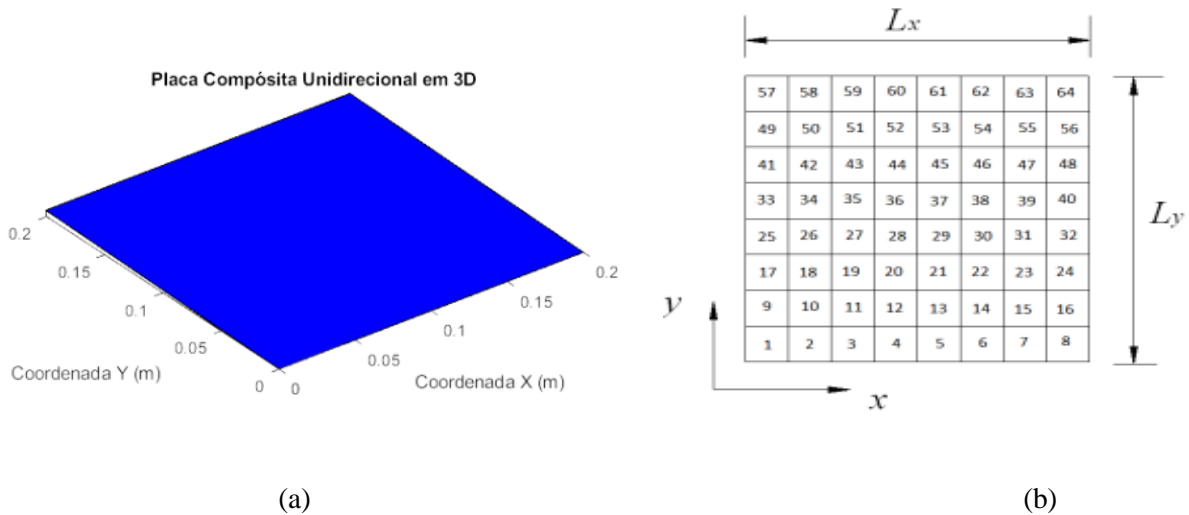
Figure 3. – (a) Composite plate; (b) Plate discretization.

The values of the material properties of this composite layer are referenced in table 1 and are provided by Diacenco (2016).

Properties of Materials	Values
$E_1 (GPa)$	172,4
$E_2 = E_3 \ (GPa)$	6,89
$G_{12} = G_{13} (GPa)$	3,45
$G_{23} (GPa)$	1,38
$\nu_{12} = \nu_{13}$	0,25
ν_{23}	0,30
$\rho(\frac{kg}{m^3})$	1566

Table 1 – Properties of the fiber-reinforced composite plate.

3.3. Reduced Stiffness by 30%

The local stiffness matrix was reduced in regions of the plate comprising twenty nodal points: 1,8,13,15,19,24,26,28,30,32,33,34,38,39,40, 41 ,45,47,55,59 according to Figure 4, which illustrates the mesh with the nodal points considered.

Through a genetic algorithm, the mentioned numbers, representing specific nodal points in a composite plate, were used to reduce stiffness in strategic regions of the material. Each affected nodal point was encoded as a gene in a binary representation, where "1" indicates stiffness reduction and "0" indicates its preservation. Starting from an initial population of random solutions, each configuration was evaluated for its effectiveness in stiffness reduction, considering the material properties. Selection, crossover, and mutation were iteratively applied to produce new generations of solutions, aiming to optimize stiffness reduction. At the end of the process, the most suitable solution was selected, indicating the regions where stiffness was reduced as desired.
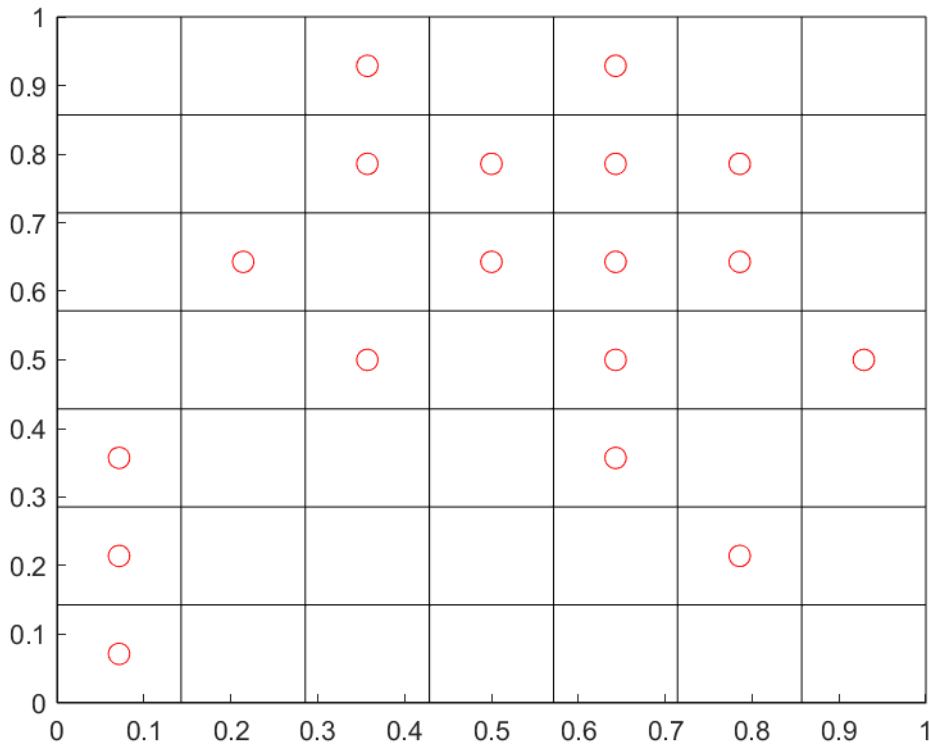
Figure 4. – Mesh with nodal points selected to reduce stiffness.

With the wonder of genetic algorithms, the best configuration was chosen:
- Population size: 100 individuals.
- Crossover probability: 0.98.
- Crossover function: 1.1.
- Stopping criteria: 200 generations.

According to the discretization of the element model in Figure 4, the x and y position of each chosen nodal point is represented in Table 2.

Nodal Point	Node x- coordinate [m]	Node y- coordinate [m]
1	0	0
8	1	0
13	0,571429	0,142857
15	0,857143	0,142857
19	0,285714	0,285714
24	1	0,285714
26	0,142857	0,428571
28	0,428571	0,428571
30	0,714286	0,428571
32	1	0,428571
33	0	0,571429
34	0,142857	0,571429
38	0,714286	0,571429
39	0,857143	0,571429

40	1	0,571429
41	0	0,714286
45	0,571429	0,714286
47	0,857143	0,714286
55	0,857143	0,857143
59	0,285714	1

Table 2 – x and y coordinates of the nodal points selected for analysis.

Table 3 shows the position of node 34 and node 45, chosen as the damage with the bias of later being compared with the coordinates found by the genetic algorithm.

Nodal Point	Node x- coordinate [m]	Node y- coordinate [m]
34	0,142857	0,571429
45	0,571429	0,714286

Table 3 – x and y coordinates of the nodal point chosen as damage.

In view of the problem, it was modelled as mono-objective, where the functional given in the equation below is minimized,

$$J = \frac{1}{2} \sum_{t=1}^{n} (d_{i(medido)} - d_{i(calculado)})^2 \; , \tag{34}$$

3.4. Numerical Simulation Using GA's

Since, the decrease in stiffness at a given nodal point of the plate affects the region around this nodal point and this region was determined as the region with the presence of damage. Of the twenty nodal points where stiffness reduction was performed, the following nodal points were chosen to compose the population 13,15,19,24,26,28,30,34,38,39,45,47,55,59 totalling fourteen nodal points, finding a 96% probability of success for the damage to be in position 34, as shown in the figure below.
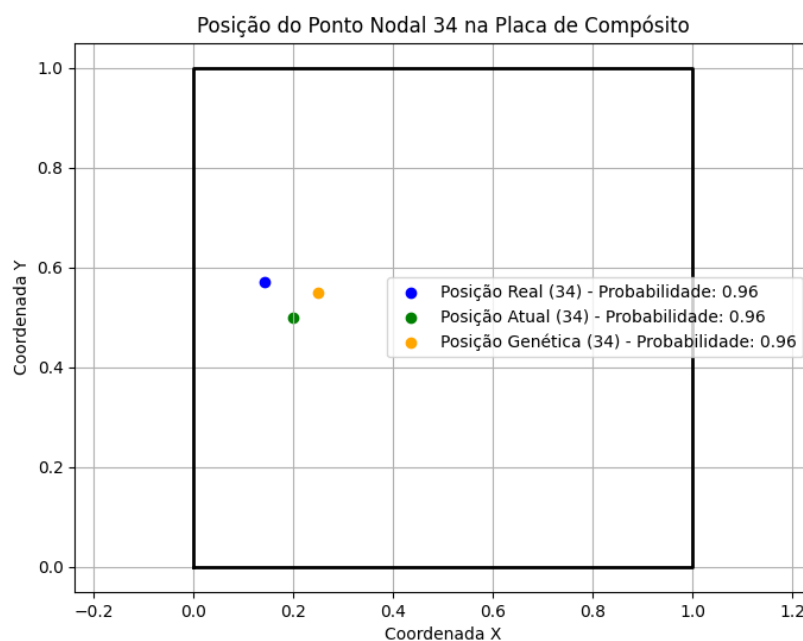
Figure 5. – 96% probability of success for damage at position 34.

Figure 6 shows the probability of success found was 51% considering the damage in position 34 and the population was composed of nineteen nodal points, leaving point 34 out as it is considered the damage.
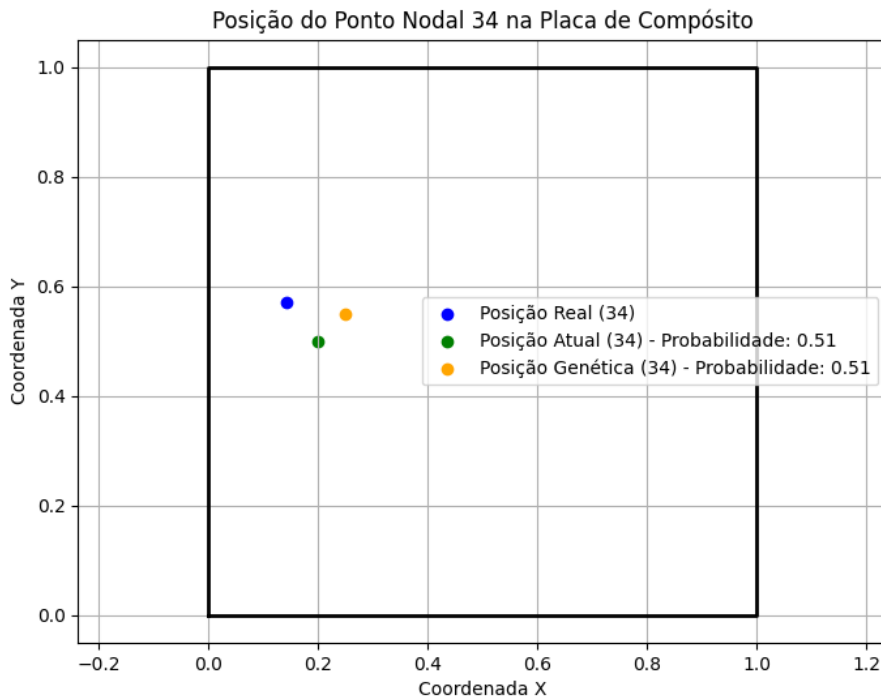
Figure 6. – 51% probability of success for damage at position 34.

Considering the damage now at position 45 and with the population of seventeen nodal points, there was the possibility of finding a 96% probability of success and this is represented by Figure 7.
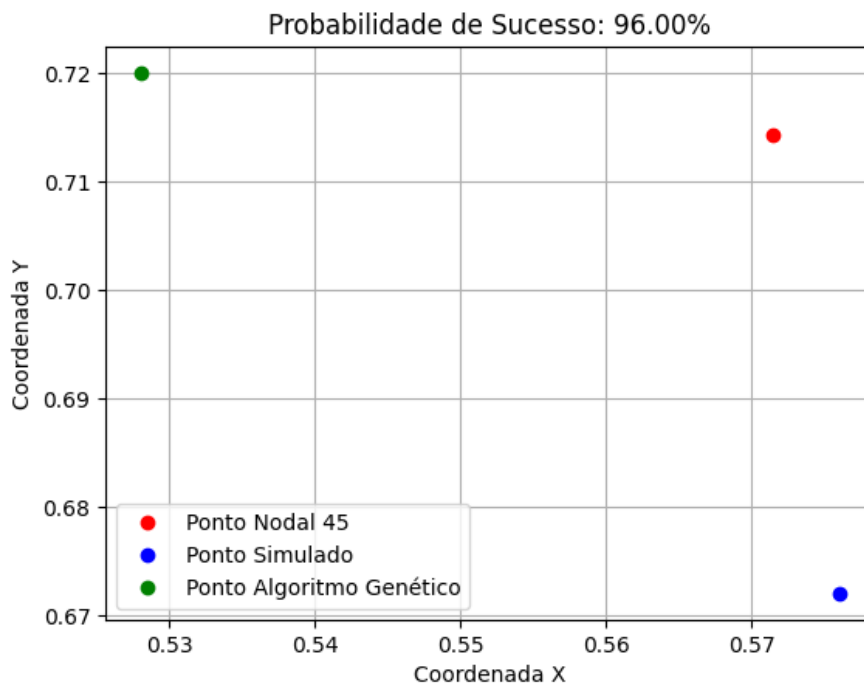
Figure 7. – 96% probability of success for damage at position 45.

Considering this same position for the damage, now with a probability of success of 21%, as shown in Figure 8.
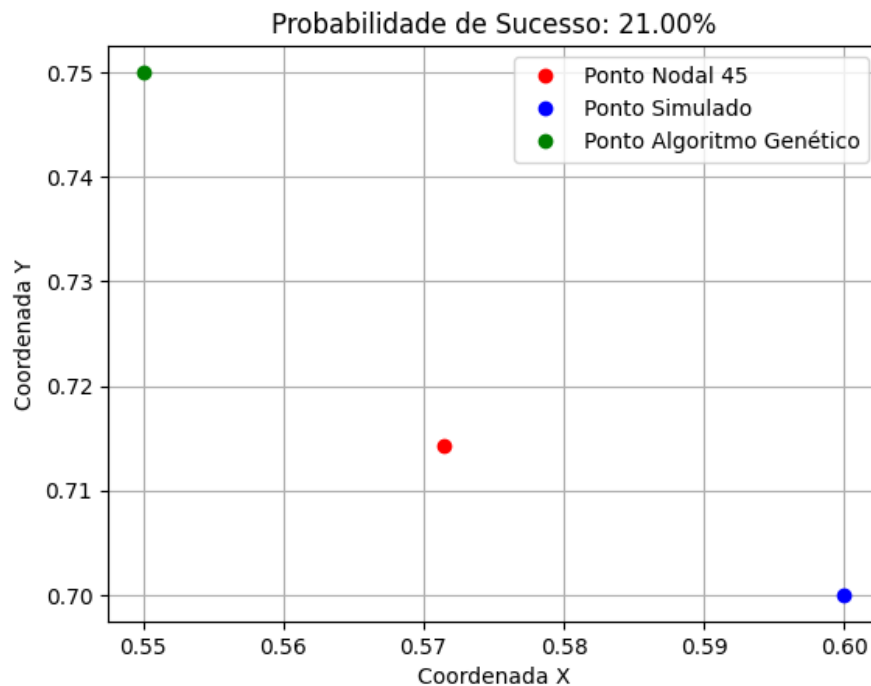
Figure 8. – 21% probability of success for damage at position 45.

4. CONCLUSIONS

4.1. Declaration of Competing Interest

A computational technical study and analysis was conducted using Genetic Algorithms in conjunction with a numerical model based on finite elements, employing the First Order Shear Deformation Theory (FSDT). This model made it possible to investigate the dynamic behaviour of a structure and obtain its responses, including vertical displacements, natural frequencies, and vibration modes, from an initial undamaged state. Then, it was possible to approach the inverse problem, using Genetic Algorithms to locate damage to the structure. The studied, analysed, and simulated damage detection model demonstrated promising results in predicting the probability of success and failure in identifying and locating damage using Genetic Algorithms. However, a significant limitation encountered was the selection of nodal positions to apply stiffness reduction, since this choice directly impacts the identification and, especially, the precise location of the damage.

5. REFERENCES

CALLISTER JUNIOR, DG, RETHWISCH, WD, Materials Science and Engineering: An Introduction 9th ed. São Paulo, LTC, 2016

DIACENCO, AA Finite Element Modeling of Composite Materials Structural Incorporating Viscoelastic Material for Passive Control of Vibration and Noise. Master's Thesis, Federal University of Itajubá, 2010.

DIACENCO, AA Optimization Modeling Applied to Sensor Topology for Identification and Location of Damage in Composite Plate. Thesis PhD, Federal University of Itajubá, 2016.

FARIA, AW Finite Element Modeling of Equipped Composite Plates of Piezoelectric Sensors and Actuators: Computational Implementation and Numerical Assessment. Dissertation (Master's) – Faculty of Engineering Mechanics, Federal University of Uberlândia, Uberlândia, 2006.

FRANCE, A. de A. Detection and Localization of Damage in Composite Materials Applied in Aircraft Using Artificial Neural Networks. 2014. 109 f.

Dissertation (master's degree) - Universidade Estadual Paulista Júlio de Mesquita Filho, Faculty of Engineering of Ilha Solteira, 2014.

GADÉA, ASM Structural Damage Identification from Minimization of Errors of Frequency Response Functions via Methods of Optimization. Postgraduate Thesis – Federal University of Rio de Janeiro, 2005.

A SEMI-ANALYTICAL MODEL FOR THERMO-MECHANICAL STRESS ANALYSIS IN COMPOSITE LAMINATES

Danilo Moura Prata[(a) *], Maurício Vicente Donadon [(b)]

(a) ⦿ 0009-0005-6474-859X (Aeronautics Institute of Technology – Brazil)
(b) ⦿ 0000-0001-9016-5340 (Aeronautics Institute of Technology – Brazil)
* Corresponding author: mouraprata@ita.br

Abstract: In carbon fiber composite fabrication, internal stresses can emerge from temperature variations during the cure cycle and the laminate may warp upon tool removal, leading to undesired geometric distortions. The present work proposed a model based on the Principle of Minimum Potential Energy (PMPE), assuming the hierarchical polynomial Bardell functions for strain-displacement relations in the Rayleigh-Ritz approximation method. The mentioned approach guarantees compatibility between the set of equilibrium equations and laminate geometric boundary conditions. The simulated analysis was carried out for different loading and layup configurations, where the model has been validated with classical examples available in the open literature including cantilever plate-like beam under concentrated and distributed loads, and a biclamped plate-like beam with a midspan concentrated load. Additional simulations were also performed on a free plate under thermal loading only, demonstrating good agreement in terms of warping results compared to results obtained using the Classical Lamination Theory (CLT) for non-symmetric laminates. For more extensive investigation, additional analyses were taken for a hybrid laminate made of Carbon-Fiber-Reinforced Polymers (CFRP) and aluminum layer, considering different geometries, layup configurations and boundary conditions, addressing the thermal loading case and effectively providing accurate the thermal effects, such as residual strains, and stresses.

1. INTRODUCTION

In advanced reinforced fibre composite structures, strategic alignment of high-strength fibres, either in preferred orientations or hybrid configurations with other materials like metals, yields materials with anisotropic properties [1]. However, during laminate composite fabrication, internal stresses may arise from temperature variations during the cure cycle, leading to undesired geometric distortions upon tool removal. These challenges are often encountered in industries such as aerospace, wind turbine, and automotive, which demands complex geometries.

These internal stresses inducing distortions in laminates being attributed to many factors such as different cure cycles and thermal expansion coefficients of the composite constituents, including fibres, matrix, and metals in hybrid layup schemes. These factors result in residual stresses and nonhomogeneous distributions of fibres in the matrix, leading to delamination. Although modelling microscale behaviours of composite materials precisely is difficult and computationally costly, variational-based methods offer analytical approaches to simulate thermal loads and compute residual stresses at a macroscale. These methods provide accurate predictions of strains and stresses using material parameters derived from characterization, facilitating the understanding of such phenomena, and improving residual strains prediction at low computation cost.

Various studies have investigated factors influencing shape distortions due to residual stresses, aiming to enhance the design of composite structures. Olumide [2] characterized thickness variation effects on shape distortions and studied carbon and glass hybrid laminates using numerical and experimental methods. Vermes

[3] proposed compensatory tool designs to mitigate warpage in asymmetric laminates, achieving good results to obtain a flat laminate. Sofia [4] used thermoplastic matrix parameters to indirectly experimental predict curvature in a hybrid beam. Cantero [5] proposed semi-analytical model for computing interlaminar stress effects in thick beams, however adding complexity to equations but offering valuable insights.

Building upon these theories, the present work aims to investigate a newly developed semi-analytical model for simulating fundamental geometric parts in structural mechanics, such as plates and beams, under mechanical and thermal loads at different boundary conditions. By utilizing engineering properties and some material parameters, such as coefficients of thermal expansion, this model streamlines the concept design step and prevents material losses during final assembly.

2. METHODOLOGY

The methodology proposed is based on the computation of Thermal Residual Strain-Stresses, and the approach is addressed by the variation-based method of Principle of Minimum Potential Energy (PMPE). The minimization of this total potential energy is taken by the Rayleigh-Ritz Approximation Solution and using the Hierarchical Polynomial Bardell Functions to describe the strain-displacement relationship. The displacement field was assumed smoothly continuous along the thickness, following the two-dimensional formulation displacement-based, as known as Classical Laminate Theory (CLT) [6].

2.1. Thermal Residual Strain-Stresses

Since laminates are cured at different temperatures from those of service, they can always face an increase in residual stresses when processing thermoset resin [7], so the thermal effects must be accounted for [8]. Also, the inherent interaction between laminate and tool part, as well the complex chemical compatibility between layers in hybrid laminates due to the different CTE of materials possess a challenge for design, even in a flat laminate manufacturing, where such thermal stress can be present. Hence the thermal analysis could address more effects to the laminate behavior than we expected being necessary to analyse the problem by inclusion of thermoelastic effects. Thus, the total strains in a single layer of laminate can be computed as a sum of all strains, which came from different natures, like thermal effects [9], as Eq. (1):

$$\{\boldsymbol{\epsilon}\}_k = [\overline{\boldsymbol{S}}]_k \{\boldsymbol{\sigma}\}_k + \Delta T \{\boldsymbol{\alpha}\}_k \tag{1}$$

The stresses involved in each lamina can be taken by inverting Eq. (1), allowing to integrate its contribution through the laminate thickness, resulting in the generalized forces and moments as Eq. (2):

$$(\{\boldsymbol{N}\}, \{\boldsymbol{M}\}) = \sum_{k=1}^{N} \int_{z_{k-1}}^{z_k} (1, z) \{\boldsymbol{\sigma}\}_k dz \tag{2}$$

As each laminae total strains are represented as $\{\boldsymbol{\epsilon}\}_k = \{\boldsymbol{\varepsilon^0}\} + z_k \{\boldsymbol{\kappa}\}$, the generalized forces and moments acting in laminate mid-plane, could be represented by combination of Eq. (1) and Eq. (2), leading to Eq. (3):

$$\begin{Bmatrix} N_x \\ N_y \\ N_{xy} \end{Bmatrix} = \begin{bmatrix} A_{11} & A_{12} & A_{16} \\ A_{12} & A_{22} & A_{26} \\ A_{16} & A_{26} & A_{66} \end{bmatrix} \begin{Bmatrix} \varepsilon_x^0 \\ \varepsilon_y^0 \\ \gamma_{xy}^0 \end{Bmatrix} + \begin{bmatrix} B_{11} & B_{12} & B_{16} \\ B_{12} & B_{22} & B_{26} \\ B_{16} & B_{26} & B_{66} \end{bmatrix} \begin{Bmatrix} \kappa_x \\ \kappa_y \\ \kappa_{xy} \end{Bmatrix} - \begin{Bmatrix} N_x^T \\ N_y^T \\ N_{xy}^T \end{Bmatrix} \tag{3a}$$

$$\begin{Bmatrix} M_x \\ M_y \\ M_{xy} \end{Bmatrix} = \begin{bmatrix} B_{11} & B_{12} & B_{16} \\ B_{12} & B_{22} & B_{26} \\ B_{16} & B_{26} & B_{66} \end{bmatrix} \begin{Bmatrix} \varepsilon_x^0 \\ \varepsilon_y^0 \\ \gamma_{xy}^0 \end{Bmatrix} + \begin{bmatrix} D_{11} & D_{12} & D_{16} \\ D_{12} & D_{22} & D_{26} \\ D_{16} & D_{26} & D_{66} \end{bmatrix} \begin{Bmatrix} \kappa_x \\ \kappa_y \\ \kappa_{xy} \end{Bmatrix} - \begin{Bmatrix} M_x^T \\ M_y^T \\ M_{xy}^T \end{Bmatrix} \tag{3b}$$

where the indices T means thermal effects, computed following the Eq. (4) below:

$$\left(\begin{Bmatrix} N_x^T \\ N_y^T \\ N_{xy}^T \end{Bmatrix}, \begin{Bmatrix} M_x^T \\ M_y^T \\ M_{xy}^T \end{Bmatrix} \right) = \sum_{k=1}^{N} \int_{z_{k-1}}^{z_k} (1, z) [\overline{\boldsymbol{Q}}_b]_k \Delta T \begin{Bmatrix} \alpha_x \\ \alpha_y \\ \alpha_{xy} \end{Bmatrix}_k dz \tag{4}$$

The stiffness laminate matrices ($[A]$, $[B]$ and $[D]$) are well known as the integration of each lamina constitutive relationship clearly demonstrated in open literature as [8] and [9]. Thus, using the sum of mechanical and thermal generalized forces and moments applied on the laminate, it's possible to evaluate the thermoelastic effects over laminate by inverting the Eq. (5) below and find strains and curvatures at midplane of laminate:

$$\begin{Bmatrix} \{\overline{N}\} \\ \{\overline{M}\} \end{Bmatrix} = \begin{Bmatrix} \{N^M\} + \{N^T\} \\ \{M^M\} + \{M^T\} \end{Bmatrix} = \begin{bmatrix} [A] & [B] \\ [B] & [D] \end{bmatrix} \begin{Bmatrix} \{\epsilon^0\} \\ \{\kappa\} \end{Bmatrix} \Rightarrow \{f\} = [C]\{e\} \tag{5}$$

2.2. Principle of Minimum Potential Energy (PMPE)

The Principle of Minimum Potential Energy (PMPE) is a foundational concept in structural mechanics, providing an alternative basis for principles like the Virtual Work theorem. It allows for deriving governing equations of continuum solids to directly determine exact or approximate solutions, intending to describe the system. Applicable across materials with linear or nonlinear constitutive behavior [10], PMPE aids in solving problem to find the stationary values of a functional concerning the problem's variables. This functional is treated as the total potential energy (Π) of a system, comprising internal energy due to deformation (U) and work done by external forces independent of deformation (V_E), this sum is denoted by [11] as Eq. (6) following,

$$\Pi = U + V_E \tag{6}$$

The minimum total potential energy is obtained by the stability of stationary points, if its value is minimum [12], yielding to equilibrium equations in terms of displacements for any elastic system, as given by Eq. (7).

$$\delta\Pi = \delta(U + V_E) = \delta(U - W) = 0 \tag{7}$$

2.3. Rayleigh-Ritz Approximation Solution

Nevertheless, for structurally complex systems, exact solutions to elastic boundary value problems are impractical [13]. However, a powerful technique within variational methods, the Rayleigh-Ritz method, addresses this challenge by providing approximate solutions. This method ensures equilibrium and compatibility by solving static equilibrium equations in terms of scalar quantity energy, representing the total system energy (Π).

In the Rayleigh-Ritz method, displacement-field equations are approximated using polynomial series with non-physical coefficients shown in Eq. (8) below, referred to as generalized coordinates, where these polynomials satisfy essential geometric boundary problem conditions.

$$\langle u_o, v_o, w_o \rangle = \sum_m \sum_n f_m(x) f_n(y) \langle q_{ij}^u, q_{ij}^v, q_{ij}^w \rangle = \langle [N_u]\{q^u\}, [N_v]\{q^v\}, [N_w]\{q^w\} \rangle \tag{8}$$

Alternatively, Eq. (8) can be written in the matrix form as follows,

$$\begin{Bmatrix} u_o \\ v_o \\ w_o \end{Bmatrix} = \begin{bmatrix} [N_u] & [0] & [0] \\ [0] & [N_v] & [0] \\ [0] & [0] & [N_w] \end{bmatrix} \begin{Bmatrix} \{q^u\} \\ \{q^v\} \\ \{q^w\} \end{Bmatrix} \Rightarrow \{d\} = [N]\{q\} \tag{9}$$

So, considering the strains in each lamina given by the linear strain-displacement relationship, the mid-plane laminate strain $\{\epsilon^0\}$ and curvature $\{\kappa\}$ can be represented as the matrixial form in Eq. (10), using these series relations mentioned above:

$$\begin{Bmatrix} \{\boldsymbol{\varepsilon}^0\} \\ \{\boldsymbol{\kappa}\} \end{Bmatrix} = \begin{Bmatrix} \varepsilon_x^0 \\ \varepsilon_y^0 \\ \varepsilon_{xy}^0 \\ \kappa_x \\ \kappa_y \\ \kappa_{xy} \end{Bmatrix} \begin{bmatrix} \begin{bmatrix} [N_{,x}^u(x,y)] & [0] \\ [0] & [N_{,y}^v(x,y)] \\ [N_{,y}^u(x,y)] & [N_{,x}^v(x,y)] \end{bmatrix} & \begin{bmatrix} [0] \\ [0] \\ [0] \end{bmatrix} \\ \begin{bmatrix} [0] & [0] \\ [0] & [0] \\ [0] & [0] \end{bmatrix} & \begin{bmatrix} [N_{,xx}^w(x,y)] \\ [N_{,yy}^w(x,y)] \\ 2[N_{,xy}^w(x,y)] \end{bmatrix} \end{bmatrix} \begin{Bmatrix} \{q^u\} \\ \{q^v\} \\ \{q^w\} \end{Bmatrix} \tag{10}$$

2.4. Hierarchical Polynomial Bardell Functions

The set of functions used in the present work is derived from the Rodrigue's form of Legendre Orthogonal Polynomial's [14], showed in Eq. (10) below:

$$f_r(\xi \ or \ \eta) = \sum_{n=0}^{r/2} \frac{(-1)^n (2r - 2n - 7)!!}{2^n n! \, (r - 2n - 1)!} (\xi \ or \ \eta)^{r-2n-1}, \qquad r > 4. \tag{11}$$

Where the non-dimensional coordinates are given by $\xi = \frac{2x}{a} - 1$ or $\eta = \frac{2y}{b} - 1$ And $r!! = r(r-2)$ and $0!! = (-1)!! = 1$. The flat plate element has now a discretization of one whole element and the interval of each variable $(\xi \ or \ \eta)$ is $[-1,1]$ as showed in Fig. 1 below, usually knowing by natural coordinates.
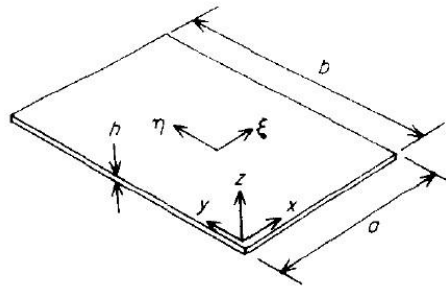
Figure 1. An example of plate element with natural coordinates, available at [15, p. 3].

The ten first Polynomial and its correspondent curve could be verified at Bardell work [14]. The four first Polynomial's ($r \le 4$) follows the same of the Euler-Bernoulli beam element and are concern to edges degrees of freedom, being used to model the cases studied. By the rule of these Euler-Bernoulli beam element polynomial´s, the first and third are related to the edge displacement, attributing either free or clamped constraint, while the second and fourth are related to the rotation of edge. From the fifth all Bardell polynomial has no effect on the boundaries, and its influence just to the displacement degrees of freedom which comprising the interval. Such approach guarantees the geometric boundary compatibility and minimum continuity required, turning easy the computation of polynomial equation series. Thus, using the Bardell functions to represent the displacement field given in Eq. (8), we achieve the set of equations in the three principal directions showed in Eq. (9), resulting in Eq. (11) for strains and curvatures:

$$\begin{Bmatrix} \{\varepsilon^0\} \\ \{\kappa\} \end{Bmatrix} = \begin{bmatrix} \frac{2}{a}[N^u_{,\xi}(\xi, \eta)] & [0] & [0] \\ [0] & \frac{2}{b}[N^v_{,\eta}(\xi, \eta)] & [0] \\ \frac{2}{b}[N^u_{,\eta}(\xi, \eta)] & \frac{2}{a}[N^v_{,\xi}(\xi, \eta)] & [0] \\ [0] & [0] & \frac{4}{a^2}[N^w_{,\xi\xi}(\xi, \eta)] \\ [0] & [0] & \frac{4}{b^2}[N^w_{,\eta\eta}(\xi, \eta)] \\ [0] & [0] & \frac{8}{ab}[N^w_{,\xi\eta}(\xi, \eta)] \end{bmatrix} \begin{Bmatrix} \{q^u\} \\ \{q^v\} \\ \{q^w\} \end{Bmatrix} \Rightarrow \{e\} = [B]\{q\} \tag{12}$$

The combination of Eqs. (5), (7) and (12) leads to the following expression for the variation of the total potential energy ($\delta\Pi = \{\delta q\}^T (\partial\Pi/\partial\{q\}) = 0$) for the plate-like beam under thermo-mechanical loads,

$$\frac{\partial\Pi}{\partial\{q\}} = \int_S [B]^T [C] [B] dS\{q\} - \int_S [B]^T \{f\} \, dS - \int_S [N]^T \{f_S\} \, dS - \int_\Gamma [N]^T \{f_\Gamma\} \, dC - \sum_i [N]^T \{f_i\} \tag{13}$$

The non-trial solution of Eq. (13) results in the following set of linear equations to be solved,

$$[K]\{q\} = \{F_f\} + \{F_S\} + \{F_C\} + \{F_i\} \tag{14}$$

Where $[K]$ is the stiffness matrix of system, and $\{F_f\}$, $\{F_S\}$, $\{F_\Gamma\}$, $\{F_i\}$ refer to the vectors associated with the midplane generalized thermo-mechanical forces, transverse force per unit of area, transverse force per unit of length and transverse concentrated force acting on the laminate, respectively. The solution of Eq. (14) allows the determination of the generalized coordinates $\{q\}$, and consequently leads to calculate the displacements and strains through Eq. (9) and (12), respectively.

The semi-analytical proposed model applied to the plate-like beam under thermo-mechanical forces, as shown in the Eq. (14) above, was developed in computing environment using the commercial platform MATLAB®, and the results are present in the next topic.

3. RESULTS AND DISCUSSION

3.1. Validation of the proposed model

The laminate stacking sequence chosen was $[0°_{(10)}]$, a symmetric laminate which could be considered isotropic material. Each lamina has the same geometry values of length $L = 254$mm , width $W = L/20$ and thickness $t = 0.127$mm , resulting in a plate-like beam geometry, and its properties are listed in Table 1 below.

Table 1. Engineering properties of laminae constituents for E-Glass Epoxy, from [8].

E_1 [MPa]	E_2 [MPa]	v_{12}	G_{12} [MPa]	α_1 [°C⁻¹]	α_2 [°C⁻¹]
53780	17930	0.25	8620	6.3×10^{-5}	20.52×10^{-5}

In sequence, the validation of the proposed model is verified by using three well know literature cases, punctual mechanical load applied to the tip of cantilever beam as the Fig. 2, distributed mechanical load applied to cantilever beam as the Fig. 3, and using mechanical load applied to biclamped beam like indicated in Fig. 4. All the results are listed in Table 2, at sequence.

$$z_{tip} = -\frac{F_0 a^3}{3EI}$$
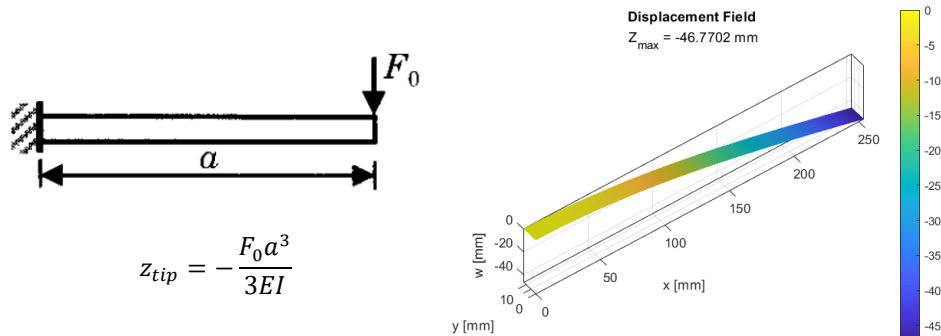
Figure 1. (a) An example of cantilever beam loaded at tip, and (b) the cantilever beam simulated using the semi-analytical proposed model.

$$z_{tip} = -\frac{q_0 a^4}{8EI}$$
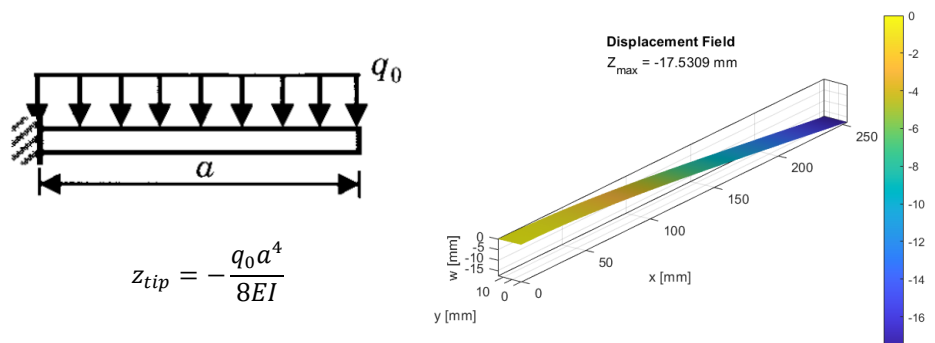
Figure 3. (a) An example of cantilever beam with distributed load, and (b) the cantilever beam simulated using the semi-analytical proposed model.

$$z_{mid-span} = -\frac{F_0 a^3}{192EI}$$
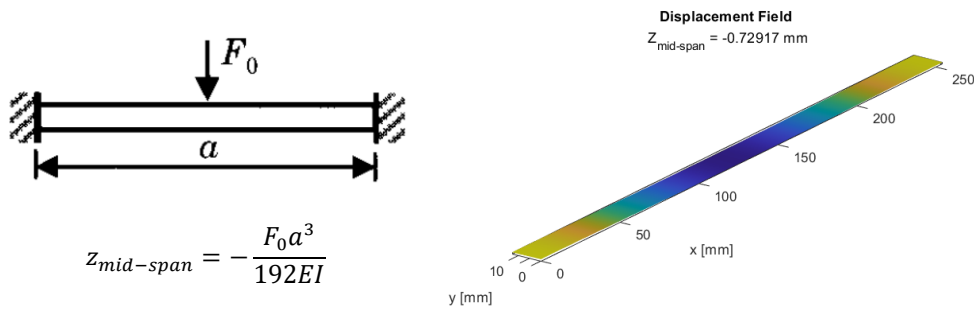
Figure 4. (a) An example of biclamped beam with punctured load, and (b) the biclamped beam simulated using the semi-analytical proposed model.

Table 2. Results for symmetric composite beam simulated.

Beam problem type	Number of terms Polynomial Series	Z_{max} [mm] (proposed model)	Z_{max} [mm] (Closed-Solution)	Relative error (%)
cantilever beam loaded at tip	6	46.5448	46.8517	0.6548
	10	46.7218	46.8517	0.2772
	15	46.7702	46.8517	0.1740
cantilever beam with distributed load	6	17.4253	17.5693	0.8199
	10	17.5075	17.5693	0.3519
	15	17.5309	17.5693	0.2190
biclamped beam with punctured load	6	0.6762	0.7320	7.6316
	10	0.7238	0.7320	1.1296
	15	0.7292	0.7320	0.3945

The listed deflections and error results indicate that the model was validated for the mechanical load.

3.2. Thermal load in hybrid laminates

The laminate stacking sequence for thermal analysis is a beam hybrid laminate $[0°_{(4)} /0°^{(Al)}]$, which are composed by layers of thermoplastic composite material and aluminium, intending simulate an experiment carried by [4]. The ply properties and engineering constants given in Table 4. Each layer has the same geometry, $L = 200$mm, $W = 26$mm and $t = 0.31$mm, whilst aluminium layer has thickness of $t = 1.25$mm. The thermal load is derived from cure degree step, $\Delta T = T_{room} - T_{cure} = -120$°C.

Table 4. Engineering properties of Toray Cetex®
TC1225 High Strength T300JB 3K Carbon and aluminium layer of Al2024-T4.

	E_1 [GPa]	E_2 [GPa]	v_{12}	G_{12} [GPa]	α_1 [°C^{-1}]	α_2 [°C^{-1}]
TC1225	58	58	0.052	3.9	1.73x10^{-5}	1.73x10^{-5}
Al2024-T4	73.1	73.1	0.33	48612 (28)	24.7x10^{-6}	24.7x10^{-6}

Analysing the equations available in [15] for curvature and deflection and using the Matlab® "fzero" function to solve the closed solution, the result for maximum beam deflection is $\delta = 8.2233$ mm. The results for deflections of closed-solution problem and convergence analysis with error achieved by the semi-analytical model proposed are listed on Table 5 below. The Fig. 5 shows the warpage of the hybrid beam laminate using the semi-analytical model proposed in face of just thermal load applied to the cantilever beam configuration.

$$\kappa = \frac{2\sin\left[\tan^{-1}(\delta/x)\right]}{\sqrt{(x^2 + \delta^2)}}$$
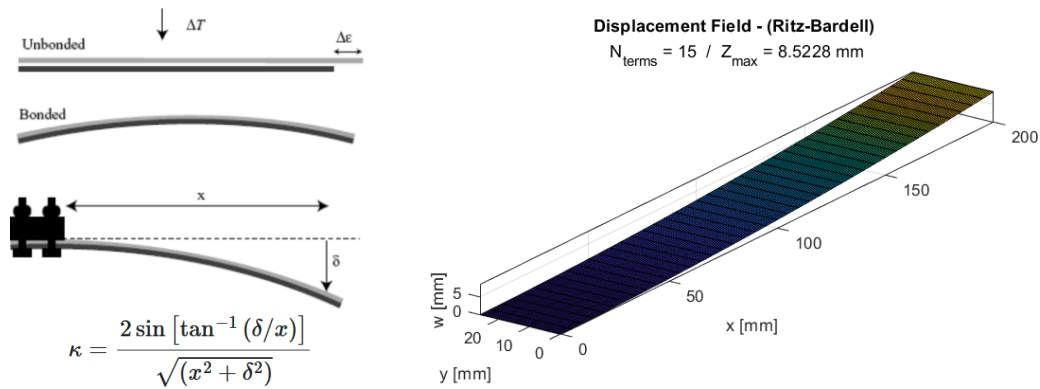
Figure 5. (a) Clamping a bimaterial strip (bonded together, the resulting internal stresses generate a uniform curvature), undergo a temperature change ΔT to allow measurement of the deflection and hence the curvature [15], and (b) the cantilever beam simulated using the present model.

Table 5. Results for cantilever hybrid beam with thermal load only.

Number of terms Polynomial Series	Z_{max} [mm] (proposed model)	Z_{max} [mm] (Closed-Solution)	Relative error (%)
6	10.9156	8.2233	32.739%
10	9.0173	8.2233	9.655%
15	8.5228	8.2233	3.642%

3.3. Simulations carried on using monolithic laminate plates.

In order to verify the proposed method to other geometries and materials, it was applied to a Carbon/Epoxy free plate under thermal load and compared to the CLT model. The engineering properties for material laminas with thickness $t = 0.19$mm are listed in Table 6 and the warpage plate result for CLT model was calculated using the equation available in [9]. The Fig. 6 below shows the perfect match of maximum displacements at z-direction and warpage.

Table 6. Engineering properties of laminae constituents for (AS4/3501-6), [9].

E_1 [MPa]	E_2 [MPa]	v_{12}	G_{12} [MPa]	α_1 [°C^{-1}]	α_2 [°C^{-1}]
142000	10300	0.28	7200	-0.9×10^{-6}	27×10^{-6}
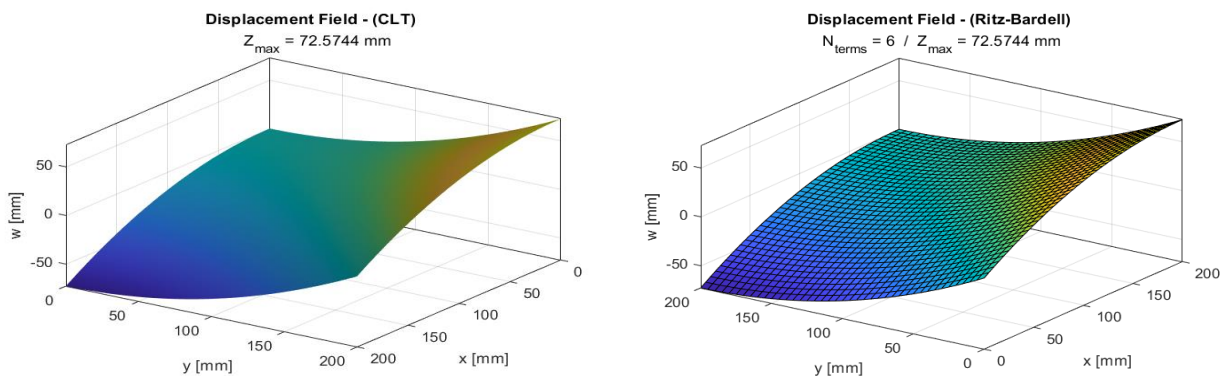
Figure 6. (a) A comparison between CLT model and the semi-analytical model proposed for a non-symmetric $[90°_{(2)}/0°_{(2)}]$ composite free plate under thermal load.

To verify the contribution of a reinforcement layer at the laminate composite plate given above, the simulations was carried out using a hybrid laminate, adding the aluminium layer, as the same thickness indicated in section 3.2 and engineering constants listed in Table 4. The results are showed at Fig. 7, following.
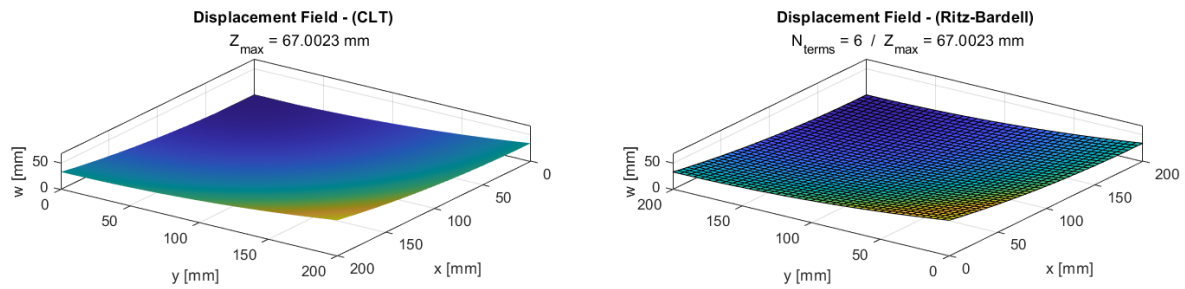
Figure 7. (a) A comparison between CLT model and the semi-analytical model proposed for a hybrid composite free plate [90°$_{(2)}$/0°$_{(2)}$/0$^{o(Al)}$] under thermal load.

Additionally, using a different layup configuration, the code developed was check-out using one of the laminate stacking sequence [45°/90°/-75°/-45°] given in [3], with each lamina material is Hexcel IM7/913 UD prepreg, whose properties could be verified at reference. The Fig. 8 shows the warpage result simulated using the semi-analytical model proposed and those obtained through FEM package simulation using ABAQUS® for a $\Delta T = -115°C$ thermal load. In simulations one whole edge plate was restrained, Clamped-Free-Free-Free (C-F-F-F) as Bardell functions combinations allows.

The value of maximum deflection in numerical results was $Z_{max} = 120\ mm$ for FEM using ABAQUS® with element type (S4R) and 72,200 elements, and the result achieved by semi-analytical model proposed using 6 terms in polynomial series was around $Z_{max} = 115\ mm$, as seen in the Fig. 8 below.
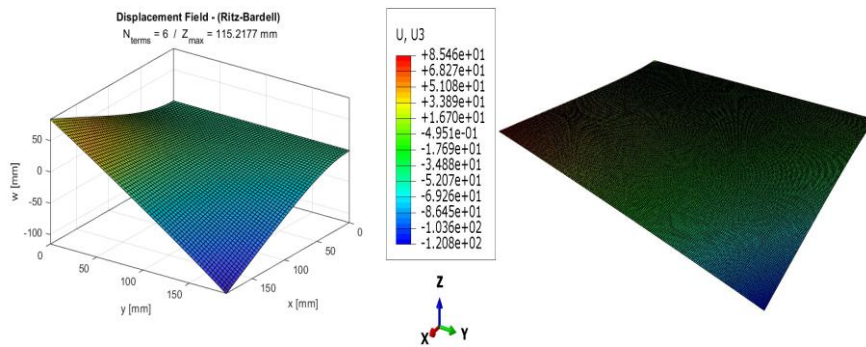
Figure 8. (a) The warpage result verified through the proposed semi-analytical model, and (b) by FEM simulation using ABAQUS® for a composite plate layup [45°/90°/-75°/-45°] under thermal load, with boundary geometric conditions Clamped-Free-Free-Free.

4. CONCLUSIONS

The simulations carried out using the proposed semi-analytical model provide results that agree fairly well with results obtained from closed form solutions. For all simulated cases a convergence study is required, where in some cases addition of high order terms are needed to improve the accuracy in results, as could be verified at biclamped beam under mechanical load in Fig. 4 and in hybrid beam under thermal load in Fig. 5. This last analysis the warpage results shows an interesting aspect of thermal effect on the laminates, indicating that its presence in composite fabrication and operation cannot be neglected.

Section of plate analysis, for hybrid laminates the warpage behavior is attenuated due the interaction between composite and metal material (Fig. 7) when compared to conventional composite laminates, as seen in Fig. 6 the high warping that nonsymmetric layup exhibits. Thus, results presented herein shows that for hybrid non-symmetric laminates the reinforcement (aluminium layer in present case) plays a crucial role in a warpage result, which indicates that any reinforcement layer should be consider during stack sequence design for composite laminate, as well these thermal effect needs to be considered in interactions between laminate and model tool, in order to achieve the desire geometry to the final part.

The model proposed herein is suitable for the exploratory application of the Rayleigh-Ritz approximation solution using Bardell polynomial functions, which is the main contribution of this work. Thus, it is possible inferring that the proposed approach can precisely compute the residual strains during cure-cycle of laminate fabrication and can reveal the strong influence of residual thermal loads in geometry final part.

The future works includes the extension of the proposed formulation to handle the kinect of cure involved in laminate fabrication, allowing the prediction of other important effect in this scenario like the chemical

residual stresses. This can be achieved either using the viscoelastic behaviour of composite constituents like shrinkage coefficients, or through phenomenological models, time-rate, or path-dependent ones where the changing of engineering properties fibre and matrix can be tracking.

4.1. Declaration of Competing Interest

The authors declare no conflict of interest.

4.2. Acknowledgements

The authors thank to the Brazilian Navy and the Laboratory of News Concepts in Aeronautics (LNCA).

5. REFERENCES

[1]   J. Sinke, Y. Wang, M. Abouhamzeh, R. Benedictus, Process Induced Warpage In Laminated Shells, 19th International Conference On Composite Materials ICCM19, p.2575 – 2582, 2013. (https://www.iccm-central.org/Proceedings/ICCM19proceedings/papers/SIN81081.pdf).

[2]   MAKINDE, Olumide Mayowa. "Prediction of Shape distortions in Composite Structures". 2018. 207f. Thesis of Doctor of Science – Instituto Tecnológico de Aeronáutica, São José dos Campos.

[3]   Bruno Vermes, Tibor Czigany, "Thermally induced mechanical work and warpage compensation of asymmetric laminates", *Composite Structures* 295, 2022. (https://doi.org/10.1016/j.compstruct.2022.115847).

[4]   SALLES LANTYER MARQUES, Sofia. "Thermal Analysis of PA6 and Residual Strain Characterization in PA6/woven carbon thermoplastic composite". 2023. 96f. Dissertation of Master of Science – Instituto Tecnológico de Aeronáutica, São José dos Campos.

[5]   J.M. González-Cantero *et al*., A new analytical model for evaluating interlaminar stresses in the unfolding failure of composite laminates, Composite Structures 147 (2016) 260–273.

[6]   André S. de Lima, Alfredo R. de Faria and José J. R. Faria, "Critical Review Of Displacement-Based Laminate Theories And Modeling Techniques", 4th BCCM Proceedings *(https://doi.org/doi/10.21452/bccm4.2018.01.02)*.

[7]   Morteza Abouhamzeh, Jos Sinke and Rinze BenedictusPrediction, Models for Distortions and Residual Stresses in Thermoset Polymer Laminates: An Overview. Journal of Manufacturing and Materials Processing, Volume 87, 2019. (http://dx.doi.org/10.3390/jmmp3040087)

[8]   Jones, R. M. *Mechanical of Composite Materials*. 2nd Edition, 1999, New York, EUA: Taylor Francis Group. (ISBN 1-56032-712-X)

[9]   Daniel, Isaac M. and Ori Ishai. *Engineering mechanics of composites*, 2nd Edition, 2006. Orford University Press. (ISBN 978-0-19-515097-1)

[10] J.N. Reddy. *Introduction to the Finite Element Method*, 4th Edition, 2019. McGraw Hill Education. (ISBN 978-1-25-986190-1)

[11] J.N. Reddy. *Mechanics of Laminated Composite Plates and Shell Theory and Analysis*, 2nd Edition, 2004. CRC Press. (ISBN 0-8493-1592-1)

[12] Megson, T. H. G. *Aircraft structures for Engineering Students*, 4th Edition, 2015. Elsevier. (ISBN-10 978-0-75066-7395)

[13] Allen D.H., Haisler W. E. *Introduction to Aerospace Structural Anal*ysis, 1985. John Wiley and Sons. (ISBN 0-471-88839-7).

[14] Bardell, N. S., "Free Vibration Analysis of a Flat Plate using the hierarchical finite element method", Journal of Sound and Vibration (1991) 151(2), 263-289.

[15] THERMAL Expansion and the Bi-Material Strip (all content). Cambridge: University of Cambridge, 2022. (https://www.doitpoms.ac.uk/tlplib/thermal-expansion/printall.php) accessed 16th April 2024.

[16] MATLAB® R2022a [Computer software]. MathWorks Inc. (https://www.mathworks.com).

[17] ABAQUS® 2022 [Computer software]. Dassault Systèms Simulia Corp (https://www.3ds.com).

EVALUATION OF MECHANICAL PROPERTIES OF LAMINATED COMPOSITE BEAMS WITH OPEN CROSS-SECTIONS

Marcelo Freires Pinto[a], Pedro Sanderson Bastos Barros[b], Luiz Antônio Taumaturgo [c], Evandro Parente Junior [d]*

(a) 0009-0002-8957-2891 (Universidade Federal do Ceará – Brazil)
(b) 0009-0001-6178-2195 (Instituto Federal do Ceará – Brasil)
(c) 0000-0003-2247-2511 (Instituto Federal do Ceará – Brazil)
(d) 0000-0003-0219-1376 (Universidade Federal do Ceará – Brazil)
    * Corresponding author: evandro@ufc.br

Abstract: The computation of cross-sectional stiffness properties of laminated composite beams and columns is important for the global analysis of these components using frame finite elements and for the evaluation of their global buckling loads. However, this computation is very complex since the equivalent stiffness properties depend on the cross-section geometry, material properties, and composite layup. Furthermore, the layup can introduce couplings between axial, bending, and twisting deformations that do not occur for beams of homogeneous and isotropic materials. Therefore, the objective of this work is to compare three different approaches to the computation of equivalent mechanical properties of laminated columns with open cross-section, using a channel section as an example. The global buckling loads obtained are compared with the results obtained using well-known programs based on the Finite Strip Method and the Finite Element Method.

1. INTRODUCTION

Composites can be used in a variety of structures, such as buildings, storage sheds, and bridge superstructures, among others. These materials are highlighted by high stress-to-weight and strength-to-weight ratios, mechanical improvements such as corrosion resistance, fatigue, thermal and acoustic insulation [1, 2].

It is well known that buckling is a crucial point in the design of laminated composite columns, as these columns are generally very slender and subject to failure under stresses lower than the strength of the material. Several works dealt with the buckling of composite columns [3, 4, 5].

Beam theories attempting to address cases of laminates with arbitrary sections result in complex formulations, and there are only a limited number of analytical solutions available for simple problems [1]. However, by introducing approximations in the kinematics deformations, it is possible to obtain solutions for more generic geometries. Cardoso et al. [6] presented simplified formulations to obtain equivalent properties. The analysis problem is discretized by a finite element technique. The structures are treated as beams resistant to torsional bending. The beam bolts are made from a set of elements that were supplied for flat-ply laminated composite panels.

Furthermore, Massa and Barbero [1] proposed a simple methodology for the analysis of thin-walled composite beams subjected to bending, torque, shear, and axial forces. The cross-section is considered by one or more segments. Modelled initially with the constitutive solution of classical lamination theory, considering a linear distribution of normal and shear strains through the thickness of the walls, as a thin plate. Warping, warping restriction, and secondary are considered. Kollar and Pluzsik [7] also presented an approximate approach that deals with beam theory for thin-walled, open, and closed-section composite beams. The

arrangement of each wall segment is arbitrary, and the effects of shear deformation and constrained warping are neglected. Closed-form expressions are developed for calculating the 4×4 stress constitutive matrix. It is also shown that the local bending stiffness of the wall segments can be neglected when the laminate is symmetric or orthotropic.

The objective of this work is to apply the methodologies proposed by Massa and Barbero [1], Cardoso et al. [6], and Kollar and Pluzsik [7] for calculating the equivalent properties of open sections and make a comparison between these theories through the calculation of global buckling loads for channel columns considering different layups.

2. METHODOLOGY

Sections 2.1, 2.2, and 2.3 present, respectively, the theories proposed by Massa and Barbero [1], Cardoso et al. [6] and Kollar and Pluzsik [7], and in 2.4 will be shown the methodology for the determination of global critical loads.

2.1. Cross-sectional Equivalent Properties by Massa and Barbero (1998)

The methodology proposed by Massa and Barbero [1] allows for the approach of open or closed cross-section laminated beams to homogeneous and isotropic materials. The theory stands out for presenting equations that not only enable simple and efficient implementation, but also lead to good results for symmetric and balanced laminates. Warping and restriction to warping are considered.

The cross-section is defined by segments that can be flat, arc-circular, and concentrated area segments, modeled with the constitutive equations of classical lamination theory. Thereby, all mechanical properties are defined by integrals over the area of the cross-section, divided over the contour and thickness of each segment.

According to Massa and Barbero [1], segment i of the cross-section is modeled as a thin plate, which has the following constitutive relationship between internal forces and strains.

$$\begin{Bmatrix} \varepsilon_x^i \\ \varepsilon_s^i \\ \gamma_{xs}^i \\ \kappa_x^i \\ \kappa_s^i \\ \kappa_{xs}^i \end{Bmatrix} = \begin{bmatrix} \alpha_{11} & \alpha_{12} & \alpha_{16} & \beta_{11} & \beta_{12} & \beta_{16} \\ \alpha_{12} & \alpha_{22} & \alpha_{26} & \beta_{12} & \beta_{22} & \beta_{26} \\ \alpha_{16} & \alpha_{26} & \alpha_{66} & \beta_{16} & \beta_{26} & \beta_{66} \\ \beta_{11} & \beta_{12} & \beta_{16} & \delta_{11} & \delta_{12} & \delta_{16} \\ \beta_{12} & \beta_{22} & \beta_{26} & \delta_{12} & \delta_{22} & \delta_{26} \\ \beta_{16} & \beta_{26} & \beta_{66} & \delta_{16} & \delta_{26} & \delta_{66} \end{bmatrix} \begin{Bmatrix} N_x^i \\ N_s^i \\ N_{xs}^i \\ M_x^i \\ M_s^i \\ M_{xs}^i \end{Bmatrix} \qquad (1)$$

where N_c^i and N_s^i are normal forces, N_{xs}^i is the shear force in the xs plane, M_x^i and M_s^i are bending moments, and M_{xs}^i is the torsional moment, ε_x^i, ε_s^i, γ_{xs}^i are the mid-place membrane strains, and κ_x^i κ_s^i and κ_{xs}^i the curvatures. The terms α_{ij}, β_{ij}, and δ_{ij} correspond to the terms of the matrices **A**, **B**, and **D** inverted.

Considering the assumption that $N_s^i = 0$ and $M_s^i = 0$ (valid for thin walls), and assuming a decoupling between membrane and shear strains ($\alpha_{16} = \beta_{16} = \delta_{16} = 0$) Eq. (1) can be reduced to:

$$\begin{Bmatrix} \varepsilon_x^l \\ \kappa_x^l \\ \gamma_{xs}^t \\ \kappa_{xs}^d \end{Bmatrix} = \begin{bmatrix} \alpha_{11} & \beta_{11} & 0 & 0 \\ \beta_{11} & \delta_{11} & 0 & 0 \\ 0 & 0 & \alpha_{66} & \beta_{66} \\ 0 & 0 & \beta_{66} & \delta_{66} \end{bmatrix} \begin{Bmatrix} N_x^l \\ M_x^l \\ N_{xs}^i \\ M_{xs}^i \end{Bmatrix} \qquad (2)$$

Finally, the expression corresponding to the reduced stiffness matrix can be determined by inverting the Eq. (2), leading to:

$$\begin{Bmatrix} N_x^i \\ M_x^i \\ N_{xs}^i \\ M_{xs}^i \end{Bmatrix} = \begin{bmatrix} A_x^i & B_x^i & 0 & 0 \\ B_x^i & D_x^i & 0 & 0 \\ 0 & 0 & F_{xs}^i & C_{xs}^i \\ 0 & 0 & C_{xs}^i & H_{xs}^i \end{bmatrix} \begin{Bmatrix} \varepsilon_x^i \\ \kappa_x^i \\ \gamma_{xs}^i \\ \kappa_{xs}^i \end{Bmatrix} \qquad (3)$$

where the terms $A_x^i, B_x^i, C_x^i, D_x^i, F_x^i \wedge H_x^i$ correspond to stiffness segments and allow for the determination of the section properties to solve the general problem of bending and torsion, and they can be calculated by:

$$A_i = \int_{-\frac{t}{2}}^{\frac{t}{2}} E_x^k dr = \sum_{k=1}^{N} E_x^k t^k \qquad B_i = \int_{-\frac{t}{2}}^{\frac{t}{2}} r E_x^k dr = \sum_{k=1}^{N} E_x^k t^k \bar{r}^k$$

$$C_i = \int_{-\frac{t}{2}}^{\frac{t}{2}} r G_{xs}^k dr = \sum_{k=1}^{N} G_{xs}^k t^k \bar{r}^k \quad D_i = \int_{-t/2}^{t/2} r^2 E_x^k dr = \sum_{k=1}^{N} E_x^k \left[\frac{(t^k)^3}{12} + t^k (\bar{r}^k)^2 \right] \qquad (4)$$

$$F_i = \int_{-\frac{t}{2}}^{\frac{t}{2}} G_{xs}^k dr = \sum_{k=1}^{N} G_{xs}^k t^k \quad H_i = \int_{-\frac{t}{2}}^{\frac{t}{2}} r^2 G_{xs}^k dr = \sum_{k=1}^{N} G_{xs}^k \left[\frac{(t^k)^3}{12} + t^k (\bar{r}^k)^2 \right]$$

where E_x^k is the equivalent elastic modulus of layer k along the x-direction, G_{xs}^k is ethe quivalent elastic transversal modulus, t^k is the thickness of layer k, r is the thickness coordinate, $\bar{r}^k$ is the distance from the middle surface of the segment to the middle surface of layer k, N is the number of layers in the segment, A_i represents the axial stiffness per unit length of the segment, B_i is the coupling between bending curvature and extensional force per unit length, D_i is the bending stiffness of the segment under bending, F_i is the in-plane shear stiffness and H_i is the twisting stiffness under a twisting moment.

Applying the Parallel Axis Theorem and summing the contributions of the segments, the mechanical moments of inertia and the mechanical product of inertia relative to the axes can be obtained by:

$$EA = \sum_{i=1}^{n} A_i b_i \qquad EI_y = \sum_{i=1}^{n} \left[\left(EI_{y'}^i \right) + A_i b_i \left(z_i + e_b \cos \alpha_y^i \right)^2 \right]$$

$$(GJ_R) = 4 \sum_{i=1}^{n} \bar{H}_i b_i \quad EI_z = \sum_{i=1}^{n} \left[\left(EI_{z'}^i \right) + A_i b_i \left(y_i - e_b \sin \alpha_y^i \right)^2 \right] \qquad (5)$$

The flexural stiffness of the segments is calculated to the neutral axis of curvature s', obtained using $z_i + e_b \cos \alpha_y^i$ and $y_i - e_b \sin \alpha_y^i$ are the coordinates of the center of the segment. EA represents the axial stiffness of the section and α_y^i are obtained by a rotation around the x-axis., where is the number of segments describing the cross-section, GJ_R is the torsional stiffness, EI_x and EI_y are the mechanical moments of inertia to axes.

2.2. Cross-sectional Equivalent Properties by Cardoso et al. (1999)

Cardoso et al. [6] introduced a methodology for the analysis of orthotropic materials under plane stress conditions. By treating beams subject to torsional bending, they utilize sections composed of flat-ply laminated composite panels, which are symmetric about their mid-plane, resulting in the elimination of all stiffness coupling terms. As a consequence, the elements exhibit orthotropic behavior in the membrane mode, thereby eliminating shear coupling effects.

Through this approach, which is based on the mechanics of composite materials, the authors consider a homogenization of the layers. The equivalent properties of the materials, derived from the unique characteristics of each constituent material, are homogeneous and orthotropic. In demonstrating this method, the authors illustrate how the mechanical properties of the equivalent orthotropic material can be evaluated by:

$$E_x^m = \frac{1}{t \alpha_{11}} \quad G_{xy}^m = \frac{1}{t \alpha_{66}} \quad G_{xy}^b = \frac{12}{t^3 \delta_{66}} \qquad (6)$$

where α_{ij} and δ_{ij} was presented in Eq. (1), and E_x^m, G_{xy}^m and G_{xy}^b are equivalent elastic constants for tensile and shear modulus, for membrane (superscript m) and bending modes (superscript b), respectively. Following this, the cross-sectional equivalent properties can be calculated by:

$$\overline{EA} = \sum_{i=1}^{NP} E_{x_i}^m A_i \quad \overline{EI}_z = \sum_{i=1}^{NP} E_{x_i}^m I_{z_i} \quad \overline{EI}_y = \sum_{i=1}^{NP} E_{x_i}^m I_{y_i} \quad \overline{EI}_{yz} = \sum_{i=1}^{NP} E_{x_i}^m I_{yz_i} \quad \overline{GJ} = \sum_{i=1}^{NP} G_{xy_i}^b J_i \quad (7)$$

being $J_i = b_i t_i^3 / 3$.

2.3. Cross-sectional Equivalent Properties by Kollar and Pluzsik (2002)

Kollar and Pluzsik [7] proposed a general theory to analyse thin-walled laminated beams and presented analytical expressions for constitutive matrix **C** for open and closed sections. The beam's wall consists of n flat segments each one may be made of composite materials with an arbitrary layup.

The procedure for obtaining the cross-section equivalent properties proposed for open-section beams consists of four steps: (*a*) the deformations in each segment must be related to axial strain, curvatures, and the rate of twist angle; (*b*) the forces in each segment of the section are determined from the strains obtained in the previous step; (*c*) the resultant normal force, as well as the bending moments and torsional moment, are obtained from the forces in each wall of the cross-section; (*d*) the stiffness matrix is established by relating the resultant forces (normal force, bending moments, and torsional moment) to the axial strain, curvatures, and rate of twist angle.

More details about the methodology used by the authors can be obtained from Kollar and Pluzsik [8] and Barros et al. [8].

2.4. Global Bucking Loads of Laminated Columns

For a simply supported laminated column (Figure 1), Barros et al. [8] show that the global buckling load can obtained by the resolution of the following equation:

$$\left(P_y - P\right) \cdot \left(P_z - P\right) \cdot \left(P_\beta - P\right) - \left(P_z - P\right) \cdot \frac{P^2 \cdot y_0^2}{r_0^2} - \left(P_y - P\right) \cdot \frac{P^2 \cdot z_0^2}{r_0^2} = 0 \tag{8}$$

being:

$$P_y = \frac{\pi^2 \cdot \overline{EI}_y}{L^2} \quad P_z = \frac{\pi^2 \cdot \overline{EI}_z}{L^2} \quad P_\beta = \frac{1}{r_0^2}\left(\overline{GJ} + \frac{\pi^2 \cdot \overline{EI}_\omega}{L^2}\right) \tag{9}$$

where L is the length of column, $\overline{EI}_y$ and $\overline{EI}_z$ are the bending stiffness, $\overline{GJ}$ is the torsional stiffness and $\overline{EI}_\omega$ is the warping stiffness, y_0 e z_0 are the distances of the mechanical centroid C to the shear center S of the cross section (see Figure 1), r_0 is the polar radius of gyration with respect to the shear center, P_y and P_z are critical loads related to pure bending, and P_β is associated with torsion and warping.

3. RESULTS AND DISCUSSION

For assessment of the presented methodologies, numerical applications for simply supported channel columns (see Figure 1) with flange width $b = 40$ mm, web height $d = 80$ mm, and total thickness $h = 1.048$ mm, were carried out for four layups and the results are compared with the Finite Strip Method (FSM) [9] using FStr (Lazzari and Batista [10, 11]) and Finite Element Method (FEM) by using ABAQUS [12].

The material properties are [13]: $E_1 = 130.71$ GPa, $E_2 = 6.36$ GPa, $G_{12} = 4.18$ GPa, and $v_{12} = 0.32$, and the considered composite layups are: L1 [0°]$_8$, L2 [(0°/90°)$_2$]s, L3 [(45°/-45°)$_2$]s, and L4 [30° /-30°]$_4$.
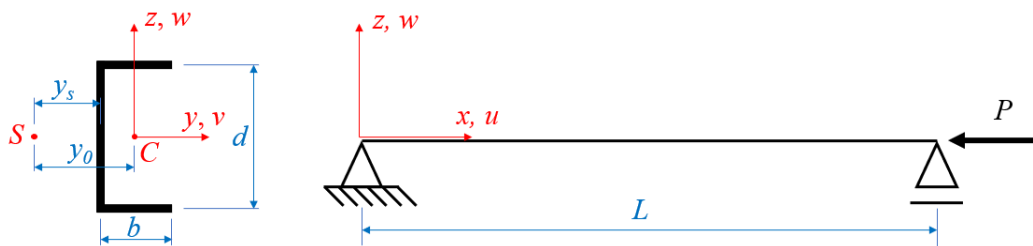
Figure 1. Geometry and boundary conditions of the columns.

For channel columns, where y is an axis of symmetry, and therefore, $z_0 = 0$, the solution of Eq. (8) indicates that the critical load will be smaller load than that obtained by pure bending around the z-axis (P_F) or by bending-torsion (P_{FT}), given by [9]:

$$P_F = P_z \qquad P_{FT} = \frac{1}{2 \cdot [1 - (y_0/r_0)^2]}\left[(P_y + P_\beta) - \sqrt{(P_y + P_\beta)^2 - 4k \cdot P_y \cdot P_\beta}\right] \tag{10}$$

where P_y, P_z, and P_β are given in Eq. (9), and $k = [1 - (y_0/r_0)^2]$.

Pluzsik and Kollar [14] indicate that for an orthotropic beam, the warping stiffness and the shear center can be evaluated by the expressions given for an isotropic beam by replacing the terms Eh by $1/\alpha_{11}$, and Eq. (6) presents a relationship between this parameter and E_x^m. Thus, the warping stiffness $\overline{EI}_\omega$ presented in Eq. (9) and the position of the shear center y_s of the channel can be determined approximately by:

$$\overline{EI}_\omega = \frac{E_x^m \cdot h \cdot d^2 \cdot b^3}{12} \cdot \frac{(3 \cdot b + 2 \cdot d)}{(6 \cdot b + d)} \quad y_s = \frac{3 \cdot b^2}{6 \cdot b + d} \tag{11}$$

The cross-sectional equivalent properties obtained by applying the methodologies of Cardoso et al. [1], Massa and Barbero [6], and Kollar and Pluzsik [7] are presented in Table 1.

It can be noted that all theories lead to very close results for cross-sectional equivalent properties and the largest difference obtained is about 4.05 % for $\overline{EI}_z$ for L2 layup between the approaches of Cardoso et al. [6] and Massa and Barbero [1]. Furthermore, Massa and Barbero [2] and Kollar and Pluzsik [7] methodologies are in very good agreement for all considered layups.

Table 1. Cross-sectional equivalent properties for the channel.

LAYUP	EQUIVALENT PROPERTIES	METHODOLOGY		
		Cardoso et al. (1999)	Massa and Barbero (1997)	Kollar and Pluzsik (2002)
L1	$\overline{EA}$ ($\times 10^7$ N)	2.1630	2.1917	2.1917
	$\overline{EI}_y$ ($\times 10^4$ N.m²)	2.2476	2.3380	2.3380
	$\overline{EI}_z$ ($\times 10^3$ N.m²)	3.5119	3.6539	3.6539
	$\overline{GJ}$ (N.m²)	0.2566	0.2566	0.2566
	$\overline{EI}_\omega$ (N.m⁴)	4.0913	4.0913	4.0913
L2	$\overline{EA}$ ($\times 10^7$ N)	1.1388	1.1539	1.1539
	$\overline{EI}_y$ ($\times 10^4$ N.m²)	1.1833	1.2309	1.2309
	$\overline{EI}_z$ ($\times 10^3$ N.m²)	1.8490	1.9239	1.9239
	$\overline{GJ}$ (N.m²)	0.2566	0.2566	0.2566
	$\overline{EI}_\omega$ (N.m⁴)	2.1540	2.1540	2.1540
L3	$\overline{EA}$ ($\times 10^7$ N)	0.2475	0.2508	0.2508
	$\overline{EI}_y$ ($\times 10^4$ N.m²)	0.2572	0.2675	0.2675
	$\overline{EI}_z$ ($\times 10^3$ N.m²)	0.4019	0.4181	0.4181
	$\overline{GJ}$ (N.m²)	1.8137	1.8137	1.8388
	$\overline{EI}_\omega$ (N.m⁴)	0.4682	0.4682	0.4682
L4	$\overline{EA}$ ($\times 10^7$ N)	0.6885	0.6977	0.6880
	$\overline{EI}_y$ ($\times 10^4$ N.m²)	0.7155	0.7442	0.7442
	$\overline{EI}_z$ ($\times 10^3$ N.m²)	1.1179	1.1631	1.1631
	$\overline{GJ}$ (N.m²)	1.4234	1.4234	1.5429
	$\overline{EI}_\omega$ (N.m⁴)	1.2842	1.2842	1.2842

For FEM analyses, a finite element mesh with 10 mm × 10 mm S8R shell elements based on Reissner-Mindlin theory was adopted. It is important to note that this element considers all couplings induced by the stacking sequence and can be applied to the analysis of shells with arbitrary layups. On the other hand, the FStr is a program based on the FSM, and it was developed for the stability analysis of thin-walled structural profiles made of isotropic and orthotropic materials and cannot be applied directly to laminates. Therefore, it was necessary to obtain the mechanical properties of an equivalent orthotropic material. These properties were obtained approach using proposed by Barbero [2], where the equivalent properties for global and local buckling are given by:

$$E_{1,eq}^{global} = \frac{1}{h \cdot \alpha_{11}} \quad E_{2,eq}^{global} = \frac{1}{h \cdot \alpha_{22}} \quad G_{12,eq}^{global} = \frac{1}{h \cdot \alpha_{66}} \quad v_{12,eq}^{global} = -\frac{\alpha_{12}}{\alpha_{11}} \tag{12}$$

$$E_{1,eq}^{local} = \frac{12}{h^3 \cdot \delta_{11}} \quad E_{2,eq}^{local} = \frac{12}{h^3 \cdot \delta_{22}} \quad G_{12,eq}^{local} = \frac{12}{h^3 \cdot \delta_{66}} \quad \nu_{12,eq}^{local} = -\frac{\delta_{12}}{\delta_{11}} \tag{13}$$

where α_{ij} and δ_{ij} are defined in Eq. (1).

Table 2 presents, respectively, the equivalent orthotropic material properties obtained by applying Eqs. (12) and (13) for the layups considered in this paper. It is important to note that for FSM, the critical loads for each layup were obtained by using the equivalent properties defined in Eqs. (12) and (13), with the lowest value for each length being considered the buckling load.

Table 2. Equivalent orthotropic material properties. Units of E_1, E_2, and G_{12} in GPa.

Layup	$E_{1,eq}^{global}$	$E_{2,eq}^{global}$	$G_{12,eq}^{global}$	$\nu_{12,eq}^{global}$	$E_{1,eq}^{local}$	$E_{2,eq}^{local}$	$G_{12,eq}^{local}$	$\nu_{12,eq}^{local}$
L2	68.817	68.817	4.180	0.0297	68.817	68.817	4.180	0.0297
L3	14.957	14.957	33.416	0.7891	14.957	14.957	33.416	0.7891
L4	41.029	8.349	25.134	1.4963	41.029	8.349	25.134	1.4963

The buckling loads were obtained using Massa and Barbero [1], Cardoso et al. [6] and Kollar and Pluzsik [7] methodologies for the channel columns for various lengths are available in Figure 2. It can be observed that there is excellent agreement in the global buckling results obtained using the cross-sectional equivalent properties and the FSM and FEM results.
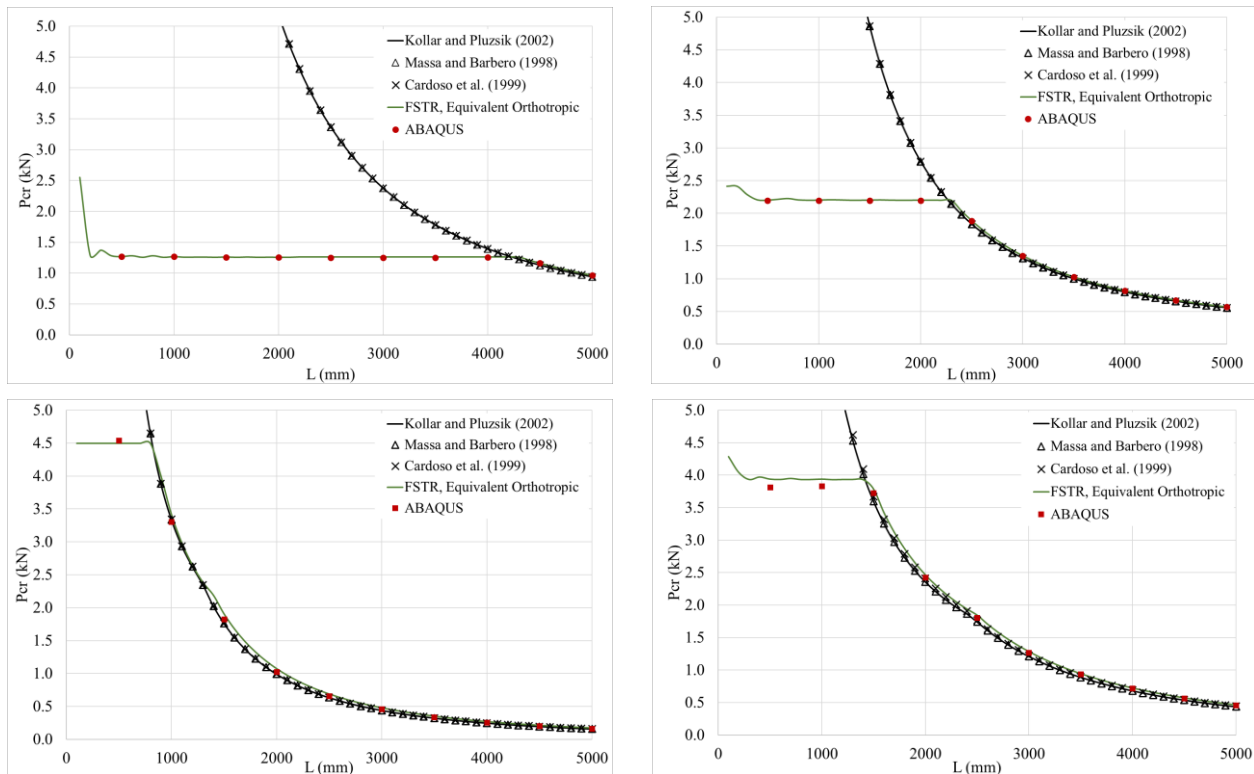
Figure 2. Signature curves for the channel columns for layups (a) L1, (b) L2, (c) L3, and (d) L4.

The lowest local buckling loads were observed for the layups L1, and L2. It can be noticed that L3, and L4 layups presented the transition between bending-torsion and bending modes at approximately $L = 1300$ mm, and $L = 2300$ mm, respectively. For laminations L1 and L2, this transition occurs in lengths outside the range presented in Figure 2, exceeding $L = 7000$ mm. Figure 3, Figure 4, and Figure 5 shows, in that order, the buckling modes obtained using ABAQUS [12] for lengths of 500 mm, 2500 mm, and 4500 mm.
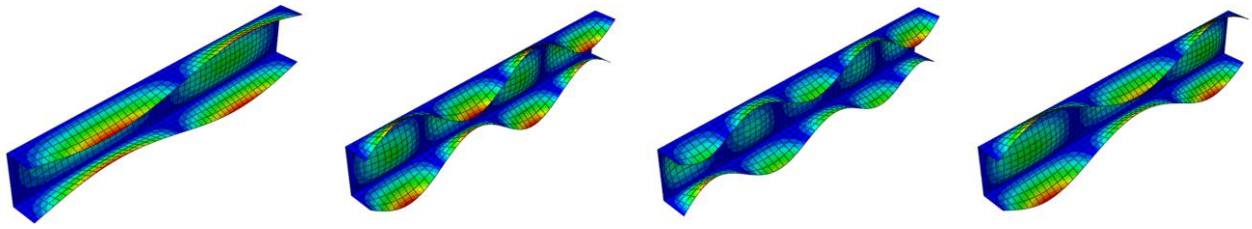
Figure 3. Buckling modes of the channels with 500 mm length for layups (a) L1, (b) L2, (c) L3, and (d) L4.
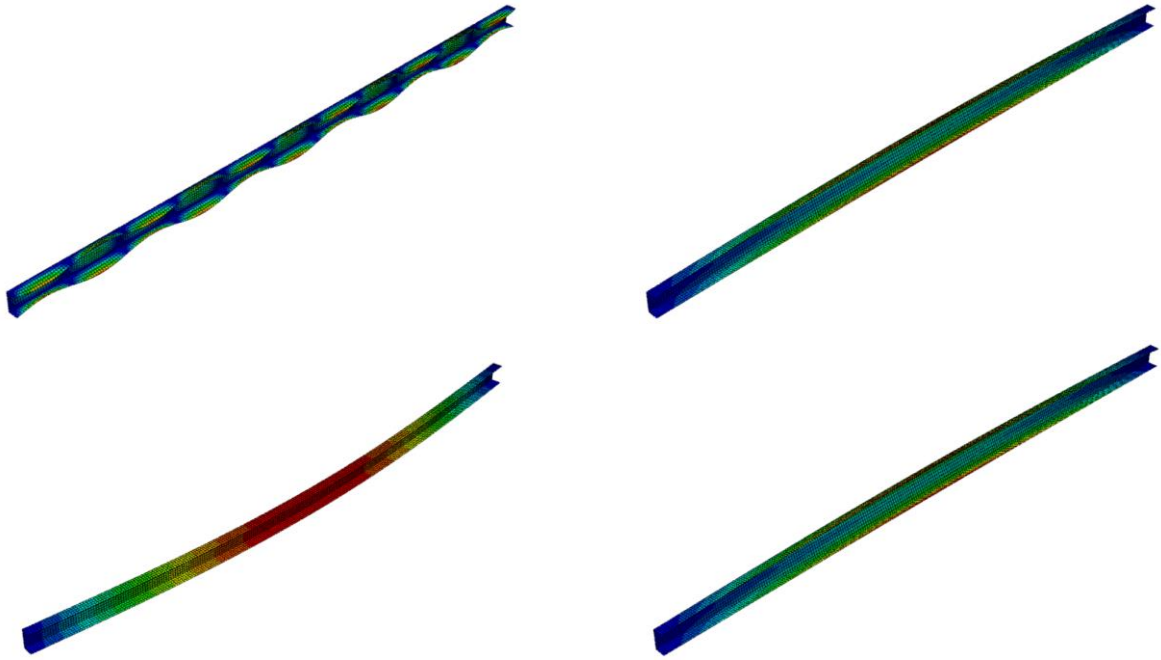
Figure 4. Buckling modes of the channels with 2500 mm length for layups (a) L1, (b) L2, (c) L3, and (d) L4.
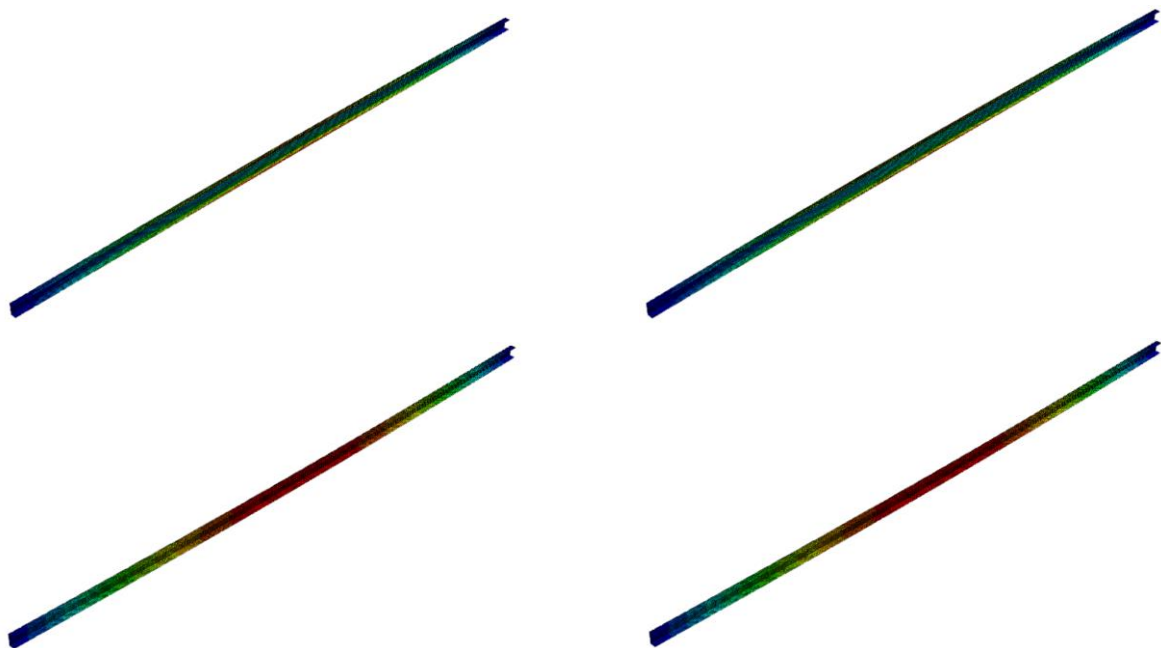
Figure 5. Buckling modes of the channels with 4500 mm length for layups (a) L1, (b) L2, (c) L3, and (d) L4.

4. CONCLUSIONS

This work presented and applied three different methodologies for the calculation of cross-sectional equivalent properties for thin-walled laminated columns and compared these theories by calculating the critical global buckling loads for laminated channel columns.

The cross-sectional equivalent properties obtained with those methodologies presented similar results, despite using different approaches. Furthermore, the application of the three approaches in the evaluation of the critical loads corresponding to the global buckling modes led to results in very good agreement with those obtained by FEM and FSM.

4.1. Declaration of Competing Interest

The authors declare no conflict of interest.

4.2. Acknowledgements

5. REFERENCES

[1] J.C. Massa, E.J. Barbero. *A Strength of Materials Formulation for Thin-Walled Composite Beams with Torsion*. J. Composite Materials, vol. 32, pp. 1560–1594, 1998.

[2] E. J. Barbero. *Introduction to composite materials design*. CRC Press, 2011.

[3] S. C. M. D'Aguiar, E. Parente Junior. *Local buckling and post-critical behavior of thin-walled composite channel section columns*. Latin American Journal of Solids and Structures, vol., 2018.

[4] L. A. T. Mororó, A. M. C. Melo, E. Parente Junior, E. Lucena Neto, and F. A. C. Monteiro. *Corotational elements for thin-walled laminated composite beams with large 3d rotations*. Thin-Walled Structures, vol. 152, pp. 106375, 2020.

[5] J. Aguiar Junior, E. Parente Junior, M. S. Medeiros Junior. *Assessment of the load-carrying capacity of laminated composite columns*. Proceedings of the 6th Brazilian Conference on Composite Materials, 2022.

[6] J. Cardoso, L. Sousa, J. Castro, A. Valido. *Design optimization of composite beam structures*. In: Oliveira, A.; Bento, J.; Pereira, E. (eds.) Proc. EPMESC VII Conf., Vol. 1, pp. 335-344. Amsterdam: Elsevier, 1999.

[7] L. P. Kollár, A. Pluzsik. *Analysis of thin-walled composite beams with arbitrary layup*. Journal of Reinforced Plastics and Composites, vol. 21, n. 16, pp. 1423–1465, 2002.

[8] P. S. B. Barros, L. A. T. Mororó, E. Parente Junior (in press). *Global buckling of thin-walled composite columns with channel sections*. Proceedings of the 7th Brazilian Conference on Composite Materials, 2023.

[9] Y. K. Cheung, L. G. Tham. Finite Strip Method. Taylor & Francis, 1998.

[10] J. A. Lazzari, E. M. Batista. *Finite strip method computer application for buckling analysis of thin-walled structures with arbitrary cross-sections*. REM - International Engineering Journal, v. 74, p. 337-344, 2021.

[11] J. A. Lazzari, E. M. Batista. *FSTr – Finite Strip Computer Application 2023 [Computer software]*. (https://sites.google.com/coc.ufrj.br/fstr).

[12] Simulia. *ABAQUS/Standard user's manual*. Version 6.12. Providence, RI, USA, 2012.

[13] H. Debski, T. Kubiak and A. Teter. *Experimental investigation of channel-section composite profiles behavior with various sequences of plies subjected to static compression*. Thin-Walled Structures, v. 71, pp. 147-154, 2013.

[14] A. Pluzsik, L. P. Kollár. Effects of Shear Deformation and Restrained Warping on the Displacements of Composite Beams. *Journal of Reinforced Plastics and Composites*, vol. 21, n. 17, pp. 1517–1541, 2002.

STABILITY ANALYSIS OF THIN-WALLED LAMINATED COMPOSITE COLUMNS USING THE FINITE STRIP METHOD

Luiz Antônio Taumaturgo Mororó[a],[*], Pedro Sanderson Bastos Barros[b], Evandro Parente Junior[c]

(a) 0000-0003-2247-2511 (Federal Institute of Ceará/Fortaleza – Brazil)
(b) 0009-0001-6178-2195 (Federal Institute of Ceará/Itapipoca – Brazil)
(b) 0000-0003-0219-1376 (Federal University of Ceará – Brazil)
* Corresponding luiz.mororo@ifce.edu.br

Abstract: Due to its high slenderness, thin-walled laminated columns might present buckling failure even when subjected to stresses much lower than the material strength. These columns can exhibit different buckling modes, depending on the cross-section geometry, material properties, composite layup, boundary conditions, and length. This work presents a simple and efficient computational approach based on the Finite Strip Method and the Classical Laminated Theory to the stability analysis of thin-walled composite columns with arbitrary layup. Despite being able to consider all possible laminate couplings, uncoupling procedures are proposed to simplify the satisfaction of the natural boundary conditions, improving the accuracy of the proposed approach. An excellent agreement was verified between the results of the proposed methodology and those obtained by the Finite Element Method and other well-known programs based on the Finite Strip Method.

1. INTRODUCTION

Due to its high slenderness, thin-walled laminated columns might present buckling failure even when subjected to stresses much lower than the material strength. Thin-walled columns can exhibit different buckling modes (*e.g.*, local, global, and distortional), depending on the cross-section geometry, material properties, composite layup, boundary conditions, and length. Like for cold-formed steel columns, the signature curve of a given cross-section is an interesting design tool for thin-walled laminated columns. This curve shows the critical load as a function of column length, allowing the simple identification of the transition between local, distortional, and global buckling modes.

The development of numerical tools capable of simulate the complex phenomena associated with the stability of thin-walled composite columns is a challenging task. In this context, several approaches have been proposed in the literature, based on the Finite Element Method (FEM) [1, 2, 3], the Rayleigh-Ritz Method [4], and the Finite Strip Method (FSM) [5, 6].

Despite being able to capture complex buckling modes for different boundary conditions, loading, cross-sections, and layups, adopting a FEM methodology to determine the signature curve is very demanding in terms of computational cost, due to the large number of degrees of freedoms required to obtain accurate responses. On the other hand, by using a Rayleigh-Ritz approach is very efficient, but it is difficult to apply to complex cross-sections and its accuracy is strongly dependent on the chosen approximate buckling modes.

The FSM can be considered a particular case of FEM. The main difference between them relies on the fact that the FEM makes use of the polynomials shape functions in all directions, while the FSM uses a combination of polynomials shape functions and trigonometric shape functions in different directions, which must satisfy essential boundary conditions [7]. This shape function separation allows the FSM to reduce the dimensionality of the problem, leading to a reduction in the inherent computational cost of the problem without loss of accuracy.

This work presents a simple and efficient computational approach based on the Finite Strip Method and the Classical Laminated Theory to the stability analysis of thin-walled composite columns with arbitrary layup. Despite being able to consider all possible laminate couplings, uncoupling procedures are proposed to simplify the satisfaction of the natural boundary conditions, improving the accuracy of the proposed approach. An excellent agreement was verified between the results of the proposed methodology and those obtained by the Finite Element Method and other well-known FSM programs.

2. METHODOLOGY

This section is dedicated to outlining the main features of the proposed approach. The formulation of FSM is summarized, providing expression for the stiffness and geometric stiffness matrices needed for the linearized buckling analysis. Furthermore, effect of the composite layup is discussed.

2.1. Finite Strip Method

In this study, a straight column is discretized with n laminated finite strip elements whose lengths are set the same of that of the column (see Figure 1). The cross section of the column is meshed with two-node strip elements on its midplane surface while spatial discretization is not employed in its longitudinal direction. The local displacements (u, v, and w) on the midplane surface in local directions (x, y, and z), respectively, at any arbitrary point within a strip is approximated by interpolating its nodal displacements with shape functions obtained by the summation of the product of polynomials functions in the transverse direction of the strip and trigonometric functions in the longitudinal direction of the strip ranging from 1 to m longitudinal terms:

$$\mathbf{u} = \mathbf{Nd} = \sum_{p=1}^{m} \mathbf{N}_p \, \mathbf{d}_p = \sum_{p=1}^{m} \mathbf{N}_p \begin{Bmatrix} u_1 \\ v_1 \\ w_1 \\ \theta_1 \\ u_2 \\ v_2 \\ w_2 \\ \theta_2 \end{Bmatrix}_p \tag{1}$$

where $\mathbf{u}$ is the vector containing local displacements at a given point, *i.e.*, $\mathbf{u} = \{u \ v \ w\}^T$, and $\mathbf{d}$ is the vector in which its elements are the degrees of freedoms (DOF) u_i, v_i, w_i and θ_i, as schematically illustrated for the first term ($p = 1$) of the simply supported end boundary condition in Fig. 1. The shape function matrix $\mathbf{N}$ can be assembled from the building block matrix $\mathbf{N}_p$ of a single longitudinal term p:

$$\mathbf{N}_p = \begin{bmatrix} N_1 \dfrac{X_p{}'}{\lambda_p} & 0 & 0 & 0 & N_2 \dfrac{X_p{}'}{\lambda_p} & 0 & 0 & 0 \\ 0 & N_1 X_p & 0 & 0 & 0 & N_2 X_p & 0 & 0 \\ 0 & 0 & H_1 X_p & H_2 X_p & 0 & 0 & H_3 X_p & H_4 X_p \end{bmatrix} \tag{2}$$
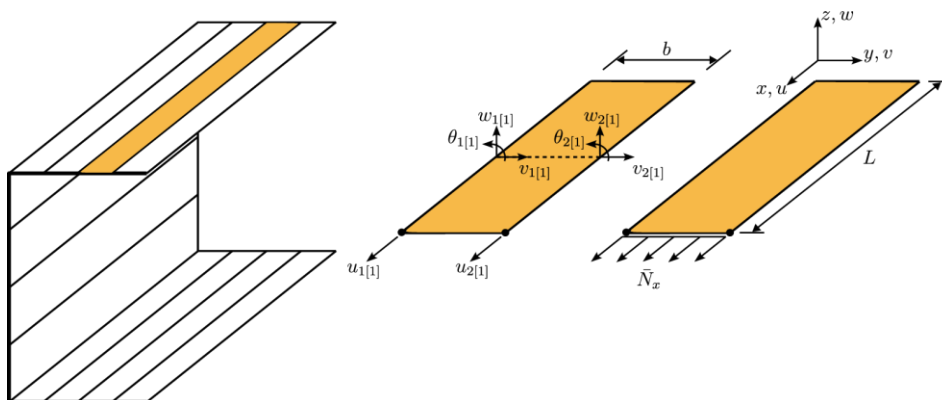
Figure 1. Finite strip discretization and DOF. Adapted from [8].

in which $N_1 = \bar{y} - 1$ and $N_2 = \bar{y}$, with $\bar{y} = y/b$, H_i are Hermite polynomials, and X_p and its derivative with respect x, $X_p{'}$, are trigonometric functions that satisfy specified boundary conditions, for instance: $X_p = \sin(\lambda_p x)$, with $\lambda_p = p \cdot \pi/L$ for a simply supported column [7, 8]. Observe that X_p is used for v and w, and $X_p{'}$ for u. This comes from the fact that each strip is treated as a beam under small strain/displacement, such that the axial displacement is determined using the slopes of the deflection.

Considering that each strip deforms as a long-laminated plate and assuming the Kirchhoff thin plate theory, the strain field for each strip can be written as:

$$\boldsymbol{\varepsilon} = \begin{Bmatrix} \varepsilon_x \\ \varepsilon_y \\ \gamma_{xy} \end{Bmatrix} = \begin{Bmatrix} \dfrac{\partial u}{\partial x} \\ \dfrac{\partial v}{\partial y} \\ \dfrac{\partial u}{\partial y} + \dfrac{\partial v}{\partial x} \end{Bmatrix} + z \begin{Bmatrix} -\dfrac{\partial^2 w}{\partial x^2} \\ -\dfrac{\partial^2 w}{\partial y^2} \\ -2\dfrac{\partial^2 w}{\partial x \partial y} \end{Bmatrix} \Rightarrow \boldsymbol{\varepsilon} = \boldsymbol{\varepsilon}_m + z\boldsymbol{\kappa} \tag{3}$$

where $\boldsymbol{\varepsilon}_m$ is the membrane strain field related to the membrane DOF (u and v), and $\boldsymbol{\kappa}$ are the curvatures of the midplane related to the bending DOF (w).

The Classical Lamination Theory (CLT) is adopted to model the laminate mechanical behavior [9, 10]. Thus, integrating the stresses through the thickness of a laminated strip, and assuming an orthotropic behavior for each ply, the generalized stress-strain relation for a single laminated strip can be written as [9, 10]:

$$\begin{Bmatrix} N_x \\ N_y \\ N_{xy} \\ M_x \\ M_y \\ M_{xy} \end{Bmatrix} = \begin{bmatrix} A_{11} & A_{12} & A_{16} & B_{11} & B_{12} & B_{16} \\ A_{12} & A_{22} & A_{26} & B_{12} & B_{22} & B_{26} \\ A_{16} & A_{26} & A_{66} & B_{16} & B_{26} & B_{66} \\ B_{11} & B_{12} & B_{16} & D_{11} & D_{12} & D_{16} \\ B_{12} & B_{22} & B_{26} & D_{12} & D_{22} & D_{26} \\ B_{16} & B_{26} & B_{66} & D_{16} & D_{26} & D_{66} \end{bmatrix} \begin{Bmatrix} \varepsilon_x \\ \varepsilon_y \\ \gamma_{xy} \\ \kappa_x \\ \kappa_y \\ \kappa_{xy} \end{Bmatrix} \Rightarrow \begin{Bmatrix} \mathbf{N} \\ \mathbf{M} \end{Bmatrix} = \begin{bmatrix} \mathbf{A} & \mathbf{B} \\ \mathbf{B} & \mathbf{D} \end{bmatrix} \begin{Bmatrix} \boldsymbol{\varepsilon}_m \\ \boldsymbol{\kappa} \end{Bmatrix} \Rightarrow \boldsymbol{\sigma} = \mathbf{C}\boldsymbol{\varepsilon} \tag{4}$$

in which A_{ij}, B_{ij} and D_{ij} are the extensional, coupling, and bending stiffness matrices, respectively, N_x, N_y and N_{xy} are the in-plane and shear stresses resultants per unit length, and M_x, M_y and M_{xy} are bending and twisting moments per unit length.

For sake of compactness, we have adopted the same symbol for the strain field in Eq. (3) and the generalized strain vector in Eq. (4); nevertheless, $\boldsymbol{\varepsilon}$ is hereafter referred to as the vector expressed in Eq. (4). Additionally, derivatives shown in Eq. (3) have been replaced with the well-known Greek letters that usually represent membrane and curvature related quantities of a plate in Eq. (4). Considering the relations in Eqs. (1), (2) and (3), the generalized strain vector in Eq. (4) can also be expressed as:

$$\boldsymbol{\varepsilon} = \sum_{p=1}^{m} \mathbf{B}_p\, \mathbf{d}_p \tag{5}$$

where $\mathbf{B}_p$ is the so-called strain-displacement matrix.

The elastic stiffness matrix, $\mathbf{k}_e$, can be derived by using the internal strain energy, U [7, 8]:

$$U = \frac{1}{2}\int_0^L \int_0^b \boldsymbol{\varepsilon}^T\,\boldsymbol{\sigma}\,dydx = \sum_{p=1}^{m}\sum_{q=1}^{m} \frac{1}{2}\mathbf{d}_p^T \left(\int_0^L \int_0^b \mathbf{B}_p^T\, \mathbf{C}\, \mathbf{B}_q\, dydx \right) \mathbf{d}_q = \sum_{p=1}^{m}\sum_{q=1}^{m} \frac{1}{2}\mathbf{d}_p^T \mathbf{k}_e^{pq} \mathbf{d}_q \tag{6}$$

$$U = \frac{1}{2}\boldsymbol{d}^T \boldsymbol{k}_e \boldsymbol{d} \tag{7}$$

where $\mathbf{k}_e^{pq}$ is the elastic stiffness matrix related to strains and stresses that come from X_p and X_q, respectively. The expressions in Eqs. (4) and (5) have been used in the second step of the mathematical development above.

The geometric stiffness matrix for an elastic buckling analysis can be derived from an additional work created by nonlinear terms only presented in ε_x of buckling displacements. Therefore, considering only axial buckling problem, the additional work V can be expressed as [7, 8]:

$$V = \frac{1}{2}\int_0^L \int_0^b \bar{N}_x \left[\left(\frac{\partial u}{\partial x}\right)^2 + \left(\frac{\partial v}{\partial x}\right)^2 + \left(\frac{\partial w}{\partial x}\right)^2 \right] dy dx = \frac{1}{2}\sum_{p=1}^m \sum_{q=1}^m \mathbf{d}_p^T \left(\bar{N}_x \, \mathbf{G}_p^T \, \mathbf{G}_q\right)\mathbf{d}_q = \frac{1}{2}\sum_{p=1}^m \sum_{q=1}^m \mathbf{d}_p^T \mathbf{k}_g^{pq}\mathbf{d}_q \quad (8)$$

$$V = \frac{1}{2}\mathbf{d}^T \mathbf{k}_g \mathbf{d} \tag{9}$$

where $\bar{N}_x$ is the traction force per unit length given by an external force, and $\mathbf{G}_p$ is the matrix containing the partial derivatives of the shape functions.

The linearized buckling analysis consists in solving the generalized eigenproblem defined by:

$$\left(\mathbf{K} + \lambda \mathbf{K_g}\right)\mathbf{\Phi} = \mathbf{0} \tag{10}$$

where $\mathbf{K}$ is the global stiffness matrix assembled through element stiffness matrices, $\mathbf{K}_g$ is the global geometric stiffness matrix assembled through element geometric stiffness matrices for the reference load, λ are the eigenvalues associated with the buckling load factors, and $\mathbf{\Phi}$ are the buckling modes.

Remarks can be made related to the integrations carried out in Eqs. (6) to (9). In classic FSM formulation, where isotropic and orthotropic materials have mostly been used, such integrations with respect the x direction are usually carried out analytically, and the following expression may be useful [7, 10]:

$$I_1 = \int_0^L X_p X_q dx = \frac{L}{2} \quad I_2 = \int_0^L X_p{}'' X_q dx = -\frac{\pi^2 p^2}{2L} \quad I_3 = \int_0^L X_p X_q{}'' dx = -\frac{\pi^2 p^2}{2L}$$

$$I_4 = \int_0^L X_p{}'' X_q{}'' dx = \frac{\pi^4 p^4}{2L^3} \quad I_5 = \int_0^L X_p{}' X_q{}' dx = \frac{\pi^2 p^2}{2L} \tag{11}$$

if $p = q$, otherwise, $I_1 = I_2 = I_3 = I_4 = I_5 = 0$. Note that these results are for the case of simply supported columns. However, when we consider a full $\mathbf{C}$ matrix (see Eq. (4)), extra integrals can be obtained due to all the possible couplings:

$$I_6 = \int_0^L X_p{}' X_q{}'' dx \qquad I_7 = \int_0^L X_p{}'' X_q{}' dx \qquad I_8 = \int_0^L X_p{}' X_q dx \qquad I_9 = \int_0^L X_p X_q{}' dx \tag{12}$$

It is noteworthy to mention that such integrals are solved numerically in this study, and they appear in terms that consist of the product of them and the quantities A_{16}, A_{26}, B_{16}, B_{26}, D_{16} and D_{26} in $\mathbf{k}_e^{pq}$ matrix.

2.2. Uncoupling procedure

The formulation presented in the previous here can account for all possible couplings that may occur in the $\mathbf{C}$ matrix for arbitrary layups. However, natural boundary conditions are not always fully satisfied due to the choice of shape functions, which in turn might decrease the accuracy of the proposed approach. For instance, the condition $M_x = 0$ must be satisfied at both ends of simply supported columns. Thus, considering Eq. (4) for symmetric laminates ($B_{ij} = 0$):

$$M_x = D_{11}\kappa_x + D_{12}\kappa_{12} + D_{16}\kappa_{xy} = 0 \tag{13}$$

This condition can be exactly satisfied in two scenarios: either D_{ij} terms are equal to zero or the curvatures are equal to zero. In practice, the former case is impossible to happen because we have, at least, non-zero values for D_{11} and D_{12} (e.g. isotropic materials). Therefore, the equality in Eq. (13) can only be met when the curvatures are zero. However, due to the shape functions adopted in this study, such equality is never satisfied when $D_{16} \neq 0$, since κ_{xy} will never be equal to zero as it depends on $\cos(\lambda_p x)$, which is not zero at the ends of the column (i.e. at $x = 0$ and $x = L$).

In addition, the series obtained by means of integrations in Eq. (12) are uncoupled for simply supported strips [11]. This means that for terms $\mathbf{k}_e^{pp}$ (when $p = q$) all the entries related to the terms in Eq. (11) are non-zero, which are the entries presented in isotropic and orthotropic materials. On the other hand, all the entries associated with the bending-twisting and stretching-shear couplings in $\mathbf{C}$ matrix (i.e. D_{16} and D_{26}) vanish because these entries are related to the quantities in Eq. (12), as shown in Figure 2.

In that spirit, we propose three different approaches that are named *full*, *stiffness*, and *flexibility* to buckling analysis of thin-walled laminated columns using FSM. The *full approach* considers all possible terms that appear in $\mathbf{C}$ matrix. In the *stiffness approach*, we straightly discard the terms D_{16} and D_{26}, keeping the

other terms unaltered. Finally, the *flexibility approach* encompasses three stages as follows. Firstly, we invert the matrix **C** to obtain the flexibility matrix (**F**). Then, the terms corresponding to B_{ij}, D_{16}, and D_{26} in **F** matrix can be zeroed, for instance. Finally, the resultant **F** is inverted so that a new uncoupled **C** matrix is obtained. However, differently from the stiffness approach, the terms of this uncoupled **C** matrix are influenced by the couplings present in the original **C** matrix.
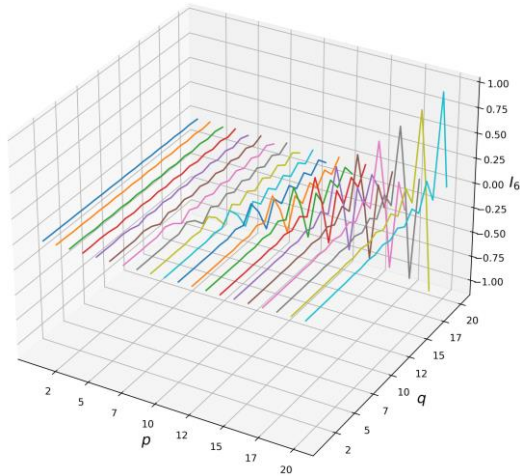
Figure 2. Normalized values for I_6.

Figure 3. Cross-sections of the columns.

3. RESULTS AND DISCUSSION

The presented formulation was implemented in the open source pyFSM toolkit at Laboratório de Mecânica Computacional e Visualização (LMCV) of Universidade Federal do Ceará (UFC). For assessment of its accuracy, stability analysis simply supported channel (flange width $b = 40$ mm and web height $d = 80$ mm) and I-section ($b = d = 40$ mm) columns (see Figure 3), both with total thickness $h = 1.048$ mm, were carried out for different layups. The material properties are [12]: $E_1 = 130.71$ GPa, $E_2 = 6.36$ GPa, $G_{12} = 4.18$ GPa, and $v_{12} = 0.32$; and the layups used are: L1 $[0°]_8$, L2 $[(0°/90°)_2]_S$, L3 $[(45°/-45°)_2]_S$, and L4 $[30°/-30°]_4$.

The obtained results are compared with CUFSM [13, 14] and FStr [15, 16] programs based on the FSM and ABAQUS [17] based on FEM. A discretization with 10 mm width finite strips was used for FSM programs, while meshes with 10 mm (channel) and 5 mm (I-section) square quadratic shell elements (S8R) was adopted for FEM. It is important to note that CUFSM and FStr programs consider only homogenous materials. Thus, they were used in this work only for columns with the L1 layup.

Figure 4 and Figure 5 presents the signature curves of channel and I-section columns, respectively. These curves show that the adopted layup has a strong influence on the buckling load of thin-walled composite columns, with the angle-ply layups (L3 and L4) layups presenting much larger buckling load than the orthotropic (L1) and cross-ply (L2) layups.

Figure 4 and Figure 5 also show the comparison of the three approaches (*full, stiffness*, and *flexibility*) proposed for consideration of the effects of laminate couplings on the critical buckling loads for the angle-ply laminates. It is important to note that this comparison makes no sense in the cases of orthotropic (L1) or symmetric cross-ply (L2) layups since they do not have coupling terms.

The differences between the three approaches are much pronounced for the angle-ply layups. The results show that *flexibility* approach gives better results, since it considers indirectly the effects of the coupling terms D_{16} and D_{26} for layup L3, and B_{16} and B_{26} for layup L4 in the constitutive matrix **C**. On the other hand, the *stiffness* approach leads to the worst accuracy since it completely neglects the effects of these terms. Finally, as discussed in Section 2.2, in the *full* approach some natural boundary conditions are not fully satisfied due to the choice of shape functions used in FSM and it leads to the differences observed in Figure 4 and Figure 5, particularly for short columns, where the local buckling mode dominates the response.

Although results have been presented for an antisymmetric angle-ply layup, it is known that these types of laminates cannot truly buckle, as they do not present a bifurcation load. This occurs due to the presence of stretch-bending coupling effects due to $B_{ij} \neq 0$. A deeper discussion about this can be found at [18, 19].

(a) L1.

(b) L2.

(c) L3.

(d) L4.

Figure 4. Signature curves for the channel column.

(a) L1.

(b) L2.

(c) L3.

(d) L4.
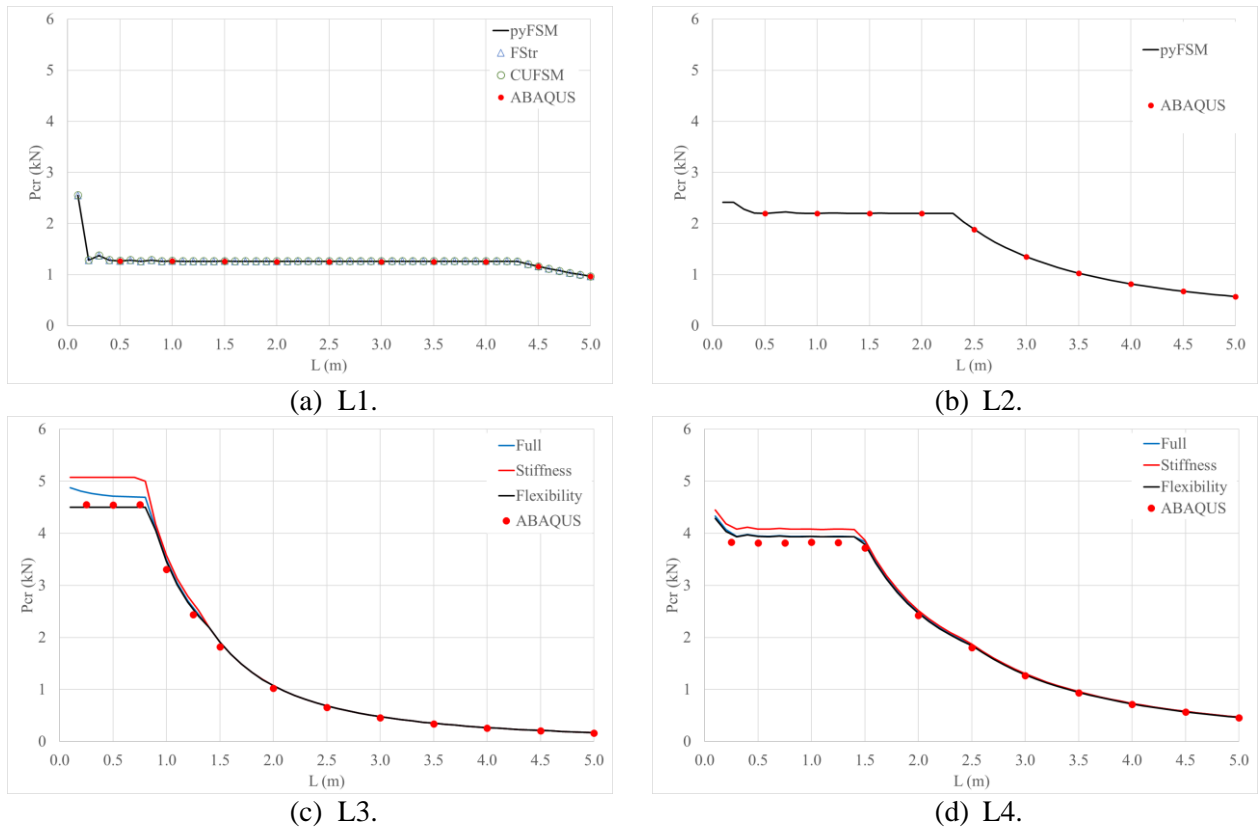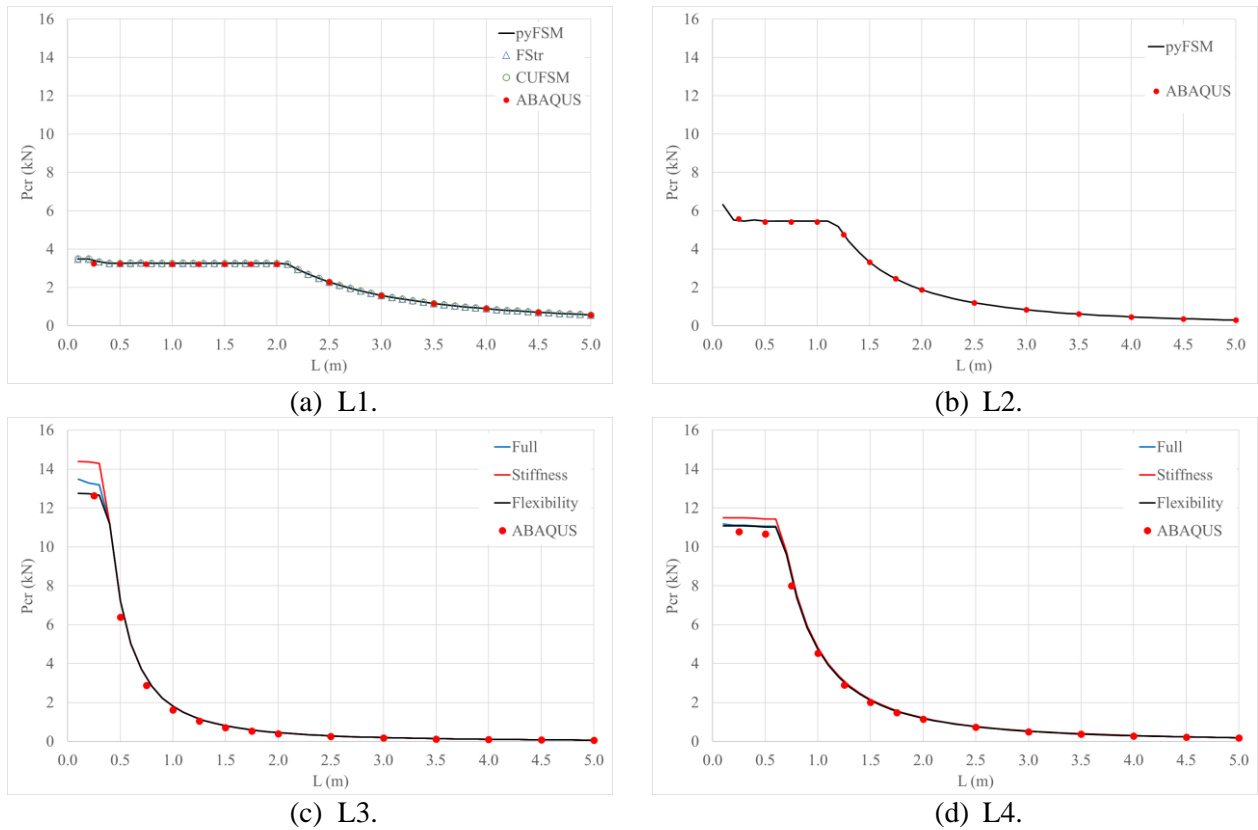
Figure 5. Signature curves for the I-section column.

It can be noticed that there is an excellent agreement in the results presented by pyFSM and those obtained by other FSM and FEM programs. The results show that for channel columns, the local buckling mode was dominant for L1 layup within the investigated length range, while global flexural-torsional and bending modes stood out for L3 and L4 layups. For the range of lengths analysed, a shift from local buckling

mode to global flexural-torsional mode was observed in all layups. However, only in layups L3 and L4 was noticed a transition from flexural-torsional mode to a bending mode. For the I-section columns only shifts from local to bending buckling mode was observed. The buckling modes obtained in pyFSM for 1000 mm length columns are presented in Figure 6 and Figure 7 for the channel and I-section, respectively.

(a) L1.   (b) L2.   (c) L3.   (d) L4.
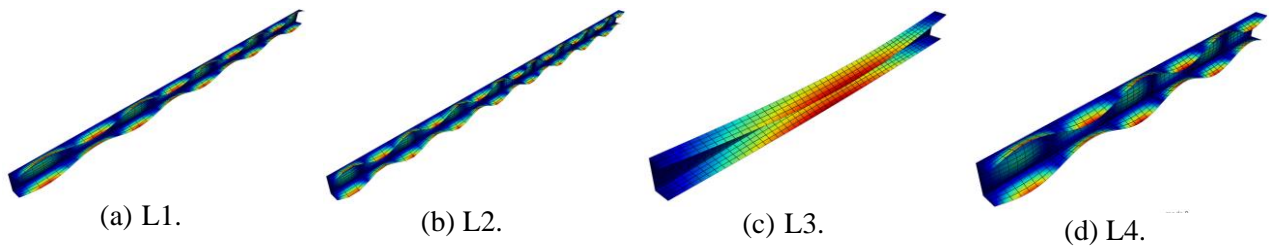
Figure 6. Buckling modes obtained in pyFSM for the channel column with 1000 mm length.

(a) L1.   (b) L2.   (c) L3.   (d) L4.
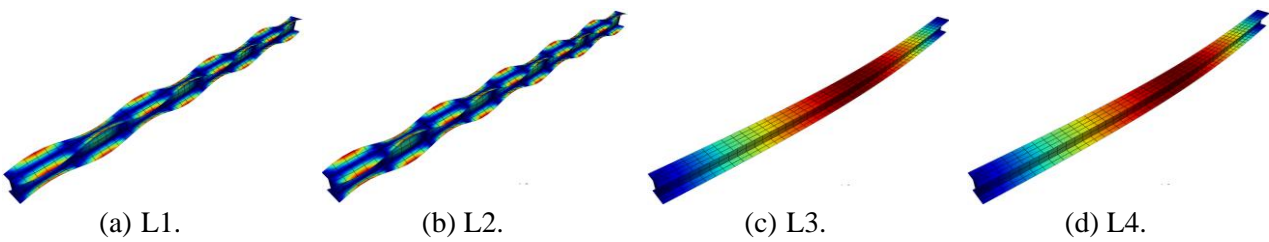
Figure 7. Buckling modes obtained in pyFSM for the I-section column with 1000 mm length.

4. CONCLUSIONS

This work presented a methodology to the stability analysis for thin-walled laminated columns with different layups using the Finite Strip Method. The Classical Laminated Theory is employed to determine the generalized stress-strain relation of a thin-walled single strip.

The proposed formulation can consider all possible couplings present in the constitutive matrix of laminates with arbitrary layups. However, numerical results show that that consideration of bending-twisting couplings decrease the accuracy of the formulation. Therefore, uncoupling procedures based on the stiffness and flexibility approaches were proposed to guarantee the satisfaction of natural boundary conditions associated with simply supports. It was verified using numerical examples that the *flexibility* approach lead to more accurate results.

The signature curves of laminate channel and I-section columns were traced for different layups and an excellent agreement was verified between the results of the proposed methodology with those obtained by FEM and FSM programs. Furthermore, the computational implementation developed in this work was capable of accurately evaluate the transition between the different buckling modes of thin-walled laminated columns with open cross-sections.

4.1. Declaration of Competing Interest

The authors declare no conflict of interest.

4.2. Acknowledgements

5. REFERENCES

[1] S.C.M. D'Aguiar and E. Parente Junior. Local buckling and post-critical behavior of thin-walled composite channel section columns. *Latin American Journal of Solids and Structures*, 15(7), e56, 2018.

[2] L.A.T. Mororó, A.M.C. Melo, E. Parente Junior. Geometrically nonlinear analysis of thin-walled laminated composite beams. *Latin American Journal of Solids and Structures*, 12(11):2094–117, 2015.

[3] L.A.T. Mororó et al. Corotational elements for thin-walled laminated composite beams with large 3D rotations. T*hin-Walled Structures*, vol. 152, pp. 106375, 2020.

[4] J. Aguiar Junior, E. Parente Junior, M.S. Mederiso Junior. Assessment of the load-carrying capacity of laminated composite columns. *In: Proceedings of the 6th Brazilian Conference on Composite Materials*, 2022.

[5] G. Akhras, M.S. Cheung, W. Li. Static and vibration analysis of anisotropic composite laminates by finite strip method. *Int. J. Solids Structures*, vol. 30, no. 22, pp. 3129-3137, 1993.

[6] D.J. Dawe. Use of the finite strip method in predicting the behaviour of composite laminated structures. *Composite Structures*, vol. 57, no. 1-4, pp. 11-36, 2002.

[7] Y.K. Cheung, L.G. Tham. *Finite Strip Method*. Taylor & Francis, 1998.

[8] Z. Li et al. Review: Contrained finite strip method developments and applications in cold-formed steel design. *Thin-Walled Structures*, vol. 81, pp. 2-18, 2014.

[9] R.M. Jones. *Mechanics of Composite Materials*. Taylor & Francis, 2nd ed., 1999.

[10] E. J. Barbero. *Introduction to composite materials design*. CRC Press, 2011.

[11] M.S. Cheung, G. Akhras, W. Li. Stability analysis of anisotropic laminated composite plates by finite strip method. *Computers & Structures*, vol. 49, no. 6, pp. 963-967, 1993.

[12] H. Debski, T. Kubiak and A. Teter. Experimental investigation of channel-section composite profiles behavior with various sequences of plies subjected to static compression. *Thin-Walled Structures*, v. 71, pp. 147-154, 2013.

[13] B.W. Schafer. *Cold-formed steel behavior and design: analytical and numerical modeling of elements and members with longitudinal stiffeners*. Dissertation (PhD) - Cornell University, Ithaca, New York, 1997.

[14] B. W. Schafer. CUFSM – Constrained and Unconstrained Finite Strip Method 2023 [Computer software]. (https://www.ce.jhu.edu/cufsm/)

[15] J. A. Lazzari, E. M. Batista. Finite strip method computer application for buckling analysis of thin-walled structures with arbitrary cross-sections. *REM - International Engineering Journal*, v. 74, p. 337-344, 2021.

[16] J. A. Lazzari, E. M. Batista. FSTr – Finite Strip Computer Application 2023 [Computer software]. (https://sites.google.com/coc.ufrj.br/fstr).

[17] Simulia. ABAQUS/Standard user's manual, Version 6.13, Providence, RI, USA, 2013.

[18] H. S. Shen. *Postbuckling behavior of plates and shells*. World Scientific Publishing Co., 2017.

[19] M. S. Qatu, A. W. Leissa. Buckling or transverse deflections of unsymmetrically laminated plates subjected to in plane loads. *AIAA Journal*, vol. 31, pp. 189–194, 1993.

6 Composites manufacturing

Organized and edited by

Sandra Maria da Luz
&
Carla Tatiana Mota Anflor

ENHANCING ADHESIVENESS OF GLASS-FIBRE COMPOSITES WITH LASER ABLATION TREATMENT

Thayane Ferreira[a], Luiza F.Soares [b], Rodrigo Teixeira Santos Freire [c], Pedro Camanho[d], Fabrizio Scarpa [e], Tulio H. Panzera[f]

(a) 0009-0008-5272-5368 (University of São João Del Rei – Brazil)
(b) 0000-0002-9339-7080 (University of São João Del Rei – Brazil)
(c) 0000-0001-5206-5639 (Federal University of São João del Rei – Brazil)
(d) 0000-0003-0363-5207 (Universidade do Porto – Portugal)
(e) 0000-0002-5470-4834 (University of Bristol, UK)
(f) 000-0001-7091-456X (Federal University of São João del Rei – Brazil)

CODE: BCCM7-48

Abstract: The adhesion of composite materials is essential in manufacturing, as it establishes a robust bond, eliminates the need for mechanical fasteners, reduces weight and cost, improves durability, and enhances manufacturing versatility. This study specifically investigates the surface treatment technique of laser ablation applied to glass fibre laminates, which creates a distinct surface topography that enhances the mechanical bonding between the parts. The investigation includes an analysis of laser cutting parameters, such as power, and their impact on the condition of the fibres. By establishing manufacturing parameters, parallel lines are created on the joints of 0° glass fibre laminates. An epoxy system serves as the matrix phase and adhesive for the composite joints, which are characterised through single-lap tests. Higher laser power leads to increased removal of the polymer matrix until fibre exposure occurs, resulting in enhanced adhesive shear strength. Treated surfaces exhibit various failure modes, including adhesive failure, cohesive failure and light-fibre-tear failure.

1. INTRODUCTION

Composite materials have found extensive use in numerous structural applications, leveraging their capacity to optimize properties and reduce weight [1, 2]. Widely applied not only in aerospace but also in naval, civil construction, orthopaedic, and sports devices [3], composites often necessitate attachment to other composite or metal structures. Traditional fasteners, such as screws and rivets, introduce stress concentrators and increase the mass of the structure. Conversely, bonding joints offer an alternative with advantages including versatility, weight reduction, improved performance, uniform stress distribution, and cost-effectiveness, making them a valuable method for creating structural joints and connections in various industries.

The reluctance to embrace bonding technology often arises from concerns about the insufficient adhesion of structural adhesives to various materials, necessitating proper pre-treatment of the substrates. Pre-treatments of adhesive joints are generally categorized as mechanical or chemical methods [4]. Chemical treatments may entail environmental and operational risks, prompting the exploration of alternatives such as laser ablation, which enhances adhesion without relying on chemicals. The effectiveness of pre-treatments is linked to the augmentation of the free surface energy and wettability of the substrate, the modification of surface morphology to increase roughness and promote mechanical interlocking, or a combination of these factors [5].

The physical surface treatment involving the removal of the matrix phase (polymer) from the surface of laminate composites, without harming their fibres, is a crucial step in enhancing adhesion and integrity. This approach enables the adhesive to directly bond to the load-transmitting fibres, eliminating the necessity for holes and mechanical fasteners. Furthermore, this process serves as an effective method for eliminating release agents from the surface, which could potentially impede adhesion [6], while also addressing potential contamination and facilitating direct fixation without compromising quality [7].

Wu et al. examined the impact of laser ablation surface treatment on the performance of AA6022-T4 joints, noting that the sample featuring a uniform and deep groove exhibited the highest shear strength. They proposed investigating the effects of grooves with varying depths on the adhesive shear strength in future studies [8].

Li et al. investigated the impact of various aspects of micro-grooves created by laser ablation—such as depth, spacing, and patterns—on the shear strength of adhesive joints between CFRP and aluminium alloy. Their findings revealed that increasing the groove depth led to a higher shear strength. However, excessive depth could result in the formation of air bubbles during the bonding process, consequently diminishing the quality of the adhesive layer [9].

Andarabi et al. applied various patterns of laser-engraved grooves on aluminium substrates, which were then evaluated in single-lap shear tests. The micro and nano-topography created on the metallic surface resulted in an increased interfacial area, mechanical interlocking, and cohesive failure at the joint interface. The outcomes of laser surface treatment were contrasted with those of an acid-alkaline chemical treatment, with the laser ablation demonstrating superior performance [10, 11].

This study details the efficacy of laser ablation treatment on glass fibre composite joints, wherein various laser cutting parameters including speed and power levels are investigated. The surface characterisation is carried out using an optical microscope, and the mechanical shear strength of the bonded joints is determined through single-lap shear testing.

2. MATERIALS AND METHODOLOGY

2.1. Materials

Glass Fibre Reinforced Polymer (GFRP) is produced by infusing four cross-ply glass fabrics, each with a 200 g/m^2 grammage. The matrix phase comprises epoxy resin (MR M) and hardener (MR 951) provided by Huntsman (Brazil), with a mixing ratio of 10:1, respectively.

2.2. Methodology

2.2.1 Fabrication of the GFRP

After cleaning the glass surface, a release agent is applied, involving three steps of release wax followed by the application of liquid release agent to facilitate easy removal of the laminate and achieve a smooth finish post-curing. Subsequently, four 320 x 360 mm^2 glass fibre fabrics and release film, peel ply, and flow are stacked. An infusion system is constructed, incorporating tubes, connectors, and valves to ensure the even distribution of resin through the glass fibres, followed by applying vacuum pressure. The pump is left in place for 1 hour, after which the parts are left under vacuum for 24 hours to complete the curing process.

2.2.2 Laser ablation parameters

To investigate the impact of speed and power parameters on the grooves created by laser ablation, cuts of 400 mm are executed using the machine Robotech 150 W (CO_2). The speed levels vary from 300 to 1000 mm/s, and the power ranges from 11 to 28W. An optical microscope is used to analyse the grooves, assess the polymer removal, examine the integrity of the fibres, and measure the cutting width.

2.2.3 Single-Lap Shear Testing

The samples are crafted using moulds created by a 3D printer, with dimensions of 25.4 x 100 mm^2 and a nominal thickness of 2.5 mm, in accordance with ASTM D5868 [12]. These moulds enable the alignment of the composite beams. Five samples are generated for each condition: (i) surface treated with laser ablation without polymer removal at 12 W power, (ii) surface treated with laser ablation without

damaging the fibres at 20 W power, and (iii) surface treated with laser ablation resulting in slight fibre damage at 28 W power. The laser grooves are lines oriented at 0°, i.e., in the longitudinal load direction.

The single lap shear test is conducted on the single overlap joints at a speed of 13 mm/min utilising a Shimadzu AGX-Plus-100 kN testing machine. This test determines the maximum force and stress sustained by the bonded joint, while the failure modes are observed following the guidelines outlined in the ASTM D5377 standard [13].

3 RESULTS AND DISCUSSION

3.1 Surface Treatment

To create three distinct grooves, power levels of 12 W, 20 W, and 28 W are specified at a speed of 700 mm/s. Notably, the 12 W level produces a rough scratch of approximately 400 μm without removing polymer from the laminate. At 20 W, polymer removal occurs while maintaining the integrity of the glass fibres, resulting in grooves of approximately 300 μm. The 28 W power completely removes the polymer, leading to fibre burning and a width similar to that of the 20 W power. Figure 1 depicts the assessment of the three surfaces via single-lap testing.
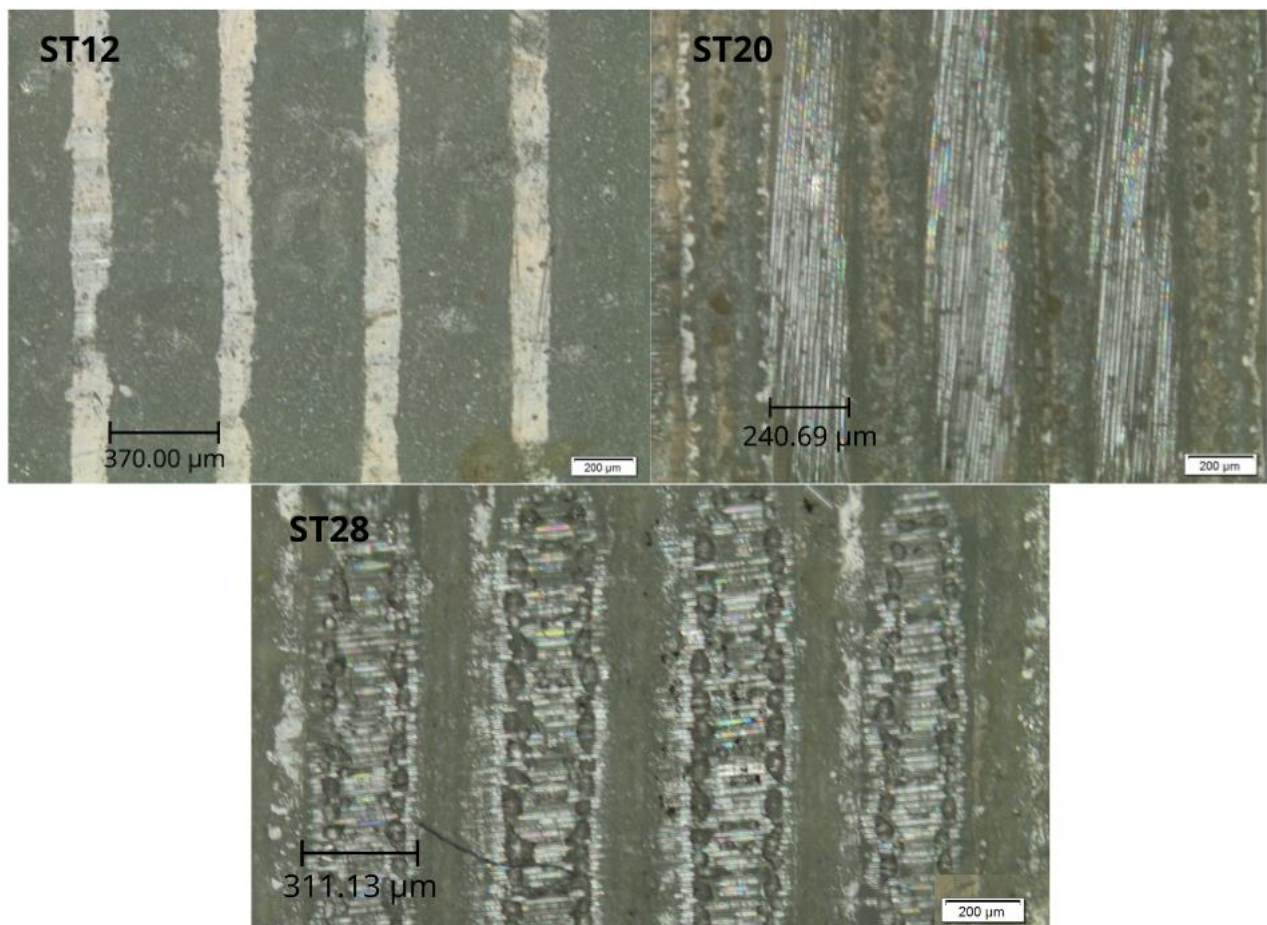
Figure 1. ST12 without total polymer removal, ST20 without damaging the fibers and ST28 causing considerable damage.

3.2 Shear Strength and Failure Modes

The results demonstrate a significant increase in shear force and strength of the joints in the presence of grooves, as depicted in Table 1. Utilising Analysis of Variance (ANOVA) and Tukey tests at a 95% confidence level, significant effects of the treatments on adhesive force and shear are indicated by p-values of 8.32e-05 and 0.005, respectively. Furthermore, Tukey's multiple comparison analysis reveals statistically different means between the treatments, with ST20 and ST28 exhibiting equivalent means denoted by sharing Letter Group A. Notably, ST20 and ST28 achieve approximately 69% higher adhesive properties than ST12. Higher laser power levels lead to exposed fibres, resulting in a rougher surface and

improved mechanical interlocking between the joint interfaces. The distinct modes of failure obtained include adhesive failure (ADH), cohesive failure (COH), and light-fibre-tear failure (LFT). ST12 samples exhibit only ADH, while ST20 samples display a combination of COH, ADH, and LFT failures and ST28 samples present both COH and LFT failures, as shown in Figure 2.

Table 1. The single lap shear test results.

Treatment	F (N)	Tukey	τ (MPa)	Tukey
ST12	2575.36±231.74	B	45.39±2.21	B
ST20	4247.40±349.89	A	76.65±9.91	A
ST28	4456.79±232.08	A	97.10±10.46	A

Figure 2. Failure modes: 12 W (left), 20 W (middle), 28 W (right) treated samples.

4 CONCLUSIONS

This study described the impact of laser ablation-treated surfaces on the performance of composite joints. The higher laser power resulted in increased removal of the polymer matrix until the fibres were exposed, leading to enhanced adhesive strength, particularly observed in treatments with higher laser power (ST20 and ST28) due to the amplified interlocking effect. Treated surfaces exhibited different failure modes, including adhesive failure (ADH), cohesive failure (COH), and light-fiber-tear failure (LFT). ST20 and ST28 samples resulted in light-fibre-tear (LFT) failure mode, while ST12 exhibited adhesive (ADH) failure only. Overall, this study demonstrates the effectiveness of laser ablation in enhancing the adhesive performance of glass fibre composite joints, thereby increasing their resistance to failure.

4.1 Declaration of Competing Interest

The authors declare no conflicts of interest.

4.2 Acknowledgements

5 REFERENCES

[1] C. Suresh Kumar, V. Arumugam, Jack J. Kenned, R. Karthikeyan & A. R. Jac Fredo (2020) Experimental investigation on the effect of glass fiber orientation on impact damage resistance under cyclic

indentation loading using AE monitoring, Nondestructive Testing and Evaluation, 35:4, 408-426, DOI: 10.1080/10589759.2019.1684491

[2]   Cascino, A., Meli, E. & Rindi, A. A strategy for lightweight designing of a railway vehicle car body including composite material and dynamic structural optimization. Rail. Eng. Science 31,340–350 (2023). https://doi-org.ez32.periodicos.capes.gov.br/10.1007/s40534-023-00312-6)

[3]   Gualberto et al., 2021 e Wang et al., 2023

[4]   Hennemann, O. D.; Brockmann, W. Surface Morphology and Its Influence on Adhesion.J. Adhes. 1981, 12(4), 297–315. DOI: 10.1080/00218468108071208.

[5]   Musiari, F., Moroni, F., & Lutey, A. H. A. (2023). Enhanced mechanical interlocking of adhesive-bonded joints via tailored serrated patterns manufactured with laser ablation. The Journal of Adhesion, 1–35. https://doi-org.ez32.periodicos.capes.gov.br/10.1080/00218464.2023.2285431

[6]   Leone C, Genna S. Effects of surface laser treatment on direct co-bonding strength of CFRP laminates. Compos Struct 2018; 194: 240–251

[7]   Özgür Bora M, Çoban O, Akman E, et al. Comparison of novel surface treatments of Al 2024 alloy for al/cfrp adhesive bonded joints. Int J Adhes Adhes 2020; 103: 102721

[8]   Y. Wu, J. Lin, B.E. Carlson, L. Peng, M.P. Balogh, N.P. Irish, M. Yu, Effect of laser ablation surface treatment on performance of adhesive-bonded aluminum alloys, Surf. Coat. Technol. 304 (2016) 340–347.

[9]   Li, H., Zhu, Y., Meng, X., Li, S., Du, W., & Qin, X. (2023). Effect of laser generated microgrooves geometric parameters on the shear strength of CFRP-Aluminium alloy adhesive joints. The Journal of Adhesion, 99(10), 1744–1767. https://doi-org.ez32.periodicos.capes.gov.br/10.1080/00218464.2022.2158731

[10]   Ala Abedinzadeh Andarabi, Karim Shelesh-Nezhad, Tajbakhsh Navid Chakherlou, The effect of laser surface structuring patterns on the interfacial resistance of aluminum joints bonded with epoxy adhesive,International Journal of Adhesion and Adhesives, Volume 114, 2022, 103101, ISSN 0143-7496, https://doi.org/10.1016/j.ijadhadh.2022.103101.

[11]   1.1. İplikçi H, Barisik M, Türkdoğan C, et al. Effects of nanosecond laser ablation parameters on surface modification of carbon fiber reinforced polymer composites. Journal of Composite Materials. 2023;57(18):2843-2855. doi:10.1177/00219983231178892).

[12]   ASTM D5868-01(2014), Standard Test Method for Lap Shear Adhesion for Fiber Reinforced Plastic (FRP) Bonding, ASTM International, West Conshohocken, PA, 2014, www.astm.org. DOI: 10.1520/D5868-01R14.

[13]   `ASTM D5377 Designation: D5573 – 99– Standard Practice for Classifying Failure Modes in Fiber–Reinforced–Plastic (FRP) Joints, ASTM International, West Conshohocken, PA, 2014, www.astm.org.`

A COMPARATIVE STUDY OF HEXAGONAL AND CIRCULAR HONEYCOMB CELLS IN 3D-PRINTED SANDWICH PANELS

Alberto Jorge Baeza Campuzano[(a)*], Rodrigo José da Silva[(b)], Márcio Eduardo Silveira[(c)], Fabrizio Scarpa[(d)], Túlio Hallak Panzera[(e)]

(a) 0000-0002-7241-6836 (Federal University of Sao Joao del Rei – Brazil)
(b) 0000-0001-8016-3165 (Federal University of São João del-Rei – Brazil and University of Bristol – United Kingdom)
(c) 0000-0001-9805-5277 (Federal University of Sao Joao del Rei – Brazil)
(d) 0000-0002-5470-4834 (University of Bristol – United Kingdom)
(e) 0000-0001-7091-456X (Federal University of Sao Joao del Rei – Brazil)
* Corresponding author: baezacaljo@gmail.com

Abstract: The honeycomb core is recognised as a crucial core material in sandwich panels. These lightweight structures are designed to meet specific mechanical requirements based on their applications. During bending characterisation, where the panels are subjected to compressive and shear loads, the core influences the stress distribution throughout the structure, impacting its overall rigidity and flexibility. The mechanical properties of the panels are influenced by the characteristics of both, the core and the skins. 3D printing offers a valuable technique for manufacturing sandwich panels with different cores, offering a better understanding of the effect of the core on their mechanical behaviour. This study compares three types of honeycomb cores (hexagonal in L- and W-direction and circular) with similar contact areas using 3D printed panels. The results show the phenomenon of wrinkling, in hexagonal cores in the L-direction. Circular cell panels exhibit high load capacity, flexural, and toughness modulus. While W-core panels demonstrate statistically similar flexural modulus and load compared to circular-core panels, reduced toughness modulus is achieved. Furthermore, L-core panels demonstrated a high toughness modulus. L-cell panels have a lower density than circular cell panels, followed by W-cell core panels, leading to reduced specific mechanical properties.

1. INTRODUCTION

Sandwich panels have been designed for many engineering applications, offering a combination of lightweight and high mechanical performance, particularly under bending. These panels typically consist of two thin sheets called skins, usually made of metal, polymers, or composites, while the core comprises thin-walled structures, lattices or scaffolds [1-3]. The panels are designed to absorb energy; however, their durability is affected by the bonding conditions [4, 5].

Tubular and hexagonal cores demonstrate excellent mechanical responses under three-point bending, compared to auxetic geometries [6, 7]. However, the fabrication of a full integral sandwich panel remains a challenge, prompting exploration of fused deposition modelling technology for 3D printing different core shape structures, such as cubic, bio-inspired structures and scaffolds [8-10].

In addition, the Finite Element Analysis (FEA) has been implemented on sandwich panels, considering static and explicit analysis with shell elements to minimise the computational cost. However, simplifications, such as removing contacts and employing linear elastic analysis, have been made [11].

Although 3D printing has been applied, a clear comparison between hexagon and circular core structures in integral sandwich panels with similar skin-core contact areas is yet to be established due to differences in composition, dimensions, and the use of metal skins. This work aims to compare circular and hexagonal (W- and L- direction) core structures in integral sandwich panels with similar skin-core contact areas.

2. METHODOLOGY

Three types of integral sandwich panels are fabricated, including circular and hexagonal (in L- and W-directions) structures, with five samples for each configuration. The panels are constructed using an Ender-3-S1, with polylactic acid (PLA) and 1.75 mm filament diameter supplied by 3DLab Brazil. The panel dimensions measure $200 \times 80 \times 15$ mm^3, with a skin thickness of 0.5 mm, as shown in Fig. 1.
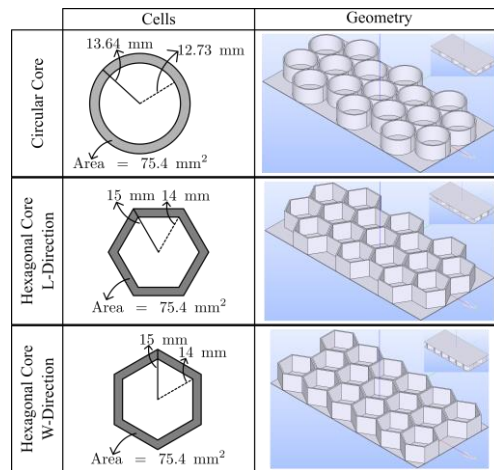
Figure 1. Dimensions of the integral sandwich panels.

The printing parameters include a nozzle and bed temperature set at 200 and 60°C, a layer height of 0.2 mm, 2 wall line count, a specified line pattern, 100% infill, and a speed of 50 mm/s for the outer wall and infill with a travelling speed of 150 mm/s and retraction speed of 40 mm/s. Supports and skirts are disabled for build plate adhesion, while the other configurations remain at their default settings. The estimated printing time is approximately 8 to 9 hours.

Three-point bending tests are conducted using an Instron machine equipped with a 50 kN load cell, employing a speed of 2 mm/min and a support span of 109 mm, following ASTM D790 [12] and ASTM C939 standards [13]. A statistical comparison is performed using ANOVA and the Tukey test, with the latter identifying equivalent means when sharing the same group letter. In case of PLA testing, five dog bone samples are fabricated according to ASTM D638 [14], reaching in a mean Young modulus of 3000.54 MPa and a Poisson´s ratio of 0.35.

The FEA analysis of the integral sandwich panels under three-point bending is carried out in Hyperworks® 2022 with the optistruct solver, taking into account the mechanical properties obtained from the PLA tensile testing. A density of 1.367 g/cm3 is considered, along with the MATS1 and PLASTIC material types, with PSOLID for the panels, PSHELL for the indenter and supports, PCONT for the contact between the panels and the rollers, the stiffness as AUTO and 0.1 as friction coefficient allowing separation.

3. RESULTS AND DISCUSSION

3.1. Three-point bending

In the linear regime, up to 1.75 mm deflection, the panels exhibit a similar mechanical response without failure. However, wrinkling becomes noticeable around 2.75 mm up to 3.4 mm in L- L-direction and circular core cells. In contrast, the W- direction does not demonstrate a wrinkling effect. All three-panel types display a maximum force of 1.1 and 1.2 kN (L and W direction). Winkling causes the upper skin to buckle either

inward or outward when the core overloads the skin under compression, resulting in the observed effects. The phenomenon occurs due to the core rigidity overloading the skin under compression [15].

A close approximation between the theoretical (535 MPa) and experimental (514 to 573 MPa) flexural modulus is achieved, indicating an almost absence of shear deformation in the linear elastic regime, as suggested in [16]. The experimental data demonstrate a variation not exceeding 7.8 %. Furthermore, the ANOVA analysis reveals P-values lower than 0.05 for all properties, meaning distinctions among the three panels. The Tukey test reveals that circular cells are statistically equivalent to panels with W-direction cores (group A) in terms of flexural modulus. However, L-direction cores exhibit a reduction of approximately 10% (group B). Moreover, circular cells have a higher modulus of toughness, while L and W- direction cores exhibit reductions of 12 and 32 %, respectively, in comparison to circular core cells. When correlating the modulus of toughness with dynamic impact response, the findings align with those reported by [1], indicating that circular cores show promise as absorbers of impact energy.

The specific bending curves for hexagonal cores exhibit differences compared to circular cores. Circular-core panels reach a force of 1.2 kN and a displacement of 3.6 mm, while the hexagonal-core panels achieve 1.1 kN and 3.5 mm in the L-direction and 2.6 mm in the W-direction. A noticeable increase in the gap between the circular and hexagonal panels is observed as the force and deformation increase (Fig. 2a). Conversely, the gap remains constant in terms of specific mechanical properties, resulting in similar behaviour up to 2.5 mm (see Fig. 2b).
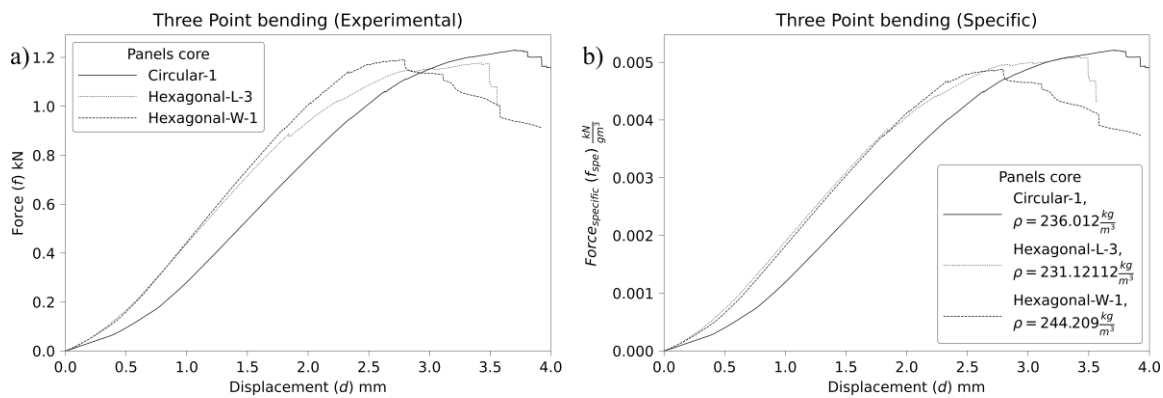
Figure 2. Typical curves under three-point bending, a) absolute force, b) specific force.

3.2. Numerical analysis

In the linear regime, the FEA analysis aligns with the experimental data. However, in the non-linear regime, a weak correlation is observed due to the anisotropic behaviour induced by additive manufacturing, as seen in Fig. 3. It is noteworthy that the W and L-direction play a significant role in the wrinkling phenomena. Specifically, the L-direction demonstrates greater rigidity than the W-direction along the longitudinal direction, resulting in an excessive load on the skin.
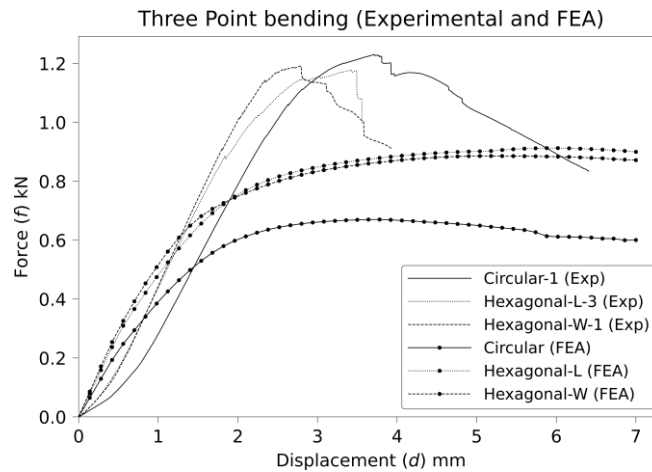
Figure 3. Details of the 3D printed panels, a) circular, b) L-direction and c) W- direction.

3.3. Failure mode analysis

In Fig. 4a, the complete melting of a circular core panel is depicted, with the cylinder fully molten, increasing resistance. In contrast, the L-core direction exhibits a cell span, leading to a sagging effect, poor adhesion and fast cooling (Fig. 4b). On the other hand, the W-direction demonstrates a sagging effect, but the corners create thread overlapping, enhancing melting and adhesion (Fig. 4c).
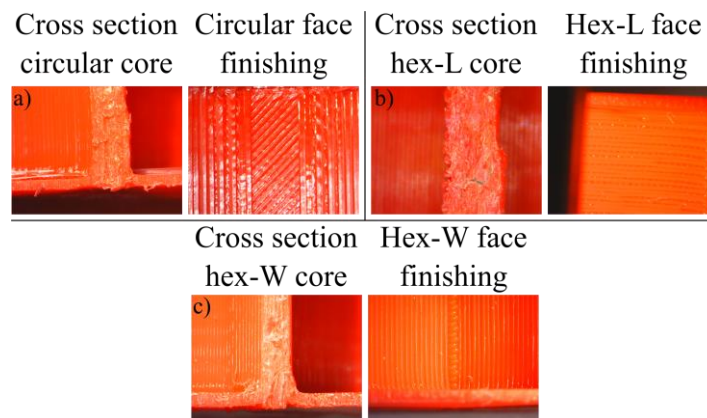
Figure 4. Details of the 3D printed panels, a) circular, b) L-direction and c) W-direction.

4. CONCLUSIONS

A comprehensive comparison of the three types of sandwich panels reveals the circular cores as the most prominent in terms of resistance in load capacity, flexural modulus and toughness. This superiority is attributed to the melting and high interaction between the threads, mitigating the effect of hanging. The W–direction panels achieve statistically equivalent flexural modulus and load capacity when compared to those made with circular cores. In contrast, the L-direction panels exhibit higher toughness than the other direction, but they tend to be less rigid due to their packing and sagging effect on the cells. The failure modes observed were wrinkling or detachment of the thread, stemming from its anisotropic behaviour induced by the 3D printer. Notably, specific properties increase when the panel reduces its weight, a phenomenon observed solely in the L-direction.

4.1. Declaration of Competing Interest

The authors declare no conflict of interest.

4.2. Fundings

4.3. Acknowledgements

5. REFERENCES

[1] N. O. Cabrera, B. Alcock, and T. Peijs. Design and manufacture of all-PP sandwich panels based on co-extruded polypropylene tapes. Composites Part B: Engineering, Volume 39(7-8) 1183–1195, 2008 (https://doi.org/10.1016/j.compositesb.2008.03.010).

[2] Meghdad Gholami, Reza Akbari Alashti, and Alireza Fathi. Optimal design of a honeycomb core composite sandwich panel using evolutionary optimisation algorithms. Composite Structures, Volume 139:254–262, 2016, (https://doi.org/10.1016/j.compstruct.2015.12.019).

[3] H. G. (Howard Godfrey) Allen. Analysis and design of structural sandwich panels., 1 edition, 1969, Pergamon Press.

[4] Zhonggang Wang, Zhendong Li, and Wei Xiong. Experimental investigation on bending behavior of honeycomb sandwich panel with ceramic tile facesheet. Composites Part B: Engineering, Volume 164:280–286, 2019, (https://doi.org/10.1016/j.compositesb.2018.10.077).

[5] Bo Cen et al. Mechanical behavior of novel GFRP foam sandwich adhesive joints. Composites Part B: Engineering, Volume 130:1–10, 2017, (https://doi.org/10.1016/j.compositesb.2017.07.034).

[6] Lívia Avila de Oliveira et al.. A novel sandwich panel made of prepreg flax skins and bamboo core. Composites Part C: Open Access, Volume 3:100048, 2020, (https://doi.org/10.1016/j.jcomc.2020.100048).

[7] Zarna, Chiara et al.. Bending properties and numerical modelling of cellular panels manufactured from wood fibre-PLA-biocomposite by 3D-printing. Composites Part A: Applied Science and Manufacturing. Volume 165. 2022, (https://doi.org/107368. 10.1016/j.compositesa.2022.107368).

[8] Xin, Zhibo et al.. Compression performance and analytical model of hexagonal-core sandwich panels fabricated by 3D printed continuous carbon fiber-reinforced thermosetting epoxy composites. Materials Research Express. Volume 9. 2022, (https://doi.org/10.1088/2053-1591/ac8a3e).

[9] Zarna, et al.. Biocomposite panels with unidirectional core stiffeners - 3-point-bending properties and considerations on 3D printing and extrusion as a manufacturing method. Composite Structures. Volume 313. 2023, (https://doi.org/116930. 10.1016/j.compstruct.2023.116930).

[10] Peng, et al.. 3D printed sandwich beams with bioinspired cores: Mechanical performance and modelling. Thin-Walled Structures. Volume 161. 2021 ,(https://doi.org/107471. 10.1016/j.tws.2021.107471).

[11] Tafazoli, Mohammad, Nouri, Mohammad. Investigation of the experimental, statistical and optimisation of 3D printed lattice core sandwich panel energy absorber with novel configuration using response surface method. International Journal of Crashworthiness. Volume 27. 2020, (https://doi.org/1-12. 10.1080/13588265.2020.1786913).

[12] ASTM International, ASTM D790/15 - Standard Test Methods for Flexural Properties of Unreinforced and Reinforced Plastics and Electrical Insulating Materials, 2015.

[13] ASTM International, ASTM C393/C393M-16, Standard Test Method for Core Shear Properties of Sandwich Constructions by Beam Flexure, 2016.

[14] ASTM International, ASTM D638-14, Standard Test Method for Tensile Properties of Plastics, 2022.

[15] Bitzer, T. Honeycomb technology:materials, design, manufacturing, applications and testing, 1st edition (1997), Springer, Glasgow. https://doi.org/10.1007/978-94-011-5856-5

[16] R. J. da Silva et al., "A core rigidity classifier method and a novel approach to account for geometric effects on the elastic properties of sandwich structures," Composite Structures, vol. 282, p. 115075, 2022, (https://doi.org/10.1016/j.compstruct.2021.115075).

MANUFACTURING AND CHARACTERISATION OF PLA/CARBON DOTS COMPOSITE MATERIALS

Alberto Jorge Baeza Campuzano[a], Rafael Barbosa Rezende[b], Nestor Cifuentes Taborda[c], Júlio César dos Santos[d], Fabiano Vargas Pereira[e], Marzio Grasso[f], André Luís dos Santos[g], Túlio Hallak Panzera[h],

(a) 0000-0002-7241-6836 (Federal University of São João del Rei – Brazil)
(b) 0009-0001-9652-4495 (Federal University of Minas Gerais – Brazil)
(c) 0000-0003-3638-7959 (Federal University of Minas Gerais – Brazil)
(d) 0000-0002-7485-491X (Federal University of São João del Rei – Brazil)
(e) 0000-0002-0784-3233 (Federal University of Minas Gerais – Brazil)
(f) 0000-0002-2684-1874 (Cranfield University – United Kingdom)
(g) 0000-0002-1738-2792 (Federal University of São João del-Rei – Brazil)
(hf) 0000-0001-7091-456X (Federal University of São João del-Rei – Brazil)

* Corresponding author: baezacaljo@gmail.com

CODE: BCCM7-61

Abstract: Carbon dots (CDs) possess exceptional properties including adjustable photoluminescence, high quantum yield, low toxicity, small size, and considerable biocompatibility. These attributes, combined with their cost-effectiveness and versatility as a carbon source, make them highly appealing for various applications in biomedicine, catalysis, and optoelectronics. In this study, carbon dots are incorporated into polylactic acid (PLA) material to fabricate composite filaments with varying concentrations of carbon nanoparticles ranging from 0.1 to 5.0 wt%. These filaments are then used to produce tensile samples via 3D printing. The presence of CDs in PLA leads to enhanced mechanical properties in the final 3D-printed samples. The fluorescence of printed samples is also analysed during mechanical characterisation, revealing a decrease in fluorescence signal along with sample width as deformation increases. Notably, the incorporation of 0.5 wt% of carbon dots results in a significant improvement of the mechanical properties of the final 3D printed product. However, higher concentrations such as 1.0, 3.0, and 5.0 wt% exhibit a greater variation in properties, likely due to manufacturing challenges and micro defects. These findings highlight the importance of meticulous optimisation of carbon nanoparticle concentration to achieve desired mechanical properties without compromising the extrusion and printing process.

1. INTRODUCTION

The inclusion of different particles into polylactic acid (PLA) has become an area of interest. Particularly, the incorporation of carbon dots (CDs) has been found to enhance the mechanical properties and stability of PLA-CD composites [1], which have been used to fabricate stents through fused deposition modelling (FDM). However, despite these advantages, the fabrication of the filament composite continues to pose challenges [2].

The extrusion process is currently employed for processing filament composites, particularly utilising single-screw technology, as it reduces degradation while ensuring consistent diameter stability. As a result, the filament is exceptionally well-suited for fused deposition modelling [3].

Following the extrusion process to create PLA-CD filaments, the FDM process facilitates further homogenisation, resulting in improved mechanical performance, as evidenced in the final product comprising PLA-bronze [4]. It is important to note that FDM has the potential to degrade the composite material; however, the inclusion of diverse additives within the composite filament mitigates this effect [5], leading to an increase in tensile strength but a decrease in compressive strength. Lastly, an enhancement in mechanical properties has been observed by varying the weight percentages of various particle reinforcements, such as bronze, copper, and carbon nanotubes [6].

This work investigates the unidirectional printing and tensile testing of PLA-CD composites, considering different inclusions of carbon dots. In addition, it conducts a correlation between fluorescence and mechanical response.

2. METHODOLOGY

The carbon dots are fabricated using a scalable method described by Wang et al. [7], with some adaptations. The composite filament is manufactured using a desktop single-screw extruder, incorporating 7 different percentages of carbon dots (CD) (0.1, 0.3, 0.5, 0.7, 1.0, 3.0, and 5.0 wt%). The processing temperature is set at 130°C to prevent degradation of the PLA polymer matrix [8]. However, the formation of clusters is more pronounced due to the re-circulation of the material as it nears the nozzle end. This phenomenon aids in memory recovery as the polymer exits the nozzle, resulting in filament expansion to a certain degree [9].

Seven unidirectional composite samples for each percentage are produced using FDM technology with a Creality® Ender 3 S1 machine, following ASTM D638 [10], with reduced thickness and width to enable fluorescence recording. The fluorescence is captured using a camera and UV light to stimulate the carbon dots. The sample´s behaviour under UV light and its response during the tensile tests are shown in Fig. 1. The tested samples are examined under an optical microscope with polarised lenses to observe the residual stresses following the tensile test.
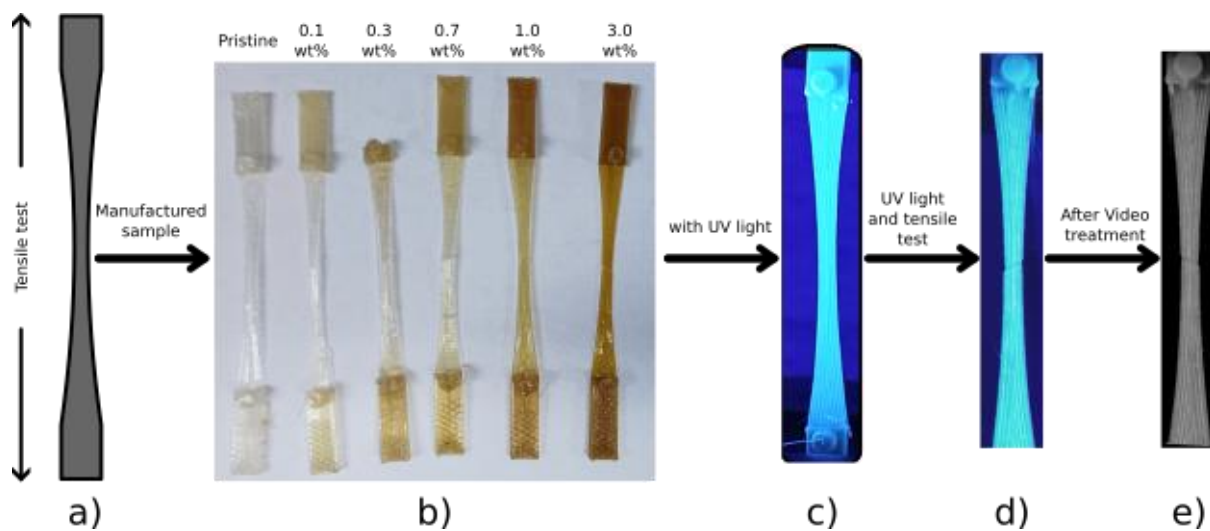
Figure 1. a) Sample design, b) manufactured sample with percentages, c)sample under UV light, d) sample after UV light exposure and failure, e) video analysis treatment.

3. RESULTS AND DISCUSSION

The tensile response reveals that the first four conditions exhibit minimal error in both Young's modulus and maximum tensile stress, making them the most promising percentages. However, higher error rates and manufacturing challenges are introduced with an increase in the percentage of CDs. In comparison, the pristine material exhibits a lower Young's modulus value than the seven percentages of CDs, while the 5 wt% condition shows similar results to the pristine material in terms of maximum tensile stress. These findings are illustrated in Fig. 2.
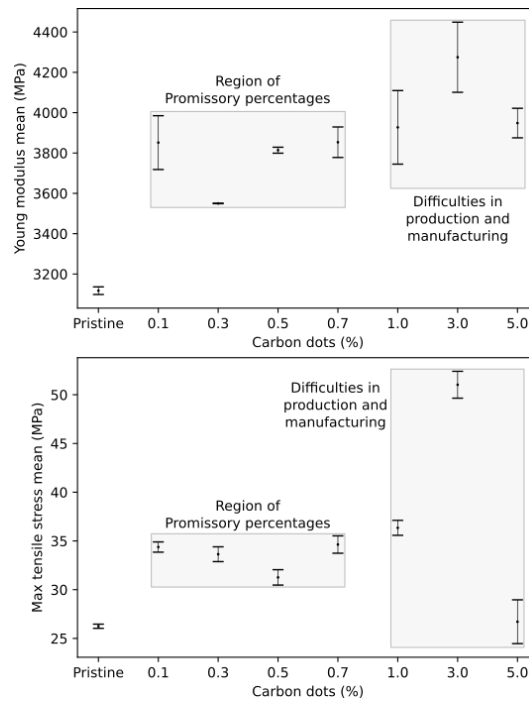
Figure 2. PLA-CDs percentage with seven samples each, upper) mean of the young modulus, lower) mean of the maximum tensile stress.

The Tukey test for the seven conditions and the pristine material indicates that samples with 0.1, 0.5, and 0.7 wt% CD exhibit equivalent means in Young's modulus and maximum tensile stress. In contrast, the last condition (5.0 wt%) and the pristine material demonstrate the lowest values for maximum tensile stress. Conversely, samples with 3.0 wt% CD achieve the highest Young's modulus and strength, as depicted in Table 1.

Table 1. Mean of the mechanical properties and Tukey test.

Material (wt%)	Mean modulus of elasticity (MPa)	Standard deviation (MPa)	Tukey test (Letter Group)	Mean tensile strength (MPa)	Standard deviation (MPa)	Tukey test (Letter Group)
Pristine (0)	3117.45	18.88	C	26.25	0.21	D
0.1	3851.70	133.43	B	34.37	0.53	BC
0.3	3549.86	1.18	BC	33.64	0.76	BC
0.5	3814.00	14.78	B	31.26	0.79	C
0.7	3853.50	75.66	B	34.63	0.89	BC
1	3927.21	182.38	AB	36.35	0.77	B
3	4274.92	173.82	AB	51.03	1.38	A
5	3948.44	73.33	AB	26.71	2.25	D

In the linear regime, there is minimal variation in fluorescence. However, as deformation increases, the tensile stress enters a non-linear regime, leading to changes in fluorescence, including an increase. An overshoot occurs, resulting in a change in fluorescence and a decrease in width. As this process progresses, distinct differences emerge in the samples with 0.1%, 0.3%, and 0.7% carbon dots. The sample with 0.7% carbon dots shows a substantial increase in fluorescence, while the other two samples demonstrate a decrease. This behaviour correlates closely with the amount of carbon dots. As the sample becomes thinner, the carbon dots disperse, providing more space for the overlapped particles in the 0.7% sample. Conversely, in the 0.1% and 0.3% samples, the particles disperse, and no additional particles fill the vacated space, resulting in a decrease in fluorescence. This phenomenon is illustrated in Figure 3.
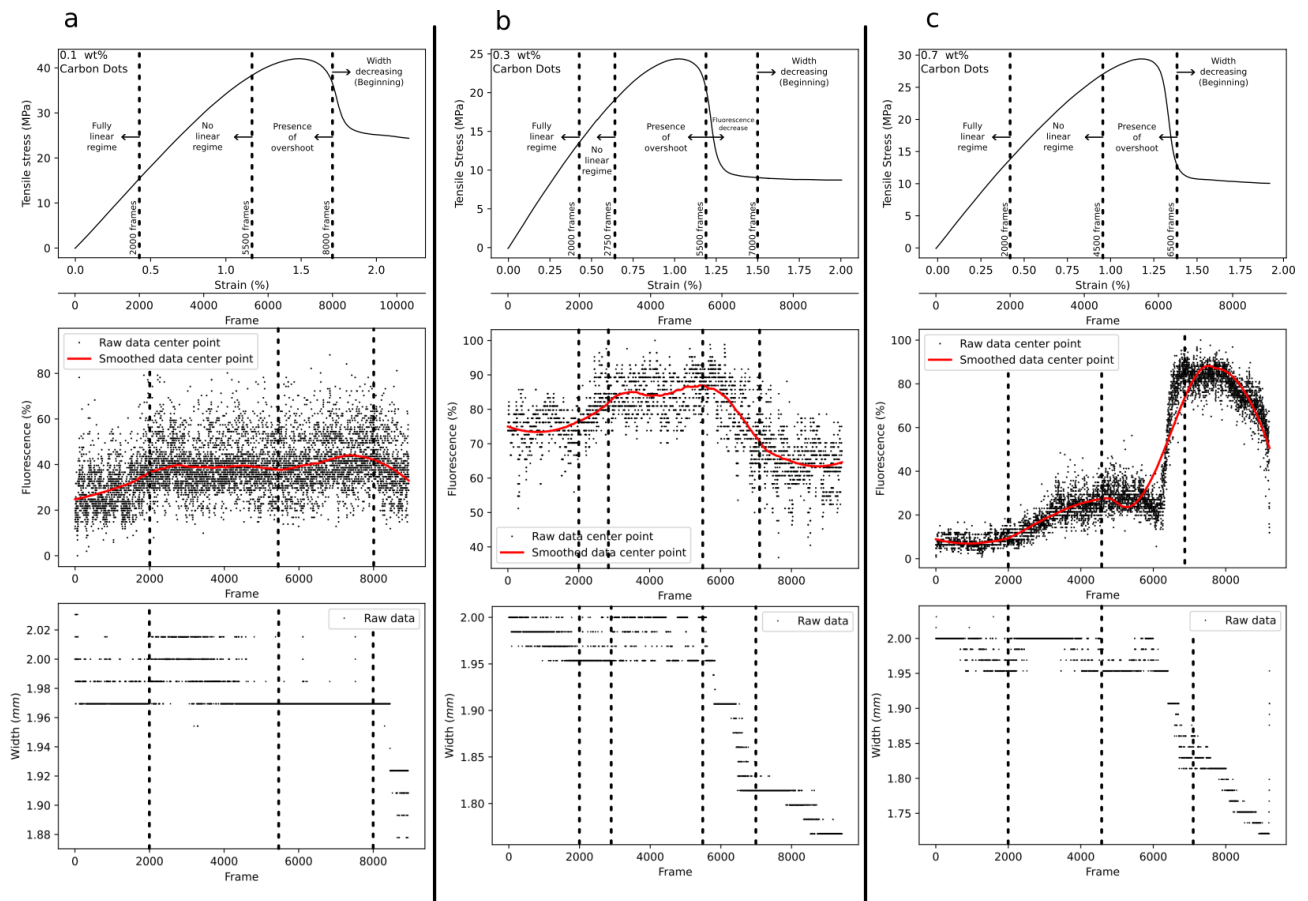
Figure 3. Correlation of the stress and strain behaviour with the florescence change during tensile analysis, a) 0.1 wt, b) 0.3 wt%, c) 0.7 wt%.

Finally, a shear effect is visible under polarised lenses, which can be attributed to both additive manufacturing and the inclusion of carbon dots as well. In essence, the inadequate interaction between printed treads becomes more pronounced with an increasing addition of CDs. This can be seen in Fig. 4.
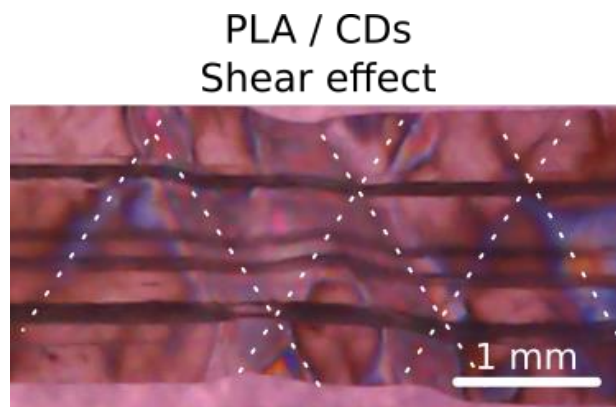
Figure 4. The shear effect caused by the carbon dots on printed threads.

4. CONCLUSIONS

The incorporation of carbon dots enhances the mechanical performance of the PLA, as the pristine material exhibits Young's modulus of 3117.45 MPa, while the PLA-CD composites present values ranging from 3549.86 to 4274.92 MPa. However, 1, 3, and 5 wt% of CDs substantially reduce Young's modulus, rendering these values statistically equivalent to that of natural PLA. In contrast, 0.1, 0.5, 0.3, and 0.7 wt% of CDs show potential for improving Young's modulus. The visible fluctuations in fluorescence, both increases and decreases, occur with the presence of carbon dots. When more than 1 wt% CD is added, the fluorescence

decreases, attributed to over-clustering, which attenuates the intensity of the sample. However, at 0.1, 0.3, and 0.7 wt% CDs, the fluorescence displays visible changes, indicating increases and decreases during different stages of the tensile test.

4.1. Declaration of Competing Interest

The authors declare no conflict of interest.

4.2. Fundings

4.3. Acknowledgements

5. REFERENCES

[1] Wang, Jun Kit et al. Polymer-Enriched 3D Graphene Foams for Biomedical Applications. ACS applied materials & interfaces, Volume 7 (2015). (https://doi.org/10.1021/ACSAMI.5B01440/ASSET/IMAGES/MEDIUM/AM-2015-01440D_0011.GIF)

[2] Mahmud Z et al. 3D-printed polymer nanocomposites with carbon quantum dots for enhanced properties and in situ monitoring of cardiovascular stents. Polym Adv Technol. Volume 33, (2022). (https://doi.org/10.1002/PAT.5572)

[3] Sarat Singamneni et al. Direct extrusion 3D printing for a softer PLA-based bio-polymer composite in pellet form, Journal of Materials Research and Technology, Volume 15, (2021). (https://doi.org/10.1016/j.jmrt.2021.08.044).

[4] Bochnia J., Kozior T., Blasiak M., The Mechanical Properties of Thin-Walled Specimens Printed from a Bronze-Filled PLA-Based Composite Filament Using Fused Deposition Modelling. Materials Volume 16, (2023). (https://doi.org/10.3390/ma16083241)

[5] Ma Z., Qian, Z., Cai, J. Effects of the manufacturing process and surface treatments on mechanical properties of PLA/SCF composites using extrusion printing. J Mech Sci Technol. Volume 36, (2022). (https://doi-org/10.1007/S12206-022-0417-Y/METRICS)

[6] Cao, D. Enhanced buckling strength of the thin-walled continuous carbon fiber–reinforced thermoplastic composite through dual coaxial nozzles material extrusion process. Int J Adv Manuf Technol, Volume 128, (2023). (https://doi.org/10.1007/s00170-023-12014-8).

[7] Dan Wang et al. Facile and Scalable Preparation of Fluorescent Carbon Dots for Multifunctional Applications, Engineering, Volume 3, (2017). (https://doi.org/10.1016/J.ENG.2017.03.014).

[8] Fabijański M. Study of the Single-Screw Extrusion Process Using Polylactide. Polymers (Basel). Volume 15(19), (2023). (https://doi.org/10.3390/polym15193878).

[9] Tang et al. State of the-Art for Extrudate Swell of Molten Polymers: From Fundamental Understanding at Molecular Scale toward Optimal Die Design at Final Product Scale. Macromolecular Materials and Engineering, Volume 305, (2020). (https://doi.org/10.1002/mame.202000340)

[10] ASTM International, ASTM D638-14, Standard Test Method for Tensile Properties of Plastics, 2022

EXPLORING THE IMPACT OF SURFACE TREATMENT BY LASER ABLATION ON THE STRENGTH OF GFRP BONDED JOINTS.

Luiza F.Soares [(a)], André Luís dos Santos [(b)], Pedro Camanho[(c)], Fabrizio Scarpa[(d)], Tulio H. Panzera[(e)]

(a) ⦿ 0000-0002-9339-7080 (University of São João Del Rei – Brazil)
(b) ⦿ 0000-0002-1738-2792 (University of São João Del Rei – Brazil)
(c) ⦿ 0000-0003-0363-5207 (Universidade do Porto – Portugal)
(d) ⦿ 0000-0002-5470-4834 (University of Bristol, UK)
(e) ⦿ 000-0001-7091-456X (Federal University of São João del Rei – Brazil)
* Corresponding author: fernandesluizasoares@gmail.com

Abstract: The strength of adhesive joints in bonded structures is influenced by various factors, including the surface treatment of the bonding region. Laser ablation surface treatment has gained attention due to its ability to enhance the strength of bonded joints while being environmentally friendly compared to chemical treatments. The parameters of the laser machine, such as speed and power, as well as the pattern of grooves created by the laser, can affect the surface treatment by ablation. In this study, the surface treatment via laser ablation using continuous straight lines oriented transversely to the load direction is investigated. The distance between the lines is studied to analyse its influence on the strength of joints and the mode of failure. A 19% improvement in shear strength is achieved compared to untreated joints. Moreover, after laser ablation treatment, adhesive failures are eliminated, and only thin-layer cohesive failure/interphase failure (TLC) is observed.

1. INTRODUCTION

Bonded joints are essential for ensuring structural integrity, strength, and specialised applications across a spectrum of industries, including aerospace, automotive, medical, and construction. The design, manufacturing, and predictive modelling of composite joints are critical considerations in the design of composite structures [1,2].

Traditional mechanical fasteners such as welds, rivets, screws, or nuts not only add mass to the structure but also introduce stress concentrators. Bonded joints have been extensively studied due to their corrosion resistance, reduced weight, improved load distribution, and fatigue resistance. Several factors influence the performance of adhesive joints, including service conditions, composition (types of adhesives and surfaces to be bonded), and the bonding process (including surface treatments and adhesive curing) [1].

Laser ablation has emerged as a novel surface treatment technique for bonded joints. This treatment not only enhances the resistance of bonded joints but also eliminates the risk of environmental damage associated with chemical agents compared to surfaces treated by chemical means [3]. Recent studies have highlighted the effects of laser ablation surface treatment on the adhesive shear strength of composite joints.

Zou et al. [4] investigated the influence of laser parameters such as power, speed, frequency, and distance between slots on the mechanical performance of metal-composite bonded joints. Li et al. [5] reported on the influence of the geometry/trajectory of the laser, including variations in orientation, distance between channels, and depth reached. Andarabi et al. [6] delved into the interaction between points and lines on joint

adhesiveness. Hande et al. [7] emphasised the importance of analysing the integrity of fibres after laser ablation processing.

The current study delves into the bonded joints of glass fibre composites, considering two laser ablation surface treatments. Single-lap tests are conducted to evaluate the shear strength and failure modes of the composite joints.

2. METHODOLOGY

2.1 MATERIALS

Glass fibre composites are produced using the resin infusion technique considering four layers of 200 g/m^2 glass fibres, a 24-hour vacuum pressure, and an epoxy system. The epoxy resin (MR M) and hardener (MR 951) from Huntsman are mixed at a 10:1 ratio to form the matrix phase. The final thickness of the glass fibre composite is 0.65 mm, and the same epoxy system is utilised both as the matrix phase and as the adhesive for joints. Surface treatment via laser ablation is carried out using the ROBOTECH CO_2 laser machine with a 150 W power.

2.2 METHODOLOGY

The glass fibre composites are cleansed with alcohol to eliminate the release agent used during infusion. The surface treatment is determined based on preliminary investigations, involving continuous straight lines oriented transversely at the load direction (Figure 1). Laser processing is fine-tuned to remove the matrix phase while preserving the integrity of the fibres, with defined parameters of a speed of 700 mm/s and a power of 22.5 W. Three different surface treatments are under consideration, including no laser ablation treatment, with line spacings (d) of 0.25 mm and 0.5 mm. The grooves created by the laser are examined using an optical microscope to measure the exposed area of the glass fibre.
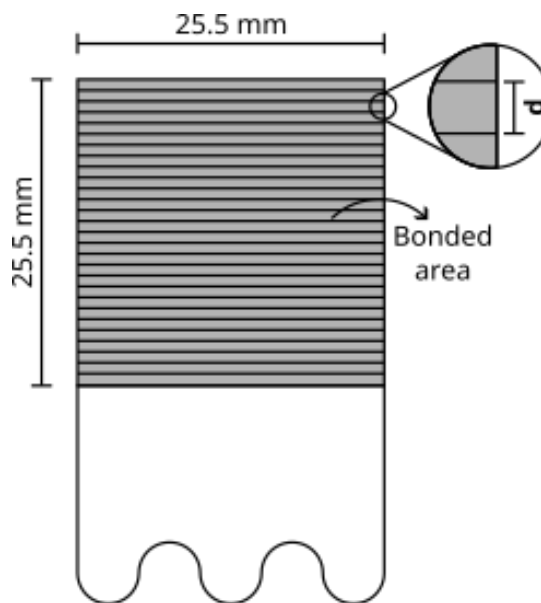
Figure 1. Schematic representation of bonded area and surface treatment.

Single-lap shear tests are carried out in accordance with the ASTM D5868[8] standard at a velocity of 13 mm/min, utilising a bonded area of 25.5 × 25.5 mm², as illustrated in Figure 1. The maximum shear force and stress are recorded. The adhesive thickness measures approximately 0.8 mm. Analysis of fracture modes follows the guidelines outlined in ASTM D5573[9].

3. RESULTS AND DISCUSSION

3.1 SURFACE TREATMENT

Figure 2 depicts the microstructural analysis for each surface treatment: (A) untreated, and (B-C) laser ablation surface treatments. It is observed that the glass fibres remain unburned after laser processing. When

d equals 0.25 mm, the laser grooves overlap, whereas no overlapping occurs when d equals 0.5 mm. Furthermore, it is noted that with d=0.25 mm, an area of approximately 1.2×1.2 mm² of resin is removed, while for d=0.5 mm, an area of approximately 1.5×0.3 mm² is observed.
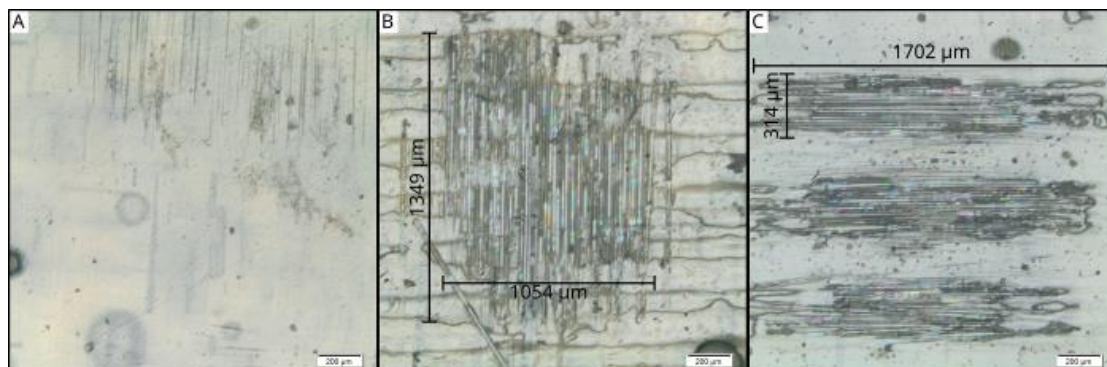
Figure 3. Surface treatment A- untreated, B- d=0.25mm and C- d=0.5 mm.

3.2 SINGLE-LAP TESTING

Table 1 presents the results of the maximum shear force and stress obtained from the single-lap shear test. An Analysis of Variance (ANOVA) is conducted to evaluate differences among the means, with P-values of 0.0005 and 0.0007 for shear force and stress, respectively, indicating significant differences in at least one condition. Subsequently, Tukey's multiple comparison analysis (refer to Table 1) is carried out, revealing statistically different means between all treatments at a 95% confidence level. The untreated samples exhibit the lowest shear properties (3805 N and 5.81 MPa), while those treated with laser processing at d= 0.5 mm achieve the highest shear force and stress values, measuring 4621 N and 6.92 MPa, respectively.

Table 1. Single-lap test results

Surface Treatment	Shear force (N)	Tukey test	Shear stress (MPa)	Tukey test
untreated	3805 ± 21	C	5.81 ± 0.06	C
d = 0.25 mm	4178 ± 160	B	6.26 ± 0.19	B
d = 0.5 mm	4621 ± 107	A	6.92 ± 0.19	A

3.3- FRACTURE MODES

Figure 3 illustrates the surfaces of typical samples after single-lap testing: untreated (left), d=0.25 mm (centre), and d=0.5 mm (right). The samples subjected to laser surface treatment display a consistent fracture mode, identified as thin-layer cohesive failure/interphase failure (TLC). In contrast, the untreated samples exhibit two distinct types of failures: TCL failure and adhesive failure/interfacial failure (ADH).

Figure 3. Failure modes: untreated (left), d=0.25mm (centre) and d=0.5 mm (right) samples

4. CONCLUSIONS

Glass fibre composite joints were evaluated with a focus on surface treatments conducted through laser ablation processing. Treated composite joints exhibit a 19% higher shear strength compared to untreated joints, with the typical fracture mode being a thin-layer cohesive failure/interphase failure (TLC) in treated composite joints. The optimisation of "d" to maximise the shear strength of the adhesive composite joints will be the scope of future investigations.

Declaration of Competing Interest

The authors declare no conflicts of interest.

4.1. Acknowledgements

5. REFERENCES

[1] Gualberto, Hiasmim Rohem; do Carmo Amorim, Felipe; Costa, Hector Reynaldo Meneses. A review of the relationship between design factors and environmental agents regarding adhesive bonded joints. Journal of the Brazilian Society of Mechanical Sciences and Engineering, v. 43, n. 8, p. 389, 2021. (https://doi.org/10.1007/s40430-021-03105-2)

[2] Wang, Dawei et al. Increasing strength and fracture toughness of carbon fibre-reinforced plastic adhesively bonded joints by combining peel-ply and oxygen plasma treatments. Applied Surface Science, v. 612, p. 155768, 2023.(https://doi.org/10.1016/j.apsusc.2022.155768)

[3] MUSIARI, Francesco; MORONI, Fabrizio; LUTEY, Adrian Hugh Alexander. Enhanced mechanical interlocking of adhesive-bonded joints via tailored serrated patterns manufactured with laser ablation. The Journal of Adhesion, p. 1-35, 2023.(https://doi.org/10.1080/00218464.2023.2285431)

[4] ZOU, Xin et al. Laser surface treatment to enhance the adhesive bonding between steel and CFRP: Effect of laser spot overlapping and pulse fluence. Optics & Laser Technology, v. 159, p. 109002, 2023.(https://doi.org/10.1016/j.optlastec.2022.109002)

[5] LI, Hao et al. Effect of laser generated microgrooves geometric parameters on the shear strength of CFRP-Aluminium alloy adhesive joints. The Journal of Adhesion, v. 99, n. 10, p. 1744-1767, 2023.(https://doi.org/10.1080/00218464.2022.2158731)

[6] ANDARABI, A. A.; SHELESH-NEZHAD, K.; CHAKHERLOU, T. N. The effect of laser surface structuring patterns on the interfacial resistance of aluminum joints bonded with epoxy adhesive. International Journal of Adhesion and Adhesives, v. 114, p. 103101, 2022. (https://doi.org/10.1016/j.ijadhadh.2022.103101)

[7] İPLIKÇI, Hande et al. Effects of nanosecond laser ablation parameters on surface modification of carbon fiber reinforced polymer composites. Journal of Composite Materials, v. 57, n. 18, p. 28432855, 2023.(https://doi.org/10.1177/00219983231178892)

[8] GERMANO BRAGA, Guilherme et al. Fully biobased composite and fiber-metal laminates reinforced with Cynodon spp. fibers. Polymer Composites, v. 44, n. 1, p. 453-464, 2023.(https://doi.org/10.1002/pc.27109)

[9] ASTM D5868-01(2014), Standard Test Method for Lap Shear Adhesion for Fiber Reinforced Plastic (FRP) Bonding, ASTM International, West Conshohocken, PA, 2014, www.astm.org.

[10] ASTM D5377 Designation: D5573 − 99- Standard Practice for Classifying Failure Modes in Fiber-Reinforced-Plastic (FRP) Joints, ASTM International, West Conshohocken, PA, 2014, www.astm.org.

UHPC WITH NANOMATERIALS AND CARBON FIBERS: A REVIEW

Amanda A. Souza[(a)*], Leila A. de C. Motta[(b)]

(a) 0009-0008-5602-5705 (Federal University of Uberlandia – Brazil)
(b) 0000-0002-1597-2297 (Federal University of Uberlandia – Brazil)
* Corresponding author: amanda.souza2@ufu.br

Abstract: Ultra-High-Performance Concrete (UHPC) is a composite material expected to exhibit high-performance in terms of compressive and tensile strength, durability, and toughness. UHPC without fibers is a brittle composite; therefore, the introduction of fiber reinforcement is necessary to meet the requirement for good toughness. Carbon materials can be used for this purpose at nano, micro, and millimetric scales. These materials have desirable characteristics as reinforcements for UHPC, as they are lightweight, have a high modulus of elasticity, small diameter, and high strength. Research have been conducted by countries such as China, South Korea, the United States, and Croatia, particularly focusing on nanomaterials. However, the use of fibers at millimetric scales is still in its early stages. Therefore, to better understand the subject and the techniques used in studies of UHPC with the incorporation of carbon materials, this article presents a systematic review with quantitative and qualitative analyses of the searched data. Studies were searched in 387 databases, yielding 13 articles across three databases. The reviewed articles emphasize the importance of using carbon materials as reinforcement for UHPC, as a solution to control crack propagation, improve mechanical properties and dynamic performance. the remarkable structural capacity of UHPC when reinforced with carbon materials.

1. INTRODUCTION

Ultra High-Performance Concrete (UHPC) stands as a highly promising composite, enabling the fabrication of exceptionally slender and lightweight components while maintaining remarkable high compressive and tensile strength. Its intricate composition and interaction among constituents yield exceptional rheological properties, such as workability and self-densification, due to its dense and uniform microstructure. A superior strength and toughness ensure heightened durability compared to conventional concrete [1–3].

The high performance of UHPC is attributed to the high compactness of its granular components. To achieve greater grain packing, coarse aggregates are excluded from the mix, eliminating the transition zone, and increasing the surface area of the grains [4]. Therefore, this material is composed cement, quartz sand, microfillers such as silica fume, fly ash, and metakaolin, low water content, superplasticizer admixture, and a small percentage of fibers [5–8]. For authors [9] the cement composition for UHPC should have moderate fineness and a low content of hydrated tricalcium aluminate (C_3A) due to its rapid reaction upon contact with water, which could cause an undesirably fast initial setting time.

Without the presence of fibers, UHPC tends to fracture in a brittle manner, while the addition of fibers enhances the flexural strength and ductility of the composite [10–12]. Several types of fibers are used, including metallic, synthetic, glass, high-performance polymeric, and carbon fiber materials [13]. Carbon materials are incorporated to UHPC at nano, micro, and millimeter scales [14,15] to enhance the mechanical properties of the microstructure, increase interlaminar fracture toughness, control microcrack growth, improve

ductility, enhance thermal conductivity and electromagnetic shielding effectiveness, as well as strengthen energy absorption capacity and resistance to abrasion [16–19].

Carbon materials are ideal for reinforcing advanced concretes due to their lightweight nature, high specific modulus, high strength, and toughness, as well as resistance to moisture and a variety of solvents, acids, and bases[20,21]. This article offers a comprehensive systematic review of UHPC studies utilizing carbon materials, delving into both quantitative and qualitative aspects to provide a thorough understanding of the subject matter and the associated techniques.

2. LITERATURE REVIEW

The review of recent literature, considering the last 5 years (2019-2024), was systematically conducted by the Periodicals Portal of the Coordination for the Improvement of Higher Education Personnel (CAPES), an agency linked to the Ministry of Education (MEC), which is the most relevant and trusted scientific repository in Brazil. It provides diverse content produced nationally and internationally for the academic community, including references, patents, statistics, audiovisual materials, technical standards, theses, dissertations, books, and reference works.

A total of 387 databases were consulted to select those containing full-text open access articles, abstracts, and reference works, as well as those dealing with Engineering/Civil Engineering in their respective categories and subcategories. Thus, out of the 387 databases, 22 were chosen to search for journal articles with open access and Qualis A.

The syntax used to enhance the search on the topic of interest was: "ultra-high-performance concrete" OR "UHPC" AND "carbon fibers" OR "carbon materials". As a result, 3 out of the 22 databases yielded articles with the used syntax, totaling 13 articles. Table 1 shows the publications found in the searches, their respective authors, the three databases used - Compendex (Engineering Village - Elsevier), CrossRef Search, and ScienceDirect (Elsevier) - publication year, and country of origin.

Table 1. Publications found in the research.

Article	Title	Authors	Database	Year of Publication	Country of Origin
1	Carbon nanofibers (CNFs) dispersed in ultra-high-performance concrete (UHPC): Mechanical property, workability, and permeability investigation	Linfei Li, Boning Wang, Mija H. Hubler	Compendex on Engeneering Village	2022	USA
2	Experimental characterization and analytical assessment of compressive behavior of carbon nanofibers enhanced UHPC	Milana Cimesa, Mohamed A. Moustafa	Compendex on Engeneering Village	2022	USA
3	Experimental study on the salt freezing durability of multi-walled carbon nanotube ultra-high-performance concrete	Guifeng Liu et al.	Compendex on Engeneering Village	2022	China
4	Hybrid effects of carbon nanotubes and steel fiber on dynamic mechanical properties of ultra-high-performance concrete	Shaojie Li et al.	Compendex on Engeneering Village	2023	China
5	Investigating the influence of multi-walled carbon nanotubes on the mechanical and damping properties of ultra-high-performance concrete	Wenhua Zhang et al.	Compendex on Engeneering Village	2020	China
6	Preparation and properties of nano-carbon black modified ultra-high-performance concrete	Linbin Wang et al.	Compendex on Engeneering Village	2022	China
7	Tailoring anti-impact properties of ultra-high-performance concrete by	Jialiang Wang et al.	Compendex on	2021	China

	incorporating functionalized carbon nanotubes		Engeneering Village	
8	The critical incorporation concentration (CIC) of dispersed carbon nanotubes for tailoring multifunctional properties of ultra-high-performance concrete (UHPC)	Myungjun Jung et al.	Compendex on Engeneering Village	2022	South Korea
9	Carbon nanotubes (CNTs) in ultra-high-performance concrete (UHPC): Dispersion, mechanical properties, and electromagnetic interference (EMI) shielding effectiveness (SE)	Myungjun Junga et al.	CrossRef Search	2020	South Korea
10	Synergistic integration of waste fibres and supplementary cementitious materials to enhance sustainability of ultra-high-performance concrete (UHPC)	Antonija Oceli´c, Ana Bari˘cevi´c , Marina Fran˘ci´c Smrki´c	Science Direct	2023	Croatia
11	Micromechanical properties of interfacial transition zone between carbon fibers and UHPC matrix based on nano-scratching tests	Haoliang Huanga et al.	Science Direct	2023	China
12	Interfacial bond between modified micro carbon fiber and high-strength cement pastes in UHPC: Bond-slip tests and molecular dynamic simulation	Haoliang Huanga et al.	Science Direct	2023	China
13	Experimental study on the thermal properties of a novel ultra-high-performance concrete reinforced with multi-scale fibers at elevated temperatures	Yibo Chena et al.	Science Direct	2022	China

3. RESULTS AND DISCUSSION

Beyond the remarkable tensile and compressive strengths already achieved, UHPC with carbon materials, reduces permeability [22], and shows promise for good frost and salt erosion resistance, especially in maritime environments [23]. It offers benefits in shielding against electromagnetic interference, sensitivity to deformation and damage sensing, and exhibits good thermal and electrical conductivity [24] Additionally, it contributes to enhancing damping properties [25], besides showing improvements in workability, water absorption, and shrinkage due to drying[26].

The high density of the cementitious matrix of UHPC is attributed to the compactness of the fine mixture components, while the inserted fibers, of adequate length, fit into the interstices without disturbing the natural packing [8]. Carbon materials reinforce UHPC through bridging and pore filling, acting as nucleation agents during hydration and modifying the hydrate microstructure [18]. Bridging effect reduces the accumulated stress at the crack tips, redirecting it towards the cement matrix and delaying propagation [27]. In summary, carbon materials reduce voids and cracks, decreasing composite porosity [26,28].

However, the carbon reinforcement materials used - carbon nanofibers, carbon nanotubes, multi-walled carbon nanotubes, carbon black nanoparticles, and carbon fibers - tend to agglomerate due to Van der Waals forces, forming defective sites in UHPC, requiring an optimal proportion [27,29,30]. Additionally, dispersing reinforcements in cementitious materials is challenging due to their hydrophobic characteristics, high specific surface area, and aspect ratio [25]. Various dispersion methods are applied to overcome this difficulty, as listed in Table 2.

Carbon materials range from nano, micro and millimeter-scales, as indicated in Table 2. These lengths and particle sizes have been studied to fill mesopores (4.5 to 25 nm) and micropores (<4.5 nm) with similar sizes [18]. Figure 1 shows the percentage of different carbon materials chosen in the 13 articles found.

Table 2. Carbon materials and methods of dispersion of these materials in UHPC.

Article	Carbon material dispersed in UHPC	Material Dimension		Dispersion method
		Length/ Particle Size	Unit	
1	Carbon Nanofiber (CNF)	50-200	μm	Chemical surfactant high range water reducer and ultrasonic treatment.
2	Carbon Nanofiber (CNF)	*1	*1	NF dispersed in admixtures resulting in a dense paste.
3	Multi-walled carbon nanotubes (MWNTs)	5-50	μm	The mixture of CNT, water, and surfactant was magnetically stirred with Polyvinylpyrrolidone (PVP), and then subjected to ultrasonic treatment.
4	Carbon nanotubes (CNT)	10-30	μm	Chemical surfactant (Polycarboxylate superplasticizer) and ultrasonic treatment. Surface treatment of CNTs by low-temperature plasma modification.
5	Multi-walled carbon nanotubes (MWNTs)	10-50	μm	Water-Reducing chemical surfactant and ultrasonic treatment.
6	Nano-carbon black (NBC)	5-100	nm	Water-Reducing chemical surfactant and ultrasonic treatment.
7	Multi-walled carbon nanotubes (CNT)	0,5-2	μm	Surface treatments of CNTs through hydroxylation (MH) and carboxylation (MC), for better dispersion.
8	Multi-walled carbon nanotubes (MWNTs)	12	μm	Suspension composed of nanotubes dispersed in distilled water.
9	Multi-walled carbon nanotubes (MWNTs)	10-70	μm	Sonication and subsequent mixing with superplasticizer.
10	Carbon fiber (CF)	10	mm	Did not use any specific method.
11	Carbon nanotubes (CNF) e Carbon fiber (CF)	CNT = 15-30	μm	Water-Reducing chemical surfactant and superficial treatment of CFs with epoxy coating, gas oxidation, hydrophilic epoxy coating, electrochemical oxidation.
		CF= 1,00	mm	
12	Carbon fiber (CF)	26	μm	Surface treatment of CFs through grafting of carboxyl groups, anodization, and epoxy coating.
13	Carbon nanotubes (CNF) e Carbon fiber (CF)	CNT = 15-30	μm	Aqueous dispersion with water, carbon nanotubes, and dispersing agent were mechanically stirred and ultrassonic treatment.
		CF= 1,00	mm	

¹) This symbol indicates that the length dimensions and particle size were not mentioned.
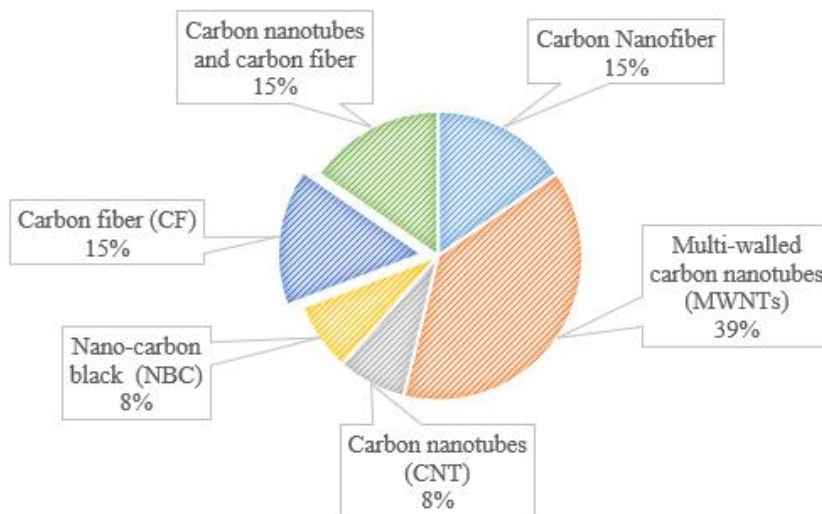
Figure 1. Percentage of carbon materials

Multi-walled carbon nanotubes appear in greater numbers (39%), which may be due to their characteristics being superior to single-walled carbon nanotubes [31] and their operation at the microscale. Although carbon fibers possess excellent properties such as low density, high tensile strength, and good chemical stability [32,33], there is a gap in undertanding their behavior in UHPC. Similarly, carbon black nanoparticles have shown effectiveness in enhancing the mechanical properties and drying shrinkage of UHPC;but further studies are needed to comprehensive understanding, including the durability performance of UHPC reinforced with this material.

The American standard ASTM C1856 establishes that the minimum compressive strength of Ultra-high Performance Concrete (UHPC) should be 120 MPa after 28 days of curing [34]. Table 3 lists the maximum values of mechanical properties cited in the compiled articles. All articles fall under the category of UHPC, except for the study referenced in article 10, in wich the authors adopted a definition predating the current standard, and article 11, which does not mention the compressive strength test, focusing on the micromechanical properties of the interface between carbon fiber and the UHPC matrix. Article 7, which used multi-walled carbon nanotubes as reinforcement, achieved the highest compressive strength of the UHPC tested, approximately 250 MPa. Only 38% of the articles investigated the tensile strength of their UHPC samples at 28 days, shows a tensile strength value of 38.50 MPa, which is over 7 times higher than that of conventional concrete.

The water-cement ratio ranged from 0.16 to 0.37. A low water-cement ratio reduces voids between particles increasing compactness density [35]. These low water-cement ratios were achievable due to advancements in superplasticizer technology, which enable better particle dispersion, resulting in a more fluid cement paste with improved workability [36].

An important property when working with fibers is toughness, which refers to the ability of fibers to absorb energy and undergo plastic deformation before rupturing. This property is typically measured by the area under the stress-strain curve up to the point of rupture [37]. In Table 3, toughness is presented with different units, due to the various approaches adopted by the authors, with most opting to explore it as specific energy absorption capacity, calculated by dividing toughness by the cross-sectional area of the specimen [21].

Table 3. Mechanical Properties of UHPC with Carbon Materials.

Article	Water Cement Ratio	Maximum Compression Strength at 28 days (MPa)	Maximum tensile strength at 28 days (MPa)	Toughness
1	0,18	140,00	20,90	775 N.mm
2	*2	130,90	*2	*2
3	0,19	123,20	13,90	*2
4	0,18	189,30	*2	2,74 Mj/m³

5	0,16	123,50	26,30	*2
6	0,18	145,40	38,50	*2
7	0,37	250,00	*2	8000 KJ/M³
8	0,24	164,00	*2	*2
9	0,23	177,10	*2	*2
10	0,22	105,00	14,30	307.8 ± 34.6 N/m
11	0,19	*2	*2	*2
12	0,23	130,00	*2	*2
13	0,35	135,00	*2	*2

²) This symbol indicates that the maximum compression strength and/or maximum tensile strength and/or toughness were not mentioned.

4. CONCLUSIONS

Composite materials represent an innovative technology that combines various properties to produce high-performance, durable, and efficient products. Recently, there has been a growing interest in Ultra-High-Performance Concrete (UHPC) when incorporated with carbon fibers, nanofibers, nanotubes, and carbon black particles. Recent studies have explored the effects of these composites, highlighting their significant positive influence on mechanical strength, permeability, durability, and other important properties.

The 13 articles selected in this systematic review focus their efforts on studying and understanding the interaction between the cementitious matrix and the reinforcing material, recognizing that effective dispersion of these small-scale materials is a significant challenge. In response to this issue, the articles highlight the dispersion methods employed to prevent the agglomeration of carbon materials. Among these methods, aqueous dispersion with the addition of carbon material to water and chemical surfactants, combined with ultrasonic treatment, emerge as the most used to ensure a homogeneous distribution of the reinforcing materials within the cementitious matrix.

The compiled results reveal that the inclusion of carbon materials can lead to significant improvements in both compressive and tensile strength, as well as an increase in the toughness of UHPC. Additionally, there is an observed enhancement in the workability of the material and a reduction in drying shrinkage. These findings suggest considerable potential for the application of UHPC reinforced with carbon materials in a wide range of environments and service conditions, highlighting its versatility and robustness as a high-performance construction material.

The investigated carbon materials exhibit a wide range of sizes, ranging from five nanometers to 10 millimeters. It is noteworthy that carbon nanotubes are predominant in the research, especially in the range of 5 to 70 micrometers. These dimensions of carbon materials allow them to fill and function as bridges in the voids and interstices within the structure of UHPC. This process has a direct impact on delaying the formation of cracks caused by shrinkage, contributing to the enhancement of the durability and strength of the composite material.

Due to the limited number of articles found on the topic across such a vast array of databases - a total of 387 - it suggests that research on UHPC with carbon materials is still in its initial stages, particularly concerning the addition of millimeter-scale fibers. Despite the existing gaps in the full understanding of the behavior and performance of UHPC reinforced with carbon materials, the results obtained so far are encouraging and indicate a promising path in the development of next-generation construction materials. This suggests that there is significant potential for substantial advancements in this field as more research is conducted and innovative technologies are developed.

4.1. Declaration of Competing Interest

The authors declare that they have no known competing financial interests or personal relationships that could have appeared to influence the work reported in this paper. even if the authors have no competing interest, it is necessary to declare as follow: The authors declare no conflict of interest.

4.2. Fundings

4.3. Acknowledgements

5. REFERENCES

[1] Liang X, Wu C, Su Y, Chen Z, Li Z. Development of ultra-high-performance concrete with high fire resistance. Constr Build Mater 2018; 179:400–12. https://doi.org/10.1016/j.conbuildmat.2018.05.241.

[2] Li J, Wu Z, Shi C, Yuan Q, Zhang Z. Durability of ultra-high-performance concrete – A review. Constr Build Mater 2020;255. https://doi.org/10.1016/j.conbuildmat.2020.119296.

[3] Wu Z, Khayat KH, Shi C, Tutikian BF, Chen Q. Mechanisms underlying the strength enhancement of UHPC modified with nano-SiO2 and nano-CaCO3. Cem Concr Compos 2021;119. https://doi.org/10.1016/j.cemconcomp.2021.103992.

[4] Cechella G, Paulo I, Bernardo H, Tutikian F. Concreto de Alto e Ultra-Alto Desempenho. 2011.

[5] Azmee NM, Shafiq N. Ultra-high-performance concrete: From fundamental to applications. Case Studies in Construction Materials 2018;9. https://doi.org/10.1016/j.cscm.2018.e00197.

[6] Mishra O, Singh SP. An overview of microstructural and material properties of ultra-high-performance concrete. J Sustain Cem Based Mater 2019; 8:97–143. https://doi.org/10.1080/21650373.2018.1564398

[7] Seyam AM, Balázs GL. A Review in Technologies, Definitions, Properties and Applications of Ultra High-Performance Concrete (UHPC). Concrete Structures 2023; 24:105–11. https://doi.org/10.32970/cs.2023.1.15.

[8] DE LARRARD F. Concrete Mixture Proportioning: A Scientific Approach. Modern Concrete Technology. vol. 9. 1999.

[9] Wille KNAE; P-MGJ. Ultra-High-Performance Concrete with Compressive Strength Exceeding 150 MPa (22 ksi): A Simpler Way. ACI Mater J 2011; 108:46. https://doi.org/10.14359/51664215.

[10] McSwain AC, Berube KA, Cusatis G, Landis EN. Confinement effects on fiber pullout forces for ultra-https://doi.org/10.1016/j.cemconcomp.2018.04.011.high-performance concrete. Cem Concr Compos 2018; 91:53–8.

[11] Khalil N, Assaad JJ. Bond properties between smooth carbon fibre-reinforced polymer bars and ultra-high-performance concrete modified with polymeric latexes and fibres. European Journal of Environmental and Civil Engineering 2022; 26:6211–28. https://doi.org/10.1080/19648189.2021.1934554.

[12] Šahmenko G, Krasnikovs A, Lukašenoks A, Eiduks M. Ultra high-performance concrete reinforced with short steel and carbon fibers. Vide. Tehnologija. Resursi - Environment, Technology, Resources, vol. 1, Rezekne Higher Education Institution; 2015, p. 193–9. https://doi.org/10.17770/etr2015vol1.196.

[13] Gong J, Ma Y, Fu J, Hu J, Ouyang X, Zhang Z, et al. Utilization of fibers in ultra-high-performance concrete: A review. Compos B Eng 2022;241. https://doi.org/10.1016/j.compositesb.2022.109995.

[14] Meng W, Khayat KH. Effect of graphite nanoplatelets and carbon nanofibers on rheology, hydration, shrinkage, mechanical properties, and microstructure of UHPC. Cem Concr Res 2018; 105:64–71. https://doi.org/10.1016/j.cemconres.2018.01.001.

[15] Lamba N, Raj R, Singh P. Mechanical response of recycled carbon fiber reinforced polymer fibers in high-strength concrete. Mater Today Proc 2023; 78:603–7. https://doi.org/10.1016/j.matpr.2022.11.477.

[16] Ladani RB, Ravindran AR, Wu S, Pingkarawat K, Kinloch AJ, Mouritz AP, et al. multi-scale toughening of fibre composites using carbon nanofibres and z-pins. Compos Sci Technol 2016; 131:98–109. https://doi.org/10.1016/j.compscitech.2016.06.005.

[17] Peyvandi A, Sbia LA, Soroushian P, Sobolev K. Effect of the cementitious paste density on the performance efficiency of carbon nanofiber in concrete nanocomposite. Constr Build Mater 2013; 48:265–9. https://doi.org/10.1016/j.conbuildmat.2013.06.094.

[18] Jung M, Lee Y soon, Hong SG, Moon J. Carbon nanotubes (CNTs) in ultra-high-performance concrete (UHPC): Dispersion, mechanical properties, and electromagnetic interference (EMI) shielding effectiveness (SE). Cem Concr Res 2020;131. https://doi.org/10.1016/j.cemconres.2020.106017.

[19] Ahmed Sbia L, Peyvandi A, Soroushian P, Lu J, Balachandra AM. Enhancement of Ultrahigh Performance Concrete Material Properties with Carbon Nanofiber. Advances in Civil Engineering 2014;2014. https://doi.org/10.1155/2014/854729.

[20] Coleman JN, Khan U, Blau WJ, Gun'ko YK. Small but strong: A review of the mechanical properties of carbon nanotube-polymer composites. Carbon N Y 2006; 44:1624–52. https://doi.org/10.1016/j.carbon.2006.02.038.

[21] William D. Callister Jr, DGR. MATERIALS SCIENCE AND ENGINEERING: AN INTRODUCTION, NINTH EDITION. vol. 9. LTC — Livros Técnicos e Científicos Editora Ltda; 2018.

[22] Li L, Wang B, Hubler MH. Carbon nanofibers (CNFs) dispersed in ultra-high-performance concrete (UHPC): Mechanical property, workability and permeability investigation. Cem Concr Compos 2022;131. https://doi.org/10.1016/j.cemconcomp.2022.104592.

[23] Liu G, Zhang H, Liu J, Xu S, Chen Z. Experimental Study on the Salt Freezing Durability of Multi-Walled Carbon Nanotube Ultra-High-Performance Concrete. Materials 2022;15. https://doi.org/10.3390/ma15093188.

[24] Li S, Yan J, Ma H, Lyu X, Zhang Y, Du S. Hybrid effects of carbon nanotubes and steel fiber on dynamic mechanical properties of ultra-high-performance concrete. Mater Res Express 2023;10. https://doi.org/10.1088/2053-1591/acbd1b.

[25] Zhang W, Zeng W, Zhang Y, Yang F, Wu P, Xu G, et al. Investigating the influence of multi-walled carbon nanotubes on the mechanical and damping properties of ultra-high-performance concrete. Science and Engineering of Composite Materials 2020; 27:433–44. https://doi.org/10.1515/secm-2020-0046.

[26] Wang L, Li G, He C, Tang Y, Yi B. Preparation, and properties of nano-carbon black modified ultra-high-performance concrete. Case Studies in Construction Materials 2022;17. https://doi.org/10.1016/j.cscm.2022.e01378.

[27] Wang J, Dong S, Pang SD, Yu X, Han B, Ou J. Tailoring Anti-Impact Properties of Ultra-High-Performance Concrete by Incorporating Functionalized Carbon Nanotubes. Engineering 2022; 18:232–45. https://doi.org/10.1016/j.eng.2021.04.030.

[28] Chen Y, Zhang Y, Zhang S, Guo Q, Gao Y, Zhang T, et al. Experimental study on the thermal properties of a novel ultra-high-performance concrete reinforced with multi-scale fibers at elevated temperatures. Constr Build Mater 2023;366. https://doi.org/10.1016/j.conbuildmat.2022.130229.

[29] Cimesa M, Moustafa MA. Experimental characterization and analytical assessment of compressive behavior of carbon nanofibers enhanced UHPC. Case Studies in Construction Materials 2022;17. https://doi.org/10.1016/j.cscm.2022.e01487.

[30] Huang H, Luo J, Peng C, Sun T, Deng T, Hu J, et al. Interfacial bond between modified micro carbon fiber and high-strength cement paste in UHPC: Bond-slip tests and molecular dynamic simulation. Cem Concr Compos 2023;142. https://doi.org/10.1016/j.cemconcomp.2023.105168.

[31] Jung M, Park J, Hong S gul, Moon J. The critical incorporation concentration (CIC) of dispersed carbon nanotubes for tailoring multifunctional properties of ultra-high-performance concrete (UHPC). Journal of Materials Research and Technology 2022; 17:3361–70. https://doi.org/10.1016/j.jmrt.2022.02.103.

[32] Byrne EM, McCarthy MA, Xia Z, Curtin WA. Multiwall nanotubes can be stronger than single wall nanotubes and implications for nanocomposite design. Phys Rev Lett 2009;103. https://doi.org/10.1103/PhysRevLett.103.045502.

[33] Bentur Arnon, Mindess Sidney. Fibre reinforced cementitious composites. Taylor & Francis; 2007.

[34] Huang H, Peng C, Luo J, Sun T, Deng T, Hu J, et al. Micromechanical properties of interfacial transition zone between carbon fibers and UHPC matrix based on nano-scratching tests. Cem Concr Compos 2023;139. https://doi.org/10.1016/j.cemconcomp.2023.105014.

[35] Standard Practice for Fabricating and Testing Specimens of Ultra-High-Performance Concrete 1 n.d. https://doi.org/10.1520/C1856_C1856M-17.

[36] Šerelis E, DELIGIA M, VAITKEVIČIUS V, KERŠEVIČIUS V. Influence of Water to Cement Ratio with Different Amount of Binder on Properties of Ultra-High-Performance Concrete. Journal of Sustainable Architecture and Civil Engineering 2015;10. https://doi.org/10.5755/j01.sace.10.1.7166.

[37] Chandra S, Björnström J. Influence of cement and superplasticizers type and dosage on the fluidity of cement mortars-Part I. n.d.

EXPERIMENTAL EVALUATION OF THE TOW TENSION FLUCTUATIONS DURING FILAMENT WINDING OF A PRESSURE VESSEL

Artem Andrianov

0000-0002-3987-6267 (University of Brasília – Brazil)
Corresponding author: andrianov@aerospace.unb.br

Abstract: The main focus of the study was on the search for a machine path that would not require a mechanism to rewind the tow over the packages during the filament winding process of a pressure vessel with elliptic domes, making the filament winding equipment less expensive. Consequently, the tow tension fluctuations were measured for various machine paths of a lathe-type winder. To make the experimental results reproducible, analytical equations were derived for both the fiber and machine paths. At least four machine paths were under consideration including the trajectory with a constant free-hanging fiber length. For one of the tested machine paths, the tow tension was near zero for a period enough to provoke a slippage of the tow from the surface of the mandrel. The machine path that is given by a combination of several trajectories demonstrated more effective behaviour than the one with a constant free-hanging fiber length.

1. INTRODUCTION

During filament winding, a delivery eye lays a tow impregnated with a resin along a geodesic or non-geodesic path on the surface of a rotating mandrel. The simultaneous translation of the delivery eye together with the rotation of the mandrel is referred to as the machine path (or machine trajectory), while the positioning of the fiber on the surface of a mandrel is referred to as the fiber path. In general, there are two methods of machine path generation [1]. The simplest one is the constant free fiber length method which establishes a constant free-hanging fiber distance between the delivery eye and the point at which the fiber is tangent to the surface of a mandrel. In this method, a nearly constant fiber feed rate can be achieved that reduces fluctuations in the fiber tension [2]. The fiber tension is an important technological parameter as it affects the fiber compaction in a wound composite structure and, as a result, improves its mechanical properties [3]. Another method is to establish a control surface (or an enveloping surface) so that the delivery eye belongs to the surface in the process of winding. Several commercial programs are available on today's market for the generation of a machine path [4], however, there is minimal information about the computation procedure. Both general approaches and detailed solutions on the computation of the machine path for a pressure vessel with hemispherical domes are given in reference [5]. However, no information is provided on the dynamic behavior of the free-hanging fiber, which is of significant importance as it affects the fiber feed rate [6]. The computing procedure of the machine path for the revolution structures is provided in reference [7] together with the resultant trajectory data for the winding process without a jerky motion of the delivery eye and with minimum variation in fiber tension. However, as the author underlines, the algorithm for the optimized trajectory is not provided in the paper. The dynamics of the free-hanging fiber can be evaluated numerically or experimentally [6]. A general winding equation suitable to deal with every possible winding machine configuration is suggested together with a numerical solver in the study [8]. The dynamic behavior is given in terms of the consumed fiber acceleration as a function of time; however, the data on the fiber tension fluctuations are not provided.

The primary objective of the presented study was to measure the tow tension fluctuations for various machine trajectories of a low-cost lathe-type winder during filament winding of a cylindrical pressure vessel with elliptic domes. The study intended to find a trajectory that does not require a mechanism to rewind the tow over the packages during the winding process at both low and high winding speeds. Moreover, simple and comprehensive analytical equations for both fiber and machine paths were derived to make the experimental results reproducible.

2. METHODOLOGY

The experimental setup involved the use of a wet filament winding technique (Fig. 1). The package with a carbon tow 12K was installed in a creel together with a magnetic powder brake. The brake provided precise torque control for the rotating package to preset the desired value of the tow tension. The tow tension was measured at the exit from the creel and after a drum-type impregnator. The experimental layout did not include either an active control of the torque (such as a combination of a dancer mechanism with feedback from tension sensors) or a mechanism to rewind the tow over the packages during the winding process. In these conditions, it was expected that high amplitude fluctuations of the tow tension would be defined by the machine path. Other low amplitude fluctuations could be caused by the kinematics and vibration of the winder, the friction between the tow and the winder guides, and the movement of the unwind point of the tow along the package (Fig. 1b). These low amplitude fluctuations were evaluated by the measurements of the tow tension during filament winding of the tow over a Ø151 mm cylindrical mandrel with a 90-degree winding angle.

Several configurations of the mandrel with high and low length-to-diameter ratios were used to evaluate the effect of a machine path on high amplitude fluctuations of the tow tension. In this paper, the results were provided only for the mandrel with a relatively high length-to-diameter ratio (Table 1).
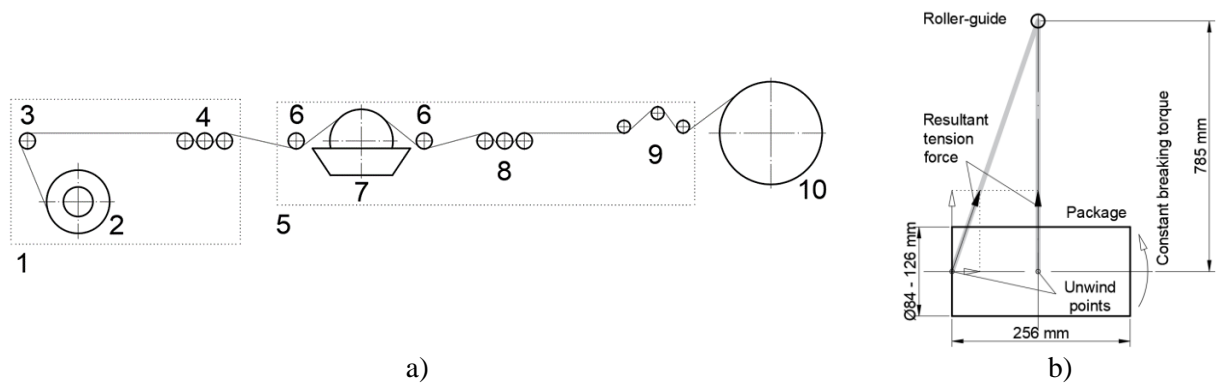
Figure 1. Experimental layout (a) and configuration of the creel (b): 1) creel, 2) tow package with a magnetic powder brake, 3) roller, 4) tension sensor, 5) winder's carriage, 6) static bars, 7) drum-type impregnator, 8) tension sensor, 9) delivery eye, 10) mandrel

A typical low-cost 4-axis lathe winder [5], was used as a part of the experimental layout. The lathe winder was controlled by a Mach3 control system that as a typical CNC system interrelates the increments of the axes (or degrees of freedom) by linear interpolation according to the prescribed feed rate [6]. The feed rate was limited by the acceleration and maximum speed of the following four axes: X is the rotation of the mandrel, Y is the linear translation of the carriage along the mandrel's axis, Z is the linear translation of the delivery eye across the mandrel's axis and A is the eye-rotation axis.

Table 1. Geometry of the mandrel with a relatively high length-to-diameter ratio (HLD).

Cylindrical casing		Elliptic dome				
Radius R_c, mm	Length, mm	Minor semi-axis length b, mm (parallel to the axis of rotation)	Major semi-axis length R_c, mm (radial direction)	Radius of polar opening r_p, mm	Ratio $c = \frac{R_c}{b}$	Ratio $e = \frac{r_p}{R_c}$
75.5	328	30.0	75.5	53.4	2.52	0.71

To exclude the effect of fiber slippage on the tension measurements, the tow was laid along a geodesic trajectory. At least four machine trajectories were computed for the unique geodesic fiber path with the use of

analytical equations derived by referring only to analytic geometry (in this paper, the solution was given only for two machine paths). The fiber path was given in terms of three coordinates of a Cartesian coordinate system, whose origin is fixed in the center of one of the polar openings (Fig. 2). The z-coordinates of the interface planes between the geometrical shapes of the mandrel are denoted as S1, S2, and S3. The machine path, as well as the fiber path, is given only for the translation of the delivery eye in the positive direction of the z-axis, which is denoted as a forward stroke. Either the machine path or the fiber path for a return stroke is the symmetric image for the respective path computed for a forward stroke with respect to a plane of symmetry of the mandrel (the symmetric image could be displaced in a circumferential direction about the axis of rotation of the mandrel depending on the winding parameters).

Two different approaches for the computation of the winding speed were used for some of the trajectories. The first approach assumed that the feed rate was constant (F = const) for all increments of the axes that led to the varying winding speed. In the second approach, the feed rate was adjusted for every increment in such a way that the winding speed would be constant (V = const). The winding velocity and the feed rate were selected in such a way that the winding productivity would be the same for all trajectories.

3. RESULTS AND DISCUSSION

3.1. Fiber path

The coordinates of the fiber path as most of the following parameters are given as functions of the z-coordinate:

$$
\begin{aligned}
x_M(z) &= r(z)\cos\big(\Phi(z) + \varphi(z)\big) \\
y_M(z) &= r(z)\sin\big(\Phi(z) + \varphi(z)\big) \\
z_M(z) &= z
\end{aligned}
\tag{1}
$$

where $r(z)$ is the radius of the mandrel's contour (Table 2), $\Phi(z)$ is the turn-around angle of the mandrel about axis z, and $\varphi(z)$ is the turn-around angle of the mandrel about axis z introduced to match the fiber path at the interfaces between the cylindrical casings and elliptic domes (Table 3).

3.2. Machine path

The machine path is given in terms of three coordinates of the mentioned Cartesian coordinate system. The coordinates x and y are given as follows:

$$
\begin{aligned}
x_E(z) &= \frac{z_E(z) - z}{p(z)} m(z) + x_M(z) \\
y_E(z) &= \frac{z_E(z) - z}{p(z)} n(z) + y_M(z)
\end{aligned}
\tag{2}
$$

where $z_E(z)$ is the z-coordinate of the machine path, and $m(z)$, $n(z)$ and $p(z)$ are the x-, y- and z-components of the direction vector of a free-hanging fiber respectively, given as:

$$
\begin{aligned}
m(z) &= \frac{dr(z)}{dz}\cos(\Phi(z) + \varphi(z)) - r(z)\frac{d\Phi(z)}{dz}\sin(\Phi(z) + \varphi(z)) \\
n(z) &= \frac{dr(z)}{dz}\sin\big(\Phi(z) + \varphi(z)\big) + r(z)\frac{d\Phi(z)}{dz}\cos\big(\Phi(z) + \varphi(z)\big) \\
p(z) &= 1
\end{aligned}
\tag{3}
$$

The equation for the coordinate $z_E(z)$ depends on the method of machine path generation. The z-coordinate of the machine path computed by the constant free fiber length method is given as:

$$
z_E(z) = \frac{\lambda \cdot p(z)}{\sqrt{m(z)^2 + n(z)^2 + p(z)^2}} m(z) + z_M(z)
\tag{4}
$$

where $\lambda = const$ is a minimal free-hanging fiber length defined by an operator in such a manner that a collision of the delivery eye with the mandrel would not occur (Fig. 2a).

In this cylindric control surface method (Fig. 2b), the z-coordinate of the machine path is given as:

$$z_E(z) = \frac{-B_1(z) + \sqrt{B_1(z)^2 - 4 \cdot A_1(z) \cdot (C_1(z) - T^2)}}{2 \cdot A_1(z)} \tag{5}$$

where $T = const$ is the radius of the cylindric control surface, whose axis coincides with the axis z (or the axis of the mandrel). This radius is defined by an operator.

Table 2. Geometry of the mandrel's contour

Intervals	Radius	Derivative of the radius
Front dome $0 < z < S1$	$r_f(z) = c\sqrt{b^2 - (\frac{1}{c}\sqrt{R_c{}^2 - r_p{}^2} - z)^2}$	$dr_f(z)/dz = \dfrac{\sqrt{R_c{}^2 - r_p{}^2} - c \cdot z}{\sqrt{b^2 - (\frac{1}{c}\sqrt{R_c{}^2 - r_p{}^2} - z)^2}}$
Cylinder $S1 \le z < S2$	R_c	0
Aft dome $S2 \le z < S3$	$r_r(z) = c\sqrt{b^2 - (z - S2)^2}$	$dr_r(z)/dz = \dfrac{c(S2 - z)}{\sqrt{b^2 - (z - S2)^2}}$

Table 3. Angular parameters for the computation of fiber path

Intervals	$d\Phi(z)/dz$	$\Phi(z)$	$\varphi(z)$
Front dome $0 < z < S1$	$d\Phi_f(z)/dz = \dfrac{\sqrt{b^2 + (S1 - z)^2(c^2 - 1)}}{c(b^2 - (S1 - z)^2)}$ $\times \dfrac{r_p}{\sqrt{c^2(b^2 - (S1 - z)^2) - r_p{}^2}}$	$\Phi_f(z) = \displaystyle\int_0^z \frac{d\Phi_f(z)}{dz}dz$	$\varphi_f(z) = 0$
Cylinder $S1 \le z < S2$	$d\Phi_c(z)/dz = \dfrac{\tan(\text{asin}\,(r_p/R_c))}{R_c}$	$\Phi_c(z) = (z - S1)$ $\times \dfrac{\tan(\text{asin}\,(r_p/R_c))}{R_c}$	$\varphi_c(z) = \Phi_f(S1)$
Aft dome $S2 \le z < S3$	$d\Phi_r(z)/dz = \dfrac{\sqrt{b^2 + (z - S2)^2(c^2 - 1)}}{c(b^2 - (z - S2)^2)}$ $\times \dfrac{r_p}{\sqrt{c^2(b^2 - (z - S2)^2) - r_p{}^2}}$	$\Phi_r(z) = \displaystyle\int_{S2}^z \frac{d\Phi_r(z)}{dz}dz$	$\varphi_r(z) = \Phi_f(S1) + \Phi_c(S2)$

The coefficients $A_1(z)$, $B_1(z)$ and $C_1(z)$ are computed as follows:

$$A_1(z) = \frac{m(z)^2 + n(z)^2}{p(z)^2}$$

$$B_1(z) = 2\left[\frac{m(z)x_M(z) + n(z)y_M(z)}{p(z)} - \frac{z(m(z)^2 + n(z)^2)}{p(z)^2}\right] \tag{6}$$

$$C_1(z) = \frac{z}{p(z)}\left[\frac{z(m(z)^2 + n(z)^2)}{p(z)} - 2(m(z)x_M(z) + n(z)y_M(z))\right] + x_M(z)^2 + y_M(z)^2$$

In the complex control surface method, a combination of the constant free fiber method $\lambda = const$ together with the cylindrical control surface method is under consideration. One more control surface has been introduced to make a smooth connection between the cylindric control surface and the constant free fiber

trajectory. The surface is an ellipsoid whose center of symmetry coincides with the center of symmetry of the elliptic surface of the aft dome. The semi-axis of the ellipsoid along the z-axis is equal to C.

In the two control surfaces method, a combination of two surfaces is under consideration: the elliptic surface (ellipsoid) over the dome and the cylindrical one over the central portion of the mandrel.
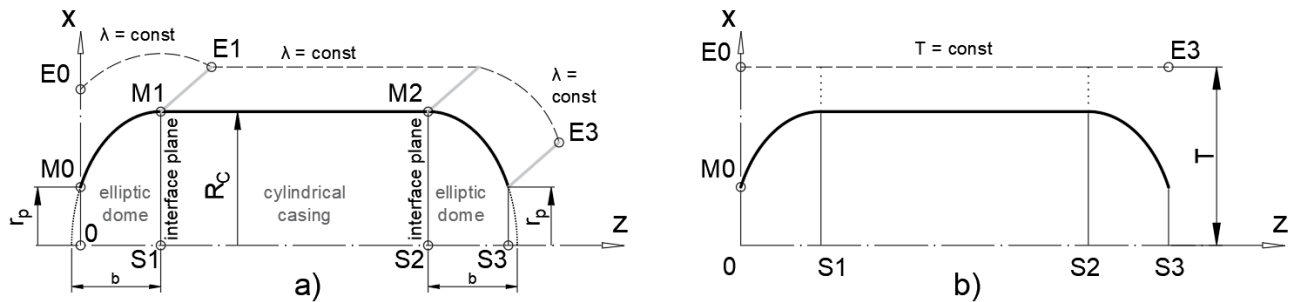
Figure 2. Schematic illustration of the machine paths computed by various methods: a) constant free fiber length method, b) cylindric control surface method.

3.3. Computation results

The coordinates of the initial point of the delivery eye E0 were the same for all trajectories except the trajectory $T = const$ (Fig. 3). The coordinates of point E0 satisfied the condition of non-collision between the delivery eye and the mandrel (Table 4). The trajectory $T = const$ was closer to the mandrel's surface than the other trajectories as the delivery eye had no limitations for a lateral collision. The coordinates of the final point E3 for all trajectories except the trajectory $T = const$ were equal too. The trajectories computed by the complex control surface method (complex) and the constant free fiber length method ($\lambda = const$) followed the same curve at the end of the plot (Fig. 3).

Table 4. Parameters of the trajectory for non-collision conditions (in millimeters)

Method	Constant free fiber length method	Cylindric control surface method	Complex control surface method	Two control surfaces method
Trajectory label	$\lambda = const$	$T = const$	$Complex$	$2\ surfaces$
Parameter, mm	$\lambda = 100$	$T = 95$	$\lambda = 100$	$C = 73$
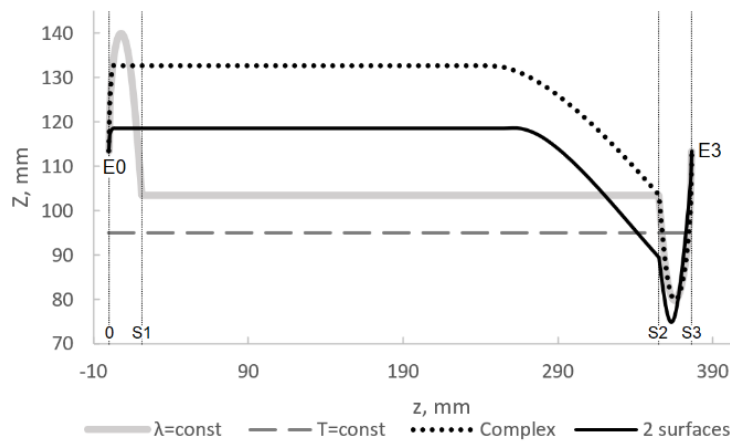
Figure 3. The linear translation of the delivery eye across the mandrel's axis Z

3.4. Tow tension fluctuations

The tension fluctuations were not plotted for the trajectory $T = const$ because the tension was so low in the range $S2 \leq z < S3$ that the tow slipped from the surface of the mandrel making the winding process unfeasible at the adopted experimental conditions. The spectrum of the tension fluctuations for the other trajectories during filament winding of the tow over the HLD mandrel had a downward peak in the range $S2 \leq z < S3$ (Fig. 4). The drop in tow tension probably was caused by the winder control features: at point M2 (Fig.

238

2a), the rotational speed of the axis X decreased significantly to make the other axes complete their increments in conditions of the limitations imposed on the maximal velocity and acceleration of the axes.

The detailed analysis of the downward peaks has shown that the least value of the tow tension measured by sensor 8 was zero for the trajectory *2 surfaces* and close to zero for the trajectory $\lambda = const$, while the minimum value of the tow tension for the *complex* trajectory was observed in the range of 300-600 cN (Fig. 5). As the mean values of the tow tension measured by both sensors slightly varied with the type of trajectory and the least coefficient of variation was demonstrated by the *complex* trajectory (Table 5), one could conclude that the depth of the peak was affected by the machine path. However, the machine path (or the free fiber length), as well as the winding velocity, were the same in the range $S2 \leq z < S3$ for both *complex* and $\lambda = const$ trajectories (Fig. 3), thus the expected dynamic behavior should be the same. The difference in the peak depth was probably caused by the speed of the axis Y in point M2, which was different for the mentioned trajectories, or by the measurement uncertainty. The differences between the minimal values of the tow tension measured for the *complex* and $\lambda = const$ trajectories were of the same order as their standard deviations (Table 5). The highest coefficient of variation was observed at the trajectory *2 surfaces*, which was tested at the constant feed rate.

Table 5. Mean values of the tow tension

Tension Sensor	Trajectory	Winding speed	Mean, cN	Standard deviation, cN	Coefficient of variation, %
4	$\lambda = const$	V=3450 mm/min	1139	208	18.3
	Complex	V=3450 mm/min	1122	176	15.7
	2 surfaces	F=8000 units/min	1169	227	19.4
8	$\lambda = const$	V=3450 mm/min	2155	389	18.0
	Complex	V=3450 mm/min	2162	319	14.8
	2 surfaces	F=8000 units/min	2151	448	20.8
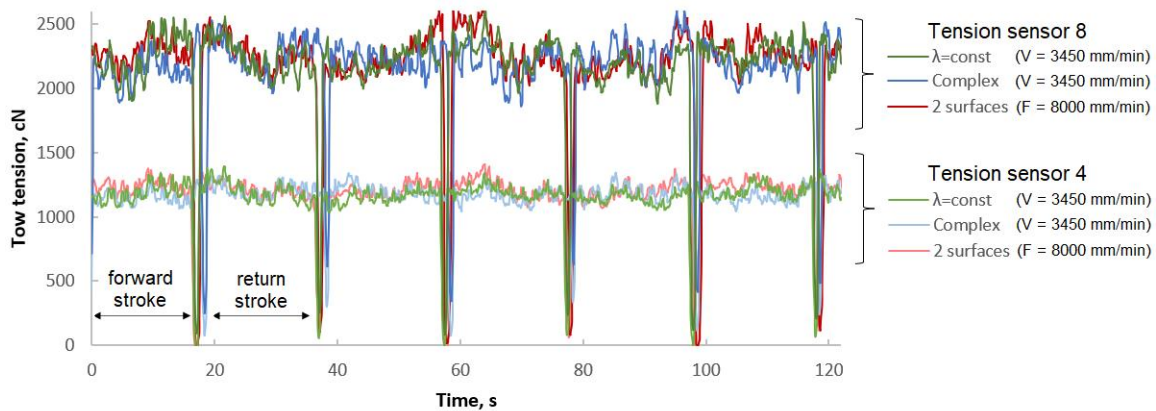
Figure 4. The tension fluctuations measured for the HLD mandrel
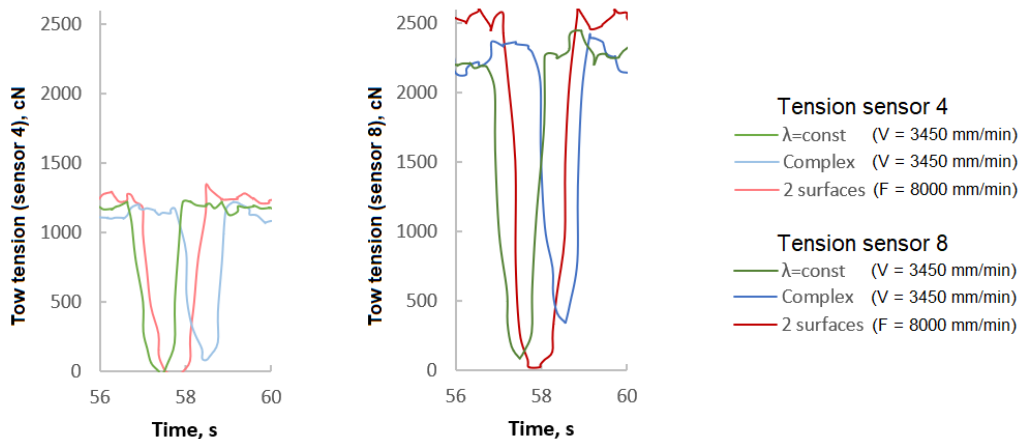
Figure 5. A detailed view of downward peaks in the range 56-58 s

4. CONCLUSIONS

There can be an almost infinite number of different machine trajectories for the manufacturing of a cylindric pressure vessel with elliptic domes by the filament winding technique depending on the combination of the control surfaces, however, some of them cannot be realized without a rewinding mechanism of the package or a tension compensator. As shown for the particular configuration of the mandrel, a machine path that follows only a cylindrical control surface is among these machine trajectories. The tow tension at this path was near zero for a period enough to provoke a slippage of the tow from the surface of the mandrel.

For the majority of the computed machine paths, the tow tension fluctuations were about some average value during most of the winding trajectory with an abrupt and short-term decrease in tension right after the interface casing-to-dome. However, the minimum value of the tow tension drop was significantly above zero only for the machine path computed by the complex control surface method. In conditions when a tension compensator is not installed and the creel is equipped only with the mechanism providing precise torque control for the rotating package, the *complex* machine path is preferable for the filament winding of a pressure vessel as compared to the machine path with a constant fiber length.

4.1. Declaration of Competing Interest

The author declares no conflict of interest.

4.2. Acknowledgements

5. REFERENCES

[1] S.T. Peters. *Composite Filament Winding*, 2011, ASM International. (ISBN 0-61503-722-5).
[2] F. Abdel-Hady. Theoretical Approach to Wind Elbow Structure. *Journal of Reinforced Plastics and Composites*, Volume 25, No. 4, 2006. (https://doi.org/10.1177/0731684405060579).
[3] D. Cohen. Influence of filament winding parameters on composite vessel quality and strength. *Compos Part A: Appl Sci Manuf,* 28(12):1035–47, 1997. (https://doi.org/10.1016/S1359-835X(97)00073-0).
[4] T. Sofi, S. Neunkirchen, R. Schledjewski. Path calculation, technology and opportunities in dry fiber winding: a review. *Advanc. Manuf.: Polymer & Composites Science*, 2018. (https://doi.org/10.1080/20550340.2018.1500099)
[5] A. Andrianov et al. A Low-Cost Filament Winding Technology for University Laboratories and Startups. *Polymers*, 14, 2022. (https://doi.org/10.3390/polym14051066)
[6] S. Koussios. *Filament Winding: A Unified Approach*, 2004, Delft University Press. (ISBN 90-407-2551-9).
[7] F. Abdel-Hady. Filament Winding of Revolution Structures. *Journal of Reinforced Plastics and Composites*, 2005. (https://doi.org/10.1177/0731684405047772).
[8] S. Koussios et al. Filament Winding. Part 2: Generic Kinematic Model and Its Solutions. *Composites Part A: Applied Science and Manufacturing*, 2004. (https://doi.org/10.1016/j.compositesa.2003.10.004).

Evaluation of the mechanical properties of ABS/Sugarcane bagasse composites made from recycled ABS

Luana Alves Patrocínio[(a),*], Gisele D. C. Antolin[(b)], Mauricio Q. Antolin[(c)], Mônica C. C. dos Santos[(d)]

(a) ⓘ 0009-0007-2456-9428 (State University of Rio de Janeiro – Brazil)
(b) ⓘ 0000-0003-0123-3183 (State University of Rio de Janeiro – Brazil)
(c) ⓘ 0000-0002-1887-1694 (State University of Rio de Janeiro – Brazil)
(d) ⓘ 0000-0002-4520-7625 (State University of Rio de Janeiro – Brazil)
* Corresponding author: luanapatrocinio11@hotmail.com

Abstract: ABS, a commonly used 3D printing material, can be recycled despite it being a non-renewable source. However, thermal degradation can cause structural changes, reducing its mechanical properties and optical properties. Adding fibers to ABS creates a composite material, improving recycling. This study compares the mechanical properties of ABS-based samples: pure 3D printed ABS (non-recycled), ABS Recycled (pure ABS) and ABS/Sugarcane bagasse composites. For this, mechanical resistance, impact resistance and morphological analyzes of these materials were carried out. Results show that ABS/sugarcane bagasse samples have lower impact resistance and elasticity due to fiber distribution and orientation. Recycling ABS is a viable option for reducing 3D printing's environmental impact, and adding natural fiber from sugarcane bagasse is a good reinforcement choice.

1. INTRODUCTION

3D printing is a technology that has transformed the way objects are manufactured, allowing the creation of parts from digital models, which are produced by the layer-by-layer deposition of material [1]. One of the most commonly used materials in 3D printing is Acrylonitrile Butadiene Styrene (ABS) thermoplastic, a petroleum-derived resin formed by combining three monomers: acrylonitrile, butadiene, and styrene. ABS has been widely adopted due to its versatility, heat and cold resistance, appealing visual appearance, and ability to be molded by injection or extrusion. Moreover, despite being made from a non-renewable source, its thermoplastic nature allows for recycling [2], potentially addressing the issue of the large quantity of 3D-printed ABS parts that are daily discarded.

Nevertheless, it is observed that the recycling of polymeric materials result in a significant reduction in their mechanical strength, due to structural changes associated with thermal degradation [3]. Consequently, various strategies have been proposed for the reuse of these materials without compromising their properties. One such strategy involves the formation of composite materials by introducing natural fibers into the material intended for recycling [3, 4].

In recent years, literature has seen numerous studies aiming to obtain composites from an ABS matrix, using fibers such as eucalyptus fiber [5], acrylic fiber [6], and coconut fiber [7]. Given the vast diversity of natural fibers in Brazil, other proposals can still be explored, such as sugarcane bagasse fibers.

Sugarcane bagasse fibers stand out among plant fibers due to their widespread availability in Brazilian soil, originating from sugarcane agro-industries. After the milling and juice extraction process, the fibrous residue known as sugarcane bagasse is widely used as fuel to generate electricity within these industries.

However, a significant portion of this resource is not reused, resulting in a substantial amount of waste [8], which could be used to enhance the mechanical properties of recycled ABS, thereby addressing two issues: the large amount of waste ABS from the 3D printing process and sugarcane bagasse fibers. Thus, this study aims to analyze the influence of adding sugarcane bagasse to recycled ABS from the 3D printing process.

2. METHODOLOGY

Parts made of pure ABS, 3D printed, have been manufactured at the Modeling and Visualization Laboratory (LabMov) of the State University of Rio de Janeiro (UERJ), using the following manufacturing parameters: 100% infill, extrusion temperature of 225ºC, and print speed of 120 mm/s. These parts will be referred to as non-reprocessed pure ABS.

After undergoing the manufacturing process and mechanical testing, some 3D printed parts are deemed unusable and often disposed of incorrectly. Consequently, research on material recycling is highly relevant. To evaluate the mechanical properties of recycled ABS material, these parts were manually reduced to the appropriate dimensions for passage through a knife mill with a 10-mesh screen, yielding powdered material. These samples will be referred to as pure ABS and will be used to assess the effect of reprocessing on the material's mechanical properties.

A third group of samples were manufactured from powdered pure ABS (matrix) reinforced with sugarcane bagasse fibers. These samples will be called ABS/Sugarcane. For the latter categories, the fibers were subjected to the acetylation process. In the acetylation process, the fibers were immersed in a 1% aqueous NaOH solution for 1 hour. They were then rinsed repeatedly until they reached a neutral pH and dried in an oven at 60°C for 24 hours. The mercerized and dried fiber samples were placed in a container, submerged in a thermostatic bath containing a mixture of acetic anhydride and acetic acid in a ratio of 1.5:1.0. After the reaction time, the samples were washed in running water and then in distilled water to remove the product until they reached neutral pH.

Before starting the production of the composites, both the fibers and the ABS were dried in an oven at a temperature of 60ºC. The fibers remained for 24 hours, while the ABS dried for 8 hours. After this stage, the fibers underwent a grinding process, using a 10 mesh. Then the materials, respecting their appropriate proportions, were sent to the manufacturing process. After this process, the materials (ABS powder and fibers) were duly weighed, in the mass proportion 45/05 for every 45g of ABS, 5g of reinforcing filler was used, in this case, sugarcane bagasse.

Finally, the powdered material was placed under a hollow mold until it was filled and taken to a hydraulic press at a temperature of 225ºC. After this, the parts went through two degassing processes and were then pressed at 5 tons for five minutes. After this time, the mold was taken to a cold hydraulic press and pressed at 3 tons to solidify the parts for another five minutes.

It is worth noting that in this manufacturing process, specimens were made in order to carry out Charpy tests according to the standard (ASTM D6110) and tensile tests (ASTM D638 type V). Another important issue is that the composites were made with staple fibers, i.e. short fibers as a reinforcing phase placed randomly inside the matrix [12]. After the mechanical tests, scanning electron microscopy (SEM) analyses were carried out to check the adhesion of the fibers to the matrix.

3. RESULTS AND DISCUSSION

The results obtained during the tensile test for the ABS/Sugarcane bagasse, Reused ABS samples and ABS non-reprocessed are presented in detail in Table 1. This table includes information such as the modulus of elasticity (E), tensile strength (σr), maximum stress (σm) and yield strength (σe).

As observed in Table 1, reprocessing significantly reduces the mechanical strength of this material. This is due to several causes, the most important being the loss of molecular mass [13]. Among the samples analyzed, it was observed that ABS/sugarcane bagasse had higher maximum stress values than pure ABS. The literature [14] indicates that parts made from recycled ABS tend to have lower mechanical strength than the original material before the recycling process. This decrease in strength can be attributed to the presence of voids within the recycled ABS samples, which appear during the pressing process, as illustrated in figure 1. It is assumed that these voids may be related to various causes, such as: insufficient mold temperature and the degassing process carried out quickly, which may have meant that the air did not have time to escape.

Thus, the increase in these values when compared to pure ABS may indicate that the sugarcane bagasse can be successfully incorporated into thermoplastic matrices, showing optimum dispersion of the fiber in the matrix during processing.

TABLE 1: RESULTS OBTAINED FOR THE MECHANICAL TESTS

Parts	ABS (Non-reprocessed)	ABS/Sugarcane bagasse	Pure ABS
σm (MPa)	30.89±1.38	14.98 ± 4.65	7.83±0.35
σr (MPa)	29.79±1.32	10.71±5.36	5.66±0.12
E (MPa)	360±40	210±50	400±59
σe (MPa)	16.36±0.43	6.22±1.63	7.52±0.51
Impact resistance (J/m)	91.85±4.48	69.56±15.28	133.04±23.07

Figure 1: Void inside of the part after the tensile test. Source: Author (2024)

The adhesion of the fibers to the matrix was assessed using scanning electron microscopy of the fractures obtained in the tensile strength tests, as shown in figure 2. As can be seen in figure 2, the fibers in this material are detached from the polymer fibers, suggesting little affinity between the phases. As pointed out by reference [8], this characteristic can lead to a reduction in the mechanical strength values of the parts.
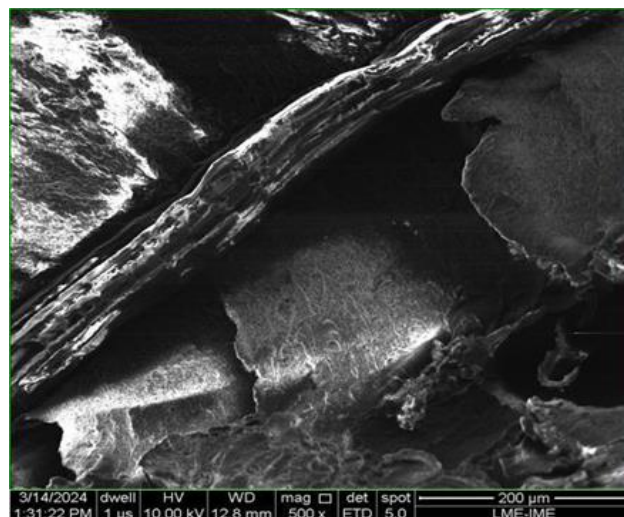
Figure 2: Scanning electron microscopy of ABS/Sugarcane parts. Source: Author (2024)

The parts made with the ABS/Sugarcane material had a value of 6.22 MPa, compared to the parts made with the reused material without the addition of a reinforcing filler, which had a value of 7.52 MPa. Based on the standard deviation of the different materials, it can be seen that there was no appreciable change, as the values found in both tests were similar.

With regard to the modulus of elasticity of the ABS/Sugarcane material and impact resistance, we can see that its value was reduced with the addition of fibers. A material's impact resistance is related to its energy absorption capacity (in the elastic and plastic phases). The yield strength is associated with the material's resistance in the elastic phase. Thus, the reduction in the value of this property may be related to the fact that

the angle of orientation of the microfibrils in relation to the longitudinal axis, which determines the stiffness of the fibers, or to the random way in which the fibers were placed [15].

In addition, it is believed that the low values found for modulus of elasticity and impact resistance may be a reflection of adhesion problems between the fibers and the material matrix. This could be solved by changing the chemical treatment procedures or the composition of the composites, increasing the amount of reinforcing fiber.

However, with the small addition of 0.5g of sugarcane to 0.45g of ABS, it was possible to increase the maximum strength of the reprocessed material. It is therefore possible that with the addition of more sugarcane fiber, the mechanical strength of the reprocessed material will be close to that of the 3D printed ABS.

4. CONCLUSIONS

Reusing ABS is a viable alternative for reducing the environmental impact generated by 3D printing. As well as promoting sustainable practices, the ABS recycling process can also result in savings for the user, who has the opportunity to reuse the material in new projects. So, as observed in this work, the mechanical properties of recycled materials tend to be lower than those parts with added reinforcement. This can be attributed to the presence of voids in the material, possibly due to flaws in the recycling process.

Therefore, according to this study, the addition of sugarcane bagasse fiber increased the maximum strength of the parts compared to reused ABS. It should be noted that this is a sustainable practice, since the sugarcane fiber would no longer be used after its useful life.

Nevertheless, it was observed in this work that the addition of sugarcane fibers in small quantities (5g) failed to improve the other mechanical properties of the parts. Therefore, the next steps for this work are to change the treatment of the fibers and the mass proportion of the composites.

4.1. Acknowledgements

5. REFERENCES

[1] F.R. Ishengoma, A B. Mtaho. *3D Printing: Developing Countries Perspectives.* International Journal of Computer Applications (0975 – 8887) Volume 104, 2014

[2] M.I. Mohammed, et al. EcoPrinting: Investigating the use of 100% recycled Acrylonitrile Butadiene Styrene (ABS) for Additive Manufacturing. In: *Solid Freeform Fabrication 2017: Proceedings of the 28th Annual International Solid Freeform Fabrication Symposium – An Additive Manufacturing Conference.*

[3] F.R. KLEIN. *Estudo da degradação termomecânica e fotooxidativa de poli(acrilonitrila-butadieno-estireno) para fins de reciclagem primária. Master's dissertation. Postgraduate Degree in Materials Science and Engineering*, Federal University of Santa Catarina, 2009.

[4] E. LIGOWSKI et al. *Composite materials based on sugarcane fibers and recycled polymers obtained through the extrusion technique.* Polymers: Science and Technology, v. 25, n. 1, p. 70-75, 2015.

[5] M.M. Schwartz. *Composite Materials: Processing, Fabrication and Applications (Vol. 2).* 1st Edition, 1996, Prentice Hall. (ISBN: 978-0133000399).

[6] W. O. DOMINGUES. *Produção do compósito de fibra de eucalipto (Eucalyptus) com matriz polimérica de ABS.* 2019. 58 f., il. Course Conclusion Paper. University of Brasília, Brazil, 2019.

[7] D. Conto et al. *Propriedades de Compósitos ABS/fibra acrílica*, in: XVII Encontro de Jovens Pesquisadores as UCS, Brasil, 2009

[8] M.H. Ishizaki, et al. *Mechanical and Morphological Characterization of Polypropylene and Green Coconut Fiber Composites: Influence of Fiber Content and Mixing Conditions.* Polymers: Science and Technology, vol. 16, n° 3, p. 182-186, 2006. (http://dx.doi.org/10.1590/S0104-14282006000300006)

[9] J.P.M. OLIVEIRA. *Compatibilização de compósitos de PEBD reforçados com o bagaço da cana-de-açúcar.* 2019. 51 p. Course Conclusion Paper, Department of Materials Engineering, Federal Technological University of Paraná. Brazil, 2019.

[10] Y.H. LOH, et al. *Sugarcane bagasse—The future composite material: A literature review.* Resources, Conservation and Recycling, v. 75, p. 14–22, 2013. (http://dx.doi.org/10.1016/j.resconrec.2013.03.002).

[11] L.H. Carvalho et al. *Properties of polyester/hibrid sisal-glass fabrics.* Polímeros-ciência e Tecnologia, 16, 2006. (http://dx.doi.org/10.1590/S0104-14282006000100009)

[12] K.F. Timbó, et al. *The influence of fiber positioning on the mechanical strength of composites*. Brazilian Journal of Development, 2020. (https://doi.org/10.1046/j.1365-2842.2001.00792.x)

[13] J.E. McIntyre, *The Historical Development of Polyesters*. John Wiley & Sons, LDT eBooks, p.1-28, 21, jun. 2004. (https://doi.org/10.1002/0470090685.ch1).

[14] L. Q. ALMEIDA. *Reciclagem de ABS oriundo da indústria automobilística: influência do processamento por termoformagem e do envelhecimento nas propriedades mecânicas.* Course Conclusion Paper. Graduation in Materials Engineering. Federal University of São Carlos, Brazil, 2022.

[15] B.F.M. de Castro. *Estudo e Caracterização Mecânica de Compósitos Reforçados com Fibras Naturais*, Master's dissertation, Instituto Politecnico do Porto, Portugal, 2013.

DYNAMICAL MECHANICAL PROPERTIES OF EPOXY COMPOSITES WITH IONIC LIQUID-MODIFIED ARAMID PULP

Eduardo F. Kerche[(a)*], Joziel A. da Cruz[(b)], Amanda A.X. da Silva[(c)], Henri S. Schrekker[(d)], Sandro C. Amico[(e)]

(a) ⓘ 0000-0003-1361-0708 (TRL9 Tech – Experimental and Development Research in Physical and Natural Science, Mundo Street 121, Salvador, 41301-110, Brazil);
(b) ⓘ 0000-0001-5123-1608 (Textile Engineering Department, Federal University of Santa Catarina, João Pessoa Street 2750, Blumenau, 89036-002, Brazil);
(c) ⓘ 0000-0001-6897-2576 (Federal University of Goiás, EMC – School of Electrical, Mechanical and Computer Engineering, Universitária Avenue 1488, Goiânia, 74605-010, Brazil);
(d) ⓘ 0000-0002-8173-3841 (Laboratory of Technological Processes and Catalysis, Federal University of Rio Grande do Sul, Bento Gonçalves Avenue 9500, Porto Alegre, 91501-970, Brazil);
(e) ⓘ 0000-0003-4873-2238 (PPGE3M, Federal University of Rio Grande do Sul, Bento Gonçalves Avenue 9500, Porto Alegre, 91501-970, Brazil).
* Corresponding author: eduardo.kerche@trl9.tech

Abstract: Three ethanolic solutions containing imidazolium ionic liquid (IL) were used for the surface modification of an aramid pulp (AP) to improve its interaction with epoxy resin. Composites were prepared by casting, with 0.4 parts per hundred of AP (untreated, or treated). Scanning electron microscopy (SEM), cryogenic fracture, and dynamic mechanical analysis (1 Hz) were performed. IL creates AP microfibrils that can better interact with AP and epoxy. IL-modified AP presented greater defibrillation with stronger interactions with the polymeric matrix, minimizing fibre pull-out. Morphological changes were partly responsible for the improvement in the dynamical mechanical response of the AP-IL/epoxy composites. The differences in normalized storage modulus (Ec/Em) between untreated and IL-treated AP composites in the elastic and rubbery regions were not significant. In the loss modulus curves, the composites with untreated-AP presented a small shoulder, close to 75 °C, which may be ascribed to the formation of aggregates. However, tan delta curves did not present significant differences. Despite that, a slight shift of tan delta peak to higher temperatures occurred for both HO_2 and $(HO_2)_2$. This paper address on the importance of ionic liquid using as filler treatment for the improvement of interaction of aramid pulp with epoxy matrix.

1. INTRODUCTION

Several types of fillers and reinforcements are used for the improvement of the physical-mechanical response of epoxy [1, 2], and poly-*p*-phenyleneterephthalamide (PPTA) has been reported in recent research [3]. PPTA may replace more conventional fillers, such as carbon black, silica, and even graphene and its derivatives [4]. Enhanced nitrile butadiene rubber [5], styrene-butadiene rubber [6, 7], rigid polyurethane foam [8] and epoxy-based composites [3] may be prepared with PPTA.

Aramid pulp (AP) is one of the forms of PPTA, being a hard, non-toxic and fibrillated filler. Fibrillated reinforcements present greater ability to intertwine with polymeric matrices what may lead to the formation of a stronger interface with improved characteristics compared to particulate fillers [9]. Despite the benefits, adjacent PPTA chains present extensive hydrogen bonding between carbonyl and NH groups, along with

aromatic π-π stacking interactions [10, 11]. This leads to an inert and smooth surface, which limits interactions with polymeric matrices and, consequently, its applicability in composites [12].

Imidazolium-based ionic liquids (IL) may interact both with AP and epoxy matrix through secondary bonds, including hydrogen bonding and aromatic π-π stacking. Within the tested IL, 1-butyl-3-methylimidazolium chloride (C$_4$MImCl) formed the strongest hydrogen bond with the hardener, which also suggested stronger interaction with cured epoxy. The IL 1-carboxymethyl-3-methylimidazolium chloride (HO$_2$CC$_1$MImCl) and 1,3-dicarboxymethylimidazolium chloride ((HO$_2$CC1)$_2$MImCl) also established strong hydrogen bonds with the hardener [3, 13].

Various IL have been reported to efficiently compatibilize AP with polymer matrices. These IL treatments potentially have lower cost and are more environmentally friendly compared to other AP surface treatment techniques such as plasma, ultraviolet and nanostructure depositions [14]. Such IL treatment was associated with positive characteristics related to AP defibrillation and IL-polymer physical-chemical interactions.

The objective of this study was to further evaluate the role of imidazolium IL in the compatibilization of AP with triethylene tetramine cured epoxy resin, including a more detailed analysis of the viscoelastic response. Along with the IL that had provided the most promising composite in the previous study, C$_4$MImCl (Fig. 1), two different chloride-based IL HO$_2$CC$_1$MImCl (Fig. 1) and (HO$_2$CC1)$_2$MImCl (Fig. 1) were also investigated, functionalizing the imidazolium cation with carboxylic acid groups. Those IL were evaluated due to their strong hydrogen bonding potential, as previous stated.
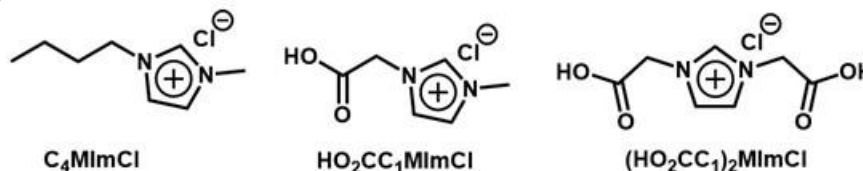
Figure 1: Chemical structures of the IL investigated as compatibilizers in AP/epoxy composites.

2. METHODOLOGY

DGEBA GY-260 Araldite® epoxy resin and triethylenetetramine (TETA) hardener AH-260 were purchased from Huntsman Co. (São Paulo, Brazil). C$_4$MImCl (95% purity) was acquired from Sigma-Aldrich (St. Louis, USA). Commercial aramid pulp (AP) was kindly donated by Dupont®, having length of 0.5–1 mm and bulk density of 48–160 kg.m^{-3}. All commercial chemicals were used as received. HO$_2$CC$_1$MImCl and (HO$_2$CC$_1$)$_2$MImCl were synthesized following literature procedures [15–18]. AP was immersed in an ethanolic solution with 5 wt.% of IL in relation to the AP mass (IL content chosen based on previous results [3]). The AP-IL mixture was placed in an ultrasonic bath at 50 °C for 30 min, left to evaporate the solvent for 24 h at room temperature, then placed in a vacuum oven for 12 h at 110 °C.

The as-received AP and AP-IL were characterized with field emission gun scanning electron microscopy (FEG-SEM), in a Jeol JSM 6060 SEM equipment operating at 10 kV, and energy-dispersive X-ray spectroscopy (EDS). Epoxy-based composites were prepared by adding 0.4 phr of untreated or IL-treated AP to the epoxy resin and mechanically stirring for 5 min at room temperature. Subsequently, the TETA hardener (13.0 phr) was added, and the mixture ultrasonicated for 10 min in an ultrasonic bath. The mixture was then degassed through cycles of negative pressure (−0.8 bar for 10 min) and atmospheric pressure (for 10 min) to remove entrapped air. Composites were molded by casting into silicone molds and curing at room temperature and post-curing in an air-circulation oven at 60 °C for 12 h [13]. The composites were codified in agreement with the type of AP added: AP (untreated AP), C$_4$ (AP + C$_4$MImCl), HO$_2$ (AP + HO$_2$CC$_1$MImCl) and (HO$_2$)$_2$ (AP + (HO$_2$CC$_1$)$_2$MImCl). AP content into the composites and procedure were defined based on the results of a previous study [3]. The morphology of cryogenically fractured epoxy and its composites was evaluated with the same FEG-SEM equipment used for the characterization of the AP fillers.

DMA was performed with specimens of the same dimensions of the flexural tests. A three-point bending clamp was used in a TA Instruments DMA 2980 equipment at 1, 10 or 100 Hz, from 30 °C to 200 °C. (Please, inform which heating rate was used.) The glass transition temperature (T$_g$) was determined from the tan delta peak. Effectiveness of the filler reinforcement in all composites was assessed based on the C constant, as in a previous work [11], equation 1:

$$C=\left(\frac{\left(E'_g/E'_r\right)_{Composite}}{\left(E'_g/E'_r\right)_{neat\ rubber}}\right) \tag{1}$$

where: E'_g and E'_r are the storage moduli related to the glassy and rubbery regions, respectively.

3. RESULTS AND DISCUSSION

Fig. 2 presents SEM images of the cryogenic fractured samples. The composites reinforced with untreated or IL-treated AP (Fig 3A-D) presented a rougher fracture surface, related to crack growth deviation when the material fractured. Besides, due to the low compatibility between untreated AP and epoxy, a tendency towards AP aggregation is evidenced in Fig. 3C. The formation of aggregates can be ascribed to the relatively strong intermolecular fibril interactions (mainly π–π stacking and hydrogen bonding), which also resulted in resin-poor regions [19]. The poor fiber-polymer interaction in composite AP is shown in Fig. 2A (circle highlighting the poorly attached epoxy/AP interface) [14, 20] and Fig. 2A-B (many pull-out holes identified in the circles).

When AP was treated with IL (Fig. 2C-D), micro-AP fibrils with lower aspect ratio are present, represented in the circle in Fig. 2C and the arrow in Fig. 2D. This can be related to hydrogen bonding and π–π stacking between IL and AP, disrupting the self-intermolecular bonding of AP [7]. Such microfibrils may avoid AP detachment from the epoxy matrix, increasing the interfacial interaction between AP and epoxy.
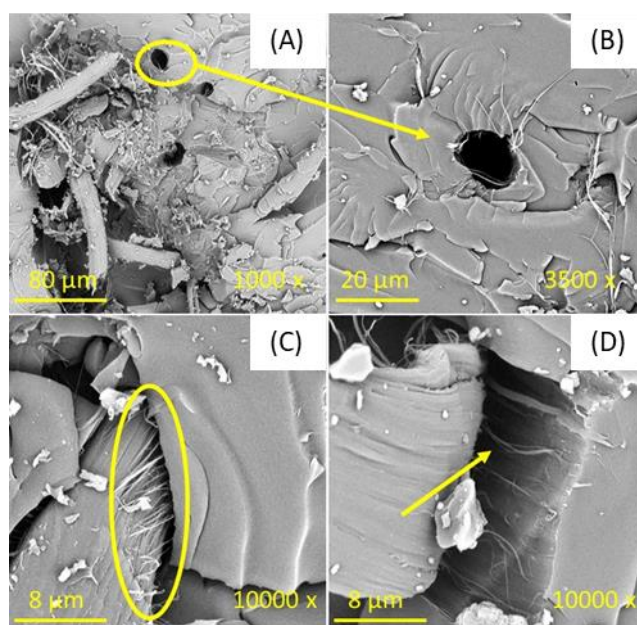
Figure 2: SEM images of fractured samples of epoxy AP composites (A-B), C_4 (C) and HO_2 (D).

Fig. 3 presents the non-isothermal DMA curves, obtained at 1 Hz, for epoxy and its composites. Table 1 presents the main properties obtained from these curves (E_c and E_m are storage moduli of the composite and neat epoxy, respectively). Comparing with the AP composite, the C parameters of the composites C_4 and HO_2 presented higher values, whereas the $(HO_2)_2$ composite presented a lower value. This suggests that the studied IL have distinct effects on the reinforcement-matrix interaction (weaker for C_4 and HO_2 and stronger for $(HO_2)_2$), with varied degrees of AP defibrillation, IL compatibilization and AP dispersion [4, 13].

In the loss modulus curves (see Fig. 3B), the AP composite presented a small shoulder close to 75 °C, which may be ascribed to the formation of aggregates [3]. In general, the tan delta curves did not present significant differences at 1 Hz frequency. Despite that, a slight shift of the tan delta peak to higher temperatures occurred for HO_2 and $(HO_2)_2$.

The parameter of full width at half maximum (FWHM) of the tan delta curves may also be used to assess the composite homogeneity. The lower the FWHM, the higher the homogeneity, and the higher the tan delta peak height, generally, the greater the interaction between the composite components, which may be governed by the interface [3, 4]. From Table 1, neat epoxy presented a lower FWHM due to the absence of a

second phase. As for the composites, the values were somewhat similar, which may again be related to the low AP content used as reinforcement, although it was slightly lower for composite $(HO_2)_2$.
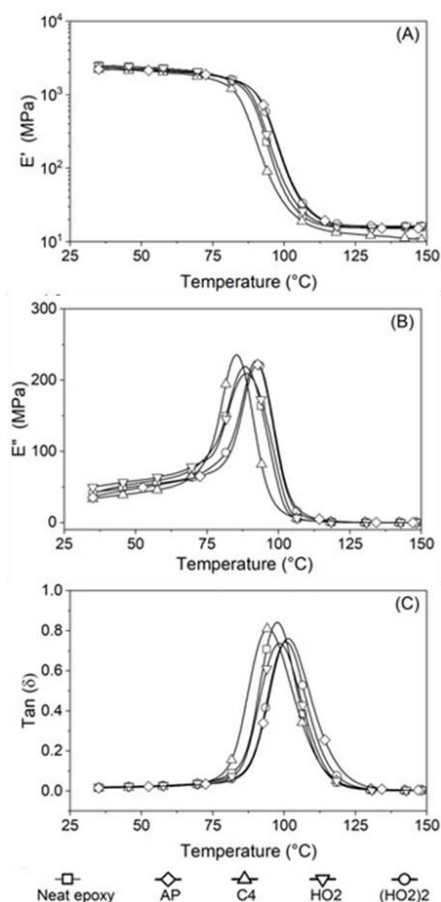
Figure 3: DMA curves of epoxy and its composites analyzed at 1 Hz: (A) Storage modulus, (B) Loss modulus and (C) tan delta.

Table 1: Viscoelastic parameters from DMA, obtained at 1 Hz, for epoxy and its composites.
"Please, inform what the letters 'a' and 'b' used in the table mean."

Parameter	Neat epoxy	AP	C_4	HO_2	$(HO_2)_2$
E'_c/E'_m (at 40 °C) [a]	1.00	0.90	0.90	1.00	0.95
E'_c/E'_m (at 140 °C) [a]	1.00	0.97	0.72	1.02	1.04
C (40/140 °C) [a]	1.00	0.93	1.24	0.97	0.91
E'' (MPa)	220.0	223.2	235.3	208.5	226.9
Peak height [b]	0.84	0.76	0.81	0.74	0.74
FWHM (°C) [b]	15.7	17.9	18.6	17.5	16.4

4. CONCLUSIONS

Ethanolic solutions containing IL proved to be a suitable modifier for aramid pulp. Modified-AP proved to have more significant interaction with epoxy matrix, compared to untreated AP. The composite with AP treated with $(HO_2)_2$ showed improved dynamical-mechanical response as well as C parameter was lower for those samples. Although those C_4 samples presented improved mechanical response previous reported.

4.1. Declaration of Competing Interest

The authors declare no conflict of interest.

4.2. Fundings

4.3. Acknowledgements

5. REFERENCES

1.   Mostovoy A, Shcherbakov A, Yakovlev A, et al (2022) Reinforced Epoxy Composites Modified with Functionalized Graphene Oxide. Polymers 2022, Vol 14, Page 338 14:338. https://doi.org/10.3390/POLYM14020338

2.   Lazzari LK, Neves RM, Kerche EF, et al (2024) Biochar from poultry litter as reinforcement used in epoxy-based composites: mechanical and dynamic mechanical properties. Polymer Bulletin 1–16. https://doi.org/10.1007/S00289-023-05128-2/TABLES/3

3.   Kerche EF, da Silva VD, Fonseca E, et al (2021) Epoxy-based composites reinforced with imidazolium ionic liquid-treated aramid pulp. Polymer (Guildf) 226:123787. https://doi.org/10.1016/j.polymer.2021.123787

4.   Kerche EF, Demétrio da Silva V, da Cruz JA, et al (2023) Aramid pulp modified with imidazolium ionic liquids as a potential replacement for carbon black in fluorinated rubber composites. Polym Compos. https://doi.org/10.1002/PC.27288

5.   Zhang R, Yuan X, Sun R, et al (2023) Preparation and properties of the aramid pulp/nitrile butadiene rubber composites with compatibilization of ionic liquids. Polym Compos. https://doi.org/10.1002/PC.27217

6.   Silva VD da, Jacobi MM, Schrekker HS, Amico SC (2018) Aramid pulp with physisorbed imidazolium ionic liquids for solvent-casted enhanced styrene-butadiene rubber composites. J Appl Polym Sci 135:46693. https://doi.org/10.1002/app.46693

7.   Silva VD da, Jacobi MM, Schrekker HS, Amico SC (2019) Imidazolium ionic liquid compatibilizers in melt-blended styrene-butadiene rubber/aramid pulp composites. Polymer Bulletin 76:3451–3462. https://doi.org/10.1007/s00289-018-2550-4

8.   Kerche EF, Demétrio da Silva V, Jankee G da S, et al (2021) Aramid pulp treated with imidazolium ionic liquids as a filler in rigid polyurethane bio-foams. J Appl Polym Sci 138:50492. https://doi.org/10.1002/app.50492

9.   Dalmas F, Cavaillé JY, Gauthier C, et al (2007) Viscoelastic behavior and electrical properties of flexible nanofiber filled polymer nanocomposites. Influence of processing conditions. Compos Sci Technol 67:829–839. https://doi.org/10.1016/J.COMPSCITECH.2006.01.030

10. Silva VD da, Barros ÍR de, Conceição DKS da, et al (2020) Aramid pulp reinforced hydrogenated nitrile butadiene rubber composites with ionic liquid compatibilizers. J Appl Polym Sci 137:48702. https://doi.org/10.1002/app.48702

11. Kerche EF, Neves RM, Ornaghi HL, et al (2022) The influence of Ionic liquid concentration on microcrystalline cellulose modification. Carbohydrate Polymer Technologies and Applications 100211. https://doi.org/10.1016/J.CARPTA.2022.100211

12. Moraes C V, Silva VD da, Castegnaro M V, et al (2020) Lightweight Composites through Imidazolium Ionic Liquid Enhanced Aramid − Epoxy Resin Interactions. ACS Appl Polym Mater 2:1754–1763. https://doi.org/10.1021/acsapm.9b01145

13. Kerche EF, Kairytė A, Członka S, et al (2023) Imidazolium Ionic Liquids as Compatibilizer Agents for Microcrystalline Cellulose/Epoxy Composites. Polymers (Basel) 15:333. https://doi.org/10.3390/POLYM15020333/S1

14. Zhang B, Jia L, Tian M, et al (2021) Surface and interface modification of aramid fiber and its reinforcement for polymer composites: A review. Eur Polym J 147:110352

15. Gisbert P, Trillo P, Pastor IM (2018) Comparative Study of Catalytic Systems Formed by Palladium and Acyl-Substituted Imidazolium Salts. ChemistrySelect 3:887–893. https://doi.org/10.1002/SLCT.201702818

16. Lu L, Jieshan Y, Shitao Y, et al (2018) Stability and activity of cellulase modified with polyethylene glycol (PEG) at different amino groups in the ionic liquid [C2OHmim][OAc]. Chem Eng Commun 205:986–990. https://doi.org/10.1080/00986445.2018.1428191

17. Huang Z, Wang Y, Zhang N, et al (2018) One-Pot Synthesis of Ion-Containing CO2-Based Polycarbonates Using Protic Ionic Liquids as Chain Transfer Agents. Macromolecules 51:9122–9130. https://doi.org/10.1021/ACS.MACROMOL.8B01834

18. Prabhakara MD, Maiti B (2020) Ionic liquid-immobilized proline(s) organocatalyst-catalyzed one-pot multi-component Mannich reaction under solvent-free condition. Research on Chemical Intermediates 2020 46:4 46:2381–2401. https://doi.org/10.1007/S11164-020-04096-W

19. Pistor V, Ornaghi FG, Ornaghi HL, Zattera AJ (2012) Dynamic mechanical characterization of epoxy/epoxycyclohexyl–POSS nanocomposites. Materials Science and Engineering: A 532:339–345. https://doi.org/10.1016/J.MSEA.2011.10.100

20. Mallick PK (2007) Fibre-reinforced composites materials, manufacturing and design, 3rd ed. CRC Press, New York

BIODEGRADABLE VISCOELASTIC POLYURETHANE FOAM FOR SUSTAINABLE ENGINEERING PROJECTS

André Alves Guimarães[(a)*], André Luís dos Santos[(b)], Rodrigo Teixeira Santos Freire [(c)]; Luiza Fernandes Soares[(d)]; Túlio Hallak Panzera [(e)];

(a) 0009-0009-1515-7311 (Federal University of São João del-Rei – Brazil)
(b) 0000-0002-1738-2792 (Federal University of São João del-Rei – Brazil)
(c) 0000-0001-5206-5939 (Federal University of São João del-Rei – Brazil)
(d) 0000-0002-9339-7080 (Federal University of São João del-Rei – Brazil)
(e) 0000-0001-7091-456X (Federal University of São João del-Rei – Brazil)
* Corresponding author: andre.guima2001@hotmail.com

CODE: BCCM7-179

Abstract: Developing biodegradable viscoelastic polyurethane foam from renewable sources is a significant step towards sustainable engineering projects. This foam, composed of two polyols (RD70-B and AGT 1315-B) and a diisocyanate (RD70-A) manufactured from castor oil, aims to reduce environmental impacts and contribute to a circular economy. The foams are analysed for various characteristics, including expansion rate, bulk density, tensile and compressive modulus. The study found that foams containing at least 30% of RD70-A and 30% to 50% of RD70-B expanded correctly, without permanent contractions, achieving a mean bulk density of 0.25 g/cm³, tensile modulus of 255 kPa and compressive modulus of 228 kPa.

1. INTRODUCTION

One of the greatest challenges facing modern industry is the acquisition of versatile materials that do not contribute to global warming. In recent decades, there has been a significant increase in the use of non-biodegradable polymeric materials resistant to natural decomposition conditions. Improper disposal of these materials in nature leads to issues such as waste accumulation and pollution of landscapes and natural habitats, including rivers and seas.

Research indicates that around 30% of the waste volume discarded in the environment is comprised of plastic materials [1]. Lambert and Martin [2] reported that out of the 8300 million metric tons of plastic produced between 1905 and 2015, 4900 tons were discarded (59%), 2500 tons (30%) have been in use, and only 800 tons were recycled. This means that only 9% of all polymer materials produced worldwide have been recycled. A method to reduce the impact of improper plastic disposal is to invest in the manufacturing of biodegradable materials, which can decompose entirely after being discarded. This decomposition process involves microorganisms breaking down their molecules and internal structures, allowing them to be assimilated by the environment and preventing excessive waste accumulation [3].

An increasingly promising material gaining traction in the scientific community is polyurethane foam derived from castor oil, a plentiful tropical plant found in Brazil. This alternative technology holds the potential to replace petroleum-derived polyurethane foams, which are non-renewable and non-biodegradable. As a result, extensive research has been conducted to explore its various applications [4]. These applications include the automotive industry for manufacturing vehicle seats, and the construction sector for thermal and acoustic insulation [5].

Vinay et al. [6] also utilised foam in the healthcare industry, suggesting the use of castor oil-based foams for constructing wheelchair seats and mattresses to explore their antibacterial properties. Their research revealed an enhancement in the antibacterial characteristics of the castor oil-based foams, along with an improvement in their mechanical properties compared to traditional polyurethane foams. Shaik [7] synthesised polyurethane foams made from castor oil and lithium hydroxide. Their study characterised properties such as density, cell morphology, phase morphology, and thermomechanical properties, revealing that the properties of the synthesised foams surpassed those of conventional polyurethane foams. Martins [8] combined castor oil-based polyurethane foam with banana peel fibres to create a biocomposite, analysing its physical properties with and without the incorporation of fibres. The fibres led to increased foam density and thermal stability, along with a reduction in pore size and crystallinity. Iqhrammullah et al. [9] manufactured foams from castor oil and combined them with zeolite, bentonite, and activated carbon to eliminate heavy metals from aqueous media originating from industrial waste. Their analysis involved laser-induced breakdown spectroscopy (LIBS) and characterisation through infrared spectroscopy methods and scanning microscopy, successfully removing heavy metal ions from water and achieving success in their research. Establishing complete certainty and confidence in this new material within the industrial realm necessitates further exploration of its properties. Lee et al. [10] highlighted that despite the rising promise of foams derived from vegetable oils due to their cost-effectiveness, natural abundance, and ease of extraction, petroleum derivatives continue to dominate the commercial market. Additionally, Olszewski et al. [11] underscored the importance of studies comparing compression properties with foam composition and how the material's stoichiometry influences its overall performance.

The present study focuses on developing flexible and biodegradable foams using raw materials supplied by Imperveg (Brazil). A vegetable-based polyurethane derived from Ricinus communis oil, devoid of solvents and heavy metals, is utilised to create a non-toxic and biodegradable product. The study investigates the foam's density, expansion rate, compression modulus, and structure.

2. METHODOLOGY

2.1. Materials

The focal material of this study is a biodegradable elastomeric foam comprising three components: two polyols, labelled by the company as RD70-B and AGT 1315-B, and one pre-polymer RD70-A, all of which are not commercially available. The density of the liquid components was concurrently determined in a related study by Soares [12], who examined the same raw materials produced by Imperveg (Brazil). Table 1 presents the density and molecular weight values of the oils utilized.

Table 1. Physical-chemical properties of the components.

Commercial Name	Density (g/cm³)	Molecular weigh
RD70-A	1.26	250.3
RD70-B	0.99	298.46
AGT 1315-B	0.98	250 - 1000

Initially, preliminary tests are carried out to determine the experimental conditions conducive to producing an elastic foam. Subsequently, the expansion rate, compressive and tensile properties, and microstructural analysis are conducted.

2.2. Expansion rate

In the preliminary test, nine conditions were previously defined, each featuring distinct proportions between the two polyols and the pre-polymer, as illustrated in Table 2. The efficacy of each expansion was analysed based on three criteria: (i) complete curing of the material; (ii) flexibility characteristic and (iii) ease of demoulding and good surface quality. Complete curing of the material is confirmed when the final foam is non-sticky, signifying a complete reaction of all components. The elastic characteristic is evaluated by manually compressing the samples and observing if they deform and promptly regain their original shape. Surface quality is assessed by inspecting the foam after demoulding and checking for tears or defects on the surface. Each expanded sample consists of 5.5 g of the total mixture, and the mixture fabrication is conducted manually. A polymer mould of 25 x 25 x 25 mm³ is used. Upon mixing the three components, an exothermic

reaction takes place, leading to expansion and the formation of the foam. This growth typically occurs between 15 and 20 seconds after the commencement of the manual mixing process of the components.

Table 2. Composition of the foams.

Experimental conditions	% RD-A	% RD-B	% AGT-B
M1	45	45	10
M2	40	45	15
M3	30	70	0
M4	30	50	20
M5	30	45	25
M6	30	40	30
M7	30	30	40
M8	25	50	25
M9	20	60	20

2.3. Expansion Rate and Density

The expansion rate is a property that signifies the volumetric increase following the reaction between all components and can be defined as the ratio between the volume of the sample after and before mixing. The principle of water displacement is employed to determine the foam's final volume. This is achieved by placing the sample in a 500 ml beaker along with an aluminium block of 49.32 cm³, which serves to keep the sample submerged. The measurement methodology proceeds as follows:

I. The sample with the block is placed in the beaker, and the volume is then adjusted to the 500 ml mark with water.

II. Subsequently, the sample with the block is removed from the container, and water is added again to the 500 ml mark. The volume of water added in this step corresponds precisely to the value of the sample volume plus the volume of the aluminium block.

III. Finally, the volume of the block is subtracted from the total volume obtained, thus yielding the value of the sample volume. This procedure was carried out in triplicate for each sample to avoid parallax errors and provide greater reliability in the experimental results. The final response was obtained by averaging the three measurements.

Density stands as one of the paramount properties of foams. The foam density test is carried out following the ASTM D1622/D1622M [13,14] standard, involving the measurement of the foam's mass using a balance with a precision of 0.001g, and determining its volume. Samples with dimensions of 25x25x25 mm³ are employed for this test.

2.4. Compressive testing

The compression test is performed utilising an Instron testing machine (Figure 1) by the ASTM D1621-16 (2018) standard. While this standard is specifically tailored for tests on rigid foams, it is selected as a reference due to its parameters being better suited to the project. The test is executed using a 1 kN load cell, with test specimens measuring 15x15x15 mm³, and a test speed of 1.5 mm/min. The samples are compressed until they reach 60% of their total thickness. Subsequently, a stress versus strain graph is generated to calculate the foam's elasticity modulus, and the foam structure recovery rate is also determined.
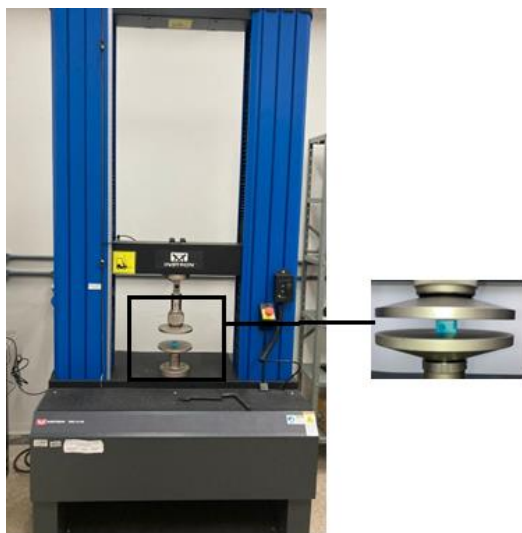
Fig.1. Compression testing

2.5. Tensile testing

The tensile test is carried out using an Instron testing machine by the ASTM D3574-17 (Test E) standard, employing a 1 kN load cell. The test specimens are laser-cut following specimen type D412-A, at a test speed of 500 mm/min. Tensile specimens are depicted in Figure 2. The samples are subjected to tension until rupture, yielding a stress-strain graph. The foam's elasticity modulus is derived from the slope of the line in the elastic regime within the deformation interval from 4% to 8%.
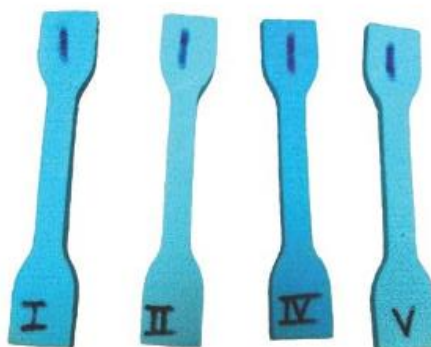
Fig.2. Tensile test specimens.

2.6. Statistical Analysis

The data obtained are subjected to statistical analyses using the Minitab software. The elastic modulus values for each test are analysed to identify any statistical differences among the samples. This involves employing analysis of variance (ANOVA) and Tukey's test for comparisons. Tukey's test serves as a complement to the analysis of variance, allowing the identification of any contrasts between two means and enabling the differentiation of experimental conditions through categorized and ordered groups in alphabetical order. Group A is consistently categorized as the one with the highest experimental absolute value, and experimental conditions sharing the same group are considered equal. To validate ANOVA, normality tests are conducted using the Ryan Joiner and Kolmogorov-Smirnov methods.

3. RESULTS AND DISCUSSION

3.1. Preliminary Tests

Following the preliminary test, samples M4, M5, M6, and M7 met the necessary prerequisites. Table 3 details the ultimate characteristics of each sample after a 14-day curing period, as specified by the manufacturer. However, conditions M8 and M9 did not achieve complete curing of the components, and therefore, their mechanical properties were not analysed.

Table 3. Preliminary evaluation.

Samples	Full curing	Foam type	Demoulding	Defects
M1	Yes	Rigid	Easy	none
M2	Yes	Rigid	Easy	none
M3	Yes	Flexible	Easy	Contractions after cure
M4	Yes	Flexible	Easy	none
M5	Yes	Flexible	Easy	none
M6	Yes	Flexible	Easy	none
M7	Yes	Flexible	Easy	none
M8	No	-	Hard	Superficial defects
M9	No	-	Hard	-

3.2. Expansion Rate and Density

Table 4 presents the results of density and expansion rate for M4-M7 conditions. It is observed that, although the density values are very close for all analysed conditions, the largest difference between the expansion rates is approximately 13%.

Table 4. Density and expansion rate values

Samples	Density (g/cm^3)	Expansion rate (%)
M4	0.24 ±0.01	5.41 ±0.18
M5	0.28 ±0.01	4.93 ±0.33
M6	0.24 ±0.01	4.79±0.09
M7	0.25 ±0.01	5.34 ±0.33

3.3. Compressive properties

Figures 3, 4, 5, and 6 depict the stress-strain curves of samples M4-M7, while Table 5 presents the mean compressive modulus values with their respective Letter Group (Tukey test). Similar letters indicate equivalent means considering a 95% confidence level. The modulus varies significantly due to differences in the manufacturing proportions of each sample, notably, a decrease in the percentage of component RD 70-B, offset by an increase in AGT 1315-B, resulting in an elevation of the material's elasticity modulus. An 88% increase is found between M5 and M7.

Table 5. Compressive modulus.

Sample	Modulus of elasticity (kPa)	Letter Group
M4	139 ± 15	C
M5	135 ± 7	C
M6	184 ± 6	B
M7	255 ± 6	A
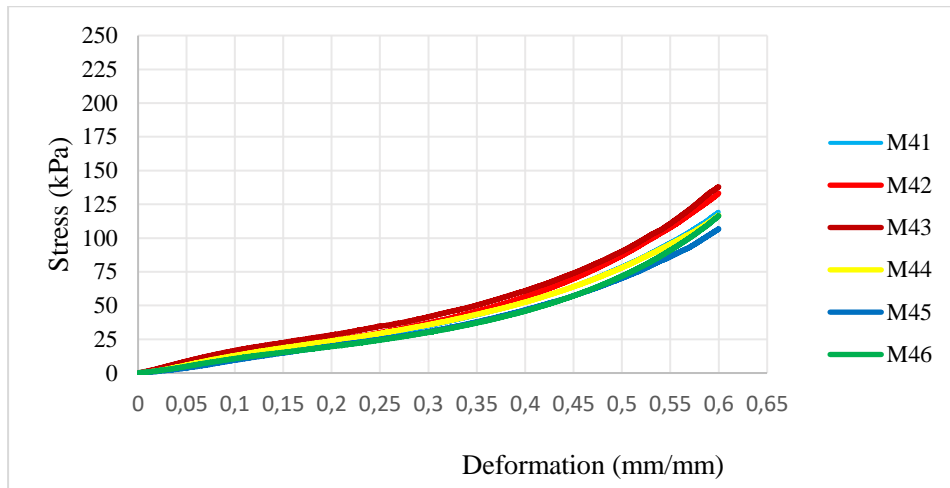
Fig. 3. Compressive stress-strain curve for M4 samples.
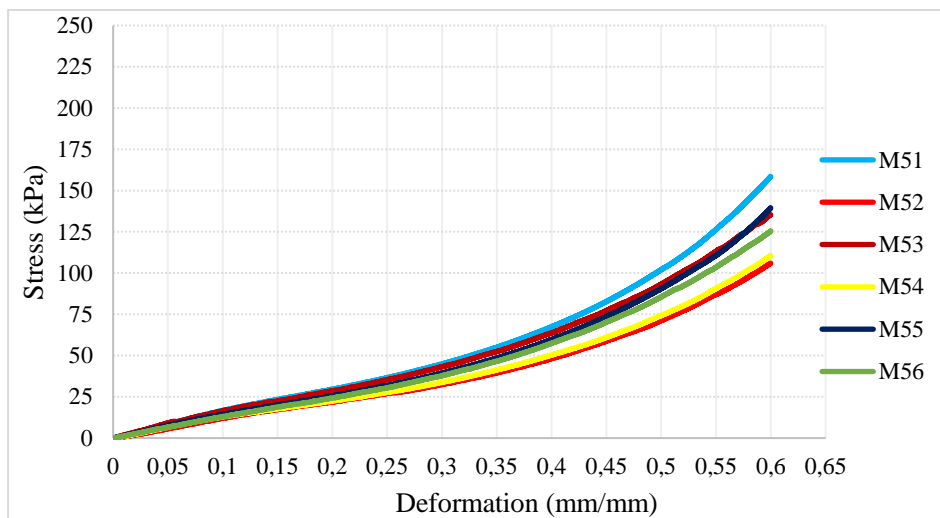
Fig. 4. Compressive stress-strain curve for M5 samples.
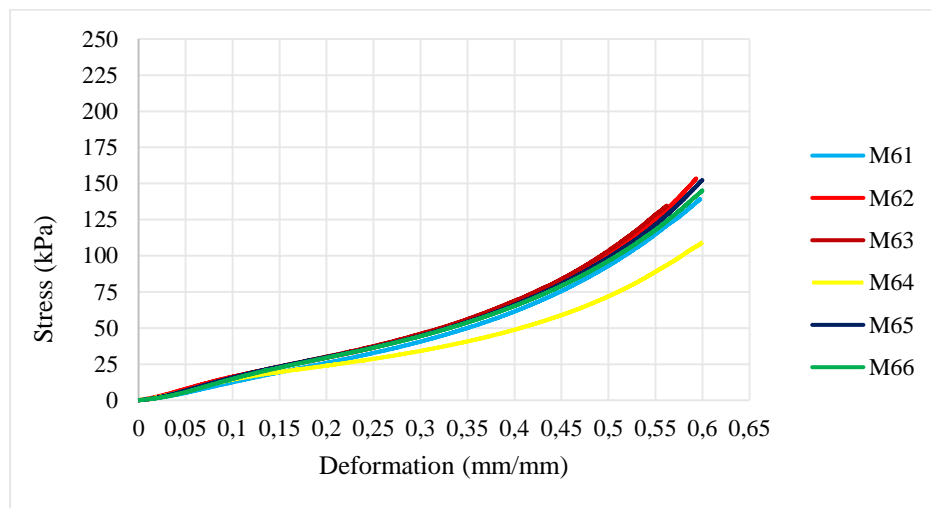
Fig. 5. Compressive stress-strain curve for M6 samples.
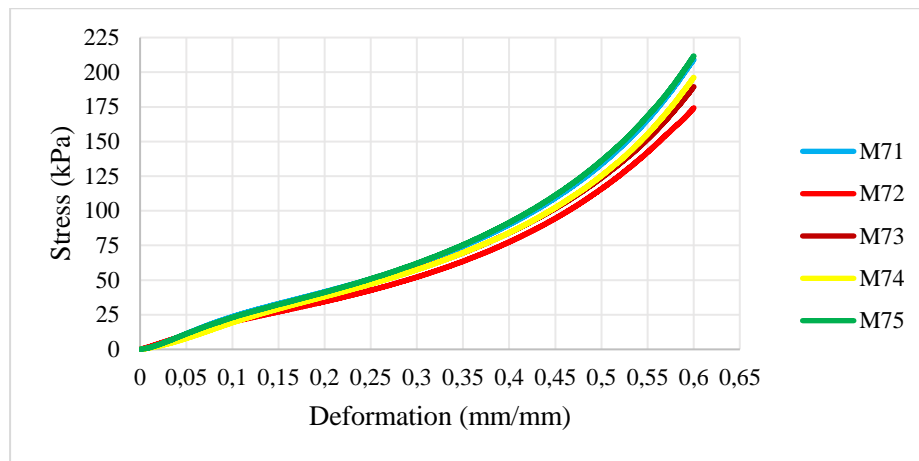
Fig. 6. Compressive stress-strain curve for M7 samples.

The castor oil-based foams exhibit elastomeric behaviour, as described by Gibson and Ashby [15]. After the load removal, all samples were re-measured with a digital calliper, revealing a 100% size recovery.

3.4. Tensile properties

Figures 7, 8, 9, and 10 display the stress-strain curves of the samples under tension, while Table 6 presents their elastic modulus values, followed by Tukey test analysis. Samples M4, M5, and M6 share Group b, indicating equivalent means. The M7 sample achieves the highest tensile modulus.

Table 6. Tensile modulus

Sample	Modulus of elasticity (kPa)	Letter Group
M4	134 ± 5	B
M5	135 ± 13	B
M6	150 ± 25	B
M7	228 ± 10	A
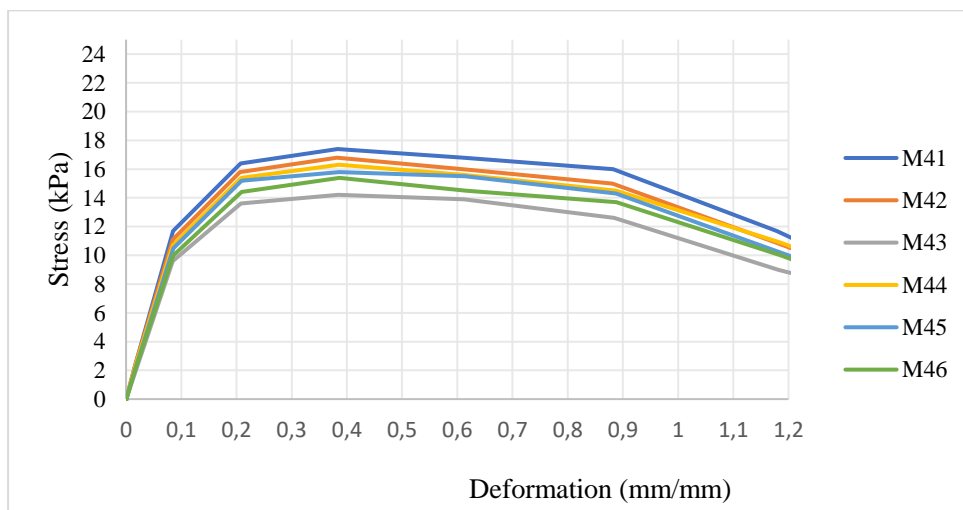
Fig. 7. Tensile stress-strain curve for M4 samples.
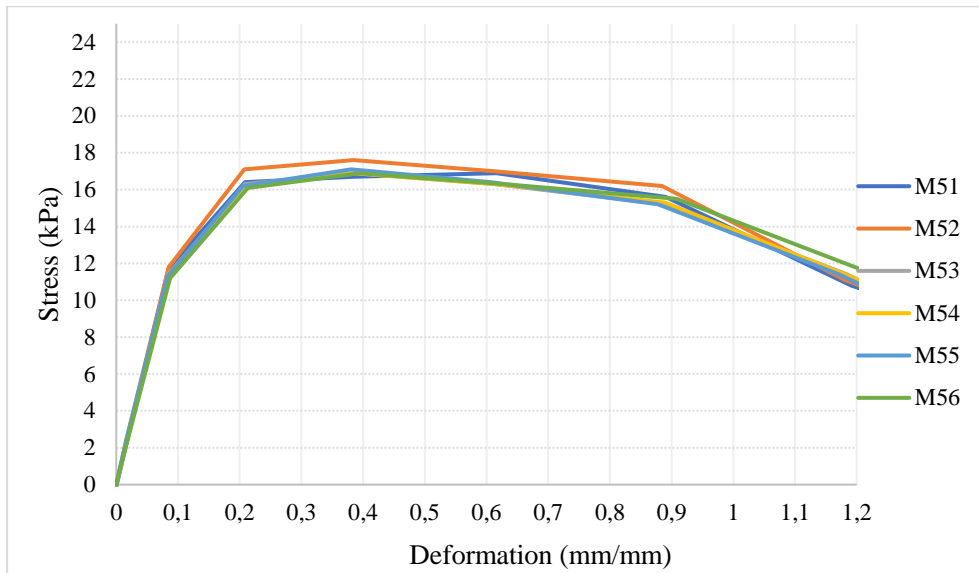
Fig. 8. Tensile stress-strain curve for M5 samples.
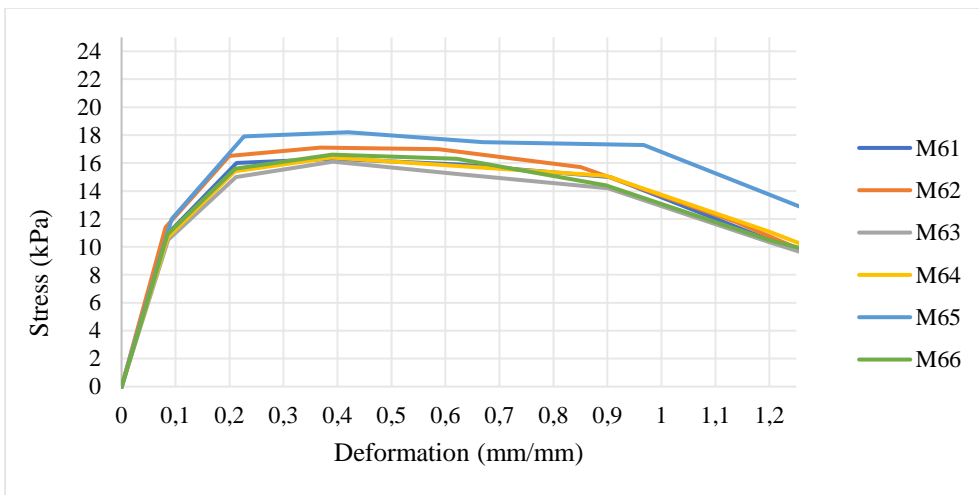
Fig. 9. Tensile stress-strain curve for M6 samples.
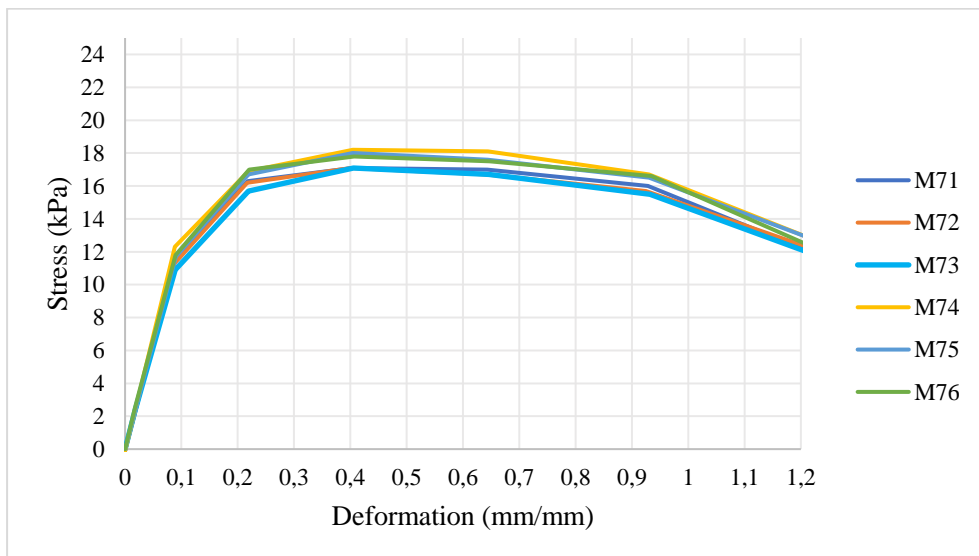
Fig. 10. Tensile stress-strain curve for M7 samples.

3.5. Statistical Analysis

Figure 11 compares the elastic modulus under tension and compression for each composition. As indicated in Table 5, samples M4 and M5 exhibit similar compressive moduli, while M4, M5, and M6 possess similar tensile moduli (Table 6). Sample M7 achieves the highest tensile and compressive moduli.
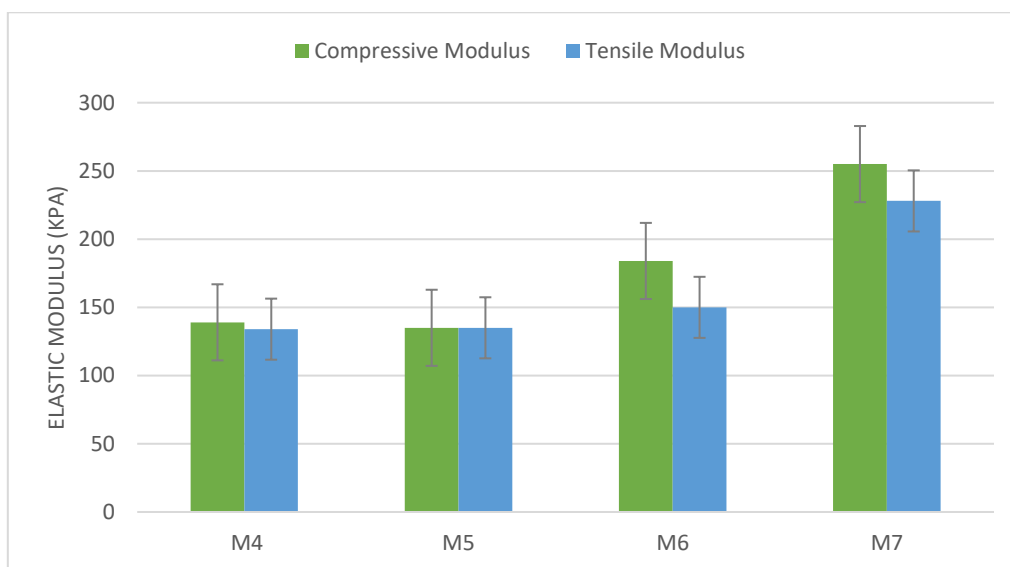
Figure 11. Elastic modulus comparison

To compare the data obtained from the tensile and compression tests, an ANOVA is conducted to determine the variances between the loads. Table 7 presents the variance of the elastic modulus as a function of the applied load. The analysis indicates that there is no significant difference between the elastic modulus obtained through compression or tension.

Table 7. ANOVA: Comparison between compressive and tensile modulus values

Anova	P value	R^2 (aj)	P value Ryan Joiner	P value Kolmogrov-Smirnov
Compressive values	0.000	96.54%	>0.150	0.097
Tensile values	0.000	87.13%	>0.100	>0.150

3.6. Microstructure analysis

The microstructural analysis of samples M4-M7 is conducted using an optical microscope, revealing predominantly closed and rounded cells of varying sizes. Figure 12 provides a visual representation of the structures of samples M4 (a), M5 (b), M6 (c), and M7 (d) at 50× magnification.
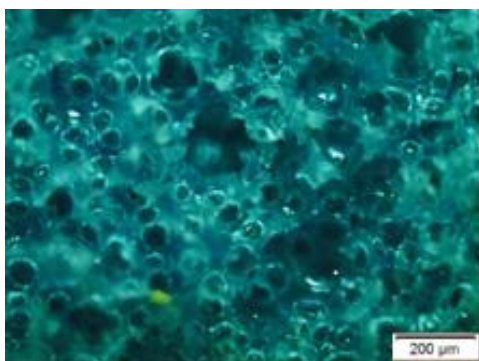
(a) Microstructure M4 foam.
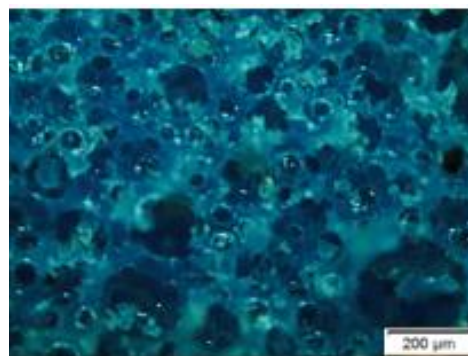
b) Microstructure M5 foam.
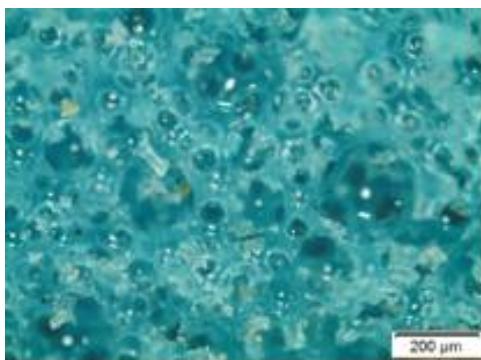
c) Microstructure M6 foam.
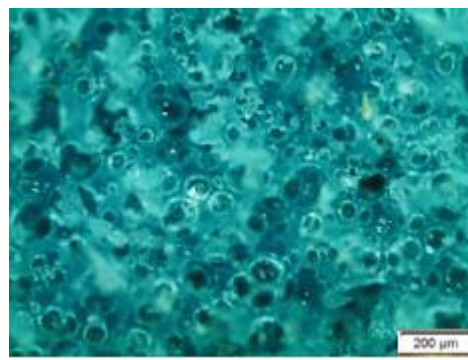
d) Microstructure M7 foam.

4. CONCLUSIONS

Out of the nine analysed conditions, only samples M4, M5, M6, and M7 met all three established prerequisites for achieving a flexible foam. Notably, despite varying proportions of polyols, these samples demonstrated similar densities and microstructures. The properties that exhibited differences among the conditions were the expansion rate and the elasticity moduli. The former displayed a modest variation of 13% between its highest and lowest values, while the latter showed a more substantial difference of 89% under compression and 70% under tension. A comparison of the results from the tensile and compressive testings revealed similar elasticity modulus values for samples with the same proportion. Specifically, sample M5 exhibited identical modulus values for tension and compression, while M4 showed a difference of 4%, M6 22%, and sample M7 12%, all with a higher compression modulus. Furthermore, the compression test unveiled the viscoelastic behaviour of the foams, achieving a complete recovery of 100% after compression of 60% of the original size.

Declaration of Competing Interest
The authors declare no conflict of interest.

Acknowledgements

5. REFERENCES

[1]   Bernardino D, Franz B. Lixo flutuante na Baía de Guanabara: passado, presente e perspectivas para o futuro. Desenvolvimento Meio Ambiente 2016; 38. http://dx.doi.org/10.5380/dma.v38i0.47024
[2]   Lambert S, Martin W. Environmental performance of bio-based and biodegradable plastics: the road ahead. Chemical Society Reviews 2017; 46. http://dx.doi.org/10.1039/c7cs00149e
[3]   Cangemi J, Santos A, Neto S, Chierice G. Biodegradation of polyurethane derived from castor oil. Polímeros 2008; 18. https://doi.org/10.1590/S0104-14282008000300004
[4]   Hsieh C, Chen YC. Synthesis of bio-based polyurethane foam modified with rosin using an environmentally-friendly process. Journal of Cleaner Production 2020; 276. https://doi.org/10.1016/j.jclepro.2020.124203
[5]   Moon J, Kwak S, Lee JY, Kim D, Ha J, Oh JS. Recycling of bio-polyurethane foam using high power ultrasound. Polymer 2020; 186. https://doi.org/10.1016/j.polymer.2019.122072
[6]   Vinay C, Varma M, Chandan M, Sivabalan P, Jaiswal A, Swetha S et al. Study of castor oil-based auxetic polyurethane foams for cushioning applications. Polymer International 2021; 70. https://doi.org/10.1002/pi.6259
[7]   Shaik AH, Banerjee S, Rahman A, Agashe S, Khan A, Chandan MR. One-step synthesis and characteristics of LiOH-castor oil based stable polyurethane foam. Journal of Polymer Research 2021; 28. https://doi.org/10.1007/s10965-021-02580-4
[8]   Martins L, Zanini N, Pinheiro L, Mulinari D. Valorization of Banana Peel Waste Used as Filler in Castor Oil Polyurethane Foam for Vegetal Oil Sorption. Journal of Natural Fibers 2022; 19. https://doi.org/10.1080/15440478.2021.1958414

[9]   Iqhrammullah M, Marlina M, Hedwig R, Karnadi I, Olaiya NG, Haafiz MM et al. Filler-Modified Castor oil-based polyurethane foam for the removal of aqueous heavy metals detected using laser-induced breakdown spectroscopy (LIBS) technique. Polymers 2020; 12. https://doi.org/10.3390/polym12040903

[10]   Lee J, Kim SH, Oh KW. Bio-based polyurethane foams with castor oil based multifunctional polyols for improved compressive properties. Polymers 2021; 13. https://doi.org/10.3390/polym13040576

[11]   Olszewski A, Kosmela P, Piasecki A, Zukowska W, Szcedanski M, Wojtasz P. Comprehensive investigation of stoichiometry–structure–performance relationships in flexible polyurethane foams. Polymers 2022; 14. https://doi.org/10.3390/polym14183813

[12]   Soares LF. Planejamento estatístico de mistura para caracterização de espuma biodegradável de mamona. Dissertação (Mestrado em Engenharia Mecânica). Universidade Federal de São João del Rei (UFSJ), São João del Rei, MG, 2022.

[13]   ASTM D1622/D1622M. Standard Test Method for Apparent Density of Rigid Cellular Plastics, 2014.

[14]   ASTM D1621-16. Standard Test Method for Compressive Properties of Rigid Cellular Plastics, 2018.

[15]   Gibson L, Ashby M. Cellular Solids: Structure and Properties. Cambridge University Press & Assessment, Cambridge, UK, 1999.

FEASIBILITY ASSESSMENT OF SIC-BASED COMPOSITES IN THE NUCLEAR INDUSTRY

Marcella C. Velloso[a] *, Carlos Henrique da L. Barbosa [b], Erica S. Souza [c], Francisco José de O. Ferreira [d], Frank F. Sene[e], Eduardo de S. Lima[f].

(a) 0000-0002-9006-6411 (Military Institute of Engineering – Brazil)
(b) 0000-0002-9166-2442 (Military Institute of Engineering – Brazil)
(c) 0009-0005-9163-4459 (Institute of Nuclear Engineering and State University of RJ – Brazil)
(d) 0009-0007-2045-9985 (Institute of Nuclear Engineering – Brazil)
(e) 0000-0001-6885-043X (Institute of Aeronautics and Space – Brazil)
(f) 0000-0001-6795-9927 (Military Institute of Engineering – Brazil)
* Corresponding author: marcella.candido@ime.eb.br

Abstract: Currently, an advanced SiC/Al_2O_3-based composite is under investigation for applications in the nuclear industry. This composite is formulated to provide exceptional radiation resistance and mechanical strength properties, rendering it suitable for the harsh environments prevalent in nuclear reactors. Experiments involve the utilization of electromagnetic radiation techniques to assess the structural integrity of the composite under simulated nuclear conditions. The investigation revolves around scrutinizing the diffusion and distribution patterns of elements within the composite, as well as assessing any potential alterations in crystal structure resulting from radiation exposure. Preliminary findings suggest that the composite exhibits substantial resistance to radiation-induced degradation while preserving its fundamental mechanical properties. Furthermore, electromagnetic radiation offers insights into the distribution of failures and discontinuities within the material, facilitating ongoing enhancements in its design and manufacturing processes. These discoveries hold promise for advancing the development of more sophisticated and safer materials for nuclear applications. Such advancements could enhance the efficiency and safety of nuclear power while opening avenues for further exploration in this domain.

1. INTRODUCTION

The demand for advanced materials in the nuclear industry has been a constant, driven by the need to develop components capable of withstanding the extreme conditions found in nuclear reactor environments [1,2]. In response to this demand, silicon carbide-based composites have garnered interest due to their exceptional properties of radiation resistance and mechanical strength [3,4]. In this context, the present study focuses on evaluating the feasibility of SiC/Al_2O_3 composites for applications in the nuclear industry.

These composites represent a promising class of materials due to the combination of the individual properties of these components. Silicon carbide (SiC) is known for its chemical stability, high resistance to elevated temperatures, and exceptional radiation resistance [5,6]. On the other hand, alumina (Al_2O_3) offers high mechanical strength and durability [7,8]. Combining these materials into a composite can potentially provide an effective solution to the challenges faced in the nuclear industry.

This study's primary objective is to evaluate the response of SiC/Al_2O_3 composites to ionizing radiation and examine their structural integrity under simulated nuclear operating conditions. By utilizing advanced analysis techniques, including electromagnetic radiation, we aim to investigate the distribution patterns of elements within the composite and any changes in the crystalline structure resulting from radiation exposure.

Additionally, we seek to provide a deeper understanding of the potential of electromagnetic radiation techniques in the non-destructive evaluation of materials, highlighting their fundamental role in developing more advanced and safer materials for nuclear applications. The findings of this study have the potential to significantly drive the advancement of material technology in the nuclear industry, contributing to more efficient and safer nuclear energy.

2. METHODOLOGY

For the preparation of the test specimens, SiC and Al_2O_3 powders manufactured by Imerys and Almatis, respectively, were used. The SiC powder from Imerys is the TREIBACHER ALODUR® Green SiC variety, characterized by its green color, alpha structure, and density of 3.21 g/cm³, while the Al_2O_3 powder from Almatis is the CT 800 SG type, with 96% purity and a density of 3.70 g/cm³. Two distinct formulations were employed in the preparation of the test specimens, as detailed in Table 1, which presents the specific proportions of SiC and Al_2O_3 in each formulation, carefully selected based on the desired properties for the final composite. In addition to the SiC and Al_2O_3 powders, a specific additive was used to aid in sintering, provided by a specialized company. The pieces were subjected to a sintering process at a temperature between 1900°C and 2100°C, aiming to achieve the desired densification and mechanical properties in the final composite.

Electromagnetic radiation inspection is a non-destructive testing technique that utilizes the penetrating property of radiation to examine the interior of materials or sealed components that require internal visual inspection without being ruptured or damaged [9]. In a radiographic inspection process, penetrating radiation - X-rays or gamma rays - reaches the material, interacts or not with it as it passes through, and upon exiting the material, reaches a radiographic film. The revealed image from this film shows internal characteristics such as structure and internal materials, density, fissures, bubbles, mass distribution, among others, that would only be observable with the rupture of the inspected material [10]. When passing through any material, electromagnetic waves are absorbed, and their intensity decays according to the formula:

$$I = Io.e - \mu x \qquad (1)$$

where I is the intensity of electromagnetic radiation after passing through the material, Io is the initial intensity, μ is the absorption coefficient of the material, and e is the base of natural logarithms, and x is the material thickness.

In the analysis of the internal structure of the composite, two main techniques were employed: electromagnetic radiation and X-ray diffraction (XRD). Electromagnetic radiation was used with a frequency on the order of 8×1014 Hz and an energy of approximately 5×1020 J.s. This technique allowed for the investigation of the structural integrity of the material and the monitoring of possible changes caused by radiation.

Furthermore, XRD was employed to investigate the crystalline phases of the composite. Using the Panalytical (IME) X'Pert MPD diffractometer from the Military Institute of Engineering, operating with cobalt Kα radiation (λ=0.17890 nm) with an iron filter. The 2θ scanning angle varied from 20 to 80°, with a step of 0.04° and 1.5 seconds per step, ensuring wide angular coverage. The acceleration voltage applied to the X-ray tube was 40 kV and the current was 40 mA, optimizing the quality of the data obtained.

These combined techniques allowed for a comprehensive characterization of the structure and properties of the composite before and after radiation exposure, providing valuable insights into its behaviour in nuclear environments.

Table 1. Proportions of SiC and Al_2O_3 in each test specimen formulation.

Test Specimen Formulation (%)	SiC	Al_2O_3
Formulation 1	40	60
Formulation 2	60	40

3. RESULTS AND DISCUSSION

The results obtained so far are promising, indicating that the SiC/Al_2O_3 composite exhibits excellent stability under radiation. The material's mechanical properties, such as Vickers hardness, remain virtually unchanged after exposure to radiation, as shown by preliminary results. Previous studies, such as those by Fortini (2023) and Zhu (2022), report Vickers hardness values (HV 0.5) between 20 and 27 GPa for SiC samples with additives, values higher than typical for ceramic materials [11,12]. However, the micrographs obtained during the Vickers tests were not clear enough to ensure the reliability of the measured values. Therefore, it will be necessary to redo the test to obtain accurate and reliable results.

The XRD analysis was performed to evaluate the crystalline structure of the SiC/Al_2O_3 composite and to assess any structural changes resulting from radiation exposure. Understanding these changes is important for determining the material's suitability for use in nuclear environments.

The X-ray diffraction patterns of SiC and Al_2O_3 samples were analyzed before and after non-destructive characterization using electromagnetic radiation. The analyses indicate that the samples exhibit well-defined crystalline phases. SiC shows characteristic peaks of the (111), (200), (220), and (311) crystal planes, while Al_2O_3 shows characteristic peaks of the (101), (110), (112), and (200) planes. The non-destructive characterization does not appear to have significantly modified the crystalline structure of the samples. However, new peaks emerged in the diffraction patterns after characterization, which may be attributed to impurities.

These results suggest that the SiC/Al_2O_3 composite maintains its structural integrity under radiation exposure. The preservation of peak positions and intensities implies that the composite's crystalline phases are stable, which correlates with the observed mechanical properties, which remained virtually unchanged after irradiation.
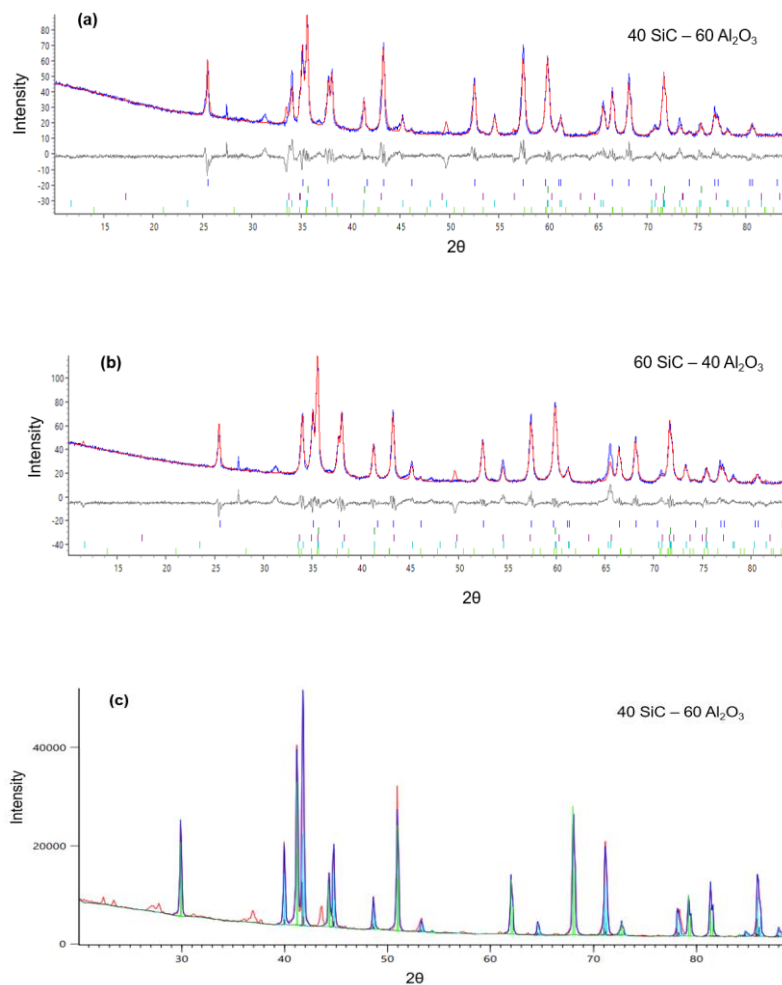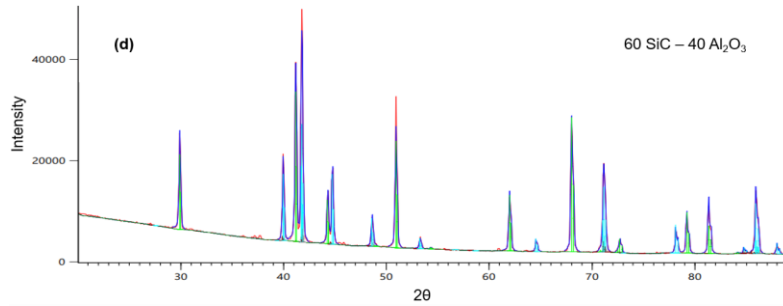
Figure 1. Presents the diffractogram of samples before and after non-destructive characterization by exposure to electromagnetic radiation

Electromagnetic wave analysis reveals a uniform distribution of failures and discontinuities, indicating a homogeneous response of the composite to radiation [10]. Figures 3 and 4 show images before and after characterization by exposure to electromagnetic radiation of the test specimens, using a non-destructive technique: (a) 40% SiC and 60% Al2O3, and (b) 60% SiC and 40% Al2O3. It is observed that both structures exhibit a uniform distribution of the material, with small regions of non-homogeneity at the edges. These analyses are fundamental for advancing materials technology in the nuclear industry, providing valuable insights for the design and optimization of radiation-resistant materials.
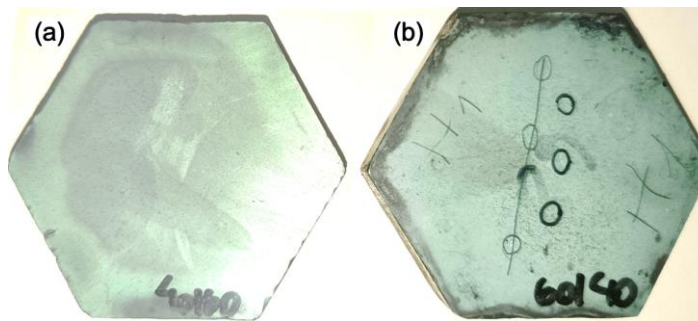
Figure 3. Image of the samples before characterization by exposure to electromagnetic radiation, (a) 40% SiC and 60% Al_2O_3, and (b) 60% SiC and 40% Al_2O_3.
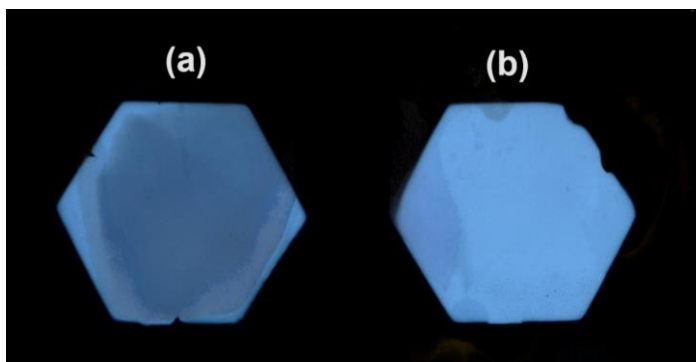
Figure 4. Radiography of the samples after characterization by exposure to electromagnetic radiation, (a) 40% SiC and 60% Al_2O_3, and (b) 60% SiC and 40% Al_2O_3.

4. CONCLUSIONS

The XRD analysis provided a detailed examination of the composite's crystalline structure before and after irradiation. The XRD patterns revealed that the major peaks at 2θ values of approximately 41.7° and 42,3°characteristic of SiC and Al_2O_3 phases remained unchanged in position and exhibited minimal variations in intensity post-irradiation. This stability in the crystalline structure suggests that the composite maintains its structural integrity under radiation, reinforcing its suitability for use in nuclear environments.

Furthermore, the use of electromagnetic radiation inspection as a non-destructive testing technique demonstrated the uniform distribution of failures and discontinuities, indicating a homogeneous response of the composite to radiation. The analysis of test specimens with different SiC and Al_2O_3 ratios (40% SiC and 60% Al_2O_3, and 60% SiC and 40% Al_2O_3) showed a consistent distribution of matter with minor regions of non-homogeneity at the edges.

Overall, these findings are fundamental for advancing material technology in the nuclear industry. The insights gained from this study contribute significantly to the design and optimization of radiation-resistant materials, enhancing the efficiency and safety of nuclear power systems.

4.1. Declaration of Competing Interest

The authors declare no competing financial interests or known personal relationships that could have appeared to influence the work reported in this article.

4.2. Acknowledgements

5. REFERENCES

[1] Yutai Katoh, Lance L. Snead. Silicon carbide and its composites for nuclear applications – Historical overview. *Journal of Nuclear Materials*, Volume 526, 2019. (https://doi.org/10.1016/j.jnucmat.2019.151849).

[2] Takaaki Koyanagi, Yutai Katoh, Takashi Nozawa. Design and strategy for next-generation silicon carbide composites for nuclear energy. *Journal of Nuclear Materials*, Volume 540, 2020. (https://doi.org/10.1016/j.jnucmat.2020.152375).

[3] R M.T.P. Rigby-Bell et al. The response of silicon carbide composites to He ion implantation and ramifications for use as a fusion reactor structural material. *Journal of the European Ceramic Society*, Volume 43, 2023. (https://doi.org/10.1016/j.jeurceramsoc.2023.07.056).

[4] H Hinoki et al. Development of Liquid Phase Sintering Silicon Carbide Composites for Light Water Reactor. *Coatings*, Volume 623, 2022. (https://doi.org/10.3390/coatings12050623).

[5] Tae-Young Cho, Young-Wook Kim. Effect of grain growth on the thermal conductivity of liquid-phase sintered silicon carbide ceramics. *Journal of the European Ceramic Society*, Volume 37, 2017. (https://doi.org/10.1016/j.jeurceramsoc.2017.04.050).

[6] Nikhil D. Andraskar, Gaurav Tiwari, Manmohan Dass Goel. Impact response of ceramic structures - A review. *Ceramics International*, Volume 48, 2022. (https://doi.org/10.1016/j.ceramint.2022.06.313).

[7] Saravanan Vanal Krishnan et al. Technical review: Improvement of mechanical properties and suitability towards armor applications – Alumina composites. Ceramics International, Volume 47, 2021. (https://doi.org/10.1016/j.ceramint.2021.05.146).

[8] Xian-Yu Jiang et al. Effect of high-enthalpy atmospheric plasma spraying parameters on the mechanical and wear resistant properties of alumina ceramic coatings. Surface and Coatings Technology, Volume 418, 2021. (https://doi.org/10.1016/j.surfcoat.2021.127193).

[9] A. R. Hussein et al. Evaluation of Electromagnetic Near-Field Measurement Technique as Non-Destructive Testing for Composite Structures. *IOP Publishing,* Volume 370, 2018. (https://dx.doi.org/10.1088/1757-899X/370/1/012002).

[10] Feifei Liu et al. Quantitative non-destructive evaluation of drilling defects in SiCf/SiC composites using low-energy X-ray imaging technique. *NDT & E International*, Volume 116, 2020, (https://doi.org/10.1016/j.ndteint.2020.102364).

[11] J. Fortini et al. Mechanical Properties of Silicon Carbide Ballistic Ceramic Doped with Silicon. *76th Annual ABM Congress – International*, São Paulo, Brazil, August 1-3, 2023.

[12] Y. Zhu et al. Effects of Sintering Additives on Microstructure and Mechanical Properties of Hot-Pressed α-SiC Ceramics. *Metallurgical and Materials Transactions*, Volume 53, 2022.

[13] O. Johnson et al. Microstructure and Properties of Al2O3–SiC. *In Proceedings of the World Congress on Engineering*, London, UK, 2–4 July 2014; Volume II, pp. 3–6

[14] I. Momohjimoh et al. Recent Advances in the Processing and Properties of Alumina–CNT/SiC Nanocomposites. *Nanomaterials*, Volume 9, 2019. (https://doi.org/10.3390/nano9010086).

EFFECT OF FIBER TENSION AND ORIENTATION ON THE PROPERTIES OF GLASS-FIBER/EPOXY FILAMENT WOUND TUBES

Diego T. de Souza[a]*, Maikson L. P. Tonatto[b], Marcelo B. Antunes[c], and Sandro C. Amico[d]

(a) 0009-0009-6316-3097 (Federal University of Rio Grande do Sul – Brazil)
(b) 0000-0002-3118-6894 (Federal University of Santa Maria – Brazil)
(c) 0009-0009-7027-879X (Lupatech – Brazil)
(d) 0000-0003-4873-2238 (Federal University of Rio Grande do Sul – Brazil)
Corresponding author: teodoro.souza@ufrgs.br

Abstract: Composite tubes, known for their durability and corrosion resistance, play a crucial role in oil extraction and water injection in wells. The production of these tubes is currently carried out by filament winding, a technique that offers a lightweight and robust solution, depositing filaments in layers. Filament tension and winding angle significantly determine the mechanical behavior of the final product, but their precise effect must be evaluated for each application. This work aims to evaluate the effect of filament tension and winding angles on the mechanical properties of composite tubes with glass-fiber/epoxy. Optical microscopy and fiber content analyses were performed on the composite to study fiber content, layer compaction and voids. Tensile testing was conducted according to ASTM D2290-19. The results indicated that applying higher tension resulted in greater compaction and less voids, thereby improving the mechanical performance of the tubes. Also, the change in winding angle affected the level of filament tension, depending on the region and geometry of the manufactured part. Understanding these factors deepens the knowledge about tube manufacturing and provides practical insights for optimizing the filament winding process and to ensure quality and performance of the products including longevity of pipelines, contributing to safety and efficiency.

1. INTRODUCTION

The development of high-performance pipes is vital for efficient and reliable transport of crude oil and refined products. Glass-fiber/epoxy tubes present themselves as interesting solutions for pipeline applications due to their superior durability and corrosion resistance. These tubes are manufactured by filament winding (FW), where fiber tension and angle are critical factors, significantly influences the final properties, such as longitudinal strength, circumferential strength, stiffness, and flexibility [1,2].

As the demand for these tubes grows, it becomes imperative to deepen the understanding on how the process parameters affect the mechanical behavior of the composite, being critical for designing robust pipeline systems capable of withstanding varied operating environments, ensuring long-term performance and integrity [3]. The applied winding tension, for instance, significantly affects the fiber content in the composite, which in turn affects its overall performance [4], in a way that, the higher winding tension, the higher the component strength [5,6,7].

This article aims at conducting a detailed investigation into the effects of fiber tension and orientation angle on the mechanical properties of glass-fiber/epoxy tubes, assessing how these two factors interact with each other and how they can be optimized to improve the performance of the tubes.

2. METHODOLOGY

The tubes were produced on a 2-axis filament winding machine, using 1100 Tex glass fiber tows from Owens Corning with 6 threads and a winding band of 36 mm, and epoxy resin from Olin. The Cadfil software was employed to calculate the best trajectories to be followed by the machine. The following lay-ups were used: $[\pm 50]_2$, $[\pm 65]_2$, or $[\pm 80]_2$. The 80° angle maximizes strength in tangential direction, especially when the final product is subjected to internal pressures, whereas the 50° angle may offers a balance of properties in tangential and axial direction [3,4].

The tension applied to the tows in the winding process was adjusted by increasing the path that the tow makes before reaching the metallic mandrel, which results in greater friction with the machine components, as depicted in Figure 1. A wet tow was fastened to a Compac digital dynamometer model IP-500 and pulled, measuring the force needed for the fibers to consistently slide through the components and onto the mandrel. Five measurements were taken for each scenario.

(a)   **(b)**   **(c)**
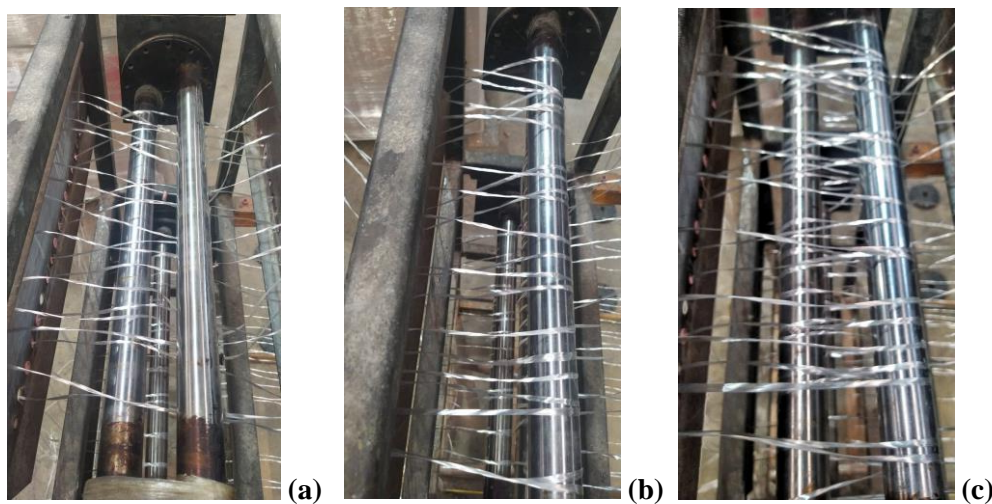
Figure 1. (a) Frictionless fiber, **(b)** fiber with 50% of maximum friction, **(c)** fiber with 100% maximum friction.

After winding, the part was cured in an oven. The final part was analyzed by optical microscopy, using a Zeiss brand microscope, Model Axio Lab.A1, with a magnification of 10x. Table 1 presents the nomenclature adopted for the samples. The fiber and resin contents were analyzed using the muffle burning method, according Method I of the ASTM D3171-22, which is based on the weight difference before and after burning of the resin at 600°C, leaving only the fiber. After cooling and weighing of the residue, the fiber and resin contents were calculated. To investigate the mechanical properties, the apparent hoop tensile test was carried out on rings cut from the tubes, based on the ASTM D2290-19 standard. The test was carried out in an universal testing machine Instron 3382 with a 100 kN load cell, as depicted in Figure 2, until the rupture of the specimens. The mean apparent tensile strength was calculated using three test specimens for each type of sample.

Table 1. Nomenclature and conditions analyzed in present study.

Sample	Angle (°)	Friction (%)
A50F0		0
A50F50	50	50
A50F100		100
A650F0		0
A65F50	65	50
A65F100		100
A80F0		0
A80F50	80	50
A80F100		100

<div align="right">(a)</div> <div align="right">(b)</div>
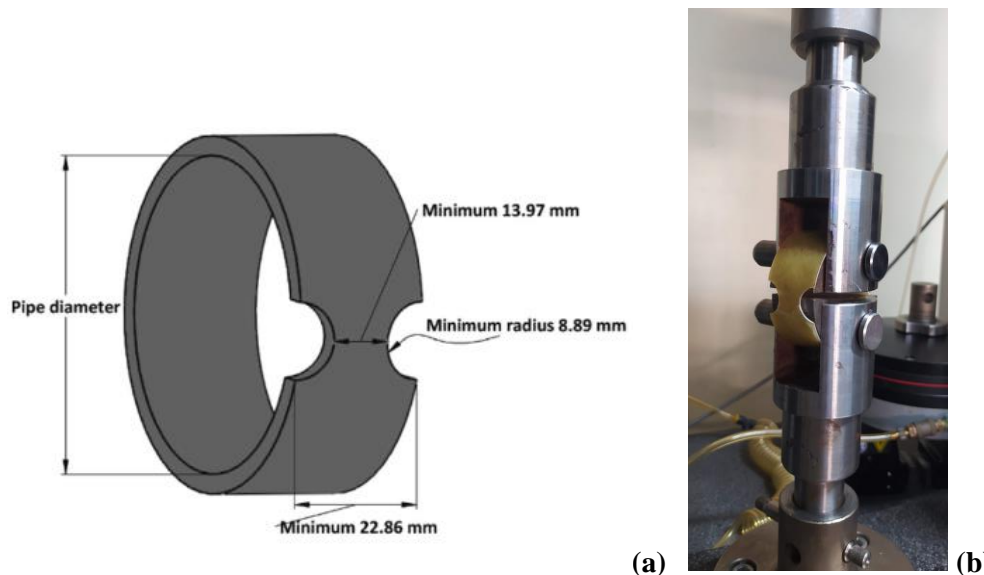
Figure 2. **(a)** Dimensions of the test specimen, and **(b)** Apparatus for the testing according to ASTM D2290-19 standard. [8].

3. RESULTS AND DISCUSSION

The fiber tension measured in the winding process for 0%, 50% and 100% of the maximum friction was 143.2±2.8 N, 186.6±1.34 N and 209.94±1.48 N, respectively. As expected, the force increased with the increase in fiber friction, in turn, exerting greater compaction of the layers of the uncured material onto the mandrel during the winding process.

Higher tension in the fibers causes resin expulsion and greater compaction due to resin expulsion, reducing tube thickness and increasing fiber content [3], as observed in Table 2. Higher tension in the fiber tow reduces its porosity and this may hinder tow impregnation in the resin bath during manufacturing, and this also has the potential to increase fiber content in the final product.

The important effect of fiber tension on compaction, as discussed, and on void content can be better appreciated in Figure 3, which shows greater compaction and reduced voids for the $[\pm 80]_2$ tubes when higher friction is applied.

Table 2. Thickness and content of tubes constituents.

Sample	Thickness (mm)	Fiber weight content (%)
A50F0	2.29	55±5.55
A50F50	2.19	66±1.47
A50F100	1.84	67±6.20
A650F0	1.85	53±2.94
A65F50	1.74	61±3.92
A65F100	1.71	60±1.81
A80F0	1.52	56±5.14
A80F50	1.50	58±4.55
A80F100	1.41	61±5.25

The tensile tests were performed on the samples and the average values, as well as their standard deviation, were calculated and from the experimental results and compiled in Table 3. A higher winding angle results in greater apparent tensile strength, as the load is more distributed to the fibers, resulting in a more linear fracture [4]. This is consistent with the current results, where the tube with a winding angle of 80° showed the highest strength. When the winding angle is less obtuse, such as 50°, resulting in poorer alignment with the load direction and greater stress concentration near the notch.

Comparing A50F0 and A50F100, there was a 35,6% increase in strength, in the same range 24,5% found when comparing A65F0 and A65F100. There was a significant increase of 50.8% when comparing A80F0 and A80F100. This increase is due to the greater compaction of the fibers aligned in the direction of the apparent tensile force. With less resin interspersed between the layers, the fiberglass reinforcements are able to perform more effectively. This is noticeable when examining the mass fraction of fiber and resin, which

increases as the tension applied to the threads during the winding process is increased. However, higher fiber tension results in greater variability in results, indicating process instability. This instability could imply loss in quality in the final product, making it less reliable.
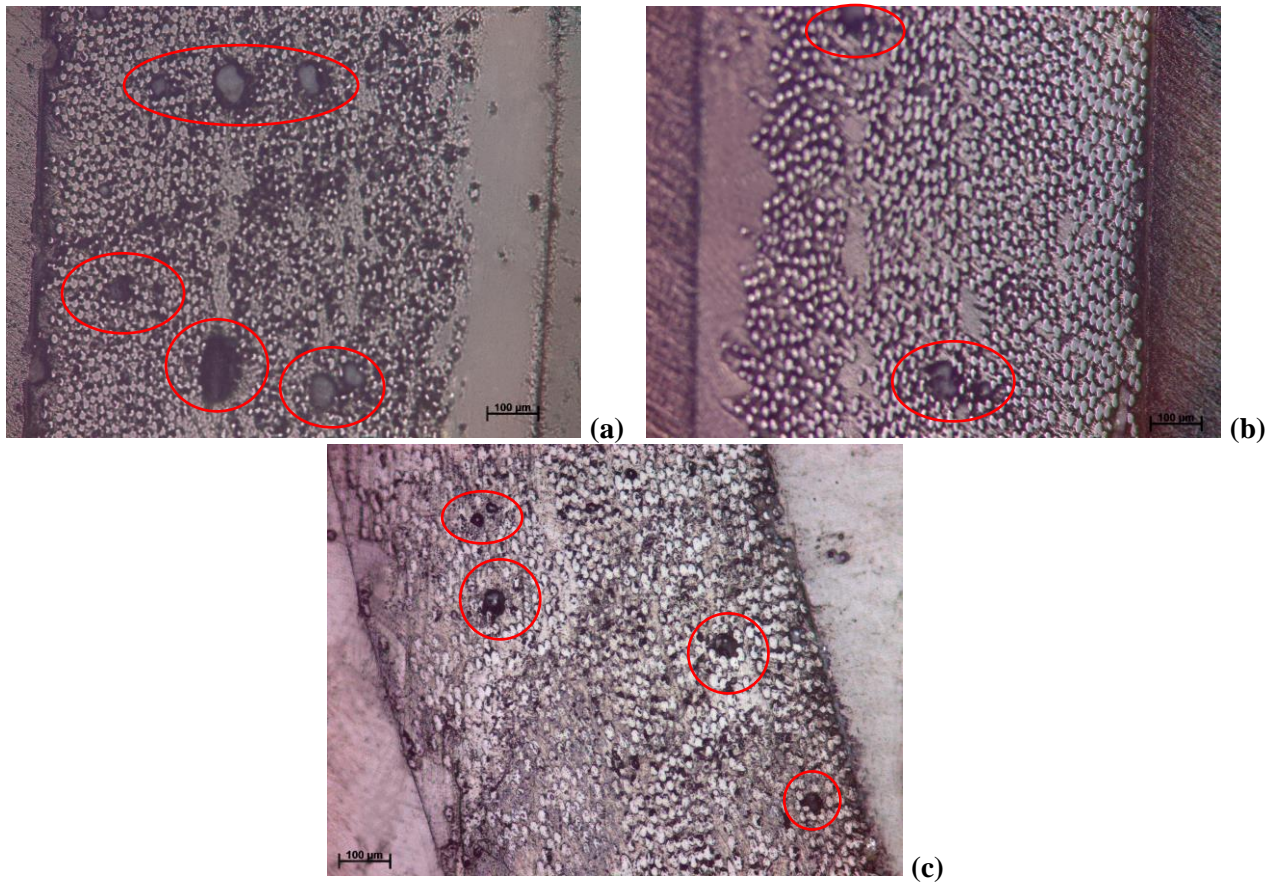
Figure 3. Micrographs of the $[\pm 80]_2$ tubes: **(a)** A80F0, **(b)** A80F50, and **(c)** A80F100. Some of the voids are identified with circles.

Table 3. Maximum load and apparent tensile strength of the tubes.

Conditions	Maximum load (N)	Apparent tensile strength (MPa)
A50F0	6456 ± 17	99.6 ± 0.3
A50F50	6787 ± 37	109.5 ± 0.6
A50F100	8051 ± 214	154.6 ± 4.1
A650F0	7889 ± 14	149.1 ± 0.3
A65F50	8577 ± 4	172.4 ± 0.1
A65F100	9665 ± 320	197.6 ± 6.5
A80F0	6719 ± 58	137.4 ± 1.2
A80F50	8816 ± 32	180.3 ± 0.6
A80F100	13671 ± 902	279.5 ± 18.4

A fractured specimen for each winding angle is presented in Figure 4. The correlation between the fracture and the obtained results can be understood in terms of micro-structure and stress distribution. In the FW process, the winding angle dictates final fiber orientation in the composite part, with a significant impact on material strength [4].

Increasing the force improves efficiency of tubular components in resisting failures, especially under loading in the fiber orientation. Also, an angle close to 90° can maximize tensile strength of the product, as it allows the fibers to be oriented in the direction of the applied load studied in this work, that is, in the hoop direction of tube [5]. However, for process and product standardization, it was observed that higher angles and

higher tensions do not necessarily result in consistently higher-quality tubes. Therefore, the selection of other angles may be reviewed depending on the application.
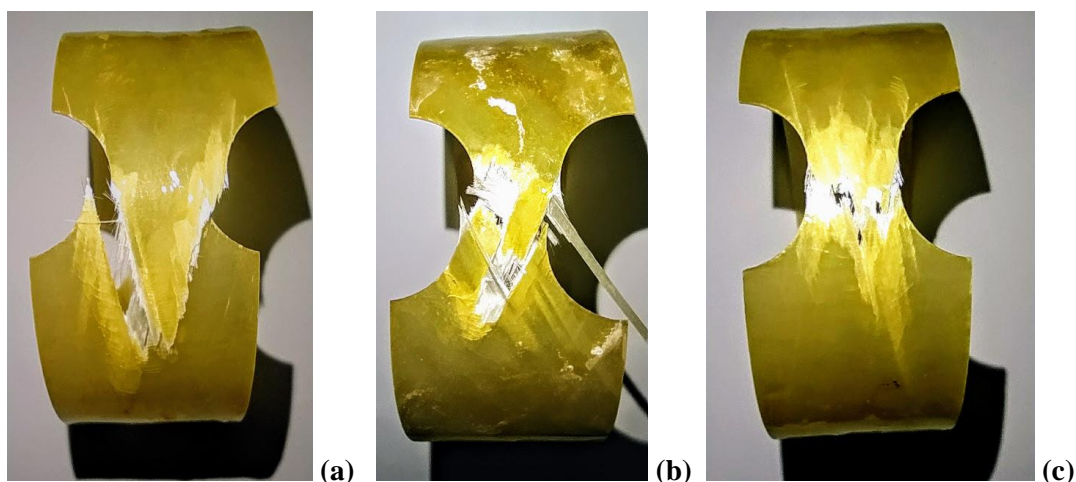
Figure 4. Fracture of the test specimens: **(a)** A50F100. **(b)** A65F100. **(c)** A80F100.

4.   CONCLUSIONS

This work investigated the behavior of tubes produced by the wet filament winding process. The increase in force applied during winding resulted in a substantial increase in apparent tensile stress of 35.4% for the samples compared from tubes A50F0 and A50F100, 24.5% for samples A65F0 and A65F100, and 50.8% for A80F0 and A80F100. However, process instability was observed for the highest force. A decrease in size and content of voids was observed, along with an increase in fiber content (5-10%).

The tensile test based on ASTM D2290-19 standard and the microscopic analysis were crucial in confirming the effect of fiber tension on the samples, contributing for a more comprehensive evaluation of the effect of those parameters on mechanical properties of the tubes. This study enabled future research on the field, indicating better approaches to further optimize the design and manufacturing process for tubes used in the oil and gas sector.

4.1. Declaration of Competing Interest

The authors declare no conflict of interest.

4.2. Acknowledgements

5. REFERENCES

[1] Błachut, Aleksander, et al. "Multiscale analysis of composite pressure vessel structures wound with different fiber tensile force." Composite Structures, 337, 2024. (https://doi.org/10.1016/j.compstruct.2024.118065).

[2] Aldoumani, Nada, et al. "Optimisation of the filament winding approach using a newly developed in-house uncertainty model." Eng 1.2 (2020): 8. (https://doi.org/10.3390/eng1020008).

[3] Ueda, Masahito, et al. "Voids in type-IV composite pressure vessels manufactured by a dry filament-winding process." International Journal of Pressure Vessels and Piping, 208, 2024. (https://doi.org/10.1016/j.ijpvp.2024.105154).

[4] Błachut, Aleksander, et al. "Influence of fiber tension during filament winding on the mechanical properties of composite pressure vessels." Composite Structures 304 (2023): 116337. (https://doi.org/10.1016/j.compstruct.2022.116337).

[5] Naseva, S., Srebrenkoska, V., Risteska, S., Stefanovska, M., & Srebrenkoska, S. "Mechanical properties of filament wound pipes: Effects of winding angles." Quality of Life, 6(1-2):10-15, 2015. (https://doi.org/10.7251/qol1501010n).

[6] Srebrenkoska, V., Zhezhova, S., & Naseva, S. "Hoop tensile properties of filament wound pipes." In: Proceedings of the International Congress on Machines, Technologies, Materials, pp. 103-106, 2015, Varna, Bulgaria. (ISSN 1310-3946).

[7] Sharma, Pranjali, et al. "Effect of tension on liner buckling and performance of a type-4 cylinder for storage of compressed gases with experimental validation." Thin-Walled Structures 189 (2023): 110928. (https://doi.org/10.1016/j.tws.2023.110928).

[8] Kara, Memduh, et al. "The effect of hydrothermal aging on the low-velocity impact behavior of multi-walled carbon nanotubes reinforced carbon fiber/epoxy composite pipes." Applied Composite Materials, 28, 2021. (https://doi.org/10.1007/s10443-021-09923-w).

7 Composite structures

Organized and edited by

Sandra Maria da Luz
&
Carla Tatiana Mota Anflor

ASSESSING THE CRASHWORTHINESS PERFORMANCE OF THIN-WALLED ALUMINUM TUBES FILLED AND NON-FILLED WITH ABS HONEYCOMB STRUCTURE

Gabriel M. Castro[a], *, Rita C. Silva [b], Alessandro B. S. Oliveira [c]

(a) 0000-0001-6388-7911 (University of Brasília – Brazil)
(b) 0000-0002-5022-8105 (University of Brasília – Brazil)
(c) 0000-0002-1298-4612 ((University of Brasília – Brazil)
* Corresponding author: castro.mgabriel@outlook.com

Abstract: Over the past few years, the number of deaths and injuries caused by traffic accidents has been rising steadily. Road traffic injury is the leading cause of death for children and young adults aged between 5 and 29 years, being the eighth leading cause of death for all age groups. Therefore, in the automotive industry, efficient structures in terms of energy absorptions are indispensable to increase passenger safety. One of the main elements widely used in vehicles due to its high energy absorption capacity is the crash box. In the literature, different energy absorbers models have been designed to minimize the injuries caused to the occupants during an impact event. Energy absorbers are systems that convert kinetic energy into another form of energy, through the plastic deformation of the structure. One of the primary geometries of these systems consists of thin-walled tubes; nonetheless, the idea of using them filled with composite honeycomb structures as hybrid specimens has not been appropriately explored. Otherwise, the use of different materials as fillers in energy absorbers systems has been increasingly explored in recent years, since they can act as a way to improve both energy absorption capacity and resist the impact of thin-walled tubes. This work aims to assess the crashworthiness of thin-walled square aluminum AL 6061 tubes non-filled and filled with ABS (Acrylonitrile Butadiene Styrene) honeycomb structure under quasi-static axial loading at a constant velocity of 1 mm/s. The ABS is an amorphous thermoplastic polymer. The specimens have patterned windows with different geometries to induce progressive buckling; the dimensions were 20x20, 15x30, and 20x30 mm², which allows the plastic deformation during compression to occur in a pre-established section, favouring the appearance of more uniform modes of deformation and improving the energy absorption capacity of the structure. Performance indicators were established to evaluate and compare the efficiency of different proposed designs. The tensile and compressive properties of the plastic material are appointed by ASTM D638-14 and ASTM C365/C365M-16, respectively. The results have shown that the honeycomb structure and the lateral windows have a significant contribution to the structure's performance indicators, which showed that windowed filled specimens perform better than non-filled tubes because the hybrid specimens presented higher values of energy absorbed.

1. INTRODUCTION

In the automotive industry, the design of efficient structures in terms of energy absorption is indispensable to increase passenger safety. Energy absorbers are systems that convert, totally or partially, kinetic energy into another form of energy, through the plastic deformation of the structure [1]. Nowadays, one of the main elements of passive safety in vehicles is the crash box placed between the bumper and the side member of different vehicles models. Therefore, many researchers have focused on these systems to better understand their mechanism deformation and absorbing kinetic energy from a collision and how to obtain good

crashworthy properties from this structure. Besides, vehicle manufacturers have invested in developing systems capable of enhancing safety features associated with lightweight materials such as using aluminum and composites [2, 3].

In experimental studies, thin-walled tubes are one of the main geometric constructions of energy absorber systems due to their relevant energy-absorbing capacity, as treated in the literature [4, 5]. In addition, another way to improve the crashworthy ability of energy absorbers is to use them filled with composite material as hybrid energy absorbers. The most usual composites used to fill these tubes are aluminum foam [6, 7], epoxy foam [8], glass-fiber reinforced polyamide [9, 10], and polyurethane foam [11].

The honeycomb is another structural solution to fill energy absorbers because of its lightweight, high out-of-plane compression properties, and good crashworthiness characteristics [12, 13]. Aluminum honeycomb filling is more weight-efficient and crush-efficient than aluminum foam filling. The higher crush efficiency of honeycomb can be explained by a greater degree of symmetry of the hexagonal cell structures over irregular foam cells [6].

The insertion of filler material in thin-walled energy absorbers leads to a higher peak force. However, hybrid tubes improve the crashworthiness of comparison hollow tubes [11, 14]. Nonetheless, the use of energy absorbers filled with thermoplastic composite in the form of honeycomb structures has not been appropriately explored. One approach to reducing the initial peak force of hybrid tubes is to provide patterned windows. According to [15], these discontinuities play the role of crash initiators by ensuring a stable collapse process and decreasing the initial peak load. Besides, windowed tubes enhance crushing performance over conventional tubes [16, 17].

This work presents the experimental crushing tests performed on honeycomb structures 3D-printed (FDM – Fused Deposition Method) with commercial ABS filament (Acrylonitrile Butadiene Styrene). The ABS is an amorphous thermoplastic polymer derived from petroleum. The glass transition temperature to the ABS is about 110º C [18]. It represents the temperature range where the polymer substrate changes from a rigid glassy material to a soft (not melted) [19]. Also, the ABS is widely used in the automotive industry due to its properties, for instance, lightweight, good chemical resistance, high resistance to cracks, and impact [20].

The ASTM D638 – 14 [21] covers the determination of the tensile properties of plastic materials. The ASTM C365/365M – 16 [22] covers the determination of compressive strength and modulus of sandwich cores. The results have shown that the composite material has good mechanical properties and may be tested as a reinforcement structure, for instance, honeycomb core, due to its high strength and lightweight.

Moreover, this work covers the assessment of the crashworthy ability of thin-walled aluminum tubes filled and non-filled with ABS honeycomb structure. The energy absorbers have patterned windows placed at the center of the tube on two opposite faces, following the dimensions 20x20, 15x30, and 20x30 mm², ensuring a progressive buckling [16]. Performance indicators established in the scientific literature allow evaluating and comparing the efficiency of different topologies [11, 23, 24]. The results show that the patterned windows and the honeycomb core significantly contribute to the structure's performance indicators.

2. METHODOLOGY

2.1. Experimental tests performed on the ABS

A commercial ABS filament of 1.75 mm in diameter was used to print the specimens for tension and compression experimental tests. The printing temperature, platform temperature, and printing speed were 255º C, 70º C, and 55 mm/min, respectively. It is noteworthy that the selected printing speed was lower than the recommended by the manufacturer to ensure a higher quality of the printing and prevent the occurrence of interlayer air gaps.

Table 1. Printing parameters for the tension specimens.

Printing parameters			
Build orientation	Raster angle	Infill density	Layer thickness
Flat	0°	100%	0.2 mm

The choice of geometrical parameters settings on the 3D printer allows for better product properties since the printing parameters significantly affect the quality of the FDM parts. Among the main geometrical parameters, build orientation, raster angle, infill density, and layer thickness have a considerable influence on the mechanical properties of the printed parts [25, 26, 27]. The printing parameters adopted for the printing parts tested to tension in the present work are listed in Table 1.

2

According to [26], the build orientation affects the mechanical properties of the printed parts, mostly in ductility. The build orientation represents how the sample is placed on the 3D printing platform. The specimens printed in the flat orientation exhibited the best mechanical properties, as previously tested by the authors.

The raster angle refers to the direction of the fused filament deposition relative to the loading of the part. Nevertheless, there is no consensus in the literature on the ideal value for the raster angle. For the tension tests, a raster angle of 0° means that the filament deposition was orientated in the load direction, improving the specimen's mechanical resistance [27].

As stated in [4], the change in infill density mainly determines the printed parts' tensile strength. The results demonstrate that a 100% infill shows the highest tensile strength in pieces. Also, the mechanical properties increase as layer thickness increases, as pointed out in [26]. The authors proposed layer thickness from 0.12 to 0.24 in the case of flat orientation, where the variations of maximum tensile and flexural strength were of little significance.

The samples were tested in an Instron Universal Testing Machining (model 8801) with a loading capacity of 100 kN. The dimensions of the test specimens are according to the standard ASTM D638-14 [21], as Type I.

A pen marking was made at thirty millimeters from both the top and bottom of the sample to place the specimens in the testing machine. In addition, a small grove was made at the center of the specimen, to induce the rupture to occur in the region where the strain gauge was fixed, as established by [21].

The testing speed was 1 mm/min, lower than that specified for specimen Type 1, according to the standard. Meanwhile, the selected rate produced a 0.5 to 5 min rupture complying with the test method. Figure 1 illustrates the specimen placed in the testing machine. The tension testing allowed determining four mechanical properties: flow stress, tensile strength at break, modulus of elasticity and elongation.

Figure 1. Specimen placed in the testing machine for test in tension.

The standards test method ASTM C365/365M – 16 [22] covers the determination of compressive strength and modulus of sandwich cores. The flatwise compressive strength and modulus are the fundamental mechanical properties of sandwich cores used in the present work.

The test method consists of subjecting a sandwich core to a uniaxial compressive force normal to the plane of the facings. The honeycomb undergoes an out-of-plane force due to the highest mechanical properties in this direction, as discussed in [28] and [29].

According to [23] and [13], the main parameters in the design of a honeycomb core that affect its mechanical properties are cell angle, thickness, and length of the cell wall. The parameters optimization led to better performance against the compressive crushing. The values of each mechanical properties were adopted as 120°, 0.4 mm, and 3 mm, respectively. From these dimensions it is possible to calculate the honeycomb density that values 260.71 kg/m³.

The density is related to the dimensions of the honeycomb cell, in other words, to the length and thickness of the cell wall. Balaji et al. [23] and Meran et al. [13] observed that higher honeycomb density led to a more significant mean crush force. It means that the honeycomb structure with a small length and thickness of the cell wall has relatively more significant crashworthiness indicators. In addition, [13] affirmed that the honeycomb structure with a 120° cell angle yields the most prominent crashworthiness parameters.

3

The printing parameters adopted for the parts tested in compression were the same as shown in Table 1, except for the raster angle of 90º and layer thickness of 0.4 mm.

A preloading of 45 N was applied to the samples, as established by the standard [22]. The testing speed was 3 mm/min, different from the suggested standard rate. Notwithstanding, the speed of testing adopted produced failure within 3 to 6 min, as prescribed in the standard.

Three stabilized specimens were tested by placing them between two thick circular plates in steel, with a thickness of 25 mm and 100 mm in diameter, adapted to an Instron Universal Testing Machine (model 8801).

2.2. Thin-walled aluminum tubes

The energy absorbers were fabricated of commercial thin-walled square tubes of aluminum AL 6160. All specimens had a length of 60 mm, cross-section width of 50 mm, and wall thickness of 1.55 mm. Young's modulus and yield stress mean values were 63 GPa and 109 MPa, respectively.

Altogether, eight samples were made, with six windowed tubes and two conventional tubes. In addition, four specimens are hybrid, i.e., filled with ABS honeycomb. The window size changes from one sample to another. The patterned windows have been positioned at the face center of the tube on two opposite faces.

The samples were cut and then machining cut to open the window. In [16], patterned windows are introduced to the thin-walled tubes. Their results have shown that windowed tubes could be grouped in three main collapse modes (symmetric, extensional, and diamond) depending on the different dimensions of the window.

Furthermore, the findings highlight that in the region of symmetric mode, the window's width is relatively small, and with the increase of window height, the collapse mode tends to become more irregular. Thus, three different topologies of lateral windows have been made; the dimensions were 20x20, 15x30, and 20x30 mm².

Figure 2 denotes the conventional tube and one windowed tube, where" w " and "h" represent the width and height of the lateral window, respectively.

| (a) | (b) |
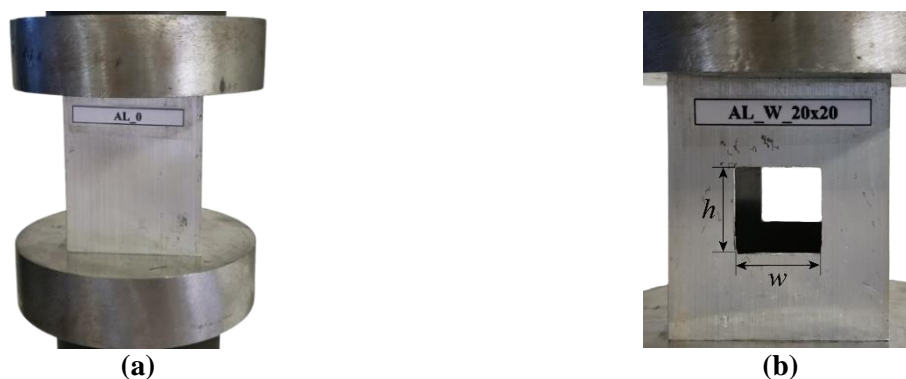
Figure 2. Energy absorbers a) conventional tube b) windowed tube.

The specimens experience quasi-static axial crushing tests at a 1 mm/min velocity in an Instron Universal Testing Machining (model 8801). Additionally, energy absorbers had their crashworthy ability evaluated based on six performance parameters: energy absorption, specific energy absorption, peak force, mean force, load ratio, and structural effectiveness, as shown in [11, 23, 24].

3. RESULTS AND DISCUSSION

3.1. Mechanical properties of the ABS polymer

Five samples were tested, as prescribed by [21]. The specimens were identified as CP_XX_YY_A_ZZ, where XX represents the adopted build orientation (F = Flat), YY refers to the raster angle, A refers to the material used to print the parts (A = ABS), and ZZ is the number of the sample.

Figure 3 illustrates the specimen after the test. Notice that the failure mode of the sample was predominantly brittle, as a rigid glassy material, as pointed out by [30] and [31]. Moreover, all of them have failed in the region of the strain gauge was fixed, as established by [21].

In addition, Figure 3 depicts the true stress versus true strain curves for the five samples tested. As aforementioned, printing parameters selection has a significant effect on the mechanical properties of the FDM

4

structures. Therefore, the adopted build orientation and the raster angle of 0º may maximize the strength of the specimens because both led the filament deposition to be put in the pull direction [27].
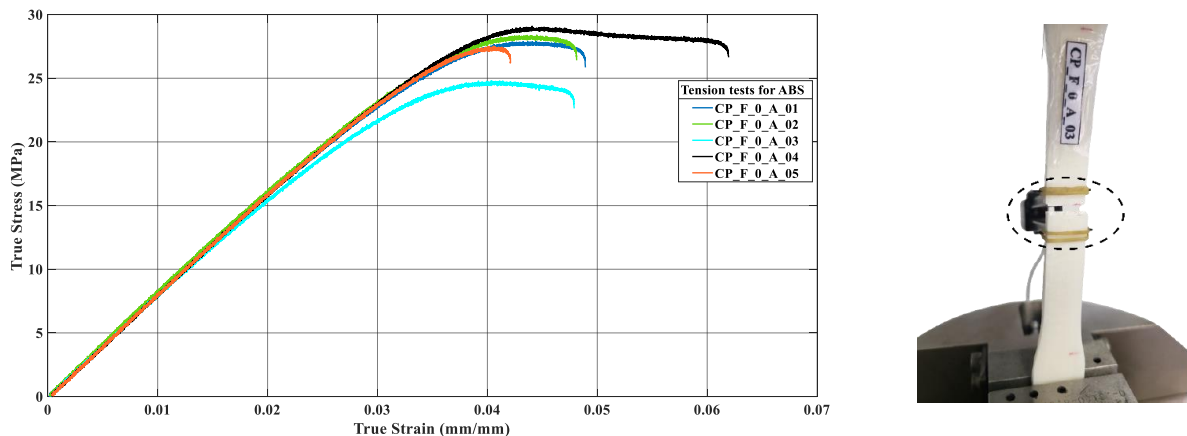
Figure 3. Curve True Stress x True Strain for test in tension.

The main results in tension obtained for the samples are according to [21]. They are flow stress, tensile strength at break, modulus of elasticity, and elongation. The flow stress represents the offset yield point where a plastic strain of 0.5% occurred (26.7 ± 1.8 MPa). This adopted value for those materials has a nonlinear elastic region [32].

The modulus of elasticity refers to the ratio between the stress and strain in the initial linear region (760.6 ± 24.3). The tensile strength at break (24.3 ± 1.5) and the elongation (5.4 ± 0.8) values in Fig. 5 are defined where the sample failed. The mechanical property of tensile strength at break is very similar to that of a manufacturer (3DLab) and Montero et al. [27].

From the compressive testing for honeycomb specimens in ABS polymer, Figure 4 depicts the samples after the crushing, where the uniform compressive failure of the sandwich core is the only acceptable failure mode. Also, illustrates the curves of load-displacement for each compressed honeycomb

Furthermore, all specimens performed a shear failure mode due to the compression, as pointed out by [33] and [34]. The dashed line illustrates the slide plane in the faces, and the arrows highlight the stress flow.
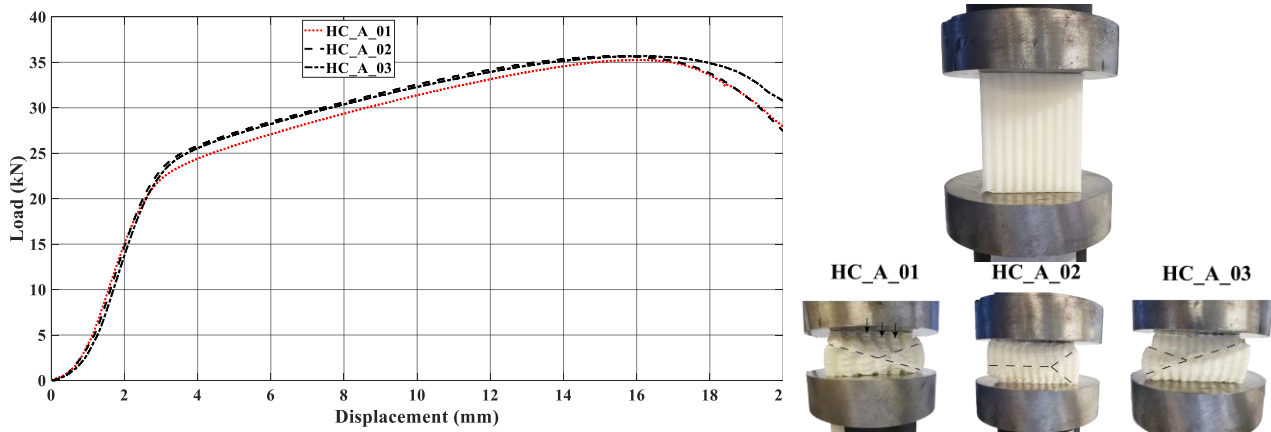
Figure 4. Curves Load-Displacement for test in compression

The main results obtained from the compression testing were established by [22]. The ultimate strength refers to the maximum compressive capacity (13.2 ± 0.1). The compressive modulus is the slope of the linear region of the stress-strain curve (5.4 ± 0.1), and the deflection stress represents a specific value of strain of about 2% (269.8 ± 4.7).

In that regard, the results showed that the ABS filament has good mechanical properties [20]. Moreover, the ABS may be tested as a reinforcement structure, for instance, honeycomb core, due to its high strength and lightweight, as discussed in [12, 13].

5

3.2. Tests results for the energy absorbers

The energy absorbers were designated as AL_X_YYxZZ, where AL is the material of the tube (AL = Aluminum), X refers to the presence of a window (0 = conventional; W = windowed), and YY and ZZ represent the dimensions of the window (15x30; 20x20; 20x30). For hybrid tubes, it was inserted FF_A to designate the ABS honeycomb structure.

Figure 5 illustrates the non-filled tubes after the crushing test. All samples failed according to a stable progressive folding mode which ensures symmetric collapse mode. The specimen AL_W_20x20 buckled following symmetric deformation mode, although having three lobes deforming inwards and one outward, as discussed by [35]. The arrow highlights the lobe, which moved outward.

| (a) AL_0 | (b) AL_W_15x30 | (c) AL_W_20x20 | (d) AL_W_20x30 |
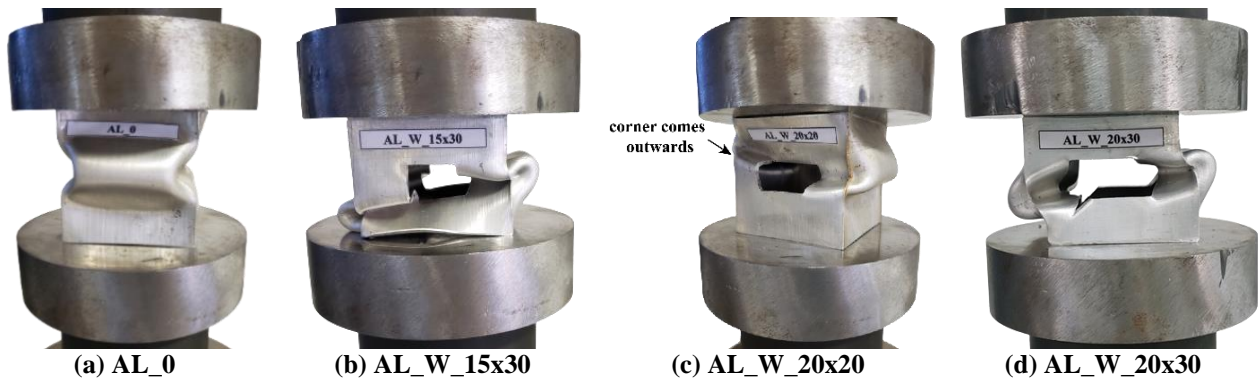
Figure 5. Non-filled tubes after the compressive test.

Figure 6 depicts the load-displacement curves for non-filled tubes. It is worth noting that there was an abrupt rise in load for all specimens followed by a sharp decrease in it, and it was more accentuated for the conventional tube (AL_0). Hence, the insertion of patterned windows has reduced the initial peak load of the tubes relative to the conventional one "0", as previewed by [16].
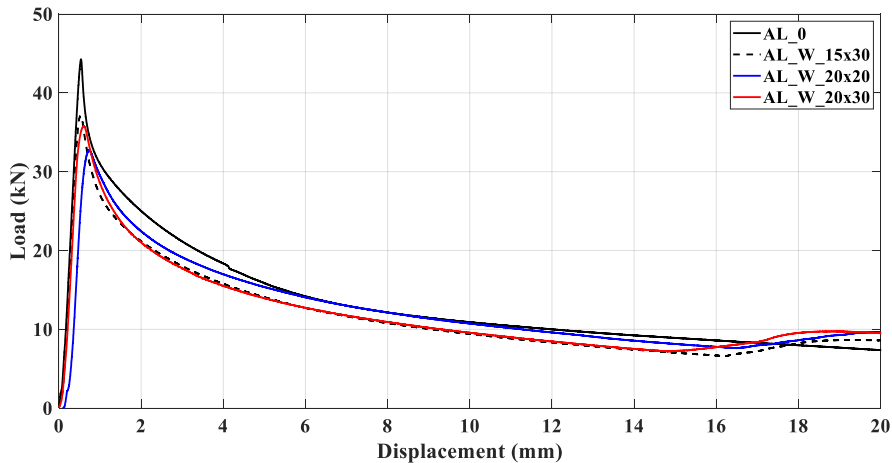
Figure 6. Curves Load-Displacement for non-filled tubes.

Table 2 outlines the results of the main performance indicators for the non-filled tubes. Those indicators are calculated from the load-displacement curves (see Fig. 6).

Briefly, Ea represents the energy absorption during the compression (area under the load-displacement curve). SEA refers to the absorbed energy related to reducing the mass of the energy absorber.

Ppeak and Pm indicate the initial peak force (obtained directly from the graph) and the mean crushing force (the ratio between the energy absorption, Ea, and the total displacement during the crushing, in case 20 mm), respectively.

LR is the load ratio, which deals with an equilibrium between the Ppeak and Pm and, the structural effectiveness (η) allows comparing the performance of energy absorbers made of different materials (aluminum and thermoplastic composite) [24].

Table 2. Performance indicators of the non-filled tubes.

6

Topologies	E_a (kJ)	SEA (kJ/kg)	P_{peak} (kN)	P_m (kN)	LR	η
AL_0	0.27	5.77	44.3	13.4	3.29	0.41
AL_W_15x30	0.24	5.48	37.1	11.8	3.15	0.43
AL_W_20x20	0.25	5.78	32.7	12.6	2.61	0.48
AL_W_20x30	0.24	6.06	35.8	12.0	2.97	0.46

The windowed tubes have reduced the P_{peak} by 26.2% - 16.3%. In terms of energy absorbed, there was no significant difference between the windowed tubes relative to the conventional tube, with a difference of up to 11%, as discussed in [16]. Besides, the windowed tubes increased the equilibrium between the forces. Thus, the specimen AL_W_20x20 was the best in performance for the non-filled tubes.

Figure 7 illustrates the hybrid tubes after the crushing test. The initial fold formed at the middle of the tube length (region of the patterned window) corroborates the feature that the patterned windows lead to plastic deformation at a predetermined area along the tube. Also, it improves the uniformity of the load-displacement behavior and controls the mode of collapse to optimize the energy absorption capacity of the tube [36, 37]. The exception was the AL_0_FF_A, whose fold started near the top end.

In addition, the filled tubes AL_0_FF_A and AL_W_15x30_FF_A presented a failure mode denoted "banana peeling", as discussed in [7]. The cause of such behavior was the major compressive strength of the composite core compared to that of the aluminum tube, see Fig. 4 and Fig. 8. It leads to a critical rupture in the tube's wall due to the compressing core being limited by the faces of the tube, consequently generating a confining pressure [38]. In fact, the AL_0_FF_A has no "escape" area, and the AL_W_15x30_FF_A is the second smallest area.

(a) AL_0_FF_A   (b) AL_W_15x30_FF_A   (c) AL_W_20x20_FF_A   (d) AL_W_20x30_FF_A
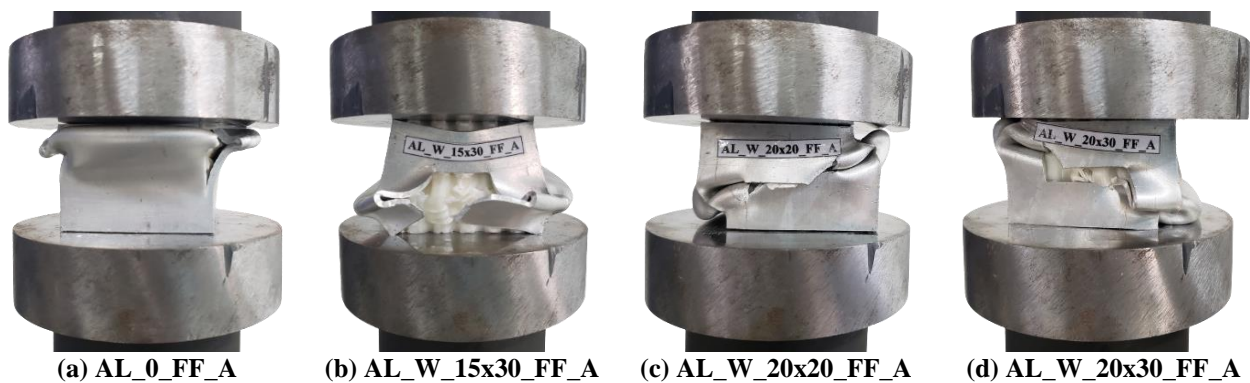
Figure 7. Hybrid tubes after the compressive test.

This critical rupture in the crushing testing is mechanically undesired because the deformation lobes development is not accomplished, reducing the energy absorption capacity of the protection system [7]. As said, the specimens AL_0_FF_A and AL_W_15x30_FF_A did not have the expected behavior. We think that a major strength metal could avoid such failure, guaranteeing hybrid tubes an adequate performance relative to the dissipation mechanism. Nonetheless, for the specimens AL_W_20x20_FF_A and AL_W_20x30_FF_A, the symmetric shear failure mode was predominant.

Figure 8 illustrates the curves of load-displacement for hybrid tubes. The LR indicator became lower in the hybrid tubes than in the hollow tubes, Fig. 12-e, indicating the contribution of the composite core. It denotes the equilibrium between the Ppeak and Pm.

In addition, hybrid tubes have higher Ppeak than non-filled, as pointed out by [11]. However, the honeycomb core attenuated the abrupt rise and decrease in the load observed for the non-filled energy absorbers.

Table 3 outlines the main results for the performance indicators for the hybrid tubes. As aforementioned, the mean values of load increase with the insertion of the honeycomb core. Additionally, the windowed tubes have reduced the Ppeak by 13.1% - 9.8%.
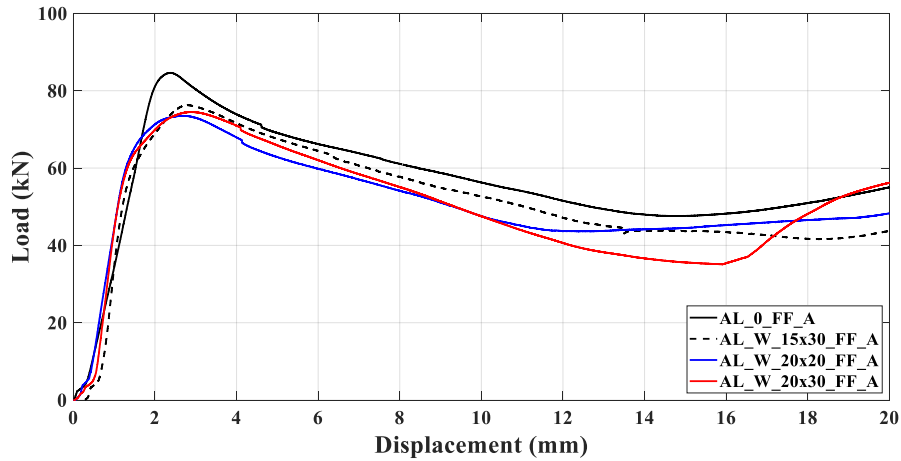
Figure 8. Curves Load-Displacement for hybrid tubes.

The energy absorption capacity and the SEA of hybrid tubes were significantly higher than non-filled ones, see Fig. 12-a and Fig. 12-b. This result agrees with [11] and, such behavior can be explained by the additional compressive deformation of the honeycomb core. Therefore, the filled thin-walled tubes have highlighted the honeycomb efficiency due to the better mechanical performance presented for the hybrid energy absorbers than non-filled energy absorbers.

It is essential to highlight that Table 3 presents the performance indicators for the specimens AL_0_FF_A and AL_W_15x30_FF_A, but their critical ruptures [7], as aforementioned, have impaired their functions as energy absorbers.

Table 3. Performance indicators of the filled tubes.

Topologies	E_a (kJ)	SEA (kJ/kg)	P_{peak} (kN)	P_m (kN)	LR	η
AL_0_FF_A	1.12	12.63	84.6	56.2	1.51	1.11
AL_W_15x30_FF_A	1.03	12.05	76.3	51.4	1.48	1.13
AL_W_20x20_FF_A	1.02	11.95	73.5	50.9	1.44	1.17
AL_W_20x30_FF_A	1.00	11.84	74.5	49.8	1.50	1.14

The specimen AL_W_20x20_FF_A achieved the best performance among the hybrid tubes, with an increase in most performance indicators over the other topologies.

Figure 12 compare the performance of the thin-walled tubes considering the indicators outlined in Tables 2 and 3. For structural efficiency, Fig. 12-f, the expected value would be one, indicating full use of the structural loading capacity. Thus, all hybrid specimens demonstrated better performance than hollow tubes, indicating the honeycomb core efficiency as filler for thin-walled tubes.
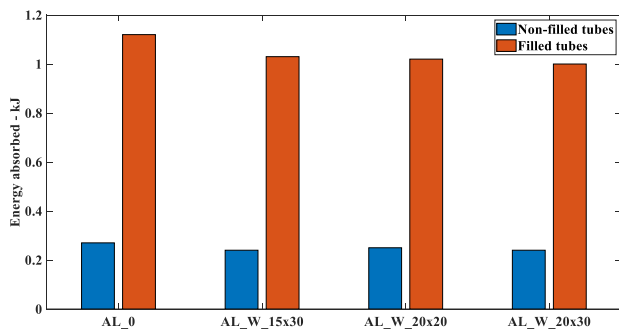
(a) Energy absorbed

(b) Specific energy absorption

8

(c) Peak force

(d) Mean force

(e) Load ratio

(f) Structural efficiency
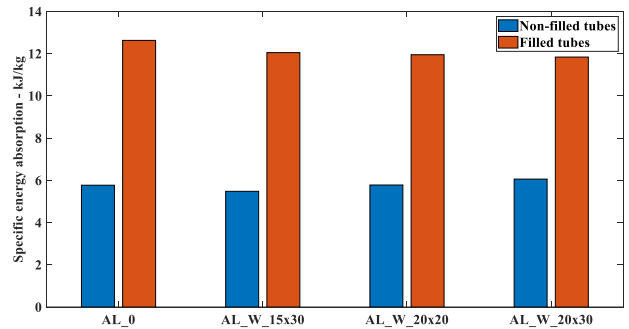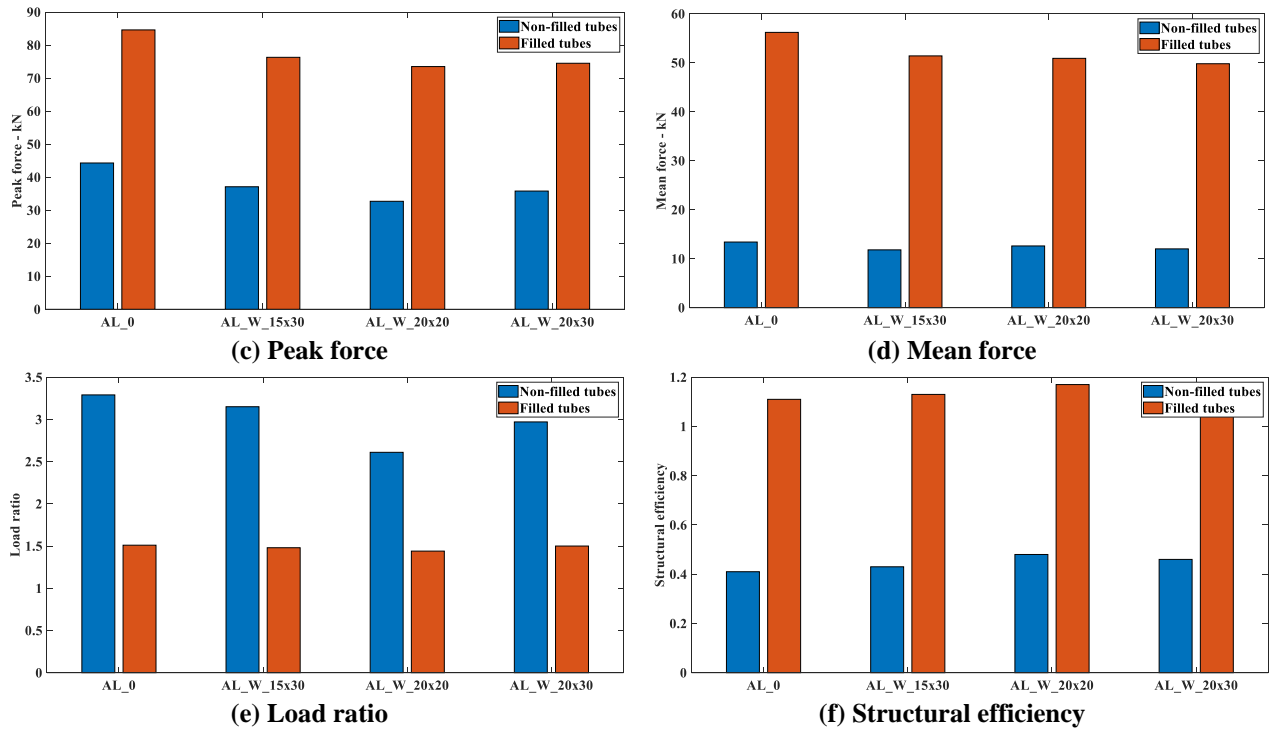
Figure 12. Comparison of performance indicators from each filled and non-filled tubes.

4. CONCLUSIONS

We have carried out experimental tests in the present work, using specimens 3D-printed with the fusion deposition method (FDM). The printing parameters were established to achieve the best performance for the samples using the ABS polymer filament. The structures were the dog bone specimen (ASTM D638-14) and honeycomb (ASTM C365/C365M-16). The preliminary tests were in tension and compression to determine the composite material's mechanical properties.

We concluded that all dog bone specimens have failed in tension as a rigid glassy material with an abrupt rupture. Three honeycomb structures have undergone compressive testing, and it was possible to obtain some mechanical properties as established by [22].

After the material evaluation based on the ASTM standards, the authors sighted ABS polymer as a reinforcement structure to energy absorbers aiming to increase their performance as an energy dissipater, due to its high strength and lightweight [12, 13].

Thus, we assessed the crashworthy ability of thin-walled aluminum tubes non-filled and filled with ABS honeycomb structure. Some of those tubes have patterned windows placed at the center of the tube on two opposites faces, following the dimensions 15x30, 20x20, and 20x30 mm2, based on the research of [16].

We concluded that windowed tubes reduced the Ppeak relative to conventional tubes, increased the equilibrium between forces, highlighted the structure's efficiency, and presented a better performance than non-windowed tubes.

Besides, the patterned windows induce the plastic deformation at a predetermined region, controlling the mode of collapse to optimize the energy absorption capacity. Nevertheless, the hybrid specimens AL_0_FF_A and AL_W_15x30_FF_A have had a critical rupture. The cause of such behavior was the major compressive strength of the composite core compared to that of the aluminum tube, see Fig. 4 and Fig. 8. It leads to a critical rupture in the tube's wall due to the compressing core being limited by the faces of the tube, consequently generating a confining pressure [38]. In fact, the AL_0_FF_A has no "escape" area, and the AL_W_15x30_FF_A is the second smallest area.

In conclusion, hybrid tubes have higher Ppeak than non-filled ones. However, the honeycomb core provoked a better equilibrium between the forces during the compressive tests. In that regard, the specimen 20x20 was the best in performance for both non-filled and filled tubes, increasing the performance indicators over the other topologies.

4.1. Declaration of Competing Interest

The authors declare no conflict of interest.

9

5. REFERENCES

[1] A.A.A. Alghamdi. Collapsible impact energy absorbers: an overview. *Thin-Walled Structures*, Volume 39, 2001. (https://doi.org/10.1016/S0263-8231(00)00048-3).

[2] N.A.Z. Abdullah et al. A review on crashworthiness studies of crash box structure. *Thin-Walled Structures*, Volume 153, 2020. (https://doi.org/10.1016/j.tws.2020.106795).

[3] N.S.B. Yusof et al. Design and materials development of automotive crash box: a review. *Ciência & Tecnologia dos Materiais*, Volume 29, 2017. (https://doi.org/10.1016/j.ctmat.2017.09.003).

[4] W. Abramowicz, N. Jones. Transition from initial global bending to progressive buckling of tubes loaded statically and dynamically. *International Journal of Impact Engineering*, Volume 19, 1997. (https://doi.org/10.1016/S0734-743X(96)00052-8).

[5] W. Abramowicz. Thin-walled structures as impact energy absorbers. *Thin-Walled Structures*, Volume 41, 2003. (https://doi.org/10.1016/S0263-8231(02)00082-4).

[6] S. Santosa, T. Wierzbicki. Crash behavior of box columns filled with aluminum honeycomb or foam. *Computers and Structures*, Volume 68, 1998. (https://doi.org/10.1016/S0045-7949(98)00067-4).

[7] A.G. Hanssen, M. Langseth, O.S Hopperstad. Static crushing of square aluminium extrusions with aluminium foam filler. *International Journal of Mechanical Sciences*, Volume 41, 1999. (https://doi.org/10.1016/S0020-7403(98)00064-2).

[8] J.M. Babbage, P.K. Mallick. Static axial crush performance of unfilled and foam-filled aluminum-composite hybrid tubes. *Composite Structures*, Volume 70, 2005. (https://doi.org/10.1016/j.compstruct.2004.08.021).

[9] M. Costas et al. Axial crushing of aluminum extrusions filled with PET foam and GFRP. An experimental investigation. *Thin-Walled Structures*, Volume 99, 2016. (https://doi.org/10.1016/j.tws.2015.11.003).

[10] M. Costas et al. Static and dynamic axial crushing analysis of car frontal impact hybrid absorbers. *International Journal of Impact Engineering*, Volume 62, 2013. (https://doi.org/10.1016/j.ijimpeng.2013.06.011).

[11] R.D. Hussein et al. Crushing response of square aluminum tubes filled with polyurethane foam and aluminum honeycomb. *Thin-Walled Structures*, Volume 110, 2017. (https://doi.org/10.1016/j.tws.2016.10.023).

[12] H. Zarei, M. Kroger. Optimum honeycomb filled crash absorber design. *Materials and Design*, Volume 29, 2008. (https://doi.org/10.1016/j.matdes.2006.10.013).

[13] A.P. Meran, T. Toprak, A. Mugan. Numerical and experimental study of crashworthiness parameters of honeycomb structures. *Thin-Walled Structures*, Volume 78, 2014. (https://doi.org/10.1016/j.tws.2013.12.012).

[14] R.D. Hussein, D. Ruan, J.W. Yoon. An experimental study of square aluminium tubes with honeycomb core subjected to quasi-static compressive loads. *Key Engineering Materials*, Volume 626, 2014. (https://doi.org/10.4028/www.scientific.net/KEM.626.91).

[15] A.G. Mamalis et al. The effect of the implementation of circular holes as crush initiators to the crushing characteristics of mild steel square tubes: experimental and numerical simulation. *International Journal of Crashworthiness*, Volume 14, 2009. (https://doi.org/10.1080/13588260902826547).

[16] J. Song, Y. Chen, G. Lu. Light-weight thin-walled structures with patterned windows under axial crushing. *International Journal of Mechanical Sciences*, Volume 66, 2013. (https://doi.org/10.1016/j.ijmecsci.2012.11.014).

[17] C. Zhou et al. The energy absorption of rectangular and slotted windowed tubes under axial crushing. *International Journal of Mechanical Sciences*, Volume 141, 2018. (https://doi.org/10.1016/j.ijmecsci.2018.03.036).

[18] A.R.T. Perez, D.A. Roberson, R.B. Wicker. Fracture surface analysis of 3D-Printed tensile specimens of novel ABS-based materials. *J. Fail. Anal. and Preven.*, Volume 14, 2014. (https://doi.org/10.1007/s11668-014-9803-9).

[19] H. Becker, L.E. Locascio. Polymer microfluid devices. *Talanta*, Volume 56, 2002. (https://doi.org/10.1016/S0039-9140(01)00594-X).

[20] A. Gnatowski et al. The research of the thermal and mechanical properties of materials produced by 3D printing method. *Thermal Sciences*, Volume 23, 2019. (10.2298/TSCI19S4211G).

[21] ASTM D638-14, Standard test method for tensile properties of plastics. ASTM International, 2014. (www.astm.org).

[22] ASTM C365/365M-16, Standard test method for flatwise compressive properties of sandwich cores. ASTM International, 2014. (www.astm.org).

[23] G. Balaji, K. Annamalai. Numerical investigation of honeycomb filled crash box for the effect of honeycomb's physical parameters on crashworthiness constants. *International Journal of Crashworthiness*, Volume 24, 2018. (https://doi.org/10.1080/13588265.2018.1424298).

[24] R.C. Silva, J.C.S. Teles, A.B.S. Oliveira. Experimental and numerical performance assessment of square aluminum and steel energy absorbers with circular hole discontinuities. *International Journal of Crashworthiness*, Volume 27, 2021. (https://doi.org/10.1080/13588265.2021.1906511).

[25] N.R.R. Royan et al. Current state and challenges of natural fibre-reinforced polymer composites as feeder in FDM-Based 3D printing. *Polymers*, Volume 13, 2021. (https://doi.org/10.3390/polym13142289).

[26] J.M. Chácon et al. Additive manufacturing of PLA structures using fused deposition modelling: effect of process parameters on mechanical properties and their optimal selection. *Materials and Design*, Volume 124, 2017. (https://doi.org/10.1016/j.matdes.2017.03.065).

[27] M. Montero et al. Material characterization of fused deposition modeling (FDM) ABS by designed experiments. In: *Rapid Prototyping and Manufacturing Conference*, 2001.

[28] H. Zhao, G. Gary. Crushing behaviour of aluminium honeycomb under impact loading. *International Journal of Impact Engineering*, Volume 21, 1998. (https://doi.org/10.1016/S0734-743X(98)00034-7).

[29] M.K. Khan, T. Baig, S. Mirza. Experimental investigation of in-plane and out-of-plane crushing of aluminium honeycomb. *Materials Science and Engineering A*, Volume 539, 2012. (https://doi.org/10.1016/j.msea.2012.01.070).

[30] C. Ziemian, M. Sharma, S. Ziemian. Anisotropic mechanical properties of ABS parts fabricated by fused deposition modelling. *Mechanical Engineering*, 2012. (10.5772/34233).

[31] N.S.F. Jap et al. The effect of raster orientation on the static and fatigue properties of filament deposited ABS polymer. *International Journal of Fatigue*, Volume 124, 2019. (https://doi.org/10.1016/j.ijfatigue.2019.02.042).

[32] W.D. Callister, D.G. Rethwisch. *Materials science and engineering: an introduction*, 8ed, 2010. J. Wiley & Sons.

[33] R.K. McFarland. Hexagonal cell structures under post-buckling axial load. *AIAA Journal*, Volume 1, 1963. (https://doi.org/10.2514/3.1798).

[34] T. Jin et al. Experimental study on the effects of specimen in-plane size on the mechanical behavior of aluminum hexagonal honeycombs. *Materials Science & Engineering A*, Volume 635, 2015. (https://doi.org/10.1016/j.msea.2015.03.053).

[35] W. Abramowicz, N. Jones. Dynamic axial crushing of square tubes. *International Journal of Impact* Engineering, Volume 2, 1984. (https://doi.org/10.1016/0734-743X(84)90005-8).

[36] G.H. Daneshi, S.J. Hosseinipour. Grooves effect on crashworthiness characteristics of thin-walled tubes under axial compression. *Materials and Design*, Volume 23, 2003. (https://doi.org/10.1016/S0261-3069(02)00052-3).

[37] A.A. Singace, H. El-Sobky. Behaviour of axially crushed corrugated tubes. *International Journal of Mechanical Sciences*, Volume 39, 1997. (https://doi.org/10.1016/S0020-7403(96)00022-7).

[38] K.-B. Park et al. Analysis of the mechanical properties of polymer materials considering lateral confinement effects. *Journal of Polymer Engineering*, Volume 39, 2019. (https://doi.org/10.1515/polyeng-2018-0299).

AN EXPERIMENTAL INVESTIGATION OF SANDWICH PANELS MADE FROM REUSED ALUMINIUM RINGS

Arthur S. Longati[(a)*], Rodrigo J. da Silva[(b)], Júlio C. dos Santos [(c)], Carlos Thomas[(d)],
Leandro J. da Silva[(e)], Túlio H. Panzera [(f)],

(a) 0009-0001-8415-4570 (Federal University of São João Del Rei – Brazil)
(b) 0000-0001-8016-3165 (Federal University of São João del-Rei – Brazil)
(c) 0000-0002-7485-491X (Federal University of São João del-Rei – Brazil)
(d) 0000-0002-2641-9411 (Universidad de Cantabria – Spain)
(e) 0000-0002-4606-3483 (Federal University of São João Del Rei – Brazil)
(f) 0000-0001-7091-456X (Federal University of São João Del Rei – Brazil)
* Corresponding author: arthurlongati@gmail.com

Abstract: Recycling waste and creating materials that can be reused is a crucial aspect of sustainability in the circular economy. This study specifically focuses on the reuse of aluminium cans as a circular honeycomb core material in sandwich structures. By utilizing this approach, significant amounts of energy and emissions associated with the refining and manufacturing processes can be saved, especially when the material meets the geometry requirements for product design. The sandwich panels developed in this study consist of galvanised steel skins, reused aluminium rings, and a castor-oil adhesive. The aluminium rings are arranged side by side to form an orthogonal core architecture. To evaluate their mechanical properties, a three-point bending test is conducted following the RJS Method and the ASTM standards C393 and D7250. The results depict that the sandwich panels can achieve a maximum load of up to 470 N. When subjected to pure bending, the panels demonstrate mean flexural stiffness and modulus of 28×10^8 N.mm^2 and 35 GPa, respectively. The findings of this study highlight the promising potential of reusing aluminium cans as a circular honeycomb core material in sandwich structures. This technology shows promise in scalability and its ability to provide secondary structural green solutions in various applications, including building and transport systems.

1. INTRODUCTION

Sandwich panels have found application in the design of various structural components, ranging from secondary to high-performance applications, representing a significant advancement in engineering and materials science [1]. This class of structures offers a unique combination of lightweight and high stiffness due to its two rigid outer thin layers (referred to as skins, faces or facesheets), which are assembled with a lightweight, thicker core [2,3].

Skins can be made of many different materials, ranging from metals such as aluminium [4] and steel [2] to non-metallic materials, such as polymer composites reinforced with carbon [5], glass [6], natural [7] and mineral fibres [8], plywood [9] and others [10]. Classifying the core type can be done either by material type or by core geometry [3, 11]. For example, the core of sandwich composites may consist of polymer [12] and metal foam [13], while in terms of application and structural design, the core may consist of honeycomb, corrugation [14], grid and bio-inspired geometry [15-19].

In recent years, the use of alternative core geometries and materials has also been evaluated [20]. Circular honeycomb cells, also known as tubular honeycomb (TH), are one of the most recently developed core topologies. THs have been used for a variety of applications ranging from supporting oil transportation

infrastructure in onshore and offshore facilities to energy-absorbing sandwich panels [4]. Oruganti and Ghosh [11] demonstrated the intrinsic stiffness and strength enhancement of TH structures due to the geometric constraints associated with the deformation of the cylinders.

By varying the core material/shape, thickness and skin material in sandwich structures, it is possible to achieve different sets of properties and target performances [21]. For this reason, it has long been an engineering challenge to find the optimal dimensioning [22]. Another challenge for researchers is to design new high-performance products without compromising the availability of resources for future generations. Recently, the scientific community has been active in the development of sustainable and high-quality sandwich panels with alternative materials from biodegradable resources with the aim of carbon neutrality [23-28]. Recent government legislation on greenhouse gas emissions is encouraging engineers and researchers in the automotive industry to produce fuel-efficient materials, replacing internal and external metal parts with lightweight green materials to improve fuel economy and reduce emissions [27].

In the given context, aluminium derived from reused cans is an abundant waste material already collected by human organisations. These cans are commonly used for packaging a wide range of beverages, including beer, soft drinks, energy drinks, and juices. Aluminium is favoured for its high recyclability without any loss of quality, making it a valuable resource in the circular economy [29]. However, instead of simply recycling this aluminium, this work proposes an innovative approach of reusing the cans as a tubular honeycomb core material. By doing so, it avoids the additional energy consumption associated with the melting and remanufacturing process. The tubular honeycomb cores can be easily obtained by slicing the aluminium cans. The sandwich panels developed in this study comprise galvanised steel skins, reused aluminium rings, and a castor-oil adhesive. These aluminium rings are arranged side by side, forming an orthogonal core architecture. To evaluate the mechanical properties of these sandwich panels, a three-point bending test is conducted following the RJS Method [30] and the ASTM standards C393 [31] and D7250 [32]. Through this analysis, researchers can assess the structural viability and load-bearing capacity of these ecological secondary solutions in various applications, including building and transport systems.

2. METHODOLOGY

2.1. Materials

The sandwich panel in this study is composed of galvanised steel skins, each approximately 0.53 mm thick. These skins provide the exterior layers of the panel, offering protection and structural support. The tubular honeycomb cores, on the other hand, are formed using reused aluminium rings. These rings have a thickness of approximately 0.14 mm and a height of 15 mm. By arranging these rings side by side, an orthogonal core architecture is achieved, contributing to the panel's structural integrity. To bond the skins to the core material, a biobased adhesive derived from castor-oil is utilized. This adhesive forms a film of approximately 1.5 mm, creating a strong and durable connection between the skins and the core.

2.2. Characterisation and manufacture

To characterise the aluminium sheet obtained from the cans, a tensile test is conducted based on the ASTM E8 standard [33], considering the circumferential direction. This test aims to determine key mechanical properties such as elastic modulus, ultimate strength, and ultimate strain. The testing is performed using an Instron testing machine equipped with a 50 kN load cell and a testing speed of 0.5 mm/min, as illustrated in Figure 1. In addition to the aluminium sheet, the mechanical properties of the other materials used in the sandwich panel construction are obtained from existing literature [36]. The galvanised steel, which serves as the skins of the panel, and the castor-oil, used as the adhesive, have their mechanical properties determined through previous research. The castor-oil adhesive used in this study is provided by the Imperveg® company based in Brazil. It consists of two components, A and B, mixed in a mass ratio of 1:1.2.
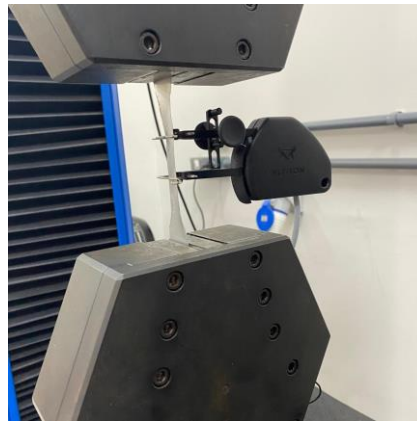
Figure 1. Tensile testing of aluminium sheet obtained from cans.

The sandwich panel is manufactured through steps designed to ensure proper assembly and curing. Here is a detailed overview of the manufacturing process: (i) galvanised steel sheets are cut to the specified panel size of 185 x 415 mm², following the ASTM C393 standard, which requires a minimum of 3 cells in width and a length of twice that of the width. Additionally, a safety margin is incorporated into the length to prevent slippage during the bending test, as recommended by the standard. The surfaces of the steel skins are degreased using an ordinary detergent and rinsed with water to remove any contaminants; (ii) the aluminium rings are cut crosswise using a Makita® marble saw. This process ensures precise dimensions and uniformity of the rings; (iii) the galvanised steel skins are inserted into polystyrene plate moulds, which are covered with film to prevent resin leakage. This setup is shown in Figure 2a; (iv) the castor-oil adhesive, composed of components A and B, is mixed for 1 minute to ensure proper blending. The mixture is then spread evenly over the surface of the galvanised steel skins, creating a uniform layer with a thickness of 1.5 mm. This step is depicted in Figure 2b; (v) the previously cut and selected aluminium rings, with a height of 15 ± 0.1 mm, which are placed on the castor-oil adhesive-coated surface. The rings are arranged side by side to form an orthogonal core architecture, as shown in Figure 2b; (vi) the mould is closed with a wooden cover and compacted at a uniaxial pressure of 0.64 kPa. This pressure is maintained for 24 hours at a room temperature of 22 ± 2ºC. This compaction process ensures proper bonding and consolidation of the panel components; (vii) after the compaction period, the material is demoulded. The second side of the sandwich panel is then bonded using the same process as the first side and (viii) the sandwich panel is cured for 14 days at an ambient temperature of 22 ± 2ºC. This curing process allows for the proper development of mechanical properties and ensures the panel's stability.
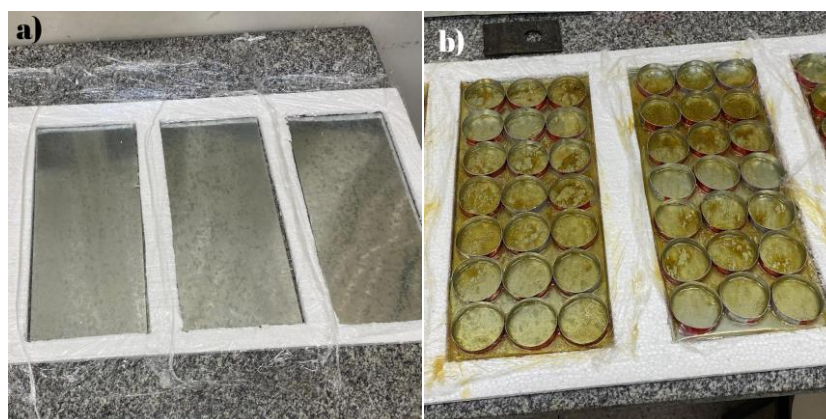
Figure 2. Panel manufacturing: (a) galvanised steel faces in the moulds, (b) aluminium rings and castor-oil adhesive spread out.

2.3. Three-point bending

To assess the mechanical properties of the sandwich panel, a three-point bending test is conducted, as depicted in Figure 3. The test utilizes a 100kN Shimadzu AG-X Plus test machine, with a crosshead speed of 6 mm/min and a span length of 370 mm. The maximum load, flexural strength, modulus, skin stress and core shear stress are determined based on ASTM standards C393 [31] and D7250 [32] and the RJS Method [30].

3

The equivalent density of the sandwich panels is also assessed by measuring the dimensions and mass of the panels using a calliper (0.01 mm) and a precision scale (0.001 g).
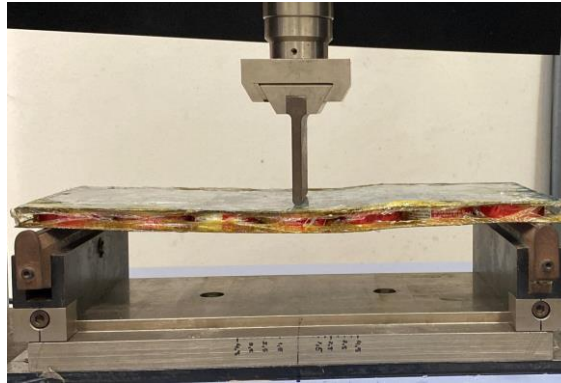
Figure 3. Three-point bending test of the sandwich panel.

2.4. Theoretical and experimental flexural modulus and core shear modulus

The RJS 2.0 Method [30,34] is employed to compare the theoretical and experimental flexural modulus of the sandwich panel. This analysis allows for the estimation of shear deformations that occur in the panel's core when subjected to bending within the elastic range. The RJS method has been extensively utilised in evaluating the mechanical properties of sandwich panels [35, 36]. By comparing the theoretically determined modulus with the experimental flexural modulus, it is possible to deduce the degree of shear deformation present in the core. A higher degree of shear deformation corresponds to a lower experimental flexural modulus. Panels that exhibit a significant difference between the theoretical and experimental flexural modulus, while maintaining the same specimen dimensions and face configuration, suggest a core with lower shear stiffness. The convergence of the experimental and theoretical flexural modulus indicates pure bending within the elastic regime. This convergence signifies that the panel is exhibiting elastic behaviour under the applied bending load [37].

The theoretical flexural modulus (E_s) is determined using Equation (1), which is derived from the homogenization concept proposed in the primary RJS Method [30]. In this equation, E_f represents the elastic modulus of the sandwich faces, while E_c represents the global elastic modulus of the core. The panel thickness and core thickness are denoted by the parameters h and c, respectively. In the calculation of the theoretical flexural modulus, Equation (1), the second term based on the core contribution (E_c) can be neglected without significant errors in cases where the core exhibits low rigidity. This is particularly applicable to flexible foams and similar materials. Therefore, for this work, only the first term of Equation (1) is considered [30, 34].

$$Es = \frac{Ef.(h^3 - c^3)}{h^3} + \frac{Ec.c^3}{h^3} \tag{1}$$

After, the experimental flexural modulus (Eexp) can be determined using Eq. 2, according to the RJS Method [30]. The support span length and sandwich width are represented by S and b, respectively. In addition, m represents the slope of the straight-line portion of the force-displacement curves.

$$Eexp = m.\frac{S^3}{4b.h^3} \tag{2}$$

The percentage comparison between experimental and theoretical flexural modulus ($100 \times Es/Exp$), also known as pure bending amount [34]. In general, to calculate the core shear modulus (G_C) using equations (3) and (4), specimens with a high degree of shear deformation are ideal. In these equations, D is the flexural stiffness calculated by multiplying the theoretical flexural modulus by the homogenized moment of inertia of the sandwich panels (b.h3/12), while U is the shear stiffness.

$$U = \frac{\sum \frac{Fi.S}{4.\left[\Delta i - \frac{Fi.S^3}{48D}\right]}.S^3}{n} \tag{3}$$

4

$$U = . \frac{b.\left(\frac{h+c}{2}\right)^2}{n} Gc \tag{4}$$

3. RESULTS AND DISCUSSION

3.1. Characterisation

Table 1 shows the mechanical properties (mean and standard deviation) of the components of the sandwich panel. The elastic modulus of the reused aluminium material accounts for approximately 22% of the galvanised steel used as skins. Concerning physical properties, the bulk density of the castor-oil adhesive is around 0.98 g/cm³ [36]. Additionally, the bulk density of the reused aluminium derived from cans is roughly 2.61 g/cm³.

Table 1. Mechanical properties of the materials used in the fabrication process of the sandwich panel.

	Elastic Modulus (GPa)		Ultimate Strength (MPa)		Ultimate strain (%)	
Properties	Tensile	Compressive	Tensile	Compressive	Tensile	Compressive
Galvanised steel (skins) *	200		-		-	
Reused aluminium (core material)	44.2 ± 5.8		134 ± 27		0.84 ± 0.64	
Castor-oil adhesive **	0.105 ± 0.004	0.0236 ± 0.0033	5.27 ± 0.62	2.20 ± 0.27	23.9 ± 4.3	12.3 ± 2.0

* Literature data. ** Experimental values reported in [36].

Table 2 shows the mean properties of the sandwich panels including maximum load and displacement, yield force and displacement, experimental and theoretical flexural modulus, yield stress and strain, ultimate stress and strain, the pure bending amount, and span to promote 95% of pure bending and the core shear modulus. Fig. 4 presents the typical bending curves for the sandwich panels.

Table 2. Mean properties of the sandwich panel.

	Yield Load (N)	Yield Displacement (mm)	Max Load (N)	Max Displacement (mm)	Experimental flexural modulus (MPa)	Theoretical flexural modulus (GPa)
Mean	278	5.91	303	7.92	872	35.2
Stdev	5	0.64	25	0.40	172	
CV (%)	2	11	8	5	20	

	Pure bending amount (%)	Span to promote 95% of pure bending (mm)	Core shear modulus (MPa)	Yield Mean Stress (MPa)	Yield Mean Strain (%)	Ultimate Stress (MPa)	Ultimate Strain (%)
Mean	2.48	10579	1.72	2.86	0.440	3.13	0.589
Stdev	-	-	0.39	0.21	0.054	0.41	0.031
CV (%)	-	-	22	12	12	13	5

5
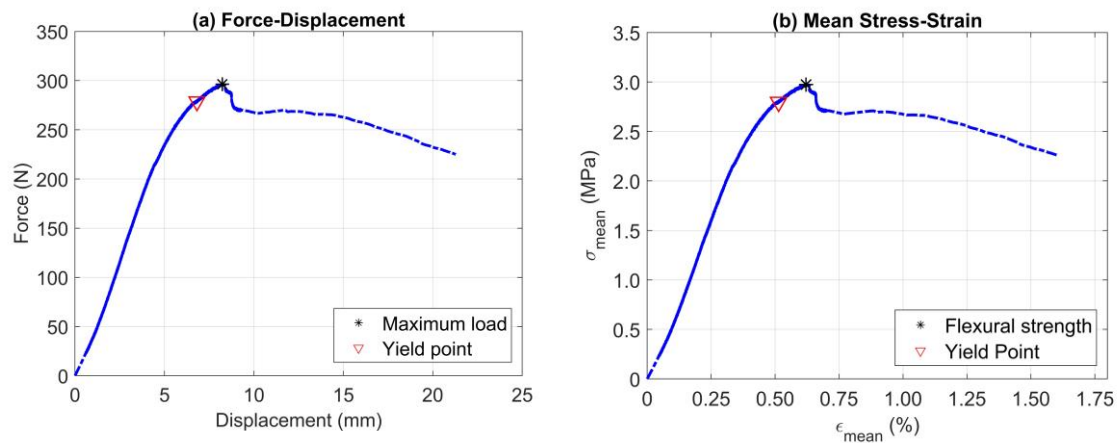
Figure 4. Typical curves of the sandwich panel: (a) Force-displacement graph, (b) Mean stress-strain graph.

It is worth noting that the mean yield and maximum loads exhibit a small standard deviation of less than 10%. Similarly, the mean yield and ultimate stresses also demonstrate a small standard deviation of less than 14%. In Figs. 4a and 4b, the yield and maximum points have been marked. As emphasized in the RJS method [34], it is observed that a higher face rigidity (200 GPa) results in a higher experimental flexural modulus (872.3 GPa) compared to the theoretical modulus. To achieve a flexural modulus of 35 GPa (indicative of pure bending), the sandwich panel requires a support span larger than 10,000 mm. This is also revealed by the pure bending amount corresponding to 2.48%. In other words, the lower the stiffness of the core relative to that of the faces, the greater the increase in the support length span should be. On the other hand, the rigid skins allow for a greater deformation of the core, which can be advantageous in certain applications focused on impact energy absorption, enhancing the modulus of toughness of the panels. The scope of future investigations will involve drop tower impact testing and three-point bending considering different adhesive thicknesses.

4. CONCLUSIONS

The sandwich panel, constructed with a reused circular aluminium core and tested with a span of 370 mm and a width of 185 mm, achieved a maximum load of up to 300 N. The mean properties, coupled with lower standard deviation values, indicate that the manual manufacturing process and the use of a biobased adhesive successfully yielded a uniform sandwich panel. The noticeable disparity between the theoretical and experimental flexural modulus signifies a significant contribution of shear deformation in the core. The combination of rigid skins and a low-stiffness core material resulted in reduced pure bending behaviour, but it also allowed for substantial deformation of the core, which can be strategically advantageous for impact absorption applications. Finally, these preliminary findings highlight the potential of these panels as both ecological and structural solutions across various applications.

4.1. Declaration of Competing Interest

The authors declare no conflict of interest.

4.2. Acknowledgements

5. REFERENCES

[1] Birman V. and Kardomateas G. A. Review of current trends in research and applications of sandwich structures. Compos B Eng 2018; 142: 221–240. DOI: 10.1016/j.compositesb.2018.01.027

[2] Howard G. Allen. *Analysis and Design of Structural Sandwich Panels*, 1st Edition, 1969. Pergamon Press. (https://doi.org/10.1016/C2013-0-02134-2).

[3] Bitzer T. *Honeycomb technology,* 1997. Springer-science + business media. (https://doi.org/10.1007/978-94-011-5856-5).

6

[4]   Gotkhindi TP, Simha KRY. In-plane effective shear modulus of generalised circular honeycomb structures and bundled tubes in a diamond array structure. Int J Mech Sci. 2015; 101:292-308. (http://dx.doi.org/10.1016/j.ijmecsci.2015.08.009).

[5]   D'Mello RJ, Waas AM. Synergistic energy absorption in the axial crush response of filled circular cell honeycombs. Compos Struct. 2012; 94:1669-76. (http://dx.doi.org/10.1016/j.compstruct.2011.12.009).

[6]   Feng Y, Qiu H, Gao Y, Zheng H, Tan J. Creative design for sandwich structures: a review. Inter J Adv Robot Syst. 2020:1-24. (http://dx.doi.org/10.1177/1729881420921327).

[7]   Huang J, Gong X, Zhang Q, Scarpa F, Liu Y, Leng J. In-plane mechanics of a novel zero Poisson's ratio honeycomb core. Composites Part B Eng. 2016; 89:67-76. (http://dx.doi.org/10.1016/j.compositesb.2015.11.032).

[8]   Huang J, Zhang Q, Scarpa F, Liu Y, Leng J. In-plane elasticity of a novel auxetic honeycomb design. Compos, Part B Eng.2018;110:72-82. (http://dx.doi.org/10.1016/j.compositesb.2016.11.011).

[9]   Cai Z-Y, Zhang X, Liang X-B. Multi-point forming of sandwich panels with egg-box-like cores and failure behaviours in forming process: analytical models, numerical and experimental investigations. Mater Des. 2018; 160:1029-41. (http://dx.doi.org/10.1016/j.matdes.2018.10.037).

[10] Lee B.C., Lee K.W., Byun J.H., Kang K-J. The compressive response of new composite truss cores. Compos, Part B Eng. 2012;43:317-24. (http://dx.doi.org/10.1016/j.compositesb.2011.08.048).

[11] Oruganti RK, Ghosh AK. FEM analysis of transverse creep in honeycomb structures. Acta Mater. 2008; 56:726-35. (http://dx.doi.org/10.1016/j.actamat.2007.10.019).

[12] Karagiozova D., Yu TX. Post-collapse characteristics of ductile circular honeycombs under in-plane compression. Int J Mech Sci. 2005; 47:570-602. (http://dx.doi.org/10.1016/j.ijmecsci.2004.11.011).

[13] Lin TC, Chen TJ, Huang JS. In-plane elastic constants and strengths of circular cell honeycombs. Compos Sci Technol. 2012; 72:1380-6. (http://dx.doi.org/10.1016/j.compscitech.2012.05.009).

[14] Oliveira PR, Panzera TH, Freire RT, Scarpa F. Sustainable sandwich structures made from bottle caps core and aluminium skins: a statistical approach. Thin-Wall Struct. 2018; 130:362-71. (http://dx.doi.org/10.1016/j.tws.2018.06.003).

[15] Kinloch AJ, Lee JH, Taylor AC, Sprenger S, Eger C, Egan D. Toughening structural adhesives via nano- and microphase inclusions. J Adhes. 2003; 79:867-73. (http://dx.doi.org/10.1080/00218460309551).

[16] Ghavami K. Bamboo as reinforcement in structural concrete elements. Cement Concr Compos. 2005; 27:637-49. (http://dx.doi.org/10.1016/j.cemconcomp.2004.06.002).

[17] Lo TY, Cui HZ, Tang PWC, Leung HC. Strength analysis of bamboo by microscopic investigation of bamboo fibre. Constr Build Mater. 2008; 22:1532-5. (http://dx.doi.org/10.1016/j.conbuildmat.2007.03.031.

[18] Li H-T, Su J-W, Zhang Q-S, Deeks AJ, Hui D. Mechanical performance of laminated bamboo column under axial compression. Compos, Part B Eng. 2015;79:374-82. (http://dx.doi.org/10.1016/j.compositesb.2015.04.027).

[19] Krause JQ, Silva FA, Ghavami K, Gomes OFM, Toledo RD Fo. On the influence of Dendrocalamus giganteus bamboo microstructure on its mechanical behaviour. Constr Build Mater. 2016; 127:199-209. (http://dx.doi.org/10.1016/j.conbuildmat.2016.09.104).

[20] Oliveira P. R. et al. Sustainable sandwich composite structures made from aluminium sheets and disposed bottle caps. *Thin-Waleed Structures,* 2017. (http://dx.doi.org/10.1016/j.tws.2017.08.013).

[21] Li W-T, Long Y-l, Huang J, Lin Y. Axial load behavior of structural bamboo filled with concrete and cement mortar. Constr Build Mater. 2017; 148:273-87. (http://dx.doi.org/10.1016/j.conbuildmat.2017.05.061).

[22] Chung KF, Yu WK. Mechanical properties of structural bamboo for bamboo scaffoldings. Eng Struct. 2002; 24:429-42. (http://dx.doi.org/10.1016/S0141-0296(01)00110-9).

7

[23] Saikia P, Dutta D, Kalita D, Bora JJ, Goswami T. Improvement of mechano-chemical properties of bamboo by bio-chemical treatment. Constr Build Mater. 2015; 101:1031-6. (http://dx.doi.org/10.1016/j.conbuildmat.2015.10.106)

[24] Gottron J, Harries KA, Xu Q. Creep behaviour of bamboo. Constr Build Mater. 2014; 66:79-88. http://dx.doi.org/10.1016/j.conbuildmat.2014.05.024).

[25] Puri V, Chakrabortty P, Anand S, Majumdar S. Bamboo reinforced prefabricated wall panels for low-cost housing. J Build Eng. 2017; 9:52-9. (http://dx.doi.org/10.1016/j.jobe.2016.11.010).

[26] Jakovljevic S, Lisjak D, Alar Z, Penava F. The influence of humidity on mechanical properties of bamboo for bicycles. Constr Build Mater. 2017; 150:35-48. (http://dx.doi.org/10.1016/j.conbuildmat.2017.05.189).

[27] Chee SS, Jawaid M, Sultan MTH, Alothman OY, Abdullah LC. Thermomechanical and dynamic mechanical properties of bamboo/woven kenaf mat reinforced epoxy hybrid composites. Compos, Part B Eng. 2019;163:165-74. (http://dx.doi.org/10.1016/jcompositesb.2018.11.039).

[28] Hartoni FJ, Anshari B, Catur AD. Effect of core and skin thicknesses of bamboo sandwich composite on bending strength. Int J Mech Eng Tech. 2017; 8:551-60.

[29] CarbonaTech. *Latas de alumínio alteram o sabor da bebida?* CarbonaTech. (https://carbonatech.com.br/aluminio-altera-saborbebida/#:~:text=Prote%C3%A7%C3%A3o%20contra%20luz%20e%20oxig%C3%AAnio,da%20bebida%20por%20mais%20tempo).

[30] R.J. da Silva et al. A core rigidity classifier method and a novel approach to account for geometric effects on the elastic properties of sandwich structures. *Composite Structures*, Volume 282, 2022. (https://doi.org/10.1016/j.compstruct.2021.115075).

[31] ASTM International. ASTM C393/C393M-16: standard test method for core shear properties of sandwich constructions by beam flexure. West Conshohocken: ASTM International; 2016.

[32] ASTM International. ASTM D7250/D7250M-16: standard practice for determining sandwich beam flexural and shear stiffness. West Conshohocken: ASTM International; 2016.

[33] ASTM International. ASTM E8/E8M-16a: standard test method for tension testing of metallic materials. West Conshohocken: ASTM International; 2016.

[34] R.J. da Silva, J.C. dos Santos, T.H. Panzera, F. Scarpa, Enhanced core rigidity classifier method (RJS 2.0): a comprehensive approach to properly measure elastic properties of sandwich structures, Compos. Struct. (Feb 2024) 117981. (https://doi.org/10.1016/j.compstruct.2024.117981, 117981).

[35] F. Napolitano, J.C. Santos, R.J. da Silva, et al., Sandwich panels made of aluminium skins and gapped-bamboo ring core, Journal of The Brazilian Society of Mechanical Sciences and Engineering, vol. 45, no. 5, Apr. 2023. (https://doi.org/10.1007/s40430-023-04140-x).

[36] R.T Lopes, R.J da Silva, R.T.S. Freire, et al., Statistical evaluation of three-point bending properties of sustainable aluminium sandwich panels with arched-core geometry, Proceedings of the Institution of Mechanical Engineers, Part L: Journal of Materials: Design and Applications 0 (0) (2023). (https://doi.org/10.1177/14644207231219647).

[37] J.C. dos Santos et al. Sandwich structures of aluminium skins and egg-box-shaped cores made with biobased foam and composites. *Journal of Building Engineering,* 88, 2024. (https://doi.org/10.1016/j.jobe.2024.109099).

STUDIES ON THE INFLUENCE OF METALLIC CORE GEOMETRY ON THE MECHANICAL PROPERTIES OF COMPONENTS FABRICATED BY ADDITIVE MANUFACTURING

Santanna, E.D.M[a*], Alberto, L.G.S[b], Anflor C.T.M.[c]

(a) 0009-0002-2397-9103 (University of Brasília – Brazil)
(b) 0009-0006-0652-3779 (University of Brasília – Brazil)
(c) 0000-0003-3941-8335 (University of Brasília – Brazil)
* Corresponding author: euclides.anna@unb.br

CODE: BCCM7-55

Keywords: Additive manufacturing, Composites, Finite Elements, Fused Deposition Modelling, Solid Mechanics.

Abstract: This study investigates the feasibility of employing metallic materials as internal reinforcement in components made through Additive Manufacturing (AM) via computational modelling. AM produced metal geometries have demonstrated promising results in various industries due to their strength and stiffness with low density. However, their complex and costly manufacturing process limits widespread use. Conversely, using AM with polymers offers an economically efficient way to produce intricate geometries precisely. The flexibility of AM allows for optimal material selection to meet specific application demands. Numerical simulations explored how different geometric configurations affect the mechanical properties of metallic reinforcements in manufactured components. Results showed satisfactory performance, though caution is needed when interpreting simulation outcomes, as real-world conditions may vary. Further studies are warranted to assess component performance in specific engineering applications. In conclusion, this study underscores the potential of metallic materials as structural reinforcement, promising benefits across diverse industrial sectors like automotive and aerospace.

1. INTRODUCTION

In the pursuit of manufacturing structures and components with greater shape freedom, the most promising alternative is additive manufacturing (AM). However, despite its numerous advantages, this technology still has limitations, such as reduced mechanical strength or high costs depending on the associated technology [1].

Fused Deposition Modelling (FDM) type additive manufacturing is a widely used technique in the production of prototypes and final parts due to its versatility and affordable cost. This method consists of depositing successive layers of molten polymeric material, which is extruded through a heated nozzle controlled by a microcontroller, onto a build platform [2]. The main advantages of FDM include the ability to create complex geometries with precision, the use of a wide range of materials, including reinforced polymers and composite materials [3]. Additionally, FDM allows for quick design adjustments and on-demand production, making it ideal for applications in industries such as automotive, aerospace, and medical [4]. However, challenges such as anisotropy and low mechanical strength of the parts limit the application of this technology in more demanding applications [5].

The main objective of this work is to investigate the influence and performance of implementing metallic reinforcements in a polymeric matrix using numerical simulation. The methodology included detailed modeling of the geometries and simulation of load conditions under bending to evaluate the strength and stiffness of the reinforced structures. Different materials and the number of reinforcements were evaluated in the analysis, as well as how these variations affect the geometry under operational conditions. The study aims to contribute to the development of methods for producing lighter and stronger geometries, considering the potential applications in various engineering fields.

2. METHODOLOGY

To study the effects of metallic reinforcement in structures manufactured by FDM, only the material properties were considered during the analyses; thus, no simulations of the AM manufacturing process were performed. The proposed geometry has a rectangular shape with dimensions of 60 x 40 x 180 mm (Fig. 1). The internal structure chosen for the matrix is triangular, resembling lattice structures. Due to these characteristics, the selected structure allows for a more uniform load distribution across the geometry.
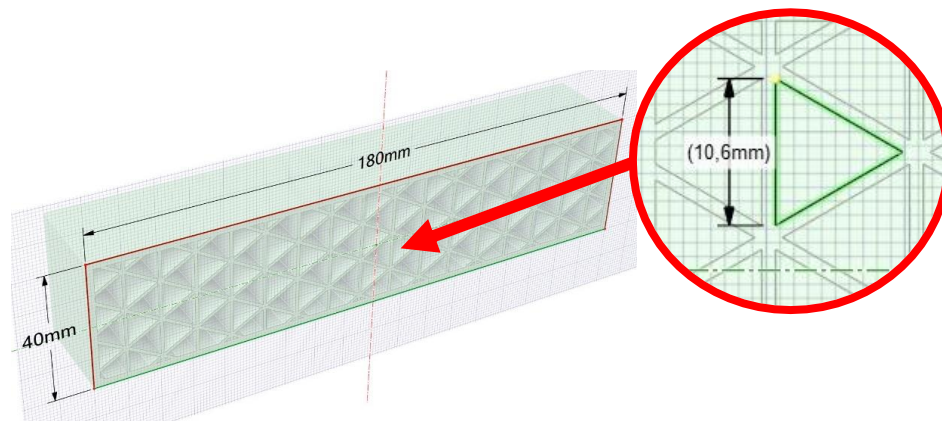
Figure 1. Geometry dimensions.

Fig. 2 presents the geometry of the reinforcement evaluated in this work. A honeycomb pattern was chosen, different from the geometry used in the matrix, to modify the load propagation and increase the distribution of stresses in the produced component [6]. To adjust the infill density of the reinforcement structure, a simulation of the matrix without reinforcements, made of Al 6061-T6, was performed. This simulation was used as a reference for the mass, displacements, and stresses parameters we aimed to achieve with the reinforced nylon geometry. Based on the reference simulation, material configurations and the number of reinforcements were proposed. Fig. 2a shows a cross-sectional view of the channels where the reinforcements will be inserted into the matrix. Fig. 2b presents an internal view of the arrangement of the reinforcements in the matrix.

Plate reinforcement channels

a)   Plate channels

b)   Reinforcements in place
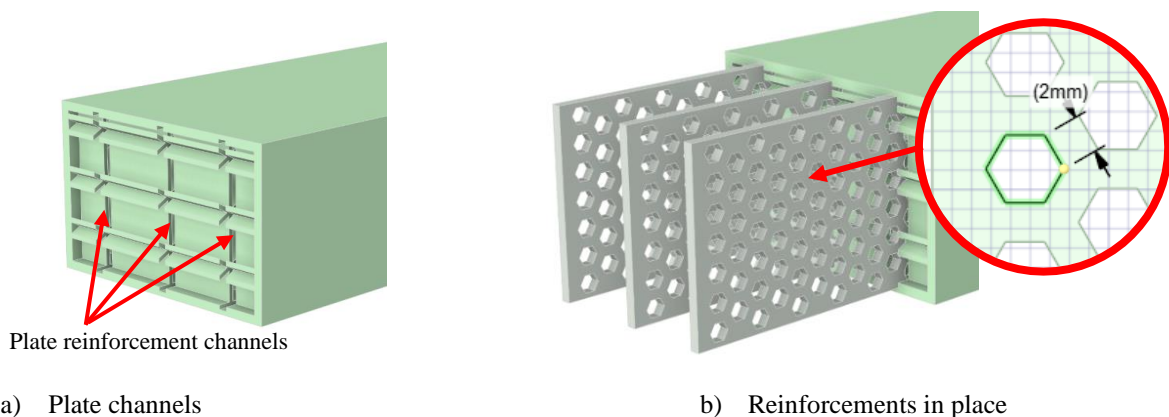
Figure 2. Internal view of reinforcements plates distribution.

2

Fig. 3 presents a diagram illustrating the manual inclusion of mechanical reinforcements during the printing process. The reinforcements have a 50% infill density relative to the effective area of the reinforcement solid. The geometry used for the infill was the honeycomb pattern, as shown in Fig. 2b [7].

| 1º Step – Start print | 2º Step – Pause Print | 3º Step – manual insert Reinforcement plate |

| 6º Step – Pos-processing | 5º Step – Repeat the process for the number of plates | 4º Step – Resume Print |
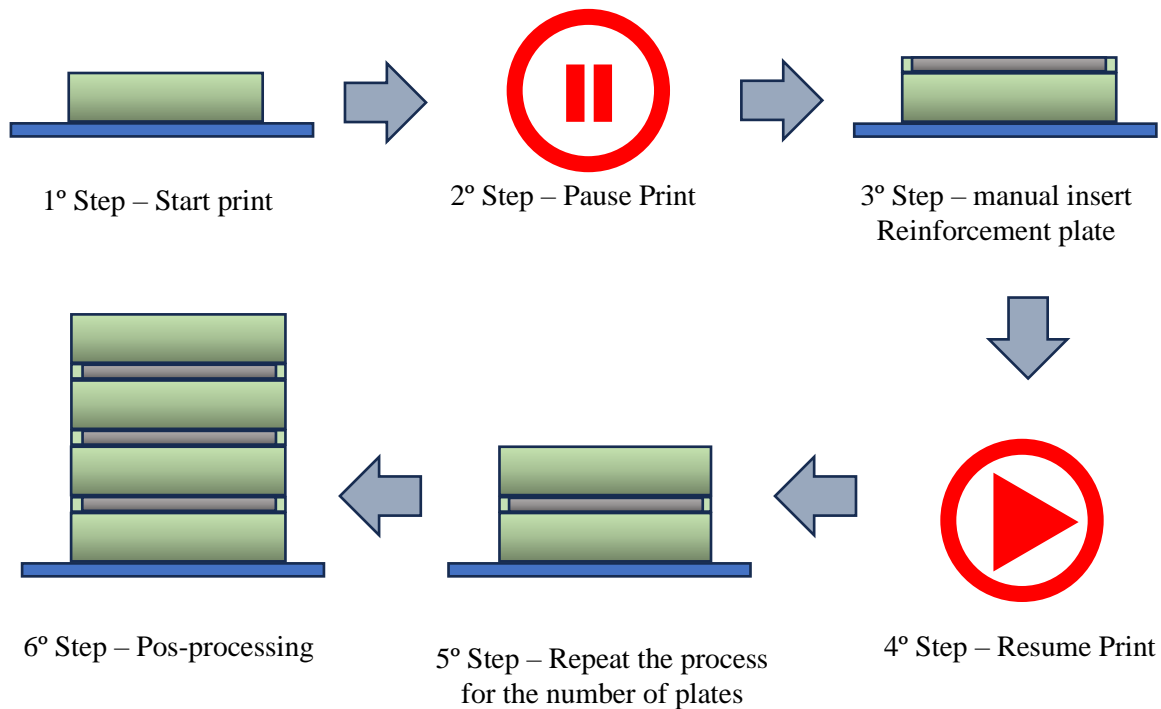
Figure 3. Scheme of the printing and reinforcement addition process.

To evaluate the mechanical performance of the structure, a study was conducted on the influence of the quantity and spatial distribution of the reinforcements within the printed layers. Additionally, two simulations were performed with components without reinforcement to compare the results between the models. The other models evaluated have reinforcements made of aluminum 6061-T6 and SAE 4340 steel, distributed in 3 and 4 plates, as shown in Table 1. The spacing between the plates was uniformly distributed based on the width of the model.

Table 1. Model configuration.

Model	Number of reinforcements
Nylon (matrix)	0
Al 6061-T6 (matrix)*	0
Nylon (matrix) +Al 6061-T6 (reinforcement)	3
Nylon (matrix) +Al 6061-T6 (reinforcement)	4
Nylon (matrix) + SAE 4340 (reinforcement)	3
Nylon (matrix) + SAE 4340 (reinforcement)	4
(Reference model)	

2.2. Material

The material used for constructing the matrix was nylon due to its mechanical properties and high elongation, making it ideal for withstanding the internal stresses resulting from the interaction between the metallic reinforcement and the internal walls of the print.

For the internal metallic reinforcement material, two variants were used: SAE 4340 steel and 6061-T6 aluminum. The properties of these materials were obtained from the Ansys® finite element software library and are listed in Table 2. SAE 4340 steel uses a plasticity model based on the Johnson-Cook parameters, 6061-T6 aluminum adopts the Steinberg-Guinan model, while nylon follows a Bilinear Isotropic model [8].

3

Table 2. Material properties.

Material Properties	Steel 4340	Al 6061-T6	Nylon
Density [Kg/m³]	7830	2703	1140
Yield Strength [MPa]	792	290	50
Shear Modulus [GPa]	81,8	27,6	3,68
Hardening Constant [MPa]	510	125	-
Hardening Exponent	0,26	0,1	-

2.1 Numerical model

The bending properties of unreinforced and reinforced plastics were conducted following the recommendations of ASTM D790 [9]. When a homogeneous elastic material is tested in bending as a simple beam supported at two points and loaded at the midpoint, the maximum stress on the outer surface of the test specimen occurs at the midpoint. Stress can be calculated for any point on the load-deflection curve using equation 1.

$$\sigma_f = 3PL \,/\, 2bd^2 \qquad\qquad\qquad (1)$$

where σ is the stress in the outer fibers at the midpoint (MPa), P is the load at a given point on the load-deflection curve (N), L is the span length (mm), b is the width of the tested beam (mm), and d is the depth of the tested beam (mm). The established boundary conditions were as follows: fixed support on the support bars located at the bottom of the model and a prescribed displacement of 30 mm at the top of the testing apparatus (Fig. 4).

The numerical simulation was conducted using Explicit Dynamics ANSYS® for nonlinear material modeling, where behaviors such as plasticity and viscoelasticity are considered. In this type of analysis, the explicit solution method is employed, as it is ideal for short-duration events with high rates of deformation. Nonlinear contact control allows for modeling complex interactions between bodies, where contacts are considered frictionless. For frictionless contact analysis, the pure penalty formulation criterion is applied. In the analysis of internal reinforcements in the proposed structures, large deformations are considered, enabling the handling of significant changes in material shape and size [10].

Figure 4. Boundary conditions.

4
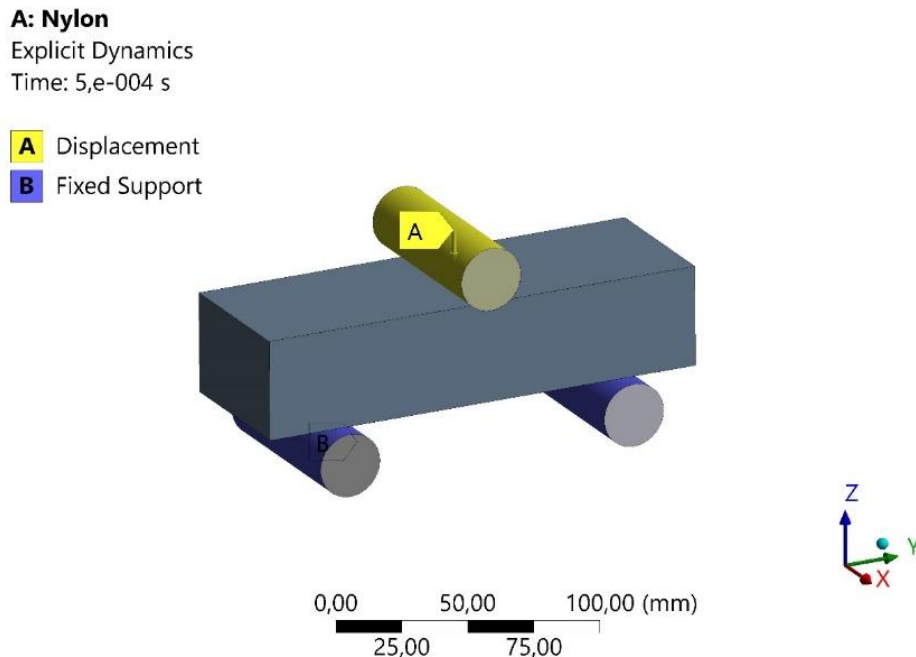
3. RESULTS AND DISCUSSION

From the simulation of the proposed geometries considering the quantity of plates and materials in their composition, it was possible to observe that the addition of metallic reinforcements has a strong influence on the geometry's strength. Fig. 5 presents the stress-strain graph with different material configurations and numbers of reinforcements. Based on the data, it can be observed that increasing the number of internal reinforcement plates results in an increment in the component's stiffness when compared to the model made exclusively of nylon.
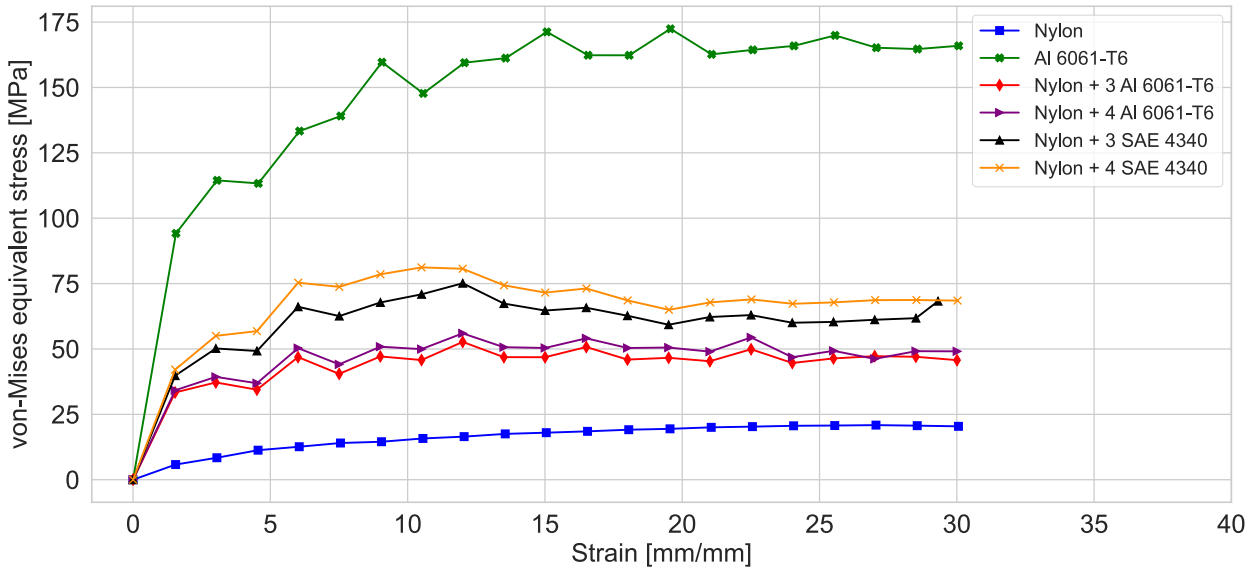
Figure 5. Mean Stress x Equivalent strain.

In Fig. 6, it can be observed that the addition of reinforcements allowed the model reinforced with SAE 4340 steel to exhibit performance comparable to the reference body made of Al 6061-T6 up to the range of 10 mm displacement. Despite the increase in maximum loading promoted by the reinforcement, when high degrees of deformation of the component are required, the results are still not close to the reference aluminum geometry.
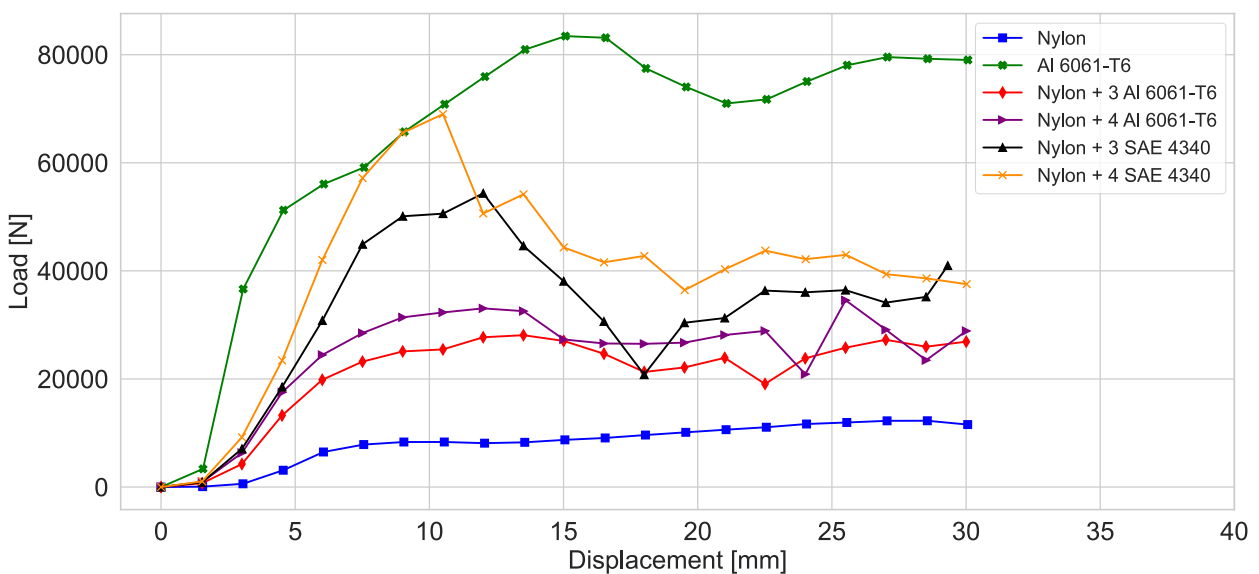
Figure 6. Load x Displacement.

5

Based on the mass distribution of the models (Fig. 7), it is possible to associate the performance improvement with the mass of the added reinforcements. From the observed data, it can be inferred that the increase in metallic reinforcement mass in the structure varies linearly and promotes convergence of the models when small displacements in the structure are observed.
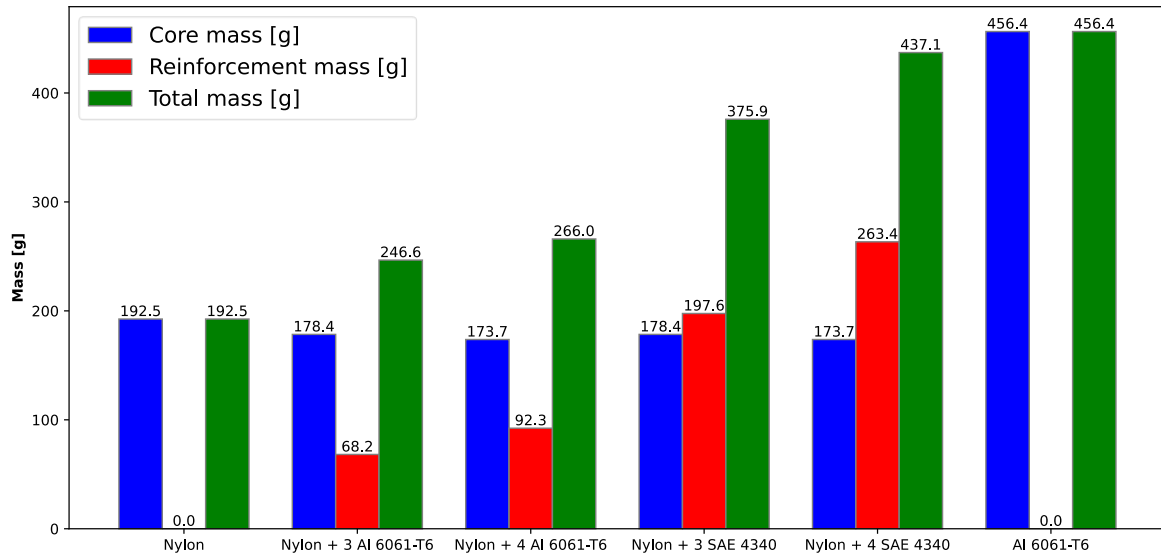
Figure 7. Mass distribution between core and reinforcement.

In Fig. 8, the structures can be comparatively evaluated under a uniform loading condition of 50KN, where it is observed that the structure with internal reinforcement exhibits a deflection 6.6 times smaller than the structure made exclusively of nylon. Additionally, the assessment of stress field distribution reveals that the reinforced body has an almost exclusive distribution on the internal plates, reducing the mechanical demand on the polymeric component of the structure.

6
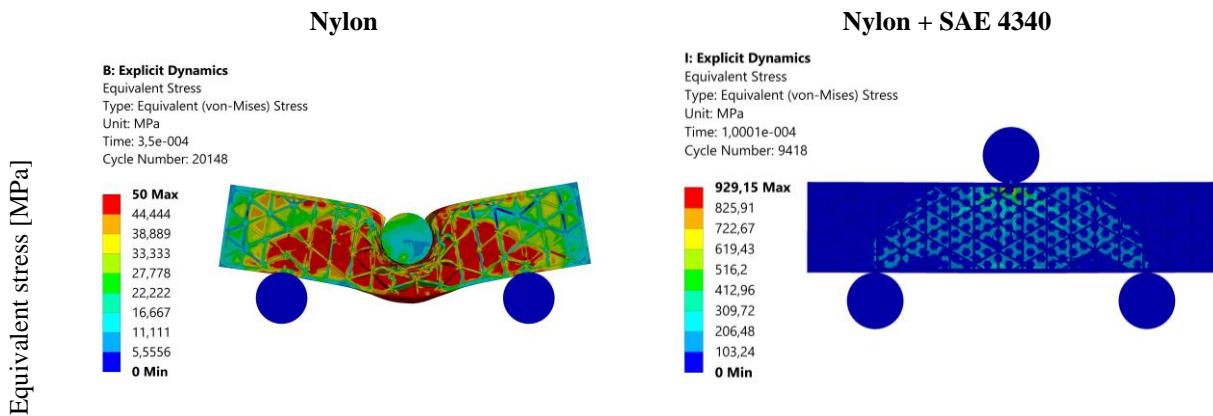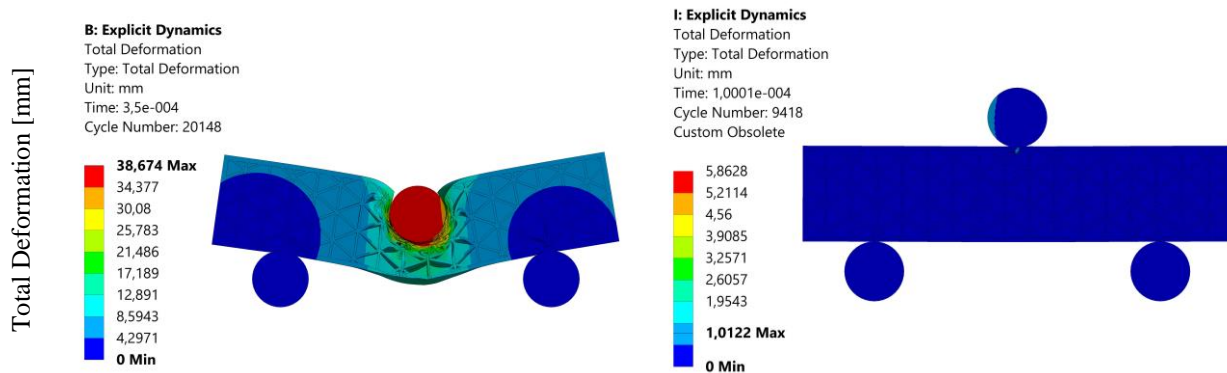
figure 8. Comparison of results across models: Equivalent Stress (MPa) and Total Deformation (mm).

4. CONCLUSIONS

The objective of this study was to investigate the performance of adding internal metallic structures as structural reinforcement in geometries manufactured by the FDM methodology. Through the evaluation of the numerical results obtained in finite element simulations, an increase in the strength of the FDM-manufactured models with reinforcement was observed compared to the unreinforced model. The reinforced model showed an increase of 82.2% in the maximum supported load, with a metallic mass 42.3% smaller than the reference model. In some specific cases of low deformations, the performance of the reinforced models approached that of the reference geometry; however, it is worth noting that the data were evaluated based on the peak values of each sample, thus it is necessary to adjust the use of reinforcements based on the application. Despite these observations, it is still necessary to conduct mechanical tests to determine the correlation between the numerical and experimental model. Additionally, further studies will be conducted regarding variations in the shape of the reinforcement component and the filling of the polymer core structure. The results obtained serve as a good reference point for further studies related to core and reinforcement density variation, with possible variations of manufacturing parameters and associated materials. With these considerations, this study contributes to the development of lighter and stronger structures, with wide application in various areas of engineering that demand such prerequisites.

4.1. Declaration of Competing Interest

The authors declare no conflict of interest.

4.2. Acknowledgements

5. REFERENCES

[1] GIBSON, L.; ASHBY, M. Cellular Solid: Structure and Properties. Cambridge Solid State Science Series, 1997. (ISBN: 0521499119, 9780521499118)

[2] CHUA, C. K.; LEONG, K. F. 3D Printing and Additive Manufacturing: Principles and Applications. World Scientific Publishing, 2015. (ISBN: 978-981-314-675-4)

[3] GIBSON, I.; ROSEN, D. W.; STUCKER, B. Additive Manufacturing Technologies: 3D Printing, Rapid Prototyping, and Direct Digital Manufacturing. Springer, 2015. (https://doi.org/10.1007/978-1-4939-2113-3)

[4] WANG, X. et al. 3D printing of polymer matrix composites: A review and prospective. Composites Part B: Engineering, 110, 442-458, 2017. (https://doi.org/10.1016/j.compositesb.2016.11.034)

[5] SUN, Q. et al. Effect of processing conditions on the bonding quality of FDM polymer filaments. Rapid Prototyping Journal, 14(2), 72-80, 2018. (DOI: 10.1108/13552540810862028)

[6] CATANA, D. I.; POP, M. A.; BRUS, D. Comparison between Tests and Simulations Regarding Bending Resistance of 3D Printed PLA Structures. Polymers, 13, 4371, 2021. (https://doi.org/10.3390/polym13244371)

[7] KAVELOĞLU, S.; TEMIZ, S. An experimental and finite element analysis of 3D printed honeycomb structures under axial compression, 2022. (DOI: 10.1177/09673911221122333)

[8] BITZER. Honeycomb technology: materials, design, manufacturing, applications and testing. Springer Science & Business Media, 2012. (https://doi.org/10.1007/978-94-011-5856-5)

[9] ASTM D790-17. Standard Test Methods for Flexural Properties of Unreinforced and Reinforced Plastics and Electrical Insulating Materials. ASTM International, 2017. ((www.astm.org))

[10] ANSYS. ANSYS engineering analysis system user's manual 2024, 2024. (https://www.ansys.com/)

Sustainable sandwich panel: harnessing the power of castor-oil polyurethane and foam

Emmanuel Sousa Lodron [a], Alexandre Silva Lacerda [b], André Luís dos Santos [c], Luísa Fernandes Soares [d], Rodrigo José da Silva [e], Carlos Thomas Garcia [f], Túlio Hallak Panzera [g]

(a) BSc Student. Centre for Innovation and Technology in Composite Materials, Federal University of São João del-Rei - Brazil)
(b) Master's Student. Centre for Innovation and Technology in Composite Materials, Federal University of São João del-Rei - Brazil)
(c) Lab Technician. Centre for Innovation and Technology in Composite Materials, Federal University of São João del-Rei - Brazil)
(d) PhD Student. Centre for Innovation and Technology in Composite Materials, Federal University of São João del-Rei - Brazil)
(e) PhD Candidate. Centre for Innovation and Technology in Composite Materials, Federal University of São João del-Rei – Brazil. University of Bristol – UK.
(f) Professor. Civil Engineering School of the University of Cantabria, Santander, Spain.
(g) Professor. Centre for Innovation and Technology in Composite Materials, Federal University of São João del-Rei - Brazil)

Abstract: The study investigates the properties of sandwich panels consisting of glass fibre composite skins and a foam core made from castor oil polyurethane. Three different configurations of skins-to-core bonding are compared, and the panels are characterised under three-point bending tests according to ASTM standard C393. Panels fully made with epoxy polymer achieve a flexural modulus of 1.61 GPa, while those fabricated with castor oil polymer achieve 1.32 GPa. Panels manufactured with epoxy composite skins and castor oil polymer adhesive reached a flexural modulus of 1.41 GPa. Other properties are calculated and analysed, demonstrating the potential of sustainable sandwich structures as an alternative to traditional epoxy panels.

1. INTRODUCTION

Composite sandwich panels are engineered by integrating two thin skins (also denoted as faces or facesheets) with a relatively thicker core structure [1]. Typically, the faces are made from a rigid material capable of withstanding high strength demands, while the core is composed of a lightweight material [2]. These sandwich structures excel at resisting flexural loads because the skins support the maximum stresses arising from bending moments while the core resists shearing and provides an increase in global thickness, thereby enhancing the second moment of area (and then the stiffness) for the beam or plate [3].

The concept of sustainability permeates various domains and is consistently emphasised in contemporary discourse. Several studies have explored sandwich panels made from traditional materials (e.g., metallic skins, synthetic foam cores, and fossil-based adhesive bonding) to enhance mechanical properties in terms of absolute and weight-specific measures [4]. However, the use of such materials, which may have significant environmental impacts and pose challenges for recycling, is not suitable for developing eco-friendly structures [5,6]. To address these concerns, eco-friendly composites have emerged as a potential solution, reducing reliance on unsustainable and harmful materials [7,8].

The current study aims to compare similar sandwich structures across different synthetic and biobased systems for the skins and the faces-to-core adhesive. Three configurations of sandwich panels are proposed: (i) composite skins made of glass-fibre and epoxy matrix, bonded to the core employing an epoxy polymer; (ii) composite skins built of glass-fibre and epoxy matrix, attached to the core utilising a biobased castor-oil polymer; and (iii) skins composed of glass-fibre and castor-oil polymer matrix, fixed to the core through a biobased castor-oil polymer. All three configurations have a core made of castor-oil polyurethane foam. Three-point bending tests are conducted following ASTM Standards [8-10], and the flexural properties are thoroughly compared across a statistical approach.

2. METHODOLOGY

2.1. Materials

2.1.1. Glass fibre laminates

The facing composite materials are manufactured using the vacuum infusion technique, in which the matrix polymers are prepared employing bi-component resin. After preparing the fluid resin mixture, it is placed in a vacuum chamber to remove the bubbles formed from the mixing process. Then, the infusion technique is initiated, and the resin is sucked with a vacuum pump, impregnating the glass fibre in a proper bag. Two laminates are produced using 200 g/m^2 cross-ply fabric. The configuration with epoxy polymer matrix is made with 43 g of fabric and 22.8 g of bi-component resin, resulting in a laminate with 65.8 g in mass. In contrast, the lamina with castor-oil polymer matrix is fabricated employing 44 g of fabric and 17.64 g of resin, resulting in a laminate with 61.64 g of mass.

2.1.1. Castor oil foam

Castor-oil foam production involves using three specific components in precise quantities while maintaining controlled environmental conditions. The laboratory is maintained at a temperature of 22°C with a relative humidity of 47%. The proportions required to produce this foam are outlined in Table 1. A mould is used to shape the foam, as depicted in Figure 1a. Additionally, it is crucial to allow sufficient time for the material to cure effectively. After moulding, the foam remains in the mould for three days before being removed, followed by a two-week curing process, as illustrated in Figure 1b.

Table 1. Castor oil foam mixing.

Component	Mass [g]
Component A (Isocyanate)	227.76
Component B (Polyol)	247.79
H_2O	9.20
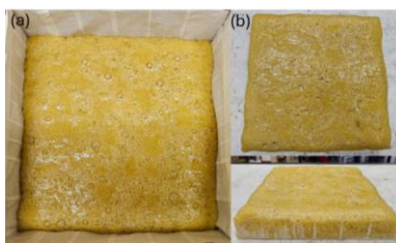
Figure 1. (a) Castor oil foam mixture poured into the mould for shaping and (b) foam core after demoulding.

2.2. Sandwich panel manufacturing and testing

The manufacturing of the sandwich panels adheres C393/C393M-20 [9] for panel dimensions. By the standard requirements, a minimum of five specimens are used to validate the results. The dimensions of the sandwich panels are provided in Table 2.

Table 2. Sandwich panel aimed dimensions.

Dimension	Measurement [mm]
Length	200
Width	24
Thickness	12

The experiments are designed to investigate the impact of two different types of polymer systems used as matrix phase (laminate) and face-to-core adhesive on the bending performance of the panels. This design approach enables valuable insights into the optimal combination for achieving desired mechanical characteristics. Table 3 provides an overview of the setup for the proposed experimental design.

Table 3. Experimental design.

Setup	Matrix Phase (Laminate)	Adhesive (Face-Core)	Abbreviation
S1	Castor Oil	Castor Oil	MMM
S2	Epoxy	Castor Oil	EME
S3	Epoxy	Epoxy	EEE

The manufacturing process of the sandwich panels involves bonding the composite laminate skins to the foam core. Initially, the foam block is pre-cut using a band saw and then undergoes laser cutting processing to achieve the core dimensions. Both the laminates and foams are cut using a Robotech laser cutting machine (500 W). Figure 2 illustrates the laser cutting machine and the bandsaw tools (a) and (b).
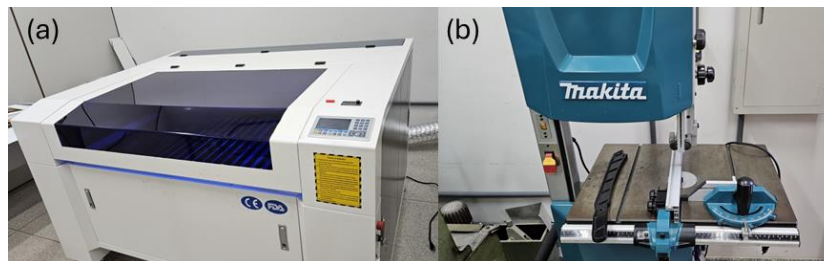
Figure 2. (a) Laser cutting and (b) bandsaw machines.

Before face-to-core bonding, the skin laminates undergo sanding on the surfaces intended for attachment to the foam core to enhance adhesion. The first skin of each panel is placed into a mould, and the resin is evenly spread over its surface. Subsequently, the foam core is positioned over the resin layer. Upon completion of resin curing (pot life), the process is repeated for the second skin. The steps of this process are shown in Figure 3a-c. Finally, the configurations of castor-oil polymer are left to cure for two weeks, while those made with epoxy polymer cure for 10 days, following manufacturer recommendations. A 20kg weight is then applied over the panels, as illustrated in Figure 4d.

3
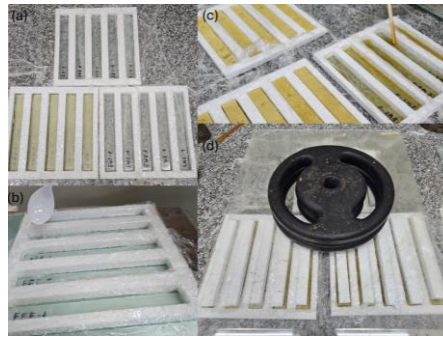
Figure 3. (a) Skins positioned in the mould, (b) epoxy resin adhesive and (c) castor oil resin application. (d) Samples during the curing process.

Table 4 exhibits the mean values of the geometrical and physical properties of the five investigated sandwich panels. Additionally, Figure 4 shows the samples before and after testing, while Figure 5 illustrates the three-point bending test, conducted with a span set to 150 mm and a crosshead speed of 5 mm/min. The mechanical properties, including (i) flexural modulus, (ii) yield mean stress, (iii) modulus of resilience, (iv) flexural strength, and (v) ultimate mean strain, are determined. The bending behaviour is analysed using MATLAB® software [10] with a dedicated script [12], and the statistical evaluation of the mechanical properties is carried out using the Minitab statistical software [13].

Table 4. Mean geometric and physical properties.

Setup	Length [mm]	Width [mm]	Thickness [mm]	Mass [g]
S1	200	25.59	13.62	25.63
S2	200	25.36	12.91	27.61
S3	200	25.14	13.27	25.41
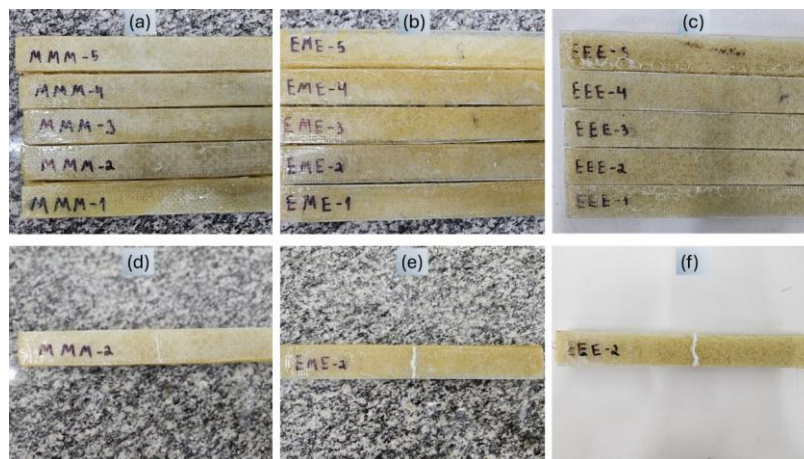
Figure 4. Samples before and after the test. (a, d) experiment 1; (b, e) experiment 2; (c, f) experiment 3.

4
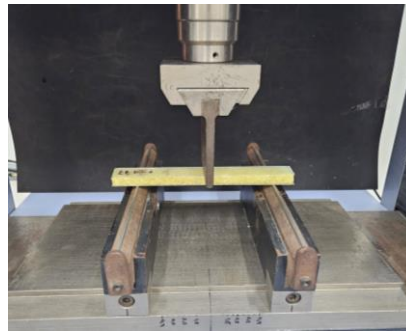
Figure 5. Three-point bending testing.

3. RESULTS AND DISCUSSION

Table 5 shows the descriptive statistics for the evaluated mechanical properties under flexural load, and the data concerning One-Way ANOVA analysis. The low values of StDev (standard deviation) and CoefVar (coefficient of variation) show that the data are statistically reliable and clustered closely around the mean values. The P-values for the Anderson-Darling test greater than 0.05 indicate that all the data have a normal distribution. Regarding Bartlett's test, P-values which are greater than 0.05 indicate a homogeneity of variances between different conditions for the target property. For data that present homogeneity of variance, the ANOVA P-value is used to check if there is a difference between the means; whilst the Welch P-value is used for the data that have non-homogeneity of variances. Flexural modulus, flexural strength and ultimate mean strain are greater than 0.05, which indicates that the means are equal. Yield mean stress and modulus of resilience are lesser than 0.05, which indicates there is at least one mean different from the others for each measured property. In the case of homogeneity of variances, Tukey's test is used to perform multiple comparisons between the means; whilst the Games-Howell test is used for data with non-homogeneity of variances. Tukey/Games-Howell tests return the same letter for statistically equal means.

In terms of yield mean stress, condition EEE (letter A) exhibits a distinct mean compared to condition MMM (letter B), while condition EME shows similarities with both (letters A and B). Concerning the modulus of resilience, condition EEE (letter A) differs from the statistically equal conditions EME and MMM (letter B). The plot interval for the evaluated mechanical properties is shown in Figure 8. Additionally, Figure 6 illustrates the typical force displacement and stress-strain curves for the evaluated conditions, while Figure 7 presents various stages of a sample. Post-testing, the core demonstrates remarkable recovery, nearly returning to its original thickness after one week (Figure 7c), highlighting the impressive restorative capacity of the castor-oil foam.
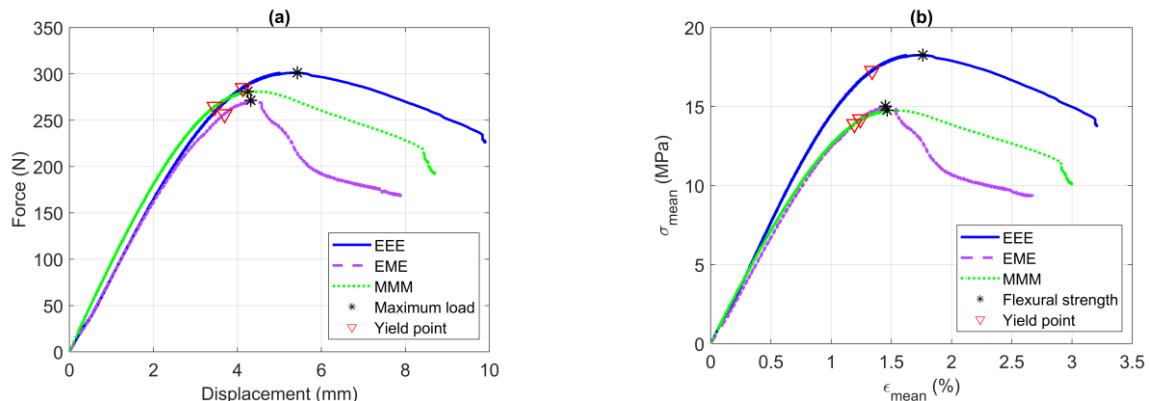
Figure 6. Typical (a) force-displacement and (b) stress-strain curves for the evaluated conditions.

5
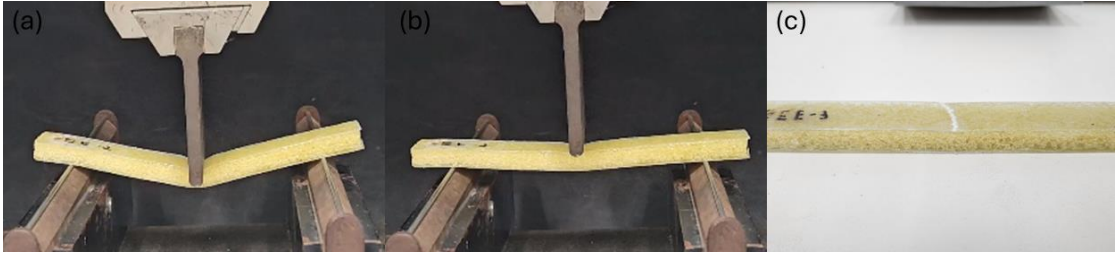
Figure 7. (a) Sample at the end of the test. (b) Sample after load removal. (c) Sample after one week of the test.

6

Table 5. Mechanical properties (descriptive statistics) and One-Way ANOVA analysis for normalised data (mean stress-strain).

Property	Flexural modulus (GPa)			Yield mean stress (MPa)			Modulus of resilience (mJ/cm$^{3)}$)			Flexural strength (MPa)			Ultimate mean strain (%)		
Condition	*EEE*	*EME*	*MMM*	*EEE*	*EME*	*MMM*	*EEE*	*EME*	*MMM*	*EEE*	*EME*	*MMM*	*EEE*	*EME*	*MMM*
Mean	1.61	1.41	1.32	18.1	14.9	13.8	134	102	96.6	19.0	15.4	14.9	1.63	1.36	1.46
StDev	± 0.22	± 0.04	± 0.19	± 2.4	± 2.1	± 1.8	± 18	± 19	± 12	± 3.3	± 1.9	± 2.3	± 0.36	± 0.07	± 0.08
CoefVar	14%	3%	14%	13%	14%	13%	14%	18%	13%	18%	13%	15%	22%	5%	5%
P-value Anderson-Darling	0.109	0.827	0.910	0.438	0.056	0.600	0.438	0.076	0.182	0.300	0.118	0.613	0.104	0.515	0.348
P-value Bartlett		0.047			0.863			0.702			0.565			0.004	
P-value ANOVA/Welch		0.172			0.021			0.009			0.055			0.132	
Tukey/Games-Howell		-		A	AB	B	A	B	B		-			-	
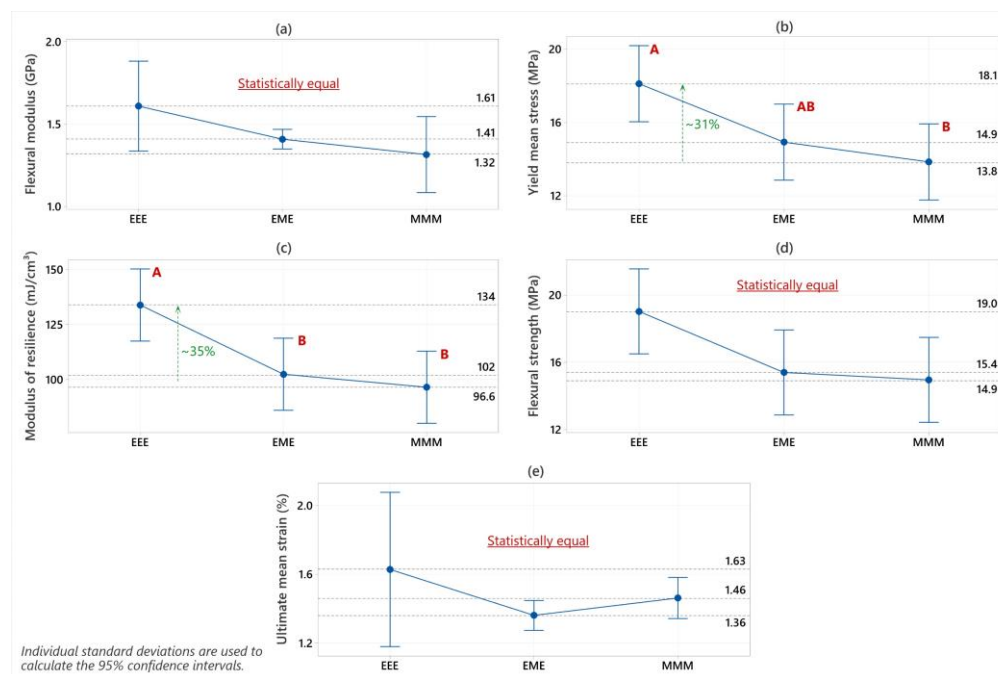
Figure 8. Plot intervals for mechanical properties: (a) Flexural modulus, (b) Yield mean stress, (c) Modulus of resilience, (d) Flexural strength, and (e) Ultimate mean strain.

7

4. CONCLUSIONS

Sandwich structures, consisting of glass fibre laminate skins and biobased cores, undergo testing via three-point bending. The primary conclusions are outlined below: i) From a statistical standpoint, the mechanical properties exhibited negligible variation, affirming the potential for substituting the epoxy system with the biobased castor-oil polymer. Notably, only the modulus of resilience and yield stress demonstrate improvement with the synthetic polymer. ii) All specimens displayed localised core crushing, with no instances of skin failure or debonding. iii) The core exhibited remarkable recovery capability after undergoing bending. iv) Panels fully made with epoxy polymer achieve a flexural modulus of 1.61 GPa, while those fabricated with castor oil polymer achieve 1.32 GPa, demonstrating the potential of sustainable sandwich structures as an alternative to traditional epoxy systems.

4.1. Declaration of Competing Interest

The authors declare no conflict of interest.

4.2. Fundings

.
4.3. Acknowledgements

5. REFERENCES

[1] Vasiliev, V.V.; Morozov, E.V. Mechanics of Laminates. Adv. Mech. Compos. Mater. Struct. 2018, 29, 191–242.

[2] Junaedi, H.; Khan, T.; Sebaey, T.A. Characteristics of Carbon-Fiber-Reinforced Polymer Face Sheet and Glass-Fiber-Reinforced Rigid Polyurethane Foam Sandwich Structures under Flexural and Compression Tests. Materials 2023, 16, 5101. https://doi.org/10.3390/ma16145101.

[3] Chan KE, Yong LA, Ko Y-F, Mendez S. Experimental and numerical studies of sustainable sandwich bio-composites derived from plant-based resources. Journal of Sandwich Structures & Materials. 2017;19(2):192-215. doi:10.1177/1099636215608785.

[4] Pablo Resende Oliveira, Michael May, Tulio Hallak Panzera, et al. Bio-based/green sandwich structures: A review, Thin-Walled Structures, Volume 177, 2022, 109426, ISSN 0263-8231, https://doi.org/10.1016/j.tws.2022.109426.

[5] T.E. Norgate, S. Jahanshahi, W.J. Rankin. Assessing the environmental impact of metal production processes, Journal of Cleaner Production, Volume 15, Issues 8–9, 2007, Pages 838-848, ISSN 0959-6526, https://doi.org/10.1016/j.jclepro.2006.06.018.

[6] Angela Daniela La Rosa, Giuseppe Recca, John Summerscales, et al. Bio-based versus traditional polymer composites. A life cycle assessment perspective, Journal of Cleaner Production, Volume 74, 2014, Pages 135-144, ISSN 0959-6526, https://doi.org/10.1016/j.jclepro.2014.03.017.

[7] Pablo Resende Oliveira, Michael May, Tulio Hallak Panzera, et al. Reinforced biobased adhesive for eco-friendly sandwich panels, International Journal of Adhesion and Adhesives, Volume 98, 2020,102550, ISSN 0143-7496, https://doi.org/10.1016/j.ijadhadh.2020.102550.

[8] K.L. Pickering, M.G. Aruan Efendy, T.M. Le. A review of recent developments in natural fibre composites and their mechanical performance, Composites Part A: Applied Science and Manufacturing, Volume 83, 2016, Pages 98-112, ISSN 1359-835X, https://doi.org/10.1016/j.compositesa.2015.08.038.

[9] ASTM C393/C393M-20 Standard Test Method for Core Shear Properties of Sandwich Constructions by Beam Flexure. ASTM International, 2020. (www.astm.org).

[10] MATLAB® R2022a (2022). [Computer software]. Natick, MA: The Mathworks, Inc. (www.mathworks.com).

[11] Rodrigo José da Silva, "Equations for flexural tests: three- and four-point bending", nov. 07, 2022. doi: 10.5281/zenodo.7301896.

[12] R.J. Silva. (2022). Flexural tests: a Matlab® script to calculate mechanical properties and plot bending diagrams of materials from force-displacement data measured by universal testing machines. [Computer Software]. Patent number BR 51 2022 001410-6. DOI: doi.org/10.5281/zenodo.7271867

[13] Minitab® 20 Statistical Software (2021). [Computer software]. State College, PA: Minitab, Inc. (www.minitab.com).

PRELIMINARY INVESTIGATION OF CASTOR-OIL FOAM ADHESION ON ALUMINIUM THROUGH SINGLE-LAP TESTS

Luís Felipe Cabral Diogo Nogueira[1]*; Júlio Cesar dos Santos[2]; Túlio Hallak Panzera[3]; André Luís dos Santos[4]; Alexandre Einstein Vale[5]; Rodrigo Teixeira Santos Freire[6]

(1) Master's Student. Federal University of São João Del Rei (Praça Frei Orlando, 170, Centro, São João del Rei (MG), CEP 36307- 352, Brazil)
(2) Ph.D. Federal University of São João Del Rei (Praça Frei Orlando, 170, Centro, São João del Rei (MG), CEP 36307- 352, Brazil)
(3) Associate Professor. Federal University of São João Del Rei (Praça Frei Orlando, 170, Centro, São João del Rei (MG), CEP 36307- 352, Brazil)
(4) M.Sc. Federal University of São João Del Rei (Praça Frei Orlando, 170, Centro, São João del Rei (MG), CEP 36307- 352, Brazil)
(5) M.Sc. Federal University of São João Del Rei (Praça Frei Orlando, 170, Centro, São João del Rei (MG), CEP 36307- 352, Brazil)
(6) Associate Professor. Federal University of São João Del Rei (Praça Frei Orlando, 170, Centro, São João del Rei (MG), CEP 36307- 352, Brazil)
*Luís Felipe Cabral Diogo Nogueira: lfelipecdn@gmail.com

CODE: BCCM7-76

Abstract: This work investigates the adhesion of a castor-oil-based polyurethane (PU) biofoam to aluminium surfaces. The foam was fabricated using water as the blowing agent for a PU elastomer. The apparent shear strength of single-lap joints is assessed following the ASTM standard D1002. 3D-printed moulds were developed for sample preparation. The study evaluates two different bonding strategies related to resin curing: (1) Simple Cure and (2) Co-Cure with Adhesive Layer. The Simple Curing method is conducted by expanding the PU biofoam in the mould cavity in contact with the aluminium sheets. In the second method, a layer of castor-oil PU is previously applied on the internal aluminium surfaces before pouring the PU foam admixture. The foaming process thus occurs inside the mould as in (2), with the additional co-cure of the adhesive PU layer on the aluminium sheets. This study is motivated by a subsequent study on foam-core sandwich panels, in which the best face-core bonding strategy will be used.

1. INTRODUCTION

Composite materials play a fundamental role in contemporary engineering, offering an innovative approach to achieving specific properties that would not be feasible with traditional materials. In this sense, there has been a growing adoption of composite materials in a wide variety of areas, including aeronautics, automobiles, shipbuilding, railways, construction, and sports, among others. This is due to the significant advantages offered by these materials, such as high strength, high stiffness, reduced weight, reliable performance under fatigue conditions and effective resistance to corrosion [1].

In this sense, materials scientists and engineers face a significant challenge that goes beyond the development of efficient and economical products. They are also charged with promoting technological evolution without jeopardising the availability of resources for future generations. High population growth has resulted in high production and consumption of materials, which has led to the accumulation of waste and the reduction of natural resources. As a result, considerable scientific effort has been focused on reducing environmental impact through the use of alternative materials and renewable natural resources in the supply

of high-quality industrial products [2,3]. Recent studies have focused on the use of foams as the core of sandwich panels [4-6]. Such structural composites provide improved flexural stiffness at low densities. However, the adhesive strategy used for face-core bonding is essential for their mechanical performance. The single-lap shear test is frequently used to evaluate the mechanical performance of different adhesives. This study is motivated by a subsequent study on foam-core sandwich panels, in which the best face-core bonding strategy will be used.

Ostaz et al. [7] investigated the use of high-performance pressure-sensitive adhesives and VHB™ acrylic foam tapes in 2024 T-4 aluminium joints in single-lap joint (SLJ) configurations. Static load and dynamic impact tests were carried out on the joints to compare the mechanical properties before and after environmental ageing. The results showed that the acrylic tapes had lower static load resistance compared to the pressure-sensitive adhesives but absorbed impact energy in a similar way.

Malik et al. [8] used a single-lap shear strength test to investigate the effect of adding TiO2 to castor oil-based polyurethane adhesive to improve its mechanical properties. The results showed that the addition of TiO2 significantly increased the property investigated, outperforming commercial wood-bonding adhesives.

In a similar study, Santana et al. [9] evaluated the effect of inclusions of silica microparticles or cement in the joints of glass fibre laminate composites. They used the single-lap joint test as a model to comparatively assess the interlocking effect provided by silica or cement microparticles in laminated composites. Analysis of variance (ANOVA) was carried out on the results obtained, showing that cement microparticles provide superior resistance compared to silica microparticles.

Romeu et al. [10] investigated the analysis of single-lap joints using castor-oil PU and epoxy composites reinforced with glass fibres. Computer simulations (Finite-Element Method) are used to predict the stresses and strength of the adhesive layer in single-lap joints. Experimental analyses based on ASTM standards were conducted to compare the mechanical performance of epoxy and castor-oil PU in bonded joints, highlighting the potential of castor-oil PU as a viable alternative for environmentally friendly composite materials and adhesives.

Gouveia et al. [11] studied polyurethane adhesives containing Kraft lignin. Single-lap shear tests, carried out to assess the strength of wood adhesive joints, reveal that the incorporation of Kraft lignin and hydroxypropylated lignin in polyurethane adhesives resulted in higher apparent strength.

To the best of our knowledge, the adhesion behaviour of foamed castor-oil polyurethane adhesive has not yet been investigated. Therefore, the purpose of this research project is to analyse the core-face adhesion using two different bonding strategies: (1) simple cure and (2) co-curing with an adhesive layer, with the aim of characterising the apparent shear strength and joint toughness of both experimental conditions, in order to identify the best bonding strategy to manufacture sandwich panels with aluminium faces with castor-oil polyurethane biofoam core for subsequent studies. The simple-curing method is conducted by expanding the PU biofoam in the mould cavity in contact with the aluminium sheets. In the second method, a layer of PU castor oil is pre-applied to the inner aluminium surfaces before pouring the PU foam mixture. The foaming process takes place inside the mould, as in (1), with the additional co-curing of the PU adhesive layer on the aluminium sheets.

2. METHODOLOGY

2.1. Materials

The AGT 1315 bi-component resin (isocyanate and polyol), manufactured and kindly donated by Imperveg (Brazil), was used to bond the 1200 Aluminium sheets (1 mm thickness). Distilled water is used as a blowing agent, reacting with isocyanate to produce carbon dioxide (CO_2) and form the cellular structure of the foam. Poly (lactic acid) filaments were used to print 3D moulds.

2.2. Methods

Single-lap joint samples are manufactured according to ASTM D1002 [12]. Aluminium sheets are cut to the required dimensions and washed with ordinary detergent. The surface that will be in contact with the foam is then sanded lengthways with 120-grit sandpaper and subsequently paper-cleaned. Three samples are tested for each bonding strategy.

The isocyanate (A) and polyol (B) are mixed according to the manufacturer´s recommendations, taking into account the necessary correction of the isocyanate mass fraction due to the addition of water, used as a blowing agent. Four phr of water are used (per hundred resin, relative to the polyol mass), based on a previous

work by Lacerda [13]. The A/B mass fraction was corrected to 1.2/1.0 to adjust the isocyanate index to 1. The foam expands to approximately three times its liquid volume during the curing process. In addition, a 20% loss of material over the total volume during the manufacturing process was adopted. These values were defined after preliminary manufacturing tests.

The study evaluates two different bonding strategies related to the curing of the resin: (1) Simple cure and (2) Co-cure with an adhesive layer.
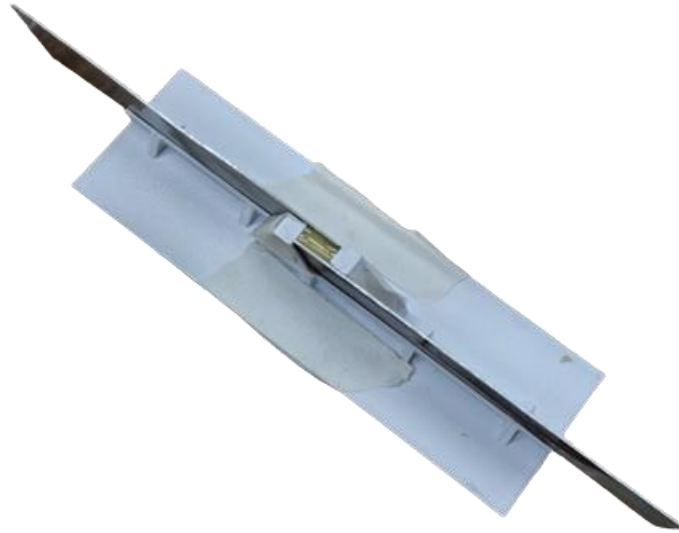
Figure 1. PLA 3D mould during the manufacture of a sample.

Samples are manufactured and stored for post-curing (15 days) in a controlled environment room at 22°C and 55% relative air humidity. The samples are then bonded to 4-mm-thick, 3-D-printed spacer blocks 24 h before testing to provide load alignment using epoxy resin (Araldite, TekBond). An additional 1-mm-thick aluminium tab is bonded on the blocks as a reinforcement and to balance frictional forces on both sides of the grip faces. The bond line is 10 mm long, and the test-grip area is 25.4 mm long. The foam adhesive bond line is 4 mm thick.

Simple-cure samples are fabricated by assembling the aluminium plates on the mould and pouring the resin into it (Figure 1). For samples fabricated with the co-cure strategy, the additional adhesive layer is obtained by applying the PU resin on the internal surface of the aluminium plates. The resin is evenly distributed by three strokes of a brush in order to apply approximately the same amount of material on the surface of the aluminium sheets in contact with the PU foam. The resin is left to stand for 50 minutes (gel time) prior to the pouring of the PU foam material. The resin used for the additional adhesive layer is prepared by mixing isocyanate and polyol according to the manufacturer´s recommendation (A/B=1.0/1.2), with no water added. The dimensions of the sample and a specimen ready for testing are illustrated in Figure (2).

(b)

(a)

3
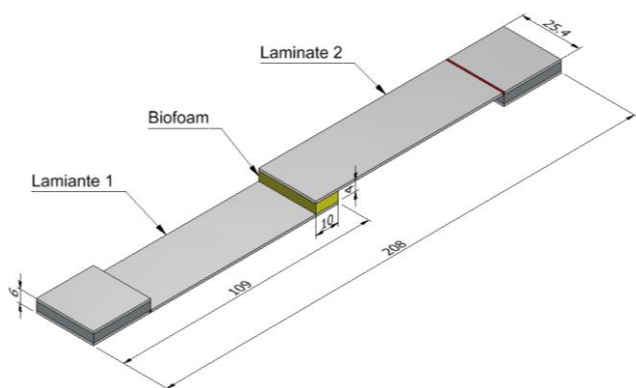
Figure 2. (a) dimensions of the sample; (b) specimen ready for testing

3. RESULTS AND DISCUSSION

Preliminary results are shown in Tables 1 and 2. The analyses revealed that the apparent shear strength (and peak force) provided by the co-cure strategy with an adhesive layer is 54% higher. The apparent shear stress is calculated considering the 10 x 25.5 mm2 bondline area. In contrast, the joint toughness for simple cure is 97% higher relative to the co-cure strategy. The joint toughness is the work exerted by the applied force to disrupt the adhesive joint, calculated as the area under the force-displacement curve. The student's t-test reveals that the peak force and apparent shear strength are significantly higher for the co-cure strategy (p-value = 0.026). In contrast, the joint toughness is significantly higher (p-value=0.033) for the simple cure strategy.

Table 1 Mechanical performance of tested single-lap joints.

Sample	Bonding Strategy	Peak Force (N)	Apparent Shear Strength (Mpa)	Joint toughness (mJ)
1.1	Simple Cure	164.08	0.64	560.13
1.2	Simple Cure	187.00	0.73	557.14
1.3	Simple Cure	222.92	0.87	711.71
2.1	Co-cure with adhesive layer	369.58	1.45	992.63
2.2	Co-cure with adhesive layer	294.07	1.15	370.83
2.3	Co-cure with adhesive layer	295.00	1.16	247.42

Table 2 Mechanical performance of tested single-lap joints: mean values.

Bonding strategy	Peak force (N)	Apparent shear strength (MPa)	Joint toughness (mJ)
Simple Cure	191 ± 30	0.75 ± 0.12	610 ± 88
Co-cure with adhesive layer	294.53 ± 0.66	1.16 ± 0.01	309 ± 87

The load-displacement behaviour of the tested samples is presented in Figure 3. It is worth noting the higher ductility and toughness of simply cured joints. The failure type displayed by all samples is cohesive, indicating an efficient surface adhesion (Figure 4). An anomalous behaviour was found for sample 2.1, for which the failure type is adhesive, and the peak force and toughness are considerably higher relative to samples 2.2 and 2.3. It is important to report that sample 2.1 has been detected as an outlier using the Weisberg t-test [14] and has not been considered for these analyses. Further investigations are being conducted to improve the statistical robustness of these preliminary findings.

4
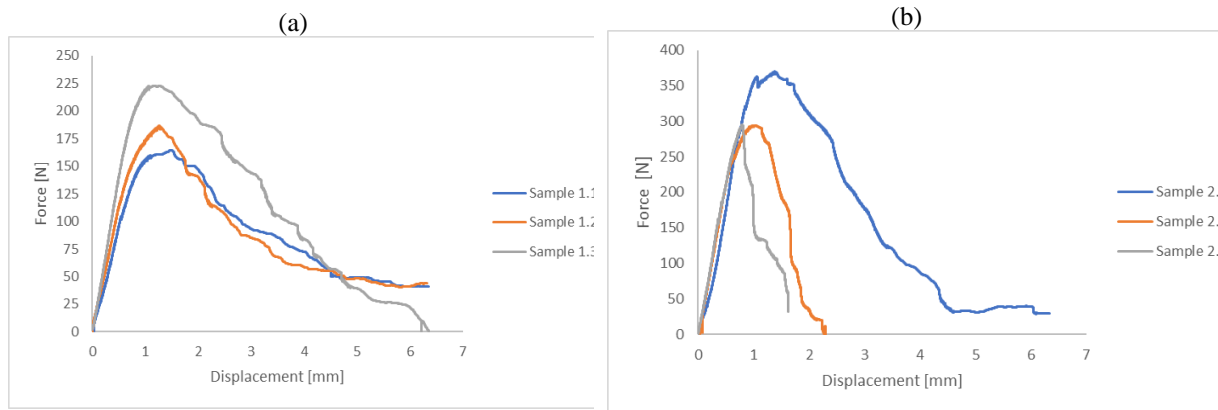
Figure 3. Behaviour of the manufactured samples in the Single-Lap test. (a) Simple Cure (b) Co-cure with adhesive layer
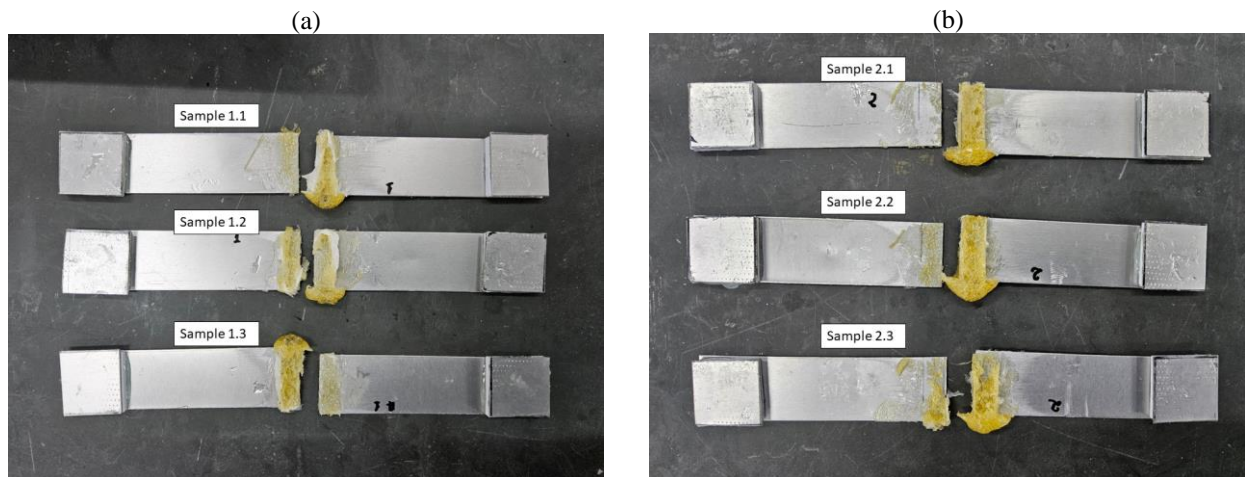
Figure 4. Type of fractures in the samples according to the adhesive strategy (a) Simple Cure (b) Co-cure with adhesive layer.

4. CONCLUSIONS

Two different bonding strategies have been evaluated using the single-lap joint test. Preliminary results indicate that the co-curing strategy with an adhesive layer provides (54%) higher apparent shear strength relative to the simple-cure strategy at the expense of a significantly lower joint toughness and fragile failure. In contrast, the energy required to tear apart simply cured adhesive joint samples is much higher (97%), indicating a ductile failure.

These results will be considered to select the most suitable bonding strategy to fabricate sandwich panels with aluminium faces and castor-oil PU foam core. Even though higher loads could, in principle, be achieved by employing the co-cure strategy, catastrophic failure should be avoided in structural composites such as sandwich panels. In view of such findings, the simple-cure strategy seems to be the best bonding strategy. Further investigation is being conducted to corroborate these conclusions.

4.1. Declaration of Competing Interest

The authors declare no conflict of interest.

4.2. Acknowledgements

5

.

5. REFERENCES

[1] DANIEL, I.M. and ISHAI, O. Engineering Mechanics of Composite Materials, Oxford University Press, 2006.

[2] ALLEN, H. G. Analysis and design of structural sandwich panels, Pergamon Press, 1969.

[3] BITZER, T. Honeycomb Technology: Materials, Design, Manufacturing, Applications and Testing, Springer, 1997.Wu, Y.; Liu, Q.; Fu, J.; Li, Q.; Hui, D.; Compos. Part B-Eng. 2017, 121, 122-133

[4] MEI, J., LIU, J., HUANG, W. Three-point bending behaviors of the foam-filled CFRP X-core sandwich panel: Experimental investigation and analytical modelling. Composite Structures, Volume 284, 2022.

[5] LI, J., YAN, Q., CAI, Z. Mechanical properties and characteristics of structural insulated panels with a novel cellulose nanofibril-based composite foam core. Journal of Sandwich Structures & Materials, 1701-1716.

[6] JUNAEDI, H., KHAN, T., SEBAEY, T. A. Characteristics of Carbon-Fiber- Reinforced Polymer Face Sheet and Glass-Fiber-Reinforced Rigid Polyurethane Foam Sandwich Structures under Flexural and Compression Tests. Materials 2023, 16, 5101.

[7] AL-OSTAZ, A., MANTENA, P. R., ANAKAPALLII, M., Hwang, S. J. Evaluation of high-performance pressure-sensitive adhesives and VHB™ acrylic foam tapes bonded aluminum joints subjected to environmental aging. Journal of Adhesion Science and Technology, 21(3-4), 339-361.

[8] MALIK, M., & KAUR, R. Mechanical and Thermal Properties of Castor Oil–Based Polyurethane Adhesive: Effect of TiO2 Filler. Advances in Polymer Technology, 37, 21637. DOI: 10.1002/adv.21637

[9] SANTANA, P.R.T., PANZERA, T.H., FREIRA, R.T.S., & CHRISTOFORO, A.L. Apparent shear strength of hybrid glass fibre reinforced composite joints. Polymer Testing, ISSN 0142-9418

[10] DA COSTA, R. R. C., DE MEDEIROS, R., RIBEIRO, M. L., & Tita, V. Experimental and numerical analysis of single lap bonded joints: Epoxy and castor oil PU-glass fibre composites. *The Journal of Adhesion*, *93*(1–2), 77–94.

[11] GOUVEIA, J. R., Leonardo D. ANTONINO L. D., Guilherme E. S. GARCIA G.E.S., Lara Basílio TAVARES L.B., Amanda N. B. SANTOS, A.N.B., dos SANTOS, D.J. Kraft lignin-containing polyurethane adhesives: the role of hydroxypropylation on thermomechanical properties, The Journal of Adhesion, 97:15, 1423-1439.

[12] ASTM D1002-10, 'Standard Test Method for Apparent Shear Strength of Single-Lap-Joint Adhesively Bonded Metal Specimens by Tension Loading (Metal-to-Metal)', ASTM International,

[13] LACERDA, Alexandre Silva. Investigation of the mechanical properties of castor-oil polyurethane foams and their reinforcement with cellulose microfibrils. Master's thesis (Mechanical Engineering) – Federal University of São João del-Rei, São João del-Rei, 2024.

[14] R. J. SEELY, L. MUNYAKAZI, J. HAURY, H. SIMMERMAN, W. H. RUSHING e T. F. CURRY, "Demonstrating the Consistency of Small Data Sets," BioPharm International, pp. 36-58, 2003.

6

ECO-FRIENDLY SANDWICH PANELS MADE OF BAMBOO-ARCH CORE, ALUMINIUM SKINS, AND BIO-BASED ADHESIVE: A PRELIMINARY INVESTIGATION

Vanessa Melo Gomes[(a)*], Sofia Dehaini Garcia[(b)], Rodrigo José da Silva[(c)], Carlos Thomas[(d)], Tulio Hallak Panzera[(e)]

(a) 0009-0009-4833-6172 (Federal University of São João del Rei - Brazil)
(b) 0000-0002-8316-0012 (Federal University of São João del Rei - Brazil)
(c) 0000-0001-8016-3165 (Federal University of São João del Rei - Brazil)
(d) 0000-0002-2641-9411 (University of Cantabria - Spain)
(e) 0000-0001-7091-456X (Federal University of São João del Rei - Brazil)

* Corresponding author: vanessamelogomes@hotmail.com

Abstract: This study investigates the fabrication and testing of sandwich panels composed of aluminium faces and bamboo-based cores with semicylindrical shapes. Two core configurations are explored: unidirectional and alternated alignment of the semicylinders. A biobased adhesive derived from castor oil is used for bonding the skins to the core. The panels are characterised via a three-point bending test to statistically compare their ultimate mean stress. Results demonstrate significant potential for combining sustainability with effective mechanical performance across the proposed sandwich structures. The panels exhibit a load capacity of up to 6 kN under three-point bending, with the alternated core configuration enhancing flexural strength by up to 9% compared to the unidirectional architecture.

1. INTRODUCTION

Lightweight structures, such as sandwich panels, have become increasingly common across various sectors that demand high performance, such as aerospace, automotive, civil construction, and naval industries. These panels typically comprise two thin faces (also denoted as skin or facesheets) of material with high rigidity and resistance, enclosing a thick low-density material core [1-4]. The faces are usually made of metals such as aluminium or steel, fibre-reinforced laminated composites or particles, plywood, or similar materials. The core can consist of polymeric and metallic foams, natural materials, and concrete, among others [5]. The core can be designed in various geometries, including honeycomb structures, corrugated plates, foams, and lattices [6-10].

The mechanical performance of sandwich panels greatly depends on the adhesive's ability to transfer loads between the faces and core. Controlling the quantity of adhesive and applying surface treatments, especially on metallic surfaces, is crucial to enhance structural rigidity. Therefore, the selection of adhesive significantly influences the performance of the sandwich structure. Biobased adhesives present an eco-friendly option, offering reduced or nearly negligible environmental impact and satisfactory interaction between the faces and the core [11,12].

The global pursuit of sustainable materials has intensified as the focus shifts towards minimising environmental impacts. The integration of ecodesign principles and the circular economy, rooted in economic viability, has gained traction and is gradually influencing everyday research activities [13]. Within this eco-friendly framework, bamboo has re-emerged as a promising material for composite development, boasting

inherent qualities such as renewability, biodegradability, low treatment cost, rapid growth, and very low density. Abundant in tropical and subtropical regions, bamboo features a circular cross-section with unidirectional fibres enveloped in a lignin matrix [14,15]. Recent research has delved into bamboo's potential as a core material in sandwich panels, revealing promising results in structural applications. These studies underscore bamboo's potential to enhance flexural capacity and meet structural demands [16-18].

This study investigates sandwich panels composed of aluminium faces and bamboo-based cores, using bamboo culms cut across the median plane parallel to the longitudinal direction to create gutter-like semicylindrical geometries. Two core configurations are proposed: one with aligned semicylinders (unidirectional) and the other with alternating semicylinders. The bonding of faces to the core is achieved using a castor-oil biobased adhesive. As an initial evaluation, this research statistically compares the panels' ultimate mean stress under a three-point bending load.

2. METHODOLOGY

Sandwich structures consist of two identical faces made of an aluminium alloy with a thickness of 0.65 mm (ISO 2024 - T3) and bamboo semicylinders as the core. The bamboo is collected from the green areas at the Federal University of São João del-Rei (UFSJ - Santo Antônio Campus, 21°08'27"S 44°15'40" W) (Fig. 1a). Previous studies [13,17] have utilised bamboo rings with a diameter of approximately 30 mm as a core material, achieving improved mechanical performance. In this sense, bamboo with diameters of Ø35 mm and Ø30 mm are gathered. The bamboo is treated with a boric acid solution (3% mass/volume percentage) and copper sulfate (1% mass/volume percentage) [19]. The faces-to-core adhesive system comprises a polyurethane-based polymer derived from castor oil, with a density of 0.88 g/cm³, supplied by Imperveg® (Brazil).
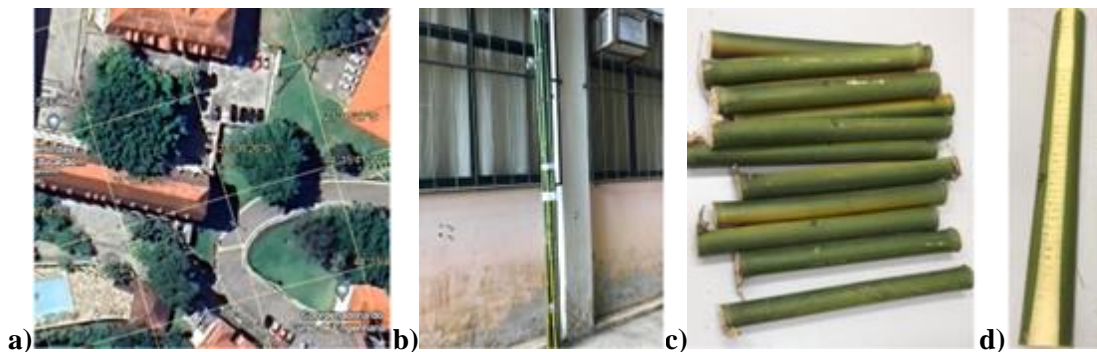
Figure 1. a) Location of the area where bamboo culms are sourced. b) Primary drying of the culms. c) Bamboo culms cut into sections. d) Culms after the upper surface has been smoothed.

The bamboo culms are pre-selected as the desired diameter and, after harvest, left in a vertical position for 14 days to allow the starch in the stalks to deplete [17]. This drying process occurs in an open environment with ample natural ventilation, away from direct sunlight (Fig. 1b). After this initial drying period, the culms are cut into semicylinders with the nodes removed, and their upper parts are smoothed (Fig. 1c,d). A secondary selection is performed to discard semicylinders with diameters below the desired and stipulated size. The semicylinders are immersed in a solution prepared with 3% boric acid (insecticide) and 1% copper sulfate (fungicide) for the preventive treatment of potential biological damage, thereby increasing the longevity of the fabricated components (Fig. 2a) [19]. After being completely submerged for seven days, the semicylinders are placed in an oven at 50°C for three days to dry them. Subsequently, to prevent potential cracks resulting from the high-temperature process, it is deemed necessary to naturally extend the drying time. Therefore, the semicylinders are once again positioned vertically position in a controlled environment (23°C and 55% humidity) for an additional four months (Fig. 2b). During this period, regular visual inspections are conducted to monitor and prevent any further issues. The semicylinders are repositioned in the drying row at least once a week to ensure proper air circulation across all samples.

All faces used in this study are cut from a single aluminium plate to ensure uniform mechanical properties. The dimensions of each face are 105 mm x 285 mm2. After cutting, the faces are cleaned with neutral soap, followed by a manual abrasive sanding process to create small scratches, enhancing adhesion. Subsequently, the faces are thoroughly rinsed with running water, dried, and stored until the day of panel assembly (Fig. 2c).
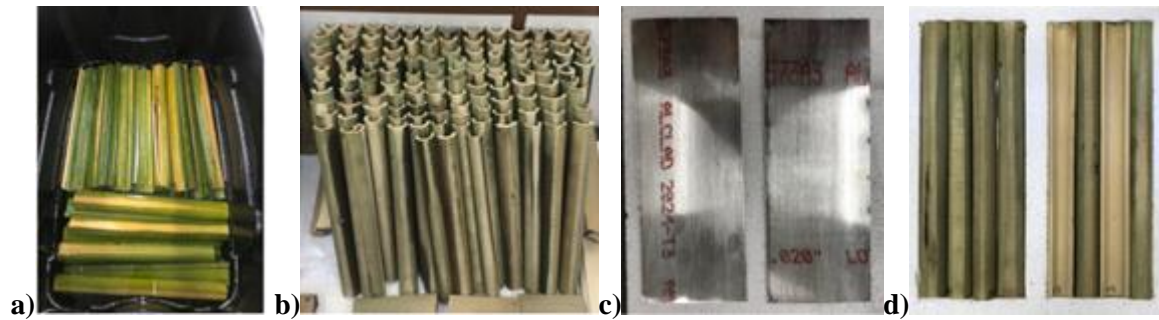
Figure 2. a) Bamboo treatment process. b) Semicylinders arranged for final drying. c) Aluminium faces after abrasive treatment. d) Core assembly process.

A polystyrene sheet is cut and prepared with plastic film and release wax to serve as a containment for applying liquid resin over the faces and then assembling the core by positioning the bamboo semicylinders over the adhesive. The assembly sequence of the two proposed conditions for the core arrangement (unidirectional and alternated) is illustrated in Fig. 2d. The biobased resin is applied to one of the faces and the semicylinders are positioned under the resin. A wooden plate with a load of 50 N is used to ensure evenly distributed pressure over the bamboo while the resin is drying. After 24 hours, the process is repeated for the second face. Subsequently, the panels are placed in a controlled environment (23°C and 55% humidity) for 14 days to ensure complete curing of the polymer system. The total thickness of the panels is about 16 mm.

Three-point bending tests are conducted on the panels with unidirectional and alternated semicylinders (6 specimens of each assembly model). The tests are performed using an INSTRON testing machine equipped with a 50 kN load cell, with a support span of 210 mm and a cross-head speed of 5 mm/min, following the recommendations of the ASTM standard C393 [20]. Force displacement curves are obtained, and the mean stress value (flexural strength) is estimated using the homogenisation concept, as reported by Silva et al. [21, 22]. Statistical comparison is performed through the Minitab® software.

3. RESULTS AND DISCUSSION

The statistical analysis of the ultimate mean stress (flexural strength) comparing the panels with unidirectional and alternated core architecture is presented in Table 1. The data dispersion is minimal, with a coefficient of variation of 7% and 9%. Figure 4 illustrates the typical curves obtained under three-point loading from two perspectives: (a) force-displacement and (b) mean stress-strain. The proposed panels demonstrate a load capacity of up to 6 kN. The Anderson-Darling P-values greater than 0.05 indicate that the data follow a normal distribution for both configurations (Unidirectional and Alternated), and the F test P-value greater than 0.05 provides evidence that both data have equal variances. Consequently, the Two-sample T-test can be applied for comparison, with the P-value greater than 0.05 indicating that the two configurations differ from each other. Notably, alternating the semicylinders in the core promotes an increase of approximately 9% in the flexural strength (65.9 MPa compared to 60.3 MPa).

Table 1. Statistical assessment of the flexural strength.

	Core configuration	
	Unidirectional	*Alternated*
Ultimate mean stress	60.3 ± 4.4 MPa	65.9 ± 5.7 MPa
Coeficient of variation	7%	9%
Anderson-Darling P-value	0.599	0.712
F test P-value	0.653	
Two-sample T-test P-value	0.106	
Estimated difference	5.6 MPa → Alternated architecture has about 9% more flexural strength	
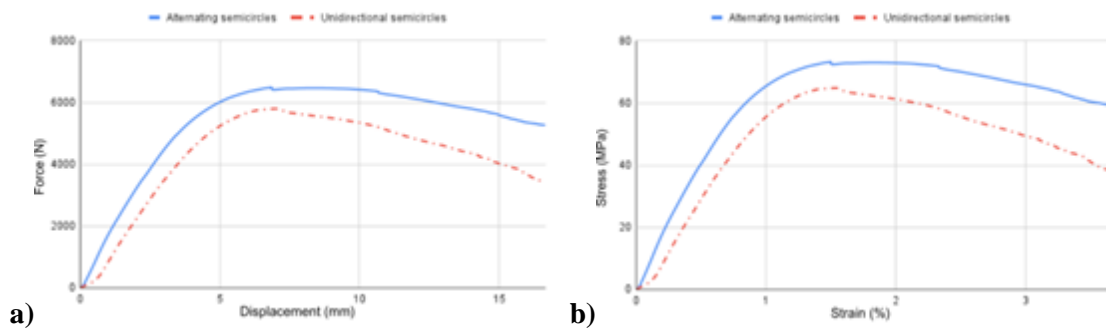
Figure 4. Three-point bending curves: (a) force-displacement. (b) mean stress-strain.

4. CONCLUSIONS

In addition to their sustainability feature, the sandwich panels demonstrated high mechanical performance, boasting a flexural load capacity of up to 6 kN. The use of an alternated core architecture resulted in a 9% increase in flexural strength compared to the unidirectional bamboo configuration. Future investigations will center on exploring the failure mode across both architectures, in addition to examining properties such as rigidity, resilience, core shear modulus, and facing stress. These further evaluations will be based on the ASTM standards and the RJS Method for mechanical assessment of sandwich structures [21,22].

4.1. Declaration of Competing Interest

The authors declare no conflict of interest.

4.2. Acknowledgements

5. REFERENCES

[1] Gibson LJ, Ashby MF. Cellular Solids: Structure and Properties, seconded, Cambridge Univ. Press, Cambridge, 2001.
[2] Ha NS, Lu GX. A review of recent research on bio-inspired structures and materials for energy absorption applications. Compos Part B-Eng 2020;181:38.
[3] Jiang MY, Shijie L, Xiao JM. Research on lightweight laminate for car bodies with excellent cushioning and energy absorption characteristics. Heliyon 2022;8:8.
[4] Oliveira PR, May M, Panzera TH, Hiermaier S. Bio-based/green sandwich structures: A review. Thin-Walled Struct 2022;177:19.
[5] Wang Z, Li Z, Xiong W. Experimental investigation on bending behavior of honeycomb sandwich panel with ceramic tile face-sheet. Compos Part B. 2019;164:280-6. http://dx.doi.org/10.1016/j.compositesb.2018.10.077.
[6]Cai Z-Y, Zhang X, Liang X-B. Multi-point forming of sandwich panels with egg-box-like cores and failure behaviors in the forming process: analytical models, numerical and experimental investigations. Mater Des. 2018;160:1029-41. http://dx.doi.org/10.1016/j.matdes.2018.10.037.
[7] D'Mello RJ, Waas AM. Synergistic energy absorption in the axial crush response of filled circular cell honeycombs. Compos Struct. 2012;94:1669-76. http://dx.doi.org/10.1016/j.compstruct.2011.12.009
[8] Feng Y, Qiu H, Gao Y, Zheng H, Tan J. Creative design for sandwich structures: a review. Inter J Adv Robot Syst. 2020:124. http://dx.doi.org/10.1177/1729881420921327.
[9] Huang J, Gong X, Zhang Q, Scarpa F, Liu Y, Leng J. In-plane mechanics of a novel zero Poisson's ratio honeycomb core. Compos, Part B Eng. 2016;89:67-76. http://dx.doi.org/10.1016/j.compositesb.2015.11.032.
[10] Huang J, Zhang Q, Scarpa F, Liu Y, Leng J. In-plane elasticity of a novel auxetic honeycomb design. Compos, Part B Eng.2018;110:72-82. http://dx.doi.org/10.1016/j.compositesb.2016.11.011.
[11] Heinrich LA (2019) Future opportunities for bio-based adhesives – advantages beyond renewability. Green Chem 21(8):1866–1888. https://doi.org/10.1039/c8gc03746a
[12] Oliveira PR, Panzera TH, Freire RT, Scarpa F. Sustainable sandwich structures made from bottle caps core and aluminium skins: a statistical approach. Thin-Wall Struct. 2018;130:362- 71. http://dx.doi.org/10.1016/j.tws.2018.06.003.

[13] Napolitano F, Santos JC, Silva RJ, Braga GG, Freire RTS, Panzera TH. Sandwich panels made of aluminium skins and gapped bamboo ring core. Journal of the Brazilian Society of Mechanical Sciences and Engineering (2023) 45:250 https://doi.org/10.1007/s40430-023-04140-x.

[14] Lo TY, Cui HZ, Tang PWC, Leung HC. Strength analysis of bamboo by microscopic investigation of bamboo fibre. Constr Build Mater. 2008;22:1532-5. http://dx.doi.org/10.1016/j.conbuildmat.2007.03.031.

[15] Saikia P, Dutta D, Kalita D, Bora JJ, Goswami T. Improvement of mechano-chemical properties of bamboo by biochemical treatment. Constr Build Mater. 2015;101:1031-6. http://dx.doi.org/10.1016/j.conbuildmat.2015.10.106.

[16] Alsubari S, Zuhri MYM, Sapuan SM, Ishak MR, Ilyas RA, Asyraf MRM. Potential of Natural Fiber Reinforced Polymer Composites in Sandwich Structures: A Review on Its Mechanical Properties. Polymers 2021;13:20.

[17] Oliveira LA, Tonatto MLP, Coura GLC, Freire RTS, Panzera TH, Scarpa F (2021). Experimental and numerical assessment of sustainable bamboo core sandwich panels under low-velocity impact. Constr Build Mater 292:123437. https://doi.org/10.1016/j.conbuildmat.2021.123437.

[18] Oliveira PR, Bonaccorsi AMS, Panzera TH, Christoforo AL, Scarpa F (2017) Sustainable sandwich composite structures made from aluminium sheets and disposed bottle caps. Thin Wall Struct 120:38–45. https://doi.org/10.1016/j.tws.2017.08.013.

[19] Sahu S, Choudhary AS, Raj S, Ghode N, Kumar A. Effect of micronutrients on yield attributes of tomato. International Journal of Agriculture and Nutrition 2022; 4(1): 34-38.

[20] ASTM (2022) Standard Test Method for Core Shear Properties of Sandwich Constructions by Beam Flexure (C393), ASTM International, West Conshohocken/USA.

[21] R. J. da Silva et al., "A core rigidity classifier method and a novel approach to account for geometric effects on the elastic properties of sandwich structures," Composite Structures, vol. 282, p. 115075, Feb. 2022, doi: https://doi.org/10.1016/j.compstruct.2021.115075.

[22] R. J. da Silva et al., "Enhanced core rigidity classifier method (RJS 2.0): a comprehensive approach to properly measure elastic properties of sandwich structures," Composite Structures, pp. 117981–117981, Feb. 2024, doi: https://doi.org/10.1016/j.compstruct.2024.117981.

A SEMI-ANALYTICAL MODEL FOR STABILITY ANALYSES OF COMPOSITE CYLINDERS ACCOUNTING FOR LOADING AND GEOMETRICAL IMPERFECTIONS EFFECTS

P. R. Santos[(a),*], M.V. Donadon [(b)] M.A. Arbelo [(c)]

(a) 0000-0003-0461-6999 (Aeronautics Institute of Technology– Brazil)
(b) 0000-0001-9016-5340 (Aeronautics Institute of Technology – Brazil)
(c) 0000-0001-5541-6773 (Aeronautics Institute of Technology – Brazil)
* Corresponding author: plinioricardodossantos@gmail.com

Abstract: In the aerospace industry, composite cylindrical shells are widely used in the design of lightweight and efficient aerospace launch vehicle (LV) structures. The development of accurate methodologies, for structural analysis of composite cylindrical shells, requires accounting for asymmetric load distribution and geometric imperfections, related to the manufacturing process. In this work, a semi-analytical model, based on the Ritz method, is proposed to evaluate the axial critical buckling load of composite cylindrical shells under initial geometric and loading imperfections. The Ritz method is based on the total potential energy and a series of functions approximates the displacement field. Usually, the approximation functions are chosen in order to meet the geometric boundary conditions. In the present work, Fourier trigonometric series in terms of sines and cosines have been used to describe the displacement field. Elastic constraints have been incorporated into the formulation in order to impose different boundary conditions along the loaded edges, allowing modeling of simply supported and fully clamped boundary conditions. The Fourier series is also employed to incorporate the loading and geometric imperfections signature from real cylinders. Simulations were performed for unidirectional tape carbon/epoxy composite cylinders, and the results are compared with numerical predictions obtained using the Abaqus Finite Element (FE) commercial software and experimental results. A fairly good agreement between predictions obtained from the proposed semi-analytical model, FE, and experimental results was found.

1. INTRODUCTION

Composite cylindrical shells have many applications, such as ducts for gas and liquid transportation, poles for transmissions and distribution lines, pressure vessels, aircraft fuselage, and aerospace launch vehicles. In these types of structures, composite usage has great advantages, such as corrosion prevention, fatigue improvements, and weight reduction. However, to reach these advantages, it is important to have analysis tools that take into account failure phenomena for composite structures. Other important considerations are the variabilities, such as those generated during the manufacturing process, that can affect considerably the structure load-carrying capability.

When in compression, thin-walled cylindrical shells are subjected to structural instability, which can drive considerably the design. In this aspect, the instability analysis can be performed by different methods. The Finite Element Method (FEM) is a common technique as it is widely used in the commercial software, such as Abaqus [1]. Rudd et al [2] developed and validated a finite element modeling methodology for designing

and analyzing composite launch-vehicle shell structures to predict buckling behavior. The model results were compared with experimental results and showed to produce accurate predictions for the buckling load and stiffness. Degenhardt et al [3] performed buckling tests and buckling simulations for composite cylinders to investigate the imperfection sensitivity and validate the applied simulation methodologies. Improved knock-down factors (the ratio of buckling loads of imperfect and perfect structures) were deduced and discussed. Priyadarsini, Kalyanaraman, and Srinivasan [4] reported a numerical and experimental study on carbon fiber-reinforced plastic (CFRP) cylinders under axial compression. Static and dynamic axial compression were considered. Measured imperfections were used in the FEM dynamic analysis. Results showed that the ultimate load is affected by the loading method and the geometric imperfections.

Many works based on energy methods can be found in the literature. In this case, the Ritz method is a good alternative. Based on the variational principles, the method applies specific approximation functions, like polynomial or trigonometric functions. This method can also be associated with the meshless methods [5]. Castro et al. [6] proposed a semi-analytical approach based on the Ritz method to solve cylinders and cones under different load cases using the classical laminate plate theory. The study showed good results compared to results from FEM. Santos and Donadon [7] investigated composite cylinders under axial loading (buckling) and internal pressurization. The results were compared with FEM and results from the literature. Cross-ply laminates showed better results when compared with angle-ply laminates. Only one term in the Fourier series was considered in the set of trigonometric functions, used to approximate the results. Furthermore, the work did not consider imperfections.

In this work, a semi-analytical approach based on the Ritz method is proposed in order to solve the instability problems of composite cylinders. The formulation considers the Reissner-Mindlin hypothesis in the strain-displacement relationships. Non-uniform loading and geometric imperfections are also studied in this paper. Three different composite cylinders were used in the study. The first one is referred to as Z11, obtained from Geier and Singh [8]. Simulation for a perfect cylinder was performed and results were compared with FEM. This study was important in order to validate the model, mainly related to cylinders with diagonal buckling modes. The second cylinder was R16, obtained from references [9] and [10]. This cylinder has geometric imperfections data available in the literature, therefore it was used in this study. The third cylinder was manufactured as part of this work at the Aeronautics Institute of Technology (ITA). The manufacturing method employed was the Vacuum Assisted Resin Transfer Molding (VARTM). Numerical results for buckling are compared with FEM and experiment results conducted by the authors of this paper.

2. FORMULATION

Figure 2 represents the cylinder model, where R is the cylinder radius; ϕ is the angle between the fibers and longitudinal cylinder direction; N_z is the axial distributed load; u, v, w, β_θ, β_z represent the displacement field and rotations; $\vec{r}$ is a position vector; and θ and z are the curvilinear coordinate system. Linear and torsional springs represent the elastic constraints in order to impose different boundary conditions, allowing modeling of simply supported, fully clamped, and conditions with real stiffness. The plies stacking sequence considers the first ply in contact with the mold and so forth.
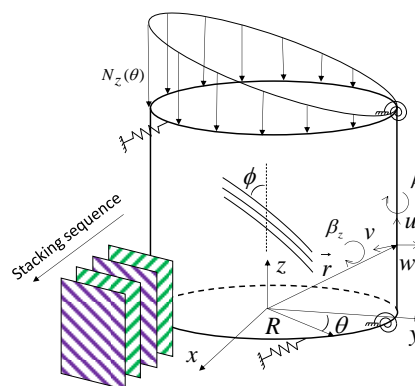
Figure 1. Cylinder representation. Elaborated by the authors.

2.1. Linear Buckling Model Accounting for Loading Imperfection

In this work, the strain-displacement relations for shells consider the Reissner-Mindlin hypothesis, i.e. straight lines normal to the undeformed middle surface remain straight but not necessarily normal to the middle surface after deformation due to the transverse shear consideration. The strain-displacement relations are taken from reference [11] and presented in a matrix form, as follows,

$$
\begin{Bmatrix} \varepsilon_z^m \\ \varepsilon_\theta^m \\ \gamma_{z\theta}^m \\ k_z \\ k_\theta \\ k_{z\theta} \\ \gamma_{zn} \\ \gamma_{\theta n} \end{Bmatrix} =
\begin{bmatrix}
\dfrac{\partial}{\partial z} & 0 & 0 & 0 & 0 \\
0 & \dfrac{1}{R}\dfrac{\partial}{\partial \theta} & \dfrac{1}{R} & 0 & 0 \\
\dfrac{1}{R}\dfrac{\partial}{\partial \theta} & \dfrac{\partial}{\partial z} & 0 & 0 & 0 \\
0 & 0 & 0 & \dfrac{\partial}{\partial z} & 0 \\
0 & 0 & 0 & 0 & \dfrac{1}{R}\dfrac{\partial}{\partial \theta} \\
0 & 0 & 0 & \dfrac{1}{R}\dfrac{\partial}{\partial \theta} & \dfrac{\partial}{\partial z} \\
0 & 0 & \dfrac{\partial}{\partial z} & 1 & 0 \\
0 & -\dfrac{1}{R} & \dfrac{1}{R}\dfrac{\partial}{\partial \theta} & 0 & 1
\end{bmatrix}
\begin{Bmatrix} u \\ v \\ w \\ \beta_z \\ \beta_\theta \end{Bmatrix}
\tag{1}
$$

In order to improve results and obtain a good agreement for the buckling loads and modes, mainly related to cases with diagonal modes, a Fourier trigonometric series $f(z,\theta)$ with two terms is considered in the displacement field approximation u, v, w, and in the rotations β_z and β_θ, as follows

$$
f(z,\theta) = \sum_{i=1}^{n}\sum_{j=1}^{m} q_{ij}^a \sin\left(\frac{i\pi z}{L}\right)\sin(j\theta) + q_{ij}^b \sin\left(\frac{i\pi z}{L}\right)\cos(j\theta)
\tag{2}
$$

Here, m and n are the number of terms used in the summation; q_{ij} are the Ritz coefficients; and L is the cylinder length. Note that approximation functions need to satisfy the geometric boundary conditions; ensure the minimum completeness, be continuous (as required in the variational methods), and be linearly independent [12]. This series can be represented in a matrix form as

$$
f(z,\theta) = \begin{bmatrix} [N_a] & [N_b] \end{bmatrix} \begin{Bmatrix} \{q_a\} \\ \{q_b\} \end{Bmatrix} = [N]\{q\}
\tag{3}
$$

Where $[N_a]$ and $[N_b]$ contains the approximation functions related to the first and second terms of the Fourier series, respectively, and $\{q_a\}$ and $\{q_b\}$ are the Ritz coefficients, related to each term, to be found later. The $f(z,\theta)$ derivatives are represented by taking the derivatives of the approximation functions $[N(z,\theta)]$.

Using Equation (3) in the strain-displacement relations to approximate the displacement field, rotations, and its derivatives, the strain-displacement components are written in a matrix form, as shown the Equation (4). The matrix form has good advantages in improving computational efficiency.

$$
\begin{Bmatrix} \varepsilon_z^m \\ \varepsilon_\theta^m \\ \gamma_{z\theta}^m \\ k_z \\ k_\theta \\ k_{z\theta} \\ \gamma_{zn} \\ \gamma_{\theta n} \end{Bmatrix} =
\begin{bmatrix}
[N_{u,z}] & [0] & [0] & [0] & [0] \\
[0] & \left[\dfrac{N_{v,\theta}}{R}\right] & \left[\dfrac{N_w}{R}\right] & [0] & [0] \\
\left[\dfrac{N_{u,\theta}}{R}\right] & [N_{v,z}] & [0] & [0] & [0] \\
[0] & [0] & [0] & [N_{\beta z,z}] & [0] \\
[0] & [0] & [0] & [0] & \left[\dfrac{N_{\beta\theta,\theta}}{R}\right] \\
[0] & [0] & [0] & \left[\dfrac{N_{\beta z,\theta}}{R}\right] & [N_{\beta\theta,z}] \\
[0] & [0] & [N_{w,z}] & [N_{\beta z}] & [0] \\
[0] & -\dfrac{[N_v]}{R} & \dfrac{[N_{w,\theta}]}{R} & [0] & [N_{\beta\theta}]
\end{bmatrix}
\begin{Bmatrix} \{q_u\} \\ \{q_v\} \\ \{q_w\} \\ \{q_{\beta z}\} \\ \{q_{\beta\theta}\} \end{Bmatrix}
\tag{4}
$$

The total potential energy is given by

$$
\pi_p = U + V = U - W \tag{5}
$$

Where U and W are the strain energy and the work done by the external forces, respectively, and V is the potential of external forces. U is given by

$$
U = \frac{1}{2}\int_S \begin{Bmatrix} \{\varepsilon_0\} \\ \{\kappa\} \\ \{\gamma_s\} \end{Bmatrix}^T \begin{bmatrix} [A] & [B] & [0] \\ [B] & [D] & [0] \\ [0] & [0] & [A_s] \end{bmatrix} \begin{Bmatrix} \{\varepsilon_0\} \\ \{\kappa\} \\ \{\gamma_s\} \end{Bmatrix} dS = \frac{1}{2}\int_S \{e\}^T [C]\{e\} dS \tag{6}
$$

Where $\{e\}$ is a vector containing the strains and $[C]$ is a matrix containing the laminate stiffness $[A], [B], [D]$ and $[A_s]$ and S is the cylinder area. To calculate the potential of the external loads, the Von-Karman non-linear strain-displacement relationship is considered [13] as shown the Equation (7).

$$
V = -\frac{1}{2}\int_S \left[N_z \left(\frac{\partial w}{\partial z}\right)^2 \right] dS \tag{7}
$$

By replacing the strain energy and the potential of the external forces in Equation (5), and taking the variational form, it is obtained

$$
\delta\pi = \{\delta q\}^T \left\{ \int_S [H]^T [C^*][H] dS + \int_S N_z \{q\}^T [H^*]^T [H^*] dS \right\} \{q\} = 0 \tag{8}
$$

Where $[H]$ is a matrix containing the approximation functions and their derivatives, after applying the variational form. Since $\{\delta q\}$ is arbitrary, the following eigenproblem is obtained,

$$
\{[K] + N_{cr_z}[K_{Gz}]\}\{q\} = \{0\} \tag{9}
$$

Here, N_{cr_z} is the buckling load (eigenvalue), $[K]$ is the stiffness matrix, and $[K_{Gz}]$ is the geometric stiffness matrix, given by

$$
[K] = \int_S [H]^T [C^*][H]\{q\} dS = \int_0^{2\pi}\int_0^L [H]^T [C^*][H]\{q\}\, dz\, R d\theta \tag{10}
$$

$$
[K_{Gz}] = \int_S N_z(\theta)[H^*]^T [H^*] dS = \int_0^{2\pi}\int_0^L N_z(\theta)[H^*]^T [H^*]\, dz\, R d\theta \tag{11}
$$

Note that load distribution $N_z(\theta)$ is integrated in order to consider any load distribution.

2.2. Geometric Imperfection

To include the geometric imperfection in the Ritz formulation, a variable $w_0(\theta, z)$ is introduced to represent the imperfection, which is measured from the perfect cylinder, as shown in Figure 2. The cylinder's displacement w is measured taking as a reference the imperfect and undeformed surface.
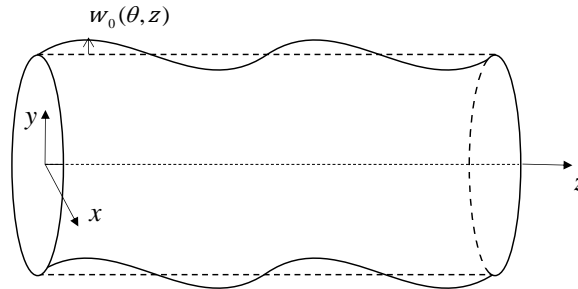
Figure 2. Representation of an imperfect cylinder. Elaborated by the author.

Then, the imperfection term is included in the non-linear kinematics relations deduction. Those relations are taken from Donnell and Sanders's theories according to references [14], [15] and [16]. In order to obtain the total potential energy, the strain energy in the longitudinal direction is given as

$$\varepsilon_1^m = \frac{\partial u}{\partial z} + \frac{1}{2}\left(\frac{\partial w}{\partial z}\right)^2 + \frac{\partial w}{\partial z}\frac{\partial w_0}{\partial z} \tag{12}$$

By neglecting the longitudinal membrane strain [17] i.e., $\varepsilon_1^m = 0$, the term $\dfrac{\partial u}{\partial z}$ is used in the work done by the external forces and the total potential energy can be written as

$$V = -\frac{1}{2}\int_S N_z \left\{\frac{1}{2}\left(\frac{\partial w}{\partial z}\right)^2 + \frac{\partial w}{\partial z}\frac{\partial w_0}{\partial z}\right\} dS \tag{13}$$

Replacing the terms of the strain energy and the potential of the external loads in Equation (5) (total potential energy) and writing in the variational form,

$$\int_S \{\delta q\}^T [H]^T \left[C^*\right][H]\{q\}\, dS - \int_S N_z \{\delta q\}^T \left\{\left[H^*\right]^T \left[H^*\right]\{q\} + \frac{1}{2}\left[H^*\right]^T \left[H_0^*\right]\{q_0\}\right\} dS = 0 \tag{14}$$

Where $\left[H^*\right]$ and $\left[H_0^*\right]$ are matrices containing the approximation functions and their derivatives related to the potential of the external energy and geometric imperfections, respectively. Finally, the Ritz vector coefficients are obtained as follows

$$\{q\} = N_z \left[[K] - N_z \left[K^*\right]\right]^{-1}\left[K_0^*\right] \tag{15}$$

Where,

$$\left[K^*\right] = \int_S \left[H^*\right]^T \left[H^*\right] dS$$

$$\left[K_0^*\right] = \frac{1}{2}\int_S \left[H^*\right]^T \left[H_0^*\right]\{q_0\}\, dS$$

The vector $\{q_0\}$ represents the imperfections coefficients. Geometric imperfections obtained in cylinders can be approximated by using the Fourier series, referred to as Half-cosine, represented by

$$w_0 = \sum_{i=0}^{n} \sum_{j=0}^{m} A_{ij} \cos\left(\frac{i\pi z}{L}\right) \sin(j\theta) + B_{ij} \cos\left(\frac{i\pi z}{L}\right) \cos(j\theta) \tag{16}$$

Here, A_{ij} and B_{ij} are amplitudes of the base functions. Expanding the last equation and using the vector form, the imperfection interpolation is rewritten as

$$w_0 = [N_0]\{q_0\} \tag{17}$$

Where $[N_0]$ is a vector containing the base functions. To find the coefficients $\{q_0\}$, a system of linear equations is solved using the Least Square Method. Note that the total distance from the perfect cylinder after deformations is $w_T = w_0 + w$.

3. NUMERICAL SIMULATIONS

Table 1 shows the mechanical and geometrical properties of the cylinders. The first case consists of a linear buckling for a uniform axial loading for cylinder Z11. Figure 3 shows the convergence for the buckling loads and buckling modes using Abaqus, where the element S8R was used, which consists of an eight-node element, with reduced integration [1]. The results are considered converged by using a number of elements greater than 3200. Figure 4 shows the convergence for buckling loads and buckling modes using the Ritz method.

Numerical simulations were performed with high spring stiffness at the edges in the order of 10^8 in order to simulate a fully clamped condition. The model showed a good convergence for m, n greater than 20.

Tabela 1. Mechanical and geometrical properties for composite cylinders used in the simulations

Cylinder	E_1 (MPa)	E_2 (MPa)	v_{12}	G_{12} (MPa)	G_{13} (MPa)	G_{23} (MPa)	Ply thickness (mm)	Stacking sequence	Lenght	Diameter
Z11	123550	8708	0.319	5695	5695	3400	0.125	[60/-60/0/0/68/-68/52/-52/37/-37]	510	500
R16	150200	8900	0.320	5100	5100	5100	0.131	[24/-24/41/-41]	500	500
ITA01	21796	21796	0.099	1677	1677	1677	0.316	[0/90/90/0]	140	235
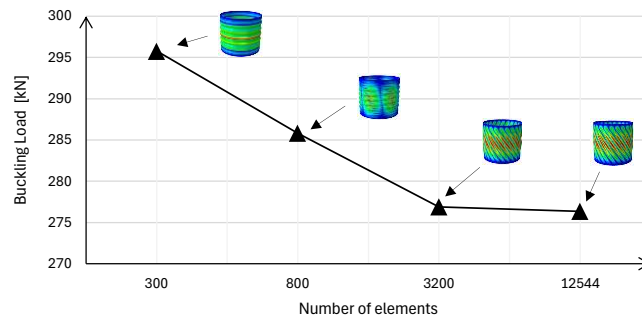
Figure 3. Convergence for the buckling loads and buckling modes using Abaqus.
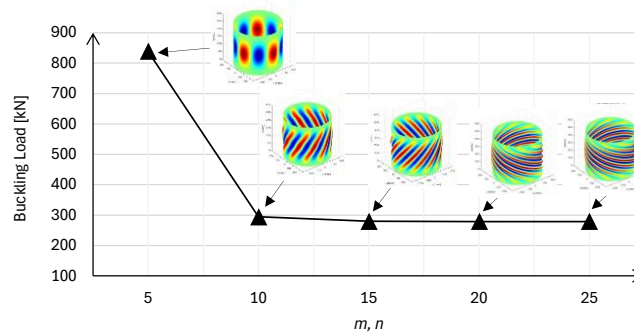
Figure 4. Convergence for the buckling loads and buckling modes using the present formulation.

Table 1 shows the comparison between FEM and Ritz for the critical loads results. A good convergence between the methods was reached using 12544 elements in Abaqus and $m = n = 20$ in the Ritz method. The relation Ritz/FEM also showed a good agreement.

Table 1. Comparison between FEM and Ritz.

FEM		Ritz		Ritz/FEM
Number of elements	Critical Load [kN]	m, n	Critical Load [kN]	
300	295.78	5	838.57	2.84
800	285.84	10	294.57	1.03
3200	276.92	15	279.49	1.01
12544	276.37	20	279.11	1.01

Two imperfect cylinders were analyzed in this work. The first one is the cylinder R16. The geometric imperfection data was obtained from the reference [18]. Fig. 5 shows the results obtained, where results for the linear case and the experiment are identified. Fig. 6 shows the results for the cylinder manufactured by the authors at ITA. Buckling results for cases of the perfect cylinder, imperfect loading, experiment, and loading imperfections including geometric imperfections are presented. The loading imperfection distribution was considered as $N(\theta) = \sin(\theta/2) - 0.1589 \cdot \sin(\theta)$, obtained through extensometer data.
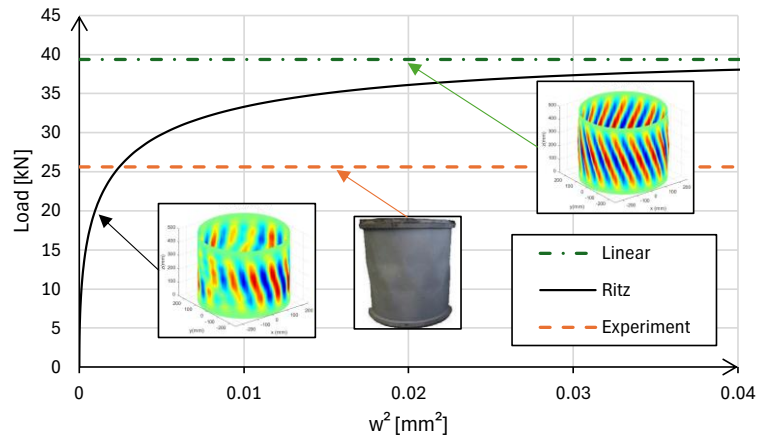
Figure 5. Instability analysis results for Cylinder R16.
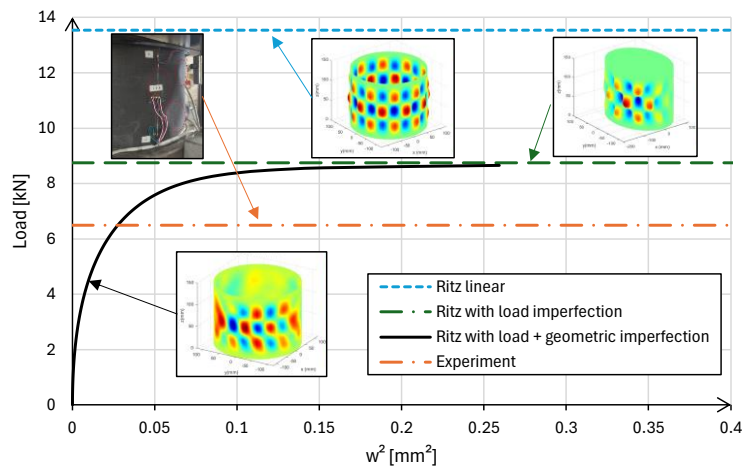
Figure 6. Instability analysis results for Cylinder ITA01.

4. CONCLUSIONS

This work presented a formulation based on the Ritz method that can simulate buckling of composite cylinders with different stacking sequences, boundary conditions, and loading. Results for perfect cylinders showed a good agreement when compared with FEM. The inclusion of loading imperfections and geometric imperfections showed to be very important since the instability results obtained through experiments of real cylinders will reflect the imperfections effects. The geometric imperfections results showed that the instability starts near the critical loads obtained from experiments, however, to capture more accurate results after the prebuckling, it is recommended to conduct non-linear analyses that can simulate post-buckling behavior.

4.1. Declaration of Competing Interest

The authors declare no conflict of interest.

4.2. Acknowledgments

5. REFERENCES

[1]   Dassault Systèmes Simulia Corp. ABAQUS/Standard User's Manual. Dassault Systèmes Simulia Corp 2011.

[2]   Rudd MT, Eberlein DJ, Waters WA, Gardner NW, Schultz MR, Bisagni C. Analysis and validation of a scaled, launch-vehicle-like composite cylinder under axial compression. Compos Struct 2023;304:116393. https://doi.org/10.1016/j.compstruct.2022.116393.

[3]   Degenhardt R, Kling A, Bethge A, Orf J, Kärger L, Zimmermann R, et al. Investigations on imperfection sensitivity and deduction of improved knock-down factors for unstiffened CFRP cylindrical shells. Compos Struct 2010;92:1939–46. https://doi.org/10.1016/j.compstruct.2009.12.014.

[4]   Priyadarsini RS, Kalyanaraman V, Srinivasan SM. Numerical and Experimental Study of Buckling of Advanced Fibre Composite Cylinders Under Axial Compression. 2012.

[5]   Santos P, Pereira MS, Donadon MV. Analysis of laminate composite plates using Moving Least Square Ritz Method. Virtual Congress: 2021. https://doi.org/10.26678/ABCM.COBEM2021.COB2021-0276.

[6]   Castro SGP, Mittelstedt C, Monteiro FAC, Arbelo MA, Degenhardt R, Ziegmann G. A semi-analytical approach for linear and non-linear analysis of unstiffened laminated composite cylinders and cones under axial, torsion and pressure loads. Thin-Walled Structures 2015;90:61–73. https://doi.org/10.1016/j.tws.2015.01.002.

[7]   Santos PR, Donadon M V. A semi-analytical model for buckling and stress analyses of pressurized composite cylinders. Journal of the Brazilian Society of Mechanical Sciences and Engineering 2023;45. https://doi.org/10.1007/s40430-023-04350-3.

[8]   Geier B, Singh G. Some simple solutions for buckling loads of thin and moderately thick cylindrical shells and panels made of laminated composite material. vol. 1. 1997.

[9]   Skukis E, Ozolins O, Kalnins K, Arbelo MA. Experimental Test for Estimation of Buckling Load on Unstiffened Cylindrical shells by Vibration Correlation Technique. Procedia Eng, vol. 172, Elsevier Ltd; 2017, p. 1023–30. https://doi.org/10.1016/j.proeng.2017.02.154.

[10] Kalnins K, Arbelo M, Ozolins O, Castro S, Degenhard R. Numerical Characterization of the Knock-Down Factor on Unstiffened Cylindrical Shells with Initial Geometric Imperfections. n.d.

[11] Lucena Neto E. Fundamentos da Mecânica das Estruturas. Florianópolis: 2021.

[12] Reddy JN. Theory and Analysis of Elastic Plates and Shells. Boca Raton: 2006. https://doi.org/10.1201/9780849384165.

[13] Don O. Brush, Bo O. Almrot. Buckling of Bars, Plates, and Shells. 1975.

[14] G.J. Simitses, I. Sheinman, D. Shaw. The accuracy of Donnell's equations for axially-loaded, imperfect orthotropic cylinders. vol. 20. 1984. https://doi.org/10.1016/0045-7949(85)90013-6.

[15] J. Arbocz. The effect of initial imperfections on shell stability: An updated review 1992.

[16] Jansen E. The influence of initial geometric imperfections on composite shell stability and vibrations. Stability and Vibrations of Thin-Walled Composite Structures, Elsevier; 2017, p. 509–48. https://doi.org/10.1016/B978-0-08-100410-4.00010-7.

[17] Timoshenko, Gere. Theory of Elastic Stability, International Student Edition, Second edition 1985.

[18] Castro SGP, Reichardt J, Burau F, Lozano E. DESICOS Plug-in for Abaqus (Version 2.4.13) 2021.

A PRELIMINARY INVESTIGATION OF PYRAMIDAL LATTICE STRUCTURES BASED ON BAMBOO ELEMENTS AND 3D-PRINTED NODES

Sofia D. Garcia [(a*)], Rodrigo J. da Silva [(b)], Rodrigo T.S. Freire [(c)], Gilberto G. del Pino[(d)], Vanessa M. Gomes [(e)], Fabrizio Scarpa [(f)], Túlio H. Panzera [(g)]

(a) 0000-0002-8316-0012 (Federal University of São João del-Rei – Brazil)
(b) 0000-0001-8016-3165 (Federal University of São João del-Rei – Brazil)
(c) 0000-0001-5206-5939 (Federal University of São João del-Rei – Brazil)
(d) 0000-0003-0754-2390 (Amazonas State University – Brazil)
(e) 0009-0009-4833-6172 (Federal University of São João del-Rei – Brazil)
(f) 0000-0002-5470-4834 (University of Bristol – United Kingdom)
(g) 0000-0001-7091-456X (Federal University of São João del-Rei – Brazil)
* Corresponding author: sofidehaini@gmail.com

Abstract: The use of lattice geometries in lightweight structural components offers numerous advantages, including superior load-carrying capacity, enhanced energy absorption, and design flexibility. This study presents a preliminary investigation into the mechanical properties of pyramidal lattice structures constructed from bamboo elements. The structures are assembled by connecting bamboo sticks with 3D-printed joints produced using fused deposition manufacturing with PLA and PETG polymers. To ensure secure attachment of the sticks and joints, a castor-oil biobased polymer is employed as the bonding phase. The mechanical properties of the pyramidal lattice structures are characterised through compression and three-point bending tests. The results demonstrate that these sustainable lattice structures exhibit an impressive loading capacity, with the ability to withstand up to 546 N under compression and approximately 90 N under bending. These findings suggest their potential for use as structural components, such as the core material of sandwich structures.

1. INTRODUCTION

Lattice structures are widely utilised in various applications due to their structural advantages, including low weight, high stiffness, and exceptional energy absorption. Ongoing developments in lattice geometries and materials aim to meet diverse structural demands and fabricate robust composites, particularly for use as sandwich materials [1]. These lattice components consist of fin elements connected and configured in different cell arrangements forming a periodic structure, such as pyramid and cubic, classified according to configuration, and selected to meet specific project requirements, showcasing remarkable mechanical strength [2].

The advancement of 3D printing techniques enables the production of intricate parts using a diverse range of materials, resulting in cost-effective and lightweight components [3]. Among the most prevalent processes is fusion deposition modelling (FDM), which utilises a thermoplastic polymer filament as the raw material. Two notable examples of feedstock for FDM include (i) PLA (Polylactic Acid), known for its biodegradability, non-toxicity, and renewable sourcing from materials like corn; and (ii) PETG (Polyethylene Terephthalate).

Renewable materials are increasingly being explored for engineering applications, aiming to minimize natural resource consumption and global pollution levels [4]. Bamboo, as an alternative to synthetic materials, serves as a renewable source of raw material, is widely available across various regions, and offers high mechanical resistance and structural lightness. Additionally, bamboo plays a vital role in carbon dioxide absorption, contributing to the reduction of greenhouse gases.

This work proposes the production and mechanical evaluation of sustainable pyramidal lattice structures through compression and bending testing. Four configurations featuring varying joint connections between bamboo sticks are fabricated by integrating two raw materials using the FDM 3D-printing process (PLA and PETG), along with two distinct joint geometries.

2. METHODOLOGY

2.1. Materials and Manufacturing

The lattice structures are composed of bamboo sticks jointed with a 3D-printed material in a semi-spherical shape. These materials are bonded using a biobased polymer derived from castor oil. The bamboo sticks possess a diameter of 1.6 mm and a length of 50 mm. Joints, shown in Fig. 1, are manufactured via 3D-printed fusion deposition using PLA and PETG materials, measuring 17.4 mm in diameter and 8.7 mm in height. These joints feature holes through which the bamboo sticks are connected. For each material, two types of joints are produced, comprising open and closed structures, as shown respectively in Figure 1a and Figure1b.

Figure 2 demonstres how joints are connected to sticks, in open geometries as presented in Figure 2a there are more openings than the necessary number of sticks used to construct the structure, and closed geometries as shown in Figure 2b posses just the necessary amount of holes so sticks can fit in. Given these two types of geometries adhesive bonding, total weight of structure and others may differ and influence in mechanical properties.

The adhesive utilised is a thermosetting polymer based on a castor-oil polyurethane system sourced from Imperveg® (Brazil). The polymer is introduced into the joints using a syringe, following which the sticks are fitted into the holes. The bonding process takes place at 25°C and 55 ± 5% humidity, and the structures undergo a 14-day curing period. Cells are fabricated in a single pyramid format, with dimensions of 67 x 67 x 45 mm³, while lattice beams with periodic pyramid format are bonded in sequence, featuring dimensions of $360 \times 67 \times 45$ mm³.
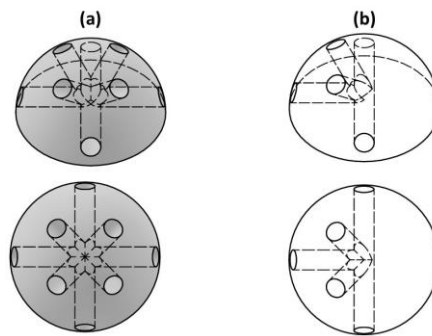
Figure 1: 3D modelling and upper view of (a) open structure and (b) closed structure joints
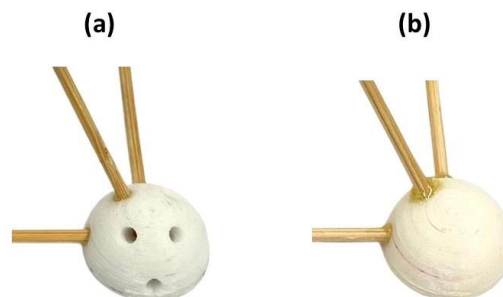
Figure 2: Joints connected to sticks (a) open structure and (b) closed structure joints

2.2. Compressive and Bending testing

The study investigates four configurations for unit cell and beam specimens. In Figure 3a, a unit cell made with PLA open joints is exhibited, while Figure 3b represents the same geometry configuration fabricated with PETG material. Additionally, Figure 3c and Figure 3d illustrate the respective joints with closed architectures. Their corresponding configurations as beam specimens are shown in Figure 4.

Mechanical properties are determined through compression tests (Figure 5a) and three-point bending tests (Figure 5b) utilising an Instron machine equipped with a 1 kN load cell. Compression tests for the unit cells are conducted at a speed of 1 mm/min, while the three-point bending tests for beam structures involve a span length of 260 mm and a cross-head speed of 2 mm/min.
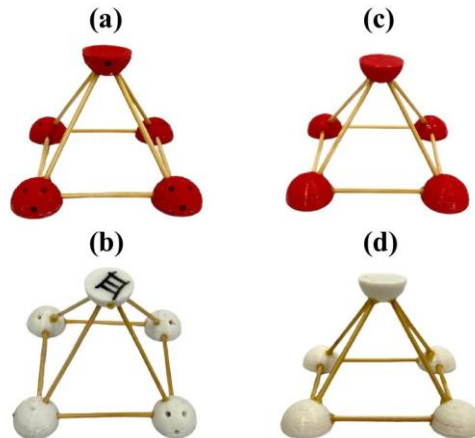
Figure 3: Unit cells made with (a) PLA open joints; (b) PETG open joints; (c) PLA closed joints; (d) PETG closed joints.
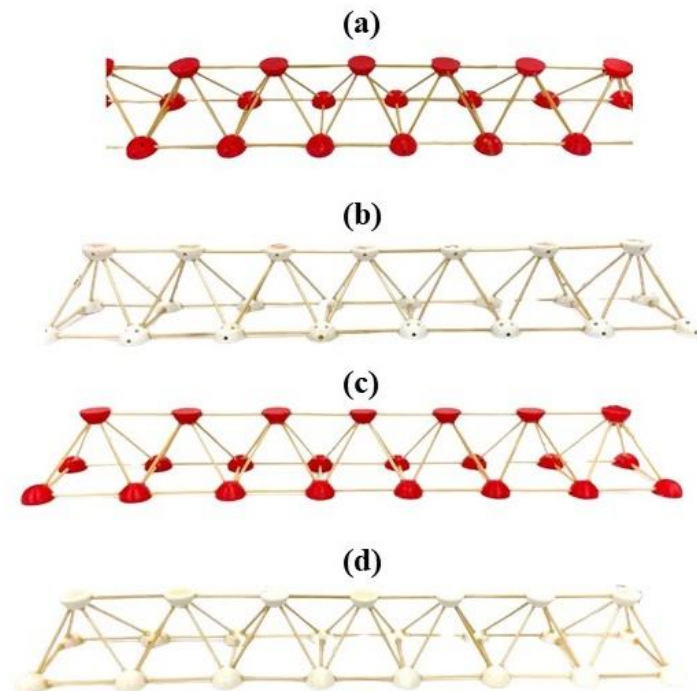
Figure 4: (a) PLA beam with open joints; (b) PETG beam with open joints; (c) PLA beam with closed joints; (d) PETG beam with closed joints.
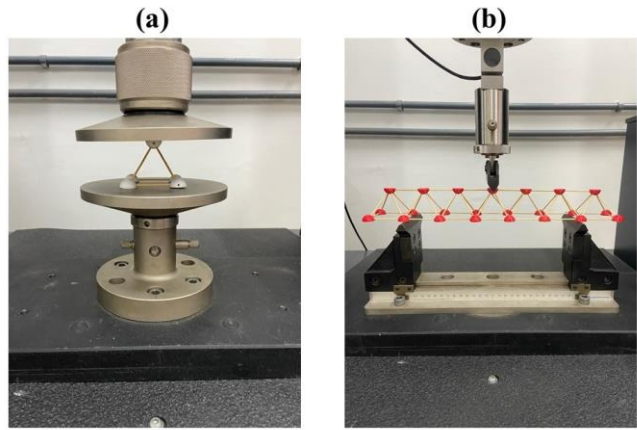
Figure 5: (a) Compression and (b) three-point bending tests.

3. RESULTS AND DISCUSSION

In Figure 6, the compressive force-displacement curves for the unit cells are presented, while Table 1 displays the mechanical properties (maximum load and displacement) obtained during the compression tests. A noticeable trend is observed in the cells constructed with PLA joints featuring closed architecture, which demonstrate a higher load capacity of up to 546 N. An increase in maximum load of 43% and 58% is observed for the PLA and PETG closed joints, respectively, in comparison to the open joint cells. When comparing the performance of PLA versus PETG material for the joints, there is a 31% i6ncrease in maximum load for the cells with open joints and a 19% increase for those with closed joints. The unit cells exhibit similar failure modes, as shown in Figure 7, wherein one stick is fractured under compressive loading.
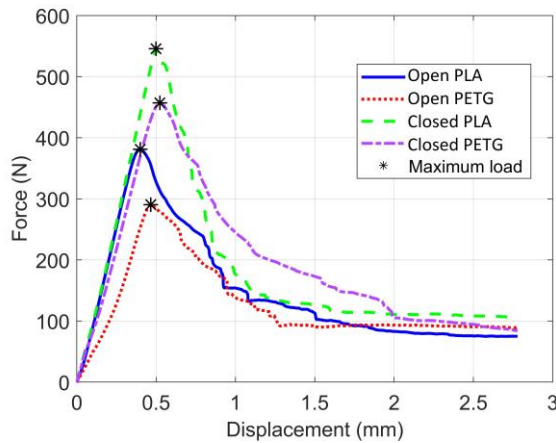
Figure 6: Typical force-displacement curves for compressive testing.

Table 1. Mechanical properties of unit cells under compression.

	Open PLA joint	Open PETG joint	Closed PLA joint	Closed PETG joint
Maximum Load (N)	381	290	546	457
Maximum Displacement (mm)	0.400	0.466	0.500	0.524
	Closed Joints Effect		**PLA Material Effect**	
	PLA Cells	**PETG Cells**	**Open Cells**	**Closed Cells**
Maximum Load	+ 43 %	+ 58%	+ 31%	+ 19%
Maximum Displacement	+ 25%	+ 12%	− 14%	− 5%
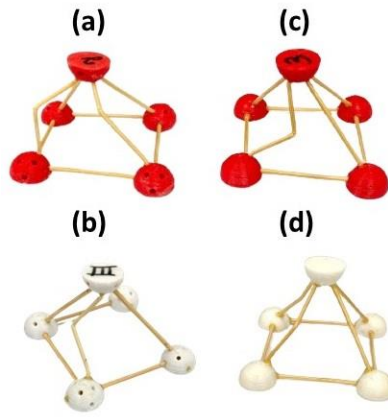
Figure 7: Unit cells after fracture composed of (a) open PLA, (b) open PETG, (c) closed PLA, and (d) closed PETG joints.

In Figure 8, the bending force-displacement curves of the lattice beams are presented, showcasing two deflections at 10 mm and 6 mm. Table 2 outlines the maximum load and its corresponding displacement. The beams with PLA joints exhibit a maximum load capacity of approximately 90 N, with minimal variation between the open and closed architectures; the closed geometry underperforms the open joints by approximately 4%. For beams constructed with PETG joints, the closed architecture demonstrates a load capacity approximately 10% lower than that of the beam with open joints. Furthermore, the PLA material for the joints demonstrates an increase in load capacity of 10% for the open architecture joint and 18% for the closed one.

Unlike the unit cells, the beams exhibit a difference in fracture, as illustrated in Figure 9. Notably, lattices constructed with PETG closed joints (Figure 9d) display distinct characteristics, attributed to stick-node debonding. This behaviour can be associated with poor adhesion between the castor-oil polymer and the PETG surface. Additionally, the open architecture joints may also encounter hindrances due to the absence or difficulty of resin spreading inside the holes.
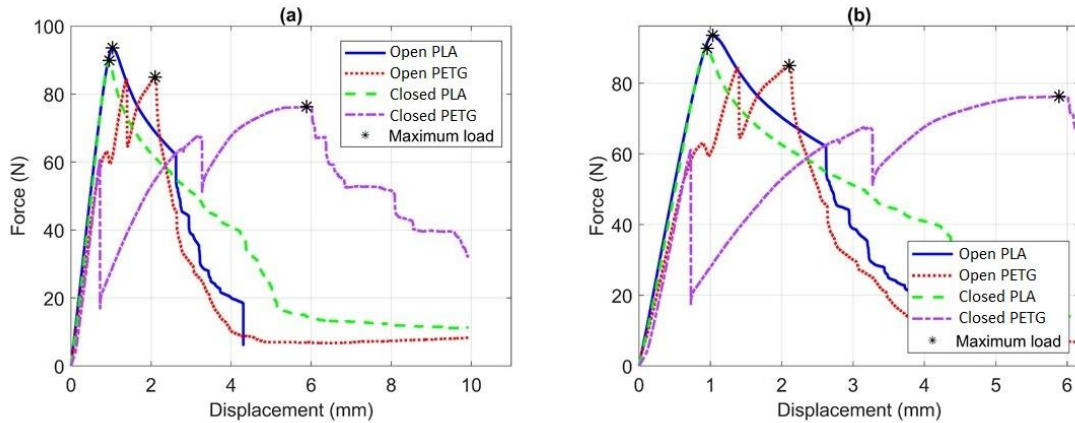
Figure 8: Force-displacement curve for three-point bending testing.

Table 2: Mechanical properties of lattice beams under three-point bending.

	Open PLA joint	Open PETG joint	Closed PLA joint	Closed PETG joint
Maximum Load (N)	93.6	85.0	89.9	76.3
Maximum Displacement (mm)	1.04	2.10	0.96	5.89
	Closed Joints Effect		**PLA Material Effect**	

	PLA Beams	PETG Beams	Open Beams	Closed Beams
Maximum Load	− 4 %	− 10%	+ 10%	+ 18%
Maximum Displacement	− 8%	+ 180%	− 50%	− 84%
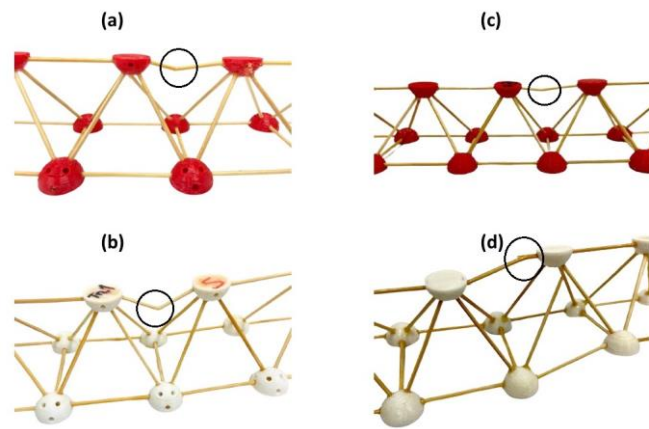
Figure 9: Lattice beams after fracture composed of (a) open PLA, (b) open PETG, (c) closed PLA, and (d) closed PETG joints.

4. CONCLUSIONS

The results indicate that pyramidal lattice structures with PLA closed joints exhibit superior performance under compression, achieving a load capacity of 546 N. This behaviour is attributed to the properties of PLA and the closed joints, which contribute to enhanced stick-node adhesion. In the three-point bending analysis, the PLA-based beam demonstrates optimal results, with a load capacity of approximately 90 N. It is observed that, in bending, the influence of the joints' geometry is minor compared to compression. Future investigations will concentrate on exploring the application of the proposed beams as the core of lightweight sandwich structures.

4.1. Declaration of Competing Interest

The authors declare no conflict of interest.

4.2. Acknowledgements

5. REFERENCES

[1] Lyes Azzouz et al , Mechanical properties of 3-D printed truss-like lattice biopolymer non-stochastic structures for sandwich panels with natural fibre composite skins. *Composite Structures*, 2019, (https://doi.org/10.1016/j.compstruct.2019.01.103)

[2] Hanfeng Yin et al. Review on lattice structures for energy absorption properties. *Composite Structures*, Volume 304, Part 1, 2023. (https://doi.org/10.1016/j.compstruct.2022.116397)

[3] Pereira, R.B.D. et al. The effect of printing parameters on the tensile properties of bidirectional PLA structures: a statistical approach. *Prog Addit Manuf 8*, 519–527 (2023).(https://doi.org/10.1007/s40964-022-00345-z)

[4] Peixing Wei, Jingxiang Chen, Yue Zhang, Lijun Pu, Wood – Based sandwich Panels: A review, *Wood Research*, 2020

OPEN-HOLE FATIGUE RESPONSE OF GLASS/EPOXY DOUBLE-DOUBLE COMPOSITE LAMINATES

Tomás Barros Vasconcelos[a], José Leandro Correia Alves[b], Evans Paiva da Costa Ferreira[c], Raimundo Carlos Silverio Freire Júnior[d], José Daniel Diniz Melo[e], *

(a) 0000-0002-4303-8741 (Federal University of Rio Grande do Norte – Brazil)
(b) xxxx-xxxx-xxxx-xxxx (Aeris Energy S.A. – Brazil)
(c) 0000-0002-4078-0537 (Federal University of Rio Grande do Norte – Brazil)
(d) 0000-0003-0920-7916 (Federal University of Rio Grande do Norte – Brazil)
(e) 0000-0002-3696-5133 (Federal University of Rio Grande do Norte – Brazil)
* Corresponding author: daniel.diniz@ufrn.br

Abstract: Double-double $[\pm\phi/\pm\psi]_n$ is a configuration of composite laminates that offers opportunities such as improved manufacturability, profile optimization by thickness tailoring and layup optimization, as compared to traditional quadriaxial laminates, which are limited to ply angles of 0°, ±45° and 90°. In this investigation, the fatigue behavior of a quadriaxial glass/epoxy laminate and a double-double of equivalent in-plane stiffness subjected to cyclic tensile loads was studied. Fatigue life diagrams showing maximum strain versus number of cycles indicated equivalent fatigue response for both configurations. In addition, due to homogenization, the damaged area observed around the open-hole was smaller for the double-double laminate as compared to the equivalent quadriaxial. In summary, this work contributes to the understanding of the mechanical behavior of double-double laminates, particularly for glass/epoxy composites.

1. INTRODUCTION

Quadriaxial (Quad) laminates based on 0°, ±45° and 90° plies have been the standard for composite structures for many years. However, with the restriction to four fixed angle orientations, the number of different permutations is limited, as compared to a continuous field of angle combinations, which has limited design and manufacturing of laminates (TSAI, 2021; VERMES et al., 2021). In addition to the four fixed angles, other guidelines for laminate design are often followed, such as mid-plane symmetry to prevent warpage, balanced layups to eliminate extension/shear coupling and at least 10% of the plies in each of the ply directions (10% rule) (HYER, 2000; BAILIER et al., 1997; SHRIVASTAVA et al., 2020; IRISARRI et al., 2009; KOGISO et al., 1994; TSAI et al., 2019).

Double-double (DD) has been proposed in the literature as a new concept for composite laminates, in which two pairs of ply angles $[\pm\phi/\pm\psi]_n$ are stacked up to form the laminate (TSAI et al., 2017). With the increase in number of repetitions of the building block $[\pm\phi/\pm\psi]_n$ that forms the DD laminate, [B] matrix and its coupling effects reduces, homogeneity is approached, and mid-plane symmetry is no longer required to prevent warpage (VERMES et al., 2021; TSAI et al., 2019; TSAI, 2022; VERMES et al., 2021).

Homogenization is an important attribute of the double-double concept. It is known that ply groups in a laminate should be dispersed to improve laminate strength and toughness (TSAI and MELO, 2015). The fewer plies in a ply group, the smaller the percentage of this ply group will be in a total laminate. Then, when a ply group fails, the effect is more localized in a dispersed laminate than in a laminate having fewer but thicker ply groups. When the dispersion in a laminate is achieved using repeated sub-laminates, the laminate becomes homogenized, as Figure 1 shows, if there is a sufficiently large number of plies. The benefits of

homogenization include increased strength and toughness; the flexural stiffness approaches that of the in-plane, and stacking sequence is not important; simpler optimization and fabrication (TSAI et al., 2017).
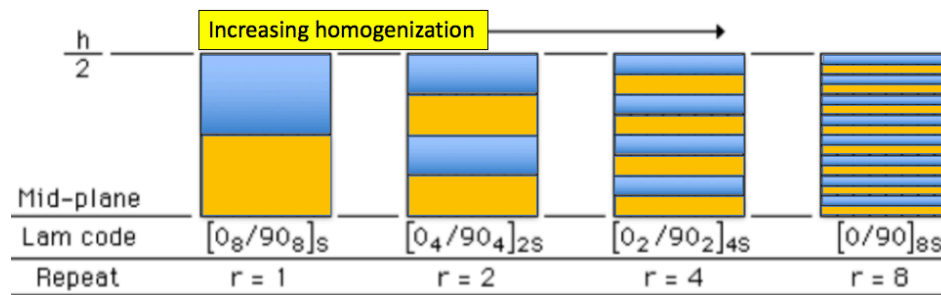
Figure 1 - Homogenization of laminates with the repetition of sub-laminates (TSAI and Melo, 2015).

The use of homogenized or uniformly dispersed laminate is an important aspect for double-double (VERMES, 2021). Homogenization is reached when $[A^*] = [D^*]$ and $[B] = 0$. Since DD laminates are built using many sub-laminates, they become naturally homogenized, and thus, the components of the $[B^*]$ matrix becomes sufficiently small and the laminate is virtually symmetric, with no warpage, as shown in Figure 2. These laminates are also easier to design and manufacture, more easily tapered and less prone to delamination (TSAI et al., 2019).
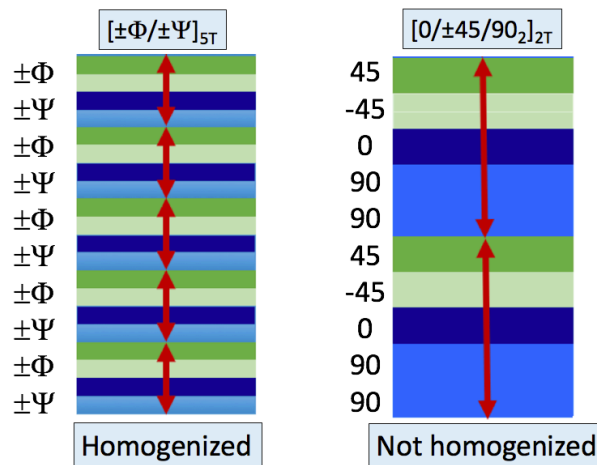
Figure 2 - DD laminates are naturally homogenized (TSAI et al., 2017).

Conventional quadriaxial laminates are difficult to be homogenized because they are not designed based on the concept of repeated sub-laminates with few plies. The use repeating sub-laminates is, therefore, a recommended design practice to obtain highly dispersed laminates (TSAI and MELO, 2014).

While ply angle tailoring expands the possibilities of achieving optimum layup (TSAI et al., 2019), homogeneity and the consequent dispensation from the requirement of mid-plane symmetry facilitate topology optimization (WANG et al., 2023). Weight reduction of double-double laminates can be achieved when tapering is also considered in the design. According to the literature, the weight reduction can reach up to 50% (TSAI, 2021).

Based on recent investigations published in the literature, there has been growing interest in double-double laminates. Most of the works has focused on carbon fiber reinforced polymers (CFRP) for aerospace applications. Nevertheless, due to the extensive use of glass fiber reinforced polymers (GFRP) in wind energy industry, the study of DD glass/epoxy laminates becomes of great interest, particularly due to the potential advantages of DD over Quads regarding manufacturability and design optimization (RAJAK et al., 2021; GOPALRAJ, 2020; RASOOL et al., 2020) (TSAI et al. 2019; TSAI et al., 2023).

In addition to the difference in properties, the GFRP plies used in the wind blade manufacturing are typically of larger thickness, as compared to the CFRP plies of the aerospace industry. Ply thickness is known to influence fatigue behavior of laminates (SIHN et al., 2007). Thus, understanding the fatigue behavior of GFRP DD laminates is of great importance if these laminates are to be considered as candidates in the design of wind turbine blades.

2. EXPERIMENTAL

Glass/epoxy laminates were designed using 16 plies, since homogenization can be achieved with this number of plies in DD laminates using repeats of a sub-laminate (TSAI, 2022; TSAI et al., 2015; ZHAO, 2023).

The traditional Quad laminate was designed using 0°, ±45° and 90° ply angles. A layup utilized in a medium-power 40 kW wind turbine blade was used as reference (ALBANESI, 2018). The number of plies was scaled down while maintaining the original proportions of angles to achieve 16 plies. Thus, the Quad stacking sequence was [±45/(0/90)3]s.

The equivalent DD laminate was designed for the same in-plane stiffness and strength as the reference Quad using equations 1 and 2, where V_1^* and V_2^* are lamination parameters, to obtain the ϕ and ψ angles (TSAI, 2019; VERMES et al., 2021; MIKI, 1982; ARTEIRO, 2020).

$$\cos(2\Psi) = V_1^* + \sqrt{-V_1^{*2} + \frac{V_2^*}{2} + \frac{1}{2}} \tag{1}$$

$$\cos(2\Phi) = 2V_1^* - \cos(2\Psi) \tag{2}$$

Using these equations, the equivalent DD laminate was defined as [±15/±75]4T, where This laminate corresponds perfectly to the original Quad's stiffness.

The material used in this investigation was epoxy resin Airstone 760E with a mixture of 30% hardener Airstone 762H and 70% Airstone 766H following a resin and hardener weight proportion of 100/32, and unidirectional glass fibers UD620 620 g/m² WindStrand 2000 from Owens Corning. Ply engineering constants for the material used are presented in Table 1.

Table 1 - Engineering Constants of E/Glass WindStrand 2000 and Epoxy resin Airstone 760E ply.

Properties	Values
E_1	44.5 GPa
E_2	12 GPa
G_{12}	3.5 GPa
v_{12}	0.31
h	0.5 mm

Source: Aeris Energy S.A.

Both laminates were manufactured by Aeris Energy S.A. using Vacuum Assisted Resin Transfer Molding (VARTM), as shown in Figure 3. All laminates were subjected to a 5h curing cycle at 80 ℃, achieving a fiber volumetric fraction of 48.5% for the Quad laminate and 49.5% for the DD.
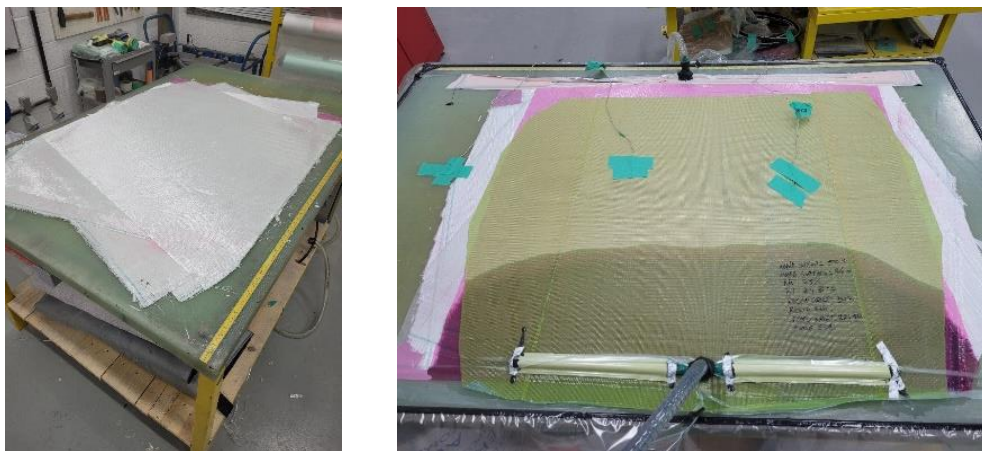
Figure 3 - VARTM utilization in the manufacturing of the laminates.

Fatigue tests were performed in an MTS LandMark Servohydraulic Universal Testing Machine, following recommendations of ASTM 7615 (2019). Nominal dimensions of specimens were 250 mm (length), 127 mm (gage length) and 36 mm (width) with a hole of 6 mm diameter drilled at the center of the specimen, resulting in a width to diameter ratio (w/D) of 6.

The specimens were mounted in the hydraulic grips of the testing machine and sinusoidal load was applied with ratio $\sigma_{min}/\sigma_{máx} = 0.1$ and frequency of 5 Hz to evaluate the fatigue behavior under cyclic tensile loading.

Cyclic tests were conducted using load control mode and the average (nominal) load in the specimens were kept at constant amplitude during the test. These load levels were selected to produce enough data points for the Strain versus fatigue cycles (ε-N) diagrams. Tests were conducted to specimen's failure or 1.5 x 10^6 cycles, which was considered as the upper limit on the number of force cycles to be applied (run-out).

Strain versus fatigue cycles (ε-N) diagrams were plotted. These diagrams were used to compare the performance of the laminates. Equation 3 (BURHAN and KIM, 2018; SUBRAMANYAN, 1976; MANDELL and MEIER, 1983) was used for linear fitting of the results.

$$\varepsilon_{max} = \alpha - \beta\,(logN) \tag{3}$$

where ε_{max} is the maximum strain per cycle, α is the interception on the Y axis, β is the slope and N is the number of cycles to failure. The parameters α and β had their variation range compared through the 95% confidence bands. Results assumed as run-out were not used for curve fitting.

In all fatigue tests, a testing setup employing a camera and background light was employed to capture images of the specimens during the tests, as shown in Figure 4.

Figure 4 – Test setup for monitoring the damage progression.

This setup allowed for monitoring the progression of damage. When bright background light shines on the specimens, cracks cause a reduction in their translucence. This change in translucence can serve as an indicator of damage. The damage, denoted as D, was expressed in terms of the change in intensity (ΔI) relative to the intensity at the initial state (I₀). These values were subsequently employed to calculate the damage progression according to equation 4:

$$D = 1 - \frac{I(N)}{I(0)} \cdot \frac{I_{ref}(0)}{I_{ref}(N)} \tag{4}$$

where the intensity of a damaged area (I) and a reference area with constant intensity throughout the tests (Iref) were considered to assure that potential variations in the background light during the tests would not interfere with the results (KRAUS, 2021; MÜLLER, 2018).

3. RESULTS AND DISCUSSION

Maximum strain versus number of cycles (ε-N) for open hole specimens are presented in Figure 5, for DD and Quad. In this case, no significant difference between the two laminates – DD and Quad – or their respective confidence bands was observed, with both laminates showing similar performance throughout the entire range.
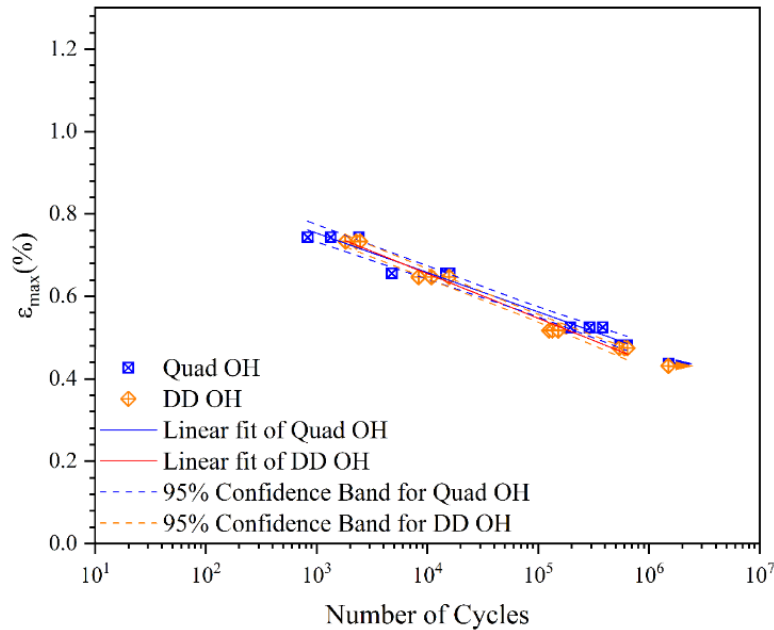
Figure 5 - ε-N diagram for Quad and DD open hole specimens.

By forcing failure away from the edges, open hole coupons can lead to a more reliable and consistent failure mode (TSAI et al., 2023). Despite the free edge stresses being reduced in this test condition, they are still present and may interfere with the results, though to a smaller extent. A smaller delaminated area was observed around the open hole in the DD laminate when compared to the Quad (Figure 6).
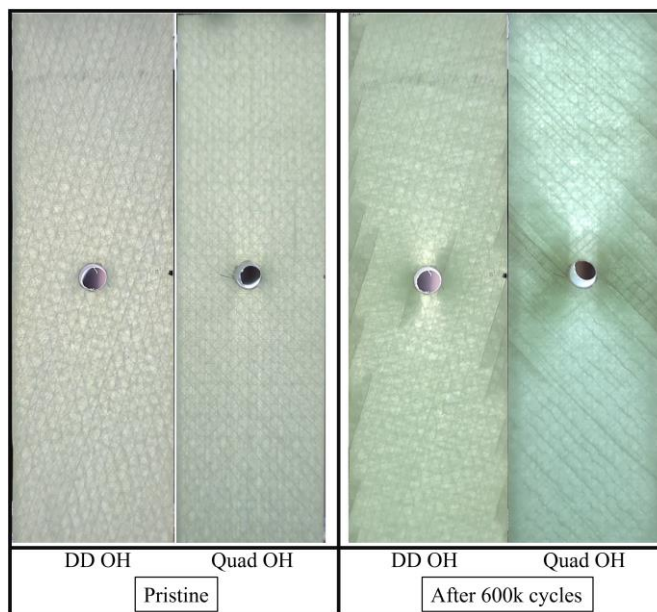
Figure 6 - Damage comparison between a DD and Quad open hole specimens under cyclic loads.

The damage progression in DD and Quad laminates is shown in Figure 7. It can be observed that damage progression is different between DD and Quad laminates. While the damaged area in DD laminates increases continuously with number of cycles, discontinuities are observed in the progression of damage of Quads. Since DD laminates are more homogenized, failure occurs with a smaller overall damaged area.
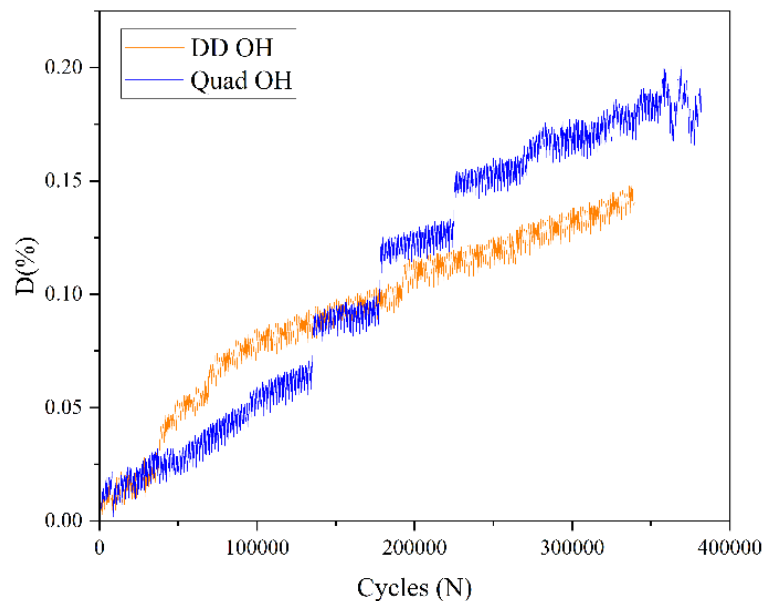
Figure 7 - Damage progression of the specimens.

4. CONCLUSIONS

Fatigue response of glass/epoxy composite laminates was studied using open hole specimens with quadriaxial and double-double layup configurations. According to the experimental results, no significant difference between the two laminates – DD and Quad – was observed for the curves of maximum strain versus number of cycles. However, a smaller delaminated area was observed around the open hole in the DD laminate when compared to the Quad. In addition, the damaged area in DD laminates increases continuously with number of cycles, while the curve of progression of damage of Quads shows discontinuities. Therefore, DD laminates can be interesting candidates as substitutes to the traditional Quad laminates for structural applications, with the reported advantages of weight reduction, homogenization, simpler ply drop strategy, efficient optimization using ply angles as a continuous variable, easier manufacturing and repair.

5. REFERENCES

Tsai SW. Double – Double: New Family of Composite Laminates, AIAA Journal. 59 (11) 4293–4305, 2021. https://doi.org/10.2514/1.J060659

Vermes B, Tsai SW, Massard T, Springer GS, Czigany T. Design of laminates by a novel "double–double" layup. Thin-Walled Structures; 165:107954; 2021. https://doi.org/10.1016/j.tws.2021.107954

Hyer M. Laminated Plate and Shell Theory, Comprehensive Composite Materials. Pergamon; 2000.

Bailie J, Ley R, Pasricha AA. A summary and review of composite laminate design guidelines. Military Aircraft Systems Division. Northrop Grumman Corporation; 1997 URL: https://docplayer.net/41811348-A-summary-and-review-ofcomposite-laminate-design-guidelines.html. (accessed 15 September 2023)

Shrivastava S, Sharma N, Tsai SW, Mohite PM. D and DD-drop layup optimization of aircraft wing panels under multi-load case design environment. Composite Structures, 248, p.112518; 2020. https://doi.org/10.1016/j.compstruct.2020.112518

Irisarri FX, Bassir DH, Carrere N, Maire JF. Multiobjective stacking sequence optimization for laminated composite structures. Composites Science and Technology 69:983–90; 2009. http://dx.doi.org/10.1016/j.compscitech.2009.01.011

Kogiso N, Watson LT, Gürdal Z, Haftka RT, Nagendra S. Design of Composite Laminates by A Genetic Algorithm with Memory. Mechanics of Advanced Materials and Structures. Sep 1;1(1): 95–117; 1994. https://dx.doi.org/10.1080/10759419408945823

Tsai SW, Sharma N, Arteiro A, et al. Composite double-double and grid/skin structures - low weight/low cost design and manufacturing, first ed. Stanford. International Paris air Show. 2019.

Tsai SW, Melo JDD, Sihn S, et al. Composite laminates: theory and practice of analysis, design and automated layup. Stanford, California: Stanford Aeronautics and Astronautics, 2017.

Tsai SW. Double-double: a new perspective in the manufacture and design of composites. Stanford, California: Stanford University; 2022.

Vermes B, Tsai SW, Riccio A, et al. Application of the Tsai's modulus and double-double concepts to the definition of a new affordable design approach for composite laminates. Compos Struct 259: 113246; 2021. https://doi.org/10.1016/j.compstruct.2020.113246.

Wang Y, Wang D, Zhong Y, Rosen DW, Li S, Tsai SW. Topology optimization of Double-Double (DD) composite laminates considering stress control. Computer Methods in Applied Mechanics and Engineering. 1;414:116191–1; 2023. https://doi.org/10.1016/j.cma.2023.116191.

Tsai SW, Melo JDD. Composite materials design and testing - unlocking mystery with invariants. Stanford: Composites Design Group; 2015.

Tsai SW and Melo JDD. An invariant-based theory of composites. Compos Sci Technol 2014; 100: 237–243. DOI:10.1016/j.compscitech.2014.06.017.

Rajak DK, Wagh PH, Linul E. Manufacturing Technologies of Carbon/Glass Fiber-Reinforced Polymer Composites and Their Properties: A Review. Polymers 13, 3721; 2021. https://doi.org/10.3390/polym13213721

Gopalraj SK, Kärki T. A review on the recycling of waste carbon fibre/glass fibre-reinforced composites: fibre recovery, properties and life-cycle analysis. SN Appl. Sci. 2, 433; 2020. https://doi.org/10.1007/s42452-020-2195-4

Rasool G, Middleton AC, Stack MM. Mapping Raindrop Erosion of GFRP Composite Wind Turbine Blade Materials: Perspectives on Degradation Effects in Offshore and Acid Rain Environmental Conditions. Journal of Tribology. 26;142(6); 2020. https://doi.org/10.1115/1.4046014

Tsai SW, Falzon BG, Aravand A. Double-double: Simplifying the Design and Manufacture of Composites Laminates. Stanford, California: Stanford University, 2023.

Sihn S, Kim RY, Kawabe K, Tsai SW. Experimental studies of thin-ply laminated composites. Compos Sci Technol 2007; 67:996–1008.

Tsai SW. Double-double: a new perspective in the manufacture and design of composites. Stanford, California: Stanford University; 2022.

Zhao K, Kennedy D, Miravete A, Tsai SW, Featherston CA, Liu X. Defining the Design Space for Double–Double Laminates by Considering Homogenization Criterion. AIAA Journal. 1–14; 2023. https://doi.org/10.2514/1.j062639

Albanesi A, Bre F, Fachinotti V, Gebhardt C. Simultaneous ply-order, ply-number and ply-drop optimization of laminate wind turbine blades using the inverse finite element method. Composite Structures, 184. 894–903; 2018. https://doi.org/10.1016/j.compstruct.2017.10.051

Miki M. Material design of composite laminates with required in-plane elastic properties. Progress in Science and Engineering of Composites 2, 1725–31; 1982.

Arteiro A, et al. A case for Tsai's Modulus, an invariant-based approach to stiffness. Compos Struct 252; 2020. https://doi.org/10.1016/j.compstruct.2020.112683

ASTM D5766-18 - Standard Test Method for Open-Hole Tensile Strength of Polymer Matrix Composite Laminates, Am. Stand. Test. Methods. 1-7; 2018. https://doi.org/10.1520/D5766_D5766M-11R18

ASTM D3479-19 - Standard Test Method for Tension-Tension Fatigue of Polymer Matrix Composite Materials, Am. Stand. Test. Methods. 1-6; 2019. https://doi.org/10.1520/D3479_D3479M-19

ASTM D7615-19 - Open-Hole Fatigue Response of Polymer Matrix Composite, Am. Stand. Test. Methods. 1-8; 2017. https://doi.org/ 10.1520/D7615_D7615M-19

Burhan I, Kim HS. S-N Curve Models for Composite Materials Characterisation: An Evaluative Review. Journal of Composites Science 2(3):38; 2018. https://doi.org/10.3390/jcs2030038

Subramanyan S. A Cumulative Damage Rule Based on the Knee Point of the S-N Curve. Journal of Engineering Materials and Technology. 98(4):316–21; 1976.

Mandell JF, Meier U. Effects of stress ratio, frequency, and loading time on the tensile fatigue of glass-reinforced epoxy. In Long-Term Behavior of Composites; ASTM STP 813; O'Brien, T.K., Ed.; American Society for Testing and Materials: Philadelphia, PA, USA, 55–77; 1983.

D. Kraus, V. Trappe, Transverse damage in glass fiber reinforced polymer under thermo-mechanical loading, Composites Part C: Open Access 5 (2021), 100147.

A. Müller, V. Trappe, S. Hickmann, H.-P. Ortwein, Investigation of the infinite life of fibre-reinforced plastics using X-ray refraction topography for the in-situ, nondestructive evaluation of micro-structural degradation processes during cyclic fatigue loading, in: Fatigue of Materials at Very High Numbers of Loading Cycles, 2018, pp. 417–439.

Wood/glass/jute hybrid-faced sandwich panel manufactured by vacuum infusion

Letícia Zimermann Pires[a]*; Joziel Aparecido Cruz[b]; Kelvin Techera Barbosa[c]; Dionatan Orestes Ramos[d]; Rafael de Avila Delucis[e]; Sandro Campos Amico[f], Andrey Pereira Acosta[g]

(a) 0009-0001-2640-7584 (Federal University of Paraná)
(b) 0000-0001-5123-1608 (Federal University Santa Catarina)
(c) 0000-0001-9894-703X (Federal University Rio Grande do Sul)
(d) 0009-0000-3968-900X (Federal University Rio Grande do Sul)
(e) 0000-0002-3657-9216 (Federal University Pelotas)
(f) 0000-0003-4873-2238 (Federal University Rio Grande do Sul)
(g) 0000-0002-5074-3772 (Federal University of Paraná)
*Corresponding author: leticiazimermann@ufpr.br

Abstract: The aim of this study is to develop a novel wood-based sandwich panel using the vacuum infusion method, with the aim of achieving exceptional mechanical performance. Pine wood veneers (W), jute non-woven fabrics (J) and glass mats (G) were used as faces, while a PET foam was used as the core and a polyester resin was used as the impregnation resin. Bulk density, flatwise and edgewise static bending were the characterisation analyses. Density varied in the sandwich panels due to the glass layers adjacent to the wood, which improved resin penetration and retention. The glass and jute reinforced sandwich panels (GWJWG) showed superior mechanical performance, with higher specific flexural modulus (E_f/ρ) and specific flexural rigidity (K/ρ), due to the strength of the glass fibre layers. SEM analysis confirmed effective interactions between core and fibres. Compared to wood-faced panels, the new panels showed significantly higher modulus of elasticity and rupture, although premature failures in the core indicate the need for tests in other orientations.

1. INTRODUCTION

The undeniable increase in the adoption of renewable-based composite materials, notably wood composites, in construction is largely due to the pressing need to mitigate the impacts of environmental catastrophes and the imperative to tackle global climate change. Wood is widely used for numerous purposes, i.e. biomass, pulp and paper production and construction [1]. The construction industry is directly dependent on the timber sector, mainly due to the unique characteristics that only this material can provide, such as thermal comfort, a remarkable relationship between mechanical performance and lightness, as well as visual comfort, among other attributes. However, it is important to note that the excessive consumption of wood around the world has contributed to an alarming increase in deforestation, especially in large countries such as Brazil, China, Russia and the United States. A study published by Mongabay (2023) [2] claimed that the global wood consumption could grow by 54% between 2010 and 2050, creating a demand for timber that would result in a "clear-cut equivalent" in area roughly the size of the continental U.S., adding 3.5 to 4.2 gigatons of carbon dioxide to the atmosphere annually for years to come. A suitable alternative to the large-scale consumption of wood of conventional origin is the adoption of exotic wood species with short planting cycles (e.g. Pinus and Eucalyptus). However, this apparently straightforward solution proves to be complex, since the rapid growth of these genera often results in inferior quality wood, making it necessary to explore other alternatives.

In the academic and industrial sectors, various methods have emerged to meet the demand for renewable materials with high physical and mechanical performance, and wood modification is a promising

solution. Numerous studies have focused on investigating the impacts of various techniques for modifying wood and its derivatives, such as thermal rectification [3], chemical modification [4], impregnation [5], impregnation of veneers for the manufacture of laminates [6] or even a combination of these treatments. However, the limitations of these techniques are evident, particularly in relation to the material's mechanical performance. Most of these studies show improvements of only around ~50% in stiffness and strength, and in the case of laminates, adhesion between the wood veneers is often compromised, resulting in significant losses in mechanical performance [6]. In this context, the use of new technologies is on the increase, especially the adoption of high-performance techniques. A particularly promising alternative has been demonstrated by Acosta and coworkers (2023) [7]. A recent study, consisting of the manufacture of high-performance wood laminates using a technique conventionally used to produce composite materials with high physical and mechanical performance, vacuum infusion. In this study, the researchers maintain that during the process of generating the interface between the veneers, there is efficient impregnation of the resin into the wood, resulting in a remarkable penetration and retention rate. The results of this research proved to be highly promising, and in subsequent work carried out by the same authors, new laminates were produced with a mechanical performance (stiffness and strength) up to approximately ~300 higher than conventional wood laminates [8]. From the research, the prospect of manufacturing high-performance sandwich panels using wood as the main component is emerging. The manufacture of sandwich panels is proving particularly attractive due in large part to the combination of low panel density and outstanding mechanical performance, resulting in exceptional specific mechanical properties.

The use of sandwich structures has evolved, becoming prominent structural and non-structural elements in the construction industry. Generally, sandwich structures consist of two extremely rigid and resistant outer layers, between which a light and flexible core is positioned. This core plays a crucial role in maintaining the separation between the outer layers and at the same time offers deformation absorption capabilities and often insulation functions. The variation in materials and thicknesses used in the outer layers and the core makes it possible to create sandwich structures with a wide range of different properties and performances. The outer layers, or 'faces', play a significant role in determining the overall mechanical performance of the sandwich panel. In the context of wood sandwich panels, these faces have certain limitations, such as low resistance to adverse weather conditions, high water absorption and, consequently, a progressive degradation of mechanical properties over time. Based on the foregoing, the aim of this study is to develop a novel wood-based sandwich panel using the vacuum infusion method, with the aim to achieve excellent mechanical performance.

2. METHODOLOGY

2.1. Raw materials

Pinus elliottii wood veneers with a thickness of ~1 mm (bulk density of 0.59 ± 0.05 g/cm³, moisture content of 9.97 ± 1.99%, and porosity of 49.25 ± 2.25%) were purchased from EcoFolhas (São Paulo, Brazil) and designated as "W". Unidirectional jute fabrics (area density of ~240 g/m²) were purchased from the Castanhal textile company (Pará, Brazil) and designated as "J". Randomly oriented glass fibre blankets (area density of ~400 g/m²) were obtained from the Owens Corning company (Toledo, USA) and designated as "G". An isophthalic unsaturated polyester with a density of 1.19 g/cm³ was used as the polymer matrix, along with a Butanox 50 initiator (1.5% by weight in relation to the resin). The viscosity of the uncured polyester resin was determined using a Brookfield viscometer equipped with a CP-40 cone-plate, set at 20 rpm at three different temperatures (20, 25 and 30 °C), with viscosity values ranging from 146.5 to 205.4 cP. The gelling time was 53 minutes, and the maximum temperature during the resin curing process reached 95.5 °C, as stipulated by the ASTM D2471 method. Closed-cell PET (polyethylene terephthalate) foam cores with a thickness of 12 mm (Divinycell PN80), purchased from Barracuda® (Rio de Janeiro, Brazil), were used as the core.

2.2. *Manufacture of the Sandwich Structures*

Sandwich structures were manufactured using a Vacuum Infusion Process (VIP) at room temperature (approximately 25 °C). First a mould release agent (carnaúba wax) was applied to the mould, then 5 sheets corresponding to the bottom face were positioned, then the Closed-cell PET was positioned and finally the 5 sheets of the top face were positioned. Two plastic spiroducts, each measuring 250 mm in length, were prepared and connected to the inlet and outlet hoses, effectively creating a rectangular injection area of 650

mm × 400 mm on a smooth surface. The inlet hose was attached to a 2 L beaker, which had been pre-filled with resin. The outlet hose was connected to a pressure vessel, serving as a Büchner flask, in conjunction with a vacuum pump. The injection area was then sealed using a vacuum bag and tacky-tape. Subsequently, the vacuum pump was activated and adjusted to maintain a constant pressure of approximately -92 kPa, ensuring a predominantly linear flow of resin. A schematic representation of all the laminates produced, their nomenclature, and their respective thicknesses is depicted in Figure 1.
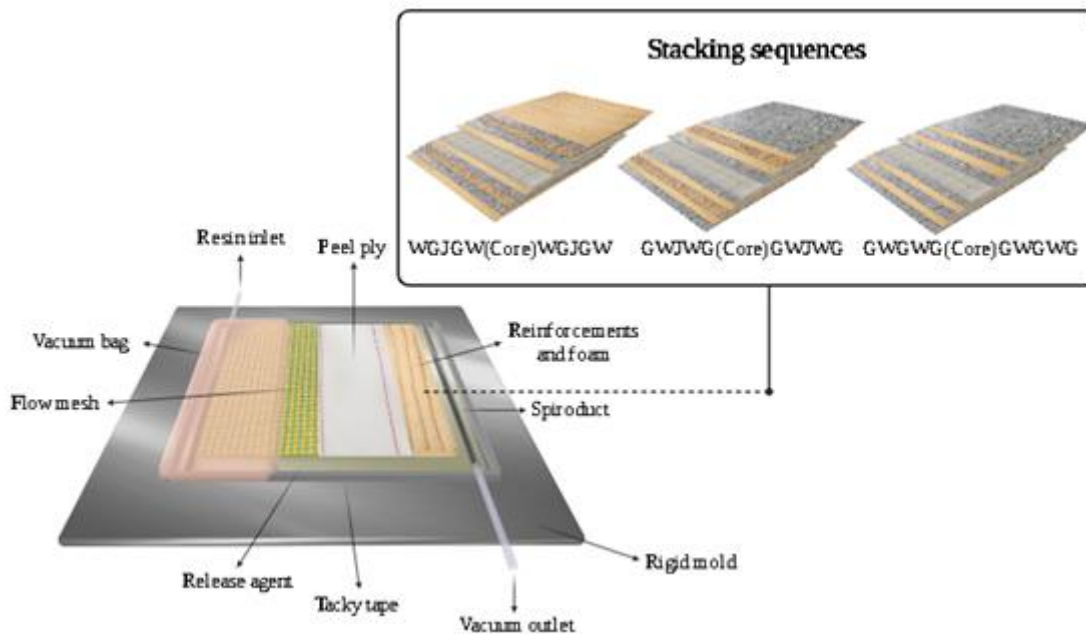
Figure 1 - Schematic representation of the stacking sequences and sandwich structures manufacturing process.

2.3. *Sandwich characterization*

The apparent density and the thickness of the faces of the sandwich panels was determined through of weight and size measurements in the panels manufactured (7.5 × 20.0 × 2.0 cm^3) for each group, using an analytical scale (0.001 g resolution) and a digital caliper (0.01 mm resolution). Flexural tests followed the standard ASTM C393. The specimens (dimensions: 200 mm × 75 mm) were loaded at a speed rate of 1.0 mm/min (up to failure) and a span/thickness ratio of 32 (≈128 mm). The interface between the veneer and the core was analysed using scanning electron microscopy (SEM). For this purpose, MA10 equipment (Zeiss Evo, Oberkochen, Germany) was used, operating at a voltage of 3 kV.

2.4 Statistical Analysis

One-Way analyses of variance (ANOVA) were applied and, whenever the null hypothesis was rejected, Tukey tests were used to compare the means. All statistical analyses were implemented at a significance level of 5%. In all the cases where ANOVA was applied, it was decided to use the error in the form of data distribution instead of the standard deviation.

3. RESULTS AND DISCUSSION

Table 1 provides an overview of the general data for the sandwich panels prepared in this study. It is evident that the GWGWG sample exhibits a higher apparent density. This phenomenon can be attributed to the high permeability of the glass mats, which potentially enhances the resin flow between and through the glass fiber mats, as reported in previous studies by Acosta and coworkers [9]. Furthermore, the glass fibers themselves are approximately five times denser than solid pine wood and roughly twice as dense as jute fibers. However, panels WGJGW and GWJWG, consisting of identical laminates but with different stacking sequences, did not exhibit significant differences, as reported in previous studies by Acosta and coworkers [9].

Table 1 - Total thickness, thickness of a single face sheet and apparent density of the manufactured sandwich structures (*different letters next to the errors in each group represent a statistical difference).

Group	Overall thickness (mm)	Face thickness (mm)	Bulk apparent density (kg/m³)
WGJGW	18.16±0.08 (b)	3.26±0.08 (a)	608.81±7,99 (b)
GWJWG	18.38±0.20 (b)	3.17±0.19 (a)	564.01±10.31 (a)
GWGWG	16.45±0.33 (a)	3.17±0.14 (a)	645.72±16.66 (c)

Numerous research studies have investigated the behavior of sandwich structures under flexural loading in the flatwise position, as they are commonly employed as structural panels for roofs, floors, walls, and bridge decks [18,19]. Figure 2 presents the results of three-point bending tests conducted in the flatwise position, including (A) flatwise representative load *vs.* displacement curves, (B) flatwise longitudinal flexural modulus, and (C) flatwise specific flexural stiffness of the fabricated sandwich structures. Concerning the specific flexural modulus, E_f/ρ, it represents the material's specific flexural rigidity.
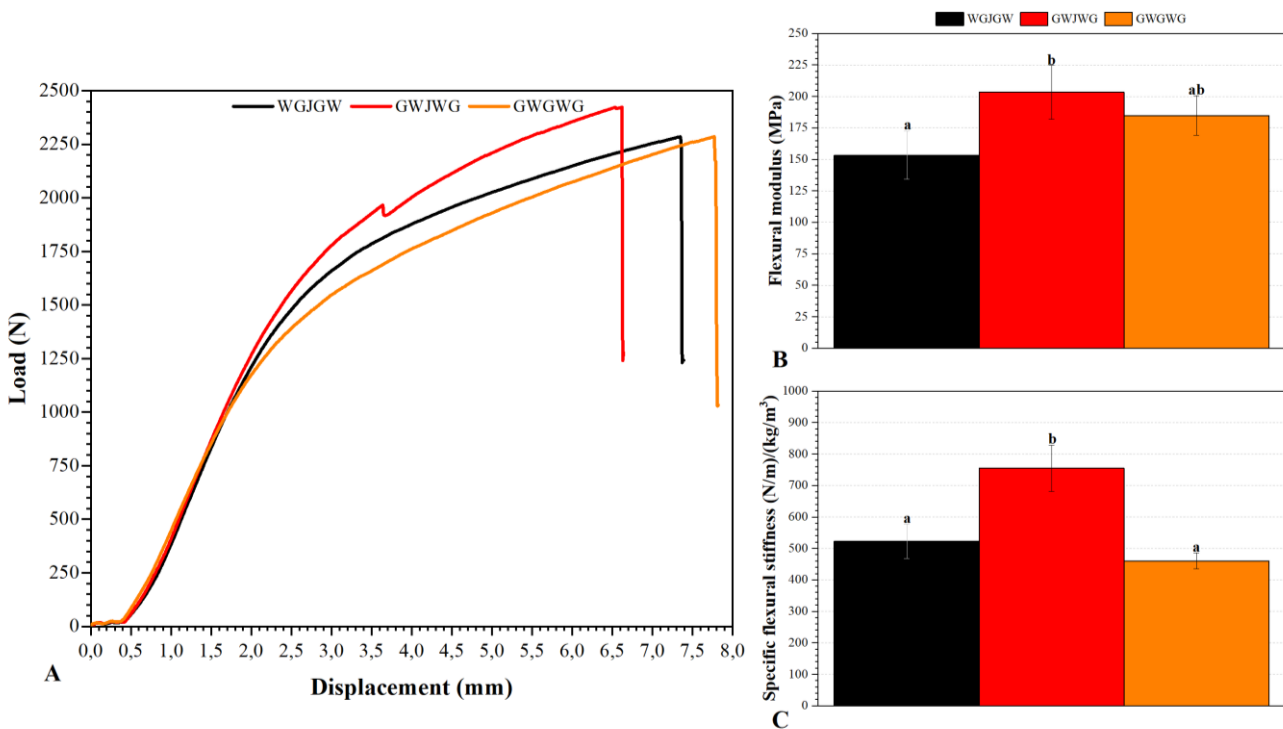
Figure 2 – Flatwise representative load vs. displacement curves (A), flatwise longitudinal flexural modulus (B) and flatwise specific flexural stiffness (C) of the manufactured sandwich structures (where: *different letters above the errors in each group represent a statistical difference)).

Shalbafan, et al. (2012) manufactured sandwich panels using a wood particleboard face and an expanded polystyrene core by hot pressing. The authors obtained modulus of rupture values of 11.5 and 10.6 MPa [10]. Compared to the panels in this study, they showed ~74% lower modulus of rupture. LI and coworkers (2014) also manufactured sandwich panels using wood derivatives with mixed faces, varying between paper and glass fibre laminates, and a triaxial core filled with polyurethane foam using the cold pressing technique. The authors obtained modulus of elasticity values of 16 to 18 MPa and values between 80.9 and 98.2 MPa [11]. Compared to the values obtained in the present study, the modulus of elasticity is ~90% higher. Another study which manufactured sandwich panels was by Lakreb and coworkers (2015) which used *Pinus Halepensis* laminates as the panel face and a core made up of agglomerated cork panels using the hot-pressing technique (SIMI), obtaining values between 1.27 and 4.60 MPa for modulus of elasticity and between 2.23 and 3.34 MPa for modulus of rupture [12]. Compared to the values obtained in this study, the modulus of elasticity is ~150% higher and the modulus of rupture ~90% higher. Thus, taking into account the studies carried out previously, parameters such as modulus of elasticity and modulus of rupture were higher in this study, which can be justified by the method used to manufacture the panels themselves, as well as the efficiency with which the adhesive was impregnated into the wood veneers, in addition to the presence of glass and/or jute fibres which favour the panel's mechanical performance.

Table 2 presents the results obtained from the flatwise flexural tests in terms of Ef/ρ (specific flexural modulus), K/ρ (specific flexural stiffness), and F_s^{ult}/ρ (specific core shear ultimate strength). Notably, the GWJWG configuration exhibited the highest value for Ef/ρ at 360.5 kPa·m³/kg, followed by WGWGW at 286.2 kPa·m³/kg and WGJGW at 251.8 kPa·m³/kg. It is worth noting that WGJGW and GWJWG sandwich structures exhibited a laminate stacking sequence effect, as observed in the literature [13]. The higher Ef/ρ value for GWJWG in comparison to WGWGW can be attributed to the presence of glass fiber layers on the surface, which possess higher mechanical strength relative to wood. A study by Da Silva and coworkers [14] demonstrated that in hybrid laminates, positioning glass fiber layers at the outer boundaries enhances mechanical performance, as most flexural rupture stresses predominantly occur in these regions. Furthermore, research suggests that mechanical behavior is enhanced when larger quantities of glass fiber layers are positioned adjacent to each other, promoting interfacial reinforcement between glass layers [8].

Table 2 - Specific flatwise flexural properties of the manufactured sandwich structures.

Group	E_f/ρ (kPa·m³/kg)	K/ρ (N/m)/(kg/m³)	F_s^{ult}/ρ (kPa.m³/kg)
WGJGW	251.8±29.0 (a)	522.6±54.5 (a)	3.38±0.08 (a)
GWJWG	360.5±36.0 (b)	755.4±73.6 (b)	3.49±0.17 (a)
GWGWG	286.2±19.1 (a)	459.7±25.7 (a)	3.43± 0.13 (a)

Where: Ef/ρ is specific flexural modulus; K/ρ is specific flexural stiffness and F_s^{ult}/ρ is specific core shear ultimate strength (*different letters next the errors in each group represent a statistical difference).

The parameter of Specific Flexural Stiffness (K/ρ) characterizes the relative stiffness concerning material density. Once again, GWJWG outperformed the other configurations, registering a value of 755.4 (N/m)/(kg/m³). Subsequently, WGWGW obtained 459.7 (N/m)/(kg/m³), while WGJGW achieved 522.6 (N/m)/(kg/m³). The higher specific flexural stiffness of GWJWG underscores the significance of optimizing the combination of skin and core materials to enhance overall stiffness [15]. The various combinations of the studied sandwich structures did not exhibit significant differences in the results of core shear ultimate strength. This is attributed to the high deformability of the faces, which induced premature core shear failure, indicating that this standard may not be suitable for the assessment of this novel material in this study.

As the study of flexural properties in the flatwise position was found to be inadequate for the material developed in this study, a transition was made to the investigation of flexural behavior in the edgewise position. According to Manalo et al. [16] in beams and similar applications, structural components are utilized in the lateral orientation to achieve increased strength and rigidity. These applications are akin to those of structural plywood loaded in the panel plane when used as the shear web of composite box beams, I-beams, or glue-laminated beams.

Fractography of the cross-section of the structure was used to reveal the interactions of the interfaces that occur in the composites. In the case of the GWGWG composite in Figure 3, it was used to reveal the interfaces between core and glass fibre that occur because of the infusion process.
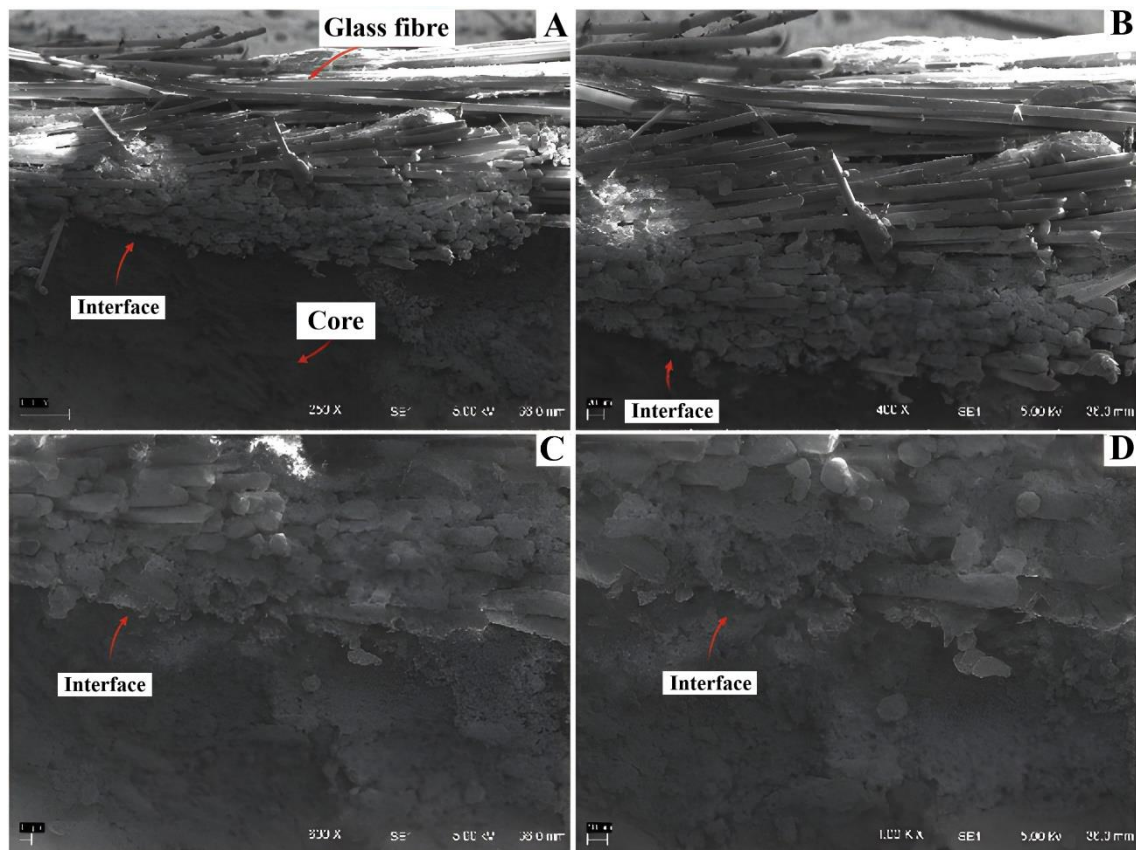
Figure 3 – SEM images of the interface of the GWGWG sandwich structure. Where: A is the image with 250× magnification; B is the image with 400× magnification; C is the image with 600× magnification and D is the image with 1000× magnification.

4. CONCLUSIONS

In this study, sandwich panels using a novel material as face reinforcement were successfully manufactured. The results showed that the density was higher (~15%) when greater quantities of wood were used on the faces (WGWGW), showing greater impregnation and retention of the resin in this case. However, the configuration with the best mechanical performance was GWJWG, with the highest values for specific flexural modulus (Ef/ρ) and specific flexural rigidity (K/ρ). This superior performance can be attributed to the presence of glass fibre layers on the surfaces, which provide greater mechanical resistance at the point of greatest stress concentration during the test. Scanning electron microscopy (SEM) analysis revealed effective interactions between the core and the glass fibres due to the infusion process. Compared to the wood-faced sandwich panels commonly reported in the literature, the panels developed showed significantly higher modulus of elasticity and modulus of rupture, indicating that the manufacturing technique, including efficient resin impregnation and the addition of glass and jute fibres, improved the mechanical properties of the panels. However, the high deformability of the faces resulted in premature failure of the core, suggesting that tests in other orientations, such as in the edgewise position, are necessary for a more adequate assessment of the material developed.

4.1 Declaration of Competing Interest

The authors declare no conflict of interest.

4.2 Acknowledgements

5. REFERENCES

[1] USDA - United States Departament of Agriculture, Solid Wood Products Annual 2023, Foreign Agric. Serv. (2023).

[2]   Mongabay, Timber harvests to meet global wood demand will bring soaring emissions: Study, (2023). https://news.mongabay.com/2023/07/timber-harvests-to-meet-global-wood-demand-will-bring-soaring-emissions-study/.

[3]   G. Bonifazi, L. Calienno, G. Capobianco, A. Lo Monaco, C. Pelosi, R. Picchio, S. Serranti, Modeling color and chemical changes on normal and red heart beech wood by reflectance spectrophotometry, Fourier Transform Infrared spectroscopy and hyperspectral imaging, Polym. Degrad. Stab. 113 (2015) 10–21. https://doi.org/10.1016/j.polymdegradstab.2015.01.001.

[4]   P. Gascón-Garrido, J. V. Oliver-Villanueva, M.S. Ibiza-Palacios, H. Militz, C. Mai, S. Adamopoulos, Resistance of wood modified with different technologies against Mediterranean termites (Reticulitermes spp.), Int. Biodeterior. Biodegrad. 82 (2013) 13–16. https://doi.org/10.1016/j.ibiod.2012.07.024.

[5]   A.P. Acosta, J. Labidi, K.T. Barbosa, N. Cruz, Termite Resistance of a Fast-Growing Pine Wood Treated by In Situ Polymerization of Three Di ff erent Precursors, (2020) 1–11.

[6]   M. Fleckenstein, V. Biziks, C. Mai, H. Militz, Modification of beech veneers with lignin phenol formaldehyde resins in the production of laminated veneer lumber (LVL), Eur. J. Wood Wood Prod. 76 (2018) 843–851. https://doi.org/10.1007/s00107-017-1275-7.

[7]   A.P. Acosta, A.A. Xavier da Silva, R. de Avila Delucis, S.C. Amico, Wood and wood-jute laminates manufactured by vacuum infusion, J. Build. Eng. 64 (2023) 105619. https://doi.org/10.1016/j.jobe.2022.105619.

[8]   A.P. Acosta, R. de Avila Delucis, S.C. Amico, Hybrid wood-glass and wood-jute-glass laminates manufactured by vacuum infusion, Constr. Build. Mater. 398 (2023) 132513. https://doi.org/10.1016/j.conbuildmat.2023.132513.

[9]   A. Pereira, R. De Avila, S. Campos, Hybrid wood-glass and wood-jute-glass laminates manufactured by vacuum infusion, Constr. Build. Mater. 398 (2023) 132513. https://doi.org/10.1016/j.conbuildmat.2023.132513.

[10]   A. Shalbafan, J. Welling, J. Luedtke, Effect of processing parameters on mechanical properties of lightweight foam core sandwich panels, Wood Mater. Sci. Eng. 7 (2012) 69–75. https://doi.org/10.1080/17480272.2012.661459.

[11]   J. Li, J.F. Hunt, S. Gong, Z. Cai, High strength wood-based sandwich panels reinforced with fiberglass and foam, BioResources. 9 (2014) 1898–1913. https://doi.org/10.15376/biores.9.2.1898-1913.

[12]   N. Lakreb, B. Bezzazi, H. Pereira, Mechanical behavior of multilayered sandwich panels of wood veneer and a core of cork agglomerates, Mater. Des. 65 (2015) 627–636. https://doi.org/10.1016/j.matdes.2014.09.059.

[13]   J.H. Song, Pairing effect and tensile properties of laminated high-performance hybrid composites prepared using carbon/glass and carbon/aramid fibers, Compos. Part B Eng. 79 (2015) 61–66. https://doi.org/10.1016/j.compositesb.2015.04.015.

[14]   R.V. da Silva, H. Voltz, A.I. Filho, M. Xavier Milagre, C. de S. Carvalho Machado, Hybrid composites with glass fiber and natural fibers of sisal, coir, and luffa sponge, J. Compos. Mater. 55 (2021) 717–728. https://doi.org/10.1177/0021998320957725.

[15]   B. Abdi, S. Azwan, M.R. Abdullah, A. Ayob, Y. Yahya, L. Xin, Flatwise compression and flexural behavior of foam core and polymer pin-reinforced foam core composite sandwich panels, Int. J. Mech. Sci. 88 (2014) 138–144. https://doi.org/10.1016/j.ijmecsci.2014.08.004.

[16]   W. Ferdous, A. Manalo, O. AlAjarmeh, A.A. Mohammed, C. Salih, P. Yu, M. Mehrinejad Khotbehsara, P. Schubel, Static behaviour of glass fibre reinforced novel composite sleepers for mainline railway track, Eng. Struct. 229 (2021) 111627. https://doi.org/10.1016/j.engstruct.2020.111627.

GLOBAL BUCKLING OF THIN-WALLED COMPOSITE COLUMNS WITH CHANNEL SECTIONS

Pedro Sanderson Bastos Barros[a], Luiz Antônio Taumaturgo Mororó[b], Evandro Parente Junior [c], *

(a) ⓘ 0009-0001-6178-2195 (Instituto Federal de Educação, Ciência e Tecnologia do Ceará – Brasil)
(b) ⓘ 0000-0003-2247-2511 (Instituto Federal de Educação, Ciência e Tecnologia do Ceará – Brasil)
(c) ⓘ 0000-0003-0219-1376 (Universidade Federal do Ceará – Brasil)
* Corresponding author: evandro@ufc.br

Abstract: This work presents a methodology to evaluate the global buckling load of laminated channel columns considering the effects of bending, bending-torsion, and restrained warping. The equivalent cross-sectional properties are obtained using a theory for thin-walled composite beams with arbitrary layup and the Rayleigh-Ritz method is applied to evaluate the global buckling loads. The accuracy of the proposed approach is assessed comparing the results obtained using the Finite Strip Method and the Finite Element Method for different layups. Very good results were obtained applying the proposed methodology.

1. INTRODUCTION

Buckling is a major concern in the design of laminated structures, since they tend to be very slender, and failure can occur with stresses much lower than the material's strength. Thin-walled laminated columns with channel section present two main buckling modes: local and global.

Debski et al. [1] presents experimental results for the local buckling of laminated channel columns with different layups and compared the results with those obtained using shell finite elements. D'Aguiar and Parente [2] proposed an approximate methodology for evaluating the local buckling load of laminated columns with channel sections and studied the post-critical behaviour of imperfect columns using shell finite elements. Aguiar et al. [3] presented comparisons between analytical, numerical, and experimental solutions for the local buckling load of thin-walled composite columns for various layups. The Finite Element Method (FEM) was used to assess approximate solutions obtained by the Rayleigh-Ritz method and to evaluate the failure load considering geometric imperfections, geometric nonlinearity, and material failure.

The global stability of columns with open cross-sections is a complex phenomenon due to the presence of different buckling modes, bending-torsion coupling and restrained warping. For columns of homogenous materials accurate closed-form expressions can be obtained using the theory of thin-walled beams with restrained warping and the Rayleigh-Ritz method [4]. Extension of this approach to laminated columns is complex due to the coupling induced by the composite layup.

Kollar and Pluzsik [5] developed a formulation to obtain a fully coupled cross-sectional stiffness matrix of thin-walled laminated beams with open or closed cross-sections with arbitrary layup. Pluzsik and Kollar [6] extended this theory developed to consider the effects of transverse shear and restrained warping. Mororó et al. [7] developed a 3D frame element for laminated beam analysis to large displacement analysis, considering moderate rotations, based on Kollar and Pluzsik [5] theory. Mororó et al. [8] proposed two frame finite elements for 3D nonlinear analyses of laminated beams with large rotations and applied these elements to the stability analysis of laminated columns and frames with different cross-sections and layups.

It is important to note the local and global buckling loads of thin-walled composite columns with open cross-section and arbitrary layup can be accurately computed using FEM. However, the application of this approach to trace the signature curve is cumbersome and presents a high computational cost. Therefore, this work presents a simple and efficient methodology for computation of the global buckling loads of laminated columns with channel sections.

2. METHODOLOGY

The methodology proposed in this work consists of two stages. In the first one, the theory of laminated beams proposed by Kollar and Pluzsik [5] and its extension presented by Pluzsik and Kollar [6] are used for determining the equivalent properties of an arbitrary cross-section. In the second stage, the Rayleigh-Ritz Method is employed to obtain semi-analytical equations for calculating the global critical loads of channel columns for different buckling modes.

2.1. Cross-sectional Equivalent Properties

Kollar and Pluzsik [5] proposed a general theory to analyze thin-walled laminated beams and presented analytical expressions for constitutive matrix ($\mathbf{C}$) for open and closed sections. The beam's wall consists of n flat segments each one may be made of composite materials with arbitrary layup.

As indicated in Figure 1-a, the following coordinate system are employed: x-y-z global coordinate system with origin at the mechanical centroid (point C); $\bar{x}$-$\bar{y}$-$\bar{z}$ global coordinate system with origin at an arbitrary chosen point (point O); x_k-r_k-s_k local coordinate system for the k-th segment with origin at the center of reference plane of the k-th segment (point c_k). Each x_k, s_k and r_k axes are, respectively, parallel to the x coordinate, along the segment and normal to the segment.

According to Classical Laminated Theory (CLT) the strain-stress relationship in the k-th segment may be given by [9]:

$$
\begin{bmatrix} \varepsilon_x^k \\ \varepsilon_s^k \\ \gamma_{xs}^k \\ \kappa_x^k \\ \kappa_s^k \\ \kappa_{xs}^k \end{bmatrix} = \begin{bmatrix} \alpha_{11} & \alpha_{12} & \alpha_{16} & \beta_{11} & \beta_{12} & \beta_{16} \\ \alpha_{12} & \alpha_{22} & \alpha_{26} & \beta_{21} & \beta_{22} & \beta_{26} \\ \alpha_{16} & \alpha_{26} & \alpha_{66} & \beta_{61} & \beta_{62} & \beta_{66} \\ \beta_{11} & \beta_{21} & \beta_{61} & \delta_{11} & \delta_{12} & \delta_{16} \\ \beta_{12} & \beta_{22} & \beta_{62} & \delta_{12} & \delta_{22} & \delta_{26} \\ \beta_{16} & \beta_{26} & \beta_{66} & \delta_{16} & \delta_{26} & \delta_{66} \end{bmatrix} \begin{bmatrix} N_x^k \\ N_s^k \\ N_{xs}^k \\ M_x^k \\ M_s^k \\ M_{xs}^k \end{bmatrix} \Rightarrow \begin{bmatrix} \boldsymbol{\varepsilon} \\ \boldsymbol{\kappa} \end{bmatrix} = \begin{bmatrix} \boldsymbol{\alpha} & \boldsymbol{\beta} \\ \boldsymbol{\beta}^T & \boldsymbol{\delta} \end{bmatrix} \begin{bmatrix} \mathbf{N} \\ \mathbf{M} \end{bmatrix} \tag{1}
$$

The relationship between the displacements and the axial strain ε_x, the curvatures κ_y and κ_z, and the first derivative of the twist angle, φ, respectively, are:

$$
\varepsilon_x = \frac{\partial u}{\partial x} \qquad \kappa_y = \frac{\partial^2 v}{\partial x^2} \qquad \kappa_z = \frac{\partial^2 w}{\partial x^2} \qquad \varphi = \frac{\partial \beta}{\partial x} \tag{2}
$$

u is the longitudinal displacement, v and w are the transverse displacements in the y and z directions, respectively, and β is the twist angle of beam. Figure 1-b shows the beam forces acting on global coordinate system for a beam with arbitrary section.

Considering arbitrary layup and arbitrary cross-section, but neglecting the effects due to transverse shear deformation and to restrained warping, the constitutive relation for thin-walled laminated composite beams can be given by:

$$
\begin{bmatrix} N_x \\ M_y \\ M_z \\ T \end{bmatrix} = \begin{bmatrix} C_{11} & C_{12} & C_{13} & C_{14} \\ C_{12} & C_{22} & C_{23} & C_{24} \\ C_{13} & C_{23} & C_{33} & C_{34} \\ C_{14} & C_{24} & C_{34} & C_{44} \end{bmatrix} \begin{bmatrix} \varepsilon_x \\ \kappa_y \\ \kappa_z \\ \varphi \end{bmatrix} \Rightarrow \boldsymbol{\sigma} = \mathbf{C} \cdot \boldsymbol{\varepsilon} \tag{3}
$$

The procedure for obtaining the cross-section equivalent properties proposed by Kollar and Pluzsik [5] for open section beams consists of four steps:

1. The deformations in each segment must be related to axial strain, curvatures, and the rate of twist angle.
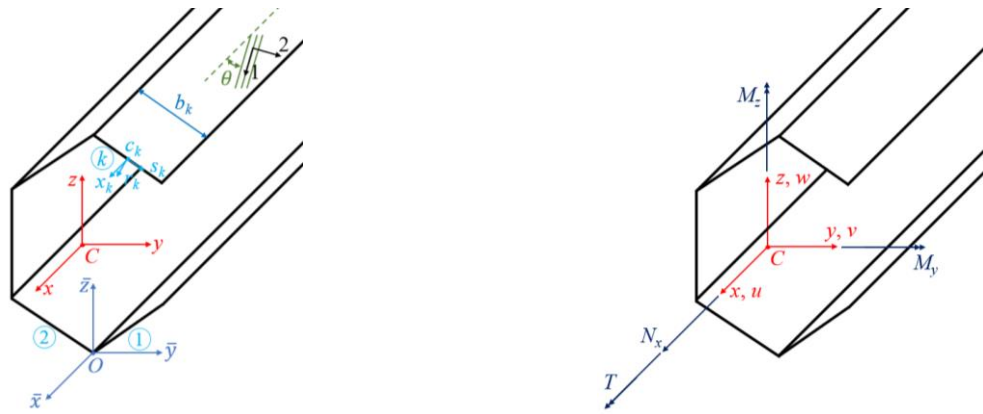
Figure 1. Thin-walled laminated beam with open cross-sections with arbitrary layup: (a) cross-section segments and coordinate systems, and (b) beam forces.

2. The forces in each segment of the section are determined from the strains obtained in the previous step.
3. The resultant normal force, as well as the bending moments and torsional moment, are obtained from the forces in each wall of the cross-section.
4. The stiffness matrix is established by relating the resultant forces (normal force, bending moments, and torsional moment) to the axial strain, curvatures, and rate of twist angle.

Applying the procedure proposed by the authors is possible to obtain the follow equation:

$$\bar{C} = R_k^T \cdot \omega_k^{-1} \cdot R_k \tag{4}$$

being:

$$
R_k = \begin{bmatrix} 1 & \bar{z}_k & \bar{y}_k & 0 \\ 0 & \cos \alpha_k & -\sin \alpha_k & 0 \\ 0 & \sin \alpha_k & \cos \alpha_k & 0 \\ 0 & 0 & 0 & 1 \end{bmatrix}, \quad
\omega_k = \frac{1}{b_k} \begin{bmatrix} \alpha_{11} & \beta_{11} & 0 & -\frac{1}{2}\beta_{16} \\ \beta_{11} & \delta_{11} & 0 & -\frac{1}{2}\delta_{16} \\ 0 & 0 & \dfrac{12}{\left(\tilde{A}_{11}\right)_k \cdot b_k^2} & 0 \\ -\frac{1}{2}\beta_{16} & -\frac{1}{2}\delta_{16} & 0 & \frac{1}{4}\delta_{66} \end{bmatrix} \tag{5}
$$

where b_k is the width of the the k-th segment, $\bar{z}$ and $\bar{y}$ are the origin coordinates of the x_k-s_k-r_k local system for the k-th segment. The angle α_k is the angle between the local s_k and global y axes. $\left(\tilde{A}_{11}\right)_k$ can be obtained by:

$$
\begin{bmatrix} \tilde{A}_{11} & \tilde{A}_{12} & \tilde{A}_{13} \\ \tilde{A}_{12} & \tilde{A}_{22} & \tilde{A}_{23} \\ \tilde{A}_{13} & \tilde{A}_{23} & \tilde{A}_{33} \end{bmatrix}_k = \begin{bmatrix} \alpha_{11} & \beta_{11} & \beta_{16} \\ \beta_{11} & \delta_{11} & \delta_{16} \\ \beta_{16} & \delta_{16} & \delta_{66} \end{bmatrix}_k^{-1} \tag{6}
$$

The Eqs. (4), (5) and (6) must be used to obtain the cross-sectional stiffness matrix of an open section beam in an arbitrarily chosen coordinate system. To determine the cross-sectional stiffness matrix in the global coordinate system, the mechanical centroid must be known. The y_c and z_c coordinates can be obtained by:

$$
\begin{bmatrix} z_c \\ y_c \end{bmatrix} = - \begin{bmatrix} \bar{W}_{22} & \bar{W}_{23} \\ \bar{W}_{23} & \bar{W}_{33} \end{bmatrix}^{-1} \begin{bmatrix} \bar{W}_{12} \\ \bar{W}_{13} \end{bmatrix} \tag{7}
$$

where $\bar{W} = \bar{C}^{-1}$. Finally, the stiffness matrix C in the global coordinate system, as shown in Eq. (3), can be obtained by:

$$W = R_b^T \cdot \bar{W}^{-1} \cdot R_b \quad \Rightarrow \quad C = W^{-1} \tag{8}$$

where:

$$\mathbf{R}_b = \begin{bmatrix} 1 & 0 & 0 & 0 \\ z_c & 1 & 0 & 0 \\ y_c & 0 & 1 & 0 \\ 0 & 0 & 0 & 1 \end{bmatrix} \tag{9}$$

To simplify the application of the Rayleigh-Ritz method, equivalent stiffness properties are considered. To compute these equivalent cross-sectional properties, the **C** matrix presented in Eqs. (3) and (8) will be inverted and the terms off the main diagonal will be neglected. Then, a new inversion is performed, resulting in a diagonalized matrix:

$$\begin{bmatrix} N_x \\ M_y \\ M_z \\ T_{sv} \end{bmatrix} = \begin{bmatrix} \overline{C}_{11} & 0 & 0 & 0 \\ 0 & \overline{C}_{22} & 0 & 0 \\ 0 & 0 & \overline{C}_{33} & 0 \\ 0 & 0 & 0 & \overline{C}_{44} \end{bmatrix} \begin{bmatrix} \varepsilon_x \\ \kappa_y \\ \kappa_z \\ \varphi \end{bmatrix} = \begin{bmatrix} \overline{EA} & 0 & 0 & 0 \\ 0 & \overline{EI}_y & 0 & 0 \\ 0 & 0 & \overline{EI}_z & 0 \\ 0 & 0 & 0 & \overline{GJ} \end{bmatrix} \begin{bmatrix} \varepsilon_x \\ \kappa_y \\ \kappa_z \\ \varphi \end{bmatrix} \tag{10}$$

where $\overline{EA}$ is the axial stiffness, $\overline{EI}_y$ and $\overline{EI}_z$ are the bending stiffness, $\overline{GJ}$ is the torsional stiffness of the cross-section. This approach allows the consideration of the couplings due to the off diagonal terms in a simple way.

Pluszik and Kollar [6] extended the theory addressed by Kollar and Pluzsik [5] by including the effects of restrained warping of the cross-section. In this work, torsional moment *T* is given by:

$$T = T_{sv} + T_\omega = \overline{GJ} \cdot \varphi + \overline{EI}_\omega \cdot \Gamma = \overline{GJ} \cdot \frac{\partial \beta}{\partial x} + \overline{EI}_\omega \cdot \frac{\partial^2 \beta}{\partial x^2} \tag{11}$$

T_{sv} is the uniform torsion component (Saint-Venant), T_ω is the non-uniform torsion component due to restrained warping, and $\overline{EI}_\omega$ is the warping stiffness.

When the layup is balanced, Pluzsik and Kollar [6] shows that the beam displacements can be approximated by combining the stiffness properties derived for a generally anisotropic beam and the warping stiffness derived for an orthotropic beam. The authors also indicates that for an orthotropic beam the warping stiffness and the shear center can be evaluated by the expressions given for an isotropic beam by replacing the terms Eh by $1/\alpha_{11}^\rho$, where h is the laminate thickness. The superscript ρ indicates that α_{11}^ρ is evaluated at the laminate "tension neutral" surface, which can be calculated by [6]:

$$\alpha_{11}^\rho = \alpha_{11} + 2 \cdot \rho \cdot \beta_{11} + \rho^2 \cdot \delta_{11} \quad \text{where} \quad \rho = -\frac{\beta_{11}}{\alpha_{11}} \tag{12}$$

The coefficients α_{11}, β_{11} and δ_{11} are obtained from the strain-stress relationship presented in Eq. (1), which are evaluated at the middle surface of the laminate.

Thus, the warping stiffness $\overline{EI}_\omega$ and the position of the shear center y_s of a channel section (see Figure 2) can be determined by [6]:

$$\overline{EI}_\omega = \frac{(1/\alpha_{11}^\rho) \cdot d^2 \cdot b^3}{12} \cdot \frac{\left[3 \cdot b/(\alpha_{11}^\rho)_f + 2 \cdot d/(\alpha_{11}^\rho)_w\right]}{\left[6 \cdot b/(\alpha_{11}^\rho)_f + d/(\alpha_{11}^\rho)_w\right]} \tag{13}$$

$$y_s = \frac{3 \cdot b^2 /(\alpha_{11}^\rho)_f}{6 \cdot b/(\alpha_{11}^\rho)_f + d/(\alpha_{11}^\rho)_w} \tag{14}$$

where the subscripts *f* and *w* in $(\alpha_{11}^\rho)_f$ and $(\alpha_{11}^\rho)_w$ refer to the flange and the web, respectively. In this work, the same layup is used in the web and flanges, therefore $(\alpha_{11}^\rho)_w = (\alpha_{11}^\rho)_f$.

2.2. Rayleigh-Ritz Method

The total potential energy of a simple supported column with open cross section is given by:

$$\Pi = U + V \tag{15}$$

where the strain energy U of the column and the potential of the applied loads V can be obtained from the expression for homogenous columns [4] using the equivalent cross-sectional stiffnesses:

$$U = \int \frac{1}{2} \boldsymbol{\varepsilon}^T \cdot \boldsymbol{\sigma} \, dx = \frac{1}{2} \int_L \left[\overline{EI}_y \cdot \left(\frac{\partial^2 v}{\partial x^2} \right)^2 + \overline{EI}_z \cdot \left(\frac{\partial^2 w}{\partial x^2} \right)^2 + \overline{GJ} \cdot \left(\frac{\partial \beta}{\partial x} \right)^2 + \overline{EI}_\omega \cdot \left(\frac{\partial^2 \beta}{\partial x^2} \right)^2 \right] \cdot dx \tag{16}$$

$$V = -\frac{P}{2} \int_L \left[\left(\frac{\partial v}{\partial x} \right)^2 + \left(\frac{\partial w}{\partial x} \right)^2 + r_0^2 \cdot \left(\frac{\partial \beta}{\partial x} \right)^2 - 2z_0 \cdot \left(\frac{\partial v}{\partial x} \right) \cdot \left(\frac{\partial \beta}{\partial x} \right) + 2y_0 \cdot \left(\frac{\partial w}{\partial x} \right) \cdot \left(\frac{\partial \beta}{\partial x} \right) \right] \cdot dx \tag{17}$$

where y_0 and z_0 are the distances of the mechanical centroid C to the shear center S of the cross section and r_0 is the polar radius of gyration with respect to the shear center, as shown in Figure 2.
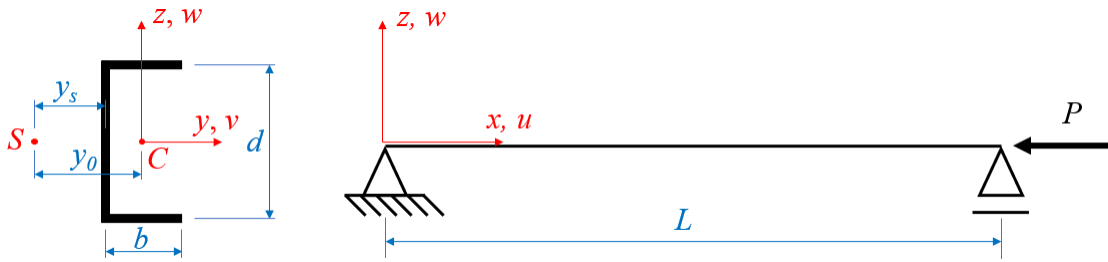
Figure 2. Geometry and boundary conditions of the columns.

For a simply supported column, the approximation functions defining the displacements in the plane of the cross-section and the twist angle presented in the previous equations are given by:

$$v(x) = v_0 \cdot sen\left(\frac{\pi x}{L} \right) \qquad w(x) = w_0 \cdot sen\left(\frac{\pi x}{L} \right) \qquad \beta(x) = \beta_0 \cdot sen\left(\frac{\pi x}{L} \right) \tag{18}$$

The critical load is defined as the load at which an equilibrium configuration is possible in a slightly deformed state. Thus, the critical load is the load at which the total potential energy is stationary. This occurs when its derivative with respect to each of the variables is zero, leading to a set of homogeneous linear equations. This set of equations has a trivial solution, where $v_0 = w_0 = \beta_0 = 0$, and a non-trivial solution, given by the solution of the following equation:

$$\left(P_y - P \right) \cdot \left(P_z - P \right) \cdot \left(P_\beta - P \right) - \left(P_z - P \right) \cdot \frac{P^2 \cdot y_0^2}{r_0^2} - \left(P_y - P \right) \cdot \frac{P^2 \cdot z_0^2}{r_0^2} = 0 \tag{19}$$

where:

$$P_y = \frac{\pi^2 \cdot \overline{EI}_y}{L^2} \qquad P_z = \frac{\pi^2 \cdot \overline{EI}_z}{L^2} \qquad P_\beta = \frac{1}{r_0^2} \left(\overline{GJ} + \frac{\pi^2 \cdot \overline{EI}_\omega}{L^2} \right) \tag{20}$$

Eq. (19) is cubic in P and its roots are the critical loads of the column. If the layup is symmetric and the cross-section is doubly symmetric, $y_0 = z_0 = 0$, and the critical loads of the column are given by Eq. (20). This indicates that P_y is the major-axis bending buckling load, P_z is the minor-axis bending buckling load, and P_β is the buckling load due to torsion and warping of the cross-section.

For channels and other mono-symmetric sections, the shear center is located at the symmetry axis. Thus, $z_0 = 0$, and Eq. (19) can be reduced to:

$$\left(P_z - P \right) \cdot \left[\left(P_y - P \right) \cdot \left(P_\beta - P \right) - \frac{P^2 \cdot y_0^2}{r_0^2} \right] = 0 \tag{21}$$

The solution of this equation indicates that the critical load of the column will be the smaller load between that the minor-axis bending ($P_F = P_z$) load and the flexural-torsional (P_{FT}) load, given by:

$$P_F = \frac{\pi^2 \cdot \overline{EI}_z}{L^2} \qquad P_{FT} = \frac{1}{2k} \left[\left(P_y + P_\beta \right) - \sqrt{\left(P_y + P_\beta \right)^2 - 4k \cdot P_y \cdot P_\beta} \right] \tag{22}$$

where $k = [1 - (y_0/r_0)^2]$.

3. RESULTS AND DISCUSSION

For assessment of the proposed approach, a numerical application for a simply supported channel column with four layups were carried out and the results are compared with the Finite Strip Method (FSM) [10] results obtained using CUFSM [11, 12] and FStr [13, 14], and Finite Element Method (FEM) using ABAQUS [15].

The geometric properties of the channel are: width b = 40 mm, height d = 80 mm (see Figure 2), and total thickness h = 1.048 mm; and the material properties used are [1]: E_1 = 130.71 GPa, E_2 = 6.36 GPa, G_{12} = 4.18 GPa, and ν_{12} = 0.32. The layups proposed are: L1 $[0°]_8$, L2 $[(0°/90°)_2]_S$, L3 $[(45°/-45°)_2]_S$, and L4 $[(30°/-30°)_4]$.

The cross-sectional constitutive matrix **C** for the laminated channel columns showed in Eq. (3) and Eq. (8) is presented in Figure 3 for the layups L1, L2, L3 and L4, respectively. The cross-sectional equivalent properties obtained by diagonalization described in Section 2.1 is presented in Table 1.

$$\mathbf{C} = \begin{bmatrix} 2.1917 \cdot 10^7 & 0 & 0 & 0 \\ 0 & 2.3380 \cdot 10^4 & 0 & 0 \\ 0 & 0 & 3.6539 \cdot 10^3 & 0 \\ 0 & 0 & 0 & 0.2566 \end{bmatrix} \qquad \mathbf{C} = \begin{bmatrix} 1.1519 \cdot 10^7 & 0 & 0 & 0 \\ 0 & 1.2309 \cdot 10^4 & 0 & 0 \\ 0 & 0 & 1.9239 \cdot 10^3 & 0 \\ 0 & 0 & 0 & 0.2566 \end{bmatrix}$$

$$\mathbf{C} = \begin{bmatrix} 2.508 \cdot 10^6 & 0 & 0 & 0 \\ 0 & 2.6753 \cdot 10^3 & 0 & -0.0379 \\ 0 & 0 & 4.1811 \cdot 10^2 & 0.0379 \\ 0 & -0.0379 & 0.0379 & 1.8388 \end{bmatrix} \qquad \mathbf{C} = \begin{bmatrix} 6.9768 \cdot 10^6 & 0 & 0 & 3.8976 \cdot 10^2 \\ 0 & 7.4422 \cdot 10^3 & 0 & 0 \\ 0 & 0 & 1.1631 \cdot 10^3 & 0 \\ 3.8976 \cdot 10^2 & 0 & 0 & 1.5647 \end{bmatrix}$$

Figure 3. Cross-section constitutive matrix **C** for the laminated columns: (a) L1, (b) L2, (c) L3, and (d) L4.

Table 1. Cross-sectional equivalent properties for the laminated columns.

Layup	$\overline{EA}$ ($\times 10^7$ N)	$\overline{EI}_y$ ($\times 10^4$ N.m²)	$\overline{EI}_z$ ($\times 10^3$ N.m²)	$\overline{GJ}$ (N.m²)	$\overline{EI}_\omega$ (N.m⁴)
L1	2.1917	2.3380	3.6539	0.2566	4.0913
L2	1.1539	1.2309	1.9239	0.2566	2.1540
L3	0.2508	0.2675	0.4181	1.8388	0.4682
L4	0.6880	0.7442	1.1631	1.5429	1.2842

For the finite element mesh, a 10 mm S8R square element was adopted. On the other hand, it is important to note that Finite Strip Method programs, CUFSM and FStr, were developed for the analysis of columns made of isotropic or orthotropic materials. Therefore, it was necessary to obtain the mechanical properties of an equivalent orthotropic material. For this, the approach proposed by Barbero [9] was used, where the equivalent properties for global and local buckling are given by:

$$E_{1,eq}^{global} = \frac{1}{h \cdot \alpha_{11}} \qquad E_{2,eq}^{global} = \frac{1}{h \cdot \alpha_{22}} \qquad G_{12,eq}^{global} = \frac{1}{h \cdot \alpha_{66}} \qquad \nu_{12,eq}^{global} = -\frac{\alpha_{12}}{\alpha_{11}} \qquad (23)$$

$$E_{1,eq}^{local} = \frac{12}{h^3 \cdot \delta_{11}} \qquad E_{2,eq}^{local} = \frac{12}{h^3 \cdot \delta_{22}} \qquad G_{12,eq}^{local} = \frac{12}{h^3 \cdot \delta_{66}} \qquad \nu_{12,eq}^{local} = -\frac{\delta_{12}}{\delta_{11}} \qquad (24)$$

where α_{ij} and δ_{ij} are defined in Eq. (1). Table 2 and Table 3 presents the equivalent orthotropic material properties obtained applying Eqs. (23) and (24) for the layups considered in this paper.

The results obtained for the critical load of the columns for various lengths are available in Figure 4 below. There is excellent agreement in the results obtained via Rayleigh-Ritz, FEM, and FSM with equivalent orthotropic properties, except when the loss of stability is due to local buckling, which was out of scope of the present work. It is important to note that for FSM, the critical loads for each laminate were obtained by using the equivalent properties defined in Eqs. (23) and (24), with the lowest value for each length being considered the buckling load.

Table 2. Equivalent orthotropic material properties for global buckling analyses.

Layup	$E_{1,eq}$ (GPa)	$E_{2,eq}$ (GPa)	$G_{12,eq}$ (GPa)	$\upsilon_{12,eq}$
L2	68.817	68.817	4.180	0.0297
L3	14.957	14.957	33.416	0.7891
L4	41.029	8.349	25.134	1.4963

Table 3. Equivalent orthotropic material properties for local buckling analyses.

Layup	$E_{1,eq}$ (GPa)	$E_{2,eq}$ (GPa)	$G_{12,eq}$ (GPa)	$\upsilon_{12,eq}$
L2	92.219	45.400	4.180	0.0450
L3	14.753	14.753	29.545	0.7647
L4	41.029	8.349	25.134	1.4963
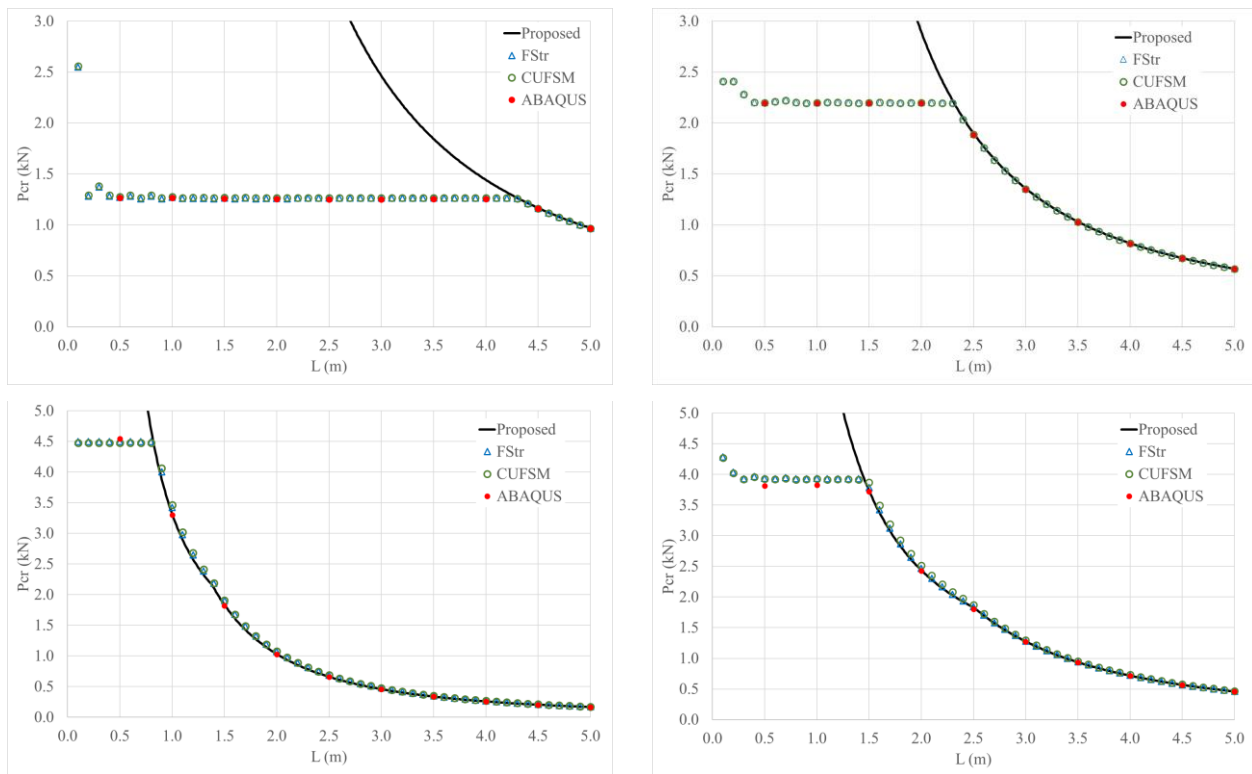
Figure 4. Signature curves of the columns: (a) L1, (b) L2, (c) L3, and (d) L4.

It was also observed that local buckling mode was dominant for L1 layup within the investigated length range, while global flexural-torsional and minor-axis bending modes stood out for L3 and L4 layups. For the range of lengths analysed, a shift from local buckling mode to flexural-torsional mode was observed in all layups. On the other hand, only in layups L3 and L4 was noticed a transition from flexural-torsional mode to a minor-axis bending mode. Figure 5 shows the buckling modes obtained in FStr for $L = 4.50$ m.
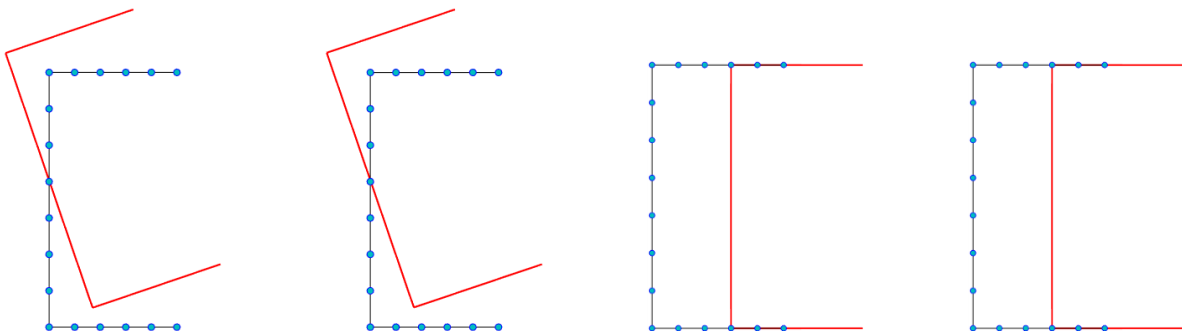
Figure 5. Buckling modes obtained in FStr for $L = 4.50$ m: (a) L1, (b) L2, (c) L3, and (d) L4.

4. CONCLUSIONS

This work presented a simple and efficient approach to evaluate the global buckling load of laminated composite channel columns considering the effects of bending, bending-torsion, and restrained warping. In this approach, the equivalent cross-sectional properties are evaluated using a well-known theory of thin-walled beams with arbitrary layups and simple closed-form expressions to evaluate the global buckling loads are obtained using the Rayleigh-Ritz method.

The signature curves of a laminate channel column were traced for different layups and an excellent agreement was verified between the results of the proposed methodology and the results obtained by the Finite Element Method and the Finite Strip Method for lengths where buckling is dominated by the global modes.

4.1. Declaration of Competing Interest

The authors declare no conflict of interest.

4.2. Acknowledgements

5. REFERENCES

[1] H. Debski, T. Kubiak and A. Teter. Experimental investigation of channel-section composite profiles behavior with various sequences of plies subjected to static compression. *Thin-Walled Structures*, v. 71, pp. 147-154, 2013.

[2] S. C. M. D'Aguiar, E. Parente Junior. Local buckling and post-critical behavior of thin-walled composite channel section columns. *Latin American Journal of Solids and Structures*, vol. , 2018.

[3] J. Aguiar Junior, E. Parente Junior, M. S. Medeiros Junior. Assessment of the load-carrying capacity of laminated composite columns. *Proceedings of the 6th Brazilian Conference on Composite Materials*, 2022.

[4] A. Chajes. *Principles of structural stability theory*. Prentice Hall, 1974.

[5] L. P. Kollár and A. Pluzsik. Analysis of thin-walled composite beams with arbitrary layup. *Journal of Reinforced Plastics and Composites*, vol. 21, n. 16, pp. 1423–1465, 2002.

[6] A. Pluzsik, L. P. Kollár. Effects of Shear Deformation and Restrained Warping on the Displacements of Composite Beams. *Journal of Reinforced Plastics and Composites*, vol. 21, n. 17, pp. 1517–1541, 2002.

[7] L. A. T. Mororó, A. M. C. Melo, E. Parente Junior. Geometrically nonlinear analysis of thin-walled laminated composite beams. *Latin American Journal of Solids and Structures*, vol. , 2015.

[8] L. A. T. Mororó, A. M. C. Melo, E. Parente Junior, E. Lucena Neto, and F. A. C. Monteiro. Corotational elements for thin-walled laminated composite beams with large 3d rotations. *Thin-Walled Structures*, vol. 152, pp. 106375, 2020.

[9] E. J. Barbero. *Introduction to composite materials design*. CRC Press, 2011.

[10] Y. K. Cheung, L. G. Tham. *Finite Strip Method*. Taylor & Francis, 1998.

[11] B. W. Schafer. *Cold-formed steel behavior and design: analytical and numerical modeling of elements and members with longitudinal stiffeners*. Dissertation (PhD) - Cornell University, Ithaca, New York, 1997.

[12] B. W. Schafer. CUFSM – Constrained and Unconstrained Finite Strip Method 2023 [Computer software]. (https://www.ce.jhu.edu/cufsm/)

[13] J. A. Lazzari, E. M. Batista. Finite strip method computer application for buckling analysis of thin-walled structures with arbitrary cross-sections. *REM - International Engineering Journal*, v. 74, p. 337-344, 2021.

[14] J. A. Lazzari, E. M. Batista. FSTr – Finite Strip Computer Application 2023 [Computer software]. (https://sites.google.com/coc.ufrj.br/fstr).

[15] Simulia. *ABAQUS/Standard user's manual*, Version 6.13, Providence, RI, USA, 2013.

Structural Analysis of a Carbon Fiber and Additive Manufactured Anti-Roll Bar for Vehicle Chassis

Luiz G.S. Alberto(a), Euclides D.M. Santanna (b), Carla T.M. Anflor

(a) [ID] 0009-0006-0652-3779 (University of Brasília – Brazil)
(b) [ID] 0009-0002-2397-9103 (University of Brasília – Brazil)
(c) [ID] 0000-0003-3941-8335 (University of Brasília – Brazil)
[a] gustavogu48@yahoo.com
[b] euclides.anna@unb.br
[c] anflor@unb.br

Abstract: This study investigates the influence of an anti-roll bar, manufactured using carbon fiber composite and additive manufacturing (AM), on high-level professional Kart vehicles designed for competitions. A computational model of the vehicle was developed to analyze the forces acting on the composite under operational conditions. External loads were determined from theoretical calculations and experimental data, accurately representing real competition conditions. The anti-roll bar geometry was designed to allow stiffness changes based on the operating angle, enabling adjustments for pilot preference. The bar was manufactured using AM, coated with carbon fiber and epoxy resin. For the numerical model, the loading condition was defined to simulate a kart taking a turn with a lateral acceleration of 2G. Using the lateral load transfer equation, a load of 270 N was applied in simulations. The ACP Pre tool in ANSYS® was used to model the composite materials, determining fiber directions and layers. Results showed that adjustments to the thickness of the anti-roll bar material influence overall stiffness, and the absence of fibrous reinforcement significantly increases structural deformation. The inclusion and variations of the anti-roll bar directly increased the overall stiffness of the model, demonstrating its strong influence on the structural and dynamic performance of professional competition karts.

1. INTRODUCTION

Karts are motor vehicles characterized by their reduced weight and tubular chassis without suspension. Competitions have played a crucial role in the technological advancement of these vehicles, driving the search for greater power, reduced weight, and increased agility on the track. To meet these demands, teams began using multiple chassis and engines, allowing for adjustments in rigidity and power for each specific track. Inspired by the automotive industry, concepts of vehicle dynamics were applied, even without suspension in karts.

During this time, while cars were built with rigid materials like steel, karts had simpler and more flexible structures, allowing the chassis to behave similarly to a suspension, especially during corners. To enhance kart dynamics, studies were conducted on lateral and longitudinal load transfer, as well as control of chassis rigidity and roll. The anti-roll bar, mentioned by [1], plays a crucial role in this process by reducing body roll by vertically connecting the wheels on the same axle. However, this bar primarily affects lateral wheel movements, with limited applicability to longitudinal movements such as acceleration and braking.

The configuration of the anti-roll bar, including its positioning, material, and geometry, directly impacts chassis rigidity. Therefore, conducting analytical studies to determine how these elements affect the rigidity of the chassis and thus choose the best configuration for each race is essential. This article aims to investigate the optimal fiber orientation configuration for a kart anti-roll bar, prioritizing the stiffness of the bar. Additionally, it seeks to determine the number of layers required for the manufacturing of a composite anti-roll bar made of polylactic acid (PLA) coated with carbon fiber.

2. METHODOLOGY

For the study of a composite anti-roll bar made of PLA via additive manufacturing (AM), coated with carbon fiber and epoxy resin, a geometry with tubular ends and an elliptical center was proposed. This design allows for stiffness adjustment depending on the bar's positioning angle. The dimensions of the PLA geometry were engineered to fit directly into the clamps of a kart chassis homologated by the Fédération Internationale de l'Automobile (FIA), with the attachment points indicated by blue circles in Figure 1 [3]. The bar has an initial thickness of 1.5 mm in PLA, which varies according to the number of carbon fiber layers. The tubular ends have an external diameter of 30 mm, and the total length of the bar is 220 mm.
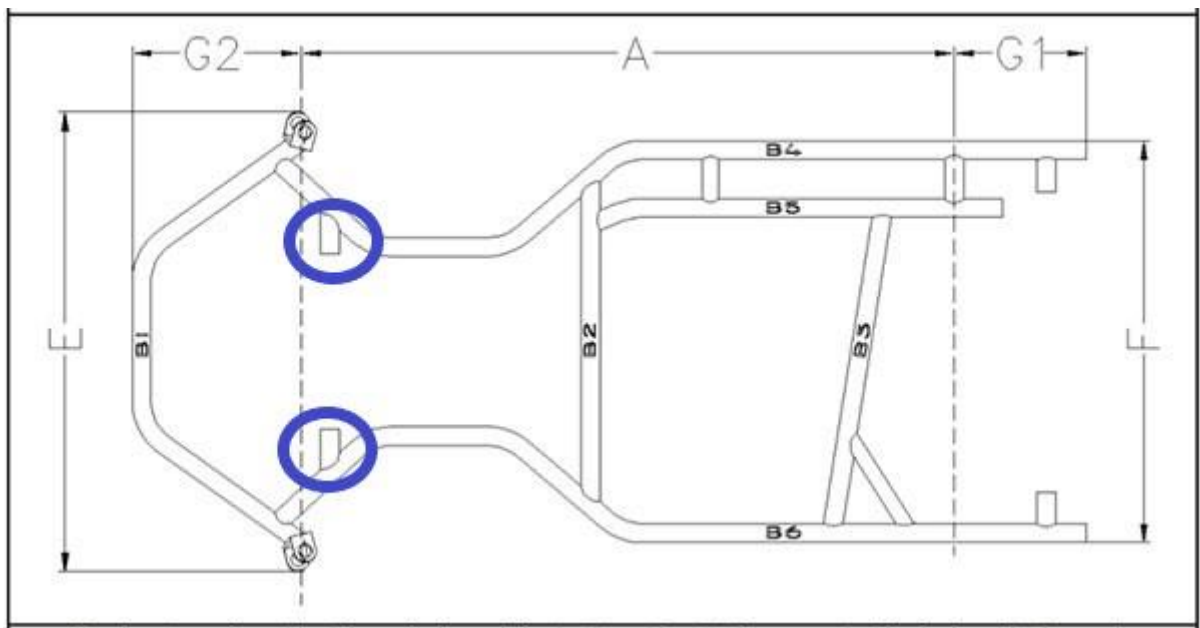
Figura 1. FIA Homologated chassis example. Fonte: FIA Karting.
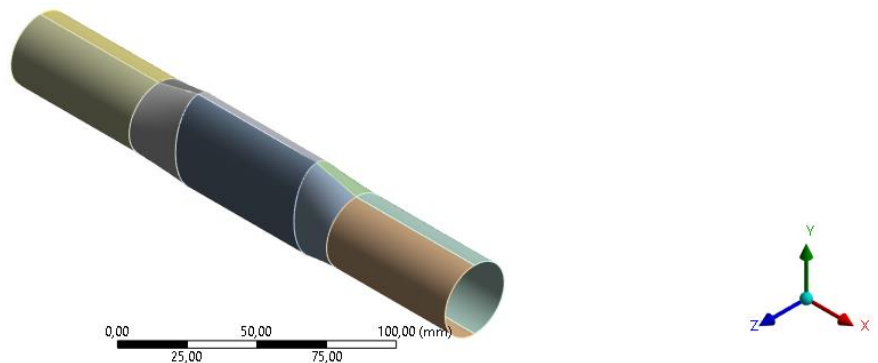
Figure 2. Anti-roll bar geometry.

The structure shown in Figure 2 is the bar manufactured in PLA by additive manufacturing, which has been coated with carbon fiber. To determine the number and orientation of the layers, numerical simulations were conducted on 9 models to find the configuration that resulted in the least total displacement of the bar under torsional conditions. The different models tested can be seen in Table 1.

Table 1: Layer orientation

Model	Number of Layers	Layer orientation in degrees
1	2	0°/90°
2	3	0°/90°/0°
3	4	0°/90°/0°/90°
4	4	0°/+45°/90°/-45°
5	2	+45°/-45°
6	3	0/+45°/-45°
7	3	45°/-45°/+45
8	2	0°/+45°
9	4	+45°/-45°/+45°/-45°

2.1 Numerical model

For the development of the numerical model, the loading condition on the bar was defined to simulate the most severe possible scenario: a kart taking a turn with a lateral acceleration of 2G, which is twice the acceleration due to gravity. The lateral load transfer equation of a vehicle defined by [1], was used to determine the loading to be applied in the simulation. See Equation 1.

$$\Delta w = \frac{w * Ay * H}{t}$$

(1)

Where w is the mass of the vehicle in Newtons (N), Ay is the lateral acceleration in (G), H is the height of the vehicle's center of gravity in meters (m), t is the track width (the distance between the wheels), and Δw is the total load transfer of the vehicle. Assuming equal load distribution between the front and rear axles, the applied load should be half the value of Δw. Therefore, for a kart weighing approximately 175 kg, with a lateral acceleration of 2G, a center of gravity height of 200 mm, and a track width of 1.3 m, the approximate load transfer to the front axle is 264 N. For the numerical simulations, a value of 270 N was used.

The numerical simulation employed the ACP Pre tool in the ANSYS® finite element software, which allows for the modeling of composite materials. This tool utilizes a method that enables the virtual lamination of the composite, thereby allowing the determination of fiber directions and layers as needed for the design [7]. Initially, the standard lamination orientation of the part was defined, starting from the face and moving outward, as shown in Figure 3 (a). The fiber orientation, indicated by the yellow arrows in Figure 3 (b), corresponds to a 0° orientation.

a) Lamination Orientation   b) Fiber orientation 0°
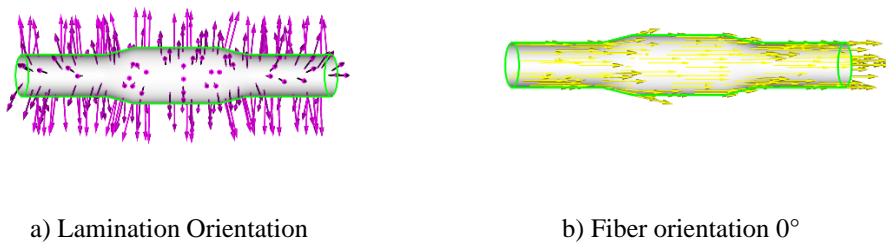
Figure 3. Reference orientations for the fibers.

For the application of boundary conditions, a load condition of 270N was applied at one cylindrical end, with the other end fixed in place, aiming to simulate the load transfer condition under the anti-roll bar. These conditions can be observed in figure 4.
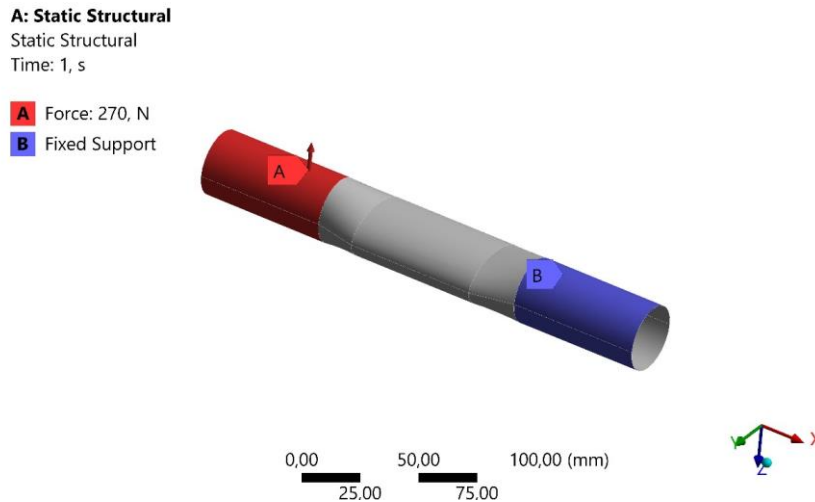
Figure 4. Boundary conditions.

2.2. Material

For the determination of material properties, [4] characterized PLA through test specimens manufactured via AM and the carbon fiber/epoxy composite test specimens through tensile tests following [5] and [6] standards. Tests were conducted on two types of carbon fiber specimens. For the purposes of computer simulation, ANSYS® only requires the moduli for each axis separately. The type 1 specimen was laminated with a woven fabric with fibers oriented at 0°/90°, while the second type was laminated with the same fabric but with an orientation of +45°/-45°. Therefore, the moduli in the X and Y directions were considered equal because, when the fabric is rotated by 90°, it retains the fiber orientation at 0° and 90° relative to the direction of tension. This consideration is also valid for the +45°/-45° specimen. For the Poisson's ratio values, the values from the ANSYS® material library were considered. The data obtained from material characterization can be viewed in Table 2.

Table 2. Material properties

Property	PLA	Carbon Fiber +45º/-45º	Carbon Fiber 0º/90º
Young's modulus - X [GPa]	3.50	39.07	66.10
Young's modulus - Y [GPa]	3.50	39.07	66.10
Young's modulus - Z [GPa]	5.24	7.50	7.50
Poisson's ratio XY	0.36	0.04	0.04
Poisson's ratio YZ	0.36	0.30	0.30
Poisson's ratio XZ	0.36	0.30	0.30
Shear modulus XY [MPa]	1927.00	34431.00	20352.00
Shear modulus YZ [MPa]	1286.98	47220.00	27911.00
Shear modulus XZ [MPa]	1286.98	47220.00	27911.00
Density [g/cm^3]	1.24	1.45	1.45

3. RESULTS AND DISCUSSION

From the simulation of the geometries with the proposed fiber orientations in Table 1, Figure 5 presents the results of maximum stress in MPa for each model, based on the von Mises criterion. It was observed that as expected for this condition, the models with a fiber orientation at 45 degrees showed the lowest stress values, with the laminate configuration of model 9 yielding the lowest result among those evaluated, at 78.357 MPa.
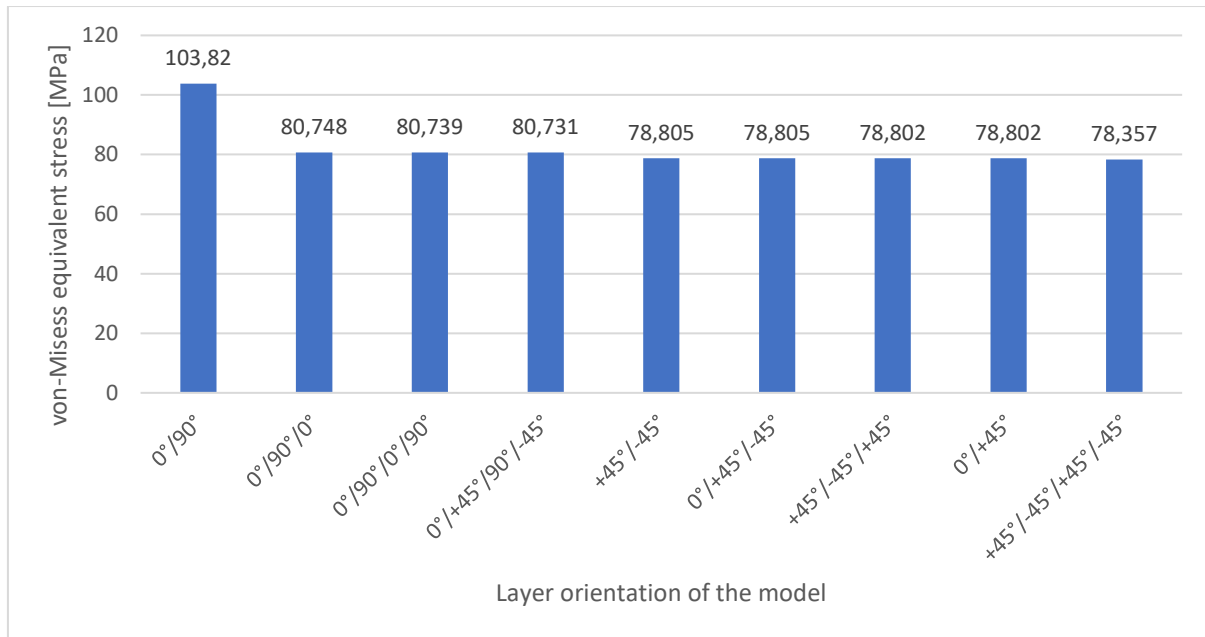
Figure 1. Mean Stress x Layer orientation

Based on Figure 6, it is possible to observe that for the total displacement, model 9, with 4 layers of fiber/epoxy and orientations at +45°/-45°/+45°/-45°, also yielded the best result, with a displacement of 0.3929mm.
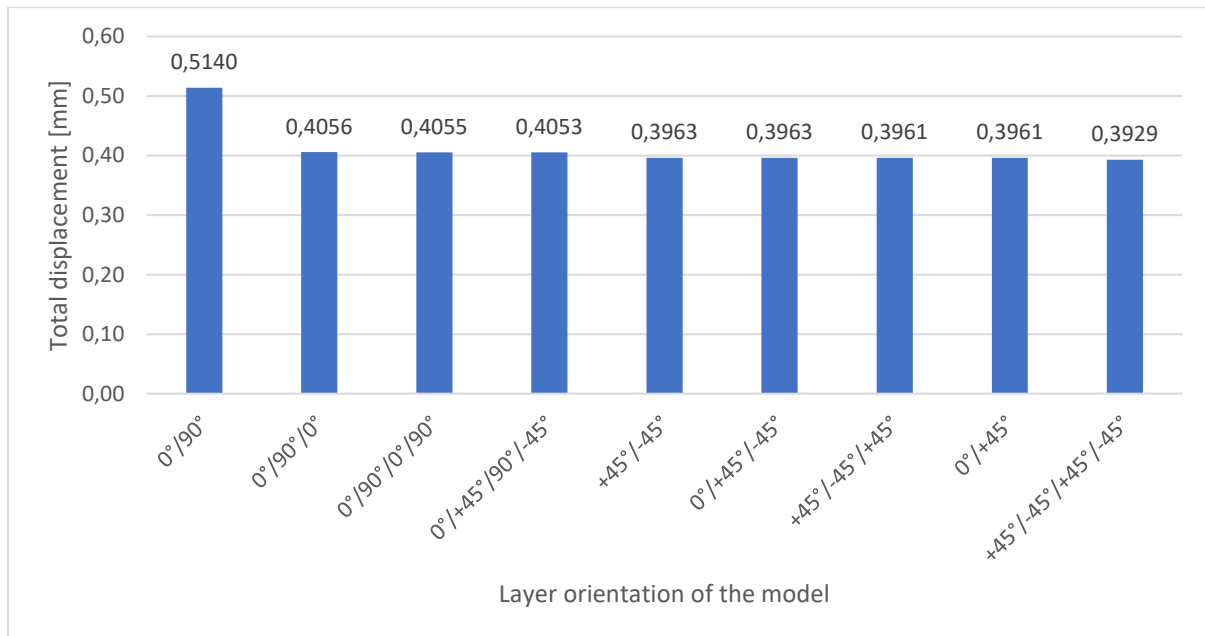
Figure 2. Total displacement x Layer orientation.

With the comparison between the models concluded, an analysis of a tenth model was conducted with the same fiber orientations as model 9, +45°/-45°/+45°/-45°, but without the use of PLA, meaning the entire bar was made solely of carbon fiber and epoxy. Comparing models 9 and 10, it was possible to observe that

PLA adds considerable reinforcement to the bar structure for this laminate configuration. The structure made only of fiber, without PLA, experiences a stress of 95.383 MPa and a total displacement of 0.4795mm, for both cases, approximately 22% higher than the structure with PLA.

With the final structure defined as that of model 9, a displacement analysis was conducted along the Y and Z axes to obtain a comparison of displacement in different bar positioning orientations so that the structure user could have more quantitative information about how changing the bar inclination would alter the kart's stiffness setup. In Figure 7 (a), setup option 1 is observable, where the loading is applied at a 45-degree angle between the Y and Z axes; as the forces are decomposed, this configuration presents the smallest total displacement. In Figure 7 (b), setup 2 shows the loading applied along the Z axis, and in Figure 7 (c), setup option 3 depicts the loading applied at a 45-degree angle between the Y and Z axes.
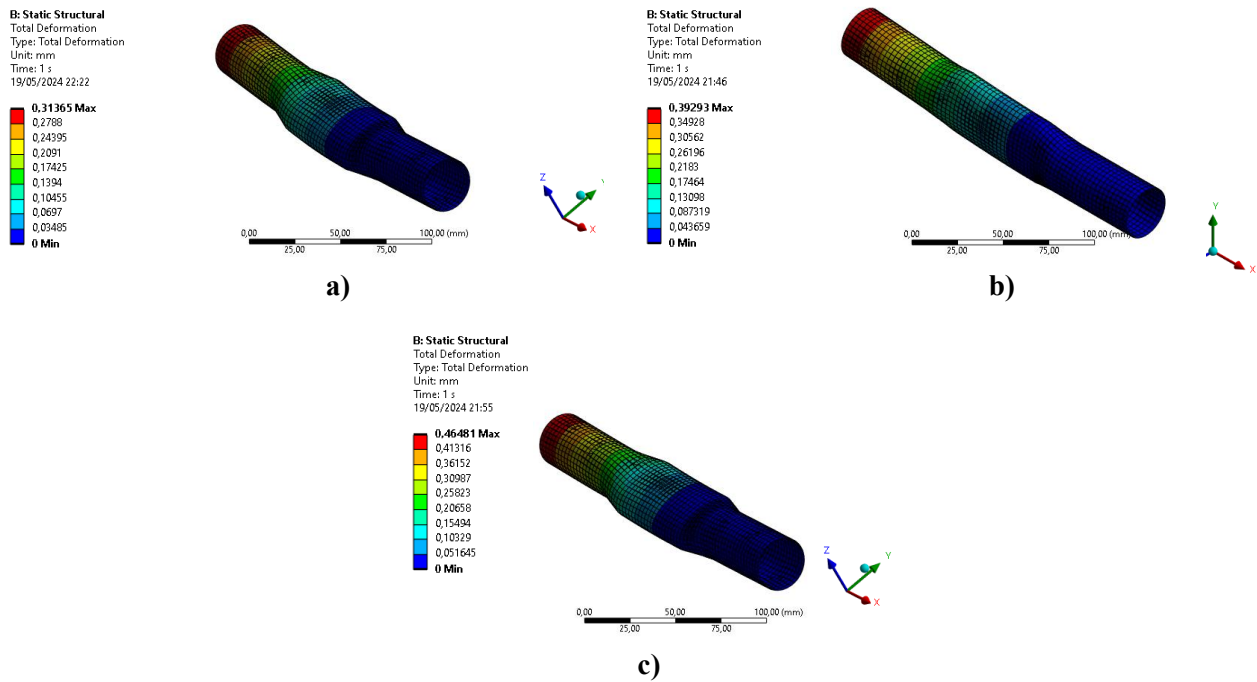
Figure 7: a) Setup 1, 45° YZ-axis, b) Setup 2, Y-axis, c) Setup 3, Z-axis.

In figure 8, It's possible to observe that there's a nearly linear variation among the setup options, thus allowing the kart engineer to adjust the setup according to their needs simply by rotating the bar around its own axis, aiming to alter the stiffness of the anti-roll bar.
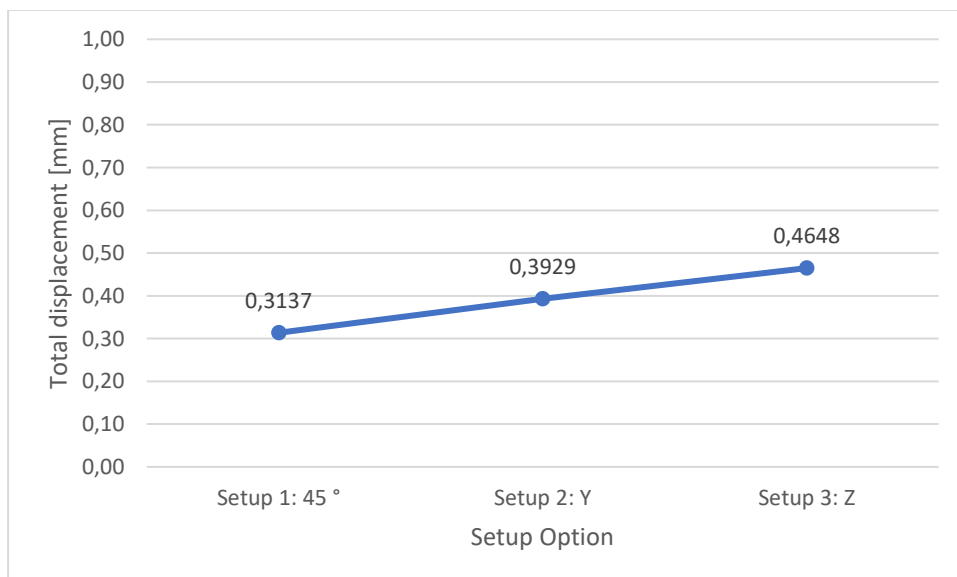
Figure 8. Total displacement x Setup Option

4. CONCLUSIONS

Based on the analyses conducted in this study, it is evident that the inclusion of PLA in the carbon fiber/epoxy composite significantly enhances the structural performance of the anti-roll bar. Comparison between models with and without PLA reinforcement revealed a notable reduction in stress and displacement of up to 22%, highlighting the beneficial effects of PLA in reinforcing the structure.

Furthermore, the investigation into different fiber orientations and ARB positioning demonstrated the versatility of the anti-roll bar design. The linear variation observed among the configuration options indicates the ease with which kart engineers can adjust the stiffness of the anti-roll bar to meet specific racing conditions. By simply adjusting the orientation of the bar, engineers can achieve the desired changes in stiffness, providing greater flexibility in optimizing kart performance.

In choosing the von Mises criterion for this analysis, considerations were made regarding the composite's composition, which includes not only fibers and matrix but also a third phase of polymeric material. This makes the von Mises criterion simpler and less computationally demanding compared to other methods such as Tsai-Wu and Hashin. Additionally, this criterion allows for comparing the developed component with others made from conventional materials like aluminium. von Mises criterion also provides a more conservative approach and requires fewer experimental data parameters, thereby facilitating practical application and obtaining reliable results. Future studies aim to explore more complex criteria and conduct comparative analyses among them.

In summary, the results of this study underscore the importance of material selection and design optimization in improving the performance of kart components. The information obtained from this research can serve as valuable guidance for engineers and designers seeking to enhance the structural integrity and performance of kart chassis components. Additionally, the methodologies employed in this study can be extended to other composite structures, contributing to advancements in lightweight and high-performance materials for various applications in the automotive industry and beyond.

4.1. Declaration of Competing Interest

The authors declare no conflict of interest.

4.2. Acknowledgements

5. REFERENCES

[1] William F. Milliken, Douglas L. Milliken. Race Car Vehicle Dynamics, 5th Edition, 1995. Society Of Automotive Engineers. (ISBN 1-56091-526-9).

[2] Homologated Equipment. FIA Karting, 2024. (https://www.fiakarting.com/page/homologated-equipament), accessed 04 October 2024.

[3] ANSYS® engineering analysis system user's manual 2024.2024 [Computer Software]. ANSYS Inc.

[4] ALBERTO, Luiz Gustavo Santos. Estudo numérico e experimental de compósitos em fibra de carbono com núcleo fabricado em manufatura aditiva. 2023. 101 f., il. Trabalho de Conclusão de Curso (Bacharelado em Engenharia Automotiva) — Universidade de Brasília, Brasília, 2023.

[5] ASTM D638. Standard test method for tensile properties of plastics. ASTM International, 2014.

[6] ASTM D3039M. Standard Test Method for Tensile Properties of Polymer Matrix Composite Materials. ASTM International, 1997.

RADIAL AND AXIAL COMPRESSIVE BEHAVIOUR OF GLASS/EPOXY FILAMENT WOUND CYLINDERS

Anderson L. Santos[(a)*], José Humberto S. Almeida Jr[(b)], Maikson L. P. Tonatto[(c)], Marcelo B. Antunes[(d)], Sandro C. Amico[(e)]

(a) 0009-0003-0252-0596 (Federal University of Rio Grande do Sul – Brazil)
(b) 0000-0002-9408-7674 (LUT University, Lappeenranta, Finland)
(c) 0000-0002-3118-6894 (Federal University of Santa Maria – Brazil
(d) 0009-0009-7027-879x (Lupatech Fiber Liners– Brazil)
(e) 0000-0003-4873-2238 (Federal University of Rio Grande do Sul – Brazil)
Corresponding author: 00222268@ufrgs.br

CODE: BCCM7-181

Keywords: GFRP, radial and axial compression, filament winding.

Abstract: Cylindrical composite structures may operate under compression loading in a variety of applications. Understanding the mechanical response of those thin-walled cylinders is complex given the multiple failure modes, such as fibre or matrix failure, delamination, or a combination of these, global or local buckling. This work focuses on studying the mechanical response of glass fibre-reinforced epoxy composites subjected to radial and axial compression loading. The cylinders (inner diameter of 70 mm) were manufactured via wet filament winding process with three layers with a fibre angle of $\pm 65°$. The physical characteristics of the samples were determined via optical microscopy analysis. The radial compression test was carried out on 140 mm long samples following the recommendations of the ASTM D2412-21 standard to obtain stiffness, percentage deflection, and stiffness factor. The cylinder subjected to radial loading has an average stiffness of 1.23 MPa, with 68% deflection and stiffness factor of 8282 mm³MPa. The failure modes were predominantly delamination in areas perpendicular to the axis of radial compression loading. Regarding the cylinders under axial compression loading, they achieved an axial compressive strength of 127 MPa with a deflection of 2.3%, and their material failure mode occurred to of 3.22 mm.

1 INTRODUCTION

Thin-walled composite cylindrical shells are widely used in structural engineering mainly due to their excellent mechanical properties and low weight. Such structures are usually manufacturing by the filament winding (FW) technique given its ability to produce solids of revolution with high repeatability given its automation character. Thin-walled composite shells are usually used in critical applications, such as aircraft fuselages, automotive drive shafts, and pressure vessels.

Composite cylinders can fail either from material failure (when a strength allowable is exceeded) or from global or local buckling due to compressive loads. Understanding how and when composite shells fail under these loads is essential for design purposes. For instance, Almeida Jr et al. [1,2] analysed computationally and experimentally the mechanical behaviour of carbon/epoxy composite cylinders with different stacking sequences under radial [1] and axial [2] compression. They found out that the main failure mode of the cylinders under radial compression is delamination, whereas thin and thick-walled cylinders in axial compression fail by buckling and material failure, respectively. Eggers et al. [3] reached similar conclusions for composite rings in radial and axial compression.

This study aims to experimentally investigate the mechanical behaviorur of glass fibre-reinforced epoxy composites under radial and axial compression loads. Cylinders with an inner diameter of 70 mm were fabricated by the wet filament winding process with three layers at a fibre angle of ±65°.

2 EXPERIMENTAL

2.1 Materials

The cylinders herein studied were produced by Lupatech Fiberware and are used in the energy sector. The test specimens were fabricated using continuous ECR-glass fibre reinforcement 1100 TEX Direct Roving and Olin Der 383 epoxy matrix. The wet filament winding process was used. The cylinders have an internal diameter of 70 mm, wall thickness of 1 mm, and length up to 15 m. After the winding process, the cylinders are cured at 160 °C for 3 h.

2.2 Physical tests

The density of the laminates was obtained using the Archimedes principle according to the ASTM D792-20 Standard Test Methods for Density and Specific Gravity (Relative Density) of Plastics by Displacement. The constituent content of the composites was carried out following the recommendations of the ASTM D3171-22 Standard Test Methods for Constituent Content of Composite Materials. The morphology of the cylinders was evaluated via optical micrographs using a Carl Zeiss Axio Scope A1 binocular optical microscope with adjustable bright-field and dark-field lighting, equipped with a 10× magnification objective lens.

2.3 Specimen preparation and mechanical tests

The length for the samples is 140 mm given that the compression platen has a diameter of 150 mm. The samples to be tested in axial compression have the same dimensions. To improve the load distribution around the edge of the samples under axial compression and hence to prevent premature failures, a resin potting procedure was performed using Alpha 163 polyester resin from Embarcol with Butanox M-50 catalyst from Induspol in a ratio of 1.5 % catalyst to resin ratio. The low-cost procedure consists of five steps, as shown in Fig. 1: (i) mold production; (ii) application of release agent; (iii) resting one edge and curing for 12 h at room temperature; (iv) resting the other edge to ensure parallelism and curing for 12 h; and (v) removal of the cylinder from the mold [3].
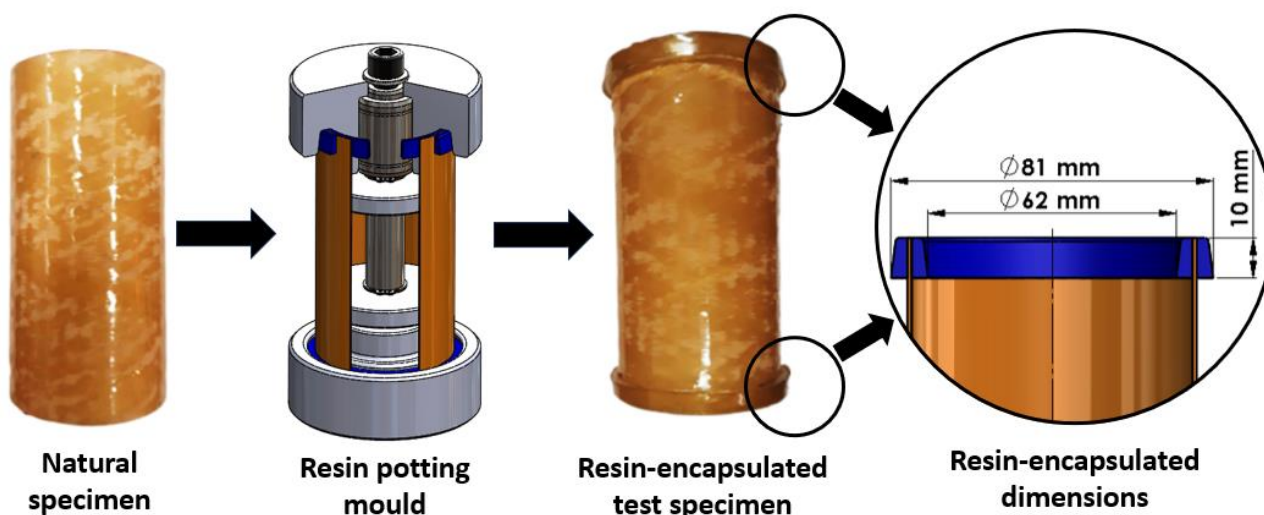
Figure 1. Description of the resin potting procedure.

The mold used to manufacture the resin potting is made of a metallic device made of carbon steel, joined and guided by a shaft and a linear bearing whose primary function is to ensure parallelism between the top and bottom surfaces of the shell. The device also includes a disk to centre the cylinder in the mold. To use the equipment, it is necessary to disassemble it into two pieces, with one half accommodating the cylinder and the second half closing it by tightening the central screw. Them, the mold is ready to receive the resin and fill

the first cavity that will form one side of the resin potting. After the curing time, the mould is rotated, and the second cavity is filled without the need for disassembly.

Five specimens were prepared and subjected in radial and axial compression loads. An Instron universal testing machine model 3382 with a load cell of 100 kN was used with compressive platens of 150 mm in diameter.

The radial compression tests were conducted following the recommendations of ASTM D2412-21 Standard Test Methods for Determination of External Loading Characteristics of Plastic Pipe by Parallel-plate Loading Materials at a speed of 12.5 mm/min. This testing method focuses on the displacement characteristics of composite tubes under parallel plate loading.

The stiffness (PS) and stiffness factor (SF) are calculated as follows (1-2):

$$PS = \frac{F}{\Delta_y} \tag{1}$$

$$SF = 0.149 \times r^3 \times PS \tag{2}$$

Where F is the applied load, Δ_y is the change in the inner diameter of the cylinder in the direction of loading.

The axial compression tests were conducted at a speed of 2.0 mm/min. The axial compressive strength (σ_x) is calculated as $\sigma_x = F/A$, where A is the cross-sectional area of the ring.

Inferential statistics were applied in the calculations of this work because it allows estimating the repeatability of measurements from a sample and extrapolating to a population. Probabilistic techniques ensure the possibility of making statements about the population based on samples within a confidence interval. The sample estimate (S) and degrees of freedom (ν) are calculated as follows (3,4):

$$S = \sqrt{\frac{\sum_{i=1}^{n}(I_i - \bar{I})^2}{n-1}} \tag{3}$$

$$\nu = n - 1 \tag{4}$$

Where n is the number of samples, I_i is the measurement of the i-th average indication out of n indications, and ν is the number of degrees of freedom. For this study, a confidence interval of 95.45% was used, and the Student's coefficient was determined by the number of samples, enabling the determination of the random error of measurements and the estimation of test repeatability.

3 RESULTS AND DISCUSSION

The average specific gravity of the samples was 1.88 ± 0.04 g/cm3, which is a dimensionless quantity. The Archimedes Principle was then applied to calculate the specific density of the GFRP composite material of the cylinder laminate, resulting in 1.87 ± 0.04 g/cm³. The resin burn-off tests revealed fibre volume fraction (V_f) of ~48% and matrix volume fraction (V_m) of ~49%, thus suggesting a void volume fraction (V_v) of ~3%. Figure 2 shows a cross-section image of the cylinder showing some voids.
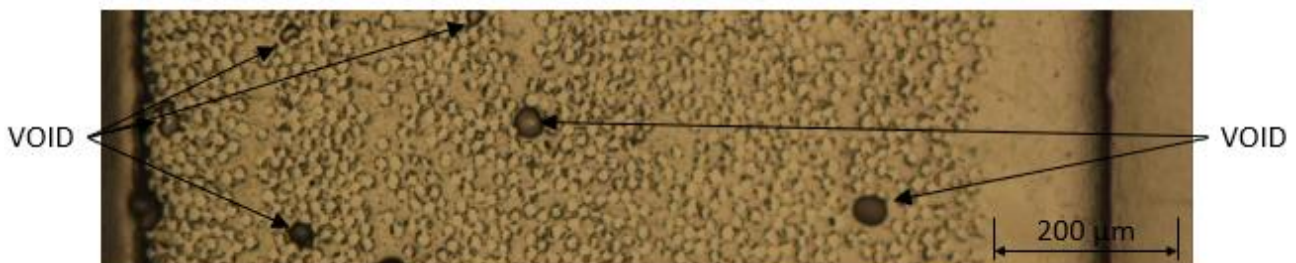
Figure 2. Cross-sectional image of a sample.

Figure 3 depicts the load-displacement curves of the radial compression tests. The curves exhibit considerable repeatability among the test specimens under axial compression loadings. Each specimen's curves demonstrate a similar dynamic response to the loading. The average peak force obtained per unit length was 27.70 ± 3.40 kN. The samples have an average stiffness of 1.23 ± 0.233 MPa and stiffness factor of $8282.65 \pm$

1559.25 mm³.MPa with a deflection of 68%. Literature indicates that for radial compression tests, the closer the winding angle is to the loading direction, the higher the maximum load achieved.
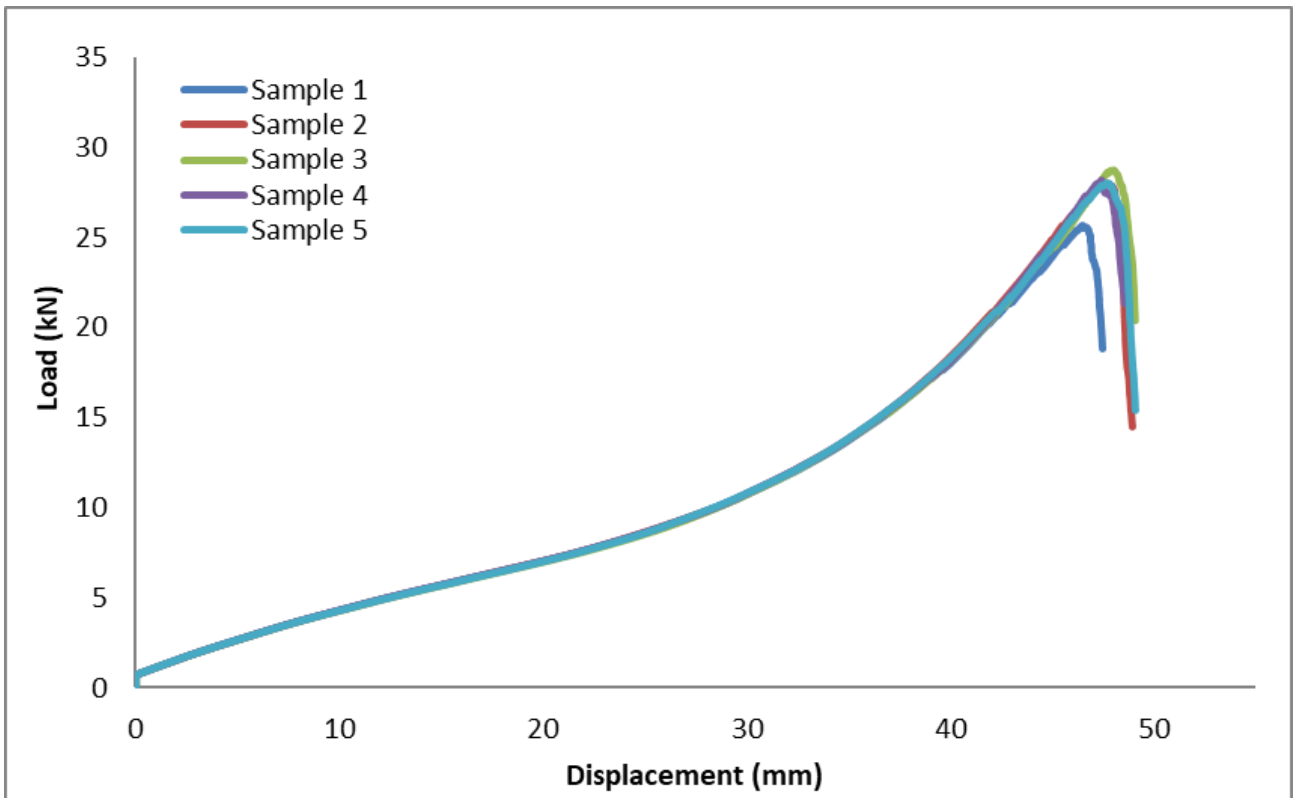
Figure 3. Load-displacement curves during quasi-static radial compression.

It is noteworthy that significant points were recorded in the deformation measurements: the onset of cracks in the epoxy matrix occurred at approximately 45% deflection with a force of 11.60 kN, while the phase of cracking of the walls and delamination between layers, at $\pm 65°$ of filament wound, occurred very close, almost simultaneously, at approximately 57% deflection with a force of 18.15 kN. Total rupture with reinforcement breakage occurred at approximately 68% deflection with a force of 27.70 kN, as shown in Figure 4.
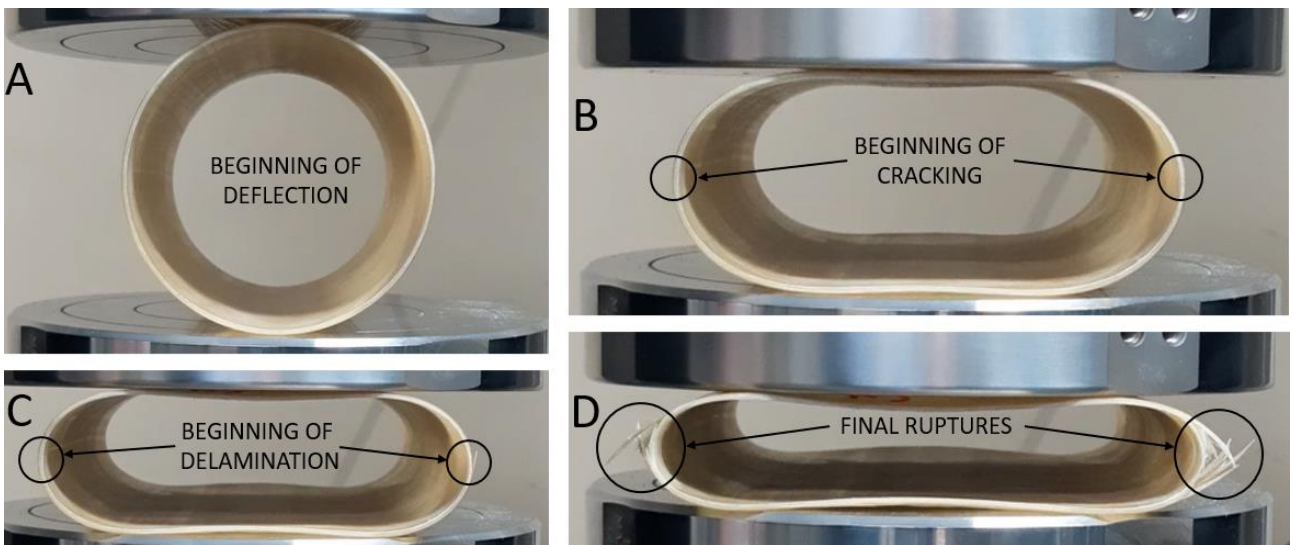
Figure 4. A) start B) cracking C) wall cracking and delamination D) of the samples under radial compression.

Figure 5 shows the load-displacement curves, which exhibited similar behavior across all axial compression tests. The response of each specimen demonstrates low dispersion, as observed in the data plot. The samples exhibited an average rupture stress of 29.77 ± 1.99 kN and an average deformation of 3.23 ± 0.50 mm. Literature indicates that for axial compression tests, the lower the winding angle, the higher the axial compressive strength, as the fiber orientation is closer to the loading direction [3].
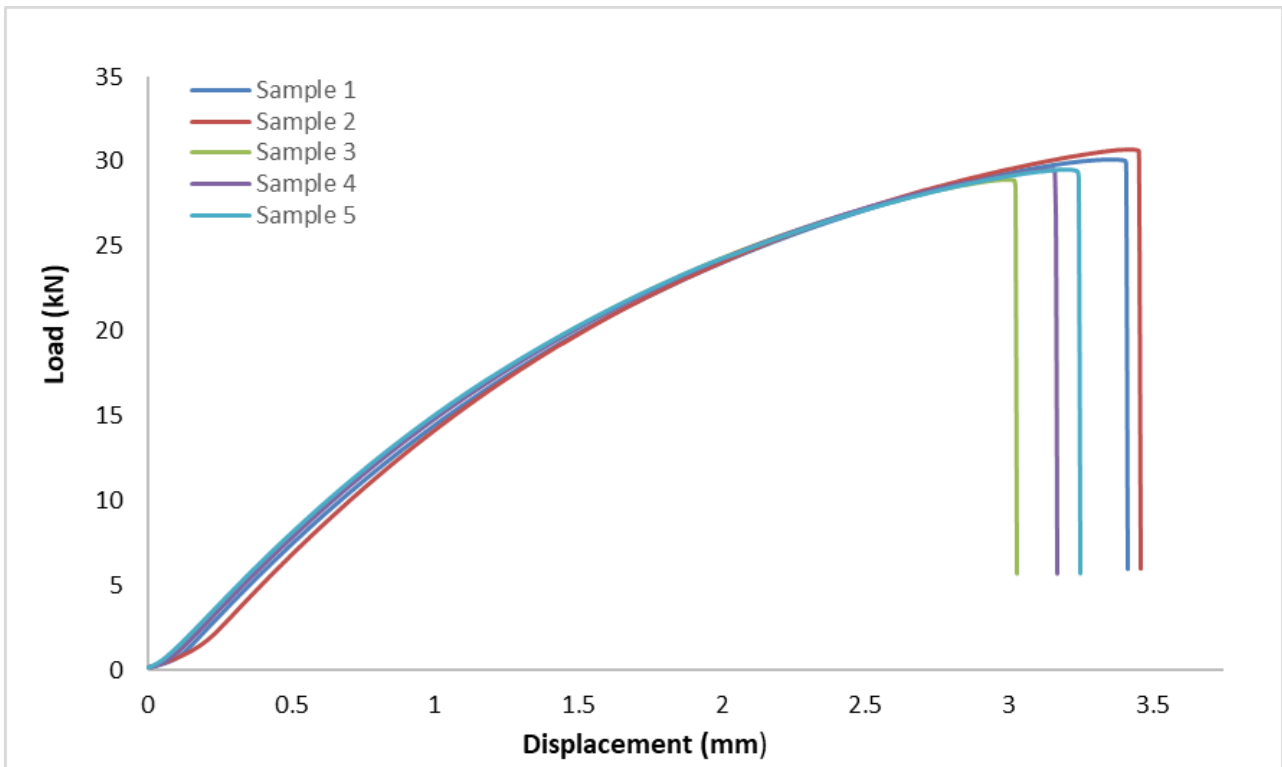
Figure 5. Load-displacement curves during quasi-static axial compression.

Figure 6 displays the test specimens after the test, exhibiting fractures due to matrix collapse and subsequent reinforcement failure, as the winding angle of the cylinder deviates significantly from the ideal angles for axial loadings, which typically require angles close to 0°
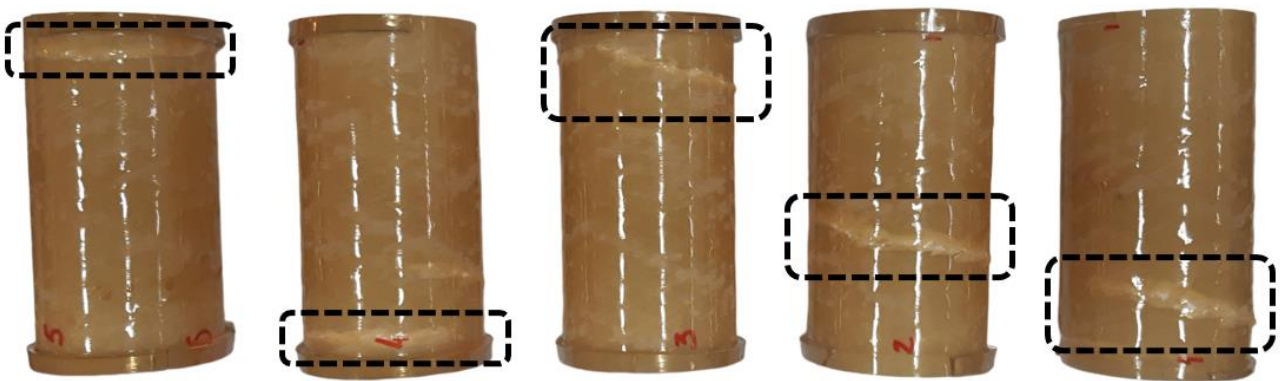
Figure 6. Failure region due to axial compression loading

4   CONCLUSIONS

In this work, the mechanical behaviour of glass fibre reinforced epoxy filament wound cylinders under radial and axial compression loads has been experimentally explored. The physical characteristics of the cylinders are: density of 1.87 g/cm^3; V_f of ~ 48% and V_m of ~ 49%. The samples subjected to radial compression load failed mostly by matrix cracking and delaminations while the samples under axial

compressions failed likely by material failure, although further investigations with optical methods, such as digital image correlation (DIC), must be performed for a more accurate failure characterisation.

4.1 Declaration of Competing Interest

The authors declare no conflict of interest.

4.2 Acknowledgements

5 REFERENCES

[1]   Almeida JHS, Ribeiro ML, Tita V, Amico SC. Damage modeling for carbon fiber/epoxy filament wound composite tubes under radial compression. Compos Struct 2017;160:204–10. https://doi.org/10.1016/j.compstruct.2016.10.036.

[2]   Almeida JHS, Tonatto MLP, Ribeiro ML, Tita V, Amico SC. Buckling and post-buckling of filament wound composite tubes under axial compression: Linear, nonlinear, damage and experimental analyses. Compos Part B Eng 2018;149:227–39. https://doi.org/10.1016/j.compositesb.2018.05.004.

[3]   Eggers F, Almeida JHS, Azevedo CB, Amico SC. Mechanical response of filament wound composite rings under tension and compression. Polym Test 2019;78:105951. https://doi.org/10.1016/j.polymertesting.2019.105951.

8 Delamination, damage and fracture

Organized and edited by

Sandra Maria da Luz
&
Carla Tatiana Mota Anflor

B-BASIS DESIGN ALLOWABLE OF OPEN HOLE TENSILE NOTCHED COMPOSITES LAMINATES USING SURROGATE MODEL

Ângelo A. Freitas [(a)*], Leonardo P. S. Ferreira [(b)], Carlos A. Cimini Jr. [(c)]

(a) 0009-0009-8113-2358 (Federal University of Minas Gerais – Brazil)
(b) 0000-0002-4963-8801 (FEMTO-ST – Université de Bourgogne Franche-Comté – France)
(c) 0000-0002-6612-0211 (Federal University of Minas Gerais – Brazil)
* Corresponding author: angeloalmeida25@gmail.com

Abstract: The study of failure in composite materials, particularly in Linear Elastic Fracture Mechanics (LEFM), has been extensively explored due to the increasing demand for predicting crack behavior. Some of the available methods are based on Classical Laminate Theory (CLT) and Tsai-Wu failure criteria for First Ply Failure (FPF) and Last Ply Failure (LPF) and their respective failure envelopes. As these methods rely on multiple tests, resulting in significant costs and labor, a novel approach using the longitudinal modulus E_1 as a single parameter to obtain the elastic properties of laminates has been proposed. This methodology simplifies testing requirements and can be expanded to predict the strength of notched laminates under tensile loading (OHT – Open Hole Tension) using laminate parameters. Despite its accuracy, this method still depends on various material and geometric parameters. Therefore, this study aims to evaluate the global sensitivity of tensile strength for different OHT laminates concerning input parameters using Sobol indices. Subsequently, an approach based on a machine learning surrogate model is proposed to generate the B-basis design allowable using relevant parameters. The proposed machine learning model reduces computational cost and speeds up analysis time.

LIST OF ACRONYMS AND ABBREVIATIONS

ANN	Artificial Neural Network
CFRP	Carbon Reinforced Fiber Polymer
CLT	Classical Laminate Theory
FFM	Finite Fracture Mechanics
FPF	First Ply Failure
LEFM	Linear Elastic Fracture Mechanics
LPF	Last Ply Failure
OHT	Open-Hole Tension
PCE	Polynomial Chaos Expansion

1. INTRODUCTION

The increasing use of composite materials, especially in the aerospace industry, has created a demand for more detailed failure analysis using Linear Elastic Fracture Mechanics (LEFM) to comprehend crack behavior in structural components. Information about different parameters (manufacturing process defects,

material properties, geometry, etc.) and their uncertainties has thus become necessary to quantify their influence on the structural design. For the design and certification process, many studies have been conducted using various specimens, geometries, and loading conditions for CFRP (Carbon Reinforced Fiber Polymer) material system. These studies employ Tsai's Modulus (ply stiffness matrix trace) [1] and the Master Ply Theory [2] using the Last Ply Failure (LPF) and First Ply Failure (FPF) failure criteria based on the Classical Laminate Theory (CLT). In this approach, a Finite Fracture Mechanics (FFM) model can be applied, where stress and energy are coupled in an analytical approach to provide a strength response for notched CFRP.

According to Furtado et al. [3], the information on longitudinal elastic modulus, uniaxial strength of the laminate, and fracture toughness comprises the recipe for calculating the remote stress at failure in an open-hole laminated specimen subjected to tension (OHT). However, determining the accurate material properties requires a long and expensive experimental testing program. To circumvent this issue, Tsai's Modulus and the master ply invariant-based concept for a specific lay-up is proposed. This allows obtaining all ply elastic properties from a single parameter E_1.

The sensitivity analysis for strength prediction of composite laminates has been studied by various authors, such as Vallmajó et al. [4] and Furtado et al. [5]. In their approach, material and geometrical properties are important for providing the correct evaluation of the notched strength, and appropriate metrics must be evaluated to account for the influence of the important parameters. Among these metrics, Sobol indices are employed in this work to assess the main effects of input parameter variances on the output results. This analysis enables the evaluation of B-basis design allowables for notched configurations of CFRP laminates, accounting for input parameters uncertainties.

Multiple simulations are needed to evaluate the uncertainty of a model. Although this can be achieved using the original model, it often leads to high computational costs. Machine-learning-based surrogate modeling techniques have received an increasing attention in recent years and can be used for sensitivity analysis and uncertainty quantification [6]. The use of surrogate models reduces the amount of computational effort needed during development phase, thereby speeding up the process.

In this paper, a study to evaluate the global sensitivity of remote stress at failure for different OHT laminates to input parameters using Sobol indices has been developed. Subsequently, an approach based on a machine learning surrogate model is proposed for generating B-basis design allowable using relevant parameters through a model design space and the Monte Carlo approach. All results obtained are also compared with numerical results presented in Furtado et al. [5]. The proposed machine learning model reduces computational costs and speeds up development time.

2. METHODOLOGY

2.1. Problem statement

Given a OHT geometry as depicted in Fig.1, this work aims to predict the B-basis design allowable considering the influence of the input parameters and their experimental uncertainties.
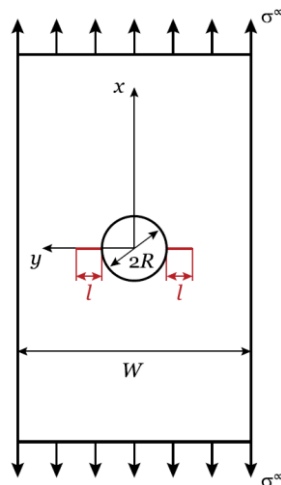
Figure 1. Geometry of the notched laminate with a central circular open hole under tensile load.
Available at [3, p.311].

The flowchart presented in Fig.2 describes the framework considered in this work. Initially, an FFM model based on the work of Furtado et al. [3] is implemented to predict the open-hole notched strength tension σ_∞ of the laminate, as described in sections 2.2 and 2.3. Then, the FFM model is used to build a dataset of σ_∞ values considering the input parameters within an experimentally determined range of values. The outputs of the model are used to conduct a global sensitivity analysis using Sobol indices, described in section 2.4. Finally, a machine learning surrogate model based on an Artificial Neural Network (ANN) is implemented to generate B-basis allowable curves considering an expected experimental distribution of input parameters, as explained in section 2.5.
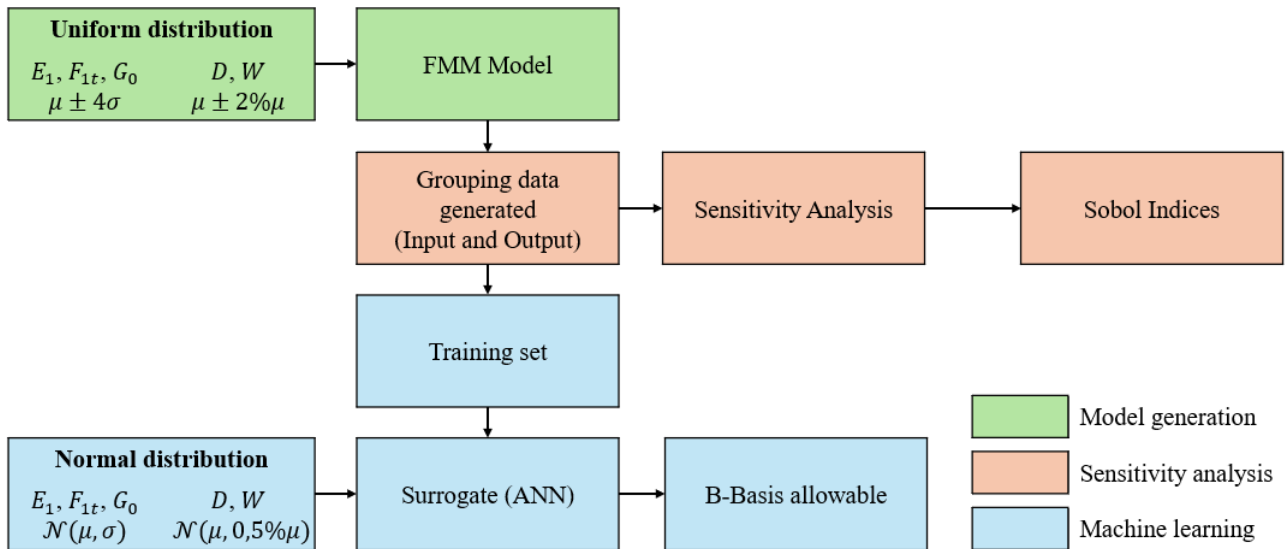
Figure 2. Diagram of the proposed framework. In the diagram, the following parameters/symbols are used: E_1 – longitudinal elastic modulus; F_{1t} – unnotched tensile strength of the laminate, G_0 – critical energy release rate; D – Diameter; W – Width; μ – mean value; σ – standard deviation, σ_∞ – open-hole notched strength tension.

2.2. Finite Fracture Mechanics model analysis

A coupled stress and energy FFM model proposed by Furtado et al. [3] is used to predict the fracture of notched composite laminates. This criterion indicates a strength response when the laminate is subjected to a remote stress, providing a good analytical way to predict the laminated plate failure. Using the ply longitudinal elastic modulus E_1, it is possible to evaluate the Tsai's Modulus (trace) according to Eq. (1), and approximate the ply's elastic properties.

$$Tr = \frac{E_1}{0.880} \tag{1}$$

The use of universal laminate factors, presented in Table 1 for Quad laminates (symmetric, balanced and with a minimum of 10% of each angle 0°, 90°, and ±45°), allows for a straightforward determination of elastic properties for any laminate or sublaminate. Then, the Unit Circle failure criterion concept introduced by Tsai and Melo [7] is applied using the ply's longitudinal tensile strength, F_{1t}, and the elastic laminated properties derived from Tsai's Modulus. Finally, the unnotched tensile strength of the laminate, X_L, is determined, enabling the prediction of composite failure using a strain space failure envelope.

Table 1. Universal laminate factors using CLT. Available at [3, p. 308].

Lay-up	$\dfrac{E_x}{Tr}$	$\dfrac{E_y}{Tr}$	$\dfrac{G_{xy}}{Tr}$	v_{xy}
Master Ply (0°)	0.880	0.052	0.031	0.320
[0°/+45°/−45°/90°]	0.336	0.336	0.129	0.308

This approach introduces an invariant-based failure analysis to define a tensile strength characteristic that remains consistent regardless of the laminate layup configuration. An Omni Strain Failure Envelope for

laminates with different ply orientations is established by using a failure criterion formulated as a tensor polynomial in strain space. This methodology involves selecting the dominant ply within each orientation in the strain space, primarily governed by the longitudinal failure of the 0° and 90° plies. These failure envelopes are invariant, meaning their shapes are unaffected by the presence of other plies [2].

Additionally, an analytical method based in fracture mechanics is applied to predict the laminate fracture toughness, G_{IC}, assuming uniform crack propagation across all plies within the laminate. This method relies on understanding the value of the critical energy release rate, G_0, and using the elastic properties of both the balanced and 0° sublaminates derived from Tsai's Modulus.

2.3. Numerical model and geometry

Using the FFM method presented in section 2.2, it is possible to predict the open-hole notched strength tension σ_∞ of a laminate with an open-hole. In this work, specimens with a quasi-isotropic layup with $[90/0/-45/45]_{3s}$ fiber orientation and a *W/D* ratio of 6 are used.

Table 2 presents the ply material data used for the system carbon-epoxy IM7/8552 [5], in which E_1 is the fiber direction Young's modulus, F_{1t} is the fiber direction tensile strength and G_0 is the critical energy release rate at the ply-level.

Table 2. Mechanical properties of IM7/8552 and standard deviation [5, p. 9].

	E_1 [MPa]	F_{1t} [MPa]	G_0 [N/mm]
Mean	171420	2323.47	206.75
Standard deviation (σ)	2380	127.45	23.64
Lower bound	169040	2196.0	183.11
Upper bound	173800	2450.9	230.39

Table 3 presents the values for the geometrical inputs used in the FFM model. Five analyses are performed, considering diameters of 2, 4, 6, 8, and 10 mm with a fixed *W/D* ratio of 6, resulting in *W* equals to 12, 24, 36, 48 and 60 mm.

Table 3. Geometrical properties used at sensitivity analysis.

Analysis		1	2	3	4	5
Diameter (D)	Mean [mm]	2.0	4.0	6.0	8.0	10.0
	Lower bound [mm]	1.96	3.92	5.88	7.84	9.80
	Upper bound [mm]	2.04	4.08	6.12	8.16	10.1
Width (W)	Mean [mm]	12.0	24.0	36.0	48.0	60.0
	Lower bound [mm]	11.76	23.52	35.28	47.04	58.80
	Upper bound [mm]	12.24	24.48	36.72	48.96	61.20

The input parameters are sampled 1,000 times and then used as inputs in the FFM model for predicting σ_∞, building a numerical dataset. The mechanical properties are sampled from uniform distributions centered in the mean value and perturbed within four standard deviations ($\pm4\sigma$) around the mean value. The authors have chosen to use four standards deviations to ensure that 99.99% of the samples would be comprised within the proposed limits, given that the mechanical properties follow a normal distribution during the B-basis allowable calculation (please refer to Section 3.3). The geometrical properties are considered as distributions centered in the mean value and perturbed within a $\pm2\%$ around the mean value, related to permissible allowances for preparing the specimens [5].

2.4. Sensitivity analysis

A global sensitivity analysis is performed using Sobol indices [8] to quantify each parameter's influence on the model's output, based on the numerical dataset described in Section 2.3. The first-order Sobol

index measures the proportion of variance in the metrics that can be attributed to a single parameter. UqLab [9] is used as a framework to implement the sensitivity analysis.

2.5. Machine learning surrogate model

A surrogate model is proposed to reduce the computational cost of running the FFM model multiple times for determining the B-basis allowables. Several techniques are available for surrogate modeling, such as the Gaussian process, Polynomial Chaos Expansion (PCE), or ANN. The surrogate model in this study is a multilayer perceptron ANN, used as an interpolation model inside the parameter search space for the properties presented in section 2.3.

The surrogate model input layer consists of five neurons, representing the five random variables, i.e., E_1, F_{1t}, G_0, D, and W, and the output layer has one neuron representing the value of σ_∞. The number of hidden layers is defined as two, with 50 and 100 neurons at the first and second hidden layers, respectively.

The neural network is trained with the numerical dataset used in the sensitivity analysis divided into training, validation, and test subsets with a ratio of 8/1/1, respectively. All input parameters are normalized between 0 and 1, and the output is normalized between –1 and 1 to improve convergence. The model is trained using the Adam optimizer [10] and an early stopping criterion based on the error in validation data.

3. RESULTS AND DISCUSSION

3.1. FFM model validation

The FFM model is implemented using the programming language Python. Considering equations presented in the work of Furtado et al. [1], a non-linear system of equations is obtained and must be solved for crack extension at failure (l) and remote stress at failure (σ_∞). The Simpson's numerical integration method is used to solve the obtained integrals.

Table 4 presents a comparison between the obtained results and numerical values available in the literature for Quad laminates with diameters of 2, 4 and 10 mm. The proposed FFM model agrees with numerical results, with a maximum difference of 1.4% in the simulation with hole diameter of 10 mm. These differences can be attributed to numerical errors in the integration process.

Table 4. Validation of mean remote stress at failure (σ_∞).

Hole diameter [mm]	σ_∞[MPa] This work	σ_∞[MPa] Furtado et al. [5]	Diference %
2	626.5	630.0	0.6
4	537.5	543.0	1.0
10	420.1	426.0	1.4

3.2. Sensitivity analysis

The 1,000 samples from the numerical dataset proposed in Section 2.3 are used to evaluate the global sensitivity of the input parameters in the FFM model results. A convergence analysis using different amounts of samples demonstrated that at least 200 samples are needed to achieve stability in the Sobol indices, as depicted in Fig. 3.
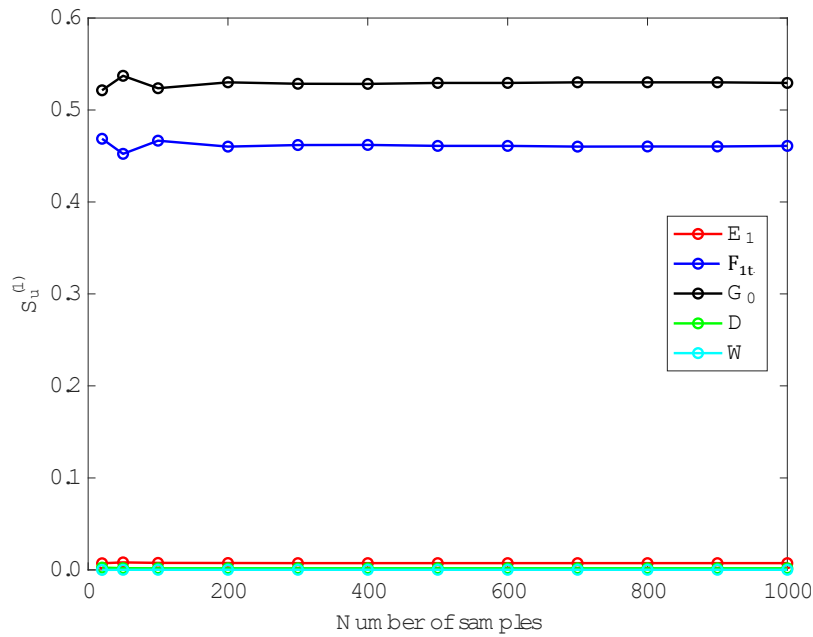
Figure 3. Sobol indices convergence analysis.

Figure 4 presents the first-order Sobol indices concerning the input parameters for mean hole diameters of 2, 4, 6, 8, and 10 mm and 1,000 random samples. The Sobol indices show that the most influential parameters are F_{1t} and G_0. The influence of F_{1t} is significant at smaller diameters, with approximately 70% of the variance in the 2 mm simulations decreasing to approximately 40% to 45% for bigger diameters. The influence of G_0 presents an opposite behavior, with a smaller influence in 2 mm, approximately 30% of the total variance, and increasing to around 55% to 60% for bigger diameters. This behavior can be attributed to problem formulation, which is more sensitive for 2 mm.
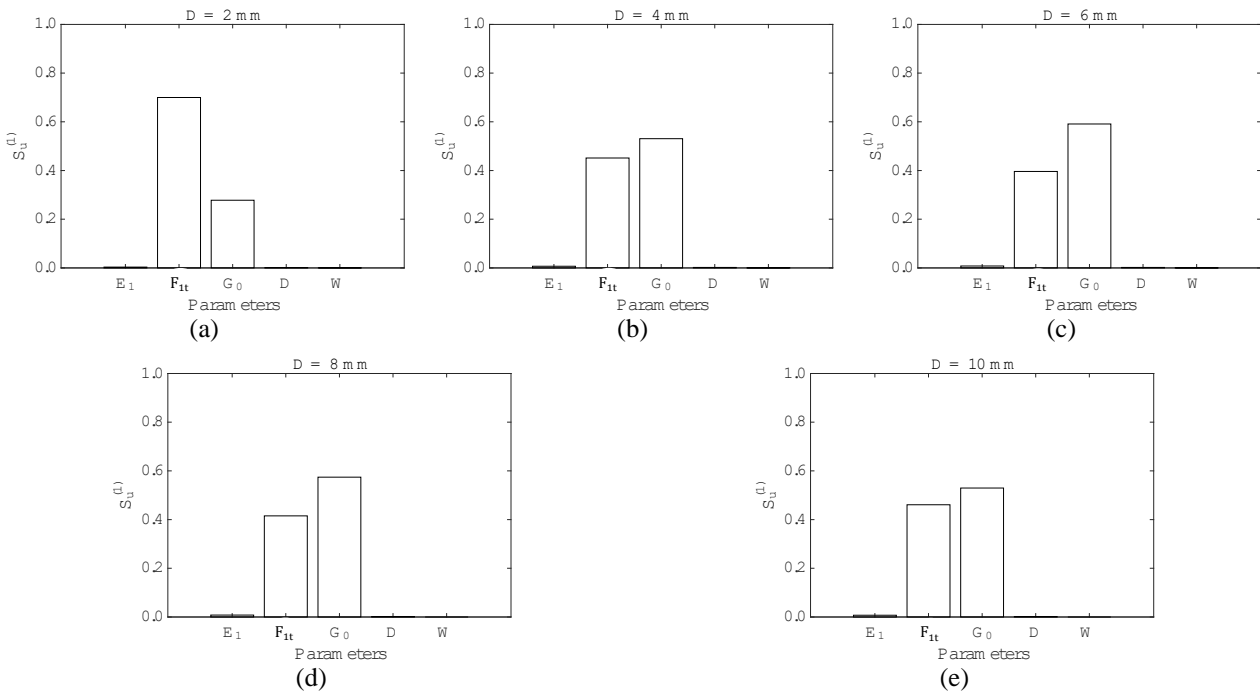
Figure 4. Results for global sensitivity analysis using Sobol indices for hole diameters of (a) 2 mm, (b) 4 mm, (c) 6 mm, (d) 8 mm, and (e) 10 mm.

The influence of the other parameters (E_1, D and W) is negligible. It is important to emphasize that the influence of the diameter and the width quantified during the global sensitivity analysis through Sobol indices refers to the variation around the mean value of the hole, not the absolute value of these geometrical properties. As presented in Table 4, the absolute value of the diameter impacts the open-hole tension stress value, but the

sensitivity analysis shows that small variations around a given value are less influential than the fluctuation of the mechanical properties, especially F_{1t} and G_0.

3.3. B-basis allowable analysis

A surrogate model is trained for each hole diameter using the 1,000 random samples for sensitivity analysis. This model serves as an interpolator within the bounds of the analysis. Figure 5 illustrates the results of training the surrogate model for a specific diameter. The errors in the training, validation, and test data are consistently less than 1% for most data points.
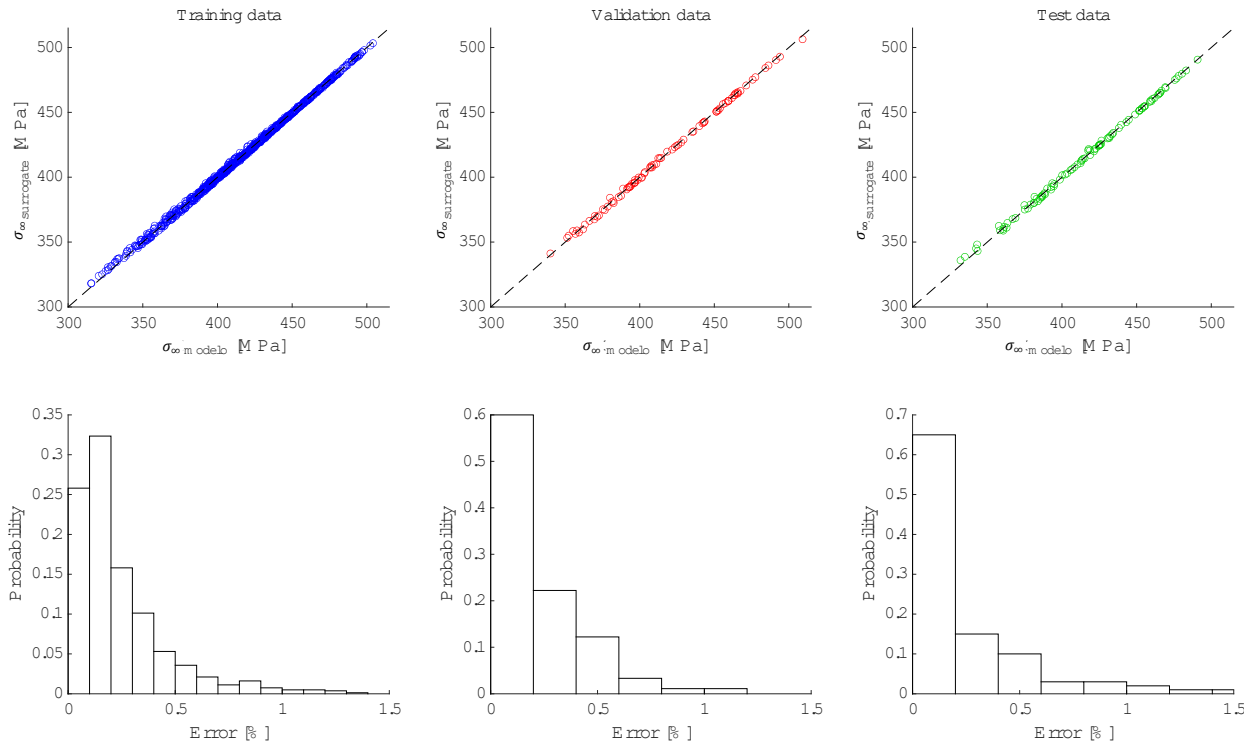
Figure 5. – ANN surrogate model predictions and error on training, validation, and test data.

Based on the mean and standard deviations shown in Table 2, 10,000 random samples are generated for each mechanical property considering a normal distribution, as depicted in Fig. 6. The geometrical properties are assumed to follow a uniform distribution bounded by $\pm 2\%$. These samples serve as input for the ANN surrogate model. Notably, the surrogate model significantly reduces computational costs. While the FFM model requires approximately 80 minutes for the 10,000 simulations, the surrogate model completes the task in just 0.15 seconds.
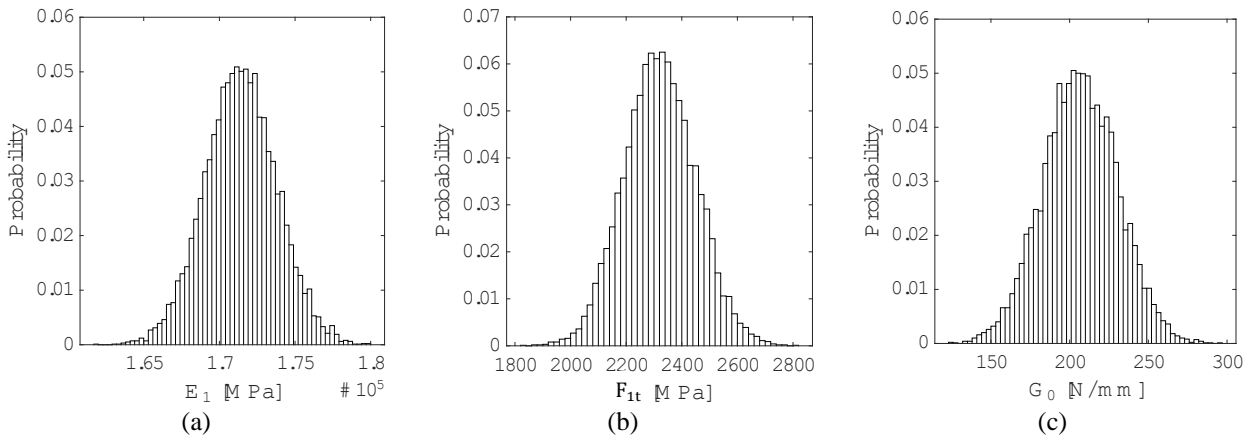
Figure 6. Normal distribution for mechanical properties: (a) E_1, (b) F_{1t}, and (c) G_0.

Figure 7 presents the open-hole tension values obtained using the surrogate model for 2, 4, 6, 8, and 10 mm hole diameters and the sampled input properties. According to MIL-Handbook-17 [11], the B-basis allowable is a 95% lower confidence interval for the tenth percentile within a predetermined population of measurements. The B-basis allowables and the mean values for the distributions are highlighted in Fig. 7. Table 5 presents the values of mean open-hole tension stress and B-basis allowables considering the obtained distributions. Note that the notched strength tension σ_∞ tends to decrease in magnitude as the hole diameter increases, as observed through the mean values of the PDFs.
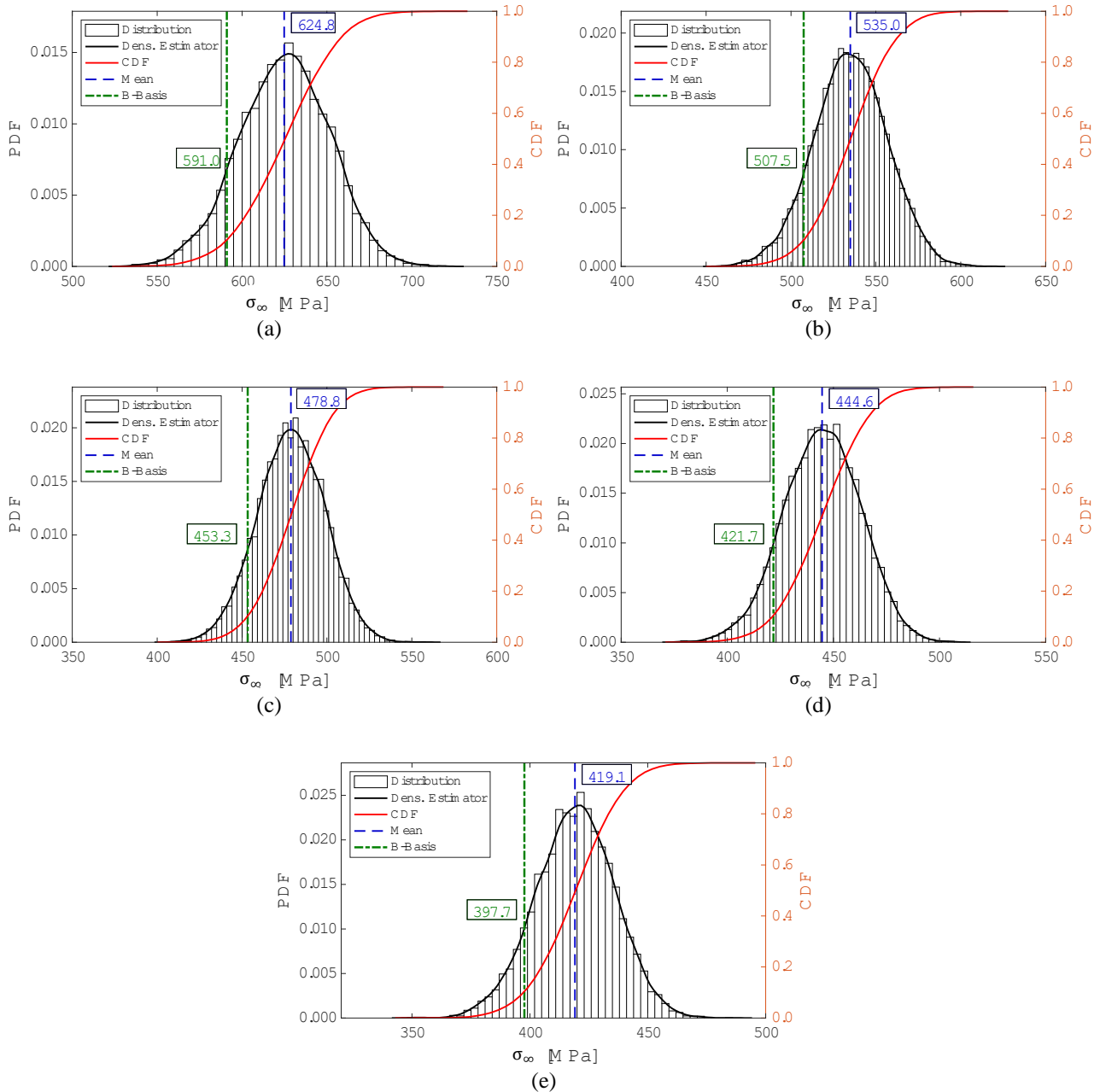
Figure 7. B-basis open-hole tension allowables for hole diameters of (a) 2 mm, (b) 4 mm, (c) 6 mm, (d) 8 mm, and (e) 10 mm.

Table 5 – B-basis design allowable results for

Hole diameter [mm]	2	4	6	8	10
Mean value [MPa]	624.8	535.0	478.8	444.6	419.1
B-basis allowable [MPa]	591.0	507.5	453.3	421.7	397.7

4. CONCLUSIONS

In this work, an FFM model was implemented to evaluate the tensile strength of a quasi-isotropic $[90/0/-45/45]_{3s}$ notched laminate with hole diameters of 2, 4, 6, 8 and 10 mm and $W/D = 6$. The notched tensile strength σ_∞ correlated well with predictions from the literature, with a maximum difference of 1.4%. The discrepancies between the results can be attributed to the numerical approach for solving non-linear equations.

A global sensitivity analysis using Sobol indices has revealed that the primary parameters influencing the model are the tensile ply's longitudinal strength, F_{1t}, and critical energy release rate, G_0. These ply strength parameters exhibit varying importance across small and large diameters. The sensitivity analysis enables a focused characterization of these properties in experimental campaigns, given their significance.

Additionally, a surrogate model has been implemented to accelerate calculations. This model significantly outperforms the original FFM model in computational efficiency and can be used within the training range as an interpolation model. Using the surrogate model, the B-basis curves for notched tensile tension σ_∞ have been obtained in open-hole configurations.

4.1. Declaration of Competing Interest

The authors declare no conflict of interest.

4.2. Acknowledgments

5. REFERENCES

[1] Arteiro A et al. A case for Tsai's Modulus, an invariant-based approach to stiffness. Composite Structures, Volume 252 :112683, 2020. (https://doi.org/10.1016/j.compstruct.2020.112683).

[2] Tsai SW, Melo JDD. An invariant-based theory of composites. *Composites Science and Technology*, Volume 100:237-43, 2014. (https://doi.org/10.1016/j.compscitech.2014.06.017).

[3] Furtado C et al. Prediction of size effects in open-hole laminates using only the Young's modulus, the strength, and the R-curve of the 0° ply. *Composites Part A: Applied Science and Manufacturing*, Volume 101:306-317, 2017. (https://doi.org/10.1016/j.compositesa.2017.04.014).

[4] Vallmajó O et al. Virtual calculation of the B-value allowables of notched composite laminates. *Composite Structures*, Volume 212:11-21, 2019. (https://doi.org/10.1016/j.compstruct.2018.12.049)

[5] Furtado C et al. A methodology to generate design allowables of composite laminates using machine learning. *International Journal of Solids and Structures*, Volume 233:111095, 2021. 10.1061/9780784413609.25710.1016/j.ijsolstr.2021.111095)

[6] Ferreira LPS et al. Bayesian data-driven framework for structural health monitoring of composite structures under limited experimental data. *Structural Health Monitoring*, Volume Online First, 2024. (https://doi.org/10.1177/14759217241236801)

[7] Tsai SW, Melo JDD. A unit circle failure criterion for carbon fiber reinforced polymer composites. *Composites Science and Technology*, Volume 123:71-78, 2014. (https://doi.org/10.1016/j.compscitech.2014.06.017).

[8] Saltelli A et al. *Global Sensitivity Analysis. The Primer*, 1st Edition, 2008. John Wiley & Sons. (https://doi.org/10.1002/9780470725184)

[9] Marelli S, Sudret B. *UQLab: A framework for uncertainty quantification in Matlab*. In: Vulnerability, Uncertainty, and Risk, 2014. ASCE Library. (https://doi.org/10.1061/9780784413609.257).

[10] Kingma DP, Ba J. Adam: A method for stochastic optimization. arXiv, Computer Science, Machine Learning, arXiv:1412.6980, 2014. (https://doi.org/10.48550/arXiv.1412.6980)

[11] MIL-HDBK-17-1F: Composite Materials Handbook, Volume 1 - Polymer matrix composites guidelines for characterization of structural materials, 2002. Department of Defense Handbook.

AN INVESTIGATION OF THE INFLUENCE OF GEOMETRICAL PARAMETERS ON THE CRACK PROPAGATION IN CFRP

Daniel M. B. Netto[a], Lucas L. Vignoli[b], Arthur Adeodato[c], Paulo P. Kenedi[d], *

(a) ⓘ 0000-0002-3265-3095 (Centro Federal de Educação Tecnológica Celso Suckow da Fonseca – Brazil)
(b) ⓘ 0000-0003-3288-3568 (Federal University of Rio de Janeiro – Brazil)
(c) ⓘ 0000-0002-0812-6594 (Rio de Janeiro State University – Brazil)
(d) ⓘ 0000-0001-5563-843X (Centro Federal de Educação Tecnológica Celso Suckow da Fonseca – Brazil)
* Corresponding author: paulo.kenedi@cefet-rj.br

Abstract: Unidirectional carbon fiber reinforced polymers (CFRP) laminates have been widely applied, mainly due to their high specific stiffness and strength. However, due to the material anisotropy, the damage initiation and propagation have very complex characteristics. In this study, a single-layered CFRP laminate with a central crack is subjected to a uniaxial tensile load (perpendicular to the crack). The material is modeled using the finite element software Ansys, considering a solid material with global linear and elastic behavior, with the addition of interface cohesive elements to represent the crack propagation. The main goal is to evaluate the influence of the ratio between the plate width and the crack length on the damage propagation up to the final failure (rupture). The results indicate that for a small ratio between the plate width and the crack length, the crack failure tends to propagate perpendicular to the central crack, which is parallel to the load direction, induced by the shear damage.

1. INTRODUCTION

The knowledge of material failure mechanisms is an important matter to the structural design. For composite materials, complex failure criteria have been proposed in the literature [1-3], by extending and adapting the isotropic failure theories to account for anisotropy and inhomogeneity. Most of them are developed for static load and severe stress concentration, like cracks, is still a problem from the modeling point of view [4].

Even considering the advances of the World-Wide Failure Exercise [5] in the damage evaluation in composite materials, there is still a gap related to the behavior of macro mechanical notched composite plates. Concerning a circular hole, Vignoli et al. [6] showed that matrix failure is dominant for damage initiation. This statement was confirmed for damage propagation numerically [7] and experimentally [8]. A discussion about different geometry variations that induce stress concentration is presented in [9].

This study aims to present a numerical and experimental analysis of the crack effects in unidirectional laminates. The archetype model of the cracked plate is shown in Fig. 1, where the cracked plate is subjected to tensile load. The numerical model, that is introduced in Section 2, is implemented using the finite element (FE) commercial software Ansys. The experimental approach conducted is introduced in Section 3. Section 4 presents the discussion of the main results, followed by the final remarks in Section 5.

1
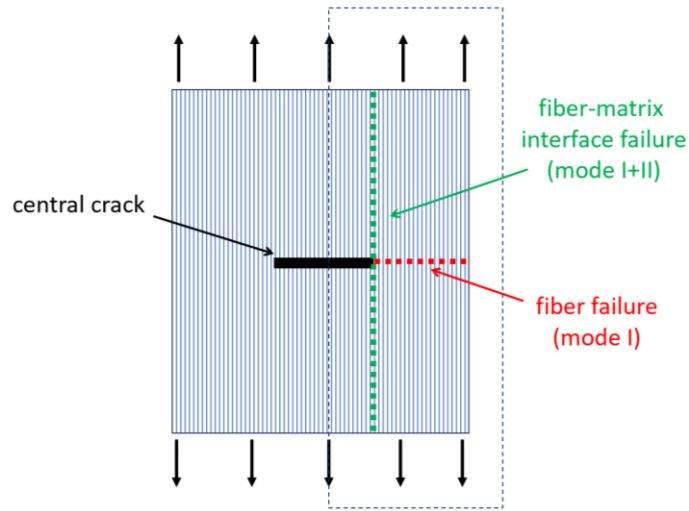
Figure 1. Schematic representation of the central crack in a unidirectional laminate.

2. NUMERICAL MODEL

This Section aims to briefly introduce the FE model developed in this study. The following hypotheses are assumed:

(i) The crack has two preferred paths to propagate, i.e. breaking the matrix or inducing the fiber-matrix debonding [10];

(ii) fiber-matrix debonding can be modeled as mixed-mode interface failure since the in-plane shear and normal tensile load imply fiber-matrix interface failure [11-13];

(iii) despite the fiber rupture is not exactly a cohesive failure, the linear behavior before damage onset and softening behavior during the damage propagation are very similar to the fiber breaking failure [14];

(iv) The material has a global linear and elastic behavior, the nonlinearity is modeled only around the fiber by using cohesive elements for fiber and fiber-matrix interface failure [15].

The cohesive element stiffnesses are computed by

$$K_I^f = \frac{E_1}{t} \tag{1}$$

$$K_I^m = \frac{E_2}{t} \tag{2}$$

$$K_{II}^m = \frac{G_{12}}{t} \tag{3}$$

where K_I^f is the normal stiffness of the elements that represent the fiber breaking, K_I^m and K_{II}^m are the normal and tangential stiffnesses of the elements that represent the fiber-matrix interface debonding, E_1 is the longitudinal elastic modulus, E_2 is the transversal elastic modulus, G_{12} is the shear modulus, and t is the thickness.

The displacements of the damage onset are computed assuming that the interface cohesive tractions are proportional to the displacements using the stiffnesses presented in Eq.(1-3). Hence,

$$u_{Io}^f = \frac{S_{11}^t}{K_I^f} = \left(\frac{S_{11}^t}{E_1}\right)t \tag{4}$$

$$u_{Io}^m = \frac{S_{22}^t}{K_I^m} = \left(\frac{S_{22}^t}{E_2}\right)t \tag{5}$$

$$u_{IIo}^m = \frac{S_{12}^s}{K_{II}^m} = \left(\frac{S_{12}^s}{G_{12}}\right)t \tag{6}$$

2

where S_{11}^t is the longitudinal tensile strength, S_{22}^t is the transversal tensile strength, and S_{12}^s is the in-plane shear strength.

To properly evaluate the damage propagation, the critical fracture energies are defined by

$$G_{Ic}^f = \frac{1}{2} S_{11}^t u_{Ic}^f \tag{7}$$

$$G_{Ic}^m = \frac{1}{2} S_{22}^t u_{Ic}^m \tag{8}$$

$$G_{IIc}^m = \frac{1}{2} S_{12}^s u_{IIc}^m \tag{9}$$

where u_{Ic}^f, u_{Ic}^f, and u_{IIc}^m are the critical displacement which results in final failure.

During the cohesive damage propagation, the debonding parameters are computed by

$$d_I^f = \left(\frac{u_I^f - u_{Io}^f}{u_I^f} \right) \left(\frac{u_{Ic}^f}{u_{Ic}^f - u_{Io}^f} \right) \tag{10}$$

$$d_I^m = \left(\frac{u_I^m - u_{Io}^m}{u_I^m} \right) \left(\frac{u_{Ic}^m}{u_{Ic}^m - u_{Io}^m} \right) \tag{11}$$

$$d_{II}^m = \left(\frac{u_{II}^m - u_{IIo}^m}{u_{II}^m} \right) \left(\frac{u_{IIc}^m}{u_{IIc}^m - u_{IIo}^m} \right) \tag{12}$$

Since the fiber-matrix interface experiences a mixed debonding, the quadratic criterion is assumed and bilinear behavior is considered for both fiber and fiber-matrix interface failure. An example of the convergent mesh is presented in Fig. 2, where the one-half symmetry is defined with 37547 quadratic plane elements and assuming the plane stress state.
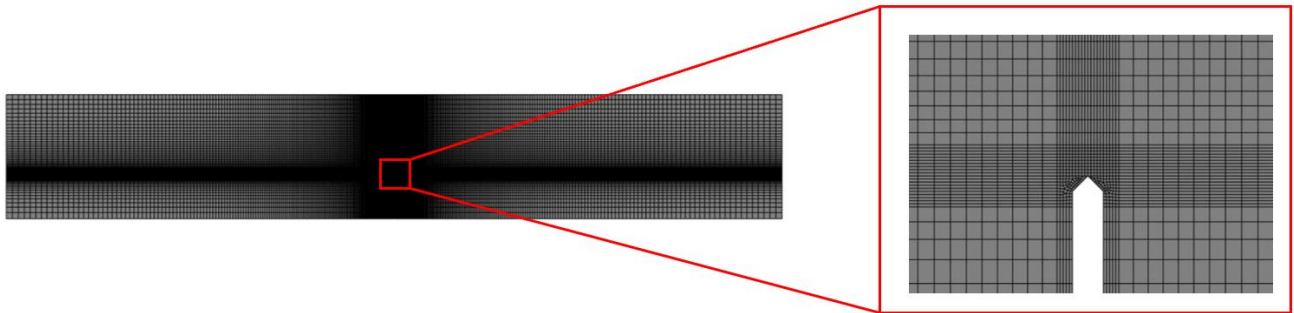
Figure 2. Convergent mesh for the FE simulations.

3. EXPERIMENTAL APPROACH

In this section, the laminate composite specimens with a central crack are described, as well as the experimental apparatus and the test itself. Fig. 3 shows the material testing machine INSTRON of 250 kN capacity with DIC accessory.

3

Figure 3. Material testing machine INSTRON of 250 kN capacity with DIC accessory and a mounted specimen.

A material testing machine INSTRON of 250 kN capacity was used, with a loadcell of 100 kN, with 1 mm/min rate, and displacement control. The digital image correlation (DIC), used in the tests, is a relatively recent form of a non-contact tracking speckles displacements, on a prepared specimen surface, to generate strain distribution of the analyzed region.

The nominal dimensions of the laminate specimens were 200 mm x 40 mm x 1 mm, with a central crack of one-third of the width. The specimens were manufactured with an epoxy matrix and unidirectional carbon fibers with three layers. The central crack was produced in two steps: initially, a hole drilling was made in the specimen center. Then using this hole, a portable saw bow jewelry wire with 0.3 mm of width was used to saw the "crack" up its final length. To use the DIC, a special surface preparation must be done in the target region of the specimens. This preparation was done in two steps: first, the target region was painted with white spray paint, and in second place, black spray paint was used to introduce black speckles on the white basis in a ratter non-uniform distribution. See Fig. 4 for a detailed photograph of the surface preparation.
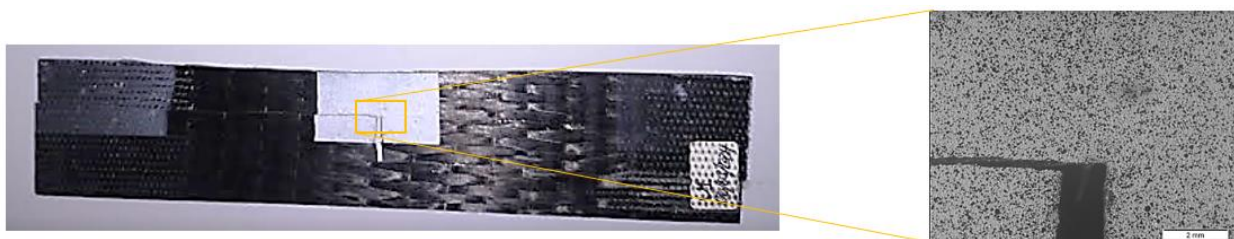
Figure 4. Laminate composite specimens with a central crack after testing.

Note that in the detailed picture shown in Fig. 4, it is quite clear that the final failure of the unidirectional specimen occurred perpendicular to the crack and parallel to the carbon fibers. Figure 5 shows the DIC strain results for the region in front of the crack tip for the unidirectional specimen.

4
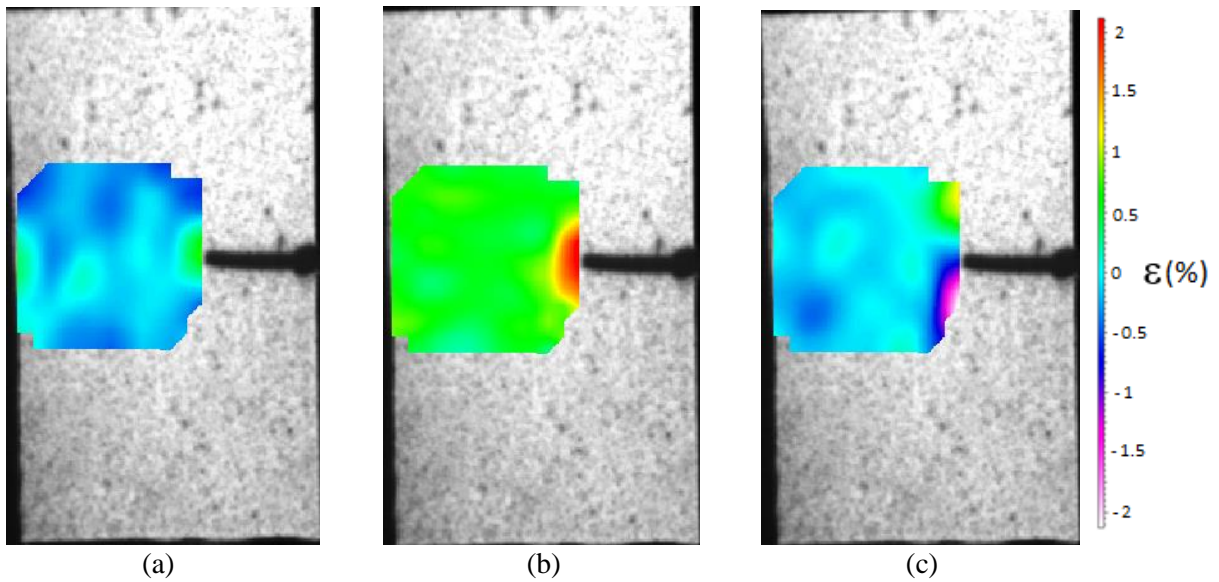
Figure 5. DIC results for the unidirectional specimen: (a) ε_{xx}, (b) ε_{yy}, and (c) ε_{xy}.

Fig.5.b shows, that around the crack tip, the red region where the ε_{yy} strains are higher. This region is related to the processed zone. An analytical estimation of the processed zone around the crack tip is in development. Also, Fig. 5.c shows relatively high ε_{xy} strains, which can be utilized to explain the preferential crack propagation in mode II.

4. RESULTS AND DISCUSSION

To implement the FE model, the laminae properties considered are: $E_1 = 112$GPa, $E_2 = 6.6$GPa, $G_{12} = 2.9$GPa, $\nu_{12} = 0.319$, $S_{11}^t = 1275$MPa, $S_{22}^t = 41$MPa, and $S_{12}^s = 31$MPa [16]. Nguyen and Waas [17] tested another CFRP are obtained $G_{Ic}^f = 40$kJ/m^2, $G_{Ic}^m = 0.29$kJ/m^2, and $G_{IIc}^m = 0.63$kJ/m^2. Since G_{Ic}^m and G_{IIc}^m are governed by the fiber-matrix interface, the values reported in [16] are assumed. On the other hand, G_{Ic}^f is governed by the fibers; hence, it is assumed that G_{Ic}^f/E_1 is the same for ref. [15] and [16], obtaining $G_{Ic}^f = 28.3$kJ/m^2.

Figure 6 shows the comparison between experimental and numerical results of the force-displacement curve. A great agreement between both approaches is realized, indicating that the cohesive elements can be applied for intra-ply crack propagation analysis in unidirectional laminates, despite this element type being initially formulated for inter-ply crack (delamination).
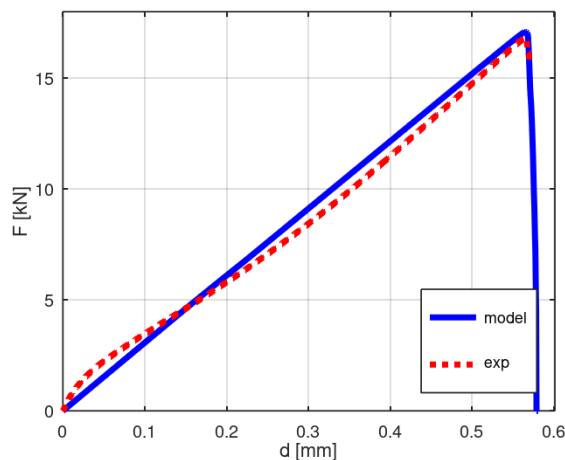
Figure 6. Validation of the FE model.

5

For a parametric analysis of the plate width, b, the force is transformed for nominal stress by applying $\sigma_n = F/bt$. Figure 7 show $\sigma_n^{max} = \max(F)/bt$ for $20\text{mm} \leq b \leq 60\text{mm}$.
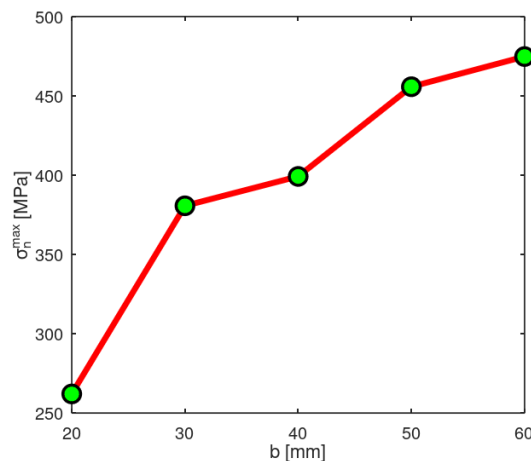
Figure 7. Parametric analysis of the maximum load according to the plate width.

When b increases, the plate tends to have the same behavior as an infinity plate. On the other hand, when b decreases the crack tends to break the plate with lower stresses.

5. CONCLUSIONS

This study presents the initial development of a novel numerical modeling approach for cracked composite plates by applying cohesive elements to model fiber breaking and fiber-matrix interface. An experimental approach is carried out to validate the FE model. At last, the influence of the plate width is investigated, indicating that the crack tends to propagate parallel to the fiber direction for shorter widths.

5.1. Declaration of Competing Interest

The authors declare no conflict of interest.

5.2. Fundings

5.3. Acknowledgements

6. REFERENCES

[1] S.W. Tsai, E.M. Wu. A general theory of strength for anisotropic materials. *J Compos Mater*, Volume 5, 58–80, 1971.(https://doi.org/10.1177/002199837100500106)

[2] Z. Hashin. Failure Criteria for Unidirectional Fiber Composites. J Appl Mech, Volume 47, 329–334, 1980. (https://doi.org/10.1115/1.3153664)

[3] A. Puck, H. Schurmann. Failure analysis of FRP laminates by means of physically based phenomenological models. *Compos Sci Technol*, Volume 58, 1045–1067, 1998. (https://doi.org/10.1016/S0266-3538(01)00208-1)

[4] L.L. Vignoli, J.T.P. Castro, M.A. Meggiolaro. Stress concentration issues in unidirectional laminates. *J Braz Soc Mech Sci Eng*, Volume 41, 1–27, 2019. (https://doi.org/10.1007/s40430-019-1965-7)

[5] M.J. Hinton, A.S. Kaddour, P.D. Soden. *Failure criteria in fiber-reinforced-polymer composites* — The World-Wide Failure Exercise. Elsevier, 2004.

6

[6] L.L. Vignoli et al. Multiscale approach to predict strength of notched composite plates. *Compos Struct*, Volume 253, 112827, 2020. (https://doi.org/10.1016/j.compstruct.2020.112827)

[7] L.L. Vignoli, J.T.P. Castro. A parametric study of stress concentration issues in unidirectional laminates. *Mech Adv Mater Struct*, Volume 28, 1554–1569, 2021. (https://doi.org/10.1080/15376494.2019.1688434)

[8] P.P. Kenedi et al. Damage tracking of notched composite plates by thermography—Experimental observations and analytical model for damage onset. *J Compos Mater*, Volume 56, 1211–1220, 2022. (https://doi.org/10.1177/00219983211072297)

[9] E. Zavvar, A.S. Hosseini, M.A. Lotfollahi-Yaghin. Stress concentration factors in steel tubular KT-connections with FRPWrapping under bending moments. *Structures*, Volume 33, 4743–4765, 2021. (https://doi.org/10.1016/j.istruc.2021.06.100)

[10] M.V. Angelo, M.L. Ribeiro, V. Tita. A computational framework for predicting onset and crack propagation in composite structures via eXtended Finite Element Method (XFEM). *Latin American Journal of Solids and Structures*, Volume 15, e70, 1–14, 2018. (https://doi.org/10.1590/1679-78254301)

[11] L.L. Vignoli et al. Micromechanical fiber-matrix interface model for in-plane shear in unidirectional laminae. *Mechanics of Advanced Materials and Structures*, online, 1–13, 2023. (https://doi.org/10.1080/15376494.2023.2259903)

[12] L.L. Vignoli et al. Analytical modeling of fiber-matrix interface failure in unidirectional laminae subjected to in-plane shear loads. *Proceedings of the Institution of Mechanical Engineers, Part L: Journal of Materials: Design and Applications*, online, 2024. (https://doi.org/10.1177/14644207241226857)

[13] L.L. Vignoli et al. Micromechanical analysis of transversal strength of composite laminae. *Compos Struct*, Volume 250, 112546, 2020. (https://doi.org/10.1016/j.compstruct.2020.112546)

[14] A. Bunsell et al. Benchmarking of strength models for unidirectional composites under longitudinal tension. *Composites Part A: Applied Science and Manufacturing*, Volume 111, 138-150, 2018. (https://doi.org/10.1016/j.compositesa.2018.03.016)

[15] L.L. Vignoli et al. An investigation about stresses and processed zone around crack tip in CFRP plates. *Journal of the Brazilian Society of Mechanical Sciences and Engineering*, Volume 45, 255, 2023. (https://doi.org/10.1007/s40430-023-04144-7)

[16] Vignoli LL, Kenedi PP, Mariano MJB. Exploring thermography technique to validate multiscale procedure for notched CFRP plates. *Compos Part C Open Access*, Volume 7, 100241, 2022. (https://doi.org/10.1016/j.jcomc.2022.100241)

[17] M.H. Nguyen, A.M. Waas. Detailed experimental and numerical investigation of single-edge notched tensile cross-ply laminates. *Composite Structures*, Volume 279, 114731, 2022. (https://doi.org/10.1016/j.compstruct.2021.114731)

7

DRILLING BEHAVIOR OF THERMOPLASTIC AND THERMOSET CFRP LAMINATES UNDER CRYOGENIC COOLING AND DRY MACHINING

Francisco A. Toti[a], Alessandra C. S. P. Tarpani[b], Alessandro R. Rodrigues[b], Marcelo F. Batista[c], José R. Tarpani [b]

(a) Faculty of Technology of Sorocaba, Center Paula Souza, SP-Brazil
(b) University of São Paulo, USP-São Carlos, SP-Brazil
(c) Institute of Education, Science and Technology of São Paulo, Araraquara, SP-Brazil
* Corresponding author: francisco.toti01@fatec.sp.gov.br

CODE: BCCM7-149

Abstract: Continuous carbon fiber-reinforced polymer composite laminates (CFRPs) are gaining popularity in high-tech areas including aeronautics and aerospace. CFRPs have traditionally been made with a thermoset matrix; however, more industries are looking into thermoplastic matrix options due to variables such as useful life and recycling. Laminated components and structures are typically subjected to machining, particularly drilling. In this context, the current study intended to assess the behavior of thermoplastic and thermoset matrix CFRP laminates in terms of the drilling energy and the torque developed during the three stages of the drilling process under dry and cryogenic cooling conditions, respectively. The results revealed that the latter drilling approach produces a larger feed force and related demand for energy in the operation than the former procedure. When machined dry, the thermoplastic laminate showed less delamination-type damage at the hole's exit than the thermoset, but cryogenic cooling caused the opposite result.

1. INTRODUCTION

CFRP laminates are frequently employed in structural components in high-tech industries, such as aerospace, due to their advanced construction requirements [1]. Its widespread use in structural components in the aerospace and automotive industries stems from its high specific strength and stiffness when compared to typical materials from the previous decade [2]. Traditionally, CFRP laminates have used thermoset resins; however, more industries are recognizing the promise of thermoplastic resins for better strength and nearly unlimited service life [3]. In this context, the introduction of new high-performance thermoplastics to replace thermosets in carbon fiber-reinforced polymers presents a new machining problem [4]. Studies on drilling-related flaws have converged on the interaction between composite laminate composition and layout, process parameters, and cooling conditions. The hole has three places where faults can be generated: at the entrance, along the surface, and at the exit, each of which may include one or more defects. These faults can cause structural and/or assembly damage; nevertheless, the extent to which a defect is related to drilling process parameters is still a hot topic in CFRP laminate literature. However, the feed rate is considered a determining factor for the occurrence of delamination defect [5,6,7,8].

2. STAGES OF THE DRILLING PROCESS

The stages of the drilling process in CFRP composite laminates are determined by the behavior of feed force versus time and/or tool displacement, beginning with the tool's transverse edges contacting the input surface and ending with the cutting edges and body exceeding the exit surface of the material to be drilled. In the present study, the drilling process was examined in three steps [9]. Stage I begins with the transverse edges

engaging the material being drilled and ends with the primary cutting edges fully engaged, gradually increasing the cutting width. Stage II begins with the tool engaging the material and concludes with the transverse edges contacting the exit surface. The cutting breadth remains constant during this step. Stage III begins after Step II and finishes after the transverse cutting edges are fully eliminated from the material and the cutting width gradually diminishes. Fig. 1 shows the drilling process.
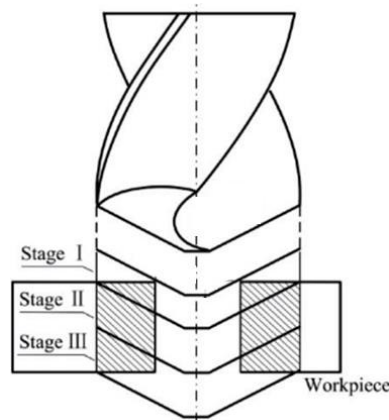
Figure 1 - Three stages of the drilling process [9].

3 EXPERIMENTAL PROCEDURES

3.1 Material, drilling process and tool

Tencate™'s PPS (Poly-Phenylene Sulfide) thermoplastic matrix reinforced with continuous carbon T300 JB fibers (C), was drilled. The PPS-C fabric layer weighed 280 g/m^2, measured 17.8 tow per inch by 17.8 tow per inch, contained 3,000 filaments per tow, and exhibited a 5HS weave pattern. The laminate had approximately 50 v% in fiber and was created by stacking 16 layers of 0/90° bidirectional fabric in the [(0/90),(+45/-45)2,(0/90)]$_4$ array for a laminate thickness of 4.7 mm. Hexcel™ EPX (Epoxy) thermoset matrix (toughened with thermoplastic elastomer particles) reinforced with continuous AGP193 carbon fibers was also machined. The EPX-C fabric layer weighed 193 g/m^2, measured 11.5 tow per inch x 11.5 tow per inch, contained 3,000 filaments per tow and exhibited a plain wave weave pattern. The laminate had approximately 60 v% in fiber and was produced by stacking 24 layers of 0/90° bidirectional fabric in the [(0/90),(+45/-45)2,(0/90)]$_6$ array for a laminate thickness of 5 mm. Full-thickness samples were cut from both the original laminates with a water-cooled rotating diamond saw. The drilling process was carried out on Romi D800 three-axis machining center tool machine with a maximum speed of 10,000 rpm and a power of 20 hp. The cutting speed (Vc) was set to 60 m/min, and the feed rate (f) were 45, 90, 180, and 360 mm/rev. For this purpose, Seco Tools Industry™ delivered a 6 mm diameter hard metal drill with a1163-6 code diamond coating and two tip angles (130º and 60º). Semper Crio Industry™ supplied the SC18 cooling system used to apply liquid nitrogen (N$_2$L).

3.2. Force, torque and energy

Graphs were generated employing the data provided on the feed force as a function of the tool's total displacement of 8 mm, and experimental values for the feed energies of the three drilling stages were obtained, as well as the contribution of the materials to the increase in torque during these steps. Two computer programs were developed using the MATLAB R2015a software, educational version. Fig. 2 and 3 depict graphs of integrated energy vs feed force and torque with and without filters, respectively.

2
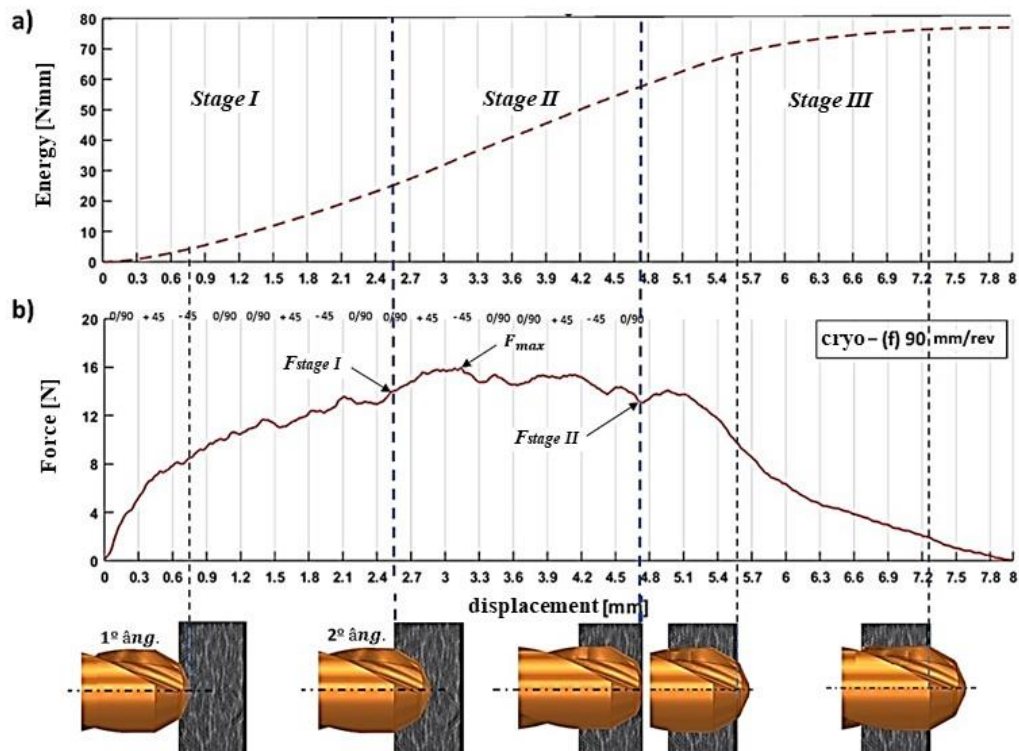
Figure 2 - Graphs generated by the computer programs referring to the PPS-C drilling test under cryogenic cooling at f = 0.090 mm/rev: (a) total feed energy, and (b) feed force.
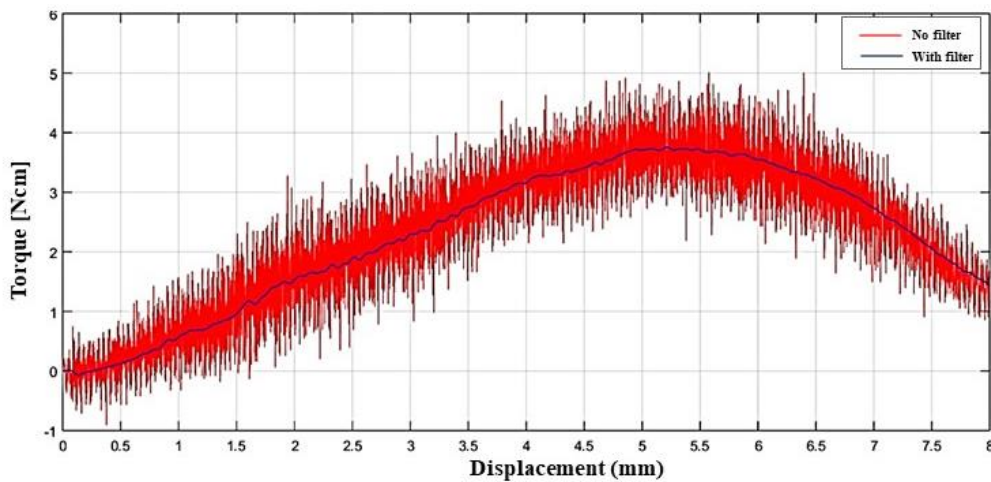
Figure 3 - Torque graph with and without filter of the PPS-C drilling test under cryogenic cooling at f = 0.090 mm/rev.

3.3 Conventional Delamination Factor

Among the factors available in the literature, the conventional one-dimensional delamination factor (F_d) [10] aims to easily analyze and compare the degree of delamination in composite laminates, being determined as a function of the ratio between the maximum diameter (D_{max}) that contains the greatest extent of delamination or cracks and the nominal diameter of the hole (D_o), as expressed in Eq. (1):

$$F_d = \frac{D_{max}}{D_o} \tag{1}$$

3

4. RESULTS AND DISCUSSION

4.1 Feed force and torque

Fig. 4a depicts the torque values acquired during dry cooling of PPS-C. In stage I, the torque increases sharply at the four feed rates. In stage II, because the tool's cutting edges are fully engaged in the material, the torque increases less sharply as the feed force stabilizes, reaching its maximum value (T_{max}) in stage III at the end of exiting the first angle at feeds of 0.045, 0.090, and 0.180 mm/rev, and at the beginning of the second angle for the feed of 0.360 mm/rev. The increase in torque in stage II can be due to friction between the tool's cutting edges and the material that progresses to the final layers of the laminate, as well as a loss of support at the hole's exit, which can cause deformations and bends, resulting in more tool contact. Tool body contact with the inner surface of the hole results in an excessive increase in torque [10]. As shown in Fig. 4b, the torque continued to increase in stage III despite a decline in input force, which could be attributed to the elastic recovery of the fibers subjected to the cutting process [11].
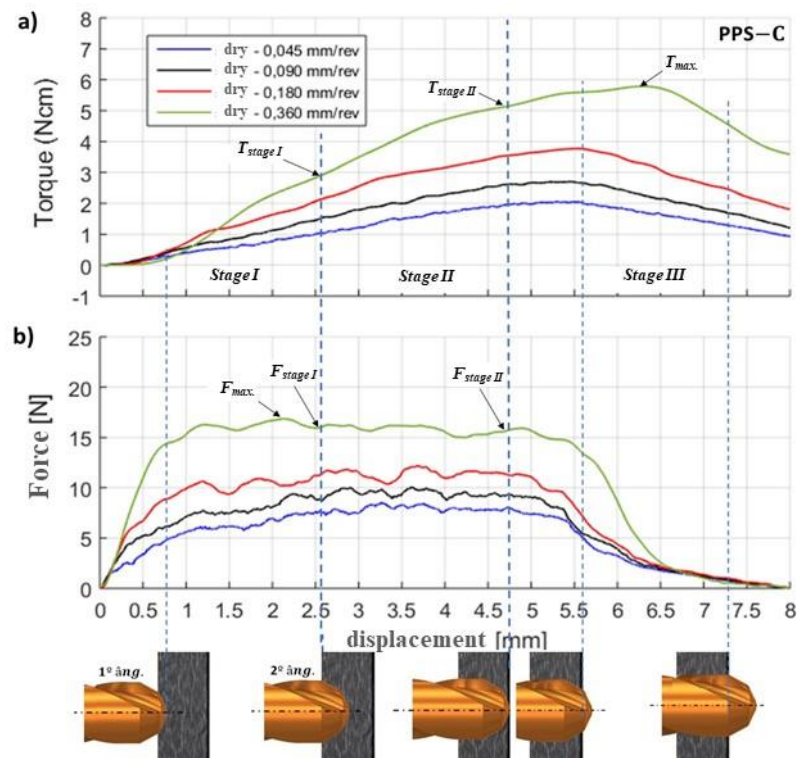
Figure 4 - Drilling test values as a function of tool feeds and displacement under dry conditions for PPS-C: (a) torque and (b) feed force.

Fig. 5a depicts torque values for the PPS-C at cryogenic cooling conditions. The values obtained for the four feed rates are higher in all stages than those obtained under dry conditions, consistent with the pattern of locating the maximum torque shown in Fig. 4a. Fig. 5b shows that the feed force values are higher than those of the dry condition in the four feeds shown in Fig. 4b, with the feed rates of 0.045 mm/rev exhibiting the greatest difference in the value of the Fmax in relation to the dry condition, indicating that the smaller the feed rate, the longer it takes for the liquid nitrogen jet (N_2L) to change the rigidity of the laminate. As the drilling temperature drops, the composite laminate becomes more rigid and, as a result, more fragile, because the matrix absorbs minimal energy [12]. The increase in feed force during cryogenic cooling can be attributed to the matrix's increased tensile strength and elastic modulus [13, 14].

4
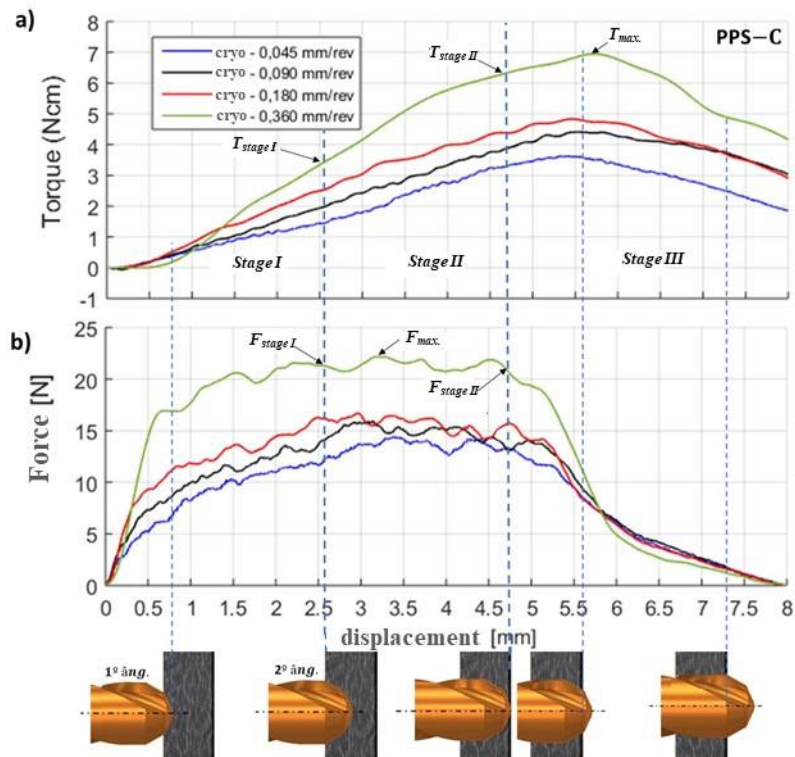
Figure 5 - Drilling test values as a function of feed rate and tool displacement under cryogenic cooling for PPS-C: (a) torque, and (b) feed force.

Fig. 6a shows the EPX-C's torque values in dry conditions. It is seen that at the end of stage I, the torque values increase with feed rate, except for 0.045 mm/rev, which remains constant in stages II and III.
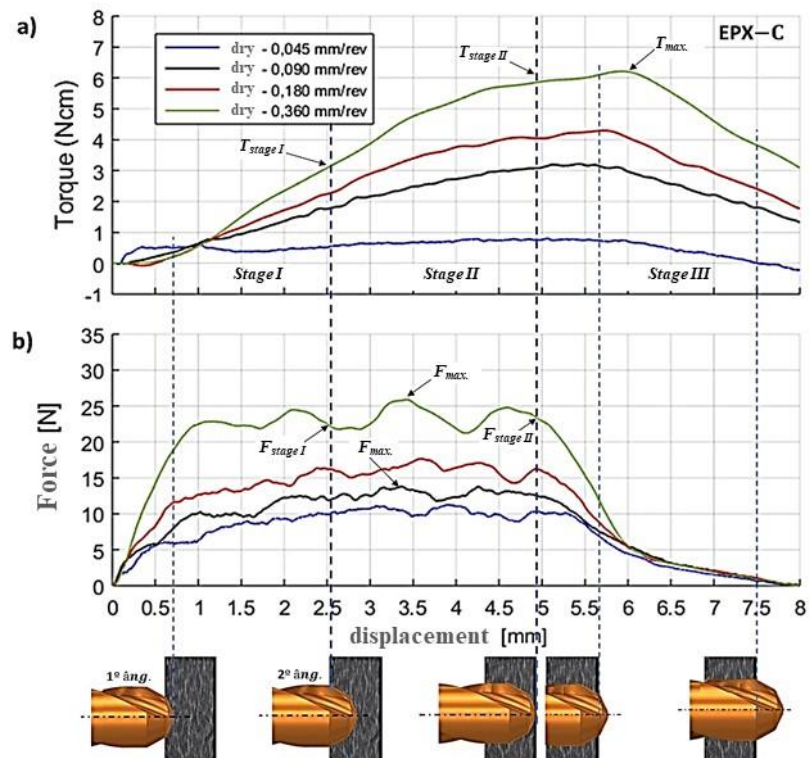
Figure 6 - Drilling test values as a function of feed rate and tool displacement under dry conditions for the EPX-C: (a) torque, and (b) feed force.

5

In stage II, the torque increases dramatically at feed rates of 0.090, 0.180, and 0.360 mm/rev, reaching its peak values in stage III. When comparing the contribution of EPX-C to the increase in torque in stages II and III to PPS-C shown in Figure 4a under dry conditions, the values are higher, but close, and can be attributed to the greater number of layers of EPX-C (24 layers) than PPS-C (16 layers), since the percentage of fiber volume is similar, but with different weights. Fig. 6b demonstrates that the F_{max} was reached with the shortest tool displacement at a feed rate of 0.090 mm/rev, and the force values in stage II are similar to those in stage I, suggesting the same behavior with respect to PPS-C. However, EPX-C shows higher values, which may be due to the thermoset matrix.

Fig. 7a shows the EPX-C's torque values under cryogenic cooling. It should be noticed that the values obtained for the four feed rates are higher in all phases than the values obtained under dry conditions, indicating the same tendency of positioning the maximum torque
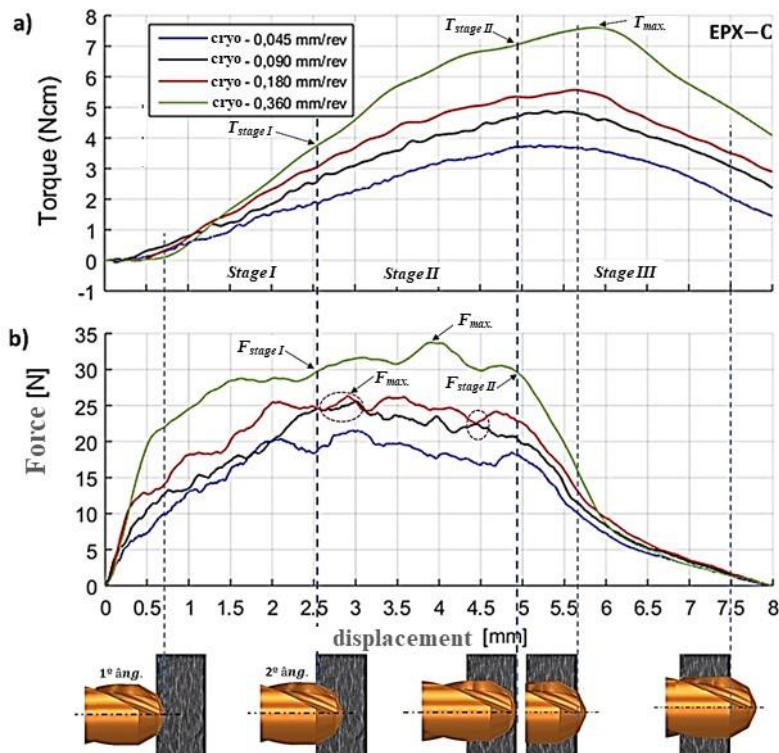
Figure 7 - Drilling test values as a function of feed rate and tool displacement under cryogenic cooling for the EPX-C: (a) torque and (b) feed force.

Fig. 7b displays the feed force values obtained under cryogenic cooling, highlighting in step II that F_{max} is achieved at near displacements at feed rates of 0.045, 0.090, and 0.180 mm/rev. Furthermore, the curves corresponding to feed rates of 0.090 and 0.180 mm/rev show equal values at two displacement positions in stage II, showing behavior similar to that of PPS-C under cryogenic cooling. This phenomenon results from signal oscillation. In stage III, the decline in force occurs more sharply until the exit from the first angle and more tenuously with the escape from the second angle than in the dry condition. A recent study [15] found opposing results in their work only in terms of T_{max}, with values under dry conditions being larger than values under cryogenic cooling, with cutting and material parameters close to those in this study. They suggested that the decreased torque could be attributable to a decrease in the friction coefficient at the tool-material interface, citing previous cryogenics research [16, 17]. The four N_2L jets spread at 90º in the axial direction of the tool may have weakened the fibers more than a single jet in the current study.

4.2 Feed energy

Fig. 8 depicts the values of total feed energy and stages I, II, and III obtained from three specimens for each feed condition under dry and cryogenic cooling circumstances, respectively, for the PPS-C laminate. Fig. 8a shows that as the feed rate increases in the order of 0.045 mm/rev, 0.090 mm/rev, 0.180 mm/rev, and 0.360

6

mm/rev, the total energy values increase during cryogenic cooling compared to the dry condition. Fig. 8b shows that the energy values in stage I are higher than those in stage III, as shown in Fig. 8d, in all feeds and both cooling conditions, due to the material's lower flexibility in this initial stage of the tool's feed, which gradually increases depending on cutting width. In stage III, the opposite occurs, as the cutting width decreases and the material is pushed by the tool's tip, providing less resistance. In addition, the energy values in stage III under cryogenic cooling are near in feed of 0.045mm/rev, 0.090mm/rev, and 0.180mm/rev, not following the increasing trend due to the feed under dry conditions, suggesting the influence of the N_2L jet on the fragility of PPSC. This is especially noticeable at a feed rate of 0.360 mm/rev, where the values are similar in both dry and cryogenic cooling circumstances because the higher the feed, the shorter the cooling period, as illustrated in Fig. 8d
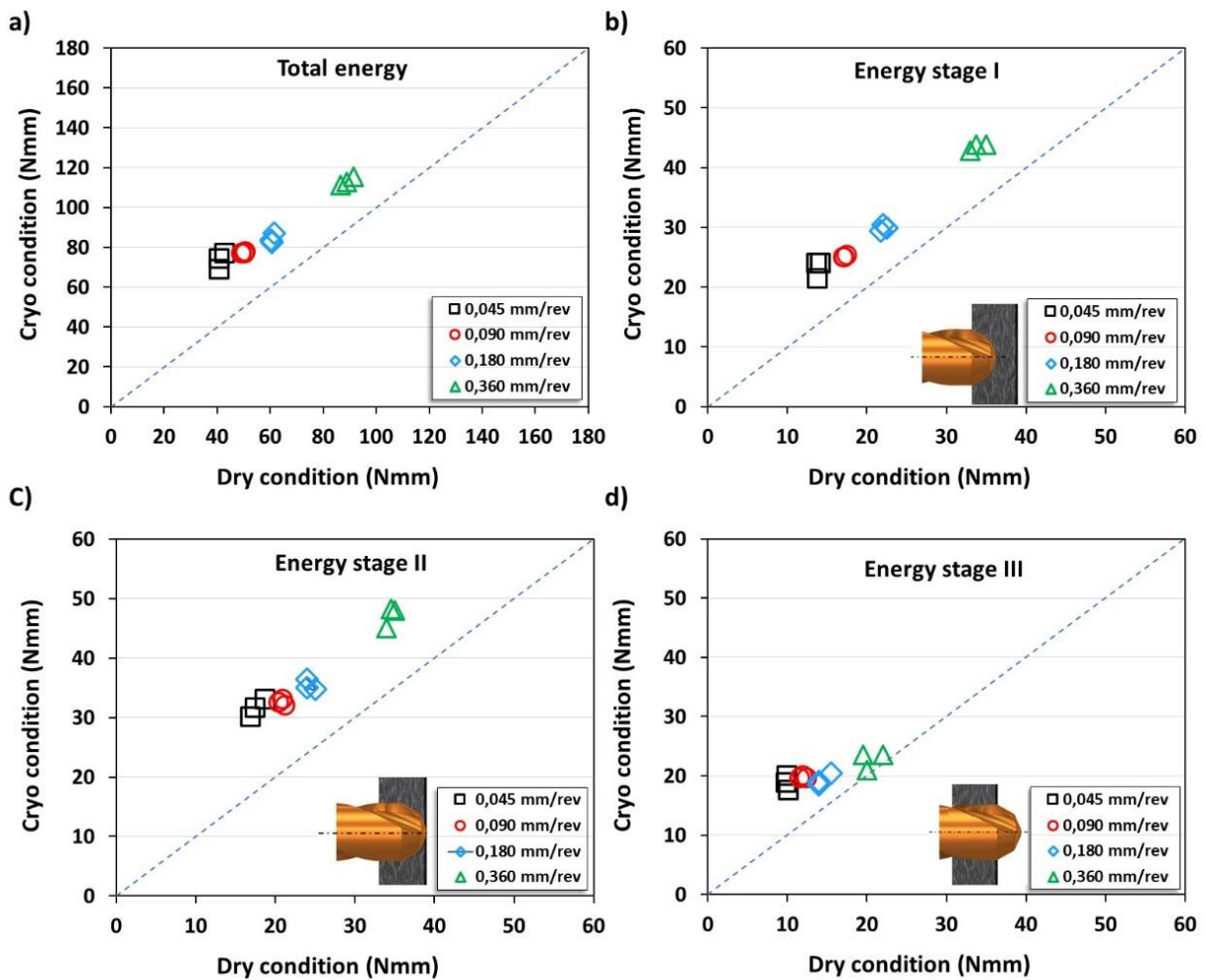
Figure 2 - Feed energy values for PPS-C under dry and N2L cooling condition: (a) total. (b) stage I. (c) stage II and (d) stage III.

Fig. 9 provides the total feed energy and phases I, II, and III for the EPX-C laminate collected from three specimens at different feed rates under both dry and cryogenic chilling conditions. Fig. 9a shows that as the feed increases in the sequence of 0.045 mm/rev, 0.090 mm/rev, 0.180 mm/rev, and 0.360 mm/rev, the total energy values increase, with cryogenic cooling being more efficient than dry cooling, as seen in the PPS-C laminate in Fig. 8a. However, the values are larger than those reported by PPS-C, as the thermoset matrix contributes more to the feed force than the thermoplastic matrix.

The matrix's contribution to the increase in feed force is owing to the predominance of its thermomechanical characteristics in the feed direction, which is stronger for matrices with higher degrees of crosslinking (high modulus of elasticity and Tg) [18]. Fig. 9b reveals that energy values in stage I are higher at all feed rates in the two cooling conditions than in stage III, as illustrated in Fig. 9d. However, the values of

7

stage III grow less significantly with an increase in feed rate during cryogenic cooling compared to the dry condition, exhibiting a different behavior from that of the PPSC laminate illustrated in Fig. 8d.

Fig. 9c shows that the energy values of stage II grow as the feed increases, with dry conditions producing lower values than cryogenic cooling. These experimentally obtained feed energy findings demonstrated the two matrices' varied behaviors and their influence on the three drilling stages. Thermoplastic composites have a high plastic deformation capacity under load, but thermoset composites are brittle and have a fundamentally different behavior, impacting the material's response to machining [19].
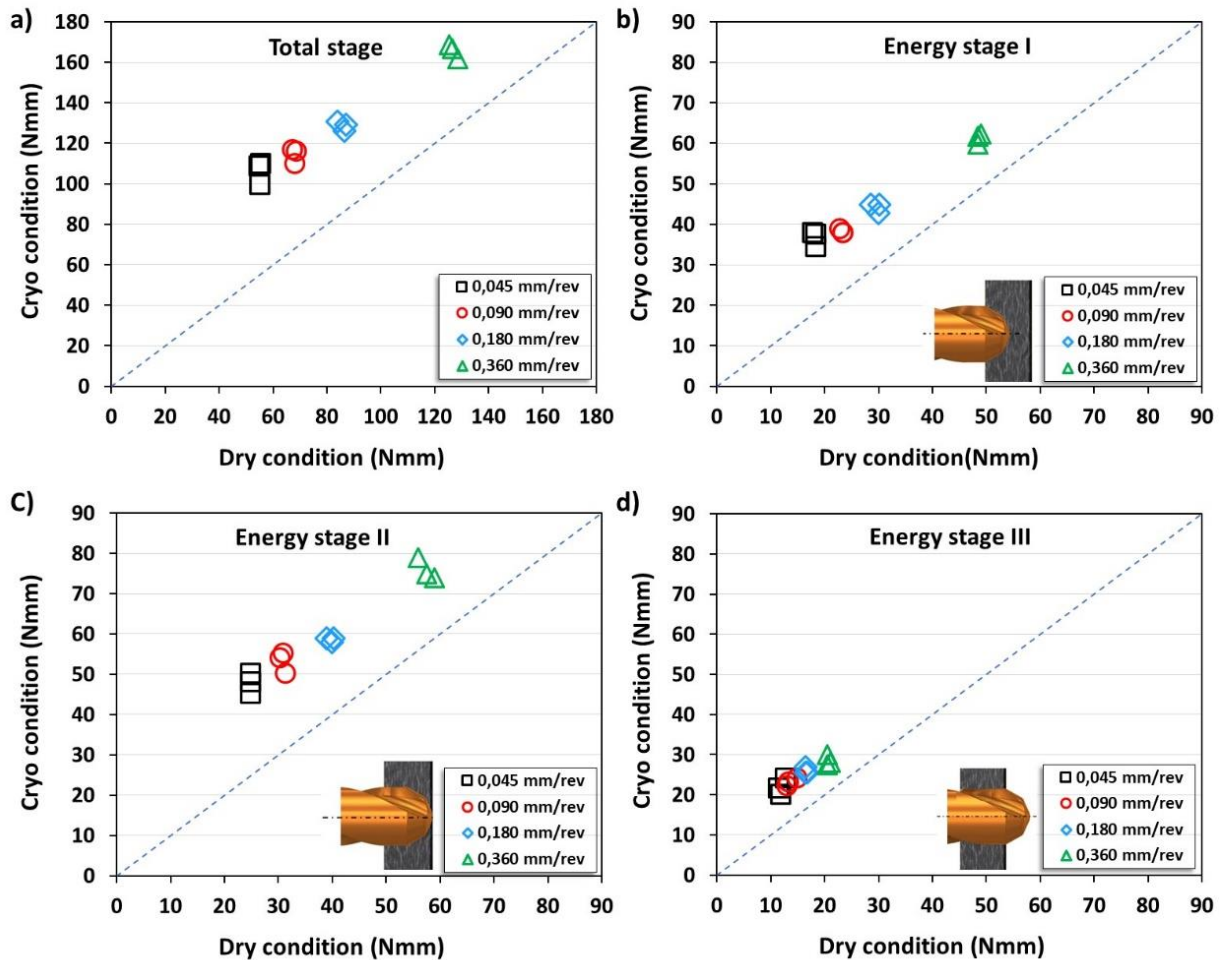
Figure 3 - Feed energy values for EPX-C under dry and cryogenic cooling conditions, respectively: (a) total, (b) stage I, (c) stage II, and (d) stage III.

4.3 Conventional delamination factor

Fig. 10 displays the conventional delamination factor (F_d) on the hole exit surface for the PPSC and EPX-C laminates. Fig. 10a for PPS-C shows that the Fd values during cryogenic cooling are greater than the dry condition values for feed rates of 0.045 mm/rev, 0.090 mm/rev, and 0.180 mm/rev, and near at 0.360 mm/rev. This proximity of values can be attributed to the N_2L jet's shorter action time in changing the stiffness of the laminate. Fig. 10b for EPX-C shows that the F_d values during cryogenic cooling are greater than the values under dry conditions at feed rates of 0.045 mm/rev, 0.090 mm/rev, and 0.180 mm/rev, and close at 0.360 mm/rev.

When the Fd values for PPS-C and EPX-C are evaluated, they behave similarly under both cooling conditions and at all feeds. However, EPX-C performed best under cryogenic cooling and PPS-C under dry

8

circumstances at feed rates of 0.045 mm/rev, 0.090 mm/rev, and 0.180 mm/rev. This occurred because the tool geometry and cutting parameters behaved similarly, and the variation in results could be attributed to the number of reinforcing layers and matrix type, given the same physical arrangement.

Another item to note is the F_d values obtained at a feed rate of 0.360 mm/rev, which were lower in the EPX-C but greatest in the PPS-C in comparison to the other feed rates. In this setting, it was expected that PPS-C, with its more ductile matrix, would produce lower values at the greatest feed rate.
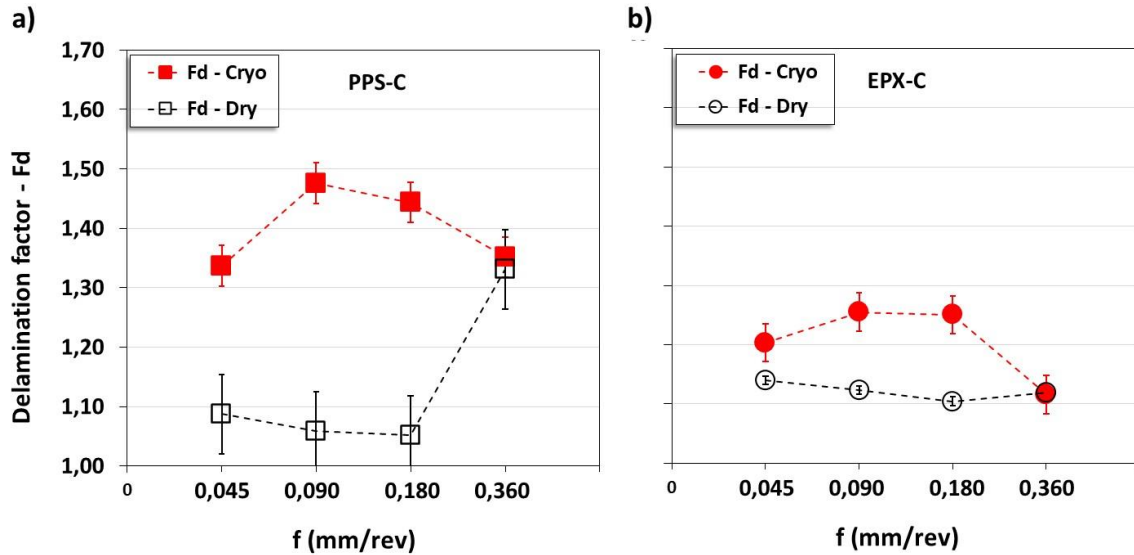
Figure 10 - F_d values at the hole exit surface as a function of feed rate under dry and cryogenic cooling conditions, respectively: (a) PPS-C, and (b) EPX-C.

5 CONCLUSIONS

The drilling test data led the following conclusions:

- In both dry and cryogenic cooling circumstances, the epoxy matrix and carbon fiber laminate produced more torque in the intermediate and final drilling stages (stages II and III) than the competing PPS thermoplastic matrix composite, which also contained carbon fibers. The thermosetting nature of the epoxy matrix, the increased number of layers, and the somewhat larger thickness of the corresponding laminate all contributed to this effect, resulting in better elastic recovery of both the matrix and reinforcing fibers throughout the cutting process.

- Machining under cryogenic chilling resulted in a higher cutting feeding force in both laminates than the dry process, which is attributed to an increase in composite stiffness when drilled under forced N_2L cooling. This was validated to the amount of energy required to feed the cutting tool in the three drilling steps (stages I–III).

- The F_d factor values demonstrated that the thermoplastic laminate PPS-C had superior machinability in the dry state than the thermoset EPX-C. However, under cryogenic cooling, the thermoset laminate outperformed the thermoplastic, which was more prone to developing delamination-type damage. This shift in matrix behavior is associated with its viscoelastic behavior, which affects its machinability differently from the thermoset matrix laminate.

5.1 Declaration of Competing Interest

The authors declare no conflict of interest.

9

ACKNOWLEDGEMENTS

REFERENCES

[1] Geier N, Szalay T, Takács M. Analysis of thrust force and characteristics of uncut fibres at non-conventional oriented drilling of unidirectional carbon fibre-reinforced plastic (UD-CFRP) composite laminates. International journal of advanced manufacturing Technology, 2019. vol. 100, p. 3139–3154.

[2] Km J, Thirumalai SK, Rendi K, Moon KP, Byeon JH. Review on the methodologies adopted to minimize the material damages in drilling of carbon fiber reinforced plastic composites. Journal of Reinforced Plastics and Composites. DOI: 10.1177/0731684418819822, 2019. vol. 38(8), p. 351–368.

[3] Li M, Soo SL, Aspinwall DK, Pearson DL. Study on tool wear and workpiece surface integrity following drilling of CFRP laminates with variable feed rate strategy. 4th CIRP Conference on surface integrity, 2018. p. 407-412.

[4] Meinhard D, Haeger A, Knoblauch V. Drilling induced defects on carbon fiber-reinforced thermoplastic polyamide and their effect on mechanical properties. Composite Structures, 2021. vol. 256, p. 113-138.

[5] Bhattacharyya D, Horrigan DPW. A study of hole drilling in Kevlar composites. Composites Science and Technology, 1998. Vol. 58, p. 267-283.

[6] Khashaba UA. Drilling of polymer matrix composites: a review. Journal of Composite materials, 2012. vol. 47-15, p. 1817-1832.

[7] Hocheng H, Tsao CC. Effects of special drill bits on drilling-induced delamination of composite materials. International Journal of Machine Tools and Manufacture, 2006. v. 46, n. 12, p. 1403–1416.

[8] Girot FG, Dau F, Gutiérrez-orrantia MA. New analytical model for delamination of CFRP during drilling. Journal of Materials Processing Technology, 2017. vol. 240, p. 332-343.

[9] Meng Q, Zhang K, Cheng H, Liu. Jiang S. An analytical method for predicting the fluctuation of thrust force during drilling of unidirectional carbon fiber reinforced plastics. Journal of Composite Material, 2015. vol. 49, p. 699-671.

[10] Chen WC. Some Experimental Investigations in the Drilling of Carbon Fiber Reinforced Plastic (CFRP) Composite Laminates. International Journal of Machine Tools & Manufacture, 1997. vol. 37, n. 8, p. 1097–1108.

[11] Kuo C, Wang C, Ko S. Wear behavior of CVD diamond-coated tools in the drilling of woven CFRP composites. Wear, 2018. vol. 398-399, p. 1–12.

[12] Bonnet C, Poulachon G, Rech J, Girard Y, Costes JP. CFRP drilling fundamental study of local feed force and consequences on hole exit damage. International Journal of Machine Tools & Manufacture, 2015. vol. 94, p. 57–64.

[13] Xia T. Investigation of Drilling Performace in Cryogenic Drilling on CFRP Composite laminates. Theses and Dissertations--Mechanical Engineering, 2014. .https://uknowledge.uky.edu/me-etds/36.

[14] Morkavuk S, Köklüa U, Bağci MB, Gemic L. Cryogenic machining of carbon fiber reinforced plastic (CFRP) composites and the effects of cryogenic treatment on tensile properties: A comparative study. Composites Part B, 2018. vol. 147, p. 1–11.

[15] Agrawal C, Khanna N, Pimenov DY, et al. Experimental investigation on the effect of dry and multi-jet cryogenic cooling on the machinability and hole accuracy of CFRP composites. Journal of materials research and technology, 2022. vol. 18, p.1772-1783.

[16] Kumar D, Gururaja S, Jawahir IS. Machinability and surface integrity of adhesively bonded Ti/CFRP/Ti hybrid composite laminates under dry and cryogenic conditions. Journal Manufacture Process, 2020. vol. 58, p. 1075-87. https://doi.org/10.1016/j.jmapro. 2020.08.064.

[17] Gupta MK, Song Q, Liu Z, Sarikaya M, Mia M, Jamil M. Tribological performance-based machinability investigations in cryogenic cooling assisted turning of a-b titanium Alloy. Tribol Int, 2021. vol. 160, p. 107-032. https://doi.org/10.1016/j.triboint. 2021.107032.

[18] Merino-pérez JL, Royer R, Merson E, et al. Influence of workpiece constituents and cutting speed on the cutting forces developed in the conventional drilling of CFRP composites. Composite Structures 140, 2016. p. 621 – 629.

[19] Marathe BA, Javali AM. Effect of drilling parameters on specific cutting energy and delamination of a composite made of unsaturated polyester resin and chopped glass fibres. Journal of Thermoplastic Composite Materials, 2016. vol. 29, p. 1261–128.

STUDY OF CRACK BEHAVIOR AND PROPAGATION USING FINITE ELEMENTS IN POLYMER STRUCTURES REINFORCED WITH CARBON FIBERS

Thamires R. Freitas [1,*], Euclides D. M. Santanna [2], Carla T. M. Anflor [3]

(1) 0009-0009-0781-6209 (University of Brasília – Brazil)
(2) 0009-0002-2397-9103 (University of Brasília – Brazil)
(3) 0000-0003-3941-8335 (University of Brasília – Brazil)
* Corresponding author: thmrs.r@gmail.com

Abstract: This numerical study addresses the behavior and propagation of cracks in geometries manufactured by additive manufacturing reinforced with carbon fiber. The specimens were fabricated by the Fused Deposition Modelling (FDM) technique. Computer modelling considered a specimen wrapped in carbon fiber and another without the reinforcement, allowing the evaluation of the fiber in the mechanical strength improvement. Both test pieces were submitted to numerical tensile tests to evaluate the crack propagation in KI mode under the presence of a central hole. The stress intensity factors in the hole zone of the samples were compared. Computational simulations were then conducted using the finite element method, employing ANSYS 2024R1 software. Numerical studies allowed the determination of the mechanical response to the addition of fiber reinforcement externally applied to the specimen. The t x FIT curves were also presented. Computer modelling enabled a wider comprehension of the mechanical component structural behavior. Specifically, the analysis provided additional insights into stress fields, deformations, and critical failure points. This study also highlights the benefits of using carbon fiber-reinforced composite materials in structures manufactured by FDM. Noticing the complexity of these objects, this article emphasizes the importance of computer simulation through preliminary studies' phase. This approach provides a broad study on the prediction of structural performance under the view of crack propagation in composite materials.

1. INTRODUCTION

The aim of fracture mechanics is to analyze the propagation of cracks in materials. The subject is particularly relevant within the aerospace, automotive, naval and civil industries. Due to its critical and often imperceptible nature, the study soon became fundamental within engineering as a tool for the validation and maintenance of materials and structures. This scenario arises from Griffth's observation that materials behave differently in the presence of a crack, especially concerning mechanical strength [1]. This behavior is quantified by the Stress Intensity Factor (SIF), which determines the stress field at the crack tip. Established by Irwin [2], SIF results from a mathematical relationship between the geometric factor of the model, the applied load and the crack size. It is therefore inferred that there is a critical SIF value at which the crack begins to propagate. This measurement is called Fracture Toughness and is an intrinsic property of each material, which is why the study of fracture plays a significant role in the project design [3].

Advances in this area have made it possible to find analytical solutions for various cases within Fracture Mechanics, such as single cracks, double cracks and cracks in central holes [4]. However, there are also situations where analytical methods are not sufficient to predict the behavior of the body satisfactorily. In these cases, an iterative numerical method should be applied to provide more accurate results for the studied problem. A solution frequently used in this field is the Finite Element Method (FEM), a mathematical tool that

consists of discretizing a continuous medium into small elements while maintaining the same properties as the original medium [5]. Widely used for the analysis of structures with complex geometries, FEM is particularly useful in Fracture Mechanics because it accurately captures the nuances present at crack tips [6]. In classical scenarios, such as in this work, FEM is used to validate analytical calculations. In order to do this, the mathematical models provided by Tada [4] are used, which frequently involve holes. Whether by means of screws or rivets, holes are highly useful in fixing components and are present in the vast majority of mechanical projects. They are especially important in Fracture Mechanics due to their stress concentration aspect. Therefore, it is essential to analyze their behavior from the perspective of crack propagation and observe the risks of failure presented by them.

With the popularization of Additive Manufacturing, specifically the Fused Deposition Modeling (FDM) technique, there has been a growing interest in polymeric materials and their characteristics. Among the main properties of these materials are low density, high flexibility and resistance to corrosion. In contrast, the polymers commonly used in additive manufacturing exhibit low fracture toughness and low mechanical strength [7]. One solution to this problem is the formation of core-polymeric structures reinforced by materials with greater mechanical strength. Thus, considering FDM, it is possible to obtain a structure with low density, complex geometry and high strength [8].

For external reinforcement, it is worth considering the exponential growth in the use of composite materials, which are known for their low density and high mechanical strength [9]. Within this context, fiber-reinforced composites are specifically useful, as can be seen in the applications of these materials in sandwich panel structures. Their major benefits include high flexural strength, lightness and stiffness [10]. Thus, it is possible to directly calculate the influence of composite strength acting on polymeric structures fabricated by additive manufacturing.

Therefore, the objective of this work is to study the behavior and propagation of cracks in geometries made with polymers and reinforced with carbon fiber. Two models are used for comparison to evaluate the influence of reinforcement on increasing the mechanical strength of the sample. The analysis makes it possible to understand not only the mechanical gain from using both materials, but also the mechanism that allows such a change in the structural performance of the model.

2. METHODOLOGY

2.1. Material Properties

The study was conducted with two samples, the first being a high-impact ABS plate and the second plate composed of a core of the same material with reinforcement of carbon fiber fabric on two of the external faces. The use of the woven instead of unidirectional fibers is justified by the greater homogeneity and orthotropy it provides, facilitating the characterization and obtaining of results in the samples. The properties of both materials are described in Tables 1 and 2 and were taken from the library of ANSYS 2024R1 software.

Table 1. Properties of high-impact ABS

Density	$1,03.10^{-6} \ kg/mm^3$
Yield stress (σ)	$27,44 \ MPa$
Young's Modulus (E)	$1628 \ MPa$
Poisson's ratio (v)	$0,4$
Fracture Toughness (K_{IC})	$3 \ MPa\sqrt{m}$

Tabela 2. Properties of woven carbon fiber

Density	$1,45.10^{-6} \ kg/mm^3$
Young's Modulus (E_x)	$59160 \ MPa$
Young's Modulus (E_y)	$59160 \ MPa$
Young's Modulus (E_z)	$7500 \ MPa$
Poisson's ratio XY (v_{xy})	4.10^{-2}
Poisson's ratio YZ (v_{yz})	$0,3$

Poisson's ratio XZ (v_{xz})	0,3

2.2. Fracture Toughness

The Stress Intensity Factor (K) is related to the mechanical strength of the material in the presence of a crack, and its general mathematical form is shown in Eq. (1).

$$K = FS\sqrt{\pi a} \qquad\qquad 1$$

where F corresponds to the geometry factor, S is the reference stress and a is the crack length. However, it is known that the expression for K can take different forms depending on the situation analyzed. In the case of a crack at the edge of a hole in a flat plate, K takes the form of Eq. (2).

$$K = F_d S\sqrt{\pi l} \qquad\qquad 2$$

The expression for Fd is presented in Eq. (3). and l corresponds to the crack length.

$$F_d = 0{,}5(3 - d)[1 + 1{,}243(1 - d)^3] \qquad\qquad 3$$

where d is the ratio between the crack size (l) and the crack length plus radius of the hole. The values used for these variables in this work are shown in Figure 1, along with the other model measurements. The plate thickness is 10 mm.
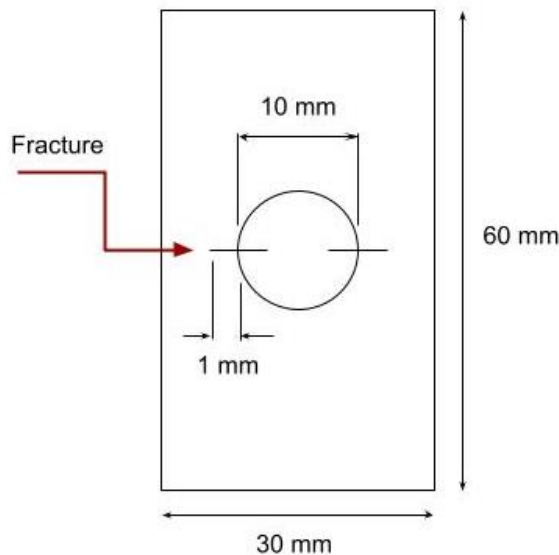
Figure 1. Geometry detail

2.3. Numerical simulation model

The numerical analysis was performed on the ANSYS 2024 R1 platform. A single mesh configuration was used for both models, which considered 1 mm for the overall element size and 0.10 mm at the crack tip. Adaptive refinement based on crack propagation was carried out using the SMART (Separating Morphing and Adaptive Remeshing) tool, a feature of the ANSYS software. However, the addition of carbon fiber surfaces resulted in slightly different meshes for each model, as shown in Table 3. The average mesh of the two models is presented in Figure 2.

Table 3. Mesh configuration for each sample

	Sample 1	Sample 2
Number of nodes	544.213	539.143
Number of elements	388.879	388.793
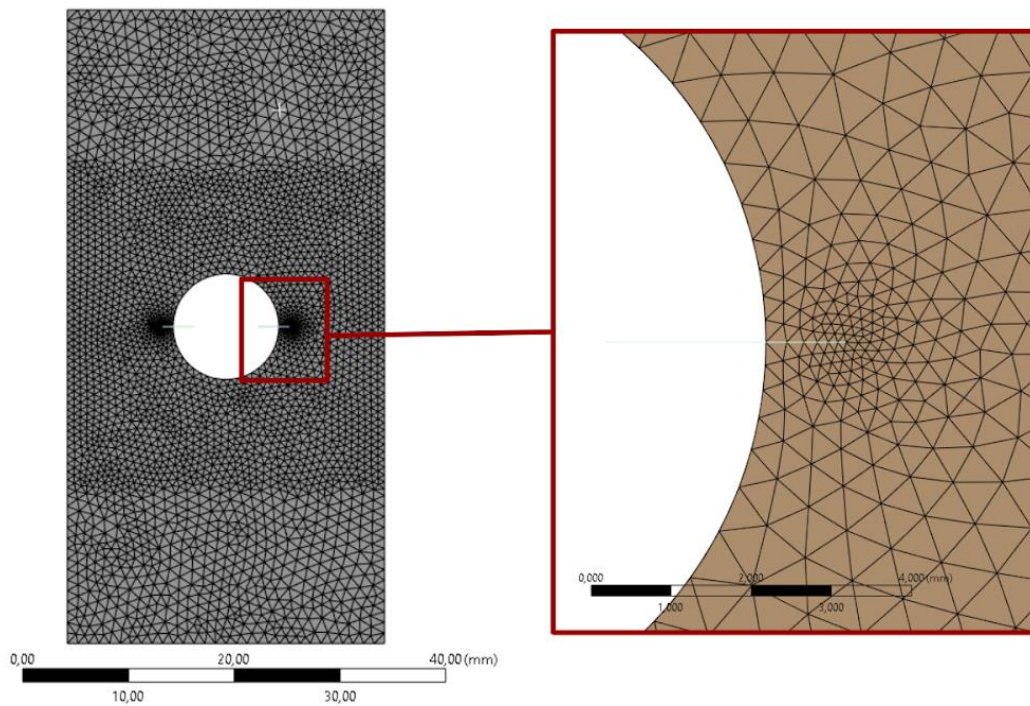
Figure 2. Detail of the mesh

To conduct the tensile study, the bottom face of the plate was fixed and the top face was subjected to a pressure of 22 MPa in the positive direction of Y, as shown in Figure 3. Additionally, a fixed displacement analysis of 2 mm was performed to compare the maximum load resisted by both models. In order to assess the influence of the number of composite layers on the increase in strength, the carbon-reinforced model was varied in 3 different thicknesses: 0.2, 0.4 and 0.6 mm.
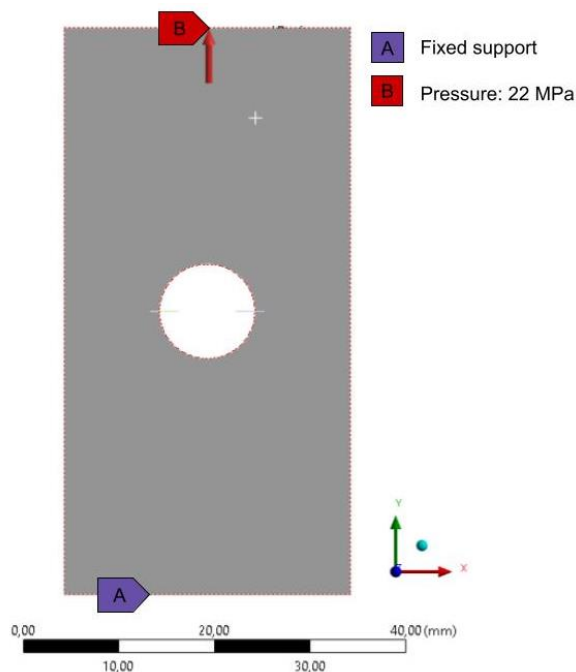
Figure 3. Boundary conditions

3. RESULTS AND DISCUSSION

The results of the Stress Intensity Factor throughout the plate thickness for each case are revealed in Figure 4, in order to understand how the stress field variations occurs within the material. The observed curves result from the Plane Stress acting on the external surface of the crack and the Plane Strain inside it. The

limiting nature of the plane stress in the transverse direction causes the crack to plasticize at that location, while the stress is released to the interior of the material. The graph also shows that the K values are reduced as the carbon fiber thickness increases, indicating an increase in the strength of the structure with composite reinforcement.

This is corroborated by Figure 5, which presents the crack extension measurements for each of the studied cases. Evaluation of the values shows that the model without composite reinforcement obtained a crack extension 1.85 times larger than the model with 0.2 mm of carbon fiber reinforcement. The other thicknesses obtained similar results, as the resisted load remained constant for the three observed cases.
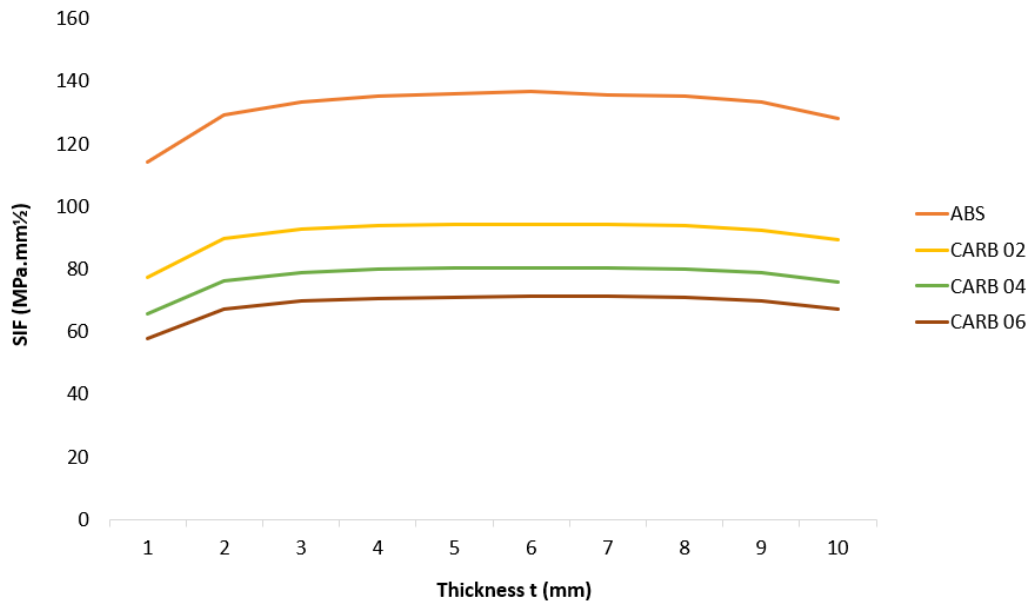
Figure 4. t x SIF curves
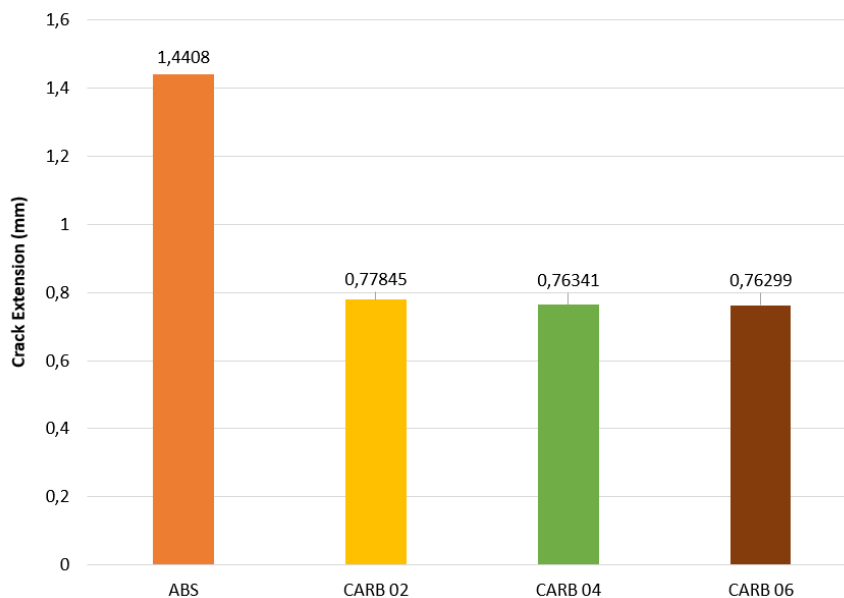
Figure 5. Crack extension for each case

The results obtained by adding carbon fiber can also be observed in terms of the maximum stresses supported by each case, as presented in Table 5. A comparison of the results from the fixed displacement analysis reveals that the structures with carbon fiber reinforcement withstand up to 7.27 times more stress than those without it. For the case with the smallest thickness, the ratio is 6.82, indicating that the number of fiber layers has little influence on the scenario studied.

Table 5. Maximum stresses for each case (MPa)

ABS	CARB 02	CARB 04	CARB 06
624,44	4262,00	4512,00	4541,70

Graphically, Figure 6 shows a comparison of the stresses resisted by two samples, Figure 6a with polymer only and Figure. 6b with 0.2 mm of carbon fiber on the sides. The images reveal that in the composite-reinforced model, stress is mostly resisted by this material. Furthermore, there is a reduction in the stress field at the crack tip from the first model to the second. An important aspect to note is the lack of homogeneity exhibited by the composite laminate (Fig. 6b), which is compatible with experimental results [11].
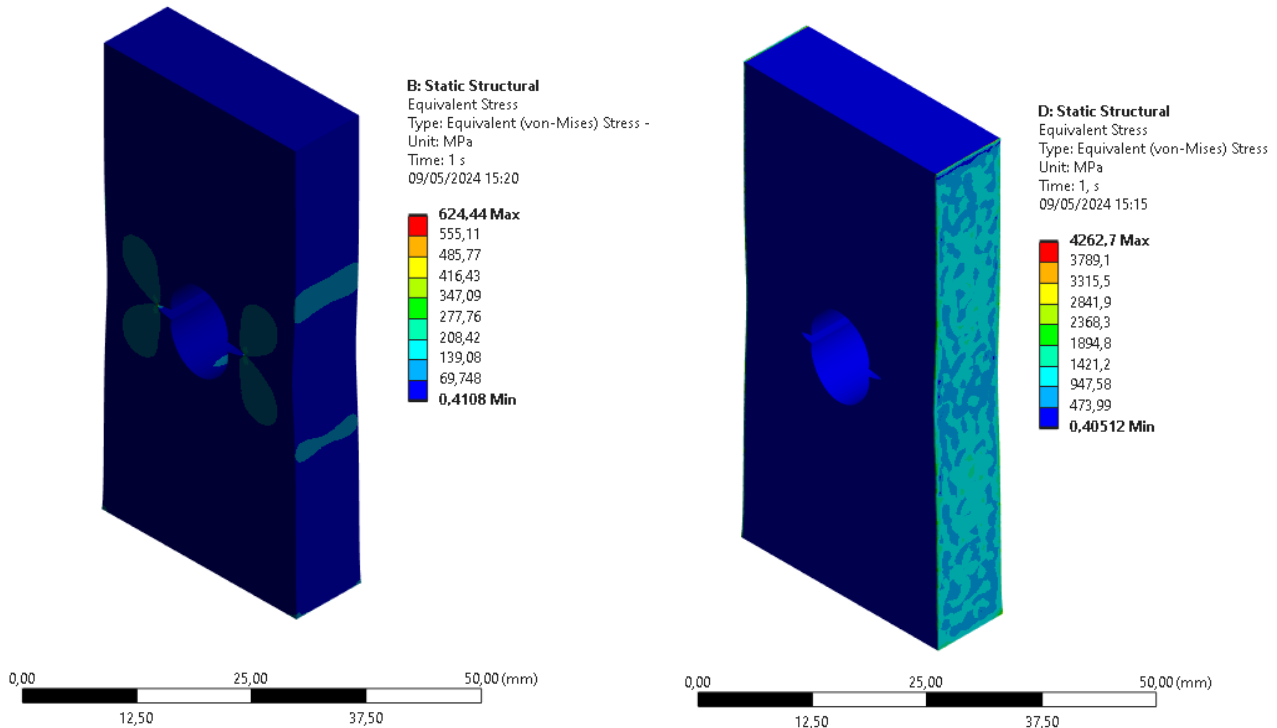
Figure 6. Comparison of stresses between the two samples: a) polymer and b) polymer coated with carbon fiber.

4. CONCLUSIONS

The present study conducted a comparative analysis of crack propagation in structures with and without composite material reinforcement. It involved a model of double crack in a central hole, for which the analytical calculation and the corresponding numerical method were presented. The obtained results were satisfactory and aligned with the literature, according to which carbon fiber reinforcement should increase the mechanical strength of the structure. For the studied case, there was a crack extension about 2 times greater in the model without reinforcement. A comparison of the stresses revealed a nearly 7-fold increase in the mechanical strength of the fiber-reinforced structures. However, further studies are warranted to investigate the influence of composite thickness on structure behavior. Furthermore, this article emphasizes the importance of numerical modelling in crack propagation research.

4.1. Declaration of Competing Interest

The authors declare no conflict of interest.

4.2. Fundings
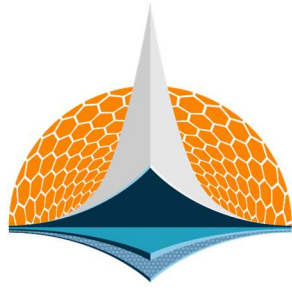
4.3. Acknowledgements

5. REFERENCES

[1] Griffith, A. A. The Phenomena of Rupture and Flow in Solids. Philosophical Transactions, Series A. Volume 221, 1920. (https://doi.org/10.1098/rsta.1921.0006)

[2] Irwin, G. R. Fracture Dynamics. Fracturing of Metals. American Society for Metals. p. 147-166, 1948.

[3] Dowling, N. E. Mechanical Behavior of Materials. 4th Edition, 2012. Pearson Education. (ISBN 10: 0-273-76455-1)

[4] Tada, H. Paris, P.C., Irwin, G. R. The Stress Analysis of cracks Handkbook. 3rd Edition, 1973. Del Research Corporation.

[5] Cook, R. D. et al. Concepts and Applications of Finite Element Analysis. 3rd Edition, 1989. John Wiley & Sons. (ISBN 0471-21207-5)

[6] Chan, S. K., Tuba, I. S., Wilson, W. K. On the Finite Element Method in Linear Fracture Mechanics. Engineering Fracture Mechanics. Volume 2, 1970. (https://doi.org/10.1016/0013-7944(70)90026-3)

[7] Callister, W. D., Rethwish, D. G. Materials Science and Engineering. 8th Edition, 2012. John Wiley & Sons. (ISBN:978-0-470-41997-7)

[8] Ilam, M. A. et al. Additive Manufacturing in polymer research: Advances, synthesis and applications. Polymer Testing. Volume 132, 2024. (https://doi.org/10.1016/j.polymertesting.2024.108364)

[9] Daniel, I. M., Ishai, O. Engineering Mechanics of Composite Materials. 2nd Edition, 2006. Oxford University Press. (ISBN 978-0-19-515097-1)

[10] Carlsson, L. A. Kardomateas, G. A. Structural and Failure Mechanics of Sandwich Composites. 1st Edition, 2011. Springer. (ISBN 978-1-4020-3224-0)

[11] Aabd-Allah, A. M., Farhan, A. M. Effect of the non-homogenity on the composite infinite cylinder of orthotropic material. Physics Letters A. Volume 372, 2008. (https://doi.org/10.1016/j.physleta.2007.08.029)

9 Design and application of composite structures

Organized and edited by

Sandra Maria da Luz

&

Carla Tatiana Mota Anflor

IMPROVING FRACTURE ENERGY IN MODE II
OF ADHESIVE JOINTS USING DOUBLE-DOUBLE LAMINATES

Ranulfo Martins Carneiro Neto(a)*, Lucas Lisbôa Vignoli, Carolina Seixas Moreira, Ney Robson Rohem, Eduardo Martins Sampaio

(a) ⬤ 0000-0001-8260-960X (Federal University of Rio de Janeiro – Brazil)
* Corresponding author: ranulfoufrj@gmail.com

Abstract: Double–Double (DD) is a new family of laminates that can revolutionize composite structures to be lighter, easier to design and lower cost to manufacture. In contrast to the classical QUAD laminates, DD laminates are not only more robust and lighter, but they also are able to accelerate manufacturing processes and reduce costs. There is an absence in the literature of studies that applied DD laminates as substrates in adhesive joints. Thus, the main innovation of this work is to investigate the behaviour of bonded joints with DD laminates substrates. For this purpose, end-notched flexure (ENF) tests with composite substrates were performed in both QUAD and DD configurations. The change in both maximum load and critical fracture energy in mode II were evaluated. Furthermore, the displacement fields for both laminates were accessed through the digital image correlation (DIC) analysis. The results indicated that the shear fracture energy can be significantly improved if DD laminates are used. The DIC analysis demonstrated the DD laminates can delay the crack propagation over the test. Moreover, the vertical displacements of DD joints were reduced in comparison to the QUAD configuration.

1. INTRODUCTION

In the realm of modern engineering, the synergy between materials science and adhesive technology has revolutionized the way we construct, assemble, and innovate. Among the myriad applications, adhesive joints with composite substrates stand out as a cornerstone of advanced manufacturing and structural design. Composites, renowned for their lightweight, durable, and tailored properties [1], offer a compelling platform for engineering solutions across industries ranging from aerospace to automotive and beyond.

Diverse methods may be applied to enhance the mechanical properties of adhesively bonded composite, such as: i) using high toughness materials on the outer surfaces of the laminates [2], ii) including spew fillets at the end of the overlaps [3], iii) shaping the adherends [4] and iv) employing specific stacking sequence of the unidirectional laminae. This last factor will be investigated in this paper.

The most common stacking sequences are from the QUAD family, where the plies have orientations of 0°, ±45°, 90°. It should be noted that the laminates from QUAD family must be symmetric and should obey the 10% rule [5]. A better family of laminate called double-double (DD) $[\pm\Phi/\pm\Psi]_n$ was recently proposed [6-8]. DD laminates are simpler than QUAD and provide a lighter structure with a faster layup for manufacturing at a lower cost [6].

In this work, we delve into the intricate world of adhesive bonding with composite substrates, exploring the influence of stacking sequence on the shear fracture energy of adhesive joints using end notched flexure (ENF) samples.

2. METHODOLOGY

The composite substrates were fabricated using the hand layup technique for unidirectional glass fiber/epoxy. As the primary objective of the study is to compare the outcomes of QUAD - $[45/90/-45/0]_{2s}$ and DD - $[67.5/-22.5/22.5/-67.5]_4$ configurations, the substrates were manufactured using two different stacking sequences, as detailed in Table 1. The laminates were manufactured at ambient temperature by layering the glass fibers on top of each other with an intermediary Pipefix lamination resin between the layers. Throughout the fabrication process, each ply was compressed with a metal roller to eliminate bubbles, ensure uniform thickness, and maintain consistency. Nylon-based peel ply layers were affixed to both upper and lower surfaces of glass FRP plates during layup. The curing of the laminates lasted 12 hours at ambient temperature.

Table 1 – QUAD and DD stacking sequence.

UNIDIRECTIONAL FIBER	QUAD (°)	DD (°)
Lamina 1	45	67.5
Lamina 2	90	-22.5
Lamina 3	-45	22.5
Lamina 4	0	-67.5
Lamina 5	45	67.5
Lamina 6	90	-22.5
Lamina 7	-45	22.5
Lamina 8	0	-67.5
Lamina 9	0	67.5
Lamina 10	-45	-22.5
Lamina 11	90	22.5
Lamina 12	45	-67.5
Lamina 13	0	67.5
Lamina 14	-45	-22.5
Lamina 15	90	22.5
Lamina 16	45	-67.5

The rectangular laminate plates were precisely cut using a machine. Figure 1 shows a schematic representation of the ENF test, where the following dimensions were adopted: $2L_2 = 130$ mm, $a_o = 45$ mm, $t_a = 0.3$ mm and $t_s = 5.8$ mm. A mold was used to bond the composite substrates, thus ensuring a constant adhesive thickness. For this purpose, a calibration wedge was placed on one end with the same desired adhesive thickness, and a double beveled plate was placed on the other end (also the same adhesive thickness), so the initial crack length was obtained. The double bevel was used to induce a cohesive fracture in the adhesive layer. The inserted plate has a length excess to assist in its removal after curing the adhesive. The adhesive was applied on both substrates after the peel ply sheets removal. In order to prevent the substrate misalignment, the specimens were positioned between the pins located over the mold. The cure time was 24-h, as recommended by the manufacturer.

`
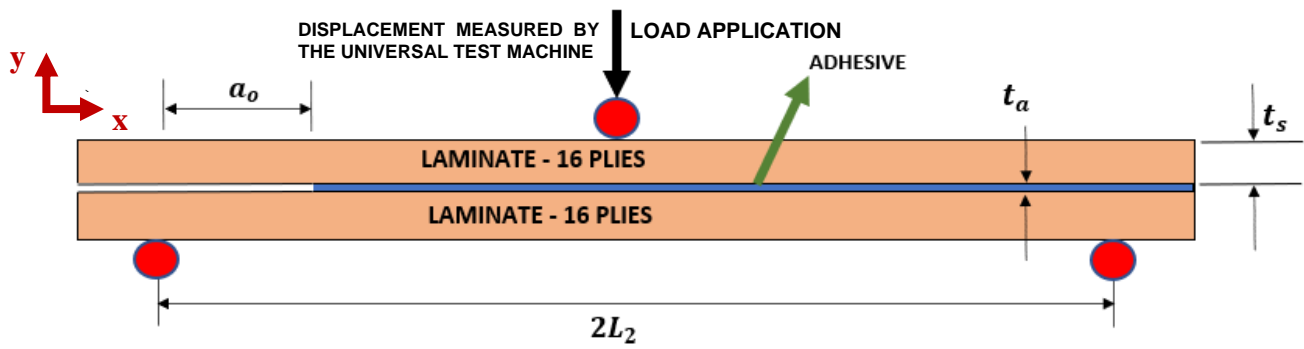
Figure 1 – Schematic representation of ENF test.

The Shimadzu universal test machine model Autography AG-X Plus 100 kN was used in all the tests, which were performed at room temperature and under displacement control of 2 mm/min. For each configuration (QUAD and DD) five specimens were tested. The load and displacement were recorded over the tests. The compliance-based beam method (CBBM) was used to obtain the fracture energy in mode II. Furthermore, two-dimensional digital image correlation (DIC) technique was used in order to access the displacement fields for both QUAD and DD configurations. The region of interest is shown in Figure 2.
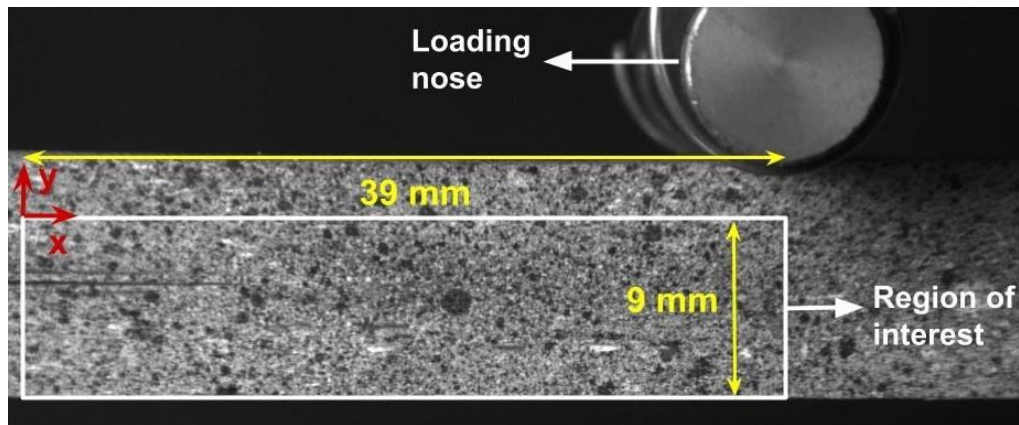
Figure 2 - Region of interest selected for digital image correlation (DIC).

3. RESULTS AND DISCUSSION

Considering the load vs. displacement curves from ENF tests (see Figure 3), good repeatability was achieved. Both loads and displacements were measured by the universal test machine. It is evident that both configurations had the same (or similar) stiffness, once this is essential to make a robust comparison between QUAD and DD configurations. The mean value of the maximum load was 13% higher for DD stacking sequence in comparison to QUAD.

Load x Displacement curve (QUAD x DD)
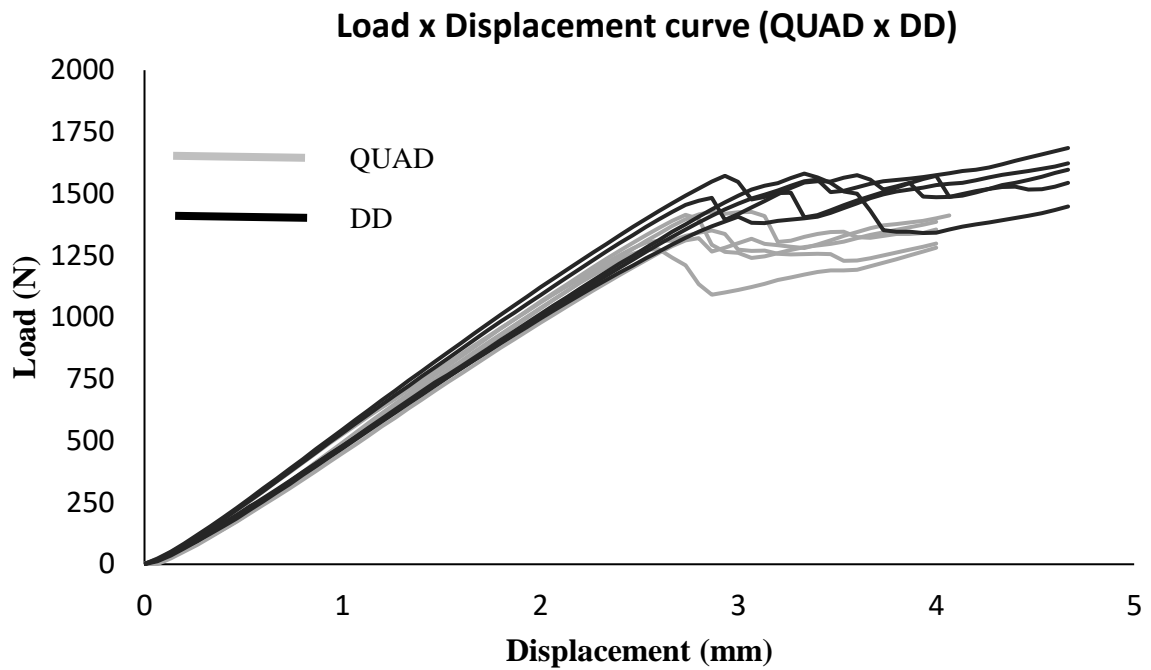
Figure 3 - Load-displacement experimental curves for the ENF tests (QUAD and DD).

For each sample, the values of G_{IIC} are obtained by the plateau observed in the Resistance curve. The critical fracture energy in mode II (G_{IIC}) was also higher for DD configurations. A very relevant increase of 38% was observed. The average values varied from 2.37 N/mm (QUAD) to 3.27 N/mm (DD), which are represented by the straight lines in Figure 4. This could mark the commencement of a new stage in the production of laminated composites, as the DD layup has the potential to streamline the comprehension of composite characteristics and ensure optimal application of the layers [9].

R-curves (QUAD x DD)

G_{IIC} (average) (DD) = 3.27 N/mm

G_{IIC} (average) (QUAD) = 2.37 N/mm
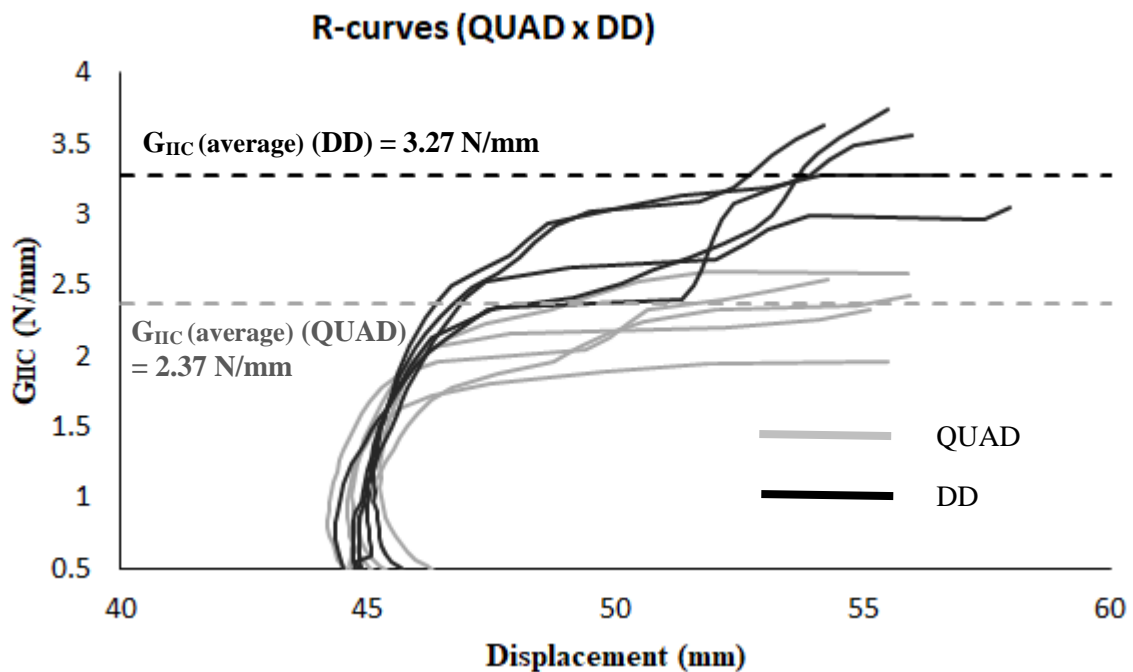
Figure 4 - Resistance curves (R-curves) of both stacking sequence QUAD and DD.

Figure 5 shows the vertical displacement fields of one specimen from QUAD and one from DD, when the machine displacement is δ = 4 mm. The areas shaded in blue highlight the most significant vertical displacement fields, as depicted by the scales in each diagram. It's noteworthy that specimens with QUAD layup exhibit greater vertical displacements compared to those with DD layup, evidenced by the increased presence of blue regions in the QUAD configuration. According to the results, it looks that DD layup may delay the crack propagation, resulting in higher values of shear fracture energy for that configurations, as already presented.
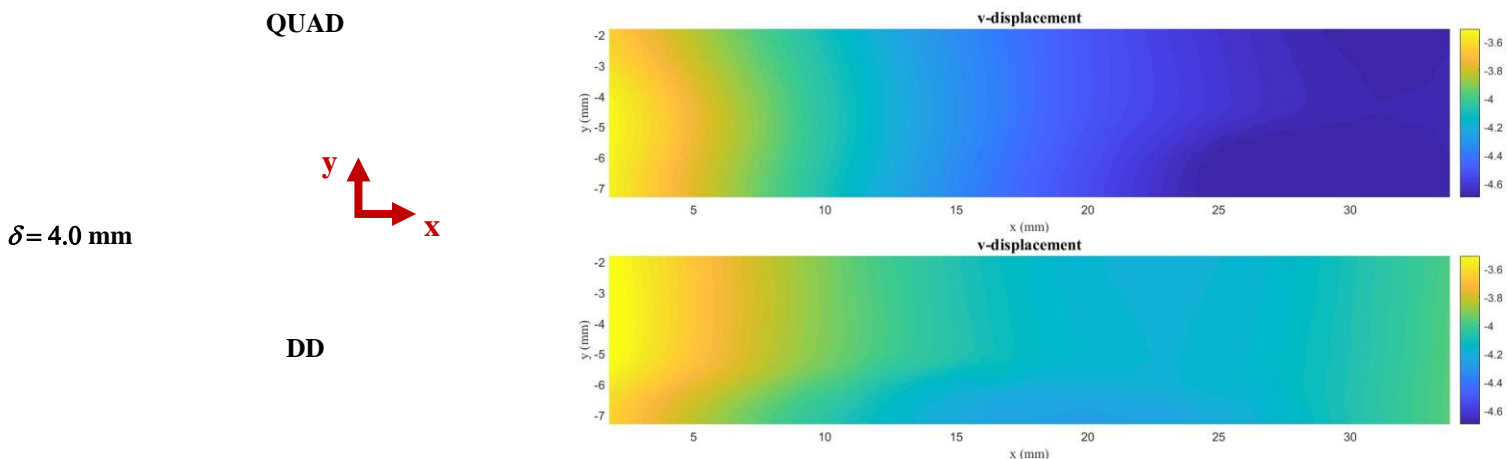
Figure 5 - Vertical displacement fields: DD configuration (sample 2) and QUAD configuration (sample 3). Images correspond to a machine displacement δ of 4 mm.

4. CONCLUSIONS

The influence of DD layup on the behaviour of adhesive joints was addressed in this work. Comparing QUAD and DD stacking sequences, both maximum load and shear fracture energy were higher for DD configuration. The increase in G_{IIC} reached 38%, which is explained by the delay in crack propagation in DD layup. Furthermore, DD layup can avoid internal defects since its manufacturing process is performed by building blocks that have a multiaxial sublaminate, providing a simpler and more homogeneous structure.

This study marks the initial attempt to assess DD laminates fabricated with GFRP. Nonetheless, the findings suggest significant potential for numerous engineering domains where adhesive joints are utilized.

4.1. Declaration of Competing Interest

The authors declare no conflict of interest.

4.2. Fundings

4.3. Acknowledgements

5. REFERENCES

References should be listed in the order mentioned in the text. Use font size 11, Times New Roman, justified

[1] Dipen Kumar Rajak, Durgesh D. Pagar, Ravinder Kumar, Catalin I. Pruncu, Recent progress of reinforcement materials: a comprehensive overview of composite materials, Journal of Materials Research and Technology, Volume 8, Issue 6, 2019, Pages 6354-6374, https://doi.org/10.1016/j.jmrt.2019.09.068.

[2] X. Shang, E.A.S. Marques, J.J.M. Machado, R.J.C. Carbas, D. Jiang, L.F.M. da Silva, Review on techniques to improve the strength of adhesive joints with composite adherends, Composites Part B: Engineering, Volume 177, 2019, 107363, https://doi.org/10.1016/j.compositesb.2019.107363.

[3] Lucas F M da Silva, R D Adams, Techniques to reduce the peel stresses in adhesive joints with composites, International Journal of Adhesion and Adhesives, Volume 27, Issue 3, 2007, Pages 227-235, https://doi.org/10.1016/j.ijadhadh.2006.04.001.

[4] da Silva LFM, Ochsner A, Adams RD (eds), Handbook of Adhesion Technology, Springer-Verlag Berlin Haidelberg, 2018. https://doi.org/10.1007/978-3-319-55411-2

[5] Irisarri F, Hicham D, Carrere N, Maire J. Multiobjective stacking sequence optimization for laminated composite structures. Compos Sci Technol 2009;69:983–90. https://doi.org/10.1016/j.compscitech.2009.01.011

[6] Vermes, B., Tsai, S.W., Riccio, A., Di Caprio, F., Roy, S., (2021a), "Application of the Tsai's modulus and double-double concepts to the definition of a new affordable design approach for composite laminates", Composite Structures, 259, 113246. https://doi.org/10.1016/j.compstruct.2020.113246.

[7] Kappel, E., (2022), "Double–Double laminates for aerospace applications — Finding best laminates for given load sets", Composites Part C: Open Access, 8, 100244. https://doi.org/10.1016/j.jcomc.2022.100244

[8] Tsai, S.W., Kappel, E., Miravete, A., Riccio, A., Di Caprio, F., Roy, S., Yeoh, K.M., Liu, J., Tay, T.E., Tan, V., Wang, D., Li, S., Xu, M., Sitnikova, E., Zheng, C., Jin, B., Arteiro, A., Sharma, N., Massard, T., (2022), "DOUBLE–DOUBLE A New Perspective in The Manufacture and Design of Composites", Composite Design Group, Stanford.

[9] Tsai, S.W., (2021), "Double–Double: New Family of Composite Laminates", AIAAJ, 59, 4293-4305.

INNOVATIVE DESIGN: EXPLORING ARCH-CORRUGATED CORES FOR LIGHTWEIGHT AND VERSATILE MODULAR SANDWICH PANELS

Gabriel Teixeira Rufino[(a)*], Maurício de Moura Nilton [(b)], Túlio Hallak Panzera [(c)]

(a) 0009-0006-3458-0236 (Federal University of São João Del Rei – Brazil)
(b) 0000-0003-0129-0655 (Federal University of São João Del Rei – Brazil)
(c) 0000-0001-7091-456X (Centre for Innovation and Technology in Composite Materials – Brazil)
* Corresponding author: gabrielrufino796@gmail.com

Abstract: Modular structures refer to a design approach that subdivides a system into smaller modules or skids, which can be independently created and utilized in different systems. These modules are distinguished by their functional partitioning and well-defined interfaces, making them an efficient and cost-effective construction method. In the realm of engineering, sandwich panels are constructed using stiff skins and a lightweight core, resulting in structures that are lightweight, rigid, and durable. These panels find applications in a wide range of engineering fields. When the core material is designed with a corrugated geometry, it offers several benefits, such as facilitating the passage of electrical conductors and pipes. This is advantageous for the construction and transportation industries, as well as for providing thermal and acoustic insulation. This study introduces an innovative framework that combines modular and sandwich designs, utilizing arch-corrugated cores. The facing and core materials are created through 3D printing using PLA (polylactic acid) and are evaluated through three-point bending tests. The arched core is investigated through six distinct arrangement configurations. The 3D printed prototypes demonstrate promising potential for modular sandwich panels, as they can adapt to different applications. This research unlocks thrilling opportunities for the future advancement and integration of modular sandwich panels in various industries.

1. INTRODUCTION

Recent advances in polymer science and engineering have led the scientific community to focus on the use of sustainable materials as a way to reduce the environmental impact of conventional materials. Biopolymers emerge as a promising solution, being non-polluting, chemically versatile, sustainable, biodegradable, and presenting a wide potential for application in various fields, including the biomedical, textile, and electronics industries, among others [1].

In the same sustainability context, sandwich structural composites have been highlighted both in the academic realm and in the industry at large due to their characteristics of lightweight and efficient structures [2]. Generally, a sandwich panel consists of two high-strength faces and a low-density core. Different materials, such as foams, aramids, aluminium alloys, wood, and polymers, have been used in the fabrication of the core of sandwich panels [3–5]. The choice of core and face material is influenced by the specific application of these structures, their load-bearing lifespan, availability, and cost [3]. Recently, 3D printing technology has been explored to produce panels with remarkable mechanical properties and a variety of patterns, with several studies conducted to investigate the characteristics and behaviour of printed sandwich panels [6–9]. In addition to materials, different core geometries have been investigated, with notable examples including the Honeycomb, featuring cells oriented perpendicular to the faces, and the corrugated core, which has cells oriented in the same direction as the faces.

In [7], the mechanical behaviour of sandwich panels composed of Honeycomb cores and faces manufactured by a 3D printer was investigated. Two types of sandwich structures were fabricated. In the first type, both the core and the outer layers were made of polylactic acid (PLA). In the second type, the outer layers were made of acrylonitrile butadiene styrene (ABS) polymer, while PLA was used for the core material. Experimental results showed that the structures exhibited distinct mechanical behaviour under bending load. The sandwich panels with outer layers and core made of PLA demonstrated significant bending properties compared to the other sample. On the other hand, [10] proposed a panel with bidirectional sinusoidal corrugated core. The study investigated the influence of the number of waves on the bending properties of panels with bidirectional or regular corrugated cores. The pattern of each corrugated core consists of a cosine curve with a certain period and amplitude. In the study [11], the effect of printed hierarchical-sinusoidal corrugated core patterns and loading direction on the bending properties of cotton/epoxy composite sandwich panels was investigated. For the cores, six sinusoidal corrugated structures were considered, and manufactured using a 3D printer and polylactic acid material. Additionally, possible arrangements (transverse or longitudinal waves, downward or upward arc) of the sinusoidal corrugated cores concerning the loading direction were considered. It was observed that, for the transverse arrangement, the bending strength of the sandwich panels is significantly improved by changing the core pattern from simple to hierarchical patterns.

It was observed in the published articles that corrugated cores are permanently bonded to the faces using adhesives. Therefore, considering the significant need to develop sustainable non-polluting materials, the aim was to develop a sandwich panel consisting of PLA faces and core through additive manufacturing via 3D printing. The corrugated core is formed by arches and reversibly fits into the faces, meaning the panel can be assembled and disassembled multiple times. This characteristic allows the panel to be adjusted to better suit each application. Different patterns were then considered for the corrugated cores. The effect of core arrangement and loading direction on bending properties was investigated.

2. METHODOLOGY

2.1. Materials

The sandwich panel components are made from 1.75 mm diameter PLA filament, a biobased thermoplastic polymer supplied by 3D LAB – Brazil. The properties of the PLA material can be found in Table 1. Samples are manufactured using a Creality Ender-3 3D printer.

Table 1. Mechanical properties of printed PLA. Available at [12].

Properties	Values
Density [g/cm^3]	1.20
Yield strength [MPa]	24.80
Ultimate tensile strength [MPa]	46.0
Elastic modulus [GPa]	1.90
Elongation [%]	3.69

2.2. Sandwich Panel Design

The core geometry is designed with arched corrugation, incorporating two types of arches with different fittings as well as a semi-arch. The geometric characteristics of the facing and core materials are illustrated in Fig. 1. Six different core arrangements considering (i) the downward or upward disposition of the arches, (ii) alternating or similar patterns and (iii) with or without semi-arches, are established and encoded (Fig. 2).
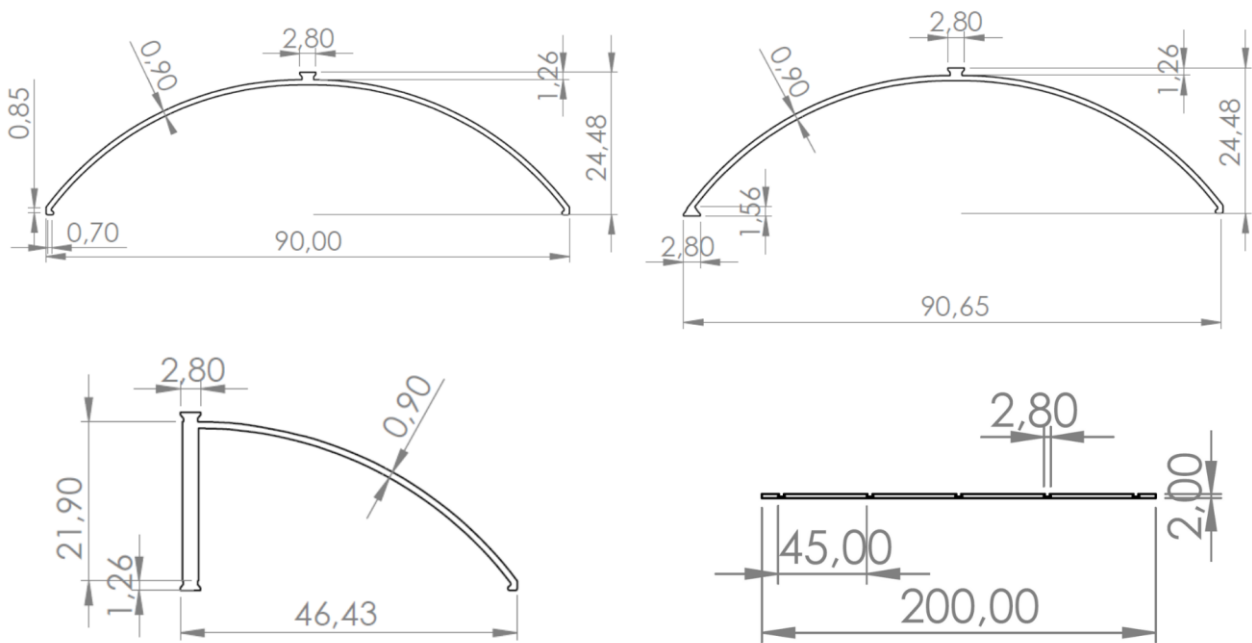
Figure 1. Details of the geometric properties of the components. Dimensions in millimetres.
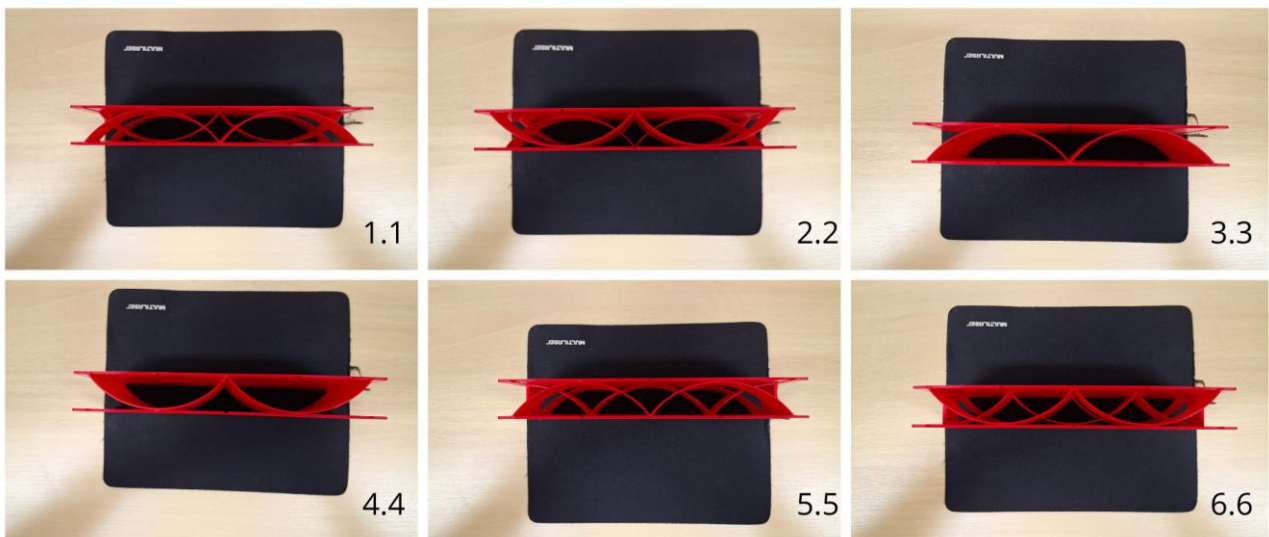
Figure 2. Studied core configurations.

The components of the sandwich panels are modelled in SolidWorks software, and then the cores and faces are printed using Creality software and an FDM Ender 3 printer. Initially, a panel composed of six equal arcs arranged alternately is manufactured using the FDM method. The printing parameters included a nozzle temperature of 200°C and a bed temperature of 60°C, as recommended by the manufacturer. The dimensions of the outer layers are set at 75×200 mm² by ASTM C393 [13] standard, and the panel has a thickness of 26.7 mm. A preliminary test revealed that using equal arcs with filled ends through an insert led to unsatisfactory behaviour as they quickly came apart. To ensure the uniformity of the arcs, the decision was made to reinforce them by using complete fittings for greater stability at the junction (Fig. 3).
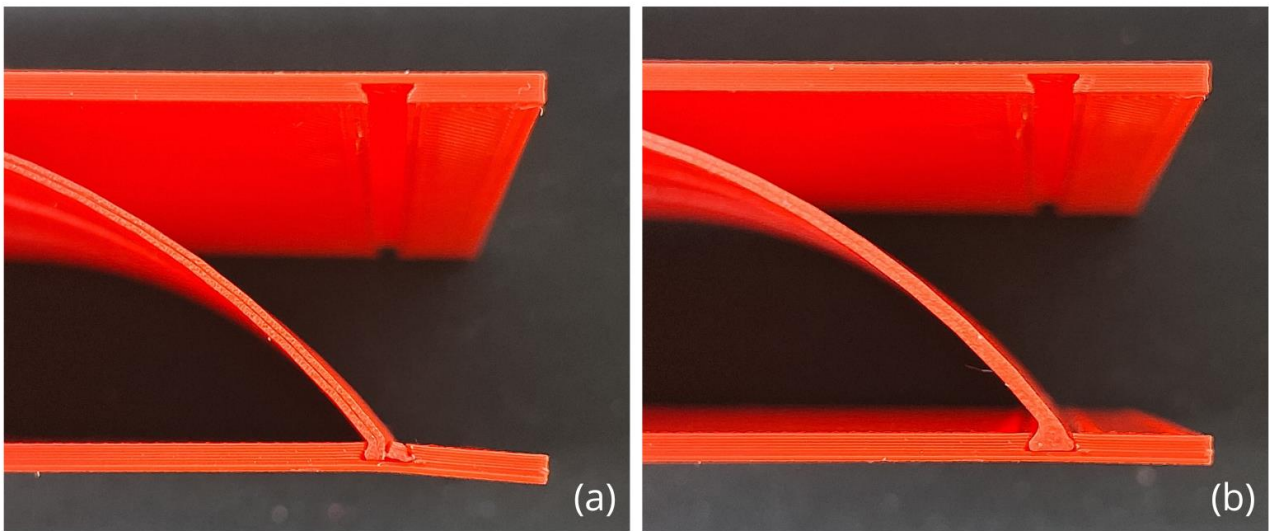
Figure 3. Type of end-fitting: (a) with insert and (b) without insert (full attachment).

2.3. Panel Testing

To assess the mechanical properties of the sandwich panels, specimens undergo flexural testing (Fig. 4). The samples are tested under three-point bending conditions with displacement control, in line with the specifications outlined in ASTM C393 [13] standard. The load-deflection curve of the prepared samples is recorded using an Instron EMIC 23-100 testing machine. Following ASTM C393 [13] standard requirements, the test is carried out at a crosshead speed of 8 mm/min to ensure failure occurs between 3 and 6 minutes. Additionally, a 1 kN load cell is utilized to record the applied load. Three specimens are manufactured and tested for each configuration.
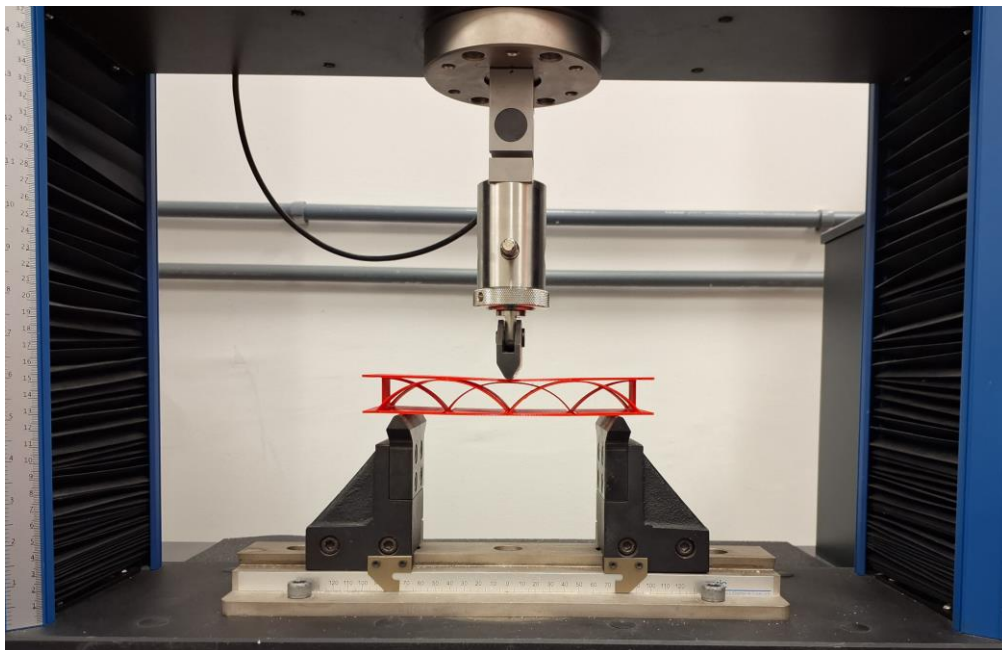
Figure 4. Three-point bending test.

The ultimate shear strength of the core and the bending stress on the faces of the sandwich panels under bending are determined. The ultimate shear strength of the core in a sandwich structure is calculated according to Eq. (1) [13].

$$F_s^{ult} = \frac{P_{max}}{(d + c)b} \tag{1}$$

Here P_{max} represents the maximum force on the force-deflection curve, d denotes the panel thickness, c represents the core thickness, and b indicates the panel width. Furthermore, the bending stress on the face is calculated using Eq. (2) [13].

$$\sigma = \frac{P_{max}S}{2t(d+c)b} \tag{2}$$

Here, S denotes the support span, and t represents the thickness of the sandwich panel face. The values of the geometric properties used in Eqs. (1) and (2) are listed in Table 2.

Table 2. Geometric dimensions of the panels used.

Parameter	Values [mm]
d	26.7
c	22.7
b	75.0
S	150.0
t	2.0

3. RESULTS AND DISCUSSION

3.1. Load-Deflection Curves

Figure 5 illustrates the typical load versus deflection curves of the sandwich panels. It is evident that the panel composed of the corrugated core (6.6.) made with arcs arranged upwards, including semi-arcs, achieves the highest maximum supported load. Furthermore, it is observed that the panels withstand more load when the arcs are turned upwards, as seen in configurations 2.2, 4.4, and 6.6.
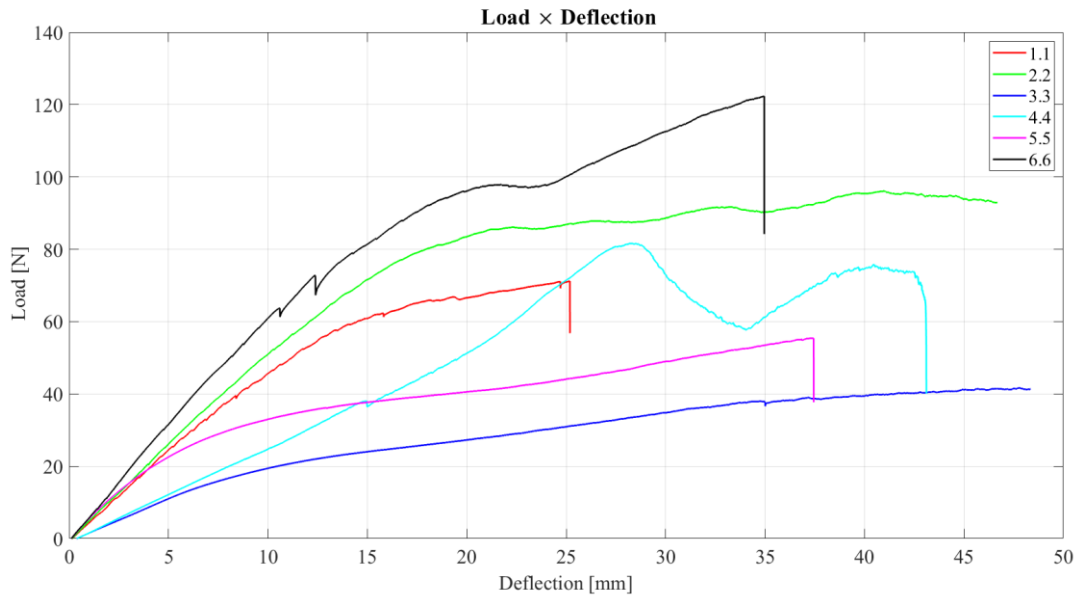
Figure 5. Results of the three-point bending tests.

Panels 2.2 and 3.3 experience significant deformation, leading to slipping on the support during the test without rupture occurring (Fig. 6). Three conditions were established as criteria for panel failure and test termination: panel fracture, disengagement of any arch, or exceeding the maximum test time (6 min) without rupture.
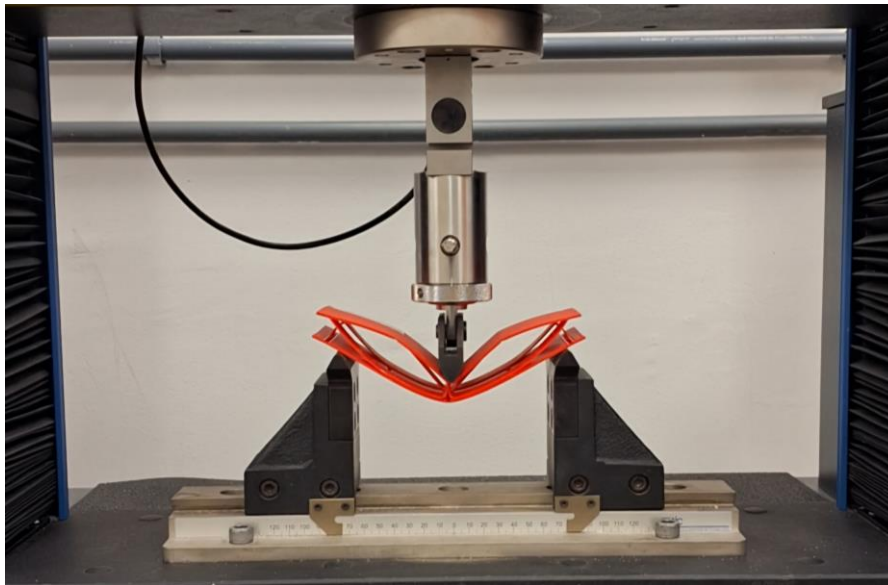
Figure 6. Example of excessive deformation and slipping of panel 2.2.

3.2. Mechanical Properties

Table 3 displays the mean maximum loads for each configuration and the evaluated mechanical properties. Except for panels 1.1 and 4.4, the standard deviation values indicate a moderate dispersion, suggesting that the manufacturing process has been satisfactorily executed, maintaining uniformity among the replicates.

Table 3. Mean of the results obtained for the panels.

Panel	P_{med}[N]	F_s^{ult}[kPa]	σ [kPa]
1.1	73.25±9.80	20.20	741.36
2.2	92.56±3.35	25.50	937.68
3.3	38.56±3.07	10.41	390.25
4.4	72.21±10.41	19.50	731.08
5.5	54.65±0.69	15.47	553.14
6.6	119.60±2.33	32.28	1210.56

4. CONCLUSIONS

The proposed modular sandwich panel has demonstrated a versatile design, resulting in impressive mechanical performance. The utilization of the arched corrugated core has led to higher bending deformation, meeting the mechanical requirements for protection and energy absorption in various engineering applications. In conclusion, this study highlights the significant impact of the arrangement of the arcs on the properties of the panel. Placing the arcs upwards provides better support for bending efforts compared to a downward position. Additionally, the use of semi-arcs at the panel ends positively contributes to supporting the efforts. By altering the core pattern, the ultimate shear strength of the core and the bending stress of the faces are significantly increased. Finally, it is recommended to investigate the behaviour of impact energy absorption, as well as the thermal and acoustic properties of these versatile modular sandwich panels.

4.1. Declaration of Competing Interest

The authors declare no conflicts of interest.

4.2. Acknowledgements

5. REFERENCES

[1] Z. U. Arif et al. Biopolymeric sustainable materials and their emerging applications. *Journal of Environmental Chemical Engineering*, Volume 10, 2022. (https://doi.org/10.1016/j.jece.2022.108159).

[2] J. M. Davies. *Lightweight Sandwich Construction*, 1st Edition, 2008. John Wiley & Sons. (ISBN: 978-0-632-04027-8).

[3] V. Birman, G. A. Kardomateas. Review of current trends in research and applications of sandwich structures. *Composites Part B: Engineering*, Volume 142, 2018. (https://doi.org/10.1016/j.compositesb.2018.01.027).

[4] Z. Liu, H. Chen, S. Xing. Mechanical performances of metal-polymer sandwich structures with 3D-printed lattice cores subjected to bending load. *Archives of Civil and Mechanical Engineering*, Volume 20, 2020. (https://doi.org/10.1007/s43452-020-00095-1).

[5] A. Kavianiboroujeni, A. Cloutier, D. Rodrigue. Low-velocity impact behaviour of asymmetric three-layer sandwich composite structures with and without foam core. *Polymers Polymer Composites*, Volume 25, 2017. (https://doi.org/10.1177/096739111702500507).

[6] L. Azzouz et al. Mechanical properties of 3-D printed truss-like lattice biopolymer non-stochastic structures for sandwich panels with natural fibre composite skins. *Composite Structures*, Volume 213, 2019. (https://doi.org/10.1016/j.compstruct.2019.01.103).

[7] S. Brischetto et al. 3D FDM production and mechanical behavior of polymeric sandwich specimens embedding classical and honeycomb cores. *Curved and Layered Structures*, Volume 5, 2018. (https://doi.org/10.1515/cls-2018-0007).

[8] D. Harland, A. W. Alshaer, H. Brooks. An experimental and numerical investigation of a novel 3D printed sandwich material for motorsport applications. *Procedia Manufacturing*, Volume 36, 2019. (https://doi.org/10.1016/j.promfg.2019.08.003).

[9] K. Essassi et al. Experimental and analytical investigation of the bending behaviour of 3D-printed bio-based sandwich structures composites with auxetic core under cyclic fatigue tests. *Composites Part A: Applied Science and Manufacturing*, Volume 131, 2020. (https://doi.org/10.1016/j.compositesa.2020.105775).

[10] V. Daliri, A. Zeinedini. Flexural behavoiur of the composite sandwich panels with novel and regular corrugated cores. *Applied Composite Materials*, Volume 26, 2019. (https://doi.org/10.1007/s10443-019-09761-x).

[11] M. Shahkarami, A. Zeinedini. Flexural Properties of 3D-printed hierarchical-sinusoidal corrugated core sandwich panels with natural fiber reinforced skins. *Polymers and Polymer Composites*, Volume 30, 2022. (https://doi.org/10.1177/09673911221101299).

[12] 3DLAB. *3DLAB Soluções em Impressão 3D*. 3DLAB, 2024. (https://3dlab.com.br/), accessed 17 April 2024.

[13] ASTM C393, Standard Test Method for Core Shear Properties of Sandwich Constructions by Beam Flexure. ASTM International, 2011. (www.astm.org).

EXPLORING DOUBLE-DOUBLE LAMINATES FOR GFRP APPLICATIONS: MULTISCALE MODEL AND EXPERIMENTAL VALIDATION

Lucas L. Vignoli[(a), *], Ranulfo M. Carneiro Neto[(b)], Carolina S. Moreira[(c)], Arthur Adeodato[(d)], Paulo P. Kenedi[(e)], Eduardo M. Sampaio [(f)]

(a) 0000-0003-3288-3568 (Federal University of Rio de Janeiro – Brazil)
(b) 0000-0001-8260-960X (Federal University of Rio de Janeiro – Brazil)
(c) 0000-0002-0175-9102 (Rio de Janeiro State University – Brazil)
(d) 0000-0002-0812-6594 (Rio de Janeiro State University – Brazil)
(e) 0000-0001-5563-843X (Centro Federal de Educação Tecnológica Celso Suckow da Fonseca – Brazil)
(f) 0000-0002-0339-0716 (Rio de Janeiro State University – Brazil)
* Corresponding author: ll.vignoli@mecanica.coppe.ufrj.br

Abstract: Double-double (DD) laminate is a family of unidirectional laminates recently proposed with a great potential for composite structural optimization. Due to the homogenization capability, several advantages have been demonstrated when compared with traditional QUAD laminates. However, most of the investigations found in the literature study carbon fiber reinforced polymers (CFRP). Regarding the great application potential of glass fiber reinforced polymers (GFRP), this is one of the first efforts to analyze DD laminates made by GFRP. The DD laminate $[67.5/-22.5/22.5/-67.5]_4$ and the QUAD laminate $[45/90/-45/0]_{2s}$ are selected for the present investigation considering their stiffness equivalence. First, the laminates are manufactured by hand layup and tensile tests are performed for four specimens for each laminate. The longitudinal elastic modulus of the laminates is the unique property experimentally measured for the proposed analytical model. The novel multiscale approach combines the trace theory, the VSPKc micromechanical model, the classical laminate theory and the Hashin failure criterion. The results of the experimental tests indicate that both laminates have the same stiffness and the difference between the average strengths is insignificant. The comparison between the experimental results and the proposed model estimations shows an error smaller than 2%, highlighting the model capability.

1. INTRODUCTION

In recent years, some innovative design methodologies for carbon fiber reinforced polymers (CFRP) structures have been proposed by Prof. Tsai and his group. In summary, three main advances can be pointed out: trace theory [1], also known as Tsai's modulus [2, 3]; unit circle failure criterion [4]; and double-double (DD) laminates [5].

Tsai's modulus aims to decrease the number of mechanical tests required to obtain CFRP. The mains concept is that the trace of the plane stress stiffness matrix is an invariant for CFRP and normalized relations are proposed. With this basis, only one elastic property is required to complete characterize CFRP materials in the elastic regime [6]. Despite the empirical foundation of this theory, an theoretical proof of its the mechanical consistence is proposed in [7]. Also aiming to decrease time and cost with experimental data, a unit circle on the normalized strain space is proposed to evaluate laminate strength, where the strains are normalized in relation to the tensile and compressive failure strains [8]. To facilitate the manufacture and optimization of composite laminates, DD were proposed, where the stacking sequence is basically defined by $[\pm\psi/\pm\phi]_n$,

where ψ and ϕ are continuous variables that can be designed to achieve the stiffness and strength requirements [9]. Compared with traditional QUAD laminates, the laminate does not need to be symmetric neither to follow the 10% rule [10].

Despite the growing popularity of these theories [11-15], they were proposed for CFRP. Regarding the great applications of glass fiber reinforced polymers (GFRP), the present investigation is part of an effort to extend these advances for GFRP. The extension of the trace theory for GFRP was performed using asymptotic homogenization and machine learning, obtaining novel equations for the normalized properties [16,17]. The application of DD laminates made by GFRP in bonded joints was discussed in [18].

In the present study, DD and QUAD laminates subjected to tensile load are investigated. The multiscale analytical model is introduced in Section 2. The results and discussion are presented in Section 3. A summary of the main conclusions is presented in Section 4.

2. METHODOLOGY

This Sections aims to explain the analytical methodology adopted in this investigation. First, the DD laminates are introduced regarding the stiffness equivalence with QUAD laminates. Next, a combined approach mixing the Tsai's modulus and the VSPKc micromechanical model is discussed. At last, the macromechanical Hashin failure criterion is presented.

2.1. Double-Double Laminates

The stiffness equivalence between DD and QUAD laminates can be established considering the classical laminate theory. The laminate extensional stiffnesses matrix is defined by [19]

$$A = \sum_{n=1}^{N} C^{(g)}(z_{n+1} - z_n) \tag{1}$$

where z_n and z_{n+1} are the positions of the lamina beginning and end on coordinate through the laminate thickness, and $C^{(g)}$ is the lamina stiffness matrix in global coordinate system computed

$$C^{(g)} = R_\sigma^{-1} C R_\epsilon \tag{2}$$

where

$$C = \begin{bmatrix} \dfrac{1}{E_1} & -\dfrac{v_{12}}{E_1} & 0 \\ -\dfrac{v_{12}}{E_1} & \dfrac{1}{E_2} & 0 \\ 0 & 0 & \dfrac{1}{G_{12}} \end{bmatrix}^{-1} \tag{3}$$

$$R_\sigma = \begin{bmatrix} \cos^2\alpha & \sin^2\alpha & 2\sin\alpha\cos\alpha \\ \sin^2\alpha & \cos^2\alpha & -2\sin\alpha\cos\alpha \\ -\sin\alpha\cos\alpha & \sin\alpha\cos\alpha & \cos^2\alpha - \sin^2\alpha \end{bmatrix} \tag{4}$$

$$R_\sigma = \begin{bmatrix} \cos^2\alpha & \sin^2\alpha & \sin\alpha\cos\alpha \\ \sin^2\alpha & \cos^2\alpha & -\sin\alpha\cos\alpha \\ -2\sin\alpha\cos\alpha & 2\sin\alpha\cos\alpha & \cos^2\alpha - \sin^2\alpha \end{bmatrix} \tag{5}$$

where E_1 is the longitudinal elastic modulus, E_2 is the transversal elastic modulus, G_{12} is the in-plane shear modulus, v_{12} is the in-plane Poisson's ratio and α if the angle between the fiber orientation and the longitudinal axis.

The equivalence between DD and QUAD laminates is obtained evaluating the elements of the main diagonal of A. In this study the QUAD laminate $[45/90/-45/0]_{2s}$; according to Tsai et al. [10], a perfect stiffness equivalence is achieved for the DD laminate $[67.5/-22.5/22.5/-67.5]_4$.

2.2. Trace Theory

Tsai and Melo [4] proposed that the unique independent property of CFRP unidirectional lamina is trace of the plane stress stiffness matrix. Mathematically, the trace theory knows as Tsai's modulus for CFRP is defined by

$$tr(\boldsymbol{C}) = \frac{E_1}{E_1^*} = \frac{E_2}{E_2^*} = \frac{G_{12}}{G_{12}^*} \tag{6}$$

$$\nu_{12} = \nu_{12}^* \tag{7}$$

where E_1^*, E_2^*, G_{12}^*, and ν_{12}^* are the normalized properties.

Despite this original theory was limited to CFRP, Vignoli et al. [16,17] used the asymptotic homogenization method and machine learning to derive the following expressions for the normalized properties for GFRP laminae

$$E_1^* = (-1.067 \times 10^{-3})tr(\boldsymbol{C}) + 0.744 \tag{8}$$

$$E_2^* = (1.046 \times 10^{-3})tr(\boldsymbol{C}) + 0.137 \tag{9}$$

$$G_{12}^* = (2.427 \times 10^{-4})tr(\boldsymbol{C}) + 0.049 \tag{10}$$

$$\nu_{12}^* = (-4.792 \times 10^{-4})tr(\boldsymbol{C}) + 0.326 \tag{11}$$

2.3. VSPKc Micromechanical Model

To evaluate the lamina strengths, the VSPKc micromechanical model is applied. Despite this model was first proposed for the effective elastic properties [20], it has been extended for the lamina strengths successfully [21-23]. Considering that the laminate is subjected to a tensile load, the longitudinal tensile strength, S_{11}^t, the transversal tensile strength, S_{22}^t, and the in-plane shear strength, S_{12}^s, must be obtained. For S_{11}^t the fiber failure is assumed, while the fiber-matrix interface failure is dominant for S_{22}^t and S_{12}^s. Hence, the following expressions are defined [23,24]

$$S_{11}^t = \left[V_f + (1 - V_f)\left(\frac{E_m}{E_f}\right) \right] S_f^t \tag{12}$$

$$S_{22}^t = (1 + a_{22})\left(\frac{E_2}{E_m}\right) S_i^n \tag{13}$$

$$S_{12}^s = 2\sqrt{\frac{V_f}{\pi}}\theta_d S_i^{sl} + 2G_m\left\{2\sqrt{\frac{V_f}{\pi}}[I(90°) - I(\theta_d) - 1] + 1\right\}\epsilon_{12}^{max} \tag{14}$$

where V_f is the fiber volume fraction, E_m is the matrix elastic modulus, E_f is the fiber elastic modulus, S_f^t is the fiber tensile strength, S_i^n is the interface normal strength, S_i^{sl} is the interface longitudinal shear strength, G_m is the matrix shear modulus, ϵ_{12}^{max} is the maximum in-plane shear strain for the lamina failure, and

$$a_{22} = 2\sqrt{\frac{V_f}{\pi}}\left[\left(\frac{E_m}{E_f}\right) - 1\right] \tag{15}$$

$$a_{12} = 2\sqrt{\frac{V_f}{\pi}}\left[\left(\frac{G_m}{G_f}\right) - 1\right] \tag{16}$$

$$\theta_d = \text{acos}\left(\frac{S_i^{sl}}{2G_m\epsilon_{12}^{max} - a_{12}S_i^{sl}}\right) \tag{17}$$

$$I(\theta) = \frac{\theta}{a_{12}} - \left(\frac{1}{a_{12}\sqrt{a_{12}^2 - 1}}\right)\ln\left[\frac{a_{12} + \cos\theta + \left(\sqrt{a_{12}^2 - 1}\right)\sin\theta}{a_{12}\cos\theta + 1}\right] \tag{18}$$

2.4. Hashin Failure Criterion

Hashin [25] proposed a failure criterion able to differentiate the fiber and matrix failure and without any calibrated parameter required. These advantages, combined with the good correlation with experimental data make this criterion very popular in the literature [26-28]. For tensile load, the fiber and matrix failure functions are

$$f_f = \left(\frac{\sigma_{11}}{S_{11}^t}\right)^2 + \left(\frac{\sigma_{12}}{S_{12}^s}\right)^2 \tag{19}$$

$$f_m = \left(\frac{\sigma_{22}}{S_{22}^t}\right)^2 + \left(\frac{\sigma_{12}}{S_{12}^s}\right)^2 \tag{20}$$

where σ_{ij} are the stress components in the laminae.

The fiber and matrix damages take place when $f_f = 1$ and $f_m = 1$, respectively. For the damage propagation up to the rupture, the material properties degradation approach is applied. If $f_f = 1$, $E_1 \rightarrow (1 - d_f)E_1$, $G_{12} \rightarrow (1 - d_f)G_{12}$, and $\nu_{12} \rightarrow (1 - d_f)\nu_{12}$, where d_f is the fiber damage variable. On the other hand, if $f_m = 1$, $E_2 \rightarrow (1 - d_m)E_2$, and $G_{12} \rightarrow (1 - d_m)G_{12}$, where d_m is the matrix damage variable. d_f and d_m can be estimated by the following expressions

$$d_f = 1 - \left(\frac{E_1^d}{E_1}\right) \tag{21}$$

$$d_m = 1 - \left(\frac{E_2^d}{E_2}\right) \tag{22}$$

Assuming that the matrix can still bearing the load when the matrix is damaged and that the transversal failure represents the interface failure from micromechanical point of view, E_1^d and E_2^d are derived using the VSPKc model and are expressed by

$$E_1^d = E_m\left(1 - V_f\right) \tag{23}$$

$$E_2^d = E_m\left(1 - \sqrt{\frac{V_f}{\pi}}\right) \tag{24}$$

3. RESULTS AND DISCUSSION

The composite laminates were manufactured using the hand layup process for unidirectional glass fiber/epoxy with two different stacking sequences: QUAD $[45/90/-45/0]_{2s}$ and DD $[67.5/-22.5/22.5/-67.5]_4$. The process was carried out at room temperature by stacking the glass fibers on top of each other with an intermediary Pipefix lamination resin between the layers. The epoxy matrix bisphenol A (resin) has a polyamide-based catalyst. During the manufacturing process each ply was compacted with a metal roller aiming to remove bubbles, ensure consistent thickness, and preserve homogeneity. Nylon-based peel ply layers were applied to both top and bottom surfaces of GFRP plates during layup. The application of peel ply sheets aids in the release of volatiles and air from the laminate during the curing process that took 12h at room temperature.

Four specimens for each laminate were manufactured and tested in tension following the D3039/D3039M [29] recommendation. The results of the tensile tests are presented in Fig. 1, where indeed we can realize that DD and QUAD have the same stiffness, which is 16.1GPa. The average strengths of the QUAD and of the DD are 262.8MPa and 257.9MPa, respectively. The strength of the QUAD laminate is 1.9% higher than the strength of the DD. The blue vertical line indicates the maximum tensile strain based on the unit circle failure criterion [4], demonstrating that the experimental results are coherent.
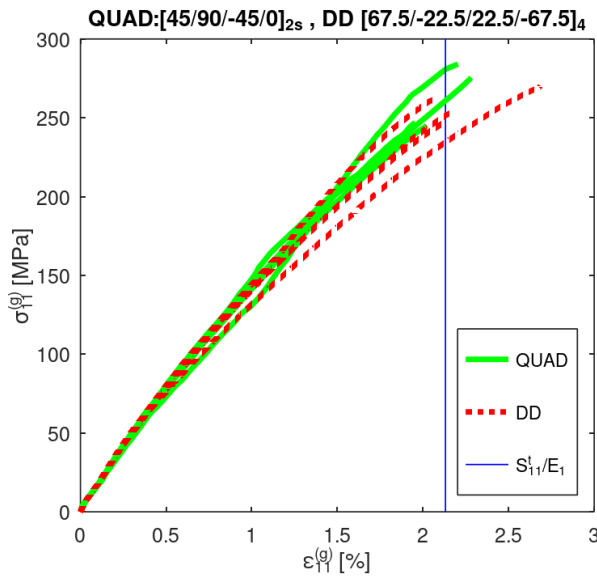
Figure 1. Experimental results of the tensile tests for QUAD and DD laminates.

The laminae properties were not measured, only the whole laminate. Hence, the first step of the proposed modeling approach is to obtain the lamina elastic properties. Based on the classical laminate theory [30], the laminate longitudinal modulus is

$$E_x = \frac{A_{11}A_{22} - A_{12}^2}{tA_{22}} \tag{25}$$

where t is the total laminate thickness and A_{ij} are defined in Eq.(1).

Since $E_x = 16.1\text{GPa}$ was obtained experimentally, the trace theory presented in Section 2.2 can be applied to compute the $tr(C)$, which is the unique independent elastic property following the Tsai's modulus idea. The result of the absolute error according to $tr(C)$ is presented in Fig. 2, indicating an agreement between experimental data and analytical model for $tr(C) = 46.9\text{GPa}$. For $tr(C) = 46.9\text{GPa}$ the laminae properties are: $E_1 = 32.6\text{GPa}$, $E_2 = 8.7\text{GPa}$, $G_{12} = 2.8\text{GPa}$, and $\nu_{12} = 0.303$.
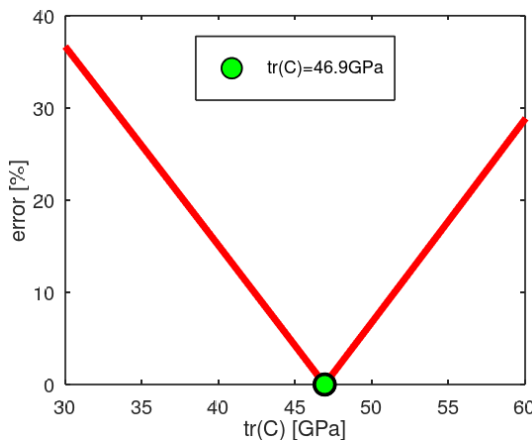
Figure 2. Average absolute error of E_x according to $tr(C)$.

The next step required for the analytical modeling proposed is to obtain the lamina strengths S_{11}^t, S_{22}^t, and S_{12}^s. The fiber and matrix properties also were not measured. To fix this issue the experimental data reported is [31] is used as reference, where a GFRP was also investigated. The authors listed the following material properties: $E_f = 80\text{GPa}$, $\nu_f = 0.2$, $E_m = 3.35\text{GPa}$, and $\nu_m = 0.35$; $V_f = 0.62$, $E_1 = 53.48\text{GPa}$, $E_2 = 17.7\text{GPa}$, $G_{12} = 5.83\text{GPa}$, $S_{11}^t = 1140\text{MPa}$, $S_{22}^t = 35\text{MPa}$, $\epsilon_{12}^{max} = 2\%$, and $S_{12}^s = 72\text{MPa}$. Solving an inverse problem, the fiber tensile strength and the interface strengths obtained are: $S_f^t = 1705.3\text{MPa}$, $S_i^n = 44.5\text{MPa}$, and $S_i^{sl} = 71.5\text{MPa}$. To extend these results of the tested material, it assumed that the fiber, matrix

and interface properties can be considered approximately the same to apply the VSPKc micromechanical model. This is a fundamental hypothesis which allows the analytical modeling implementation without need to additional experimental tests to compute S_{11}^t, S_{22}^t, and S_{12}^s.

For the QUAD and DD, where $E_1 = 32.6$GPa, the fiber volume fraction can be computed by applying the rule of mixture [32]; i.e. $V_f = (E_1 - E_m)/(E_f - E_m) = 0.38$. By applying $S_f^t = 1705.3$MPa, $S_i^n = 44.5$MPa, and $S_i^{sl} = 71.5$MPa into Eq.(12-14), the lamina strengths for the tested GFRP are: $S_{11}^t = 694.0$MPa, $S_{22}^t = 38.6$MPa, and $S_{12}^s = 76.8$MPa. At last, for the complete implementation, replacing $E_m = 3.35$GPa and $V_f = 0.38$ into Eq.(21-24), $d_f = 0.94$, and $d_m = 0.75$.

Once all the material parameters are obtained using only E_x measured experimentally and implementing the combined approach mixing the trace theory, VSPKc model and solving an inverse problem, the laminates response to the tensile load estimated are presented in Fig. 3 for the QUAD and DD. The laminate strength for the QUAD measured experimentally is 262.8MPa, while the proposed model estimation is 258.5MPa. For the DD, the experimental strength is 257.9MPa and the model estimation is 254.3MPa. For both, the error between the model estimation and the experimental result is smaller than 2%. This result indicate a promising approach to decrease abruptly the number of experimental tests required to design composite structures.
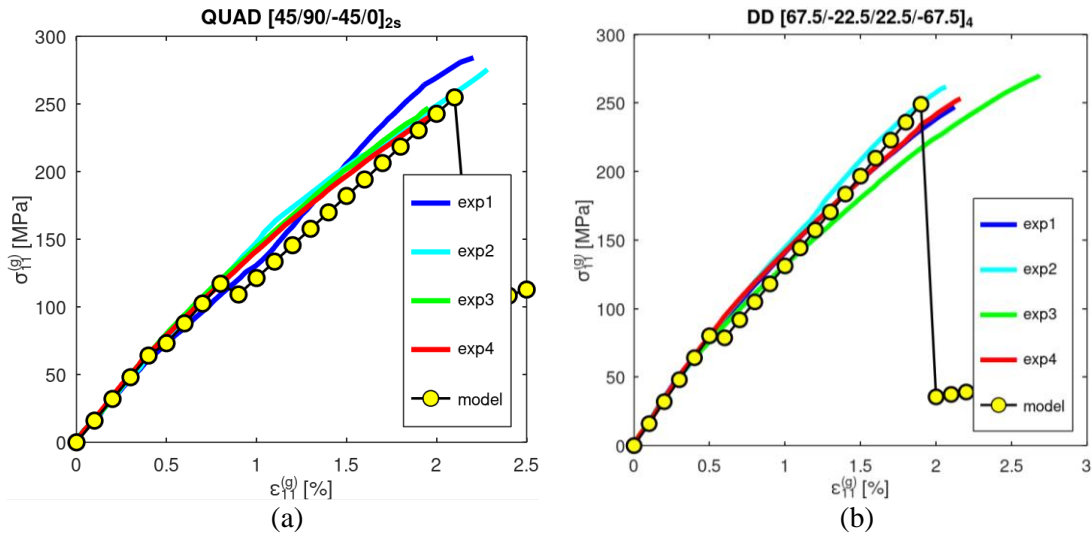
Figure 3. Comparison between experimental stress-strain curves with the analytical estimations: (a) QUAD; (b) DD.

4. CONCLUSIONS

DD laminates have been widely explored in the literature for CFRP, but there are few investigations about the applications of this new family of laminates for GFRP. This study is a contribution to the effort to apply the DD design concept for GFRP comparing the QUAD $[45/90/-45/0]_{2s}$ and DD $[67.5/-22.5/22.5/-67.5]_4$. The experimental results indicate that both laminates have the same stiffness and strength. Additionally, an analytical model is developed, where the laminate longitudinal elastic modulus is used as input and the other properties are obtained combining the trace theory with VSPKc micromechanical model. The experimental and numerical results show an error smaller than 2%, indicating the modeling reliability.

4.1. Declaration of Competing Interest

The authors declare no conflict of interest.

4.2. Fundings

4.3. Acknowledgements

5. REFERENCES

References should be listed in the order mentioned in the text. Use font size 11, Times New Roman, justified, Paragraph spacing: 0 pt before and 6 pt after, without left indent, as follow:

[1] S.W. Tsai, J.D.D. Melo. An invariant-based theory of composites. Composites Science and Technology, 100, 237-243, 2014.

[2] L.L. Vignoli et al. Trace theory applied to composite analysis: A comparison with micromechanical models. Composites Communications, 25, 100715, 2020.

[3] A. Arteiro et al. A case for Tsai's modulus, an invariant-based approach to stiffness, Composite Structures, 252, 112683, 2020.

[4] S.W. Tsai, J.D.D. Melo. A unit circle failure criterion for carbon fiber reinforced polymer composites. Composites Science and Technology, 123, 71-78, 2016.

[5] S.W. Tsai. Double-double: new family of composite laminates. AIAAJ, 59, 4293-4305, 2021.

[6] S.W. Tsai, J.D.D. Melo. Composite Materials Design and Testing - Unlocking Mystery with Invariants. Stanford Composites Design Group, 2015.

[7] L.L. Vignoli el al. Theoretical justification of Tsai's modulus based on micromechanical analysis. Composites Science and Technology, 238, 110041, 2023.

[8] S.W. Tsai et al. Composite Double-Double and Grid/Skin Structures - Low Weight/Low Cost Design and Manufacturing, Stanford Composites Design Group, 2019.

[9] B. Vermes et al. Design of laminates by a novel ''double–double'' layup. Thin-Walled Structures, 165, 107954, 2021.

[10] S.W. Tsai et al. DOUBLE– DOUBLE Simplifying the Design and Manufacture of Composite Laminates. Stanford: Composite Design Group, 2023.

[11] S. Shrivastava et al. D and DD-drop layup optimization of aircraft wing panels under multi-load case design environment. Composite Structures, 248, 112518, 2020.

[12] A. Vijayachandran, A. Waas. On the use of non traditional stacking to maximize critical buckling loads in flat composite panels. Composite Structures, 261, 113320, 2021.

[13] E. Kappel. Double-double laminates for aerospace applications — finding best laminates for given load sets. Composites Part C: Open Access, 8, 100244, 2022.

[14] R.D. Cunha et al. Low velocity impact response of non-traditional double double laminates. Journal of Composite Materials, 57, 1807-1817, 2023.

[15] G.C. Alves, L.L. Vignoli R.M.C. Neto. Damage onset in CFRP single lap joint for DD and QUAD laminates. J Mech Sci Technol, 38, 157–162, 2024.

[16] L.L. Vignoli et al. Micromechanical fiber-matrix interface model for in-plane shear in unidirectional laminae. Mechanics of Advanced Materials and Structures, 0, 1–13, 2023.

[17] L.L. Vignoli et al. Buckling Analysis of Thin-Walled Structures Based on the Trace Theory – A Simple and Efficient Approach for Mechanical Characterization of GFRP. Submitted.

[18] R.M.C. Neto et al. Increase of shear fracture energy of adhesive joints using double-double laminates. The Journal of Adhesion, 1–19, 2024.

[19] J.N. Reddy. Mechanics of Laminated Composite Plates - Theory and Analysis. 2nd ed., CRC Press, 2003.

[20] L.L. Vignoli et al. A Novel Micromechanical Model Based on the Rule of Mixtures to Estimate Effective Elastic Properties of Circular Fiber Composites. Appl Compos Mater, 29, 1715–1731, 2022.

[21] L.L. Vignoli et al. Micromechanical fiber-matrix interface model for in-plane shear in unidirectional laminae. Mechanics of Advanced Materials and Structures, 0, 1–13, 2023.

[22] L.L. Vignoli et al. Analytical modeling of fiber–matrix interface failure in unidirectional laminae subjected to in-plane shear loads. Proceedings of the Institution of Mechanical Engineers, Part L: Journal of Materials: Design and Applications, 0, 2024.

[23] L.L. Vignoli. Is the out-of-plane shear strength an independent property? A micromechanical perspective about a macromechanical question. Journal of Composite Materials, 57, 4379-4388, 2023.

[24] L.L. Vignoli et al. Micromechanical analysis of longitudinal and shear strength of composite laminae. Journal of Composite Materials, 54, 4853-4873, 2020.

[25] Z. Hashin. Failure criteria for unidirectional fiber composites. J Appl Mech, 47, 329-334, 1980.

[26] A.P.C. Duarte, A. Díaz Sáez, N. Silvestre. Comparative study between XFEM and Hashin damage criterion applied to failure of composites. Thin-Walled Structures, 115, 277-288, 2017.

[27] E.J. Barbero, M. Shahbazi. Determination of material properties for ANSYS progressive damage analysis of laminated composites. Composite Structures, 176, 768-779, 2017.

[28] M. Trombini et al. 1D higher-order theories for quasi-static progressive failure analysis of composites based on a full 3D Hashin orthotropic damage model. Composites Part B: Engineering, 270, 111120, 2024.

[29] ASTM D3039/D3039M-08. Standard Test Method for Tensile Properties of Polymer Matrix Composite Materials.

[30] E.J. Barbero. Introduction to composite materials design. 3rd edition, CRC Press, 2018.

[31] A.S. Kaddour et al. Mechanical properties and details of composite laminates for the test cases used in the third world-wide failure exercise. J Compos Mater, 47, 2427–2442, 2013.

[32] L.L. Vignoli et al. Comparative analysis of micromechanical models for the elastic composite laminae. Composites Part B, 174, 106961, 2018
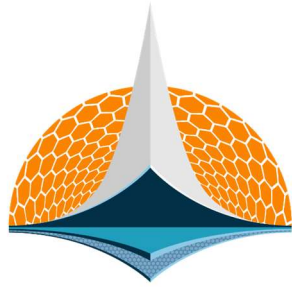
10 Durability of composite materials

Organized and edited by

Sandra Maria da Luz
&
Carla Tatiana Mota Anflor

DEGRADATION ARAMID FIBER STUDY FROM BALLISTIC PANELS USED IN BRAZILIAN FEDERAL POLICE VESTS BETWEEN 2015 AND 2020

Juliana Laura A. P. Maschwitz, Alessandro B. de S. Oliveira, Rita de Cássia Silva, Eberth de Almeida Corrêa, Demétrio Antônio da Silva Filho

Mechatronics Department, Technology Faculty (University of Brasília – Brazil)
Corresponding author: julianalalves@gmail.com.br

Abstract: The aramid fiber, introduced by DuPont in 1971, met the expectations of many lines of business, revolutionized protective gear across numerous industries; in this field, the ballistic vests manufacturing for militaries and law enforcement agents worldwide have been privileged with the launched by this lightweight and flexible material in contrast to the existing ones. In addition, this material has proven to be advantageous for various industries, including automotive, aeronautical, and aerospace, as well as for the production of cables, helmets, and ballistic protection panels used in automobiles.

A preliminary experimental analysis was conducted to assess the effectiveness of aramid fibers in the ballistic panels, considering that they could be degraded over time and affected by the various manners of use. These vests were purchased by the Brazilian Federal Police in 2014. Such analysis allowed us to determine how well the fibers met their primary function and how effectively they provided safety measures. Five ballistic vests used by the police in Brasília/DF were randomly sampled.

The proposed method consists of a Thermogravimetric Analysis (TGA) and Differencial Scanning Calorimetry (DSC), to examine the degradation of woven ballistic fibers, and gather data for comparison against safety performance standards. The aim is to determine if the material can meet the high ballistic performance required by security agencies.

The results indicate significant fiber degradation, suggesting they may no longer meet the safety requirements for their intended use. In light of these findings, the research recommends studies using Dynamic Mechanical Analysis (DMA) techniques shortly.

1. INTRODUCTION

Aramid fibre, scientifically described as paraphenylene terephthalamide (PPTA), commercially known as KEVLAR®, has outstanding properties, such as high strength, low density, dimensional and thermal stability; all of which attract attention, as it can be used for a variety of applications, such as aeronautical engineering, aerospace, cable manufacturing, helmets, ballistic protection and others.

Created on the basis of industrial demand, this meant creating a material that was light, strong, durable and flexible enough for certain applications. In this field, aramid fiber has been widely used by the war industry, necessarily in the creation of ballistic protection.

Its use in the manufacture of panels for ballistic protection vests was practically consolidated with the launch of the material by the American company DuPont in the 1970s, precisely because of its high impact resistance and low density [1]; this has allowed public safety officers around the world to wear protective vests made of material that is more resistant than steel by approximately seven times per unit.

Aramid is an organic fiber belonging to the family of aromatic polyamides. It is a long-chain polyamide [1] and is a polymer in which approximately 85% of the amide bonds are directly linked to two aromatic rings, which distinguishes it from conventional polyamides such as nylon [2] .The repeating units (meros) of the polymer attached to the aromatic ring have a rectilinear arrangement; this para-orientation makes the molecular chain super rigid, with a high modulus of elasticity, high tensile strength, low density and low deformation (excellent dimensional and thermal stability). In addition, the mechanical properties of interest are basically determined by the integrity of the chemical bonds, through hydrogen bridges, of the amide functional group, followed by the respective weights and molecular orientations, as well as the presence of water and roughness in the fibers [3].

Once the launch has been completed, it was made feasible by company with several types of Kevlar® yarns, known as grids, wich be different each others by mechanical properties. The grids lauched by DuPont are: Kevlar® 29, 49, 119, 129 e 149. The grids most commonly used by ballistic protection industries is fabric made from Kevlar® 29 e Kevlar®49, owing their high modulus of elasticity and consequent impact resistance.

The appropriate ballistic performance of the final composition of a given piece of equipment necessarily involves understanding exposure processes (what types of threats, sources of shock waves and the environment in which they occur)[4], mapping indices which make it possible to select the right raw material for the case (such as modulus and characteristic stress that the material is capable of withstanding), identifying factors which tend to degrade the material and reduce durability, and consequently the performance and safety standards required – temperature, humidity and possible exposure to acidity are examples of these factors. Once the equipment has been produced (ballistic panel and appropriate protective covers), the next step is to understand the environmental elements that can deteriorate or contribute to the material's useful l; and in this case, there are many publications that address these factors, describing the nuances of how degradation occurs or even a reasonable way of reducing it.

In accordance with the exposures above, Liu et Yu (2006) investigated the termal stability from eight (08) types of high performance fibers [5]; in this case, has classified the degradation characteristic temperatures for *para-aramids* Kevlar® 29, 49, 129 and Twaron® 2000, Terlon®, Kermel®, PBO (*poly(p-phenylene benzobisoxazole*)) and UHMW-PE (*ultra high molecular weight polyethylene*). Therefore, they had concluded that the most important characteristic temperature for evaluate degradation is the temperature on initial of the process (T_i), where Kevlar® 29, 49, 129 respectively presented the values: 480, 474.7 e 464.2ºC. The researchers had completed their investigation by calculating and presenting the activation energies of each of these fibers, using Freeman-Carrol method – to known activation energy associated in this process means understanding equipment's life cycle[5]; thus, the all fibers Kevlar's activation energy studied are similar and ecqual to 0.37 KJ/mol (in NO_2) and 0.45 KJ/mol (in Atmosphere).

In 2010, study performed by Arrieta *et al.*investigated the age process of high performance polymer blend (Kevlar® and Poly-benzimidazole), and has explained that the loss of tensile strength occurs because of decrease in crystallinity by heat flow [6]. Furthermore, changes observed in the original Polymer structure occurs due to the scission of the polymer chain, and result in a loss molecular weight and mechanical properties.

In 2011, a research by Cai *et* Yu investigated the thermal degradation of high-performance Kevlar® 49, 129 (Poly(p-phenylene terephtamide), Nomex (polysophtaloyl methaphenileny diamine), and PBO (poly(p-phenylene benzobisoxazole) fibers using Termogravimetry (TG) [7]. In general terms, the results of fabric's pyrolysis has generated residues, mainly of: CO, CO_2, NO, NO_2. In addition, the initial degradation temperatures (T_{onset}) ranged from 423.7 to 648ºC; Kevlar® 49 has presented 548.1ºC and Kevlar® 129 has presented 542.4ºC. The final degradation temperatures (T_{endset}) were 643.7ºC for Kevlar®49 and 660.4ºC for Kevlar®129.

In the same year, NR Council *et al.* (2011) published a book entitled *Opportunities in Protection Materials Science and Technology for Future Army Applications*[4] in which they devoted part of a chapter to explaining that environmental factors such as UV radiation, humidity and extreme temperatures, in combination or not, can degrade aramid fibers, thus reducing ballistic performance. At the time, has mentioned that in case of helmets, the use of resin was recommended to make the material homogeneous and waterproof, in order to improve the operating conditions of the equipment.

It is important to consider that the development of this high-performance synthetic fiber dates back approximately 50 years, and was relatively new and disruptive at the time of its launch. Since then, there has been a great deal of contemporary research concerned not only with mechanisms to improve ballistic performance and control degradation, but also with cost reduction, biodegradability, minimizing material damage and risks in production processes, improved thermal characteristics, ease of economic evaluation, as well as maintaining or improving the original modulus of elasticity and resistance and characteristics of the synthetic fibre.

And in an attempt to mitigate the deleterius effects of the aggressive environment, several studies have shown that the synthetic material has previously been treated with saline solutions at various concentrations and/or reinforced with natural fibers and *nanofillers*, in order to improve fiber interlocking and promote the thermal stability of the ballistic composite fabric; the studies presented below confirm the understanding that these procedures have shown promise in delaying or combating degradation, with the consequent improvement in the ballistic performance of the material.

In 2013, S.Li *et al.* investigated the ultraviolet radiation effects in the poly(p-phenylene terephthalaraid) fibers. They concluded that short-term exposures were capable of altering the surface of the material, causing changes in the chemical structures of the fiber's surface while preserving its core [8]. Thus, increases in UV radiation exposure time caused decreases almost linear in tensile properties; in addition, has noticed that these changes were capable to cause fluctuations in fiber performance. Meanwhile, they observed that these indices almost stabilized, when the exposure time exceed three hours.

Study performed by Monteiro *et al.* (2018) [9] aproached the use of aramid's reinforcement with natural fiber such as *fique plant* (from the botanical genus *furcraea andina*, belonging to the family *agavaceae*). The research presented several environmental factors in degradation contributing and highlighted the thermal degradation; in this case, they has concluded that the addition of natural fiber presented an increase of thermal stability with performance similar to Kevlar®. In this same research, they mentioned several possibilities of natural fiber's for the same purpose, such as: coin fiber, coconut, sisal, curauá and piassava); and finally, they highlighted production costs analysis: using *fique plant* as reinforcement produces an equipment thirteen times cheaper than the material with only synthetic fiber.

Yuan *et al.* (2018) evaluated nanoparticles POOS (glycidyl polyhedral oligomeric silesquioxanes) applications [10] in Meta-aramid and Polytetrafluoretilene hybrid fabrics (Nomex/PTFE). The research showed significant results in terms of increased roughness of the fibers studied, as well as increased resistance to UV rays. In addition, the tensile properties of the new material showed an increase of 24.3% compared to the untreated material. It is important to note the increase in roughness, where the study showed an increase of 46.8% in the fibers tested; because according to [4], roughness contributes greatly to the ballistic resistance desired in high performance ballistic fabrics.

A study by Naturazzi et al. in 2021 [11] presented the state of the art in the use of various types of natural fibers as an alternative to Kevlar® in the manufacture of multilayer ballistic panels (aramid + natural fiber). He mentioned coconut, pineapple, palm, jute, sisal, corn, bamboo and marijuana fibers as possible applications. Of course, he points out the drawbacks of using them in their natural state, emphasizing the need for prior treatment to modify their surfaces to make them compatible with the synthetic polymer matrix. By using jute fiber impregnated with polyester resin to provide adhesion to the aramid, the material met the *National Institute of Justice (NIJ)* Level III test standard using 7.62mm ammunition, with a plasticine deformation less than the 44mm required by the aforementioned standard.

Still in this context of reinforcing natural fibers, in 2022 Gladys et al. carried out research using *snake grass fiber*[12]. Firstly, the fiber was treated with a NaOH solution in concentrations of 5%, 10% and 15% to contribute to thermal stabilization and finally to improve the surface roughness of the natural fibers used, in order to provide a better interlocking between them and to promote correct adhesion to the synthetic fiber and additional *fillers*. The study concluded that for the natural fiber treated at a concentration of 5%, there were gains in thermal and mechanical properties; at percentages above 5%, the alkaline solution did not bring any benefits, as it degrades the fiber. In the same study, the Al2O3 *nanofiller* was added to investigate possible increases in ballistic resistance. An addition of 8% alumina *filler* resulted in a 68.80% increase in the energy absorbed by the material.

In a comprehensive review of the degradation mechanisms of aramid fabrics exposed to aggressive environments by Xu et al. in 2022, the effects of four environmental factors were described: ultraviolet radiation (UV), thermal fluctuation, humidity, and acidic and basic environments [3]. Ultraviolet radiation causes a decrease in tensile strength and tear strength of about 40% and 79.9%, respectively, after 144 hours of exposure. Thermal properties are also affected by UV exposure; after 1 hour of exposure, the initial decomposition temperature of aramid decreased from 423.8°C to 384.3°C [3]. The same study also indicated that ballistic resistance was reduced by 20% after exposure to ultraviolet rays, since the performance analyzed in ballistic fabrics is closely related to tensile properties and failure due to pulling of threads from the fabric. With regard to thermal variation, research shows that heating the material to temperatures around 300°C is capable of reducing the tensile strength by about 30%; this is because the increase in temperature modifies the microcrystalline structure of aramid - it should be remembered that the strength of the fiber is given by the para-orientation of its aromatic rings, where the increase in temperature is capable of modifying this micromolecular organization. Humidity also has a degenerative effect, since the presence of amide causes the

fibers to degrade by hydrolysis, drastically reducing tensile strength and consequently ballistic performance [3]. Finally, in acidic environments, changes in the mechanical behavior of the fibers have been observed, in particular a decrease in tensile strength, due to the oxidation of the fiber surface and the consequent breaking of the bonds of the amides present [3].

In the light of this knowledge, understanding the durability of high-performance fabrics, the conditions under which they deteriorate and/or the ways in which they can be preserved is fundamental in order to prescribe the correct fiber for certain uses and to make proper use of the guarantees offered by manufacturers; in this field, given the high cost of the finished product, understanding the conditions under which it should be used in order to extract maximum performance from this noble material is fundamental for the safety of the public user.

Thus, in the context of the use of ballistic protection vests in the Federal Police, acquired in 2014 and put into use in 2015, the general objective of this work is to determine whether there has been degradation of the aramid fiber used in the fabrics used to make the equipment in question. The occurrence of degradation implies the use of a material unsuitable for its intended purpose; it is therefore essential to determine whether degradation has occurred, and if so, at what point in the material's service life.

For this purpose, the technical parameters provided by the manufacturer of the aramid fabrics (KEVLAR®, DuPont) are studied and compared with the data obtained from the preliminary thermogravimetric (TG) and differential scanning calorimetric (DSC) tests.

2. METHODOLOGY

2.1. Materials

The materials analyzed are ballistic vests for tactical and ostensible use, for use by the police force of the Federal Police Department - MJSP. The vests were purchased in 2014 and manufactured in 2015. In addition, they only had a one (01) year warranty - at the time of purchase, there were no control criteria for receiving the parts, nor was there a requirement for a minimum warranty of five (05) years, as is currently the case. They were distributed to all troops in the 26 states of the Federation in 2015; the parts under analysis were only used in the Federal District during their warranty period.

Figure 1. (a) Vest in front-panel view; (b) Open vest with front and back panel view.

Their storage conditions prior to expiration are uncertain; when they were collected for this experiment after expiration, they had been stored in cardboard boxes in the 2nd basement of the PF headquarters for approximately three (03) years, coexisting in damp and moldy conditions.

The samples prepared and examined in the materials laboratory are KEVLAR® ballistic fabric discs approximately 15 mm in diameter. Extraction and preparation were performed in two (02) steps:

Stage 1 - Extraction: The vests were catalogued numerically; then the ballistic panels were removed from their outer and inner covers, so that from a total of 40 vests, 4 samples could be extracted by cutting out

the bottom of the ballistic panels. The cut was made in this position of the panel in order to keep its geometry as close as possible to the original configuration, so that its performance could be measured later in a ballistic laboratory test.
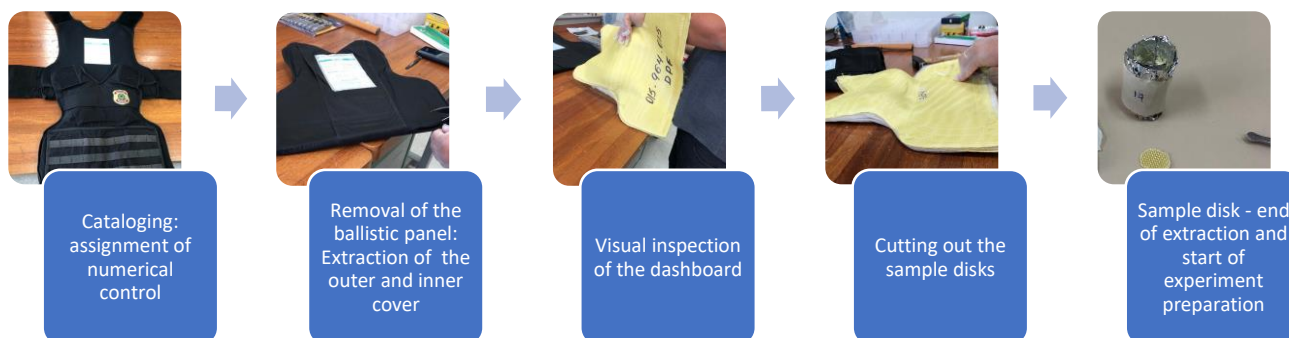
Figure 2. Diagram of Step 1 of the experiment - sample extraction and control.

2ª Etapa - Preparo: a partir da etapa anterior, foram escolhidas amostras retiradas de quatro (04) coletes. Os materiais extraídos dos coletes são pequenos discos de tecido KEVLAR®, com aproximadamente 15mm de diâmetro. Eles foram fragmentados em pequenas fibras, colocados em copinhos feitos com papel alumínio, e levados para estufa a temperatura de 80°C por aproximadamente 3h30min. Após esse processo, foram colocados em dessecador para resfriamento e manutenção da desidratação imposta pós-estufa.
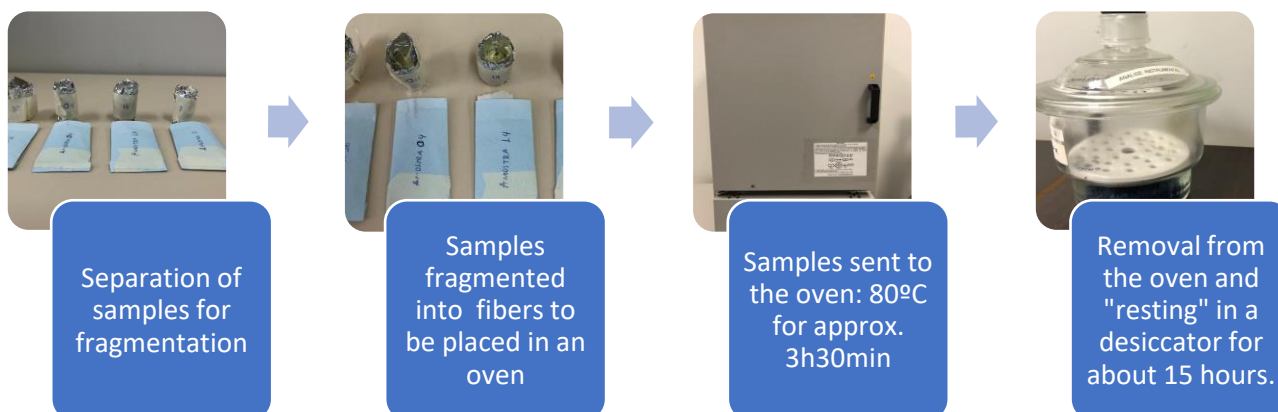
Figure 3. Diagram of Step 2 of the Experiment - Sample Preparation.

Finally, the material was extracted once more from a collection that had been preserved in a similar manner to that of an unexposed sample (virgin sample). Steps 1 and 2 were repeated for this final item in the experiment in order to obtain the control sample.

2.2. Procedures

The samples were subjected to thermal analysis using a simultaneous TGA/DSC thermal analyzer, model SDT Q600 (TA Instruments).

Figure 4. Simultaneous Thermal Analyzer model SDT Q600 (TA Instruments).

The quantities of each material sampled are presented in Table 3, with values ranging from approximately 8.00g to 13.00g. The samples were placed in a ceramic crucible under an atmosphere of N_2 (nitrogen) with a flow rate of 100mL/min, at a heating rate of 10ºC/min. A preliminary series of tests was conducted, commencing at room temperature and concluding at 900°C for the initial sample. The subsequent experiments commenced at room temperature and concluded at 800°C.

3. RESULTS AND DISCUSSION

Table 3. The presentation of thermal information..

Amostras	Inicial Mass (mg)	T_g / C_p (ºC)	T_i	T_{onset} (ºC)	T_{pico} (ºC)	T_{endset} (ºC)	Waste (%)	ΔH (J/g)
Sample Vest 16	11.06	179.28	530.00	570.00	575.74	600.00	32.00	332.90
Sample Vest 04	8.05	101.55	486.67	573.33	578.02	600.00	36.47	257.70
Sample Vest 14	12.89	173.89	516.22	559.46	574.83	589.20	32.00	169.50
Sample Vest 07	8.59	192.80	500.00	558.33	577.91	588.89	36.15	133.20
Sample Vest 17	9.31	159.82	514.28	554.29	575.49	577.14	34.00	112.70

Prior to the discussion of the results, it is important to note that the receipt of materials was not under control at the time, and the bidding procedure did not specify the type of grid to be used in the ballistic fabric (whether Kevlar® 29 or 49). Consequently, some results appear to be aramid fiber, as illustrated in Figure 5.

Prior to conducting the thermal analysis on the SDT Q600 Simultaneous Thermal Analyzer, it is important to note that the samples for vests numbers 04 and 07 exhibited significant deterioration. Additionally, sample 04 exhibited a color that differed from the characteristic color of the Kevlar® under study (it should have been golden yellow, but it was whitish).
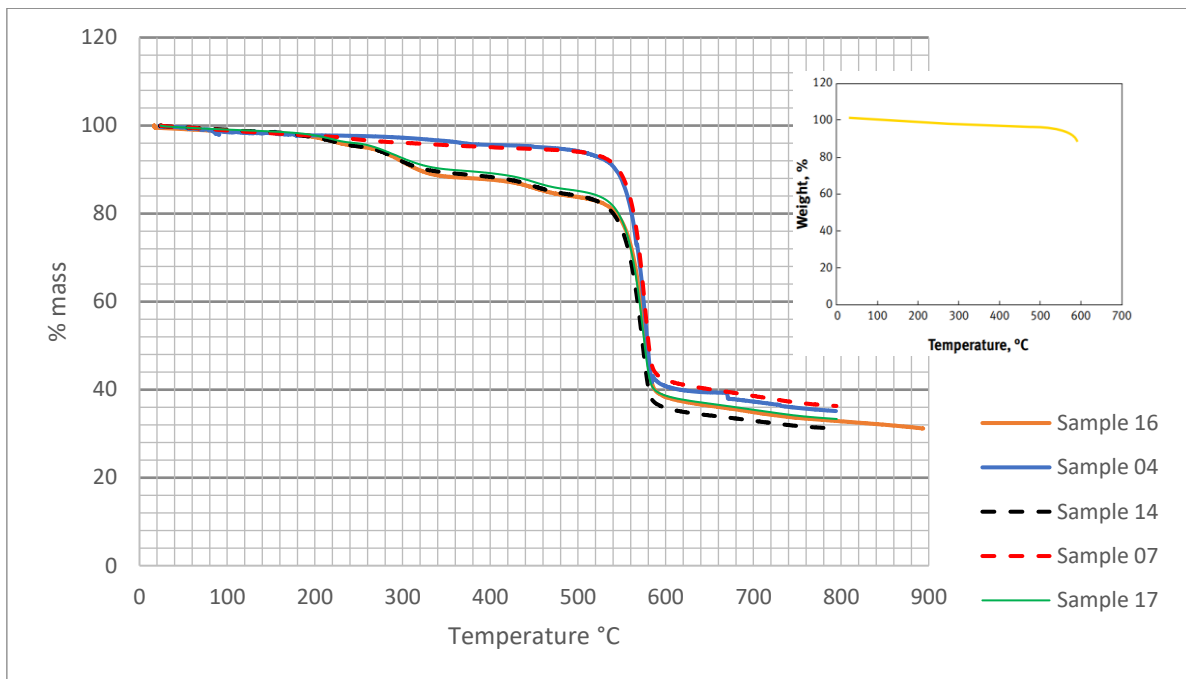
Figure 5. TG characteristic curve of the fibers sampled, with exposure to nitrogen at 10°C/min.

A comparison of the graph in the top right-hand corner, provided by the manufacturer to portray the typical curve of TG exposed to nitrogen at a rate of 10ºC/min, as reproduced in the experiment, with the shape of the graph generated using the samples collected reveals a significant discrepancy. This indicates the possibility of a mixture of fibers or other compounds in the yarns used to manufacture the ballistic fabric, or even a mixture of a resin other than the polymer in question, the type of which cannot be identified using this technique.

The samples obtained from vests 14, 16, and 17 do not initially align with the characteristic TG graph provided by the manufacturer. Instead, they appear to exhibit two distinct stages of degradation before reaching the peak. The manufacturer of aramid asserts that the initial decline is solely due to water loss. However, given the differing graphical behavior observed in the material under study, it is possible that a mixture of materials is present, which cannot be identified using the techniques employed.
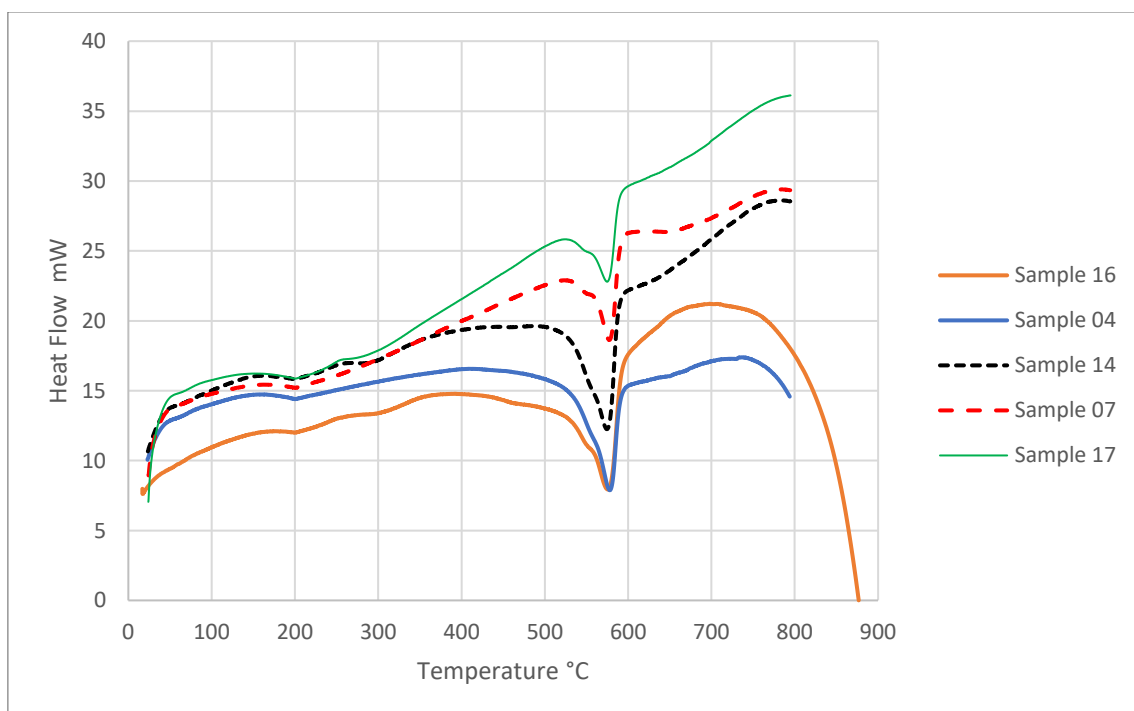
Figure 6. DSC characteristic curves of the aramid samples of each of the vests evaluated.

Upon analysis of the DSC curves of the ballistic vests, it was observed that sample vest 04 exhibited an initial degradation temperature of approximately 51°C lower than the manufacturer's indications. Specifically, decomposition was observed to occur at 486.67°C, which was found to be lower than the expected value of around 538°C. A comparison of Table 3 with the data reveals a discrepancy between the glass transition temperature indicated by the company and the value observed in the test. While the company indicates values in the 149 to 179°C range, the value found was 101.55°.

All of the vests exhibited a lower initial degradation temperature (Ti) than that indicated by the manufacturer, which suggests that the test was conducted on a degraded material.

4. CONCLUSIONS

This study was a first look at the state of the raw material used in the ballistic panels of the vests of the Federal Police, during the warranty period of the manufacturers.

In this case, it is crucial to recognize that there is no method for verifying the proper maintenance of the material by users. Furthermore, the Brazilian manufacturer did not implement quality control procedures during the production process.

The carried out testes by SDT Q600 Simultaneous Thermal Analyzer, TG and DSC according methodology presented, has permitted the acquisition of additional data regarding the recent state of the samples. The known numbers from the experiment suggest at least two hypothesis:
   a. The fibers exhibited considerable degradation;
   b. A composite material was observed, but the specific composition of the materials within it could not be determined.

These hypotheses have been proposed due to the discrepancies between the results obtained from the experiment and those previously reported by aramid fiber manufacturer.

Therefore, with the experiment results, it's possible to deduce that studied fibers do not perform according minimum securities standards due the several fiber's degradation. This study will be complemented, in a short future, with FTIR analysis and dynamic mechanical analysis (DMA) to certify if the material adhere standards, and if there is possibility for usage according safety recquirements.

5. REFERENCES

[1]   L. Loureiro, 'Reutilização de fibras de Para-Aramida como Reforço Mecânico em Poliamida 6,6.', 2016.

[2]   DuPont, 'KEVLAR ® ARAMID FIBER TECHNICAL GUIDE', 2017.

[3]   Y. Xu, H. Zhang, and G. Huang, 'Review on the mechanical deterioration mechanism of aramid fabric under harsh environmental conditions', *Polymer Testing*, vol. 128. Elsevier Ltd, Nov. 01, 2023. doi: 10.1016/j.polymertesting.2023.108227.

[4]   NR Council et al, *Opportunities in Protection Materials Science and Technology for Future Army Applications*. Washington, DC: National Academies Press, 2011. doi: 10.17226/13157.

[5]   X. Liu and W. Yu, 'Evaluating the thermal stability of high performance fibers by TGA', *J Appl Polym Sci*, vol. 99, no. 3, pp. 937–944, Feb. 2006, doi: 10.1002/app.22305.

[6]   C. Arrieta, E. David, P. Dolez, and V. K. Toan, 'Thermal aging of a blend of high-performance fibers', *J Appl Polym Sci*, vol. 115, no. 5, pp. 3031–3039, Mar. 2010, doi: 10.1002/app.30825.

[7]   G. M. Cai and W. D. Yu, 'Study on the thermal degradation of high performance fibers by TG/FTIR and Py-GC/MS', *J Therm Anal Calorim*, vol. 104, no. 2, pp. 757–763, May 2011, doi: 10.1007/s10973-010-1211-0.

[8]   S. Li, A. Gu, J. Xue, G. Liang, and L. Yuan, 'The influence of the short-term ultraviolet radiation on the structure and properties of poly(p-phenylene terephthalaramide) fibers', *Appl Surf Sci*, vol. 265, pp. 519–526, Jan. 2013, doi: 10.1016/j.apsusc.2012.11.038.

[9]   S. N. Monteiro *et al.*, 'Fique fabric: A promising reinforcement for polymer composites', *Polymers (Basel)*, vol. 10, no. 3, Feb. 2018, doi: 10.3390/polym10030246.

[10]   J. Yuan, Z. Zhang, M. Yang, W. Wang, X. Men, and W. Liu, 'POSS grafted hybrid-fabric composites with a biomimic middle layer for simultaneously improved UV resistance and tribological properties', 2018.

[11]   N. M. Nurazzi *et al.*, 'A review on natural fiber reinforced polymer composite for bullet proof and ballistic applications', *Polymers (Basel)*, vol. 13, no. 4, pp. 1–42, Feb. 2021, doi: 10.3390/polym13040646.

[12]   A. Kumaresan Gladys, V. S. Muthuvelu, K. Kumar, and K. Ganesh, 'Energy absorption performance of Kevlar/snake grass fiber composites under ballistic impact test with nano Al2O3 inclusion', *Polym Compos*, 2022, doi: 10.1002/pc.26911.

A NEURAL NETWORK-DRIVEN METHODOLOGY TO PREDICT FATIGUE LIFE OF TIRE COUPLINGS

Lourenço S. Daudt[(a)*], Rogério J. Marczak[(b)]

(a) 0009-0002-7693-8292 (Federal University of Rio Grande do Sul – Brazil)
(b) 0000-0001-5760-3468 (Federal University of Rio Grande do Sul – Brazil)
* Corresponding author: lourencodaudt@gmail.com

Abstract: Tire couplings are widely used in the industry. These products, predominantly made of fiber-reinforced rubber, exhibit nonlinear behaviour that makes fatigue study more challenging compared to linear materials. Additionally, fatigue testing of these products is time-consuming, potentially causing delays in production. Therefore, a methodology to rapidly predict the fatigue life of these products, considering not only the raw material but also the manufacturing process, is highly desirable. Previous research has established a relationship between static and fatigue tests using artificial neural networks, but these analyses were only performed with standardized test specimens. In this study, a methodology to predict fatigue life using artificial neural networks and static tests of the final product was developed, also considering manufacturing process characteristics. For this, data such as hardness, the results of a coupling torsion test, with outputs being torque at 10° and 20° of deformation were used. The results demonstrated that the neural network was effective in predicting good approximations for the fatigue life of the coupling.

1. INTRODUCTION

Flexible couplings play a crucial role in transmitting torque between misaligned rotating shafts, being essential in sectors such as mining and oil and gas [1]. In the Brazilian context, tire couplings are widely used, standing out for their ability to handle radial and angular misalignments, ensuring long durability. These products are predominantly made of a composite material, specifically fiber-reinforced rubber. Therefore, the non-linearity of this composite, which is hyperelastic and anisotropic, and the complexity in load distribution make the analysis of these couplings more challenging, hindering the attainment of analytical solutions for the involved stresses.

Additionally, manufacturing imprecision increases the variability of the final product, especially during mounting and vulcanization. This imprecision, combined with complex geometry and various loads, underscores the need for an experimental approach focused on the final product, rather than relying exclusively on standardized test bodies.

The fatigue of these couplings, often associated with misalignments and variations in transmitted torque [2], presents a significant prediction challenge, potentially occurring unpredictably after installation. Considering this, this research proposes an innovative approach that combines experimental tests and computational modelling to anticipate the lifespan of elastomers subjected to cyclic loading.

Specifically, this study aims to develop a methodology capable of predicting the fatigue life of a composite material, more specifically a tire coupling, based on static tests, using artificial neural networks (ANNs). These static tests are approximately 100 times faster than fatigue tests, thus bringing a crucial time benefit to the industry.

Previous studies have predicted the fatigue life of materials with ANNs: tests of uniaxial tensile fatigue were conducted on vulcanized natural rubber samples in dumbbell shape. Based on the data from these tests, a backpropagation neural network (BPNN) model was developed to estimate the fatigue life of the natural rubber samples [3]. A predictive model was developed using a backpropagation artificial neural network (BP-ANN) to estimate fatigue properties of natural rubber (NR) composites. By utilizing mechanical and viscoelastic properties as input data and fatigue life as output, with a remarkable prediction accuracy of 97.3% [4]. Multiaxial fatigue experiments were conducted on hyperelastic chloroprene rubber (CR) reinforced with tungsten nanoparticles, proposing a semi-empirical fatigue model ε-N. Additionally, machine learning models were employed for fatigue life prediction, with the Deep Neural Network demonstrating superior accuracy (14,3% error) [5]. The capability of Artificial Neural Networks (ANN) was successfully demonstrated to accurately predict fatigue failure in fiber-reinforced composite materials, even for materials not included in the network training [6]. Rotating bending fatigue performance was examined across various composite shaft types and utilized ANN predictions to complement experimental findings. Results indicated that the ANN effectively predicted fatigue life in composite materials [7].

2. METHODOLOGY

The proposed methodology aims to test and validate a method for determining fatigue life through rapid tests using artificial neural networks (ANN). This network is fed with static tests of the final product on the Static Test Machine (STM) and hardness as inputs. Each dataset is analysed along with the number of cycles of a dynamic fatigue life test with the final product on the Dynamic Test Machine (DTM), which is the network's output, with the purpose of training it. The objective of the network is therefore to predict fatigue life, i.e., the estimated number of cycles on the dynamic machine.

The first phase of the methodology begins with the manufacture of 11 flexible elements. This process is strategically designed to encompass a representative range of raw material and process conditions.

The second stage focuses on conducting tests. The first is hardness testing. The Quasi-Static test is the second, conducted on the STM, testing each piece until 20° of torsion, providing a thorough evaluation of static characteristics. The third and final test is conducted on the DTM, providing valuable information on the fatigue life of the final product, which is the most relevant result.

The third stage is the development of the neural network, involving training and validation in the MATLAB environment. The goal is to empower the neural network to extract complex patterns from the data obtained from 11 flexible elements in the STM and durometer, comparing them with the results of the dynamic test. In the final phase of this stage, the methodology proposes the testing of the ANN using two flexible elements not used during training and new static and dynamic tests. These three stages form a comprehensive and innovative strategy, providing an in-depth analysis of the fatigue life of flexible elements manufactured under various process conditions.

2.1. Tire Coupling

Tire couplings consist of two metallic hubs and one flexible element, typically made of fiber-reinforced rubber. Is the case of the Antares AT 50, object of this study and presented in Figure 1, the flexible element features a rubber matrix reinforced with four layers of polyamide fibers arranged at 45°/135°/45°/135°. A sectioned flexible element is shown in Figure 2, where is possible to see the fiber layers.

Figure 1. AT 50 – AT 50 tire coupling type used in the present study.

Figure 2. Sectioned view of the composite element, showing the layers of fibers.

The flexible element is a toroid with metallic flanges on both sides. The combination of its geometry and the non-linear stress-strain relations hinders the possibility of a purely analytical solution.

Tire couplings can be considered composite structures. The isotropic hyperelastic rubber matrix provides firmness without losing flexibility, while the anisotropic polyamide fibers bear the torque load. This material combination allows the coupling to withstand significant deformations while maintaining structural integrity. The specific fiber orientations optimize load distribution and improve the coupling's ability to counterpart stresses in specific directions.

A previous study [8] analysed this tire coupling's structure by characterizing the material's constitutive relations. The researchers divided the tire into two layers: the outer layer, made solely of rubber, was modelled using the Yeoh model (isotropic hyperelastic), and the inner layer, made of fiber and rubber, was modelled using the Holzapfel-Ogden-Gasser model (anisotropic hyperelastic). This approach resulted in a complex finite element model capable of accurately simulating a torsion test.

2.2. Testing Proceeding

Aiming the hardness measurements, the tip of the analogical Shore A durometer is placed at the external side of the flexible element, in 5 different points around the toroid. Then, the average is calculated.

The Static Test Machine (STM), shown in Figure 3 and whose schematic diagram is illustrated in Figure 4, constitutes a fundamental component in the process of evaluating the mechanical performance of the elastic couplings. Its design encompasses a drive system composed of a gearmotor and a gearbox, responsible for inducing a constant rotation of 1 rpm in the coupling under analysis. Subsequently, an encoder is installed in the system to measure the angle of rotation of the shaft. Following this, the coupling to be tested is installed, in this case, the AT 50. On the opposite side, the machine is firmly fixed by means of a lever arm, whose opposite end is positioned on a load cell. As the drive system applies load to the coupling causing it to twist, the encoder records the angle, and the load cell records the corresponding increase in load. This load, when multiplied by the length of the arm, is converted into torque, providing essential data on the mechanical characteristics of the component.

Figure 3. Static Test Machine
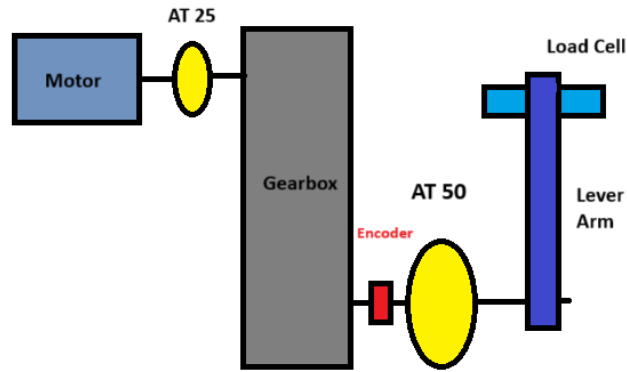
Figure 4. Schematic illustration of the STM

In practice, the result of this test is represented by a curve that relates the angle of deformation (expressed in degrees) measured by the encoder to the torque (expressed in Nm) measured by the load cell. This graphical representation offers a detailed and quantitative view of the torsional stiffness of the flexible element. Each one of the 11 flexible elements is tested until 20° of torsion. This angle was selected based on the range of torque observed during the startup phase of an electric motor, which constitutes a high but frequently occurring load for the coupling, as determined by manufacturer measurements. Each sample is tested four times to verify the Mullins effect and to check if the coupling suffers any damage, which would be indicated by an increasing flexibility over repeated tests. Then, the torque (Nm) vs. deformation (°) curve is obtained with the last test. More specifically, the torque at 10° and at 20° of deformation.

Each one of the 11 pieces then go through a fatigue life test on the Dynamic Testing Machine (DTM), operated by a 2 HP motor at 1800 rpm. This machine, depicted in Figure 5 and schematically illustrated in Figure 6, is connected to an Antares AT 25 (tire coupling) and then to a gearbox with a ratio of 1:150, resulting in an output rotation of 12 rpm. At this output, the coupling under test is located - usually an AT 50, as in this test case. Afterwards, there is a pair of bearings. Then, a 0,5 m torque arm is connected to the shaft. In this arm, loose weights are inserted, which the system will rotate in an unbalanced manner. After that, there is another pair of bearings. Finally, there is a rotation counter that records the number of cycles performed by the machine, which is the output of the neural network.

Figure 5. Dynamic Test Machine (MTD)
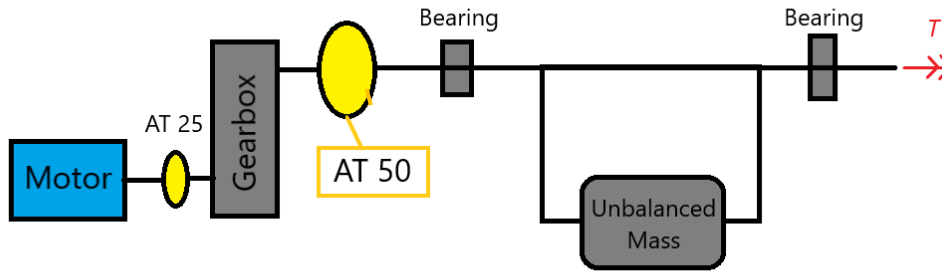
Figure 6. Schematic illustration of the DTM

During the upward cycle of the mass, the torque is positive because the coupling pulls the mass. However, during the downward cycle, the torque becomes negative because the coupling needs to hold the mass. Thus, the machine generates a torque curve with a zero average, where the maximum torque practically coincides in magnitude with the minimum torque. This maximum torque is determined by the eccentric mass. In this setup, the total torque was set to 548 Nm. Specifically, the torque arm alone generates 195 Nm, and an additional mass of 79.3 kg is applied to achieve the total torque.

The fatigue life test follows the DIN 740-2 [9] standard, with a mean torque T_N equal to zero and a maximum torque of T_{max}. For the flexible element to be approved, it must withstand at least 50,000 cycles. The oscillation frequency (f_{osc}) should be up to 10 Hz, provided it does not result in overheating of the system. In the case of the test in question, the frequency is 12 rpm, or 0.2 Hz. Furthermore, to expedite the testing process, the torque was elevated to 548 Nm, resulting in a reduction in the number of cycles, as shown in section 3. Nevertheless, given that the primary objective of this methodology is to predict the cycle count rather than to validate the coupling, deviating from the stipulated 50,000 cycles outlined by DIN 740-2 is not a problem.

2.3. Artificial Neural Network

In the context of modelling and computational analysis, an artificial neural network was developed in the MATLAB environment, with the Neural Network Fitting toolbox. The training data for the network include hardness, static test results (torque at 10° and at 20°), and the results of the fatigue life test (number of cycles, being this last one the output of the ANN) of 9 specimens. The neural network was trained to establish complex relationships between these parameters, providing an effective tool for predicting the mechanical performance of elastomeric couplings.

After the completion of training, the neural network was tested with input data from 2 specimens not used in training. The obtained results were compared with the physical values obtained from fatigue life tests for each specimen, allowing the assessment of the predictive performance of the neural network. Calculating the percentage of accuracy will provide a quantitative measure of the neural network's precision in predicting the mechanical behaviour of elastomeric couplings under different manufacturing conditions. This integrated approach, combining physical experimentation and computational modelling, enables a comprehensive analysis of the mechanical properties of elastomeric couplings and validation of the effectiveness of the developed neural network.

Afterwards, if the methodology is validated, the operator can conduct a torsion test at the STM and acquire the hardness measures. With these parameters, the ANN would yield a predictive estimate of the anticipated number of cycles in the fatigue test.

3. RESULTS AND DISCUSSION

Four static tests were conducted on each sample to assess both the Mullins effect and the possibility of damage in the composite material. For instance, as depicted in Figure 7, which illustrates the results of the four tests performed on sample number 3, the initial test (highlighted in red) exhibited slightly higher stiffness compared to the subsequent tests. Conversely, the stiffness observed in the subsequent tests was slightly lower but remained consistent across them, indicating a potential influence of the Mullins effect rather than damage to the material.
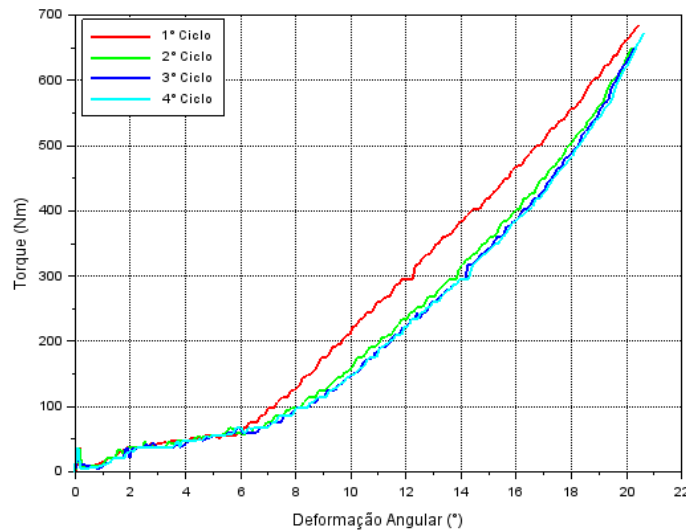
Figure 7. Comparison of stiffness in four static tests of sample 3.

The results of hardness, torque at 10° and at 20° in the STM, and the fatigue life of 9 flexible elements are displayed in Table 1. This dataset of 9 specimens was used to train the neural network.

Table 1. Training and validation samples

Specimen	Hardness (Shore A)	Torque @ 10° (Nm)	Torque @ 20° (Nm)	Actual Fatigue Life (cycles)	Predicted Fatigue Life (cycles)
1	62,0	184,04	734,11	9.458	9.458
2	61,5	190,83	706,04	11.942	11.942
3	63,0	175,73	688,31	5.420	5.420
4	62,0	192,86	721,76	15.360	15.360
5	63,0	192,74	761,64	16.157	16.157
6	62,0	191,69	757,39	10.092	10.092
7	62,5	209,13	800,01	36.240	36.240
8	62,5	191,70	750,07	19.086	19.086
9	62,0	205,70	746,99	18.767	18.767

The network was trained using Levenberg-Marquardt as algorithm. It was generated with one hidden layer of 10 neurons. As can be seen, the mean square error of the training was 0, and the resultant R^2 was 1, indicating that the response surface generated by the ANN is capable of reproducing exactly the experimental tests. This is a direct consequence of the small number of tests used to train it. It is expected that, for a high number of specimens, the errors will be measurable. Following this, two more samples were employed to test the ANN, and their results are presented in Table 2.

Table 2. Testing Samples

Specimen	Hardness (Shore A)	Torque @ 10° (Nm)	Torque @ 20° (Nm)	Actual Fatigue Life (cycles)	Predicted Fatigue Life (cycles)	Error (%)
10	63,0	193,13	750,16	13.952	12.514	10,3%
11	62,0	192,60	735,49	13.972	14.649	4,8%

The errors can be considered highly acceptable given that the material was a hyperelastic composite and the tests were conducted on the final product. The ANN yielded a remarkably low average error rate of 7,6%. Consequently, the overall predictive accuracy is deemed successful for these samples, underscoring the ANN as a promising tool for predicting the fatigue life of composite tire couplings.

The MSE of the testing step was $1,26 \cdot 10^6$. The resultant R² of the ANN, including the testing samples, was 0,9981. The graphs of predicted outputs versus actual fatigue life of the training samples, the test samples and from all 11 samples together are shown in Figure 8.
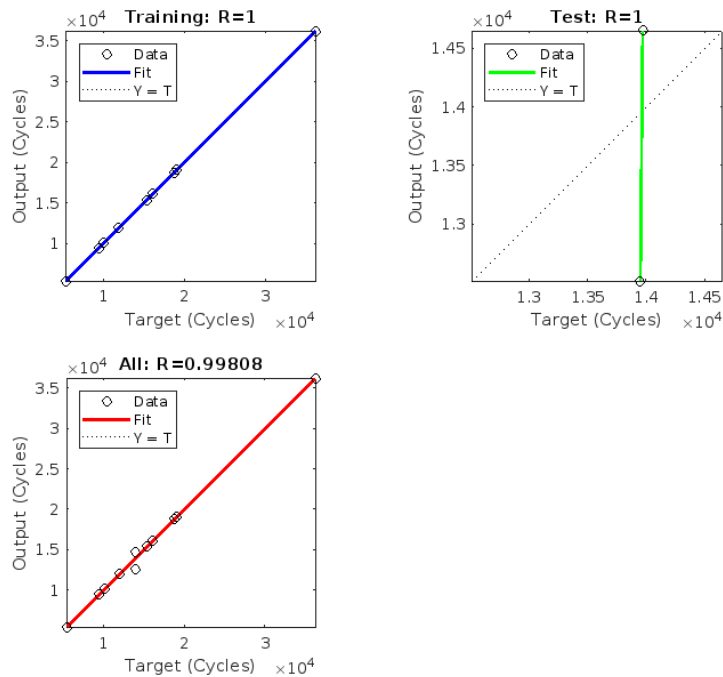
Figure 8. ANN prediction x actual fatigue life.

As comparison, 28 methods of linear regression were tested in MATLAB considering all 11 samples. The best performance was Support Vector Machine (SVM), which yielded R² = 0,6786. The graph of predicted versus actual response is shown in Figure 9.
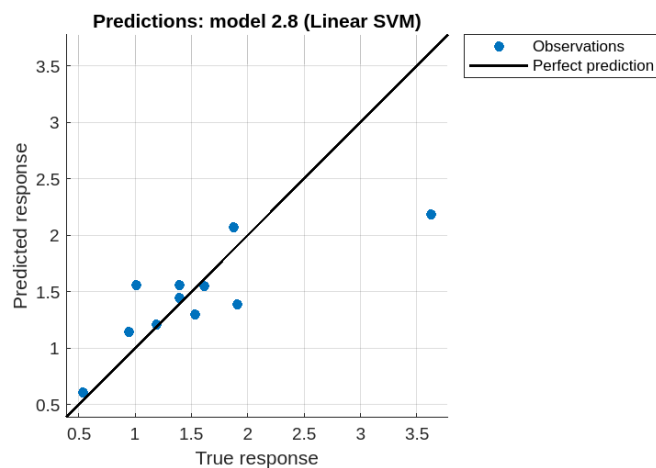
Figure 9. SVM linear regression prediction x actual fatigue life

4. CONCLUSIONS

The preliminary findings underscore the high promise of the proposed methodology, indicating its potential utility in using static tests in conjunction with Artificial Neural Networks (ANN) for rapid and

reasonably accurate prediction of fatigue life in materials. With an error rate of 7,6%, the developed ANN can be considered suited for this problem.

Furthermore, the ANN results were significantly better than those obtained through linear regression methods, demonstrating that it is a superior tool for this purpose. The enhanced predictive capability of the ANN highlights its robustness in capturing the complex, non-linear relationships inherent in hyperelastic composite materials, which the linear regression methods failed to address adequately. This superiority makes the ANN a more reliable and precise option for predicting fatigue life of these products.

However, with the number of samples used so far, it is important to address that, even though artificial neural networks have the potential to predict systems with evolving loading conditions, the current ANN can provide a response similar to a fitting curve.

To further validate and refine this approach, it is recommended that a minimum of ten additional specimens be subjected to both training and validation processes for the ANN, with an additional two specimens reserved exclusively for testing purposes. This expanded dataset will enable a more comprehensive assessment of the methodology's efficacy within this specific domain, enhancing confidence in its applicability and reliability for future fatigue life predictions of this product.

4.1. Declaration of Competing Interest

The authors declare no conflict of interest.

4.2. Acknowledgements

5. REFERENCES

[1] Johnson, C. M. An introduction to flexible couplings. *World Pumps*, Volume 1996, 1996. (https://doi.org/10.1016/S0262-1762(99)81001-3).

[2] Jon R. Mancuso. *Couplings and Joints: design, selection & application*. 2nd Edition, 1999. CRC Press. (https://doi.org/10.1201/9781482292275)

[3] Liu, X., Zhao, X., & Shangguan, W. B. Fatigue life prediction of natural rubber components using an artificial neural network. *Fatigue & Fracture of Engineering Materials & Structures*, Volume 45, 2022. (https://doi.org/10.1111/ffe.13690).

[4] Xiang, K. L., Xiang, P. Y., Wu, Y. P. Prediction of the fatigue life of natural rubber composites by artificial neural network approaches. *Materials & Design*, Volume 57, 2014. (https://doi.org/10.1016/j.matdes.2013.12.044).

[5] Choi, J., Quagliato, L., Lee, S., Shin, J., e Kim, N. Multiaxial fatigue life prediction of polychloroprene rubber (CR) reinforced with tungsten nano-particles based on semi-empirical and machine learning models. *International Journal of Fatigue*, Volume 145, 2021. (https://doi.org/10.1016/j.ijfatigue.2020.106136)

[6] Al-Assadi, M., Kadi, H. E., e Deiab, I. Predicting the fatigue life of different composite materials using artificial neural networks, *Applied Composite Materials*, Volume 17, 2009. (https://doi.org/10.1007/s10443-009-9090-x)

[7] Hassan, A. K. F., Mohammed, L. S., Abdulsamad, H. J. Experimental and artificial neural network ANN investigation of bending fatigue behavior of glass fiber/polyester composite shafts, *Journal of the Brazilian Society of Mechanical Sciences and Engineering*, Volume 40, 2018. (https://doi.org/10.1007/s40430-018-1098-4)

[8] Vieceli, B. C. et al. A technique for structural finite element modeling of fiber-reinforced rubber composite used in flexible couplings. In: *Proceedings of the 2nd Ibero-American Conference on Composite Materials – IAMaC*, p. 149-154, 2023.

[9] DIN 740-2, Power Transmission Engineering; Flexible Shaft Couplings; Parameters and Design Principles. DIN Standards, 1986. (www.din.de/en)

11 Failure of composites

Organized and edited by

Sandra Maria da Luz
&
Carla Tatiana Mota Anflor

FAILURE PREDICTION IN COMPOSITE LAMINATES BY MACHINE LEARNING

Paola M. Albino[a], Herbert M. Gomes [b], *

(a) 0009-0007-2815-9565 (Federal University of Rio Grande do Sul, Brazil)
(b) 0000-0001-5635-1852 (Federal University of Rio Grande do Sul, Brazil)
* Corresponding author: herbert@mecanica.ufrgs.br

Abstract: Composite materials are being widely used nowadays. There are economic and structural advantages in replacing materials with these new ones due to their good weight/stiffness ratio and cost. There are currently several constitutive and failure models to represent the constitutive behavior up to the failure of these materials, but not all of them have adequate accuracy. Models such as Tsai-Wu, Tsai-Hill, Hashin, etc. have limitation in application for some ranges of the behavior of composite materials. Much attention has been paid to Machine Learning (ML) tools in recent decades due to their good learning and generalization capabilities, as well as their ability to capture tendencies from scarce experimental data. This work aims to apply the ML tool to learning to predict failure onset on laminated composites. This paper begins with a survey for experimental data from biaxial tests and the generation of a database following a methodology already used in other papers. A class of ML, Neural Networks, is used to train experimental data and then validated with unseen data. Preliminary results indicate that it is possible to accurately model behavior directly from experimental data without the need to idealize combinations of principal stresses and stress invariants. Results relating to failure prediction of the materials investigated are presented to show the effectiveness of the proposed use of ML in this area.

1 Introduction

The use of ML in the modelling of failure surfaces in composite materials represents an innovative and effective approach to predicting the behavior of these materials under different conditions. The importance of this application lies in its ability to deal with the complexities inherent in composite materials, such as heterogeneity, anisotropy and non-linearity, in a more accurate and efficient way than traditional methods. ML, in particular, can explore complex patterns in failure data, capturing non-linear relationships that may escape conventional approaches. By integrating ML algorithms, such as artificial neural networks (ANN), support vector machine (SVM) or decision trees (DT), into failure prediction models, it is possible to significantly improve prediction capabilities, leading to a deeper and more accurate understanding of the behavior of composite materials. The ML's ability to learn from experimental data, adapting to new information and continually improving its predictions makes its use very attractive.

The use of ML in constitutive modelling is not new (Ghabhousi et al., 1991). Recently it has been used for metallic materials (Lourenço et al., 2022). Specifically for the ANN use to the constitutive modelling of composite material, a comprehensive review can be found in Liu et al. (2021). There, it was surveyed two main research areas: discovering unknown constitutive laws and accelerating multiscale modelling. The discovery of unknown constitutive laws is hindered by the scarcity of directly paired experimental data, and the paper proposes using indirect data derived from experimental measurements through physics-based models as a potential solution. The study also discusses the lack of physical interpretation in ANN models and

the computational expense of high-fidelity simulation models. The trend of combining ANN models with physics, experimentation, and data science to build a hybrid system that maximizes the capabilities of each component is highlighted in the conclusion.

In a recent study conducted by Fontes and Shadmehri (2023) a data-drive Deep Neural Networks (DNN) was used to predict the failure strengths of several types of laminates. The experimental database to train the DNN was based on WWFE-1 and the predictive capabilities of DNN was compared to conventional analytical failure theories. The study aimed to address the limitations of previous models by creating a framework that could generalize input features and predict failure for various laminate angles and loading scenarios. The paper also discussed the neural network architecture and training methodology used in the study. Laminae strength properties ($\sigma_{1,ult}^T$, $\sigma_{1,ult}^C$, $\sigma_{2,ult}^T$, $\sigma_{2,ult}^C$, $\tau_{12,ult}$), the ultimate Cartesian stress ratios (σ_x/σ_y, σ_x/τ_{xy}, σ_y/τ_{xy}, etc.), the order and orientation of the layup, and cases of symmetry were the input values for training. The results showed that the DNN outperformed conventional theories in predicting failure strengths for multiple types of laminates. However, the study highlighted the need for comprehensive experimental data to improve the model's predictive ability. They found that the trained DNN followed the general trends observed in the experimental data. Also it was highlighted the need for experimental training data that covers the entire input space, since where there was few data, the DNN behaved weak in making predictions outside the variability of the input experimental data.

2 Theoretical Basis

2.1 Artificial Neural Networks

Artificial Neural Networks (ANN) are machine learning-based computer algorithms that resemble biological neurons in terms of their fundamental structure. One basic kind of neural network is feedforward, in which the connections between nodes do not form cycles. For supervised learning tasks like regression and classification, they are frequently used. An input layer, hidden layers, and an output layer make up the network architecture. Using optimization algorithms such as backpropagation, training includes modifying weights in order to minimize the discrepancies between expected and actual outputs. Natural language processing and image recognition have seen successful applications of feedforward neural networks. An artificial neural network, or ANN, with architecture [4 5 3 2] is shown operating in Figure 1. Every neuron unit functions as $y = f(\mathbf{W}^T\mathbf{X} + b$, where), $\mathbf{X}$ the vector of input signals, f is a nonlinear activation function, $\mathbf{W}^T\mathbf{X}$ is the vector of weights, and b is the trigger threshold. Training is done by applying the backpropagation algorithm and minimizing (with a learning rate η) of an error function, which is usually the Mean Squared Error, or MSE.
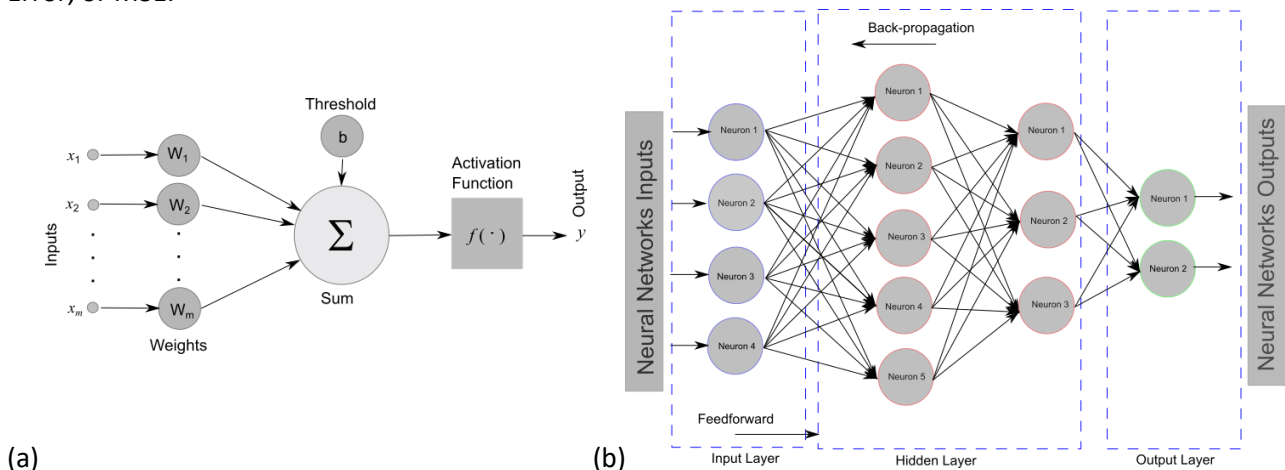
Fig. 1 (a) Neuron activity function representation. (b)ANN representation with a [4 5 3 2] architecture.

2.2 Classic Failure Criteria

Many failure criteria exist to predict composite failure like maximum stress, maximum strain, Larc03, Larc05, but without loss of generality, this paper will be focused on the Tsai-Wu, Tsai-Hill and Hashin. The

Tsai-Wu failure criteria is a widely used mathematical model for predicting the failure of composite materials under various loading conditions. It was developed by Tsai and Wu (Tsai, 1965 and Tsai and Wu, 1971) in the field of composite mechanics by a generalization of the Tsai-Hill theory to include stress and strength interactions in the fiber and matrix directions. The criterium assess the failure potential based on the combination of normal and shear stresses in the principal material directions and is expressed as an inequality, where the failure is predicted when the computed value exceeds a certain threshold. The in-plane form of the Tsai-Wu failure criterion for a composite material with stresses in the main direction of orthotropic material (normal and shear stresses) is given by (Kaw, 2006) $H_1\sigma_1 + H_2\sigma_2 + H_6\tau_{12} + H_1\sigma_1^2 + H_{22}\sigma_2^2 + H_{66}\tau_{12}^2 + 2H_{12}\sigma_1\sigma_2 < 1$, where σ_1, σ_2 and τ_{12} are the in-plane stresses and $H_1 = (\sigma_{1,ult}^C - \sigma_{1,ult}^T)/(\sigma_{1,ult}^T \sigma_{1,ult}^C)$, $H_{11} = 1/(\sigma_{1,ult}^T \sigma_{1,ult}^C)$, $H_2 = (\sigma_{2,ult}^C - \sigma_{2,ult}^T)/(\sigma_{2,ult}^T \sigma_{2,ult}^C)$, $H_{22} = 1/(\sigma_{2,ult}^T \sigma_{2,ult}^C)$, $H_6 = 0$, and $H_{66} = 1/\tau_{12,ult}^2$ are material-dependent parameters. For the Mises-Hencky criterion, $H_{12} = -0.5\sqrt{1/(\sigma_{1,ult}^T \sigma_{1,ult}^C \sigma_{2,ult}^T \sigma_{2,ult}^C)}$. For Tsai-Hill Failure criteria it is assumed that failure in the material takes place only when the distortion energy is greater than the failure distortion energy of the material. Hill adopted the von Mises' distortional energy yield criterion to anisotropic materials and Tsai adapted it to a unidirectional lamina. It is defined as: $(G_1 + G_3)\sigma_1^2 + (G_1 + G_3)\sigma_2^2 + 2G_3\sigma_1\sigma_2 + 2G_4\tau_{23}^2 + 2G_6\tau_{12}^2 < 1$, where $G_1 = 0.5(2/\sigma_{2,ult}^T{}^2 - 1/\sigma_{1,ult}^T{}^2)$, $G_2 = 0.5(1/\sigma_{2,ult}^T{}^2)$, $G_3 = 0.5(1/\sigma_{1,ult}^T{}^2)$, $G_6 = 0.5(1/\tau_{12,ult}{}^2)$.

Hashin (1980) failure criteria, provides individually tensile and compressive fibre failures and tensile and compressive matrix failures modes independently, as follows and described in Wang and Duong (2016): for tensile mode $\sigma_1 > 0$ then $(\sigma_1/\sigma_{1,ult}^T)^2 + (\tau_{12}/\tau_{12,ult})^2 = 1$, for compressive fiber mode $\sigma_1 < 0$ then $\sigma_1 = \sigma_{1,ult}^C$, for tensile matrix mode $\sigma_2 > 0$ then $(\sigma_2/\sigma_{2,ult}^T)^2 + (\tau_{12}/\tau_{12,ult})^2 = 1$ and finally for compressive matrix mode $\sigma_2 < 0$ then $[\sigma_2/(2\tau_{23,ult})]^2 + \{[\sigma_{2,ult}^C/(2\tau_{23,ult})]^2 - 1\}(\sigma_2/\sigma_{2,ult}^C) + (\tau_{12}/\tau_{12,ult})^2 = 1$, where generally $\tau_{23,ult} = 0.5\tau_{12,ult}$ for CFRP. For Tsai-Hill failure criteria.

3 Methodology

This study intends to use an ANN to learn the failure envelopes for composite laminates and plane in shear stress strain, similar to those used in (Hinton et al., 2004). So, the data used in this study was gathered from the WWFE-1 (Hinton et al.,2004), section 2, articles 2.1 and 2.2 that are concerned to Lamina properties, lay-up configurations and loading conditions for a range of fiber reinforced composite laminates (FRCL), and the Biaxial experimental test results for strength and deformation of those laminates. The input data included the elastic constants, stress strain curves and strengths for four unidirectional laminae and their constituents.

3.1 Data Augmentation

To increase the number of points for better data analysis, a custom function was used. This function was applied to the original data and then fitted using the scipy.optimize.curve_it from the SciPY library. After fitting the parameters and computing a covariance matrix, new data points were generated. These additional points were filtered using numpy.convolve, combined with a function to define the filter of the moving average, called windows_size. This procedure was used to smooth the curve to avoid noise, and then these new points were saved for inclusion in the ANN's dataset to improve accuracy.

4 Numerical results

Figure 2.a shows the results for the ultimate failure (envelope) for GFRP (Glass-Epoxy) using the trained ANN and a comparison with other failure surface (Tsai-Wu, Tsai-Hill and Hashin). It also shows a characteristic strain-stress curve (orange) of the material. According to the ANN failure surface and Tsai-Wu, it is predicted the material to fail before the actual experimental failure (GRPF), while according to the other classical failure surface, the prediction is right. With the same method but now for a different material, T300 Carbon/Epoxy, it shown that this material is predicted to fail in the right stress state for any of the surfaces, inclusive for the trained ANN, as shown in Figure 2.b.

(a)

(b)
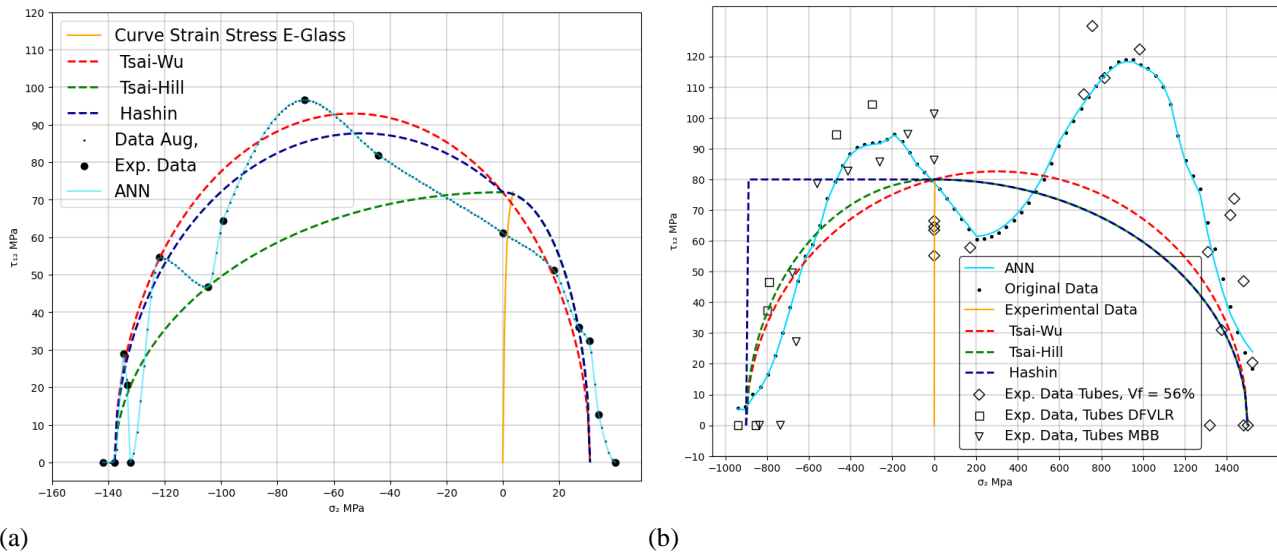
Fig. 2 Results from WWFE-I for (a) GFRP and (b) CRFP criteria and the trained ANN along with Tsai-Wu, Tsai-Hill and Hashin failure criteria. The orange curve represents one stress path.

5   Final Remarks and conclusions

This paper presents the results of the implementation of ANNs for predicting stress-strain and surface failure curves for different composite materials. The dataset was based on experiments from WWFE-1 (Hinton et al., 2004). The data augmentation technique was used to improve the number of training data and accuracy. The validation dataset showed a low MSE, indicating the ability of the trained ANN architecture to generalize, however a dataset with less uncertainty would render better generalization. Once the model is trained, it would be implemented in a finite element software.

5.1   Declaration of Competing Interest

The authors declare no conflict of interest.

5.2   CRediT author statement

Albino, P. M.: Methodology, Software, Writing-original draft. **Gomes, H. M.**: Conceptualization, Formal Analysis, Supervision, Writing-review.

6   References

[1] Fontes, A., Shadmehri, F. 2023. Data-driven failure prediction of Fiber-Reinforced Polymer composite materials. Engineering Applications of Artificial Intelligence, V. 120, Art. ID: 105834, doi:10.1016/j.engappai.2023.105834

[2] Hashin, Z., 1980. Failure criteria for unidirectional fiber composites. J. Appl. Mech. 47, 329–334. doi: 10.1115/1.3153664.

[3] Hinton, M. J., Kaddour, A. S., Soden, P.D. 2004. Failure Criteria in Fibre Reinforced Polymer Composites: The Worldwide Failure Exercise (WWFE-1). First Edition. Elsevier Ltd. Hinton, M.J., Kaddour, A.S., Soden, P.D. Editors, Oxford, UK, 1255p. ISBN: 0-08-044475-X.

[4] Ghabhoussi J., Garret Jr., J.H., Wu, X. Knowledge-based modelling of material behavior with neural networks. Journal of Engineering Mechanics, Vol. 117, No. 1, 1991. doi: 10.1061/(ASCE)0733-9399(1991)117:1(132)

[5] Kaw, A. K. mechanics of Composite Materials. 2006. Second Edition. CRC Taylor and Francis, Boca Raton, FL, USA, ISBN 0-8493-1343-0.

[6] Liu, X., Tian, S., Tao, F., Yu, W. 2021. A review of ANN in the constitutive modelling of composite materials. Composites Part B, V.224, Article ID: 109152. doi: 10.1016/j.compositesb.2021.109152.

[7] Lourenço, R., Campos, A. A., Georgieva, P. 2022. The use of ML techniques in material constitutive modelling for metal forming process. Metals, V.12, 427. doi:10.3390/met12030427

[8] Tsai, S., 1965. Strength characteristics of composite materials. NASA CR-224.

[9] Tsai, S., Wu, E., 1971. A general theory of strength for anisotropic materials. Journal of Composite Materials, V.5, pp.58-80. doi: 10.1177/00219983710050.

[10] Wang, C. H., Duong, C. N. 2016. Bonded Joints and Repairs to Composite Airframe Structures. Oxford, UK, Elsevier. ISBN: 978-0-12-417153-4.

MECHANICAL CHARACTERIZATION OF CARBON/EPOXY LAMINATES MANUFACTURED BY FILAMENT WINDING

*Maria Fernanda S. Pimentel[a)], Danilo F. Duarte [(b),] Gabriel B.P. de Knegt [(c),] Artem Andrianov [(d),]

(a) 0000-0002-5951-196X (University of Brasília – Brazil)
(b) 0009-0000-7676-1656 (University of Brasília – Brazil)
(c) 0009-0008-8642-204X (University of Brasília – Brazil)
(d) 0000-0002-3987-6267 (University of Brasília – Brazil)
* Corresponding author: pimentel.maria@aluno.unb.br

CODE: BCCM7-89

Keywords: mechanical properties, filament winding, flat mandrel

Abstract: The objective of the work was to compare the engineering properties of flat laminates manufactured by filament winding with the use of two different methods for specimen preparation. The laminate of the first method was manufactured by the direct filament winding of a carbon tow impregnated with epoxy resin onto a flat mandrel. The laminate of the alternative method was manufactured by winding the same tow onto a cylindrical mandrel. The uncured laminate was removed from the mandrel and then placed onto a flat mold covered with a vacuum bag to finish the curing process. The engineering constants of the specimens cut from both laminates were measured through the use of ASTM methods. The results showed that the engineering constants were higher for the specimens manufactured by the alternative method. These specimens had less porosity and higher fiber volume fraction, which was proven by an optical technique based on an image analysis of micrographs of the test coupons.

INTRODUCTION

Several standard procedures are known to determine the engineering properties of composite laminates manufactured by filament winding [1]. In some of the procedures, flat test specimens are cut from the laminates following the recommended geometry. There may be different methods for how the laminates are manufactured and one of them is dry or wet filament winding onto a flat mandrel [2-7]. In this method (hereafter, the flat mandrel method), the laminates may have a concave shape after the curing process due to residual stresses [8]. Another method is the filament winding over a cylindrical mandrel (hereafter, the cylindrical mandrel method). The specimens are cut directly from the cured composite tube [9] or, first, the laminate is cut out from the mandrel and then placed onto a flat mold before the curing process. In the former method [10], the specimens are not completely flat due to the curvature of the tube, while in the latter method, both the induced fiber tension and the radial stress caused by the curvature of the mandrel are lost.

The objective of the work was to compare the measured engineering properties of the flat specimens manufactured by both methods. To preserve the radial stress in the latter method the laminate was cured in a vacuum bag. The required properties were measured for a single orthotropic lamina. The lamina was considered a part of a composite structure, whose stress-strain behavior was given by a plane stress model (for instance, such as a thin-walled pressure vessel). In plane stress conditions, the lamina can be characterized by four independent engineering constants [11]: longitudinal modulus of elasticity E_1, transverse modulus of elasticity E_2, Major Poisson's ratio v_{12} and shear modulus G_{12}. In the actual version of the paper, the results were presented only for the longitudinal properties.

METHODOLOGY

2.1 Constituents of the composite material

Continuous carbon fiber tows based on polyacrylonitrile Teijin Carbon HTS45 E23 12K (Table 1) and epoxy resins of different grades produced by Huntsman (Table 2) were used for the manufacturing of test specimens.

Table 1. Properties of the carbon fiber tow (as declared by local supplier Texiglass)

Parameter	Minimal	Nominal	Maximal
Mass per unit length ρ_f, tex	720	800	880
Density ρ, g/cm^3	1.77	1.80	1.83
Tensile strength F_{1f}, MPa	4050	4500	4950
Modulus of elasticity E_{1f}, GPa	228	240	252

Table 2. Cure schedules for three types of resin-impregnated tows

Designation	Resin composition	*η at 25°C, mPa·s	Cure schedule
LY1564	Araldite LY1564/XB3473	1000-1200	2h at 120°C + 4h at 180°C
GY260	Araldite GY260/XB3473	5200-6000	
LY5052	Araldite LY5052/Aradur TM5052	600-700 (to 1500 after 56-60 min)	1h at 160°C + 2h at 180°C (tow) and 0.5h at 130°C + 12 h at 160°C (laminate)

*manufacturer's data

2.2 Manufacturing and characterization of the specimens

The resin-impregnated and consolidated test specimens were prepared to determine the impregnation quality of the tow by resins with various viscosities. The apparatus for automated impregnation consisted of two steel circular bars with a diameter of 20 mm arranged at a distance of 320 mm (Fig. 1a). The angular velocity of the apparatus was 12.5 rev/min and the winding pitch was 8 mm. The gap between the doctor blade and the impregnation drum was 0.33 mm. Polymerization was carried out in an electric oven by the cure schedules depending on the resin grade (Table 2).

The standard ASTM D4018-17 was used to measure the modulus of elasticity and the resin content of the resin-impregnated and consolidated carbon fiber tow. The strain was measured by a built-in linear variable differential transformer sensor at a standard head displacement rate of 2 mm/min with the use of the testing machine Instron 8801.
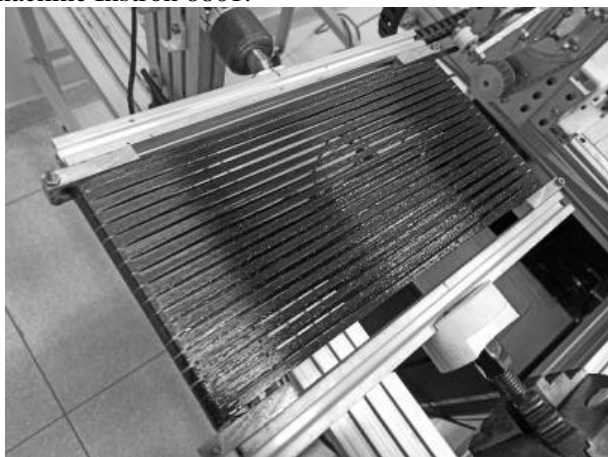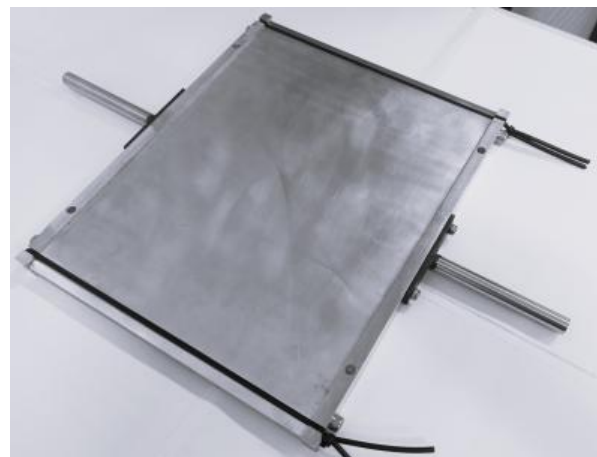
a)   b)

Figure 1. Apparatus for the test specimens of the resin-impregnated and consolidated carbon fiber tow (a) and the mandrel for the filament winding of flat laminates (b)

To manufacture unidirectional flat laminate, the carbon tow was impregnated with GY260 epoxy composition and wound in two successive layers onto an aluminum flat mandrel made in accordance with the standard ISO 01268-5-2001 (Fig. 1b). The angular velocity of the mandrel at winding was 12.5 rev/min, and

the winding pitch was 0.85 mm. The required final thickness of the flat specimen was obtained by adjusting the distance between the former and the outer-mold pieces of the mandrel.

Another unidirectional flat laminate was manufactured by impregnation of the tow with LY1564 composition and winding in five successive layers onto the aluminum flat mandrel. The angular velocity of the mandrel at winding was the same as for the previous laminate, but the winding pitch was 4 mm.

Finally, one more unidirectional laminate was manufactured by winding the carbon tow in six successive layers onto a 151 mm diameter cylindrical mandrel covered with a nylon release fabric in the same way as shown for the laminate $[\pm45°]_n$ in Fig. 2a. After winding the last layer, the laminate was covered with another nylon release fabric to prevent fiber pull-out during cutting and transferring of the uncured laminate from the mandrel to the mold. The epoxy composition used for the specimen was LY5052. The angular velocity of the mandrel at winding was 15.8 rev/min, and the winding pitch was 5 mm. The uncured laminate was cut off from the mandrel with the use of a mini-grinder and placed onto a flat mold (Fig. 2b). Then the laminate was covered with a breather fabric to allow the escape of excess gas and resin during cure. The applied cure schedule was 30 minutes at 130°C and 12 hours at 160°C.

a)   b)
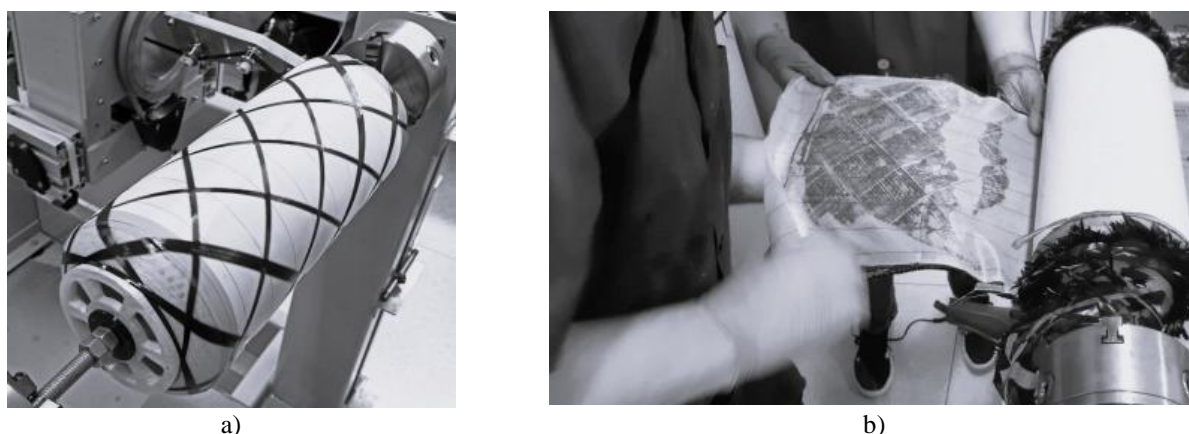
Figure 2. The manufacturing process of the flat specimens $[\pm45°]_n$ by the alternative method: a) filament winding of the carbon tow onto a cylindrical mandrel, b) removing of the laminate from the mandrel.

After the curing process, the test specimens with dimensions 250x15 and 250x15 mm were cut from a flat specimen with the use of a diamond pattern router bit of a 3-mm in diameter composed of AlTiN-coated solid carbide. The tensile properties of the test specimens were determined by ASTM 3039/D3039M-00 at the displacement rate of 2 mm/min.

The fiber volume ratio was determined using an optical technique based on an image analysis of micrographs of transverse cross sections of the coupons. The fiber volume ratio was calculated as a ratio of the area of the fiber cross sections to the total area within the frame of the micrograph. The thresholding tool of the open-source software ImageJ 1.53e was used to determine the area of fiber cross sections on the 8-bit micrograph with a magnification of 400x.

RESULTS AND DISCUSSION

The least average resin content was observed for the tow impregnated with LY1564 epoxy composition at the higher coefficient of variation (Table 3), which could be caused by its relatively low viscosity and extremely high pot life at normal temperature. The tensile chord modulus of the LY1564 tow was the least among the tested tows and was lower than the modulus of elasticity declared by the manufacturer by 13%.

Table 3. Characteristics of the impregnated and consolidated carbon fiber tow

Resin	Resin content (weight percent) V_m	Coefficient of variation	Tensile chord modulus of the fiber E_{1f}	Coefficient of variation
	%	%	GPa	%
LY1564	34.8	18.1	209	9.0
LY5052	43.8	5.8	216	1.7
GY260	52.9	2.7	218	1.6

The measured tensile properties of the test specimens manufactured with the use of the flat mandrel were not high (Table 4). The failure character was LAT, SGM or SGR (ASTM 3039). This behavior was

caused by the low fiber volume fraction and high porosity of the specimens (Fig. 3). In general, the voids and pores do not affect greatly fiber-dominated tensile properties of the polymer composites, however, they may affect the packing geometry of the fibers. The tensile stress-strain curves shown in Fig. 4 revealed several drops in stress due to the failure of individual fibers before the stress reached its ultimate value. Probably, the resin was unable to consolidate some fibers (or clusters of fibers) due to the high porosity, causing the failure of individual fibers. Moreover, the local fiber distortion could occur due to the remarkable size of the voids.

Table 4. Tensile properties of the specimens manufactured with the use of the flat mandrel

Resin	Tensile strength F_{1t} MPa	Coefficient of variation %	Tensile chord modulus E_{1t} GPa	Coefficient of variation %	*Fiber Volume ratio V_f %
GY260	1555	2.6	85.3	0.8	40.0
LY1564	1327	5.6	77.0	2.9	36.9

*The coefficient of variation is above 20%
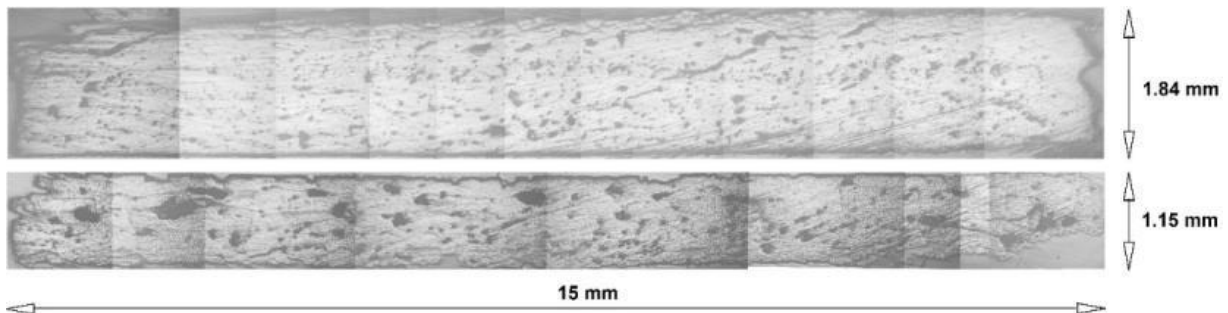
Figure 3. Consolidated micrographs 40x for two flat specimens manufactured by the flat mandrel method and impregnated with GY260 (top) and LY1564 (bottom) compositions.

a)   b)
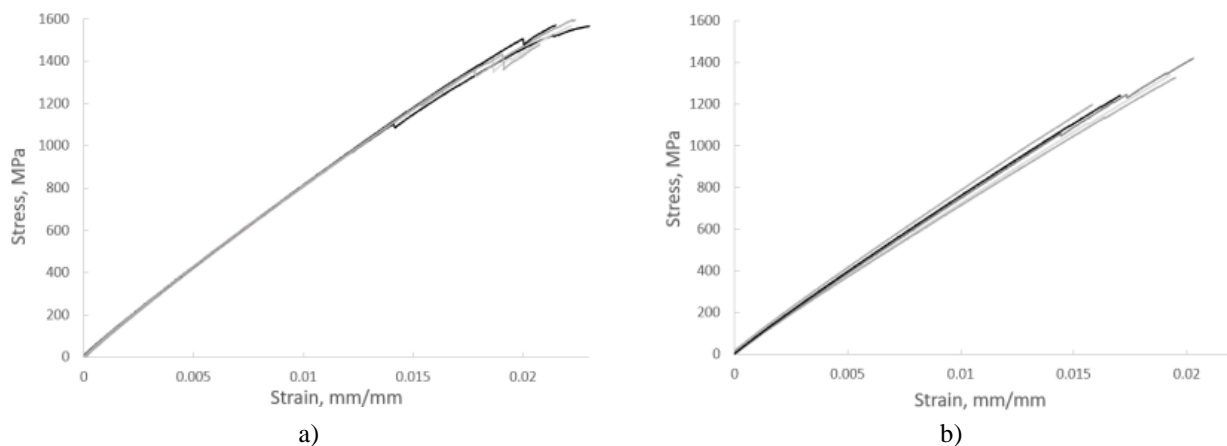
Figure 4. The tensile stress-strain curves of the specimens manufactured by the flat mandrel method and impregnated with GY260 (a) and LY1564 (b) compositions

The specimens manufactured by the flat mandrel method were impregnated with resins of different viscosity, so a possible effect of the resin on the porosity was excluded. However, some pores could be a result of more complex local curing effects. Thus, the specimens manufactured by the alternative method were impregnated with cold cure resin composition LY5052.

The failure character of the specimens manufactured with the use of the cylindrical mandrel was predominantly SGM/SGR (ASTM 3039). They were less porous compared to the specimens manufactured by the flat mandrel method (Fig. 5). Moreover, the size of the voids was significantly lower. As a result, the fiber volume ratio and the tensile properties of these specimens were higher (Table 5). Worth noting that the dispersion of the measured data was also higher for the specimens manufactured by the cylindrical mandrel method. At least three out of eight specimens failed without a drop in stress (Fig. 6).

The lower porosity and higher fiber volume ratio of the specimens were caused by the better conditions for the fiber compaction in the process of filament winding. The tow tension induced radial pressure over the mandrel with non-zero curvature. As a result, the specimens were less porous than those manufactured by

winding the tow onto a flat mandrel, whose curvature was zero. It was difficult to find a spot without voids as shown in Fig. 7a in the specimens fabricated by the flat mandrel method since most of the micrographs were saturated with both resin and voids (Fig. 7b,c). The micrographs of the specimens fabricated by the cylindrical mandrel method had few voids and their size was of the same order of magnitude as a couple of fiber diameters (Fig. 8a,b), while some voids in the specimens fabricated by the flat mandrel method were even larger than the thickness of a ply (Fig. 3). The boundaries between the plies were possible to distinguish only for the specimens manufactured by the cylindrical mandrel method (Fig. 8c).
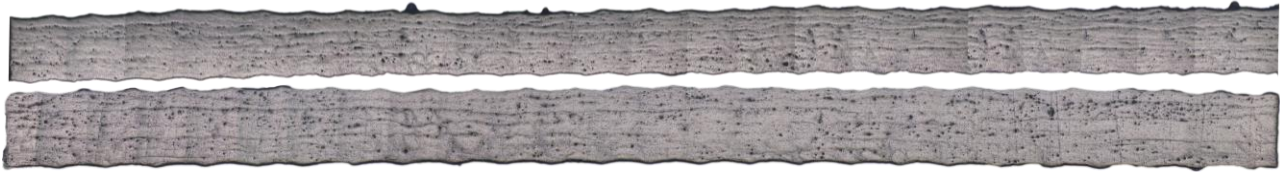
Figure 5. Consolidated micrographs 40x for two flat specimens manufactured by the cylindrical mandrel method and impregnated with LY5052 composition (dimensions of the sections are 0.9x15 mm).

Table 5. Tensile properties of the specimens manufactured with the use of the cylindrical mandrel

Resin	Tensile strength F_{1t} MPa	Coefficient of variation %	Tensile chord modulus E_{1t} GPa	Coefficient of variation %	Fiber Volume ratio V_f %	Coefficient of variation %
LY5052	2233	10.7	106.5	11.8	54.4	3.5

a)   b)
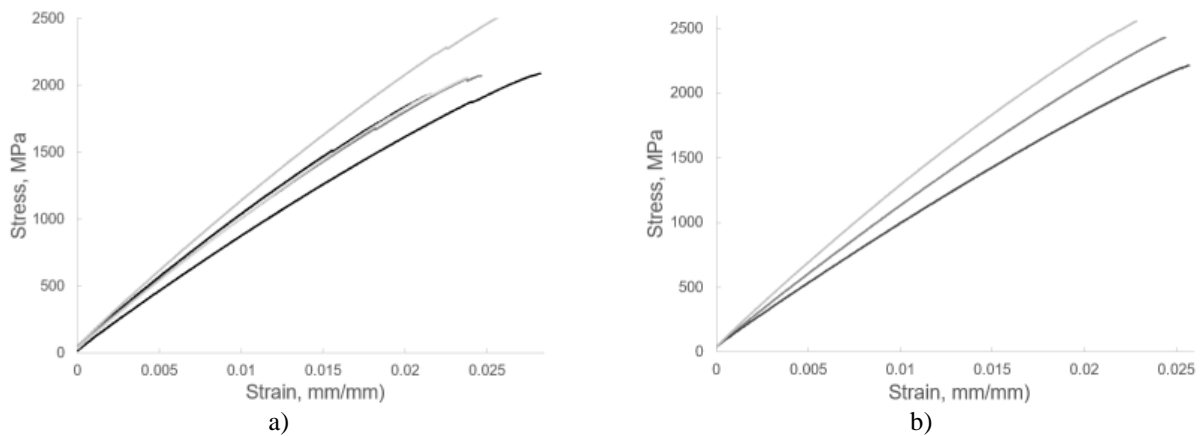
Figure 6. The tensile stress-strain curves of the specimens manufactured by the cylindrical mandrel method and impregnated with LY5052 composition: a) the curves with several drops in stress due to the failure of individual fibers (5 specimens), b) the curves without drops in stress (3 specimens)

a)   b)   c)
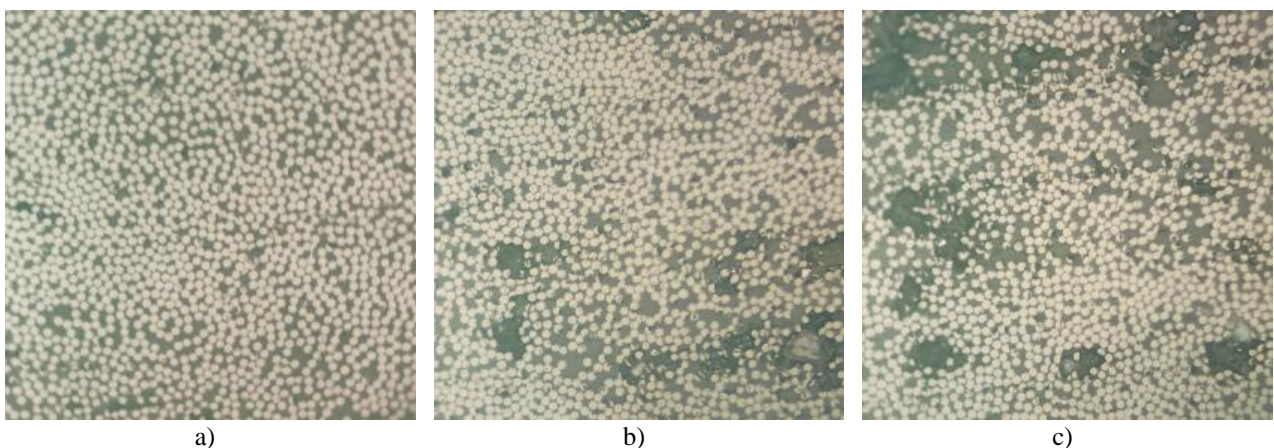
Figure 7. Micrographs x400 of the specimens manufactured by the flat mandrel method and impregnated with LY1564 composition: a) relatively high saturation of fibers, b) high saturation of fibers to the top-left and a high concentration of resin and voids at the bottom-right c) voids at the bottom surrounded by fibers with a high concentration of resin and voids at the top

a)   b)   c)
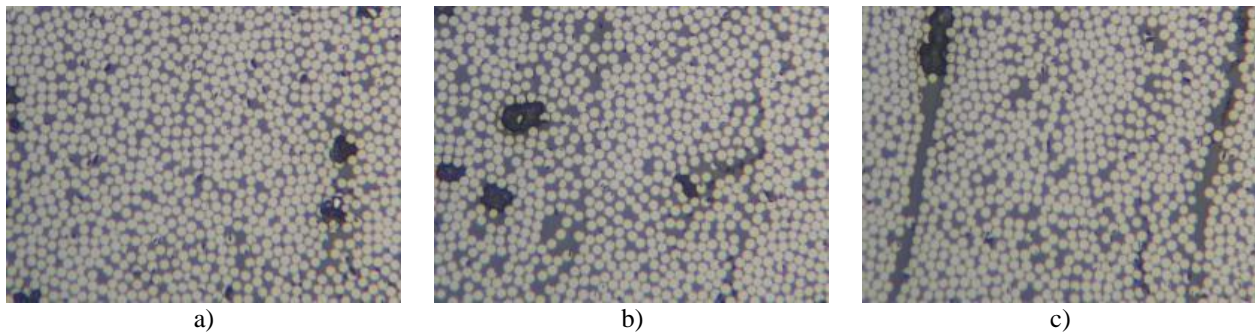
Figure 8. Micrographs x400 of the specimens manufactured by the cylindrical mandrel method and impregnated with LY5052 composition: a) relatively high saturation of fibers with small voids to the right,b) typical pores and relatively high concentration of resin to the right, c) boundaries of a ply.

CONCLUSIONS

The flat mandrel method is not an appropriate method for the manufacturing of test specimens by the wet filament winding technique because of the low fiber compaction. The specimens manufactured by the method are full of voids and the fiber volume ratio is relatively low for the technique despite the normal pressure induced in the mold. As a result, the tensile properties are low. To improve the tensile properties of the specimens, the cylindrical mandrel method must be used with the curing of the laminate in a flat mold covered with a vacuum bag, which contributes to fiber compaction.

Declaration of Competing Interest

The authors declare no conflict of interest.

Acknowledgments

REFERENCES

[1] S.T. Peters. *Composite Filament Winding*, 2011, ASM International. (ISBN 0-61503-722-5).

[2] Isaac M. Daniel, Ori Ishai. *Engineering mechanics of composite materials*, 2nd Edition, 2006. Oxford University Press. (ISBN 978-0-19-515097-1)

[3] C.V. Reddy et al. Mechanical characterization of unidirectional carbon and glass/epoxy reinforced composites for high strength applications. In: M*aterials today: Proceedings*, v. 4, n. 2, p. 3166-3172, 2017. (https://doi.org/10.1016/j.matpr.2017.02.201.).

[4] P. Bere and J.B. Krolczyk. Determination of mechanical properties of carbon/epoxy plates by tensile stress test. In: *E3S Web of Conferences.*, v. 19 p. 03018. 2017. (https://doi.org/10.1051/e3sconf/20171903018.).

[5] C.V. Reddy et al. Mechanical Characterization of Carbon/Epoxy Unidirectional and Bidirectional Composites for Structural Application. *International Journal of Engineering Research & Applications (IJERA)*, v. 8, n. 7, p. 21-24, 2018.

[6] J.H.S.A. Júnior et al. Engineering Properties Of Carbon/Epoxy Filament Wound Unidirectional Composites. In: *European Conference On Composite Materials*, vol.16, p. 1-8, 2014.

[7] E. Kessler et al. Investigation of mechanical properties of filament wound unidirectional basalt fiber reinforced polymers for automotive and pressure vessel application. ICCM 20. *In 20 th International Conference on Composite Materials,* p. 1-10, 2015.

[8] T. K. Hwang et al. Evaluation of fiber material properties in filament-wound composite pressure vessels. *Composites Part A: Applied Science and Manufacturing*, v. 43, n. 9, p. 1467-1475, 2012. (https://doi.org/10.1016/j.compositesa.2012.04.005)

[9] M.H Lapena and G. Marinuccib. Mechanical characterization of basalt and glass fiber epoxy composite tube. *Materials Research*, v. 21, p. e20170324, 2018. (http://dx.doi.org/10.1590/1980-5373-MR-2017-0324)

[10] W. Toh et al. Material characterization of filament-wound composite pipes. *Composite Structures*, v. 206, p. 474-483, 2018.. (https://doi.org/10.1016/j.compstruct.2018.08.049.

[11] Y.K. Okten and C. Kaynak. Mechanical performance of composite flat specimens and pressure vessels produced by carbon/epoxy towpreg dry winding. *Journal of Reinforced Plastics and Composites*, v. 42, n. 11-12, p. 558-576, 2023. (https://doi.org/10.1177/07316844221134029)

[12] S.H. Yoon and J.Y. Kim. Effects of winding process variables on tensile properties of filament wound structures using split disk test. *Journal of the Society of Materials Science*, v. 5, n. 2, p. 104-109, 1999. (http://dx.doi.org/10.2472/jsms.48.6Appendix_104)

[13] J.G.H. Bouwmeester et al. Carbon/dyneema® intralaminar hybrids: New strategy to increase impact resistance or decrease mass of carbon fiber composites. In: *ICAS2008 conference anchorage,* p. 1-6, 2008.

[14] L. Chinchan et al. *Mechanical Testing of Polymeric Composites for Aircraft Applications: Standards, Requirements and Limitations* In: *Advanced materials (S.H. Chang et al).* Volume 152, Springer. (doi 10.1007/978-3-319-03749-3)

[15] M.H. Lapena et al. Mechanical characterization of unidirectional basalt fiber epoxy composite. In: *Proceedings of the 16 th European Conference on Composite Materials ECCM*. . p. 22-26, 2014.

SHORT-BEAM STRENGTH OF GLASS FIBER-EPOXY COMPOSITES WITH HEALING AGENT

Francisco de Assis da Silva Júnior [a]*, Rafaela Jordania Marinho França [b] **, João Felipe Barros Pontes [c], José Daniel Diniz Melo [d], Ana Paula Cysne Barbosa [e], Raimundo Carlos Silverio Freire Júnior [f]

(a) 0009-0007-2018-9911 (Federal University of Rio Grande do Norte – Brazil)
(b) 0000-0001-8233-7608 (Federal University of Rio Grande do Norte – Brazil)
(c) 0009-0009-6267-395X (Federal University of Rio Grande do Norte – Brazil)
(d) 0000-0002-3696-5133 (Federal University of Rio Grande do Norte – Brazil)
(e) 0000-0002-9510-4851 (Federal University of Rio Grande do Norte – Brazil)
(f) 0000-0003-0920-7916 (Federal University of Rio Grande do Norte – Brazil)
*fas-junior@hotmail.com
**rafaelajmfranca@gmail.com

Abstract: Glass-epoxy polymer compounds are one of the most versatile materials, mainly due to their final mechanical properties. However, when subjected to service conditions, loads and environmental factors, microcracks can develop, impacting these properties. A solution proposed to extend its lifespan is the addition of a thermally activated self-healing thermoplastic, such as poly-ethylene-co-methacrylic acid (EMAA). In this work, the influence of the thermoplastic EMAA on the short-beam strength of a glass-fiber epoxy laminate was investigated. The tests followed recommendations of ASTM D2344M - and its equivalent ISO 14130. According to the experimental results, the short-beam strength of specimens with the addition of self-healing agent was virtually unaffected, with a reduction of only 3.6% in a strength of (26.57 ± 0.37) MPa.

1. INTRODUCTION

Composites are a class of materials, originating in the middle of the 20th century, resulting from the joining of two or more distinct materials (matrix and reinforcement), having properties that cannot be met separately [1][2]. Among the types of materials available for use in engineering, polymer composites have gained great prominence in the industry, due to their ability to combine characteristics such as: easy processing, weight reduction and good mechanical properties, which allows a wide variety of applications [3].

Glass fiber-epoxy composites, among these, are one of the most versatile materials, mainly due to their final mechanical properties. However, when subjected to service conditions, loads and environmental factors, they can develop microcracks, impacting their mechanical performance and reducing their life span [4].

Due to their varied microstructure, chemical compositions and manufacturing methods, materials are always susceptible to deterioration, whether through impact, creep, fatigue, corrosion or aging, causing a reduction in both useful life and reliability [5]. Composites, under high levels of deformation, have the ability to absorb part of the energy and not rupture instantly. However, due to this absorbed energy they suffer damage, which even if imperceptible to the naked eye (microcracks and internal delaminations), subsequently compromises their life in service [6].

Interlaminar shear properties of composites are highly relevant knowledge for improvement and future applications. Delamination cracks result in relatively low interlaminar properties for this type of material, even

though they have excellent in-plane mechanical properties. Laminates that present these cracks between their layers are susceptible to delamination failures when subjected to out-of-plane loads, leading to a high reduction in their mechanical properties and early structural failure [7].

It is common for these microcracks to be difficult to detect, so new techniques for healing them are of great interest for recovering the material's properties. A recent solution that has been studied to extend the useful life of these materials is the addition of a thermally activated self-healing thermoplastic in their composition, such as the additive poly-ethylene-co-methacrylic acid (EMAA), a copolymer that presents good adhesive properties and high resilience [8]. With the use of this material, when damaged, the composite can recover its properties, resulting in a reduction in the need for maintenance and an increase in usage time [4][9]. This is possible because the healing agent, once subjected to external heating, it reduces its viscosity and gains mobility, which is capable of filling microcracks [10][11].

In this context, it is necessary to disseminate knowledge that is still little explored about the action of the healing agent and reduce production costs, with studies of the influence on the mechanical behavior of the laminate with the presence of this self-healing together with the thermoset, as well as its feasibility of application based on the properties obtained. Therefore, it is important to evaluate the replacement of glass fiber-epoxy composite materials with conventional thermoset matrix by the composite added with EMAA self-healing, especially in conditions in which it presents superior performance.

In the present work, the influence of the addition of EMAA on the strength of a glass fiber-epoxy composite, was analyzed. The tests followed the standards of ASTM D2344M - Standard short beam test method for strength of polymer matrix composite materials and their laminates, as well as ISO 14130.

2. METHODOLOGY

2.1. Pre-impregnated (Prepreg) glass-epoxy

The specimens used in this research were made with prepreg Hexply® M9.6F/32%/UD1600+V50/G+F, produced by Hexcel. The prepreg input has a mass fraction of 32 wt.% of epoxy resin matrix reinforced with UD1600+V50 glass fiber (E-glass), with a density of approximately 2.56 g/cm³ and a thickness per prepreg sheet of 1 mm [12].

Various curing cycles applicable to this material are specified by the manufacturer, as detailed in Table 1. Compaction pressures vary from 0.5 to 5 bar, while heating rates range from 0.5 to 5ºC/min. The product's technical data sheet records a matrix with a glass transition temperature of 120 ºC, with a density of 1.20 g/cm³ [12].

Table 1. Curing cycles applicable to the Hexply M9.6F.

Temperature (ºC)	Time (Min)
80	510
100	100
120	40

Source: [12].

In this study, the last method was adopted for producing the specimens, which consists of a uniaxial pressing temperature of 120 ºC for a period of 40 minutes. According to the technical data sheet provided by the manufacturer, after the 30-minute curing cycle at a temperature of 140°C and pressure of 5 bar, the material has the following mechanical properties listed in Table 2 [12].

Table 2. Mechanical properties of glass-epoxy pre-preg, cured at 140ºC for 30 minutes.

Property	Value (MPa)	Methodology

Tensile strength	1160	EN ISO527
Bending strength	1370	EN 14125
Interlaminar Strength (ILSS)	55	EN 2377
Compressive strength	-	-

Source: [12].

2.2. Poly (Ethylene Co-methacrylic acid) – EMMA

In the interfacial region of the samples subjected to healing, the thermoplastic agent poly(ethylene-co-methacrylic acid) (EMAA) purchased from Sigma-Aldrich was used. This material contains approximately 15% methacrylic acid and 85% polyethylene. To optimize the dispersion of this component in the matrix, cryogenic grinding was applied to achieve a particle size distribution in the range of 125-250 µm. The additive was supplied in the form of pellets and subjected to a cryogenic grinding phase followed by sieving, in order to adjust its particle size. Subsequently, the determination of the mass of the polymer to be incorporated into the composite interfaces M_{EMAA} was carried out using Equation (1).

$$M_{EMAA}= M_t \text{ x } \% \text{ matrix} \times \% \text{ additive} \tag{1}$$

Where M_t denotes the total mass of the composite, multiplied by the mass fraction of the matrix and the percentage of the desired additive for this specific application, that is, 32%. The experimental specimens were made by adding 10% mass with respect to the final weight of the thermoset matrix contained in the prepreg. To carry out this procedure, each sheet was individually weighed and then the total mass of the composite was calculated.

Once this value was obtained, this quantity was evenly distributed between the three interfaces present in the layering of the test specimen sheets. Substituting the known values in Equation (1), it will take the form shown in Equation (2).

$$M_{EMAA}= 0{,}032 \text{ x } M_t \tag{2}$$

Table 3 presents essential characteristics and properties of this polymer, including its melting point and glass transition, as provided by the manufacturer.

Table 3. Property of EMAA.

Properties	Value
Flow index	60 g/10 min
Composition	15% methacrylic acid
Toughness	46 Shore D (ASTM D2240)
Fusion point	76ºC
Density	0.941 g/mL (at 25ºC)

Source: [13].

2.3. Sample preparation

The test specimens were manufactured with uniaxial hot pressing for 40 minutes at 120 ºC using a 30 cm square carbon steel detachable mold, as shown in Figure 1. After the set time, the mold was removed from the press and opened to remove the manufactured material. The prepreg laminate used is unidirectional and was placed into the mold with the configuration of 0°/90°/90°/0°, forming a stack of 4 layers of glass-epoxy pre-impregnated, resulting in a thickness of approximately 5mm.

Figure 1. Mold: base with busbars and metal sheet for compression used to make 30 x 30 cm plates.

In the composites containing the healing agent (10 wt.%), calculated from the total mass of resin present in the laminate with the 4 prepreg sheets, 27 g of thermoplastic were added dispersed in each interface of the laminate, i.e., 9 g for each of the 3 interfaces present; and so, the thermoplastic was added alternately to the prepreg laminae.

2.4. Interlaminar Strength Test - ILSS

The test used to evaluate the strength of the material was a short beam test, in accordance with ASTM D2344M - Standard Test Method for short-Beam Strength of Polymer Matrix Composite Materials and Their Laminates and its equivalent ISO 14130 - Determination of Apparent Interlaminar Strength by Short- Beam Method. This test determines the strength of a composite material laminated with three short distance bending points [14][15].

To carry out the test, the universal testing machine model AG-I from Shimadzu, with a capacity of 250 KN (Figure 2 (a)), was used. In order to adapt the machine to the test, the apparatus represented in Figure 2 (b) was used, consisting of a base with two lower support rollers, a roller to be placed on the sample and a cleaver to compress the upper roller.

(a)   (b)

Figure 2. (a) Shimatzu AG-I machine and (b) Apparatus assembled with sample.

In this test, the upper roller has a diameter of 6 mm and the two that support the sample are approximately 3 mm. The cleaver will exert compression effort on the larger roll up to the maximum point of strength, when the test will be completed [14].

The base is equipped with screw-on guides that allow to vary the distance between the sample support points. This is because, according to standards, the size of the samples and supports were well defined. The dimensions of the samples were defined based on a thickness of 5 mm, following the aforementioned standards:

- The length is six times the value of the thickness, therefore, 30 mm;
- The width is twice as large as the thickness, that is, 10 mm;
- As for the supports, they must be 20 mm apart.

Once the maximum shear force was defined for the samples, the short-beam strength was calculated using Equation (3).

$$F^{sbs} = 0.75 \times \frac{P_m}{b \times h} \tag{3}$$

Where F^{sbs} is the short-beam strength, P_m is maximum load observed during the test, b is the width and h is the thickness of the sample.

3. RESULTS AND DISCUSSION

After carrying out ILSS tests on glass-epoxy prepreg samples with and without EMAA, the effect of the self-healing agent was analyzed in terms of its strength, Figure 3(a), (b). In Figure 3(a), there is the stress-displacement graph, with the result of the shear test behavior of unmodified samples, without the presence of EMAA.
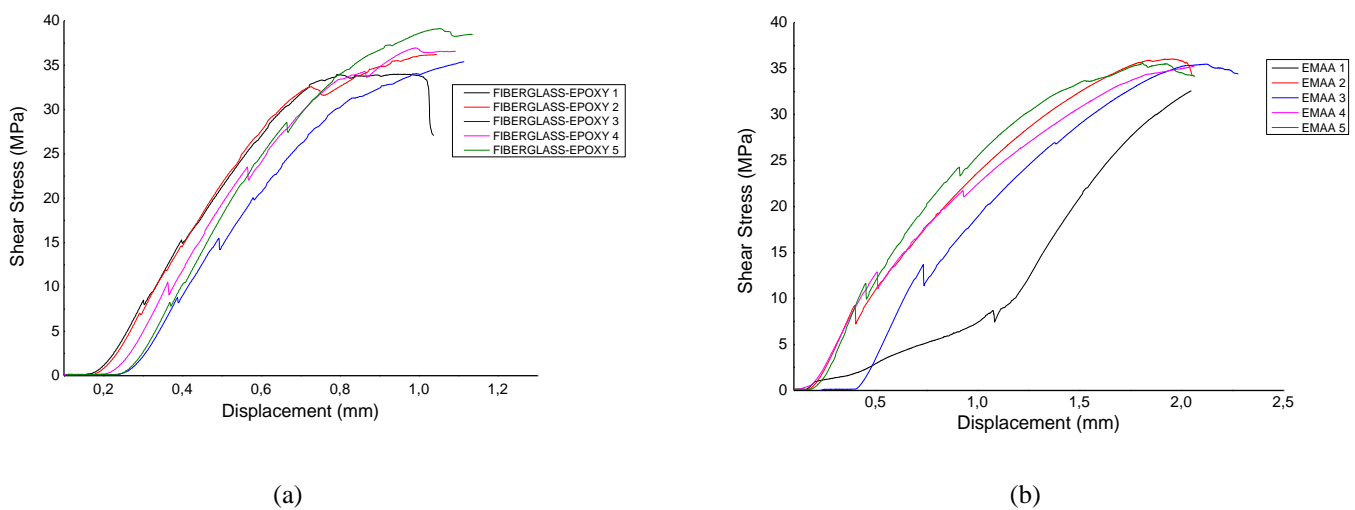
Figure 3. ILSS for glass-epoxy composite samples: (a) Without EMAA; (b) With EMAA.

Considering the stress behavior as a function of deformation of the glass fiber composite, which is predominantly brittle, while the epoxy matrix phase is relatively ductile, the graph can be subdivided mainly into two stages, in accordance with [2]: In the first stage, both the fibers and the matrix undergo elastic deformation; Generally, this part of the curve is linear. Typically, for a composite of this type, the matrix begins to flow and deform plastically, while the fibers continue to elongate elastically, since the tensile strength limit of the fibers is significantly greater than the yield strength of the matrix. This process constitutes the second stage (approximately 0.6 mm of displacement); generally, almost linear, but with a reduced slope compared to the first stage. Furthermore, when moving from the first to the second stage, the proportion of the applied load supported by the fibers increases. Through data processing, a short-beam strength of approximately (27.57 ± 1.40) MPa was obtained.

According to the standard [14], used in this test, different failure mode results can be obtained in ILSS tests: interlaminar shear, flexion, inelastic deformation. In the study, after carrying out the ILSS tests, results suggest, based on the characteristics of the fracture, an interlaminar shear failure mode, similar to the results present in the literature. [16], state that by employing a test specimen with a short-beam geometry, this test provides maximum interfacial adhesion strength when subjected to flexural loading at three points. Failure in this case occurs in the midplane parallel to the fibers in a shear mode, and the fracture load is interpreted as a measure of the interlaminar strength of the composite. Figure 4 illustrates the results of the ILSS test for samples with the presence of the EMAA self-healing agent.

In figure 3 (b), with the addition of EMAA, a curve with behavior similar to that obtained without the presence of self-healing is observed, with a value of (26.57 ± 0.37) MPa, for strength. From the values obtained for the laminate with the presence of self-healing agent, the short-beam strength was virtually unaffected, with a reduction of approximately 3.6% for this property.

Works such as [8], in the study on unmodified epoxy and with the addition of EMAA self-healing, for unmodified epoxy, a storage modulus with a higher value compared to the material modified with

thermoplastic was obtained. This result is already expected, since the modulus of the thermoplastic material is lower than the modulus of the epoxy resin. Thus, the addition of this thermoplastic reduced the elastic modulus and this decrease in modulus may be related to changes in the formation of the epoxy network close to the particles during curing, suggesting the formation of a chemically interconnected interphase between the epoxy and EMAA, as explained in the article [8].

In this context, there is also a study by [17], with the investigation of the use of EMAA for healings in epoxy resins, in which the addition of self-healing particles to the resin caused a drop in the modulus. This observed reduction is in accordance with existing literature on thermoplastic or rubber-hardened epoxy resins, based on [18], in which the use of thermoplastic polymers in rigid epoxy resins can result in an increase in fracture resistance and a decrease in the modulus of elasticity of the material.

In this way, results suggest that the presence of EMAA self-healing in the studied laminate (glass-epoxy), influences the mechanical behavior of the material, due to the addition of this thermoplastic which has a lower modulus of elasticity compared to the thermoset matrix, which reflected in the slight drop in interlaminar shear stress.

However, given the increasing applicability of thermosetting matrices in composites (such as epoxy resin), and according to [17], the highly cross-linked structure of these materials makes them fragile and susceptible to the formation of microcracks that are difficult to detect. Thus, it becomes valid to analyze the feasibility of using self-healing with its advantages in different applications, with virtually no loss in strength. Accordingly, in recent years there have been proposals for the development of epoxy resins with self-healing capacity, aiming to restore the strength of damaged components. This initiative seeks to make these materials safer to use, increase their reliability and facilitate their maintenance [17].

4. CONCLUSIONS

According to the experimental results, a drop in the stiffness of the laminate was evidenced with the addition of EMAA. However, short-beam strength was virtually unaffected, with a reduction of approximately 3.6% in its strength. Therefore, this change suggests being a property of interest for analysis, depending on the specific application and project requirements, considering the benefits presented by the aforementioned material.

5. REFERENCES

[1] I. M Daniel; O. Ishai. Engineering mechanics of composite materials. 2 ed. New York. Oxford University Press, 2006. Development, 9(8). DOI: 10.33448/rsd-v9i8.5640

[2] W. D. Callister. Materials science and engineering: an introduction. Rio de Janeiro: LTC, 2016.

[3] M. Biron. Thermoset and composites: technical information for plastics users. Oxford. Elsevier Advanced Technology, 2004.

[4] A. P. C Barbosa et al. Effects of accelerated aging on carbon fiber/epoxy composites. 2017. Compos Part B Eng 110:298–306

[5] P.S.C. P da Silva, Mechanical behavior and fracture of metallic components and structures, 1999.

[6] C. Fortes, "Fracture Mechanics," Mater. Construction. and Principles of Science and Eng. Mater., no. 51, pp. 241–280, 2010

[7]. S. Wang et al. Interlaminar Shear Properties of Z-Pinned Carbon Fiber Reinforced Aluminum Matrix Composites by Short-Beam Shear Test. Materials (2018) 11(10) 1874. Doi:10.3390/ma11101874.

[8] B.L Silva et al. The role of poly (ethylene-co-methacrylic acid) (EMAA) on curing kinetics and thermomechanical properties of epoxy. Polymer Bulletin (2022) 79(5) 3291-3307. doi: 10.1007/s00289-021-03650-9

[9] J.P. Pascault, RJJ Williams. Epoxy Polymers: New Materials and Innovations, 1st ed. WileyVCH, Weinheim, (2010).

[10] T. W. Loh et al. Ultra-resistant and healingable carbon/epoxy composite insitu with EMAA. Compos Part A ApplSciManufact 143:106206, 2021.

[11] T. W Loh et al. Intralaminar hardened carbon/epoxy composites exhibiting self-healing capabilities. International Conference on Composite Materials, Non-Series, 1214–1222, 2020.

[12] HEXPLY M9.6F. C. Modified et al., "Product Data Sheet: N-Lok Product Data Sheet: N-Lok," vol. 1450, no. 07315745, pp. 5–7, 2008.

[13] Sigma Aldrich. Product Catalog: Poly(ethylene-co-methacrylic acid) (EMAA). Available at: https://www.sigmaaldrich.com/. Accessed on June 20, 2023.

[14] ASTM D2344M-22, Standard Test Method for Short-Beam Strength of Polymer Matrix Composite Materials and Their Laminates. West Conshohocken, July 15th. 2022. DOI: 10.1520. International Organization for Standardization.

[15] ISO 14130 - Determination of Apparent Interlaminar Shear Strength by Short-Beam Method. Ed. 1. Dec. 1997.

[16] G. M. Candido et al. Effects of hydrothermal conditioning on the interlaminar shear strength of carbon/epoxy laminates. Brazilian Congress of Engineering and Materials Science. Annals. São Paulo: 2000.

[17] S. Meure et al. Polyethylene-co-methacrylic acid healing agents for mendable epoxy resins. Crown Copyright 2009 Published by Elsevier Ltd. on behalf of Acta Materialia Inc..doi:10.1016/j.actamat.2009.05.032.

[18] A. C. Garg; YW Mai. Compos Sci Technol 1988 - 31:179.

12 FRP in concrete, steel and composite steel/concrete structures

Organized and edited by

Sandra Maria da Luz
&
Carla Tatiana Mota Anflor

MACHINE LEARNING WITH DATA AUGMENTATION FOR CONCRETE CONSTITUTIVE MODELLING

Paola M. Albino[a], Herbert M. Gomes [b], *

(a) ⓘ 0009-0007-2815-9565 (Universidade Federal do Rio Grande do Sul – Brazil)
(b) ⓘ 0000-0001-5635-1852 (Universidade Federal do Rio Grande do Sul – Brazil)
* Corresponding author: herbert@mecanica.ufrgs.br

CODE: BCCM7-6

Abstract: Reinforced concrete structures are still a very common composite material in Civil Engineering due to their low cost and high performance in buildings and structures. The behavior of such material is highly nonlinear even in the early stages of loading. Failure modes such as cracking, crushing, splitting, etc. can lead the material to ultimate strength. Plasticity and viscoelasticity are also responsible for the nonlinear behavior. A set of experimental data, reported as a database by Kupfer et al. (1969), is used for such behavior in plane stress, for various stress ratios and concrete strengths. So, like the paper of Ghabhoussi et al (1991), a Machine Learning (ML) approach to model the nonlinear behavior (stress-strain curves) of concrete is proposed in this paper. Techniques of data augmentation are used to expand the original database and different ML models. The results show that ML can predict and represent very well the nonlinear behavior by comparing the experimental stress-strain curves with those obtained by ML. Furthermore, the ML was able to predict the Failure Surface (for any failure mode) for the concrete.

1   Introduction

Artificial neural networks (ANNs), commonly referred to as neural networks, are computational models that are modeled after the architecture and operation of biological neural networks found in the human brain. They are made up of layers of networked nodes, also referred to as neurons or units. Every neuron in the network takes incoming signals, processes them using an activation function, and then outputs a signal that could be transmitted to other neurons (Ghabhoussi et al., 1999). The field of material modeling has seen a revolution recently due to breakthroughs in neural networks, particularly in creative learning algorithms. Constitutive modeling in information science is learning about a material and expressing it with an emphasis on its intricate behavior. Neural networks' capacity for self-organization and learning can be used to create behavioral models of materials if there is enough information on the materials' responses to outside stimuli.

This paper improves, with the data augmentation technique, an ANN model (Ghabhoussi et al, 1991) to predict stress-strain curves for concrete in a biaxial stress state, based on experimental data from (Kupfer et al, 1969).

2   Theoretical Basis

Artificial Neural Networks (ANN) are computer algorithms based on the concept of machine learning. The basic structure behind ANNs is similar to that of a biological neuron, i.e.: body, transmission lines, axon, and dendrite. Feedforward neural networks are a fundamental type of artificial neural network where connections between nodes do not form cycles. Information flows in one direction, from input nodes through

hidden layers (if present) to output nodes. These networks are commonly used for supervised learning tasks such as classification and regression. The network architecture consists of an input layer, one or more hidden layers, and an output layer. Each layer contains interconnected nodes (neurons), and connections between nodes are associated with weights that are learned during training. Feedforward neural networks utilize activation functions to introduce nonlinearity into the network, enabling them to learn complex patterns and relationships in the data. Training typically involves adjusting the weights of connections using optimization algorithms such as backpropagation to minimize the difference between predicted and actual outputs (Haykin, 1998). Feedforward neural networks have been successfully applied in various domains, including image recognition and natural language processing, and are used in this paper. In the training phase, the output signal is sent back to the input in an interactive process to reduce the error. Truncation takes place using criteria such as the number of interactions or the final admissible error. Figure 1 illustrates the operation of an artificial neural network, ANN, with several 4 input neurons, 2 hidden layers with 5 and 3 neurons, and an output layer with 2 neurons (with architecture [4 5 3 2]). Each neuron unit operates as $y = f(\mathbf{W}^{\mathrm{T}}\mathbf{X} + b)$, where $\mathbf{W}^{\mathrm{T}}$ is the vector of weights b the threshold for trigger (to be determined), $\mathbf{X}$ the vector of input signals, and f a nonlinear activation function. The training is performed by minimization (using a learning rate η) of an Error function (generally the MSE, Mean Squared Error) and using the backpropagation algorithm.
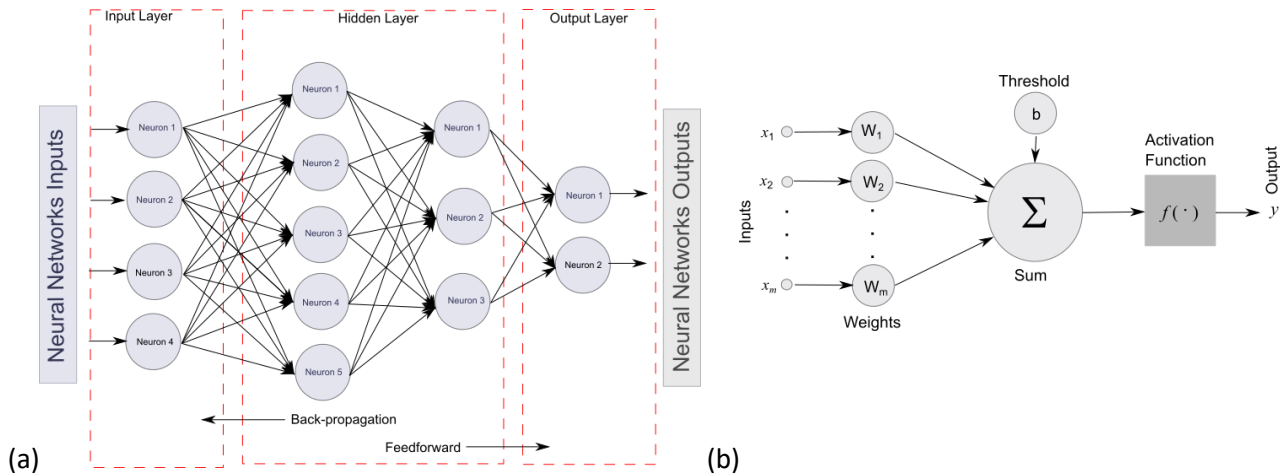
Fig. 1 (a)ANN representation with a [4 5 3 2] architecture. (b) Neuron activity function representation.

3   Methodology

All the data was digitized from the Kupfer et al (1969) curves till failure composed by $\sigma_1/f_c \times \varepsilon_1$, $\sigma_1/f_c \times \varepsilon_2, \sigma_2/f_c \times \varepsilon_1$ and $\sigma_2/f_c \times \varepsilon_2$ where σ_1 and σ_2 are the principal stresses, ε_1 and ε_2 are the principal strains and f_c is the compressive ultimate strength of concrete, all obtained in a series of experimental tests. The architecture used by Ghabhoussi et al, 1991 is depicted in Figure 2. Thus, the input parameters are the principal stresses, the principal strains of a certain point the stress-strain curve, and the incremental principal stresses to obtain the next point in the graph. The output was the incremental principal strains, $\Delta\boldsymbol{\epsilon}^{k+1} = \mathcal{N}_1(\boldsymbol{\sigma}^k, \boldsymbol{\epsilon}^k, \Delta\boldsymbol{\sigma}^k)$, where $\boldsymbol{\sigma}$ and $\boldsymbol{\epsilon}$ are the principal stress and strain, respectively, k is an incremental step and $\mathcal{N}$ represents the ANN. For a Finite Element Method implementation, the incremental stresses become de output, and the incremental strains, the inputs, $\Delta\boldsymbol{\sigma}^{k+1} = \mathcal{N}_2(\boldsymbol{\sigma}^k, \boldsymbol{\epsilon}^k, \Delta\boldsymbol{\epsilon}^k)$.
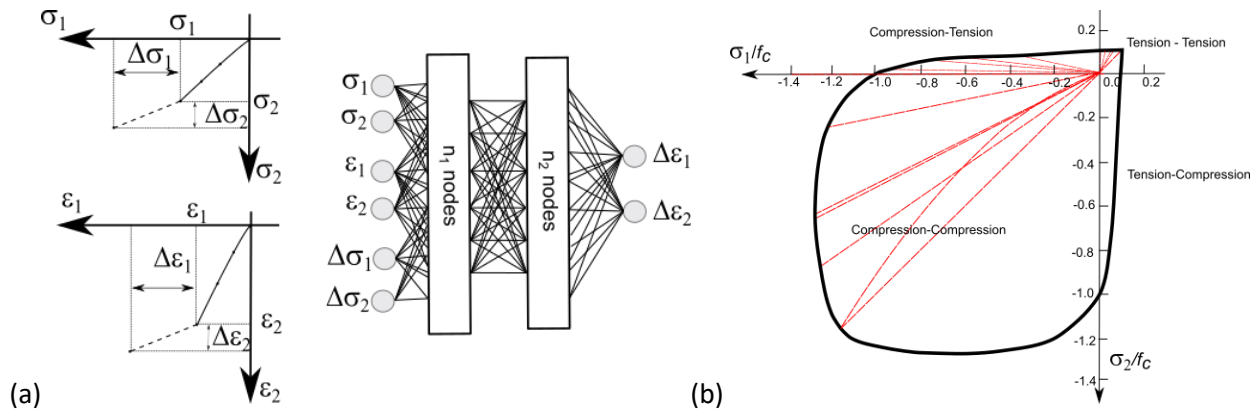
Fig. 2 (a) Architecture used by Ghabhoussi et al, 1991 for the biaxial stress-strain curve constitutive modeling. (b) Experimental stress paths (Kupfer et al., 1991) that compose the dataset for training and validation curves.

Values for the principal stress ratio to define the stress-strain paths used for training and validating (Fig. 2b) are: σ_1/σ_2 ={-1/-1;-1/-0.52;-1/0.0; -1/-0.2;-1/-0.5; -1/-0.7;-1/0.204;-1/0.103;-1/0.052;-1/0.02;-1/0.04;-1/0.10; 1/1; 0.55/1; 0/1; 0.25/1; 0.5/1} and also $\{\sigma_2 = 0.343\sigma_1 - 0.571\sigma_1^2$ and $\sigma_2 = -0.221\sigma_1 - 0.214\sigma_1^2$. In the end, there were 26 graphs, each with two principal stress versus principal strain, totaling 52 stress × strain experimental graphs.

3.1 Data Augmentation

For the data augmentation, it was chosen to interpolate the points from the digitized/discretized curves using spline curves that, in the end, fitted very well with all the experimental data. Afterward, the fitted spline curves were resampled with a higher number of points, 10 times more data than the original experimental data. Typical digitized experimental data (symbols) and the augmented data (dashed line) are presented in Fig.3.
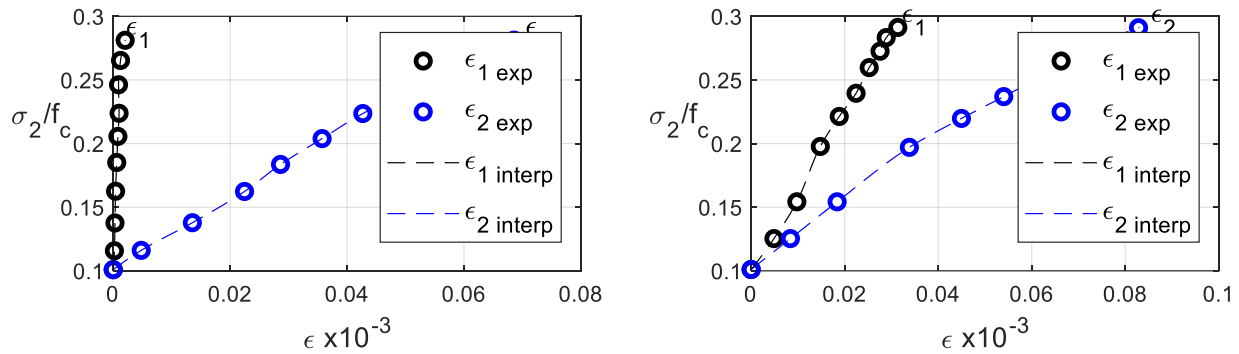
Fig. 3 Typical digitized original experimental data(symbols) and the augmented data by spline interpolation (dashed lines).

4 Numerical results

The best architecture for the ANN used was [12 15 4]. All the dataset was randomly separated in in training, validating and testing sets with a proportion of 70%, 15%, and 15%. The Levenberg Marquardt backpropagation algorithm was used for the task. Figure 4 shows the MSE error and a comparison of the 2 outputs $\Delta\varepsilon_1, \Delta\varepsilon_{12}$ for the testing set (unseen data by the ANN), showing the ANN was correctly trained, presenting a good generalization without overfitting.
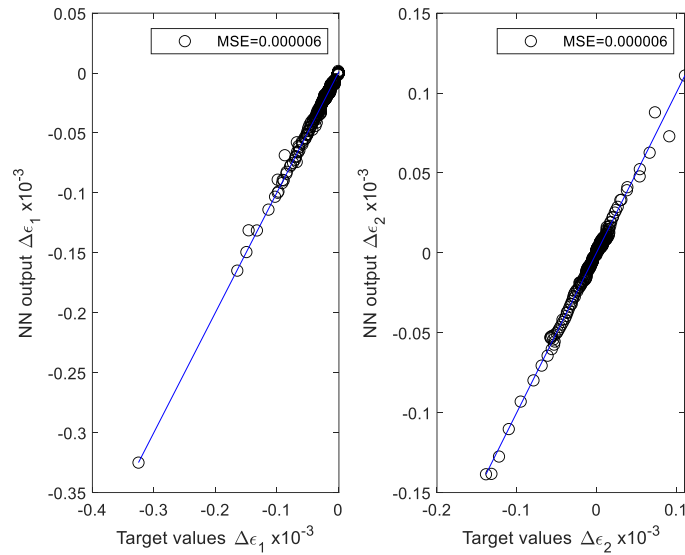
Fig. 4 Typical MSE error for the two outputs $\Delta\varepsilon_1$ and $\Delta\varepsilon_2$ for the trained ANN in the validation set.

Figure 5 shows some comparative curves corresponding to the validation data set for the stress-strain curves with a good correlation with the experimental data from Kupfer et al. (1969). Figure 6 shows that using the same ANN, one can notice that the failure prediction is quite good (cyan continuous line) when compared to the previous original experimental data (black dots) for the surface failure of plain concrete.
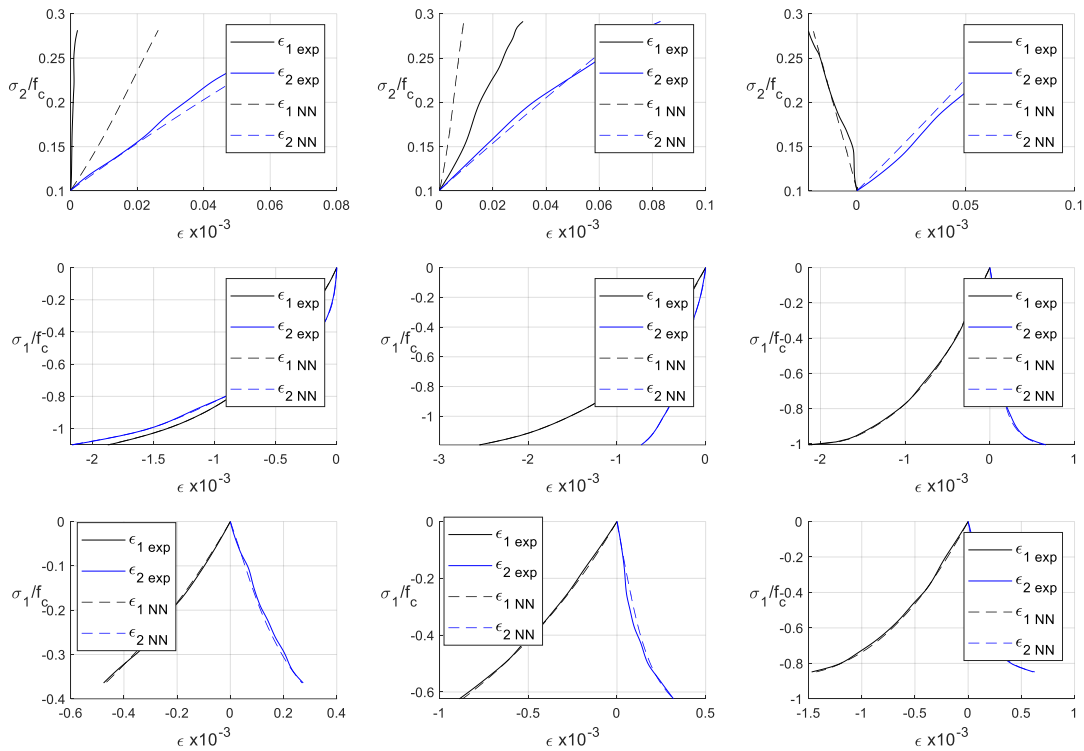
Fig. 5 Typical results after training for $\sigma/f_c \times \varepsilon$ curves compared to the experimental data (dashed line are the ANN prediction).
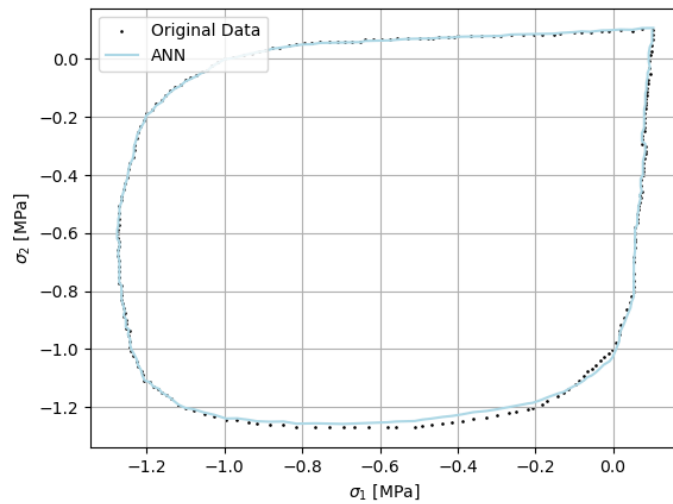
Fig. 6 Results after training for $\sigma_1 \times \sigma_2$ curve compared to the experimental data(dots) and ANN prediction (cyan continuous line).

Combined with this surface, the algorithm can also determine how far away a particular point is from failure based on where it is within the surface, whether it's far away or not. Figure 7 shows the module of a distance vector based on the nearest point (perpendicular) to the surface for both (a)Experimental Data and (b)ANN. One can notice that the values are slightly different, presenting a difference of up to 2%.

5 Final Remarks and Conclusions

The presented paper implemented feedforward-backpropagation ANNs to predict stress-strain curves for the composite material concrete. The dataset was based on experiments from Kupfer et al. (1969) and the data augmentation technique was used to improve the training. The MSE error was very low in the validation dataset, meaning a good generalization for the trained ANN architecture and confirmed by the superposition of the predicted-measured stress-strain curves in several scenarios of the plane stress. The proposed methodology is ready for practical implementation in a Finite Element software as a material nonlinearity module in future studies.
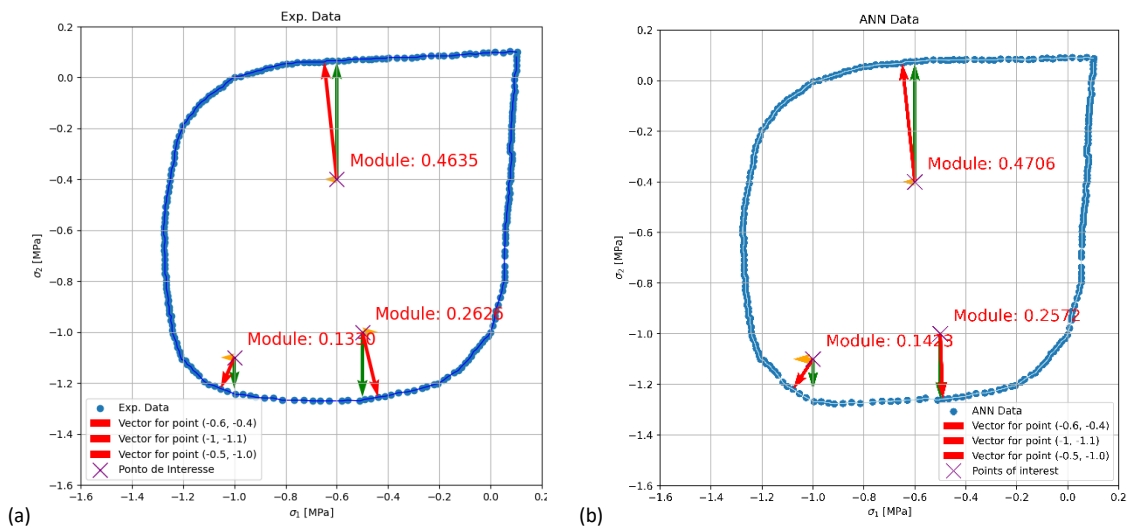
Fig. 7 Results after training for $\sigma_1 \times \sigma_2$ curve compared to the (a) Experimental data (blue dots) and (b) the trained ANN prediction (cyan dots).

5.1 Declaration of Competing Interest

The authors declare no conflict of interest.

5.2 CRediT author statement

Paola M. Albino: Methodology, Software, Writing-original draft. **H. M. Gomes**: Conceptualization, Formal Analysis, Supervision, Writing-review.

References

[1] J. Ghabhoussi, J.H. Garret Jr., X. Wu. Knowledge-based modelling of material behaviour with neural networks. Journal of Engineering Mechanics, Vol. 117, No. 1, January, 1991. DOI: 10.1061/(ASCE)0733-9399(1991)117:1(132)

[2] J. Ghabhoussi, X. Wu, G. Kaklauskas. Neural Network material modelling. Statyba, 5:4, 250-257, 1999. DOI: 10.1080/13921525.1999.10531472.

[3] H. Kupfer, H. K. Hilsdorf, H. Rusch. Behavior of concrete under biaxial stresses. J. Am. Concr. Inst., 66(8), 656-666. 1969.

[4] Haykin, S. 1998. Neural Networks: A Comprehensive Foundation, 2nd. Edition, 842p.

APPLICATION OF ARTIFICIAL NEURAL NETWORK IN PREDICTING THE MECHANICAL PERFORMANCE OF REINFORCED CONCRETE COLUMNS CONFINED WITH CFRP

Matheus de S. Santos[(a)*], Francisco E. Júnior [(b)]

(a) ⓘ 0000-0001-5882-2080 (University of Brasília – Brazil)
(b) ⓘ 0000-0002-9353-1083 (University of Brasília – Brazil)
* Corresponding author: matheusdesantanaeng19@gmail.com

CODE: BCCM7-46

Abstract: The investigation of the flexural-compression resistance capacity of columns reinforced with composite materials has been the subject of study by several researchers. Among these materials, Carbon Fiber Reinforced Polymers (CFRP) stand out for their excellent resistance and rigidity properties. From a technical aspect, the prediction of maximum force and respective displacement in structural designs plays a crucial role. Therefore, an artificial neural network (ANN) machine learning model was used to determine the values of force, lateral displacement, and influence of reinforcement in reinforced concrete columns confined with CFRP. The neural network used a set of 176 numerical data from columns with a square cross section, developing a model with 5 input variables, 4 output variables and 2 hidden layers composed of 26 and 23 neurons, respectively. In terms of results, the model showed promising performance with R² values of 0.91 and overall mean squared error (MSE) of 0.025 for the normalized data. The results confirmed the model's ability to reliably reproduce the mechanical performance of reinforced columns.

1. INTRODUCTION

External restraint with CFRP has been the subject of increasing investigation as an effective tactic for reinforcing reinforced concrete elements [1-3]. Among the different types of structural elements, columns can be reinforced in axial compression and flexion using the partial or total containment method with externally adhered CFRP wraps [4-7]. The containment provided by the composite induces a multiaxial variation in the concrete tensions, leading to an increase in its strength and ductility, thus preventing premature failure of the column [8]. Several factors influence this performance gain, such as the properties of the composite, the geometry of the columns and the characteristics of the concrete. Therefore, current research aims to understand the best combination of reinforcement and structure that results in the most effective performance in terms of force and displacement.

Anticipating the performance of these adapted columns is essential to optimize material selection, ensuring structural safety during the implementation of this method [8]. In this context, artificial intelligence emerges as a promising tool to predict performance, identify potential security risks, and avoid excessive costs, while maintaining the effectiveness and reliability of expected results [9]. In the field of artificial intelligence, machine learning techniques stand out, which offer an approach to predict the maximum resistance of columns reinforced with composites based on previously established data sets [10].

Among a variety of models, Artificial Neural Networks (ANNs) have been widely applied in different fields of civil engineering, from assessing the structural integrity of buildings to characterizing and modeling new materials, through optimizing reinforcement and repair techniques, and in the design of roads and bridges [11]. Studies highlight the ability of ANNs to identify complex correlations between various input and output parameters, working with data sets of various sizes [8, 10, 12].

Thus, machine learning techniques emerge as promising alternatives to support reinforcement initiatives. However, the application of these techniques to predict the behavior of reinforced structures is still restricted, often limited to a single type of performance. Furthermore, they rarely consider the impact of loading conditions on strength, a crucial aspect of effective design. In this scenario, this article proposes to estimate the predicted behavior and analyze the influence of reinforcement in reinforced concrete structures. The objective is to implement a reliable ANN model to predict the compressive strength and lateral displacement capacity of confined carbon fiber columns under eccentric loading, examining regression metrics to evaluate the model's performance and analysing its predictive quality.

2. METHODOLOGY

To achieve the established objective, three tools were used: Microsoft Excel, ABAQUS and MATLAB software. Due to its ability to model a variety of materials using the finite element method, ABAQUS version 6.14 was used to build the numerical database. Excel version 2311 was used to organize the input and output database during model pre-processing, as well as to manipulate the variables and analyze the results after processing by the ANN. MATLAB, in version R2018b, played a crucial role in the learning, validation and testing stages of the performance prediction network. The choice of this software was motivated by the inclusion of the Neural Network Toolbox, which offers several training algorithms for ANNs, allowing multiple simulations to be carried out in the search for the most appropriate model for the proposed objective.

The results achieved so far are partial and are part of broader ongoing research. This other research will add the rupture mode as an output variable and will use cross-validation as a network training criterion.

2.1. Numerical modeling

Parametric numerical models of columns subjected to flexion-compression were developed, using experimental data obtained from tests carried out by [13] and numerically confirmed by [14]. In set B of columns, four samples were selected and divided into two subgroups. The first subgroup was tested with a nominal eccentricity (*e*) to cross-sectional height (*h*) of 0.46, while the second subgroup had an *e/h* ratio of 0.60. Each subgroup consists of a control unconfined sample and a sample completely confined with a layer of CFRP as specified in Table 1. The concrete measurements and the layout of the steel reinforcement are illustrated in Fig. 1.

Table 1. Characteristics of the experimental test. Available at [13, p. 2331].

Group	Charging condition	Section format	Reinforcement condition	Column designation
B	Eccentric (*e/h*=0.46)	Square	No confinement	SN-e1
			Full confinement	SF-e1
	Eccentric (*e/h*=0.60)	Square	No confinement	SN-e2
			Full confinement	SF-e2

After carrying out the laboratory tests and obtaining the results, [14] proceeded with the numerical validation process using the ABAQUS software, as shown in Fig. 1. To achieve this, the author chose to employ the constitutive model known as Concrete Damaged Plasticity (CDP), which incorporates material plasticity curves and damage evolution curves. CFRP was represented as linear elastic until failure, while steel was characterized by elastic-plastic behavior with linear hardening.

As illustrated in the graphs in Fig. 2, the numerical curves accurately reproduced the evolution of the experimental test curves, for both eccentricities, demonstrating an excellent adjustment in relation to the maximum resistant force and the corresponding lateral displacement. This result indicates that the calibration process was successful, confirming the suitability of the finite element models presented to analyze the behavior of reinforced concrete columns confined with CFRP. Therefore, these validated models were used to create the database for this research.
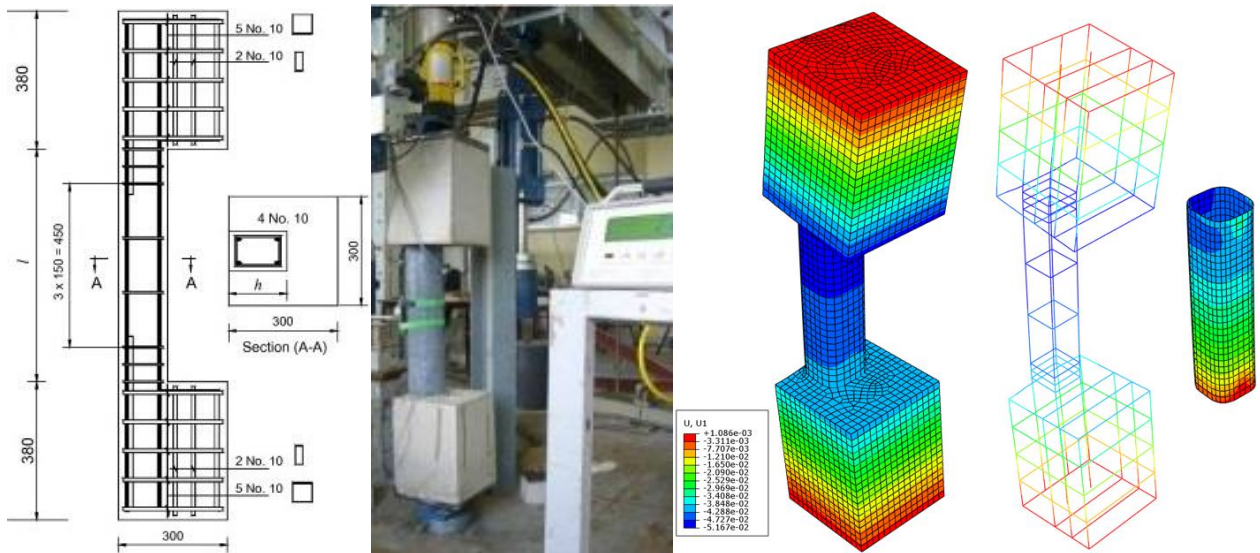
Figure 1. Experimental test and numerical modeling of confined columns. Available at [13, p. 2333-2334].
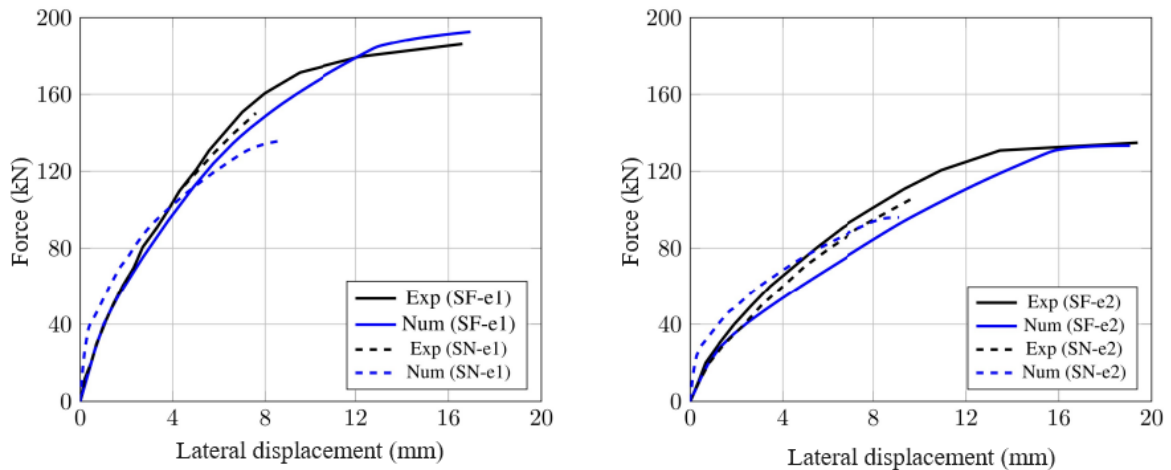
Figure 2. Force-displacement curves of the columns obtained in numerical simulations compared to experimental curves. Available at [14, p. 100].

2.2. Definition of input variables

The performance and influence of confinement are determined by variables such as the compressive strength concrete (f_{ck}), the corner radius of the square sections (r), the thickness of the blanket (number of layers - n), the modulus of elasticity of the composite (E_f) and eccentricity ratio (e/h). Therefore, these data are considered as input variables. This definition is based on several research studies that have explored various reinforcement configurations. It was observed that the factors that most influence the efficiency of CFRP application are related to the properties of the materials and to the geometry of the columns [15-17].

2.3. Database

After determining the input variables, the calibrated numerical models were expanded to perform a parametric study that encompassed 176 columns. Table 2 below shows the statistical summary of the data set, including the smallest value, mean, standard deviation and maximum value for all variables used in the ANN. For each input parameter, 4 numerical levels were considered, given that all variables are quantitative.

Regarding the results, 4 output variables were selected, grouped into two categories: mechanical performance indicators, which include the maximum compression force - F_c and the corresponding lateral displacement - δ_l measured at an average height of the test area; and indicators of mechanical improvement, represented by the percentage increase in resistance - F_c (%) and lateral displacement - δ_l (%) in relation to numerical samples without reinforcement with CFRP.

Table 2. Statistical database synthesis.

	f_{ck} (MPa)	E_f (GPa)	$n°$	r (mm)	e/h	F_c (kN)	δ_l (mm)	F_c (%)	δ_l (%)
Minimum	20	230	1	10	0.46	100.3	4.13	-5.6	9.4
Average	34.4	401	2.5	25.4	0.53	262.6	19.7	49.2	133.9
Standard deviation	11.2	161.9	1.1	15.6	0.07	69.5	4.6	32.8	52.7
Maximum	50	690	4	50	0.67	431.4	36.3	150.6	376.8

2.4. ANN model definition

The definition of the ANN included an iterative process of training, validation and testing, exploring different configurations until identifying a model that best fit the data set. We chose to use the MATLAB *feedforward* network and the *trainbfg* training algorithm. This algorithm presents fast convergence, being especially effective in networks with few neurons [18]. The data set from the numerical simulations was compiled and later normalized to vary from -1 to 1, according to Eq. (1).

$$x_{normalized} = \frac{x - x_{min}}{x_{max} - x_{min}} \tag{1}$$

Subsequently, the data was randomly divided into 80% for the training set, 10% for validation and 10% for testing. These sets were then incorporated into the ANN model, and the results obtained were evaluated using regression metrics. After several iterations, it was determined that the model with two hidden layers offered the most satisfactory results. The final configuration of the ANN in this study presented two intermediate layers with 26 and 23 neurons, respectively, as shown in Fig. 3, where x_n represents the inputs and y_n the outputs. The activation functions adopted were *purelin* and *poslin*, respectively.
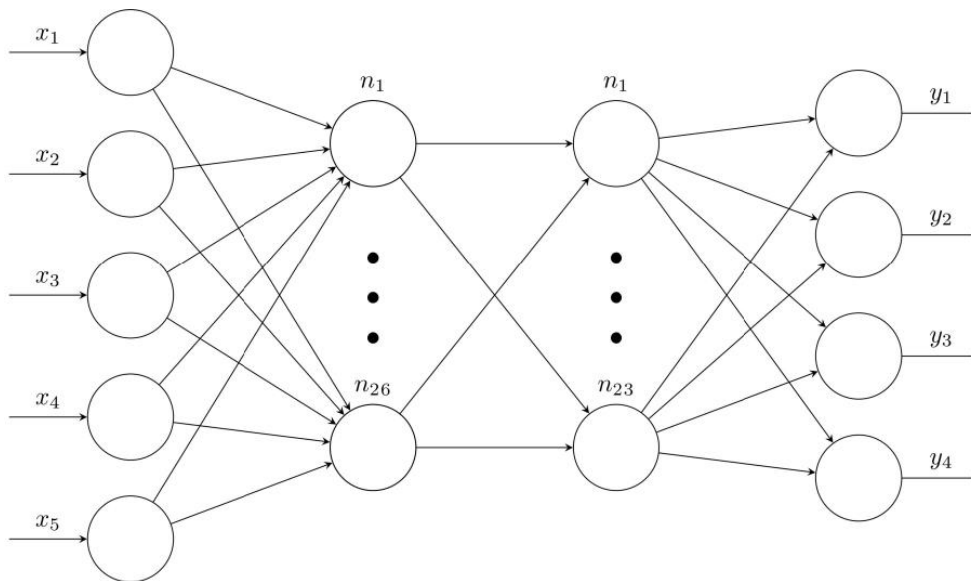
Figure 3. Definitive configuration of the ANN used.

3. RESULTS AND DISCUSSION

Table 3 shows ANN performance metrics for test data for all output variables. According to the magnitude of the values of compression and displacement forces, the MAE indices are judged to be satisfactory. However, there were considerable differences between some predicted resistance results and actual data, resulting in a high MSE due to the magnification of these squared discrepancies. In this context, RMSE analysis is commonly used for a clearer interpretation of the metric. This is because RMSE preserves the unit at the same scale as the original data, indicating that outliers are not exerting a significant influence on the model predictions.

In Fig. 4, the dispersion between the actual values and those predicted during the data test is shown, in relation to the line of equality. It was noted that the force values are distributed within a range of +15% to -10% compared to the line of equality, indicating a consistent distribution across various force ranges. As for lateral displacement, the data is spread out in the range of +35% to -10%, with a significant concentration of results around the average. Therefore, qualitatively, the test data related to compressive strength exhibits a more accurate representation.

Table 3. Performance indicators achieved in predicting column behavior.

Metric	Data	Mechanical behavior		Mechanical improvement	
		F_c (kN)	δ_l (mm)	F_c (%)	δ_l (%)
R^2	Test	0.96	0.69	0.86	0.73
MAE	Test	9.40	1.38	9.98	12.30
MSE	Test	154.55	3.83	171.72	261.46
$RMSE$	Test	12.43	1.96	13.10	16.17
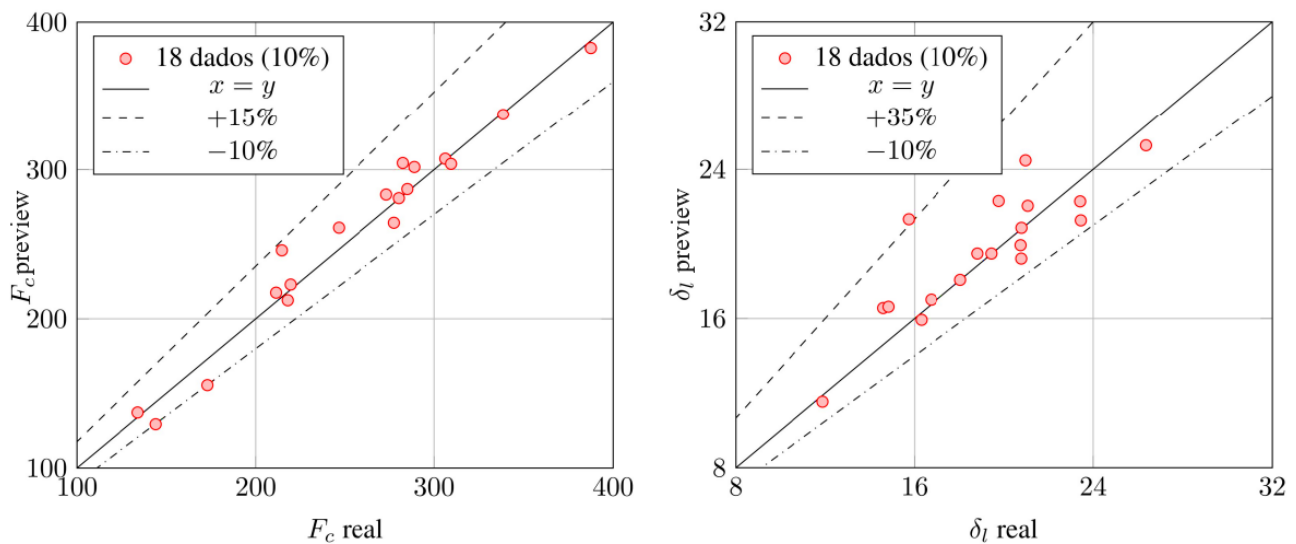
Figure 4. Mechanical behavior test data results.

The use of ANN also made it possible to predict the percentage influence of CFRP on strength and deformation compared to unconfined columns. The MAE and RMSE values presented in Table 3 were higher than those of the mechanical performance variables. These discrepancies can be explained by the different scales of the variables, especially the variable δ_l (%), which presents the greatest variation among all the values in the database.

Figure 5 illustrates the reason for the high metrics identified for the variable Fc (%). Approximately 28% of the data lies outside the acceptable range of +32% and -37% in relation to the line of equality, indicating a greater percentage error.

When analysing the outputs of the data set, it is observed that a portion of these results correspond to the columns that experienced a loss of resistance with the increase in reinforcement. Therefore, for a greater proximity of the points in relation to the line of equality, it is imperative to increase the amount of data associated with a lower level of confinement and a greater eccentricity ratio. This is because the number of data that showed a reduction in resistance was significantly lower compared to those that demonstrated a gain.

As for the variable δ_l (%), Fig. 5 shows that the predicted values were close to the numerical results, exhibiting a variation in relation to the line of equality that ranges from +34% to -22%. Furthermore, it is noted that different percentage ranges were considered for both variables analysed, without a centralized concentration in a specific region. This suggests that the model is effective in predicting the influence of reinforcement compared to unreinforced samples.
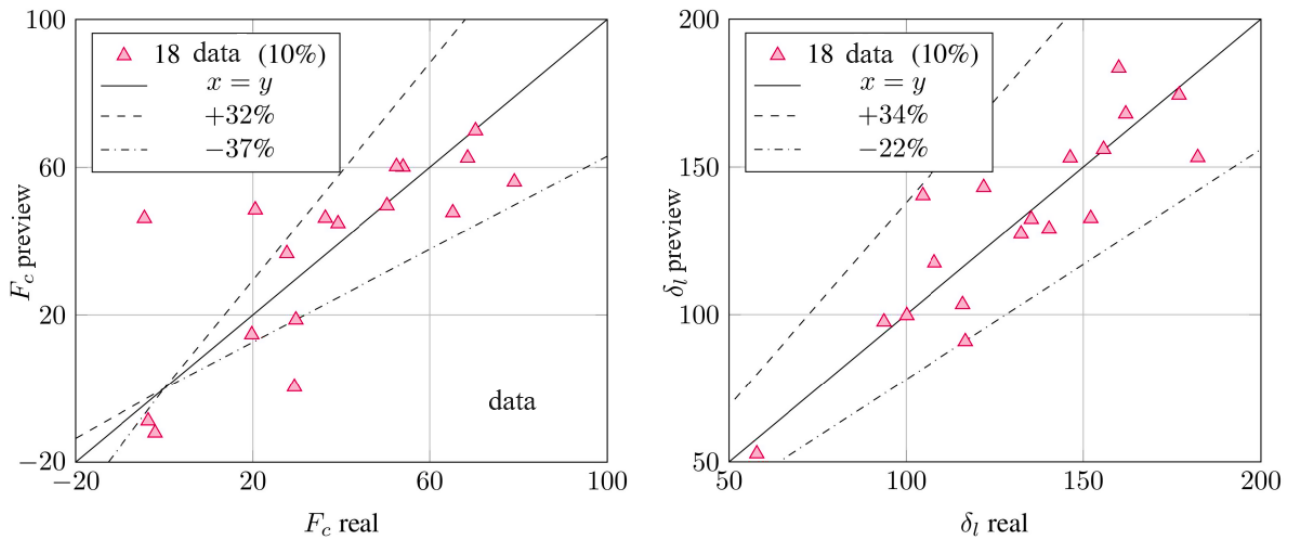
Figure 5. Mechanical improvement test data results.

3.1. Boxplot graphics

Boxplot graphs were created for the MSE values obtained from 40 independent ANN tests used to visualize the data distribution and identify outliers. These boxplots provide information about the network's prevision ability, as the lower the MSE, the better the prevision.

When observing the boxplots in Fig. 6, it is noticeable that the variable Fc (kN) presents the lowest error values and a more restricted dispersion in the results, followed by the variable Fc (%). However, the data referring to lateral displacement demonstrated higher errors, with the variable δ_l (mm) being the one with the most striking difference between the maximum and minimum values, in addition to a higher box, indicating greater variability in the results. The variable Fc (%) was the only one to exhibit symmetry, suggesting a normal distribution in the data set. On the other hand, the other variables showed asymmetry in MSE values, with a greater concentration of data in the upper part of the boxplots, that is, above the median.
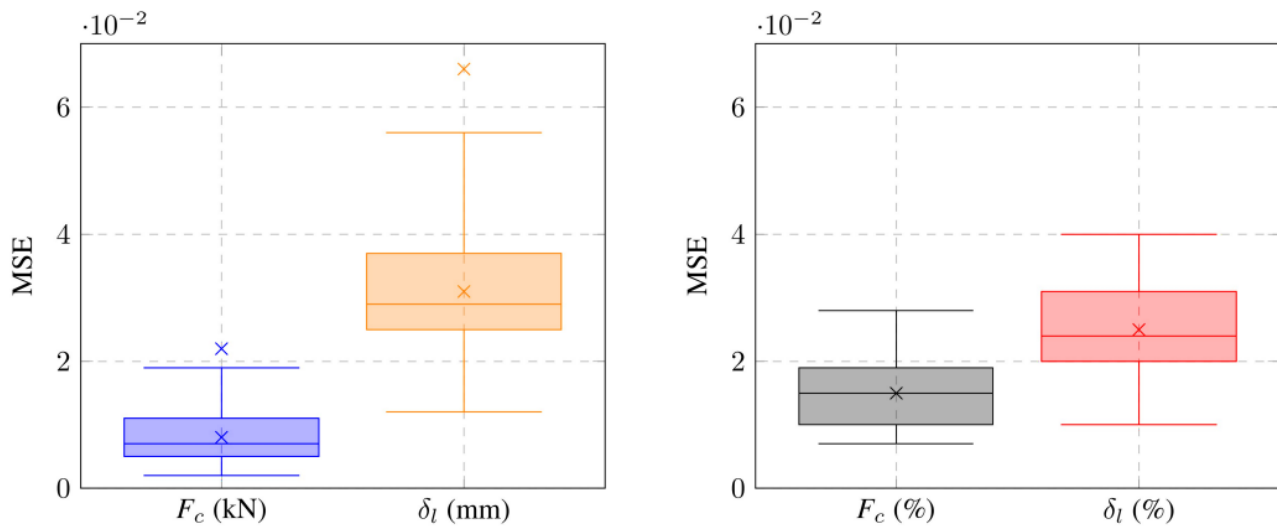
Figure 6. Comparative boxplots of MSE for outputs.

The boxplots associated with mechanical performance presented one outlier each, while those related to improvement revealed no discrepancies with the main data. Given this situation, a comparison proposed by [19] was carried out to evaluate the MSE and R² in two models, considering the presence and absence of suspected outliers. No significant differences were identified between the results obtained, suggesting that the outliers are just extreme values.

4. CONCLUSIONS

With the objective of developing a useful tool for the structural design of reinforced concrete elements confined with CFRP, this research developed a model using Artificial Neural Networks to estimate the load capacity and displacement of columns subjected to flexion-compression. Based on the results obtained, we have:

a) The results of the test data validated the efficiency of the model in reproducing in a reliable, simple and economically accessible way the behavior of force and lateral displacement, while also quantifying the influence of reinforcement on the percentage increase in resistance and deformation. The final ANN model showed a total R^2 of 0.91.

b) The use of numerical data in ANN applications does not receive much attention in the literature. However, to improve the adaptation of the model to the real world, it is crucial to augment the dataset with numerical validations from other experimental research, as well as incorporating new factors such as column heights and different cross-sectional geometries.

c) It is important to highlight that the use of CFRP for confinement affects other properties of the columns, such as the failure mode. Therefore, when undertaking the project, it is essential to ensure that the chosen level of confinement does not result in brittle failure of the structures.

For future investigations, it is recommended to include data from columns subjected to biaxial eccentric loads, in addition to developing new models to predict the behavior of different types of elements reinforced with CFRP. This may include strengthening beams in bending and shear, as well as seismic strengthening of walls, among other examples.

4.1. Declaration of Competing Interest
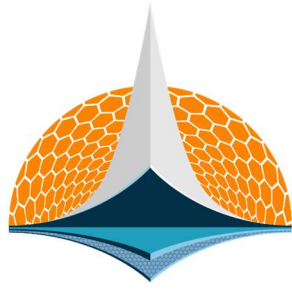
The authors declare no conflict of interest.

4.2. Acknowledgements

5. REFERENCES

[1] A. Chalot, L. Michel, E. Ferrier. Experimental study of external bonded CFRP-concrete interface under low cycle fatigue loading. *Composites Part B: Engineering*, Volume 177, p. 107255, 2019. (https://doi.org/10.1016/j.compositesb.2019.107255).

[2] R. Ismail *et al*. Experimental study of circular hollow reinforced concrete column strengthened with partial carbon fibre reinforced polymer (CFRP) confinement. In: *IOP Conference Series: Materials Science and Engineering*, Volume 615, n. 1, p. 012075, 2019. (https://doi.org/10.1088/1757-899X/615/1/012075).

[3] S. Kaeseberg, D. Messerer, K. Holschemacher. Assessment of standards and codes dedicated to CFRP confinement of RC columns. *Materials*, Volume 12, n. 15, p. 2390, 2019. (https://doi.org/10.3390/ma12152390).

[4] C. Chastre, M.A. Silva. Monotonic axial behavior and modelling of RC circular columns confined with CFRP. *Engineering Structures*, Volume 32, n. 8, p. 2268-2277, 2010. (https://doi.org/10.1016/j.engstruct.2010.04.001).

[5] I.B.R. Widiarsa, M.N. Hadi. Performance of CFRP wrapped square reinforced concrete columns subjected to eccentric loading. *Procedia Engineering*, Volume 54, p. 365-376, 2013. (https://doi.org/10.1016/j.proeng.2013.03.033).

[6] A.S. Abdel-Hay. Partial strengthening of RC square columns using CFRP. *HBRC Journal*, Volume 10, n. 3, p. 279-286, 2014. (https://doi.org/10.1016/j.hbrcj.2014.01.001).

[7] F. Michelli, A. Cascardi, M.A. Aiello. Pre-load effect on CFRP-confinement of concrete columns: Experimental and theoretical study. *Crystals*, Volume 11, n. 2, p. 177, 2021. (https://doi.org/10.3390/cryst11020177).

[8] P. Chen *et al*. Prediction of mechanical behaviours of FRP-confined circular concrete columns using artificial neural network and support vector regression: Modelling and performance evaluation. *Materials*, Volume 15, n. 14, p. 4971, 2022. (https://doi.org/10.3390/ma15144971).

[9] Y. Pan, L. Zhang. Roles of artificial intelligence in construction engineering and management: A critical review and future trends. *Automation in Construction*, Volume 122, p. 103517, 2021. (https://doi.org/10.1016/j.autcon.2020.103517).

[10] K. Miao *et al*. Machine learning-based model for the ultimate strength of circular concrete-filled fiber-reinforced polymer-steel composite tube columns. *Construction and Building Materials*, Volume 394, p. 132134, 2023. (https://doi.org/10.1016/j.conbuildmat.2023.132134).

[11] Y. Huang, J. Li, J. Fu. Review on application of artificial intelligence in civil engineering. Computer Modeling in Engineering amp; *Sciences*, Volume 121, n. 3, p. 845-875, 2019. (https://doi.org/10.32604/cmes.2019.07653).

[12] X. Xue *et al*. Machine learning approach for prediction of lateral confinement coefficient of CFRP-wrapped RC columns. *Symmetry*, Volume 15, n. 2, p. 545, 2023. (https://doi.org/10.3390/sym15020545).

[13] T.E. Maaddawy, M.E. Sayed, B. Abdel-Magid. The effects of cross-sectional shape and loading condition on performance of reinforced concrete members confined with carbon fiber-reinforced polymers. *Materiais & Design* (1980-2015), Volume 31, n. 5, p. 2330-2341, 2010. (https://doi.org/10.1016/j.matdes.2009.12.004).

[14] M. S. Santos. Modelagem numérica de pilares curtos de concreto confinados com PRFC solicitados por força de compressão concêntrica e excêntrica. Dissertation (Master's) - Technology Center, Federal University of Ceará, Fortaleza, 117 f, 2022.

[15] D.S. Oliveira, R. Carrazedo. Numerical modeling of circular, square, and rectangular concrete columns wrapped with FRP under concentric and eccentric load. *Revista IBRACON de Estruturas e Materiais*, Volume 12, n. 3, p. 518-550, 2019. (https://doi.org/10.1590/S1983-41952019000300006).

[16] M.F. Fahmy, Z. Wu. Evaluating and proposing models of circular concrete columns confined with different FRP composites. *Composites Part B: Engineering*, Volume 41, n. 3, p. 199-213, 2010. (https://doi.org/10.1016/j.compositesb.2009.12.001).

[17] D. Mostofinejad, N. Moshiri, N. Mortazavi. Effect of comer radius and aspect ratio on compressive behavior of rectangular concrete columns confined with CFRP. *Materials and Structures*, Volume 48, n. 1-2, p. 107-122, 2013. (https://doi.org/10.1617/s11527-013-0171-9).

[18] S. Ding, Q.H. Wu. A matlab-based study on approximation performances of improved algorithms of typical bp neural networks. *Applied Mechanics and Materials*, Volume 313, p. 1353-1356, 2013. (https://doi.org/10.4028/www.scientific.net/AMM.313-314.1353).

[19] S. Walfish. A review of statistical outlier methods. *Pharmaceutical technology*, Volume 30, n. 11, p. 82, 2006.

13 Laminated composites

Organized and edited by

Sandra Maria da Luz
&
Carla Tatiana Mota Anflor

Fire behavior of wood-glass and jute-glass hybrid laminates manufactured by vacuum infusion

Ohayna Lisboa Santos[a*]; Andrey Pereira Acosta[b]; Letícia Zimermann Pires[c]; Daniele Battegazzore[d]; Alberto Frache[e]; Pedro Henrique Gonzalez de Cademartori[f]; Sandro Campos Amico[g]

(a) ◉ 0009-0000-2624-9611 (Federal University of Paraná)
(b) ◉ 0000-0002-5074-3772 (Federal University of Paraná)
(c) ◉ 0009-0001-2640-7584 (Federal University of Paraná)
(d) ◉ 0000-0002-6829-5605 (Politecnico di Torino)
(e) ◉ 0000-0002-2572-3235 (Politecnico di Torino)
(f) ◉ 0000-0003-3295-6907 (Federal University of Paraná)
(g) ◉ 0000-0003-4873-2238 (Federal University Rio Grande do Sul)
*Corresponding author: ohayna.lisboa@ufpr.br

Abstract: This study explores the fire behavior of wood-glass and jute-glass hybrid laminates, with a focus on the influence of jute and wood veneers as a new material for composite production. Five-layer hybrid laminates were manufactured using the vacuum infusion process (VIP). Combustion and carbonization performance were assessed using a cone calorimeter based on the ISO5660 method. The study evaluates flammability through key parameters including ignition time, heat release rate, and smoke production. The results indicated that the ignition time was significantly longer (c.a. 64 s) for the glass-jute laminate (GJGJG), compared to the wood-glass laminate (WGWGW) (c.a. 53 s). The heat release rate of laminates containing organic components is higher than sample composed only of glass mat (G5) but they are all lower than the polyester reference resin. WGWGW compared to the GJGJG sample is able to produce a good quality protective shield and therefore postpone the occurrence of the heat release peak. By this way, the fire growth rate index (FIGRA) best performance resulted to the WGWGW sample (2.7±0.3 kW/m²*s) which is even better than the G5 sample. The total smoke released value was highest for polyester, 7361±839 m²/m², followed by WGWGW 2873±188 m²/m² and J5 2484±216 m²/m². Among the hybrid laminates the best performance is obtained by GJGJG 1860±49 m²/m² that compared to the G5 laminates it was only ~36% higher. Specific extinction area (SEA) is a smoke parameter related to the mass of the samples, the best result is obtained by WGWGW with 697±31 m²/kg.

1. INTRODUCTION

The growing demand for environmentally conscious products in the construction industry, driven by public policies and concerns about environmental health, has driven the replacement of conventional materials such as glass with lower impact options such as plant fibers. Lignocellulosic materials, sourced from renewable plants and trees, inherently offer biodegradability and a lower carbon footprint compared to traditional synthetic fibers [1]. As highlighted in a comprehensive review, plant-based materials offer versatility in applications ranging from construction and furniture sectors to emerging domains like adsorption materials and electrode components. In this context, hybrid laminate composites have emerged as a prominent alternative, offering a combination of robust mechanical properties, affordable costs and compliance with environmental regulations [2].

These laminates, made up of fabrics and/or fiber mats, are mostly made of glass, due to its low cost and excellent mechanical properties. Studies have reported that hybrid laminates can achieve increased

tensile strength, bending strength, impact strength, compression-after-impact strength, reduced water absorption, and improved thermal stability compared to their single-component counterparts [3]. Hence, in plant-based hybrid laminates, glass layers can mitigate some detrimental characteristics of the lignocelulosic ones such as seasonality, limited mechanical properties, high water absorption, suboptimal hydrophobicity and vulnerability to fracture, making them less desirable for certain applications (e.g. civil construction, furniture, etc.) [4].

In fact, the use of lignocellulosic materials to manufacture hybrid laminates has emerged over the last few years in the structural composites segment [5]. Dias et al. [12] for example, investigated the influence of hybridization with jute and glass fabrics on the physical and mechanical properties of laminates manufactured by vacuum infusion process (VIP). Recently, Acosta et al. [6] proposed the use of balsa wood veneers as an alternative material that has a higher volume production and lower cost (depending on the region) compared to other fibers (e.g. jute, sisal, ramie, etc.). Although this is nothing completely new in the literature, these laminates using glass have already been well explored from the point of view of mechanical and physical properties [7]. However, wood is a material considered to be a thermal insulator and, especially in the case of structural applications, it is extremely important to assess its fire behavior, a fact that is not found in the literature in the form of laminates produced by VIP.

Most of the studies focused on studying the behavior of laminates in relation to fire concentrate on exploring laminates produced with commonly used natural mats or fabrics (e.g. jute, cotton, bamboo, ramie, etc.). For example, Zuhudi et al. [8] evaluated the influence of fire on hybrid laminates of polypropylene, bamboo fabrics and glass (BGPP). The BGPP were manufactured by replacing around 30% of the glass fiber with bamboo fabric, using the compression molding technique. The results of the calorimeter cone tests revealed a superior performance of the hybrid composites, BGPP, compared to the glass-propylene composites, with a significant 19% reduction in the heat release rate and smoke release, as well as having a 67% higher ignition time compared to the glass-propylene composite [8]. In addition, Barczewski et al. [9] studied the fire exposure behavior of hybrid epoxy and flax cotton laminates (EP/FF) by adding proportions of 1-10 wt% of micrometric expanded vermiculite (VMT). The addition of VMT quantities of 1 and 2 wt% enabled a 60 % reduction in the heat release rate (HRR) and a 20 % reduction in the total heat release rate, compared to EP/FF [9].

Despite the growing research into the fire behavior of laminates, it is important to highlight the scarcity of studies into laminates manufactured by VIP, mainly using wood, precisely because wood-based laminates manufactured by VIP are an innovation in laminates in the literature. VIP involves the use of vacuum pressure to drive resin into a dry fiber lay-up, ensuring complete saturation and optimal distribution of the resin throughout the composite structure. This process has been reaching great attention for its ability to provide a balance of performance, cost-efficiency, and environmental sustainability compared to other composite manufacturing methods such as hand lay-up, RTM, and filament winding [10]. Its advantages in terms of uniform resin distribution, reduced void content, and environmental benefits make it a preferred choice for producing high-quality composite laminates across various industries [11]. This research aims to address the existing research gap by exploring the fire behavior of wood-glass and jute-glass hybrid laminates, utilizing a cone calorimeter, with a special emphasis on evaluating the effect of natural based components.

2. METHODOLOGY

1 mm-thick *Pinus elliottii* wood veneers (with an apparent density of 0.59 ± 0.05 g/cm³, moisture content of 9.97 ± 1.99%, and porosity of 49.25 ± 2.25%) [7] were purchased from EcoFolhas (São Paulo, Brazil). Unidirectional jute fabrics (with an area density of ~239 g/m²) were sourced from Castanhal Textile Company (Pará, Brazil). Randomly oriented glass mats (with an area density of ~400 g/m²) were obtained from Owens Corning (Toledo, USA). Pine veneer, jute fabric, and glass mat are denoted as "W", "J", and "G", respectively. An unsaturated isophthalic polyester resin (with a density of 1.19 g/cm³) and a Butanox 50 initiator (comprising 1.5% by weight relative to the resin) were used as the polymer matrix

The laminates were manufactured using the vacuum infusion process (VIP) at room temperature (~25 ℃) by stacking five layers oriented lengthwise, except for the glass mats, which were randomly oriented. The manufacturing and stacking configuration was based on a sequence of previously published articles [7]. The following laminate stacking sequences were used: GGGGG (G5), JJJJJ (J5), WGWGW, and GJGJG, to investigate fire behavior in relation to hybridization. The samples reached similar apparent densities obtained with the measurement of the weight of the sample divided by their volume calculated with

the dimensions measured with a digital caliper. They range from 0.95±0.02 g/cm³ of J5 sample to 1.64±0.02 g/cm³ of G5 sample. The GJGJG sample has a density of 1.16 g/cm³ and WGWGW of 1.03 g/cm³. The fire behavior of hybrid laminates and pure resin was assessed using NOSELAB ATS s.r.l. cone calorimeter apparatus in accordance with ISO 5660. Compared to the ISO 5660 standard, the sample size was adapted to dimensions of $50 \times 50 \times 2\text{-}4$ mm³. These samples were securely positioned within an aluminum sample holder and exposed to irradiation at 35 kW/m² using a horizontal configuration setup.

The cone tests were conducted three times for each laminate, and standard deviation values were calculated for the following parameters: ignition time (TTI, s), peak heat release rate (pHRR, kW/m²), time to peak (TTP, s), total heat release (THR, MJ/m²), total smoke release (TSR, m²/m²), optical transmittance percentage (%), carbon monoxide (%) and carbon dioxide (%) presence in the exhaust air flow. Horizontal burning tests on $125 \times 13 \times 2\text{-}4$ mm³ samples were carried out in accordance with UL 94HB in a NOSELAB ATS s.r.l. cabin to obtain the burning rate (V). One sample per group was evaluated for this test. Before the flammability and combustion tests, the samples were conditioned in a climate chamber at 23 ±1 ºC and 50% of relative humidity for a minimum of 48 h, as suggested by standard ISO5660. One-Way analyses of variance (ANOVA) were applied and, whenever the null hypothesis was rejected, Tukey tests were used to compare the means with 5% of significance level. In all cases where ANOVA was applied, data distribution was used to represent the error instead of the standard deviation.

3, RESULTS AND DISCUSSION

The first analysis reported is the cone calorimetry test under a heat flow of 35 kW/m² in a horizontal position. The main data obtained from this analysis are reported in Table 1 and then discussed individually.

Table 1. Main data and standard deviations measured in combustion in the cone calorimeter tests.

Sample	TTI (s)	TTP (s)	pHRR (kW/m²)	THR (MJ/m²)	TSR (m²/m²)	SEA av. (m²/kg)	MARHE (kW/m²)	FIGRA (kW/m²*s)	Residue (%)
Polyester	58±1	166±3	971±103	116±12	7361±839	1227±8	492±3	5.8±0.5	0.1±0.1
G5	55±15	94±12	322±6	25.1±2.3	1365±191	825±92	141±11	3.5±0.4	62.4±2.3
J5	45±1	105±6	794±45	53.0±7.6	2484±216	825±31	332±23	7.5±0.6	0.5±0.1
GJGJG	64±3	121±8	395±7	40.2±5.1	1860±49	835±90	191±8	3.3±0.2	34.7±1.9
WGWGW	53±3	165±8	453±43	76.5±5.8	2873±188	697±31	270±13	2.7±0.3	1.9±1.1

The time to ignition (TTI) of the different samples were reported in the first column of Table 1. The TTI is the time required to start burning due to the radiation of heat onto a sample surface in the presence of a spark. The lower the TTI, the more flammable is the material [20]. Considering the TTI necessary for the neat resin used for infusion to ignite (58±1 s), this time is brought deeply forward for the samples J5 (45±1 s) and only slightly for the WGWGW sample (53±3 s). On the other hand, TTI is postponed for the samples GJGJG (64±3 s) and G5 (55±15 s).

These observations can be attributed to the presence of lignocellulosic material on the face of the WGWGW and J5 laminates. Components like cellulose and hemicellulose in these materials significantly increase their flammability [12]. Conversely, laminates containing glass exhibit longer burn times, particularly on the face, due to the inorganic nature of glass. Composed of 70-75% silica (SiO_2), sodium carbonate, and calcium carbonate, glass offers greater resistance to fire exposure [12]. The similarity between the reference polyester and G5 can be explained by the high permeability of glass mats during infusion, which can facilitate the flow of resin through fiberglass mats.

Thermal conductivity can also contribute to the first stages of heating and decomposing of the surface of the samples. Wood and jute, for example, have values of conductivity of ~0.1 to ~0.2 W/ (m.K) [13], i.e. higher thermal conductivity compared to glass but similar to the infusion resin. Thermal properties pertain to a material's ability to conduct, store, and dissipate energy. Lower thermal conductivity values accelerate carbonization and temperature accumulation on the surface, leading to quicker pyrolysis and

carbonization of the material [12]. This may be an explanation for the variability of samples with more insulating material on the surface such as G5.

Parameters such as HRR, pHRR and THR are important to determine, as they give a general indication of the size of the fire and how quickly it spreads [14]. The speed with which thermal energy is generated by the combustion of a material is important, especially for structural composites, as it indicates its potential fire risk and combustibility, since materials that release smoke and toxic gases relatively quickly are more dangerous than those that do so more slowly [10]. Figure 1A shows the results obtained in relation to the heat release rate (HRR), while Figure 1B refers to the statistical difference according to the confidence interval. Differences can be seen in the time taken for the different laminates to combust, as well as the pure resin. The polyester resin, used for the matrix of the composites, showed the highest HRR peak value (971 ± 103 kW/m²), which is related to its chemical composition, containing a considerable amount (35-40%) of styrene in this particular case, as well as highly volatile ester groups [15]. Combustion lasts a long time with a progressive increase of HRR in the first stage and a long combustion of the charred part in the final part of the test which brings the duration of the flaming phase to over 300s.

The G5 sample presents an extremely reduced HRR trend compared to the polyester resin. Indeed, the peak is reduced to 322 ± 6 kW/m². This fact is certainly due to the part of glass which, not being combustible, limit the release of energy during the combustion of the specimen. The combustion time is almost halved with respect to the neat resin (161 s) and the peak of heat release appears earlier (TTP 94 ± 12 s vs 166 ± 3 s). The opposite formulation sample, the J5 one, composed of resin and organic material, presents a behavior similar to the neat resin with an even sharper peak at 794 ± 45 kW/m² and a TTP of 105 ± 6 s. The entire combustion process appears to be the fastest of the samples examined with an average combustion phase around 115 s. The two samples containing the hybrid layers between glass and organic substances present similar behavior to each other with the presence of a first small peak in the first stages of combustion (20-30 s from starting of flame) probably due to the resin presence. Subsequently, in both cases, there is a protective layer formation phase which can be made of glass or the carbonized organic material or the combination of them. During this period the HRR curve essentially remains constant or decreases significantly. This phase lasts shorter for the GJGJG sample which then presents the HRR peak of 395 ± 7 kW/m² at 121 ± 8 s while it lasts longer for the WGWGW sample and causes a higher in intensity peak of 453 ± 43 kW/m² postponed until 165 ± 8 s. Probably the WGWGW compared to the GJGJG sample is able to produce a good quality protective shield and therefore postpone the occurrence of the peak. However, having a larger quantity of organic content than the GJGJG produces a slightly higher peak.
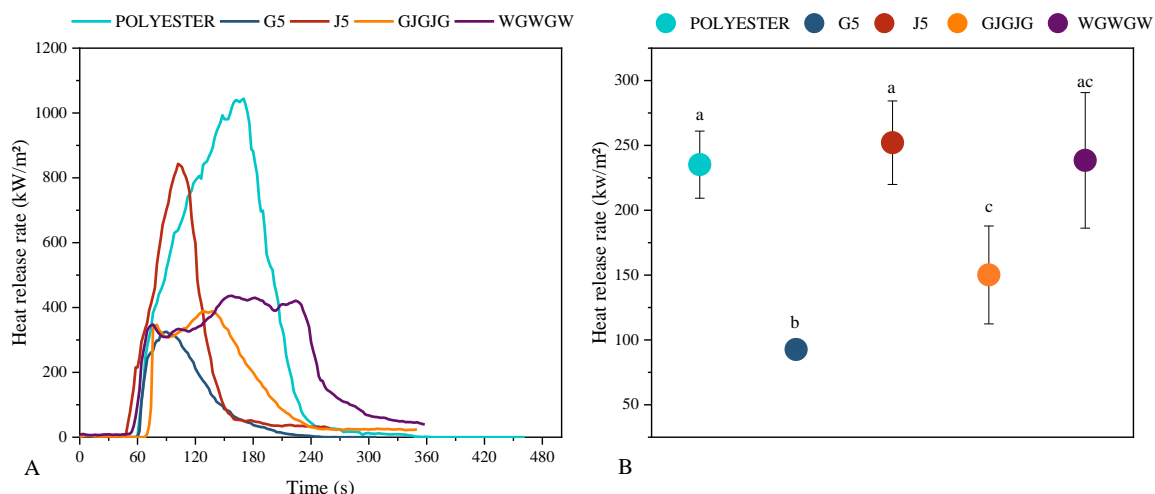
Figure 1. Heat release rate as a function of time for each group analyzed (A) and the average values of the heat release rate and confidence interval of 95% (B). Different letters above the errors in each group represent a statistical difference.

Finally, it is important to note that the WGWGW hybrid laminate, predominantly composed of wood veneers, especially in its surface layer, exhibited a heat release time that ranged on average from 53 seconds to 255 seconds. This range is significantly higher compared to the other laminates, showing fire resistance and delayed carbonization. These results highlight the effectiveness of hybrid laminates in improving their properties when exposed to heat, especially those where the hybridization chosen was with wood and glass

[16]. To further highlight this fact, a parameter widely used in the flame retardancy literature named FIGRA (fire growth rate index) has been reported in Table 1. This value is obtained by dividing the pHRR by the time at which this peak is obtained, i.e. the TTP. It is therefore evident as the smaller this parameter is, better is the behavior. The best performance result is attributed to the WGWGW sample (2.7±0.3 kW/m²*s) which is even better than the G5 sample (3.5±0.4 kW/m²*s).

MARHE (kW/m²) is the maximum average rate of heat emission is a parameter similar to HRR that is used in large scale tests as single burning item (SBI). Basically, it can be observed how the ratios between the analyzed samples remain the same compared to the value reported with pHRR. The best performance is obtained by the G5 sample with 141±11 kW/m² and the worst by the neat polyester resin 492±3 kW/m².

The J5 and polyester sample showed a greater deviation in HRR compared to other laminates, likely due to its higher void content, as reported by Acosta et al. [14]. Void spaces within the material can act as pockets for the accumulation of combustible gases, promoting faster and more intense combustion when exposed to heat [17]. Additionally, the presence of voids can alter the heat transfer mechanisms within the material, leading to localized hotspots and uneven combustion. This can result in fluctuations and deviations in the HRR measurements. The voids may also affect the thermal stability and decomposition pathways of the material. The increased void content can facilitate the escape of volatile components and combustion products, influencing the combustion kinetics and heat release characteristics during the test [18].

Figure 2A shows the curves for the total heat release (THR) of the laminates, while Figure 2B shows the statistical differences according to the confidence interval of 95%. It can be seen that the WGWGW hybrid laminate showed statistically higher values (76.5±5.8 MJ/m²) than the GJGJG (40.2±5.1 MJ/m²), corroborating the theory that the material present on the surface of the hybrid laminate has a significant influence on heat release. This is evidenced by the presence of glass (an inorganic non-combustible material), which showed lower average values [19]. Finally, the G5 mono-component laminate had statistically lower average values than pure resin (~-78%, 25.1±2.3 MJ/m²), since pure resin has low fire resistance and tends to release a considerable amount of heat in a short period of time [15]. It is important to emphasize that, despite the resin having low fire resistance, an improvement in combustion performance was observed for all laminates. Even WGWGW, which is an interesting alternative, combining fire resistance with low raw material costs for composites, as well as wood being an environmentally friendly material reach a reduction of 34% with respect the neat resin [20].
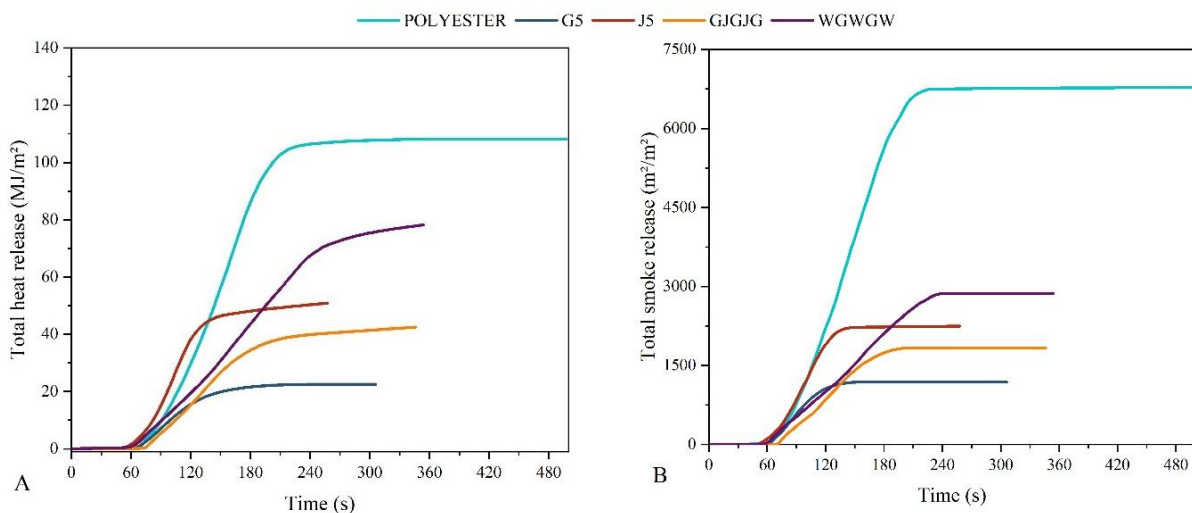
Figure 2. Total heat release (THR) as a function of time for each group analyzed (A) Total smoke release (TSR) as a function of time for each group analyzed (B).

Figure 2B shows total smoke release curve (TSR) in relation to time for the different laminates produced, as well as for the pure resin. One of the problems associated with fires is the smoke produced. Smoke means the mixture of pyrolysis products and air near the site of the fire and represents potential hazards because it interacts with light to obscure vision and probably it contains harmful and toxic substances [21]. This makes it interesting to determine the amount of smoke production. In general, for the materials under study, the value of smoke formed was highest for polyester, 7361±839 m²/m², followed by WGWGW 2873±188 m²/m² and J5 2484±216 m²/m². Among the hybrid laminates the best performance is

obtained by GJGJG 1860±49 m²/m² that compared to the G5 laminates it was only ~36% higher. The amount of total smoke released during the burning of materials such as wood and jute, which have organic compounds in their composition which also includes the release of carbonized particles, organic vapours and gases, it is expected to be greater than glass mat, as it has no smoke release [14].

Specific extinction area (SEA, m²/kg) is the ratio of smoke production to specimen mass loss averaged over the test duration. This parameter is interesting, compared to the others reported on the smokes produced, because is related to the mass of the sample and not to its exposed surface. By this way, it is possible to compare samples that have significantly different masses like those under this study. According to this processing, the polyester resin has the highest SEA value of 1227±8 m²/kg. On the contrary, the samples G5, J5 and GJGJG are fully comparable with values around 825 m²/kg and the best result is obtained by WGWGW with 697±31 m²/kg. This is mainly due to the fact that the WGWGW sample was the heaviest between the laminates.

Burning materials can result in the emission of gases that are harmful to the environment and human health. Initially, during incomplete combustion, carbon monoxide (CO) and soot are released. Later, these gases are oxidized to form carbon dioxide (CO_2) and water, representing the complete combustion of the material [22]. Figures 3A and B show the results of the measurements of the percentage in the instrument's exhaust air of carbon monoxide (CO) and carbon dioxide (CO_2) during the combustion of the different laminates. The results show that the wood-glass and jute-glass composites showed more than 50% of reduction in CO and CO_2 maximum peak of emissions compared to polyester resin. The best performance is obtained by the G5 sample.

The lower CO and CO_2 values observed for the G5 hybrid laminate in Figure 3 can be attributed to the inherent properties of glass fibers. Glass fibers are non-combustible and can act as an effective barrier to heat transfer, thereby reducing the rate of combustion and the subsequent emission of gases like carbon monoxide (CO) and carbon dioxide (CO_2). Therefore, the inert nature of glass fibers ensures minimal contribution to gas emissions during the combustion process, which explains the lower values of CO and CO_2 observed for the G5 laminate compared to other hybrid laminates containing natural fibers.

In addition, another two-component laminate GJGJG, despite having glass sheets on the face, showed higher CO/CO_2 emissions than the single-component laminate G5. This is probably related to the configuration of the laminate since jute fabric is used between the glass mats [6].
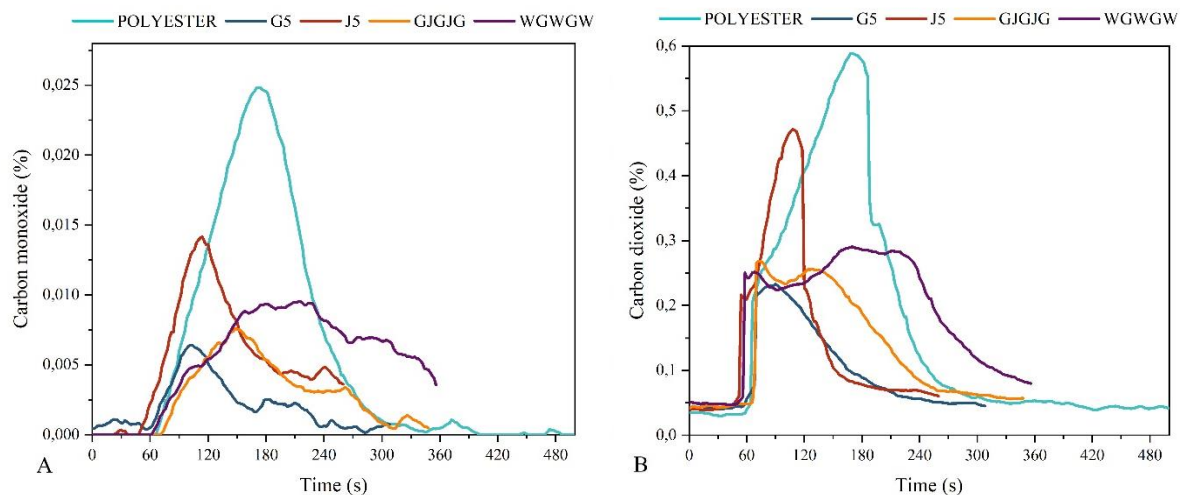
Figure 3. A) Carbon monoxide and B) Carbon dioxide as a function of time for each group analyzed.

4. CONCLUSIONS

This comprehensive study provided insights into the fire behavior of various hybrid laminates, emphasizing the role of materials like wood, jute, and glass in influencing combustion characteristics. Laminates containing lignocellulosic materials, particularly WGWGW and J5, exhibited good flammability attributed to components like cellulose and hemicellulose. In contrast, those with glass showed enhanced fire resistance, with longer burn times, thanks to their inorganic nature and thermal stability.

The heat release rate (HRR) was highest for polyester resin, likely due to its volatile esters and styrene content. However, the WGWGW laminate, enriched with glass, displayed improved fire resistance and delayed carbonization, highlighting the pivotal role of glass in influencing combustion kinetics. Moreover, laminates with wood and jute released a great quantity of smoke due to their organic composition but in any case, less than the neat resin. In contrast, the incorporation of glass in hybrid laminates significantly reduced smoke production, suggesting its potential in mitigating environmental hazards during fires.

In terms of harmful gas emissions, hybrid laminates generally exhibited reduced CO/CO_2 emissions compared to pure polyester and J5 laminates. This reduction can be attributed to glass fibers acting as barriers, limiting heat conduction and reducing oxygen exposure during combustion.

Looking ahead, optimizing laminate configurations for superior fire resistance without compromising mechanical and functional properties is a promising avenue for future research. Exploring interactions between wood, jute, and glass can further refine our understanding and contribute to the evolution of innovative, fire-resistant composite materials. Evaluating the burning characteristics of the material under fire conditions stands out as a crucial future study. In conclusion, while glass fiber laminates generally exhibited superior fire performance, wood-glass and jute-glass hybrid laminates, with their distinct advantages and positive influence on combustion performance, offer viable alternatives. Thus, selecting the most suitable material hinges on specific application requirements. Future studies with expanded sample sizes, different burning conditions and rigorous statistical analyses are warranted to corroborate these findings and offer definitive material selection guidelines for specific applications.

4.1 Declaration of Competing Interest

4.2 Fundings

4.3 Acknowledgements

5 REFERENCES

[1] Z. Lou, Z. Zheng, N. Yan, X. Jiang, X. Zhang, S. Chen, R. Xu, C. Liu, L. Xu, Modification and Application of Bamboo-Based Materials: A Review—Part II: Application of Bamboo-Based Materials, Forests. 14 (2023). https://doi.org/10.3390/f14112266.

[2] F. Chen, J. Deng, X. Li, G. Wang, L.M. Smith, S.Q. Shi, Effect of laminated structure design on the mechanical properties of bamboo-wood hybrid laminated veneer lumber, Eur. J. Wood Wood Prod. 75 (2017) 439–448. https://doi.org/10.1007/s00107-016-1080-8.

[3] A.H.M. Shamim Hasan, M.A. Chowdhury, A. Almahri, M.A. Kowser, M.S. Alam, M.B.A. Shuvho, R.S. Alruwais, N. Hossain, M.R. Rahman, M.M. Rahman, Physical, thermal, and mechanical properties of Al2O3/SiO2 infused jute/glass fiber resin composite materials in relation to viscosity, Polym. Compos. 43 (2022) 3971–3982. https://doi.org/10.1002/pc.26671.

[4] M. Arulmurugan, A.S. Selvakumar, K. Prabu, G. Rajamurugan, Effect of barium sulphate on mechanical, DMA and thermal behaviour of woven aloevera/flax hybrid composites, Bull. Mater. Sci. 43 (2020) 1–10. https://doi.org/10.1007/s12034-019-2018-7.

[5] T. da C. Dias, A.A.X. da Silva, M.L.P. Tonatto, S.C. Amico, Experimental Investigation on the Mechanical and Physical Properties of Glass/Jute Hybrid Laminates, Polymers (Basel). 14 (2022) 4742. https://doi.org/10.3390/polym14214742.

[6] A.P. Acosta, A.A. Xavier da Silva, R. de Avila Delucis, S.C. Amico, Wood and wood-jute laminates manufactured by vacuum infusion, J. Build. Eng. 64 (2023) 105619.

https://doi.org/10.1016/j.jobe.2022.105619.

[7] A.P. Acosta, R. de Avila Delucis, S.C. Amico, Hybrid wood-glass and wood-jute-glass laminates manufactured by vacuum infusion, Constr. Build. Mater. 398 (2023) 132513. https://doi.org/10.1016/j.conbuildmat.2023.132513.

[8] N.Z.M. Zuhudi, R.J.T. Lin, K. Jayaraman, Flammability, thermal and dynamic mechanical properties of bamboo-glass hybrid composites, J. Thermoplast. Compos. Mater. 29 (2016) 1210–1228. https://doi.org/10.1177/0892705714563118.

[9] M. Barczewski, K. Sałasińska, W. Raś, A. Hejna, S. Michałowski, P. Kosmela, J. Aniśko, A. Boczkowska, M. Szostak, The effect of hybridization of fire retarded epoxy/flax-cotton fiber laminates by expanded vermiculite: Structure-property relationship study, Adv. Ind. Eng. Polym. Res. 6 (2023) 181–194. https://doi.org/10.1016/j.aiepr.2023.01.005.

[10] P.A. Arrabiyeh, D. May, M. Eckrich, A.M. Dlugaj, An overview on current manufacturing technologies: Processing continuous rovings impregnated with thermoset resin, Polym. Compos. 42 (2021) 5630–5655. https://doi.org/10.1002/pc.26274.

[11] T. Wang, K. Huang, L. Guo, T. Zheng, F. Zeng, An automated vacuum infusion process for manufacturing high-quality fiber-reinforced composites, Compos. Struct. 309 (2023) 116717. https://doi.org/10.1016/j.compstruct.2023.116717.

[12] M.A. AlMaadeed, R. Kahraman, P. Noorunnisa Khanam, N. Madi, Date palm wood flour/glass fibre reinforced hybrid composites of recycled polypropylene: Mechanical and thermal properties, Mater. Des. 42 (2012) 289–294. https://doi.org/10.1016/j.matdes.2012.05.055.

[13] Z. Pásztory, S. Fehér, Z. Börcsök, The effect of heat treatment on thermal conductivity of paulownia wood, Eur. J. Wood Wood Prod. 78 (2020) 205–207. https://doi.org/10.1007/s00107-019-01470-3.

[14] Q. Xu, L. Chen, K.A. Harries, F. Zhang, Q. Liu, J. Feng, Combustion and charring properties of five common constructional wood species from cone calorimeter tests, Constr. Build. Mater. 96 (2015) 416–427. https://doi.org/10.1016/j.conbuildmat.2015.08.062.

[15] D. Romanzini, F. Cuttica, A. Frache, A.J. Zattera, S.C. Amico, Thermal and fire retardancy studies of clay-modified unsaturated polyester/glass fiber composites, Polym. Compos. 38 (2017) 2743–2752. https://doi.org/10.1002/pc.23872.

[16] Q. Wu, K. Chi, Y. Wu, S. Lee, Mechanical, thermal expansion, and flammability properties of co-extruded wood polymer composites with basalt fiber reinforced shells, Mater. Des. 60 (2014) 334–342. https://doi.org/10.1016/j.matdes.2014.04.010.

[17] H.T. Nguyen, K.T.Q. Nguyen, T.C. Le, L. Soufeiani, A.P. Mouritz, Predicting heat release properties of flammable fiber-polymer laminates using artificial neural networks, Compos. Sci. Technol. 215 (2021). https://doi.org/10.1016/j.compscitech.2021.109007.

[18] M. Debuyser, J. Sjöström, D. Lange, D. Honfi, D. Sonck, J. Belis, Behaviour of monolithic and laminated glass exposed to radiant heating, Constr. Build. Mater. 130 (2017) 212–229. https://doi.org/10.1016/j.conbuildmat.2016.09.139.

[19] H. Yang, Y. Jiang, H. Liu, D. Xie, C. Wan, H. Pan, S. Jiang, Mechanical, thermal and fire performance of an inorganic-organic insulation material composed of hollow glass microspheres and phenolic resin, J. Colloid Interface Sci. 530 (2018) 163–170. https://doi.org/10.1016/j.jcis.2018.06.075.

[20] J. Kim, J.H. Lee, S. Kim, Estimating the fire behavior of wood flooring using a cone calorimeter, J. Therm. Anal. Calorim. 110 (2012) 677–683. https://doi.org/10.1007/s10973-011-1902-1.

[21] F. Girardi, E. Cappelletto, J. Sandak, G. Bochicchio, B. Tessadri, S. Palanti, E. Feci, R. Di Maggio, Hybrid organic-inorganic materials as coatings for protecting wood, Prog. Org. Coatings. 77 (2014) 449–457. https://doi.org/10.1016/j.porgcoat.2013.11.010.

[22] M.J. DiDomizio, P. Mulherin, E.J. Weckman, Ignition of wood under time-varying radiant exposures, Fire Saf. J. 82 (2016) 131–144. https://doi.org/10.1016/j.firesaf.2016.02.002.

INFLUENCE OF HYBRIDIZATION ON THE MECHANICAL PROPERTIES OF SISAL/CARBON AND SISAL/GLASS FIBER METAL LAMINATES

Vilson D. Libera Junior [(a), *], Sandra M. da Luz [(b)]

(a) 0000-0001-5557-7331 (Federal Institute of Education, Science and Technology of Goiás – Brazil)
(b) 0000-0002-2223-0021 (University of Brasília – Brazil)
* Corresponding author: vilson.dalla@ifg.edu.br

Abstract: Fiber-metal laminates (FML) are advanced composite materials that combine the desirable properties of metals and fiber-reinforced polymer (FRP), effectively overcoming the limitations of each material individually. This combination improves the fatigue and impact resistance compared to conventional monolithic aluminum. Despite this, the difference between the individual mechanical properties of raw FML composition results in delamination and premature failure in structural applications. Natural fibers can be an excellent alternative to solve this issue as they have low modulus and moderate elongation. Furthermore, these environmentally friendly fibers can increase the FML's sustainability. In this context, this study aims to evaluate the influence of hybridization on the mechanical properties and failure mechanism of hybrid fiber metal laminates with sisal and synthetic fibers. Initially, synthetic fiber (carbon and glass) and sisal fiber prepregs were produced. FRP, FMLs, and hybrid FLMs groups were manufactured through hot-pressing. The FMLs cluster had a metallic layer of 2024-T3 aluminum on the external face. Data on the tensile mechanical properties of all laminates were obtained through tensile tests coupled with the Digital Image Correlation (DIC) technique. Microtomography was conducted on the fracture region after the specimen's tensile test, and the images were used to evaluate the extent of damage and its influence on the mechanical properties. Individual analysis of FRP laminates showed distinct mechanical behaviors among the FRP laminates. The addition of the metallic layer and the production of FML directly influenced the mechanical properties, with moderate changes in mechanical strength, strain, and Young's modulus, except in the sisal FML, where tensile strength was enhanced compared to individual sisal FRP. Hybrid FMLs adjusted properties according to the nature of the fibers, with good compatibility between fibers, which exhibited similar modulus. Microtomography revealed early breakage of carbon fibers in the hybrid composites, resulting in low deformation in the specimen, affecting their final mechanical strength. The total breakage of sisal fibers was not observed, indicating the better elongation of this fiber. Delamination between layers in the hybrid laminates was observed and can be associated with the deformation incompatibility between the applied fibers.

1. INTRODUCTION

Fiber-metal laminates (FML) are advanced composite materials that combine the desirable properties of metals and fiber-reinforced polymer (FRP), effectively overcoming the limitations of each material individually [1]. This combination improves the fatigue and impact resistance compared to conventional monolithic aluminum. Carbon and glass are the most investigated and used fibers in FMLs [2].

Despite the FML's advantages, the difference between the individual mechanical properties of raw layer composition results in delamination and premature failure in structural applications [3]. To solve this issue, incorporating natural fibers can be a good alternative, as they have low modulus and moderate elongation. Furthermore, these fibers are environmentally friendly and can increase the FML's sustainability.

Biocomposites reinforced with natural fibers have been used in various applications and stand out for their low cost and non-abrasive properties during processing [4]. However, polymer composites reinforced with natural fibers can be limited to non-structural applications due to their susceptibility to biodegradation at high humidity and temperature and the high variability in mechanical properties [5,6]. Consequently, a standard method for overcoming these problems is "hybridization", i.e. combining natural fibers with synthetic fibers, which improves the mechanical properties of the final composite [7].

The mechanical properties of FMLs in engineering structures have been extensively explored through physical tests, numerical methods, analytical models, bending performance, impact resistance, and fatigue evaluation. Studying these properties and other analysis techniques, such as Digital Image Correlation (DIC), has been growing steadily. This method can be applied to measure the deformations of the hybrid component. Generally, they indicate that the FML increased strength and strain rate depends on the nature and sequence of stacking between the metal and FRP layers [8–10]. X-ray microtomography is another interesting technique for observing the fracture modes of FML compounds. This analysis makes it possible to visualize and analyze the internal structure and fracture mechanisms of FMLs at a microscale level [11]. In this context, this study aims to evaluate the influence of hybridization on the mechanical properties and failure mechanism of hybrid fiber metal laminates with sisal and synthetic fibers.

2. METHODOLOGY

2.1. Materials

The prepregs were produced using unidirectional sisal fabrics, prepared according to the procedure described in [12]. Unidirectional carbon fiber (UC300) and glass fiber E fabrics (VEW130), both from Barracuda Advanced Composites, were used as the polymeric matrix. Araldite® LY 1564 epoxy resin and Aradur® 22962 curing agent from Huntsman Advanced Materials were also used.

The aluminum alloy used to produce the FMLs was aeronautical aluminum 2024-T3, with 0.5 mm thickness. Aluminum sheets were cut and anodized according to the technique explained in Libera Junior et al. [12].

2.2. Prepregs manufacturing

The matrix solution was produced at room temperature by mixing appropriate quantities of DGEBA epoxy monomer with the curing agent. The resin/curing agent ratio used was 25 phr as recommended by the manufacturer. The resin/curing agent combination was degassed for 5 minutes in an ultrasonic bath in a Kondorteck device.

Subsequently, unidirectional sisal, carbon, and glass fabrics were impregnated with the matrix solution by manual lamination using a flexible spatula and a cylindrical compressor roller. The final thickness of the sisal fiber prepreg was ~0.5 mm, and the carbon and glass fiber prepreg's thickness was ~0.35 mm. The fiber volume fraction about the matrix for all the prepregs was around 50%. The prepregs produced were packaged and protected from the weather using polyethylene film.

The prepregs were left to cure for 3 hours at room temperature (~25°C) until the matrix in the prepreg appeared as a sticky, semi-solid material (Stage B). Afterward, to slow down the matrix curing process, the prepregs were stored in a refrigerator at -18 °C for later production of FRP and fiber-metal laminates.

2.3. Production of FRP and FML laminates

This study produced two groups of laminates. The first group consists of three types of FRP laminates made from unidirectional carbon, glass, and sisal fiber prepregs. Their production is essential for obtaining the mechanical properties of each composite individually.

The second group consisted of two different types of FMLs: non-hybrids, characterized by the exclusive presence of a kind of FRP composite, and hybrids, which incorporate two different types of FRP composites in alternating compositions between synthetic FRP and natural fibers.

Table 1 show the composition and detailed distribution of the layers of FRP laminates and FMLs. The C_8 nomenclature represents, in sequence, the type of unidirectional prepreg used (C—carbon, G—glass or S—sisal) and the number of layers in the laminate (8, 6, 4, 2 or 1).

Table 1. Composition and layer distribution of FRP and FML laminates.

Laminate	Sequence	Number of layers				Thickness (mm)	Area density (g/cm²)
		A	C	G	S		
Aluminum	[Al]	1	0	0	0	0.491 ± 0.002	0.134 ± 0.000
Carbon	[C$_8$]	-	8	-	-	2.767 ± 0.053	0.291 ± 0.023
Glass	[G$_8$]	-	-	8	-	2.564 ± 0.113	0.400 ± 0.006
Sisal	[S$_6$]	-	-	-	6	2.177 ± 0.058	0.285 ± 0.009
Carall	[Al/C$_6$/Al]	2	6	-	-	3.297 ± 0.061	0.585 ± 0.005
Glare	[Al/G$_6$/Al]	2	-	6	-	3.052 ± 0.113	0.624 ± 0.025
Siral	[Al/S$_4$/Al]	2	-	-	4	2.649 ± 0.058	0.464 ± 0.015
CaSiral	[Al/C$_2$/S$_2$/C$_2$/Al]	2	4	-	2	3.087 ± 0.026	0.557 ± 0.009
SiCarall	[Al/S$_1$/C$_4$/S$_1$/Al]	2	-	4	2	3.133 ± 0.057	0.562 ± 0.012
GlaSiral	[Al/G$_2$/S$_2$/G$_2$/Al]	2	4	-	2	3.457 ± 0.072	0.648 ± 0.011
SiGlare	[Al/S$_1$/G$_4$/S$_1$/Al]	2	-	4	2	3.227 ± 0.039	0.626 ± 0.011

The laminates were manufactured using the hot compression molding technique in a hydraulic press with 300 x 300 mm heated plates (WABASH, 10000 psi). The prepregs were thawed at room temperature for 1 hour and then stacked on top of each other or on top of the aluminum layers according to the sequences set out in Table 1. The layers were placed under a peel-ply film, followed by a layer of release film, as shown in the diagram in Fig. 1.
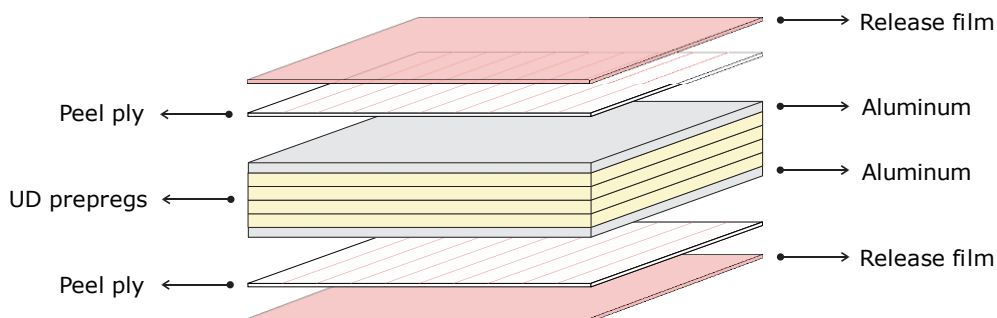
Figure 1. Layer stacking scheme for pressing the FMLs.

The material was then inserted into the machine press, where a pressure of 5 MPa was applied. The plates were then heated at a rate of 5 °C/min between room temperature and 80 °C, after which the set was kept in an isotherm for 30 min. After the curing time, the heating was stopped, and the composites were removed. The plates were then subjected to the post-curing process in an oven for 1 hour at a temperature of 100 °C.

2.4. Mechanical characterization coupled with DIC

To obtain the specimens from the FRP and FML laminate plates, a Newton mechanical guillotine cutting machine model 2x1220 mm was used. After cutting, the specimens were sanded on a sander (Polipan - 2D Double Motorized Polisher) for greater finish and dimensional accuracy.

The specimens for the DIC-coupled tensile test were prepared according to the recommendations of ASTM D3039 [13]. The surface of the specimens was then prepared for DIC analysis. In this procedure, the specimens were initially painted with white spray paint, and micro-drops of black paint were applied to the initially painted surface using a soft bristle brush (Fig. 2).
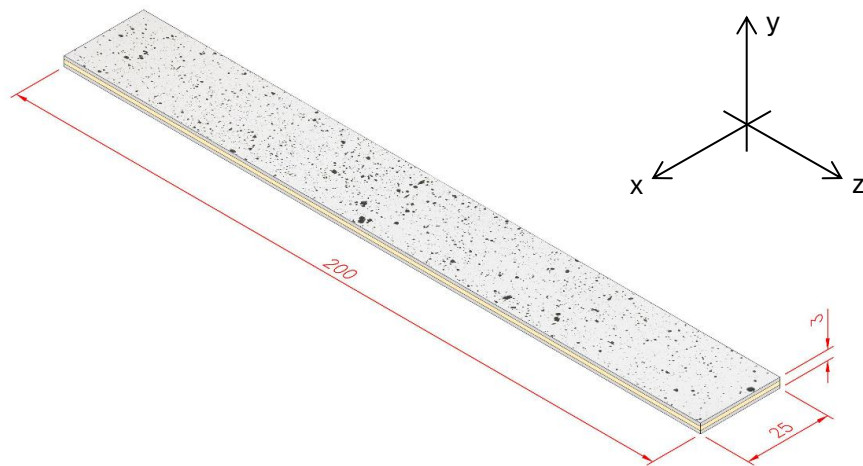
Figure 2. The finished specimen for tensile strength analysis coupled with DIC with prepared surface and dimensions in millimetres.

The tensile tests were carried out by ASTM D3039 [13]. They were carried out on a universal mechanical testing machine, INSTRON 8801, with a 100 kN load cell. Five specimens were tested for each group, and the test speed was 2 mm/min.

Specimens' deformation data during the tensile test was obtained using the DIC technique with the Dantec Dynamics Q-400 system. This system determines the three-dimensional properties of materials in tensile, torsion, bending, or combined tests. In this procedure, two cameras were installed in front of the mechanical testing machine, with the focus adjusted to the position of the specimen being analysed. A red lamp between the cameras evenly illuminated the sample's surface. During the test, images were captured at 1s intervals. The recording started at the same time as the tensile test, so the data obtained from both analyses could be synchronized later. The images were analysed, and the X and Y axes deformations were obtained using ISTRA 4D software (Dantec Dynamics).

2.5. X-ray microtomography and failure mechanism analysis

X-ray tomography analysis was carried out on the FML samples tested in the tensile test to assess the laminates' failure mechanism. The failure modes observed were associated and identified by ASTM D3039 [13]. In addition, the failures were correlated with the composition of the constituent layers, tensile strengths, and the occurrence of delamination in each group of FMLs.

The samples were scanned at the University of Brasilia using a HELISCAN MARK 1 platform. X-rays were generated using a voltage of 120 kV and a current of 80 μA. The helical scans (scan + vertical displacement) were carried out at an average voxel size of 12 μm and lasted between 1 and 4 hours, depending on the type of laminate. The beam source was configured with a microfocus for thin materials, and the flat screen detector had 3040×3040 pixels. The data was acquired using Qrumba software, and the images were reconstructed using Qmango software. Two images were selected for each FML group, one showing the fracture region in the transverse direction (XY axis) and the other in the longitudinal direction (YZ axis).

In addition, photographs of the longitudinal region showing the complete specimen were taken with a Canon EOS Rebel-T7 camera as supplementary material to analyze each PC's behavior after the test and evaluate the failure mechanism.

3. RESULTS AND DISCUSSION

3.1. Mechanical properties

The tensile stress-strain curves (σ - ε) for the FRP with single reinforcement (carbon, glass, and sisal), non-hybrids, and hybrids FMLs were obtained. The strain displayed in the curves of Fig. 3 corresponds to the y-axis strain measured using the DIC technique.

Maximum stresses and strains were recorded at the point of failure, illustrating a typical tensile failure of ductile materials. In general, the samples failed at the center of the specimen which may be related to the plane of maximum shear stress. Therefore, the effect of stress hardening is negligible in the presented stress-strain curves.
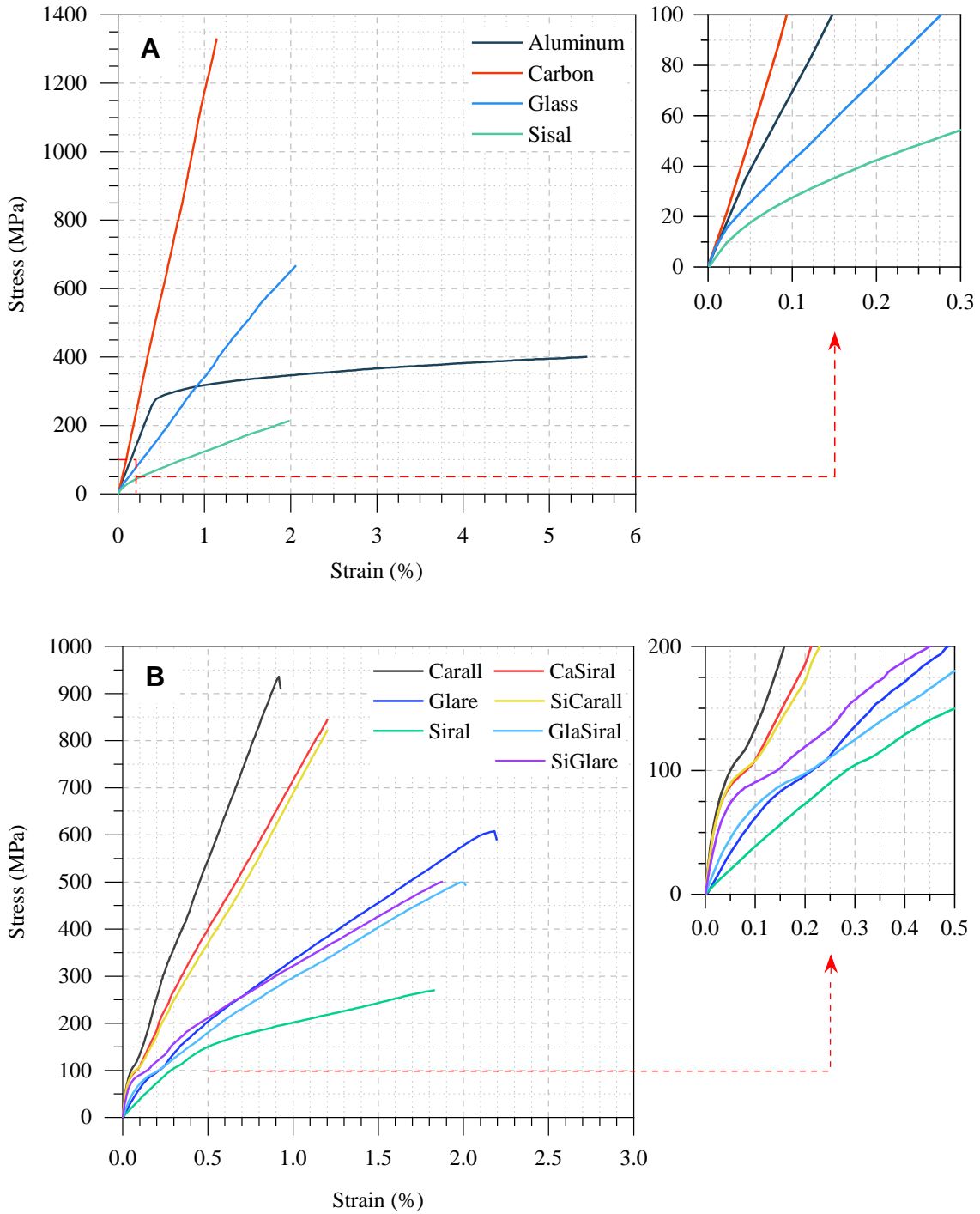
Figure 3. Stress-strain curves of Aluminum, FRP laminates (a) and FMLs (b).

The stress-strain curves of aluminum and FRP laminates shown in Fig. 3a behave differently due to the individual properties of each material, which significantly impact the potential hybridization process between the reinforcements. As expected, the carbon fiber composite showed the highest mechanical strength, followed by the glass and sisal fiber laminates.

In addition, the stress-strain curves of the FMLs shown in Fig. 3b indicate a similar behavior to that present by the FRP laminates individually. Furthermore, the FMLs combination of aluminum and FRP laminates produced a variation in the laminate's initial stage strain intensity [1]. Generally, it is also possible to observe a slight deviation of stress-strain curves between the non-hybrid and hybrid FMLs with the same synthetic fiber composition.

Table 2 summarizes the mean values of the tensile test data, such as failure stresses (σ_y), failure strains (ε_f), Young's modulus (E), and Poisson's ratio (n). Additionally, the standard deviation values were provided.

Table 2. Summary of tensile properties of Aluminum, FRP laminates, and FMLs.

Laminate Group	Laminate	Failure stress (σ_y) (MPa)	Failure Strain (ε_f) (%)	Young's modulus (GPa)	Poisson ratio (v)
Aluminum	Aluminum	387.31 ± 11.84	4.54 ± 0.75	73.61 ± 4.32	0.33 ± 0.02
FRP	Carbon	1269.49 ± 97.19	1.18 ± 0.08	112.51 ± 1.92	0.34 ± 0.01
	Glass	654.61 ± 33.50	2.08 ± 0.02	34.15 ± 2.41	0.27 ± 0.02
	Sisal	188.15 ± 24.09	1.80 ± 0.21	19.86 ± 0.95	0.46 ± 0.01
Non-hybrids FMLs	Carall	903.35 ± 0.09	0.98 ± 0.09	101.85 ± 1.59	0.34 ± 0.01
	Glare	508.86 ± 0.11	2.27 ± 0.11	47.75 ± 1.51	0.29 ± 0.03
	Siral	260.78 ± 0.09	1.92 ± 0.09	41.72 ± 1.98	0.41 ± 0.01
Hybrids FMLs	CaSiral	869.23 ± 0.09	1.33 ± 0.09	77.86 ± 4.04	0.37 ± 0.01
	SiCarall	827.97 ± 0.06	1.33 ± 0.06	79.98 ± 0.39	0.38 ± 0.01
	GlaSiral	483.6 ± 0.09	2.13 ± 0.09	43.98 ± 1.99	0.34 ± 0.01
	SiGlare	505.5 ± 0.18	2.14 ± 0.18	44.16 ± 2.8	0.34 ± 0.01

As anticipated, the FML Carall exhibited the highest tensile strength following the carbon fiber FRP performance. Nevertheless, a slight decrease in tensile strength was noted after incorporating aluminum into the FML [14]. This can be attributed to the significant elongation of aluminum and its low strength as shown in Fig. 3a. It can be observed that the hybridization of FML did not significantly affect its mechanical properties, as the CaSiral and SiCarall laminates exhibit a reduction in strength of 7.2% and 12.7%, respectively. The same behavior was observed for hybrid FMLs with sisal and glass fibers.

According to the hybridization effect in FMLs, the position of the sisal FRP layer did not significantly affect the hybrid FML's mechanical properties. However, in FMLs GlaSiral and SiGlare, it was observed that the sisal fiber core was 4.3% less effective in improving tensile properties.

3.2. Failure mechanism analysis by X-ray microtomography

Fig. 4 shows the X-ray microtomography of hybrid FMLs composed of carbon and sisal FRPs. Two images were selected for each FML, with one illustrating the fracture area (region of interest) in the transverse direction (XY) and the other in the longitudinal direction (YZ). The fractures were evaluated by considering not just the size and arrangement of the cracks but also how the different FML layers interacted with each other.
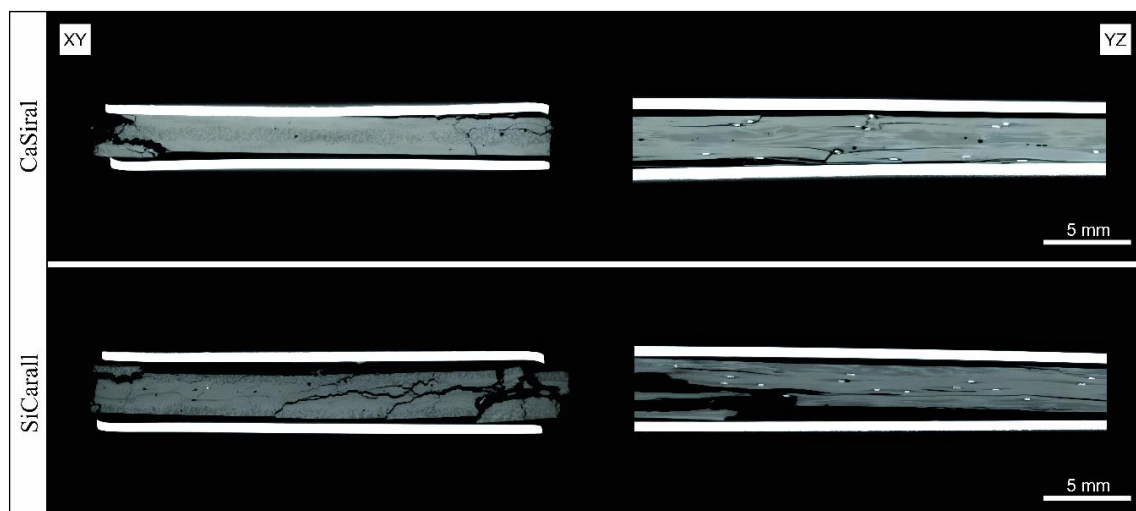
Figure 4. X-ray microtomography of CaSiral and SiCarall hybrid FMLs.

In the CaSiral FML, it is observable that the fracture has extended throughout the FRP layers. However, observing the longitudinal specimen fracture, while the carbon FRP layer suffered several fractures,

the sisal FRP layer remained unbroken. This phenomenon can be attributed to the more considerable elongation in the sisal FRP, as observed in Fig. 3a, indicating that sisal fibers inside the hybrid FML contributed to better stress dispersion, improving tensile properties [11]. In contrast, both layers of FRP in the SiCarall FML present an early delamination, which resulted in the layers breaking when the specimen failed.

X-ray microtomography of GlaSiral and SiGlare hybrid FMLs is shown in Fig. 5. In contrast to FMLs manufactured with carbon fiber, the sisal and glass fibers interacted more efficiently due to their similar Young's modulus. Consequently, both fibers exhibited nearly elongation, resulting in uniform layer rupture. However, the XY cross-sectional photography reveals a roughly fractured glass fiber FRP due to its inherently brittle nature. The hybridization pattern improved glass and sisal fiber interaction because of the associated elongation properties, as data in Table 2 indicates better interaction in this laminate.
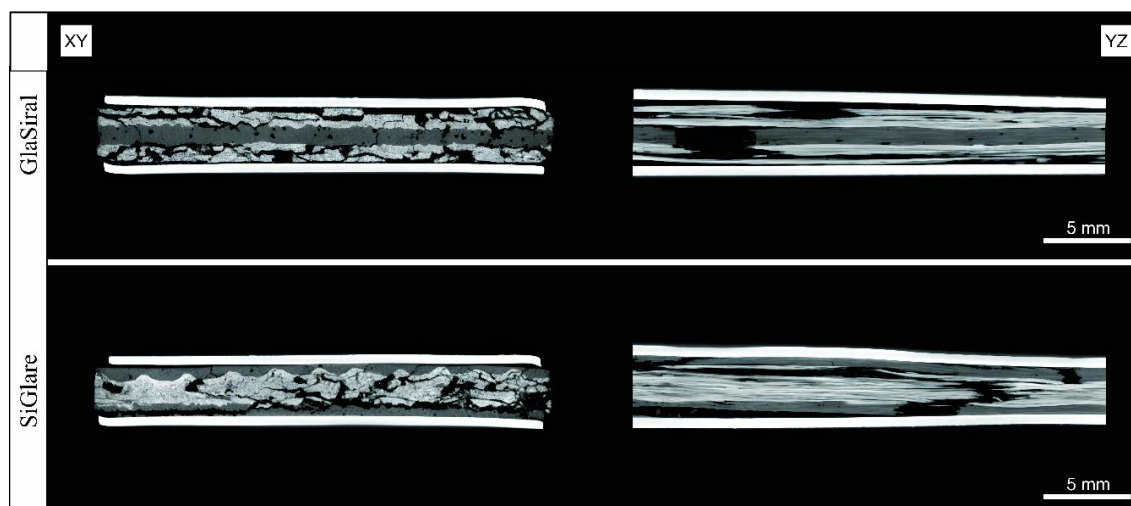
Figure 5. X-ray microtomography of GlaSiral and SiGlare hybrid FMLs.

4. CONCLUSIONS

The stress-strain curves of FRP with single reinforcements and hybrid FMLs displayed distinct mechanical behaviors influenced by the properties of the composition materials. Carbon fiber composites, followed by glass and sisal fibers, exhibited the highest strength. Among FMLs, Carall had the highest tensile strength. The stress-strain curves indicated minimal differences between non-hybrid and hybrid FMLs, suggesting that hybridization with natural fibers did not significantly change their mechanical properties, an excellent effect for obtaining more sustainable composites.

Hybridization of FMLs did not significantly impact tensile stress, with CaSiral and SiCarall showing 7.2% and 12.7% strength reductions, respectively. Similar behavior was observed in hybrid FMLs GlaSiral and SiGlare. Sisal and glass fibers interacted more efficiently in these laminates because of their similar Young's modulus, resulting in uniform elongation before the layers ruptured. According to the X-ray microtomography analysis, CaSiral showed early fractures in the carbon FRP layer, while sisal FRP remained intact due to better elongation and stress dispersion. Despite this, GlaSiral and SiGlare had efficient sisal-glass fiber interaction, leading to uniform deformation at rupture.

In this context, the FML hybridization had no significant impact on its mechanical properties, making it a more environmentally friendly and sustainable option than traditional FML materials.

4.1. Declaration of Competing Interest

The authors declare no conflict of interest.

4.2. Acknowledgments

5. REFERENCES

[1] Sasso M, Mancini E, Dhaliwal GS, Newaz GM, Amodio D. Investigation of the mechanical behavior of CARALL FML at high strain rate. Compos Struct 2019; 222:110922. https://doi.org/10.1016/j.compstruct.2019.110922.

[2] Ding Z, Wang H, Luo J, Li N. A review on forming technologies of fibre metal laminates. International Journal of Lightweight Materials and Manufacture 2021; 4:110–26. https://doi.org/10.1016/j.ijlmm.2020.06.006.

[3] Boer T de. Next Generation Fibre Metal Laminates. Fibre Metal Laminates 2001:39–51. https://doi.org/https://doi.org/10.1007/978-94-010-0995-9_3.

[4] Libera Junior VD, Teixeira LA, Amico SC, Maria da Luz S. Processing, thermal and mechanical properties of composite laminates with natural fibres prepregs. Polymers and Polymer Composites 2022;30. https://doi.org/10.1177/09673911221087591.

[5] Teixeira LA, Libera Junior VD, Luz SM. Chemical treatment of curaua fibres and its effect on the mechanical performance of fibre/polyester composites. Plastics, Rubber and Composites 2021;50:189–99. https://doi.org/10.1080/14658011.2020.1862978.

[6] Al-Hajaj Z, Sy BL, Bougherara H, Zdero R. Impact properties of a new hybrid composite material made from woven carbon fibres plus flax fibres in an epoxy matrix. Compos Struct 2019; 208:346–56. https://doi.org/10.1016/j.compstruct.2018.10.033.

[7] Khalid MY, Al Rashid A, Arif ZU, Ahmed W, Arshad H, Zaidi AA. Natural fibre reinforced composites: Sustainable materials for emerging applications. Results in Engineering 2021; 11:100263. https://doi.org/10.1016/j.rineng.2021.100263.

[8] Sun J, Daliri A, Lu G, Ruan D, Lv Y. Tensile failure of fibre-metal-laminates made of titanium and carbon-fibre/epoxy laminates. Mater Des 2019; 183:108139. https://doi.org/10.1016/j.matdes.2019.108139.

[9] Sharma AP, Khan SH, Parameswaran V. Experimental and numerical investigation on the uni-axial tensile response and failure of fibre metal laminates. Compos B Eng 2017; 125:259–74. https://doi.org/10.1016/j.compositesb.2017.05.072.

[10] Sharma AP, Velmurugan R. Uni-axial tensile response and failure of glass fibre reinforced titanium laminates. Thin-Walled Structures 2020; 154:106859. https://doi.org/10.1016/j.tws.2020.106859.

[11] Hussain M, Imad A, Nawab Y, Saouab A, Herbelot C, Kanit T. Effect of matrix and hybrid reinforcement on fibre metal laminates under low–velocity impact loading. Compos Struct 2022;288. https://doi.org/10.1016/j.compstruct.2022.115371.

[12] Libera Junior VD, Luz SM. Experimental processing of fibre-meal laminates with hybrid reinforcement of Synthetic and natural fibres composites. 6th Brazilian Conference on Composite Materials, 2022, p. 317–22.

[13] ASTM International. ASTM D3039 - Standard Test Method for Tensile Properties of Polymer Matrix Composite Materials. Annual Book of ASTM Standards 2017. https://doi.org/10.1520/D3039.

[14] He W, Wang C, Wang S, Yao L, Cui L, Xie D. Characterizing and predicting the tensile mechanical behavior and failure mechanisms of notched FMLs—Combined with DIC and numerical techniques. Compos Struct 2020;254. https://doi.org/10.1016/j.compstruct.2020.112893.

TORSIONAL TEST ON GLASS/EPOXY AND SISAL/EPOXY TUBULAR COMPOSITES

Celso A. M. Oliveira [a], Linconl A. Teixeira [b], Larissa C. Ribeiro [c]*, Sandra M. Luz [d].

(a) 0009-0003-3288-2300 Automotive Engineering (University of Brasília – Brazil)
(b) 0000-0002-2922-3027 Engineering Materials Integrity Graduate Program (University of Brasília – Brazil)
(c) 0009-0000-6596-2081 Aerospace Engineering (University of Brasília – Brazil)
(d) 0000-0002-2223-0021 Engineering Materials Integrity Graduate Program (University of Brasília – Brazil)
* Corresponding author: larissa.ribeiro013@gmail.com

CODE: BCCM7-39

Abstract: Composite materials have been studied and validated through several tests. However, research on torsional behavior in tubular structures remains limited. Tubular configurations are standard in diverse engineering fields, and composites, particularly those reinforced with synthetic and natural fibers, hold promise for advancing technology by offering a combination of good strength and low density. This study aims to comparatively characterize laminated composite tubes fabricated from sisal fiber and glass fiber/epoxy through torsion tests. Prepregs were manufactured using the hand lay-up technique with synthetic glass fiber and pre-treated sisal fiber (5% w/v NaOH) to enhance matrix adhesion. The fiber and matrix volume ratio were kept constant at 30% (v/v) fiber and 70% (v/v) matrix to ensure a fair comparison. Specimens were fabricated using the roll wrap method, where prepregs were manually wound onto tubular molds and subjected to torsion tests to obtain torque-deformation curves. The analysis revealed that glass fiber has a superior torsional modulus, approximately 46% higher than sisal fiber. Nonetheless, sisal fiber demonstrates potential applicability as a substitute for glass fiber in select projects contingent upon specific performance criteria. This investigation provides valuable insights into the torsional behavior of composite materials, guiding material selection for engineering applications.

1. INTRODUCTION

Composite materials have emerged as an integral aspect of modern engineering and design, revolutionizing industries like aerospace and automotive, among others. The innovation in the composite area has allowed significant weight reduction in structural design. These materials strive to amalgamate two or more distinct physical properties from their constituents to create a novel material that excels in efficiency and sophistication for its intended purpose [1, 3].

Metals are known for their superior mechanical properties. However, they often lack in areas such as weight efficiency and environmental friendliness. In contrast, composite materials, particularly those composed of thermosetting epoxy matrices and synthetic fibers, struggle with recyclability issues [4, 5]. After thermosetting matrices undergo curing or polymerization, they cannot be repurposed, and any attempt to heat the material results in its degradation or a decline in structural integrity [6]. Addressing the ecological concerns associated with these synthetic composites requires the exploration of sustainable alternatives that offer comparable characteristics suitable for practical use. Natural fibers present a promising solution in this context.

Natural fibers offer a compelling alternative to synthetic fibers such as glass and carbon in composite materials. They boast biodegradability, good mechanical properties, and cost-effectiveness [7]. As environmentally friendly and cost-effective options, natural fibers are in high demand across industries,

ensuring a sustainable future for composite materials. Ongoing studies are exploring their potential in biodegradable polymers, aiming to boost their versatility and advantages [8]. One standout natural fiber for industrial applications is sisal (*Agave sisalana*), widely available in Brazil. However, natural fibers also face challenges in composite use, requiring compatibility with the matrix, especially polymeric ones, to maintain mechanical properties. Chemical treatments with alkaline solutions are commonly used to enhance adhesion by dissolving fiber amorphous portions [9].

Pre-impregnated materials or prepregs, among polymer composites, stand out for their ease of use, straightforward commercialization, and high-quality finish. Combined with well-preserved mechanical properties, these characteristics result in a highly marketable material widely employed across various high-performance industries [4, 5]. Prepregs involve impregnating fibers (in the form of unidirectional tapes or fabrics) with a semi-cured polymer resin matrix. To prevent further curing, they are stored at low temperatures and can be fully cured through either temperature or pressure increases upon use. An effective curing process is essential for maintaining material integrity [5].

Composite materials used in shafts, tubes, bars, and across industries require torsional behavior analysis. These components, including transmission shafts, steering rods, and drills, undergo torsion and are increasingly prevalent in Formula 1, aircraft, and conventional cars [10]. Torsion involves shear stress and deformation when torque is applied to a bar with any cross-section [11]. Therefore, this study aims to characterize and compare laminated sisal and glass fiber/epoxy composite tubes through torsion tests.

2. METHODOLOGY

2.1. Materials and Manufacturing

SisalSul from Brazil supplied the sisal fibers. Before the chemical treatment, the sisal fibers (average length 60 cm) were cut to a 20 cm length. Then, the sisal fibers were treated with a 5% (w/v) sodium hydroxide (NaOH) solution, and the fibers were mercerized at a ratio of 10:1 (solution: fiber) at 70 °C for 2 h under manual stirring. After the chemical treatment, the fibers were washed with distilled water until neutral pH and dried at room temperature for 120 h. The glass fiber (VRW700) was supplied by E-composites.

The polymeric matrix was prepared by mixing proper quantities of epoxy resin Araldite LY 1564 BR and a specific hardener Aradur 42 in a proportion of 100:25, both from HUNTSMAN. The composites were developed with 30% (v/v) by roll wrap method, and the fiber orientation was 45º for all composites, as shown in Fig. 1. Also, all composites had an internal diameter of 9.4 mm and an average length of 12 mm. The following materials were obtained: sisal/ epoxy and glass/ epoxy.
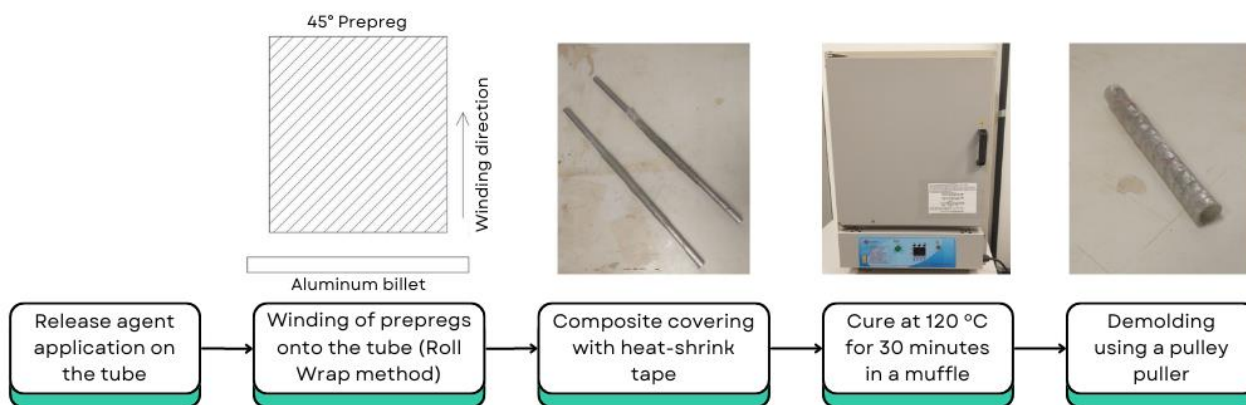
Figure 1. Steps to obtain the tubular composites.

2.2. Torsional Test

The torsional test was performed on a universal testing machine (Instron MT2, Instron, USA) equipped with 225 Nm (2000 lb-in) of torque and a maximum speed of 60 RPM. The test was carried out under a constant rotation speed of 1º/s. The angle of twist is defined by Eq. (1) [11]:

$$\phi = \frac{T.L}{G.J} \tag{1}$$

Where T is the torque, L is the tube length, G is the shear modulus, and J is the polar moment of inertia. The polar moment of inertia of the tube was determined using Eq. (2) [11]:

$$J_{tube} = \frac{1}{32}\pi.(de^4 - di^4) \tag{2}$$

Where de is the external diameter and di is the internal diameter.

3. RESULTS AND DISCUSSION

Fig. 2 shows the torsional curve obtained from the average samples of glass/epoxy and sisal/epoxy composites. The recorded torque for the glass/epoxy composites (sample 3) was 7.24 N·m at a torsion angle of 0.29 (16.6º). In contrast, the sisal/epoxy composites (sample 2) exhibited a torque of 5.01 N·m at a twist angle of 0.22 rad (13.2º). These values highlight the differential resistance capacities between the two materials.
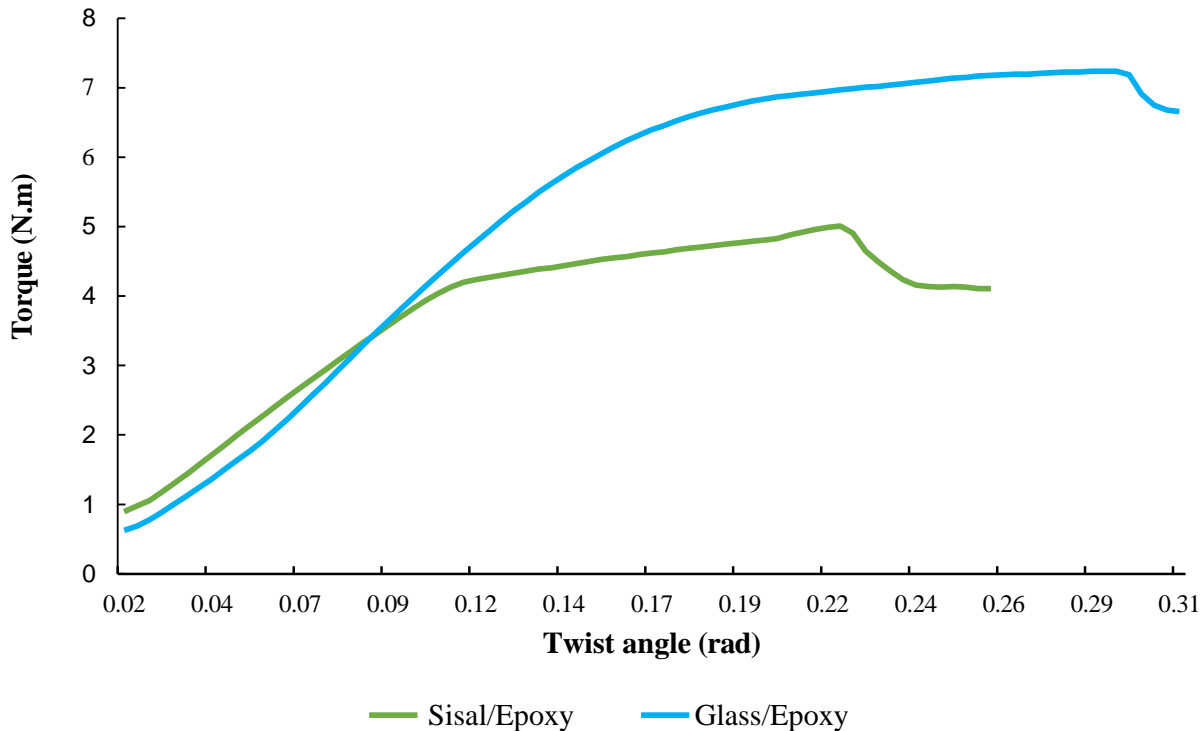
Figure 2. Torque vs. twist angle average samples of sisal/epoxy and glass/ epoxy composites.

The graph in Fig. (2) displays a nonlinear relationship between torque and twist angle for sisal/epoxy and glass/epoxy composites. Initially, both materials show a proportional increase in torque with the twist angle, indicating elastic behavior. However, as the twist angle increases, the torque for both composites deviates from linearity. For the sisal/epoxy composite, the torque peaks and then decreases, suggesting the onset of damage or material failure. The glass/epoxy composite exhibits a higher peak torque and a more pronounced nonlinearity, indicating a higher resistance to twisting but also showing signs of material failure at higher twist angles. This nonlinear behavior likely occurs due to the progressive damage accumulation in the material, micro-cracking, fiber-matrix debonding, and eventual failure under increasing torsional loads.

Given the complexity of the nonlinear behavior observed in Fig. (2), an approximate estimate of the shear modulus at the moment of fracture was made. Equation (2) was employed to determine the polar moment of inertia (J) for each sample. Utilizing the calculated polar moment of inertia and the data obtained from the torsion tests, the shear modulus for each sample was subsequently computed using Eq. (1), isolating the

parameter. Table 1 presents the results from the torsional tests conducted on glass/epoxy and sisal/epoxy composites, including the calculated parameters derived from these measurements.

Table 1. Torsional properties of sisal/epoxy and glass/epoxy composites.

Composite	Sample	Length (m)	Maximum Torque (N.m)	Break Angle (rad)	Moment of Inertia (10^{-9} m^4)	Shear Modulus (GPa)
Sisal/epoxy	1	0.102	6.70	0.23	1.935	1.54 ± 0.06
	2	0.100	5.01	0.23	1.730	1.26 ± 0.06
	3	0.102	2.32	0.12	1.572	1.25 ± 0.06
	4	0.097	3.00	0.11	2.260	1.17 ± 0.06
	5	0.104	5.24	0.17	2.296	1.39 ± 0.06
Average		-	4.45 ± 0.79	0.17 ± 0.026	-	1.32 ± 0.06
Glass/epoxy	1	0.098	8.51	0.20	1.730	2.41 ± 0.31
	2	0.097	7.57	0.16	1.605	2.86 ± 0.31
	3	0.097	7.24	0.29	1.487	1.62 ± 0.31
	4	0.101	8.20	0.15	1.654	3.34 ± 0.31
	5	0.098	7.10	0.21	1.630	2.03 ± 0.31
Average		-	7.72 ± 0.027	0.20 ± 0.025	-	2.45 ± 0.31

In mechanical strength tests, glass/epoxy composites exhibited significantly higher mechanical strength than sisal/epoxy composites. Specifically, a notable difference was observed in maximum torque values, with sisal fiber being 42% less effective. However, this disparity decreased when examining the break angle, showing a 15% advantage for glass/epoxy composites. Additionally, regarding shear modulus, glass/epoxy composites outperformed sisal fiber by approximately 46%. Overall, the results underscore the superior mechanical resistance of glass/epoxy composites over sisal/epoxy composites.

Notable differences emerge when comparing the torsional properties of glass/epoxy composites from these experiments to those reported in the article by Jun Ke et al. [12]. The experiments recorded a 7.24 N·m torque at a torsion angle 16.6º for glass/epoxy composites. In contrast, the article reports a significantly higher maximum torque of 40.33 N·m with a maximum rotation angle of 11.16º per unit thickness for pure glass fiber circular tubes. These discrepancies can be attributed to the superior mechanical properties and advanced fabrication techniques employed in the article's study, such as using a two-dimensional braiding method and specific resin infusion processes [12].

Comparing the results for sisal fiber composites with the pure ramie circular tubes discussed in the article by Jun Ke et al. [12], several distinctions in torsional performance and configuration are evident. The sisal/epoxy composites, configured with a unidirectional orientation of 45º, demonstrated a 5.01 N·m torque at a torsion angle of 13.2º. In contrast, the article reports that pure ramie circular tubes, configured using a two-dimensional braiding method, exhibited a higher maximum rotation angle of 13.97º per unit thickness and a maximum torque per unit wall thickness of 22.24 N·m. The ramie fibers' superior performance can be attributed to their higher tensile strength and Young's modulus, which enhance mechanical properties and provide a more effective stress distribution under torsional loads. Moreover, the two-dimensional braided configuration of the ramie fibers contributes to improved torsional stiffness and load transfer efficiency, compared to the unidirectional orientation of the sisal fibers. The superior interfacial bonding between ramie fibers and the resin matrix further enhances the load-bearing capacity of the ramie composites. This comparison underscores that while both fibers are sustainable options, ramie fibers, with their stronger mechanical properties and advantageous braided configuration, offer superior torsional resistance [12].

The torsional resistance of fiber-reinforced composites during testing is predominantly influenced by several characteristics of the fibers, including their inherent mechanical properties, the fiber content within the composite, fiber orientation, fiber length, and the quality of the fiber-matrix interface. These factors collectively play a crucial role in determining the overall torsional resistance of the composite material.

Despite glass fiber demonstrating superior mechanical properties compared to sisal fiber due to its higher strength, it was decided to utilize sisal fiber. This choice was influenced by sisal fiber's biodegradability and lower density relative to glass fiber. Furthermore, data on the torsional behavior of sisal fiber in the

literature is scarce. Despite a 46% reduction in strength compared to fiberglass, these attributes render sisal fiber a preferred choice for specific applications. Moreover, it was observed that fiber orientation and the manufacturing method significantly affect mechanical outcomes. All specimens were produced manually, which may introduce variability in the results. Specifically, the manufacturing process for sisal fiber is entirely manual, involving the manual stitching and arrangement of fiber sheets, potentially introducing errors associated with this process. In contrast, the glass fibers were perfectly oriented, mitigating this issue during manufacturing.

The high variations in the obtained shear modulus (G) values, particularly for the glass/epoxy samples (1.62 to 3.34 GPa) compared to the sisal/epoxy samples (1.17 to 1.54 GPa), can be attributed to several factors inherent to the materials and manufacturing processes. Glass fibers, while offering superior mechanical properties, can exhibit significant variability due to inconsistencies in fiber quality, alignment, and distribution within the epoxy matrix, as well as variations in the fiber volume fraction and curing conditions during composite fabrication. These factors contribute to a wider range of mechanical properties in glass/epoxy composites. In contrast, sisal fibers, being natural and typically hydrophilic, seemed to interact more consistently with the epoxy matrix due to the chemical treatment, resulting in a narrower range of G values. This suggests that while natural fiber composites may have lower absolute mechanical properties, they could offer more predictable and uniform performance.

During the development of the project, several difficulties were encountered. The first obstacle was the resin used in the prepreg: initially, the HEX-135 resin with FAST hardener cured quickly, making it difficult to roll the tube. Switching to LY 1564 resin, which has a slower curing process, facilitated handling. The second obstacle was the surface of the test specimen; the prepreg opened in the oven, but the use of shrink tape solved the problem, forming a smoother surface. The third obstacle was removing the tubes from the aluminum molds, which initially caused damage due to the cured resin adhering to the mold. Repeated application of release agent, forming a thin film, allowed for the removal of the tubes without damage.

4. CONCLUSIONS

Torsional tests on sisal/epoxy and glass/epoxy tubular composites revealed that glass/epoxy composites have a superior torsional modulus, attributed to the inherent strength and consistent orientation of glass fibers. In contrast, sisal/epoxy composites, while exhibiting a lower torsional modulus, offer notable advantages such as biodegradability and lower density. These results suggest that optimizing fiber arrangement and improving matrix adhesion with natural fibers could significantly enhance the properties of natural fiber composites.

To enhance sisal/epoxy composites, better fiber alignment can reduce stress concentrations and improve load distribution, while improved adhesion between fibers and the matrix increases stress transfer efficiency. Overall, although glass/epoxy composites currently outperform sisal/epoxy composites, advancements in fiber arrangement and adhesion could significantly improve the performance of sisal/epoxy composites, making them a viable, sustainable, and lightweight alternative.

4.1. Declaration of Competing Interest

The authors declare no conflict of interest.

4.2. Acknowledgments

5. REFERENCES

[1] B. L. S. Lopes. *Polímeros reforçados por fibras vegetais uma revisão sobre esses compósitos.* 1st Edition, 2017. Blucher. (978-85-8039-292-0).

[2] T. Sinmazçelik et al. A review: Fibre metal laminates, background, bonding types and applied test methods. *Materials & Design*, Volume 32, 2011. (https://doi.org/10.1016/j.matdes.2011.03.011).

[3] C. A. M. Oliveira. Análise torsional comparativa entre laminados de fibras de vidro e sisal em compósitos tubulares. Bachelor's dissertation. University of Brasília, Brasília, 2023.

[4] K. K. Kar. *Composite materials: processing, applications, characterizations*, 2017. Springer Berlin Heidelberg. (978-36-6249-514-8).

[5] H. Lengsfeld et al. *Composite Technology: Prepregs and Monolithic Part Fabrication Technologies,* 2nd Edition, 2021. Carl Hanser Verlag. (978-1-56990-825-9).

[6] V. D. Libera Junior. Laminados de fibra de curauá/epóxi obtidos a partir de pré-impregnados. Master's dissertation. University of Brasília, Brasília, 2019.

[7] A. B. Bevitori. Avaliação das Propriedades e Estrutura de Fibras de Rami e seus Compósitos Poliméricos. Doctoral dissertation. State University of North Fluminense, Rio de Janeiro, 2014.

[8] J. N. Seixas, J. E. GRANADA. Compósitos de Polipropileno Reforçados com Fibras Naturais do Talo da Banana em Diferentes Granulometrias. *Revista Brasileira de Engenharia e Sustentabilidade*, Volume 5, 2018. (https://revistas.ufpel.edu.br/index.php/rbes/article/view/279).

[9] L. A. Teixeira. O efeito da modificação química das fibras de curauá nas propriedades morfológicas, térmicas e mecânicas de compósitos de poliéster. Master's dissertation. University of Brasília, Brasília, 2019.

[10] M. C. Rezende, E. C. Botelho. O Uso de Compósitos Estruturais na Indústria Aeroespacial. *Polímeros: Ciência de Tecnologia*, Volume 10, 2000.

[11] F. P Beer et al. *Torsion*. In: *Mechanics of Materials*, 8th Edition, 2019. McGraw Hill. (978-12-6011-327-3).

[12] K. Jun et al. Torsional mechanical properties and damage mechanism of glass fiber-ramie hybrid circular tube. *Composite Structures*, Volume 327, 2024. (https://doi.org/10.1016/j.compstruct.2023.117680).

CHARACTERIZATION OF DAMAGE DUE TO BALLISTIC IMPACT ON THIN-WALLED EPOXY FIBERGLASS LAMINATES

*Gabriel B.P. de Knegt[a], Danilo F. Duarte [b,] Bruno Telles [c,] Artem Andrianov [d]

(a) ⓘ 0009-0008-8642-204X (University of Brasília – Brazil)
(b) ⓘ 0009-0000-7676-1656 (University of Brasília – Brazil)
(c) ⓘ 0000-0003-2106-9085 (Civil Police of the Federal District – Brazil)
(d) ⓘ 0000-0002-3987-6267 (University of Brasília – Brazil)
* Corresponding author: gabriel.knegt@aluno.unb.br

Abstract: The paper presents the results of the damage characterization due to a ballistic impact of a 0.22 projectile in 1-1.5 mm thick epoxy fiberglass laminates manufactured by various techniques. The focus of the study is on the assessment of the applicability of the damage data for a shooting incidence reconstruction. The constituents of the laminates are epoxy resins of cold and hot curing, plane weave and biaxial E-glass clothes, and glass roving. The characterization of the laminates involves optical microscopy and standard test method for flexural stiffness. The damages caused by straight-shooting and shooting at an angle of 45° are characterized by the ellipse method and evaluation of the delaminated area by image processing. The damage produced by the ballistic impact varies with the technique, manufacturing quality, and reinforcement pattern of the thin-walled fiberglass laminates.

1. INTRODUCTION

Glass fiber-reinforced polymers (GFRP) or fiberglass plastics are typical representatives of fiber-reinforced polymer composites that can be found in everyday life in civil engineering, electronics, furniture, piping, and transport vehicles [1]. Among other synthetic fibers, glass fibers are the most widely used due to their availability and cost-effective properties [2]. The market of GFRP is growing fast and wide, and the number of scientific publications about fiberglass is still increasing [3]. Several techniques were developed for the manufacturing of GFRP [4]. In these conditions, it seems that GFRP together with other polymer composites are displacing conventional materials and may become a subject matter of common scene evidence in criminalistics, for instance, as a structural component of an aircraft or a sailboat with traces of a ballistic impact. The effects of a ballistic impact, such as the shape and dimension of the hole, the projectile's entrance or exit side, and the direction of travel of the projectile are of great importance in a shooting incidence reconstruction [5]. These effects are well-studied in commonly used materials, such as metals, glass, plastics, etc [6]. The study of ballistic impact on GFRP was initiated during World War II to evaluate its ballistic protection performance [7]. Until the present moment, the ballistic protection performance of GFRP has been under investigation both individually and in comparison with other polymer composites [8,9].

The effects of a high-velocity ballistic impact (above 100 m/s) are related to the local response of the targeted composite [10]. Several failure mechanisms, which have been observed as the local response of a general laminate, occur in stages throughout the penetration process and depend on indenter geometry. These mechanisms are delamination (matrix cracking), fiber tension failure (fiber breakage, which can be followed by a petal formation on the exit side of a laminate), transverse shear failure (punching or shear plugging), hole expansion (compression of the fibers around the indenter) and hole friction. No information was found on the local response of the targeted GFRP composite, whose thickness is significantly less than 3 mm. There is also

little information on the effect of the manufacturing methods and related defects on the mechanical properties of the GFRP composite, which may affect the elastic response of the laminate to a ballistic impact.

The objective of the presented study is to evaluate and characterize the damage of the orthogonal and oblique ballistic impact produced by low caliber projectiles in 1-1.5 mm thick GRFP laminates manufactured by different techniques with the use of various reinforcement and matrix materials.

2. METHODOLOGY

2.1. Materials and manufacturing techniques

Several techniques and glass fibers were used to manufacture 1-1.5 mm GFRP laminates (Table 1). In the hand lay-up, glass cloth was positioned on the plane surface of an aluminum female mold, which was covered with a carnauba release wax, and wetted with liquid resin using a consolidation roller (Figure 1a). After impregnation and overlapping of 5 plies, the press-type female mold was covered by a male closure. The distance between the plane surfaces of the female mold and male closure was regulated to control the thickness of the laminate.

In the vacuum bagging, the sealant tacky tape was placed around the perimeter of a 6 mm thick tempered glass covered with a carnauba release wax. The glass cloth was laid up over the glass and wet out manually with a roller. Then the impregnated plies were covered with a release fabric and breather material and put under vacuum in a thin-film bag to compact the laminate and remove excess resin (Figure 1b). In the infusion vacuum process, the installation was the same as in the previous technique except that the resin was driven into the laminate through a flow-media positioned between the transparent thin-film bag and the release fabric (Figure 1c). A different non-woven reinforcement, more appropriate for the manufacturing method, was used.

In the wet filament winding process, the glass roving was wound over a plastic mandrel (Figure 2a) in such a way that the layup over the cylindrical part of the mandrel, made of a Ø150mm smooth PVC tube, and printed PETG domes would be [±45]. Then the uncured structure was covered with release fabric to cut out the pre-impregnated laminate over the cylindrical part of the mandrel (Figure 2b). Finally, the separated rectangular portion of the laminate was cured in the same mold that was used for the hand lay-up process (Figure 2c).

Table 1. Materials and manufacturing techniques.

Method (laminate series)	Number of plies	Reinforcement	Resin / hardener (viscosity at 25°c, MPa·s / cure schedule)
Vacuum bagging (VB)	5	Plain weave E glass cloth, 300 g/m^2	Araldite LY5052 / Aradur 5052 (600-700 / 7 days at 25°C)
Vacuum infusion (VI)	5	Biaxial non-woven E glass fabric [±45], 300 g/m^2	
Hand lay-up (HL)	5	Plain weave E glass cloth, 300 g/m^2	Araldite LY 1564 / Araldite XB 3473 (1000-1200 / 30 min at 130°C + 12 h at 160°C)
Filament winding (FW)	1	Glass roving 2400 tex, angle-ply layup [±45]	

2.2. Characterization

The flexural stiffness was measured following the ASTM D 7264/D 7264M – 07 standard following Procedure A, a three-point system where simply supported beam is loaded at its center [11]. For all manufacturing methods used, the 13-mm width specimens were cut in such a way that about half of the fibers would be oriented in the spanwise direction of the specimen. The optional support span-to-thickness ratio of 40:1 was used for most of the laminates (HL, VI, and VB) except those manufactured by filament winding, whose span-to-thickness ratio was 16:1, since the specimens were too thin to use the 40:1 ratio. The density of the laminates was measured by the water displacement method.

The void volume ratio (porosity) was determined using an optical technique based on image analysis of micrographs of transverse cross sections of the coupons. The void volume ratio was calculated as a ratio of the area covered by black pixels representing voids and pores to the total area within the frame of the

micrograph. The thresholding tool of the open-source software ImageJ 1.53e was used to determine the area of black pixels on the 8-bit micrograph with a magnification of 100x.

| (a) | (b) | (c) |
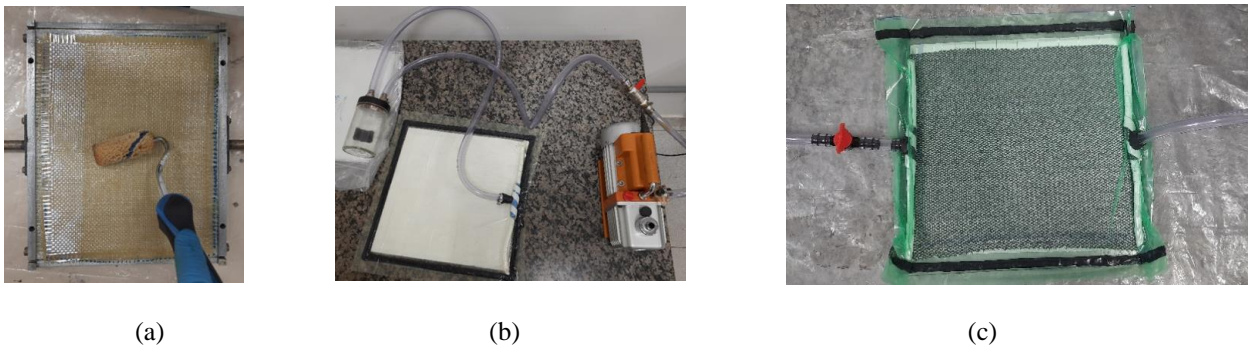
Figure 1. Manufacturing of the GFRP laminates by (a) hand lay-up, (b) vacuum bagging, and (c) vacuum infusion processes.

| (a) | (b) | (c) |
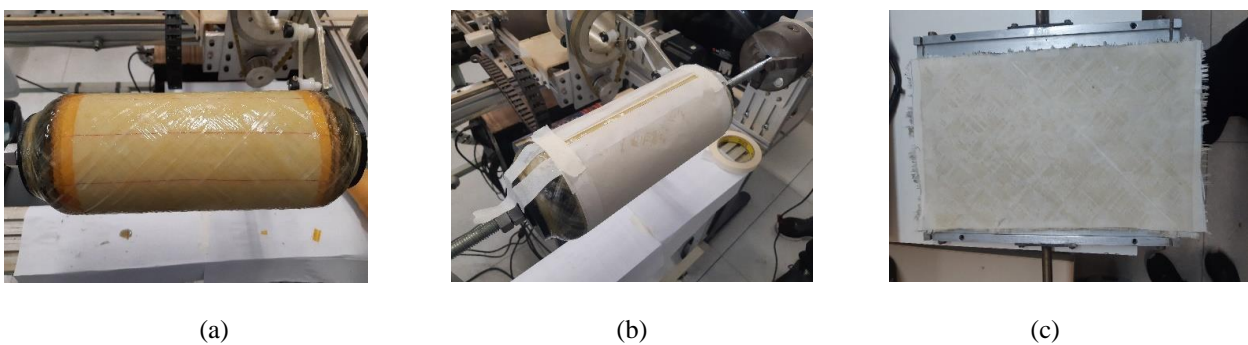
Figure 2. Manufacturing of the GFRP laminates by filament winding: (a) winding over a plastic mandrel, (b) preparation of the laminate to cut out the ±45 ply wound over the cylindric part of the mandrel, (c) wound laminate on the plane surface of the female mold.

The laminates were subjected to a ballistic impact of a 0.22 caliber projectile with kinetic energy of 159J. Each target laminate was positioned 1 meter beyond the muzzle of a firearm and fixed onto a cardboard shooting target by only two bulldog clips. The effects of at least two values of incidence angle θ (the angle between the projectile velocity vector and the laminate surface) were under investigation (Table 2), the different angles were achieved by moving the weapon to the desired incidence angle while keeping the same range from the laminates.

Table 2. Number and thickness of specimens.

Manufacturing technique and the abbreviation of the laminate series	The number of specimens (and mean thickness in mm ± coefficient of variation) at the given test conditions	
	0.22 caliber	
	$\theta = 90°$	$\theta = 45°$
Vacuum bagging (VB)	5 (1.22±1.6%)	6 (1.47±0.9%)
Vacuum infusion (VI)	4 (1.32±3.1%)	4 (1.44±2.7%)
Hand lay-up (HL)	3 (1.31±5.3%)	3 (1.16±2.2%)
Filament winding (FW)	10 (1.12±17.3%)	6 (1.17±3.3%)

The damage produced by the ballistic impacts was photographed from the entrance side. Besides the qualitative assessment of the observed damages, the images were used to measure the delaminated area with the software ImageJ. After the images had been properly scaled, the delaminated area was delimited with the polygon section tool (Figure 3a) and automatically measured by the software.

The ellipse method was used to estimate the incidence angle of a projectile [6,12]. In the method, the damaged site of the laminates subjected to an oblique ballistic impact is delimited with an ellipse, whose semi-axes are measured (Figure 3b). In the study, the procedure was carried out by two independent persons to estimate the repeatability and subjectivity of the measurements. The incidence angle was calculated with Eq. (1).

$$\theta = arcsin\frac{b}{a} \tag{1}$$

where a is the semi-major axis and b is semi-minor axis of the ellipse.

| (a) | (b) |
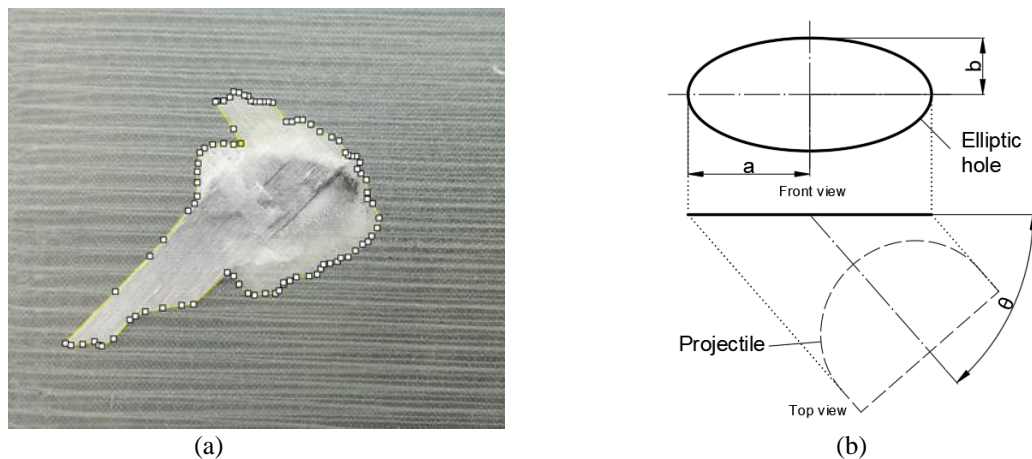
Figure 3. Measurements of the delaminated area and the incidence angle.

3. RESULTS AND DISCUSSION

3.1. Mechanical behavior of the laminates

The VI-series laminates demonstrated the highest mean value of the modulus of elasticity (Table 3), while the least modulus of elasticity was observed for the FW-series laminate (worth noting, that the ASTM D 7264/D 7264M – 07 standard does not recommend comparing the data obtained from different support span-to-thickness ratios) [11]. The high mechanical properties of the VI-series laminate are probably caused by the use of non-woven reinforcement where the fibers are straight and not interlaced. Moreover, the observed porosity for the VI-series laminates was the lowest (Figure a), which is a common feature of the manufacturing technique.

The stiffness of polymer composites in the fiber direction is usually dominated by the fiber properties [13]. The modulus of elasticity of the HL series and VB series laminates are practically the same because of the identical plane weave reinforcement. The density of the HL series laminate is less than that of the VB series due to the high porosity of the former (Figure b). The mold manufactured following the ISO standard [14] was intentionally used without O-ring gaskets to allow leakage of the resin out of the mold and, thus, remove the excess resin. As a result, a significant portion of the resin leaked out from the mold affecting the porosity of the HL series laminates. The same ISO standard mold was used for the curing process of the FW series laminates. The porosity of these laminates was higher than in the laminates of the VI and VB series, but significantly less than in the HL series laminates. The latter effect is probably caused by the difference in the impregnation methods inherent to the manufacturing techniques.

3.2. Ballistic Test

All laminates of the HL series were perforated through by a .22 caliber projectile at the orthogonal ballistic impact. The shape of the delaminated area was uniform and close to circular (Figure 5a). At the oblique impact, the 0.22 caliber projectile did not perforate through the thickness of two HL series laminates. After partial penetration had occurred, the projectile passed between the plies and exited from the lateral side of the

Table 3. Mechanical properties of the GFRP

Laminate series	Density MV, g/cm³	Porosity MV, %	Modulus of elasticity MV, GPa	SD, GPa
Vacuum bagging (VB)	1.97	5.63	24.1	1.32
Vacuum infusion (VI)	1.82	4.40	93.5	4.79
Hand lay-up (HL)	1.74	28.70	25.2	0.96
Filament winding (FW)	1.87	12.17	4.8	0.94

(a)   (b)

Figure 4. Micrographs of the section (x100) with high concentration of pores and voids: (a) VI series, (b) HL series.

laminate (Figure 5b). Most likely, the high interlaminar porosity (Figure 4b) provoked the change in projectile obliquity, because the effect was observed only in the HL series laminates.

The same pattern of the delaminated area as in the HL series laminates was observed in the VB series laminates at the orthogonal impact (Figure 6a). As in the HL series laminates, there was no hole-expansion and plugging, despite the projectiles having penetrated through the thickness of the laminates. The circumferential or elliptical dark stains shown in Fig. 5 and 6 are referred to as bullet wipe marks [6,15], whose presence indicates the projectile's entrance side.

At the oblique impact, only one of the VB series laminates was not perforated through the thickness by a .22 caliber projectile (Figure 6b), however, the delaminated area after the ricochet had the same shape as in other laminates of the series perforated by 0.22. The direction of a 0.22 caliber projectile could be determined by the close-to-elliptical shape of the bullet wipe and the location of the delaminated area in relation to the impact side. The delamination predominantly occurs along the trajectory of the projectile propagation inside the laminate.

(a)   (b)
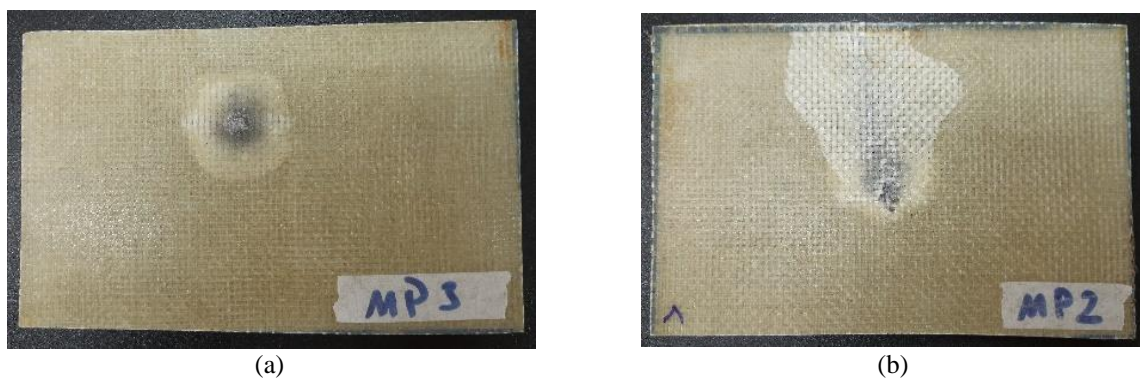
Figure 5. Characterization of the damage due to (a) orthogonal and (b) oblique ballistic impact in the HL series laminates.

(a)   (b)
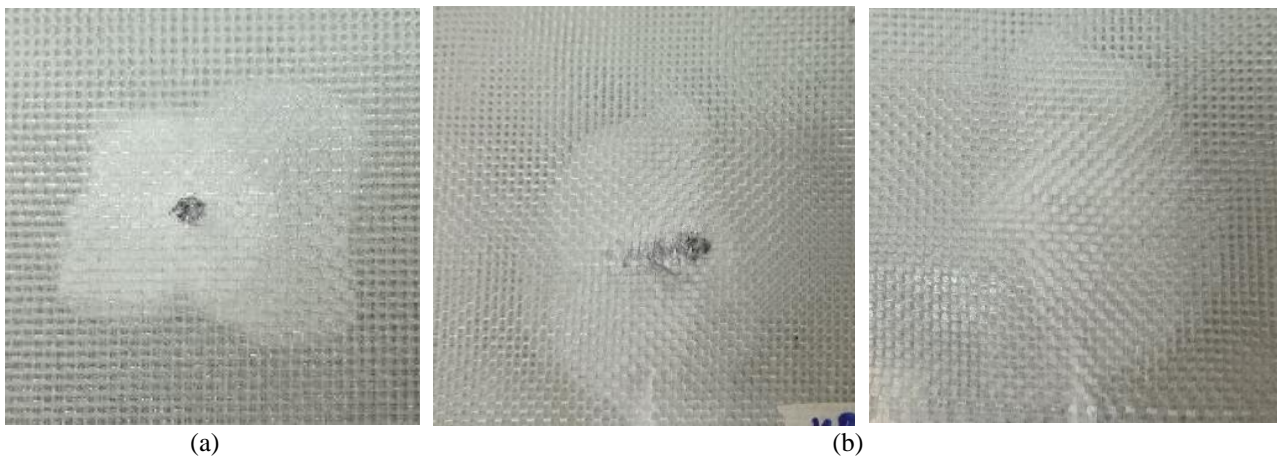
Figure 6. Characterization of the damage due to ballistic impact in the VB series laminates: (a) $\theta = 90°$; (b) $\theta = 45°$, ricochet (front and back faces are shown).

The faintly distinguishable distortion of the fibers and their discontinuity (Fig. 6b) indicates the site of impact. None of the damage produced by a 0.22 projectile is suitable for the definitive evaluation of the caliber. However, the same problem is common even for isotropic and non-fibrous materials [15]. Following the data in Table 4, the delaminated area in the VB series laminates is larger compared to other laminates.

Table 4. Delaminated area in mm² and measured incidence angle for impacts at 45 degrees

| Laminate series | Incidence angle | | | | Angle independent measurer No | | | |
| | $\theta = 90°$ | | $\theta = 45°$ | | 1st | | 2nd | |
	MV	SD	MV	SD	MV, °	CV, %	MV, °	CV, %
VB	2681	723	4999	2532	41.2°	8.5	35.6°	20.9
VI	1872	524	2103	141	—	—	—	—
HL	1471	406	3307	1120	42.8°	4.8	40.4°	10.2
FW	2079	873	1939	940	44.6°	0.9	42.0°	6.6

The pattern of the delaminated area of the FW series laminates differs from the laminates reinforced by plane weave. The delamination in the FW series laminates occurs between the glass rovings along the direction of reinforcement (Figure 7a). The peeling of entire rovings occurs because only one angle ply was manufactured (Table 1). Such a damage pattern makes it impossible to determine the direction of the projectile in the FW series laminates, while in most of the laminates reinforced with the plane weave cloth the delamination occurs along the projectile trajectory inside the laminate right after the bullet wipe (Figure 5b). However, the shape of the bullet wipe marks is elliptical-like, which indicates at least the plane of the projectile trajectory. Neither hole expansion nor plugging was observed for both orthogonal and oblique impacts.

The damage pattern of the VI series laminates was the combination of both previous patterns: the delamination between the plies was accompanied by the peeling of entire rovings (Fig. 7b). All laminates except one were perforated through the thickness by a .22 caliber projectile at the orthogonal impact. At the oblique impact, none of the 0.22 caliber projectiles was able to perforate through the thickness of the laminates. The projectiles left no clear wipe marks on the surface of the VI series laminates, making it impossible to evaluate the incidence angle by the dimensions of the ellipse. However, the data on the measurements of the incidence angle are available for the rest of the laminates (Table 4). The mean values of the measured incidence angles are close to the true angles used in the firing tests.

4. CONCLUSIONS

The damage produced by the ballistic impact of 0.22 caliber projectiles varies with the manufacturing technique and the nature of the constituents of the thin-walled GFRP laminates. At least two typical damage patterns and their combination were observed depending on the reinforcement type. The damage pattern produced by the projectiles in the laminates reinforced by the plain weave cloth was the most preferable from the point of view of the shooting incidence reconstruction, as made it possible to determine both the projectile's entrance side and the direction of travel of the projectile by the shape of the wipe marks and the configuration of the delaminated area. The damage pattern of the laminates reinforced by the glass roving in the form of the individually delaminated rovings allowed only the evaluation of the entrance side and the plane of the projectile trajectory. Moreover, the manufacturing defects, such as excessive porosity, might affect the elastic response in the laminates.

| (a) | (b) |
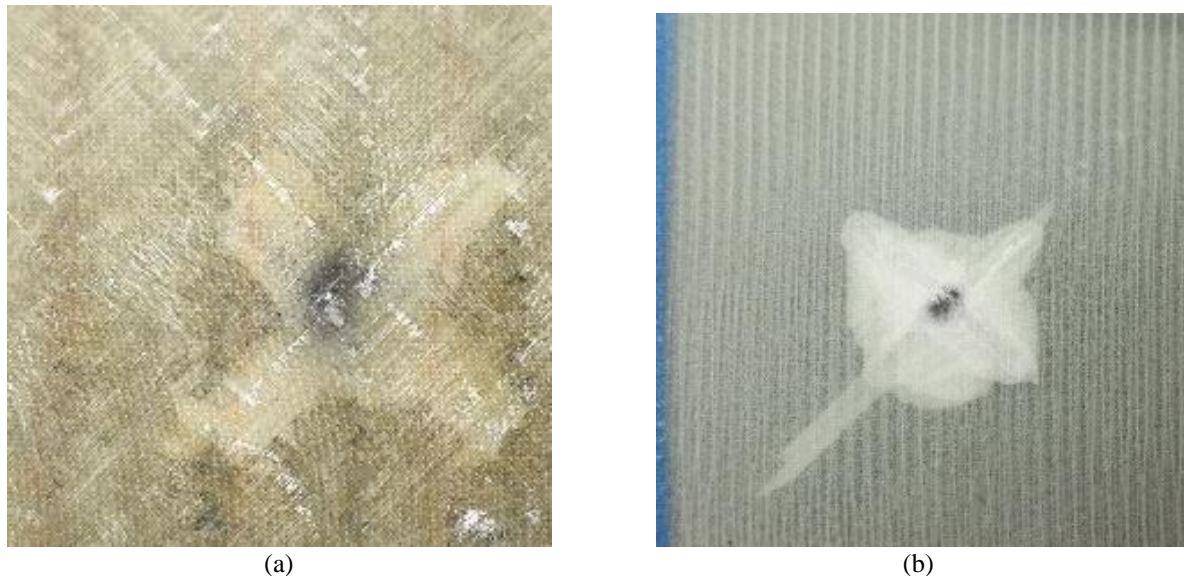
Figure 7. Characterization of the damage due to ballistic impact of .22 in the FW (a) and VI (b) series laminates ($\theta = 90°$)

An important feature of the thin-walled GFRP laminates was the absence of the hole-expansion and plugging common for the thick-walled laminates even when the projectiles penetrated through the thickness of the laminates. With these conditions, the evaluation of the projectile's direction by the probing method or by using the 3-dimensional shape of the lead-in becomes impossible. The ellipse method applied to the wipe marks could be a proper solution for the estimation of the incidence angle of a projectile, however, other than 45-degree incidence angles must be experimentally tested.

4.1. Declaration of Competing Interest

The authors declare no conflict of interest.

4.2. Acknowledgements

5. REFERENCES

[1]   T.P. Sathishkumar, S. Satheeshkumar, J. Naveen. Glass fiber-reinforced polymer composites - A review. *Journal of Reinforced Plastics and Composites,* Volume 33, 2014. (https://doi.org/10.1177/0731684414530790).

[2]   D.K. Rajak, et al. Fiber-reinforced polymer composites: Manufacturing, properties, and applications. *Polymers*, Volume 11, 2019. (https://doi.org/10.3390/polym11101667).

[3]   J. Singh, et al. Properties of Glass-Fiber Hybrid Composites: A Review. *Polymer - Plastics Technology and Engineering*, Volume 56, 2017. (https://doi.org/10.1080/03602559.2016.1233271).

[4]   H.S. Ashrith, T.P. Jeevan, J. Xu. A Review on the Fabrication and Mechanical Characterization of Fibrous Composites for Engineering Applications. *Journal of Composites Science*, Volume 7, 2023. (https://doi.org/10.3390/jcs7060252).

[5]   T.A. Warlow. *Firearms, the Law and Forensic Ballistics*. 1st Edition, 1996. CRC Press. (https://doi.org/10.4324/9781482290523).

[6]   M.G. Haag. *Shooting Incident Reconstruction*. In: *Encyclopedia of Forensic Sciences (*M.M. Houck*),* 3rd Edition, 2023. Elsevier. (https://doi.org/10.1016/B978-0-12-823677-2.00248-8).

[7]   R.C. Laible. Ballistic Materials and Penetration Mechanics. *The American Journal of Forensic Medicine and Pathology*, Volume 3, 1982. (https://doi.org/10.1097/00000433-198206000-00020).

[8]   H. Barhoumi, et al. Review of ballistic protection materials: Properties and performances. *Journal of Reinforced Plastics and Composites,* Volume 42, 2022. (https://doi.org/10.1177/07316844221137920).

[9]   G.G. Ojoc, et al. Glass fibers for impact protection systems. A review. *IOP Conference Series: Materials Science Engineering*, Volume 485, 2019. (https://doi.org/10.1088/1757-899X/485/1/012019).

[10]   A. Shahkarami, et al. *Material responses to ballistic impact*. In: *Lightweight Ballistic Composites: Military and Law-Enforcement Applications (A. Bhatnagar)*, 1st Edition 2006. Woodhead Publishing. (https://doi.org/10.1533/9781845691554.1.72).

[11]   ASTM D7264/D7264M – 07. Standard Test Method for Flexural Properties of Polymer Matrix Composite Materials. ASTM International, 2007. (www.astm.org)

[12]   E.J.A.T. Mattijssen, W. Kerkhoff. Bullet trajectory reconstruction - Methods, accuracy and precision. *Forensic Science International,* Volume 262, 2016. (https://doi.org/10.1016/j.forsciint.2016.03.039).

[13]   I.M. Daniel, O. Ishai. *Engineering mechanics of composite materials*, 2nd Edition, 2006. Oxford University Press. (ISBN 978-0-19-515097-1)

[14]   ISO 1268-5. 2001. Fibre-reinforced plastics – Methods of producing test plates – Part 5: Filament winding. International Organization for Standardization, 2001. (www.iso.org)

[15]   B.J. Heard. *Handbook of Firearms and Ballistics: Examining and Interpreting Forensic Evidence*, 2nd Edition, 2008. Wiley. (https://doi.org/10.1002/9780470694589).

QUASI STATIC INDENTATION TESTS TO PREDICT LOW VELOCITY IMPACT BEHAVIOUR OF ARAMID/S2-GLASS/EPOXY HYBRID LAMINATES

Amanda A. X. da Silva[(a), *], Mohammad Rezasefat [(b)], Andrea Manes [(c)], Sandro C. Amico [(d)]

(a) 0000-0001-6897-2576 (Federal University of Goiás – Brazil)
(b) 0000-0002-9381-9773 (Politecnico di Milano – Italy)
(c) 0000-0001-7485-8980 (Politecnico di Milano – Italy)
(d) 0000-0003-4873-2238 (Federal University of Rio Grande do Sul – Brazil)
* Corresponding author: amanda.albertin@ufg.br

Abstract: Low velocity impact (LVI) loadings are critical in-service conditions for any structural component, but are particularly significant for laminate composite structures. Although the impact loading is a peculiar loading condition, the use of quasi-static indentation (QSI) tests to correlate and predict low or high velocity impact behaviour of laminate composites remains a challenge. Therefore, the aim of this study is to evaluate the effect of hybridization of aramid/S2-glass/epoxy hybrid laminates subjected to QSI tests, as well as the potential use of QSI tests to predict the response to low velocity impacts. Six different laminates were manufactured using vacuum infusion moulding. The specimens include monolithic specimens made of aramid fabrics ($[K]_{4S}$) and S2-glass fabrics ($[G]_{8S}$) and four interply hybrids ($[G_6K_5]$, $[G_2K]_{S2}$, $[G_4K_2]_S$ and $[G_8K_4]$). Quasi-static indentation tests and low velocity impact tests with different levels of energy (18 J, 36 J, and 72 J) were conducted. Hybridization demonstrated a positive effect on energy absorption and peak force in both indentation and LVI tests. QSI tests showed promise in predicting the response of hybrid laminates to low velocity impacts, with similarities in peak force and energy absorption capacity. Finally, the research indicates the suitability of certain hybrids for applications with impact loadings.

1. INTRODUCTION

Low velocity impact (LVI) loadings are critical in-service conditions for any structural component, but even more critical for composite structure. Laminate composites are more vulnerable to impact damage than metallic materials, for example, during maintenance or manufacturing operations, internal damage such as delamination, matrix cracking, and fiber breakage could be generated in the laminate composite through impact loading at low velocity [1]. These internal damages can result in premature failures or catastrophic failures in the laminates during their service. Another type of loading that creates damages in laminates and resembles LVI is Quasi-Static Indentation (QSI), QSI test consist in applying on the material a transverse load perpendicular to the indented surface via a hemispherical indenter. The impactor of an LVI drop tower is in free fall before hitting the surface of the composite, the indenter of a QSI test is brought into contact with the surface prior to the test, thus, both testing methods are comparable in their working principle, expect that one is dynamic in nature while the other is quasi-static [2].

QSI tests can provide meaningful evidence of the damage events occurring during a low velocity impact, since the impact duration is much longer than the time required by the propagating waves to travel from the impact site to the supports or free edges [3]. The results of a QSI test may be used to study the damage mechanism and to predict the dynamic behaviour of the material[4]. Several researchers [5–10] showed the similarities between low velocity impact and QSI tests. In a study conducted by Nettles and Douglas [11] on quasi-isotropic carbon/epoxy laminated showed no distinct differences between QSI and LVI tests based on

the peak force. Likewise, Suresh Kumar et al. [12] reached the same conclusion on quasi-isotropic glass/epoxy, glass/basalt/epoxy and glass/carbon/epoxy composite laminates, their results indicated that there were no significant differences in dent depth, back surface crack size and force-displacement curve behaviour. Zhang et al. [13] developed a work with laminates composed of carbon fiber and bismaleimide resin were subjected to both LVI and QSI tests. The results of these experiments demonstrated comparable delamination patterns and a consistent trend in delamination size across the thickness direction of the laminates.

The impact resistance of laminate composites can be increased by improving fiber/matrix interface adhesion, matrix modification, and fiber hybridization [14]. Hybridization used in laminates may be an effective method of improving the capability to absorption energy and penetration resistance [3]. The quasi static penetration resistance of glass fiber laminates hybridized with Kevlar fibers was investigated by Al-Kinani, Najim and Moura [16]. Hybrid laminates with different stacks (only four layers) were subjected to different nose shape indenters for characterization of hybrid effect. As conclusions, the hybridization improved the penetration resistance which was independent of Kevlar layer position, and, the back face of laminates was mostly affected by the Kevlar layers position. An experimental investigation of the effect of hybridization on quasi-static indentation and LVI behaviour of S-glass/E-glass/epoxy, carbon/E-glass/epoxy and Kevlar/E-glass/epoxy interply hybrid composites was performed by Vasudevan et al.[17]. As a result, the E-glass/epoxy and Kevlar/E-glass/epoxy composites presented the higher energy absorption capacity, thus, the Kevlar/E-glass/epoxy interply hybrid composites are recommended for crashworthiness applications.

The impact load involves a number of other loads, the use of QSI tests (simpler tests) to correlate and predict low or high velocity impact behaviour of laminate composites remain a challenge and a current research topic for numerous researchers[12,18–21], as well as, with hybrid laminates the challenge is even greater and with few results in the literature. The authors have already evaluated the effects of hybridization on low-velocity impacts [22–25] and on mechanical properties and quasi-static indentations [26] separately, however, no comparison between the behaviour and damage generated in the LVI and QSI tests was carried out. Hence, the present study focuses on the evaluation of the physical, QSI, and LVI properties (drop weight) of S2-glass/aramid hybrid laminates as a function of the hybridization and pairing effect. And, evaluate the use of QSI test to predict the low velocity impact behaviour of the hybrid laminates.

2. METHODOLOGY

Plain-weave Kevlar®29 fabric (440 g/m², 0.62 mm thickness, with 7 threads per centimeter) sourced from Dupont, and Hexcel® 8 harness satin S2-glass fabric (302 g/m², 0.24 mm thickness, with 22 threads per centimeter) were employed as reinforcement materials. The laminates were fabricated using a mixture of epoxy resin AR260 and AH260 hardener (AR/AH260) at a ratio of 100g/26g, respectively, the components of which were supplied by Barracuda Advanced Composites.

Vacuum infusion moulding was the chosen manufacturing process. Prior to processing, the fabrics underwent a drying procedure at 100°C for 2 hours to eliminate moisture content. After infiltration at approximately -1 bar, the plates were subjected to a 24-hour curing process under vacuum conditions. Subsequently, the composite was extracted and subjected to post-curing treatment lasting 16 h at 65°C.
A total of six laminate stacks were fabricated, as depicted in Figure 1, with four of them being hybrids. The stacking sequences were carefully determined to ensure that the final thickness of approximately 4 mm was maintained across all configurations. In the case of the asymmetric stacks, denoted as $[G_8K_4]$ and $[G_6K_5]$, only one side of the laminate was subjected to testing, specifically the stiffer surface featuring S2-glass fiber fabric. This decision was grounded in existing literature, which indicates that aramid/glass hybrid laminates with layers of glass fibers on the impact surface exhibit enhanced energy absorption characteristics [16,25]. Additionally, the selection of non-symmetric laminates, such as G_6K_5 and G_8K_4, has yielded superior outcomes in prior studies conducted by the authors, manifesting higher absorbed energies [22,29].

$[K]_{4S}$ $[G_6K_5]$ $[G_2K]_{2S}$ $[G_4K_2]_S$ $[G_8K_4]$ $[G]_{8S}$
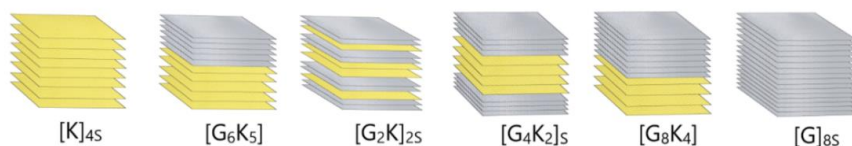
Figure 1. Stacking sequence of the laminates and nomenclature adopted.

Density of the laminates was evaluated according to ASTM D792 standard. Their constituents' content, namely, overall fiber content (V_f), and aramid (V_K), glass (V_G), matrix (V_m), and void (V_v) volume fraction, were determined according to ASTM D3171.

2.1 Low velocity impact tests

The drop weight impact tests were performed according to the ASTM D7136 standard, similar to the previous work [22]. The tests were performed at the *Politecnico di Milano* with the drop weight impact tower. The composite laminates were impacted with a hemispherical impactor with a diameter of 16 mm with three different levels of energy (nominally, 18 J, 36 J and 72 J). An optical sensor was used to measure the initial velocity of the impactor before the onset of impact and the impactor was equipped with a load cell to record the contact force between the specimens and the impactor during the impact event. The specimen was clamped to a rigid plate with 125×75 mm² free rectangular area using four fixtures equipped with rubber dampers. After each impact, the impactor was stopped with a pneumatic arm to block any additional and unwanted impact between the impactor and the specimen.

2.2 Quasi-static indentation tests

Indentation tests were performed according to ASTM D6264, similar to the work undertaken previously [26], by a universal testing machine (Instron) having load capacity of 100 kN. Test speed of indenter was set to 1.25 mm/min (loading and unloading), until 13 mm of displacement. Three test samples (150 mm x 150 mm) for each configuration were tested. Samples were constrained by means of two steel plates having a circular cut-out ($\emptyset = 125$ mm) and then they were subjected to concentrated loading along the out of plane direction by using a hemispherical indenter ($\emptyset = 16$ mm) in the middle of sample. The maximum force (F_{max}) is defined by the peak of load, the maximum energy (E_{max}), is obtained by area under the force-displacement curve until the maximum displacement (13 mm), and the absorbed energy (E_{abs}), is obtained by area under the force-displacement curve considering the loading and unloading process. One-way analyses of variance (ANOVA) were conducted, and in cases where the null hypothesis was rejected, Tukey tests were employed to assess mean differences. All statistical analyses were conducted at a significance level of 5%.

3. RESULTS AND DISCUSSION

Table 1 shows the primary characteristics of the laminates. The $[K]_{4S}$ exhibited the highest overall fiber content (63%), while $[G]_{8S}$ had the lowest (47%), and the overall V_f decreases with the incorporation of more glass layers (S2). Similar to the findings presented by the authors in a previous study [29], this can be attributed to differences in fabric architecture, and the use of aramid allows for greater compaction under the maximum pressure (-1 bar) available during the vacuum infusion processing. Furthermore, as the number of glass layers increases, there is a decrease in void content (V_v), likely attributed to the higher permeability of the S2-glass fabric, which facilitates resin flow within the preform [30]. The thickness of all laminates was approximately to 4.00 ± 0.03 mm. Since the S2-glass fiber has a higher density than aramid fiber, the density of the laminates increases with the incorporation of more glass layers.

Table 1. General characteristics of the laminates.

Laminate	Density [g/cm³]	V_m [%]	V_m [%]	V_v [%]
$[K]_{4S}$	1.188 ± 0.014	62.9 ± 1.6	23.6 ± 1.9	13.5 ± 0.3
$[G_6K_5]$	1.431 ± 0.001	61.1 ± 0.1	29.8 ± 0.6	9.1 ± 0.1
$[G_2K]_{2S}$	1.478 ± 0.014	59.7 ± 0.1	30.9 ± 0.7	9.5 ± 0.1
$[G_4K_2]_S$	1.459 ± 0.003	58.6 ± 0.3	31.1 ± 0.5	10.4 ± 0.3
$[G_8K_4]$	1.473 ± 0.010	56.5 ± 0.1	33.9 ± 0.7	9.6 ± 0.2
$[G]_{8S}$	1.746 ± 0.006	46.7 ± 0.2	49.8 ± 0.9	± 0.2

The experimental results for force-time, energy-time and force-displacement of all laminates subjected to impacts of 19 J (20 J), 36 J (40 J) and 72 J (80 J) are discussed by the authors in previous works [23,31].

Typical force-displacement curves of the QSI and drop weight tests with different energies (19 J, 36 J and 72 J) of all laminates can be seen in Figure 2. Observations of rebounding, penetration and perforation of the impactor were made across various cases during the conducted test campaign. For 19 J and 36 J impacts, the impactor consistently exhibited rebounding characteristics across all configurations. However, in the case of 72J impacts, the impactor rebounded when impacting $[G]_{8S}$, nearly penetrated the hybrid configurations, and perforated the $[K]_{4S}$. These observations align with the force-displacement curves depicted in Figure 2, showcasing close ($[G]_{8S}$), semi-open (hybrids, $[G_6K_5]$, $[G_2K]_{2S}$, $[G_4K_2]_S$, $[G_8K_4]$), and open ($[K]_{4S}$) characteristics for the respective configurations.

The obtained results of impact response are compiled in Table 2. The ratio of absorbed energy to impact energy (E_A/E_I), referred to as the energy absorption ratio, is defined as the quantification of energy absorption. The energy absorption ratio increases with the increase in impact energy for all configurations, consequently yielding broader force-displacement curves for impacts with higher energy levels. The increase in energy absorption ratio is due to the more severe damage that occurs when the impact energy is higher.

Table 2. Characteristics of the impact response of the studied laminate configurations.

Laminate	Peak force (kN)			Maximum displacement (mm)			E_A/E_I		
Energy	19 J	36 J	72 J	19 J	36 J	72 J	19 J	36 J	72 J
$[K]_{4S}$	5.92	7.28	8.24	6.55	9.47	-	0.32	0.62	0.89
$[G_6K_5]$	5.93	7.64	8.61	6.27	8.92	14.96	0.54	0.68	0.95
$[G_2K_2]_{2S}$	6.14	9.18	9.64	6.14	8.63	15.73	0.38	0.64	0.98
$[G_4K_2]_S$	6.18	8.69	9.36	6.11	8.48	13.88	0.48	0.66	0.92
$[G_8K_4]$	6.36	7.80	8.36	6.04	8.82	16.69	0.50	0.68	1
$[G]_{8S}$	6.84	9.18	9.37	5.51	7.38	11.95	0.22	0.49	0.84

Table 3 shows the properties obtained from the QSI tests of each laminate. The representative force-displacement curves of QSI and LVI tests of each laminate can be seen in the Figure 2. The laminate with the highest E_{abs}, E_{max} and F_{max} as the $[G_6K_5]$ hybrid, with six layers of S2-glass in the indentation side follow with five layers of aramid. The $[G_8K_4]$ hybrid, presented statistically similar values for all properties, all have S2-glass in the indentation surface. The same hybrids laminates presented the highest values of E_A/E_I from LVI tests for all energies. All hybrids exhibited energy absorption capacity (E_A/E_I) greater them monolithic stacks, $[K]_{4S}$ and $[G]_{8S}$.

The first layers of the laminate are compressed during penetration (QSI and impact tests); thus, the compression strength of the outer laminate layers is crucial. S2-glass fibers exhibit a higher compressive modulus than aramid fibers, thus, their presence in the first layers seems to be more beneficial. During the next stage of penetration, the fibers are sheared and stretched. At the last stage, once the neutral layers are penetrated, fiber layers become stretched. The use of fibers with higher elongation and strength seems to be justified in last stage, properties linked to aramid fibers, more ductile than S2-glass fibers. Similar conclusions were reached by Pach and Kuterek [4], who observed higher strength to indentation in carbon–aramid laminates if carbon fibers were present on the outer layers. The authors explain that this layout allowed the aramid fibers present on the stretched side of the sample to absorb more energy.

Comparing the laminates with an equal number of aramid and S2-glass layers, $[G_2K_2]_{2S}$, $[G_4K_2]_S$, and $[G_8K_4]$, the symmetric laminates exhibited statistically similar values, but the asymmetric laminate, $[G_8K_4]$, presented one of the best results for the (QSI) indentation strength. So, the stacking sequence has significant effect on the maximum force and energy absorbed (QSI tests). In the LVI tests, as the impact energy increased, the influence of the stacking sequence on the impact properties was reduced, showing a greater difference in lower energy impacts (20 J), and the alternating laminate $[G_2K_2]_{2S}$ presented the lowest value of E_A/E_I but with similar peak force to the other two hybrids, $[G_4K_2]_S$ and $[G_8K_4]$.

Table 3. Elaborated data from the QSI test.

Laminate	F_{max} [kN]	E_{max} [J]	E_{abs} [J]	Difference[%] Peak Force/F_{max}
$[K]_{4S}$	8.61 ± 0.16 [CD]	55.20 ± 1.98 [C]	45.81 ± 2.03 [BC]	4-15%
$[G_6K_5]$	9.86 ± 0.35 [F]	62.31 ± 5.11 [D]	54.83 ± 4.91 [D]	13-23%
$[G_2K_2]_{2S}$	7.39 ± 0.25 [B]	49.85 ± 1.94 [AB]	43.65 ± 1.28 [ABC]	24-30%
$[G_4K_2]_S$	7.96 ± 0.78 [BC]	52.60 ± 2.70 [ABC]	45.68 ± 2.46 [BC]	9-18%
$[G_8K_4]$	9.46 ± 0.23 [EF]	60.72 ± 4.78 [D]	52.07 ± 4.41 [D]	12-18%
$[G]_{8S}$	5.90 ± 0.34 [A]	54.20 ± 0.94 [BC]	41.38 ± 0.95 [AB]	56-58%

(A), (B), (C), (D) and (E) represent different families according to ANOVA ($p < 0.05$).
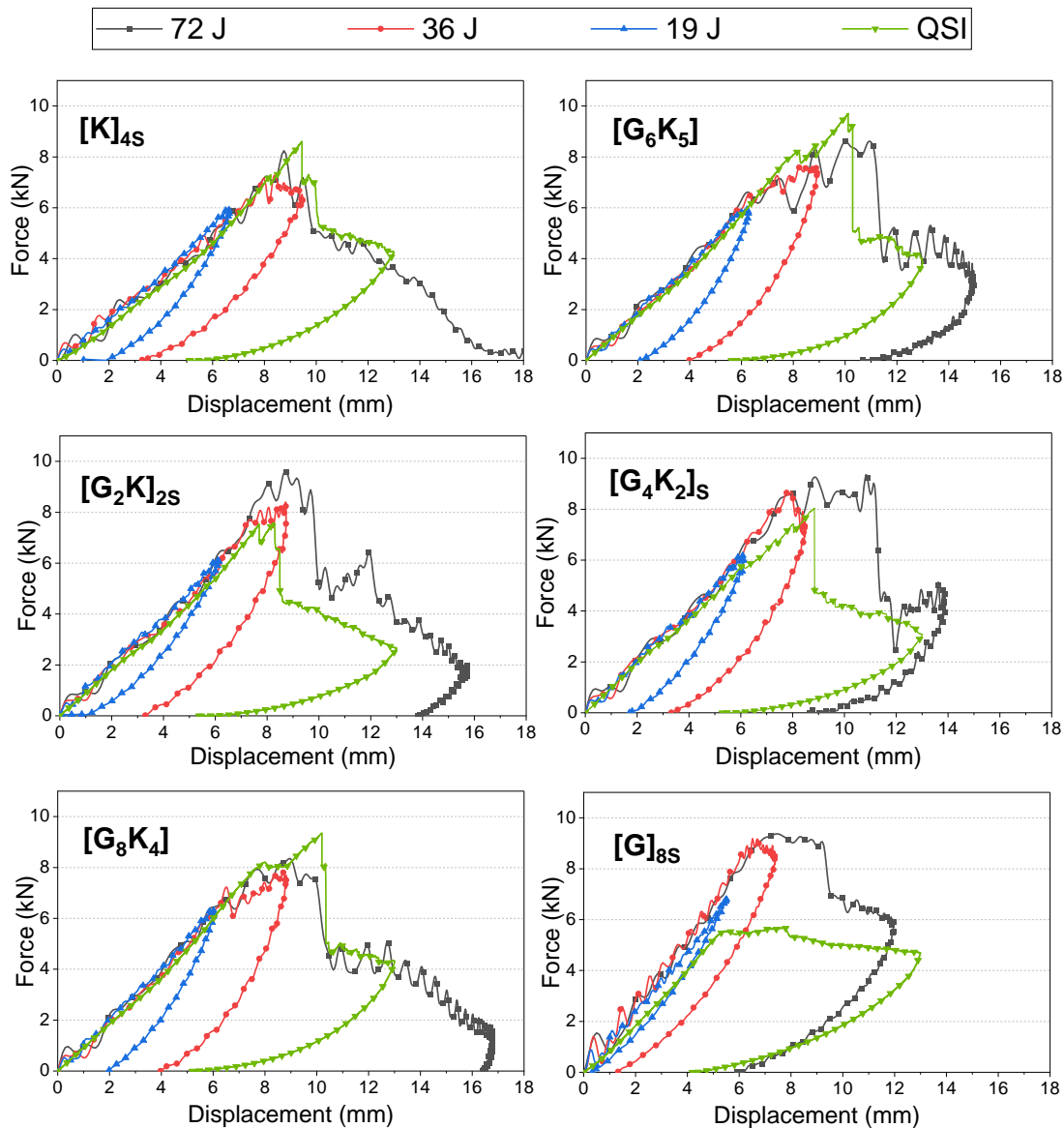
Figure 2. Typical force-displacement curves of the QSI and drop weight tests with different energies (19 J, 36 J and 72 J) of all laminates.

Finally, analyzing the behavior of the LVI tests and the QSI tests (Figure 2), the impact stiffness of the LVI curves (19 J, 36 J and 72 J) presented very similar behavior to the QSI tests, and the peak force (F_{max}) for the aramid and hybrid laminates of QSI tests presented close values with the 36 J and 72 J curves of LVI tests, see the range of difference values in Table 3, comparing the peak force (36 J and 72 J curves) and F_{max} of QSI tests. The QSI tests showed E_{abs} of 50-60 J (Table 3), intermediate values of the absorbed energies (E_A) obtained with in the LVI tests with initial impact energy of 36 J and 72 J. With LVI tests nearest to the E_{abs} exhibited during the QSI tests, more similar curves can be reached [2]. On the other hand, the S2-glass laminate, [G]$_{8S}$, did not show similarities in the peak force (difference of 56-58%) and in the behavior of the curve comparing the QSI and LVI tests, with the increase of the test velocity, the material presents a greater strength (peak force) and stiffness to the impact/indentation (rate-dependency), similar that report in [32].

3.1 Damage analysis

Figure 3 shows the post-mortem damages observed at the cross sections after the QSI and LVI tests (72 J). Similar damage patterns and failure mechanisms were evident in both tests, and included matrix cracking, fiber breakage, delamination and permanent indentation [26,31]. Notably, laminates subjected to LVI tests (72 J) exhibited a heightened extent of damage, characterized by deeper permanent indentation, forming a distinct "V-shaped" damage region[22], in contrast to those subjected to QSI tests. This discrepancy aligns with expectations owing to the different absorbed energies. In the QSI tests, wherein displacements reached up to 13 mm, the absorbed energy was approximately 50 J. Conversely, LVI tests absorbed energies

ranging from 60 to 72 J, indicating a propensity for greater damage but with identical propagation of damages. Consequently, the results of QSI tests offer substantive insights into damage occurrences during low-velocity impacts, facilitating predictions regarding the dynamic behavior of hybrid composite laminates [4,33].
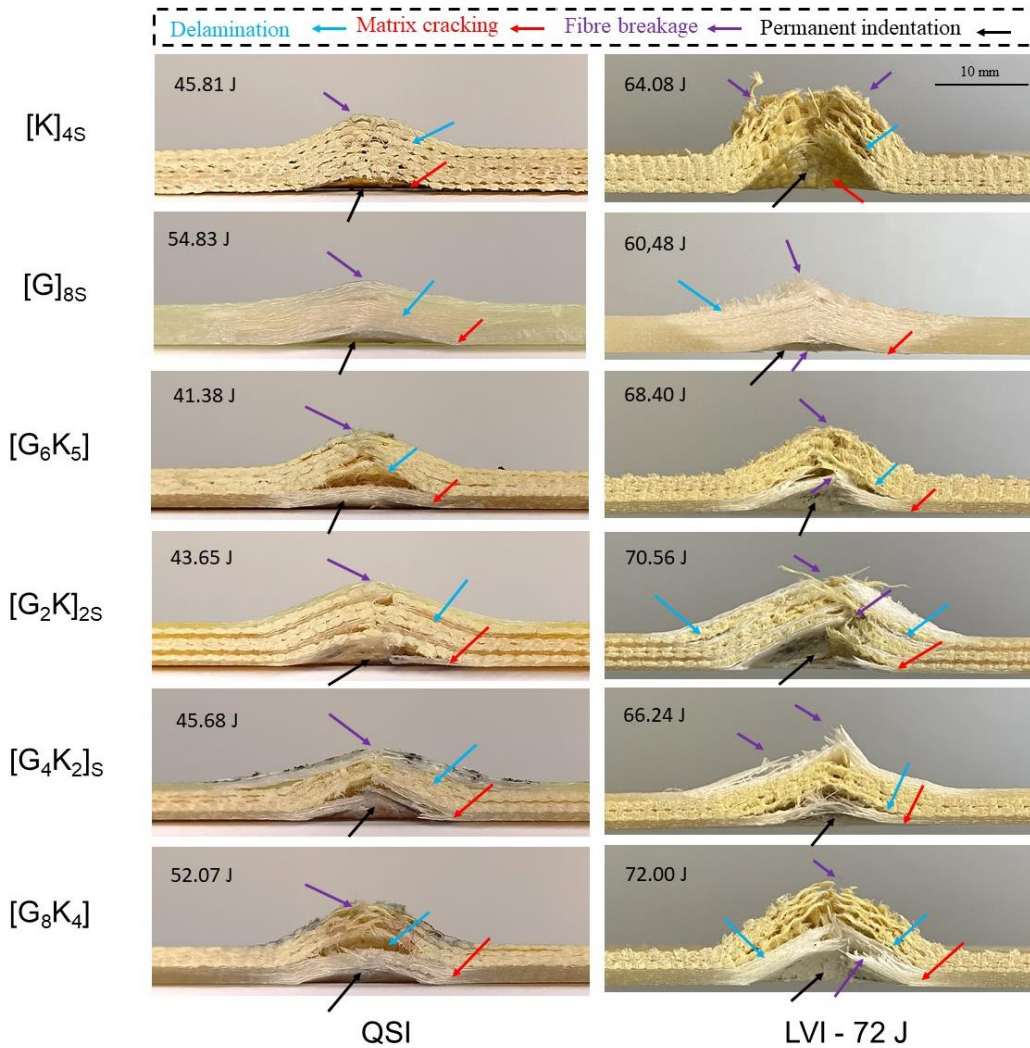
Figure 3. Cross-section damages of all laminates after QSI tests and drop weight tests with 72 J. Energy values inside each picture repost absorbed Energy.

4. CONCLUSIONS

Aramid/S2-glass/epoxy laminates were successfully obtained by vacuum infusion and hybridization improved the final quality of the composites, with a reduction in void content for the hybrid laminates compared to pure aramid.

Hybridization influences the impact response. At lower impact energy, the increase in aramid ratio leads to higher displacement, lower impact force and lower impact stiffness.

The hybridization presented a positive hybrid effect in the energy absorption and peak force in indentation and LVI tests. The asymmetric hybrid laminates, [G_6K_5] and [G_8K_4], with S2-glass on indentation surface, exhibited the E_{abs} and F_{max} higher than pure laminates, [K]$_{4S}$ and [G]$_{8S}$, so the hybridization allowed to achieve greater energy absorption capacity. The pairing effect has influence in the QSI properties and more effective influence in LVI test in lower impact energies.

The QSI tests presented a promissory option to predict the response of hybrid laminates in low velocity impacts, indicating similarities in peak force and capacity of absorption energy and propagation of damages, allowing indicate the more provide hybrid to be used applications with impact loadings.

In general, hybridization of aramid with S2-glass lead to easier manufacturing by vacuum infusion, increased energy absorption capability, therefore it may lead to an optimized application in rigid composite reinforcements.

4.1. Declaration of Competing Interest

The authors declare no conflict of interest.

4.2. Acknowledgements

5. REFERENCES

[1] Safri SNA, Sultan MTH, Jawaid M, Jayakrishna K. Impact behaviour of hybrid composites for structural applications: A review. Compos B Eng 2018;133:112–21. https://doi.org/10.1016/j.compositesb.2017.09.008.

[2] Leroy A, Scida D, Roux É, Toussaint F, Ayad R. Industrial Crops & Products Are there similarities between quasi-static indentation and low velocity impact tests for flax-fibre composites ? Ind Crops Prod 2021;171:113840. https://doi.org/10.1016/j.indcrop.2021.113840.

[3] Wagih A, Maimí P, Blanco N, Costa J. Composites : Part A A quasi-static indentation test to elucidate the sequence of damage events in low velocity impacts on composite laminates. COMPOSITES PART A 2016;82:180–9. https://doi.org/10.1016/j.compositesa.2015.11.041.

[4] Pach J, Kuterek E. Investigation of the Quasi-Static Penetration Resistance Behaviour of Carbon / Aramid Fibre-Reinforced PP Laminate. Materials 2021;14:1–17. https://doi.org/https://doi.org/10.3390/ma14040709.

[5] Lee SM, Zahuta P, Corpornrioti C. Instrumented Impact and Static Indentation of Composites. J Compos Mater 1991. https://doi.org/DOI: 10.1177/002199839102500205.

[6] Aoki Y, Suemasu H, Ishikawa T. Damage propagation in CFRP laminates subjected to low velocity impact and static indentation 2014:37–41. https://doi.org/10.1163/156855107779755318.

[7] Hongkarnjanakul N, Rivallant S, Bouvet C, Miranda A, Hongkarnjanakul N, Rivallant S, et al. Permanent indentation characterization for low-velocity impact modelling using three-point bending test. J Compos Mater 2014:1–14. https://doi.org/10.1177/0021998313499197.

[8] Kaczmarek H, Maison S. Comparative Ultrasonic Analysis of Damage CFRP Under Static Indentation and Low-Velocity Impact. Compos Sci Technol 1994;51:11–26.

[9] Wu Z, Zhang L, Ying Z, Ke J, Hu X. Low-velocity impact performance of hybrid 3D carbon / glass woven orthogonal composite: Experiment and simulation. Composites Part B 2020;196:108098. https://doi.org/10.1016/j.compositesb.2020.108098.

[10] Jackson R, Jr CC, Use T. The Use of Impact Force as a Scale Parameter for the Impact Response of Composite Laminates 2021:282–9.

[11] Nettles AT, Douglas MJ, Dominion O. to Low-Velocity of Quasi-Static Impact Alabama. 2000.

[12] Kumar CS, Arumugam V, Santulli C. Characterization of indentation damage resistance of hybrid composite laminates using acoustic emission monitoring. Composites Part B 2017;111:165–78. https://doi.org/10.1016/j.compositesb.2016.12.012.

[13] Zhang J, Zhao L, Li M, Chen Y. Compressive fatigue behavior of low velocity impacted and quasi-static indented CFRP laminates. Compos Struct 2015;133:1009–15. https://doi.org/10.1016/j.compstruct.2015.08.046.

[14] Zhang C, Rao Y, Li W. Low-velocity impact behavior of intralayer hybrid composites based on carbon and glass non-crimp fabric. Compos Struct 2020;234:111713. https://doi.org/10.1016/j.compstruct.2019.111713.

[15] Pach J, Kuterek E. Investigation of the Quasi-Static Penetration Resistance Behaviour of Carbon / Aramid Fibre-Reinforced PP Laminate. Materials 2021;14:1–17. https://doi.org/https://doi.org/10.3390/ma14040709.

[16] Al-Kinani R, Najim F, Moura MFSF De. The Effect of Hybridization on the GFRP Behavior under Quasi-Static Penetration n.d.:37–41. https://doi.org/10.1080/15376494.2012.680672.

[17] Vasudevan A, Senthil Kumaran S, Naresh K, Velmurugan R. Layer-wise damage prediction in carbon/Kevlar/S-glass/E-glass fibre reinforced epoxy hybrid composites under low-velocity impact loading using advanced 3D computed tomography. International Journal of Crashworthiness 2019;0:1–15. https://doi.org/10.1080/13588265.2018.1511234.

[18] Leroy A, Scida D, Roux É, Toussaint F, Ayad R. Are there similarities between quasi-static indentation and low velocity impact tests for flax-fibre composites? Ind Crops Prod 2021;171. https://doi.org/10.1016/j.indcrop.2021.113840.

[19] Serna Moreno MC, Horta Muñoz S. Mechanical response of ±45° angle-ply CFRP plates under low-velocity impact and quasi-static indentation: Influence of the multidirectional strain state. Compos Sci Technol 2020;194. https://doi.org/10.1016/j.compscitech.2020.108145.

[20] Spronk SWF, Kersemans M, De Baerdemaeker JCA, Gilabert FA, Sevenois RDB, Garoz D, et al. Comparing damage from low-velocity impact and quasi-static indentation in automotive carbon/epoxy and glass/polyamide-6 laminates. Polym Test 2018;65:231–41. https://doi.org/10.1016/j.polymertesting.2017.11.023.

[21] Saeedifar M, Najafabadi MA, Zarouchas D, Toudeshky HH, Jalalvand M. Barely visible impact damage assessment in laminated composites using acoustic emission. Compos B Eng 2018;152:180–92. https://doi.org/10.1016/j.compositesb.2018.07.016.

[22] Rezasefat M, Gonzalez-Jimenez A, Ma D, Vescovini A, Lomazzi L, da Silva AAX, et al. Experimental study on the low-velocity impact response of inter-ply S2-glass/aramid woven fabric hybrid laminates. Thin-Walled Structures 2022;177:109458. https://doi.org/10.1016/j.tws.2022.109458.

[23] Rezasefat M, da Silva AAX, Amico SC, Giglio M, Manes A. Repeated impact behaviour of inter-ply hybrid aramid/S2-glass epoxy laminates. Thin-Walled Structures 2023;186. https://doi.org/10.1016/j.tws.2023.110680.

[24] Rezasefat M, Ma D, da Silva AAX, Colombo C, Amico SC, Giglio M, et al. Multi-criteria decision-making analysis and numerical simulation of the low-velocity impact response of inter-ply S2-glass/aramid woven fabric hybrid laminates. Compos Struct 2023;312:116867. https://doi.org/10.1016/j.compstruct.2023.116867.

[25] Fulginiti F, Rezasefat M, Xavier da Silva A, Amico SC, Giglio M, Manes A. Experimental and numerical studies on the repeated low-velocity impact response and damage accumulation in woven S2-glass fibre/epoxy composites. Advanced Composite Materials 2023;00:1–26. https://doi.org/10.1080/09243046.2023.2178272.

[26] Da Silva AAX, Araújo Silva ÍJ de, Miranda ACM, Manes A, Amico SC. Influence of hybridization on the mechanical and dynamic mechanical properties of aramid/S2-glass hybrid laminates. Mater Today Commun 2022;32. https://doi.org/10.1016/j.mtcomm.2022.104021.

[27] Bandaru AK, Vetiyatil L, Ahmad S. The effect of hybridization on the ballistic impact behavior of hybrid composite armors. Compos B Eng 2015;76:300–19. https://doi.org/10.1016/j.compositesb.2015.03.012.

[28] Muhi RJ, Najim F, de Moura MFSF. The effect of hybridization on the GFRP behavior under high velocity impact. Compos B Eng 2009;40:798–803. https://doi.org/10.1016/j.compositesb.2009.08.002.

[29] Da Silva AAX, Scazzosi R, Manes A, Amico SC. High - Velocity Impact Behavior of Aramid / S2 - Glass Interply Hybrid Laminates. Applied Composite Materials 2021. https://doi.org/10.1007/s10443-021-09946-3.

[30] Da Silva AAX, Souza JA, Manes A, Amico SC. In-plane Permeability and Mechanical Properties of R-Glass/Aramid Hybrid Composites. J Mater Eng Perform 2020;29:4484–92. https://doi.org/10.1007/s11665-020-04944-1.

[31] Rezasefat M, Gonzalez-Jimenez A, Ma D, Vescovini A, Lomazzi L, da Silva AAX, et al. Experimental study on the low-velocity impact response of inter-ply S2-glass/aramid woven fabric hybrid laminates. Thin-Walled Structures 2022;177:109458. https://doi.org/10.1016/j.tws.2022.109458.

[32] Djele A, Karakuzu R. An experimental study on quasi-static indentation, low-velocity impact and damage behaviors of laminated composites at high temperatures 2021. https://doi.org/10.1177/09673911211016932.

[33] Wagih A, Maimí P, Blanco N, Costa J. A quasi-static indentation test to elucidate the sequence of damageevents in low velocity impacts on composite laminates. Composites: Part A 2016;82:180–9. https://doi.org/10.1016/j.compositesa.2015.11.041.

14 Micromechanics

Organized and edited by

Sandra Maria da Luz
&
Carla Tatiana Mota Anflor

MICROMECHANICAL STUDY OF THE BAHAVIOR OF UNIDIRECTIONAL COMPOSITES DURING HOT PRESSING MANUFACTURING

Gustavo Henrique da Silva [(a), *], Murilo Sartorato [(b)]

(a) 0009-0000-1983-6228 (São Paulo State University "Júlio de Mesquita Filho" – Brazil)

(b) 0000-0002-2904-9954 (São Paulo State University "Júlio de Mesquita Filho" – Brazil)

* Corresponding author: gustavo.silva13@unesp.br

CODE: BCCM7-56

Keywords: hot pressing, representative volume element, finite element analysis

Abstract: The present work is focused on implementing a numerical methodology to study the manufacturing process of structural laminated unidirectional carbon fibre-epoxy and/or carbon fibre-PEEK composite plates via hot pressing; in particular, temperature distributions and residual thermal stresses will be studied as a function of composite thickness and heating and cooling curves for different cases of non-uniform fibre distributions. Through the numerical routine developed in Python/MATLAB based on previous works from the literature using quasi-Newton optimization with L-BFGS-B approximation of Hessian matrix of the minimum distance between randomly generated sets of fibres, Representative Volume Elements (RVE) with non-uniform distributed fibres are generated for different levels of fibre volume fraction and the different levels of non-uniformity dispersion in the matrix. These RVE are implemented in ANSYS Workbench through Python scripting automatization where the external applied mechanical pressure and temperature of the plates used during the manufacturing process necessary for matrix consolidation are simulated. From the simulations, average temperature and stress field distributions are obtained through several slices of the simulated coupon for different values of pressure, temperature curves and thicknesses are compared. The size of the slices and number of realizations needed for statistical convergence of the results are also shown.

1. INTRODUCTION

Laminated structural composite materials based on polymeric matrices and ceramic fibres (carbon, e-glass, aramid) have extensive applications in the aerospace and aeronautical industries due to their unique combination of properties that make them highly suitable for various components and structures. Several advantages exist regarding their usage over classic materials such as aluminium alloys: weight reduction due to the smaller density; higher specific mechanical properties like stiffness, resistance and residual strength; higher corrosion resistance under moisture, salt and temperature variations; high fatigue resistance depending on the plies alignment; and high design flexibility by shaping and molding components to more complex shapes compared to traditional materials. This versatility allows for innovative designs that optimize aerodynamics and efficiency [1].

However, the quality of the final components when considering the chemical consolidation of the polymeric matrix is complex and dependent on the kind of process used and fine control of the different parameters. In this work, a study focusing on the analysis of the temperature and the residual thermal stress distributions in structural laminated composites with unidirectional fibres manufactured with hot press plates is performed. Hot pressing, or hot consolidation, is a versatile and efficient method for producing composite materials with a wide range of properties and applications. It is employed in industries such as aerospace, automotive, and construction to manufacture lightweight, strong, and durable parts and components. [2]. The basic steps involved in hot pressing a laminated composite are as follows: the composite material typically

consists of two or more layers of different materials, such as fibres or fabrics, which are stacked and impregnated with a polymeric matrix; the composite is then cut to the desired shape and size and placed between two metal plates, which are heated to specific temperatures and pressures. These plates are typically made of steel or aluminium, with their size and shape varying depending on the application. Finally, the plates are pressed together with a force ranging from several hundred to several thousand pounds per square inch (psi). Simultaneously, the plates are heated to a temperature typically between 75 ºC and 200 ºC, depending on the material of the matrix used. The pressure and heat cause the composite matrix to bond and form a solid, homogeneous material. Once the hot pressing is complete, the plates are cooled to room temperature, potentially using a specific cooling curve, and the composite material is removed from the press. (Jones, 1998; Reddy, 2004). An example of this process can be found in Fig. 1.
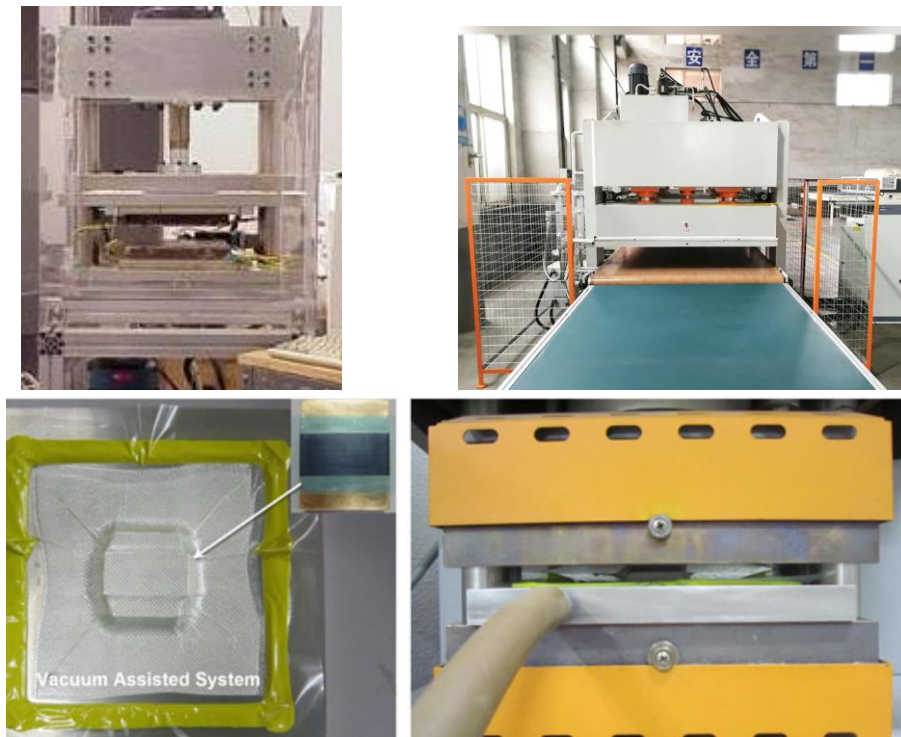
Figure 1. Hot pressing manufacturing process in: (a) laboratorial scale (Adapted from [3]); (b) industrial scale (Adapted from [4]); (c) pressing chamber on a hot plate vacuum assisted process (VAS - adapted from [5]).

(a)   (b)
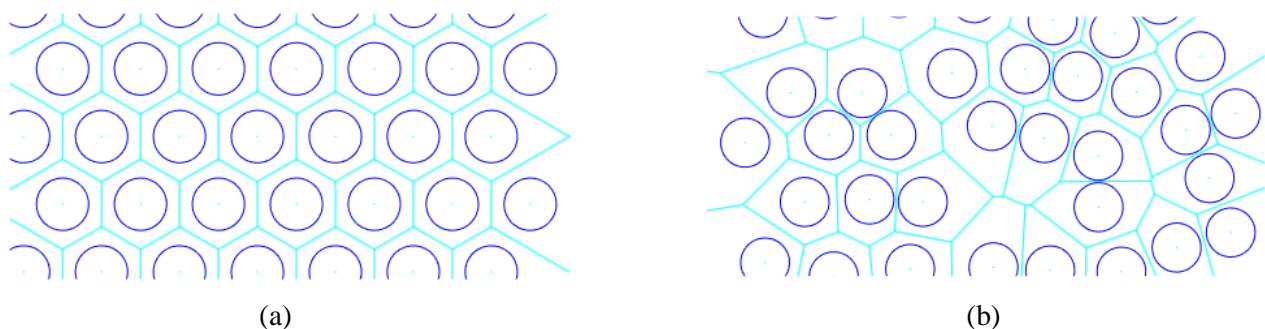
Figure 2. (a) Uniform distributed fibres. (b) Non-uniform distributed fibres. (Adapted from [9]).

However, this heating and cooling cycle results in thermally induced stresses due to the material's thermal expansion. Particularly in thick laminates and/or composites composed of matrices and fibres with significantly different thermal conductivities, the temperature distribution across the thickness and between different plies may be non-uniform, leading to residual stresses during the cooling stage that can warp the plates. Therefore, this study aims to investigate this procedure from the perspective of temperature application on the upper and lower edges of a composite plate and to examine the level of residual stress generated for different temperatures and different heating and cooling curves, considering homogenized models and microstructures of fibres distributed non-uniformly.

To achieve this, a finite element model is proposed on a heterogeneous micro scale (fibre and matrix) with a non-uniform distribution of fibres, as depicted in Fig. 2. Various studies employ the approach of heterogeneous models of microstructure. These results have been previously studied for intralaminar damage [6] and fatigue behaviour [7,8], but have not been applied to the study of thermal residual stresses.

2. METHODOLOGY

The methodology of the work can be summarized by the flow-chart in Fig. 3. Follows a deeper explanation of how the micro scale geometry is created, how the finite element model is implemented including boundary conditions and other solver characteristics and, which study cases were simulated and how the post processing was done for the statistical analysis.
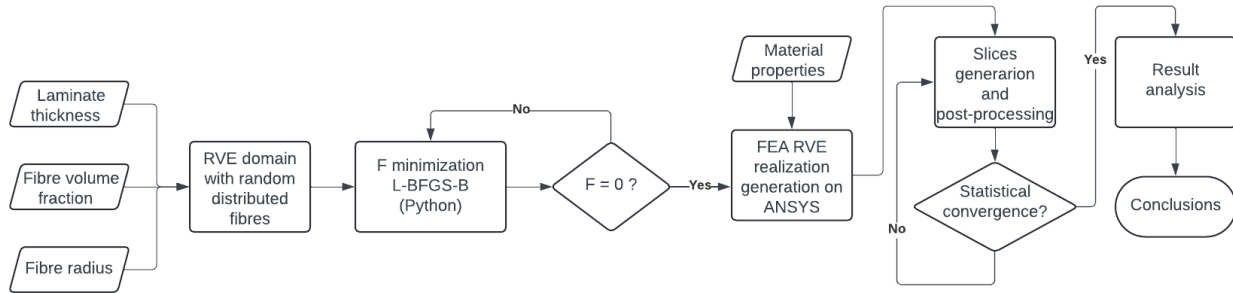
Figure 3. Methodology applied for the RVE generation and thermos-mechanical simulations.

2.1. Non-uniform micro scale geometry creation algorithm

The non-uniform distributed fibres geometry is created using the following procedure, based on the work of [10]. The geometry is created in two steps: first the RVE domain is created and populated by uniformly randomly distributed circles, initially ignoring possible superposition; then an optimization algorithm is run over the position and distances between each fibre to guarantee a given gap between neighbouring fibres is respected.

The RVE domain is a rectangle with dimensions defined as such: height (L_y) is fixed as the thickness of the target laminate; width (L_x) is taken to be such that a number of vertical slices of the RVE can be created that both statistically converge for the results of a given realization (shown in the results to be found to be two) while every horizontal line cutting the slices contains, on average, at least seven fibres, three fibres neighbouring the centre slice from either side, as shown by [6] that this configuration fully captures the influence of each fibre on the centre fibre of that region. This domain is populated by a number of fibres n calculated from the size of the RVE and the desired fibre volume fraction by means of Eq. (1).

$$n = \frac{L_x L_y}{\pi r^2} \qquad (1)$$

For a given random pair of fibre inclusions ij, their superposition can be quantified by the function f Eq. (2),

$$f_{ij} = (\bar{d}_{ij} - d_{ij})H(\bar{d}_{ij} - d_{ij}) \qquad (2)$$

where d_{ij} is the Euclidian distance between the centre of a pair i-j of fibre inclusions; $\bar{d}_{ij}$ is the distance of the closest approach for i and j , which is the sum of their respective radius plus the minimum allowable gap if both are circles; and H is the Heaviside function. f is positive in the case of a superposition and null if the inclusions are with at least a distance equal to a gap of g . Then for a given distribution of n fibres a function F (Eq. (3)) can evaluate the level of superposition of inclusions in the RVE by summing the function f over every possible pair of fibres.

$$F = \sum_i^{n-1} \sum_{j,i \neq j}^n f_{ij} \qquad (3)$$

The following optimization problem can be formulated in Eq. (4):

$$\min F(x, y), \; given \; x_i \in [r, L_x - r], \; y_{\{i} \in [r, L_y - r], \forall i, j \in [1, n] \tag{4},$$

It was demonstrated in [9] that any of F local minima will result in a configuration of inclusions that do not overlap, and at most, only touch, resulting in an RVE with no superposition of fibres. The authors argued that numerical approximations, tolerances and float errors will make it improbably that any fibre touching would occur, however this approach can lead to extremely small distance between fibres which would penalize mesh generation in a finite element analysis and may increase computational cost to unfeasible levels. As such a minimum gap value is introduced to by artificially increasing the radius of each inclusion to guarantee a minimum distance between each pair by using $\overline{d}_{ij} = r + g$.

The optimization problem was solved by [10] using a Newton approach by analytically calculating the Hessian matrix using the gradient of F. This approach however was found to be inefficient given that the gradient of F includes unstable terms near the edge cases because of the Heaviside function. As such we opted to use a quasi-Newton approach numerically approximating the Hessian matrix using the BFGS method [11]. This change both increased the stability of the method and decreased the computational time needed to find a suitable minimum. Further studies showed that the whole approximation was not needed, and a limited BFGS approach using the L-BFGS-B method [12,13] was enough for most of the cases and the increase gain in memory allocation allowed larger models with larger fibre volume fraction and thicknesses to be ran.

2.2. Finite element model

Given a cloud of points with the centre of fibres obtained through the aforementioned optimization algorithm, a finite element model of the RVE consisting in the bidimensional cross-section of a laminate with fibres all aligned in the same direction is constructed. The optimization algorithm, as function of the desired thickness and fibre volume fraction, is ran inside a Python automatization script in ANSYS that automatically creates the circular geometric partitions and material assignments for matrix and fibres. The mesh is automatically generated using a quad-dominant approach with quadratic thermo-mechanical coupling elements with an element size of 1 µm, which was found to be enough to guarantee mesh convergence. The initial temperature was set to 25 °C through the whole RVE.

For boundary conditions, the left and right edges of the RVE were free, the temperature in the top and bottom surfaces were given as the ideal cure temperatures for the chosen material, and can be expressed as function of the t_{ramp}, t_{cure}, t_{min}, T_{cure} temperatures given by Fig. 4 (a), T_∞ is set to be 25 °C. No periodic boundary conditions were applied; the results were obtained from a subset of the model far away from the left and right boundaries to guarantee that the edge effects were not contaminating the results. This approach tends to increase the computational cost and size of the RVE needed but guarantees a statistically significant geometry given the non-uniform fibre distribution.

An example of an RVE with the boundary conditions applied can be seem in Fig. 4 (b).

(a)	(b)
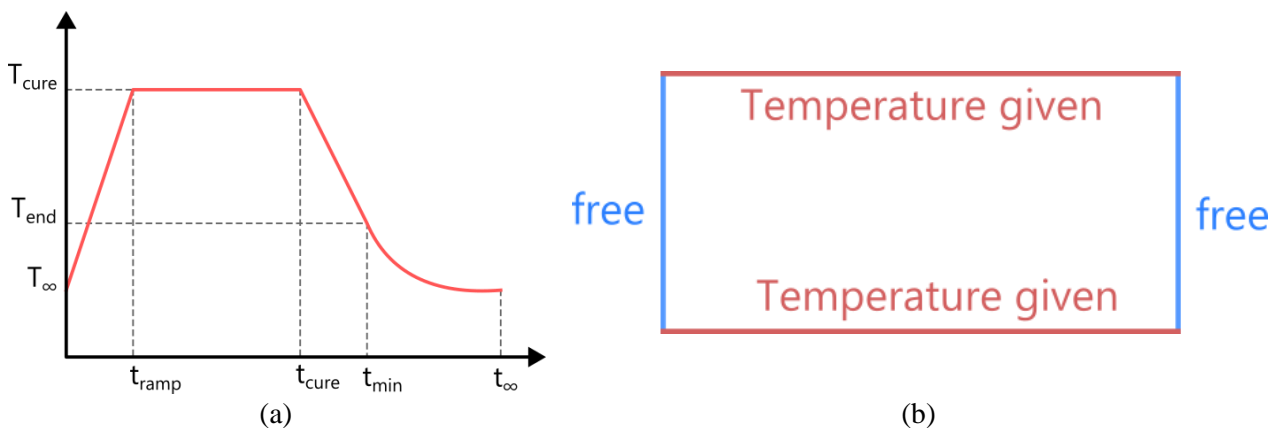
Figure 4. (a) Nomenclature of the temperature ramp boundary condition; (b) boundary conditions.

2.3. Study cases and post-processing

Given the methodology and finite element models defined on the previous sessions, different study cases were made to study the influence of different parameters of the manufacturing process on the thermal and mechanical characteristic formed on the microstructure. Materials for matrix and fibre were chosen and

properties found on Table 1 were used for all studies. Then, first a mesh convergence analysis was done to guarantee the precision of the results. The time step was taken to be 5 ms for the implicit time integration.

Table 1. Materials and geometric properties used in the study cases.

Property	Matrix	Fibre
E [GPa]	4.34	230
v [m/m]	0.38	0.25
C [J/kg K]	1100	777.1
α [μ/K]	46.8	-0.410
r [μm]	N/A	0.35

Table 2. Temperature boundary conditions.

Quantity	T_{cure} [ºC]	T_{end} [ºC]	t_{ramp} [s]	t_{cure} [s]	t_{min} [s]
Value	400	50	0.01	0.02	0,05

Several realizations of different RVEs for varying levels of thickness, fibre volume fraction, and temperature ramps were analysed using the following methodology: each RVE realization was cut into slices of equal length, each slice containing at least seven fibres diameters on average for every horizontal line cutting it; for every slice a centre line was used as reference to obtain the temperature over thickness distribution. An increasing number of slices was tested until a statistically significant mean value for the temperature distribution over times of interest was obtained. The geometry and methodology of this process is described in Fig. 5: each of the red and yellow rectangles are a "slice", which are defined by the distance L taken as 7 fibre diameters; within each slice its centre line is used as reference to obtain the temperature distribution through thickness. This process is made since previous literature works show that the influence of the neighbouring fibres over a centre reference fibre remains for a region of about 3 neighbouring fibres.
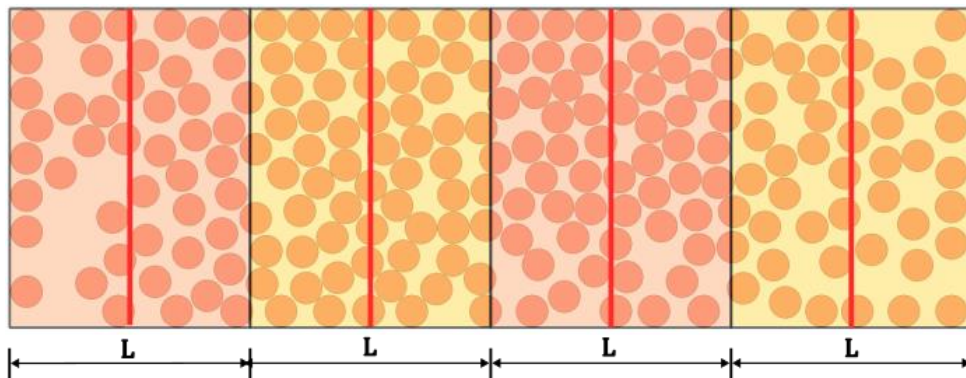
Figure 5. RVE with the definition of slices (red and yellow areas), spaced by 7 fibre diameters; the centre line of each slice (red lines) is used as a reference path for the temperature distributions.

3. RESULTS AND DISCUSSION

An example of the RVE obtained from algorithm optimization for each analysis is shown in Fig. 6, as well a mesh generated for this RVE.
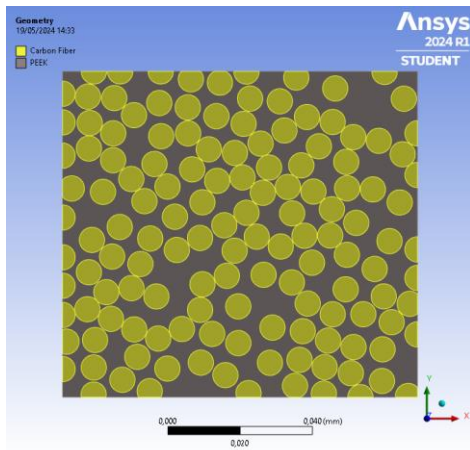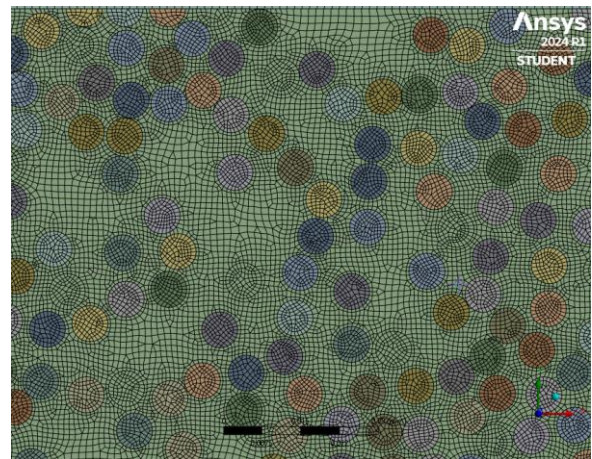
(a)   (b)

Figure 6. (a) example of a RVE obtained from algorithm optimization and (b) the mesh generated for each simulation.

For each RVE model, the process for obtaining the maximum temperature is identical. A necessary study for slices convergence is shown in Fig. 7.
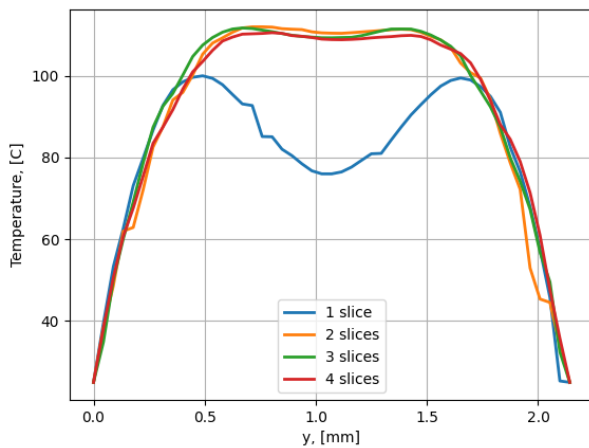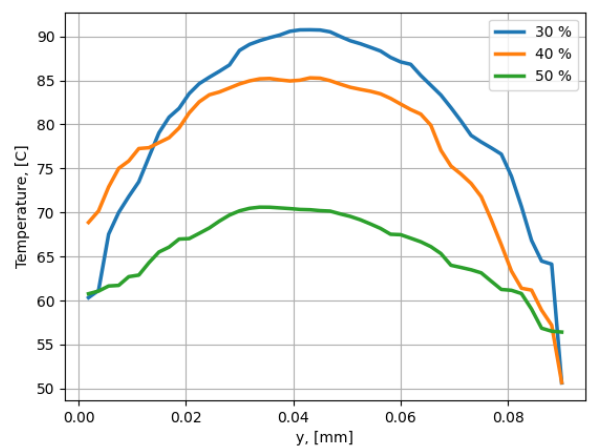
(a)   (b)

Figure 7. (a) Temperature distribution over thickness showing statistically significant mean value; (b) temperature over thickness for three different fibre volume fractions.
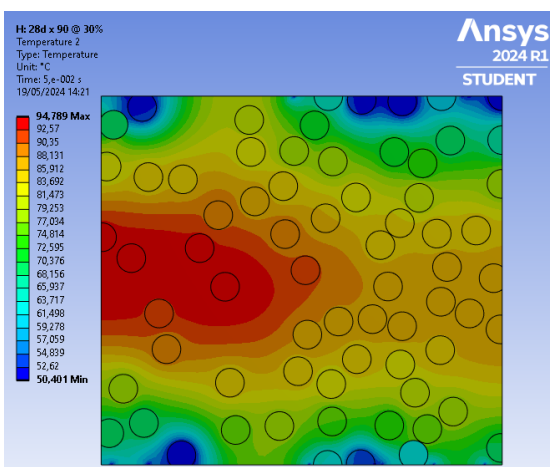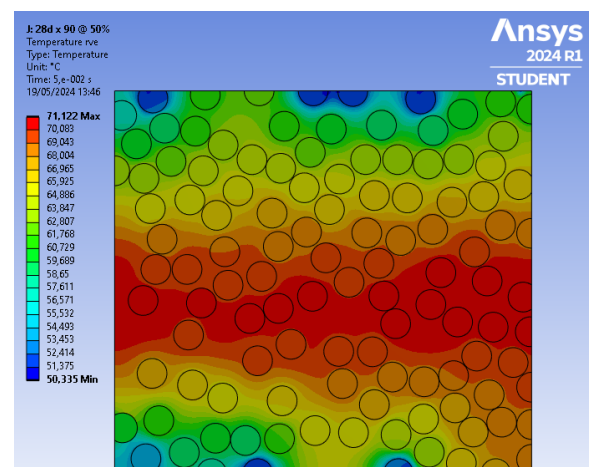
(a)   (b)

Figure 8. Temperature distribution in the RVE (a) for 30% fibre volume fraction and (b) 50% fibre volume fraction.

Due to the statistic results in Fig. 7 (a), the simulations took two slices of fibre representation as it is enough to give the temperature distribution over thickness without any disturbance. Fig. 7 (b) shows the temperature distribution through the thickness for different fibre volume fractions for a specified begging time, which shows a different thermal conductivity and its effects on the temperature at the middle of a layer. Fig. 8 shows how the distribution happens on the whole cross-sections, showing that for some realizations the temperature distributions and heat flow is asymmetrical, which can lead to different levels of curing, consolidations or pockets of over-cured matrix due to overshoot of temperature when only controlling the borders, even for the case of thin layers.

Fig. 9 presents a quantitative analysis of the results depicted in Fig. 8 (a), with the representative volume element divided into two sections (left and right) to analyse the asymmetrical temperature distribution. The analysis is conducted at the centre of each section.
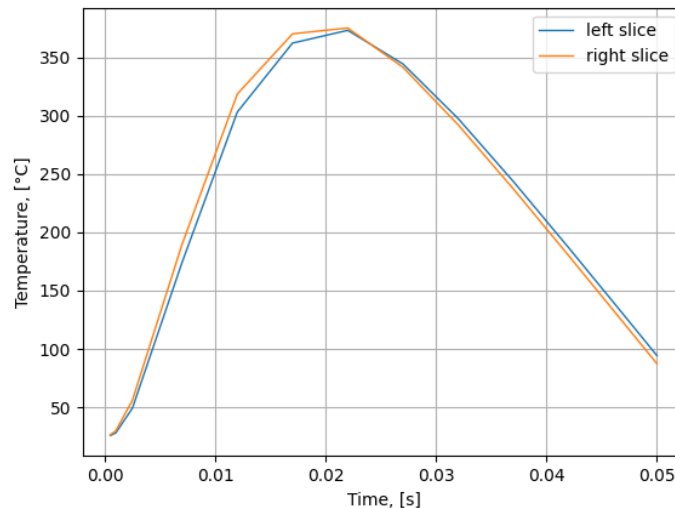
Figure 9. Temperature over time for the 30% fibre volume fraction RVE. The temperature is taken at the centre of each slice.

4. CONCLUSIONS

A methodology to study the manufacturing process of hot pressing for consolidating composite materials was successfully created, including the generation and automatization of a finite element model considering the non-uniform distribution of fibres. The process was successful and can easily create different statistically significant microstructure realizations. The process was used with different values of fibre volume fraction and a temperature ramp for carbon fibre and poly(ether ether ketone) (PEEK). The conclusions were that an increase in the fibre volume fraction in the RVE model causes a significant decrease in the maximum temperature obtained in the centre of the composite material, which may be an aggravating factor for the consolidation process of the polymer matrix in its manufacturing process. The non-uniform distribution of fibres can create asymmetrical distributions of temperature that can lead to wrongly cured matrix on areas of matrix rich pockets and may lead to defects. As such, more studies need to be done to better understand these mechanisms and correlate the non-uniformity, heat flux analysis and defects.

4.1. Declaration of Competing Interest

The authors declare no conflict of interest.

4.2. Fundings

4.3. Acknowledgements

5. REFERENCES

[1] Jones RM. Mechanics of composite materials. 2nd ed. Boca Raton, FL: CRC Press; 1998.

[2] Reddy JN. Mechanics of Laminated Composite Plates and Shells. CRC Press; 2003. https://doi.org/10.1201/b12409.

[3] Carvalho L, Ranita J, Martins J, Garrido N, Costa C. INFLUÊNCIA DO CICLO DE PRENSAGEM NA QUALIDADE DO AGLOMERADO DE PARTÍCULAS DE MADEIRA FABRICADO COM UM TEOR ELEVADO DE PARTÍCULAS RECICLADAS, 2005.

[4] SAMACH. Hot Pressing Composite Production Line (samach.cn) 2024.

[5] Nam TH, Goto K, Oshima K, Premalal EVA, Shimamura Y, Inoue Y, et al. Mechanical property enhancement of aligned multi-walled carbon nanotube sheets and composites through press-drawing process. Advanced Composite Materials 2016;25:73–86. https://doi.org/10.1080/09243046.2014.985419.

[6] Asp LE, Berglund LA, Talreja R. Prediction of matrix-initiated transverse failure in polymer composites. Compos Sci Technol 1996;56:1089–97. https://doi.org/https://doi.org/10.1016/0266-3538(96)00074-7.

[7] Maragoni L, Carraro PA, Quaresimin M. Effect of voids on the crack formation in a [45/−45/0]s laminate under cyclic axial tension. Compos Part A Appl Sci Manuf 2016;91:493–500. https://doi.org/https://doi.org/10.1016/j.compositesa.2016.02.018.

[8] Carraro PA, Maragoni L, Quaresimin M. Prediction of the crack density evolution in multidirectional laminates under fatigue loadings. Compos Sci Technol 2017;145:24–39. https://doi.org/https://doi.org/10.1016/j.compscitech.2017.03.013.

[9] Sartorato M. A numerical homogenization technique for unidirectional composites using polygonal generalized finite elements. Proceedings of the Institution of Mechanical Engineers, Part L: Journal of Materials: Design and Applications 2022;236:1351–63. https://doi.org/10.1177/14644207211046320.

[10] Nakka R, Harursampath D, Pathan M, Ponnusami SA. A computationally efficient approach for generating RVEs of various inclusion/fibre shapes. Compos Struct 2022;291:115560. https://doi.org/10.1016/j.compstruct.2022.115560.

[11] Jorge Nocedal, Stephen J. Wright. Numerical Optimization. Springer New York; 2006. https://doi.org/10.1007/978-0-387-40065-5.

[12] Byrd RH, Lu P, Nocedal J, Zhu C. A Limited Memory Algorithm for Bound Constrained Optimization. SIAM Journal on Scientific Computing 1995;16:1190–208. https://doi.org/10.1137/0916069.

[13] Zhu C, Byrd RH, Lu P, Nocedal J. Algorithm 778: L-BFGS-B. ACM Transactions on Mathematical Software 1997;23:550–60. https://doi.org/10.1145/279232.279236.

[14] *Supplier Data – Polyetheretherketone (PEEK).* AZO Materials, 2003. (https://www.azom.com/properties.aspx?ArticleID=1882), accessed 11 May 2024.

[15] *HPMs – High-performance materiais: PEEK.* AIKOLON, 2019. (https://www.aikolon.fi/en/products/high-performance-plastics/peek), accessed 11 May 2024.

[16] *PEEK Virgin.* MATMATCH, 2024. (https://matmatch.com/materials/keyu011-peek), accessed 11 May 2024.

[17] *Mitsubishi Chemical Advanced Materials Ketron® 1000 PEEK, Extruded Unfilled Polyetherether Ketone (ASTM Product Data Sheet).* MATWEB. (https://www.matweb.com/search/DataSheet.aspx?MatGUID=53b9159c018544a599a06726922c9b8e&ckck=1) , accessed 11 May 2024.

[18] *T300 Carbon Fiber Sheet.* MATMATCH, 2024. (https://matmatch.com/materials/jinj0001-t300-carbon-fiber-sheet), accessed 11 May 2024.

[19] *Toray T300 Carbon Fiber.* MATWEB. (https://www.matweb.com/search/DataSheet.aspx?MatGUID=86d0be5b80514c66b2c91e3357c57a1f), accessed 11 May 2024.

[20] Z. Dai et al. Effect of heat treatment on carbon fiber surface properties and fibers/epoxy interfacial adhesion. *Applied Surface Science*, Volume 257, 2011. (https://doi.org/10.1016/j.apsusc.2011.04.129)

[21] L. Feuillerat et al. Effect of poly(ether ether ketone) degradation on commingled fabrics consolidation. *Composites Part A: Applied Science and Manufacturing,* Volume 149, 2021. (https://doi.org/10.1016/j.compositesa.2021.106482)

FAILURE ENVELOPE FOR UNIDIRECTIONAL LAMINAE SUBJECTED TO TRANSVERSAL AND OUT-OF-PLANE SHEAR LOADS

Lucas L. Vignoli[(a), *,] Arthur Adeodato[(b)], Marcelo A. Savi[(c)], Pedro M.C.L. Pacheco[(d)], Alexander L. Kalamkarov[(e)]

(a) ● 0000-0003-3288-3568 (Federal University of Rio de Janeiro – Brazil)
(b) ● 0000-0002-0812-6594 (Universidade do Estado do Rio de Janeiro – Brazil)
(c) ● 0000-0001-5454-5995 (Federal University of Rio de Janeiro – Brazil)
(d) ● 0000-0002-3374-5119 (Centro Federal de Educação Tecnológica Celso Suckow da Fonseca – Brazil)
(e) ● 0000-0002-9964-5882 (Dalhousie University – Canada)
* Corresponding author: ll.vignoli@mecanica.coppe.ufrj.br

Abstract: Unidirectional laminae are transversally isotropic materials with five independent elastic properties and six strengths. For the elastic properties, Tsai's modulus has been successfully applied to decrease the number of experimental tests required for characterization. On the other hand, few advances can be found for the strengths. However, for transversal and out-of-plane shear loads, experimental evidence indicates that the interface failure tends to be predominant, i.e. the out-of-plane shear strength may be related to the transversal tensile and compressive strengths since there are only two interface strengths on the transversal plane, namely normal and shear strengths. In this study, the VSPKc micromechanical model is applied to obtain the interface strengths from the transversal tensile and compressive strengths. Next, the out-of-plane shear strength is obtained based on the interface strengths. At last, the interface failure for combined transversal and out-of-plane shear loads is evaluated to generate the micromechanical-based failure envelope. The results indicate an average error of 6% for the out-of-plane shear strength compared with experimental data of three CFRP (Carbon Fiber Reinforced Polymer) laminae, indicating the model capability, the consistency of the failure envelope obtained, and the possibility of avoiding the experimental test for the out-of-plane shear load.

1. INTRODUCTION

Due to the multiscale nature of composite materials, the design of composite structures requires many variables [1], which makes the implementation of optimization routines a hard task [2]. For unidirectional laminates, which is the focus of this investigation, the laminae are transversally isotropic. Hence, five elastic properties and six strengths are necessary [3].

The most considerable recent advance to decrease the number of experimental tests for mechanical characterization is known as Tsai's modulus. Tsai and Melo [4] proposed a trace-relation where only one elastic property is required. Despite the original theory being limited to CFRP (carbon fiber reinforced polymers) subjected to plane stress state, it was extended to 3D stress state as well as other fiber types [5-7]. This considerable innovative theory is very helpful for different applications [8-10] and many studies indicating the reliability of Tsai's modulus can be found in the literature [11-13].

Concerning the trial to relate lamina strengths also aiming to decrease the number of experimental tests, the most promising way is the investigation of the correlation between the transversal tensile strength, S_{22}^t, the transversal compressive strength, S_{22}^c, and the out-of-plane shear strength, S_{23}^s. As reviewed by Vignoli [14], despite some existent proposals in the literature [15-18], the applications of the VSPKc micromechanical

model obtain the best fit with experimental data. Although the VSPKc model was first proposed to compute the effective elastic properties [19], some recent studies indicate that it can also be applied for the strengths [20,21].

The goal of the present investigation is to evaluate the laminae failure subjected to transversal tensile and compressive load with the out-of-plane shear load. To deal with this analysis, the proposed approach combines the Tsai's modulus and the VSPKc model. After this Introduction, the novek methodology is explained in Section 2. The results are presented in Section 3, and the final remarks are pointed out in Section 4.

2. METHODOLOGY

Tsai and Melo [4] proposed that the unique independent property of CFRP unidirectional lamina is trace of the plane stress stiffness matrix. This proposal was extended to 3D stress states and can be expressed by the following equation [5]

$$tr(\boldsymbol{C}) = \frac{E_1}{E_1^*} = \frac{E_2}{E_2^*} = \frac{G_{12}}{G_{12}^*} = \frac{G_{23}}{G_{23}^*} \tag{1}$$

where $\boldsymbol{C}$ is the stiffness matrix, E_1 is the longitudinal elastic modulus, E_2 is the transversal elastic modulus, G_{12} is the in-plane shear modulus, G_{23} is the out-of-plane shear modulus, and $E_1^* = 0.7349$, $E_2^* = 0.04351$, $G_{12}^* = 0.0261$, and $G_{23}^* = 0.0148$ are the normalized properties.

For the present study, main relation derived directly from Eq.(1) is

$$G_{23} = \left(\frac{G_{23}^*}{E_2^*}\right) E_2 \tag{2}$$

(a)

(b)
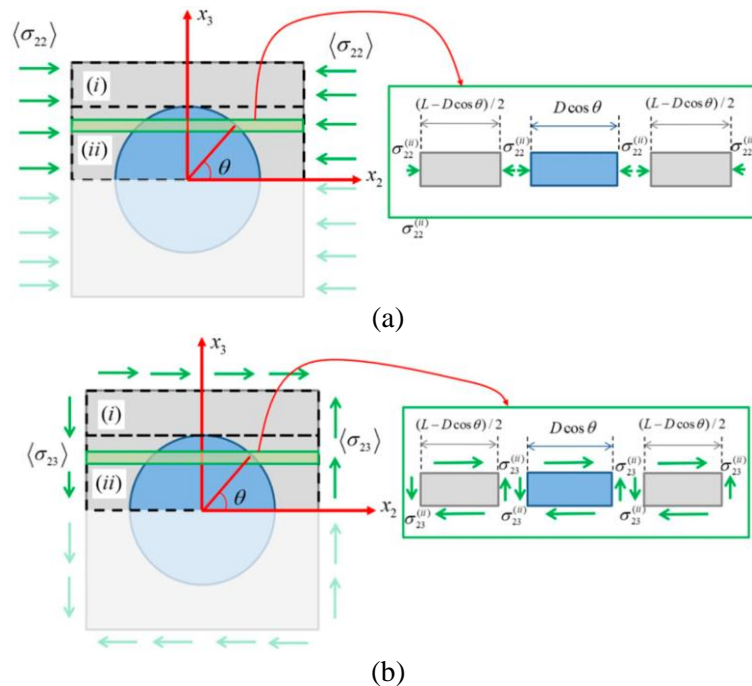
Figure 1. Load distribution inside the unit cell according to the VSPKc model: (a) transversal load; (b) out-of-plane shear load.

The consistency between Tsai's modulus and VSPKc micromechanical model was demonstrated by Vignoli et al. [22]. According to the VSPKc model [14], the macromechanical load distribution inside the unit cell is represented in the Fig. 1, and the interface tractions for combined transversal normal and out-of-plane shear loads using the superposition principle is

$$\tau_{rr}(\sigma_{22}, \sigma_{23}, \theta) = \left(\frac{E^m}{E_2} \frac{\cos^2 \theta}{1 + a_{22} \cos} \right) \sigma_{22} + \left(2 \frac{G^m}{G_{23}} \frac{\cos \theta \sin \theta}{1 + a_{23} \cos \theta} \right) \sigma_{23} \tag{3}$$

$$\tau_{r\theta}(\sigma_{22}, \sigma_{23}, \theta) = \left(-\frac{E^m}{E_2} \frac{\cos \theta \sin \theta}{1 + a_{22} \cos} \right) \sigma_{22} + \left(\frac{G^m}{G_{23}} \frac{\cos^2 \theta - \sin^2 \theta}{1 + a_{23} \cos \theta} \right) \sigma_{23} \tag{3}$$

where τ_{rr} and $\tau_{r\theta}$ are the normal and shear interface traction, E^m is the matrix elastic modulus, $G^m = E^m/2(1 + v^m)$ is the matrix shear modulus, v^m is the matrix Poisson's ratio, $0° \leq \theta \leq 90°$ is the angle used to map the interface, and

$$a_{22} = 2 \left[\left(\frac{E^m}{E_2^f} \right) - 1 \right] \sqrt{\frac{V_f}{\pi}} \tag{4}$$

$$a_{23} = 2 \left[\left(\frac{G^m}{G_{23}^f} \right) - 1 \right] \sqrt{\frac{V_f}{\pi}} \tag{5}$$

where V_f is the fiber volume fraction, E_2^f is the fiber transversal elastic modulus, and G_{23}^f is the fiber out-of-plane shear modulus.

The interface failure function can be defined by [23,24]

$$f(\sigma_{22}.\sigma_{23}, \theta) = \left(\frac{\max(0, \tau_{rr})}{S_n^i} \right)^2 + \left(\frac{\tau_{r\theta}}{S_s^i} \right)^2 \tag{6}$$

where S_n^i is the interface normal strength, S_s^i is the interface shear strength, and the failure happens when $f = 1$. Note that $f = f(\sigma_{22}, \sigma_{33}, \theta)$ because $\tau_{rr} = \tau_{rr}(\sigma_{22}, \sigma_{23}, \theta)$ and $\tau_{r\theta} = \tau_{r\theta}(\sigma_{22}, \sigma_{23}, \theta)$.

Based on this theoretical background, the proposed methodology is implemented following the steps:

i) the inputs are $V_f, E_2, S_{22}^t, S_{22}^c, E^m, v^m, E_2^f, G_{23}^f$;

ii) S_n^i and S_s^i can be computed evaluating $\max[f(S_{22}^t, 0, \theta)] = 1$ and $\max[f(-S_{22}^c, 0, \theta)] = 1$;

iii) once S_n^i and S_s^i are obtained, S_{23}^s is computed by applying $\max[f(0, S_{23}^s, \theta)] = 1$;

iv) to obtain the failure envelope, for any angle α in the plane $\sigma_{22} - \sigma_{23}$, $\sigma_{22} = r \cos \alpha$ and $\sigma_{23} = r \sin \alpha$, where r is defined by $\max[f(r \cos \alpha, r \sin \alpha, \theta)] = 1$.

3. RESULTS AND DISCUSSION

For the implementation of the proposed methodology, the experimental data from three CFRP laminae were compiled from [26] are listed in Table 1. As introduced in Section 2, these are the input required for the proposed methodology.

Table 1. Experimental properties of CFRP laminae [27].

CFRP	#	V_f	E_2[GPa]	S_{22}^t[MPa]	S_{22}^c[MPa]	E^m[GPa]	v^m	E_2^f[GPa]	G_{23}^f[GPa]
IM7/8552	1	0.6	0	73	185	4.08	0.38	19	7
G40-800/5260	2	0.6	10	75	210	3.45	0.35	19	7
AS4/3501-6	3	0.6	11	48	200	4.2	0.34	15	7

Figure 2 shows the interface strengths for the three CFRP laminae. The IM7/8552 (#1) represents the composite with highest strengths, while the AS4/3501-6 (#3) has the smallest strengths. Additionally, the AS4/3501-6 (#3) the unique case with $S_s^i > S_n^i$.
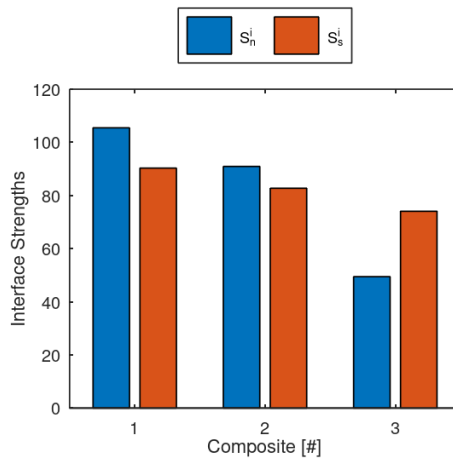
Figure 2. Interface strengths computed using the VSPKc micromechanical model.

The distributions of the interface tractions and of the failure functions for $\sigma_{22} = S_{22}^t$ and $\sigma_{22} = -S_{22}^c$ are presented in Fig. 3 and 4, respectively. Despite the failure function introduced in Eq.(6) considers the interaction between S_n^i and S_s^i, the results for $\sigma_{22} = S_{22}^t$ indicate that the failure happens in $\theta = 0°$, where $\tau_{r\theta} = 0$, and the results for $\sigma_{22} = -S_{22}^c$ indicate that $\tau_{rr} < 0$ for any θ. Hence, τ_{rr} can be directly computed evaluating $\sigma_{22} = S_{22}^t$ and $\tau_{r\theta}$ is obtained analysing $\sigma_{22} = -S_{22}^c$.
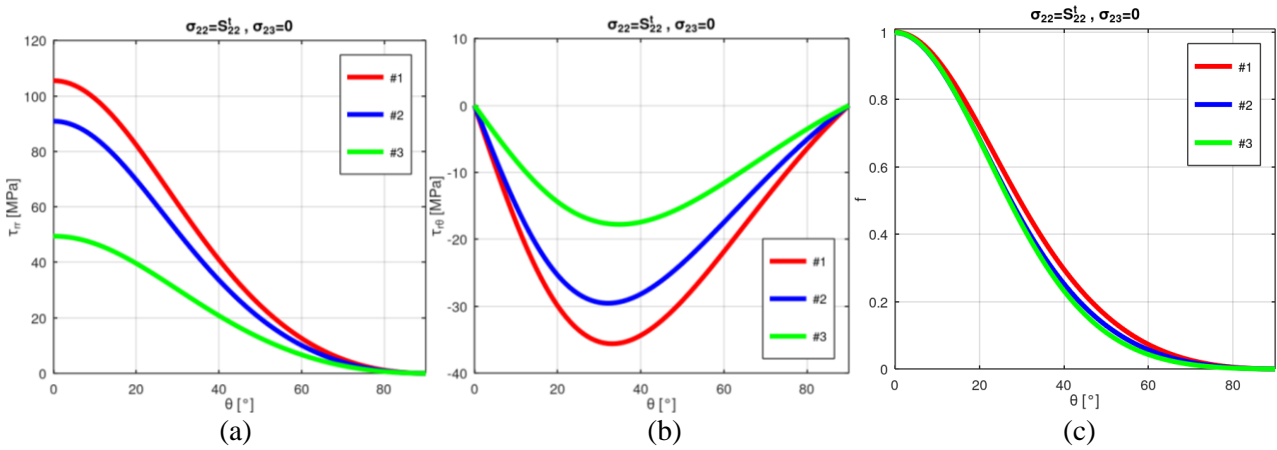
Figure 3. Normal interface traction (a), shear interface traction (b), and failure function (c) distribution for transverse tensile load with $\sigma_{22} = S_{22}^t$.
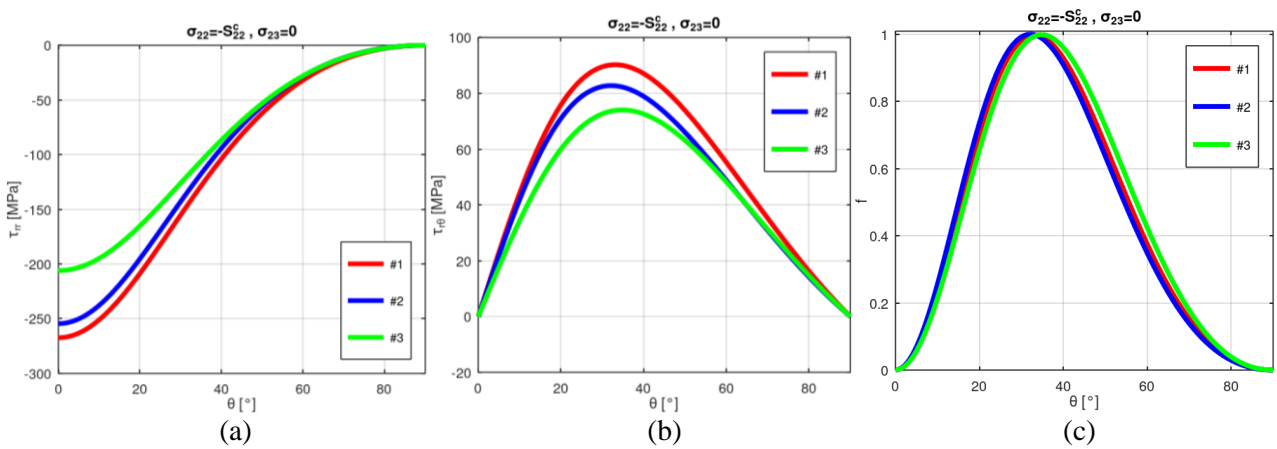
Figure 4. Normal interface traction (a), shear interface traction (b), and failure function (c) distribution for transverse compressive load with $\sigma_{22} = -S_{22}^c$.

The estimations of G_{23} using Tsai's modulus and S_{23}^s using the VSPKc model are presented in Fig, 5 considering the ratio between the model and the experimental data. For both properties, the maximum error is around 10% and the average error is around 5%, highlighting the capability of the proposed methodology.
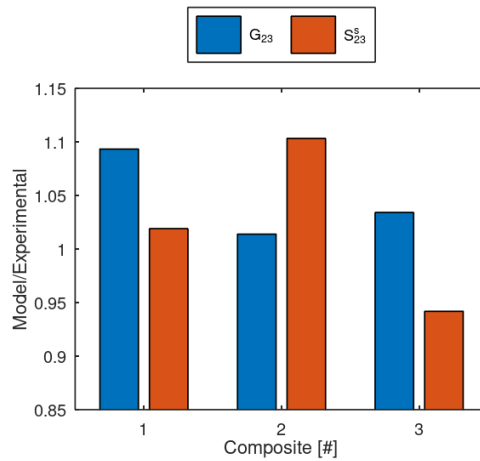
Figure 5. Validation of the experimental estimation for G_{23} and S_{23}^s using Tsai's modulus and VSPKc model.

The variations of the interface tractions and of the failure function for $\sigma_{23} = S_{23}^s$ is presented in Fig. 6. These results indicate that the out-of-plane shear strength for IM7/8552 (#1) and G40-800/5260 (#2) are dominated by $\tau_{r\theta}$, while for AS4/3501-6 (#3) the influence of τ_{rr} is predominant.
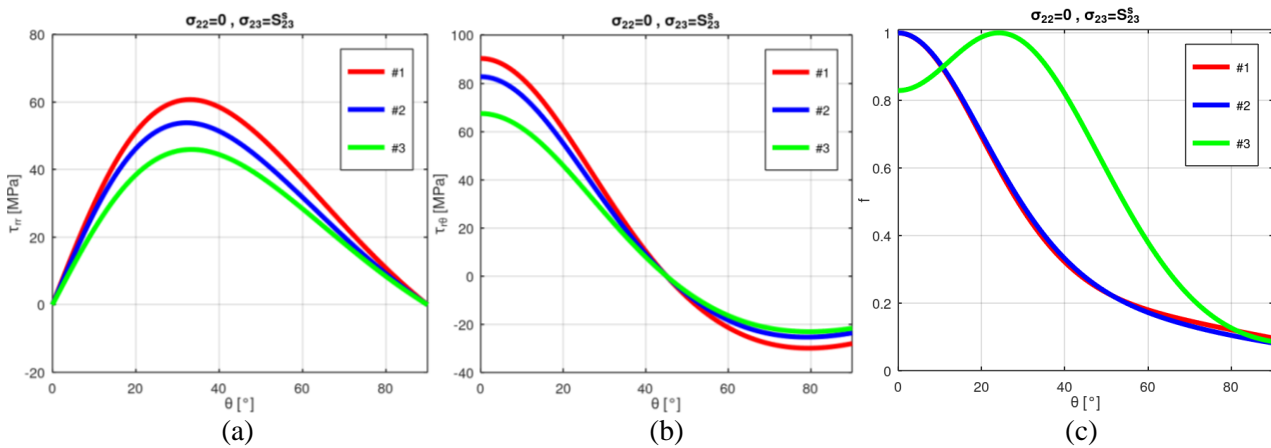
Figure 6. Normal interface traction (a), shear interface traction (b), and failure function (c) distribution for out-of-plane shear load with $\sigma_{23} = S_{23}^s$.
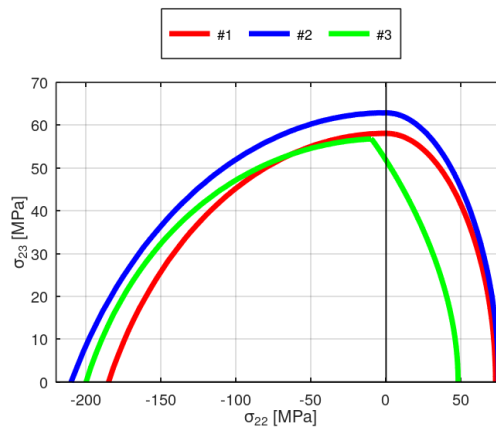
Figure 7. Micromechanical failure envelopes.

Once the novel methodology proposed is validated, it is extended to analyse the failure envelope in the $\sigma_{22} - \sigma_{23}$ plane. The results obtained are presented in Fig. 7 for the three laminae. For all of them, the right side of the graphic indicate the failure dominant by τ_{rr} and part where $\tau_{r\theta}$ is prevalent is on the left side. For IM7/8552 (#1) and G40-800/5260 (#2) a smooth transition is realized with $\sigma_{22} > 0$, and a more abrupt transition is obtained for AS4/3501-6 (#3) with $\sigma_{22} < 0$.

4. CONCLUSIONS

A novel methodology is proposed in this study combining the Tsai's modulus and the VSPKc micromechanical model to evaluate the failure of unidirectional laminae subjected to transversal normal and out-of-plane shear loads. As results, the experimental tests to measure G_{23} and S_{23}^s can be avoided for CFRP with average errors smaller than 10%. Additionally, the approach presented is able to predict the failure envelope on the plane $\sigma_{22} - \sigma_{23}$ considering the interface failure.

4.1. Declaration of Competing Interest

The authors declare no conflict of interest.

5. REFERENCES

[1] L.L. Vignoli, M.A. Savi. Multiscale failure analysis of cylindrical composite pressure vessel: a parametric study. Latin American Journal of Solids and Structures, 15, 2018.

[2] I.V. Andrianov, J. Awrejcewicz, V.V. Danishevs'kyy VV. Asymptotical mechanics of composites - modelling composites without FEM. Springer, 2018.

[3] E.J. Barbero. Introduction to composite materials design. 3rd edition, CRC Press, 2018.

[4] S.W. Tsai, J.D.D. Melo. An invariant-based theory of composites. Compos Sci Technol, 100, 237–243, 2014.

[5] S.W. Tsai, J.D.D. Melo, S. Sihn, A. Arteiro, R. Rainsberger, Composite Laminates - Theory and practice of analysis, design and automated layup, Composites Design Group, Department of Aeronautics & Astronautics, Stanford University, Stanford, 2017***

[6] R.M. Guedes. Validation of trace-based approach to elastic properties of multidirectional glass fibre reinforced composites. Compos Struct, 257, 113170, 2021.

[7] L.L. Vignoli et al. Using asymptotic homogenization and machine learning to derive a 3D trace theory for GFRP. Mechanics of Advanced Materials and Structures, 0, 1–13, 2024.

[8] S.W. Tsai et al. DOUBLE– DOUBLE Simplifying the Design and Manufacture of Composite Laminates. Stanford: Composite Design Group, 2023.

[9] L.L. Vignoli, P.P. Kenedi, M.J.B. Mariano. Exploring thermography technique to validate multiscale procedure for notched CFRP plates. Composites Part C: Open Access, 7, 100241, 2022.

[10] R.D. Cunha et al. Low velocity impact response of non-traditional double double laminates. Journal of Composite Materials, 57, 1807-1817, 2023.

[11] S.K. Ha, C.A. Cimini. Theory and validation of the master ply concept for invariant-based stiffness of composites. J Compos Mater, 52, 1699–1708, 2018.

[12] A. Arteiro et al. A case for Tsai's Modulus, an invariant-based approach to stiffness", Compos Struct 252: 112683

[13] L.L. Vignoli et al. Trace theory applied to composite analysis: A comparison with micromechanical models. Compos Commun, 25, 100715, 2021.

[14] L.L. Vignoli. Is the out-of-plane shear strength an independent property? A micromechanical perspective about a macromechanical question. Journal of Composite Materials, 57, 4379-4388, 2023.

[15] S.J. DeTeresa, G.J. Larsen. Reduction in the Number of Independent Parameters for the Tsai-Wu Tensor Polynomial Theory of Strength for Composite Materials. J Compos Mater, 37, 1769–1785, 2003.

[16] C.G. Davila, P.P. Camanho, C.A. Rose. Failure Criteria for FRP Laminates. J Compos Mater, 39, 323–345, 2005.

[17] R.M. Christensen. 2013 Timoshenko Medal Award Paper - Completion and Closure on Failure Criteria for Unidirectional Fiber Composite Materials. J Appl Mech, 81, 011011, 2014.

[18] S. Li, M. Xu, E. Sitnikova. The Formulation of the Quadratic Failure Criterion for Transversely Isotropic Materials: Mathematical and Logical Considerations. Journal of Composites Science, 6, 82, 2022.

[19] L.L. Vignoli et al. A Novel Micromechanical Model Based on the Rule of Mixtures to Estimate Effective Elastic Properties of Circular Fiber Composites. Appl Compos Mater, 29, 1715–1731, 2022.

[20] L.L. Vignoli et al. Micromechanical fiber-matrix interface model for in-plane shear in unidirectional laminae. Mechanics of Advanced Materials and Structures, 0, 1–13, 2023.

[21] L.L. Vignoli et al. Analytical modeling of fiber–matrix interface failure in unidirectional laminae subjected to in-plane shear loads. Proceedings of the Institution of Mechanical Engineers, Part L: Journal of Materials: Design and Applications, 0, 2024.

[22] L.L. Vignoli, et al. Theoretical Justification of Tsai's Modulus based on Micromechanical Analysis. Compos Sci Technol, 238, 110041, 2023.

[23] R.Q. Macedo et al. Intraply failure criterion for unidirectional fiber reinforced composites by means of asymptotic homogenization. Compos Struct, 159, 335–349, 2017.

[24] L.L. Vignoli et al. Micromechanical analysis of transversal strength of composite laminae. Compos Struct, 250, 112546, 2020.

ABRASIVE WEAR OF CARBON NANOSTRUCTURES AND EPOXY RESIN COMPOSITES

H. Guimarães[(a)*], K. Sales de Oliveira[(b)], J. A. da Cruz [(c)], S. C. Amico [(d)], T. Doca[(e)]

(a) 0009-0003-4063-5131 (University of Brasília – Brazil)
(b) 0000-0002-0509-9842 (University of Brasília – Brazil)
(c) 0000-0001-5123-1608 (Universidade Federal do Rio Grande do Sul – Brazil)
(d) 0000-0003-4873-2238 (Universidade Federal do Rio Grande do Sul – Brazil)
(e) 0000-0001-5376-5590 (University of Brasília – Brazil)

*Corresponding author: 190029404@aluno.unb.br

Abstract: Epoxy resin is a thermoset polymer, with a relatively high mechanical and thermal resistance when compared to other polymers. Studies regarding its wear behavior when combined with carbon based nanofillers have been made, but there seems to be a gap in the literature regarding micro-abrasion. This work aims to study the tribological performance of pure epoxy resin and epoxy resin reinforced with carbon nanotubes or graphene platelets. Micro-abrasive wear tests are conducted using a rotating sphere tribometer. The worn volume is measured via confocal microscopy. It was possible to conclude that the addition of graphene as filler lubricates the surface, reducing mass loss and wear rates. Carbon nanotubes influenced the composite's brittleness, and the configuration with higher filler addition presented lower wear resistance.

1. INTRODUCTION

Due to their low friction, high corrosion resistance, and reduced production costs, reinforced polymers offer an attractive alternative to typical metallic coatings. However, low mechanical and thermal resistance hinders its use for a broader range of applications. In that context, filler materials, such as carbon nanotubes (CNT) and graphene nanoplatelets (GNP), could improve the mechanical performance of epoxy resin, resulting in effective and low-cost coating materials.

Some aspects of the wear behavior of carbon nanostructures-epoxy composites can be found in the literature. Campo et al. [1] evaluated the wear performance of multi-walled carbon nanotubes-epoxy composites through pin-on-disk tests. Higher concentrations of reinforcements reduced mass loss and wear rate, though, for concentrations below 0.5%, the friction coefficient increased. Yan et al. [2] investigated epoxy reinforced with aligned carbon nanotubes under lubricated conditions. The composite yielded wear rate and friction coefficient lower than pure epoxy. Pure epoxy also seemed to suffer from both fatigue and abrasive wear, while for the composites the abrasion mechanism was predominant. Hussein et al. [3] studied the wear resistance of graphene, carbon fiber, and carbon nanotubes reinforced epoxy. For graphene and carbon fiber, an increase in filler concentration promoted consistent improvement in wear rates. For carbon nanotubes, an optimal addition is identified at around 3%, likely due to an increase in brittleness for higher concentrations. Dong et al. [4] examined friction coefficient and wear rates of multi-walled carbon nanotubes epoxy matrix composites, under dry sliding contact conditions. The friction coefficient is reduced up until 1.5% filler concentration, after which it assumes a stable value, while wear rates increase after that concentration value.

It can be noted that the behavior recorded followed a somewhat regular tendency, however, no studies contemplating rotating sphere tests have been found. Micro-scale abrasive tests are often used to

evaluate thin coatings, and they also allow mapping out possible variations in wear resistance along a surface due to the reduced size of the wear scars [5]. This work aims to evaluate the wear performance of carbon nanostructures-epoxy resin composites in micro-scale abrasive tests. Two concentrations are studied for each nanostructure (CNT or GNP): 0.5% and 1.0%, besides the reference configuration (pure epoxy). Rotating sphere tests are conducted, and wear scar depth, diameter, and volume are measured via confocal microscopy. The results are used to determine abrasive wear coefficients. The study of the scars is also carried-out to determine qualitative aspects related to the wear mechanisms involved.

2. METHODOLOGY

2.1. Materials

All specimens were manufactured by the *Laboratório de Materiais Poliméricos (Universidade Federal do Rio Grande do Sul)*. Epoxy resin AR260 was mixed with triethylenetetramine HY 951 at 100:13 mass ratio. The resin was degassed for five minutes and cured at room temperature for 24 hours, and post-curing followed for 3 hours at a temperature of 100°C. For the composites, STREM Chemicals fillers were mixed via mechanical stirring at 13000 rpm and by sonication (60% amplitude, pulses on/off, 60 s/60 s) in an ice bath. GNP width varied between 6-8 nm. CNT is multi-walled, with a diameter of 140 nm and average length of 7 µm.

The prismatic specimens, squared section of 25 x 25 mm, were polished, to control thickness (5.00 ± 0.05 mm) and flatness. Initial surface average roughness (Ra) was measured for reference, results are listed in Table 1.

Table 1. Average roughness

	Epoxy resin	**0.5% CNT**	**1.0% CNT**	**0.5% GNP**	**1.0% GNP**
Ra (µm)	0,164	0,077	0,191	0,136	0,098

2.2. Experimental Procedure

The micro-abrasive wearrotating sphere tests are carried out in an Anton Paar CAT[2] Calotest (Fig. 1). An AISI 420 steel sphere, with a diameter, *d,* equal to 15 mm, is selected. A rotating speed, *n*, of 1000 rpm and an inclination angle equal to 30° (with the horizontal plane) have been established following the guidelines of the equipment manual and after preliminary testing. A solution of 1 µm aluminum oxide and deionized water, at a volume ratio of 30:70, is prepared, and it is fed to the interface sphere-specimen at a rate of 1 mL/min. The use of an abrasive medium is recommended to accelerate the process and to ensure consistent wear marks. Four testing times are selected for the evaluation of the wear rate: *t* = 3, 5, 7.5, and 10 min.
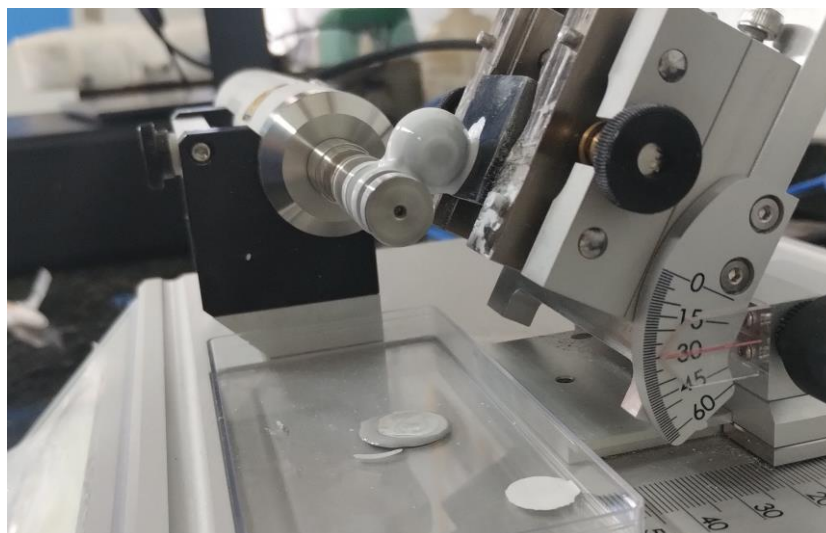
Figure 1. Experimental setup of the abrasive wear test using a AISI 420 steel sphere rotating.

Measurement of scar depth and diameter is made in two perpendicular directions at the centre of the spherical caps. Worn volume, *V,* is measured using a computational tool available in the confocal microscope software. The sliding distance, *S,* can be determined using Eq. (1).

$$S = \pi d n t \quad (1)$$

The product of the sliding distance and normal load can be correlated with the worn volume via Archard's Law, as follows,

$$S \cdot N = \frac{V}{k} \quad (2)$$

3. RESULTS AND DISCUSSION

Fig. (2) presents the worn volume measured for each sliding distance. All configurations presented linear growth of the worn volume with the increase in sliding distance, as predicted by Eq. (2). Pure epoxy, 0.5% GNP and 1.0% CNT exhibited the lowest resistance, while 1.0% GNP and 0.5% CNT lost less volume for the same sliding distances. Pure epoxy and both CNT configurations presented the least consistent behavior. That could be due to the presence of defects, resulting from the fabrication process, which may have increased brittleness locally. Also, uneven filler distribution and fiber orientation could have influenced wear resistance.
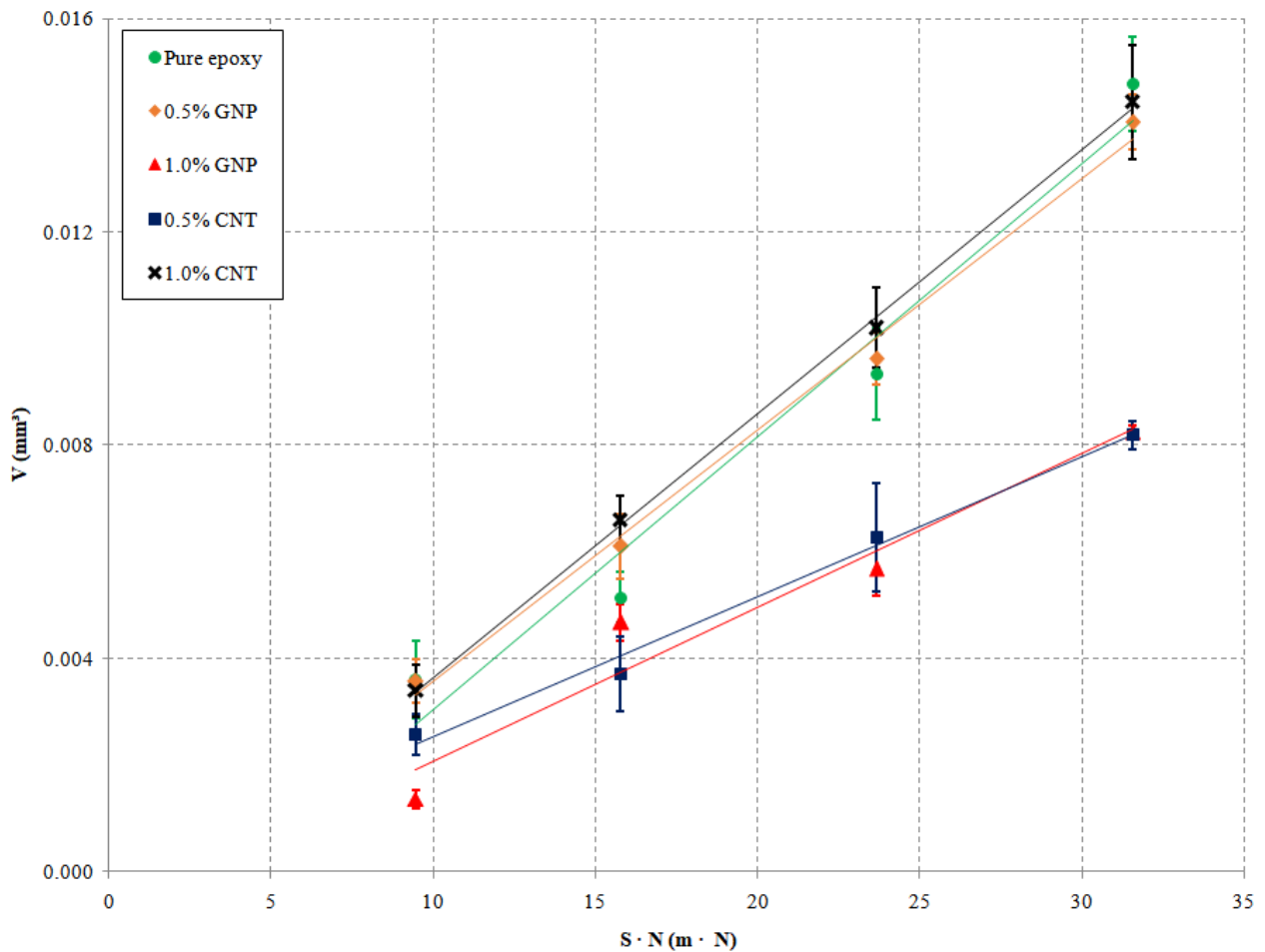
Figure 2. Wear volume *versus* the
sliding distance multiplied by
the normal load.

Fig. (3) displays the values of wear coefficients for each configuration. For both filler concentrations, GNP reduced the wear coefficient, with 1.0% GNP yielding an improvement of 44% in tribological performance. The graphene platelets likely act as a solid lubricant in the interface metal-polymer, reducing wear rate and mitigating material loss. As for CNT, at 0.5%, the wear coefficient assumes the lowest value between all configurations, with a 49% improvement in wear resistance when compared to the reference configuration. However, at 1.0%, CNT presents the worst behavior among the composites. Previous indentation tests [6] showed that the addition of 0.5% CNT reduces hardness and as such, might also decrease brittleness. However, at 1.0%, hardness assumes a value comparable to pure epoxy's, which explains the slim difference observed in both volume loss and wear coefficient for those configurations.
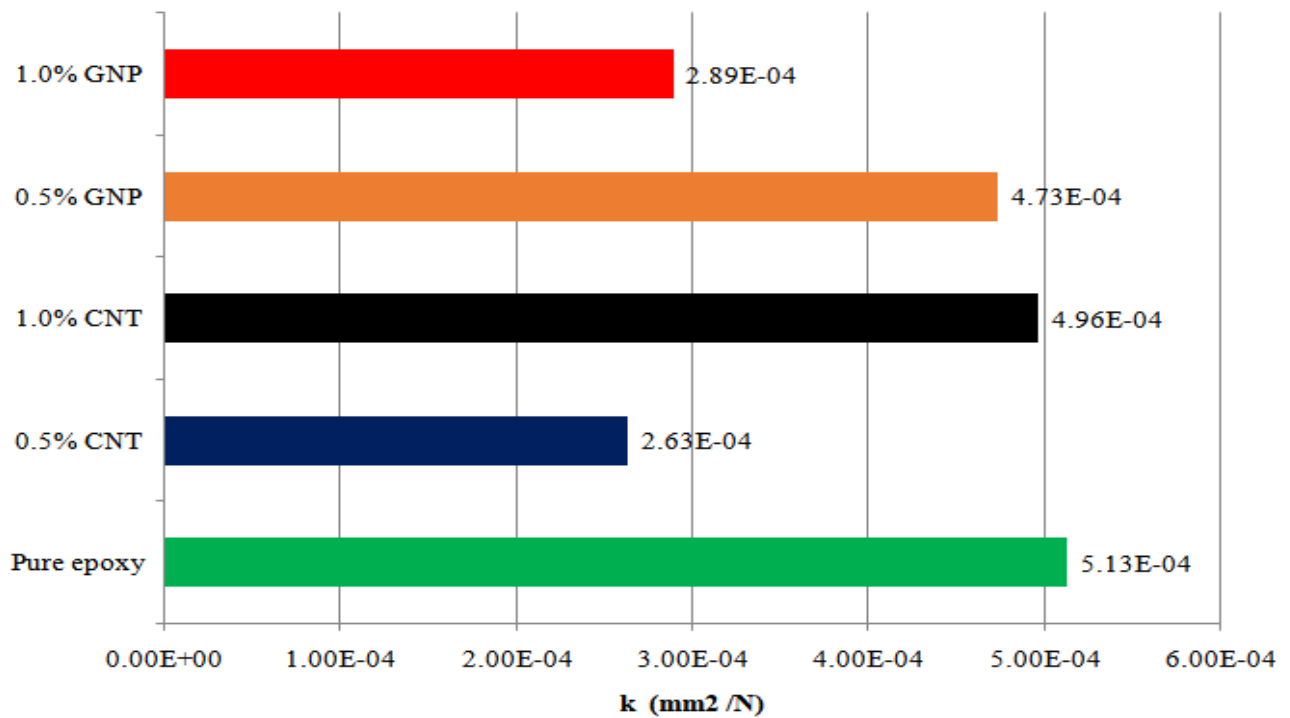
Figure 3. Measured abrasive wear coefficients, k [mm^2/N].

It was also possible to evaluate the wear scars qualitative aspects. Figure 4 displays the wear scars generated at $t = 5$ min for all configurations. Wear tracks along the sliding direction are clear in all configurations, along with the presence of nicks that likely occur due to defects in the matrix. 0.5% CNT and 1.0% GNP also present furrows, mostly concentrated near the center of the marks. For 1.0% CNT it was identified the presence of circular surface defects, both outside and in the wear scar. Those defects likely intensified the loss of mass and increased wear rates for the configuration. Besides, all configurations incur some degree of circularity deviation, which are higher for 1.0% GNP and 0.5% CNT. During the test, the sphere presents low amplitude displacement on the axis (wobbling). This causes the diameter measured in the horizontal to be slightly larger, especially for better lubricated surfaces and softer materials.

a) **Pure epoxy**
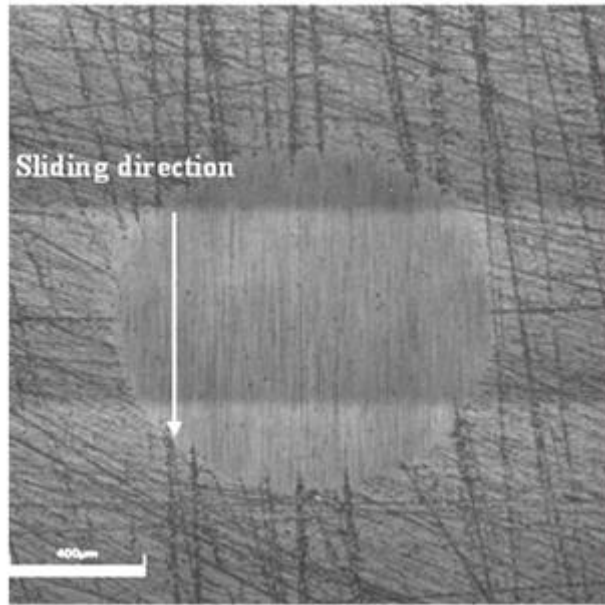
b) 0.5% GNP
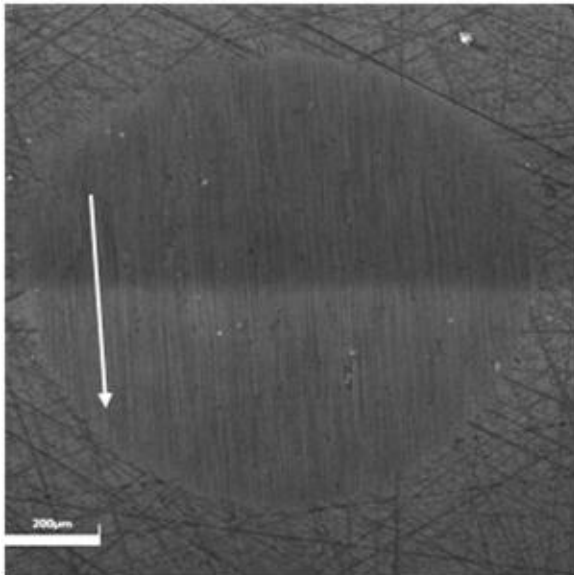
c) 1.0% GNP
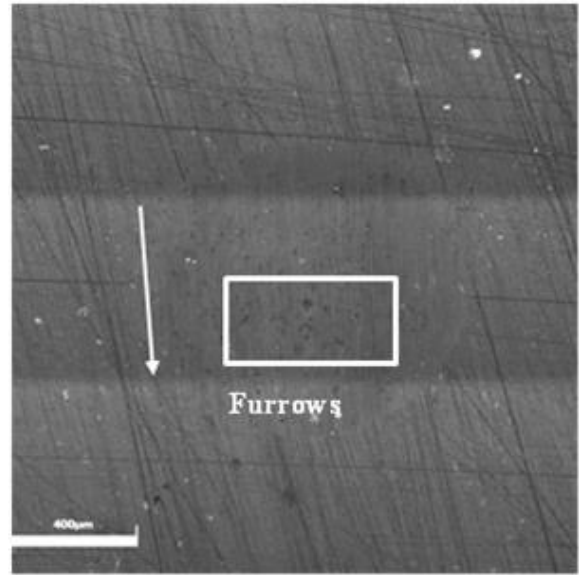
d) 0.5% CNT
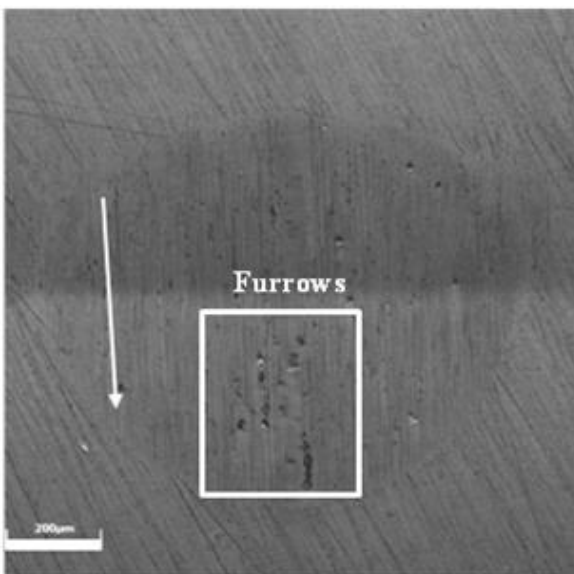
e) 1.0% CNT
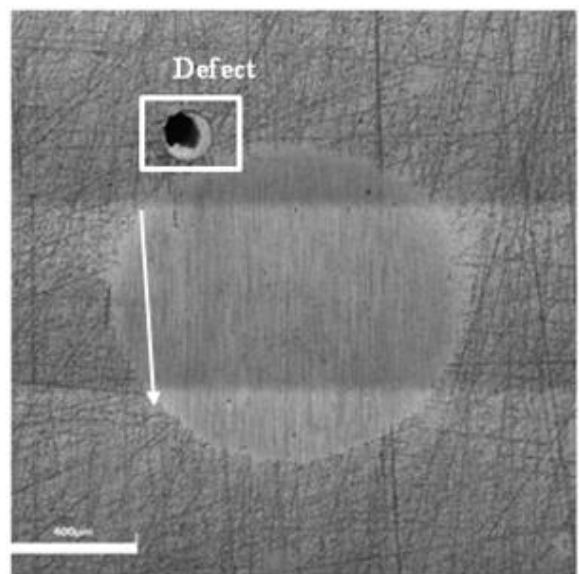
Figure 4. Representative microscopy view of the wear scars for t = 5 min.

4. CONCLUSIONS

In this work, it was possible to explore the wear behavior of carbon nanostructures reinforced epoxy, through micro-scale abrasive tests. GNP improved tribological performance for both concentrations, by acting as a lubricant and hence reducing friction and material loss. 0.5% GNP yielded a slight improvement, but at 1.0% concentration, the wear coefficient is decreased in 44%. CNT's effect on the wear behavior correlated to material hardness. 0.5% CNT resulted in the lowest wear coefficient, improving the reference configuration in 49%, while 1.0% CNT resulted in the highest, its wear coefficient differing from pure epoxy by only about 3%. The study of the wear scars showed that furrows formed on the surface of 0.5% CNT and 1.0% GNP, and that surface defects may have impacted 1.0% CNT wear rate.

Declaration of Competing Interest

The authors declare no conflict of interest.

Funding

REFERENCES

[1] M. Campo, A. Jiménez-Suárez, & A. Ureña. Effect of type, percentage and dispersion method of multi-walled carbon nanotubes on tribological properties of epoxy composites. *Wear*, Volume 324, 2015 (https://doi.org/10.1016/j.wear.2014.12.013)

[2] Lei Yan et al. Friction and wear properties of aligned carbon nanotubes reinforced epoxy composites under water lubricated condition. *Wear,* Volume 308.1-2, 2013 (https://doi.org/10.1016/j.wear.2013.10.007)

[3] Seenaa I. Hussein et al. Effect of incorporation of conductive fillers on mechanical properties and thermal conductivity of epoxy resin composite. *Applied Physics A,* Volume 124, 2018 (https://doi.org/10.1007/s00339-018-1890-0)

[4] B. Dong et al. Study on tribological properties of multi-walled carbon nanotubes/epoxy resin nanocomposites. *Tribology Letters,* Volume 20, 2005 (DOI: 10.1007/s11249-005-8637-8)

[5] Ian Hutchings and Philip Shipway. *Tribology: friction and wear of engineering materials*. 2nd Edition. 2017. Butterworth-Heinemann. (ISBN: 978-0-08-100910-9)

[6] H. Guimarães et al. Tensile and indentation tests on carbon nanostructures and epoxy resin composites. In: Anais do 17° Congresso Brasileiro de Polímeros. 451-455. 2023. (ISBN 978-85-63273-55-0)

15 Modelling, simulation and testing of composites, sandwich and adaptive structures

Organized and edited by

Sandra Maria da Luz
&
Carla Tatiana Mota Anflor

EXPERIMENTAL RADIAL COMPRESSION ANALYSIS OF VARIABLE-ANGLE TOW FILAMENT-WOUND COMPOSITE CYLINDERS WITH AND WITHOUT STRESS CONCENTRATORS

Gabriel S. C. Souza[(a),*], Rui Miranda Guedes[(b)], Sandro Campos Amico[(c)], Volnei Tita[(d)]

(a) 0000-0002-9677-5024 (University of São Paulo – Brazil)
(b) 0000-0001-5513-9155 (University of Porto – Portugal)
(c) 0000-0003-4873-2238 (Federal University of Rio Grande do Sul – Brazil)
(d) 0000-0002-8199-1162 (University of São Paulo – Brazil, and University of Porto – Portugal)
* Corresponding author: gabrielsales@usp.br

Abstract: This study aims to experimentally analyze variable-angle tow filament-wound composite (VAT-FWC) cylinders subjected to radial compression with and without stress concentrators. Tests are conducted using universal testing machines, evaluating both intact cylinders and those containing holes with elliptical geometry until failure. Initially, the cylinders are analyzed in the linear elastic regime to obtain their stiffnesses, and then they are subjected to crushing tests to study the initiation and propagation of damage in them. The specific energy absorption (SEA) and crushing force energy (CFE) are computed and compared between samples with and without holes to assess the crashworthiness of these thin-walled cylinders. Force-displacement curves are generated and detailed *post-mortem* inspections of the cylinders are carried out to examine their morphology and damage mechanisms during testing. A thorough discussion regarding the initiation and progression of failure mechanisms is conducted, with these results providing a solid foundation for further computational studies of these structures, such as using the finite element method.

1. INTRODUCTION

Filament winding is a widely used manufacturing method for making fiber-reinforced composite parts with various geometries, including spherical, cylindrical, elliptical, and rectangular shapes. In this process, continuous fiber tapes are wrapped around a rotating mandrel along predefined paths. Its popularity, particularly in the aerospace industry, stems from its high quality, repeatability, cost-effectiveness, and productivity [1]. The past 34 years have seen the development of new advanced materials known as variable-angle tow (VAT) composites, pioneered by Hyer and Charette [2]. This type of material takes the concept of optimizing structural performance in composites to the maximum, as the fibers are arranged in curvilinear paths within the same layer, resulting in a dependence of the fiber angle on the spatial coordinates. Despite its potential, the utilization of VAT composites began to gain momentum in the 2010s due to improvements in manufacturing technologies [3], primarily involving advanced fiber placement (AFP) [4], tailored fiber placement (TFP) [5], and laser-assisted fiber placements [6]. These recent developments were mainly focused on flat structures, focusing on the mechanical, vibrational, and buckling/post-buckling behaviors of these laminates [7]. Recently, Maciel et al. [8] conducted a bibliometric study concerning VAT composites and warned that with current FW technology, the amount of manufacturing defects is higher for VAT filament-wound composites (VAT-FWC) than it is for conventional (non-VAT) ones. In the research, an experimental assessment of fiber, matrix, and void volume fractions is also done, concluding that the composite quality, e.g., void content, is also higher for conventional filament-wound parts, indicating that further developments in the FW technology are needed for the reliable utilization of it for the VAT concept. Moreover, to the authors'

knowledge, there are only three works in the literature concerning VAT-FWC [9-11]. Thus, this study aims to experimentally investigate the mechanical behavior, the influence of stress concentrators, damage onset and propagation, morphology of failure, and crashworthiness of VAT-FWC cylinders under radial compressive loads. These findings will contribute to the development of analytical, computational, and hybrid analyses in the field.

2. METHODOLOGY

The material set is a composite towpreg of TORAYCA T700S-12K-50C carbon fiber reinforcement combined with a UF3369 TCR epoxy resin matrix. In total, three cylinders were manufactured, with two of them having a length of 150 mm and 176.8g, while the other has a length of 200 mm and 238.9g, aiming also to assess the size effect on the mechanical response.

2.1. Manufacturing and Machining

Manufacture of the cylinders was done utilizing the same approach of Almeida Jr. et al. [11], with an MF Tech Kuka robot arm model KR 140 L100-2. Summarizing, the VAT-FWC cylinder is sectionally conventional, and the final structure can be thought of as a spanwise stacking of multiple filament-wound composite rings with different fiber orientations as detailed in Figure 1.
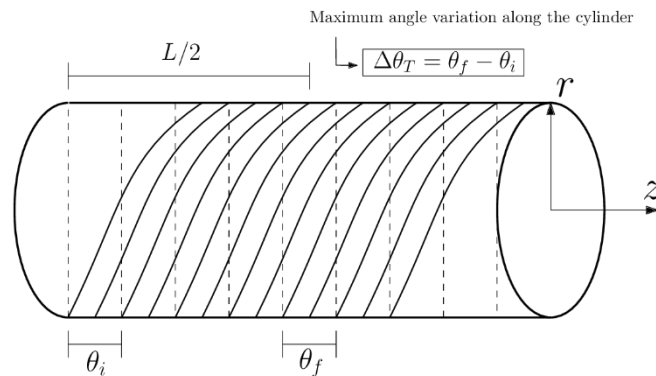
Figure 1. VAT-FW cylinder sections definition.

The final structures have a 136 mm inner diameter and a 2.0 mm average wall thickness, which is not constant as characteristic of filament-wound parts, but, for simplicity, here it is considered as it is, with the fiber orientation along the longitudinal direction varying from 52º at the cylinders' ends (θ_i) up to 62º at their center (θ_f), with each subsection of it having $\pm 2°$ of fiber orientation to its neighbors. These angles and their variations are selected to avoid high wall-thickness fluctuations that are more prominent in VAT tubes. Making use of and adapting the notation coined by Gürdal and Olmedo [12], hereinafter, these cylinders are denoted as $\Delta\theta_s < \theta_i|\theta_f >$. In it, $\Delta\theta_s$ is the angular variation from one section to the other with this parameter being controlled by deciding the minimum and maximum angles, and the number of subsections of the VAT cylinder. It follows,

$$\Delta\theta_s = \pm \frac{\Delta\theta_T}{[(N-1)/2]}, \tag{1}$$

that, in the case of the current work, gives the angular variation above-described for $N = 11$.

Drilling of the elliptical holes is done on a computerized controlled milling machine, with a Palbit HC38AS drilling tool which is a good choice for composite materials due to its solid carbide material and cylindrical shank of 3.0 mm diameter with 4 teeth at a 5000 rpm spindle speed and 1000 mm/min cutting feed rate to avoid the development of delamination due to machining. Also, the temperature was monitored throughout the process with a Fluke Tix580 thermal camera to check if the machining process induces fiber and/or matrix degradation. Data was treated using SmartView Classic 4.4 and the maximum recorded temperature was 27.7 ºC (carbon emissivity of 0.8 as recommended by the developer), as depicted in Figure 2 which also shows the temperature histogram and its three-dimensional distribution during one machining process.

(a)   (b)
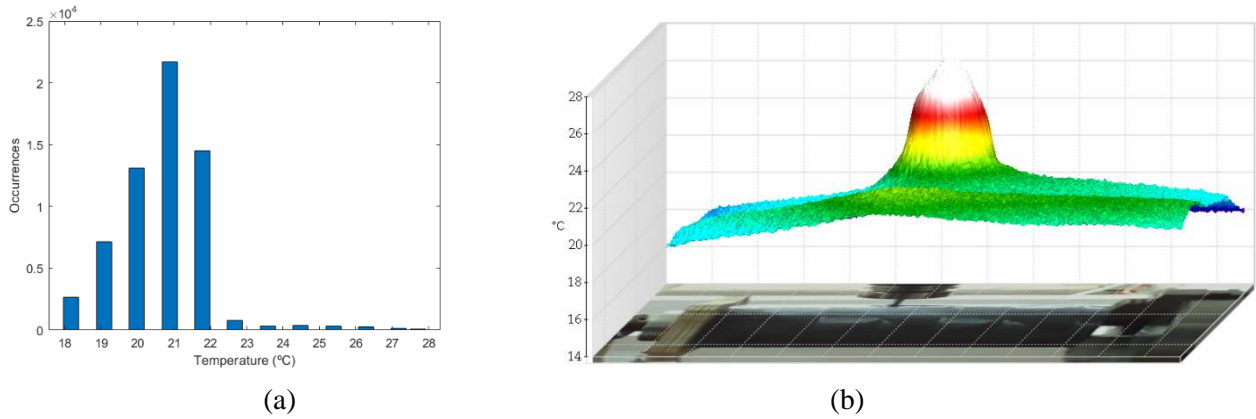
Figure 2. Temperature histogram (a) and corresponding 3D distribution (b) during hole drilling.

After analyzing the harvested data and carrying out visual inspections, no damage or degradation is reported. It is also worth mentioning that, these machining parameters and the shape and size of the holes were previously defined after some experimental and computational tryouts. All cylinders were perforated with elliptical holes measuring 16 mm in the major radius and 6 mm in the minor radius.

2.2. Experimental Procedures

Radial compression tests are conducted in several stages using universal testing machines. Initially, to obtain the stiffnesses of intact cylinders, tests were conducted in the linear-elastic regime using a homemade machine developed at INEGI with a load capacity of 12 kN at a displacement rate of 1.2 mm/min. Subsequently, the tubes are drilled, and the tests are repeated in the presence of the stress concentrator for comparison. This is done within the elastic regime and on this machine because the load cell has high resolution since the load capacity of the machine is not excessively high.

Then, for the damage development and crashworthiness analyses, the now-drilled cylinders are taken to an Instron 5900R (load capacity of 200 kN) for a third round of radial compression tests, which are now crushing ones conducted until the onset of the self-contact phase. These are all performed at a displacement rate of 5.0 mm/min, which, although different from that used in the previous ones, does not significantly affect the results as it falls within the range (0.5 to 12.0 mm/min) of the quasi-static regime. During these tests, image acquisition is performed using a CANON digital camera to carry out the damage characteristics analyses and for Digital Image Correlation (DIC) investigations which will be further explored in future publications. Figure 4 depicts the experimental setups for the linear-elastic tests (Fig. 4(a)) and for the crushing tests (Fig. 4(b)).

(a)   (b)
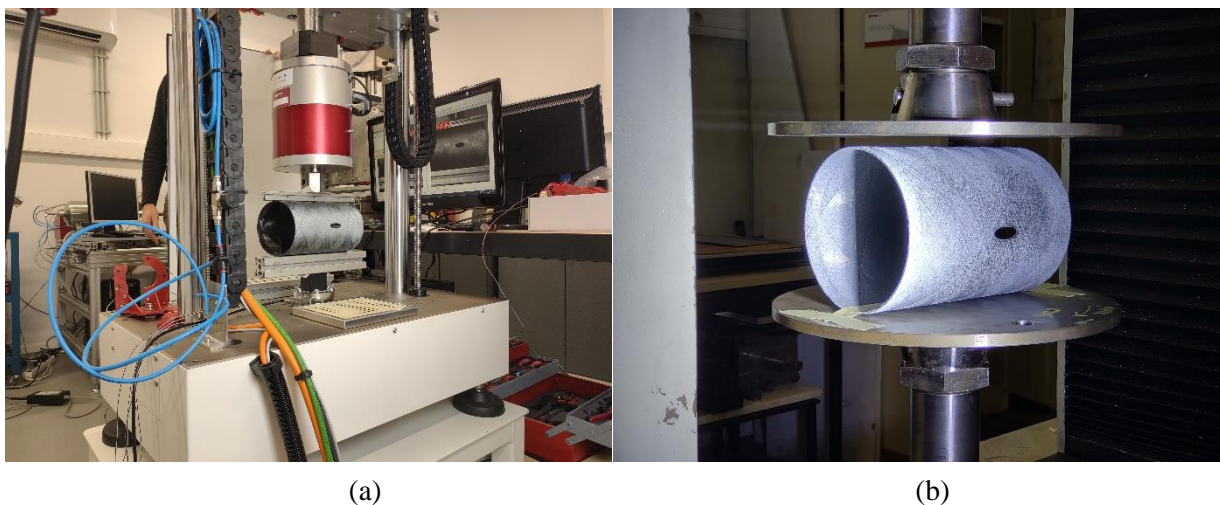
Figure 4. Experimental radial compression setups for the linear-elastic (a) and crushing (b) tests.

2.3. Stiffness and Crashworthiness Parameters

According to ASTM D2412 [13], the tube deflection ratio ($P = \Delta y/d$) is related to its stiffness (PS) through Eq. (2), given as

$$PS = \frac{F}{\Delta y}\left(1 + \frac{P}{2}\right)^3, \tag{2}$$

where Δy is the radial deflection, F is the applied load, and d is the outside diameter. Also, the term inside the parenthesis on the right-hand side of Eq. (2) can be thought of as a correction factor of the pipe stiffness and it remains valid assuming that the pipe maintains an elliptical shape during load. The parameter PS relates to the pipe stiffness factor (SF) by,

$$SF = EI = 0.149r^3 \times PS, \tag{3}$$

in which r is the cylinder mid-wall radius.

To conduct the crashworthiness analyses, some concepts from the work of Li et al. [14] are used. In these, four structural performance indices are defined, which assess the energy absorption capacity of the tubes when laterally crushed under quasi-static conditions. These indices are the peak crushing force (PCF), mean crushing force (MCF), specific energy absorption (SEA), and crushing force efficiency (CFE).

When analyzing the force-displacement curves of radially loaded composite cylinders, it is notable that they experience three distinct behaviors. Initially, there is the linear-elastic phase, followed by the progressive crushing stage, and finally, the self-contact stage. The latter, although similar to that experienced by metallic materials, is not exactly a stage of densification of the composite tube, even though there is a noticeable increase in force values. Hence, it is worth mentioning that all crashworthiness indices are evaluated in the pre-self-contact stages, as when these structures pass these, this type of analysis loses its purpose. So, denoting the total displacement up to the self-contact phase by δ, the MCF is calculated as the average force until there, given by:

$$MCF = \frac{1}{\delta}\int_{y=0}^{y=\delta} F(y)dy, \tag{4}$$

where $F(y)$ is the load response. Notice that the MCF value given by Eq. (4) can be interpreted as the total energy absorption capacity of the composite tube.

The SEA index can be seen as the most important for crashworthiness analyses since it represents the energy absorbed per unit mass of the tube. In this way, it is possible to compare various tubes composed of different materials, cross-sections, and masses. Thus, the mass of the portion that effectively participates in energy absorption (m) is defined by,

$$m = \frac{M\delta}{H}, \tag{5}$$

in which M and H are the total mass and the lateral height of the cylinder. Using Eq. (5), the SEA is given by,

$$SEA = \frac{\int_{y=0}^{y=\delta} F(y)dy}{m}. \tag{6}$$

The CFE, on the other hand, is given as the ratio between the energy absorption capacity and the maximum crushing load. Therefore,

$$CFE = \frac{MCF}{PCF}. \tag{7}$$

In other words, the higher the CFE, the better the energy absorption capacity coupled with a minimization of the maximum crushing force the structure has, which is important when looking at the problem from a human wellness perspective.

3. RESULTS AND DISCUSSION

3.1. Force-Displacement Curves

As discussed, the experiments are conducted in three stages. Firstly, in order to obtain the stiffnesses for the cylinders, tests are carried out in the linear-elastic regime. Then, tests are conducted until self-contact is reached. Also, to avoid slippage of the samples, a preload of approximately 100 N is used for all crushing tests. Figure 5 presents the results obtained for the cylinders of 150 mm and 200 mm.

(a)   (b)
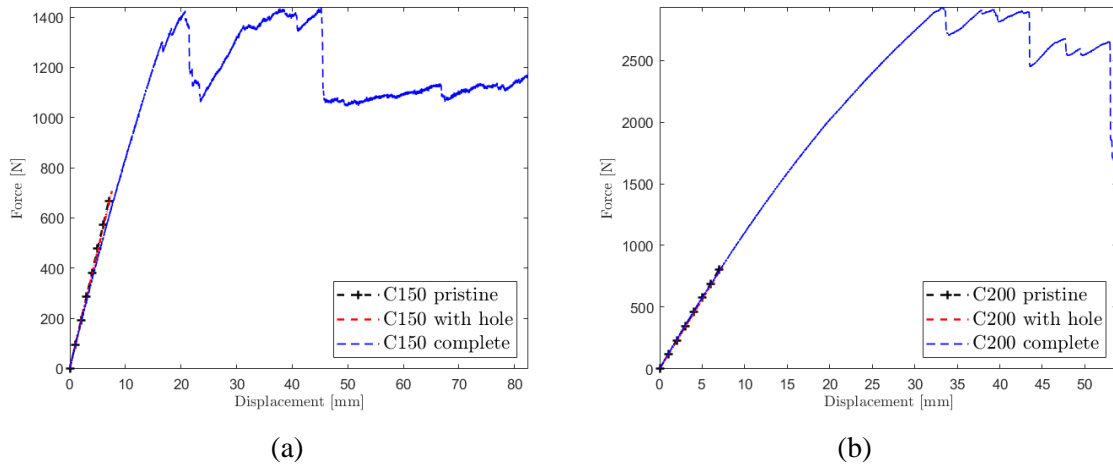
Figure 5. Force-displacement curves for the 150 mm (a) and 200 mm (b) cylinders.

It can be observed that for both cylinders, there is no notable decrease in stiffness between the tests, demonstrating that they remained in the elastic regime and that during the initial tests, there was no introduction of damage or permanent deformations in the samples. In fact, only one of the 150 mm cylinders is depicted, as the result presented is representative of both tests. This can be verified in Figure 6, where the results obtained for all cylinder crushing tests are represented. Furthermore, the characteristic evolution of their shape during the tests is also shown.
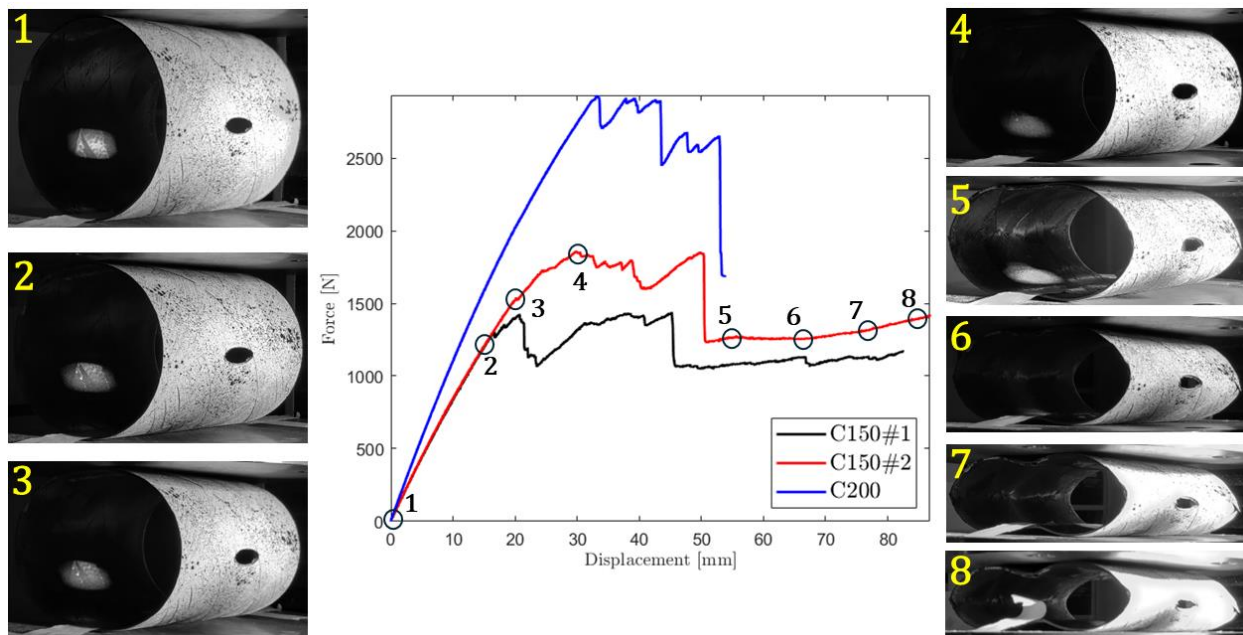
Figure 6. Crushing force-displacement curves and typical deformation history.

When comparing the plotted curves, it's evident that the longer cylinder exhibits slightly higher stiffness than the shorter ones. In addition, it is observed that the former has a higher peak load (~3000 N)

compared to the latter (~1650 N), even though these occur at similar displacement levels. All curves follow a similar pattern, starting with a linear-elastic zone, followed by a drop in stiffness leading to a peak force value, and then a sudden decrease in force. The initial stiffness drop occurs due to cracks forming in the region where the cylinder contacts the loading platen, which eventually propagates, causing the first drop in loading observed in the curves. Once the contact between the platen and the specimen is fully re-established, the curves stabilize with a regain in force values as displacement increases. Some drops originate from subsequent failures occurring at the base of the cylinder. Conversely, the subsequent abrupt drops occur due to the initiation and rapid propagation of cracks in the inner layer of the cylinder in the region of the holes, accompanied by an almost constant plateau in the force level that persists until the end of the tests. In the case of the 200mm cylinder, three sudden drops in force values are observed. This can be attributed to the cylinder's larger size, which results in longer subregions compared to the 150mm cylinders. Consequently, failures occurring due to the contact of the base with the sample are more noticeable because they are physically more extensive. Now, utilizing Eqs. (2) and (3) and noting that the cylinders maintain an elliptical cross-section until the occurrence of the largest force drops (related to failure in the region of the holes – point 5 in Figure 6), Table 1 presents the results concerning the stiffness parameters of the samples.

Table 1. Experimental VAT-FWC cylinders stiffness parameters.

Sample	Pipe Stiffness (**kN/m**)	Stiffness Factor (**N. m^2**)
C150#1	86.68	4.061
C150#2	85.37	3.999
C200	124.66	5.841
Average	98.90	4.634
Standard Deviation	17.54	0.856
Interval of Confidence (95%)	±19.84	±0.968

3.2. Lateral Crashworthiness and Damage Characteristics

The crushing tolerance of the cylinders is evaluated using the parameters previously discussed. Thus, Table 2 presents the results obtained during the tests.

Table 2. Experimentally obtained crashworthiness parameters for the VAT-FWC cylinders.

Sample	Mean Crushing Force (kN)	Specific Energy Absorption (kJ/kg)	Crushing Force Efficiency (−)
C150#1	1.093	0.927	0.759
C150#2	1.339	1.136	0.718
C200	2.039	1.707	0.695

It is observed that the C200 cylinder has higher values of the MCF and SEA parameters, as expected since it has a longer length and therefore more material resists crushing, i.e., greater m, resulting in higher energy absorption capacity. In terms of efficiency, the C150 cylinders have a slightly higher CFE value. Regarding failure mechanisms, a *post-mortem* analysis of the cylinders was conducted. Initially, the presence of holes does not induce damage initiation in the stress concentrator, as discussed. Figure 7 shows several images of a representative cylinder after testing.
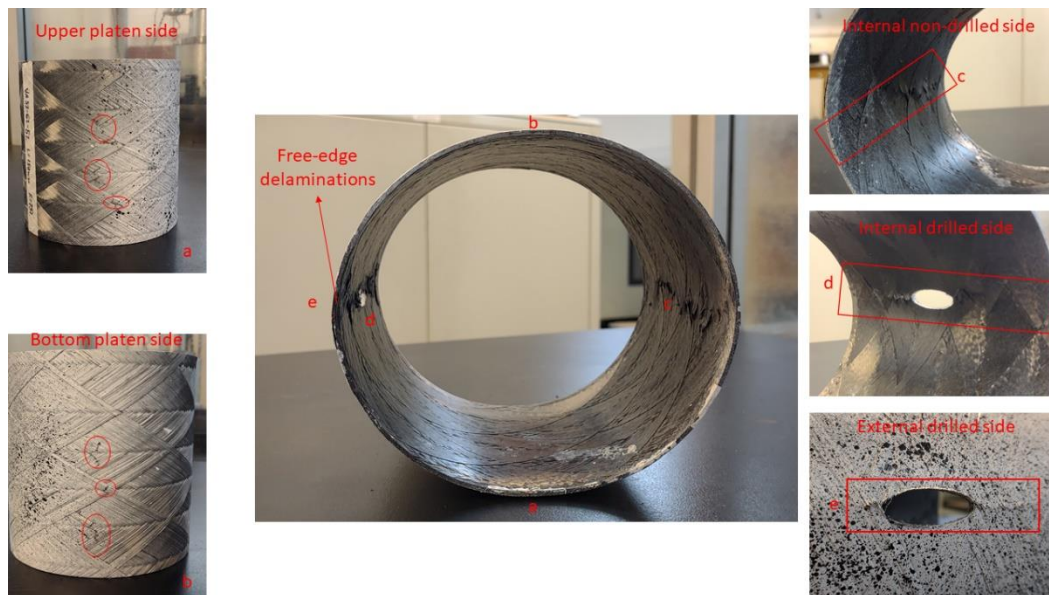
Figure 7. Typical *post-mortem* morphology of VAT-FWC cylinders under radial compression.

First, it is observed that the cylinders exhibit cracks in the region of contact with the force applicator (Fig. 7(a)) and the support base (Fig. 7(b)), i.e., in the outermost layer. These cracks develop following the orientation of the fiber, particularly initiating in the central region. Subsequently, still in the contact zone, other cracks appear in various spread areas along the cylinder but do not necessarily coalesce as they have a more or less transverse morphology. These mechanisms characterize various failures, initially related to matrix failure and later to the fiber. Until the end of the tests, only a few cracks are noticeable in the inner layers of the cylinder in the contact region, which appear only at the base. The first noticeable drops in force in the force-displacement curves occur due to the appearance and longitudinal coalescence of cracks in the hole region in the innermost layer of the same (Fig. 7(d)). This mechanism primarily characterizes matrix failure under compression, which, after a certain point, also occurs on the other side of the cylinder, in the region without the hole (Fig. 7(c)). Furthermore, there is a contribution from the fiber kinking mechanism (fiber micro buckling) at this stage. Continuing with the test, it is observed that cracks appear mainly due to the matrix failure mechanism under tension in the outer layer of the hole region (Fig. 7(e)), where maximum circumferential strain values are present and, at the end of the test, this also occurs for the side with no hole of the cylinder. In all tests, delaminations in the cylinders happen due to large deformations, and by construction, there is a high stiffness gradient along the thickness of the samples (they are like two sub-layers at 0/90 to form a complete layer). However, as these occur at the neutral axis where maximum shear and minimum normal stresses are present, in the case of radial compression, this failure mechanism is not relevant to the overall behavior of the cylinders, and there is no evident effect on the force-displacement curves.

4. CONCLUSIONS

A relevant experimental study was conducted on VAT-FWC cylinders under radial compression up to failure. Evaluation of pertinent parameters such as stiffness, crush tolerance, failure mechanisms, and failure morphology was done. Throughout the study, some conclusions were drawn: 1) Delamination, under radial compression, only contributes to the progressive and permanent loss of stiffness and facilitates the initiation and propagation of other more relevant damage mechanisms, thus indirectly responsible for the failure and being concentrated on the free edges of the cylinders; 2) The presence of the elliptical hole does not affect the overall elastic response of the tubes, only bringing forward the onset of damage at that region; 3) On the other hand, the length of the cylinder does affect the quantitatively the behavior of the tubes; 4) The winding pattern, also known as mosaics, plays an important role in the mechanical behavior of FW parts, being also responsible for damage nucleation and development. The conclusions drawn can be verified by experimental digital image correlation and computational simulations using the finite element method, which will be explored in future works.

4.1. Declaration of Competing Interest

The authors declare no conflict of interest.

5. REFERENCES

[1] Q. Wang. et al. Prediction of void growth and fiber volume fraction based on filament winding process mechanics. *Composite Structures*, Vol. 246, 2020. (doi.org/10.1016/j.compstruct.2020.112432).

[2] M.W. Hyer, R.F. Charette. Innovative design of composite structures: use of curvilinear fiber format to improve structural efficiency. *NASA Technical Reports*, No. TR-87-5, 1987. (ntrs.nasa.gov/citations/19870016936).

[3] K.C. Wu, Z. Gürdal, J.H. Starnes. Structural response of compression-loaded, tow-placed, variable stiffness composite panels. In: *AIAA/ASME/ASCE/AHS/ASC Structures, Structural Dynamics and Materials Conference*, 2002. (doi.org/10.2514/6.2002-1512).

[4] Z. Wu, G. Raju, P.M. Weaver. Framework for the buckling optimization of variable-angle tow composite plates. *AIAA Journal*, Vol. 53, 2015. (doi.org/10.2514/1.J054029).

[5] J.H.S. Almeida Jr., L. Bittrich, A. Spickenheuer. Improving the open-hole tension characteristics with variable-axial composite laminates: Optimization, progressive damage modeling and experimental observations. *Composites Science and Technology*, Vol. 185, 2020. (doi.org/10.1016/j.compscitech.2019.107889).

[6] G. Clancy et al. In-line variable spreading of carbon fibre/thermoplastic pre-preg tapes for application in automatic tape placement. *Materials & Design*, Vol. 194, 2020. (doi.org/10.1016/j.matdes.2020.108967).

[7] C. González et al. Structural composite for multifunctional applications: Current challenges and future trends. *Progress in Materials Science*, Vol. 89, 2017. (doi.org/10.1016/j.pmatsci.2017.04.005).

[8] M.M.A.D. Maciel et al. Evolution of variable angle tow composite structures: Data analysis and relevance of the theme. *Proceedings of the Institution of Mechanical Engineers, Part L: Journal of Materials: Design and Applications*, Vol. 0, 2024. (doi.org/10.1177/14644207241240048).

[9] Z. Wang et al. Reliability-based buckling optimization with an accelerated kriging metamodel for filament-wound variable angle tow composite cylinders. *Composite Structures*, Vol. 254, 2020. (doi.org/10.1016/j.compstruct.2020.112821).

[10] Z. Wang et al. Lightweight design of variable-angle filament-wound cylinders combining kriging-based metamodels with particle swarm optimization. *Structural and Multidisciplinary Optimization*, Vol. 65, 2022. (doi.org/10.1007/s00158-022-03227-8).

[11] J.H.S. Almeida Jr. et al. Design, modeling, optimization, manufacturing and testing of Variable-angle filament-wound cylinders. *Composites Part B: Engineering*, Vol. 225, 2021. (doi.org/10.1016/j.compositesb.2021.109224).

[12] Z. Gürdal, R. Olmedo. In-plane response of laminates with spatially varying fiber orientations: Variable stiffness concept. *AIAA Journal*, Vol. 31, 1993. (doi.org/10.2514/3.11613).

[13] ASTM D2412-21. Standard test method for determination of external loading characteristics of plastic pipe by parallel-plate loading. ASTM International, 2021. (www.astm.org/d2412-21.html).

[14] X. Li et al. Lateral crashworthiness performance of CFRP/aluminum circular tubes with mesoscopic hybrid design. *Composites Part B: Engineering*, Vol. 251, 2023. (doi.org/10.1016/j.compositesb.2022.110489).

PARAMETRIC OPTIMIZATION OF COMPOSITE BEAMS WITH NON-SYMMETRIC CROSS-SECTION UNDER FOUR-POINT BENDING

Tiago Balestro [(a)]*, Letícia Vedana de Andrade [(b)], Adelano Esposito[(c)]

(a) ⓘ 0009-0002-0247-8043 (Federal Institute of Education, Science, and Technology of Rio Grande do Sul – Brazil)
(b) ⓘ 0009-0009-2070-4244 (Federal Institute of Education, Science, and Technology of Rio Grande do Sul – Brazil)
(b) ⓘ 0000-0001-7383-0062 (Federal Institute of Education, Science, and Technology of Rio Grande do Sul – Brazil)
* Corresponding author: tiagobalestro@hotmail.com

CODE: BCCM7-64

Abstract: This work presents a parametric optimization study of composite beams with non-symmetric cross-sections subjected to four-point bending. Utilizing the first-order beam theory tailored to the composite nature of the cross-section, the sandwich beam is modelled. The optimization process employs the particle swarm optimization method to minimize the mass of the structure while respecting material limit stress and geometrical requirements. The optimization problem is formulated to handle a combined set of discrete and continuous variables. The study presents results pertaining to stiffness, mass reduction, and mid-span deflection, followed by an analysis of the optimization solution.

1. INTRODUCTION

The ultimate characteristic of a sandwich beam could be aptly enunciated as its ability to achieve exceptional flexural stiffness solely through the geometric arrangement of its structural components. Yet this idea may have held significant importance during the early stages of its theoretical development, contemporary applications in diverse sectors, such as aerospace, demand a refined examination of its design variables, where naturally arises the need for optimal sandwich parameters. In this point of view, numerous studies have introduced approaches to optimize sandwich structures through the years.

Hudson [1] employed multi-objective Particle Swarm Optimization (PSO) to obtain optimized stiffness, mass, and cost of the sandwich beam. The free variables considered were face thickness, and the face and core materials. Optimization using the finite elements method is presented by Stolpe [2] where the effect of fibre orientation and layer thickness is considered and optimal conditions for the design of slender laminated composite structures are investigated. Bru [3] presented a Genetic Algorithm to minimize the material cost of strengthening timber beams, while respecting the limit state of deflection, according to a building code, as well as the ultimate limit states for flexural and shear behaviour. Kovács [4] focused on optimization for minimum cost and maximum stiffness, using a multi-algorithm approach. For the case of a symmetrical cross-section sandwich beam, a three-step optimization is presented by Irisarri [5], where the overall optimization is divided into small optimization problems, and more than one optimization method is employed. A more extensive account of the optimization of composite sandwich structures can also be found at [5].

Although the literature provides a vast array of optimization objectives and free variables, each tailored to specific problems and objectives, there are important features that shall be employed to contribute directly to the real application of lightweight structures. Namely, the use of a non-symmetric cross-section, which

permits a more effective material distribution, particularly significant in materials like Glass Fiber Reinforced Polymer (GFRP), where compressive and tensile strengths may vary considerably [6]. Additionally, for real application and large-scale production, discrete values of face thickness might be necessary to accomplish industrial processes, i.e. a large-scale pultrusion process, or equally, codes specification. In this way, the present study focuses attention on implementing these characteristics, in order to obtain optimal dimensions such that it minimizes the mass of the structure respecting constraints of material stress and specific geometric constraints.

2. METHODOLOGY

2.1. Sandwich Beam Model

The beam is modelled following the conception developed by Allen [7] and Plantema [8], as outlined in Zenkert's presentation [9]. The model applied to the problem is summarized below. No consideration of weak core or thin face was done, as possible accordingly to [9]. Fig. 1a presents the boundary conditions of the loaded beam, resembling those presented by Almutairi, perhaps in the current investigation the structure represents a non-symmetric cross-section optimized beam.
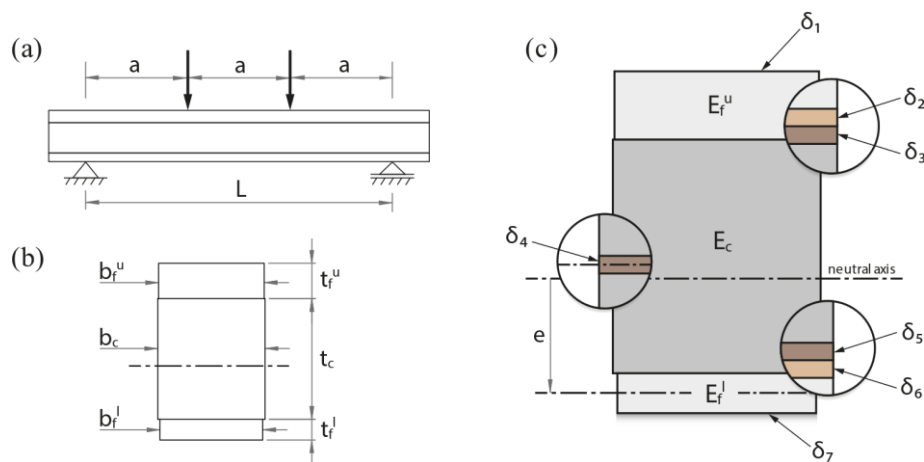
Figure 1. (a) Four-Point bending of a sandwich beam. (b) Cross-section dimensions. (c) Cross-section view of face infinitesimal elements where stresses shall be evaluated.

The normal stress for the infinitesimal face element $i = \delta_1, \delta_2, \delta_3, \delta_4, \delta_5, \delta_6, \delta_7$ is given by

$$\sigma_i = -\frac{MzE_i}{D} \tag{1}$$

where E_i stands for the modulus of elasticity of the material at the i face in consideration and D is the flexural rigidity. Analogously, the shear stress τ_i for the face elements $i = \delta_3, \delta_4, \delta_5$, is given respectively by

$$\frac{V}{D}E_1 t_1 (d-e), \quad \frac{V}{D}\left[E_2 t_2 e + \frac{1}{8}E_c(-2e+t_2)^2\right], \quad \frac{V}{D}E_2 t_2 e \tag{2}$$

Clearly, for the faces δ_2 and δ_6, the shear values are the same as in the faces δ_3 and δ_5, respectively.

These equations were obtained from the corresponding shear stress equations presented in [9] and substituting the independent variable z by its value on the desired face element, that is, in the contact between faces and core, and beam's neutral axis. Perhaps the shear stress is evaluated in the adhesion zone between each face and core, the adhesive is not modelled as a physical material of the structure, the only effect analysed is its capability to withstand shear stress.

Utilizing the Timoshenko beam theory, the mid-span deflection of the sandwich beam is expressed by,

$$\Delta(L/2) = \frac{Pa}{24D}(3L^2 - 4a^2) + \frac{Pa}{S} \tag{3}$$

The stress limit of the materials was modelled with the use of Tsai-Wu failure criteria for the faces and Hoffman failure criteria for the core, therefore, being appropriate to validate the model using the data from [10], wood for the core, and GFRP for upper and lower faces. An important consideration of these failure criteria, that is, the consideration of the yield stress as the maximum acceptable value, makes it possible to

consider the wood at the core as a linear material. Since no transverse applied stress σ_2 is present, both the Tsai-Wu and Hoffman failure criteria are simplified to Eq. (9).

The materials properties used to validate the model were obtained from the experimental study of [10], except face compressive strength, which was taken as 0.55 % of the tensile strength value [6], and GFRP face density, obtained from [11].

2.2. Discrete and Continuous Variables Formulation for Design Optimization

The simultaneous optimization of face and core parameters, involving discrete and continuous design variables, respectively, produces an optimization problem of combinatorial nature. Thus, to achieve the simultaneous optimal solution, the problem is firstly established by considering two types of variables. Discrete values taken from standards reference lists are set for the face parameters, thicknesses t_f, and width b_f. For the core, continuous-sized variables are linked.

Furthermore, as typically set, the optimization problem shall minimize the objective function while satisfying specified constraints. For the case in consideration, it is equivalent to minimizing the mass while satisfying materials' strength and geometric requirements. In this context, a mathematical expression was developed to model and determine the thicknesses and width of the individual layers in a GFRP-wood sandwich beam, ensuring both satisfactory mechanical performance and minimal self-weigh.

The objective function of self-weight (f_w) optimization for discrete and continuous variables, by assembling all constraints into a single formulation, was computed as follows.

$$
\begin{aligned}
&\text{Find} && \mathbf{X} = \{x_1(t_c), x_2(b_c)\}^T, \\
& && \alpha = \left\{\alpha_1\left(t_f^u, b_f^u\right), \alpha_2\left(t_f^l, b_f^l\right)\right\}^T, \\
&\text{Min} && f_w(\mathbf{X}, \alpha) = L\left(\rho_c x_1(t_c) x_2(b_c) + \rho_f \sum_{i=1}^{2} \alpha_i(t_f, b_f)\right) \\
&\text{s.t.} && g_j(\mathbf{X}, \alpha) \le 0 \; j = 1, \cdots, m, \\
& && x_i^L \le x_i \le x_i^U \; i \in I_C, \\
& && \alpha_k^L \le \alpha_k \le \alpha_k^U \; k \in K_D,
\end{aligned}
\tag{4}
$$

where $\mathbf{X}$ is a vector of continuous sized variables, including core thickness, $x_1(t_c)$, and core width, $x_2(b_c)$; α represents the available discrete values, listed in ascending order, where $\alpha_1\left(t_f^u, b_f^u\right)$ and $\alpha_2\left(t_f^l, b_f^l\right)$ corresponds to the rectangle-shaped sections of the upper and lower faces, respectively, as defined in Fig. 1b. The objective function is represented by $f_w(\mathbf{X}, \alpha)$, and $g_j(\mathbf{X}, \alpha)$ is the j-th constraint function; m denotes the sum of the constraints, including mechanical strength and geometrical requirements. ρ_f and ρ_c are the densities of the facing and core materials respectively, and L is the length of the sandwich beam. I_C denotes the set of indices for continuous design variables; I_D denotes the set of indices for discrete design variables; x_i^L and x_i^U denote the lower and upper limits for the design variables that are continuous i.e. $i \in I_C$; α_k^L and α_k^U represents the side constraints for the design variables that are discrete i.e. $k \in K_D$;

The optimization problem addressed herein, according to Eq. (4), is of constrained nature, and therefore, a transformation is needed to describe it as an unconstrained optimization problem. This process is achieved by using a penalty function, f_p, defined by the summation of all active constraint violations, computed accordingly to Eq. (5)

$$
f_p = \sum_{j=1}^{n_c} v_{c_j}
\tag{5}
$$

where j is increased from 1 to n_c, which is the total number of constraints; v_{c_j} is the j-th violation constraint, given by Eq. (6)

$$
\begin{aligned}
&\text{if } g_j < 0 \text{ then } v_{c_j} = |g_j| \\
&\text{if } g_j \ge 0 \text{ then } v_{c_j} = 0
\end{aligned}
\tag{6}
$$

where g_j are the normalized constraints, from Eq. (8) to Eq. (9). There are several applications and methods of penalty functions. A very comprehensive review of such techniques is covered in [12]. In the present work, an expression for the unconstrained objective function, f_w, is shown in Eq. (7),

$$f_o(\mathbf{X}, \alpha) = f_w(\mathbf{X}, \alpha)\left(1 + f_p\right)^{\beta} \tag{7}$$

where the total mass of the structure, $f_w(\mathbf{X}, \alpha)$, is the sum of the mass of the wood and GFRP components. β is a penalty coefficient, taken as 2.0 in this work, as suggested by [13, 14].

Strength constraints are given in Eq. (8). σ_{ycf} and σ_{ytf} are the allowable stresses in compression and tension of GPRF faces, respectively. τ_{ybond} is the shear strength of the adhesive.

$$
\begin{aligned}
g_{\delta 1} &= 1 - \sigma_{\delta 1}/\sigma_{ycf} \geq 0 \\
g_{\delta 7} &= 1 - \sigma_{\delta 7}/\sigma_{ytf} \geq 0 \\
g_{ybond} &= 1 - \tau_{\delta 3}/\tau_{ybond} \geq 0 \\
g_{ybond} &= 1 - \tau_{\delta 5}/\tau_{ybond} \geq 0
\end{aligned}
\tag{8}
$$

In Eq. (9), τ_{12} represents the shear stress acting, and S is the shear strength of the ply. The orientation of τ_{12} and S are parallel to the face shown in Fig. 1a. In Eq. (9) τ_{12} and σ_1 are replaced by their corresponding values on the face element in consideration, that is, with $i = \delta_2, \delta_3, \delta_4, \delta_5, \delta_6$. The longitudinal tensile and compressive strength are represented respectively by X_t and X_c.

$$g_i = 1 - \left[\left(\frac{1}{X_t} - \frac{1}{X_c}\right)\sigma_1 + \frac{\sigma_1^2}{X_t X_c} + \left(\frac{\tau_{12}}{S}\right)^2 \right] \geq 0 \tag{9}$$

Physical limits, the size constraints, for the beam are set as follows,

$$
\begin{aligned}
1 &\leq t_f^u, t_f^l \leq t_c \\
1 &\leq b_f^u, b_f^l \leq b_c \\
t_f^u &+ t_f^l + t_c \leq 91 \\
b_c &\leq 60
\end{aligned}
\tag{10}
$$

with dimensions in mm.

2.3. Particle Swarm Optimization

The development of theories aiming to optimize problems has been based on mathematical programming. The basic idea shared by some methods is that the gradient of the function to be optimized has important information to quickly find an optimum solution for a specific problem. However, when dealing with highly nonlinear, non-convex, non-differentiable, (i.e., problems where the mass reduction conflicts with stress or displacement constraints, and especially discrete design variables), these methods may present some convergence difficulties.

Inspired on social behaviours observed in nature, such as insects, birds, and fish groups, the PSO algorithm was originally proposed by [15] as a stochastic optimization method where each particle, which represents a potential solution of the problem, surrounds the hyperspace guided by its flight experience allied to the experience from the particle set as whole, named swarm. For instance, each particle flies over the hyperspace influenced by its own best position as well as the best position found by its neighbours [16]. Among the key advantages of PSO is its ease of implementation and programming. Given sufficient computation time, PSO is always capable of converging to the global optimum. This capability stems from its ability to simultaneously analyse a broad spectrum of randomly generated solutions, making it less prone to converge to local optima.

3. RESULTS AND DISCUSSION

3.1. Discrete and Continuous Variables Formulation for Design Optimization

To test and validate the numeric computational routines implemented here, the case study proposed consists of minimizing the weight of the timber beam, with a cross-section of 60×91 mm (width $\times$ depth) and 1800 mm length (L). The value of load was selected equal to the ultimate load of the unreinforced beam, set as 16 kN. Consequently, the proposed optimization method is applied to a change of configuration of the timber beam, corresponding to the geometry shown in Fig. 1a, to ascertain the optimal thicknesses and width for each layer in a GFRP-wood sandwich beam, ensuring both satisfactory mechanical performance and minimal self-weight.

The statistical results of ten independent evaluations are presented in Table 1, along with the PSO setup parameters used. It can be noticed that there is a small deviation from each independent run mean value. Due to the use of analytical modelling based on bending theory for structural calculations, the total computational expense is minimal, enabling a substantial number of evaluations.

Table 1. Result of structural optimization.

Mean mass (kg)	Standard deviation	N° of particles	Mean n° of iterations	ω	c_1	c_2
7.7316	0.1013	35	137	0.75	1.96	1.85

ω = velocity momentum; c_1 = cognitive constant; c_2 = social constant.

Table 2 shows the best result obtained by the optimization routine, which was used in the comparison. The wood-mass reduction is about 36.58% concerning the reference mass. Using GFRP reinforcement alone reduces mid-span displacement by 38.28% and increases equivalent bending stiffness by 64.15%.

Table 2. Result of structural optimization.

	Wood	GFRP	Δ	D	t_f^u	b_f^u	t_f^l	b_f^l	t_c	b_c
Initial design	5.14	-	75.60	44.46	-	-	-	-	91	60
Optimization	3.26	4.47	46.66	72.98	12.70	50.80	9.53	50.80	68.16	50.80
Difference (%)	36.58	-	38.28	64.15	-	-	-	-	-	-

Δ = maximum displacement of mid-span in **mm**. D = equivalent bending stiffness in **kNm²**. $t_f^u, b_f^u, t_f^l, b_f^l, t_c, b_c$ are in **mm**. Wood and GFRP represent mass, in kg.

Fig. 2 shows the evolution and behaviour of the best solutions found by the PSO routine over the iteration cycles until convergence was reached by the implemented method. The graph in Fig. 2a represents the convergence history of the best value of the objective function, found by the swarm, as well as the associated mean value of each cycle, from the positions of all particles. In relation to Fig. 2b, the graph shows the fluctuation from the design variables' point of view, along with PSO's convergence history; such fluctuation features the objective function minimizing process.

(a) Convergence of particles. (b) Behaviour of design variables.
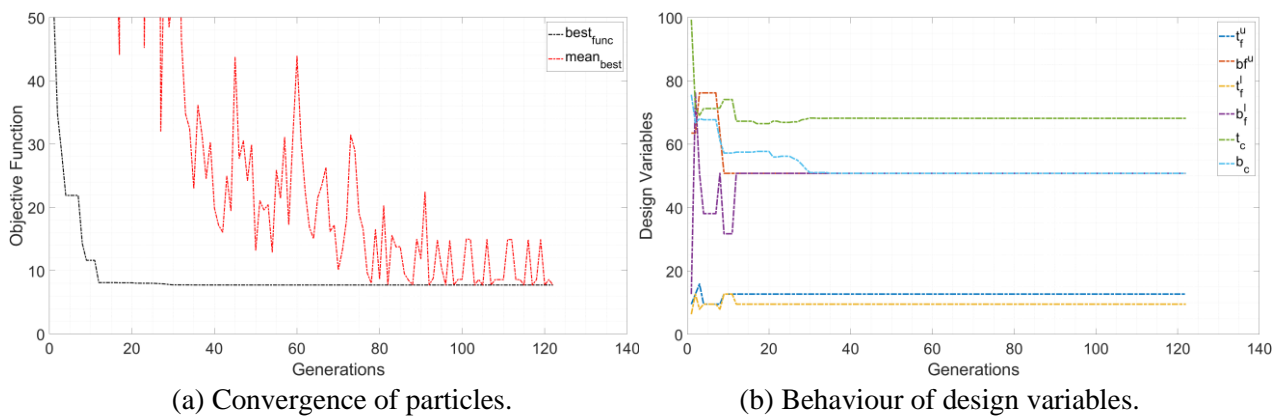
Figure 2. Convergence history.

Fig. 3 and Fig. 4 show the objective function domain relative to the discrete (rectangle-shaped sections of the upper and lower faces, $t_f^u \times b_f^u$ and $t_f^l \times b_f^l$, respectively) and continuous (width-thickness values, t_c and b_c, respectively) variables. The graphical representation illustrates the constraints imposed by the mechanical resistance (strength constraints) of the face sheets, C^{face}, core material, C^{core}, and geometrical requirements (size constraints), $C^{\text{geometrical}}$. The unconstrained, $\Omega_{\text{unconstrained}}$, feasible, Ω_{feasible}, and failure, Ω_{failure}, regions are represented on the Fig. 3 and Fig. 4.

(a) Thickness of the core times rectangle-shaped section of the upper faces.

(b) Thickness of the core times rectangle-shaped section of the lower faces.
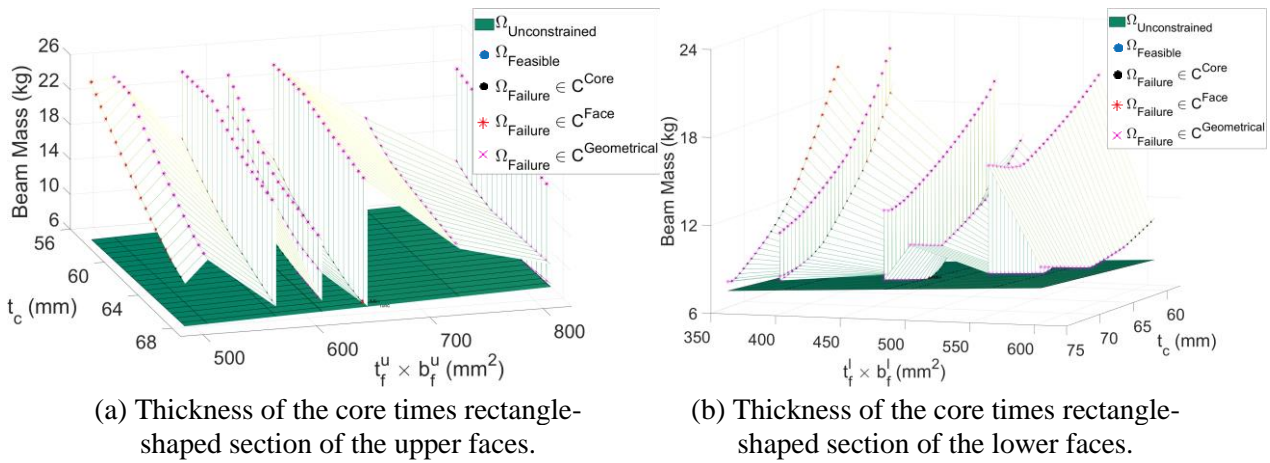
Figure 3. Objective function, when combined the full ranges of continuous and discrete variables.

(a) Rectangle-shaped section of the upper and lower faces.

(b) Thickness and width of the core
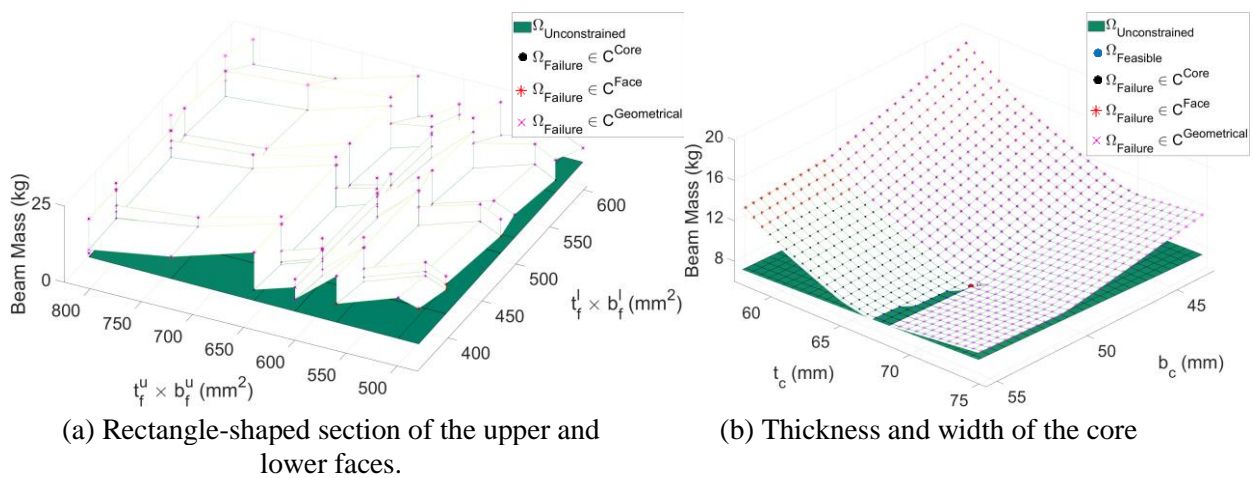
Figure 4. Objective function, when combined the full ranges of continuous and discrete variables.

As it can be seen, from Fig. 3 and Fig. 4, the surfaces in green over an inclined plane relate to the objective function without penalties being applied, i.e., feasible design. This is the reason behind the uniform shape presented by this view of the function. In contrast, when considering the effects of violated constraints being applied to the objective function, using the penalty function, it is observed that the originally flat domain develops a fluctuation, which is anchored in the points associated with the strength and geometrical constraints. It is noted that the applied penalty will ensure the formation of a single global minimum that belongs to the objective function's safety domain. Finally, it may be noted that the discrete optimization results to a highly nonlinear function, leading to visible fluctuations that indicate the presence of local minima within the discretized domain. These minima are particularly defined by gaps resulting from variable discontinuity, which potentiates the application of heuristic methods, such as PSO, for this type of problem.

4. CONCLUSIONS

The present work employed a heuristic optimization method, the PSO, to find an optimal solution for a non-trivially convergent function in the sense of deterministic optimization methods. Hence, the following can be highlighted.

The considerable density of the GFRP increased the total mass of the beam since the wood considered was lighter occupying the same region. However, when considering the application of wood only at the core, it represents wood economy alongside better mechanical properties, mainly a higher flexural stiffness. Additionally, the beam analytical modelling provided a suitable framework for fast computation of an objective function with several local minima, improving the efficiency in terms of computational cost, and therefore, a faster convergence rate.

4.1. Declaration of Competing Interest

4.2. Fundings

4.3. Acknowledgements

5. REFERENCES

[1] C. W. Hudson, J. J. Carruthers, A. M. Robinson. Application of particle swarm optimisation to sandwich material design. *Plastics, Rubber and Composites*, Volume 38, 2009. (doi 10.1179/174328909X387829).

[2] J. P. Blasques, M. Stolpe. Maximum stiffness and minimum weight optimization of laminated composite beams using continuous fiber angles. *Struct Multidisc Optim*, Volume 43, 2011. (doi 10.1007/s00158-010-0592-9).

[3] D. Bru et al. Structural optimization of timber beams with composite materials. *WIT Transactions on The Built Environment*, Volume 168, 2015. (doi 10.2495/SD150521).

[4] G. Kovács et al. Analysis and optimum design of fibre- reinforced composite structures. *Struct Multidisc Optim*, Volume 28, 2004. (doi 10.1007/s00158-004-0425-9).

[5] F.-X. Irisarri et al. A general optimization strategy for composite sandwich structures. *Struct Multidisc Optim*, Volume 63, 2021. (doi 10.1007/s00158-021-02849-8).

[6] A. Ineia et al. Barras de fibra de vidro, uma alternativa inovadora e suas potencialidades: revisão bibliográfica. *Tecno-Lógica*, Volume 25, 2021. (doi 10.17058/tecnolog.v25i2.16214).

[7] H. G. Allen. *Analysis and Design of Structural Sandwich Panels*. Pergamon Press, 1969. (ISBN 9780080128702).

[8] F. J. Plantema. *Sandwich Construction*. John Wiley & Sons, 1966.

[9] D. Zenkert. *An Introduction to Sandwich Construction*. Engineering Materials Advisory Services, 1995. (ISBN 9780947817770).

[10] A. D. Almutairi, Y. Bai, W. Ferdous. Flexural behaviour of GFRP-Softwood sandwich panels for prefabricated building construction. *Polymers*, Volume 15, 2023. (doi 10.3390/polym15092102).

[11] M. N. Bin Kamarudin et al. Buckling analysis of a thin-walled structure using finite element method and design of experiments. *Aerospace*, Volume 9, 2022. (doi 10.3390/aerospace9100541).

[12] C. A. C. Coello. Theoretical and numerical constraint-handling techniques used with evolutionary algorithms: a survey of the state of the art. *Computer Methods in Applied Mechanics and Engineering*, Volume 191, 2002. (doi 10.1016/S0045-7825(01)00323-1).

[13] O. Hasançebi et al. Performance evaluation of metaheuristic search techniques in the optimum design of real size pin jointed structures. *Computers & Structures*, Volume 87, 2009. (doi 10.1016/j.compstruc.2009.01.002).

[14] O. Hasançebi et al. Comparison of non-deterministic search techniques in the optimum design of real size steel frames. *Computers & Structures*, Volume 88, 2010. (doi 10.1016/j.compstruc.2010.06.006).

[15] R. Eberhart and J. Kennedy. A new optimizer using particle swarm theory. In: Proceedings of the Sixth International Symposium on Micro Machine and Human Science, pp. 39-43, 1995. (doi 10.1109/MHS.1995.494215).

[16] F. van den Bergh and A. Engelbrecht. A study of particle swarm optimization particle trajectories. *Information Sciences*, Volume 176, 2006. (doi 10.1016/j.ins.2005.02.003).

DESIGN AND ANALYSIS OF LAMINATE LAY-UPS FOR COMPOSITE PRESSURE VESSELS FOR AIR STORAGE

Martin H. M. Maruyama*[(a)], Lucas L. Agne [(b)], Sandro C. Amico [(c)], Maikson L. P. Tonatto [(d)]

(a) 0000-0002-2606-581X (Federal University of Santa Maria – Brazil)
(b) 0009-0009-2470-724X (Federal University of Santa Maria – Brazil)
(c) 0000-0003-4873-2238 (Federal University of Rio Grande do Sul – Brazil)
(d) 0000-0002-3118-6894 (Federal University of Santa Maria – Brazil)
* Corresponding author: martin.maruyama@acad.ufsm.br

Abstract: Composite overwrapped pressure vessels (COPV) are structures designed to contain various types of fluids, usually compressed natural gas, hydrogen, oxygen or air, and became a recent solution for conventional pressure vessels due to its low weight and high strength. In order to prevent failure, they must be well-designed and validated. Air storage for braking systems usually utilizes metallic pressure vessels and no study about COPV for this application was found. This study aims at studying the behaviour of Type IV COPV for air storage solutions in which different laminates are used as the composite shell. The methodology was divided into analytical and numerical phases, using Python scripts, and modelling and simulation analysis, respectively. The best four lay-ups were modelled and analysed using Abaqus software and Woundsim plugin, and compared to analytical results. Burst pressure was compared using Tsai-Wu, Tsai-Hill and maximum stress failure criteria. Total mass data was obtained from the numerical models. Analytical and numerical models presented similar values for burst pressure, with a maximum difference of 10.41%, and the influence of total mass on mechanical strength was evidenced.

1. INTRODUCTION

Pressure vessels (PV) are structures designed to storage and transport various types of fluids under high-pressure conditions. Typically, these structures are made of metallic material due to the high mechanical strength properties and safety factor. On the other hand, metallic PVs are also heavy due to their high-density materials and have poor fatigue and corrosion properties. In order to deal with this issue, composite overwrapped pressure vessels (COPV) became an efficient solution [1].

Structures such as PV and COPV are divided in 5 different categories: Type I (it is the commonly used full-metallic pressure vessel); Type II (it is the first type of COPV, with a metallic liner overwrapped with composite material on the cylindrical region); Type III (metallic liner full overwrapped with composite material); Type IV (polymeric liner full overwrapped with composite material and metallic boss); and Type V (full composite with metallic end boss pressure vessel without liner) [2]. Among all PV types, the COPV Type IV is the most reliable and studied solution of all, being 70-80% lighter than PV Type I [1], presenting low permeability, easy manufacturing, high cyclic fatigue life and high burst pressure properties [2]. This type of COPV is typically used in applications for storage of high-pressure gases such as CNG (compressed natural gas), hydrogen, oxygen and air [1-3]. PVs for air storage are typically used in auxiliary braking systems on heavy vehicles such as buses and trucks, however it is uncommon to see COPV on this application or even studies on literature that analysed such systems with COPV.

Since Type IV COPVs have complex designs, it is crucial to ensure that the minimal requirements according to the standards are met and verified through proper testing and inspection. In order to verify the

reliability of these structures and reduce manufacturing costs, many authors utilize numerical models to optimize material properties, vessel geometry, burst pressure, stacking sequence, processing parameters and other variables that may affect the COPV project. Jebeli and Heidari-Rarani (2022) performed a study of Type IV COPV by simulating a numerical model with Abaqus software and WCM plugin to analyze the burst pressure with Puck failure criteria and considering bilinear cohesive law on the interface between liner, boss and composite regions to simulate the debonding due to temperature variations [2]. Ramirez et al. (2015) presented simulation and experimental results of burst tests of a Type IV COPV for hydrogen storage, which numerical model was simulated considering continuum damage to the composite structure to predict accurately the material behavior, while the experimental burst test was conducted in order to validate the numerical model and certify that a safe failure will occur [4]. Sharma and Neogi (2023) analyzed critical parameters on a numerical model of a Type IV COPV for compressed gas storage such as composite thickness distribution, fiber bandwidth, volume fraction and winding pattern and its effects on burst pressure, failure characteristics and weight of the vessel in order to compare with a manufactured experimental model [5].

Therefore, this study focuses on a Type IV COPV for air storage using finite element (FE) and analytical models in order to simulate their mechanical behavior when subjected to internal pressure, addressing the effect of different lay-ups on weight and burst pressure.

2. ANALYTICAL CALCULATIONS

To reduce the number of sequences that would be modelled and analysed in numerical models, a script was written in Python language based on the Classical Theory of Laminates [6]. The COPV model was subject to internal pressure and performed using different failure criteria for composite materials: Tsai-Hill, Tsai-Wu and maximum stress criteria.

The Python script requires the following data in order to calculate the failure criteria values for the COPV: composite material properties, number of layers, stacking sequence, cylinder radius and internal pressure. Since the laminate adopted the Classical Theory of Laminates, it is subjected to forces and moments, the applied pressure is decomposed as vectors on the x and y axis by multiplying it by the radius of the cylinder. The burst pressure that the COPV must withstand, according to BS EN 286-1 standard [7], corresponds to the value calculated in Eq. (1):

$$5 \cdot PS \cdot \frac{R_{m,act}}{R_m} \cdot \frac{e_{ms}}{e_s - t_s - c_s} \tag{1}$$

where, PS is the maximum working pressure of the COPV, $R_{m,act}$ is the actual tensile strength as measured on the plate used for the vessel, R_m is the minimum value of tensile strength, e_{ms} is the measured thickness before the pressure test, e_s is the nominal wall thickness, t_s is the absolute value of the negative tolerance and c_s is the shell corrosion allowance. The Eq. (1) was simplified and reduced to the Eq. (2):

$$P_{b,min} = 5 \cdot PS \tag{2}$$

where, $P_{b,min}$ is the minimum burst pressure and PS was adopted as 1.0 MPa, resulting in a minimum burst pressure of 5.0 MPa for this study.

First, the minimum number of layers is studied. To determine that for a particular stacking sequence, an initial $[\pm\alpha]_n$ stacking sequence is created, where α represents the orientation of the layers (in this case $\alpha = 55°$) and n is an integer value that represents a multiple of the stacking sequence (n = 1, 2, 3, …). The stacking sequence is inserted on the Python script and the internal pressure is varied from 1 to 10 MPa until all failure criteria reach a value equal to 1, meaning that the input pressure results in failure for that stacking sequence. The minimum number of layers on the stacking sequences is determined if the safety factor SF is equal or greater than 1.5, according to the Eq. (3):

$$SF = \frac{P_{b,min}}{P_i} \tag{3}$$

where, P_i is the applied internal pressure.

After that, a single angle stacking sequence study is developed. The angles that are more likely to withstand the minimum burst pressure are chosen. The stacking sequences are analysed in the format $[\pm\beta]_n$, where β is an integer value of angle that varies from 10° to 88° (practical limits) and n is the minimum number of layers determined earlier. The stacking sequence is inserted on the script and then pressure from 1 to 10 MPa is applied. The burst pressure for each angle is registered and the safety factor SF is calculated with the Eq. (3).

After ranking the best angles according to the safety factor, the top three proceed to the final step of the analysis. Considering the best angles and the minimum number of layers, a list of stacking sequences is created using another Python script to generate all possible stacking sequences that follow the defined

characteristics (maximum number of layers and chosen angles). After running the script, 64 different stacking sequences were created and analysed to determine each *SF*.

From the initial 64 stacking sequences, only 4 presented a *SF* equal or greater than 1, which means that the applied internal pressure was greater than 5.0 MPa. These 4 stacking sequences were approved and used in the following numerical study.

3. NUMERICAL MODEL

The models are built using Abaqus/Standard version 2024. The Type IV COPV model is created using the main parts of the structure, *i.e.*, liner, boss and composite layers. The vessel design is a 3D model (Figure 1a), but, in order to reduce the processing time and simplify the analysis, a 2D-axisymmetric model with ¼ symmetry is created (Figure 1b). In order to consider the composite layers, the Woundsim plugin is used. The composite layup imports the external surface contour points of the liner from the 2D-axisymmetric model geometry in Abaqus. With the liner surface plotted, it is possible to create the stacking sequence by inserting the plies orientations, properties and thicknesses for each sequence. The complete composite layup is plotted along with the liner as shown in Figure 1c.
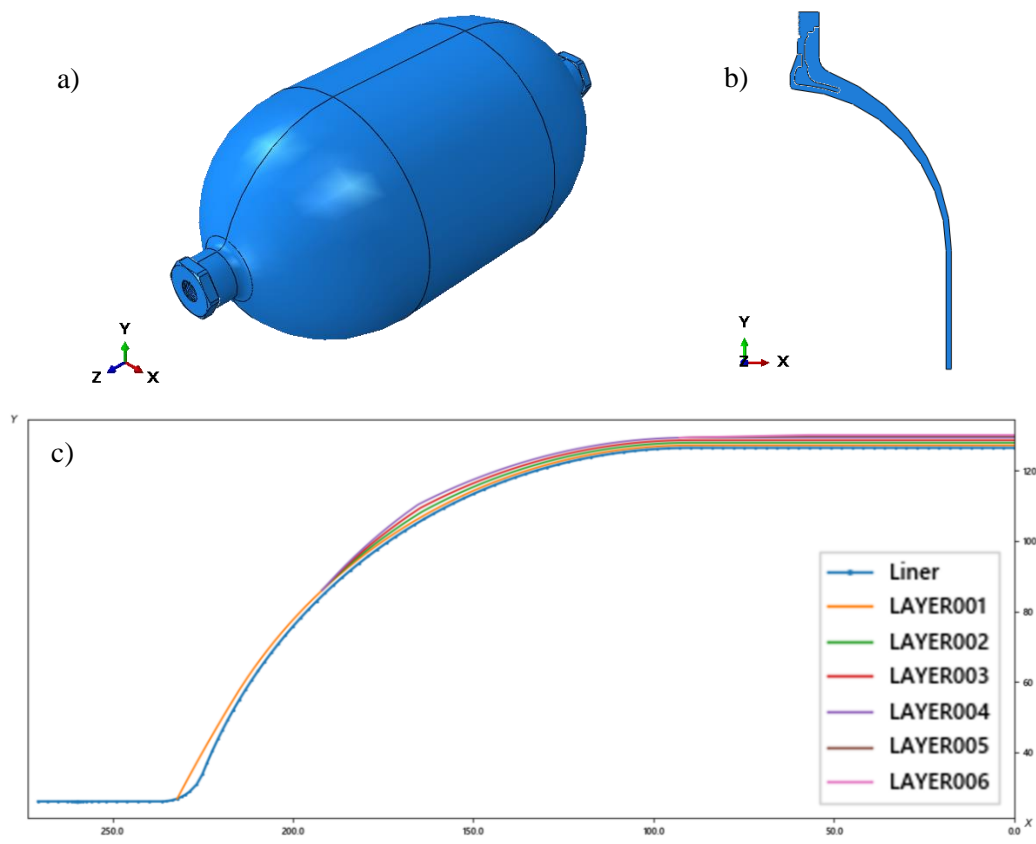
Figure 1. a) COPV 3D model, b) COPV 2D-axisymmetric model, and c) Plot of the liner and composite layup.

The contact between liner and composite is performed as bonded and the contact between boss and liner is performed as frictionless. The mesh for the model is built using SAX1 type elements with a total of 24236 elements along the dome, cylinder and boss regions, and the step is set with a pressure of 10.0 MPa applied on liner internal surface and a concentrated force in the boss region representing the pressure on the poppet if the COPV is sealed, with initial increment of 0.01 and minimal increment of 10^{-5}. The boundary condition is set as symmetry on y-axis on the bottom nodes of liner and composite layup. The Abaqus model is then created assembling the liner and the composite layup (Figure 2).

The liner, boss and composite properties are presented in Tables 1-2. The liner properties were obtained from experimental tests.The composite material is exported to the Woundsim plugin and then assembled with the creation of the composite layups or stacking sequences later on the Woundsim configuration step. The layer thickness is given as a function of the radius and calculated in Woundsim considering the Conservation of Volume method, given by Eq. (4):

$$t(r) = \frac{t_{tl} \cdot cos(\theta_{tl})}{cos(\theta_r)} \tag{4}$$

where t_{tl} represents the thickness at the tangent line, θ_{tl} is the winding angle at the tangent line and θ_r is the winding angles calculated for the defined radius. As the winding process reaches the dome region, angle evolution occurs and the variation for the angles is given by Eq. (5):

$$\theta(R) = sin^{-1}\left(\frac{R_0}{R}\right) \pm \delta\left(\frac{R - R_0}{R_{tl} - R_0}\right)^n \tag{5}$$

where R is the radial distance from the centre line to a point in the layer, R_0 is the radial distance from the centre line to the turnaround point, R_{tl} is the radius at the dome-cylinder tangent line, δ is the difference in degree between the frictionless winding angle and the winding angle calculated by the first term and n is the frictionless to friction angles interpolation parameter. The comparison between analytical and numerical model is made in the cylindrical region since it presents constant angle and thickness, unlike the dome and polar regions. The burst pressures calculated in the cylindrical region using the same failure criteria (Tsai-Wu, Tsai-Hill and maximum stress) are compared with those from the analytical results.
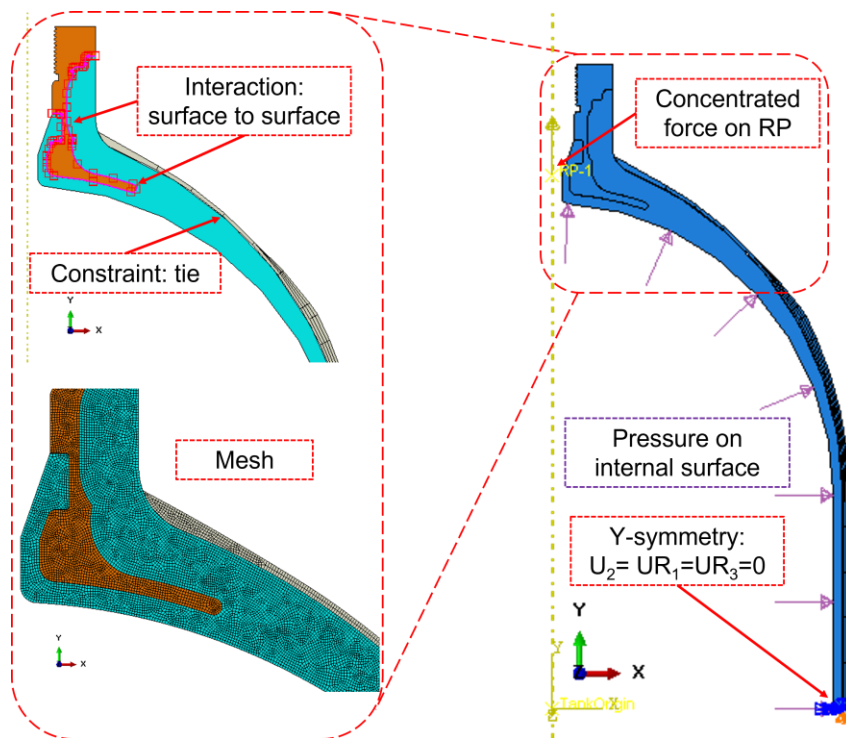
Figure 2. Abaqus model configuration.

Table 1. Liner and boss material properties.

	Liner	Boss [8]
Density, ρ	0.95 g/cm³	2.70 g/cm³
Elastic modulus, E	0.337 GPa	68.900 GPa
Poisson's ratio, ν	0.46	0.33

Table 2. Composite material properties [9].

Density, ρ	1.862 g/cm³
Elastic modulus in direction 1, E_1	43.810 GPa
Elastic modulus in directions 2 and 3, E_2 and E_3	5.568 GPa
Poisson's ratio in planes 12 and 13, ν_{12} and ν_{13}	0.286
Poisson's ratio in plane 23, ν_{23}	0.239
Shear modulus in planes 12 and 13, G_{12} and G_{13}	2.962 GPa

Shear modulus in plane 23, G_{23}	3.658 GPa
Longitudinal tensile strength, X_t	1400 MPa
Longitudinal compressive strength, X_c	759.7 MPa
Transversal tensile strength, Y_t	55.7 MPa
Transversal compressive strength, Y_c	104.9 MPa
Shear strength in plane 12, S_{12}	89.6 MPa

4. RESULTS AND DISCUSSION

In this section, the results for four different stacking sequences of a Type IV COPV for air storage from the analytical results (from the Python script) and the numerical results (from Abaqus simulation) are analysed. The profile of the final COPV model and the fiber orientations in the composite layer is represented by the UVARM1 variable in the analysis phase, illustrated in Figure 3.
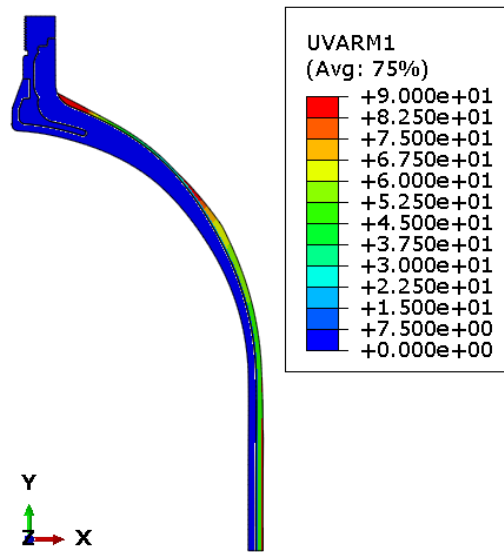
Figure 3. COPV composite fiber's angles.

Figure 4 compares burst pressure from the analytical (A) and numerical (N) models in the cylindrical region of the COPV. The best four stacking sequences are referenced as Seq_1, Seq_2, Seq_3 and Seq_4, respectively. It is observed that the numerical values (N) for Seq_1, Seq_3 and Seq_4 according to Tsai-Wu, Tsai-Hill and maximum stress failure criteria are greater than the analytical values (A). The largest difference was 10.41% for Seq_1 using Tsai-Hill criterion, and the smallest difference was 3.71% for Seq_3 using Tsai-Hill criterion. The Seq_1 showed the largest average difference (9.45%) between A and N models for the three criteria, while Seq_3 showed the smallest (4.41%). Based on the adopted standard, the burst pressure of all N and A models overcome 5.0 MPa, except Seq_4 for maximum stress and Tsai-Hill's analytical models.
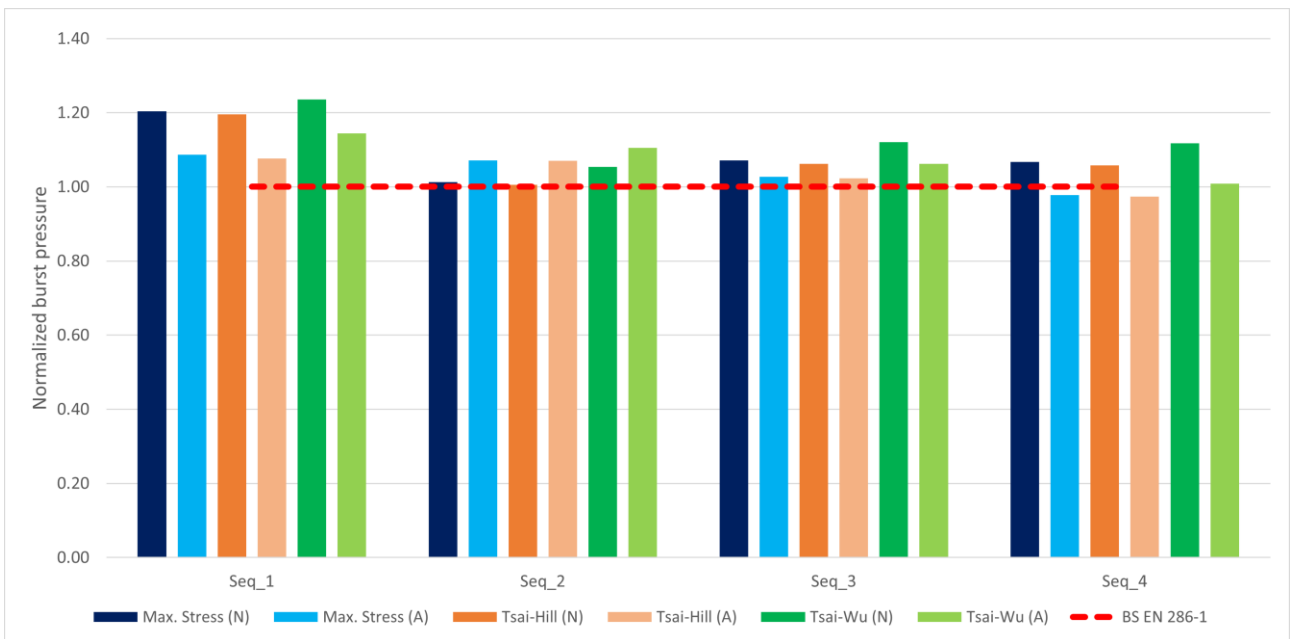
Figure 4. Normalized burst pressure in the cylinder region for analytical (A) and numerical (N) models using maximum stress, Tsai-Hill, and Tsai-Wu failure criteria.

Figure 5 compares the total mass of COPV for the four selected sequences. The total mass is calculated using the total mass of the composite layup given by Woundsim and the mass of liner and boss. The COPV with Seq_1 presented the greatest total mass, 5.26% higher than the average mass, whereas Seq_3 showed the lowest total mass, 2.03% below the average mass.
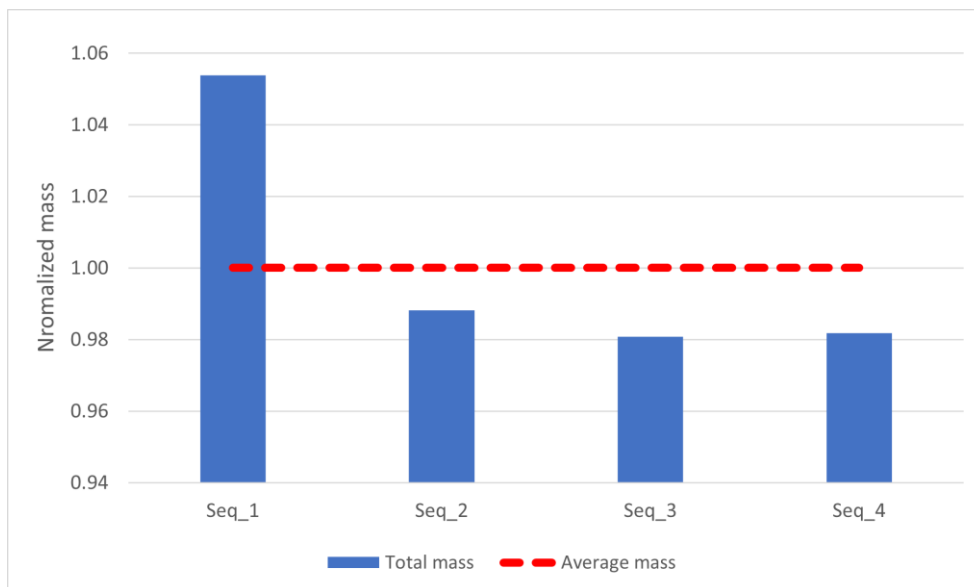
Figure 5. Normalized total mass, in relation to average mass, of COPV for each composite layup.

5. CONCLUSIONS

The present work consisted in analysing and comparing the performance of Type IV COPV for air storage considering different stacking sequences for the composite shell, considering burst pressure and total mass. The use of an analytical script for the initial study of possible stacking sequences proved helpful in reducing the number of stacking sequences to model, optimizing the analysis time demand. It was also considered reliable since the differences between numerical and analytical models were small. The sequence 1 showed the greatest burst pressure and total mass among the selected stacking sequences, meaning that the mass of the composite has some influence on the mechanical strength of the COPV. The sequence 3 showed the lowest differences between numerical and analytical models for three failure criteria, being the most reliable in this study.

5.1. Declaration of Competing Interest

The authors declare no conflict of interest.

5.2. Fundings

5.3. Acknowledgements

6. REFERENCES

[1] M. Azeem, H.H. Ya, M.A. Alam et al. Application of Filament Winding Technology in Composite Pressure Vessels and Challenges: A Review. *Journal of Energy Storage*, Volume 49, 2022. (https://doi.org/10.1016/j.est.2021.103468).

[2] M.A. Jebeli, M. Heidari-Rarani. Development of Abaqus WCM plugin for progressive failure analysis of type IV composite pressure vessels based on Puck failure criterion. *Engineering Failure Analysis*, Volume 131, 2022. (https://doi.org/10.1016/j.engfailanal.2021.105851)

[3] N.H. Farhood, S. Karuppanan, H.H. Ya et al. Burst pressure investigation of filament wound type IV composite pressure vessel. *AIP Conf. Proc.*, Volume 1901, 2017. (https://doi.org/10.1063/1.5010482).

[4] J.P. Berro Ramirez, D. Halm, J.C. Grandidier et al. 700 bar type IV high pressure hydrogen storage vessel burst - Simulation and experimental validation. *International Journal of Hydrogen Energy*, Volume 40, 2015. (https://doi.org/10.1016/j.ijhydene.2015.05.126).

[5] P. Sharma, S. Neogi. Performance-based design and manufacturing of filament wound Type-4 cylinders for compressed gas storage, *Composite Structures*, Volume 309, 2023. (https://doi.org/10.1016/j.compstruct.2023.116710).

[6] F. Levy Neto, L.C. Pardini. *Compósitos estruturais: Ciência e Tecnologia*, 2nd Edition, 2016. Editora Blucher. (ISBN: 8521210795, 9788521210795).

[7] BS EN 286-1, *Simple unfired pressure vessels designed to contain air or nitrogen. - Part 1: Pressure vessels for general purposes*. The British Standards Institution, 2024. (https://standardsdevelopment.bsigroup.com/projects/2019-01914#/section)

[8] M. Nebe, A. Soriano, C. Braun et al. Analysis on the mechanical response of composite pressure vessels during internal pressure loading: FE modeling and experimental correlation, *Composites Part B: Engineering*, Volume 212, 2021. (https://doi.org/10.1016/j.compositesb.2020.108550).

[9] Mech-GCOMP® 2024 [Computer software]. GCOMP/UFRGS. (www.ufrgs.br/mechg).

EXPERIMENTAL INVESTIGATION OF THE UNIAXIAL RATCHETING BEHAVIOR OF POLYPROPYLENE MATRIX

Fábio C. Castro[a],*, Jonatan R. Moura[b], Arthur S. Maciel[c], Leonardo V.A. Duarte[d]

(a) ⓘ 0000-0001-9005-6961 (University of Brasília – Brazil)
(b) ⓘ 0009-0002-5392-2888 (University of Brasília – Brazil)
(c) ⓘ 0009-0000-2162-5286 (University of Brasília – Brazil)
(d) ⓘ 0009-0007-4784-7769 (University of Brasília – Brazil)
* Corresponding author: fabiocastro@unb.br

Abstract: Components made of polymers or composite materials with a polymeric matrix are widely used in today's industry and, in many applications, they must withstand cyclic loads. In this scenario, accurate modeling of the stress-strain response of polymers is crucial for a reliable prediction of the durability of a component. In this work, uniaxial stress-controlled tests were conducted on polypropylene to characterize its ratcheting behavior. Asymmetrical cyclic loadings were applied at different loading rates, mean stresses, and peak stress hold times. The experimental results showed that these parameters influence the strain response of polypropylene and should, therefore, be described by cyclic constitutive models.

1. INTRODUCTION

Reliable lifetime prediction of engineering components made of polymer, or polymeric composites, requires an accurate stress and strain analysis. Since the 1960s, there has been significant progress on theoretical and numerical models to aid this analysis [1–3]. Nonetheless, further research on the constitutive behavior and failure mechanisms of polymeric materials is still needed for safety and reliability purposes, especially in situations involving cycling loading. A major difficulty in predicting the stress-strain response of polymers is that they exhibit a complex nonlinear and time-dependent behavior, which is related to their molecular nature and morphological structure.

Engineering components are often subjected to loading histories that cycle asymmetrically about zero. This situation may result in a progressive accumulation of inelastic deformation, which is called ratcheting. This phenomenon may harm the integrity of structural parts by producing dimensional changes in the parts or by activating damage mechanisms in the material. There are many recent studies on the ratcheting behavior of polymers and polymeric composites (see [4–10] and references therein), which have been motivated by the importance of these materials in today's industry. However, accurate modeling and a detailed understanding of the characteristic behavior of polymeric materials is still a challenging task.

The present study is concerned with the experimental characterization of the uniaxial ratcheting behavior of polypropylene at room temperature. This material in its pure form, or with reinforcements, has been widely used in applications involving cyclic loads [10]. The test data obtained can be useful in the development of cyclic constitutive models for polymers.

2. METHODOLOGY

The material investigated in this study was polypropylene. It was acquired in the form of a square plate with a side of 600 mm and a thickness of 5 mm. Specimens with rectangular cross sections of 24 mm by 5 mm and length of 165 mm were machined from plate.

The experimental setup for the characterization of the ratcheting behavior of polypropylene is shown in Fig. 1a. The tests were conducted in force control using an MTS servohydraulic machine equipped with a load cell of 5 kN. The strain in the gage section of the specimen was measured with an MTS 634.11 extensometer, which has a gage length of 25 mm and a range of -10% to 20%. All tests were conducted at room temperature. The influence of the mean stress, stress rate, and peak stress hold time on the time-dependent strain of polypropylene was investigated for the stress history shown in Fig. 1b, where the stress was defined as the axial force divided by the initial cross-sectional area of the specimen. The loading parameters considered in the test are listed in Table 1.

The tests had a short duration (less than 5 h) and were not conducted up to failure. While the authors recognize the importance of the problem of long-term ratcheting in engineering applications, short-term tests were deliberately performed to reduce the duration of the experimental program. Moreover, with a view to future modeling of the time to failure of polymers under cyclic loading, we realize that a clear understanding of the stress-strain behavior is required before introducing damage into the analysis.

Ratcheting refers to the progressive cycle-by-cycle accumulation of strain due to unsymmetrical stress cycling. To quantify the ratcheting behavior, the ratcheting strain ε_r corresponding to the loading cycle N was defined by

$$\varepsilon_r = \frac{\varepsilon_{max} + \varepsilon_{min}}{2} \tag{1}$$

where ε_{max} e ε_{min} where are the maximum and minimum values of the strain during the loading cycle. For each test, the variation of the ratcheting strain with the number of cycles was obtained by postprocessing the raw data. It should be noted that, in some cases, the strain response during the first cycles was not shown because transient effects related to the force control might be confused with the real strain behavior of the material.

a   **b**
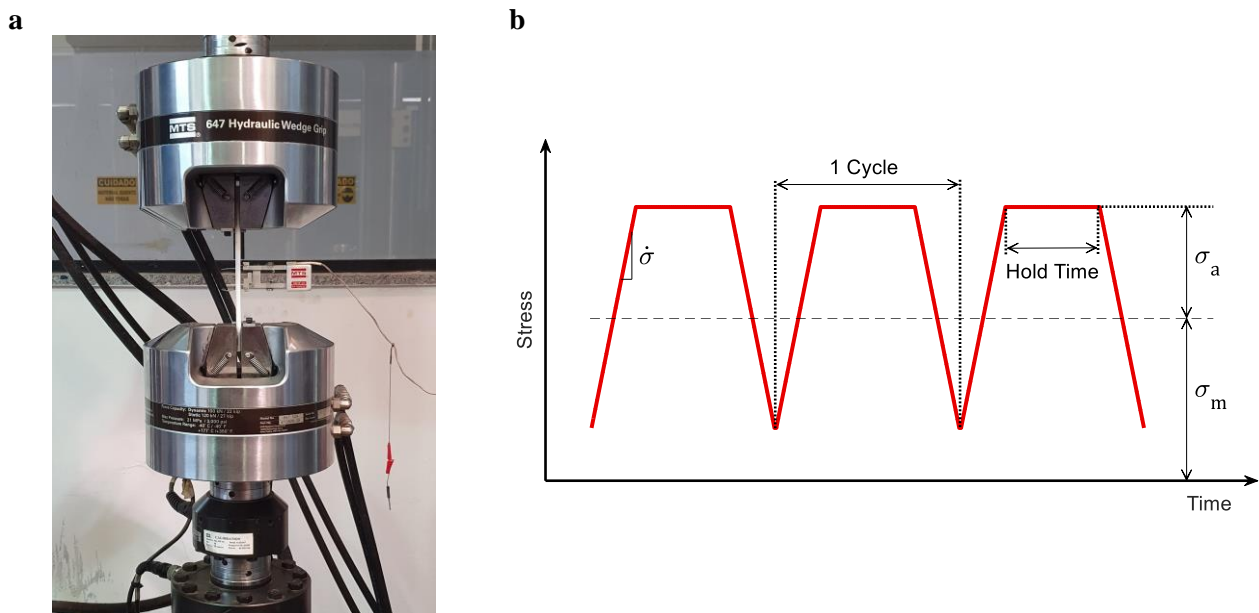
Figure 1. (a) Experimental setup for ratcheting test of polypropylene. (b) Stress history used in the tests.

Table 1. Parameters of the stress-controlled tests.

Test No.	σ_m (MPa)	σ_a (MPa)	$\dot{\sigma}$ (MPa/s)	Hold Time (s)
1	2.6	7.7	1.2	–
2	6.3	7.7	1.2	–
3	9.4	7.7	1.2	–
4	9.4	7.7	3.1	–
5	9.4	7.7	31	–
6	9.4	7.7	1.2	5
7	9.4	7.7	1.2	20
8	9.4	7.7	3.1	5

3. RESULTS AND DISCUSSION

Engineering components often operate under loads that vary asymmetrically about zero, which results in a mean stress superimposed on an alternating stress. It is therefore important to understand the mean stress effect on the cyclic strain behavior of polymers. The experimental results of the tests conducted on polypropylene under various mean stresses are presented in Fig. 2., where the ratcheting strain of each cycle is plotted against the number of cycles. The slope of this curve is the ratcheting rate which provides the increment of strain ratcheting per cycle. The results show that the mean stress influences the magnitude and the rate of the ratcheting strain. For a mean stress greater than 2.6 MPa, the ratcheting strain becomes proportional to the number of cycles (i.e., the ratcheting strain rate reaches a constant value) after an initial transient of about 100 cycles.
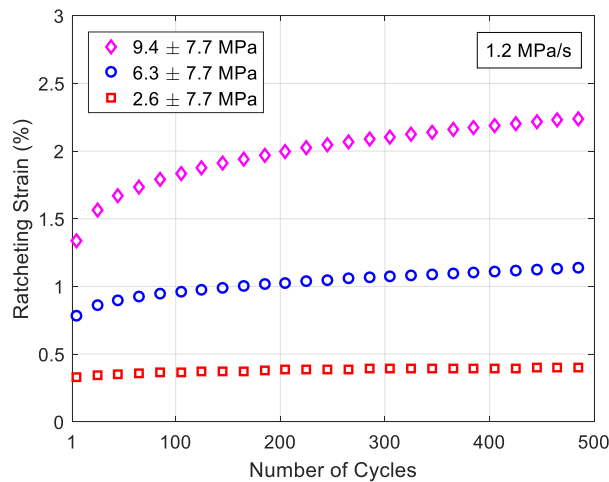
Figure 2. Mean stress effect on ratcheting strain for a stress history with stress amplitude $\sigma_a = 7.7$ MPa and stress rate of 1.2 MPa/s.

Experimental results have shown that ratcheting of polymers typically exhibits a time-dependent behavior. To investigate the effect of time-related loading parameters on the ratcheting strain response of polypropylene, tests were conducted with different stress rates and peak stress hold times. Fig. 3 shows the results of tests performed at loading frequencies of 0.04, 0.1, and 1 Hz, which corresponded to stress rates of 1.2, 3.1, and 31 MPa/s, respectively. It can be seen that, after an initial transient period, a steady state behavior characterized by a constant ratcheting rate is achieved. Also, higher stress rates resulted in lower magnitudes of ratcheting strain and ratcheting rates.
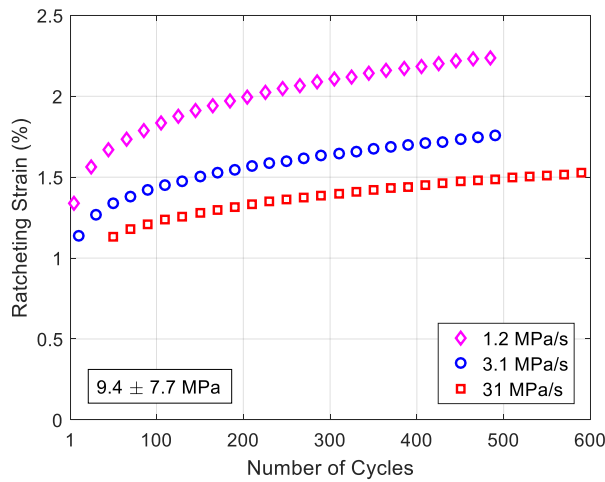
Figure 3. Stress rate effect on ratcheting strain for a stress history with $\sigma_m = 9.4$ MPa and $\sigma_a = 7.7$ MPa.

Engineering components that work under cyclic loads may experience dwell periods of constant loading. For a polymer subjected to a stress history, creep of the material during this period can influence the amount of accumulated strain, when compared to similar loading histories without hold times. For the polypropylene under investigation, the results of the tests performed with peak stress hold times of 5 s and 20 s are shown in Figs. 4a and b, respectively. It can be seen that longer hold times resulted in higher magnitudes and rates of strain ratcheting. It is interesting to compare the stress-strain hysteresis loops of tests with and without a holding period at the peak stress, as shown in Fig. 5. These results show that the peak stress hold produces an amount of creep at each loading cycle. As a consequence, the strain ratcheting is higher, the ratcheting rate is faster, and more energy is dissipated per cycle (hysteresis loops have a larger area).
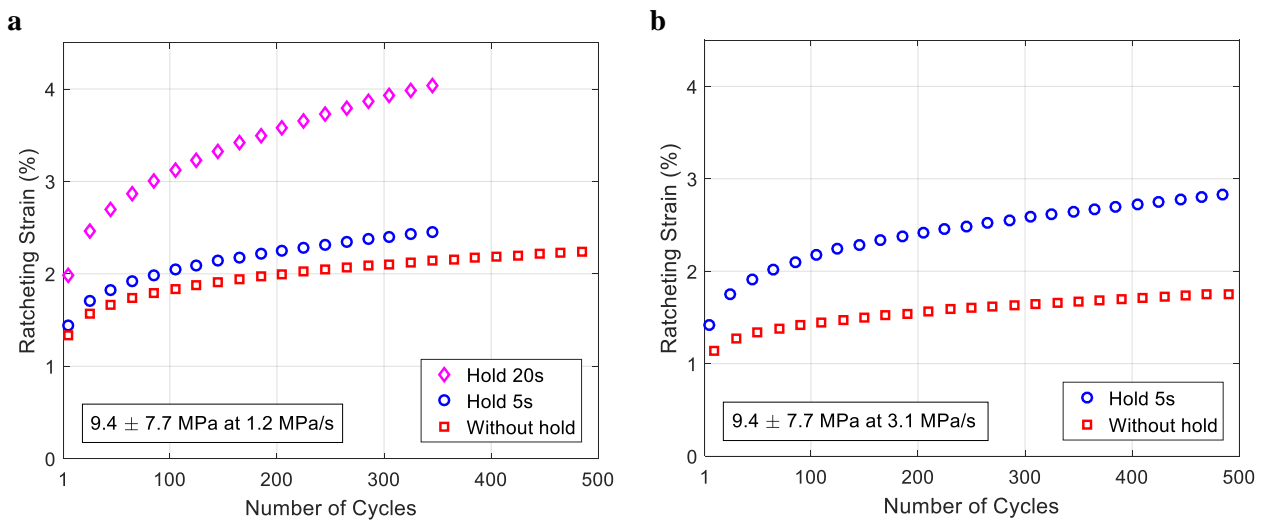
Figure 4. Peak stress hold-time effect on ratcheting strain for a stress history with $\sigma_m = 9.4$ MPa and $\sigma_a = 7.7$ MPa and stress rates of (a) 1.2 MPa/s and (b) 3.1 MPa/s.

4. CONCLUSIONS

The study has described a series of stress-controlled uniaxial tests on polypropylene at room temperature. The material was subjected to triangular stress histories, in some cases with a peak stress hold period, for a short duration (less than about 5 hours). The ratcheting responses measured allows to conclude that the loading parameters investigated (mean stress, stress rate, and hold time) have a significant influence on the time-dependent strain and should, therefore, be included in any proper modeling of the cyclic constitutive behavior of polypropylene.
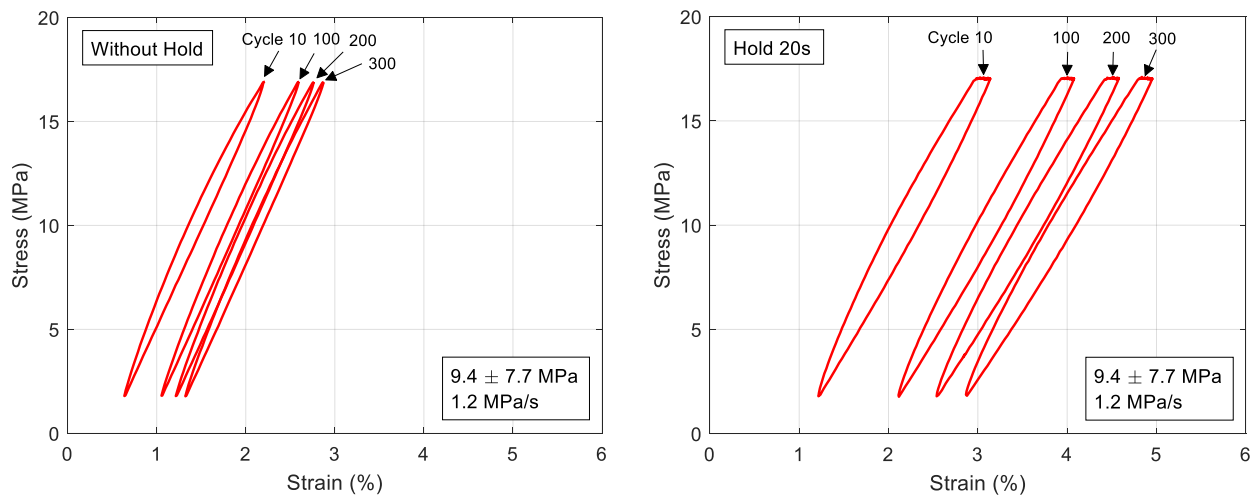
Figure 5. Stress-strain hysteresis loops of tests conducted without and with peak stress hold.

4.1. Declaration of Competing Interest

The authors declare no conflict of interest.

4.2. Acknowledgments

5. REFERENCES

[1] R.A. Schapery. Nonlinear viscoelastic solids. *International Journal of Solids and Structures*, Volume 37, 2000. (https://doi.org/10.1016/S0020-7683(99)00099-2).

[2] A. Wineman. Nonlinear viscoelastic solids–A Review. Mathematics and Mechanics of Solids, Volume 14, 2009. (https://doi.org/10.1177/1081286509103660).

[3] J.S. Bergstrom. *Mechanics of Solid Polymers*, 1st Edition, 2015. William Andrew. (https://doi.org/10.1016/C2013-0-15493-1).

[4] G. Kang et al. Uniaxial ratchetting of polymer and polymer matrix composites: Time-dependent experimental observations. *Materials Science and Engineering A*, Volume 523, 2009. (https://doi.org/10.1016/j.msea.2009.06.055).

[5] C. Yu. Viscoelastic–Viscoplastic Cyclic Deformation of Polycarbonate Polymer: Experiment and Constitutive Model. *Journal of Applied Mechanics*, Volume 83, 2016. (https://doi.org/10.1115/1.4032374).

[6] A. Krairi, I. Doghri. A thermodynamically-based constitutive model for thermoplastic polymers coupling viscoelasticity, viscoplasticity and ductile damage. *International Journal of Plasticity*, Volume 60, 2014. (https://doi.org/10.1016/j.ijplas.2014.04.010)

[7] C. Kaijuan et al. Effect of crystalline content on ratchetting of ultra-high molecular weight polyethylene polymers: Experimental investigation and constitutive model. *Mechanics of Materials*, Volume 133, 2019. (https://doi.org/10.1016/j.mechmat.2019.03.007).

[8] R. Song et al. A thermodynamically consistent model for viscoelastic polymers undergoing microstructural changes. *International Journal of Engineering Science*, Volume 142, 2019. (https://doi.org/10.1016/j.ijengsci.2019.05.009).

[9] F. Lu et al. Study on the ratchetting behavior of glass fiber-reinforced epoxy composites: Experiment and theory. *Polymer Testing*, Volume 117, 2023. (https://doi.org/10.1016/j.polymertesting.2022.107875).

[10] J. Karger-Kocsis. Fatigue performance of polypropylene and related composites. In: Polypropylene. Polymer Science and Technology Series, Volume 2, 1999. Springer, Dordrecht. (https://doi.org/10.1007/978-94-011-4421-6_31).

16 Multifunction composites

Organized and edited by

Sandra Maria da Luz
&
Carla Tatiana Mota Anflor

EVALUATION OF BIOSILICATE® FUNCTIONALIZATION BY RF AND ABIPPS PLASMA THROUGH SOLID MALEIC ANHYDRIDE

Camila Thais Mamani[a]*, Beatriz Goulart Hespanhol da Silveira[b], Davi João Espíndola[c], Daniel Aparecido Lopes Vieira da Cunha[d], Lidiane Cristina Costa[e], Luiz Antonio Pessan[f], Teresa Tromm Steffen[g]Daniela Becker[h]

(a) 0009-0009-6285-315X (Santa Catarina State university – Brazil)
(b) 0009-0009-2423-3363 (Santa Catarina State university – Brazil)
(c) 0009-0003-0385-2292 (Santa Catarina State university – Brazil)
(d) 0000-0003-0291-4896 (Santa Catarina State university – Brazil)
(e) 0000-0002-0280-6994 (São Carlos Federal university – Brazil)
(f) 0000-0001-8363-9122 (São Carlos Federal university – Brazil)
(g) 0000-0001-6608-8269 (Santa Catarina State University – Brazil)
(h) 0000-0003-3250-576X (Santa Catarina State university – Brazil)
* Corresponding author: camilathaismamani@gmail.com

Abstract: Bioglass has earned space in tissue engineering due to its chemical composition similar to human bone, and being highly bioactive. Among the various existing bioglasses, Biosilicate®, developed by the Department of Materials Engineering at the Federal University of São Carlos (DEMa/UFSCar), presents the chemical elements silicon, oxygen, sodium, calcium, and phosphorus (Si, O, Na, Ca, and P) and has crystallinity close to 100%. Due to this, Biosilicate® has been used as a filler with Lactic polyacid (PLA), resulting in a promising composite material to produce scaffolds used in bone regeneration. Conventional techniques to produce polymer composites usually employ high temperatures and shear rates, which can result in severe polymer degradation in the presence of certain bioactive fillers. Particle surface modification could overcome these processing difficulties. However, there are a lot of studies using the chemical route to do the surface modification and few studies using plasma. Due to this, this work aims to evaluate the functionalization of Biosilicate® using maleic anhydride (MA), as a functionalization agent, by applying RF plasma under mild conditions such as low power and short times. The mixture of Biosilicate® with MA was performed manually in a mass proportion of 90:10 (Biosilicate®:MA). The samples were treated by 35 W Radio Frequency source in a capacitively Couple Plasma reactor for a period of 5 and 15 minutes. The treatment was made in a reactor manufactured specifically for the experiments in this study, and all the treatments used Argon as a working gas (22,33 sccm). After plasma, treated samples were washed with methanol to remove unreacted MA molecules, and characterized by FTIR (Fourier Transform Infrared Spectroscopy) to evaluate the Biosilicate® functionalization. As a result, it was noted that the treatments were not succeed. Because of this result, it was changed to an asymmetric pulsed plasma with 400 V for 1h, after these changes the Biosilicate® could be functionalized.

1. INTRODUCTION

PLA and Biosilicate® are promising composites for manufacturing scaffolds, as PLA has good mechanical resistance to fulfill necessary load functions, and Biosilicate® has osteoinductive behavior when

implanted in the body. It presents the chemical elements silicon, oxygen, sodium, calcium, and phosphorus (Si, O, Na, Ca, and P), and, unlike other bioglass, it has a crystallinity close to 100% [1].

However, the presence of Biosilicate® severely degrades the PLA matrix during their processing due to the chain split through the reaction between the Si-O groups present on the surface of the Biosilicate® and C=O groups present in the polymer structure at high temperatures that consequently reduce the molar mass and viscosity, resulting in the reduction of the thermal stability [2,3]. Since the combination of PLA and Biosilicate® shows promise, one way to mitigate this process and preserve the molar mass of the polymer matrix would be to modify the surface of this particle to control the release of ions present on the surface of the particles.

There are a lot of researchers functionalization of bioburdens using the chemical route mechanism [4,5]and even using plasma [3], but it´s rare to explore the functionalization of the Biosilicate® material using the plasma technique. Plasma differs from other methods because it is a fast, clean process, free of contaminants, reproducible, and considered chemically efficient [6].

Besides, studies show that plasma throughout radiofrequency is commonly used to functionalize ZnO ,carbon nanotube in times of 5 and 15 minutes and power of 35W [7,8]. However, studies that could functionalize Bioglass 45S5, which has a similar Biosilicate® structure, had used higher power and time of treatment to have a successful functionalization. Based on that, a power source that has been used to guarantee more power is ABiPPS (Asymmetric Bipolar Plasma Power Supply).

In short, based on the motivations and problems presented, this work aims to evaluate the Biosilicate® functionalization using the functionalization solid agent the Anhydride maleic by radio frequency (RF) plasma in times of 5 and 15 minutes and also using the ABiPPS plasma in 1 hour of treatment.

2. METHODOLOGY

The materials used were Biosilicate®, which was manufactured according to the processing steps described in patent filing code WO 2004/074199, and it was donated by Vitreous Materials Laboratory (LaMaV) from the Department of Materials Engineering (DEMa/UFSCar). As functionalization agent material it was used 99% maleic anhydride (Aldrich Chemistry), and the gas used to open the plasma discharge was ultrapure argon (99.999%). For the vacuum filtration procedure, treated samples were mixed with methanol obtained from the company Dinâmica Química Contemporânea Ltda, with a minimum dosage of 99.8%.

The plasma reactor was homemade and has a cylindrical sample holder (h=1.2 cm, Ø=5.4 cm). Initially, the mixture of Biosilicate® with the functionalizing agent was manually performed. Mixing with maleic anhydride (Biosilicate_MA) followed the procedure described by [7] in a 90:10 mass ratio. The parameters of the RF plasma treatment were chosen based on previous works [7,8] The system was first evacuated to a base pressure of 1×10^{-1} Torr. Then, with an argon flow of 195 sccm, the working pressure of 1 Torr was established. The argon flow, without plasma discharge, was maintained for 10 minutes to contribute to the cleaning of the discharge environment. Finally, the plasma treatment was carried out for 5 and 15 minutes with a radio frequency power of 35 W, or using ABiPPS (Asymmetric Bipolar Plasma Power Supply). For ABiPPS, the chosen parameters were: four intercalated positive and negative peaks of 400V, during 1 microsecond each, separated by 10us time off. The treatment lasted 1 hour.

After functionalization, the samples were mixed with methanol, considering the proportion of 1g of sample to 100 ml of methanol, in a Becker and stirred for 12 hours using a magnetic stirrer. Then, the mixture was vacuum filtered to remove possible unreacted molecules of the functionalizing agent. The solid samples obtained from the vacuum filtration were kept in an oven at 50°C for 1 hour. Samples were characterized by Fourier transform infrared spectroscopy (FTIR). For the FTIR analysis, 32 scans were performed in the spectral region from 4000 to 400 cm^{-1}, with a resolution of 4 cm^{-1}, using the transmission mode with KBr chips.

3. RESULTS AND DISCUSSION

After plasma treatment by RF and ABiPPS source, the surface of the modified Biosilicate® particles was analyzed by FTIR. Fig.1 shows the FTIR spectra for Biosilicate, Anidride Maleiche (AM), and the RF plasma treated samples for 5 minutes (BIO+AM_5min) and 15 minutes (BIO+AM_15min).
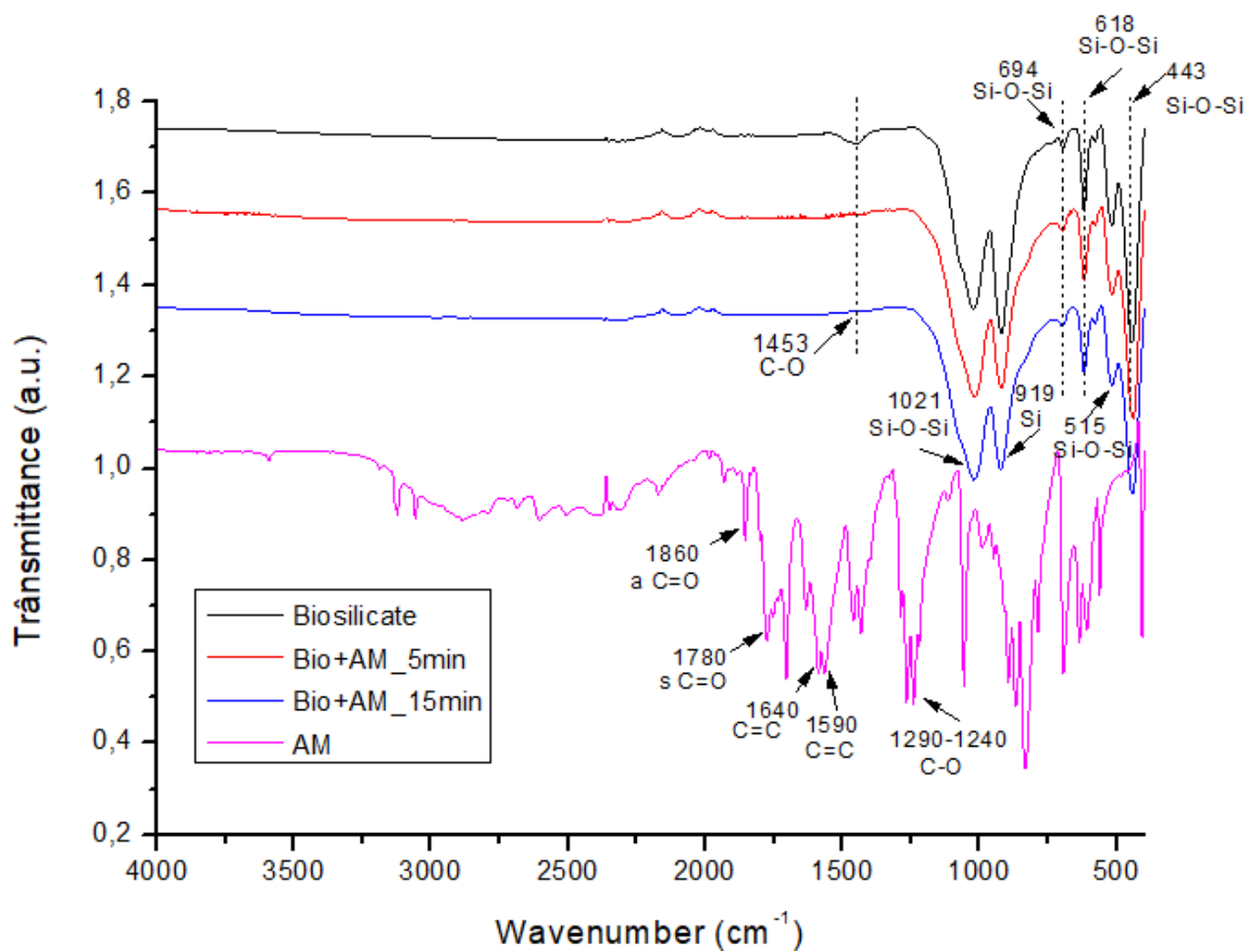
Figure 1. FTIR spectra for Biosilicate®, treated Bio+AM_5min , treated Bio+AM_15min samples, and AM.

The Biosilicate® spectrum shows a band in the region of 1453 cm^{-1} associated with the C–O vibration mode [9], while the bands 443cm^{-1}, 515cm^{-1}, 618cm^{-1} and 1021cm^{-1} are related to the stretching vibration of Si-O-Si [10]. The absorption band at 919 cm^{-1} is related to SiO banding vibration [10]. Regarding the spectrum of the maleic AM sample, a band in the region of 1780 cm^{-1} is associated with the symmetrical elongation of the C=O. Already, the band in the region 1860 cm^{-1} is related to asymmetric elongation of the C=O. At 1640 and 1590 cm^{-1} the bands refer to the elongation of the C=C bond, and in the region from 1290 to 1240 cm^{-1}, the bands correspond to the elongation of the C-O bond of the MA ring [8].

For treated samples by RF plasma (BIO+AM_5min and BIO+AM_15min), as shown in both spectrums, are the same as the Biosilicate® spectrum, which indicates that the functionalization by RF plasma it was too mild. This result can be associated with the parameters that were set in plasma. Some studies used plasma RF with higher times and powers [3], it could functionalize the Bioglass® 45S5 by plasma using the parameters of 80W and 45 minutes of treatment. Besides, based on the experiment done by [4,5] they could have a successful functionalization in ZnO surface using plasma RF with a power of 100W and 5 hours of treatment. Taking into consideration the studies mentioned, it was changed the source of power from RF to a more powerful source of energy: ABiPPS, and also increased the time of treatment. Fig 2 shows the spectra for the treated ABiPPS sample.
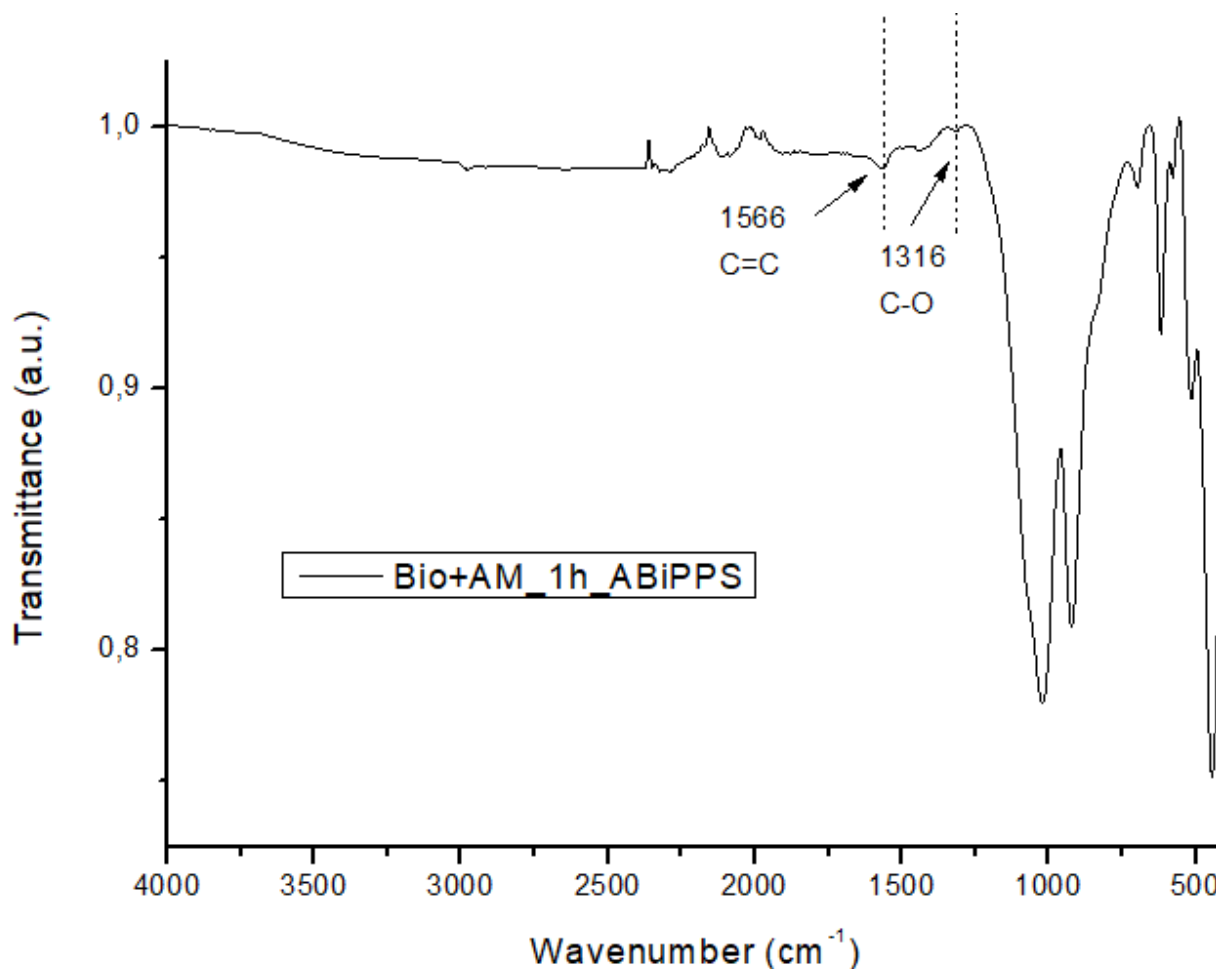
Figure 2. FTIR spectra for treated Bio+AM_1h_ABiPPS sample.

It can be noticed in Fig.2 the band 1566 cm^{-1} refers to the elongation of the C=C bond and 1316 cm^{-1} corresponds to the elongation of the C-O bond of the MA ring. It is attributed to the asymmetric and symmetric stretching of the carboxylic acid salt functional group (COO-) [8]. The carboxylic acid salt functional group formation makes sense because of the Biosilicate® structure that contains a lot of metals that can bond and form the acid. The presence of signals from MA in the sample may indicate that the functionalization process was successful.

4. CONCLUSIONS

Although the RF plasma treated samples showed that the Biosilicate® was not functionalized, after changing the parameters of the plasma process, it means increased power by changing the power source from RF to ABiPPS and also increased the time of treatment from 5 and 15 minutes to 1 hour, it was possible to see evidence of functionalization in FTIR characterization when the bands from MA was found in the samples treated by ABiPPS plasma and from this process the study will be continued.

4.1. Declaration of Competing Interest

The authors declare no conflict of interest.

5. REFERENCES

[1] Zanotto D. E, Ravagnani C, Peitl O, Panzeri H, Lara EG. *Process and compositions for preparing particulate, bioactive or resorbable biosilicates for use in the treatment of oral ailments*. Patent WO 2004074199 A1, 2007

[2] Blacker J., Maquet V.,J´erome R.,Boccaccini A. R. and Nazhat S. N., *Mechanical Properties of Highly Porous PDLLA/Bioglass Composite Foams as Scaffolds for Bone Tissue Engineering*, Acta Biomater., 2005, 1, 643–652.

[3] Larrañaga, A.; Petisco, S.; Sarasua, J. *Improvement of thermal stability and mechanical properties of medical polyester composites by plasma surface modification of the bioactive glass particles*. Polym. Degrad. Stab. 2013, 98, 1717–1723. [Google Scholar] [CrossRef].

[4] Ciolan, Mihai Alexandru; Motrescu, Iuliana; Luca, Dumitru; Nagatsu, Masaaki. *Mass spectrometric study of Ar/NH3surface wave plasma utilized for surface functionalization of ZnO nanoparticles*. Japanese Journal Of Applied Physics, [S.L.], v. 53, n. 1, p. 010207, 30 dez. 2013. IOP Publishing. http://dx.doi.org/10.7567/jjap.53.010207.

[5] Ciolan, Mihai Alexandru; Motrescu, Iuliana; Sugiura, Kuniaki; LUCA, Dumitru; Nagatsu Masaaki. *Tailoring the Surface Functionalities of Radio Frequency Magnetron- Sputtered ZnO Thin Films by Ar/NH3 Gas Mixture Surface-Wave Plasmas*. Langmuir,[S.L.], v. 34, n. 38, p. 11253-11263, 29 ago. 2018. American Chemical Society (ACS). http://dx.doi.org/10.1021/acs.langmuir.8b01183.

[6] SILIPRANDI, R. A. Atmospheric *Pressure Plasmas for Surface Modifications*. 2007. 167 f. 2007.

[7] T.T. Steffen et al. Carbon nanotube plasma functionalization: *The role of carbon nanotube/maleic anhydride solid premix*. Applied Surface Science, 491, 2019. (https://doi.org/10.1016/j.apsusc.2019.06.176).

[8] Klok, Larissa et al. *Plasma functionalization of zinc oxide nanoparticles through organic compounds*. 6th Brazilian Conference on Composite Materials. August,2022. (doi.org/10.29327/566492)

[9] Vikash Kumar Vyas; A Sampath Kumar, S P Singh; Ram Pyare. *Effect of nickel oxide substitution on bioactivity and mechanical properties of bioactive glass*. Bull. Mater. Sci., Vol. 39, No. 5, September 2016, pp. 1355–1361. ©Indian Academy of Sciences. DOI 10.1007/s12034-016-1242-7

[10] Pereira M. A.; Oliveira J. E. ; Fonseca C. S. *Influence of the use of rice husk as source of silica on the sol-gel synthesis of bioglass*. Cerâmica 67 (2021) 333-337 http://dx.doi.org/10.1590/0366-69132021673833134

17 Nanocomposites

Organized and edited by

Sandra Maria da Luz
&
Carla Tatiana Mota Anflor

IMPROVEMENTS IN THE MECHANICAL PROPERTIES OF EPOXY ADHESIVES WITH PLASMA-FUNCTIONALIZED CARBON NANOTUBES

Elton J. Sehnem[(a)*], Ricardo de Medeiros[(b)], Teresa T. Steffen[(c)], Daniela Becker[(d)]

(a) 0009-0002-6817-9476 (Santa Catarina State University – Brazil, elton.js@edu.udesc.br)
(b) 0000-0002-8055-3275 (Santa Catarina State University – Brazil, ricardo.medeiros@udesc.br)
(c) 0000-0001-6608-8269 (Santa Catarina State University – Brazil, teresa.ts@udesc.br)
(d) 0000-0003-3250-576X (Santa Catarina State University – Brazil, daniela.becker@udesc.br)

Abstract: Bonded joints are becoming an option to replace or support traditional mechanical fixation methods in composite material laminates. This study aimed to investigate how incorporating functionalized and non-functionalized carbon nanotubes affects the mechanical properties of the commercial epoxy adhesive and e-composites AR/AH-345. The nanotubes were functionalized by radiofrequency plasma by adding 10% m/m of urea in the presence of argon and/or nitrogen. Test specimens were manufactured according to ASTM standard type I. The pure adhesive constituents were manually mixed, while in the nanocomposites containing 0.3% m/m of carbon nanotubes, the nanoparticles were incorporated into the resin using a torque rheometer. Test specimens were evaluated using an Instron universal testing machine and an extensometer. Results showed that the test specimens with non-functionalized carbon nanotubes exhibited no significant changes compared to the matrix. However, the sample functionalized with gas mixture (argon and nitrogen) for 10 minutes demonstrated a 10% increase in elastic modulus and approximately 21% in fracture stress compared to the pure adhesive. These results suggest that longer functionalization times and the presence of nitrogen on the surface of the nanotubes enhance dispersion and interfacial interaction of the nanoparticle with the matrix, thereby improving the stiffness of the adhesive.

1. INTRODUCTION

Modern industrial needs, especially in applications sensitive to component weight like aeronautics and aerospace, have led to the analysis and development of materials that fulfill the requirements while exhibiting a high strength-to-weight ratio [1]. Fiber-reinforced composite materials have emerged as a promising alternative to replace other material classes in complex and advanced applications. In the aerospace industry, composite materials are already a reality; for example, the Boeing 787 commercial aircraft incorporates carbon fiber composites in 50% of its structure, resulting in a 20% reduction in fuel consumption compared to similar-sized aircraft and doubling the fuselage maintenance interval [2]. The expanding use ofcomposite materials has increased geometric and dimensional complexity in component manufacturing, often requiring the joining of multiple parts, requiring fastening methods between the parts.

Traditional bonding methods involve mechanical fastening through screws or rivets, usually through post-manufacture drilling, allowing for positioning freedom and alignment corrections during final assembly. However, post-manufacture mechanical fastening can lead to detrimental effects on the assembly properties, acting as points of delamination initiation, fiber breakage, and stress concentration [3].

An alternative method that circumvents to solve these issues is adhesive bonding. This process involves the application of a polymeric material between the composite layers, which, upon solidification, promotes adhesion between the parts, ensuring a more uniform stress distribution within the joint region [5]. as Additionally, the adhesive bonding acts as an electrical insulator and exhibiting higher fatigue resistance compared to traditional mechanical fastening methods.

Among commercial adhesives, epoxy is commonly used due to its good mechanical properties, wide service temperature range, and compatibility with various substrates [6]. To achieve complex and high-performance applications, there's growing interest in incorporating nanoparticles into adhesives to enhance their mechanical characteristics. In a thesis by Reis [7], multi-walled carbon nanotubes (MWCNTs) were added to the epoxy-based adhesive SikaPower 456LB. Nanocomposites with 0.25%, 0.5%, and 1.0% MWCNTs showed an increase in apparent shear strength of 9%, 12%, and 14%, respectively, compared to pure SKP-456LB adhesive. After aging in humidity and salt spray, nanocomposites with 1% MWCNTs corresponded to an increase in shear strength of 15% and 12%, respectively, compared to pure epoxy.

Carbon nanotubes are widely used in nanocomposites, mainly due to their high modulus of elasticity, a property that compensates for the deficiency of many polymeric matrices [8]. However, efficient sharing of properties between reinforcement and matrix depends on the interaction between the components and nanoparticles' good dispersion and distribution. One technique that enables the improvement of the interaction of the dispersed phase with the matrix is plasma functionalization, which provides the nanotube, through chemical and physical attack, reactive sites on its surface that enable the covalent bonding of chemical groups (Fig. 1), when in contact with the matrix, promote anchoring and interaction with it, improving the properties of the nanocomposite [9].
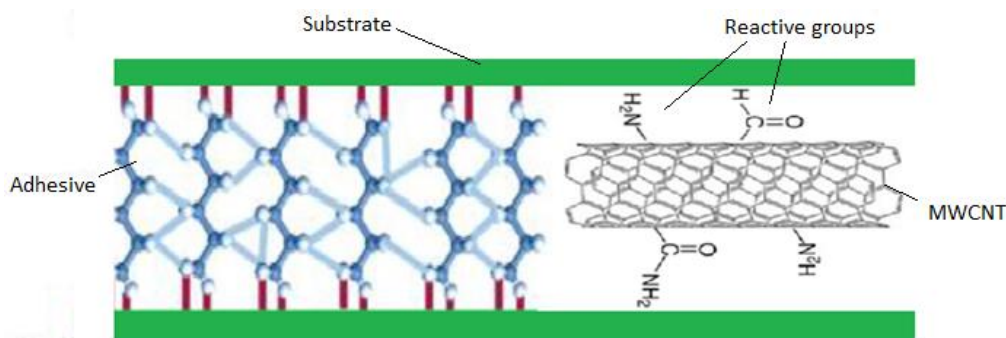
Figure 1. Illustration of adhesion forces and functional groups generated by functionalization.

In the study proposed by Steffen [10], carbon nanotubes were plasma-functionalized in similar conditions with developed in this paper and added to a commercial epoxy resin, resulting in a 22% increase in elastic modulus and a 4% increase in hardness, supporting the expectations of improvements in the mechanical properties of the epoxy adhesive that we used.

This paper aims to investigate the influence of carbon nanotubes with and without plasma functionalization on the mechanical properties of epoxy-based adhesive. The mechanical properties will be analyzed through tensile testing, acquiring stress-strain curves and extracting key properties. Additionally, transmission electron microscopy images will be taken to evaluate the nanoparticles' dispersion and distribution in the matrix.

2. METHODOLOGY

The specimens were manufactured with the bicomponent epoxy adhesive AR/AH-345 provided by e-composites. The main mechanical characteristics are a 3095 MPa elastic modulus and a tensile strength of 53 MPa. The carbon nanotubes utilized were multi-walled, sourced from Chengdu Organic Chemicals Co. Ltd, TNIM4 category, with purity greater than 85%. For the plasma treatment, ultra-pure gases of argon and nitrogen were employed, boasting a putity level of 99.999%.

Plasma-functionalized nanotubes were syntherized in a homemade reactor (Fig. 2), consisting of a radio frequency (RF) power source operating at 13,56 MHz, a glass vacuum chamber, a thermocouple, a pressure gauge, and a gas inlet system equipped with a flowmeter. The functionalization process took place in a dielectric barrier discharge (DBD) configuration, with two parameter variations: one involving argon with a 5 minutes discharge time (NTC_0.3_F5) and another utilizing a combination with argon and nitrogen with a 10 minutes discharge time (NTC_0,3_F10), both with a real power of 35W. After the sample was inserted into

the reactor, it was evacuated until the base pressure of approximately 4.0×10^{-2} Torr, then the nitrogen flow was initiated until the system pressure reached 2.8×10^{-1}, followed by the argon flow until 9.0×10^{-1}. A 15-minute waiting period was allowed for gas flow and system pressure stabilization.
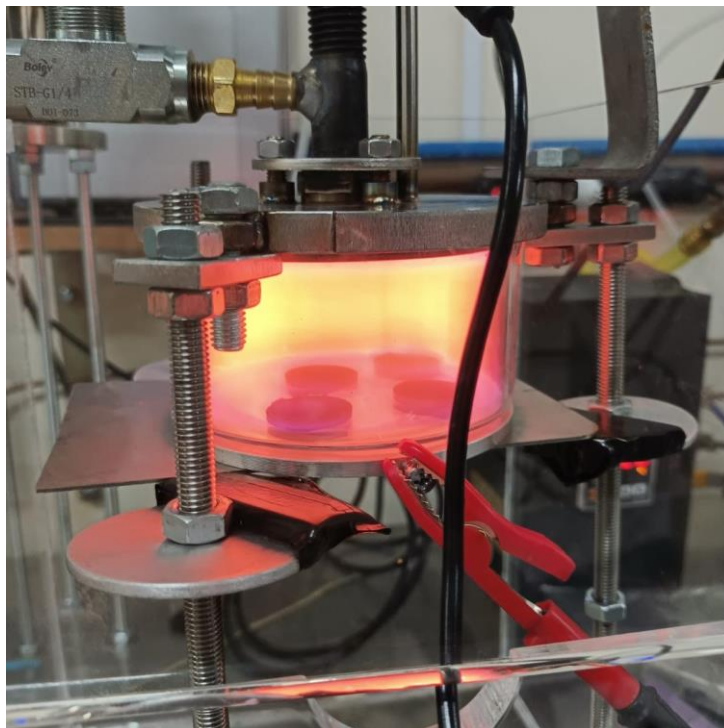
Figure 2. Plasma reactor detail.

The epoxy resin AR-345, component A of the adhesive, and the catalyst AH-345, component B, were thoroughly hand-mixed in the ratio specified by the manufacturer, 100A/45B. Carbon nanotubes, 0.3% by mass, were pre-incorporated into component A using a torque rheometer (Thermo Scientific Haake Rheomix 600), operating at 23°C and 100 rpm, for 10 minutes, before being subsequently mixed with component B. Five test specimens were manufactured for each of the variations, and the one with the highest discrepancy in modulus of elasticity value from each set was eliminated. After the entire process of preparing the components and their respective mixtures, a uniform mass was obtained, carefully introduced into the silicone molds using a spatula and allowed to cure for a minimum of 24 hours at room temperature before demolding and subjected to tests. Mechanical properties were carried out through tensile tests using an Instron Universal Testing Machine and an extensometer with a crosshead displacement velocity, as recommended by ASTM D638, at 5 mm/min. Stress-strain curves were obtained, and the modulus of elasticity and ultimate strength were determined. After the tensile test, a transmission electron microscope (TEM) was used to examine the nanoparticles dispersion.

3. RESULTS AND DISCUSSION

The tensile test indicated no significantly differences in elastic modulus for samples containing 0.3% w/w non-functionalized nanotubes (0.3_NTC) and for 0.3_NTC_F5 samples. This similarity in values can be atttibuted to the weak interaction between the matrix and the reinforcement, because the non-functionalization or its short-term process proved inadequate in generating a reactive groups in a sufficient number to significantly alter the nanocomposites properties. However, samples containing functionalized nanotubes for 10 minutes in an argon and nitrogen environment (0.3_NTC_F10) exhibited a 10% increase in elastic modulus and a 21% increase in rupture stress when compared to the pure adhesive. These findings are depicted in Fig. 3 and summarized in Table 1.
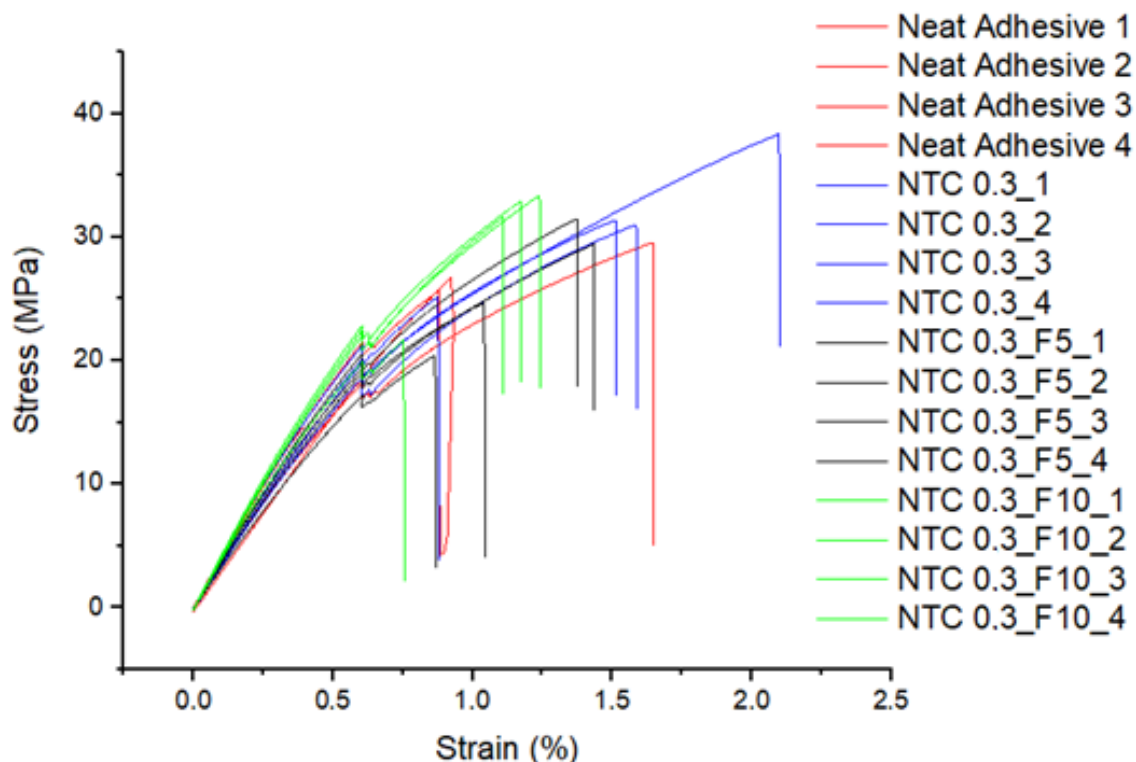
Figure 3. Stress-strain curves.

Table 1. Mechanical properties – mean values

Specimen	Elastic Modulus [MPa]	Fracture Stress [MPa]
Neat Adhesive	3778.8 ± 464.7	27.4 ± 1.6
0.3_NTC	3813.1 ± 314.2	30.5 ± 3.9
0.3_NTC_F5	3620.5 ± 284.7	29.2 ± 3.2
0.3_NTC_F10	4146.8 ± 123.1	33.1 ± 1.3

The mechanical properties improvements observed in 0.3_NTC_F10 samples are consistent with the literature findings [11], which indicate that longer exposure times to the plasma process enhance functionalization efficiency and increase the number of reactive groups attached to the nanotube walls. The presence of nitrogen on the nanotube surface also improves interaction with the epoxy matrix, promoting the epoxide ring opening, thus generating strong interaction between matrix and reinforcement through the carbon bond saturation [12].

A notable aspect highkighted in Fig 5 is the the TEM image of the nanotubes in the 0.3_NTC_F10 sample. Despite some   aglomeration, there are visible spaces between them, characteristic of the functionalization effect caused by the amine and carboxyl groups attached to their walls [13]. These functional groups hinder closer proximity, contributing to improved dispersion and reinforcing effects within the matrix.
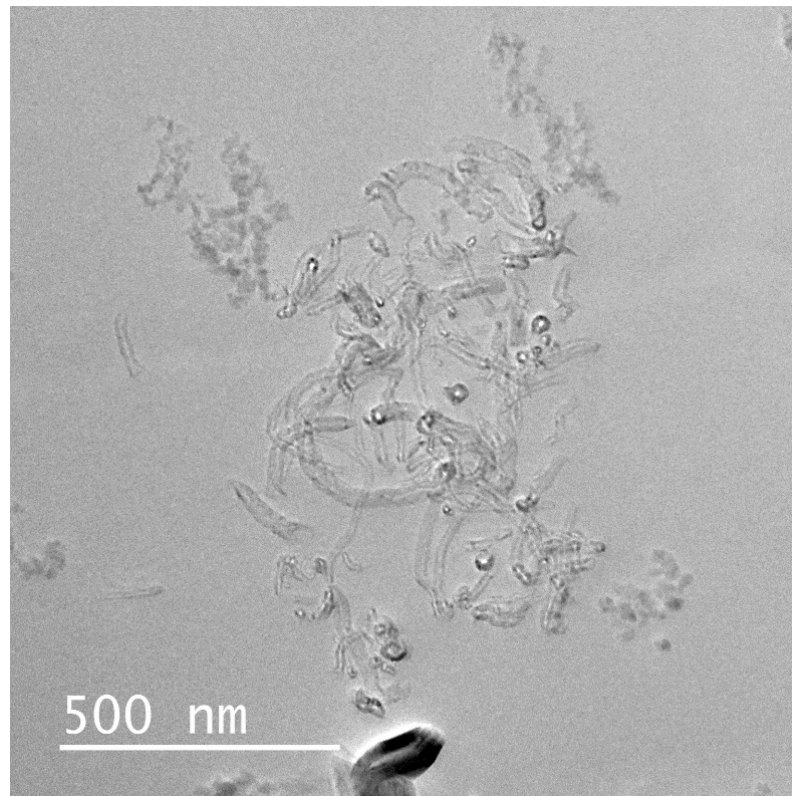
Figure 5. Transmission microscopy of carbon nanotubes.

4. CONCLUSIONS

The results demonstrate that the nanoparticle incorporation, whether without functionalization or with 5 minutes of functionalization, did not significantly affect the mechanical properties of the epoxy matrix. This lack of effect can be attributed to inadequate reinforcement dispersion and distribution, leading to unchanged properties. However, the absence of nitrogen and the shorter exposure time to the process resulted in weak interaction between the nanoparticles and the matrix, unable to promote sufficient stress transfer to increase the sample stiffness.

In contrast, the 0.3_NTC_F10 samples exhibited a significant increase in the elasticity modulus and the rupture stress. This indicates that nitrogen was crucial to promote the insertion of reactive groups on the nanotube walls, increasing the interaction with the epoxy matrix and reducing the mobility of the chains through their interlocking. Overall, these findings emphasize the importance of nitrogen and longer functionalization times in optimizing the mechanical properties of nanocomposites.

4.1. Declaration of Competing Interest

The authors declare no conflict of interest.

4.2. Fundings

4.3. Acknowledgements

5. REFERENCES

[1] McIlhagger A, Archer E, McIlhagger R (2020) 3—manufacturing processes for composite materials and components for aerospace applications, pp59–81. Available at: http://www.sciencedirect.com/science/article/pii. (B9780 08102 6793000034).

[2] Engenharia FEG. Aplicação de Fibra de Carbono na Indústria Aeronáutica. (http://engenhariafeg.com.br/2011/seminarios/a2/a2.pdf.), accessed 04 March 2024.

[3] S. Omairey et al. Defects and uncertainties of adhesively bonded composite joints. SN Applied Sciences, Volume 3:769, 2021. (https://doi.org/10.1007/s42452-021-04753-8).

[4] Jeevi G, Nayak SK, Abdul Kader M. Review on adhesive joints and their application in hybrid composite structures. Journal of Adhesion Science and Technology 33(14):1497–1520, 2019 (10.1080/01694243.2018.1543528).

[5] Banea, M. & Silva, L.F.M.. Adhesively bonded joints in composite materials: An overview. Proceedings of The Institution of Mechanical Engineers Part L-journal of Materials-design and Applications - PROC INST MECH ENG L-J MATER. 223. 1-18. 2009 (10.1243/14644207JMDA219).

[6] E.C. Monteiro; A.F. Avila,. The Carbon Nanotubes Effect into Single-lap Joint Failure Modes and Load Capacity: a Macromechanical Analysis. *Materials Research*, volume 20, n. suppl 1, p. 143–152, 2018. (https://doi.org/10.1590/1980-5373-MR-2017-0442)

[7] M.O. Reis. Desenvolvimento e Caracterização de um Adesivo Epóxi Nanomodificado e Avaliação De desempenho das juntas adesivadas. Tese de Doutorado, Universidade Federal de Minas Gerais – UFMG, 2022.

[8] S. HUSSAIN. et al. Growth and Plasma Functionalization of Carbon Nanotubes. Journal of Cluster Science, v. 26, n. 2, p. 315–336, 2015, (10.1007/s10876-015-0862-1)

[9] Ana Rudawska. Adhesives and Adhesive Joints in Industry Applications, 1st Edition, 2019. Intechopen. (http://dx.doi.org/10.5772/intechopen.77485).

[10] T.T. Steffen. Funcionalização de nanotubos de carbono por plasma rádio frequência e sua influência em nanocompósitos de epóxi/Teresa. Dissertação de mestrado, Universidade do Estado de Santa Catarina – UDESC, 2017.

[11] Z. Chen. Et al. Improving the mechanical properties of epoxy using multiwalled carbon nanotubes functionalized by a novel plasma treatment. Composites Part A: Applied Science and Manufacturing. 45. 145 - 152. 2013 (10.1016/j.compositesa.2012.09.005).

[12] P.M. Ma. et al. Dispersion, Interfacial Interaction and Re-Agglomeration of Functionalized Carbon Nanotubes in Epoxy Composites. Carbon. 48. 1824-1834. 2010 (10.1016/j.carbon.2010.01.028).

[13] B.B Ruelle. et al. Surface treatment of carbon nanotubes via plasma technology. 1. ed. Oxford: Woodhead Publishing Limited 2011 (10.1533/9780857091390.1.25).

INVESTIGATION OF THE MECHANICAL PROPERTIES OF A CASTOR-OIL POLYURETHANE FOAM REINFORCED WITH CELLULOSE MICROFIBRILS

Alexandre S. Lacerda[(a) *], Júlio Cesar dos Santos[(b)], Túlio H. Panzera[(c)], Carlos Thomas[(d)], Ana Cimentada[(e)], Rodrigo T. S. Freire [(f)]

(a) 0009-0000-2825-0288 (Federal University of São João del-Rei – Brazil)

(b) 0000-0002-7485-491X (Federal University of São João del-Rei – Brazil)

(c) 0000-0001-7091-456X (Federal University of São João del-Rei – Brazil)

(d) 0000-0002-2641-9411 (University of Cantabria– Spain)

(e) 0000-0003-3256-7047 (University of Cantabria– Spain)

(f) 0000-0001-5206-5939 (Federal University of São João del-Rei – Brazil)

* Corresponding author: alexandresilac@gmail.com

Abstract: This work investigates the enhancement of mechanical properties of a castor-oil polyurethane biofoam by cellulose microfibrils (CMF). Samples were manufactured at different mass fractions of CMF (0, 0.3 and 0.6 phr) and tested under uniaxial compression to analyse the elastic modulus and collapse stress. The foam morphology was investigated by microtomography, and the bulk density of the samples was also measured to obtain the specific modulus and collapse stress. Samples were tested in the parallel and perpendicular directions relative to foam expansion, making it possible to assess the anisotropy of the mechanical properties of the material. Tukey's multiple comparison test was employed to analyse the effects of CMF on the material. Samples present an anisotropic behaviour with a higher specific elasticity modulus in the expansion direction. The addition of cellulose microfibrils increases the compressive elastic modulus up to 60%. Microtomography revealed an open-cell foam with a porosity of around 89% and an anisotropy index of 1.19.

1. INTRODUCTION

Polyurethane (PU) is a very versatile material used in a variety of applications, such as the automotive, furniture, and civil construction industries, mostly in the form of foams. Produced from the reaction between an isocyanate and a polyol, PU is conventionally derived from petroleum. However, especially to environmental concerns, alternative ecological, sustainable sources have been proposed. Several types of natural polyols are found in soybeans [1], castor beans [2], sugar cane [3], and palm [4].

The mechanical properties of PU foams can be improved by incorporating reinforcing phases into the polymer matrix. Cellulose microfibrils (CMF) provide efficient reinforcement due to their high specific surface area (surface-to-volume ratio). Offering high elastic modulus and tensile strength and low oxygen permeability, combined with a low cost, abundance and ecological cycle, the use of CMF as a reinforcement in polymers has grown over the last decade [6-10].

In this context, this work investigates the mechanical properties of open-cell, castor-oil polyurethane foams reinforced with cellulose microfibres. The dispersion method proposed by Zhou et al. [11] is employed. These authors have successfully manufactured castor-oil polyurethane foams reinforced with carrot nanocellulose, improving the mechanical properties of the material with good particle dispersion.

2. METHODOLOGY

2.1. Materials

The two-component castor-oil polyurethane resin AGT1315 was kindly donated by Imperveg (Brazil). Cellulose microfibres from Norway spruce were kindly supplied by Borregaard (Norway). Distilled water was used as the blowing agent. A co-solvent (1,4-dioxane) was purchased from Êxodo Científica (Brazil). Dimethylpolysiloxane (50.76 wt% in SiO_2) was purchased from Nanofarma. The dual-function catalyst 1,4-diazabicyclo [2.2.2] octane (Merck, Germany) was used.

2.2. Samples and compression tests

Samples were manufactured in a 250 x 250 x 100 mm MDF mould with an open top, which allows free foam expansion in the vertical direction. Samples were cut and tested following the ASTM D1621-16 standard on an INSTRON Emic 23-100 universal testing machine with a load cell of 50 kN and a testing speed of 3 mm/min. The isocyanate (A) and polyol (B) were mixed according to the manufacturer´s recommendations (A/B=1/1.2 in mass). Water was used as the blowing agent, and the isocyanate index (moles of NCO radicals/moles of OH radicals) was adequately corrected to one, resulting in a ratio A/B of 1.1/1.0 in mass.

2.3. Dispersion of microfibrils in polyol

Three mass fractions were considered, namely 0 phr, 0.3 phr, and 0.6 phr (per hundred resin, relative to the polyol mass content).

The adequate dispersion of cellulose nanoparticles in (hydrophobic) polyol is difficult to achieve. For this matter, Zhou et al. have reported a successive co-solvent-assisted dispersion strategy, which is used in this work [11]. The cellulose microfibrils were initially homogenised in the polyol in a beaker and mixed using an Ultra-Turrax homogeniser for three minutes at 10000 rpm. Half of the dioxane total mass was then added and mixed for three additional minutes at 10,000 rpm.

The solution was then transferred to a thermomagnetic mixer at 500 rpm and 70 °C for one hour. The remaining dioxane was subsequently added. The mass of the solution was continually monitored on a scale to check the evaporation of both water and dioxane. Considering the size of the moulds used, the complete evaporation would take nearly 24 hours, and the stirring process would proceed overnight. The total mass of dioxane used was twice the mass of polyol.

2.4. Preparation of nanocomposite foams

Once CMF was dispersed in polyol, the heat was turned off, and the mixture was stirred until room temperature was achieved. Distilled water (4 phr, parts per 100 resin, relative to the polyol mass), catalyst (0.5 phr) and surfactant (4 phr) were added and mixed again using Ultra-Turrax for 3 minutes and 10,000 rpm for good dispersion. Finally, the isocyanate is added and manually mixed thoroughly for homogenisation. The mixture was poured into the mould. The foam expanded in a few minutes, and it was already dry to the touch in about 5 minutes. The foam was kept in the mould for one day and post-cured for seven days in a controlled environment room at 22 °C and 55% relative air humidity. Samples were then cut to the specified dimensions using a band saw (Figure 1) and post-cured for three days before tests were carried out. Three repetitions of six samples were considered for each test direction.

Figure 1. Image of a PU foam sample that was used for compressive tests (0.6 phr CMF)

The microtomographic analysis of foam samples was carried out at the Laboratory of the Materials Science and Technology Division (Ladicim) at the University of Cantabria (Spain). A Bruker SkyScan 1172 X-ray microtomograph with a 10W X-ray source.

3. RESULTS AND DISCUSSION

The mean values for bulk density, elastic modulus and specific elastic modulus under uniaxial compression tests for each CMF mass fraction are listed in Table 1, along with their respective standard deviation (SD) and coefficient of variation (CV). The bulk density was obtained by measuring the weight of each sample on a laboratory scale (0.01 g precision) by its respective volume, obtained with a micrometre. Tukey's multiple-comparison test results are also presented. This test executes a pairwise comparison among the average values obtained for each response variable (density, elastic modulus and specific elastic modulus). Different letters are attributed to statistically different averages. Averages that share the same letter are not statistically different from each other. Figure 2 displays representative stress-strain curves for the compression tests performed in the direction parallel to the foam expansion.
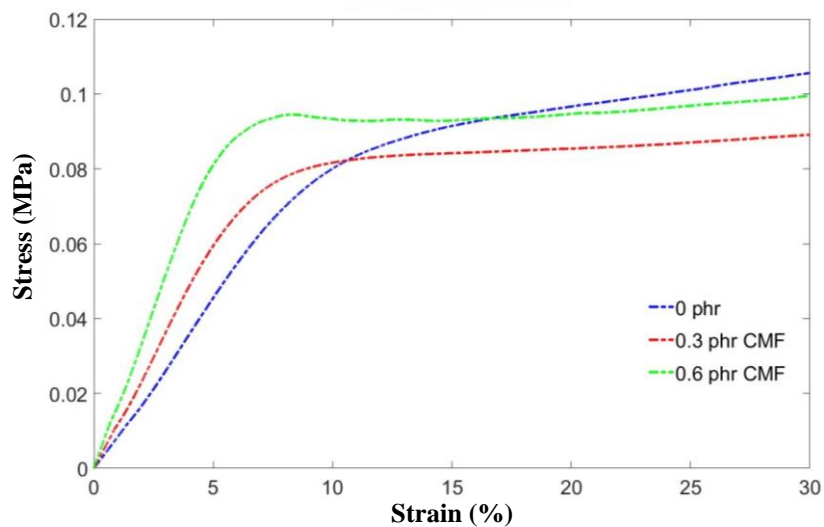
Figure 2. Stress-strain curves obtained from compression tests (parallel to foam expansion).

Table 1. Density, elastic modulus and specific elastic modulus (parallel to foam expansion).

Property	Density (kg/m³)			Elastic modulus (MPa)			Specific elastic modulus (kPa*m³/kg)		
MCF mass fraction	0	0.3	0.6	0	0.3	0.6	0	0.3	0.6
Mean value	46.4	37.8	36.6	0.83	1.06	1.35	17.9	28.2	36.5
SD	± 4.6	± 2.5	± 4.5	± 0.17	± 0.13	± 0.34	± 2.7	± 5.3	± 6.7
CV	9.9%	6.6%	12.3%	20.5%	12.3%	25.2%	15.1%	18.8%	18.4%
Tukey	A	A	A	A	A	A	A	AB	B

Even though the bulk density and elastic modulus do not statistically differ at a 5% significance level, it is possible to observe a downward trend in density values and an upward trend in elastic modulus values. However, the combined effects of MCF on density and stiffness lead to a significant mechanical effect: cellulose microfibrils significantly increase the specific elastic modulus. In fact, an additional analysis shows that an increase in the significance level to 6% is already enough to detect a significant decrease in density with 0.6 phr of MCF. The same effect is observed in the elastic modulus, considering a significance level of 8%.

Compared to the sample without CMF, the density of the 0.3 phr samples decreases by 18% and the 0.6 phr by 21%, demonstrating a tendency of CMF to decrease the density. The elastic modulus increases by around 28% at 0.3 phr and 63% at 0.6 phr. The effects of MCF on the specific elastic modulus are even stronger, reaching 58% at 0.3 phr and 104% at 0.6 phr. Similar results were reported by Zhou et al., with an increase in compressive elastic modulus of 23% and 63% at 0.25 phr and 0.5 phr, respectively, for PU foams reinforced with cellulose microfibres extracted from carrots. The authors, however, did not observe a reduction in density, even though they recognised that microfibrils may act as nucleation sites for pores. The compressive elastic modulus was higher, though, since foams presented closed pores, ranging from 3.5 with no MCF to 5.7 MPa with 0.5 phr of MCF. Samples were tested along the direction of foam expansion.

In this work, samples are also tested in the direction perpendicular to the foam expansion to investigate anisotropy. The results are similar to those obtained in the parallel direction. However, the compressive elastic modulus is slightly lower, ranging from 0.80 MPa to 1.14 MPa, indicating a small index of anisotropy (
Table 2).

Table 2. Density, elastic modulus and specific elastic modulus (perpendicular to foam expansion).

Property	Density (kg/m³)			Elastic modulus (MPa)			Specific elastic modulus (kPa*m³/kg)		
MCF mass fraction	0	0.3	0.6	0	0.3	0.6	0	0.3	0.6
Mean value	45.7	35.8	38.0	0.80	0.80	1.14	17.8	22.6	29.8
SD	± 5.1	± 1.5	± 4.8	± 0.13	± 0.14	± 0.31	± 4.2	± 4.2	± 5.2
CV (%)	11.2	4.2	12.6	16.2	17.5	27.2	23.6	18.6	17.4
Tukey	A	A	A	A	A	A	A	AB	B

The results reveal a total porosity of 88.71% and an open-cell porosity of 88.70%. An anisotropy of 1.19 was detected, indicating that cells are slightly elongated in the foam-expansion direction (Figure 3).
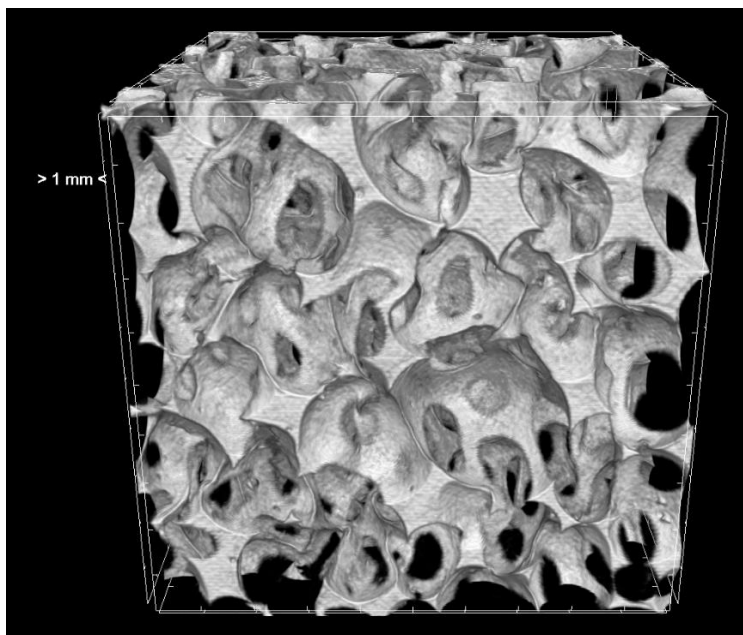
Figure 3. Image obtained of PU foam by microtomography.

4. CONCLUSIONS

Castor-oil PU foams reinforced with cellulose microfibres (CMF) were successively fabricated. Despite the laborious homogenisation process of CMF in polyol, the increase in specific elastic modulus is significantly high, reaching up to 103% with 0.6 phr of CMF.

The addition of 0.6 phr of CMF provided the best results, generating a gain in stiffness with a simultaneous decrease in bulk density.

Microtomography results reveal a total porosity of 88.71% and an open-cell porosity of 88.70%, with an anisotropy degree of 1.19.

The manufactured MCF-reinforced bio-foams are a promising alternative to petroleum-based foams, providing competing stiffness values at low density.

4.1. Declaration of Competing Interest

The authors declare no conflict of interest.

4.2. Acknowledgments

5. REFERENCES

[1] M. O. Seydibeyoğlu et al. Green polyurethane nanocomposites from soy polyol and bacterial cellulose. *J Mater Sci.* 48, 2013. (https://doi.org/10.1007/s10853-012-6992-z).

[2] A. I. Cordero et al. The role of nanocrystalline cellulose on the microstructure of foamed castor-oil polyurethane nanocomposites. *Carbohydrate Polymers.* 134, 2015. (https://doi.org/10.1016/j.carbpol.2015.07.077).

[3] A. A. A. Hakim et al. Preparation and characterization of rigid polyurethane foam prepared from sugar-cane bagasse polyol. *Materials Chemistry and Physics.* 129, 2011. (https://doi.org/10.1016/j.matchemphys.2011.04.008).

[4] X. Zhou, M. M. Sain, K. Oksman. Semi-rigid biopolyurethane foams based on palm-oil polyol and reinforced with cellulose nanocrystals. Composites: Part A: Applied Science and Manufacturing. 83 2016. (https://doi.org/10.1016/j.compositesa.2015.06.008).

[5] D. Klemm et al. Cellulose: Fascinating biopolymer and sustainable raw material. Angewandte Chemie International edition. 44, 2005. (https://doi.org/10.1002/anie.200460587).

[6] H. P. S. A. Khalil, A. H. Bhat, A. F. I. Yusra. Green composites from sustainable cellulose nanofibrils: A review. Carbohydrate Polymers. 87, 2012. (https://doi.org/10.1016/j.carbpol.2011.08.078).

[7] N. Lavoine et al. Microfibrillated cellulose–Its barrier properties and applications in cellulosic materials: A review. Carbohydrate Polymers. 90, 2012. (https://doi.org/10.1016/j.carbpol.2012.05.026).

[8] K. Y. Lee et al. On the use of nanocellulose as reinforcement in polymer matrix composites. Composites Science and Technology. 105, 2014. (https://doi.org/10.1016/j.compscitech.2014.08.032).

[9] M. Mariano, E. N. Kissi, A. Dufresne. Cellulose nanocrystals and related nanocomposites: Review of some properties and challenges. Journal of Applied Polymer Science Part B: Polymer Physics. 52, 2014. (https://doi.org/10.1002/polb.23490).

[10] K. Oksman et al. Review of the recent developments in cellulose nanocomposite processing. Composites Part A: Applied Science and Manufacturing. 83, 2016. (https://doi.org/10.1016/j.compositesa.2015.10.041).

[11] X. Zhou et al. Dispersion and reinforcing effect of carrot nanofibers on biopolyurethane foams. Materials and Design. 110, 2016. (https://doi.org/10.1016/j.matdes.2016.08.033).

OBTAINING AND CHARACTERIZING POLYACRYLONITRILE (PAN) MATS REINFORCED WITH GRAPHENE

Isabela Luiza Rodrigues Cintra[a]*, Jefferson Patricio Nascimento [b], Felipe Vicente Kodaira[c], Luis Rogerio de Oliveira Hein[d], Michelle Leali Costa[e], Edson Cocchieri Botelho[f]

(a) 0000-0002-7005-4106 (São Paulo State University - Brazil)
(b) 0000-0002-8756-011X (São Paulo State University - Brazil; Technological for Research Institute - Brazil)
(c) 0000-0002-3775-3386 (São Paulo State University - Brazil)
(d) 0000-0002-9266-0668 (São Paulo State University - Brazil)
(e) 0000-0001-9492-8544 (São Paulo State University - Brazil; Forza Composites - Brazil)
(f) 0000-0001-8338-4879 (São Paulo State University - Brazil)

* Corresponding author: isabela.cintra@unesp.br

CODE: BCCM7-42

Keywords: Graphene, Nanocomposite, Poliacrilonitrile, Electrospinning, Liquid phase Exfoliation.

Abstract: Graphene-reinforced polymeric mats, obtained through the electrospinning process, have gained significant attention in recent years due to their unique properties and the possibility of application in various sectors such as water treatment and purification. In this work, polyacrylonitrile (PAN) mats were obtained and characterized by electrospinning with two concentrations (10μg/mL and 39μg/mL) of graphene with the aim of evaluating the effect of this carbon nanomaterial on the structure, morphology and thermal stability of the mats produced. The graphene used in this work was produced by liquid phase exfoliation assisted by cavitation from two types of natural crystalline graphite, aiming to obtain few-layer graphene. The graphene dispersions produced were characterized by UV-VIS (ultraviolet-visible) to estimate the concentration/yield of the exfoliation process and average number of layers and to prepare the mats, parameters of the electrospinning process already defined in previous works were used. The morphology and structure and thermal stability of the graphene mats produced were verified using scanning electron microscopy (SEM), Fourier transform infrared absorption spectroscopy (FTIR) and thermogravimetry (TGA). Using SEM images, it was possible to verify the diameter of the fibers, as well as their morphology. Through FTIR analysis, functional groups characteristic of the polymer and graphene were observed and through TGA analysis, it was verified that when the graphene content in the mats is increased, its thermal stability also increases.

1. INTRODUCTION

Nanocomposites are considered promising materials and have increasingly more fields of research and attract the interest of researchers, due to their properties and wide application possibilities. Polymeric nanocomposites (PNC) are made up of polymers or copolymers with the addition of nanofillers or nanoparticles. There are many methods for preparing polymer nanocomposites, the best-known methods are in situ polymerization, melt extrusion, electrospinning and dispersion or mixing of solutions [1]. Among these methods, electrospinning is considered a simple, cheap, and multifunctional technique to manufacture nanocomposites [2]. The basic electrospinning system consists of a syringe with needle, flow pump, a high voltage source and a grounded collector, variations may apply. During this process, the polymer solution is pumped at a constant rate. Under the effect of applied voltage, the polymer solution is loaded and stretched to

form fibers due to electrostatic repulsions and surface tension. The polymer jet is elongated, forming fibers, which are deposited in the grounded collector [2,3].

To obtain nanocomposites, several materials can be used as nanofillers. Graphene is a carbonaceous nanomaterial, which has been widely used as a nanofiller in nanocomposites. It is a two-dimensional material consisting of sp^2 hybridized carbon atoms arranged in a hexagonal lattice. In particular, the mono- and few-layer graphenes (up to ten layers of carbon atoms in sp^2 hybridization), have desirable properties such as high surface area, exceptional electrical and thermal conductivity, as well as unique mechanical and optical properties [4]. Such properties have potential applications in a number of technologies, especially in the area of nanocomposites. Several techniques can be used to obtain graphene and its derivates, such as liquid-phase exfoliation (LPE), micromechanical exfoliation, supramolecular assembly, plasma and laser techniques, chemical vapor deposition (CVD) methods and chemical synthesis [2,3]. However, the LPE is one of the most promising processes for the industrial production of graphene for presenting scalability, versatility and relatively low cost compared to other methods. The LPE is a "top-down" method where natural graphite is exfoliated through high-shear mixing or sonication, obtaining a stable dispersion of defect-free graphene with few layers [4].

Within this context, the obtaining of electrospun polymer nanocomposites with different amounts of graphene produced by LPE was studied in this work, analyzing the influence of this amount on the properties and morphology of the fibers obtained.

2. METHODOLOGY

2.1 Materials

In carrying out this work, the flake natural graphite (Graflake 99580) and expanded graphite (HC30), supplied by Nacional de Grafite company, were used as a precursor material to study graphene production by LPE. The solvents N-methyl-2-pyrrolidone (NMP) and dimethylformamide (DMF) with analytical purity (PA 99%), from the company Neon Comercial Reagentes Analíticos Ltda., were used to obtain graphene dispersions. For electrospinning the blankets, the polymer polyacrylonitrile (PAN) ($\overline{Mn}$) = 267,000 gmol^{-1}) was used, supplied in powder form by Radici Fibras Company.

2.2 Methodology

2.2.1 Production of Graphene Dispersions

The LPE process mechanically assisted by cavitation (sonication by bath ultrasound) was used with the aim to obtain dispersions with an adequate concentration of defect-free and with structural quality few-layer graphenes for polymer nanocomposite application. For this, the process variables were studied, as shown in Table 1, where T_s is the sonication time, T_C and F_C the centrifugation time and centrifugation force, respectively.

Table 1- Parameters used in the LPE process for graphene production.

Experiments	$T_{S\,(min)}$	Precursor Graphite	$T_{C\,(min)}$	$F_{C\,(rpm)}$
1	30	Graflake	30	2000
2	60	Graflake	30	2000
3	30	HC30	30	2000
4	60	HC30	30	2000
5	30	Graflake	30	4000

2.2.2 Solvent exchange

It is known that the LPE process can produce graphene homogeneous with few-layers and defects-free, being a widely used technique. However, a challenge for application of graphene produced by LPE in polymer nanocomposites is the low yield ($\leq$ 0,1 %) of process [6]. Due to this, in the literature, some ways of increasing the concentration of graphene obtained via LPE have been addressed. One of the possible routes is the exchange of solvents [5].

For this, the dispersion obtained was dried in an oven at 150°C for a period of 72 hours to eliminate the solvent. Subsequently, the dried graphene was subjected to the LPE process again, in the solvent DMF, used for electrospinning the blankets.

2.2.3 Electrospinning of blankets

The PAN and PAN/graphene blankets were obtained through the electrospinning process. The equipment used consists of a high voltage source, a rotating collector, a dosing pump, glass syringe and stainless-steel needle. For electrospinning the blankets, 19 kV voltage, flow rate of 0.05 mL/min, rotation of 40 rpm and working distance of 10cm were used.

2.2.4 Characterization techniques
2.2.4.1 Ultraviolet–visible Spectroscopy (UV-Vis)

UV-vis characterization was carried out in a PerkinElmer (Lambda25) in a range of 190 to 800 nm, with a scanning speed of 480 nm/min, with a 1 nm slit and 0.5 nm of resolution. The samples were placed in a quartz cuvette with a 10 mm optical path. The equipment used can be found in the Electrolytic Plasma Laboratory, at Unesp Guaratinguetá.

Additionally, to evaluate the effectiveness of the parameters used, equations were used to estimate the concentration of graphene in the dispersion, using the Lambert-Beer law (Equation 1) applied in a way adapted to the case in question, and the average number of layers of graphene obtained, estimated using the equation developed by Backes and collaborators [7], for dispersions in NMP solvent.

$$\text{Ext}_{750} = \varepsilon_{750} \times C \times l \ (1) \qquad\qquad N = 35{,}7 \times (\varepsilon_{550} / \varepsilon_{325}) - 14{,}8 \ (2)$$

Where:

Ext_{750} is extinction value at 750 nm of the spectra obtained; ε_{750} is the extinction coefficient in 750 nm (5450 L.g^{-1}.m^{-1}) calculated by Backes and collaborators [7]; $\varepsilon_{550} / \varepsilon_{325}$ is the ratio between the extinction value at 550 nm and 325 nm of the spectra obtained; C is the concentration; l is the optical path and N is average number of layers.

2.2.4.2 Scanning Electron Microscopy (SEM)

The SEM was employed to assess the presence of defects and the morphology of graphene-coated electrospun mats. For this purpose, (1 x 1) cm samples were affixed to double-sided carbon tape and coated with a thin layer of gold. The scanning electron microscope used was a Zeiss EVO LS 15 model, located in the Microscopy and Microanalysis Laboratory at UNESP Guaratinguetá. Fiber diameters were quantified using the freely accessible Image J imaging software, with 100 measurements performed on each sample.

2.2.4.3 Fourier-Transform Infrared Spectroscopy (FTIR)

The verification of possible changes in the structure of the blankets with the addition of graphene was carried out by FTIR analysis. This analysis was conducted on a PerkinElmer Spectrum 100 FTIR equipment, using the attenuated total reflectance (ATR) system. The spectrum was obtained in the mid-infrared region (4000 to 400 cm^{-1}), with a total of 32 scans and resolution of 4 cm^{-1}. The equipment used is available at the Plasma and Applications Laboratory of the Faculty of Engineering, UNESP, Guaratinguetá campus.

2.2.4.4 Thermogravimetric analysis (TGA)

Thermogravimetric analysis was used to evaluate the thermal stability of blankets with different percentages of graphene. For this, around 3 mg of the material were analysed, where they were subjected to heating from 25 to 1000 °C, under a nitrogen atmosphere of 100 mL/min and a heating rate of 20 °C.min^{-1}. The equipment used is from the SII Nanotechnology brand, model TG/DTA 6200 and is available at the Department of Technology and Materials (DMT) at FEG/UNESP- Guaratinguetá Campus.

3. RESULTS AND DISCUSSION

3.1 Graphene Production

3.1.1   UV-Vis

The dispersions obtained by LPE process were characterized by UV-Vis to obtain to estimate the concentration and average number of layers of the graphenes obtained. In Figure 1, the spectra obtained for graphene dispersions are presented.
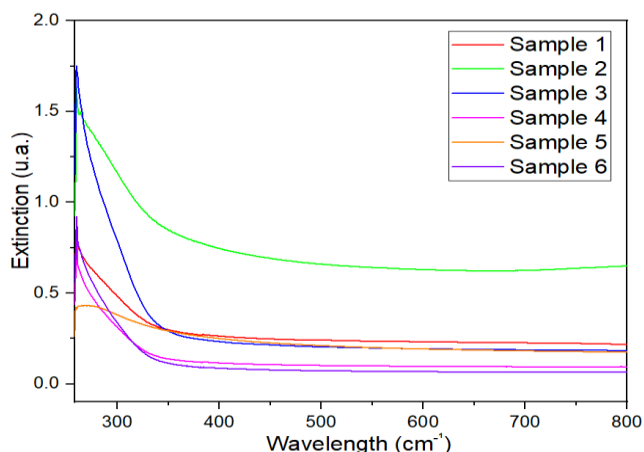
Table 2- Estimated concentration values and number of layers for graphenes obtained by LPE process.

Experiments	Concentration (μg/mL)	Number of layers
1	7	10
2	10	9
3	3	2
4	5	4
5	3	7

Figure 1- UV-Vis spectra obtained for graphene dispersions

As can be seen in Figure 1, all samples presented spectra characteristic of graphene, with a pronounced peak at approximately 260 nm. According to Tseng [8], this peak is characteristic of the μ- μ* transition of graphene. Using extinction values at E_{325}, E_{550} and E_{750}, estimates of the number of layers and concentration of graphene were calculated. In Table 1, the estimated values of the concentration of graphene in solution (calculated from Equation 1), and the number of layers (calculated from Equation 2) are presented.

With the data obtained, it was found that the dispersions presented a low concentration of graphene, being lower for *Samples 3 and 5*. It was observed that *Sample 2* presented a higher concentration value and low number of layers, indicating that, among the parameters studied , those used for exfoliation of this sample are more suitable.After investigating the best parameters for obtaining graphene via UV-VIS, around 30 mL of the dispersion (*Sample 2*) was dried with the aim of obtaining graphene in powder form. Then, the dried graphene was added to the PAN/DMF solution for electrospinning the blanket.

To obtain a higher concentration of graphene for incorporation into the PAN by electrospinning, around 300 mL of new dispersion using the parameters of *Sample 2* was prepared and subsequently dried in an oven to eliminate the solvent. The graphene in powder form was dispersed in DMF and subjected to the sonication step again. The graphene concentration and number of layers were also estimated, where values of 39 µg/mL (four times higher value) and 10 were found, respectively.

3.1.2   Characterization of Electrospun Blankets

SEM analysis was carried out with the aim of verifying the morphology of the fibers of the blankets with different graphene contents, in addition to estimating the average diameter of the fibers. SEM images showing the morphology of PAN/graphene electrospun blanket produced from dispersions with 10 µg/mL and 39 µg/mL are presented in Figures 2 and 3, respectively.

Figure 2- PAN/graphene electrospun blanket produced from dispersion with 10µg/mL.
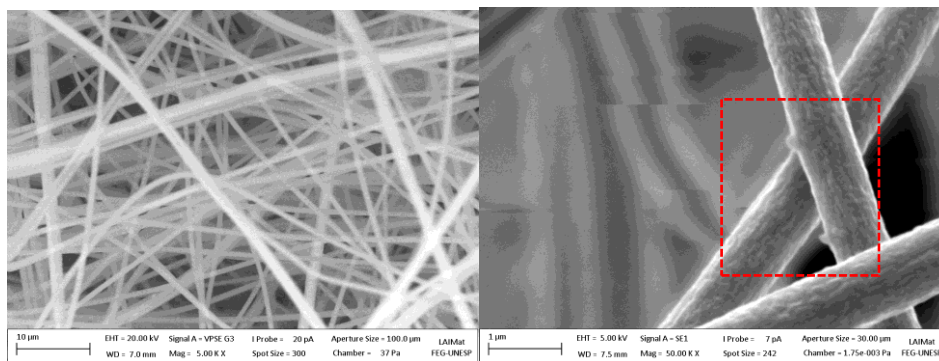
Figure 3- PAN/graphene electrospun blanket produced from dispersion with 39µg/mL.
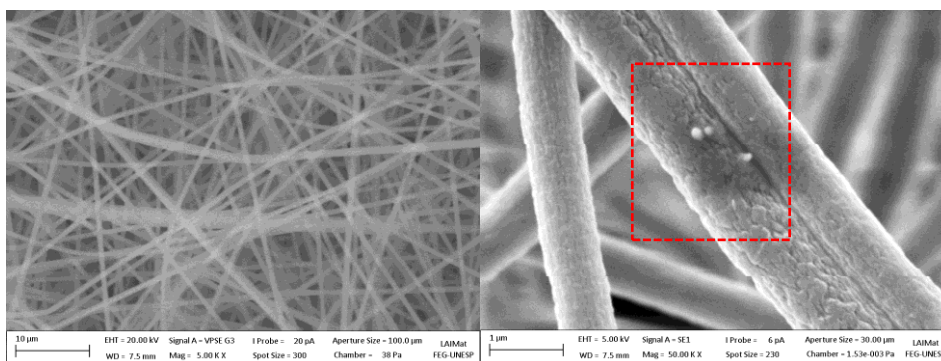
From the microscopy images of the graphene blankets, it was possible to observe that they all had uniform fibers and were free of defects. It is not possible to observe the presence of graphene on the blankets surface and, therefore, it is necessary to employ other characterization techniques such as transmission electron microscopy (MET) and Raman mapping. Using microscopy images, the average diameters of the fibers of each blanket were also quantified and Table 3 shows the diameter values.

Table 3- Average diameter of electrospun blanket fibers obtained.

Sample	Average diameter (µm)	Standard deviation
0 µg/mL	130	±10
10 µg/mL	161	±24
39 µg/mL	120	±12

According to Table 3, it is possible to observe that the blanket with 10 µg/ml of graphene had a larger average diameter of the fibers, when compared to the pure PAN blanket. This can be attributed to the change in the viscosity of the polymer solution caused by the addition of the nanofiller. However, it is necessary to carry out a study regarding the effect of the amount of nanofiller added on the viscosity of the solution to draw concrete conclusions. It is also possible to observe that with the increase in the amount of graphene in the blanket to 39 µg/ml, there was a decrease of approximately 20% in the diameter of the fibers, when comparing the blanket with 10 µg/ml and 7% when compared to the blanket of PAN without graphene.
Khan and collaborators [1], obtained electrospun polyacrylonitrile (PAN) blankets with different graphene contents in their composition (0.5% by weight, 1% by weight and 3% by weight), and observed that with the increase in graphene content in the blanket there was a decrease of around 20% in the diameter of the fiber obtained."

3.1.3   Fourier-Transform Infrared Spectroscopy (FTIR)

FTIR analysis was carried out with the aim of verifying the occurrence of structural changes in the blankets after the addition of graphene. Figure 4 shows the spectra obtained for the blankets.

Figure 4- Spectra of graphene blankets obtained.
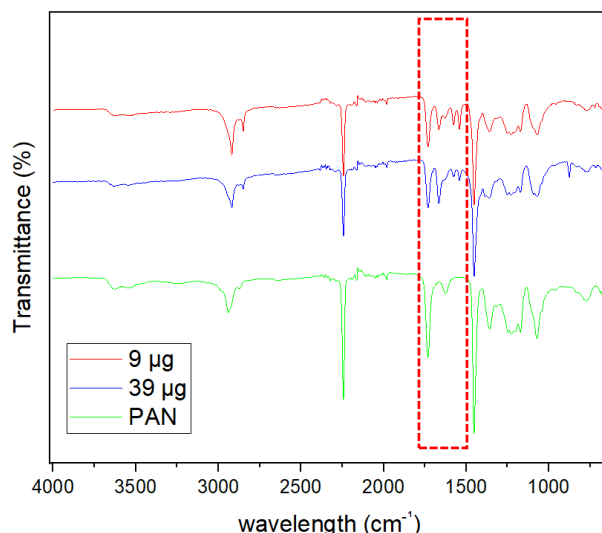
In the spectrum of the blankets, bands at 1359 cm^{-1} and 1075 cm^{-1} are visible, related to the polar-polar interaction between the S=O and C≡N groups. In the PAN spectrum, the band at 2936 cm^{-1} is also observed, corresponding to the C-H stretching of aromatic methoxyl groups and methyl and methylene groups of side chains [9]. At 2240 cm^{-1}, 1729 cm^{-1} and 1455 cm^{-1} characteristic bands of PAN are visible, both in the pure polymer and in the graphene blankets. The band at 2240 cm^{-1} comes from the stretching of C≡N bonds, the band at 1720 cm^{-1}, attributed to vibrations of C=O bonds, referring to hydrolysed nanofibers and/or residual solvent (DMF) and the band at 1455 cm^{-1} refers to the vibration of aliphatic CH groups (CH, CH$_2$ and CH$_3$) [10, 9]

In the graphene blankets, it is possible to observe the appearance of new bands in 1664 cm^{-1}, 1576 cm^{-1} and 1542 cm^{-1} and the decrease in the band in 1625 cm^{-1} and 1733 cm^{-1}, which may indicate the presence of the graphene into the polymer and a possible chemical interaction and/or the presence of DMF residue. According to Tucureanu, [9] the bands present between 1580–1530 cm^{-1} can be attributed to the amide group II (-CO–NH–). According to Cetiner [11], the absorption bands that appear at 1660 cm^{-1} are characteristic of the stretching of the double bonds between carbon and oxygen in DMF. In the spectra, the peak was shifted to 1666 cm^{-1} in the presence of PAN. The amide nitrogen of DMF has primary affinity for the nitrile group of PAN. Therefore, this small change may result from the interaction of the amide nitrogen and the nitrile group in the presence of DMF. Furthermore, it is possible to observe a peak in the spectra at 1732 cm^{-1} which, can be attributed to the stretching of the carbonyl (C=O) [11, 9] However, the appearance of these bands must be better understood and correlated with other characterization techniques, such as X-ray photoelectron spectroscopy (XPS).

3.1.4   Thermogravimetric Analysis (TGA)

Thermogravimetric analysis was used to verify any possible changes in the thermal stability of the blankets, caused by the addition of graphene. In Figure 6, the thermogravimetric curves (TGA) and derived thermogravimetric curves (DTG) of the blankets are presented. The TGA/DTG data are in Table 4.

Figure 6- TGA curve (a) and DTG curve (b) of PAN/Graphene electrospun mats
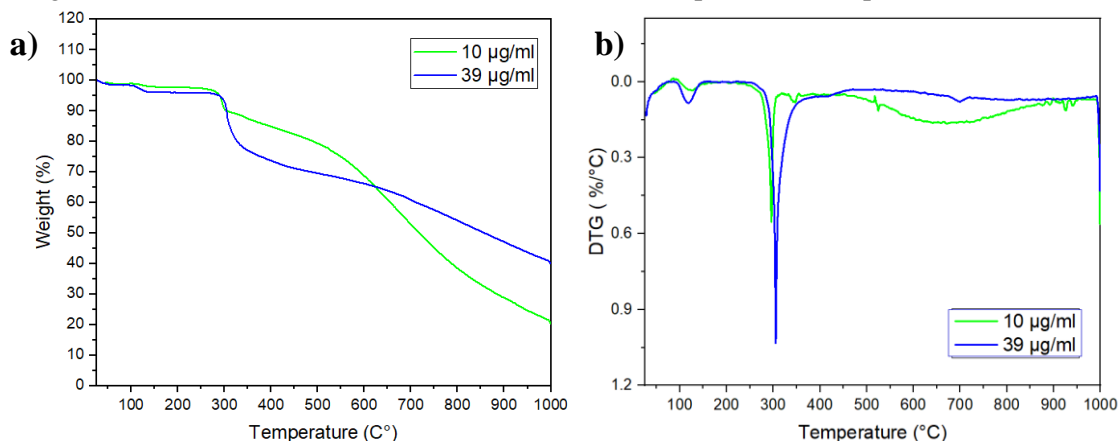
Table 4 - Derived thermal parameters from TGA/DTG curves of PAN and PAN/Graphene electrospun mats.

Sample	Ti$_1$ (°C)	M$_1$ (%)	Ti$_2$ (°C)	M$_2$ (%)	Ti$_3$ (°C)	M$_3$ (%)	R (%) at 950 °C
10 µg/mL	86	3.5	219	8.3	452	58.3	29.5
39 µg/mL	84	4.2	256	26.5	467	27.1	43.2

Legend: Ti – temperature initial of decomposition; M: weight loss; R: residue.

Using the data presented in Table 1, it is possible to verify that the PAN blanket with 10 µg/mL of graphene and the blanket with 39 µg/mL of graphene presented at least three thermal events. In both samples it is possible to observe the occurrence of a thermal event with a small loss of mass up to approximately 100 °C, attributed to the evaporation of water and elimination of residual solvent [1]. In the sample with 10 µg/mL of graphene, the second thermal event occurs at 219°C with a weight loss of 8%. The third thermal event takes place at a temperature of 452°C with a mass loss of 58%, with the residue of 29.5% in weight at 950°C. For the sample with higher concentration of graphene, the second thermal event occurs at 256°C with weight loss of 26%, and the third thermal event at 467°C with weight loss of 27%. According to Khan et al [1], at 270 °C carbonation occurs, eliminating of non-carbon factors (N_2, NH_3, HCN, CO_2, and CO) and at temperatures above 300 °C, polymer decomposition occurs.

It is possible to observe that after the process, the blanket with the highest graphene content have around 45% more residue, as expected due to the presence of a greater amount of graphene in the sample. Thus, it can be stated that PAN blanket with 39 µg/mL has greater thermal stability than the sample PAN blanket with 10 µg/mL.

4. CONCLUSIONS

Blankets with different graphene contents were electrospun to evaluate the effect of graphene content on PAN blankets. Graphene was produced in the laboratory via LPE process and the parameters for obtaining graphene have been optimized. The electrospun mats were characterized in terms of their morphology through SEM analysis and chemical structure through FTIR and their thermal stability was verified by TGA.

Through SEM images, it was possible to observe that the addition of graphene in the quantities studied does not result in the appearance of defects in the electrospun fibers, however it favors the obtaining of fibers with a smaller diameter due the presence of a conductive material like graphene. In the spectra obtained by FTIR, the appearance in the blankets is visible with new bands which can possibly be attributed to graphene and/or DMF residue and a decrease in bands attributed to PAN. Lastly, TGA analysis revealed that the blanket containing a higher concentration of graphene exhibited enhanced thermal stabilization and retained a greater quantity of material at the conclusion of the process.

With this, it is concluded that graphene can favor the obtaining of blankets with uniform fibers, free of defects and with a reduced diameter.

Declaration of Competing Interest

The authors declare no conflict of interest.

REFERENCES

[1] KHAN, T. et al. Graphene-embedded electrospun polyacrylonitrile nanofibers with enhanced thermo-mechanical Properties. J Nanopart Res, 4, 2023.

[2] Kausar, A. et al. Nanocomposite Nanofibers of Graphene fundamentals and Systematic Developments. J. Compos. Sci., 7, 2023. (https://doi.org/10.3390/jcs7080323)

[3] Al-Dhahebi, A.M.; Gopinath, S. C.; Saheed, M. S. M. Graphene impregnated electrospun nanofiber sensing materials: a comprehensive overview on bridging laboratory set-up to industry. Nano Convergence, 7, 2020 (https://doi.org/10.1186/s40580-020-00237-4)

[4] Dias, M. L. et al. Electrospun Nanofibers of Poly(lactic acid)/Graphene Nanocomposites . J Nanosci Nanotechnol, 4, 2017. (doi: 10.1166/jnn.2017.12679. PMID: 29652121).

[5] XU, y. et al. Liquid-Phase Exfoliation of Graphene: An Overview on Exfoliation Media, Techniques, and Challenges. Nanomaterials,8, 2018. doi:10.3390/nano8110942

[6] Paton, K. R. et al. Scalable production of large quantities of defect-free few-layer graphene by shear exfoliation in liquids. Nature Materials, 13, 2014. (10.1038/NMAT3944)

[7] BACKES, C. et al. Spectroscopic metrics allow in-situ measurement of mean size and thickness of liquid-exfoliated graphene nanosheets. Nanoscale, v. 8, p. 4311–4323, 2016

[8] Tseng, K. et al. Characteristic Analysis and Electrical Conductivity of Graphene and Graphene-Nanosilver Prepared by Electrical Spark Discharge Method. Research Square, 1, 2023. (https://doi.org/10.21203/rs.3.rs-919197/v1)

[9] Ţucureanu, V.; Matei, A.; Avram, A. M. FTIR Spectroscopy for Carbon Family Study, Critical Reviews in Analytical Chemistry, 6, 2017. DOI: 10.1080/10408347.2016.1157013.

[10] KARBOWNIK, I. et al. The Preparation and Characterization of Polyacrylonitrile-Polyaniline (PAN/PANI) Fibers. *Materials, 12, 2019. (*https://doi.org/10.3390/ma12040664).

[11] Cetiner, s. et al. Polymerization of pyrrole derivatives on polyacrylonitrile matrix, FTIR–ATR and dielectric spectroscopic characterization of composite thin films. Synthetic Metals, 160, 2010. (10.1016/j.synthmet.2010.03.007)

THERMAL AND MECHANICAL ANALYSES OF A GRAPHENE ACRYLONITRILE STYRENE ACRYLATE COMPOSITE FOR ADDITIVE MANUFACTURING USE

Fernando Alves Guimarães[a]*, Luis Felipe de Paula Santos [b], Fabio Roberto Passador [c], Michelle Leali Costa[d]

(a) 0000-0003-3423-2291 (São Paulo State University (UNESP), Brazil)
(b) 0000-0002-5089-1089 (Instituto de Pesquisa Tecnológicas (IPT), Brazil and São Paulo State University (UNESP), Brazil)
(c) 0000-0001-5239-5962 (Federal University of São Paulo (UNIFESP), Brazil)
(d) 0000-0001-9492-8544 (São Paulo State University (UNESP), Brazil and Forza Composites, Brazil)
* Corresponding author: fernando.a.guimaraes@unesp.br

CODE: BCCM7-43

Abstract: Nanostructured composites have garnered remarkable interest in recent years due to their potential to improve material properties across industries. Their ability to integrate nanoscale fillers into conventional matrices allows for precise control over material structure and performance. This control has sparked widespread interest as researchers and industries explore the applications of nanostructured composites in fields such as aerospace, automotive, electronics, energy, and biomedicine. Graphene is one of the most promising reinforcements due to its exceptional mechanical strength, high electrical conductivity, enhanced thermal conductivity, low density, biocompatibility, and chemical stability. Additive manufacturing presents a compelling approach to overcome this challenge by integrating graphene's remarkable properties with the versatility of this manufacturing method. Acrylonitrile-styrene-acrylate copolymer (ASA) is a thermoplastic polymer prized for its outstanding ultraviolet resistance, weatherability, chemical resistance, and mechanical strength. ASA can be used in outdoor applications such as automotive parts and building materials. ASA maintains its properties even under harsh environments, thus making it a promising polymer for additive manufacturing. In this work, the effect of adding graphene to ASA and the effect on thermal and dynamic-mechanical properties was studied. ASA filament reinforced with 0,5 et% of graphene was prepared using a twin-screw extruder alongside neat ASA filament as a reference material. The study aims to understand the impact of low content of graphene reinforcement on the thermal and dynamic-mechanical performance of nanocomposites. For this reason, the filaments were evaluated by thermogravimetric analysis (TGA), differential scanning calorimetry (DSC), and dynamic mechanical analysis (DMA). Regarding processability, it was possible to observe a good mixture of graphene with the polymer matrix, enabling the formation of filaments. The thermal properties were slightly affected by the addition of small amounts of this filler.

1. INTRODUCTION

Interest in graphene surged after 2004 when K. Novoselov and A. Geim achieved the 2D carbon structure through micromechanical exfoliation. Over the past two decades, substantial expansion in graphene research and development across various fields has occurred. Graphene's physical properties have paved the way for enhanced composite materials for electronic devices, sensors, medical biosensors, filtration membranes, energy generation, and storage solutions [1]. High-purity graphene exhibits outstanding electrical conductivity (around 6000 S/cm), thermal conductivity (around 5000 W/(m³K)), and mechanical properties surpassing those of conventional engineering materials, with a tensile strength of 130 GPa and Young's modulus of 1 TPa [2,3]. Graphene finds diverse applications with these properties, primarily as a composite material reinforcement [2,4].

Acrylonitrile-styrene-acrylate copolymer (ASA) is an amorphous thermoplastic polymer with many advantages over other commonly used polymers for additive manufacturing, such as ABS (acrylonitrile-butadiene-styrene copolymer) [5]. It has many uses, especially in in automotive applications such as exterior siding, mirror housing, and electronics components, due to its weather and UV resistance capabilities, high glass transition temperature, and oil-heat resistance for preventing discoloration [6,7].

Thus, this research examines how incorporating graphene into ASA filaments influences their thermal and dynamic-mechanical properties. ASA filaments and ASA/graphene filaments with 0.5 wt% of graphene were prepared in two steps: first the compositions were prepared using a twin-screw extruder and the filaments were prepared using a mini-extruder with a specific die to prepare filaments. The investigation endeavours to elucidate the effects of minimal graphene reinforcement proportions on the dynamic-mechanical and thermal properties of the nanocomposite.

2. METHODOLOGY

2.1. Materials

ASA was supplied by SABIC Innovative Plastics South America (Brazil) with a melt flow index (MFI) of 11.1 g/10 min (260 °C/5 Kg). A premium graphene powder was supplied by 2D Materials Pte Ltd (2DM)-Singapore, with an average particle size of 1 to 3 µm, purity of 90% and with 1-2 layers. The graphene was supplied by 2DM through TEXIGLASS.

The extrusion process was performed in a co-rotational twin-screw extruder (model AX16:40DR - AX Plásticos) with modulated screws profiles with two kneading zones, a diameter (D) of 16 mm and L/D of 40. The processing parameters applied were a temperature profile of 200/210/210/215/220 °C (from feed zone to die), a feeding screw speed of 30 rpm, a twin-screw speed of 100 rpm, and a water bath for cooling the material at the end. After the extrusion, the material was pelletized and dried under the same conditions.

The filaments were prepared via extrusion in a lab-scale line for filaments supplied by Filmaq3D®/Brazil, which consisted of an extruder, filament puller rollers, and a filament winder. The extruder was operated at 240 °C, and the filaments were cooled with air, pulled at controlled speed, and the filament diameter was continuously measured, maintaining (1.75 ± 0.05) mm. Finally, the filament was coiled in a commercial 3D printing coil. The FFF process of the filaments was performed in a 3D printer, Sethi S3X, for the preparation of DMA samples. The printing parameters that were used for all samples can be seen in Table 1.

Table 1. Printing Parameters.

Parameter	Value
Wall Thickness	0.5 mm
Wall Layers	3
Layer Height	0.2 mm
Top and Bottom Layers	2
Infill	100%
Infill Pattern	Align
Raster Angle	0º
Extrusion Temperature	250ºC
Bed Temperature	120ºC
Printing Speed	40 mm/s

2.2. Thermogravimetric Analysis (TGA)

TGA was carried out using a TG/DTA6200 EXSTAR6000 machine in neat ASA and ASA/0.5 wt% graphene. The tests were evaluated in a synthetic air atmosphere (100 mL/min) using a platinum pan, the initial temperature was set as 25 ºC up to 700 ºC, at a heating rate of 10°C/min, the sample weights for the neat ASA an ASA/0.5% Graphene were 10.23mg and 9.79mg respectively.

2.3. Differential Scanning Calorimetry (DSC)

DSC analyses were conducted based on ASTM D3418 on TA Instruments equipment, model Q20. The analyses were carried out in duplicate for the neat ASA samples and the ASA/0.5 wt% graphene filament. All tests were done using the same parameters with a single heating run starting from 25 ºC up to 220 ºC with a heating rate of 20 ºC/min, the pan used was a hermetic platinum pan, the purge gas was nitrogen with a flow rate of 40 mL/min. The weight of each sample can be seen in Table 2.

Table 2. Mass of DSC samples.

	ASA		ASA/0.5% Graphene	
	Sample 1	Sample 2	Sample 3	Sample 4
Weight	10.0 mg	10.8 mg	10.7mg	10.6mg

2.4. Dynamic Mechanical Analysis (DMA)

DMA analyses were performed according to the ASTM D7028 standard, which aims to evaluate the viscoelastic behavior of the samples and the glass transition temperature (T_g). The following parameters were used: dual cantilever mode, temperature range from 25 ºC to 200 ºC, heating rate of 5 ºC.min^{-1}, nitrogen atmosphere with a flow of 100 mL.min^{-1}, frequency of 1 Hz, amplitude of 10 µm, load of 2000 mN, the samples were made using the 3D printer, Sethi S3X, with dimensions of (50 x 14 x 3) mm. Figure 1 depicts the neat ASA and ASA/0.5% graphene samples.

After production, the samples were measured with calipers at three different points along its length, width and thickness, one measurement in each extremity and one at the center, the average of each measurement was used for the analysis.

3. . RESULTS AND DISCUSSION

3.1. TGA

The thermogravimetric analysis comparison between both samples was made to verify the influence of graphene in the thermal stability and degradation temperature of the composite. The comparison can be seen in the Figure 1.

a)   b)
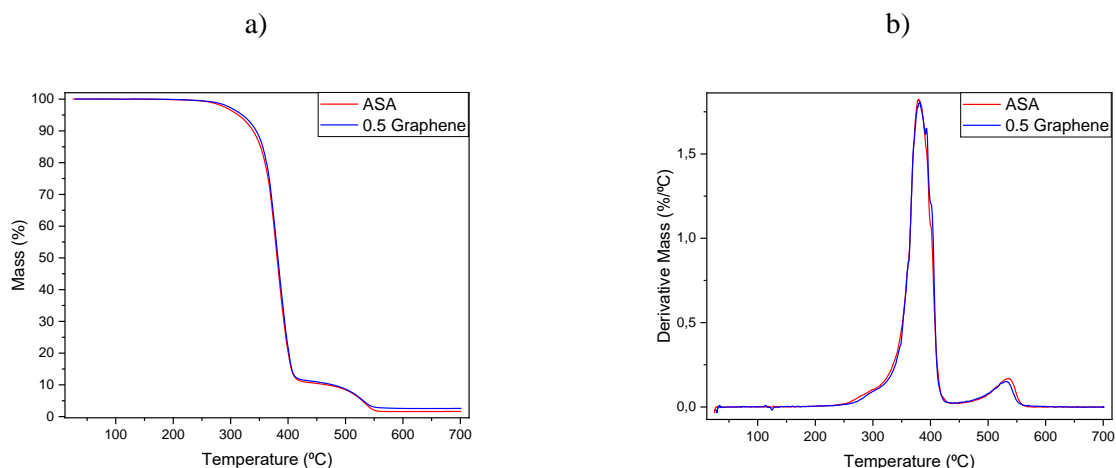
Figure 1. TGA curves of both samples. a) mass loss comparison and b) DTG comparison.

For both filaments it was observed two thermal events, the first one can be attributed to the degradation of styrene and acrylate parts of the polymer while the second one can be attributed to the degradation of the acrylonitrile. The degradation temperatures, loss percentages and ash percentages can be seen Table 3.

Table 3. TGA data for neat ASA and ASA/0.5% graphene comparison.

	1st Degradation Temperature	Loss %	Peak DTG	2nd Degradation Temperature	Loss %	Peak DTG	Ash %
Neat ASA	227 ºC	88.5%	378.9ºC	437.4 ºC	9.0%	536.6 ºC	1.6%
ASA/0.5% graphene	229 ºC	88.2%	381.5ºC	444.5 ºC	7.9%	546.2 ºC	2.6%

From the temperatures, it can be seen that there was virtually no difference in the first degradation temperature due to the addition of 0.5% Graphene, although a small variation in the second thermal event's temperature, loss percentage, and residue percentage was noted.

3.2. DSC

The DSC analysis was carried out to evaluate the influence of the graphene reinforcement in the glass transition temperature (Tg) of the material, this temperature is critical for the additive manufacturing process for it dictates the working temperature of the filament. The test curves of each material can be seen in Figure 2.
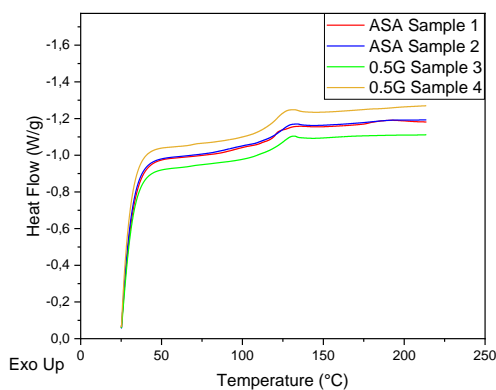
Figure 2. DSC Comparison between neat ASA and ASA/0.5% graphene.

The values of each sample's glass transition and the mean temperatures of each material can be seen in Table 4. Analyzing both graph and table, it can be seen that the Tg was not significantly affected by the addition of the graphene reinforcement.

Table 4. Tg values of the samples obtained by DSC.

	ASA Sample 1	ASA Sample 2	ASA/0.5% graphene Sample 3	ASA/0.5% graphene Sample 4
Tg	120ºC	121ºC	119ºC	121ºC
Mean	121ºC ± 0.5		120ºC ± 1.0	

3.3. Geometric Stability

A short analysis of the measurements of the DMA sample was made to verify the effects of graphene in the geometric stability of the material. The results can be seen in Table 5.

Table 5. Mean and Standard Deviation of Measurements.

	Length Mean (mm)	Width Mean (mm)	Thickness Mean (mm)
ASA Sample 1	50.68 ± 0.072	14.94 ± 0.165	3.31 ± 0.121
ASA Sample 2	50.62 ± 0.015	14.92 ± 0.070	3.25 ± 0.072
ASA/0.5% graphene Sample 3	50.07 ± 0.012	14.23 ± 0.040	2.95 ± 0.130
ASA/0.5% graphene Sample 4	50.02 ± 0.015	14.20 ± 0.055	2.97 ± 0.101

The standard deviation of the first ASA sample was higher than the other samples, but there is virtually no difference between sample 2, sample 3 and sample 4. However, when taking at account the project dimension of (50 x 14 x 3) mm, it can be seen that graphene reinforced samples were more accurate than the ASA samples. This can be seen more clearly in Figure 3.

c)
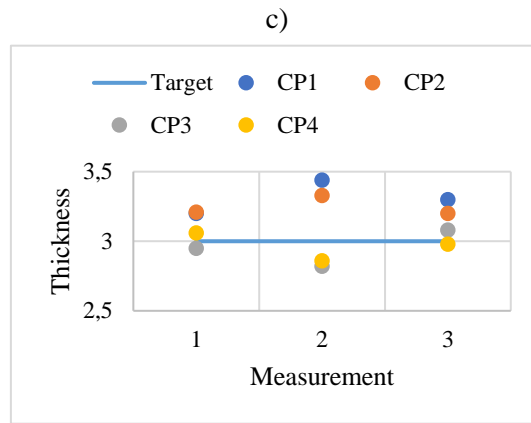
Figure 3. Dimension Measurements. a) Length, b) Width, and c) Thickness Measurements.

Considering the observed difference, the addition of graphene affects the dimensional precision of 3D printing parts. This can be attributed possibly due to graphene good thermal conductivity.

3.4. DMA

DMA analysis was caried out to further investigate the effects of the reinforcement in the Tg and also evaluate the effect of the graphene reinforcement in the material stiffness. The resulting curves of two representing samples can be seen in Figure 4 and Table 6.

a)

b)

c)
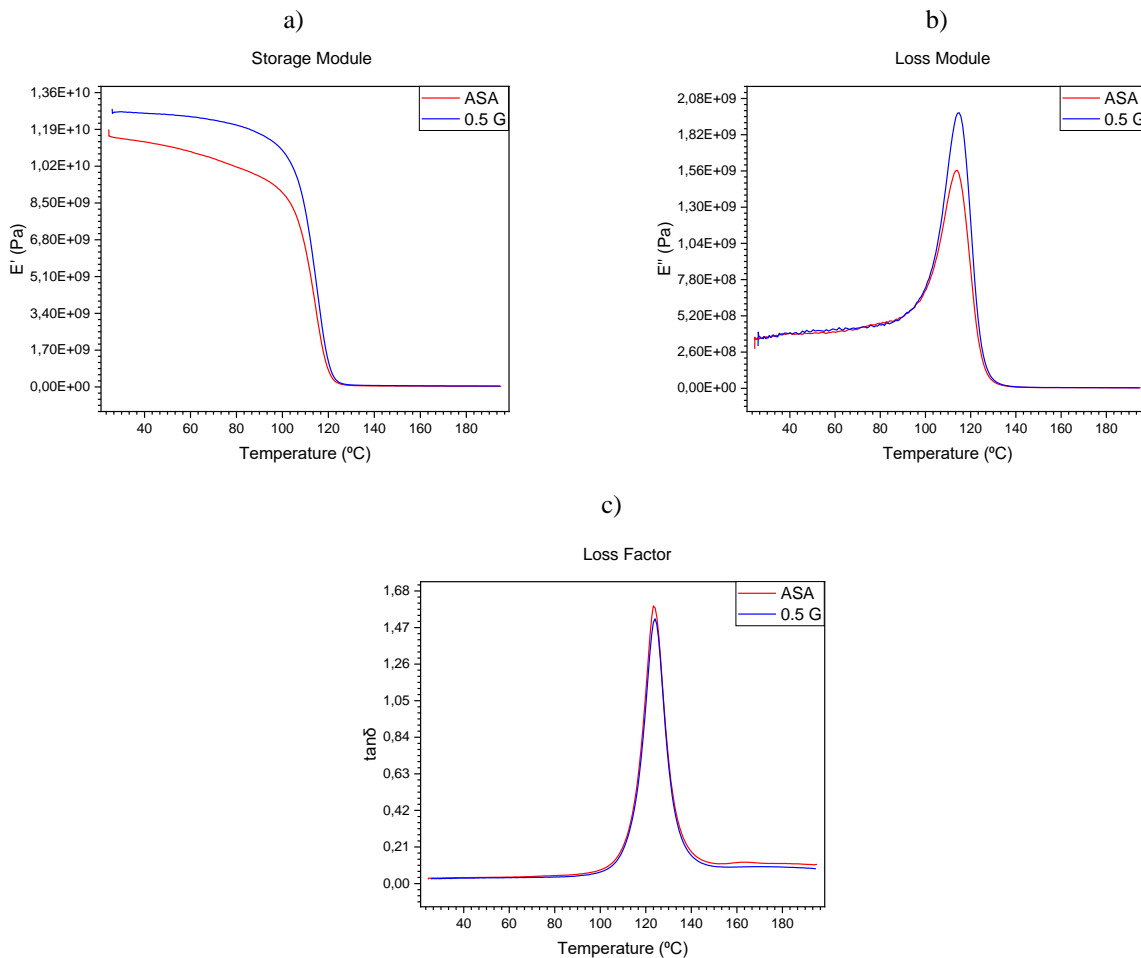
Figure 4. DMA curves of Neat ASA and ASA/0.5% graphene, (a) storage modulus, (b) loss modulus, and (c) tan δ.

Table 6. Results of DMA analysis.

	T$_{Onset}$ E' (°C)	Peak E" (°C)	Peak tanδ (°C)	Storage Modulus at 30°C (GPa)
ASA Sample 1	103	113	123	11.86
ASA Sample 2	99	115	124	11.30
Mean	101 ± 2	114 ± 1	124 ± 0.5	11.58 ± 0.28
ASA/0.5% graphene Sample 3	101	114	124	13.94
ASA/0.5% graphene Sample 4	99	115	124	11.63
Mean	100 ± 1	115 ± 0.5	124 ± 0	12.79 ± 1.16

Comparing the results of the DSC and DMA analysis it confirms that the graphene reinforcement does not significantly affect the Tg of the nanocomposite, but it does affect the storage modulus, even a small addition of 0.5% wt has shown an increase in 10.4% in the storage modulus, indicating an increase in material stiffness.

It can also be noted that in the graphene reinforced samples, a lateral wall detachment was observed, meaning that with modification in the printing parameters and sample design even better results can be expected. Test samples after the DMA analysis can be seen in Figure 5.

Figure 5. Test Samples after the Analysis. a) ASA Sample before analysis; b) ASA/0.5% graphene Sample before analysis c) ASA Sample after analysis; d) ASA/0.5% graphene Sample after analysis

4. CONCLUSIONS

It can be concluded that an addition of 0.5 wt% graphene did not affect the working temperature of the material since both Tg and degradation temperature remained similar. However, it can be noted an increase in geometrical stability possibly due to good thermal conductivity of the graphene. It also can be concluded that even the addition of small content of graphene provide a positive impact in the viscoelastic properties with increase in the material stiffness and an improvement in the printing factors and sample design might yield even better results.

4.1. Declaration of Competing Interest

The authors declare no conflict of interest.

4.2. Fundings

4.3. Acknowledgements

5. REFERENCES

[1]   Oliveira RA, Nascimento JP, Zanin MHA, Santos LFP, Ribeiro B, Guimarães A, et al. Manufacturing Free-Standing Graphene Oxide/Carbon Nanotube Hybrid Papers and Improving Electrical Conductivity by a Mild Annealing Treatment. Materials Research 2022;25. https://doi.org/10.1590/1980-5373-MR-2022-0131.

[2]   Jin J, Rafiq R, Gill YQ, Song M. Preparation and characterization of high performance of graphene/nylon nanocomposites. Eur Polym J 2013;49:2617–26. https://doi.org/10.1016/j.eurpolymj.2013.06.004.

[3]   Jia F, Fagbohun EO, Wang Q, Zhu D, Zhang J, Gong B, et al. Improved thermal conductivity of styrene acrylic resin with carbon nanotubes, graphene and boron nitride hybrid fillers. Carbon Resources Conversion 2021;4:190–6. https://doi.org/10.1016/j.crcon.2021.05.001.

[4]   Gong L, Yin B, Li LP, Yang MB. Nylon-6/Graphene composites modified through polymeric modification of graphene. Compos B Eng 2015;73:49–56. https://doi.org/10.1016/j.compositesb.2014.12.009.

[5]   Camposeco-Negrete C. Optimization of printing parameters in fused deposition modeling for improving part quality and process sustainability n.d. https://doi.org/10.1007/s00170-020-05555-9/Published.

[6]   Rakshit R, Kalvettukaran P, Acharyya SK, Panja SC, Misra D. Development of high specific strength acrylonitrile styrene acrylate (ASA) structure using fused filament fabrication. Progress in Additive Manufacturing 2023;8:1543–53. https://doi.org/10.1007/s40964-023-00420-z.

[7]   Kechagias JD, Ninikas K, Vakouftsi F, Fountas NA, Palanisamy S, Vaxevanidis NM. Optimization of laser beam parameters during processing of ASA 3D-printed plates. International Journal of Advanced Manufacturing Technology 2024;130:527–39. https://doi.org/10.1007/s00170-023-12711-4.

EFFECT OF NANODIAMOND FUNCTIONALIZATION ON THE THERMO-MECHANICAL BEHAVIOR OF BIONANOCOMPOSITES

Maria Eduarda A. Ribeiro[(a)] *, Antonio S. Ferri[(b)], Ruben J. Sanchez Rodriguez [(c)]

(a) 0000-0002-9033-1828 (Universidade Estadual do Norte Fluminense Darcy Ribeiro – Brazil)
(b) 0009-0009-0492-4394 (Universidade Estadual do Norte Fluminense Darcy Ribeiro – Brazil)
(c) 0000-0002-1434-5144 (Universidade Estadual do Norte Fluminense Darcy Ribeiro – Brazil)
    * Corresponding author: ribeiromaria.doc@gmail.com

Abstract: Nanotechnology is a multidisciplinary field of science, and developing nanocomposites is a versatile way to obtain specific properties by adding to a matrix low fillers' content. This work aimed at fabricating nanocomposites based on poli(3-hydroxybutyrate-co-hydroxyvalerate) (PHBHV) with 1.5 wt% of three different nanodiamond (nD): pristine nD (M), hydrogen-functionalized nD (H) and amino-functionalized nD (A). nD nanoparticles were dispersed in chloroform under sonication for 5 min. Then, each dispersion was mixed to PHBHV solution and submitted to sonication for more 2 min. Injection molded specimens were produced [(60 x 13 x 3) mm]. The effect of nD functional surface was evaluated by thermogravimetric analysis (TGA) and flexural tests. The incorporation of nD-M and nD-A delayed the initial and maximum degradation temperature of PHBHV in about 4 ºC. In contrast, nanocomposites with nD-H did not have significant changes on thermal stability. The addition of nD-M and nD-A also increased the elastic modulus of nanocomposite in more than 15%, while no statistical variation was observed for sample H. The presence of acid groups on nD-M and amine groups on nD-A may introduce interactions with polymer matrix, contributing to some changes on these thermo-mechanical properties.

1. INTRODUCTION

Carbon nanomaterials, such as graphene, carbon nanotubes, nanodiamonds, and fullerene are very known for their unique mechanical, thermal, and electrical properties [1]. Nanodiamonds (nD) are multifunctional nanoparticles with average size of 5 nm. They are known by their high hardness, thermal conductivity, thermal and chemical stability, and biocompatibility. Often produced by detonation, nD presents a large number of functional groups, such as carboxyls, carbonyls, hydroxyls, ethers, epoxy. Combining their large surface area and aspect ratio, the incorporation of nD on polymer nanocomposites results in a series of advantages, such as enhanced mechanical, thermal, electrical, and barrier properties [2-4]. Additionally, the non-toxicity of nD makes them very interesting for biomedical applications, such as tissue regeneration, drug delivery, imaging, and sensors [3]. Recently, a study showed the benefits of easy nD modification on cancer treatment [5]. Other work investigated the low quantity incorporation of fluorescent nanodiamonds on polycarbonate (PCL) composites. The nD reduced the enzymatic degradation rate of PCL and allowed the image monitoring [6].

The use of nD as a mechanical reinforcement on polymers is widely studied with proved improvements on stiffness and strength [7-9]. However, to achieve it, some challenges may be faced. In general, nanoparticles shown an intrinsic agglomeration tendency. Regarding nD, besides the small size, their variety of functional groups increases this behavior. Some studies evidenced that surface functionalization of nD may contribute to the nanoparticles disaggregation and may generate interactions to the polymer matrix, favouring a good interface particle/polymer [10].

Considering these observations, this study aims at investigating the effect of three different functionalized nanodiamonds on bionanocomposites based on poly(3-hydroxybutyrate-co-hydroxyvalerate) (PHBHV). The commercial nanodiamonds were the pristine one, hydrogen and amino groups functionalized nD. Thermo-mechanical analyses were carried out to observe the effect of functionalization on nanocomposites behavior.

2. METHODOLOGY

2.1. Materials

The materials used in this work are listed below: Poly(3-hydroxybutyrate-co-hydroxyvalerate) with 6% HV (PHBHV) was obtained from PHB Industrial (Brazil), with molar mass (Mw) of 101,820 g/mol and polydispersity of 1.99, determined by gas permeation chromatography (GPC). Three different functionalized-nanodiamonds were purchased from Carbodeon Ltd. Oy (uDiamond, Finland): pristine nD (M), hydrogen-functionalized (H) and amino-functionalized (A). All of them presented high purity (~97%) and average particle size of 4-6 nm. Chloroform (99.5%) was used as solvent.

2.2. Nanocomposites preparation

The nanocomposites were produced with 1.5 wt% of pristine and functionalized-nD. To obtain nanocomposites with good nanoparticles dispersion, nD was firstly dispersed in chloroform solution, under sonication probe technique for 5 min at 40% of amplitude and 30 s of pulse on/off, previously investigated by [7]. The nD dispersion was added to PHBHV solution, and the mixed solution was submitted to sonication for 2 min at the same conditions. The solid material (PHBHV/nD) was obtained through solvent evaporation at 160 rpm and water bath at 45 ºC, under vacuum atmosphere. This solid material was collected, dried at 45 ºC and used to feed a benchtop injection machine. The barrel temperature was 174-178 ºC, mold temperature was 50-70 ºC and pressure was 6 bar.

2.3. Nanocomposites characterization

Injection-molded specimens of (60 x 13 x 3) mm were used to investigate the mechanical properties of nanocomposites, according to ASTM D790- 17 [11], to calculate the elastic modulus (E), flexural strength (σ_m) and elongation at break (ε). The flexural test (n=5) was performed with support distance of 45 mm, and speed of 1.1 mm/min at room temperature. Thermogravimetric analysis (TGA) was carried out on each component and nanocomposites (8 mg), under oxidative atmosphere, with airflow of 100 mL/min, heating rate of 10 ºC/min and temperature range of 30 to 950 ºC. From TGA, the initial degradation temperature (T_{onset}) and maximum degradation temperature were obtained. To evaluate the thermal stability of each nanocomposite and PHBHV, the heat resistance index (T_{HRI}) was calculated, according to the Eq. (1) [12]:

$$T_{HRI} = 0.49 * [T_{5\%} + 0.6 * (T_{30\%} - T_{5\%})]$$

(1)

Where $T_{5\%}$ e $T_{30\%}$ represent the thermal decomposition temperature at 5 and 30% weight loss, respectively. Differential scanning calorimetry (DSC) was performed under nitrogen flow of 50 mL/min, and heating hate of 10 ºC/min from -40 to 190 ºC on samples of 6-8 mg placed on aluminium pan.

3. RESULTS AND DISCUSSION

The effect of nD functionalization on PHBHV thermo-mechanical properties will be discussed in this section. To introduce, according to [13], pristine nD presents lots of carboxylic groups and a heterogeneous surface. In contrast, nD functionalization reduces the variety of functional groups as well as their quantity. In the case of nD-H, the hydrogenated surface introduces a hydrophobic behavior to the nanoparticle, which could improve the nD affinity to hydrophobic polymers, such as PHBHV. The nD-A are functionalized with amino-groups, which may covalently interact to carbonyls groups of PHBHV.

Thus, regarding the thermal characterization of nanocomposites components, it is seen in Table 1 that even with different functionalization, nanodiamonds are particles of high thermal stability, with initial thermal decomposition occurring around 500ºC. On the other hand, as known, PHBHV degrades at a single step event starting at about 280ºC. The incorporation of nD-M and nD-A slightly prevented the thermal degradation, dislocating the T_{onset} at about 4ºC and T_{max} at 2 and 3 ºC to higher temperatures. A more accurate method to

verify the effect of nanoparticles on composites thermal stability is to measure the heat resistance index, in which a correlation between temperatures at defined degradation points reveals whether the nanocomposite is more stable or not compared to neat polymer. Higher the T_{HRI}, higher the thermal stability. In this study, the differences were subtle, but nanocomposite A revealed the higher index. Other works have reported the same behavior of amino-nanodiamons on different polymer matrixes [7,12].

In general, incorporating inorganic nanoparticles to polymer matrixes may increase the thermal stability of nanocomposites. However, to observe this behavior, some conditions may occur, such as good dispersion, filler/matrix interactions, and barrier effect [14]. Regarding nanodiamonds, at the same time they are very thermally stable, they are good thermal conductors, allowing a good temperature homogenization throughout the material and preventing overheating in certain regions of the sample. Thus, it is assumed that nD-M and nD-A achieved stronger interactions to PHBHV than nD-H.

Finally, the percentual residue measured at 400 ºC (temperature in which PHBHV is completely degraded, and nD is remains stable) indicates that all nanocomposites presented about 2 wt% of nD. This value is slightly smaller than the theorical one (1.5 wt%) due to polymer losses during the processing, resulting in accumulated concentration of nD.

Table 1. Thermal decomposition temperatures of PHBHV and nanocomposites.

Sample	T_{onset} (ºC)	T_{max} (ºC)	Residue (%)	T_{HRI}
nD-M	545.8	632.7	-	-
nD-H	550.2	614.3	-	-
nD-A	550.0	610.4	-	-
PHBHV	280.8	292.8	-	135.6
M	284.4	294.7	2.3	137.1
H	279.5	290.4	2.1	136.1
A	284.5	295.4	2.0	138.0

DSC curves, registered in Fig. 1, shows that nD-H incorporation did not change de crystallization behavior of PHBHV, which is characterized by the formation of different crystals with multiple melting peaks, and also melting-recrystallization-melting phenomena, evidenced by the small peaks at higher temperatures [15]. On the other hand, the third melting peak is not observed for samples M and A, suggesting a more uniform crystal morphology. These observations indicate possible different dispersion states and interaction levels of nD and PHBHV, also evidenced by TGA.
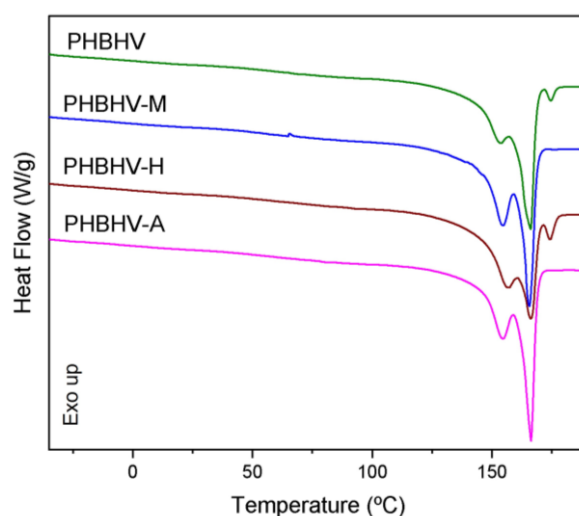
Figure 1. DSC curves of PHBHV and nanocomposites.

Despite the functionalization, nD is a nanoparticle of high stiffness (E~1000GPa) [14]. Several studies have reported the increase of elastic modulus of polymer matrix when incorporating nD. In this study, it is observed, in Fig. 2, that the addition of nD in PHBHV resulted in an increase of elastic modulus, especially

for samples M and A, which achieved an average E about 16 and 21% higher than neat PHBHV. According to ANOVA test, the significance between groups was 0,001 (p<0,05), indicating a statistical difference between PHBHV and nanocomposites. To predict which group presented statistical difference, Tukey analysis was applied, showing sample A is statistically higher than PHBHV.
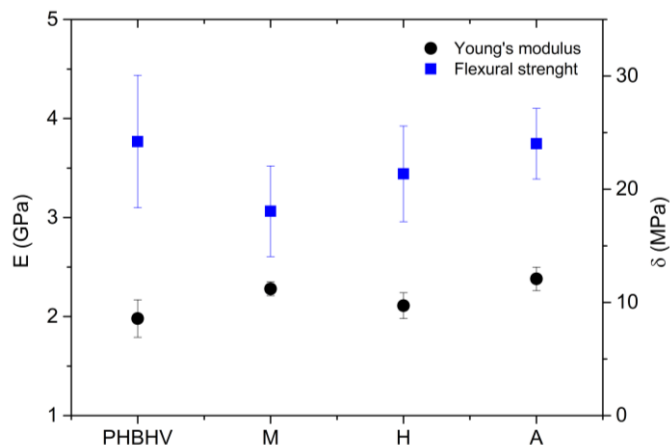
Figure 2. Elastic modulus and flexural strength of PHBHV and nanocomposites.

Regarding the flexural strength, the incorporation of different nD resulted in a slight reduction of average strength value, as listed in Table 2. However, the variation was reduced from PHBHV to nanocomposites, especially for sample A. Weibull analysis, shown in Fig. 3, revealed that group A presents a higher reliability among all studied groups, which means that nD-A improve de applicability of PHBHV nanocomposites, allowing a more accurate level of confidence while use.

Table 1. Mechanical properties of PHBHV and nanocomposites.

Sample	E (GPa)	σ_m (MPa)	ε (%)
PHBHV	1.96±0.20	24.21±5.86	1.02±0.41
M	2.28±0.07	18.05±4.01	0.84±0.18
H	2.11±0.13	21.36±4.22	0.76±0.17
A	2.38±0.11	24.04±3.12	0.93±0.07
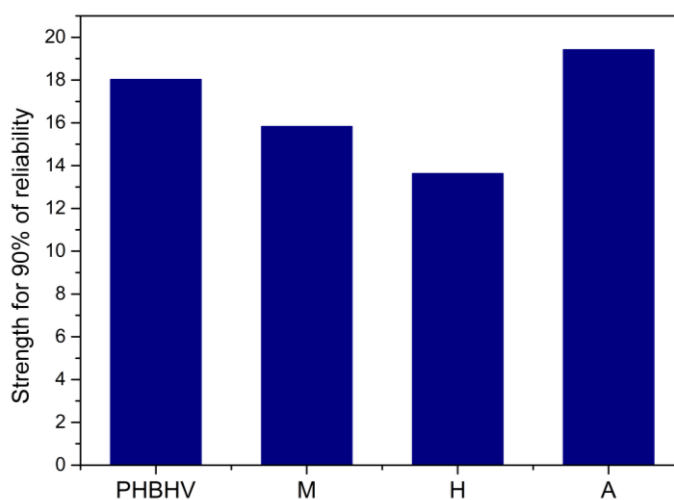
Figure 3. Elastic modulus and flexural strength of PHBHV and nanocomposites.

4. CONCLUSIONS

In this work, nanocomposites of biopolymer PHBHV with three different commercial nanodiamonds were successfully produced. The nD had different functional groups on their surface (pristine, hydrogenated and aminated nD). The thermal and mechanical behavior of nanocomposites were investigated aiming at to evaluate whether nD functionalization has a strong impact on nanocomposites performance. From TGA, it was concluded that all nanocomposites had similar amounts of nD, around 2 wt%, allowing the accurate effect of nD functionalization, without external interference, such as higher loading. The incorporation of nD-M and nD-A slightly postponed the thermal degradation of PHBHV, which was proven by the increase of heat resistance index. The effect of nD-M and nD-A was also verified on the stiffness of nanocomposites, which were approximately 16 and 22% higher than neat PHBHV. On the other hand, nD-H had no effect on thermal degradation profile of PHBHV and did not cause any statistical difference on elastic modulus. In general, the low nD loading, and the even smaller number of functional groups available to interact with polymer may have not been enough to generate huge differences on the thermo-mechanical properties evaluated in this study. However, there are evidence that amino group may create stronger interactions with PHBHV than the heterogeneous surface of nD-M and hydrogenated groups of nD-H. Further analysis may be done to better understand these observations.

4.1. Declaration of Competing Interest

The authors declare no conflict of interest.

4.2. Fundings

4.3. Acknowledgements

5. REFERENCES

[1] G. Maduraiveera, W. Jin. Carbon nanomaterials: Synthesis, properties and applications in electrochemical sensors and energy conversion systems. *Materials Science and Engineering: B*, Volume 272, 2021. (https://doi.org/10.1016/j.mseb.2021.115341).

[2] M. Khan et al. Surface optimization of detonation nanodiamonds for the enhanced mechanical properties of polymer/nanodiamond composites. *Diamond and Related Materials*, Volume 107, 2020. (https://doi.org/10.1016/j.diamond.2020.107897).

[3] T.L.A. Montanheiro et al. A brief review concerning the latest advances in the influence of nanoparticle reinforcement into polymeric-matrix biomaterials. *Journal of Biomaterials Science, Polymer Edition*, Volume 31, 2020. (https://doi.org/10.1080/09205063.2020.1781527).

[4] V.N. Mochalin, Y. Gogotsi. Nanodiamond–polymer composites. *Diamond and Related Materials*, Volume 58, 2015. (https://doi.org/10.1016/j.diamond.2015.07.003).

[5] J. Cui et al. Enhanced in vivo antitumor efficacy through the nanodiamond mediated co-delivery of drugs. *Journal of Drug Delivery Science and Technology*, Volume 88, 2023. (https://doi.org/10.1016/j.jddst.2023.104984).

[6] X. Wu et al. Melt electrowritten scaffolds containing fluorescent nanodiamonds for improved mechanical properties and degradation monitoring. *Bioprinting*, Volume 32, 2023. (https://doi.org/10.1016/j.bprint.2023.e00288).

[7] M.E.A. Ribeiro et al. Poly (3-hydroxybutyrate-co-3-hydroxyvalerate) and amino-functionalized nanodiamond bionanocomposites for bone tissue defect repair. *International Journal of Biological Macromolecules*, Volume 226, 2023. (https://doi.org/10.1016/j.ijbiomac.2022.11.221).

[8] S. Morimune-Moriya et al. Development and characterization of strong, heat-resistant and thermally conductive polyimide/nanodiamond nanocomposites. *Polymer*, Volume 230, 2021. (https://doi.org/10.1016/j.polymer.2021.124098).

[9] T. Remis et al. Study on structure, thermal behavior, and viscoelastic properties of nanodiamond-reinforced poly (vinyl alcohol) nanocomposites. *Polymers*, Volume 13, 2021. (https://doi.org/10.3390/polym13091426).

[10] V.N. Mochalin et al. Covalent incorporation of aminated nanodiamond into an epoxy polymer network. *ACS nano*, Volume 5, 2011. (https://doi.org/10.1021/nn2024539).

[11] ASTM D790-17, Standard Test Methods for Flexural Properties of Unreinforced and Reinforced Plastics and Electrical Insulating Materials. ASTM International, 2017. (www.astm.org).

[12] B. Nan et al. Covalently introducing amino-functionalized nanodiamond into waterborne polyurethane via in situ polymerization: Enhanced thermal conductivity and excellent electrical insulation. *Colloids and Surfaces A: Physicochemical and Engineering Aspects*, Volume 596, 2020. (https://doi.org/10.1016/j.colsurfa.2020.124752).

[13] V. Mochalin et al. The properties and applications of nanodiamonds. *Nature Nanotechnology*, Volume 7, 2011. (https://doi.org/10.1038/nnano.2011.209)

[14] Y-Q. Zhao et al. Nanodiamond/poly (lactic acid) nanocomposites: Effect of nanodiamond on structure and properties of poly (lactic acid). *Composites Part B: Engineering*, Volume 41, 2010. (https://doi.org/10.1016/j.compositesb.2010.09.003).

[15] M. Cakmak et al. The effect of copolymer composition on the spatial structural hierarchy developed in injection molded bacterial poly(3- hydroxybutyrate-co-3-hydroxyvalerate) parts. *Polymer*, Volume 46, 2005. (https://doi.org/10.1016/j.polymer.2005.02.071).

EVALUATING THE DISPERSION METHODS OF GRAPHENE OXIDE AND THEIR IMPACT ON THE THERMAL AND DYNAMIC MECHANICAL PROPERTIES OF EPOXY NANOCOMPOSITES

Fillip C.Alves[a]*, Luis F.P. Santos[b], Heitor L.O. Junior[c], Edson C.Botelho[d], Michelle L.Costa[e]

(a) 0000-0003-1032-0078 (São Paulo State University – Brazil)
(b) 0000-0002-5089-1089 (São Paulo State University / Institute for Technological Research – Brazil)
(c) 0000-0002-0005-9534 (São Paulo State University – Brazil)
(d) 0000-0001-8338-4879 (São Paulo State University – Brazil)
(e) 0000-0001-9492-8544 (São Paulo State University – Brazil)
* Corresponding author: fillip.cortat@unesp.br

CODE: BCCM7-62

Abstract: Thermosetting polymer matrices offer a combination of mechanical, thermal, and chemical properties. When combined with other materials, they are often chosen for their ability to reduce weight without compromising strength, which is crucial for aerospace and automotive industries, where fuel efficiency and performance are paramount. The incorporation of nanofillers is promising, especially when using graphene-based materials such as carbon nanotubes, graphene, and graphene oxide (GO), which tend to enhance matrix properties. The main challenge is the dispersion of the graphene oxide into the matrix. Proper dispersion contributes to the enhancement of material properties. This study investigates the effects of GO dispersion on the thermal and viscoelastic properties of epoxy matrix nanocomposites. In this study, nanocomposites were fabricated by casting, with a concentration of 0.5% (wt/wt). Dispersion methods such as mechanical stirring, magnetic stirring, ultrasonic tip dispersion, and manual dispersion were employed. Thermal and viscoelastic properties were evaluated, including thermogravimetric analysis (TGA) and dynamic mechanical thermal analysis (DMTA). The results suggest that GO dispersion methods directly influenced the properties. Thermal stability remained unchanged, while a significant increase in storage modulus values was observed, particularly when employing ultrasonic tip dispersion. This approach stood out for promoting a 146.89% increase (E') in the glassy region.

1. INTRODUCTION

Thermosetting polymeric materials are used as a matrix in composite materials when high performance and resistance are required. Phenolic, polyester, and epoxy are the most employed resins. Particularly, epoxy resin possesses specific intriguing characteristics, such as its exceptional ability to combine superior mechanical properties with versatility in incorporating reinforcements like carbon fibers, fiberglass, and even nanoreinforcements such as carbon nanotubes or graphene-based materials like graphene and graphene oxide. However, resins generally exhibit brittleness, with low toughness and impact resistance. This is often attributed to the high crosslink density within the resin matrix [1]. Combining resin with other materials gives rise to composites that offer a remarkable strength-to-weight ratio, enabling manufacturing of lightweight, robust, and efficient structures. These materials are ubiquitous and facilitate significant advancements across various industries, such as sports equipment, automotive, aerospace, naval, and civil construction [2].

Graphene oxide (GO), a material derived from graphene, is one of the nanomaterials garnering considerable interest in manufacturing composites, particularly those with a polymeric matrix. This is due to its compact structure, large specific surface area, excellent physical barrier performance, and outstanding

physical, chemical, and mechanical properties. GO typically exhibits thicknesses of up to several tens of nanometers, with lateral dimensions on the order of micrometers. The disparity between graphene and GO arises from functional groups on the surface and edges of its structure, such as oxygen-containing functional groups, including carbonyl, hydroxyl, and epoxy groups [3-5].

The challenge of implementing nanomaterials into thermosetting matrices is closely tied to their tendency to agglomerate. Consequently, achieving good dispersion is paramount to ensuring system's homogeneity without regions containing large concentrations of agglomerated nanoreinforcements. Inadequate or inefficient dispersion can result in the reduction of specific material properties. Various techniques can be employed for nanomaterial dispersion, including mechanical stirring, magnetic stirring, and dispersion via ultrasonic probe. Wei et al. [6] investigated the effect of graphene dispersion in epoxy resin, with results indicating that sonication alone can achieve graphene dispersion in the resin. The appropriate dispersion for the studied system increased the glass transition temperature from 93.4 °C to 99.1 °C in materials reinforced with just 0.3% (w/w) of graphene compared to pure resin [6]. Hence, studies should be undertaken regarding the fabrication of nanocomposites with high-performance polymeric matrices utilizing the nanoscience/nanotechnology of graphene-based materials, which can be applied across various fields.

Thus, the objective of the present study is to evaluate different methods of graphene oxide dispersion in epoxy resin and assess the thermal stability and viscoelastic properties of the manufactured nanocomposites. Consequently, the aim is to determine the most suitable dispersion methodology for the materials.

2. METHODOLOGY

2.1. Materials

The Araldite epoxy resin and Hardener were obtained from Max Epoxi (São Paulo, Brazil), with a viscosity of 1000 – 1200 mPa·s (25 °C), and a gel time of 50 minutes (120 °C). Graphene oxide (GO) was obtained from NanoView – Applied Nanotechnology, with lateral layer dimensions of approximately 1 – 5 μm, and several layers of approximately 1 – 10 μm.

2.2. Methods

Manufacturing of the resin and nanocomposites:

To produce specimens of pure epoxy resin and nanocomposites (NC), the thermosetting epoxy matrix, Araldite and hardener were mixed in a ratio of 4:1 (w/w), respectively. Subsequently, the mixture was placed into silicone rubber molds for the curing process. For the fabrication of nanocomposites, GO was dispersed in epoxy resin at a mass fraction of 0.5%, using four different methodologies:

1. Manual Dispersion (NC1): GO was incorporated into the epoxy resin and manually dispersed using a mortar until achieving good homogeneity.

2. Mechanical Stirring Dispersion (NC2): GO was incorporated into the epoxy resin and dispersed using a mechanical stirrer with a helix, operating at 1000 rpm for 20 minutes.

3. Magnetic Stirring Dispersion (NC3): GO was incorporated into the epoxy resin and dispersed using a magnetic stirrer operating at 1000 rpm for 20 minutes.

4. Ultrasonic Tip Dispersion (NC4): GO was incorporated into the epoxy resin and dispersed using an ultrasonic tip from Sonics & Materials, model VC 750, utilizing 30% of its maximum operating amplitude (750 W) for 20 minutes.

Subsequently, the hardener was added in the established ratio for all methodologies. After adding the hardener, the nanocomposites were cast into silicone rubber molds and placed in a vacuum oven at -0.8 bar for 15 minutes or until the bubbles in the resin disappeared. The materials were then cured at 120 °C for 2 hours followed by 180 °C for 4 hours.

Thermogravimetric Analysis:

Thermogravimetric analyses (TGA) were performed using the SII Nanotechnology equipment - Seiko Model TG/DTA 6200, available at the Department of Materials and Technology (DMT) of UNESP – Campus Guaratinguetá. For the analyses, the following parameters were employed: approximately 10 mg of sample mass, platinum sample holder, a heating rate of 10 °C/min, nitrogen inert atmosphere with a flow rate of 100

mL/min, temperature range from 25 °C to 800 °C, and alumina as the reference material. The analysis was conducted on the epoxy resin without the addition of nanoreinforcements, and nanoreinforcements were added to samples prepared using the different dispersion methods. The objective was to assess the thermal stability of the resin and to determine whether the studied dispersion methods influenced the thermal stability of the final material.

Dynamic Mechanical Thermal Analysis:

The equipment used for the analysis was the SII Nanotechnology – SEIKO, model DMS 6100. The parameters employed for these analyses were as follows: three-point bending mode, nitrogen atmosphere with a flow rate of 100 mL/min, oscillation amplitude of 10 μm, frequency of 1 Hz, and a heating rate of 3 °C/min. The samples were fabricated for the test with dimensions of (55 x 10 x 2.5) mm, and a temperature range from 25 °C to 200 °C. The calculation of the reinforcement effectiveness coefficient (C) was performed using Eq. (1) to assess the effectiveness of the nanoreinforcement (C) on the storage modulus. The effectiveness of the nanoreinforcement occurs when there is improved stress transfer at the interface created between the reinforcement and the matrix.

$$C = \frac{\left(\frac{E'_g}{E'_r}\right)_{Nanocomposite}}{\left(\frac{E'_g}{E'_r}\right)_{Epoxy}} \tag{1}$$

where E'_g and E'_r are the storage modulus in the glassy and rubbery regions, respectively. For this study, temperatures of 30°C and 190°C were selected.

The degree of entanglement density (N) can be applied to evaluate the dispersion of nanofillers in the polymer matrix. The degree of entanglement density is based on Eq. (2):

$$N = \frac{E'}{6RT} \tag{2}$$

where E' is the storage modulus at a given temperature, R is the gas constant, and T is the absolute temperature (in Kelvin).

The reinforcement efficiency (r) is also derived from E' and is calculated according to Eq. (3):

$$r = \frac{E_c - E_m}{E_m \ x \ V_f} \tag{3}$$

where r is the nanoreinforcement efficiency factor, E_c is the storage modulus of the nanocomposite, E_m is the storage modulus of the epoxy matrix, and V_f is the volume fraction of the filler (GO).

3. RESULTS AND DISCUSSION

Fig. 1 shows the thermogravimetric analysis of pure epoxy resin and epoxy/GO nanocomposites fabricated using different dispersion methods. In Fig. 1(a), the weight variation with temperature is depicted, and it can be observed that both the neat resin and the nanocomposites exhibit a single thermal decomposition stage. The temperature of the maximum degradation rate, defined by the peak of the derivative thermogravimetric curves (DTG) (Fig. 1(b)), was not highly influenced by the incorporation of the nanoreinforcement and the dispersion methods used; its value was approximately 385 °C, attributed to the complete degradation of the epoxy network [7]. This analysis allowed us to determine the temperature of thermal stability of the resin and nanocomposites, thereby enabling us to limit the temperature range used in dynamic mechanical analysis (DMA). The application should be restricted to temperatures below the material's onset degradation temperature, close to 325°C. The result showed values similar to those of other studies using epoxy resins as matrices for structural composites [8,9].
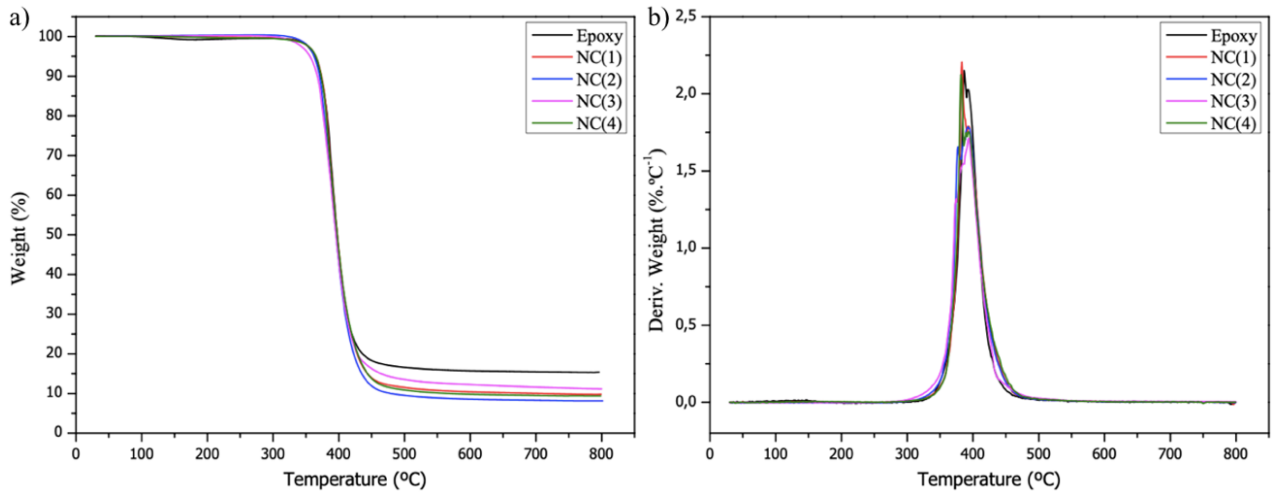
Figure 1. Thermogravimetric analysis of epoxy resin and nanocomposites a) mass variation b) derivate mass variation.

The curves constructed from the results of the dynamic mechanical analysis for epoxy resin and nanocomposites, with different dispersion methods, are represented in Fig. 2. A characteristic behaviour can be observed with increasing temperature, that is, for the storage modulus (E') (Figure 2(a)) there was a decrease in the modulus as a function of temperature, for the loss modulus (E") and damping factor (tan δ or tan delta) initially there was a linearity and then an increase in the property with increasing temperature (Fig. 2(a) and Fig. 2(b)).
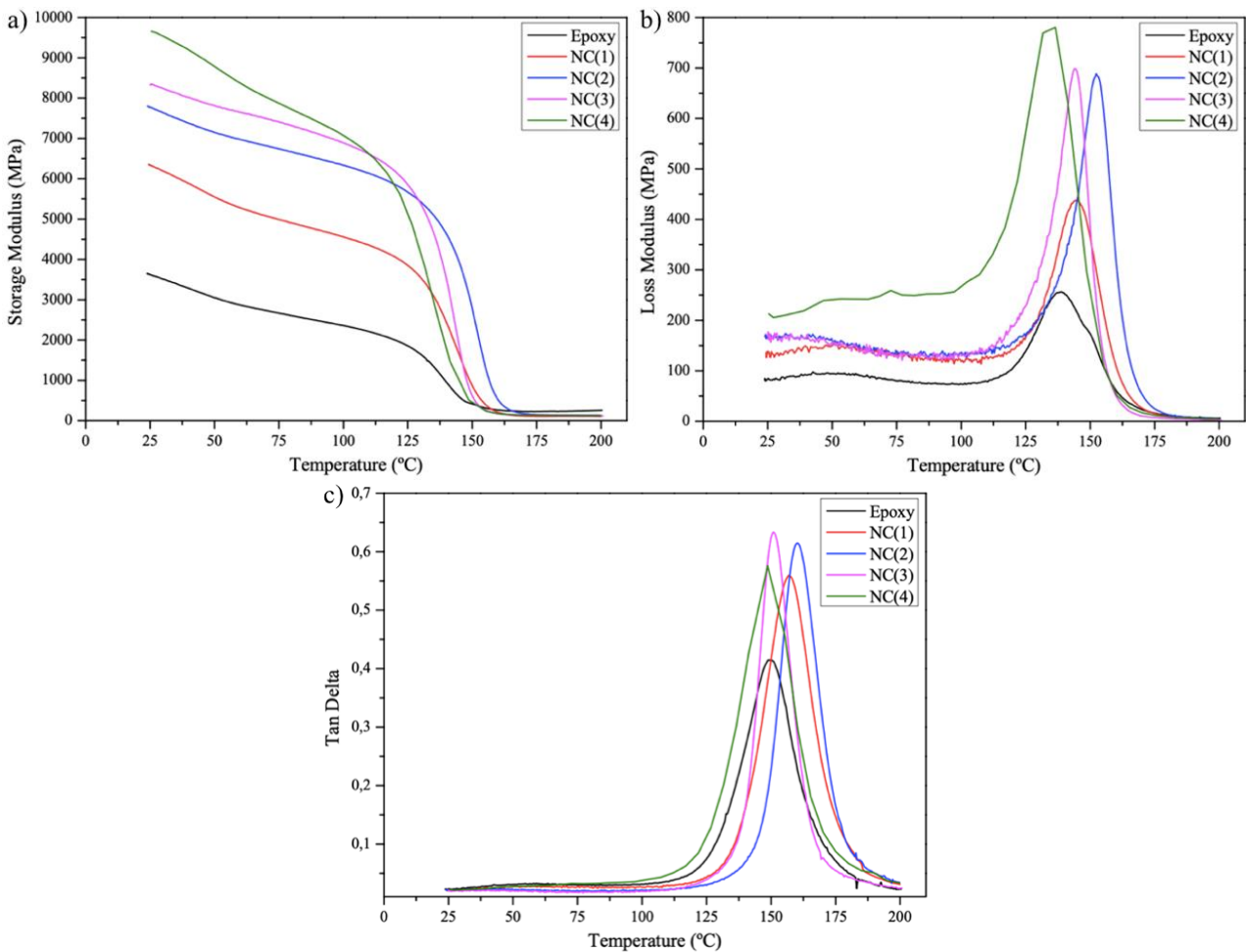
Figure 2. Dynamic-mechanical analysis for epoxy resin and nanocomposites a) E', b) E", and c) tan δ.

According to Fig. 2(a), the addition of GO and different dispersion methods used significantly influenced the values of the storage modulus. At room temperature (25 °C), in the glassy region, the

incorporation of GO into the epoxy resin contributed to the highest values of the storage modulus. Manual dispersion (NC1) contributed to the lowest value of the storage modulus, followed by dispersion with a mechanical stirrer (NC2), dispersion with a magnetic stirrer (NC3), and dispersion using an ultrasonic probe (NC4), which presented modulus values of 6300 MPa, 7600 MPa, 8300 MPa, and 9700 MPa, respectively. This parameter is of great relevance for the application of the material since it refers to the elastic response of the material, represented after an applied loading.

The difference found in the storage modulus values of the samples is likely due to the difference in the dispersion method used. Nanoreinforcements dispersed properly tend to increase the properties of the matrix due to the better interface between the phases, influencing mechanical loading. Thus, the materials tend to be stiffer, which justifies the higher modulus values of the nanocomposite NC4. It can be observed that sample NC4 exhibits a more pronounced reduction in modulus compared to the others. Samples NC1, NC2, and NC3 showed a more stable decline in this temperature range compared to sample NC4, which may be related to a higher content of aggregated GO nanoparticles, indicating that they acted as a barrier, restricting the movement of polymer chains and reducing the slope of the curve in this region. The behaviour of sample NC1 showed a lower capacity to store energy compared to the other nanocomposites, possibly due to the poorer homogeneity of the nanoreinforcement in the polymer matrix, as it underwent manual dispersion. However, the dissipation of stored energy occurs more gently over time and temperature. The storage modulus values in the elastomeric region did not vary significantly, being close to 190 MPa, indicating that the dispersion method did not influence in this region.

In Fig. 2(b), the loss modulus of the samples is observed. The behaviour exhibited by the materials indicates that the dispersion method and the addition of GO influenced the results. In the glassy region, nanocomposites exhibited higher modulus values compared to the pure resin. Through the loss modulus, it is possible to verify the maximum energy dissipation, represented by peaks in the glass transition region, due to the movement of the polymer chains. In the glassy region, sample NC4 exhibited the highest modulus value. This result corroborates with the earlier discussion regarding the storage modulus, where the higher energy storage capacity presented by sample NC4, as well as the more abrupt reduction in modulus, led to a greater dissipation of energy. Consequently, the loss modulus in this region was higher.

The graphs presented in Fig. 2(c) represent the samples behavior regarding the loss tangent. For all samples, the presence of a characteristic peak located in the glass transition region. Through the analysis of this peak, the glass transition temperature of the composites was determined, as well as the maximum value found for tan δ [10]. These values, the maximum of tan δ and the corresponding temperature at this maximum are listed in Table 1.

Table 1. Relevant results of DMA for the epoxy resin and for the nanocomposites manufactured by different methods.

Sample	E'$_{g\ 30\ °C}$ (MPa)	E'$_{r\ 190\ °C}$ (MPa)	C	Peak height (tan δ)	Tg (°C) Tan δ	N	r
Epoxy	3755.78	208.98	-	0.4144	148.7620	-	-
NC1	6280.69	157.83	2.21	0.5594	156.7683	0.4155	1.3445
NC2	7505.94	194.36	2.15	0.6145	160.1391	0.4966	1.9970
NC3	8229.68	184.14	2.48	0.6335	150.8592	0.5445	2.3824
NC4	9272.58	197.16	2.61	0.5959	150.8590	0.6135	2.9378

The observed difference, even if slight, may be due to the different dispersion methods used to fabricate each sample and, thus, the homogeneity of the system. This difference is attributed to each sample ability to store and dissipate energy. Samples that showed a smoother energy dissipation in the glassy region resulted in the transition occurring over a broader temperature range compared to the others. The nanoreinforcement dispersed using the ultrasonic probe, represented by sample CN4, allowed for more energy to be accumulated. However, the nanofillers dispersed through this method cannot retain this energy; hence, the dissipation occurs more rapidly.

It is essential to highlight that the relaxation process of polymers and composites is highly complex and depends on various factors such as stress loading, particle/matrix interaction, temperature, etc. It has been found in several studies that the reinforcement effect observed in the glassy region did not necessarily reflect a shift towards higher temperatures in the maximum value of glass transition temperature, as observed in this study [11]. The glass transition temperature obtained from the tan δ curves, and the calculated effectiveness

coefficient C are presented in Table 1. The effectiveness values of the nanoreinforcement coefficient C for the samples were similar, with the lowest values obtained for the nanocomposites produced by methods NC2, NC1, NC3, and NC4, which demonstrates, based on the results obtained, that the dispersion methods were efficient. The higher effectiveness value of C presented by sample NC4 may be due to the considerably higher storage modulus value (146.89 % higher than pure epoxy resin) in the glassy region, indicating good dispersion of GO in the polymer matrix, and the low values presented by the storage modulus in the elastomeric region, where the implementation of nanoreinforcement showed no influence.

Table 1 presents the degree of entanglement density N for each studied nanocomposite. The entanglement degree (N) was applied to evaluate the dispersion of GO in the polymer matrix. Higher N values suggest lower interaction between the nanofillers, contributing to a lesser tendency for agglomerate formation [12]. The nanocomposite produced by method NC4 showed higher N values followed by NC3, NC2, and NC1, respectively. The observed trend suggests a higher degree of satisfactory dispersion for NC4, which may be related to the efficiency regarding the dispersion method of GO in the polymer matrix. A more adequate dispersion implies a lower interaction between the GO layers. The same trend was observed for calculating the reinforcement efficiency factor r, where NC4 showed the highest value, followed by NC3, NC2, and NC1, respectively. This trend, as verified through the calculation of the entanglement degree, suggests that the NC4 method is more efficient for the dispersion of GO.

4. CONCLUSIONS

The possibility of dispersing graphene oxides in epoxy resin was verified using the different methodologies studied. There was no formation of visible GO agglomerates. The implementation of the nanoreinforcement did not alter the thermal stability of the epoxy matrix, nor did the techniques used for the dispersion of the nanoreinforcement. All dispersion methods studied contributed to an increase in the storage modulus in the glassy region, with dispersion through the ultrasonic probe presenting the highest E' value (146.89 % higher than pure resin). Thus, the most efficient method for nanoparticle dispersion in epoxy resin for the processing of epoxy/GO nanocomposites proved to be using the ultrasonic probe.

4.1. Declaration of Competing Interest

The authors declare no conflict of interest.

4.2. Acknowledgements

5. REFERENCES

[1] O. Zabihi et al. A technical review on epoxy-clay nanocomposites: Structure, properties, and their applications in fiber reinforced composites. *Composites Part B*: Engineering, Volume 135, 2018. (https://doi.org/10.1016/j.compositesb.2017.09.066).

[2] F.C. Alves et al. Influence of void content and morphology on the creep behavior on glass/epoxy composites. *Composites Communications*, Volume 25, 2021. (https://doi.org/10.1016/j.coco.2021.100712).

[3] M.A.A. Ahmad et al. Dynamic mechanical analysis of graphene nanoplatelets/glass reinforced epoxy composite. *Journal of Physics*, Volume 2051, 2021. (https://doi.org/10.1088/1742-6596/2051/1/012046).

[4] Q. Zhai, S. Feng. Preparation, structure control and application of graphene oxide. *Chemical Industry and Engineering Progress*, Volume 39, 2020. (https://doi.org/ 10.16085/j.issn.1000-6613.2019-1424).

[5] X. Chen et al. In-situ crosslinking reaction of graphene oxide & waterborne epoxy resin to construct continuous phase anticorrosive coating. *Arabian Journal of Chemistry*, Volume 17, 2024. (https://doi.org/10.1016/j.arabjc.2024.105795)

[6] J. Wei et al. Graphene Nanoplatelets in Epoxy System: Dispersion, Reaggregation, and Mechanical Properties of Nanocomposites. *Journal of Nanomaterials*, Volume 2015, 2015. (https://doi.org/10.1155/2015/561742).

[7]   R.M. Neves et al. Enhancing thermal and dynamic-mechanical properties of epoxy reinforced by amino-functionalized microcrystalline cellulose. *Journal of Applied Polymer Science*, Volume 138, 2021. (https://doi.org/10.1002/app.5132).

[8]   F.C. Alves et al. The relation of porosity and creep behavior of glass fiber/epoxy composite: Design of experiments approach. *Polymer Composites*, Volume 42, 2021. (https://doi.org/10.1002/pc.26267).

[9]   F.M. Monticeli et al. On the 3D void formation of hybrid carbon/glass fiber composite laminates: a statistical approach. *Composites Part A*: Applied Science and Manufacturing, Volume 137, 2020. (https://doi.org/10.1016/j.compositesa.2020.106036).

[10] E.D. Zantto, J.C. Mouro. The glassy state of matter: Its definition and ultimate fate. *Journal of Non-Crystalline Solids*, Volume 471, 2017. (https://doi.org/10.1016/j.jnoncrysol.2017.05.019).

[11] R.M. Neves et al. Creep and stress relaxation behavior of functionalized microcrystalline cellulose/epoxy composites. *Cellulose*, Volume 30, 2023. (https://doi.org/10.1007/s10570-022-05020-8).

[12] J. Jyoti et al. Dynamic mechanical properties of multiwall carbon nanotube reinforced ABS composites and their correlation with entanglement density, adhesion, reinforcement and C factor. *RSC Advances*, Volume 6, 2016. (https://doi.org/10.1039/C5RA25561A).

SENSOR MADE OF CARBON NANOTUBES AND CARBON BLACK IN RUBBER MATRIX FOR MONITORING BOLTED JOINTS

Eduardo Preto[a], Pedro Ramos Barboni[b], José Antonio Malmonge[c], and Samuel da Silva* [d]

(a) 0000-0001-9970-8938 (UNESP - Universidade Estadual Paulista, Departamento Engenharia Mecânica – Ilha Solteira/SP - Brazil)
(b) 0009-0006-6135-6635 (UNESP - Universidade Estadual Paulista, Departamento Engenharia Mecânica – Ilha Solteira/SP - Brazil)
(c) 0000-0002-1773-3142 (UNESP - Universidade Estadual Paulista, Departamento de Física e Química – Ilha Solteira/SP - Brazil)
(d) 0000-0001-6430-3746 (UNESP - Universidade Estadual Paulista, Departamento Engenharia Mecânica – Ilha Solteira/SP - Brazil)
* Corresponding author: samuel.silva13@unesp.br

Abstract: Mechanical structures are systems present in several areas of the modern world and monitoring them is essential to guarantee the safety of everything around them. Damage identification and monitoring techniques are diverse but focus on dynamic measures that require high costs in equipment and specialized labor. In this context, this work presents a new sensor developed by a natural rubber matrix with carbon black and carbon nanotubes incorporated. This nanocomposite has piezoresistive properties, which makes it possible to perform static measurements, requiring low investment in equipment training to perform the analysis. To better understand the behavior of the sensor, tests were performed on the tensile machine to evaluate the piezoresistive response. Furthermore, rubber was used in bolted joints made of composite material to identify the torque variation in tightness in the bolts and verify the piezoresistive property under compression. The piezoresistive test showed results that validate the material's properties and thus make it possible to apply the nanocomposite as a resistive sensor under deformation. Finally, the application to bolted joints showed promising results, identifying the torque variation in this type of structure with high precision.

1. INTRODUCTION

In February 2024, a Boeing airplane had an emergency door blown off due to missing screws, and after inspections, the investigation revealed loose bolts that were under-torqued [1,2]. Therefore, monitoring techniques that can identify this type of problem are essential to ensure the safety of the structure and the people who use it. The literature presents several studies applying Structural Health Monitoring (SHM) methods to identify these tips of structural damage. Almost all these techniques analyze dynamic measurements, which require expensive sensors and equipment, and high knowledge and training for the operators [3–5].

At the same time, there have been considerable advances in the production and development of nanomaterials. In this context, researchers have developed studies to combine these materials with others known in the literature. In this way, these materials with both properties make it possible to perform new applications [6,7]. The sensors used with these nanocomposites show promising results in bioelectronic devices [8,9], electronics [10,11], engineering [12–16], and among others.

This paper presents the study of a new sensor made of natural rubber, carbon nanotubes, and carbon black. This material has a piezoresistive effect, which gives it conductive properties that can vary according to

the level of deformation. In this context, the aim is to apply this sensor to detect the loosening of bolted joints since the torque applied to the bolts generates compression deformation in the sensor and, due to this property, the resistivity corresponding to each level can be related, thus identifying, and monitoring possible damage to the structure using static measurements.

2. METHODOLOGY

This section describes the methodology used to produce the nanocomposite used in this project. Following this, it was performed the material's characterization tests to validate its properties and then was used to identify torque variation in bolted joints. Finally, the methodology for identifying damage in bolted joints using the nanocomposite is presented.

2.1. Nanocomposite production

The nanocomposite production used the following materials:
- Natural Rubber (NR);
- Chloroform PA (Pure for Analysis);
- Carbon black (CB) with an average diameter of 35 nm, density of 0.1 gcm³, surface area of 1000 m^2g^{-1}, and electrical conductivity of 200 Sm^{-1};
- Multilayer carbon nanotube (CNT) acquired from CTNano (Nanomaterials Technology Center - UFMG), with purity greater than 95% and with approximately 5% contaminants ($Al_2O_3 - Co - Fe$), length from 5 to 30 μm, diameter 10 to 30 nm, surface area of 100 m^2g^{-1} and electrical conductivity in the order of 100 to 200 Sm^{-1};
- Zinc Oxide, Sulfur, and ZDEC (Di-etil Di-tiocarbamato de Zinco) for vulcanization.

The sensor's base material is natural rubber extracted from *Hevea brasiliensis*. The process involves treating the rubber to remove the present proteins, leaving only the polymer behind. Subsequently, the polymer is cut into small pieces, placed in chloroform, and subjected to magnetic stirring for solubilization, with a concentration of 5% by mass.

The CB and CNT guarantee material conductivity. Both are mixed in chloroform mutually with vulcanizing agents and prepared in an airtight jar to prevent the chloroform from evaporating. This solution is placed in an ultrasonic bath to disperse the nanomaterials and the components responsible for vulcanization.

As shown in Fig. 1, the two solutions are mixed to form the nanocomposite. The final solution is kept under magnetic stirring for 24 hours to allow the components to homogenize. After this period, the solution is poured into a Petri dish for the chloroform to evaporate. The final material was placed in the oven at a temperature of 90°C and kept there for three hours for the rubber to vulcanize.
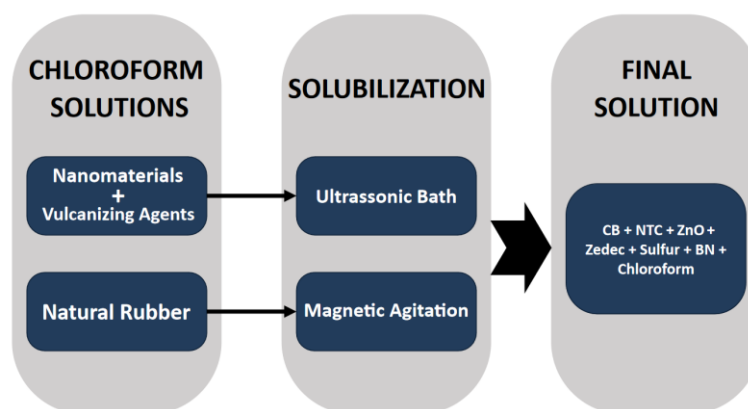
Figure 1. Flowchart of the methodology applied to the production of conductive rubber from solubilization in chloroform to the joining of solutions to obtain the final solution.

The samples produced in this paper contain 5% CB and 1% CNT. This percentage ensures the material is at the percolation limit, making the system more sensitive when deformed, as it varies between conductive and insulating. If the nanomaterial concentration is high, the material has low electrical resistance attributable to the many paths, and deformations generate low variation in conductivity.

Figure 2 shows the material and its properties. The nanocomposite combines the properties of rubber and nanomaterials, as it has flexibility and piezoresistivity, making it possible to use it as a sensor. In addition, the sensor produced has an average thickness of 270 µm, ensuring it can be deformed until it loses its percolation.

2.2. Piezoresistivity behavior

The piezoelectric effect can be characterized using a cyclic loading test with a pre-defined deformation, and the sample used has a length of 50 mm and a width of 5 mm. The test was performed on the INSTRON universal testing machine, and the sensor was analyzed in two deformation cycles: 1 mm and 3 mm. Piezoresistivity was measured using the Keitlhey 238 voltage source, which supplies an electric voltage and obtains the electric current passing through the sample. Figure 3 shows the experimental apparatus, in which the specimen was fixed to the traction machine by pneumatic clamps, and insulating material was used to ensure that all the electrical voltage was applied to the sample.
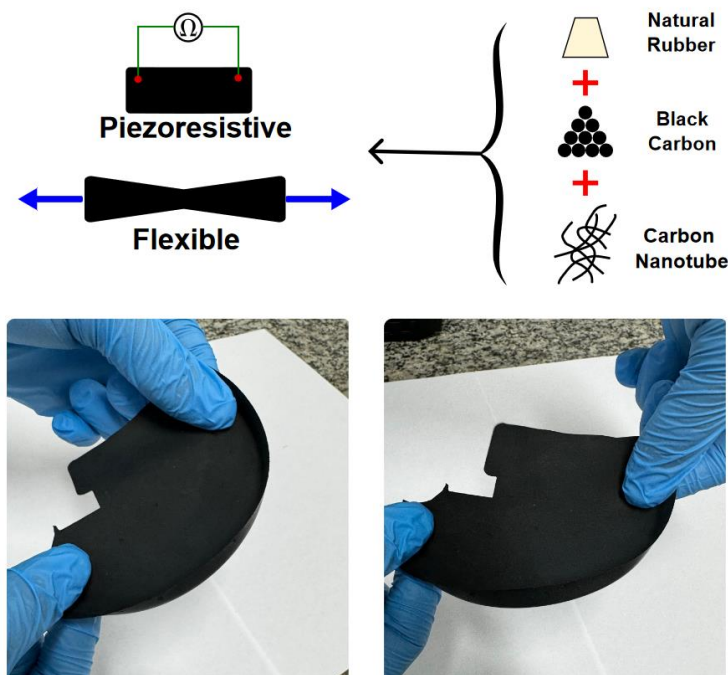
Figure 2. The upper image represents a schematic of the nanocomposite properties, and the lower image shows the material produced by applying the methodology.
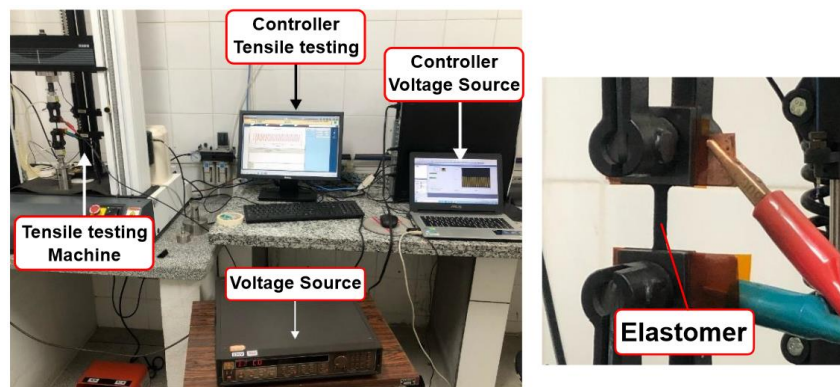
Figure 3. An experimental bench composed of a tensile testing machine to promote deformation and a voltage source that measures the piezoresistivity of the nanocomposite.

In this test, the cyclic deformation cycle was measured, and the material's resistive response was checked by measuring the electric current passing through it. The material was checked to determine whether it showed a variation in electrical resistance when deformed and whether the sensor was sensitive to these levels of deformation.

2.3. Determining torque variation

The sensor measurements are made statically by obtaining the electrical resistance value. The measured values are in the MΩ range, and the acquisition board cannot perform the measurement directly. An alternative would be to use a voltage source, but a buffer circuit was used to simplify the acquisition and reduce equipment costs. This voltage divider requires a reference resistor to enhance sensitivity in the measurements. Therefore, for high-resistance sensors, the reference resistor must be increased. In addition, a TL071 integrated circuit is used, which allows measurements to be made with a conventional acquisition board since the circuit can reduce the impedance and acquire the signal correctly.

The bolted joint is monitored using a 50 x 5 mm section of the nanocomposite produced. The sensor is positioned between the two beams to be screwed together, and in the area between the two bolts, the support manufactured by 3D printing was used to fix the bolted joint when applying the torque to the system does not move. The initial torque applied to the structure is 1.4 Nm, and it varies from 0.4 Nm to 5.8 Nm. The electrical resistance is measured for each torque level.

The ELVIS II system (Environment Laboratory Virtual Instrumentation Suite) was made for the buffer circuit and the acquisition, and LabView was the interface between the board and the computer. The data was collected for 60 seconds, and the average was calculated for each torque level. Finally, the data was normalized to generalize and used 1.4 Nm torque level as the reference. Figure 4 shows a representation of the circuit, the sensor positioned on the bolted joint, and the circuit assembled in ELVIS II.
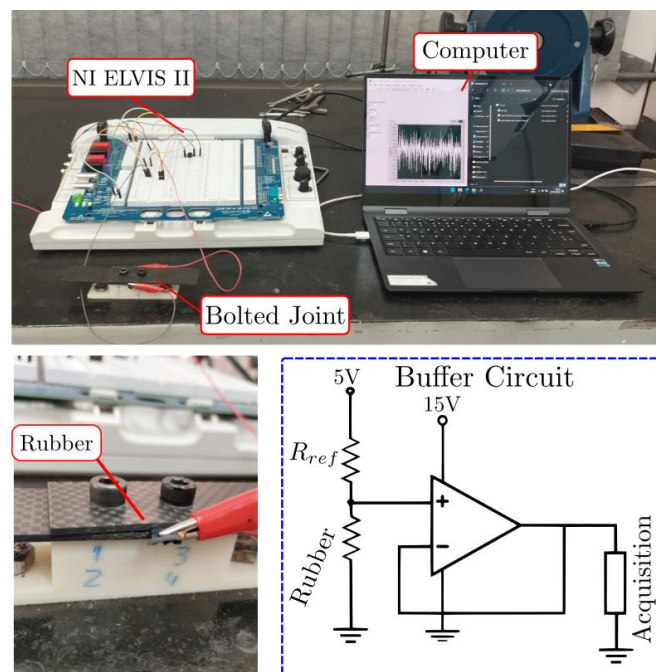
Figure 4. An experimental bench was used in this test and a buffer circuit was used to measure the resistance.

3. RESULTS AND DISCUSSION

Figure 5 shows the results of the piezoresistivity characterization. The resistivity of the sensor varies as it undergoes deformation, as can be seen by the curves in red. Due to vulcanization, the sensor returns to its initial resistance condition without the presence of residual deformations. The amplitude of the sensor's electrical current variation tends to increase as the deformation applied by the traction machine increases, indicating that it is sensitive to different levels of deformation. Furthermore, the sensitivity of the sensor can be analyzed, since for low deformations it has variations of approximately 50%. Also, it appears that the current variation is proportional to the deformation, with the response peaks corresponding to the deformation multiplied by the current variation when deformed by 1 mm. Another factor present is the lag of the current peaks with the deformation, this is the result of the creation of new current paths during the accommodation of the sensor right after the peak of deformation and this lag tends to increase, reaching almost 2 seconds for the largest deformation.
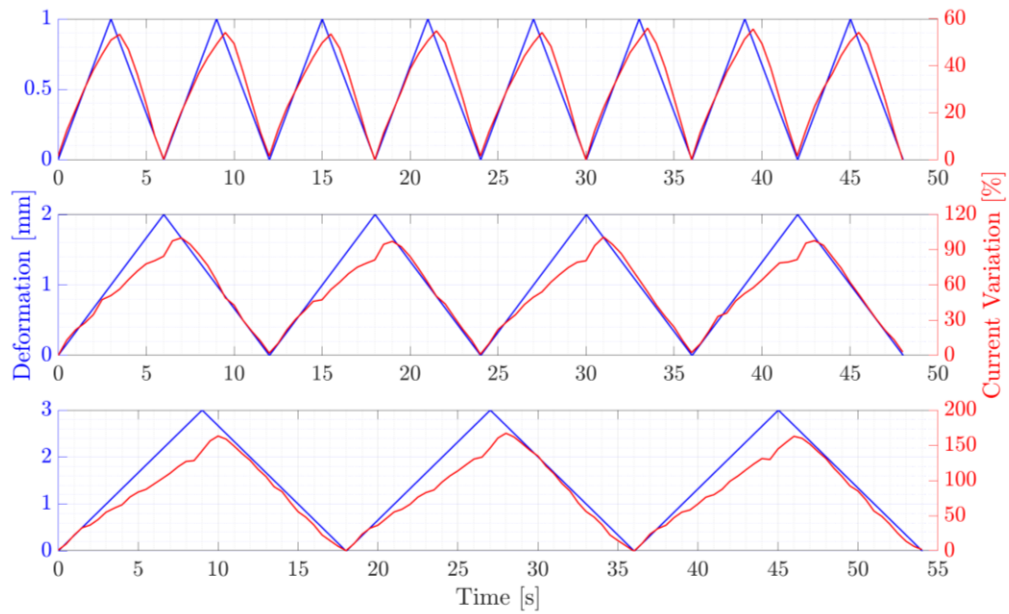
Figure 5. Piezoresistive response to deformation is shown in red and the deformation applied is shown in blue.

The variation in normalized resistance measurements is presented in Fig. 6. It shows that a high level of torque promotes an increase in resistance variation because the sensor tends to lose conductivity when it undergoes deformation. In some cases, close levels of torque do not show much variation, but if more widely spaced torque levels are analyzed, the difference in electrical resistance tends to become clearer and indicates the variation in torque across the sensor. Furthermore, it is worth mentioning that the sensor operates at a certain level of torque, so for higher torque levels it tends to be isolating and lose sensitivity and saturation. Likewise, depending on the sensitivity, the sensor requires a deformation that causes changes in its distribution of nanomaterials, so for low levels of torque, no variation in resistance may be identified.
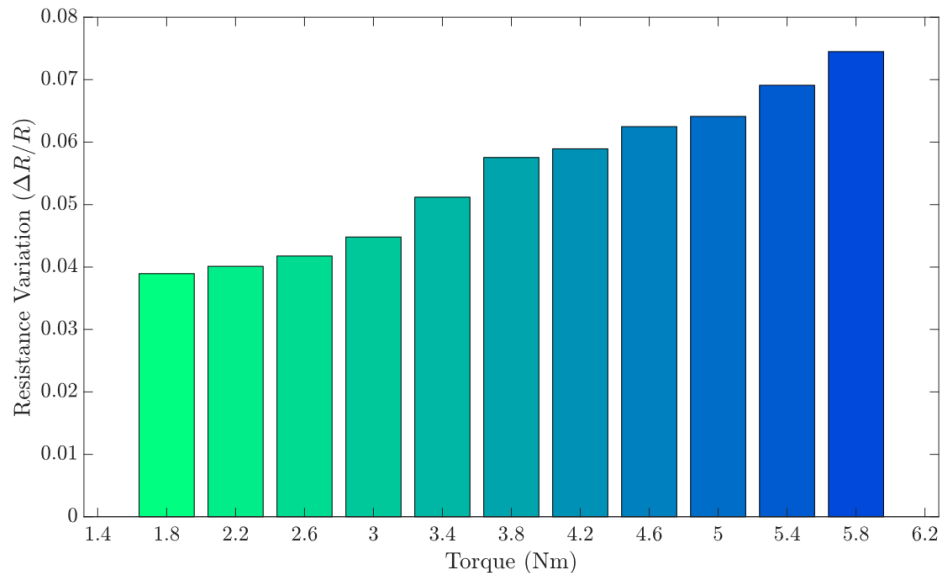
Figure 6. Piezoresistive response of sensor for different torque levels in a bolted joint.

4. CONCLUSIONS

The nanocomposite used as a sensor showed promising results in detecting the loss of tightness in bolted joints. It can identify low torque variations without taking dynamic measurements. Moreover, it holds promising potential for operation within systems featuring low and high torque levels. Developing the sensor for specific tightening ranges involves establishing the ratio of CNT and CB that ensures its sensitivity. The nanocomposite used as a sensor showed also adequate results in detecting the loss of tightness in bolted joints.

It can identify low torque variations without taking dynamic measurements. Moreover, it holds promising potential for operation within systems featuring low and high torque levels. Developing the sensor for specific tightening ranges involves establishing the ratio of CNT and CB that ensures its sensitivity. In addition, the thickness variation in the sensor makes it possible to check the sensitivity related to this parameter. An important aspect will be studying compression vulcanization techniques, which can offer increased rigidity and function effectively at higher torque levels.

4.1. Fundings

5. REFERENCES

[1]   Key bolts were missing from a Boeing door plug that blew out in mid-air, report says | CNN Business (https://edition.cnn.com/2024/02/06/business/ntsb-boeing-alaska-door-plug-blowout-faa/index.html), accessed April 12, 2024.

[2]   Porta ejetada durante voo: avião saiu da fábrica sem parafusos na porta, conclui relatório dos EUA sobre o caso | Mundo | G1. (https://g1.globo.com/mundo/noticia/2024/02/06/porta-ejetada-durante-voo-eua-dizem-que-aviao-estava-sem-parafusos-em-relatorio-final.ghtml), accessed April 12, 2024.

[3]   Lopes KW, Gonsalez-Bueno CG, Inman DJ, Bueno DD. On the modeling of circular piezoelectric transducers for wave propagation-based structural health monitoring applications. Journal of Intelligent Material Systems and Structures, Volume 32, 2023. (https://doi.org/10.1177/1045389X2211476)

[4]   Cortez NE, Filho J V., Baptista FG. A new microcontrolled structural health monitoring system based on the electromechanical impedance principle. Structural Health Monitoring, Volume 12, 2012. (https://doi.org/10.1177/14759217124611)

[5]   Baptista FG, Budoya DE, de Almeida VAD, Ulson JAC. An Experimental Study on the Effect of Temperature on Piezoelectric Sensors for Impedance-Based Structural Health Monitoring. Sensors, Vol 14, 2014. (https://doi.org/10.3390/S140101208).

[6]   Banerjee SS, Arief I, Berthold R, Wiese M, Bartholdt M, Ganguli D, et al. Super-elastic ultrasoft natural rubber-based piezoresistive sensors for active sensing interface embedded on soft robotic actuator. Appl Mater Today. Volume 14, 2021. (https://doi.org/10.1016/J.APMT.2021.101219).

[7]   Bokobza L. Multiwall carbon nanotube-filled natural rubber: Electrical and mechanical properties. Express Polym Lett. Volume 6, 2012. (https://doi.org/10.3144/EXPRESSPOLYMLETT.2012.24).

[8]   Song E, Li J, Won SM, Bai W, Rogers JA. Materials for flexible bioelectronic systems as chronic neural interfaces. Nature Materials. Volume 19, 2020. (https://doi.org/10.1038/s41563-020-0679-7).

[9]   Li Z, Liu H, Ouyang C, Hong Wee W, Cui X, Jian Lu T, et al. Recent Advances in Pen-Based Writing Electronics and their Emerging Applications. Adv Funct Mater. Volume 26, 2016. (https://doi.org/10.1002/ADFM.201503405).

[10]   Li Q, Chen L, Gadinski MR, Zhang S, Zhang G, Li H, et al. Flexible high-temperature dielectric materials from polymer nanocomposites. Nature. Volume 523, 2015. (https://doi.org/10.1038/nature14647).

[11]   Khan Y, Thielens A, Muin S, Ting J, Baumbauer C, Arias AC. A New Frontier of Printed Electronics: Flexible Hybrid Electronics. Advanced Materials. Volume 32, 2020. (https://doi.org/10.1002/ADMA.201905279).

[12]   Tai G, Wei D, Su M, Li P, Xie L, Yang J. Force-Sensitive Interface Engineering in Flexible Pressure Sensors: A Review. Sensors. Volume 22, 2022. (https://doi.org/10.3390/S22072652).

[13] Li X, Li P, Wu Z, Luo D, Yu HY, Lu ZH. Review and perspective of materials for flexible solar cells. Materials Reports: Energy, Volume 1, 2021. (https://doi.org/10.1016/J.MATRE.2020.09.001).

[14] Thostenson ET, Chou TW. Carbon nanotube-based health monitoring of mechanically fastened composite joints. Compos Sci Technol. Volume 68, 2008. (https://doi.org/10.1016/J.COMPSCITECH.2008.05.016).

[15] Ashrafi B, Johnson L, Martinez-Rubi Y, Martinez M, Mrad N. Single-walled carbon nanotube–modified epoxy thin films for continuous crack monitoring of metallic structures. Structural Health Monitoring. Volume 11, 2012. (https://doi.org/10.1177/1475921712449509).

[16] Takiuti BE, Júnior VL, Brennan MJ, Sakamoto WK, Malmonge JA, Orlandi MO. Development and characterization of an ITO nanocomposite film sensor for damage detection. Conference Proceedings of the Society for Experimental Mechanics Series. Volume 7, 2016. (https://doi.org/10.1007/978-3-319-29956-3_1/COVER).

THE INFLUENCE OF PLASTICIZERS ON THE CONDUCTIVITY OF NANOCOMPOSITE FILMS OF REGENERATED CELLULOSE AND SILVER NANOPARTICLES

Lays F. de M. S. Kataoka [a]*, Michaella S. B. Fialho [b], Maria del P. H. Falla [c], Sandra M. da Luz [d]

(a) 0000-0003-1766-7509 (University of Brasília – Brazil)
(b) 0000-0002-8709-7081 (University of Brasília – Brazil)
(c) 0000-0003-1623-9510 (University of Brasília – Brazil)
(d) 0000-0002-2223-0021 (University of Brasília – Brazil)
* Corresponding author: lays.furtado94@gmail.com

Abstract: Conductive films of regenerated cellulose can be promising for applications in electronic devices, aiming to replace synthetic polymers and high-density rigid glasses, which cause environmental impacts due to accelerated consumption of non-renewable and non-biodegradable resources. However, the application of these films faces structural challenges that may compromise their performance, and the addition of plasticizers appears as a possible solution to improve the physical properties of these materials, such as conductivity. This work studied the conductivity of nanocomposite films of regenerated cellulose and silver nanoparticles (AgNPs) as a function of different plasticizers. To obtain the films, bleached cellulose extracted from jute fiber was used, dissolved in an aqueous solution of NaOH and regenerated in water. The methodology involved the addition of 15 wt.% of carboxymethylcellulose (CMC), sorbitol, and glycerol as plasticizers for the films. Additionally, AgNPs were synthesized from sodium borohydride and silver nitrate and incorporated into the nanocomposites (0.5 wt.%). The conductivity of the nanocomposite films was obtained through sheet resistance measurements using the Vander Pauw Method. Overall, the nanocomposites showed a significant improvement in conductivity, ranging from 10^{-2} to 10^{-1} S/cm compared to the nanocomposite without plasticizer. The CMC plasticizer provided the best conductivity values in the nanocomposite, followed by glycerol and then sorbitol.

1. INTRODUCTION

Environmental and economic concerns have been driving research in designing new materials for electronic devices [1]. Electronic devices primarily comprise fossil-origin polymers and rigid, dense glasses, which have environmental impacts due to the accelerated consumption of non-renewable resources [2]. Thus, biopolymers derived from renewable natural resources can mitigate environmental impacts at the end of life of these devices [1,3], besides offering attractive properties such as non-toxicity, biodegradability, compostability, biocompatibility, and film-forming capacity [4,5].

Among biopolymers, cellulose is abundant, renewable, and naturally occurring, obtainable from natural fibers, such as jute. Additionally, it can be used to produce conductive films through cellulose regeneration and applied in sensors, transistors, solar cells, supercapacitors, electromagnetic shielding, and other electronic elements [5]. To obtain regenerated cellulose films, cellulose must undergo a dissolution process and subsequent coagulation. Among the cellulose solvent systems, alkaline solutions like sodium hydroxide (NaOH) are considered economical and do not use or produce toxic substances or derivatives

throughout the process [6]. To provide conductivity in these regenerated cellulose films, conductive materials such as silver nanoparticles can be inserted during cellulose regeneration, resulting in excellent conductivity [7].

In a previous study, the obtained film showed promising conductivity results. However, the film's structure proved fragile because, in general, the mechanical properties of films obtained by aqueous NaOH-based solvents, even with additives, are affected [6,7]. Thus, incorporating plasticizers can improve their flexibility, elasticity, and strength while reducing their rigidity and fragility [8].

The proper selection of plasticizers is influenced by various factors, such as compatibility between the polymers used and the desired final properties [9]. In regenerated cellulose conductive films, the insertion of plasticizers should be a focus of study as they can promote various changes in mechanical properties, transmittance, chemical composition, thermal stability, and conductivity [10]. Among the plasticizers, glycerol, sorbitol, and carboxymethylcellulose (CMC) are derived from renewable sources and can produce regenerated cellulose films [11]. Therefore, these regenerated cellulose conductive films can be considered a more sustainable choice than petrochemical polymers due to the use of renewable raw materials in their manufacturing and biodegradation capacity.

In regenerated cellulose conductive films, the insertion of plasticizers is a research gap. While studies on the insertion of plasticizers in regenerated cellulose films can be found, they are not used in films with the insertion of conductors. Hence, in this study, we evaluated the conductivity of regenerated cellulose film from jute fibers by adding silver nanoparticles (AgNPs) and CMC, sorbitol, or glycerol as plasticizing agents.

2. METHODOLOGY

2.1. Synthesis of silver nanoparticles

To obtain the silver nanoparticle solution, 450 mL of an 18.0×10^{-6} mol/L sodium borohydride (NaBH$_4$, 98%, Dynamic) solution was kept below 3 °C in an ice bath and added to an Erlenmeyer flask under vigorous magnetic stirring. Through a burette, 150 mL of a 9.0×10^{-6} mol/L solution of silver nitrate (AgNO$_3$, 99.9%, Neon) was added at an additional rate of 1 drop/s. The chemical reaction between NaBH$_4$ and AgNO$_3$ in those concentrations resulted in AgNPs at 250 ppm. To avoid silver nanoparticle aggregation, the solution was stabilized with 0.6 g of CMC (Sigma–Aldrich), which coats the nanoparticles.

2.2. Obtaining Regenerated Cellulose Films (RCF) with Silver Nanoparticles

The bleached jute cellulose was obtained in previous work [7]. Then, it was ground in an automatic analytical mill Quimis Q298A for 30 seconds. Depending on the sample, as shown in Table 1, each solution was prepared as follows: To obtain the RCF film, 2.2 g of cellulose was dissolved in 100 mL of a pre-cooled solution (-12°C for 18 h) containing 8% (w/v) NaOH solution. The solution was kept in a freezer for at least 18 h to reach around -12°C equilibrium to achieve the cooling conditions. Also, to obtain the RCF with the AgNPs, 26 mL of nanoparticle solution at 250 ppm was added to achieve 0.5 wt.% of silver nanoparticle content before the pre-cooling. To prepare the RCF films with the plasticizers, the CMC, sorbitol (98%, Dynamic), and glycerol (98%, Synth) in an amount corresponding to 15 wt.% concerning cellulose were added to the pure RCF solution. The exact process was performed for the nanocomposites, which resulted in nanocomposites containing 15 wt.% of plasticizer and 0.5 wt.% of silver nanoparticle. To dissolve the solution, all samples were submitted under vigorous stirring at 3000 rpm and room temperature every 7 min.

Table 1. Composition of regenerated cellulose films.

Sample	Plasticizer (wt.%)	AgNP (wt.%)	Sample	Plasticizer (wt.%)	AgNP (wt.%)
RCF	-	-	RCF - Sorbitol	15% Sorbitol	-
RCF - AgNP	-	0.5%	RCF - Sorbitol - AgNP	15% Sorbitol	0.5%
RCF - CMC	15% CMC	-	RCF - Glycerol	15% Glycerol	-
RCF - CMC - AgNP	15% CMC	0.5%	RCF - Glycerol - AgNP	15% Glycerol	0.5%

To mold the films and regenerate the cellulose, the mixture containing cellulose and nanoparticles was subjected to centrifugation at 4000 rpm for 10 min to exclude the undissolved part and perform degassing. Then, 7 mL of the resulting solution was poured onto a polypropylene Petri dish with a diameter of 85 mm. The RCF and nanocomposite films were pre-dried at room temperature for 18 h until gelation. Afterward, the

sample was immersed in a water bath (distilled water) at room temperature for 15 min to thicken and regenerate the cellulose. Finally, the films were dried at room temperature for 48 h before the characterization.

2.3. Electrical Measurements of Films by the Van der Pauw Method

Using the Van der Pauw method for thin film characterization, sheet resistance measurements of nanocomposite films were acquired via four-point measurements utilizing the Agilent B1500A Semiconductor Device Analyzer. The samples underwent current ranging from 100 uA to 1 mA with a 10 uA increment, reaching a maximum of 1 V. To calculate resistivity and conductivity, film thicknesses were gauged using a Mitutoyo digital micrometer (with an error margin of 0.001mm), measured at 10 points across the material.

From the sheet resistance measurements (R_s), expressed in units of ohms per square ($\Omega/\square$) e and the uniform thickness of the films (t), the sheet resistivity (ρ_s) can be obtained using Equation 1.

$$\rho_s = R_s . t \quad [\Omega . cm] \tag{1}$$

Where the sheet conductivity (σ_s) can then be calculated using Equation 2:

$$\sigma_s = \frac{1}{\rho_s} \quad [S/cm] \tag{2}$$

3. RESULTS AND DISCUSSION

3.3 Electrical Characterization of Films

The conductivity of regenerated cellulose films can be influenced by the concentration of AgNPs [7]. Nevertheless, there is a lack of literature examining these films with the inclusion of plasticizers. Thus, due to their nearly two-dimensional structure, the Van der Pauw method enables the assessment of the electrical characteristics of these nanocomposite-regenerated cellulose films, thereby minimizing experimental inaccuracies such as those arising from contact misalignment [12].

Figure 1 shows graphs of sheet resistance measurements for one sample of each nanocomposite film carried out by the Van der Pauw method. The graph provides the film's sheet resistance ($\Omega/\bullet$) and the potential difference (DeltaV) generated as a function of the applied electrical current (i) to the film. The sheet resistance taken for each sample is the highest value measured in the sheet resistance curve, denoted as R-sheet.

The DeltaV curve is generated by varying voltage as a function of the defined applied current in the system. This voltage variation calculates the sheet resistance of the samples according to Equation 2. The sheet resistance is obtained at its maximum value, given by the highest point of the curve [13,14].

Silver nanoparticles (AgNP) were deposited onto the nanocomposite films to act as a conductive electron pathway. The sheet resistance of all samples was measured at current (I) values of 0.0001 A. In all nanocomposites, there was a decrease in sheet resistance with the applied current. For the plasticized nanocomposites, the R-sheet and DeltaV curves are similar, and starting from 0.0004 A, the R-sheet curve begins to stabilize with sheet resistance below 500 ($\Omega/\square$), and at 0.001 A, it varies between 170 and 200 ($\Omega/\square$).

For the RCF - AgNP film, there is oscillation throughout the current application range, as seen in a previous study [7], both for R-sheet and DeltaV. Despite the decrease in sheet resistance with increasing current, the structure of pure regenerated cellulose may cause resistivity in the film, since incorporating plasticizers into the nanocomposites shows smooth and regular curves and decreasing sheet resistance.

Other studies have shown the effect of increased conductivity with plasticizer incorporation. Composite films of polyurethane/regenerated cellulose nanoparticles (RCNs)/PEDOT showed increased conductivity with incorporating RCNs acting as plasticizers, improving the films' mechanical properties [10]. In polyaniline and nitrile rubber blends, conductivity increased using imidazolium-based ionic liquids as plasticizers [15]. Table 2 shows the conductivity average values of the nanocomposite films.
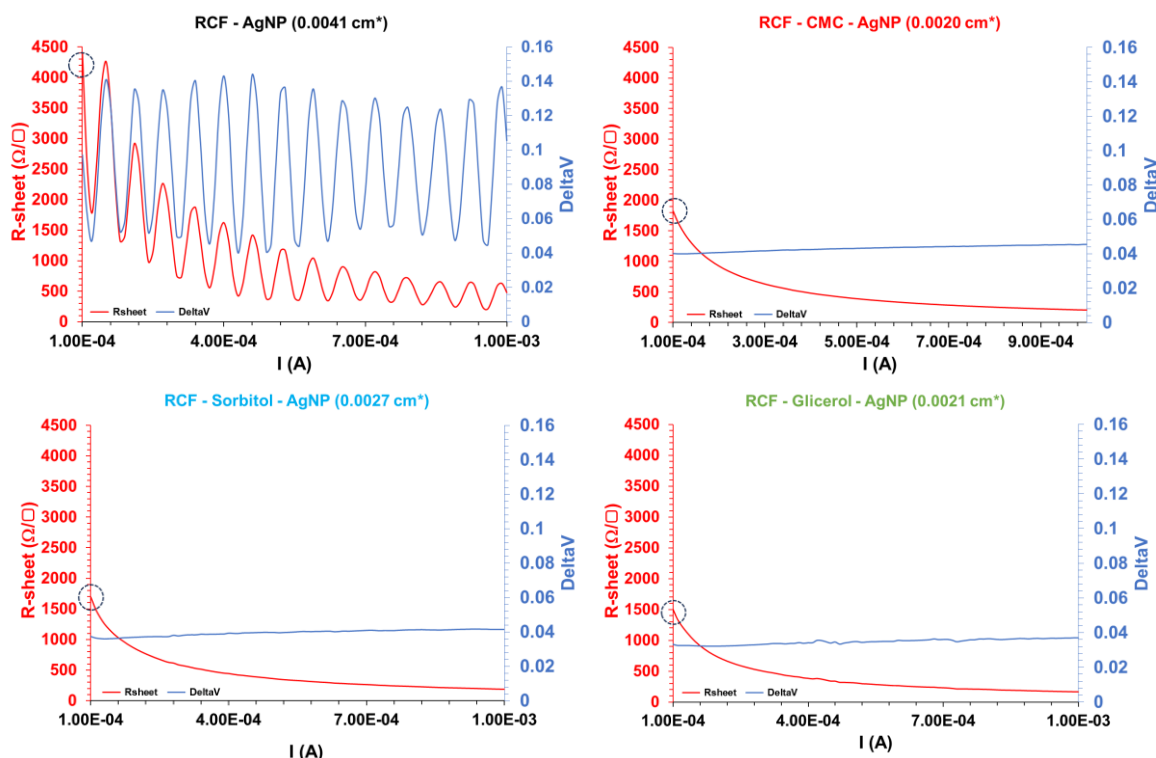
Figure 1. Resistance sheet and DeltaV graphs as a function of applied current for nanocomposite films using Van der Pauw's four-point method.

Table 2. Conductivity data for nanocomposites.

Sample	Conductivity Average (S/cm) [*1]
RCF - AgNP	0.06836 ±0.0230
RCF - CMC - AgNP	0.2682 ± 0.0504
RCF - Sorbitol - AgNP	0.1774 ± 0.0359
RCF - Glycerol - AgNP	0.2260 ± 0.0506
RCF [*2] [7]	3.28×10^{-2}
RCF – 0.290% AgNP [*2] [7]	5.32×10^{-2}

[*1] Three films of each nanocomposite studied were analyzed. For each film, electrical measurements were carried out in quadruplicate. [*2] Literature data.

Due to the inclusion of plasticizers, nanocomposites incorporating these components experienced an enhancement in conductivity, transitioning from the range of 10-2 to 10-1 in comparison to RCF—AgNP with identical nanoparticle content. This resulted in an increase of 292% for RCF—CMC—AgNP, 159% for RCF—Sorbitol—AgNP, and 231% for RCF—Glycerol—AgNP.

As a plasticizer, CMC yielded superior conductivity values in the nanocomposite, followed by glycerol and sorbitol. The variance in conductivity between the plasticized films RCF - CMC - AgNP with higher conductivity and RCF - Sorbitol - AgNP with lower conductivity was 51.2%.

The electrical data for pure RCF and the nanocomposite containing 0.290% AgNP, as detailed in Table 2, indicate that increasing the silver nanoparticle content from 0.290% to 0.5% in RCF – AgNP (without plasticizer) resulted in a 28.5% increase in conductivity. Furthermore, there was a remarkable 717.8% increase in the conductivity of RCF - CMC – AgNP compared to the conductivity of pure RCF [7].

Conductive films of regenerated cellulose in the order of magnitude of 10-2 to 10-1 S/cm, found for the nanocomposite films in this study, may show potential promise for applications such as supercapacitors [16–18], deformation sensors [19], electromagnetic interference shielding [20,21], and antistatic cellulose films [22].

4. CONCLUSIONS

The nanocomposites containing plasticizers exhibited a significant improvement in conductivity due to the incorporation of these components, transitioning from the range of 10^{-2} to 10^{-1} compared to RCF - AgNP with the same nanoparticle content, as well as showing smooth and regular curves in sheet resistance, indicating effective film plasticization. There was an increase of 292.3% for RCF - CMC - AgNP, 159.50% for RCF - Sorbitol - AgNP, and 230.6% for RCF - Glycerol - AgNP compared to RCF - AgNP. The CMC plasticizer provided better conductivity values in the nanocomposite, followed by glycerol and sorbitol. Therefore, it is possible to observe that plasticizers directly influenced the nanocomposites' conductivity.

Based on the results, the RCF—CMC—AgNP nanocomposite exhibited the best application properties in terms of conductivity. However, the mechanical properties of this nanocomposite should be evaluated to determine if it is indeed the nanocomposite with the best properties for electronic device applications.

4.1. Declaration of Competing Interest

The authors declare no conflict of interest.

4.2. Acknowledgements

5. REFERENCES

[1] Alves C, Ferrão PMC, Silva AJ, Reis LG, Freitas M, Rodrigues LB, et al. Ecodesign of automotive components making use of natural jute fiber composites. J Clean Prod 2010;18:313–27. https://doi.org/10.1016/j.jclepro.2009.10.022.

[2] Wang S, Lu A, Zhang L. Recent advances in regenerated cellulose materials. Prog Polym Sci 2016;53:169–206. https://doi.org/10.1016/j.progpolymsci.2015.07.003.

[3] Leao AL, Rowell ; Roger, Tavares N. Applications of Natural Fibers in Automotive Industry in Brazil — Thermoforming Process. Science and Technology of Polymers and Advanced MateriJJ/s 1998:755–61. https://doi.org/doi:10.1007/978-1-4899-0112-5_66.

[4] Van Vlierberghe S, Dubruel P, Schacht E. Biopolymer-based hydrogels as scaffolds for tissue engineering applications: A review. Biomacromolecules 2011;12:1387–408. https://doi.org/10.1021/bm200083n.

[5] Liu X, Xiao W, Ma X, Huang L, Ni Y, Chen L, et al. Conductive Regenerated Cellulose Film and Its Electronic Devices – A Review. Carbohydr Polym 2020;250:1–16. https://doi.org/10.1016/j.carbpol.2020.116969.

[6] Budtova T, Navard P. Cellulose in NaOH–water based solvents: a review. Cellulose 2016;23:5–55. https://doi.org/10.1007/s10570-015-0779-8.

[7] Kataoka LF de MS, Leão RM, Gontijo AB, Falla M del PH, Luz SM. Regenerated cellulose films from jute fibers applied in conductive nanocomposites. Mater Today Commun 2022;33. https://doi.org/10.1016/j.mtcomm.2022.104645.

[8] Callister W, Rethwisch D. Materials science and engineering: an introduction. Materials Science and Engineering. vol. 94. 7th ed. New York: John Wiley & Son; 2007.

[9] Cheremisinoff NP. Advanced Polymer Processing Operations. 1st ed. New Jersey: Noyes Publications; 1998.

[10] Choi SM, Han SS, Shin EJ. Highly Stretchable Conductive Nanocomposite Films Using Regenerated Cellulose Nanoparticles. ACS Appl Polym Mater 2020;2:4387–98. https://doi.org/10.1021/acsapm.0c00294.

[11] Pang J, Liu X, Zhang X, Wu Y, Sun R. Fabrication of cellulose film with enhanced mechanical properties in ionic liquid 1-allyl-3-methylimidaxolium chloride (AmimCl). Materials 2013;6:1270–84. https://doi.org/10.3390/ma6041270.

[12] Pauw LJ van der. A method of measuring specific resistivity and Hall effect of discs of arbitrary shapes. Philips Research Report 1958;13:1–9.

[13] Technologies K. Sheet Resistance/Resistivity Measurement Using a Source/Measurement Unit (SMU) - Application Note 2016.

[14] Luz GVS, Hui WangS, Roncoleta RC, Nogueira PHO, Brasil LM, Hidalgo P. Assembly and characterization of ZnO nanoparticles for Grätzel's solar cells. Adv Mater Lett 2018;9:284–90. https://doi.org/10.5185/amlett.2018.1599.

[15] Prudêncio L, Camilo FF, Faez R. Líquidos iônicos como plastificantes em blendas de borracha nitrílica/polianilina. Quim Nova 2014;37:618–23. https://doi.org/10.5935/0100-4042.20140103.

[16] Liu S, Yu T, Wu Y, Li W, Li B. Evolution of cellulose into flexible conductive green electronics: A smart strategy to fabricate sustainable electrodes for supercapacitors. RSC Adv 2014;4:34134–43. https://doi.org/10.1039/c4ra07017h.

[17] Zhao D, Chen C, Zhang Q, Chen W, Liu S, Wang Q, et al. High Performance, Flexible, Solid-State Supercapacitors Based on a Renewable and Biodegradable Mesoporous Cellulose Membrane. Adv Energy Mater 2017;7. https://doi.org/10.1002/aenm.201700739.

[18] Tian J, Peng D, Wu X, Li W, Deng H, Liu S. Electrodeposition of Ag nanoparticles on conductive polyaniline/cellulose aerogels with increased synergistic effect for energy storage. Carbohydr Polym 2017;156:19–25. https://doi.org/10.1016/j.carbpol.2016.09.005.

[19] Mun S, Zhai L, Min SK, Yun Y, Kim J. Flexible and transparent strain sensor made with silver nanowire-coated cellulose. J Intell Mater Syst Struct 2016;27:1011–8. https://doi.org/10.1177/1045389X15577651.

[20] Chen J, Xu J, Wang K, Qian X, Sun R. Highly Thermostable, Flexible, and Conductive Films Prepared from Cellulose, Graphite, and Polypyrrole Nanoparticles. ACS Appl Mater Interfaces 2015;7:15641–8. https://doi.org/10.1021/acsami.5b04462.

[21] Lee TW, Jeong YG. Regenerated cellulose/multiwalled carbon nanotube composite films with efficient electric heating performance. Carbohydr Polym 2015;133:456–63. https://doi.org/10.1016/j.carbpol.2015.06.053.

[22] Huang HD, Liu CY, Zhang LQ, Zhong GJ, Li ZM. Simultaneous carbon nanotube/cellulose conductive nanocomposite film reinforcement and toughening by interfacial hydrogen bonding. ACS Sustain Chem Eng 2015;3:317–24. https://doi.org/10.1021/sc500681v.

THERMAL CHARACTERIZATION COMPARISON BETWEEN COMMERCIAL PLA AND PLA/GRAPHENE FILAMENTS

Fernando Henrique Rufino Resende[a]*, Carlos Eduardo Moraes[b], Luis Felipe de Paula Santos[c], João Victor Passos Neves Gomes [d], Larissa Stieven Montagna [e], Jefferson Patrício Nascimento [f], Bruno Ribeiro[g], Edson Cocchieri Botelho[h], Michelle Leali Costa[i]

(a) ⓘ 0009-0000-4454-6580 (UNESP - São Paulo State University and Maxion Wheels - USA)
(b) ⓘ 0000-0001-7095-1029 (UNESP - São Paulo State University – Brazil)
(c) ⓘ 0000-0002-5089-1089 (Laboratório de Estruturas Leves – LEL/IPT – Brazil; UNESP - São Paulo State University – Brazil)
(d) ⓘ 0000-0002-6825-7238 (Institute for Technological Research - Brazil)
(e) ⓘ 0000-0002-7947-3112 (Laboratório de Tecnologia em Polímeros e Biopolímeros – TecPBio; Universidade Federal de São Paulo – UNIFESP - Brazil)
(f) ⓘ 0000-0002-8756-011X (Laboratório de Estruturas Leves – LEL/IPT – Brazil; UNESP - São Paulo State University – Brazil)
(g) ⓘ0000-0002-0078-9641(Laboratório de Estruturas Leves - LEL/IPT; UNESP - São Paulo State University - Brazil)
(h) ⓘ 0000-0001-8338-4879 (UNESP - São Paulo State University – Brazil)
(i) ⓘ 0000-0001-9492-8544 (Instituto Ganesha de Inovação – Tecnologia e Ciência- Brazil; UNESP - São Paulo State University – Brazil)
* Corresponding author: fernandohrresende@hotmail.com

Abstract: The primary objective of this study is to characterize two types of commercial filaments (PLA and PLA/graphene) and assess the influence of graphene on their thermal properties. The filaments characterization was performed using the following techniques: helium pycnometer density; X-ray diffraction (XRD); Raman spectroscopy; scanning electron microscopy (SEM); differential scanning calorimetry (DSC), thermogravimetry (TGA), and thermomechanical analysis (TMA). The results obtained by helium pycnometer density, XRD, Raman, and SEM confirmed the presence of graphenic material in the PLA/graphene filament. The glass transition and melting temperatures of PLA identified in this study exhibited an analogous value to PLA/graphene, and the melting enthalpy values were the same (28 J/g in both cases). The thermal decomposition temperature of PLA was 241°C, while the PLA/graphene was 254°C, indicating that graphene material may contribute to the increase in the decomposition temperature of PLA. The value obtained for the coefficient of thermal expansion of PLA and PLA/graphene was 87 μm/m°C. Finally, it can be concluded that the PLA/graphene filament could not present noteworthy variation in analyzed properties compared to PLA, indicating that a true composite was not formed and that graphenic material functions merely as a filler within the PLA matrix.

1. INTRODUCTION

The demand for polymers in the automotive industry has changed considerably in recent years. The natural evolution scenario, combined with the need to reduce carbon dioxide (CO_2) emissions, greatly valued the use of this type of material. With the popularization and increasing use of electric cars worldwide and the demand to adapt to this reality, the need to make them lighter emerged on the market, aiming to increase

autonomy and, thus, efficiency. One of the methods to achieve this objective is to reduce vehicle weight by using non-metallic materials, where polymers stand out, mainly those reinforced with continuous fibers, short fibers, and graphene materials, among others [1].

The automotive industry has increasingly sought to use additive manufacturing in addition to focusing on the use of polymers. This method has revolutionized how the parts are being produced, allowing the development of products quickly without the need for molds. This technology has advantages compared to conventional processes, such as versatility, cost reduction, production agility, etc. [2].

Among the polymers currently available, one that has stood out mainly for its use in additive manufacturing is PLA, a biodegradable aliphatic polyester from renewable resources with high rigidity, high mechanical resistance, and ease of use [3].

Another material that has stood out is graphene, considered the fundamental building block of all graphitic forms of carbon, formed by a single layer of carbon atoms, possessing excellent physical properties, such as high modulus, high thermal conductivity, high electronic mobility, etc. Since it has all the advantages mentioned above, it has been used in several applications, such as energy storage materials, electronic devices, nanocomposites, etc. [4].

Recent studies have demonstrated that graphene-reinforced PLA nanocomposites are promising for obtaining improved mechanical properties of parts produced using the additive manufacturing method [3]. Thus, this study aims to characterize two types of commercial filaments (PLA and PLA/graphene) and assess the influence of graphene on their thermal properties.

2. METHODOLOGY

2.1. Materials

The materials used in this study were 3D printer filaments made from two different types of materials: PLA and PLA/graphene. Both were purchased from Voolt3D company. The filament diameter is 1.75mm, and the recommended printing temperature is 190°C to 210°C. The bed temperature should be above 60°C.

The filaments supplier (Voolt3D) did not provide further information about their graphene (type of graphene, quantity, concentration, etc.).

2.2. Methods

The equipment used for the specific mass test was the Helium Pycnometer from Quantachrome Instruments, model Ultrapyc 1200e, with a pressure of 17 MPa. This equipment uses helium gas to calculate the volume and provides the specific mass based on the measurement sample mass. The equipment performs three-volume and density measurements and prints all values with the average and standard deviation. This study analyzed a PLA filament sample and a PLA/graphene filament sample were analyzed. Each sample was measured three times. They have a diameter of 1.75 mm and a length of approximately 17 mm.

The X-ray diffraction test was carried out using Bruker equipment, model D8 Advance Eco, with a Copper (Cu) tube with a wavelength of 1.5418 Å, voltage of 40 kV, and current of 25 mA. The scanning speed was 10°/min and an angular increment of 0.01°. The diffractogram was obtained in the region of $2\theta = 10\text{-}50°$.

The morphology of the cryo-fractured surface of the PLA and PLA/graphene samples was investigated on FEI (Inspect S50) equipment operated at 12.5 keV. The sample was fractured with liquid nitrogen fixed in an aluminum sample holder and metalized with a thin layer of gold.

DSC analyses were conducted using TA Instruments equipment, model Q20. PLA and PLA/graphene samples weighing approximately 5 mg were encapsulated in an aluminum sample holder and heated from 30°C to 230°C at a heating rate of 10°C/min in an N2 atmosphere of 50 mL/min. Later, an isotherm at 230°C for 5 minutes was applied, followed by cooling to 30°C at a heating rate of 10°C/min. Finally, the sample was re-heated from 30°C to 230°C at a heating rate of 10°C/min.

TGA analyses were performed on the SII Nanotechnology equipment, model TG/DTA 6200. The samples (~10 mg) were heated from 30°C to 900°C at a heating rate of 10°C /min in nitrogen atmosphere (100 mL/min) and synthetic air (100 mL/min).

Thermomechanical analysis (TMA - SII Nanotechnology, TMA/SS6100 model) was carried out to obtain linear thermal expansion coefficients of both materials. The temperature range was 25°C to 140°C, with a heating rate of 3°C/min, tested in thermal expansion mode. The analyzed samples had dimensions of 10 mm x 10 mm.

The Raman spectroscopy measurements were performed on a Witec Alpha 500RA Raman/AFM spectrometer equipped with a confocal microscope. CCD detectors in single spectrum mode were conducted

in three different regions, ranging from 500 cm-1 to 3500 cm-1, using a 532 nm laser line (2.33 eV) with ~0.5 mW power, three accumulations with integration time of 120s, diffraction grating of 600 lines/mm, and 100x objective. The PLA and the PLA/graphene materials were embedded in resin with subsequent sanding and polishing steps for all measurements. The obtained spectra were analyzed using Peak Fit software using theoretical adjustment with a Lorentzian function.

3. RESULTS AND DISCUSSION

3.1. Specific mass

The PLA sample mass was 0.1417g, while the PLA/graphene mass was 0.1377g. The Table 1 provides information about volume, specific mass, and standard deviation from helium pycnometer measurements.

Table 1. PLA and PLA/graphene filaments specific mass.

Material	Standard deviation (volume)	Volume (average) [cm^3]	Specific mass (average) [g/cm^3]
PLA	0.0011	0.1000	1.4174
PLA/graphene	0.0018	0.0961	1.4336

As can be seen the specific mass of the PLA/graphene filament is 1.14% greater than the specific mass of the PLA material. This difference may corroborate the existence of graphene material in the composition of the PLA/graphene filament.

3.2. X-ray diffraction (XRD)

Figures 1a and 1b represent the diffractograms for neat PLA and the PLA/graphene composite. According to the results, PLA presents a characteristic diffraction peak at 2Θ = 17°, belonging to the plane (200/110), corresponding to the α shape of PLA. The incorporation of graphene particles is responsible for the appearance of a peak at 2Θ = 26.8° belonging to the (002) plane, commonly found in graphene materials [5]. These results may indicate that the graphene material existing in the PLA/graphene filament may consist only of layers of graphene or even a mixture of graphene, graphite, or graphite nanoplates, corroborating the Raman result.
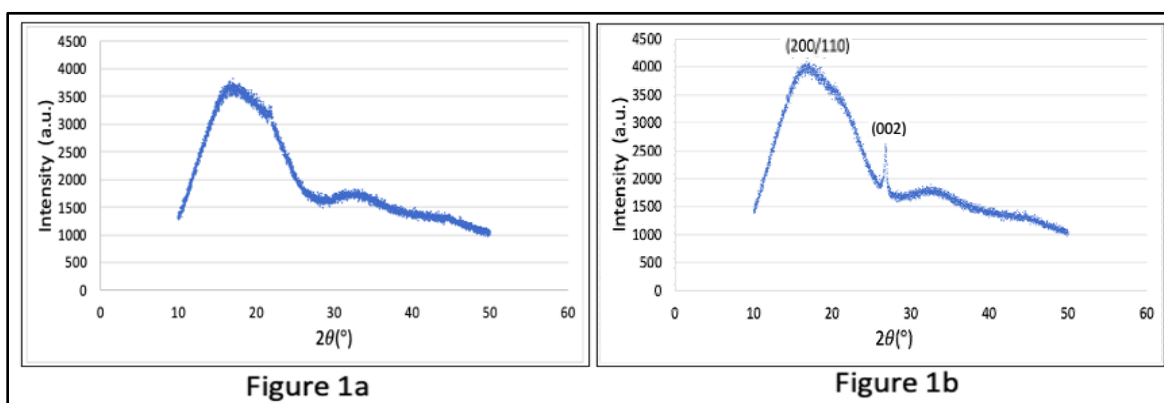
Figure 1. X-ray diffraction diagram for the PLA **(1a)** and PLA/graphene **(1b)** filament.

The Raman spectroscopy spectra (Figure 2) obtained in different sample regions present all the PLA characteristic bands according to the literature: (~2951 cm^{-1}), (~3006 cm^{-1}), (~2889 cm^{-1}), (~881 cm^{-1}) and (~705 cm^{-1}) [6].
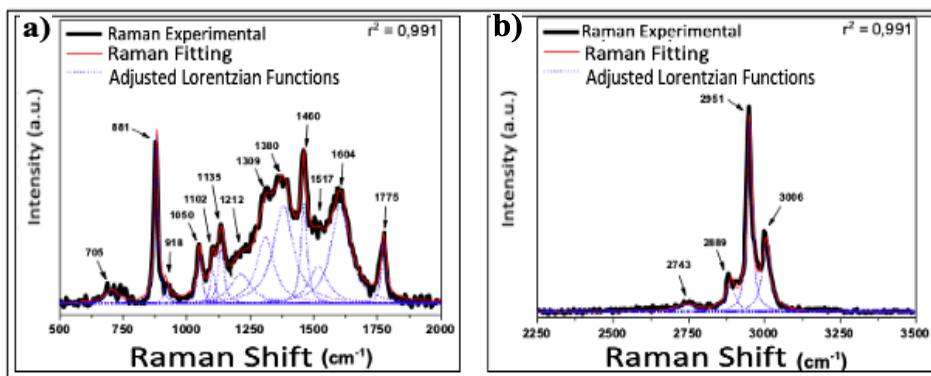
Figure 2. PLA Raman spectrum in the ranges of 500 cm^{-1} to 2000 cm^{-1} **(a)** and 2500 cm^{-1} to 3500 cm^{-1} **(b).**

It can be seen, in Figure 3, that the Raman spectra of the PLA/graphene material obtained in different sample regions present all the characteristic bands of graphene materials: D(~1357 cm^{-1}), G(~1588 cm^{-1}), D'(~1626 cm^{-1}) and 2D(~2700 cm^{-1}) [7]. This graphene material can be graphite/graphene nanoplates, micro graphite or graphite, being corroborated by the XRD results. It is worth mentioning that as this filament is commercial, there is no information whether it is added with graphene or graphene oxide. However, based in the literature [3] and the observed profile of the 2D band (Figure 3b) in the Raman test, it is possible to deduce that the material incorporated is probably graphene and not graphene oxide. Nevertheless, more in-depth characterizations with other techniques, such as Fourier-transform infrared spectroscopy (FTIR) and X-ray photoelectron spectroscopy (XPS) are necessary to confirm this observation.
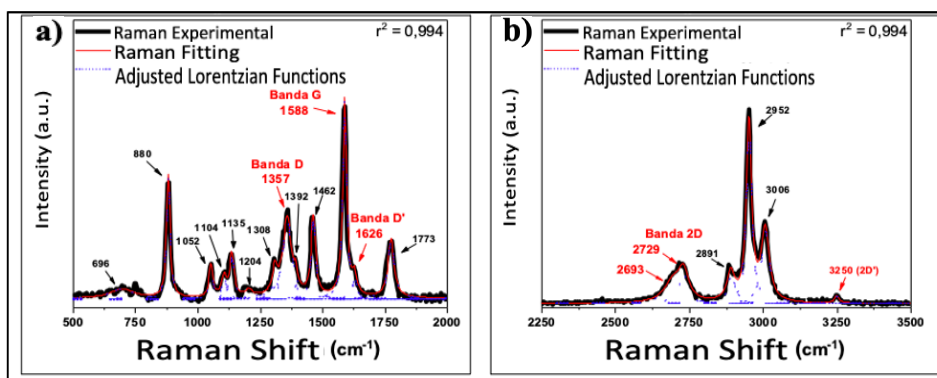
Figure 3. PLA/graphene Raman spectrum in the ranges of 500 cm^{-1} to 2000 cm^{-1} **(a)** and 2500 cm^{-1} to 3500 cm^{-1} **(b).**

3.3. Scanning Electron Microscopy

The morphology of the PLA/graphene filament was evaluated by SEM and is shown in Figures 4a and 4b. The graphene dispersion in the polymer matrix is observed to be relatively homogeneous throughout the studied area (blue arrows in the figure). The particles appear to have 10-30 µm sizes, suggesting the incorporation of non-exfoliated material (graphite or nanographite). In addition to the particles mentioned, smaller particles, ranging from 2 to 5 µm, are distributed throughout the sample, which suggests the presence of graphene particles in the PLA matrix. It is worth mentioning that as this filament is commercial, there is no information on whether it is added with graphene or graphene oxide. As suggested in the literature [3], however, based on the observed profile of the 2D band in the Raman test, it is possible to conclude that the material is graphene, not graphene oxide.
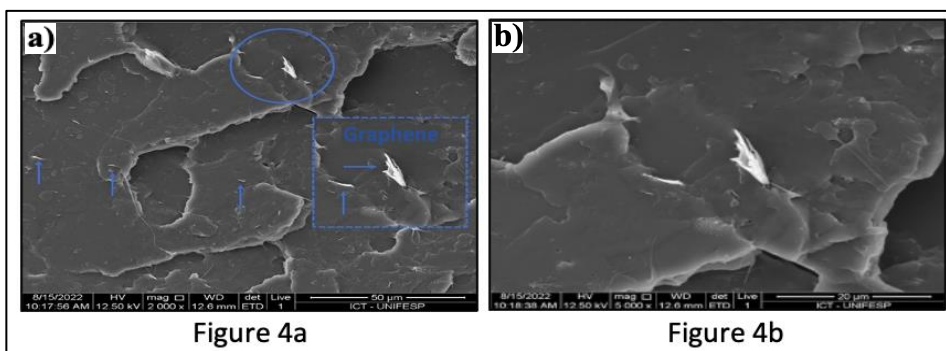
Figure 4. SEM image for the PLA/graphene filament - 2,000x **(a)** and SEM image for the PLA/graphene filament - 5,000x **(b)**

3.4. Differential Scanning Calorimetry

The DSC analyses were performed in dual scan; that is, the samples were heated, cooled, and heated again. Figures 5,6 and 7 show the DSC curve of the PLA filament and the PLA/graphene filament for the first heating, cooling, and second heating.
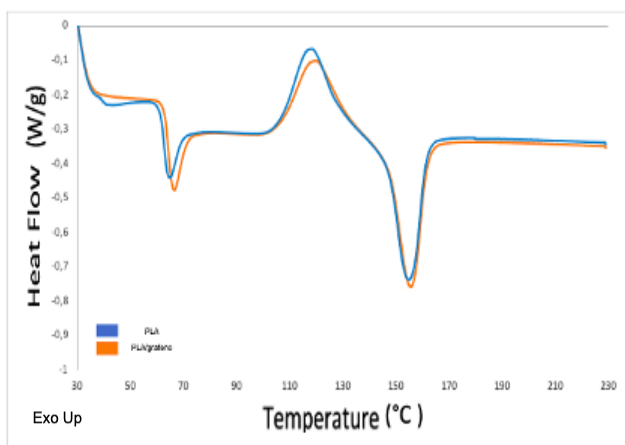
Figure 5. PLA and PLA/graphene curves: first heating.
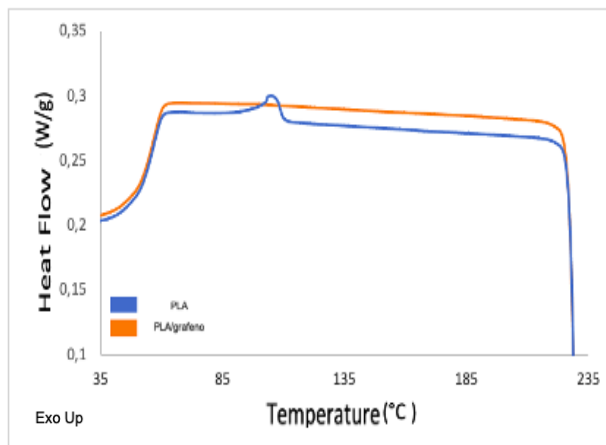
Figure 6. PLA and PLA/graphene curves: cooling.
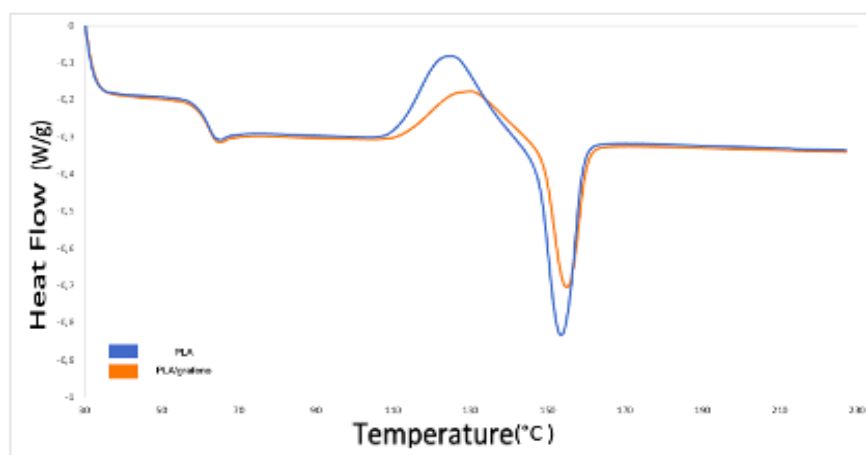
Figure 7. PLA and PLA/graphene curves: second heating.

As Figure 7 shows, unlike the first heating curve, the PLA filament does not have an endothermic peak associated with the glass transition temperature (Tg) once the material already had the thermal relaxation process. The Table 2 shows the results obtained from the DSC analyzes.

Table 2. Thermal properties from the DSC tests.

Thermal Property	Thermal Event	PLA	PLA/graphene
Melting temperature	First Heating	155 °C	156 °C
	Second Heating	153 °C	155 °C
Glass transition temperature (Tg)	First Heating	61 °C	63 °C
	Second Heating	61 °C	61 °C
Enthalpy of fusion	First Heating	28 J/g	28 J/g
	Second Heating	26 J/g	18 J/g
Crystallization temperature	First Heating	118 °C	120 °C
	Second Heating	125 °C	130 °C
	Cooling	105 °C	N/A

3.5. Thermogravimetry

Figure 8 shows the TGA/DTG curve of the PLA filament performed in an N_2 atmosphere. It can be observed that the PLA thermal decomposition occurs in at least two steps, confirmed by the presence of two peaks in DTG. From 98 °C to 117 °C, there is a slight loss of 0.4% of the material weight, and this loss may correspond to the presence of volatiles such as moisture or other low molecular weight fractions. The second weight loss of 94.5% occurs between 241 °C and 494 °C. At the end of the analysis, a weight residue of 3.3% was observed at 885 °C. Based on the blue curve in Figure 8, which represents the derivate weight, it is observed that the maximum weight loss peak, where the mass weight loss is most significant, occurs at a temperature of approximately 365 °C. This temperature value is very similar to that found in the literature for neat PLA filaments, whose values range from 360 °C to 364 °C [8].
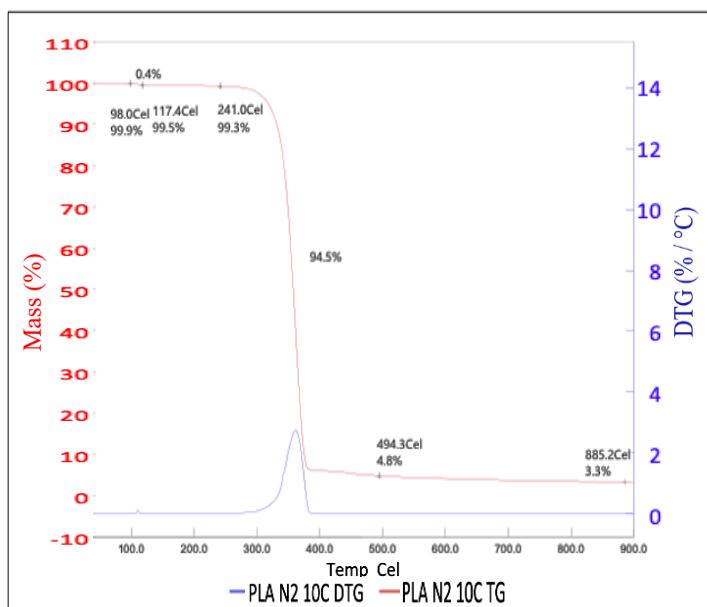
Figure 8. TGA/DTG curves of PLA
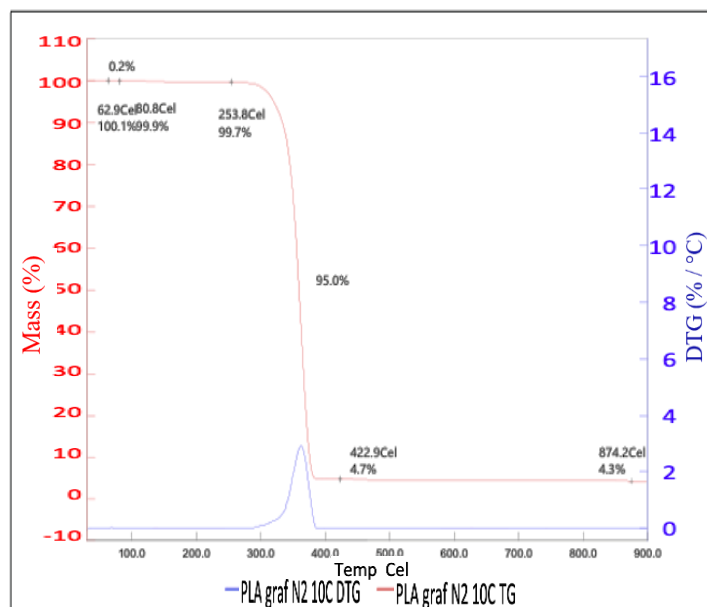
Figure 9. TGA/DTG curves of PLA/graphene

Figure 9 shows the weight/derivative weight curves of the PLA/graphene filament carried out in a N_2 atmosphere. It can be observed that the thermal decomposition of PLA/graphene occurs in at least one step, confirmed by the presence of a peak in derivative weight curve. The 95% weight loss occurs between 254°C and 423°C. At the end of the analysis, a weight residue of 4.3% was observed at 874°C. Starting from the premise that in the TGA analysis of neat PLA, a weight residue of 3.3% was observed and in PLA/graphene a weight residue of 4.3% was observed, it can be inferred that the difference of 1.0% is relative to the presence of graphene in the filament. As the supplier does not inform the content of graphene present in the sample, the

TGA analysis can be an indication of this concentration . This result corroborates the result of the specific mass test.

It can also be stated that the thermal decomposition event at 241°C observed for the neat PLA filament is delayed by the presence of graphene in the PLA/graphene filament, since this one occurs at 254°C. This behavior of improving the thermal stability of the PLA/graphene composite, compared to the neat PLA filament, can be explained by the presence of the barrier effect of the graphene layers, which causes the limitation of the emission of degradation gases and the heat transmission. Therefore, resulting in a material thermal stability improvement [9].

3.6. Thermomechanical Analysis (TMA)

Figure 10 shows the TMA curves for PLA and PLA/graphene filaments. The blue line represents the PLA curve, while the orange line represents the PLA/graphene curve. According to PLA curve, it is observed that with the increase of the temperature, firstly, the material thermal expansion occurs, accompanied by the PLA glass transition temperature (T_g), which can be verified at 63°C (similar to the value obtained in the DSC experiment: 61°C). Then, a second thermal event is observed, the PLA softening approximately at 84°C, which is related to its melting temperature. The PLA thermal expansion coefficient value obtained was 88 µm/m°C.
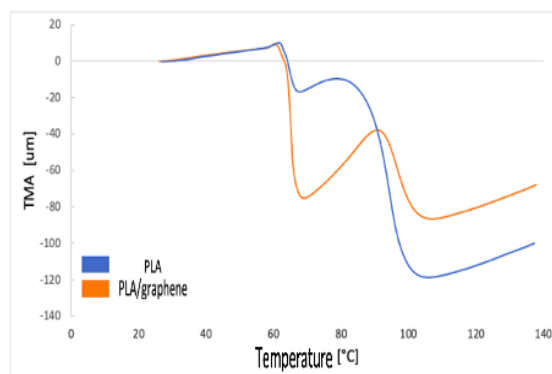
Figure 10. Curva de TMA dos filamentos de PLA e PLA/grafeno.

According to the PLA/graphene curve, two thermal events are observed. Firstly, a material thermal expansion occurs, accompanied by PLA/graphene glass transition temperature (T_g), which can be verified at 61°C (the same value obtained in the DSC test). Then, a second thermal event is observed: the PLA/graphene softening at approximately 96°C, which is related to its melting temperature.

Although no variation in Tg was observed with the addition of graphene to the filament, the softening temperature increased by 14% in PLA/graphene compared with neat PLA filament. The value obtained for the PLA/graphene thermal expansion coefficient was 87 µm/m°C. Therefore, it can be stated that there was no significant variation in the filament linear thermal expansion coefficient with the graphene addition.

4. CONCLUSIONS

Based on the tests performed and subsequent analysis, the main points to be highlighted are:

- The results of the specific mass test show that the PLA/graphene filament has a specific mass 1.14% higher than the specific mass of neat PLA. This difference may corroborate the existence of graphene material in the composition of the PLA/graphene filament.

- Analysis of the X-ray diffraction test on the PLA material indicates that a characteristic diffraction peak occurs for this filament, as observed in the literature, corroborating the results found. The incorporation of graphene particles is responsible for the appearance of a peak at $2\Theta = 26.8°$ belonging to the (002) plane, commonly found in graphene materials. This result agrees with what was found in the Raman and SEM tests. Therefore, the X-ray technique also proves the presence of graphene material in the PLA/graphene filament.

- The Raman spectra obtained from both PLA and PLA/graphene are in accordance with the literature, presenting all the characteristic bands of their respective materials. Regarding the PLA/graphene filament, graphene material (graphite/graphene nanoplate, micrographite, or graphite) exists in its composition, which is even supported by SEM results. Based on the profile observed in the 2D band in the Raman test, there is graphene and not graphene oxide.

- The SEM analysis reveals a relatively homogeneous dispersion of graphene in the polymer matrix. The particles appear to have sizes of the order of 10-30 µm, suggesting the incorporation of non-exfoliated material (graphite or nanographite). There is also the presence of smaller particles, ranging from 2 to 5 µm, distributed throughout the sample, which indicates the presence of graphene particles in the PLA matrix.

- The PLA glass transition temperature is close to that observed for PLA/graphene. The peak melting temperature of neat PLA filament is also similar to PLA/graphene, as well as the melting enthalpy values. Therefore, the addition of graphene to the PLA filament did not significantly change its thermal properties.

- The thermal decomposition temperature of 241°C observed for the neat PLA filament is delayed by the presence of graphene in the PLA/graphene filament since this occurs at 254°C.

- By TMA, it was observed that, although there was no significant variation in T_g with the addition of graphene to the filament, the softening temperature increased by 14% concerning the neat PLA filament. According to the results obtained, there was no significant variation in the linear thermal expansion coefficient of the filament with the addition of graphene.

- Finally, it can be concluded that the commercial PLA/graphene filament could not show notable variation in the analyzed properties compared to neat PLA, indicating that a true composite was not formed, and the graphene material only works as a filler within the PLA matrix. In further papers, the weight ratio of graphene into PLA will be determined and studied.

4.1. Declaration of Competing Interest

The authors declare no conflict of interest.

4.2. Acknowledgments

5. REFERENCES

[1] Compostos. *Indústria automotiva e o impacto dos veículos elétricos no uso de polímeros*. COMPOSTOS, 2021. (https://www.compostos.com.br/blog/industria-automotiva-e-polimeros), accessed 24 September 2023.

[2] Equipe Totvs. *O que é manufatura aditiva, tecnologias, vantagens e muito mais*. TOTVS, 2022. (https://www.totvs.com/blog/gestao-industrial/manufatura-aditiva), accessed 12 November 2023.

[3] L.V. Cambraia et al. Desenvolvimento de filamentos de PLA e óxido de grafeno para melhoria termomecânica de peças produzidos por impressão 3D. *Brazilian Journal of Development*, Volume 6, 2020. (https://doi.org/10.34117/bjdv6n9-419).

[4] S. Pattnaik, M.K. Sutar. Graphene Base Nanocomposites: An overview. *Materials Today: Proceedings*, Volume 18, 2019 (https://doi.org/10.1016/j.matpr.2019.07.572).

[5] J. Liesenfeld. Efeito do pós-processamento por recozimento sobre as propriedades do PLA impresso com e sem adiao de grafeno. LIESENFELD, 2023. (https://repositorio.ufsm.br/bitstream/handle/1/29629/DIS_PPGEM_2023_LIESENFELD_JANAINA.pdf?sequence=1 &isAllowed=y), accessed 10 January 2024

[6] A. Bouamer et al. Characterization of the Polylactic acid stretched uniaxial and annealed by Raman spectrometry and Differential scanning calorimetry. *IOP Conf. Series: Materials Science and Engineering*, Volume 461, 2019 (https:// doi:10.1088/1757-899X/461/1/012006)

[7] L. V. Cambraia. Desenvolvimento de filamentos de PLA e óxido de grafeno para melhoria termomecânica de peças produzidos por impressão 3D. *Brazilian Journal of Development,* Volume 6, 2020. (https:// doi:10.34117/bjdv6n9-419)

[8] L. Santana et al. Avaliacão da Composição Química e das caracteríticas térmicas de filamentos de PLA para impressoras 3D de código aberto. *Congresso Nacional de Engenharia Mecânica - CONEM 2016*, p. 1-9, 2016. (https://doi.org/10.20906/CPS/CON-2016-0378)

[9] R. B. Valapa, G. Pugazhenthi, V. Katiyar. Effect of graphene content on the properties of poly(lactic acid) nanocomposites. *RSC Advances*, Volume 5, 2015. (https://doi.org/10.1039/c4ra15669b).

DURABILITY OF FIBER-CEMENT REINFORCED WITH NATURAL FIBERS: A SYSTEMATIC REVIEW

Lóren F. Cruz [a], Arthur B. Aramburu[b]; Rafael A. Delucis [c], *

(a) ⓘ 0009-0001-0123-8497 (Federal University of Pelotas – Brazil)
(b) ⓘ 0000-0001-9842-6904 (Federal University of Rio Grande do Sul – Brazil)
(c) ⓘ 0000-0002-3657-9216 (Federal University of Pelotas – Brazil)
* Corresponding author: rafael.delucis@ufpel.edu.br

Abstract: Natural fibers have emerged as an economically and environmentally appealing material for reinforcing fiber-cement composites. However, there remains considerable scope for studying the durability of this composite, with a lack of standardized protocols for such investigations and a notable absence of systematic reviews on the subject. Durability is a crucial property for construction materials intended for long-term use, hence this systematic review addresses studies conducted on the durability of fiber-cement reinforced with natural fibers, aiming to provide a comprehensive overview of durability testing, with a focus on accelerated aging procedures in research on this material. Using the PRISMA protocol, 41 articles from databases such as SciFinder, Scopus, and Web of Science were analyzed, highlighting wood cellulosic pulp cellulosic pulp and sisal as predominant fibers. Wetting and drying cycles were the most used tests, followed by freeze-thaw cycles. The main characterization techniques were flexural strength testing and scanning electron microscopy. Results indicate that the durability of these composites is enhanced by specific fiber treatments, offering promising prospects for practical applications. Ultimately, the recognized patterns and prospective outlooks are outlined to aid in the more straightforward recognition of principal deficiencies and possibilities in the field.

1. INTRODUCTION

For a considerable time, asbestos constituted the predominant fiber in the fiber-cement market. However, presently, numerous countries enforce prohibitions on its usage due to the health complications afflicting workers involved in its production and handling. Consequently, extensive research endeavors have been undertaken to explore ecologically and economically viable reinforcement fibers for fiber-cement, including those derived from plant sources [1,2].

The utilization of plant fibers offers advantages such as low density, high specific mechanical strength, reduced cost, carbon neutrality, biodegradability, and favorable acoustic and thermal properties. However, their use in cementitious composites necessitates attention to certain challenges, such as water absorption, loss of ductility in humid and alkaline environments, and high variability of mechanical characteristics.

Studies on the durability of fiber-cement composites reinforced with plant fibers are also important, as adverse environments or structures exposed to severe weather conditions are critical factors in common applications of fiber-cement. Furthermore, the number of studies related to the durability of fiber-cement composites reinforced with plant fibers is also low. With a better understanding of the durability of these materials, it will be possible to promote their wider use in the construction industry, contributing to more sustainable and efficient construction practices.

Accelerated aging tests, *e.g.*, wet/dry (W/T) and freeze/thaw (F/T) cycling are laboratory procedures designed to simulate the harsh environmental conditions to which a material may be exposed during its lifespan

within a relatively short period. The aim is to replicate, in a short timeframe, the aging effects that would typically occur over several years in real-world situations.

Systematic reviews are more commonly found in fields such as Medicine, Psychology, Education, and Sciences, resulting in a scarcity of works of this nature in the field of Engineering. To date, the systematic review by Ahmad et al. [3], which addresses the mechanical properties of fiber-cement composites reinforced with plant fibers, has been the only one found on a subject similar to the present study. Therefore, the objective of this work is to conduct a systematic review to analyze the landscape of accelerated aging tests conducted to assess the durability of fiber-cement composites reinforced with plant fibers.

2. LITERATURE REVIEW

The aim of this review is to examine the application of accelerated aging tests in assessing the durability of fiber-cement composites reinforced with plant fibers. To achieve this, this systematic review was conducted following the methodological guidelines of the PRISMA protocol [4].

The articles were searched in three databases, SciFinder (http://www.scifnder.cas.org), Scopus (www.scopus.com), and Web of Science (www.webofknowledge.com). The search terms used were "(fiber OR fibre) AND cement AND (durability OR endurance) AND ("accelerated aging" OR cycles OR intemperism) AND properties". The results were limited to English articles published between 2013 and 2023, excluding reviews, conference papers, and book chapters. Duplicate articles from the database were then excluded. This selection and analysis of articles were conducted in September 2023.

Finally, the following exclusion criteria were applied: 1) The studied fibers were not of plant origin; 2) The type of composite studied was different from fiber-cement or mortar; 3) The article did not involve accelerated aging. To apply these exclusion criteria, the titles and abstracts of the papers were examined. After the application of the exclusion criteria, the included articles had their full text analyzed.

3. RESULTS AND DISCUSSION

With the search across the indicated databases, a total of 518 documents were found. After applying filters (date, article type, and language), the search resulted in 409 papers. Removal of duplicate articles yielded 292 documents. Finally, after applying exclusion criteria, 41 papers were considered relevant and included in the study. Figure 1 illustrates the papers selection process.
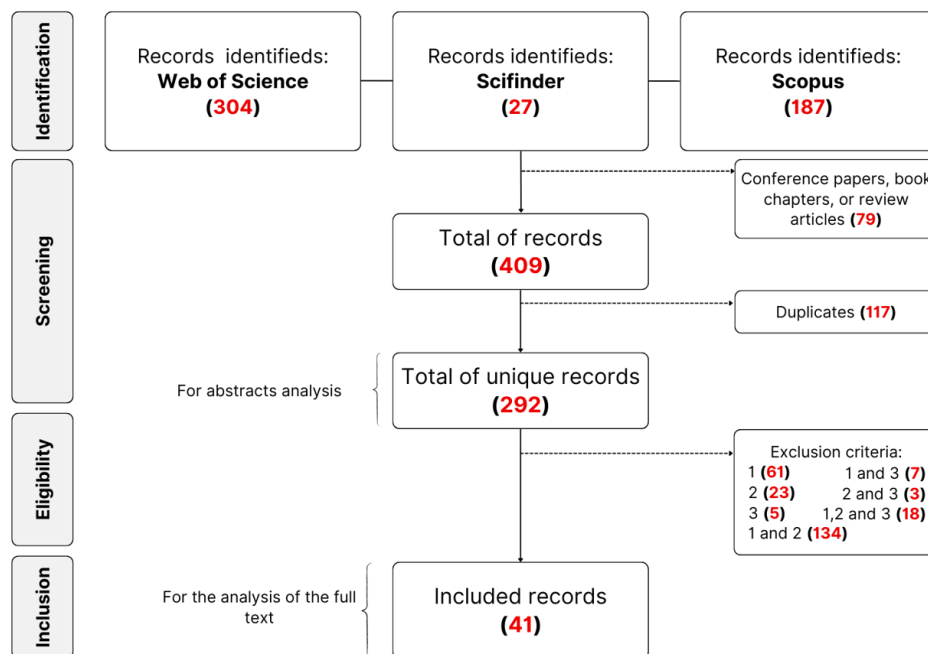
Figure 1. Flowchart depicting the systematic review process, following the guidelines outlined in the PRISMA protocol.

Table 1 summarizes the main information found in the papers selected for this review, including the types of fibers used, characterization and accelerated aging tests conducted, as well as reinforcements and fillers utilized.

Table 1. Utilized fibers, accelerated aging tests, characterization assays, fillers/reinforcements.

Reference	Fiber	Accelerated Aging Method	Reinforcement/ filler
[5]	coconut	W/D, induced reactions	Natural latex, silica fume and metakaolin
[6]	wood cellulosic pulp	W/D	quartz silica mineral addition
[7]	hemp	W/D, F/T	-
[8]	wood cellulosic pulp	W/D	PET bottle waste
[9]	sisal	W/D	diatomaceous earth
[10]	sisal	W/D, F/T, immersion	-
[11]	wood cellulosic pulp	W/D	-
[12]	fir	W/D	slag
[13]	wood cellulosic pulp	W/D	coal mining waste and limestone filler
[14]	sisal	W/D	-
[15]	bamboo	W/D	-
[16]	sisal, curaua and jute	W/D	-
[17]	ensete ventricosum	W/D	metakaolin, fly ash and slag
[18]	curaua	W/D	metakaolin and fly ash
[19]	abaca, cabuya and sisal	W/D	silica
[20]	wood cellulosic pulp	W/D	ground carbonate material
[21]	coconut	W/D	-
[22]	wood cellulosic pulp	W/D	-
[23]	sugarcane bagasse	W/D	-
[24]	flax	W/D	metakaolin
[25]	curaua and wood cellulosic pulp	W/D	limestone
[26]	coconut and flax	F/T	air-lime
[27]	wood cellulosic pulp	W/D	coal mining waste and limestone filler
[28]	hemp	W/D	fly ash
[29]	curaua	W/D	hydrated lime
[30]	eucalyptus, banana pseudostem, coffee husk and coconut shell	W/D	Agricultural limestone and polyether carboxylic additive (ADVA)
[31]	Tucum palm, razor grass, jute and piaçava	W/D	Fly ash and metakaolin
[32]	sisal	F/T	MCC powder, CTAB

[33]	wood cellulosic pulp	W/D	ground limestone filler
[34]	flax	W/D	silica fume and metakaolin
[35]	wood cellulosic pulp	W/D	microsilica powder
[36]	wood cellulosic pulp	W/D	cement and metakaolin
[1]	rice husk	F/T	-
[37]	wood cellulosic pulp	W/D	limestone
[38]	açai	W/D	hydrated lime
[39]	sisal	W/D	rice husk ash, metakaolin, nanoclay and fly ash
[40]	sisal	W/D	silica fume and metakaolin
[41]	hemp	W/D	Nanoclay and calcined nanoclay
[42]	wood cellulosic pulp	W/D	ground limestone
[43]	kenaf	biological agents	-
[44]	giant miscanthus	F/T	Fly ash and synthetic zeolite

In Figure 3a, the number of occurrences of the most commonly used types of fibers in the selected papers can be observed. In addition to the fibers presented in the figure, the utilization of fibers such as abaca, açaí, sugarcane bagasse, bamboo, rice husk, coffee husk, coconut husk, ensete, eucalyptus, banana leaf, razor grass, kenaf, giant miscanthus, rice straw, tucum palm, piassava, and banana pseudostem was also observed, albeit each with only one occurrence. There is a predominance of wood cellulosic pulp cellulosic pulp as the main plant fiber in fiber-cement composites. This fiber is likely the most used due to its abundance, as the fiber-cement industry benefits from the established cellulose production industry, which extracts tons of cellulose fibers every day, especially for paper production, although other applications are currently highly targeted with the widespread use of digital media. Among the 41 studies analyzed, 28 different types of tests were conducted for material characterization. In Figure 3b, the frequency of occurrence of the main tests used for the characterization of fiber-cement composites can be observed. Flexural strength and scanning electron microscopy were the most commonly used tests, occurring in approximately 83% and 63% of the studies, respectively.
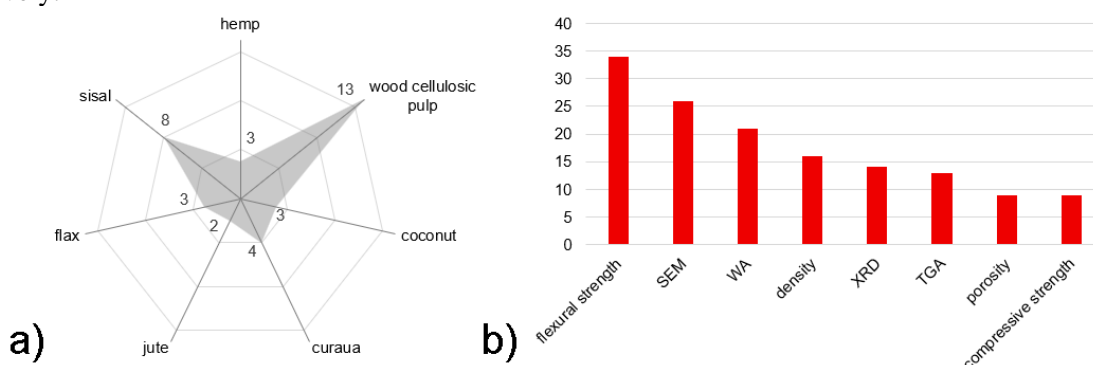
Figure 2. Most studied plant fibers (a) and main characterization assays performed (b).

3.1. Durability tests

In the analyzed papers, six different types of durability tests were utilized: wet/dry cycles, freeze/thaw cycles, induced reactions, exposure to biological agents and immersion. It is important to highlight that besides the mentioned tests in this review, there are various other accelerated aging tests, such as weathering resistance test and fatigue resistance test. The occurrence of accelerated aging tests applied in the studies can be observed in Figure 5. It is noticeable that wetting and drying cycles were significantly more utilized, present in 87.8% of the articles. Freezing and thawing cycles were the second most used test type, with a 12.1% occurrence, while induced reactions occurred in only one article, as did immersion and exposure to biological agents.
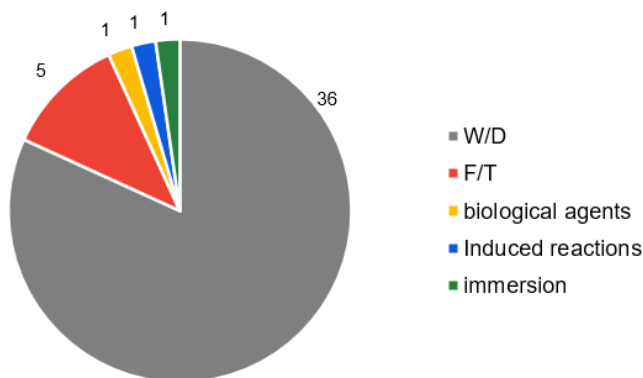
Figure 3. Accelerated aging methods performed.

3.2. Durability of fiber-cement composites with treated fibers

To enhance the properties of fiber-cement reinforced with plant fibers, treatments such as hornification, accelerated carbonation, and pulp refining can be applied. Of the 17 studies that provided comparisons between treated and untreated composites, 16 reported an improvement in durability in the treated samples compared to the untreated controls. However, despite the improvement in initial mechanical performance (at 28 days of curing), composites reinforced with refined eucalyptus pulp (mechanical treatment) exhibited inferior mechanical performance after 200 cycles of accelerated aging compared to the material reinforced with untreated fibers. This can be attributed to the lower mineralization of the fibers and the fact that the untreated ones present higher initial mechanical strength [16].

Regarding hornification, it has been reported that the treatment reduces water absorption capacity and increases the dimensional stability of the cellulose paste while preserving the original chemical composition of the plant pulp. In addition to improving mechanical properties, it enhances interfacial shear strength and tensile strength after accelerated aging [13,16,19,37,39]. However, physical properties after cycles of accelerated aging indicate that hornification would not significantly interfere with the material's physical properties [23].

When it comes to accelerated carbonation, Cabral et al. [23] considered the accelerated carbonation curing process efficient, as it generated densification in the matrix and preserved the sugarcane bagasse particles after the accelerated aging test composed of 200 wet/dry cycles. Significant decreases in water absorption and air permeability were also observed [11,37]. When comparing untreated and NaOH-treated Curauá fibers, [29] found that accelerated aging caused a greater reduction in tensile strength in untreated fibers, while treated fibers exhibited greater adherence to the matrix and a lesser reduction in tensile strength.

In addition to treatments on fibers, some studies indicate an improvement in the durability of fiber-reinforced composites that undergo alterations in the composition of the cementitious matrix. Mármol et al. [35] describes that samples manufactured with a composition of 60% MgO and 40% SiO2 do not show a significant reduction in the Modulus of Rupture (MOR), nor do they exhibit changes in deformation at the rupture point after aging; however, in the material produced with Portland cement, these properties reduce drastically. Moreover, Wei et al. [39] points out that the addition of RHA as a partial substitute for cement not only enhances the initial mechanical properties of sisal fiber-reinforced mortar but also promotes a considerable improvement in flexural strength and toughness of the composites, especially after undergoing wetting and drying cycles.

The inclusion of polymeric additives in the matrix can also bring benefits to the durability of fiber-reinforced composites, reducing interfacial debonding in the transition zone, and improving their microstructure by limiting pore/void expansion during cycles [15]. Partial substitution of cement with metakaolin, slag, and fly ash can also be favorable. Although sometimes exhibiting lower initial mechanical strength than samples made with Portland cement, the substitutions have proven effective in preventing degradation after accelerated aging, reducing fiber mineralization [17].

Wei et al. [9] established an important linear relationship between the tensile strength of aged plant fibers and the CH content of cement matrices. There was a 42% reduction in the cellulose content of the fiber incorporated into pure cement after 20 cycles of wetting and drying, resulting in a loss of tensile strength in the fiber. A lesser reduction in cellulose content occurred when part of the cement was replaced by

diatomaceous earth and limestone in the matrix, leading to a cellulose content 50% higher compared to the control group.

4. CONCLUSIONS

This systematic review provided an overview of durability tests applied in studies aimed at the development of fiber-reinforced cement composites with plant fibers. Through the analysis of the 41 articles included in this research, it was possible to conclude that there is a wide variety of fibers studied, with wood cellulosic pulp and sisal being the most researched, and the most applied durability test was the wetting and drying cycles. A greater durability was observed after exposure to durability tests in composites that underwent some form of treatment. The durability of composites reinforced with natural fibers has proven to be satisfactory for the applications proposed by the studies analyzed. In the context of wetting and drying cycles, there was a predominance of cycles with a total duration of up to 24 hours, and the most used range of cycle numbers was between 101 and 200 cycles. Additionally, there was a gap regarding the comparison between different quantities and durations of cycles, as well as different durability tests, which would provide relevant information about the behavior of samples subjected to different conditions. It is suggested that this gap be addressed in future research.

4.1. Declaration of Competing Interest

The authors declare no conflict of interest.

4.2. Fundings

5. REFERENCES

[1]   Feng B, Liu J, Lu Z, Zhang M, Tan X. Study on properties and durability of alkali activated rice straw fibers cement composites. J Build Eng 2023;63:105515. https://doi.org/10.1016/j.jobe.2022.105515.

[2]   Wei J, Ma S, Thomas DG. Correlation between hydration of cement and durability of natural fiber-reinforced cement composites. Corros Sci 2016;106:1–15. https://doi.org/10.1016/j.corsci.2016.01.020.

[3]   Ahmad W, Khan M, Smarzewski P. Effect of Short Fiber Reinforcements on Fracture Performance of Cement-Based Materials: A Systematic Review Approach. Materials (Basel) 2021;14:1745. https://doi.org/10.3390/ma14071745.

[4]   Shamseer L, Moher D, Clarke M, Ghersi D, Liberati A, Petticrew M, et al. Preferred reporting items for systematic review and meta-analysis protocols (PRISMA-P) 2015: elaboration and explanation. BMJ 2015;349:g7647–g7647. https://doi.org/10.1136/bmj.g7647.

[5]   Silva EJ da, Marques ML, Velasco FG, Fornari Junior C, Luzardo FM, Tashima MM. A new treatment for coconut fibers to improve the properties of cement-based composites – Combined effect of natural latex/pozzolanic materials. Sustain Mater Technol 2017;12:44–51. https://doi.org/10.1016/j.susmat.2017.04.003.

[6]   Urrea-Ceferino GE, Panesar DK, Savastano H. Adjusting curing parameters for innovative and durable vegetable fibre-cement composites. Cem Concr Compos 2019;103:121–33. https://doi.org/10.1016/j.cemconcomp.2019.04.028.

[7]   Kosiachevskyi D, Abahri K, Daubresse A, Prat E, Chaouche M. Assessment of the hygrothermal, microstructural and chemical evolution of a hemp-based cementitious mortar under ETICS total weathering aging protocol. Constr Build Mater 2022;314:125471. https://doi.org/10.1016/j.conbuildmat.2021.125471.

[8]   Farrapo CL, Fonseca CS, Pereira TGT, Tonoli GHD, Savastano Junior H, Mendes RF. Cellulose Associated with Pet Bottle Waste in Cement Based Composites. Mater Res 2017;20:1380–7. https://doi.org/10.1590/1980-5373-mr-2017-0183.

[9]   Wei J, Gencturk B. Degradation of Natural Fiber in Cement Composites Containing Diatomaceous Earth. J Mater Civ Eng 2018;30. https://doi.org/10.1061/(ASCE)MT.1943-5533.0002486.

[10] Wei J, Meyer C. Degradation rate of natural fiber in cement composites exposed to various accelerated aging environment conditions. Corros Sci 2014;88:118–32. https://doi.org/10.1016/j.corsci.2014.07.029.

[11] Teixeira RS, Tonoli GHD, Santos SF, Savastano H, Protásio TP, Toro EF, et al. Different ageing conditions on cementitious roofing tiles reinforced with alternative vegetable and synthetic fibres. Mater Struct 2014;47:433–46. https://doi.org/10.1617/s11527-013-0070-0.

[12] Huang Y, Tan J, Xuan X, Wei S, Liu L, Yu S, et al. Durability of plant fiber reinforced alkali activated composites. Constr Build Mater 2022;314:125501. https://doi.org/10.1016/j.conbuildmat.2021.125501.

[13] Eduardo Mejia-Ballesteros J, Rodier L, Filomeno R, Savastano Jr. H, Fiorelli J, Frias Rojas M. Effect of activated coal waste and treated Pinus fibers on the physico-mechanical properties and durability of fibercement composites. Constr Build Mater 2023;392:132038. https://doi.org/10.1016/j.conbuildmat.2023.132038.

[14] Neves Junior A, Ferreira SR, Toledo Filho RD, Fairbairn E de MR, Dweck J. Effect of early age curing carbonation on the mechanical properties and durability of high initial strength Portland cement and lime-pozolan composites reinforced with long sisal fibres. Compos Part B Eng 2019;163:351–62. https://doi.org/10.1016/j.compositesb.2018.11.006.

[15] Akinyemi BA, Omoniyi TE. Effect of experimental wet and dry cycles on bamboo fibre reinforced acrylic polymer modified cement composites. J Mech Behav Mater 2020;29:86–93. https://doi.org/10.1515/jmbm-2020-0009.

[16] Ferreira SR, Silva F de A, Lima PRL, Toledo Filho RD. Effect of hornification on the structure, tensile behavior and fiber matrix bond of sisal, jute and curauá fiber cement based composite systems. Constr Build Mater 2017;139:551–61. https://doi.org/10.1016/j.conbuildmat.2016.10.004.

[17] Tsegaye Beyene M, Kingne F, Tsangouri E, Kadi M El, Adugna Demissie T, Rahier H, et al. Effect of matrix modification on the durability of cementitious composites reinforced with aligned Ensete fibre. Constr Build Mater 2023;363:129706. https://doi.org/10.1016/j.conbuildmat.2022.129706.

[18] Zukowski B, dos Santos Mendonça YG, de Andrade Silva F, Toledo Filho RD. Effect of moisture movement on the tensile stress–strain behavior of SHCC with alkali treated curauá fiber. Mater Struct 2020;53:49. https://doi.org/10.1617/s11527-020-01486-9.

[19] Ardanuy M, Claramunt J, Ventura H, Manich AM. Effect of Water Treatment on the Fiber–Matrix Bonding and Durability of Cellulose Fiber Cement Composites. J Biobased Mater Bioenergy 2015;9:486–92. https://doi.org/10.1166/jbmb.2015.1545.

[20] Tonoli GHD, Santos SF, Teixeira RS, Pereira da Silva MA, Rocco Lahr FA, Pescatori Silva FH, et al. Effects of Eucalyptus pulp refining on the performance and durability of fibre-cement composites. J Trop For Sci 2013;25:400–9.

[21] Bui H, Levacher D, Boutouil M, Sebaibi N. Effects of Wetting and Drying Cycles on Microstructure Change and Mechanical Properties of Coconut Fibre-Reinforced Mortar. J Compos Sci 2022;6:102. https://doi.org/10.3390/jcs6040102.

[22] Ballesteros JEM, Santos SF, Mármol G, Savastano H, Fiorelli J. Evaluation of cellulosic pulps treated by hornification as reinforcement of cementitious composites. Constr Build Mater 2015;100:83–90. https://doi.org/10.1016/j.conbuildmat.2015.09.044.

[23] Cabral MR, Nakanishi EY, Fiorelli J. Evaluation of the Effect of Accelerated Carbonation in Cement–Bagasse Panels after Cycles of Wetting and Drying. J Mater Civ Eng 2017;29. https://doi.org/10.1061/(ASCE)MT.1943-5533.0001861.

[24] Ramirez M, Claramunt J, Ventura H, Ardanuy M. Evaluation of the mechanical performance and durability of binary blended CAC-MK/natural fibe composites. Constr Build Mater 2020;251:118919. https://doi.org/10.1016/j.conbuildmat.2020.118919.

[25] Teixeira RS, Santos SF, Christoforo AL, Payá J, Savastano H, Lahr FAR. Impact of content and length of curauá fibers on mechanical behavior of extruded cementitious composites: Analysis of variance. Cem Concr Compos 2019;102:134–44. https://doi.org/10.1016/j.cemconcomp.2019.04.022.

[26] Maia Pederneiras C, Veiga R, de Brito J. Incorporation of Natural Fibres in Rendering Mortars for the Durability of Walls. Infrastructures 2021;6:82. https://doi.org/10.3390/infrastructures6060082.

[27] Mejia-Ballesteros JE, Rodier L, Filomeno R, Savastano Jr H, Fiorelli J, Rojas MF. Influence of the

fiber treatment and matrix modification on the durability of eucalyptus fiber reinforced composites. Cem Concr Compos 2021;124:104280. https://doi.org/10.1016/j.cemconcomp.2021.104280.

[28] Poletanovic B, Janotka I, Janek M, Bacuvcik M, Merta I. Influence of the NaOH-treated hemp fibres on the properties of fly-ash based alkali-activated mortars prior and after wet/dry cycles. Constr Build Mater 2021;309:125072. https://doi.org/10.1016/j.conbuildmat.2021.125072.

[29] Azevedo ARG de, Klyuev S, Marvila MT, Vatin N, Alfimova N, Lima TES de, et al. Investigation of the Potential Use of Curauá Fiber for Reinforcing Mortars. Fibers 2020;8:69. https://doi.org/10.3390/fib8110069.

[30] Teixeira JN, Silva DW, Vilela AP, Savastano Junior H, de Siqueira Brandão Vaz LEV, Mendes RF. Lignocellulosic Materials for Fiber Cement Production. Waste and Biomass Valorization 2020;11:2193–200. https://doi.org/10.1007/s12649-018-0536-y.

[31] Filho AS, Parveen S, Rana S, Vanderlei R, Fangueiro R. Micro-structure and mechanical properties of microcrystalline cellulose-sisal fiber reinforced cementitious composites developed using cetyltrimethylammonium bromide as the dispersing agent. Cellulose 2021;28:1663–86. https://doi.org/10.1007/s10570-020-03641-5.

[32] da Fonseca RP, Rocha JC, Cheriaf M. Mechanical Properties of Mortars Reinforced with Amazon Rainforest Natural Fibers. Materials (Basel) 2020;14:155. https://doi.org/10.3390/ma14010155.

[33] da Costa Correia V, Santos SF, Soares Teixeira R, Savastano Junior H. Nanofibrillated cellulose and cellulosic pulp for reinforcement of the extruded cement based materials. Constr Build Mater 2018;160:376–84. https://doi.org/10.1016/j.conbuildmat.2017.11.066.

[34] Claramunt J, Fernández-Carrasco LJ, Ventura H, Ardanuy M. Natural fiber nonwoven reinforced cement composites as sustainable materials for building envelopes. Constr Build Mater 2016;115:230–9. https://doi.org/10.1016/j.conbuildmat.2016.04.044.

[35] Mármol G, Savastano H, Tashima MM, Provis JL. Optimization of the MgO SiO2 binding system for fiber-cement production with cellulosic reinforcing elements. Mater Des 2016;105:251–61. https://doi.org/10.1016/j.matdes.2016.05.064.

[36] Correia V da C, Santos SF, Mármol G, Curvelo AA da S, Savastano H. Potential of bamboo organosolv pulp as a reinforcing element in fiber–cement materials. Constr Build Mater 2014;72:65–71. https://doi.org/10.1016/j.conbuildmat.2014.09.005.

[37] Ballesteros JEM, Mármol G, Filomeno R, Rodier L, Savastano H, Fiorelli J. Synergic effect of fiber and matrix treatments for vegetable fiber reinforced cement of improved performance. Constr Build Mater 2019;205:52–60. https://doi.org/10.1016/j.conbuildmat.2019.02.007.

[38] de Azevedo ARG, Marvila MT, Tayeh BA, Cecchin D, Pereira AC, Monteiro SN. Technological performance of açaí natural fibre reinforced cement-based mortars. J Build Eng 2021;33:101675. https://doi.org/10.1016/j.jobe.2020.101675.

[39] Wei J, Meyer C. Utilization of rice husk ash in green natural fiber-reinforced cement composites: Mitigating degradation of sisal fiber. Cem Concr Res 2016;81:94–111. https://doi.org/10.1016/j.cemconres.2015.12.001.

[40] Claramunt J, Ardanuy M, Fernandez-Carrasco LJ. Wet/Dry Cycling Durability of Cement Mortar Composites Reinforced with Micro- and Nanoscale Cellulose Pulps. BioResources 2015;10. https://doi.org/10.15376/biores.10.2.3045-3055.

[41] Hakamy A, Shaikh FUA, Low IM. Effect of calcined nanoclay on the durability of NaOH treated hemp fabric-reinforced cement nanocomposites. Mater Des 2016;92:659–66. https://doi.org/10.1016/j.matdes.2015.12.097.

[42] Filomeno RH, Rodier LB, Ballesteros JEM, Rossignolo JA, Savastano H. Optimizing the modified atmosphere parameters in the carbonation process for improved fiber-cement performance. J Build Eng 2020;32:101676. https://doi.org/10.1016/j.jobe.2020.101676.

[43] Amiandamhen SO, Osadolor SO. Recycled waste paper–cement composite panels reinforced with kenaf fibres: durability and mechanical properties. J Mater Cycles Waste Manag 2020;22:1492–500. https://doi.org/10.1007/s10163-020-01041-2.

[44] Savic A, Antonijevic D, Jelic I, Zakic D. Thermomechanical behavior of bio-fiber composite thermal insulation panels. Energy Build 2020;229:110511. https://doi.org/10.1016/j.enbuild.2020.110511.

ENHANCING CFRP PROPERTIES WITH MICRO-FIBRILLATED CELLULOSE: A STUDY ON INTERPHASE AND MATRIX MODIFICATION

F.J. Goyo-Brito[a]*, G.S.C. Souza[b], V. Tita[c], J.R. Tarpani[d]

(a) 0000-0002-7666-9080 (University of Sao Paulo – Brazil)*
(b) 0000-0002-9677-5024 (University of Sao Paulo – Brazil)
(c) 0000-0002-8199-1162 (University of Sao Paulo – Brazil)
(d) 0000-0003-1201-8999 (University of Sao Paulo – Brazil)

* Corresponding author: francisco.goyo@gmail.com

Abstract: This study investigates the effects of microfibrillated cellulose (MFC) on the mechanical and physical properties of carbon fiber-epoxy composites. The MFC was added to the matrix and/or at the interface between the fiber and the matrix through the use of solvents. Mechanical properties were evaluated through low-velocity impact tests, while physical properties were evaluated through Vickers microindentation. The results showed that the addition of MFC at the interface and/or in the matrix improved the mechanical properties of the composites, specifically the interlaminar shear strength (F3P) and the impact resistance. The addition of MFC at the interface resulted in a higher F3P compared to the addition of MFC in the matrix alone. The impact resistance was also improved, with the lowest value of the parameter Du-Dm observed in the composites reinforced with MFC in the matrix and interface. Furthermore, the addition of MFC in the matrix and/or at the interface resulted in an increase in the hardness of the epoxy resin, as measured by Vickers microindentation. These findings suggest that the addition of MFC can effectively improve the mechanical and physical properties of carbon fiber-epoxy composites, with potential applications in various industries.

1. INTRODUCTION

Despite their outstanding performance, carbon fiber reinforced polymers (CFRP) have some limitations, such as brittleness, low interfacial adhesion, and low fracture toughness. These limitations led to research efforts to improve the mechanical properties of CFRPs, including the addition of micro/nanoreinforcements, which can significantly improve the interfacial bonding between the fiber and the matrix, leading to increased strength and toughness. [1]

Micro/nano-reinforcements are materials with dimensions in the micrometer or nanometer range that can be added to the polymer matrix or to the interphase to enhance the mechanical properties of the composite. [2].

The micro-fibrillated cellulose (MFC) is a renewable, biodegradable, and sustainable nanomaterial derived from wood pulp fibers. It has excellent mechanical properties, such as high stiffness, high aspect ratio, and high specific surface area. The addition of MFC to the epoxy matrix has been shown to improve the mechanical properties of the resulting composite. MFC can be used as a coating for fibers [3] or added to the matrix [4] to improve the mechanical properties of the interphase and polymer.

Generally, thermoset matrix materials exhibit brittleness, which consequently heightens the vulnerability to delamination in composite materials. Among the various matrix systems available, the carbon fiber reinforced epoxy matrix system is widely favored for engineering applications, owing to its remarkable

weight reduction capabilities and superior two-dimensional performance. However, the composite's interlaminar fracture toughness in the thickness direction is severely compromised due to the inherently low fracture toughness of the epoxy matrix.[5]

Previous research has shown conflicting results on the impact performance of MFC-reinforced composites. Some studies have reported an improvement in impact resistance with the addition of MFC [6], while others have reported a decrease in impact resistance.[7] Therefore, there is a need for a comprehensive study on the effect of MFC on the mechanical behaviour of CFRP composites to better understand the potential benefits and limitations of using MFC as a reinforcement material.

The objective of this study is to investigate the effect of MFC on the impact behaviour of CFRP composites. Specifically, the study aims to evaluate the mechanical properties of the composites under quasi-static and dynamic tests. The study will also investigate the effect of the MFC location within the composite, either in the epoxy matrix or at the interface between the matrix and the carbon fibers, on the impact behaviour of the composite.

2. METHODOLOGY

2.1. Materials

The epoxy matrix used in this study was Epikote RIMR035 C resin and hardener Epikure RIMH 037 hardener, which were supplied by Hexion ™ Brazil. The carbon fibers used were PAN-based unsized, 0.40 mm thick, 3K filaments per bundle, bidirectional twill weave fabric with an areal weight of 200 g/m², five bundles/cm in both the warp and weft directions, provided by Fibertex Brazil™. and the MFC was obtained from Borregaard. Microfibrils of cellulose water paste Exilva F 01-V, 10 wt. % MFC was synthesized and provided by Borregaard™, Norway.

Preparation of MFC-coated carbon fibers: Rectangular Twill wave Carbon Fibers (CF) were cut and dried at 100 °C for 3 hours. MFC/water suspensions at 0.1% were produced by mixing MFC and distilled water with an Ultra-Turrax homogenizer (IKA T25). The CF were coated with MFC by infusion coating processes, using the 0.1% MFC suspension in deionized water for both. The coated fibers were then dried in an oven at 100 °C for 1 hour to evaporate the water and to fix the MFC on the surface of the fibers.[8]

Preparation of MFC-reinforced epoxy matrix: To prepare MFC-reinforced epoxy matrix, the as-received MFC suspension was first diluted and subjected to solvent exchange using polar organic solvents, specifically Ketone (KET) and isopropyl alcohol (ALC). This was done via liquid-liquid extraction to remove any impurities using a KASVI centrifugation machine at 5 minutes at 1000 rpm. The supernatant solvent (mixed of alcohol or ketone and water) was removed, refilling with new solvent. This process was repeated 10 times.

After the exchange, the solvents were removed by roto-evaporation to produce MFC gels containing either acetone (MFC-KET) or isopropyl alcohol (MFC). The MFC gels were separately added to the epoxy resin and the partial solvents were evaporated.

The concentration of MFC was adjusted to 0.75% wt. for MFC(Ket) and 0.5% wt. for MFC(Alc). The mixture was heated under mechanical agitation at 60ºC for MFC(Ket) and 80ºC for MFC(Alc), the mixtures were weighted and maintained at these temperatures until the variation in weight between measures were less than 0.01 g. Then, the curing agent was added while stirring the mixture with the heating off. The same process was also performed for neat resin (EPX), so for epoxy containing MFC from acetone and isopropyl alcohol solvent exchange processes, named EPXMFC(Ket) and EPX-MFC(Alc) respectively.

CFRP laminates manufacturing: Resin infusion under flexible tooling was used to permeate the preforms containing non-coated CFs (Reference) and CF-MFC coated and dried preforms. The preforms were infused with resin under a vacuum bagging pressure of -80 KPa, with a total filling time of 10 min. The resin was cured at room temperature for 24 hours and post-cured in an oven at 70 °C for 5 hours. The size of the resulting composite laminates was 100x150x0.5 mm3, with the two plies of CF fabrics maintaining the same stacking order for both MFC and resin infusion.

2.2. Experimental

Microhardness Vickers: Microhardness measurements using a Vickers pyramidal diamond indenter were conducted on a microhardness testing machine (Micromet 2100 Series Microhardness Testers, Buehler, Lake Bluff, IL, USA). Each sample was subjected to ten measurements, applying a load of 3 N during 10 seconds.

Low-velocity impact test: The ASTM D7136 [9] standard specifies a rectangular specimen to be impacted by a hemispherical aluminium indenter, the prior being fixed by four toggle clamps attached to an inertial base. The specimens for impact test were extracted from laminates with seven layers (COLOCAR TABLA CON ESPESURAS) of twill-wave CF under their specific conditions of nano/micro reinforcement.

The drop-weight characteristics and parameters selected for the impact tests are listed in Table 1 while Figure 1 shows the results compendium of the drop tests embodying the force, displacement and energy histories and the force displacement curves of the events.

Table 1. Low-velocity test impact parameters.

Impactor mass (kg)	Test height (m)	Initial velocity (m/s)	Total impact energy (J)	Impactor radius (mm)	Impactor material
4.826	0.072	1.187	3.40	8	Aluminum

Figure 1. Impactor, specimen, and clamping apparatus.

3. RESULTS AND DISCUSSION

3.1. Microhardness Vickers

The table 2 provided shows the Vickers hardness values for neat epoxy and epoxy composites with MFC added using solvents (alcohol and ketone) on the first day and after 30 days. The results showed that the addition of MFC using solvents led to a significant increase in the epoxy resin's hardness compared to neat epoxy. The highest increase was observed in the composite reinforced with MFC added using alcohol, with a hardness of 16.2 HV on day 1 and 16.4 HV on day 30, compared to 12.5 HV for neat epoxy.

The composite reinforced with MFC added using ketone also showed an increase in hardness, with values of 15.7 HV on day 1 and 15.4 HV on day 30.

The observed increase in hardness is likely due to the MFC's high aspect ratio and strong interfacial adhesion with the epoxy resin, which can lead to the formation of a rigid network that resists deformation [10]. Additionally, the solvents used to incorporate the MFC may have facilitated the dispersion and alignment of the MFC in the epoxy resin, leading to a more uniform distribution of the reinforcement and enhanced mechanical properties [11].

The addition of MFC through the use of solvents can significantly improve the hardness of epoxy resin, with alcohol being the most effective solvent for the incorporation of MFC. These findings have important implications for the development of new epoxy-based materials with enhanced mechanical properties for a wide range of applications.

Table 2. Values of hardness by Vickers micro-indentation for neat epoxy and composites micro-reinforced with MFC added using solvents as alcohol and/or ketone.

Specimen	HV day 1	HV day 30
EPX	12.5	12.7
EPX-MFC(Alc)	16.2	16.4
EPX-MFC(Ket)	15.7	15.4

3.1. Low velocity impact test

Force Histories
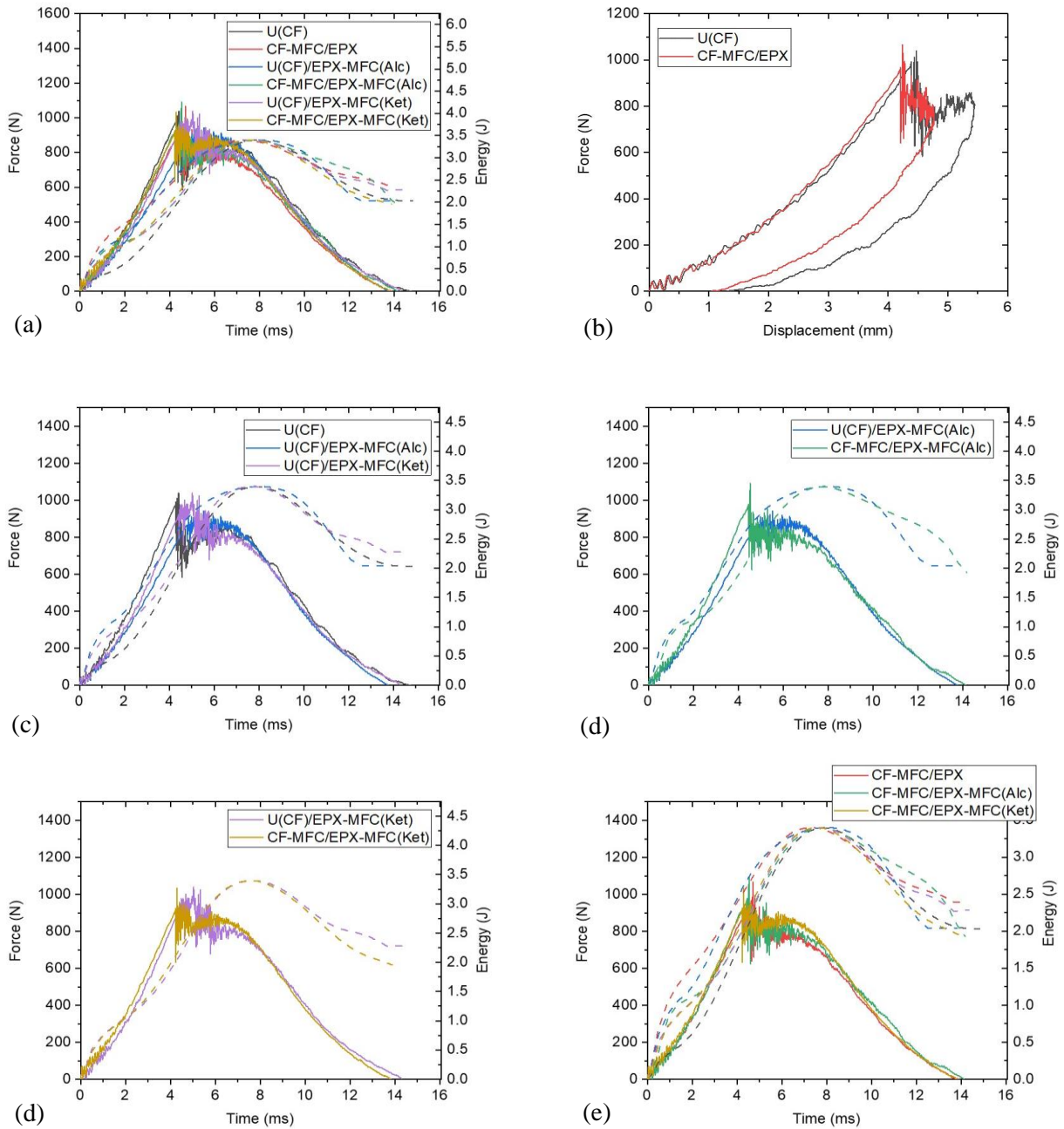
Figure 3. Force and energy curves of CFRP with micro/nano-reinforcements of cellulose in the interphase.

Figure 3 shows the Force-Time curves obtained from the impacted composite laminates, revealing the behaviourmof supercritical impact for all the specimens impacted.

Supercritical impact events occur above the damage threshold of the composite laminate, inducing damages as matrix and delaminations. The curves exhibit similar behaviour indifferent ranges. In the initial phase of contact (0-1 ms), there is a region of high-frequency oscillations resulting from the initial contact between the specimen and the dart.

The top of the curves indicates the maximum force value sustained by the laminate before a major failure, as delaminations occur. Previous to the Fm oscillations can be observed, those oscillations start at a point of the curve where the first noticeable force drop is observed and is associated with events such as matrix cracking before delamination.

Oscillations after the big drop is related mainly to the propagation of the previous damages and fiber breakages. The time associated to those parameters is also important for the analysis.[12]

The peak force values indicate that the specimens reinforced with MFC (CF-MFC/EPX, U(CF)/EPX-MFC(Alc), CF-MFC/EPX-MFC(Alc), U(CF)/EPX-MFC(Ket), CF-MFC/EPXMFC(Ket)) have higher impact resistance compared to the unreinforced specimen (U(CF)). This can be seen from the higher peak force values recorded for the MFC-reinforced specimens, indicating that they were able to withstand greater impact forces.

Furthermore, the time to peak force and time to initial damage values for the MFC-reinforced specimens were generally lower than the values for the unreinforced specimen.

This suggests that the MFC-reinforced specimens were able to reach their maximum force and initial force more quickly, which is indicative of a stiffer material.

It is important to note that there are some differences in the impact test parameters depending on the role of the MFC as reinforcement, working as interphase, or as matrix micro-reinforcement. For instance, the peak force value for U(CF)/EPX-MFC(Alc) is lower than the peak force value for CF-MFC/EPX-MFC(Alc), but the time to peak force and time to initial force are both higher. This may be due to differences in the role of the MFC and its distribution in the composite [13].

Moreover, the time to peak force values obtained for the specimens indicate that the addition of MFC coating and MFC-reinforced epoxy matrix can also improve the energy absorption capacity of the composite materials. This is because the time to peak force is directly proportional to the energy absorption capacity of the composite, as a longer time to peak force indicates that the material can dissipate more energy before failure. The specimens with MFC coating and MFC-reinforced epoxy matrix exhibited longer time to peak force values than the uncoated specimens, which suggests that the composites were able to absorb more energy during the impact loading.

In Figure 3 are also represented the curves of energy-time. Since the impact load is applied to a plate or laminate, the energy absorbed by the material increases with the load until it reaches its peak. Initially, the applied energy is absorbed elastically, resulting in elastic deformations, and the material retains this elastic energy [14].

However, after reaching the maximum energy threshold, the laminate rebounds back to the impactor. If the impact energy exceeds the elastic energy, it is considered that the remaining energy is absorbed by the laminate in the form of various damage modes such as delamination, fiber and matrix-induced failures, and plastic deformation. The amount of energy absorbed by the laminate, before it undergoes major damage or before the initiation of major damage, will be named E[Fm], and it is related to delamination and matrix crack propagation [15].

The results from the Energy-Time curves in Figure 3 reveal some interesting insights into the effect of MFC on the mechanical properties of the composites. In general, the addition of MFC in both the interphase and matrix has led to an increase in the total impact energy absorbed by the composites. Specifically, the CF-MFC/EPX and U(CF)/EPX-MFC(Ket) specimens exhibited the highest impact energies at 3.4 J. This increase in absorbed energy indicates an improvement in the density of absorbed energy of the composite material, which is desirable for applications where impact resistance is critical.

Moreover, the addition of MFC in the interphase and matrix has also led to a decrease in the amount of elastic energy stored in the material. This suggests that the composites with MFC are able to absorb more energy during the impact event, rather than storing it as elastic energy. This is consistent with the observed increase in absorbed energy and improved the density of absorbed energy.

Comparing the effect of MFC in the interphase versus the matrix, the CF-MFC/EPX and U(CF)/EPX-MFC(Ket) specimens with MFC added to the matrix exhibited higher absorbed energy than the U(CF)/EPXMFC(Alc) and CF-MFC/EPX-MFC(Alc) specimens with MFC added to both the interphase and matrix. This suggests that the addition of MFC in the matrix has a greater impact on the energy absorption capacity of the composite.

However, it is important to note that the CF-MFC/EPXMFC(Alc) specimen exhibited the highest amount of energy at peak force, indicating that the MFC addition in the interphase may contribute to an increase in the initial stiffness of the composite material.

These results suggest that the addition of MFC can improve the mechanical properties of carbon fiber-epoxy composites, with specific effects depending on the location of MFC addition (interphase or matrix) and

the process of for the addition of MFC in the matrix. Further studies can be conducted to investigate the optimal amount and distribution of MFC in the composite material for specific applications.

Residual Displacement
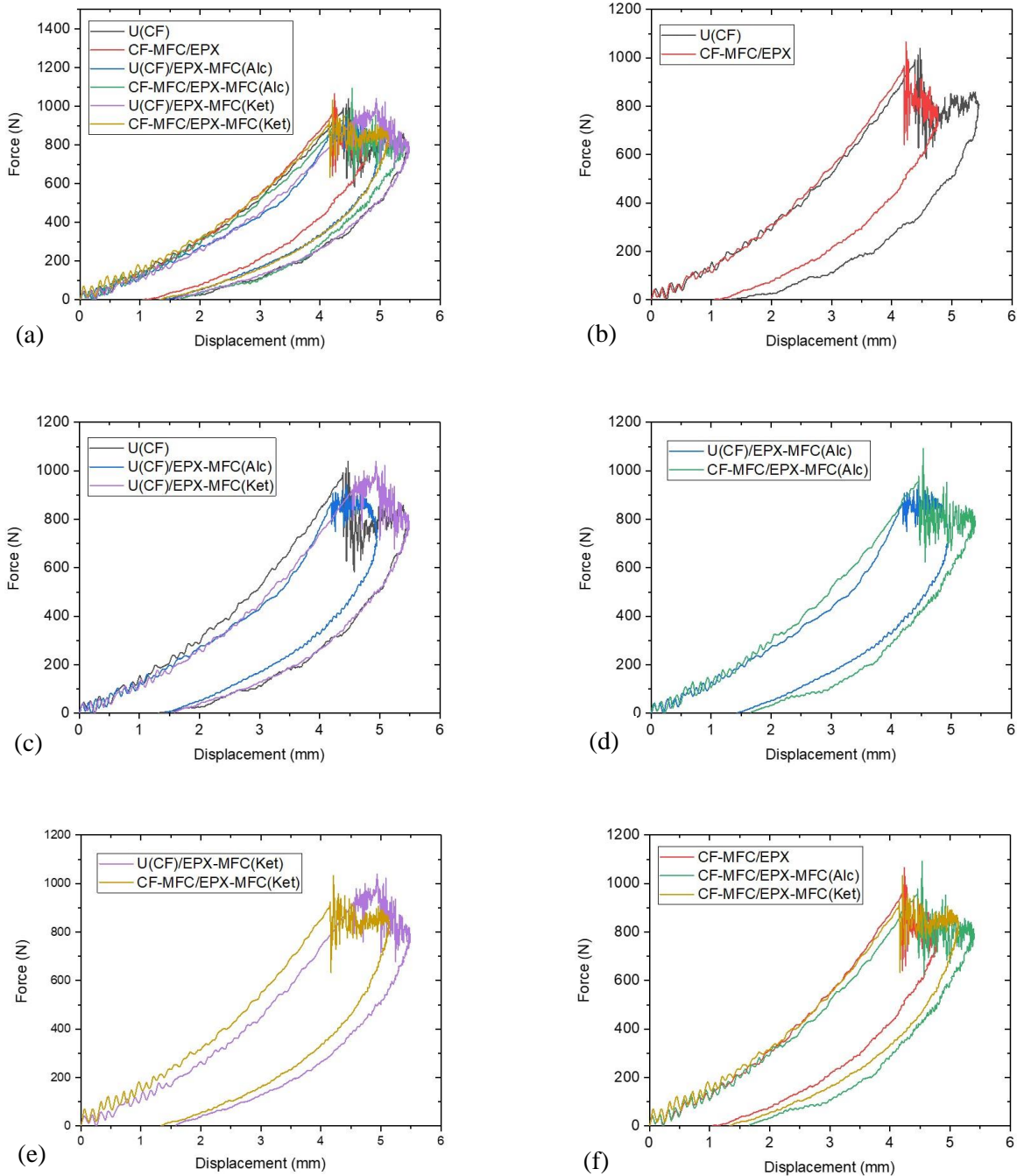
Figure 4. Indentation curves of CFRP with micro/nano-reinforcements of cellulose in the interphase and/or in the matrix.

The curves plotted in Figure 4 show the displacement parameters extracted from the indentation curves of all specimens. The parameter Dm represents the projectile displacement corresponding to the peak load, whereas Du represents the overall laminate displacement or maximum projectile displacement. The parameter Du-Dm represents the difference between Du and Dm, which indicates the structural integrity of the laminate. Lower values of Du-Dm suggest better structural integrity of the laminate.

Comparing all specimens, it can be observed that the addition of MFC in the matrix and the interface improved the structural integrity of the laminate as indicated by the lower values of Du-Dm. The specimens with MFC in the matrix and interface (CF-MFC/EPX-MFC(Alc) and CFMFC/EPX-MFC(Ket)) showed the lowest Du-Dm values, indicating better structural integrity compared to the other specimens.

In particular, the addition of MFC in the interface resulted in a significant improvement in the structural integrity of the laminate compared to the specimens without MFC in the interface (U(CF) and CF-MFC/EPX). This can be attributed to the ability of MFC to improve interfacial bonding between the matrix and reinforcement, leading to better load transfer and improved structural integrity.

In terms of percentage difference, the addition of MFC in the interface resulted in a reduction of Du-Dm by approximately 48.5% and 35.5% for U(CF)/EPX-MFC(Alc) and CFMFC/EPX-MFC(Alc), respectively, compared to U(CF) and CF-MFC/EPX. On the other hand, the addition of MFC in the matrix resulted in a reduction of Du-Dm by approximately 23.2% and 6.7% for CF-MFC/EPX-MFC(Alc) and CF-MFC/EPX-MFC(Ket), respectively, compared to CFMFC/ EPX.

These results suggest that the addition of MFC in the interface has a greater effect on improving the structural integrity of the laminate compared to the addition of MFC in the matrix.

4. CONCLUSIONS

The low-velocity impact test reveals that MFC enhances the mechanical properties of composite laminates, increasing their impact resistance and stiffness. The role and distribution of MFC, whether as reinforcement, interphase, or matrix micro-reinforcement, lead to variations in the impact parameters. MFC addition in both the interphase and matrix increases the total impact energy absorbed by the composites, improving their energy density. However, the location of MFC addition and the process for its addition in the matrix can have specific effects on the mechanical properties of the composites.

4.1. Declaration of Competing Interest

The authors declare no conflict of interest.

4.2. Fundings

5. REFERENCES

[1] L. Gorbatikh, B. L. Wardle, S. V. Lomov, Hierarchical lightweight composite materials for structural applications, Mrs Bulletin 41 (2016) 672–677. (https://doi.org/10.1557/mrs.2016.170)
[2] J. Karger-Kocsis, H. Mahmood, A. Pegoretti, All-carbon multi-scale and hierarchical fibers and related structural composites: A review, Composites Science and Technology 186 (2020) 107932. (https://doi.org/10.1016/j.compscitech.2019.107932).
[3] B. E. B. Uribe, E. M. S. Chiromito, A. J. F. Carvalho, J. R. Tarpani, Low-cost, environmentally friendly route for producing CFRP laminates with microfibrillated cellulose interphase., Express Polymer
Letters 11 (2017). (https://doi.org/10.3144/expresspolymlett.2017.6).
[4] V. Carvelli, T. Fujii, K. Okubo, The effect of microfibrils cellulose modified epoxy on the quasi-static and fatigue behaviour of open hole carbon textile composites, Journal of Composite Materials 52 (2018)
3365–3380. (https://doi.org/10.1177/0021998318765623).
[5] V. Dikshit, S. K. Bhudolia, S. C. Joshi, Multiscale polymer composites: A review of the interlaminar fracture toughness improvement, Fibers 5 (2017) 38. (https://doi.org/10.3390/fib5040038).
[6] K. Katagiri, N. Kishimoto, H. Yamaguchi, T. Okumura, S. Kawakita, S. Honda, K. Sasaki, Effects of stacking sequences of nonhydrophobic cellulose nanofiber dispersion layer on impact properties of carbon fiber/cellulose nanofiber reinforced epoxy composite, Mechanics of Advanced Materials and Structures 30 (2023) 582–591. (https://doi.org/10.1080/15376494.2021.2018743).
[7] V. Carvelli, A. Betti, T. Fujii, Fatigue and izod impact performance of carbon plain weave textile reinforced epoxy modified with cellulose microfibrils and rubber nanoparticles, Composites Part A: Applied Science and Manufacturing 84 (2016) 26–35. (https://doi.org/10.1016/j.compositesa.2016.01.005).

[8] A. C. S. P. Tarpani, M. M. Á. Maciel, J. R. Tarpani, V. Tita, Investigation on the existence of physical-chemical interaction between epoxy matrix and fibrillated cellulose in nano/microcomposites, Proceedings of BCCM 5 (2021).

[9] ASTM International. (2019). ASTM D7136/D7136M-19, Standard Test Method for Measuring the Damage Resistance of a Fiber-Reinforced Polymer Matrix Composite to a Drop-Weight Impact Event. West Conshohocken, PA: ASTM International. (https://www.astm.org).

[10] W. J. Orts, J. Shey, S. H. Imam, G. M. Glenn, M. E. Guttman, J.-F. Revol, Application of cellulose microfibrils in polymer nanocomposites, Journal of Polymers and the Environment 13 (2005) 301–306. (https://doi.org/10.1007/s10924-005-5514-3).

[11] A. Isogai, Development of completely dispersed cellulose nanofibers, Proceedings of the Japan Academy, Series B 94 (2018) 161–179. (https://doi.org/10.2183/pjab.94.012)

[12] S. K. Bhudolia, S. C. Joshi, Low-velocity impact response of carbon fibre composites with novel liquid methylmethacrylate thermoplastic matrix, Composite Structures 203 (2018) 696–708. (https://doi.org/10.1016/j.compstruct.2018.07.066).

[13] K. Katagiri, N. Kishimoto, T. Okumura, S. Kawakita, S. Honda, K. Sasaki, Effects of cellulose nanofiber content on impact properties of carbon fiber reinforced epoxy composites with the cellulose nanofiber dispersion layer, Mechanics of Advanced Materials and Structures 29 (2022) 6087–6095. (HTTPS://DOI.ORG/10.1080/15376494.2021.1972369).

[14] M. Ali, S. C. Joshi, Impact damage resistance of CFRP prepreg laminates with dispersed CSP particles into ply interfaces, International Journal of Damage Mechanics 21 (2012) 1106–1127. (https://doi.org/10.1177/1056789511429143).

[15] M. Ali, S. C. Joshi, Damage evolution in glass/epoxy composites engineered using core–shell microparticles under impact loading, Journal of Materials Science 48 (2013) 8354–8367. (https://doi.org/10.1007/s10853-013-7635-8).

COMPOSITE FILM BASED ON QUATERNIZED STARCH AND REINFORCED BY CRYSTALLINE NANOCELLULOSE WITH ANTIMICROBIAL ACTIVITY AGAINST BACTERIA AND CORONAVIRUS

Guilherme R. Carvalho [a]*, Camila Dameliana[b], Marta C. T. Duarte[c], Liliane M.F.Lona [d]

(a) 0000-0001-6542-4881 (University of Campinas– Brazil)
(b) 0000-0002-6855-2499 (University of Campinas– Brazil)
(c) 0000-0001-7604-629X (University of Campinas– Brazil)
(d) 0000-0001-5304-9025 (University of Campinas– Brazil)

* Corresponding author: gr.carvalho@yahoo.com.br

CODE: BCCM7-152

Keywords: Quaternized cassava starch, Crystalline nanocellulose, Film, Coronavirus.

Abstract: A new composite film with antiviral and antibacterial properties, called Q-CS/CNC, was developed using cassava starch-modified (Q-CS) with GTMAC and reinforced with crystalline nanocellulose (CNC). The addition of CNC significantly increased thickness, tensile strength, and stiffness. The Q-CS/CNC film demonstrated the ability to inactivate 99% of the coronavirus in just 1 min and inhibit Staphylococcus aureus and Escherichia coli growth. These effects are attributed to the electrostatic interaction of quaternary amino groups, derived from GTMAC, grafted onto starch, with the phospholipid membrane of microorganisms. The results highlight the potential use of Q-CS/CNC film as antimicrobial packaging, especially against coronavirus.

1. INTRODUCTION

Plastic films used in packaging are a potential source of contamination by microorganisms, including SARS-CoV-2, which can remain active for up to three days [1]. In addition to SARS-CoV-2, bacteria such as *Staphylococcus aureus* and *Escherichia coli* are also capable of infecting plastic surfaces [2]. Given this context, strategies to develop plastic films capable of inactivating microorganisms, aiming to mitigate contamination, become crucial.

Cassava starch (CS) is a promising option for producing plastic films, especially in the food industry, given its low cost, high availability, and biodegradability [3,4]. Furthermore, modifying starch with antimicrobial compounds, such as quaternary ammonium salts (QAS), ensures antimicrobial properties in plastic films [5].

The quaternization of cassava starch with QAS, such as glycidyltrimethylammonium chloride (GTMAC), is a promising approach for developing plastic films with antimicrobial activity. However, starch-based plastic films face limitations in their mechanical properties, such as low tensile strength [6]. However, the addition of crystalline nanocellulose (CNC) significantly enhances these properties [7]. Therefore, the objective of this study is to produce a plastic film based on quaternized cassava starch, reinforced with CNC, with antiviral activity against coronavirus and antibacterial activity against *S. aureus* and *E. coli*, in addition to determining its mechanical properties.

2. METHODOLOGY

2.1. Materials

The materials used in this study were: (i) cassava starch (CS) (Yoki Food S.A, Brazil); (ii) glycidyltrimethylammonium chloride (GTMAC) (Sigma Aldrich, Brazil); (iii) glycerol (Sigma Aldrich, Brazil), used as a plasticizer; (iv) crystalline nanocellulose (CNC) (CelluForce®, Canada).

2.2 Quaternization of starch and elemental analysis

Initially, an aqueous suspension of CS was prepared by dissolving 20 g of this biopolymer in 400 mL of distilled water. Then, a 1M NaOH solution was gradually added to the starch suspension until reaching pH 12. The system was heated to 65 °C, with constant stirring at 450 rpm. For the quarternization reaction, 40 g of GTMAC was added to the mixture, keeping the pH adjusted. The reaction continued for 20 hours at 65 °C, under continuous stirring. Subsequently, HCl was added to lower the pH to a value between 6 and 7, interrupting quaternization. The quaternized cassava starch suspension (Q-CS) was then precipitated with excess acetone, vacuum filtered, washed with ethanol and distilled water (1:1 by volume), and lyophilized at - 40°C. Elemental carbon, hydrogen, and nitrogen composition were analyzed using a CHN analyzer with a thermal conductivity detector. The percentage of nitrogen was determined by the degree of substitution (DS) (Kjeldahl method), following the methodology described by Ribeiro de Carvalho et al. [5].

2.3 Films preparation

The casting technique was used to produce the films [8]. Initially, 4.0 g of Q-CS were suspended in 100 mL of distilled water containing 1.0 g of glycerol. This suspension was gradually heated to 70 °C, with constant stirring at 1000 rpm. Then, 0.4 g of CNC was added to the Q-CS suspension, maintaining the temperature and stirring for 40 min. After that, 20 g of the suspension was poured into acrylic Petri dishes (90 × 15 mm) and dried at 50 °C for 24 h. The films were placed in desiccators with a saturated magnesium nitrate solution (60% relative humidity) for two days for characterization. A Q-CS film was produced without CNC for comparison. The resulting films were named Q-CS and Q-CS/CNC, representing quaternized and quaternized starch with cellulose nanocrystals.

2.4 Thickness and mechanical properties

The thickness of the samples was measured with a digital micrometer (0.001 mm resolution) from Mitutoyo, Japan, at ten random points on the film. Tensile strength (RT, MPa), percentage elongation at break (E, %), and modulus of elasticity (ME, MPa) were measured with a texturometer (model TA.XT2, Stable Micro System SMD) following the method ASTM D882-12 standard [9] (initial clamping distance = 50 mm and test head displacement speed = 10 mm s^{-1}). Ten specimens measuring 80 mm long and 25 mm wide were used.

2.5 Antimicrobial activity

The agar diffusion method was used to evaluate the antimicrobial activity of the films [2,10]. Square samples measuring 0.5 cm x 0.5 cm of each formulation, including the control film, were placed on plates containing nutrient agar previously inoculated with 100 μL of a solution containing approximately 108 CFU/mL of the microorganisms tested: *Staphylococcus aureus* ATCC 6538 and *Escherichia coli* ATCC 11775. Analyzes were performed in triplicate, with samples incubated at 37 °C for 24 h. The MHV-3 coronavirus was used in contact with the L-929 fibroblast cell line for antiviral activity assays [11,12]. The culture medium was prepared with DMEM (Dulbecco's Minimum Essential Medium) containing 2 to 10% FBS (Fetal Bovine Serum). Sequential virus dilutions were prepared in 96-well plates (2 x 10^5 cells/well). The film was placed in direct contact with the virus for 1 min.

3. RESULTS AND DISCUSSION

3.1 Chemical reaction and elemental analysis

The quaternization reaction involves the nucleophilic replacement of the hydroxyl groups of cassava starch by the quaternary ammonium compound (GTMAC), as illustrated in Figure 1. The degree of substitution

(DS) obtained for cassava starch was 0.551, indicating that quaternization was satisfactory [13,14] .This result suggests that modified starch is a promising choice for developing plastic films with antimicrobial properties.
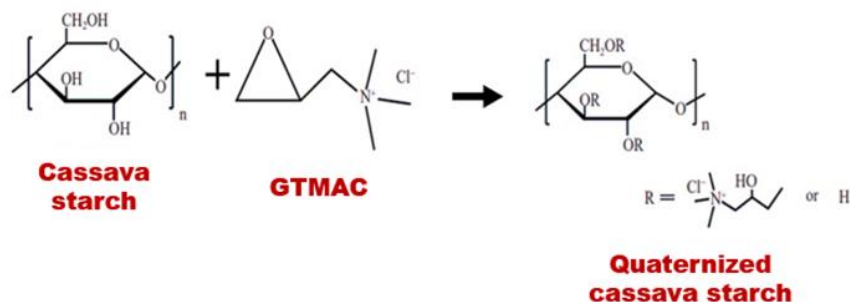
Figure 1. Scheme of chemical reaction of quaternization of cassava starch with GTMAC [5].

3.2 Thickness and mechanical properties

Thickness values and mechanical properties are presented in Table 1.

Table 1. Thickness and mechanical properties of films.

Film	Thickness (mm)	Tensile strength (TS) (MPa)	Elongation at break (EB) (%)	Modulus of elasticity (ME) (MPa)
Q-CS	0.118 ± 0.016[b]	1.42 ± 0.12[b]	34.5 ± 8.7[a]	111.2 ± 13.34[b]
Q-CS/CNC	0.164 ± 0.007[a]	2.04 ± 0.15[a]	28.3 ± 7.7[a]	233.4 ± 14.56[a]

The incorporation of CNC resulted in a significant ($p<0.05$) increase in thickness, with the Q-CS/CNC film being 38.9% thicker than the Q-CS film. This increase in thickness is attributed to the more significant amount of total solids due to the presence of CNC. Other studies investigating starch-based films reinforced with cellulosic material observed the same effect [3,15].

The addition of CNC significantly ($p<0.05$) increased the tensile strength (TS) of the Q-CS/CNC film by 43.6% compared to the Q-CS film. This improvement is attributed to the uniform distribution of particles in the starch matrix due to the nanometric dimensions of the CNC and the rigid properties of the crystalline celluloses that reinforce the material [6,16]. Regarding elongation values at break, no significant differences were observed ($p>0.05$). This suggests that the incorporation of CNC did not affect the elongation of the films under the processing conditions used. Furthermore, both the Q-CS film and the Q-CS/CNC film showed higher elongation percentages when compared to those reported for other types of starch-based films [3,17]. Similarly to the TR values, the presence of CNC increased the elastic modulus (EM) of the quaternized starch-based film by around 109%. This increase results from hydrogen interactions between the CNC and the hydroxyl groups of the starch after quaternization, which reduces the mobility of the polymer matrix, making the film more rigid [6].

3.2 Antimicrobial activity

The Q-CS/CNC film demonstrated rapid activity against the coronavirus, achieving 99% virus inactivation in just 1 min after contact. This antiviral effect is attributed to electrostatic interactions between the positively charged nitrogen atoms of quaternized cassava starch and the negative charges in the phospholipid membranes of the virus [18,19]. These interactions lead to the collapse of viral structures, resulting in the inactivation of the coronavirus (Figure 2) [5]. Furthermore, the Q-CS/CNC film demonstrated antibacterial activity against the tested bacteria, with inhibition zones of 376 mm and 357 mm for *S. aureus* and *E. coli*, respectively. This effectiveness in inactivating bacteria suggests that the film can be used as antimicrobial packaging.
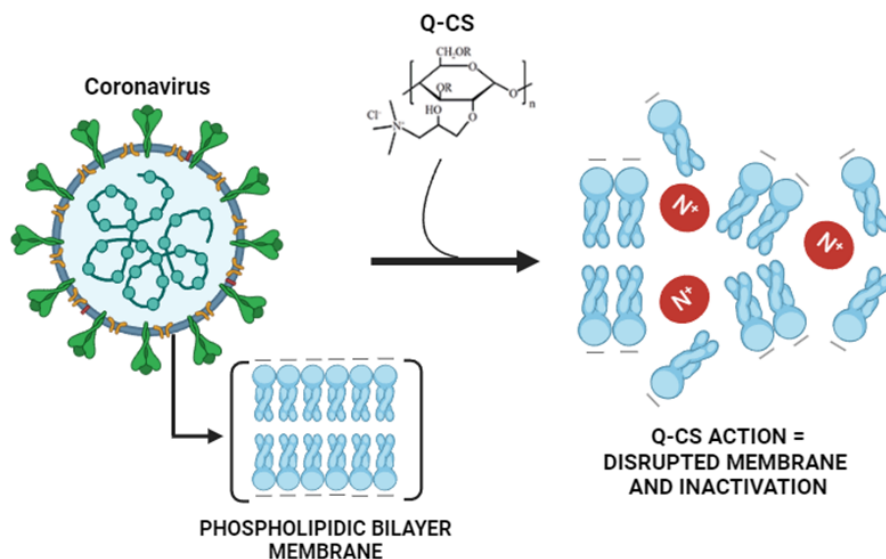
Figure 2. Mechanism of action of Q-CS against the MHV-3 coronavirus.
Red spheres symbolize positively charged nitrogen atoms [5].

4. CONCLUSIONS

In this study, we developed a new antimicrobial composite film based on quaternized cassava starch reinforced with crystalline nanocellulose (CNC). The starch modification resulted in a degree of substitution 0.552, as confirmed by elemental analysis. Adding CNC to the modified starch film increased the thickness and mechanical strength. The Q-CS/CNC film stood out for its notable antibacterial activity against E. coli and S. aureus, in addition to inactivating 99% of the coronavirus in just 1 min. This antimicrobial activity suggests that the film could be a promising option for food and surface coatings, playing a significant role in preventing contamination and combating pandemics and possible future crises involving different viruses.

4.1. Declaration of Competing Interest

The authors declare no conflict of interest.

5. REFERENCES

[1]   Z. He et al. Droplet evaporation residue indicating SARS-COV-2 survivability on surfaces, Phys. Fluids, 2021. https://doi.org/10.1063/5.0038562.
[2]   de Carvalho et al. Antiviral and antibacterial activity of sodium alginate/poly (diallyldimethylammonium chloride) polyelectrolyte film for packaging applications, Int. J. Biol. Macromol, 2023. https://doi.org/10.1016/j.ijbiomac.2023.125388.
[3]   Marques et al. Production and characterization of starch-based films reinforced by ramie nanofibers (*Boehmeria nivea*), J. Appl. Polym. Sci, 2019) 1–11. https://doi.org/10.1002/app.47919.
[4]   G.R. de Carvalho, G.S. Marques, L.M. de Matos Jorge, R.M.M. Jorge, Cassava bagasse as a reinforcement agent in the polymeric blend of biodegradable films, J, Appl. Polym. Sci, 2019. https://doi.org/10.1002/app.47224.
[5]   Ribeiro de Carvalho et al. Quaternization of cassava starch and determination of antimicrobial activity against bacteria and coronavirus, Carbohydr. Res, 2024. https://doi.org/https://doi.org/10.1016/j.carres.2024.109098.
[6]   G.R. de Carvalho et al. Effect of the addition of cassava fibers on the properties of cassava starch composite films, Brazilian J. Chem. Eng, 2021. https://doi.org/10.1007/s43153-021-00093-7.
[7]   W. Zhang et al. Improving the performance of edible food packaging films by using nanocellulose as an additive, Int. J. Biol. Macromol, 2021. https://doi.org/10.1016/j.ijbiomac.2020.10.185.
[8]   M.P. Silveira et al. Development of active cassava starch cellulose nanofiber-based films incorporated with natural antimicrobial tea tree essential oil, J. Appl. Polym. Sci, 2020.

https://doi.org/10.1002/app.48726.

[9]   ASTM International, ASTM D882–18: Standard Test Method for Tensile Properties of Thin Plastic Sheeting, West Conshohocken, 2018.

[10]   R.C. Nonato et al. Nanocomposites of PLA/ZnO nanofibers for medical applications: Antimicrobial effect, thermal, and mechanical behavior under cyclic stress, Polym. Eng. Sci, 2022. https://doi.org/10.1002/pen.25913.

[11]   R.A. Bataglioli et al. Hybrid alginate–copper sulfate textile coating for coronavirus inactivation, J. Am. Ceram. Soc, 2022. https://doi.org/10.1111/jace.17862.

[12]   G.B et al.. Calais. Bioactive textile coatings for improved viral protection: A study of polypropylene masks coated with copper salt and organic antimicrobial agents, Appl. Surf. Sci, 2023. https://doi.org/10.1016/j.apsusc.2023.158112.

[13]   C. Santinon et al. Optimization of kappa-carrageenan cationization using experimental design for model-drug release and investigation of biological properties, Carbohydr. Polym, 2023. https://doi.org/10.1016/j.carbpol.2023.120645.

[14]   R. Covis et al. Structural and rheological properties of kappa (κ)-carrageenans covalently modified with cationic moieties, J. Polym. Res, 2016. https://doi.org/10.1007/s10965-016-0971-z.

[15]   M. Safar et al. Optimization of nanocomposite films based on quinoa protein isolate incorporated with cellulose nanocrystal and starch, J. Food Process. Preserv, 2021. https://doi.org/10.1111/jfpp.15926.

[16]   L. Zhang et al. The effects of cellulose nanocrystal and cellulose nanofiber on the properties of pumpkin starch-based composite films, Int. J. Biol. Macromol, 2021. https://doi.org/10.1016/j.ijbiomac.2021.09.187.

[17]   G.F. Schutz et al. Development of Starch-Based Films Reinforced with Coffee Husks for Packaging Applications, J. Polym. Environ, 2022. https://doi.org/10.1007/s10924-022-02733-6.

[18]   C. Fidelis et al. Synthesis and characterization of n-phosphonium chitosan and its virucidal activity evaluation against coronavirus, Int. J. Biol. Macromol, 2023. https://doi.org/10.1016/j.ijbiomac.2023.125665.

[19]   J. Kerwald et al. Coating of surgical masks with quaternized chitosan aiming at inactivating coronavirus and antibacterial activity, Carbohydr. Polym. Technol. Appl, 2023. https://doi.org/10.1016/j.carpta.2023.100315.

INFLUENCE OF DIFFERENT CONCENTRATIONS OF CARBON NANOTUBES IN ELECTROSPUN PVC COMPOSITE MEMBRANES: THE EFFECTS ON MORPHOLOGY, THERMAL BEHAVIOR AND IMPEDANCE SPECTRA

Marcio Briesemeister*[(a)], Sérgio H. Pezzin[(b)], John A Gómez-Sánchez[(c)], Pedro B. Filho [(d)]

(a) 0000-0003-0707-3176 (Santa Catarina State University – Brazil)
(b) 0000-0002-5667-1968 (Santa Catarina State University – Brazil)
(c) 0000-0002-0295-1235 (Santa Catarina State University – Brazil)
(d) 0000-0002-5264-4874 (Santa Catarina State University – Brazil)
* Corresponding author: marcio.brie@gmail.com

CODE: BCCM7-157

Abstract: The present study aims to evaluate the effect of different concentrations of CNTs in PVC during electrospinning in morphological, thermal and electrical behavior of composite membranes. For this, PVC membranes containing up to 3 wt.% CNTs were electrospun from THF/DMF solutions, and subsequently characterized by thermal analyses (TG and DSC), transmission and scanning electron microscopies (FE-SEM and TEM) and electrical impedance spectroscopy (EIS). TEM images show that most of the nanotubes are encapsulated inside the fibers and oriented along them, hindering the electrical conductivity of the membranes. FE-SEM showed no significant differences in the average diameter of the fibers due to the presence of nanotubes. The CNTs caused a significant reduction (up to 20 °C) in the glass transition temperature (T_g) in relation to the resin and a positive impact on thermal stability. Due to the high porosity and encapsulation of CNTs in the fibers, which prevents the formation of a percolation network throughout the insulating matrix, no significant differences between impedance spectra of neat PVC and PVC/CNT composite membranes were found. Nyquist plots is possible to observe a charge transfer resistance of 38 Mohm and 40 Mohm, respectively, for pure PVC and PVC/CNT 3%.

1. INTRODUCTION

The advancement of electrospinning technology observed in recent decades stands out among nanofiber preparation methods due to its advantages including high control-lability, simple operation, low cost, and wide adjustability.[1] These characteristics have led to the expansion of the use of PVC for a wide variety of applications: air filtration systems, water treatment, batteries, protective clothing, among others. Due to the flexibility of the electrospinning process, it is possible to obtain nanofibers with diameters ranging from a few hundred nanometers to several micrometers. Among several interesting characteristics of electrospun PVC membranes, mechanical resistance, adjustable hydrophobicity, and high porosity can be highlighted.[2]

Although the fibers obtained by the electrospinning technique have a high surface area, high porosity and interesting electrochemical characteristics, nanofibers prepared with a single polymer often do not meet the requirements for practical applications. On the other hand, polymer nanocomposites generally exhibit multifunctional properties and have been widely used in applications in biomedicine, microwave absorption, electro-chemical and optical materials.[3] PVC is among the most used materials in the production of nanocomposites due to its characteristics already mentioned in addition to the possibility of improving its mechanical properties and high environmental resistance. [4] The application restrictions are mainly related to its high glass transition temperature (T_g), resulting from strong polar C-Cl interactions. [5]

The combination of PVC with other functional nanoparticles, such as carbon nanotubes (CNTs), in the electrospinning process makes it possible to expand the range of application of the material to energy, environmental and biomedical fields, among others. [6,7] The incorporation of carbonaceous nanofillers to the PVC matrix impacts the mobility of the polymer chains and, thus, their effect on the structure depends on a variety of factors: such as size, aspect ratio, and chemical functionalization.[8] With the addition of CNTs to the PVC matrix, some effects can be observed, such as changes in Tg and Tp (simultaneous flow temperature), due to the physical interaction between the CNTs and the polymer molecules, and the presence of an interphase between the matrix and the surface of the nanotubes. This new phase presents different properties in relation to neat PVC, promoting molecular mobility restrictions.[9] For a well-dispersed system, a small amount of nanotubes provides a large interfacial area, promoting changes in the mechanical and thermal properties of the polymer.[10]

However, no reference to the effect of nanotube addition to the electrical properties of electrospun PVC membranes have been reported so far. Thus, the present study aims to evaluate the effect of different concentrations of CNTs in PVC during electrospinning in morphological, thermal and electrical behavior of composite membranes.

2. METHODOLOGY

2.1. Materials

Homopolymer PVC (NORVIC® SP 750RA), obtained by suspension polymerization, was supplied by Braskem (Brazil). Multi-walled carbon nanotubes (MWCNTs) were purchased from Chengdu Organic Chemicals Co. Ltd. (China), batch TNIM4, with 95% puri-ty. According to the manufacturer's information, MWCNTs have an external diameter of 10-30 nm, an internal diameter of 5-10 nm and a length of 10-30 μm.

Tetrahydrofuran (THF) and dimethylformamide (DMF), both supplied by Dinâmica (Brazil) with a minimum content of 99 and 99.8%, respectively, were used as solvents. Triton-X100, supplied by Vetec Química (Brazil), was used as a surfactant.

2.2. Solution preparation

PVC solutions were prepared in THF/DMF 50/50 at a concentration of 18 wt.% containing amounts of 0%, 1%, 2% and 3% by weight of CNT. The detailed quantities of each component in the solutions are presented in Table 1.

Table 1: Composition of the PVC/CNT solutions

Name	PVC (g)	CNT (g)	Triton X-100 (g)	DMF (g)	THF (g)
Neat PVC	3.6	-	-	10	10
PVC/CNT 1%	3.6	0.036	0.118	10	10
PVC/CNT 3%	3.6	0.108	0.119	10	10

To produce the PVC/CNT solutions presented in Table 1, the 7 steps contained in Figure 1 were followed.

Figure 1: Procedure for the preparation of PVC/CNT solutions
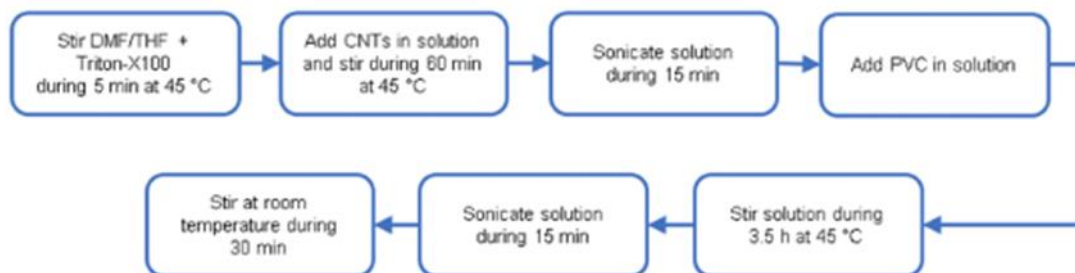
2.3. Preparation of electrospun Membranes

To produce the PVC/CNT electrospun membranes, an Eletrotech Lab EF 2B CRT 0212 electrospinning equipment, produced by DBM Eletrotech (Brazil), was used. The equipment has a rotating collector made of Ø60x200 mm aluminum, a high voltage source for up to 20 kV and two infusion pumps. Table 2 presents the settings used to produce the membranes.

Table 2: Parameters used for the electrospinning processes.

Variables	Values
Flow rate	3 mL/h
Work distance	15 cm
Collector rotation	160 rpm
Syringe	10 mL
Needle	Ø0.7x30mm
Temperature	23 °C
Humidity	42% - 55%

2.4. Thermal Characterization

Thermogravimetry (TG) was carried out in a TA Instruments Thermogravimetric Analyzer model TGA55. The heating rate was 10°C/minute, in a temperature range from 25 to 700°C, under N2 atmosphere. The samples had ca. 5 mg.

Differential Scanning Calorimetry (DSC) analyses were carried out in a NETZSCH DSC 200F3 equipment; the specimens had ca. 5 mg. The analyzes were run with heating and cooling rates of 10°C/min, under N2 atmosphere, gas flow of 40 ml/min and a closed panel system.

To obtain the first heating curves, the samples were heated from 25°C to 165°C, remaining at that temperature for 1 min. For the second heating, the material was cooled to 25°C and subsequently heated again to 165°C, remaining at that temperature for 1 min.

2.5. Morphological Characterization

Field-Emission Scanning Electron Microscopy (FESEM) was performed in a JEOL JSM-6701F operated at 10 kV. The samples were metallized with gold (Dentan Vacuum Desk V) prior to the analyses.

Transmission electron microscopy (TEM) images have been obtained with a JEOL model JEM 2100 microscope. Samples were directly electrospun on carbon sample holders with 300 mesh copper grids (CF300-Cu).

2.6. Electrical Impedance Spectroscopy (EIS)

For the EIS analyses, a MFIA equipment (Zurich Instruments) was used in the frequency range between 10 Hz and 5 MHz, at 300mV and current of 10mA. The measurements were carried out using 2 electrodes made of Ø3/16"x60 mm stainless steel with polished ground contact surfaces, at a distance of 5 mm between the electrodes. Five measurements were taken on each of the samples in the longitudinal direction in the orientation of the mem-brane production. The membranes analyzed were between 150 and 160 µm thick.

3. RESULTS AND DISCUSSION

Figure 2 shows the FESEM images and fiber size distribution histograms of PVC electrospun membranes with different CNT concentrations.

Figure 2: FESEM images of the electrospun membranes and fiber diameter histograms: a) Neat PVC; b) PVC/CNT 1 wt%; c) PVC/CNT 3 wt%
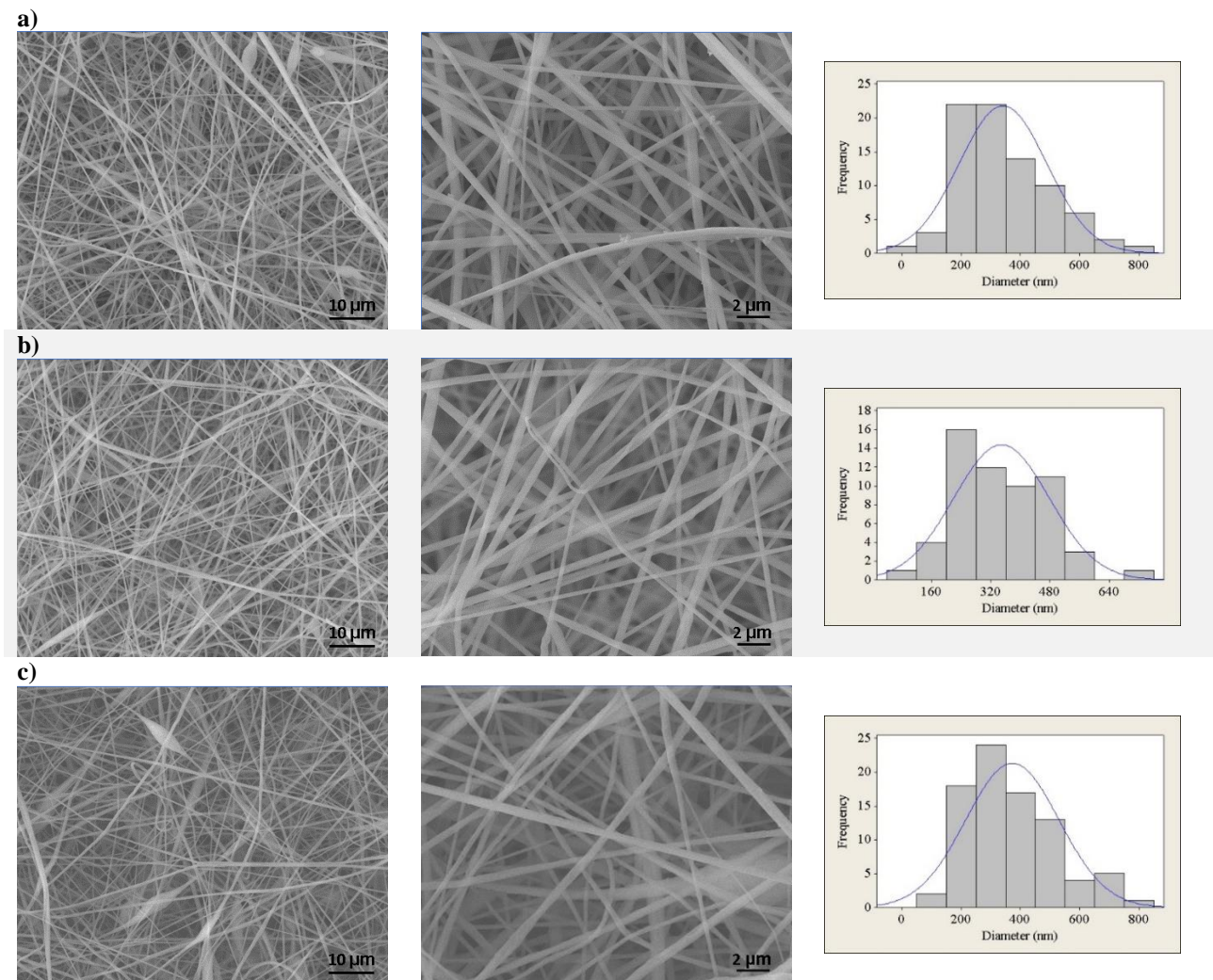
It is observed that the membranes are composed of relatively uniform fibers containing few beads and flaws, except for the membrane containing 3 wt% CNTs, in which there is a greater presence of beads next to the fibers. It has been probably caused by the formation of CNT clusters in the solution, as also observed by Mazinani and Dubois for PET/CNT electrospun membranes.[15] The fibers presented average diameters from 341 to 373 nm, without significant differences, for a significance of 95% considering the Mann-Whitney non-parametric hypothesis test.

Even though the increase in the concentration of CNTs in the solution can promote greater conductivity and a greater number of inductive charges, this did not result in a reduction in the average diameter of the fibers. It is thus suggested that the concentration of CNTs was not sufficient for percolation to occur. The results are similar to those reported by Pham and Uspenskaya, who evaluated the influence of processing variables on the diameter of PVC nanofibers electrospun from 15 wt.% solutions at a flow rate of 1mL/h.[16]

TEM images presenting the dispersion of CNTs inside electrospun PVC fibers are shown in Figure 3.

Figure 3: Dispersion 3% of CNTs inside electrospun PVC
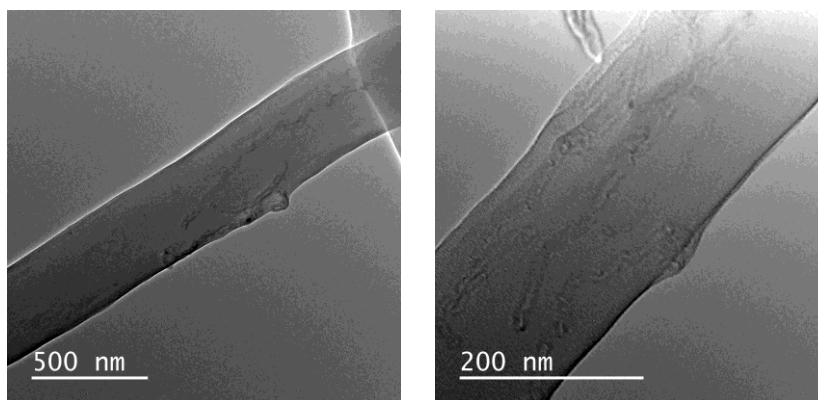
It is observed a good adhesion between the CNTs and the polymer matrix, with only few regions presenting agglomerates. Most of the nanotubes are located inside the fibers and oriented along them, i.e., encapsulated, and only a small portion is positioned on the external side of the fibers. The CNTs that are not fully encapsulated in the PVC fibers are due to their non-uniformity, presenting folds, favoring mechanical entanglement.[17]

Dror et al. proposed a theoretical model to explain the behavior of particles such as CNTs during the electrospinning process. Initially the CNTs are randomly oriented, but due to the wedge-shaped flow they are gradually oriented mostly along the streamlines so that the straight CNTs are oriented as they enter the Taylor cone.[18] It is suggested that combined with the wedge-shaped flow, the alignment of the CNTs is also favored by the action of the electric field, where, according to Yan et al., the intensity of the electric field, the exposure time, the concentration of the nanofiller and the viscosity of the solution are decisive.[17]

The thermal mass loss behavior of the PVC/CNT electrospun membranes, as well as the neat PVC resin, are shown in Figure 4.

Figure 4: Thermogravimetric curves of electrospun PVC/CNT membranes and neat SP750Ra resin
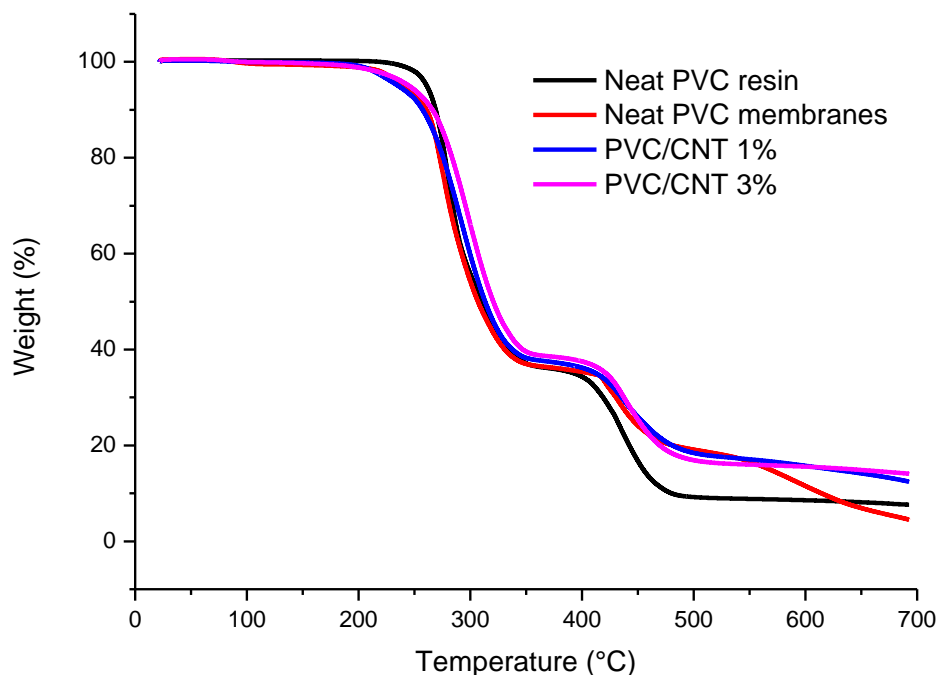
A small mass loss is observed below 150°C in the PVC/CNT membranes, which can be attributed to the vaporization of THF and DMF that were retained in the PVC matrix after electrospinning. Both PVC/CNT nanocomposites and resin present two stages of degradation. In the first stage, attributed to the PVC dehydrochlorination reaction, a mass loss of 64% is observed for the resin and 62% for the fibers containing

3% CNTs, where the mass loss begins shortly after 200°C. For the other PVC/CNT compositions, the mass loss was intermediate between the two values. In the second stage, a mass loss of 17% and 11% is observed for the resin and the nanocomposite, respectively, where the mass loss begins at around 400°C, being attributed to the rupture of the double bonds of the polyene structure, forming volatile hydrocarbons in addition to solid char residue. From 550°C on-wards, variations in the TG curves are observed, which can be attributed to the different concentrations of CNTs in the structure. Analyzing the results, the presence of CNTs in the composition provides, in general, an increase in the thermal stability of the composite. The TG curves are also similar to those found in the study by Hasan et. al., where the authors also evaluated PVC/CNT fibers.[19]

Table 3 shows the DSC detailed results for the first and second heating of PVC/CNT membranes and the neat PVC resin. The results show a well-defined trend in the reduction of the glass transition temperature (Tg) as the concentration of CNTs in the composite increases.

Table 3: Tg values from DSC curves of SP750Ra resin and PVC/CNT membranes

Name	1 st Heating (°C)	2 nd Heating (°C)
Neat PVC resin	82	82
Neat PVC membrane	79	75
PVC/CNT 1%	74	66
PVC/CNT 3%	62	61

The variation in the Tg is strongly related to the mobility of the PVC polymer chains, which can be influenced by the molecular mass, tacticity and the interaction of the nanotubes and the matrix.[20] Nevertheless, the results obtained are contrary to various studies reviewed by Tomaszewska et al.[20] where the addition of CNTs to PVC matrices provides an increase in Tg, by reducing the mobility of the polymer chains. It is suggested that it may be associated with the saturation limit and dispersion of nanotubes in the matrix, causing a plasticizing effect on the composite. The presence of agglomerates at high concentrations of CNTs may also have relatively poor interfacial interactions with the matrix.

Figure 5 presents the results of electrical impedance spectroscopy of pure PVC and 3% PVC/CNT electrospun blankets. Analyzing the results of |Z| (Figure 5a), no significant differences were found between the two samples considering the non-parametric Mann-Whitney test for a significance of 95%.

Figure 5 - Electrical Impedance Spectroscopy: a) Bode plot and b) Nyquist plot.
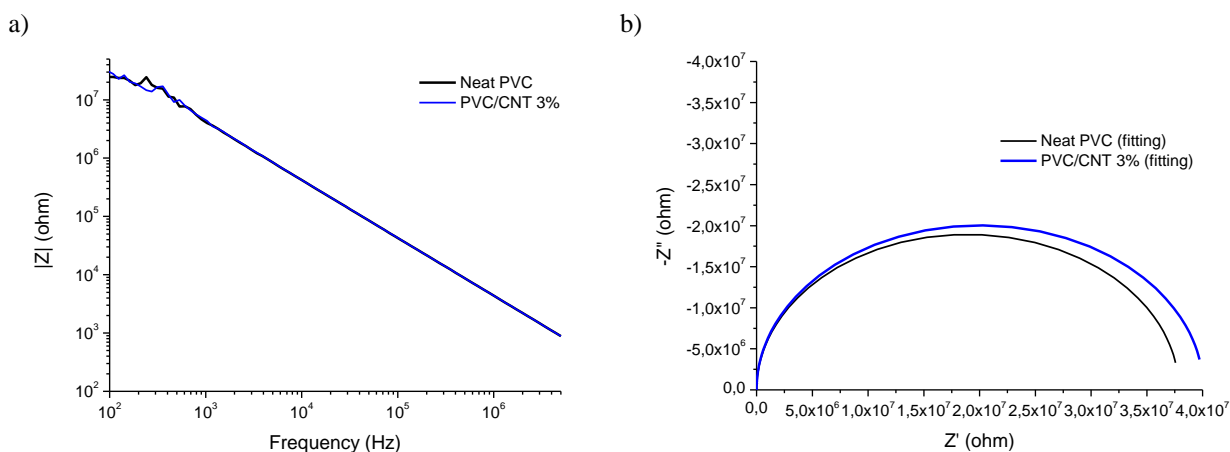
In Figure 5b, the fitting and experimental Nyquist plots for PVC and PVC/CNT 3% membranes, where it is possible to observe a charge transfer resistance of 38 Mohm and 40 Mohm, respectively, for pure PVC and PVC/CNT 3%. The results confirm the resistive characteristic of the material regardless of the presence of CNTs in the structure. I.e., the addition of 3 wt.% CNTs did not interfere with the impedance spectroscopy results. It is suggested that the reason for non-percolation was basically due to two factors: the first is the encapsulation of the vast majority of CNTs within the fibers and the second is the high porosity of the membranes caused by the spaces (voids) between the fibers.

Thus, although the high electrical conductivity of CNTs, the PVC/CNT 3% membrane, in the dry state, presented almost the same electrical behavior as the insulating porous PVC matrix, as there was no formation of a conducting network due to the encapsulation of the nanotubes within the fibers. The pores, within and

between the fibers, also play an important role in determining the physical and chemical properties of electrospun membranes.[21]

4. CONCLUSIONS

It was observed that the addition of nanotubes did not affect the average diameter of the fibers, as well as their surface morphology. However, most of the CNTs were located inside the fibers ('encapsulated') and longitudinally oriented, and just a small part of the nanotubes was positioned externally.

It can be also highlighted a significant decrease (up to 20 °C) for the PVC/CNT composite membranes, in comparison to neat PVC, which is possibly related to the 'saturation limit' of CNTs in PVC, leading to clusters, and hindering the dispersion of the nanofiller.

Regarding the results of electrical impedance spectroscopy, no significant differences were found due to the presence of CNTs in the PVC membranes, in the dry state. It is suggested that high charge transfer resistance is related to the high porosity and encapsulation of CNTs in the fibers, which prevents the formation of a percolation network throughout the insulating matrix.

4.1. Declaration of Competing Interest

The authors declare no conflict of interest.

4.2. Fundings

4.3. Acknowledgements

5. REFERENCES

[1]   He J-H, Wan Y-Q. Allometric scaling for voltage and current in electrospinning. Polymer (Guildf) 2004;45:6731–4.

[2]   Freier G. The coalescence of water drops in an electric field. J Geophys Res 1960;65:3979–85.

[3]   Schubert DW, Allen V, Dippel U. Revealing novel power laws and quantization in electrospinning considering jet splitting—Toward predicting fiber diameter and its distribution part ii experimental. Adv Eng Mater 2021;23:2001161.

[4]   Sakamoto H, Fujiwara I, Takamura E, Suye S. Nanofiber-guided orientation of electrospun carbon nanotubes and fabrication of aligned CNT electrodes for biodevice applications. Mater Chem Phys 2020;245:122745.

[5]   Wang N, Wang B, Wang W, Yang H, Wan Y, Zhang Y, et al. Structural design of electrospun nanofibers for electrochemical energy storage and conversion. J Alloys Compd 2023;935:167920.

[6]   Han W-H, Wang M-Q, Yuan J-X, Hao C-C, Li C-J, Long Y-Z, et al. Electrospun Aligned Nanofibers: A Review. Arabian Journal of Chemistry 2022:104193.

[7]   Sharafkhani S, Kokabi M. High performance flexible actuator: PVDF nanofibers incorporated with axially aligned carbon nanotubes. Compos B Eng 2021;222:109060.

[8]   ElMessiry M, Fadel N. The tensile properties of electrospun poly vinyl chloride and cellulose acetate (PVC/CA) bi-component polymers nanofibers. Alexandria Engineering Journal 2019;58:885–90.

[9]   Es-Saheb M, Elzatahry AA, Sherif E-SM, Alkaraki AS, Kenawy E-R. A novel electrospinning application for polyvinyl chloride nanofiber coating deposition as a corrosion inhibitor for aluminum, steel, and brass in chloride solutions. Int J Electrochem Sci 2012;7:5962–76.

[10]   Chiscan O, Dumitru I, Tura V, Stancu A. PVC/Fe electrospun nanofibers for high frequency applications. J Mater Sci 2012;47:2322–7.

[11]   Quoc Pham L, Uspenskaya M V, Olekhnovich RO, Olvera Bernal RA. A review on electrospun pvc nanofibers: Fabrication, properties, and application. Fibers 2021;9:12.

[12]   Namsaeng J, Punyodom W, Worajittiphon P. Synergistic effect of welding electrospun fibers and MWCNT reinforcement on strength enhancement of PAN–PVC non-woven mats for water filtration. Chem Eng Sci 2019;193:230–42.

[13] Iribarren A, Rivero PJ, Berlanga C, Larumbe S, Miguel A, Palacio JF, et al. Multifunctional protective PVC-ZnO nanocomposite coatings deposited on aluminum alloys by electrospinning. Coatings 2019;9:216.

[14] Yang X, Wang Y, Qing X. A flexible capacitive sensor based on the electrospun PVDF nanofiber membrane with carbon nanotubes. Sens Actuators A Phys 2019;299:111579.

[15] Mazinani S, Ajji A, Dubois C. Fundamental study of crystallization, orientation, and electrical conductivity of electrospun PET/carbon nanotube nanofibers. J Polym Sci B Polym Phys 2010;48:2052–64.

[16] Pham LQ, Uspenskaya M V. Morphalogy PVC nanofiber, produced by electrospinning method. International Multidisciplinary Scientific GeoConference Surveying Geology and Mining Ecology Management; SGEM: Sofia, Boulgaria 2019;19:289–95.

[17] Zhang Q, Chang Z, Zhu M, Mo X, Chen D. Electrospun carbon nanotube composite nanofibres with uniaxially aligned arrays. Nanotechnology 2007;18:115611.

[18] Dror Y, Salalha W, Khalfin RL, Cohen Y, Yarin AL, Zussman E. Carbon nanotubes embedded in oriented polymer nanofibers by electrospinning. Langmuir 2003;19:7012–20.

[19] Hasan M, Kumar R, Barakat MA, Lee M. Synthesis of PVC/CNT nanocomposite fibers using a simple deposition technique for the application of Alizarin Red S (ARS) removal. RSC Adv 2015;5:14393–9.

[20] Tomaszewska J, Sterzyński T, Woźniak-Braszak A, Banaszak M. Review of recent developments of glass transition in PVC nanocomposites. Polymers (Basel) 2021;13:4336.

[21] Wang X, Wang W, Li X, Carlberg B, Lu X, Cheng Z, et al. Investigation of dielectric strength of electrospun nanofiber based thermal interface material. 2007 International Symposium on High Density packaging and Microsystem Integration, IEEE; 2007, p. 1–6.

EVALUATION OF TENSILE STRENGTH AND MASS LOSS OF EPOXY AND SOYBEAN OIL BASED COMPOSITES WITH INSERTION OF CELLULOSE NANOCRYSTALS

Roseméri Barbosa dos Santos da Silva[(a)*], Paulo Roberto[(b)], Felipe Gabriel Santos Araújo[(c)], Gabriel Mendonça Valane[(d)], Michel Picanço Oliveira[(e)], Mateus Urbano do Nascimento[(f)]

(a) 0009-0004-6432-591X (Federal University of Espírito Santo – Brazil)
(b) 0000-0001-8594-0920 (Federal University of Espírito Santo – Brazil)
(c) 0009-0000-7069-5408 (Federal University of Espírito Santo – Brazil)
(d) 0000-0002-2736-4440 (Federal University of Espírito Santo – Brazil)
(e) 0000-0001-9241-0194 (Federal University of Espírito Santo – Brazil)
(f) 0009-0008-3032-8134 (Federal University of Espírito Santo – Brazil)
* Corresponding author: rosemeribarbosadossantos@hotmail.com

CODE: BCCM7-160

Abstract: In recent years, the need for eco-friendly materials has sparked an attempt to replace petroleum-derived polymers with biodegradable polymers. However, obtaining a high-performance biodegradable polymer is still a challenge, due to its properties being inferior to those of fossil origin. An alternative to reduce the use of petroleum-derived polymers in the development of polymeric composites are oils of vegetable origin with the subsequent addition of fillers derived from renewable sources to improve their physicochemical properties. In view of this approach, this study sought to develop an epoxy-based composite with 20% of epoxidized soybean oil in the composition of the matrix with the insertion of cellulose nanocrystals (CNC's) to the polymeric matrix in the proportion of 1%, 2% and 3%, then the composites were subjected to mechanical tensile tests, thermogravimetric analysis (TG) and scanning electron microscopy (SEM). From the analyses, it was observed that there was no gain in tensile strength, however, the addition of CNC provided an increase in the modulus of elasticity, in which the insertion of 1, 2 and 3% of CNC presented a gain of around 27, 13 and 16% to the modulus of elasticity to tensile, increasing the stiffness of the composite material. The failure behavior was characteristic of brittle fracture, while the degradation behavior of the composites was similar to that of the pure matrix with slightly lower displacements. Thus, it is possible to use CNC-reinforced epoxy and soybean oil composites in applications that require lower values of mechanical properties and in temperature conditions close to those of epoxy degradation.

1. INTRODUCTION

Thermosetting resins are widely used in coatings, adhesives, composites and other areas due to their excellent thermomechanical properties, dimensional stability and medium strength. As part of this classification, epoxies resins account for nearly 70% of the thermoset polymer market, synthesized from low molar mass prepolymers with at least two epoxide groups [1]. Bisphenol A diglycidyl ether (DGEBA) is the main precursor of epoxy resin and is synthesized by the reaction between bisphenol A (BPA) and epichlorohydrin. As a chemical derived from petroleum, BPA is classified as hazardous to human health and, for this reason, researchers have been studying the development of bio-based epoxie resins that do not use the precursor DGEBA [2].

Concomitantly, due to the growing interest in ecological materials and technologies, the application of biodegradable raw materials to obtain polymer-based composite materials with a sustainable character has

been incurred. The use of epoxidized vegetable oils as raw material plays a fundamental role in maintaining oil reserves and reducing dependence on petrochemical derivatives. In addition, its use in the formulation of resins allows the polymer to have greater flexural properties [3].

Plant-based, soybean epoxidized oil (ESO) has long been considered a viable bio-based substitute for petroleum-based epoxy resin. However, cured ESO exhibits suboptimal mechanical properties and thermal resistance for use as a thermoset. These limitations hinder the practical application of ESO thermosets [4] and, therefore, an alternative for the development of composites using ESO is to partially insert it in the formulation of the synthetic epoxy resin, providing the final compound with better thermomechanical properties, however, sustainability is partially violated.

Epoxidized vegetable oil is already used in the Polyvinyl Chloride (PVC) industry as a natural plasticizer, which gives flexibility to this polymer. Madaleno et al (2009) [5] studied the application of modified and epoxidized vegetable oil in PVC compared to the use of traditional plasticizers, such as dioctyl phthalate (DOP) and dioctyl adipate (DOA). According to the authors, the mechanical properties analysis showed that the vegetable oil was more efficient in the plasticization of PVC than the other plasticizers, confirming its potential application in PVC formulations.

Furthermore, cellulose nanocrystals (CNCs) are nanoscale biological-based materials that can be of plant origin or derived from bacteria, highly available and renewable. However, the use of CNCs as fillers in composites is also due to characteristics such as large specific surface area, high transparency, high strength, low density, and susceptibility to chemical modification [6,7]. As such, CNCs have been widely studied as micro/nano fillers to increase toughness, conductivity, tensile strength, and other performance properties of epoxy resins [8].

In view of the above, it is important to obtain green nanocomposites that exhibit considerable thermomechanical characteristics for future applications. Therefore, with the aim of ensuring such properties, this work was developed with the objective of producing an epoxy and ESO-based nanocomposite with the addition of CNCs as a reinforcing agent to evaluate the feasibility of using ESO and CNCs in obtaining epoxy-based nanocomposites.

2. METHODOLOGY

The composite materials were obtained by the insertion of cellulose nanocrystals (CNC) into epoxy resin previously mixed with 20% epoxidized soybean oil. The variations established in the compositions were made for the resin and the CNCs, as shown in Table 1.

Table 1. Produced composites and their compositions.

Treatment	Material Code Epoxi	Epoxy Resin (%)	Epoxidized Soybean Oil (%)	CNC (%)
Control	EPX00	80	20	0
	CNC01	79	20	1
CNC	CNC02	78	20	2
	CNC03	77	20	3

Initially, the CNCs in aqueous suspension were mixed with epoxidized oil. This mixture was kept on a hot plate together with a mechanical stirrer and with the aid of a thermometer, the temperature was maintained at ±103°C to ensure the evaporation of water and the concentration of CNCs in the oil. This step lasted until all the water from the initial mixture was evaporated. After eliminating all the water, the mixture containing the oil and the CNCs were added to the epoxy resin, and then mixed with a hardener component and molded into silicone forms with adapted measures to obtain tensile and flexural testing samples. Subsequently, the material remained at rest for 24 hours during the resin polymerization, and then was placed in a drying oven for 48 hours at 70°C to complete its total curing, achieving the test specimens with adaptation to standard D638 [9].

The obtained samples were mechanically tested for tensile strength in a universal testing machine Emic model DL 10000. The broken specimens were subjected to scanning electron microscopy (SEM) analysis with a JEOL microscope model JSM-IT200 to validate the fracturing surface morphology of the composites. In order to evaluate the thermal degradation behavior of the composites, thermal characterization of the samples in powder form was carried out on a LabSys Evo thermogravimetric analyzer in the temperature range of 25°C to 800°C with a heating rate of 10°C min^{-1}.

3. RESULTS AND DISCUSSION

The Figure 1 shows the representative graphs of the properties of maximum tensile strength (Figure 1-A), modulus of elasticity (Figure 1-B) and tensile toughness (Figure 1-C) of the nanocomposites with and without the addition of CNC's.

Figure 1- Mechanical properties of maximum tensile strength (a), modulus of elasticity (b) and tensile toughness (c) of nanocomposites and pure resin with ESO.
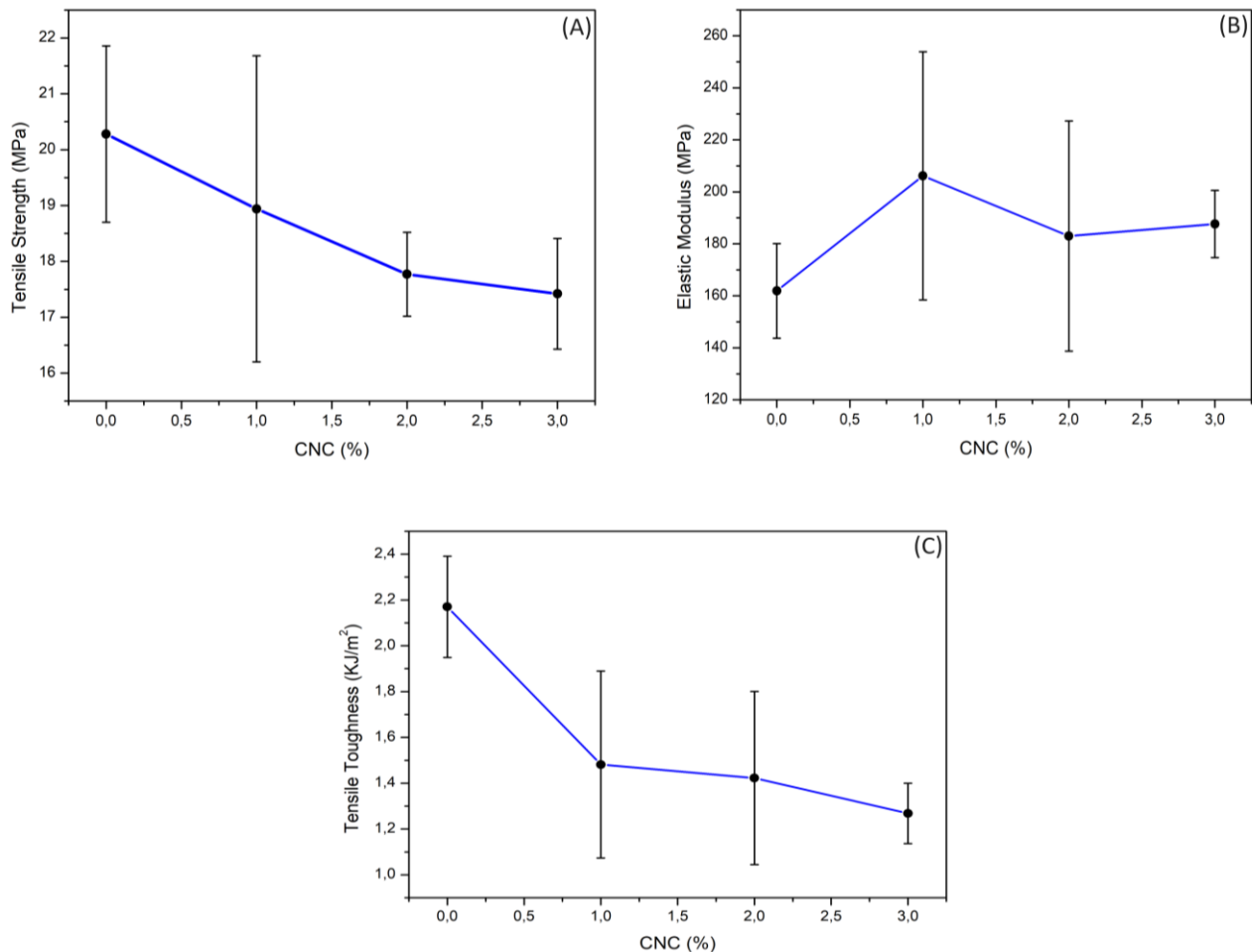
When analyzing the maximum tensile strength of the nanocomposites, it was observed that the addition of 1, 2 and 3% of CNC's to the matrix did not provide improvement in the strength results when compared to only the matrix and the different compositions of the nanocomposite. Although CNC's individually present good mechanical strength, when inserted in a polymeric matrix of non-polar character, there is an inverse effect on the tensile strength property. This may be because CNC's have a hydrophilic nature that inhibits homogeneous dispersion in hydrophobic polymer matrices producing weak interfaces, which reduces the mechanical properties of the material [10]. In this case, this fact could have promoted low results in tensile strength, mainly due to the methodological process for removing the water present in the suspension of CNC's. One way to overcome this limitation is to use coupling agent to modify the surface of the CNC's and ensure better interfacial adhesion [10]. Another factor that may have influenced the tensile strength results is the insertion of ESO in the epoxy resin formulation, which commonly has weak tensile mechanical properties [11].

Regarding the modulus of elasticity (MOE) in tension, Figure 1-B shows that the insertion of CNC's caused an increase in all compositions of the nanocomposites, with the highlight of the composite with 1% CNC's, which presented a value of 206 MPa. This behavior may be associated with the high Young's modulus of up to 140 GPa found in CNC's [12] (Grishkewich et al., 2017), while the epoxy matrix with ESO showed the lowest value for MOE. Tensile toughness, corresponding to Figure 1-C, decreased with the increase of CNC's in the nanocomposite composition, among which, the composite with 1% showed the highest tensile

toughness, while the resin with ESO remained with the maximum tensile toughness value. This fact can be interpreted due to the addition of higher molecular weight ESO to the epoxy resin, which causes an increase in the flexible properties of the epoxy resins and weak linkage between ESO and CNC[13].

The SEM images of the fracture surface of the composites found in Figure 2 help to verify how the failure in the material occurred. From Figure 2-A, we can see an aspect of a fragile fracture (red arrows), characteristic of the epoxy resin with ESO. This fracture surface also occurred for the nanocomposites (green arrows) where it is possible to observe that there was the formation of cavitations (region demarcated by circles) in the structure of the nanocomposite (Figure 2-B) which evidently contributed to low tensile strength. When dispersed in epoxy, the unreacted ESO is cavitated and leads to an increase in resistance to deformation and the initiation of cracks in the matrix. Generally, epoxy resin compounds with ESO exhibit higher flexural strength compared to pure epoxy resins [13].

Figure 2 – Scanning electron microscopy of the (a) fracture surface of the pure matrix and (b) the nanocomposite.
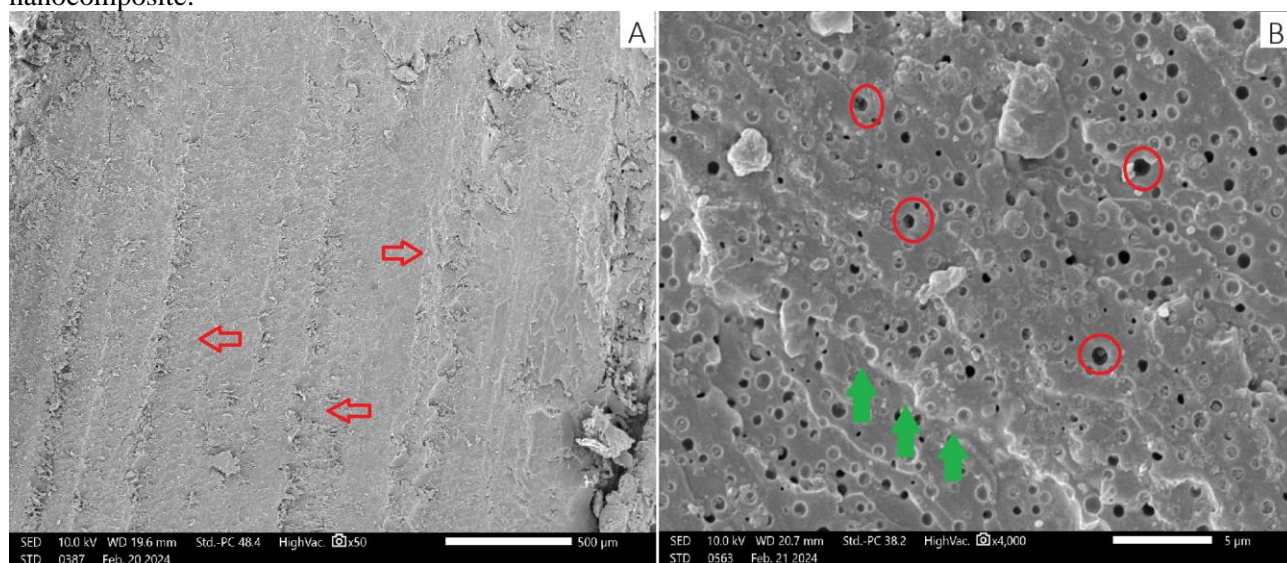
The Figure 3 shows the thermal degradation curves of the CNCs (Figure 3-A), the nanocomposites with 1, 2 and 3% of the CNC's and the pure resin (Figure 3-B). Observing the degradation curve of the CNC's, it is verified that the loss of mass up to approximately 119°C corresponds to the loss of water of the CNC's. From 230°C to 315°C there is an intense mass loss of 35% due to the degradation of the cellulosic chain, especially hemicellulose. The last stage occurred more slowly up to 400°C with the formation of carbon residue as seen in the literature [14-16].

Figure 3 – Thermogravimetric curves of (a) CNC and nanocomposites and pure resin with ESO (b).
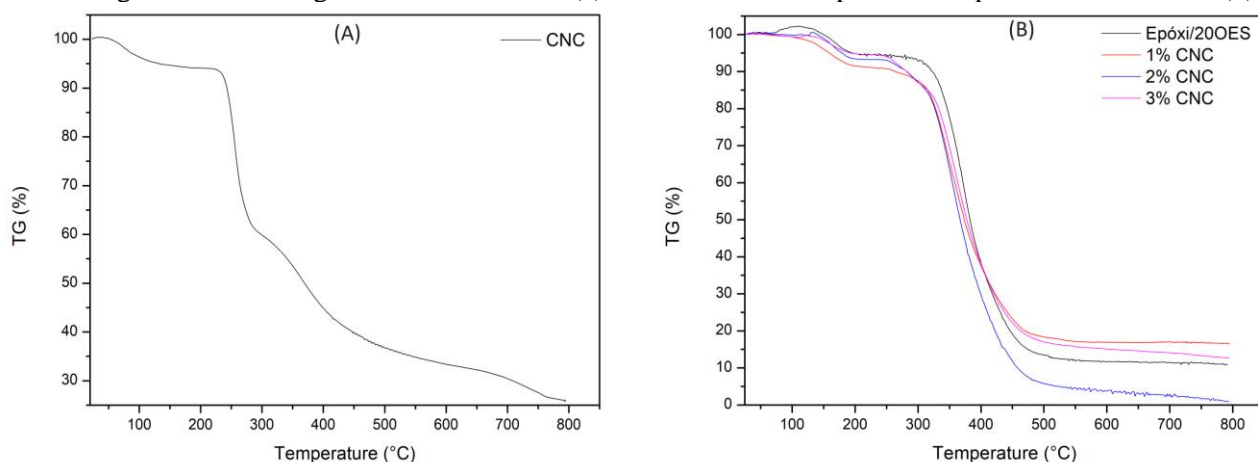
The Figure 3-B shows that the thermal degradation onset temperatures for epoxy with 20% ESO, and composites with 1, 2 and 3% CNC were 280°C, 256°C, 249°C and 246°C, respectively. It was observed that nanocomposites with CNC incorporation showed reduced thermal stability compared to epoxy with ESO. This behavior may be associated with lower CNC stability, as seen earlier. With the increase in the CNC content,

the thermal stability was slightly reduced, a behavior consistent with the stability of the separate constituents, which was also observed by other authors [11].

4. CONCLUSIONS

From the obtained and analyzed results, it is concluded that the use of epoxidized soybean oil is a viable alternative to partially replace epoxy resin in the formulation of nanocomposites; however, further study is needed to minimize the formation of cavitations in the material structure. The insertion of CNC's did not improve the tensile strength and tensile toughness properties, but with the addition of 1% of CNC's, there were improvements in the modulus of elasticity, providing greater rigidity to the nanocomposite. Regarding thermal stability, the incorporation of CNC's significantly slightly decreased the degradation temperature of the materials, indicating that at ambient conditions with temperatures up to 246°C, these materials are suitable for application. The addition of 1% of CNC's was shown to be the most suitable for the development of epoxy-based nanocomposites with epoxidized soybean oil, particularly in applications that require greater rigidity.

4.1. Declaration of Competing Interest

The authors declare no conflicts of interest in this work.

4.2. Fundings

4.3. Acknowledgements

5. REFERENCES

[1]   R. Auvergne, S. Caillol, G. David, B. Boutevin, and J. P. Pascault, "Biobased thermosetting epoxy: Present and future," *Chem Rev*, vol. 114, no. 2, pp. 1082–1115, 2014, doi: 10.1021/cr3001274.

[2]   N. Khundamri, C. Aouf, H. Fulcrand, E. Dubreucq, and V. Tanrattanakul, "Bio-based flexible epoxy foam synthesized from epoxidized soybean oil and epoxidized mangosteen tannin," *Ind Crops Prod*, vol. 128, no. November 2018, pp. 556–565, 2019, doi: 10.1016/j.indcrop.2018.11.062.

[3]   A. P. O. Costa, A. E. Gerbase, and C. L. Petzhold, "Investigação da cinética de cura por calorimetria diferencial exploratoṕria (DSC) de resinas epóxi preparadas a partir de óleo de soja epoxidado com diferentes anidridos e aminas terciárias," *Polimeros*, vol. 21, no. 2, pp. 146–150, 2011, doi: 10.1590/S0104-14282011005000022.

[4]   X. Zhen *et al.*, "Fully bio-based epoxy resins from lignin and epoxidized soybean oil: Rigid-flexible, tunable properties and high lignin content," *Int J Biol Macromol*, vol. 254, no. P2, p. 127760, 2024, doi: 10.1016/j.ijbiomac.2023.127760.

[5]   E. Madaleno, D. D. S. Rosa, S. F. Zawadzki, T. H. Pedrozo, and L. P. Ramos, "Study of the use of plasticizer from renewable sources in PVC compositions," *Polimeros*, vol. 19, no. 4, pp. 263–270, 2009, doi: 10.1590/s0104-14282009000400004.

[6]   L. Feng, M. Zhang, Y. Hua, P. Zhu, and Y. Tang, "Enhanced mechanical and thermal properties while maintaining transparency of epoxy resin film by introducing shear-oriented cellulose nanocrystals," *Prog Org Coat*, vol. 182, no. January, p. 107683, 2023, doi: 10.1016/j.porgcoat.2023.107683.

[7]   J. Wang, X. Liu, T. Jin, H. He, and L. Liu, "Preparation of nanocellulose and its potential in reinforced composites: A review," *J Biomater Sci Polym Ed*, vol. 30, no. 11, pp. 919–946, 2019, doi: 10.1080/09205063.2019.1612726.

[8]   R. Haney, R. H. Kollarigowda, L. Wiegart, and S. Ramakrishnan, "Surface-Functionalized Cellulose Nanocrystals as Nanofillers for Crosslinking Processes: Implications for Thermosetting Resins," *ACS Appl Nano Mater*, vol. 5, no. 2, pp. 1891–1901, 2022, doi: 10.1021/acsanm.1c03508.

[9]   ASTM-D638-12, "Standard Test Method for Tensile Properties of Plastics," *ASTM Standards*, vol. 08, 2014, doi: 10.1520/D0638-22.1.

[10]   H. Kargarzadeh, R. M. Sheltami, I. Ahmad, I. Abdullah, and A. Dufresne, "Cellulose nanocrystal reinforced liquid natural rubber toughened unsaturated polyester: Effects of filler content and surface treatment on its morphological, thermal, mechanical, and viscoelastic properties," *Polymer (Guildf)*, vol. 71, pp. 51–59, 2015, doi: 10.1016/j.polymer.2015.06.045.

[11]   F. Zhao, P. X. Tian, Y. D. Li, Y. Weng, and J. B. Zeng, "Fabrication of well-dispersed cellulose nanocrystal reinforced biobased epoxy composites using reversibility of covalent adaptable network," *Int J Biol Macromol*, vol. 244, no. February, p. 125202, 2023, doi: 10.1016/j.ijbiomac.2023.125202.

[12]   N. Grishkewich, N. Mohammed, J. Tang, and K. C. Tam, "Recent advances in the application of cellulose nanocrystals," *Curr Opin Colloid Interface Sci*, vol. 29, pp. 32–45, 2017, doi: 10.1016/j.cocis.2017.01.005.

[13]   S. J. Park, F. L. Jin, and J. R. Lee, "Thermal and mechanical properties of tetrafunctional epoxy resin toughened with epoxidized soybean oil," *Materials Science and Engineering: A*, vol. 374, no. 1–2, pp. 109–114, 2004, doi: 10.1016/j.msea.2004.01.002.

[14]   F. D'Acierno, W. Y. Hamad, C. A. Michal, and M. J. Maclachlan, "Thermal Degradation of Cellulose Filaments and Nanocrystals," *Biomacromolecules*, vol. 21, no. 8, pp. 3374–3386, 2020, doi: 10.1021/acs.biomac.0c00805.

[15]   J. K. Ogunjobi, A. I. Adewale, and S. A. Adeyemi, "Cellulose nanocrystals from Siam weed: Synthesis and physicochemical characterization," *Heliyon*, vol. 9, no. 1, p. e13104, 2023, doi: 10.1016/j.heliyon.2023.e13104.

[16]   V. Chaparala, G. Ravi Kiran Sastry, and P. Phani Prasanthi, "Thermal degradation study of cotton waste pulp-based cellulose nanocrystals," *Mater Today Proc*, no. xxxx, 2023, doi: 10.1016/j.matpr.2023.05.134.

ENHANCING RHEOLOGICAL PROPERTIES OF HDPE/GRAPHENE NANOCOMPOSITES THROUGH THERMOKINETIC MIXING

Lucas J. S. Nascimento[(a)]*, Tainá S. Guatimosim[(b)], Sandro C. Amico[(c)], Otávio Bianchi[(d)]

(a) 0009-0009-9899-5774 (Federal University of Rio Grande do Sul – Brazil)
(b) 0009-0000-8470-941X (Federal University of Rio Grande do Sul – Brazil)
(c) 0000-0003-4873-2238 (Federal University of Rio Grande do Sul – Brazil)
(d) 0000-0001-7493-8163 (Federal University of Rio Grande do Sul – Brazil)
* Corresponding author: lucas.jonatas@ufrgs.br

Abstract: Carbonaceous nanoparticles, like graphene, exhibit vast potential in various applications, including electrical devices, sensors, and rheological additives. In particular, graphene nanoplatelets (GNP) composed of 2 to 10 layers are an economically viable option for many uses, particularly polymeric additives. However, a significant challenge arises in their utilization, primarily related to the production process. The dispersion of graphene nanoplatelets in polymeric matrices is challenging due to the high viscosity of these matrices (>1000 Pa.s) and the limited specific energy provided by conventional processing systems. Strategies employing high shear-rates (>1000 s^{-1}) emerge as promising solutions. In this context, this study proposes an innovative approach for effectively dispersing and distributing graphene nanoplatelets in high-density polyethylene (HDPE) using a thermokinetic mixer. Notably, the effect of the residence time (10 and 20 min) at a rotation speed of 2640 rpm for the incorporation of GNP (0.1 and 1wt.%) was studied. The system temperature was kept below 110 °C to mitigate potential adverse effects such as chain splitting induced by excessive shear forces. The rheological behavior was evaluated using oscillatory rheometry (utilizing parallel-plate geometry at 190 °C) within the linear viscoelastic regime. The increase in residence time led to a corresponding rise in viscosity during the initial Newtonian plateau. This phenomenon can be attributed to improved nanoparticle dispersion, which hinders chain mobility within the matrix. Similar trends were observed concerning the storage modulus at a frequency of 0.1 rad/s. Thus, the findings suggest that prolonged residence times exhibit a positive correlation with improved rheological properties, indicating the potential for optimizing nanocomposite performance without significant drawbacks in the processing of HDPE.

1. INTRODUCTION

The evolution of nanotechnology has brought about the development of nanocomposites composed of a polymer matrix reinforced with nanoparticles dispersed on a nanoscale. These nanoparticles exhibit significantly large surface area per unit volume, typically approximately 1000 times greater than those found in conventional (micro)composites [1]. Graphene is a plane and two-dimensional structure formed by carbon atoms that are only one atom thick [2], being found in agglomerates containing a different number of packed sheets, known as platelets. They have excellent dimensional stability, thermal and electrical conductivity, flexibility, and exceptional mechanical strength [3].

The occurrence of agglomeration is common in polymer nanocomposites with graphene nanoplates (GNP), single-layer graphene (SLG), or multilayer graphene (MLG) [4]. Agglomeration is typically a result of ineffective dispersion of fillers throughout the composite during fabrication or when the volume concentration of graphene fillers surpasses a critical level. The agglomeration threshold is a crucial parameter

that indicates the development of cohesive clusters of graphene due to intermolecular van der Waals forces [5].

El Achaby et al. [6] investigated the production of nanocomposites by incorporating graphene into a high-density polyethylene (HDPE) matrix through melt-mixing using a torque rheometer. Their findings underscored the significant impact of the nanofiller shape and size on reinforcement efficacy. The superior performance of graphene nanoplatelets was attributed to their augmented surface area and nanoscale planar structure, which facilitated enhanced interfacial interactions with HDPE. Additionally, rheological percolation was observed for nanoparticle content ranging from 0.5 to 1 wt.%, with a transition from liquid-like to solid-like viscoelastic behavior. In another study, conducted by Okan [7], HDPE was compounded with thermally exfoliated graphene oxide employing a custom Gelimat thermokinetic mixing apparatus, operating at 5500 rpm and 215 °C for 45 s to ensure proper dispersion at high shear-rate. The importance of preventing graphene sheet agglomeration and restacking within the matrix was highlighted, effectively mitigating stress concentration points, particularly at 2 wt.% of thermally exfoliated graphene oxide (TEGO). Furthermore, Tarani et al. [8] was noted an increase in viscosity at low oscillation frequencies (10^{-1}-10 rad/s) concerning the average diameter of graphene nanoplatelets (GNP), possibly attributed to greater mobility restriction, and high shear-rates facilitated enhanced dispersion of these nanoparticles.

This study focuses on the production of HDPE/graphene nanocomposites with a thermokinetic mixer, particularly assessing the system processing time and rheological characteristics.

2. METHODOLOGY

2.1. Materials

HDPE developed for rotational molding (grade HD4601), with MFI of 2.0 g/10 min (190 °C, 2.16 kg – ASTM D-1238) and density of 0.942 g/cm³, was purchased from Braskem. Graphene nanoplatelets were obtained from Strem Chemicals, Inc. USA, with 6-8 nm average thickness and up to 25 µm in size.

2.2. Mixing and specimen production

The nanocomposites were prepared using a thermokinetic mixer operating at 2640 rpm with ≈200 g batches. Different mixing residence times of 10 and 20 min were evaluated for nanoparticle contents of 0.1 and 1wt.%. Emphasis was placed on maintaining the system temperature below 110 °C throughout the process.

For sample preparation, 3 g of the mixture was processed using a HAAKE MiniJet II at 180 °C using an injection pressure of 600 bar. The resulting samples exhibited dimensions of ≈58.5±0.2 × 12.3±0.1 × 3±0.1 (length × width × thickness, in mm). The introduction of neat HDPE and HDPE/GNP powders into the charging cylinder was followed by the application of pressure via a vertical steel piston to achieve uniform filling of the sample mold cavity. This process facilitated the creation of a consistent pattern across all samples, ensuring homogeneity in the resulting structures.

2.3. Characterization

Dynamic rheological properties of the material were assessed using an oscillatory rheometer (Anton Paar MCR 101). Samples were cut from injection molded plates and tested using parallel-plate geometry (d = 25 mm) operating at 190 °C. The gap distance in the parallel-plate geometry was 1 mm. Dynamic frequency sweep tests (within 0.1–500 rad/s) were performed to determine the dynamic properties of the materials, namely, complex viscosity (η^*), storage modulus (G'), and loss modulus (G'') as a function of frequency (ω).

3. RESULTS AND DISCUSSION

Figures 1(a-b) depict the values of G' and G'' as a function of frequency. In this work, the HDPE chains are expected to relax fully and exhibit terminal behavior like linear polymers with scale relations of approximately $G' \sim \omega^2$ and $G'' \sim \omega^1$ at low frequencies at the experimental temperature [9]. In the low-frequency range, the frequency-dependent behavior of HDPE was observed to follow $G' \sim \omega^{1.44}$ and $G'' \sim \omega^{0.96}$, which may be attributed to the broad molecular weight distribution. The scaling laws for the angular frequency dependence of G' and G'' of the nanocomposites are presented in Table 1.

In most nanocomposites, the slopes of G' and G'' gradually decrease with increasing nanofiller content and approach a plateau ("non-terminal behavior") indicative of pseudo-solid rheological behavior [10, 11]. Non-terminal behavior typically occurs in intercalated and exfoliated nanocomposites, where individual

lamellae or tactoids hinder the free rotation and relaxation of polymer chains. The extent of nanoparticle effects on polymer relaxation depends on the nanocomposite microstructure and nanofiller/matrix affinity. In nanocomposites with no significant interactions between the two components, G', G", and viscosity increase with angular frequency, and the curves resemble those of the pure polymer because the nanofiller does not modify the angular frequency dependency. This behavior was observed for HDPE nanocomposites with GNP processed for 10 min, where the profiles of the G' and G" curves resembled those of HDPE. Notably, for the sample with 0.1 wt.% processed for 20 min, a slight reduction in the slopes of G' and G" was observed.
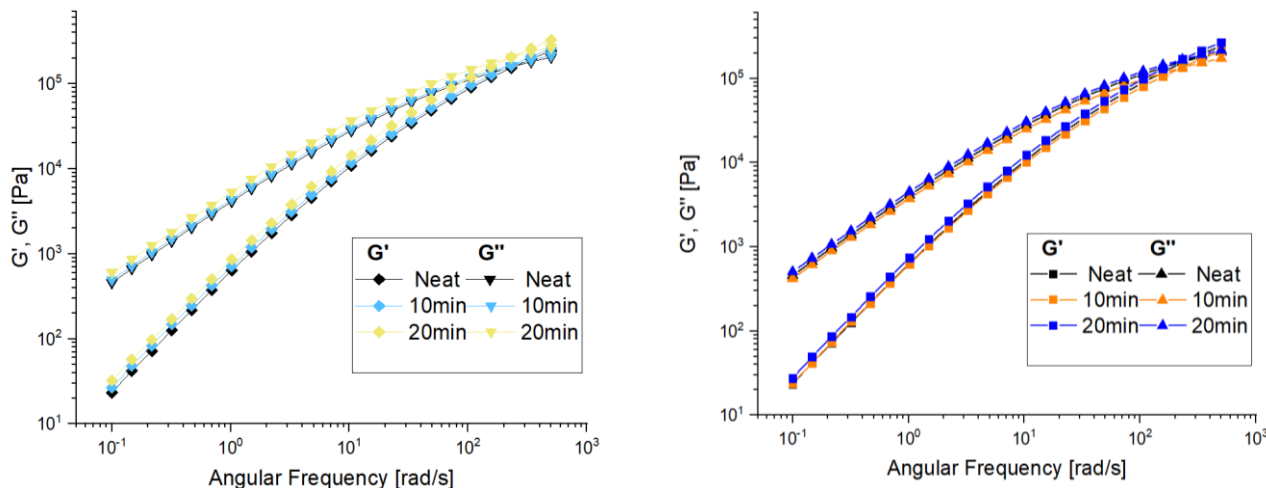
Figure 1. Storage modulus and loss modulus vs. angular frequency curves for HDPE and its nanocomposites with: (a) 0.1 wt.% GNP, and (b) 1wt.% GNP.

Table 1. Slopes of G' and G" versus angular frequency (ω) for HDPE and its nanocomposites.

Sample	Slopes for G' vs. ω (Pa/rad.s)	Slopes for G" vs. ω (Pa/rad.s)	τ_t (s)
Neat HDPE	1.44	0.96	0.0040
0.1 wt.% 10 min	1.47	0.95	0.0042
0.1 wt.% 20 min	1.42	0.94	0.0044
1 wt.% 10 min	1.47	0.96	0.0045
1 wt.% 20 min	1.44	0.96	0.0045

The crossover frequency corresponds approximately to the terminal relaxation time (reptation), τ_t, in linear polymers ($\tau_t \sim 1/\omega$ where G' = G") [12]. Assuming, as a simple approximation, the validity of this correlation for these nanocomposites, the results indicate that the nanoparticles induce a slight increase in τ_t, in other words, dynamic slowing, as depicted in Table 1. The nanoparticles can influence the dynamics of the polymer matrix in the terminal regime by slowing down the reptation dynamics due to the formation of percolated networks. However, this effect is limited, since nanoplatelet clusters may act as lubricants, which is more pronounced for 1 wt.%. GNP.

The Cole–Cole plot, a graphical representation between the imaginary viscosity (η'') and real viscosity (η'), serves as a valuable tool in analyzing the interaction between reinforcement and matrix in polymeric systems, helping identifying particle agglomerates [13]. Figure 2 shows the Cole-Cole plot of neat HDPE and HDPE/GNP composites. A study conducted by Almeida et al. [14] highlighted the presence of an arc in all samples, attributed to the absence of significant filler aggregates in the composite structure. Notably for the 1 wt.% with a residence time of 10 min, a noticeable flattening of the arc compared to HDPE was observed, indicating greater phase separation, suggesting the presence of agglomerates. The introduction of short-chain HDPE during the shear process increased the sample loss content [15], resulting in a downward shift of the peak. Furthermore, 1 wt.% GNP 10 min exhibited a marked decrease in elastic behavior compared to HDPE

and the other samples, probably related to the subsequent increase in the number of interfaces formed between particle-particles in relation to the polymer-particle interfaces, consequently contributing to the dissipation of energy.

The behavior of the Cole-Cole testing frequency influences the plot and offers insights into the inherent characteristics of the system. According to Marashdeh et al. [16], smooth semi-circular shapes in composites indicate similar relaxation times for both the matrix and the filler, a trend corroborated by the data presented in Table 1. Notably, a more pronounced curve was noted for the 0.1 wt.% GNP composite with a residence time of 20 min, suggesting improved filler dispersion and more effective interfaces within the polymeric matrix. The curves corresponding to 1wt.% GNP fell between neat HDPE and 0.1 wt.% GNP 20 min, implying a rise in the viscosity of the nanocomposites alongside the presence of agglomerate sites, given the higher energy threshold required for the dispersion of that amount of filler.
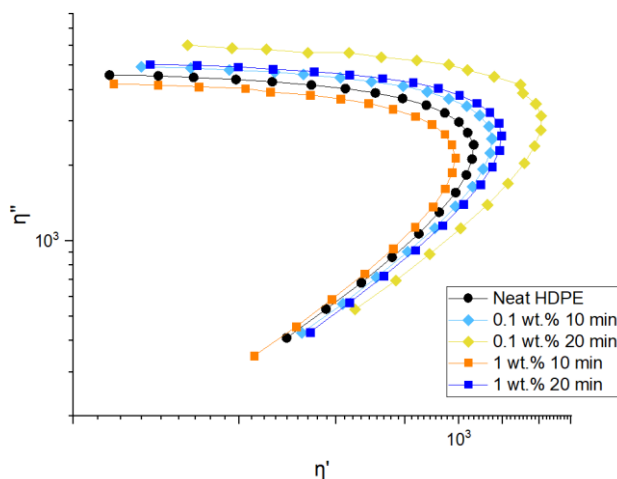
Figure 2. Cole–Cole representation for HDPE and its nanocomposites with GNP.

4. CONCLUSIONS

The rheological properties of HDPE and HDPE/GNP composites underscore the critical role of parameters like GNP amount and processing time. When HDPE/GNP composites were processed for 10 min, their rheological profiles mirrored those of pure HDPE. Conversely, at a longer processing time (20 min), a notable improvement in filler interaction was observed for the sample containing 0.1 wt.% GNP, as evidenced by the decrease in slope. Furthermore, the presence of GNP induced a slight increase in terminal relaxation time, as elucidated with the Cole-Cole plot, with the formation of nanoplatelet clusters at 1 wt.% potentially acting as lubricant. These results emphasize the pivotal role of processing time and GNP concentration in tailoring the rheological properties of nanocomposites, highlighting avenues for optimizing their performance in various applications.

4.1. Declaration of Competing Interest

The authors declare no conflict of interest.

4.2. Acknowledgements

5. REFERENCES

[1] P. M. Ajayan, L. S. Schadler and P. V. Braun. *Nanocomposite Science and Technology*, 1st Edition, 2003. Wiley-VCH GmbH & Co. KGaA. (https://doi.org/10.1002/3527602127.fmatter).

[2] A. C. Ferrari et al. Raman Spectrum of Graphene and Graphene Layers. *Physical Review Letters*, Volume 97, 2006. (https://doi.org/10.1103/PhysRevLett.97.187401).

[3] L. He et al. Thermal and Morphological Characterization of Composites Prepared by Solution Crystallization Method of High-Density Polyethylene on Carbon Nanotubes. *Polymer Composites*, Volume 31, 2010. (https://doi.org/10.1002/pc.20875).

[4] C. Li, J. Wang, Y. Su. A dual-role theory of the aspect ratio of the nanofillers for the thermal conductivity of graphene-polymer nanocomposites. *International Journal of Engineering Science*, Volume 160, 2021. (https://doi.org/10.1016/j.ijengsci.2020.103453).

[5] R. Rafiee, A. Eskandariyun. Predicting Young's modulus of agglomerated graphene/polymer using multi-scale modeling. *Composite Structures*, Volume 245, 2020. (https://doi.org/10.1016/j.compstruct.2020.112324).

[6] M. El Achaby, A. Qaiss. Processing and properties of polyethylene reinforced by graphene nanosheets and carbon nanotubes. *Materials & Design*, Volume 44, 2013. (https://doi.org/10.1016/j.matdes.2012.07.065).

[7] B. S. Okan. Fabrication of multilayer graphene oxide-reinforced high density polyethylene nanocomposites with enhanced thermal and mechanical properties via thermokinetic mixing. *Turkish Journal of Chemistry*, Volume 41, 2017. (https://doi.org/10.3906/kim-1608-53).

[8] E. Tarani et al. Insights into crystallization and melting of high density polyethylene/graphene nanocomposites studied by fast scanning calorimetry. *Polymer Testing*, Volume 67, 2018. (https://doi.org/10.1016/j.polymertesting.2018.03.029).

[9] C. I. Ferreira et al. Morphological, Viscoelastic and Mechanical Characterization of Polypropylene/Exfoliated Graphite Nanocomposites. *Polímeros: Ciência e Tecnologia*, Volume 23, 2013. (http://dx.doi.org/10.4322/polimeros.2013.066).

[10] Y. T. Lim, O. O. Park. Phase morphology and rheological behavior of polymer/layered silicate nanocomposites. *Rheologica Acta*, Volume 40, 2001. (https://doi.org/10.1007/s003970000126).

[11] G. Galgali, C. Ramesh, A. Lele. A Rheological Study on the Kinetics of Hybrid Formation in Polypropylene Nanocomposites. *Macromolecules*, Volume 34, 2001. (https://doi.org/10.1021/ma000565f).

[12] C. Dal Castel et al. The influence of interfacial agents on the morphology and viscoelasticity of PP/MMT nanocomposites. *Materials Science and Engineering C*, Volume 29, 2009. (https://doi.org/10.1016/j.msec.2008.10.012).

[13] Y. Chen et al. Rheological, thermal, and morphological properties of low-density polyethylene/ultrahigh-molecular-weight polyethylene and linear low-density polyethylene/ultra-high-molecular-weight polyethylene blends. *Journal of Applied Polymer Science*, Volume 129, 2013. (https://doi.org/10.1002/app.38374).

[14] J. F. M. de Almeida et al. Rheological, mechanical and morphological behavior of polylactide/nano-sized calcium carbonate composites. *Polymer Bulletin*, Volume 73, 2016. (https://doi.org/10.1007/s00289-016-1656-9).

[15] G. Chakraborty et al. Facile dispersion of exfoliated graphene/PLA nanocomposites via in situ polycondensation with a melt extrusion process and its rheological studies. *Journal of Applied Polymer Science*, Volume 135, 2018. (https://doi.org/10.1002/app.46476).

[16] W. F. Marashdeh, J. O. Iroh. Viscoelastic behavior and construction of master curve for graphene/polyimide nanocomposites. *High Performance Polymers*, Volume 29, 2016. (https://doi.org/10.1177/0954008316665159).

THE CONDUCTIVITY OF NANOCOMPOSITE FILMS OF HEMICELLULOSE AND SILVER NANOPARTICLES

Layse Mendes Diniz (a) Lays F. de M. S. Kataoka (b)*, Michaella S. B. Fialho (c), Wladymyr Jefferson Bacalhau de Sousa (d), Sandra M. da Luz (e)

(a) 0000-0001-5753-9443 (University of Brasília – Brazil)
(b) 0000-0003-1766-7509 (University of Brasília – Brazil)
(c) 0000-0002-8709-7081 (University of Brasília – Brazil)
(d) 0000-0002-3931-8265 (Federal University of Campina Grande – Brazil)
(e) 0000-0002-2223-0021 (University of Brasília – Brazil)
* Corresponding author: lays.furtado94@gmail.com

CODE: BCCM7-177

Abstract: Developing flexible conductive substrates has seen rapid growth for applications such as sensors. To minimize negative environmental impacts and create a sustainable future, natural polymers, such as hemicellulose, are increasingly being explored as candidates to replace conventional materials in manufacturing these devices. In this context, this work studies the conductivity of nanocomposite films of hemicellulose with silver nanoparticles. Hemicellulose was extracted from jute fibers using KOH solution 10% w/v. Then, the pure hemicellulose and hemicellulose films with silver nanoparticles (AgNPs) at 0.25, 0.50, 1, and 5 wt.% were moulded using the water casting technique. The films were analyzed using Thermogravimetry (TGA), Differential Scanning Calorimetry (DSC), and X-ray Diffraction (XRD). Electrical properties were tested using a bench multimeter. The results showed that hemicellulose films have good thermal stability. XRD revealed characteristic peaks of the amorphous structure of hemicellulose, with increased intensity of characteristic peaks with increasing AgNP content. The inclusion of silver nanoparticles not only improved electrical conductivity but also the thermal stability of the material. A higher conductivity value was only observed upon adding 0.50% AgNP. The sample with 5% AgNP achieved higher conductivity at 0.34 S/m.

1. INTRODUCTION

The demand for raw materials for sensor production inevitably leads to drastic environmental problems. Many residual energy devices do not naturally degrade [1]. In response, biopolymers occur widely in nature or are extracted from plants or animals, such as cellulose, chitosan, and starch [2]. Among the various biopolymers, hemicellulose stands out, which can be extracted from plant fibers, lignocellulosic fibers, such as jute, which can contain about 20 to 40% in its composition [3].

Hemicellulose polymers are branched, completely amorphous, partially soluble in water, and hygroscopic [4]. Compared to cellulose, hemicellulose is still a relatively understudied polymer [5]. The literature has not yet presented research employing it as a substrate for creating conductive composites incorporating silver nanoparticles to confer conductivity to the material. This approach is innovative for application in temperature, pressure, and humidity sensors. In this context, it emerges as a suitable material for this application, as besides offering environmental advantages due to its degradability, it presents low cost, good flexibility, low density, good thermal stability, and is non-toxic.

Therefore, this work explores hemicellulose as a flexible substrate for sensor application, understanding the electrical behavior of hemicellulose-based substrates aggregated with silver nanoparticles. This investigation aims to fill a gap in the literature regarding the potential of hemicellulose-based composites for sensor technology, especially their electrical properties. By studying the influence of silver nanoparticles on

the electrical conductivity of hemicellulose-based films, this research seeks to contribute to developing eco-friendly and efficient sensor materials. Additionally, it addresses the need for sustainable alternatives in sensor technology, aligning with the growing demand for environmentally friendly solutions in various industries.

Furthermore, the use of hemicellulose in sensor applications holds promise not only for its electrical properties but also for its abundance and renewability. By harnessing natural resources and integrating them into sensor technology, we can reduce reliance on non-renewable materials and minimize the environmental impact of sensor production processes. Overall, this research represents a step forward in exploring sustainable materials for sensor applications and underscores the potential of hemicellulose as a versatile and environmentally friendly substrate in sensor technology [1].

2. METHODOLOGY

2.1. Hemicellulose Extraction

Extraction procedures of hemicellulose followed the method developed by Kataoka et al, 2021 and Oliveira, 2017 [6]. Approximately 10 g of fibers were immersed in 200 mL of distilled water for 1 hour at room temperature and filtered. Then, the fibers were immersed in a 10% (w/v) KOH (Potassium Hydroxide) solution under orbital agitation at 250 rpm and mechanical agitation at 50 rpm for 3 hours. Subsequently, the fibers were filtered, and the liquid (liquor) had its pH adjusted to 4.8 using acetic acid. The liquor was left at rest for 24 hours and then centrifuged for 5 minutes at 4000 rpm.

The precipitation solution (1:10 acetic acid and ethanol) was added to the liquor. For every 100 mL of liquor, 125 mL of the solution was added. It was left at rest for 24 hours to allow the precipitation of hemicellulose. The hemicellulose portion was washed with distilled water (200 mL) three times. Finally, the hemicellulose was left to dry at room temperature for 24 hours.

2.2. Obtaining Nanocomposite Films

The films were produced using the *water-casting* technique. For this technique, hemicellulose was solubilized in distilled water at a concentration of 33% (w/v) under magnetic stirring for 2 hours at a temperature of 35°C. Afterward, the solution was centrifuged at 4000 rpm for 10 minutes and poured onto a glass plate (30 x 40 cm), allowing the film to dry at 25°C. Different concentrations of AgNPs (0.25, 0.50, 1, and 5 wt%) were incorporated to prepare conductive flexible substrates from the hemicellulose. Then, the solution was stirred magnetically for 10 minutes at 25°C. Finally, the solution was deposited on a glass plate (15 x 15 cm) until drying at room temperature and film formation.

2.3. Characterization of Nanocomposite Films

Thermogravimetry (TGA) and Differential Scanning Calorimetry (DSC) tests were conducted using a simultaneous thermal analyzer, model SDT Q600 (TA Instruments), in an alumina crucible under a nitrogen atmosphere with a flow rate of 50 mL/min. The heating was conducted from room temperature to 950 °C with a heating rate of 10 °C/min.

X-ray diffraction (XRD) analyses of the films were performed at room temperature using an XRD-7000 Shimadzu apparatus, with copper Kα radiation (1.5418 Å) at 40 kV. XRD characterization was carried out to determine the phases and crystal structures of the materials within the 2θ range of 10 to 70° with a scan speed of 2°/min.

For the electrical analysis of the nanocomposites, a digital multimeter ET-1649-Minipa was used to measure electrical voltage and electrical current. The electrical conductivity was calculated using Ohm's Law, following Equations 1, 2, and 3.

$$U = R \cdot I \quad [V] \tag{1}$$

$$R = \frac{\rho \cdot L}{A} \quad [S/cm] \tag{2}$$

$$\rho = \frac{1}{\sigma} \quad [S/cm] \tag{3}$$

Where: U = Electric voltage, R= Electric resistance, I= Electric current, $\boldsymbol{\rho}$ = Resistivity, L = conductor length in m, A= conductor cross-sectional area in m², $\boldsymbol{\sigma}$ = Conductivity

3. RESULTS AND DISCUSSION

3.1. TGA and DSC of Hemicellulose and Nanocomposite Films

Figure 1 shows the TG/DTG curves of hemicellulose and nanocomposite films. The curves show four stages of weight loss. The first peak corresponds to the onset of hemicellulose moisture loss, involving dehydration and cleavage of its side chains [7]. The second stage of weight loss corresponds to hemicellulose degradation. Hemicellulose quickly begins its decomposition between 220 and 315°C [8].
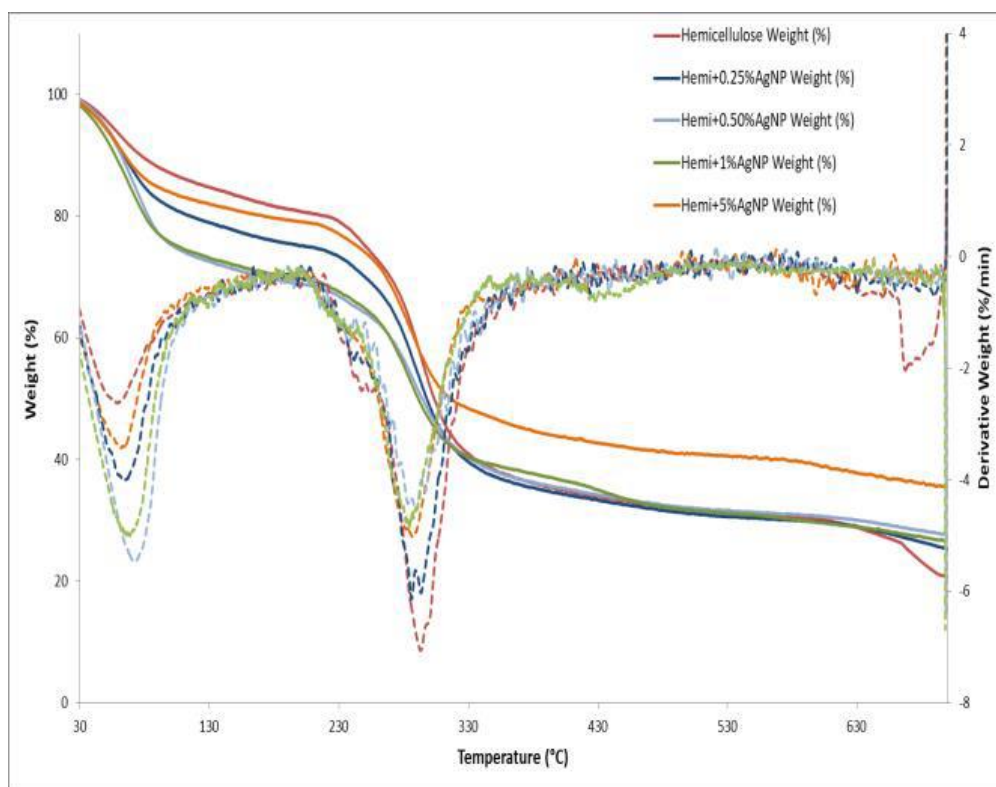
Figure 1. TG and DTG curves of hemicellulose and nanocomposite films.

The third peak, corresponding to the third stage of weight loss, is related to cellulose degradation [9]. The fourth peak, corresponding to the fourth degradation stage, is related to residues from the KOH solution (potassium oxide after burning), used in hemicellulose extraction, with its possible conversion into oxide. The thermal stability presented for the films averaged 185°C.

It was observed that introducing different concentrations of silver nanoparticles (AgNPs) into the hemicellulose matrix affected its thermal properties in a complex manner, altering the profiles of the thermal curves. During the initial phases of thermal degradation, the AgNPs accelerated the degradation of the polymeric matrix, while at higher temperatures, they contributed to greater thermal stability. The nanocomposite films showed more excellent thermal stability than the pure hemicellulose films. The presence of silver nanoparticles appears to influence the thermal stability of hemicellulose, as indicated by variations in the DTG peaks compared to pure hemicellulose. This change is attributed to metallic silver's higher inherent thermal stability [10,11].

Figure 2 shows the DSC curves, where it was possible to detect four main thermal events in the hemicellulose film. The first event is endothermic, has low energy, is around 46°C, and is related to moisture evaporation. Next is a second endothermic event related to hemicellulose's glass transition temperature (T_g), which occurs at 196°C [9,12]. The third event is exothermic, at 262.08°C, corresponding to the degradation of hemicellulose, and in the fourth event, broad and poorly defined endothermic undulations are observed without characterizing peaks. This event is attributed to the degradation of the cellulose portion in the samples, as also seen by Oliveira et al. (2022) [9]. Other events, such as another endothermic peak occurring at 768°C, can also be observed, possibly related to lignin pyrolysis. An exothermic peak at 796°C refers to residual potassium

oxides from the extraction solution. Exothermic peaks can be observed at higher temperatures, which may be related to small portions of extractives present in the samples, as also observed by Oliveira et al. (2022) [9].
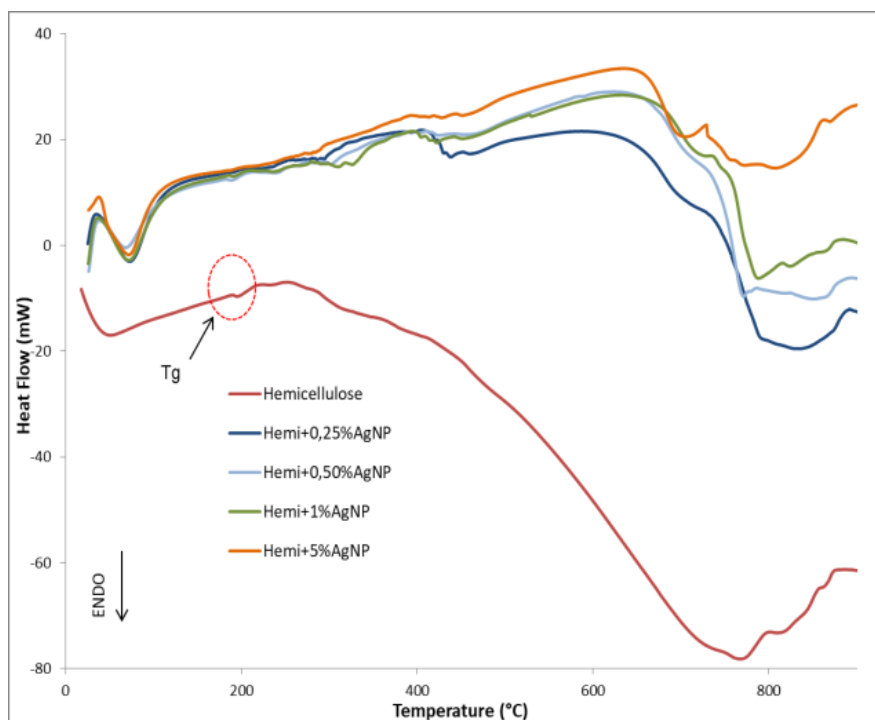
Figure 2. TG and DTG curves, and (b) DSC of hemicellulose and nanocomposite films.

3.2. DRX Analysis of Hemicellulose and Nanocomposite Films

Figure 3 shows the diffractograms of the hemicellulose films and their nanocomposites. Hemicellulose is an amorphous polysaccharide matrix, which causes its curve to lack defined and sharp peaks. This occurs due to the side chains in hemicellulose, which prevent the molecules from adopting a regular structure. X-ray diffraction analysis in amorphous materials plays a crucial role in understanding their structural properties; the diffracted X-rays do not exhibit distinct and sharp peaks as observed in crystalline substances. Instead, they present a broad and featureless diffraction pattern [13].
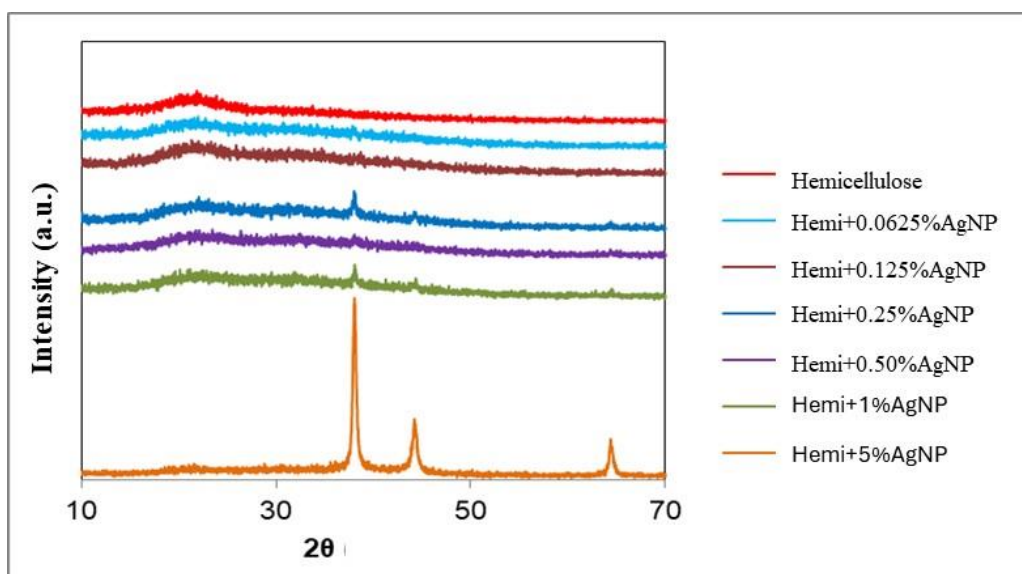
Figure 3. Diffractogram of the hemicellulose nanocomposites films.

In the curve corresponding to hemicellulose, a broad band around $2\theta = 20°$ is observed, indicating the amorphous structure of hemicellulose, as also noted by [14,15]. This same band was visible in all other curves related to hemicellulose nanocomposites with silver nanoparticles. The insertion of silver nanoparticles into

hemicellulose resulted in characteristic peaks with a face-centered cubic (FCC) structure. The three main peaks are located at $2\theta = 38°$, $44°$, and $64°$, corresponding to the crystalline planes (111), (200), and (220), respectively [16].

Furthermore, as the amount of silver nanoparticles increased, these peaks became even more intense. This curve exhibited peaks that are more representative of X-ray diffraction (XRD) patterns associated with silver nanoparticles, as documented in the literature and also reported by Zeng et al. (2020) [17]. These results indicate that the incorporation of silver nanoparticles into the hemicellulose matrix is influencing the resulting crystalline structure, thus confirming the distribution of nanoparticles in the matrix.

3.3. Influence of Electrical Properties as a Function of the AgNP Content Added to Hemicellulose

The addition of silver nanoparticles to polymeric films can lead to increased electrical conductivity. Silver is one of the metals with the highest electrical conductivity. When distributed in nanoparticles within a polymeric matrix, it can form conductive pathways that facilitate the flow of electrons [18]. Table 1 shows the hemicellulose films and nanocomposites' electrical resistance and conductivity values. From the found values of electrical current and electrical voltage, Equations 1, 2, and 3 were used to calculate the values of electrical resistance, resistivity, and, consequently, their conductivity.

Table 1. Results of electrical resistance, resistivity, and conductivity for hemicellulose and nanocomposite films.

SAMPLES	ELECTRICAL RESISTANCE (Ω)	RESISTIVITY (Ω.m)	CONDUCTIVITY (S/m)
Hemicelulose	184.60 ± 12.64	6.46 ± 0.44	0.15 ± 0.01
Hemi+0.0625%AgNP	167.99 ± 9.12	5.88 ± 0.32	0.17 ± 0.01
Hemi+0.125%AgNP	185.10 ± 15.55	6.49 ± 0.54	0.16 ± 0.01
Hemi+0.25%AgNP	164.74 ± 8.89	5.77 ± 0.31	0.17 ± 0.01
Hemi+0.50%AgNP	126.54 ± 9.13	4.43 ± 0.32	0.23 ± 0.02
Hemi+1%AgNP	92.68 ± 4.36	3.24 ± 0.15	0.31 ± 0.01
Hemi+5%AgNP	84.48 ± 2.38	2.96 ± 0.08	0.34 ± 0.01

It is observed that the addition of AgNP significantly alters the electrical properties of hemicellulose, a relevant aspect for applications in electronics and advanced materials. According to the results, the conductivity of the films increases with the reduction of electrical resistance and resistivity [19]. Samples with higher AgNP content exhibited superior conductivities. It is noted that a higher conductivity value compared to the hemicellulose film was only observed from the addition of 0.50% AgNP. At concentrations of 0.0625, 0.125, and 0.25%, changes in conductivity were minimal, suggesting ineffective dispersion of nanoparticles in the hemicellulose polymeric matrix.

Nanocomposite films with 1% and 5 wt.% of AgNP demonstrated the highest conductivities, in line with expectations. The sample with 5% AgNP achieved the lowest resistivity and, consequently, the highest conductivity at 0.34 S/m. Therefore, the higher the percentage of AgNP in the nanocomposite composition, the higher the resulting electrical conductivity, as a greater quantity of conductive nanoparticles is dispersed in the film, facilitating electron transport. However, it is essential to find a balance, as an excess of nanoparticles can lead to aggregation, forming insulating regions. Additionally, the uniform dispersion of nanoparticles is crucial to ensure the continuity of conductive pathways and, consequently, the desired conductivity [1].

The hemicellulose film without the addition of AgNP presented a low conductivity value. This is justified because hemicellulose can conduct a small amount of electrical current due to its chemical and structural properties. For example, hemicellulose is a polymer composed of various sugar units containing polar

functional groups. These groups can facilitate a certain degree of electron or ion mobility, allowing the conduction of electrical current [20].

4. CONCLUSIONS

In the present work, we verified good thermal stability for hemicellulose films and their nanocomposites. When producing hemicellulose films with different percentages of silver nanoparticles (AgNPs), it was verified that the samples with the highest nanoparticle content induced a significant increase in the electrical conductivity of the film. A probable hypothesis for the results obtained is that these nanoparticles were well dispersed in the hemicellulose matrix, with 5.0 wt% being the most appropriate for use as a sensor.

4.1. Declaration of Competing Interest

The authors declare no conflict of interest.

4.2. Acknowledgments

5. REFERENCES

[1] Du X, Zhang Z, Liu W, Deng Y. Nanocellulose-based conductive materials and their emerging applications in energy devices - A review. Nano Energy 2017;35:299–320. https://doi.org/10.1016/j.nanoen.2017.04.001.

[2] Caillol S. Special Issue "Natural Polymers and Biopolymers II." Molecules (Basel, Switzerland) 2020;26:10–2. https://doi.org/10.3390/molecules26010112.

[3] Spinacé MAS, Lambert CS, Fermoselli KKG, De Paoli MA. Characterization of lignocellulosic curaua fibres. Carbohydrate Polymers 2009;77:47–53. https://doi.org/10.1016/j.carbpol.2008.12.005.

[4] Li X, Tabil LG, Panigrahi S. Chemical treatments of natural fiber for use in natural fiber-reinforced composites: A review. J Polym Environ 2007;15:25–33. https://doi.org/10.1007/s10924-006-0042-3.

[5] Mendes FRS, Bastos MSR, Mendes LG, Silva ARA, Sousa FD, Monteiro-moreira ACO, et al. Preparation and evaluation of hemicellulose fi lms and their blends. Food Hydrocolloids 2017;70:181–90.

[6] Kataoka LF de MS, Hidalgo Falla MDP, Luz SM Da. The Influence of Potassium Hydroxide Concentration and Reaction Time on the Extraction Cellulosic Jute Fibers. Journal of Natural Fibers 2021:1–13. https://doi.org/10.1080/15440478.2021.1934934.

[7] Yeo JY, Chin BLF, Tan JK, Loh YS. Comparative studies on the pyrolysis of cellulose, hemicellulose, and lignin based on combined kinetics. Journal of the Energy Institute 2019;92:27–37. https://doi.org/10.1016/j.joei.2017.12.003.

[8] Yang H, Yan R, Chen H, Lee DH, Zheng C. Characteristics of hemicellulose, cellulose and lignin pyrolysis. Fuel 2007;86:1781–8. https://doi.org/10.1016/j.fuel.2006.12.013.

[9] Roldi-Oliveira M, Diniz LM, Elias AL, Luz SM. Hemicellulose Films from Curaua Fibers (Ananas erectifolius): Extraction and Thermal and Mechanical Characterization. Polymers 2022;14:2999. https://doi.org/10.3390/polym14152999.

[10] Rozilah A, Aiza Jaafar CN, Sapuan SM, Zainol I, Ilyas RA. The effects of silver nanoparticles compositions on the mechanical, physiochemical, antibacterial, and morphology properties of sugar palm starch biocomposites for antibacterial coating. Polymers 2020;12:1–21. https://doi.org/10.3390/polym12112605.

[11] Makvandi P, Nikfarjam N, Sanjani NS, Qazvini NT. Effect of silver nanoparticle on the properties of poly(methyl methacrylate) nanocomposite network made by in situ photoiniferter-mediated photopolymerization. Bulletin of Materials Science 2015;38:1625–31. https://doi.org/10.1007/s12034-015-0959-z.

[12] Farhat W, Venditti R, Quick A, Taha M, Mignard N, Becquart F, et al. Hemicellulose extraction and characterization for applications in paper coatings and adhesives. Industrial Crops and Products 2017;107:370–7. https://doi.org/10.1016/j.indcrop.2017.05.055.

[13] Liang T, Wang L. Thermal Treatment of Poplar Hemicelluloses at 180 to 220 °C under Nitrogen Atmosphere. BioResources 2016;12:1128–35. https://doi.org/10.15376/biores.12.1.1128-1135.

[14] Xu J, Xia R, Zheng L, Yuan T, Sun R. Plasticized hemicelluloses/chitosan-based edible films reinforced by cellulose nanofiber with enhanced mechanical properties. Carbohydr Polym 2019;224:115164. https://doi.org/10.1016/j.carbpol.2019.115164.

[15] Abdulkhani A, Najd Mazhar A, Hedjazi S, Hamzeh Y. Preparation of xylan bio-composite films reinforced with oxidized carboxymethyl cellulose and nanocellulose. Polymer Bulletin 2020;77:6227–39. https://doi.org/10.1007/s00289-019-03075-5.

[16] Ghodake G, Kim M, Sung JS, Shinde S, Yang J, Hwang K, et al. Extracellular synthesis and characterization of silver nanoparticles—antibacterial activity against multidrug-resistant bacterial strains. Nanomaterials 2020;10:1–16. https://doi.org/10.3390/nano10020360.

[17] Zeng Y, Liu Y, Wang L, Huang H, Zhang X, Liu Y, et al. Effect of Silver Nanoparticles on the Microstructure, Non-Isothermal Crystallization Behavior and Antibacterial Activity of Polyoxymethylene. Polymers (Basel) 2020;12:424. https://doi.org/10.3390/polym12020424.

[18] Rauwel P, Rauwel E, Ferdov S, Singh MP. Silver nanoparticles: Synthesis, properties, and applications. Advances in Materials Science and Engineering 2015;2015:2–4. https://doi.org/10.1155/2015/624394.

[19] Callister Jr. WD. Ciencia dos materiais - Callister.pdf. 7ª. Rio de Janeiro: LTC; 2007.

[20] Koskela S, Zha L, Wang S, Yan M, Zhou Q. Hemicellulose content affects the properties of cellulose nanofibrils produced from softwood pulp fibres by LPMO. Green Chemistry 2022;24:7137–47. https://doi.org/10.1039/d2gc02237k.

CELLULOSE AND NATURAL RUBBER NANOCOMPOSITES AEROGELS MORPHOLOGY AND THERMAL PROPERTIES

Eliza M. Sakazaki[(a)*], Laiane Carvalho[(b)], Larissa Andreani[(c)], Sandra Maria da Luz[(d)],
Leonardo F. Valadares[(e),]

(a) 0009-0006-9938-8958 (University of Brasília - Brazil)
(b) 0009-0003-6110-2721 (University of Goiás - Brazil)
(c) 0000-0002-6567-5725 (Brazilian Agricultural Research Corporation – Embrapa - Brazil)
(d) 0000-0002-2223-0021 (University of Brasília - Brazil)
(e) 0000-0002-4190-8598 (Brazilian Agricultural Research Corporation - Embrapa - Brazil)
* Corresponding author: miekazaki@gmail.com

CODE: BCCM7-178

Abstract: This study focuses on producing aerogels formed by cotton microfibrillated cellulose (MC), natural rubber latex (NR), and their nanocomposites. MC was produced through high-speed mechanical shear processes, enabling its dispersion in an aqueous medium. The nanocomposite's production occurred by blending the aqueous dispersions of microfibrillated cellulose (0.26 wt %) and the natural rubber latex (1 wt%), followed by freeze-drying. The morphology and thermal properties of aerogels were evaluated using scanning electron microscopy (SEM), thermogravimetry analyses (TGA), and differential scanning calorimetry (DSC). Aerogels with different proportions were prepared to comprehend each component's effects in the nanocomposite. Microscopy revealed the effectiveness in obtaining cellulose micro- and nanostructures using shear. All samples presented a very porous structure. The preparation of the nanocomposites allowed the uniform incorporation of cellulose into rubber despite the intrinsic differences between their composition and chemical properties. The increase in rubber the proportion promotes greater interconnectivity of macropores, rendering them denser and losing the laminar and microporous characteristics observed in aerogels with higher cellulose ratios. The aerogels exhibited satisfactory thermal stability at around 300 °C, underscores the effectiveness of the aerogel synthesis process in obtaining cellulose micro- and nanostructures through mechanical processes and in nanocomposite formation through aqueous medium followed by freeze-drying.

1. INTRODUCTION

In the pursuit of new technologies, the concern for the entire lifecycle of a material, from raw material to disposal, has become an inevitable point to consider during the development of new materials. Increasingly, efforts are directed toward more efficient solutions, sustainability, and less environmental harm, drawing inspiration from what already exists in nature.

In this context, a material that has garnered considerable attention is the aerogel. Its excellent properties, such as high porosity, high surface area, and low density, allow it to be applied in various technology fields [1,2]. It can be used for storing and transporting substances, as structuring agents, filter materials, absorbers, etc. Like a fruit, watermelon has a porous structure of fibers responsible for absorbing and encapsulating large amounts of liquid. A bone is also a porous structure designed to provide minimal

density support. This illustrates the importance of correlating the functionality of a material with its microstructural characteristics when designing a new composite.

Cellulose is the most abundant naturally occurring biopolymer, being nontoxic, biocompatible, and biodegradable [3]. Cellulose nanostructures can be used as reinforcing fillers in composites and nanocomposites [4]. Various methods are used to obtain these nanostructures, including chemical, enzymatic, and mechanical processes. In some cases, acids are used, which can be highly aggressive to the user or harmful to the environment upon disposal, or they may not yield a favourable outcome for the process.

Similarly, natural rubber is a biopolymer with various intrinsic properties derived from the latex of different types of rubber trees. It is commercially highly valuable, used to manufacture industrial and medical products, and essential for the tire and anti-vibration industries [4]. Natural rubber's key characteristics include resilience, elasticity, and abrasion resistance. Moreover, its hydrophobic and oleophilic nature offers the rubber a range of possibilities in terms of compatibility with different materials [5]. These properties can be further enhanced through manufacturing and structuring processes, thus expanding its field of application, such as in the production of aerogels.

The synthesis of rubber composites containing cellulose as reinforcing fillers, or rubber with small rubber additions, is increasingly being studied. This trend is directly related to the different properties among them. Regarding the adhesion of these materials, it isn't just the dispersion and orientation of the cellulose fibers but also the bonding forces between the polymers that influence the enhancement of mechanical properties [6,7]. Thus, the dimensions of the structures, such as fibers, and the medium in which the composites are synthesized are crucial in achieving effective matrix-fiber interaction in composites.

This study evaluated aerogels of cellulose derived from cotton and natural rubber latex, along with composites of the two materials in different proportions. The nanostructures were obtained through a mechanical shear and dispersion process. The formation of composites and aerogels occurred in an aqueous medium using freeze-drying. Freeze-drying involves a simple dehydration process that removes the solvent through sublimation at low temperatures from a previously frozen material [2]. This study aimed to analyze the effectiveness and results of the processes for synthesizing bio-aerogels from cellulose and natural rubber, aiming to create a material with high engineering utility, sustainable in nature, without chemical modification, and produced with simpler, efficient, and sustainable method.

2. METHODOLOGY

2.1. Materials

Micro and nanostructures were derived from commercial bulk cotton [Farol, Juiz de Fora MG] using the 500 W UltraTurrax disperser from IKA, using a top-down approach. The natural rubber latex was extracted from the rubber tree (*Hevea brasiliensis*) located at Fazenda Maira, in the city of Cidade Ocidental, Goiás, Brazil, and provided by Professor Dr. Floriano Pastore from the University of Brasília. The cotton dispersion and latex dilution were carried out using distilled water.

2.2. Production of cellulose aqueous dispersions

The cellulose aqueous dispersion was prepared using distilled water and commercial cotton at 0.25 wt%. The microfibrillation was adapted from the methodology used by Cheng [8]. The commercial cotton, previously dried, was untangled and cut into small pieces about 1 mm thick using scissors. Then, the cotton pieces were dispersed in water and processed in a commercial blender (Britannia, BLQ1280, 1150W) until an initial homogenization was achieved. The material was then subjected to high shear in a disperser (UltraTurrax T25 D S32, IKA) for 12 cycles of 5 minutes each, at a speed of 20,000 rpm. For the latex, the original solid content was determined and then diluted to create a colloid with 1% and 5% concentrations for producing two pure rubber aerogels and 10% for synthesizing the nanocomposites.

The preparation of the composites involved mixing the two dispersions in an aqueous medium with different ratios of solid content from each material. In addition to the pure dispersions of 100% cellulose (100/00 MC/NR) and 100% natural rubber (00/100 MC/NR), nanocomposites were created with 80% cellulose and 20% natural rubber (80/20 MC/NR), 50% cellulose and 50% rubber (50/50 MC/NR), and 20% cellulose and 80% rubber (20/80 MC/NR). The nanocomposites were then mixed and dispersed using the Ultra Turrax disperser.

2.3. Production of aerogels

The five dispersions were poured into molds and frozen at -24 °C for 24 hours, followed by -80 °C for another 4 hours. The frozen material was processed in a freeze-dryer (Liotop K 120) for 96 hours to produce the aerogel.

2.4. Material characterization

2.4.1. Density and porosity

The density (ρ_o) of each aerogel was determined using its mass (m) and its volume (v), which was calculated based on its external dimensions. The masses were determined using an analytical balance (Shimadzu, AY220), and the external dimensions were measured with a digital calliper (DIGIMESS). Three samples were considered for each dispersion, and each sample was measured three times. For each material, the mean of a triplicate was considered, and the density was calculated according to Eq. (1)

$$\rho_o = \frac{m}{v} \tag{1}$$

The calculated density ρ sub o and theoretical density ρ were considered to determine porosity, following the methodology used in [1]. The theoretical density of the biopolymers is obtained through the weighted average of the densities of the two components, according to their mass fractions, as shown in Eq. (2).

$$\rho = \frac{1}{\frac{w_1}{\rho_1} + \frac{w_2}{\rho_2}} \tag{2}$$

where w is the polymer's mass fraction and ρ is the theoretical density obtained from the literature in g/cm³. The densities used for the calculation were 1.50 g/cm³ for cellulose fibers, as referenced in [9], and 0.93 g/cm³ for natural rubber, according to reference [10]. Once the densities are determined, porosity, expressed as a percentage, can be calculated using Eq. (3).

$$porosity(\%) = \left(1 - \frac{\rho_o}{\rho}\right)100 \tag{3}$$

2.4.2. Volume shrinkage

Volume shrinkage was defined by comparing the initial volume v_o of the molded and frozen dispersion with the external volume v_e of the material after freeze-drying, i.e., in its aerogel state.

$$VS(\%) = \frac{v_o - v_e}{v_o}100 \tag{4}$$

2.5. Morphology

The aerogels' morphological analysis was carried out using a Scanning Electron Microscope (ZEISS FEG Sigma HV). The top surface of the samples was examined. Before analysis, the samples were coated with an approximately 20 nm layer of gold powder using a sputter coater (Q150T-ES Quorum Technologies).

The effectiveness of obtaining nanometric cellulose structures through the applied mechanical process was evaluated by analyzing the dimensions of the fibers in the material from the microscopy images. Using the software ImageJ, the thickness of 100 cellulose fibers was measured, and the mean and standard deviation were calculated.

2.6. Thermal Analysis

Thermal analyses were performed using a simultaneous thermal analyser TGA/DSC (TA Instruments, SDT Q600) to investigate the thermal behavior of pure aerogels and composites. Samples of approximately 9 mg of each material were placed in alumina crucibles and subjected to controlled and monitored heating,

ranging from 30 °C to 600 °C, under an inert nitrogen atmosphere at a flow rate of 100 mL/min and a heating rate of 20 °C/min. The analyses provided detailed information on the mass losses as a function of temperature increase associated with the thermal transitions of the studied materials.

3. RESULTS AND DISCUSSION

The results regarding density, porosity, and volumetric shrinkage are presented in Table 1. The table also includes the total solid content of the aqueous dispersions for each material produced before the freeze-drying process. We can relate the results of density and porosity to the solid content in each dispersion. As this content increases, density increases, while porosity decreases, as observed in [1]. Unlike the pure cellulose aerogels and composites, it was impossible to unmold the pure rubber aerogel with a 1% solid content. It remained bound to the mold used and experienced significant shrinkage when trying to remove it. Thus, a new attempt to obtain the pure rubber aerogel was made considering a 5% solid content. In this case, it was possible to get more structured material. Given this result, we see that the solid content of the rubber is an essential variable in obtaining pure rubber aerogels.

On the other hand, when comparing the pure rubber aerogel with the composite containing 80% rubber and 20% cellulose (20/80 MC/NR), despite having very similar solid contents, the latter showed the lowest volumetric shrinkage among all others developed, which indicates the influence of cellulose fibers in the material's structure.

Table 1. Physical properties of aerogels: 100/00 MC/NR, 80/20 MC/NR, 50/50 MC/NR, 20/80 MC/NR and 00/100 MC/NR

Sample	Solid/ dispersions (%w/w)	Density(g/cm³)	Porosity (%)	Volumetric Shrinkage (%)
MC pure	**0.25**	0.0039 ± 0.0002	99.73 ± 0.30	32 ± 4
80/20 MC/NR	0.31	0.0049 ± 0.0004	99.66 ± 0.03	38 ± 5
50/50 MC/NR	0.49	0.0067 ± 0.0008	99.43 ± 0.07	28 ± 8
20/80 MC	1.14	0.0119 ± 0.0004	98.82 ± 0.04	6 ± 3
NR pure	1.00	0.0114 ± 0.0001	98.77 ± 0.03	12 ± 2
NR pure*	5.00	0.0518 ± 0.0012	94.95 ± 0.16	2 ± 2

* Pure natural rubber aerogel is produced later with higher solid content.

Analyses of the structure and morphology of the aerogels were conducted using scanning electron microscopy, as shown in Fig. 1. Fig. 1a present cellulose fibers obtained through the mechanical shear and dispersion process. Visualizing a network structure with fiber thicknesses ranging from 26 to 147 nm is possible. This result demonstrates the process's effectiveness in obtaining dispersed nanostructures, according to the definition in [3]. Fig. 1b presents the aerogel with 80% cellulose and 20% rubber (80/20 MC/NR). We can observe the adhesion of small rubber particles along a cellulose fiber, indicating a good surface bonding between MC and NR.
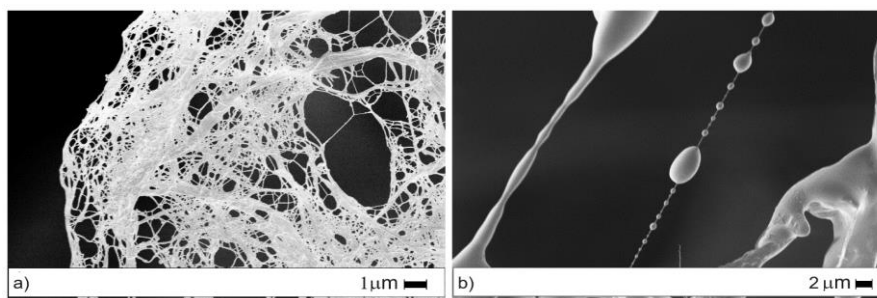
Figure 1. The SEM images of (a) cellulose pure aerogel and (b) 80/20 MC/NR nanocomposite aerogel.

Fig. 2 presents SEM images of samples of each aerogel formed, with Fig.2a and Fig.2b representing the pure cellulose and pure rubber aerogels, respectively. Generally, we can see a high degree of porosity in the aerogels and a plate-like formation pattern. The formation of a porous structure and the development of plate-like formations can be associated with synthesizing aerogels in an aqueous medium, where the dispersions are frozen and then subjected to freeze-drying. During the freezing process, ice crystals form, causing the cellulose and rubber particles to assume a specific arrangement, which remains after the water sublimates [2]. When comparing the pure aerogels, the cellulose aerogel shows a rougher appearance with micropores, unlike the pure rubber aerogel, which has a denser and more interconnected reticular structure. These same characteristics are observed progressively in the composites. Increasing the rubber proportion promotes greater interconnectivity of the macropores, making them denser and losing the laminar and microporous characteristics observed in aerogels with higher cellulose proportions.
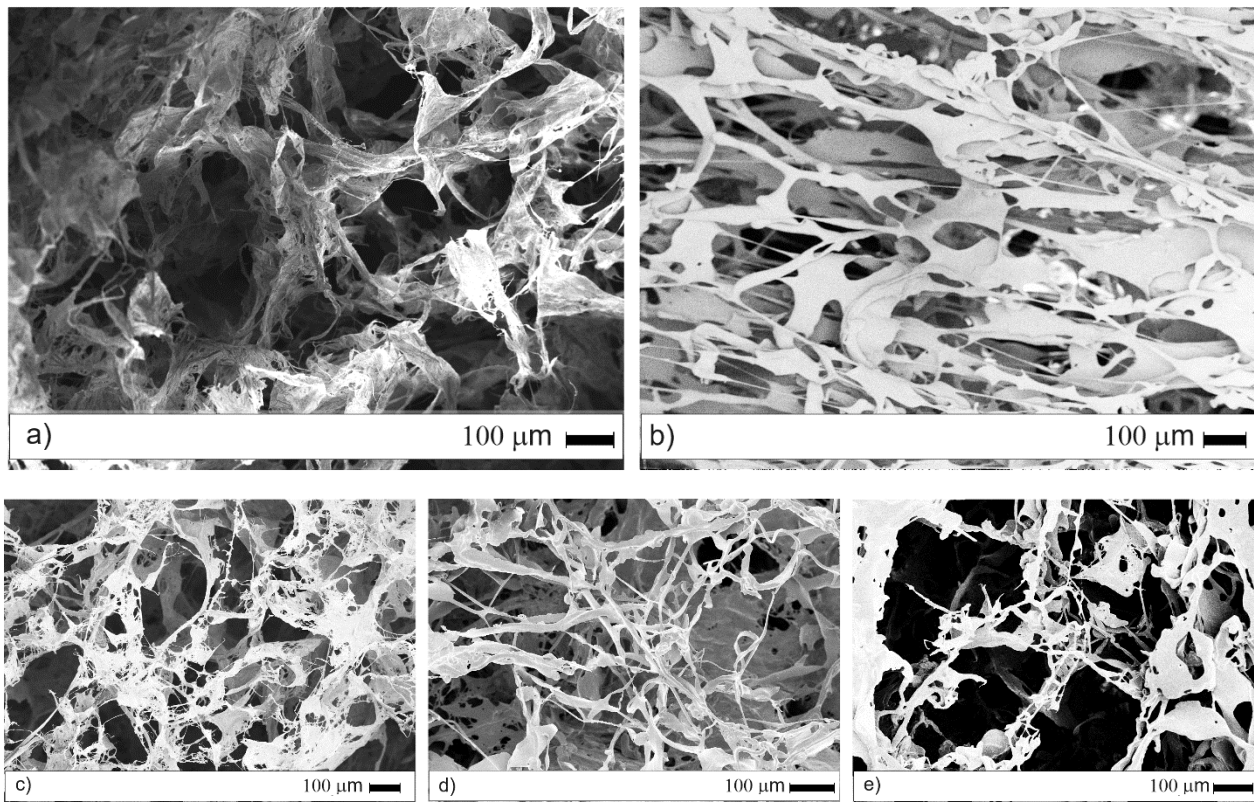
Figure 2. The SEM surface images of (a) pure cellulose 100/00 MC/NR, (b) pure natural rubber 00/100 MC/NR and (c) 80/20 MC/NR, (d) 50/50 MC/NR and (e) 20/80 MC/NR nanocomposites aerogels.

The curves thermogravimetric (TG), derivative thermogravimetric (DTG), and differential scanning calorimetry generated from the thermal analysis of the pure cellulose aerogel, the natural rubber aerogel, and their composites are presented in Figure 3. Initially, all samples exhibit a similar TG curve shape, indicating a similarity in thermal behaviour among them. In samples with higher cellulose content, most notably in pure cellulose, the first stage of degradation occurs at a temperature close to 50 °C. This weight loss can be related to the moisture content in the samples, accounting for about 6% of the total weight in pure sample 100/00 MC/NR, attributed to its hydrophilic nature. The residual weight at 600 °C was also proportional to the cellulose content, with zero residual weight for the pure rubber aerogel.

When analyzing the DSC curves in Fig. 3c, we observe that materials containing higher cellulose content have a greater enthalpy of degradation than those with higher rubber proportions. This significant difference, even with similar degradation curves, can be attributed to a better structural arrangement of cellulose molecules, resulting in increased bond energy between them. Since the analyses were conducted in an inert atmosphere, it was observed that the presence of oxygen in the cellulose molecules and its absence in the rubber molecules directly impacted the onset temperature of material degradation.
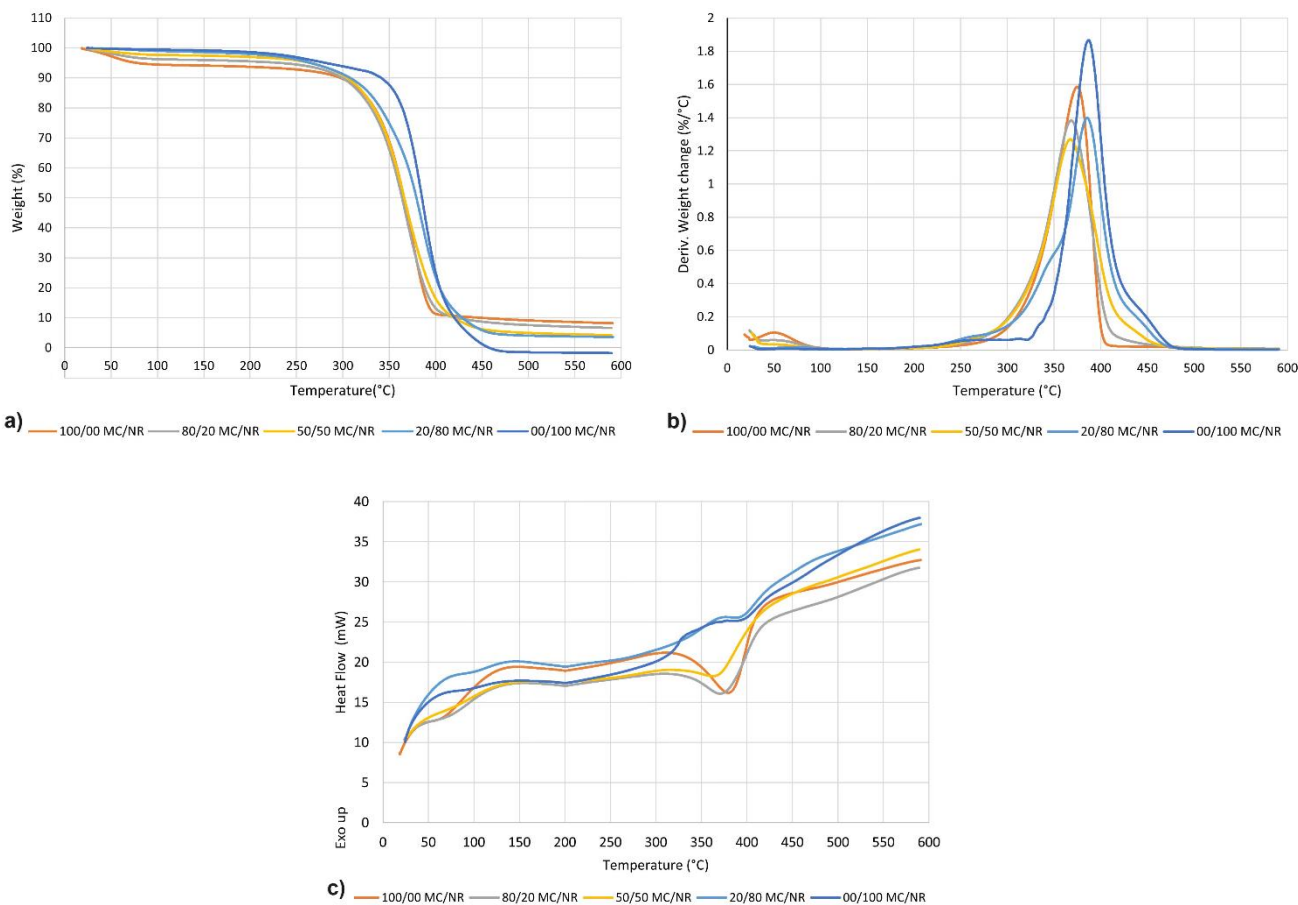
Figure 4. Thermal properties of 100/00 MC/NR, 80/20 MC/NR, 50/50 MC/NR, 20/80 MC/NR, and 00/100 MC/NR aerogels. (a) TGA, (b) DTG, and (c) DSC curves.

The main degradation temperatures of the material are presented in Table 2. The materials exhibited thermal stability up to 250 °C, with no notable differences. Regarding the pure materials, natural rubber has a higher onset temperature of degradation than cellulose. For the composites with 80% and 50% cellulose (80/20 MC/NR and 50/50 MC/NR), the T_{onset} values are lower than those of pure cellulose, indicating that degradation begins earlier in these composites than in pure cellulose. This relationship also extends to the recorded peak temperature. However, the end temperature of the event, T_{endset}, for the two composites is higher than the cellulose, indicating a broader degradation range. On the other hand, the composite with 80% rubber (20/80 MC/NR) has a higher onset temperature of degradation than cellulose and a higher peak temperature, with its end event temperature closer to the rubber. Additionally, the composites showed less intense and broader degradation peaks than pure materials, suggesting greater thermal stability [11].

The presence of a single stage of degradation in the composites indicates good dispersion and adhesion of cellulose fibers with rubber particles [12], supporting the effectiveness of the composite synthesis process in the aqueous medium.

Table 2. Thermal degradation events of aerogels.

Samples	Degradation Temperature (°C)		Residue at 600°C (%)	Maximum Degradation Temperature (T_{max}, °C)	ΔH (J/g)
	T_{onset}	T_{endset}			
Pure cotton MC	**340**	**390**	**8**	**375**	**195**
Pure NR	**360**	**415**	**0**	**387**	**14**
80/20 MC/NR	323	395	7	368	128
50/50 MC/NR	325	400	4	368	71
20/80 MC	345	410	4	385	15

4. CONCLUSIONS

Cellulose aerogels from cotton, rubber, and their composites were synthesized from an aqueous formulation followed by freeze-drying. Through a mechanical process, nanostructured particles were obtained from commercial cotton, allowing for the formation of a uniformly dispersed colloid. This resulted in a homogeneous dispersion of the composites with natural rubber latex. The morphology of the nanostructures from both materials and the aqueous medium in which they were dispersed influenced the adhesion quality, improving the material's thermal stability and conformation. Cellulose proved an important structuring agent, while rubber contributed to increased thermal stability in the composites. Water was an effective medium for obtaining composites and formulating the aerogels through freeze-drying. The method demonstrated significant effectiveness in obtaining nanostructures and synthesizing aerogels through processes that do not rely on chemical or enzymatic products, making them more accessible regarding material requirements.

5. REFERENCES

[1] Paulauskiene T, Teresiute A, Uebe J, Tadzijevas A. Sustainable Cross-Linkers for the Synthesis of Cellulose-Based Aerogels: Research and Application. J Mar Sci Eng 2022;10. https://doi.org/10.3390/jmse10040491.

[2] Abdullah, Zou YC, Farooq S, Walayat N, Zhang H, Faieta M, et al. Bio-aerogels: Fabrication, properties and food applications. Crit Rev Food Sci Nutr 2023; 63:6687–709. https://doi.org/10.1080/10408398.2022.2037504.

[3] Fernandes A, Cruz-Lopes L, Esteves B, Evtuguin D. Nanotechnology Applied to Cellulosic Materials. Materials 2023;16. https://doi.org/10.3390/ma16083104.

[4] Fiorote JA, Pereira Freire A, De D, Rodrigues S, Martins MA, Andreani L, et al. Preparation of composites from Natural Rubber and Oil Palm Empty Fruit Bunch Cellulose: Effect of Cellulose Morphology on Properties. vol. 14. 2019.

[5] Zou L, Phule AD, Sun Y, Zhu TY, Wen S, Zhang ZX. Superhydrophobic and superoleophilic polyethylene aerogel coated natural rubber latex foam for oil-water separation application. Polym Test 2020;85. https://doi.org/10.1016/j.polymertesting.2020.106451.

[6] Wongvasana B, Thongnuanchan B, Masa A, Saito H, Sakai T, Lopattananon N. Reinforcement Behavior of Chemically Unmodified Cellulose Nanofiber in Natural Rubber Nanocomposites. Polymers (Basel) 2023;15. https://doi.org/10.3390/polym15051274.

[7] Dominic MCD, Joseph R, Begum PMS, Joseph M, Padmanabhan D, Morris LA, et al. Cellulose nanofibers isolated from the Cuscuta Reflexa plant as a green reinforcement of natural rubber. Polymers (Basel) 2020;12. https://doi.org/10.3390/POLYM12040814.

[8] Cheng H, Gu B, Pennefather MP, Nguyen TX, Phan-Thien N, Duong HM. Cotton aerogels and cotton-cellulose aerogels from environmental waste for oil spillage cleanup. Mater Des 2017; 130:452–8. https://doi.org/10.1016/j.matdes.2017.05.082.

[9] Pereira ALS, Feitosa JPA, Morais JPS, Rosa M de F. Bacterial cellulose aerogels: Influence of oxidation and silanization on mechanical and absorption properties. Carbohydr Polym 2020;250. https://doi.org/10.1016/j.carbpol.2020.116927.

[10] Salmazo LO, Lopez-Gil A, Ariff ZM, Job AE, Rodriguez-Perez MA. Influence of the irradiation dose in the cellular structure of natural rubber foams cross-linked by electron beam irradiation. Ind Crops Prod 2016; 89:339–49. https://doi.org/10.1016/j.indcrop.2016.05.023.

[11] Teles VC, Roldi M, Luz SM, Santos WR, Andreani L, Valadares LF. Obtaining Plasticized Starch and Microfibrillated Cellulose from Oil Palm Empty Fruit Bunches: Preparation and Properties of the Pure Materials and Their Composites. vol. 16. 2021.

[12] Phomrak S, Nimpaiboon A, Newby BMZ, Phisalaphong M. Natural rubber latex foam reinforced with micro-and nanofibrillated cellulose via dunlop method. Polymers (Basel) 2020; 12:1–16. https://doi.org/10.3390/polym12091959.

MORPHOLOGICAL AND THERMAL CHARACTERIZATION OF PLA/NANOCELLULOSE COMPOSITES

Lucas Horiuchi[a], Katielly Polkowski[b], Marina Andrade[c], Ana Paula Gonçalves[d], Vinícius Oliveira[e], Pollyana Cardoso[f], Rodrigo Polkowski[g],*

(a) 0009-0006-7223-1897 (TRL9 LAB Testing and Technical Analysis, Salvador, BA, Brazil)
(b) 0009-0003-2554-3677 (TRL9 LAB Testing and Technical Analysis, Salvador, BA, Brazil)
(c) 0009-0005-0353-3560 (TRL9 LAB Testing and Technical Analysis, Salvador, BA, Brazil)
(d) 0000-0002-0326-5966 (TRL9 LAB Testing and Technical Analysis, Salvador, BA, Brazil)
(e) 0009-0004-9172-4692 (TRL9 LAB Testing and Technical Analysis, Salvador, BA, Brazil)
(f) 0000-0001-5633-8535 (SENAI/CIMATEC University Center, Salvador, BA, Brazil)
(g) 0000-0002-9417-0953 (TRL9 LAB Testing and Technical Analysis, Salvador, BA, Brazil)
* Corresponding author: rodrigo@trl9.tech

Abstract: Cellulose nanofibril (CNF), derived from sustainable and renewable sources, presents promising properties for various applications such as textile, biomedical field, paper products, packaging sector, etc. The incorporation of CNF into polymeric matrices can significantly improve properties, such as biodegradability and thermal stability, promoting advances in the development of sustainable and high-performance composite materials. Furthermore, these particles can act as a nucleating agent, affecting the crystallization kinetics of the polymeric matrix. Polylactic acid (PLA) is an amorphous or semicrystalline polyester obtained from renewable sources and has high rigidity and good processability. However, the low thermal stability of this polymer is still a limitation. This study aimed to evaluate the effect of CNF (1.5 and 4.5wt%) on the thermal properties, degree of crystallization, and crystallization kinetics of PLA biopolymer composites prepared in a twin-screw extruder at a temperature range of 165-190°C. Based on the results, the CNF did not increase the degree of crystallinity of PLA, possibly due to the inhibition of nucleation caused by non-cellulosic materials (waxy) present in the nanoparticles. The thermal degradation of PLA/CNF composite showed that the degradation of PLA has a peak of degradation at 358°C (Tmax) and the CNF addition has little effect on this parameter.

1. INTRODUCTION

Brazil is currently an emerging leader in the global production of cellulose from renewable sources [1], its production, when done sustainably, offers the market a biodegradable product with applications in the areas of packaging, newspapers, and printing paper [1]. However, these applications have low added value and are considered commodities. The incorporation of cellulose into polymers can lead to an increase in the mechanical properties of the material [2], opening possibilities for applications with higher value. Cellulose when isolated on a nanometric scale is known as nanocellulose. These nanostructures can present different chemical and physical behaviors when compared to those that are not on a nanometer scale (cellulose on a macro scale), resulting in the improvement of the physical and/or chemical properties in composites, due to the high surface area and greater degree of dispersion, enabling outstanding performance. Such nanoparticles can be used to improve thermal behavior of different polymers.

Cellulose nanoparticles can be used to improve thermal behavior when mixed in different polymers [3] as a nucleating agent, preventing crystal growth and improving crystallization rates, which allows greater thermal stability to the composite, creating a more homogeneous and resistant product [3].

Due to the growing negative impacts of non-biodegradable plastics on the environment, there is an increased interest in the use of biodegradable polymers, an example of poly(lactic acid) (PLA), and this interest has aroused considerable interest in academia. PLA is a biodegradable polyester, easily processed and made from starchy plant sources [4]. Although it is a biodegradable and compostable material and widely used in 3D printing and rapid prototyping its adoption is limited due to its fragility, low tenacity, and low thermal stability [4] as it degrades in one or two steps in temperatures starting at 300°C [5] in contrast to other commonly used polymers such as polypropylene (PP) and Acrylonitrile Butadiene Styrene (ABS), with the beginning of their thermal decomposition occurring between 400°C [6] and 380°C [7] respectively.

To better understand the impact of cellulose nanofibril (CNF) addition on composite properties, this study aimed to evaluate the effect of CNF (1.5 and 4.5wt%) on the thermal properties, degree of crystallization and crystallization kinetics of PLA biopolymer composites using techniques such as Differential Scanning Calorimetry (DSC), Thermal Gravimetric Analysis (TGA) and Thermal Microscopy with hot stage plate.

2. METHODOLOGY

2.1. Materials

The poly (lactic acid), PLA, with a melt flow index of 12.6 g/10min (at 210ºC, 2.16 kg) selected for sample preparation was Naturework, purchased from 3D Lab. The cellulose nanofibrils were obtained by TRL9 and the methodology used is described in detail in the patent filling phase.

2.2. Preparation of the composites

Before the extrusion step, the components of the formulation (PLA, cellulose nanofibril) were dried in an oven at 100°C for 24h and mixed manually before extrusion. Three formulations were prepared: pure PLA and two composites with 1.5 wt.% (PLA+1.5CNF) and 4.5 wt.% (PLA+4.5CNF) of cellulose nanofibril. Each formulation was prepared in a twin-screw extruder, co-rotating, screw diameter D=16 mm and L/D = 40, model DR.16.AX (AX-Plásticos Máquinas Técnicas Ltda, Diadema, Brazil). The temperature profile and screw speed used were respectively: 165/170/175/180/180/185/185/185/190°C and 140 rpm. After the stage of obtaining the filament, the composites were granulated using a rotating blades granulator coupled to the extruder.

2.3. Characterization

Differential scanning calorimetry (DSC)

Analysis was performed to evaluate the influence of the presence of nanocellulose on the glass transition temperature and melting temperature of PLA and PLA/CNF nanocomposites. The DSC analysis was performed on a TA Instruments analyzer, model DSC Q10 (TA Instruments, New Castle, USA). The samples were first heated from 25 to 300°C, with a heating rate of 10°C/min, under a nitrogen atmosphere and kept at this temperature for 3 min to remove previous thermal history. At the sequence, the samples were cooled to 25ºC with a cooling rate of -10ºC/min and maintained for 3 min. In the end, the samples were reheated (second heat) to 300°C at the same first heating rate. The thermal properties estimated from DSC curves included glass transition temperature (Tg), crystallization peak temperature (Tc), cold crystallization peak temperature (Tcc), melting peak temperature (Tm), enthalpy of crystallization (ΔHc), enthalpy of fusion (ΔHm), and the degree of crystallinity (Xc). The degree of crystallinity (Xc) of PLA and PLA/CNF nanocomposites was calculated according to Eq. (1) [8]:

$$Xc(\%) = \frac{\Delta H_{m2} - \Delta H_c}{\Delta H_{m100\%} \times W_{PLA}} \times 100 \qquad (1)$$

Where: ΔHm2 is the enthalpy of melting in the second DSC heating scan. ΔHc is the enthalpy of crystallization (in the DSC cooling run). WPLA is the PLA weight fraction in the composite. ΔHm100% is the enthalpy of melting of 100% crystalline PLA (93.0 J/g) [8].

Thermogravimetric analysis (TGA)

To evaluate the thermal stability of the nanocomposites and their degradation temperature a thermogravimetric analysis (TGA) was performed. TGA analysis of the samples was performed on a TA Instruments analyser, model Q50 (TA Instruments, New Castle, USA), in the temperature range of 25 to 1000°C, with a heating rate of 10°C/min, under an atmosphere of nitrogen.

Thermal microscopy

The thermal microscopy analysis was done using an optical microscope Zeiss with a digital camera Axio coupled with the hot stage (Linkam Scientific Instruments Ltd., Redhill, UK). A thin slice of the sample was cut with a blade and placed between 2 glass coverslips. A magnification of 50x was used on the microscope lens and the digital images were obtained using the software Axio Image Analysis. For the thermal microscopy, the hot stage was set to a rate of 10°C/min for heating from 25-250°C and 5°C/min for cooling. This analysis was carried out to observe the thermal behavior of the samples, the effect of CNF on T_g, T_m, and T_c, and the nucleation and crystallization of PLA.

3. RESULTS AND DISCUSSION

3.1. DSC Analysis

The effect of CNF on the thermal properties of PLA was evaluated using DSC. Fig. 1a, 1b, 1c, 1d shows the second heating scan and Fig. 2 shows the cooling scan after the first heating. The parameters analyzed were glass transition temperature, melting temperature, enthalpy of melt, crystallization temperature, and degree of crystallinity (Xc).

1a

2b

1c

1d
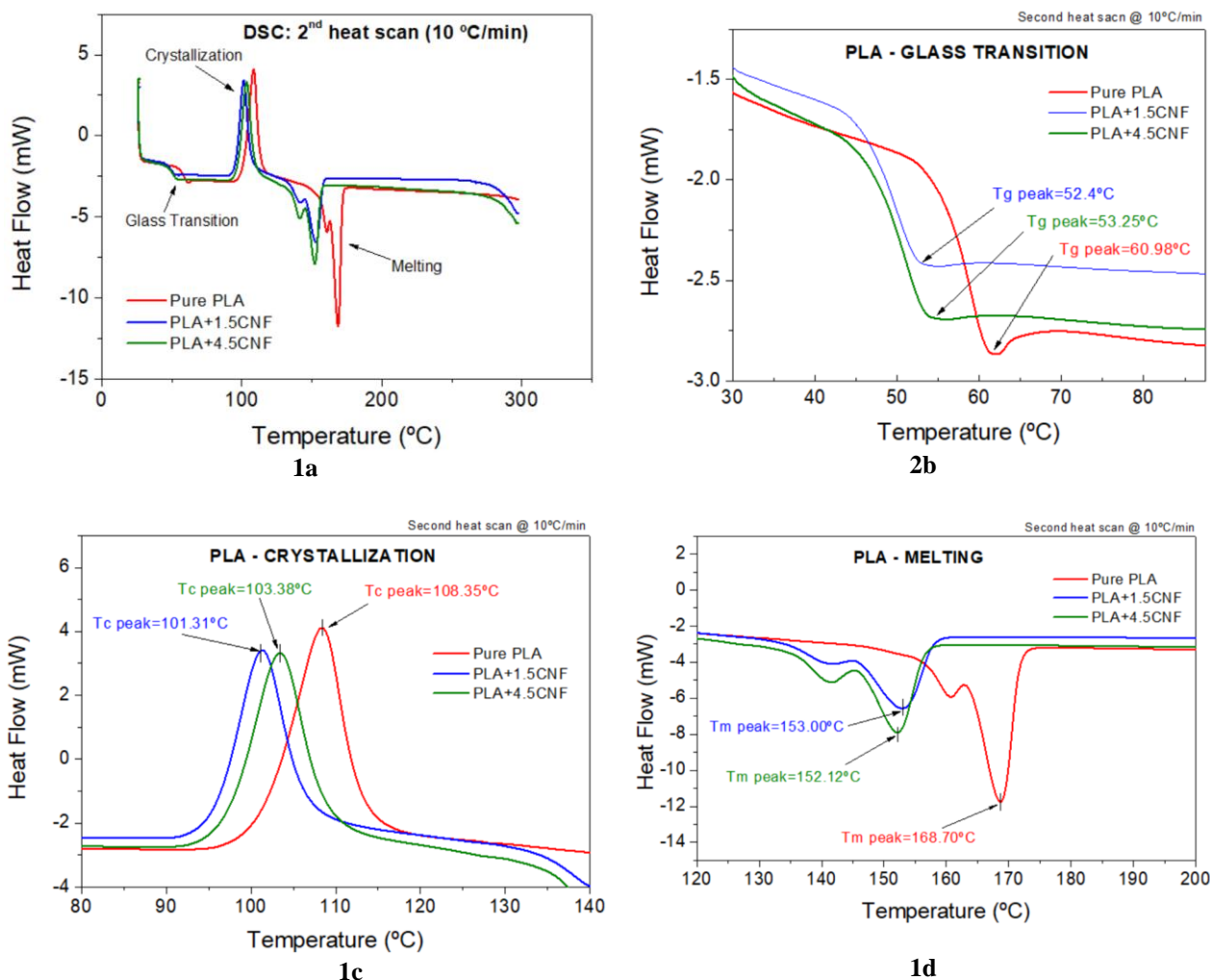
Figure 1. Second DSC heating scan from 25 to 300°C at 10°C/min. (**1a**). Complete reheating curve. (**1b**) Glass transition event. (**1c**) Crystallization event. (**1d**) Melting event.
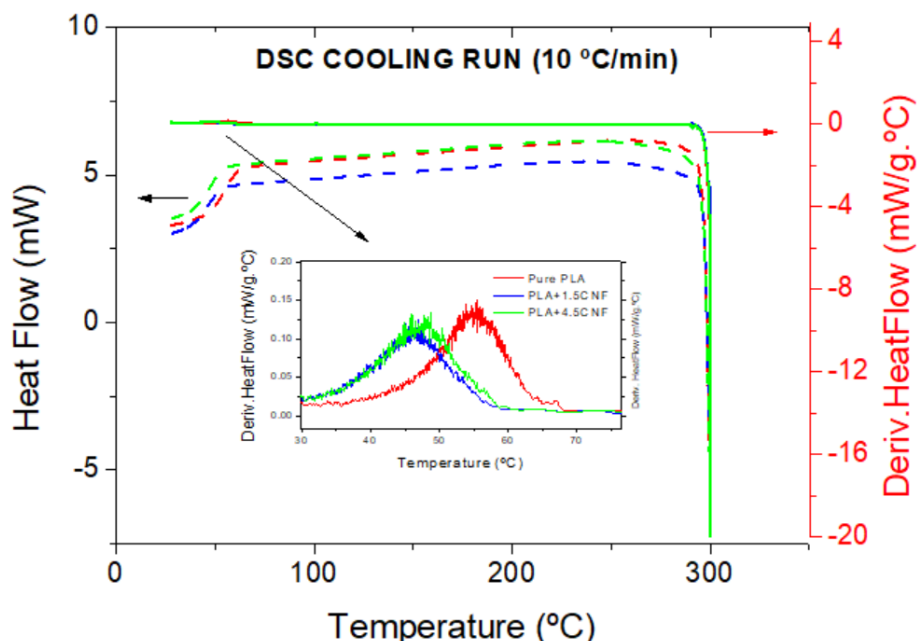
Figure 2. DSC cooling scan from 300 to 25ºC a -10ºC/min (after the first heat). The highlight (small graph) shows the glass transition of PLA at approximately 50-60ºC.

The Table 1 summarizes these thermal events obtained from DSC analysis of PLA and PLA-CNF composites. The degree of crystallinity (Xc) of pure PLA was calculated as 3.7%, consistent with literature, that found 2.3% of crystallinity [9], however the expected increase in the Xc was not observed in this work for the PLA+CNF composites. Some authors found around 30% of crystallinity for 1 to 2% of CNF, and around 40% of crystallinity with 4-5% of CNF in PLA [9,10], perhaps it was due to poor dispersion or agglomeration of CNF which can cause inhibition of crystallization of PLA or due to the heating rate not being low enough (a rate of 2 ℃/min) [9] as used in this work (10ºC/min). Furthermore, it was observed that addition of CNF promotes a decrease in the melting temperature, glass temperature and crystallization temperature, compared to pure PLA. The decrease of the Tg value caused by CNF loading, probably is influenced by increase of chain mobility, not necessarily correlated to crystallinity change [9]. Another explanation for the limited behaviour of crystallite nucleation by nanofibrils in the PLA matrix can be attributed to the waxy components present in cellulosic materials, associated to the inhibition of the growth of the PLA transcrystalline layer [11].

Table 1. Summary of DSC results for pure PLA and PLA/CNF composites:

Sample	Glass Transition	Crystallization		Melting		Cold Crystallization		Xc %
	Tg2 (ºC)	Tc2 (ºC)	ΔHc2 (J/g)	Tm2 (ºC)	ΔHm2 (J/g)	Tcc (ºC)	ΔHcc (J/g)	
Pure PLA	61.0	108.4	41.2	168.7	44.6	59.9	0.21	3.7
PLA+1.5CNF	52.4	101.3	35.4	153.0	38.2	51.9	0.87	3.1
PLA+4.5CNF	53.3	103.4	38.3	152.1	1.3	53.2	0.99	3.4

Legend: Subscript 2 refers to the second DSC heating, and subscript "cc" refers to the cold crystallization on DSC cooling run. Tg is the glass transition peak temperature. Tc is the crystallization peak temperature. Tcc is the cold crystallization peak temperature. Tm is the melting peak temperature. ΔHc2 is the enthalpy of crystallization in the second heating. ΔHcc is the enthalpy of cold crystallization. ΔHm is the enthalpy of fusion. Xc is the degree of crystallinity.

3.2. TGA/DTG

This analysis was done to perform a comparative analysis of the thermal stability and degradation of PLA when compared to composites containing cellulose nanofibril. The Fig. 3a and 3b shows the TG and DTG curves of pure PLA, PLA+1.5CNF; PLA+4.5CNF. The events relating to mass losses are summarized in Table 2. Based on the results (Tonset) it was possible to verify that there was no influence of the addition of cellulose nanofibril on the thermal stability of PLA as can be seen in the TGA curves (Fig. 3a). When evaluating the thermal behaviour of PLA, it was observed that this polymer was thermally stable up to 338.7°C, whereas the PLA+1.5CNF and PLA+4.5CNF composites were stable up to 324.6 and 331.6°C respectively. This single mass loss event is related to PLA degradation as reported in the literature [12].
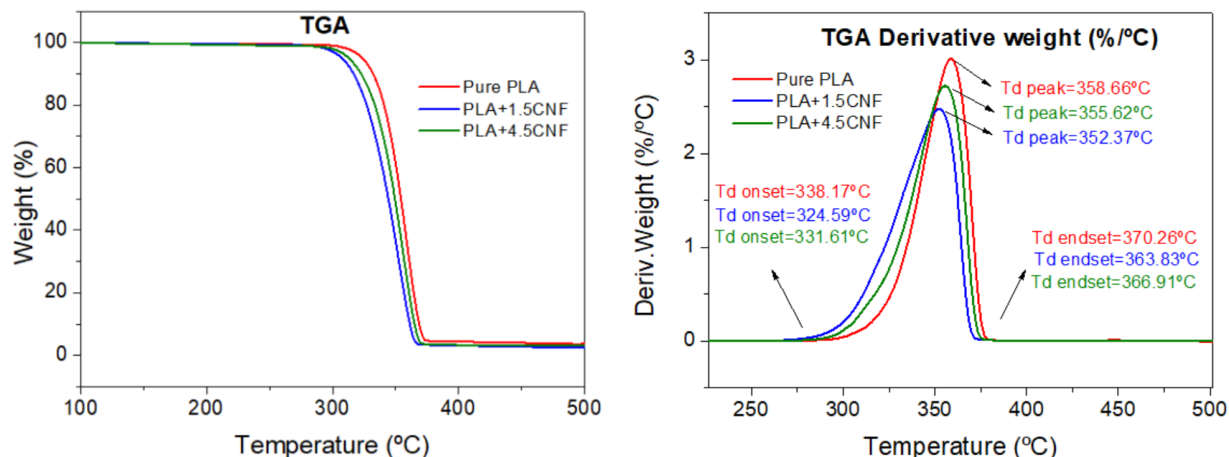
Figure 3. (a) TGA and (b) DTG curves of Pure PLA, PLA+1.5CNF; PLA+4.5CNF

Some authors reported that the addition of (3, 5, 7 and 10%) cellulose nanofibril improved the thermal stability of PLA for PLA/cellulose nanofibril composites obtained by electrospinning [13]. They observed through DTG that a thermal event for the compound occurs close to 331°C (Tmax). This value mentioned is lower when compared to the compounds obtained in this study (Tmax – Fig. 3b and Table 2), inferring that the nanocellulose used in the present study presents a promising thermal potential, although the difference between the thermal stability between PLA and the composites was not expressive.
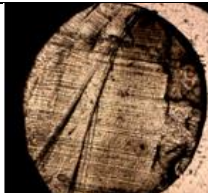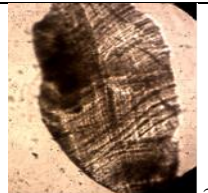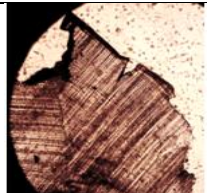
Table 2. DTG thermal events (Tonset, Tendset and Tmax) of PLA and PLA/CNF composites:

Sample	T_{onset} (°C)	T_{endset} (°C)	T_{max} (°C)
Pure PLA	338.2	370.3	358.7
PLA + 1.5CNF	324.6	363.8	352.4
PLA + 4.5CNF	331.6	366.9	355.6

A study from Cho et al [14] reported that using nanocellulose in poly(vinyl alcohol) also stated that there was no significant effect on the thermal stability of the material. The authors attributed this behaviour to the low levels (1 and 3%) of nanocellulose content used in the work, as these tend to provide a greater increase in the degradation temperature and delaying the rate of polymer degradation.

3.3. Thermal microscopy

The thermal microscopy was performed to evaluate the effect of CNF on Tg, Tm, Tc and the nucleation and growth of PLA polymeric crystallites. Fig. 4 shows images of the samples, started to 30 °C, heated until 250°C (with a rate of 10°C/min) and then cooled until 30°C (-5 °C/min). In the heating, at about 70°C occur the glass transition, and at approximately 180°C the samples begin to melt. In the cooling run, the nucleation of small PLA crystals (small bright spots) close to 111°C can be observed. This is equivalent to the crystallization observed in DSC analysis (Fig. 1a), which for PLA and CNF composite occurs at around 100-110°C (108.4°C for pure PLA, 101.3°C for PLA+1.5CNF and 103.4°C for PLA+4.5CNF).

Condition	PLA Pure	PLA+1.5CNF	PLA+4.5CNF
Heating (10°C/min) Start of analysis. Slice of sample cut using a blade. 50x nominal magnification.	40°C	30°C	30°C
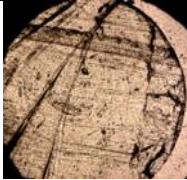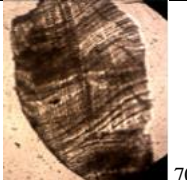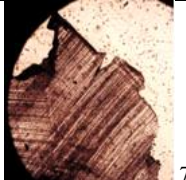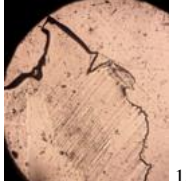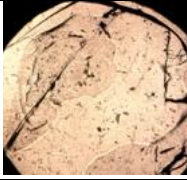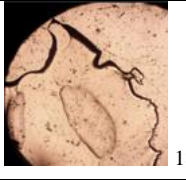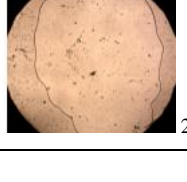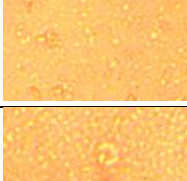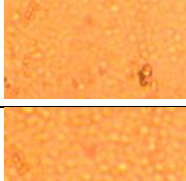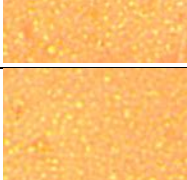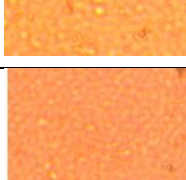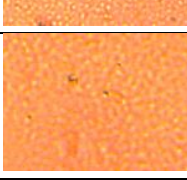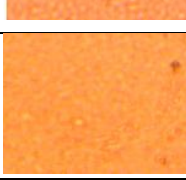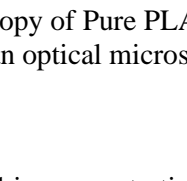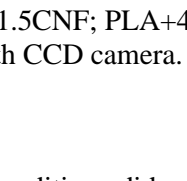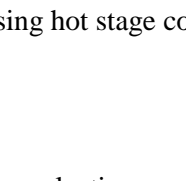
Heating (10ºC/min) 50x nominal magnification. **Glass transition temperature**	70ºC	70ºC	70ºC
Heating (10ºC/min) 50x nominal magnification.	180ºC	180ºC	180ºC
Heating (10ºC/min) 50x nominal magnification. **Starting to melt**	182ºC	182ºC	182ºC
Heating (10ºC/min) 50x nominal magnification.	250ºC	250ºC	250ºC
Cooling (5 ºC/min) **(50x nominal+100% digital zoom)** **Crystallization starting**	111ºC	--	111ºC
Cooling (5 ºC/min) **(50x nominal+100% digital zoom)**	108ºC		108ºC
Cooling (5 ºC/min) **(100% digital magnification)**	105ºC	105ºC	105ºC
Cooling (5 ºC/min) **(50x nominal+100% digital zoom)**	95ºC	95ºC	95ºC

Figure 4. Thermal microscopy of Pure PLA, PLA+1.5CNF; PLA+4.5CNF using hot stage coupled to an optical microscopy with CCD camera.

4. CONCLUSIONS

The nanocellulose evaluated in concentrations and conditions did not act as a nucleating agent with the behaviour expected to increase the degree of crystallinity of the PLA. This outcome can be attributed to non-cellulosic materials, such as waxy components present in these nanoparticles. Another factor that may have contributed to this behaviour was the low dispersion of CNF in the polymer matrix. Furthermore, the thermal stability assessed by TGA analysis showed that there was no significant difference in PLA when compared to composites, possibly due to the nanocellulose content incorporated into the polymer. Thermal microscopy showed changes in the PLA polymer film, during heating, at approximately 70ºC the film began acquired a lighter tone (in the glass transition), and at approximately 182ºC the sample melted (melting temperature). In the cooling run, nucleation can be observed with the formation of small PLA crystals (bright spots) close to 111ºC. A similar behaviour was observed in PLA/CNF composites. As future perspectives, new methods of dispersing these particles in the polymeric matrix should be studied to improve the thermal

performance of the materials, such as methods for removing waxy components, improving the melt mixture, and altering the interface between the nanoparticle and the matrix through functionalization methods.

4.1. Declaration of Competing Interest

4.2. Acknowledgements

5. REFERENCES

[1] Klein HS, Luna FV. The Development of a Modern Cellulose Industry in South America. Lat Am Res Rev 2022;57:753–74. https://doi.org/10.1017/lar.2022.65.

[2] Agbakoba VC, Mokhena TC, Ferg EE, Hlangothi SP, John MJ. PLA bio-nanocomposites reinforced with cellulose nanofibrils (CNFs) for 3D printing applications. Cellulose 2023;30:11537–59. https://doi.org/10.1007/s10570-023-05549-2.

[3] Gauss C, Pickering KL. A new method for producing polylactic acid biocomposites for 3D printing with improved tensile and thermo-mechanical performance using grafted nanofibrillated cellulose. Addit Manuf 2023;61:103346. https://doi.org/10.1016/j.addma.2022.103346.

[4] Tian J, Cao Z, Qian S, Xia Y, Zhang J, Kong Y, et al. Improving tensile strength and impact toughness of plasticized poly(lactic acid) biocomposites by incorporating nanofibrillated cellulose. Nanotechnol Rev 2022;11:2469–82. https://doi.org/10.1515/ntrev-2022-0142.

[5] Kervran M, Vagner C, Cochez M, Ponçot M, Saeb MR, Vahabi H. Thermal degradation of polylactic acid (PLA)/polyhydroxybutyrate (PHB) blends: A systematic review. vol. 201. 2022. https://doi.org/10.1016/j.polymdegradstab.2022.109995.

[6] Chiang TC, Liu HL, Tsai LC, Jiang T, Ma N, Tsai FC. Improvement of the mechanical property and thermal stability of polypropylene/recycled rubber composite by chemical modification and physical blending. Sci Rep 2020;10:1–8. https://doi.org/10.1038/s41598-020-59191-0.

[7] Alonso A, Lázaro M, Lázaro D, Alvear D. Thermal characterization of acrylonitrile butadiene styrene-ABS obtained with different manufacturing processes. J Therm Anal Calorim 2023;148:10557–72. https://doi.org/10.1007/s10973-023-12258-2.

[8] Dadbin S, Naimian F. Gamma radiation induced property modification of poly(lactic acid)/hydroxyapatite bio-nanocomposites. Polym Int 2014;63:1063–9. https://doi.org/10.1002/pi.4611.

[9] Shazleen SS, Yasim-Anuar TAT, Ibrahim NA, Hassan MA, Ariffin H. Functionality of cellulose nanofiber as bio-based nucleating agent and nano-reinforcement material to enhance crystallization and mechanical properties of polylactic acid nanocomposite. Polymers (Basel) 2021;13:1–19. https://doi.org/10.3390/polym13030389.

[10] Safdari F, Bagheriasl D, Carreau PJ, Heuzey MC, Kamal MR. Rheological, Mechanical, and thermal properties of polylactide/cellulose nanofiber biocomposites. Polym Compos 2018;39:1752–62. https://doi.org/10.1002/pc.24127.

[11] Baheti V, Mishra R, Militky J, Behera BK. Influence of noncellulosic contents on nano scale refinement of waste jute fibers for reinforcement in polylactic acid films. Fibers Polym 2014;15:1500–6. https://doi.org/10.1007/s12221-014-1500-5.

[12] Ramos M, Fortunati E, Peltzer M, Dominici F, Jiménez A, Garrigós MDC, et al. Influence of thymol and silver nanoparticles on the degradation of poly(lactic acid) based nanocomposites: Thermal and morphological properties. Polym Degrad Stab 2014;108:158–65. https://doi.org/10.1016/j.polymdegradstab.2014.02.011.

[13]   Yang Z, Li X, Si J, Cui Z, Peng K. Morphological, Mechanical and Thermal Properties of Poly(lactic acid) (PLA)/Cellulose Nanofibrils (CNF) Composites Nanofiber for Tissue Engineering. J Wuhan Univ Technol Mater Sci Ed 2019;34:207–15. https://doi.org/10.1007/s11595-019-2037-7.

[14]   Cho MJ, Park BD. Tensile and thermal properties of nanocellulose-reinforced poly(vinyl alcohol) nanocomposites. J Ind Eng Chem 2011;17:36–40. https://doi.org/10.1016/j.jiec.2010.10.006.

CELLULOSE NANOFIBRILS IN POLYMERIC FILMS - A REVIEW ON THE MECHANICAL BEHAVIOR AS A FUNCTION OF CNF DIMENSIONS

Rodrigo Polkowski[a]*, Paulo Romano Correia[b], Ana Paula Gonçalves[c], Josiane Barbosa[d]

(a) 0000-0002-9417-0953 (TRL9 Lab – Testing and Technical Analysis Ltd and SENAI/CIMATEC University Center, Salvador, BA, Brazil)
(b) 0000-0002-3666-8980 (TRL9 Tech – Research and Development, Salvador, BA, Brazil)
(c) 0000-0002-0326-5966 (TRL9 Lab – Testing and Technical Analysis Ltd, Salvador, BA, Brazil)
(d) 0000-0001-9835-8016 (SENAI/CIMATEC University Center, Salvador, BA, Brazil)
*Corresponding author: rodrigo@trl9.tech

CODE: BCCM7-196

Keywords: Cellulose Nanofibrils; Reinforcement; Polymeric Films.

Abstract:

Cellulose nanofibrils (CNFs), derived from low-cost, abundant and renewable resources, have achieved extensive research attention due to their sustainability, low density, large surface area, and unique mechanical performance when incorporated in a polymer matrix. The effect of CNF dimensions on the mechanical resistance of polymeric films remains an active area of research. While there is a consensus that CNFs can enhance mechanical properties, the exact impact of their dimensions is complex and not fully understood. In the present work, CNFs and their efficiency in acting as a mechanical reinforcement in polymer composite films were investigated, motivated by the number of cellulosic resources and availability of biomass in the South American region, mainly in the Northeast of Brazil, and also for the opportunity to provide insights for developing advanced materials with tailored properties for various applications, from packaging to electronics, and biomedical engineering. Thus, a systematic review was performed including all papers published until 2024, regarding the terms: cellulose AND (nanofibril OR nanofiber) AND reinforcement AND films, through a search of three articles databases, restricting the English language, while book chapters and conference papers were excluded. Although the literature reported the development of many types of polymeric films, this research was restricted to the most common polymers for film application. The PRISMA protocol was used to organize the information found (steps: identification, screening, eligibility, and inclusion). Overall, the findings reported that the addition of CNFs leads to an enhanced tensile modulus on the polymer matrices, representing an eco-friendly reinforcement with superior properties. The studies revealed that this outstanding mechanical performance can be attributed to the geometry of nanocellulose. CNFs of varying dimensions exhibit distinct surface charges and crystalline structures, resulting in varying degrees of entanglement through van der Waals forces, restricting the mobility of the polymer chain, and consequently preventing deformation. However, a few challenges still exist concerning the use of CNFs in polymer films, including the efficient dispersion and compatibility of nanoparticles in the matrix, and the development of suitable methods for the material processing, which also determines the final properties of the CNF-based composites.

1. INTRODUCTION

The use of CNFs derived from renewable cellulose resources presents a promising path for the sustainable development of materials [1]. Cellulose, the most abundant biopolymer on Earth, comes from various biomass raw materials, such as wood, agricultural waste and industrial by-products [2]. The Northeast region of Brazil, known for its rich biodiversity and forest resources, offers ample opportunities for the extraction and processing of cellulose-based materials.

In addition to CNFs, other cellulose derivatives, such as cellulose nanocrystals (CNCs) and microfibrillated cellulose (MFC), also have remarkable mechanical properties and have been explored in various applications [3]. These cellulose nanomaterials can be obtained by different extraction methods, including acid hydrolysis, mechanical fibrillation and enzymatic treatments, which allows for customized properties and applications [4-5].

Polymer composites with CNFs offer numerous advantages, including high mechanical strength, barrier properties and biodegradability [6-7]; attributes responsible for a wide range of applications, including the sustainable packaging sector, lightweight structural components and biomedical scaffolding [8].

In addition, advances in processing technologies, such as additive manufacturing and nanocomposite fabrication techniques, allow precise control over the dispersion and alignment of CNF within polymeric matrices, leading to improved mechanical performance and functionality. The development of environmentally friendly and economical manufacturing processes is crucial to the expansion of CNF-based materials for industrial applications [9-10].

Furthermore, exploiting synergistic effects between CNFs and other nanomaterials, such as carbon nanotubes and graphene, holds promise for progressively improving the properties and functionalities of polymer composites [11]. By taking advantage of the unique properties of CNFs and other nanomaterials, researchers can innovate and develop materials with customized properties for specific applications in electronics, energy storage, biomedical engineering, among others.

This study consists of a systematic review that aims to investigate the impact of CNF size on the tensile strength, modulus of elasticity and toughness of CNF-reinforced polymer films. CNFs have diameters ranging from 5 to 100 nm and widths varying several µm in length, exhibit a crystallinity of 50 to 70% and an extremely high surface area [12].

The PRISMA protocol [13] was used to organize the information collected, covering the stages of identification, screening, eligibility and inclusion. The results indicated that the addition of CNFs increases the tensile modulus of polymeric matrices, presenting CNFs as environmentally friendly reinforcements with superior mechanical properties. The research suggests that the remarkable mechanical performance of CNF-based composites stems from the geometric characteristics of the nanocellulose. Thus, CNFs of different dimensions exhibit distinct surface charges and crystalline structures, resulting in varying degrees of entanglement through van der Waals forces, thus allowing polymer chain mobility and deformation.

2. LITERATURE REVIEW

This study followed the PRISMA protocol (Preferred Reporting Items for Systematic Reviews and Meta-Analyses) [13] to ensure transparency and methodological rigor. Three different bibliographic databases were used: Scopus, Web of Science and MDPI with language restricted to English and publications up to March-2024. The keywords used were: "cellulose" AND ("nanofibril" OR "nanofiber") AND "reinforcement" AND "films". Despite the extensive literature documenting the development of various types of polymeric films, this study focuses on the most prevalent polymers for film applications.

Fig. 1 illustrates the workflow used to select the articles, as recommended by the PRISMA protocol. After the initial search in the databases, a total of 357 articles were obtained. The inclusion criteria covered only research articles, excluding reviews, conference papers, early access articles, book chapters, among others. In addition, duplicated articles were removed, leaving 233 publications.

In the next stage, the eligibility criteria were applied, excluding articles that did not focus on nanofibrillar cellulose, did not involve composite materials or those articles that did not include the polymers of interest (PLA, PLC, PBAT, PBS, HDPE, etc). This selection process resulted in the selection of 33 relevant articles for further analysis.
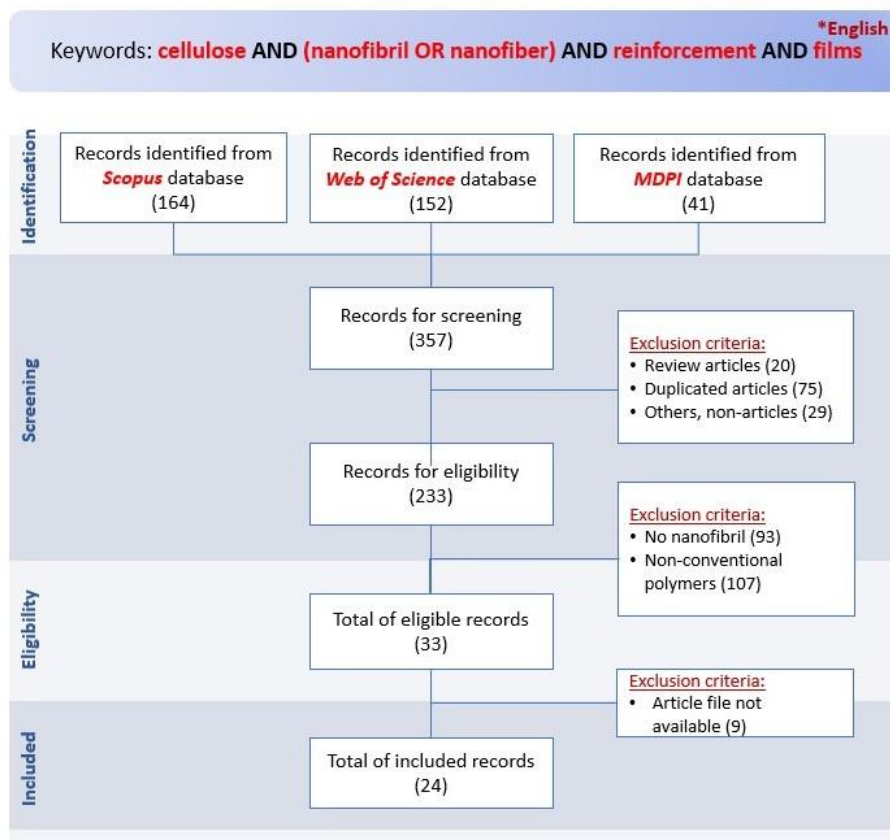
Figure 1. Systematic review flowchart, following PRISMA protocol.

Of the 33 articles, 9 were unavailable and the remaining opened access files were independently assessed for compliance, resulting in a total of 24 articles included in this study.

3. RESULTS AND DISCUSSION

Based on the analysis of data from the PRISMA protocol, a significant increase was observed in the number of articles selected in the years 2019 and 2022 (Fig. 2), indicating a growing interest and investment in studies related to composites with CNFs as a reinforcement agent. This increase in scientific production can be attributed to a combination of factors, such as technological advances, growing environmental concerns, the improved properties offered by CNFs and the diversification of potential applications for these materials.
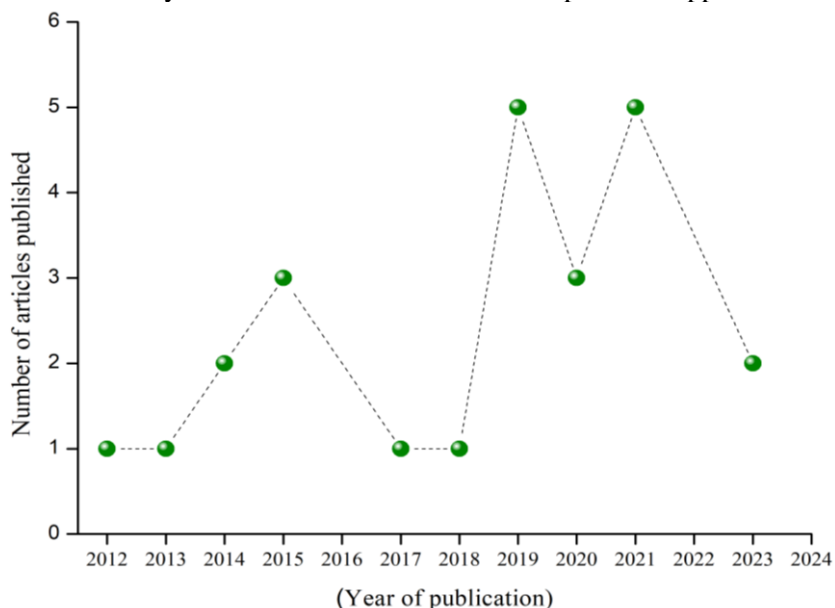
Figure 2. Temporal analysis of the selected studies by year

The articles presented a variety of types of polymers with added CNF (Fig. 3), acting as an effective reinforcement and significantly improving the mechanical properties of the polymers. The studies also show that the presence of CNF contributes to thermal stability, optical transparency and water resistance, expanding its application in sectors such as electronics, packaging, coatings and biomaterials [14].
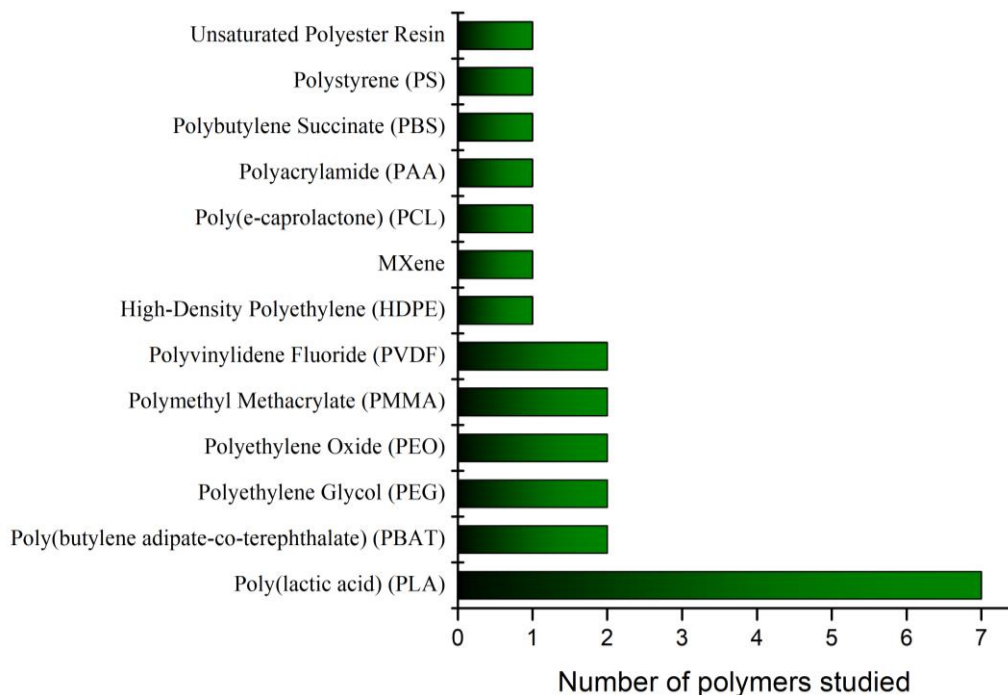
Figure 3. Polymers evaluated in the selected articles.

The addition of CNFs to biodegradable polymers such as PLA, PBAT, PCL and PBS show significant improvements in the general properties of composites, not only in terms of mechanical reinforcement, but also in terms of reducing environmental impact [15-16]. The effective interaction between CNFs and polymeric matrices results in more homogeneous composites with improved performance, expanding their application possibilities in various industrial sectors. Nanocellulose can be divided into three main classes: nanostructured materials, (cellulose microcrystals (CNF) and cellulose microfibrils (CNC) and bacterial cellulose (BC), depending on their morphologies, origin and isolation techniques [16]. This distinction between the different forms of nanocellulose is fundamental to understanding their specific properties and applications, highlighting the diversity and versatility of these nanostructured materials derived from a renewable and abundant source such as cellulose. Table 1 [17] summarizes the physical properties and sources of nanocellulose.

Table 1. The physical comparison between nanocellulose

Nanocellulose Type	Abbreviation	Sources	Dimensions
Bacterial nanocellulose	BNC	Microorganisms	Diameter: 2 - 4 nm Length: 100 nm
Cellulose nanocrystals	CNC	Plants	Diameter: 2 - 20 nm Length: 10 - 600 nm
Cellulose nanofibers	CNF	Plants	Diameter: 5 - 100 nm Length: Several μm

An in-depth analysis of the articles revealed a diversity of research incorporating CNFs into different polymers for the production of composite films. The studies investigated their mechanical properties and explored the impact of the size of the CNFs in these materials. Of the 24 articles analyzed, only 14 included complete information on the size of the CNFs used. Table 2 shows the relationship between the values of the sizes of the CNFs incorporated into the polymer composites and the effects observed on the mechanical properties.

Table 2. Articles evaluated in the systematic review by polymer type, CNFs size, concentration and mechanical properties.

Polymer Type	CNF Dimensions Diam./Length	CNF%	Mechanical Properties	Ref.
PEO	3 nm, 1500 nm	0 to 20	The composite films showed a significant increase in Young's modulus and tensile strength, from 0.2 to 2.4 GPa and from 6 to 86 MPa, respectively. However, the elongation at break decreased from 320% to 9% with increasing CNF content, resulting in harder and stronger but more brittle composites.	[14]
PLA	5 - 80 nm, N/I	1,0 3,0 and 5,0	The addition of 3% nanofibrillated cellulose (CNF) resulted in significant improvements in the mechanical properties of the nanocomposites, including increased tensile strength and elastic modulus.	[15]
HDPE	55 - 219 nm, N/I	5,0	Significant improvement in mechanical properties, with a 22% increase in tensile strength and a 98% increase in Young's modulus.	[18]
MXene	$\cong$ 20 nm, N/I	20, 50 and 60	Pure MXene film surpassed by 20% CNF in tensile strength and elongation.	[19]
PBAT	10 nm, 500 nm	0,4 to 0,8	Significant increase in modulus of elasticity by up to 75 MPa and in tensile strength by up to 35.6 MPa, in addition to a notable increase in elongation at break reaching up to 703%.	[20]
PLA	3 - 4 nm, >800 nm	0,1	Addition of 0.1 wt% functionalized CNF resulted in a significant increase in both the strength and toughness of the material.	[21]
PLA	93 - 28 nm, N/I	1,0	Average tensile strength of 37.6 ± 3.8 MPa, reflecting a 25% increase compared to pure PLA.	[22]
PLA	15.2 - 66.8 nm, several μm	0,25 0,5 and 1,0	Tensile strength were improved from 71.82 to 74.66 MPa and Young's modulus from 1,09 to 1,29	[23]
PLA	N/I, 443 nm	3,0	Initial modulus and tensile strength increased by 207.69 and 168.67% respectively compared to pure PLA film.	[24]
PBS	10 -19 nm, N/I	1, 3, 5 and 10	Increase of up to 18.8% in tensile properties, indicating significant improvements in mechanical properties.	[25]
PEG	3 nm, 1087 nm	0 - 2,5	Tensile strength and elongation at break increased considerably with increasing PEG-TOCN content from 0 to 2.5% by weight.	[26]
PEO	5 nm, N/I	10 and 5	The nanocomposite film with a 90:10 EG/CNF ratio demonstrated a tensile strength of 50.7 MPa.	[27]
PS	3 a 4 nm, 383 - 1087 nm	0,5 to 10	With 10% TOCN-310, there was a 91% increase in modulus of elasticity and 18% increase in tensile strength compared to pure PS, despite a decrease in elongation at break.	[28]
PVDF	<100 nm, N/I	0,5 to 5	The tensile modulus of CNF/PVDF films increased approximately 18% compared to the pure film.	[29]

*N/I = Not informed

Shi et al. (2019) [14] presented a CNF prepared by TEMPO-oxidization method, with homogeneous and small widths of 3 nm and a high average aspect ratio of 500. These network structures of CNF elements in the PEO matrix, without significant agglomeration, resulted in unique mechanical properties. The Young's modulus and tensile strength remarkably improved from 0.2 to 2.4 GPa and from 6 to 86 MPa, respectively, with increasing CNF addition from 0% to 20% to the PEO matrix.

Abdulkhani et al. (2014) [15] in turn, addressed the importance of additives in optimizing the performance of the composite, highlighting their influence on the adhesion between the polymer matrix and the reinforcing fibers, the transfer of tensions and the crystallinity matrix. The addition of modified cellulose nanofibers to PLA nanocomposites is evaluated in relation to the material's mechanical and thermal properties. In the study, revealed that the addition of CNFs to PLA can affect the crystallinity of the polymer due to their ability to act as nucleation points for PLA crystallization. The presence of CNFs can interfere with the crystalline structure of PLA, leading to changes in molecular organization and crystal formation.

Dias et al., (2021) [18] studied the interaction between high-density polyethylene (HDPE) and ethylene vinyl alcohol copolymer (EVAL), which played a key role in improving adhesion and dispersion of nanocellulose (CNF) in the ternary matrix. The presence of CNF in the matrix influences the surface tension and chemical compatibility of the components, directly impacting on the final properties of the nanocomposites. CNF acted as a nucleation agent, influencing the crystallinity and mechanical properties of the materials. The crystallinity of the nanocomposite increased by up to 35.2% compared to those of neat HDPE. The study highlights the innovation of a low-energy process free of harmful organic solvents to obtain a homogeneous distribution of CNF in HDPE. CNF dispersion was achieved through a melt blending process, with the EVAL copolymer playing a crucial role as a bridge between HDPE and CNF.

Geng et al. (2018) [21] noted in their work that PEG-grafted cellulose nanofibers have demonstrated much better dispersion in PLA matrix as compared with unmodified CNF. The CNF prepared by TEMPO-oxidization method exhibit average width of 4.3 nm for the CNF-g-PEG, which is slightly larger than that of the CNFs (3.6 nm) owing to the grafted PEG layer covering the surface of the CNFs. No apparent difference between the average lengths of the CNF (820 nm) and CNF-g-PEG (830 nm), indicating that the treatment of PEG grafting was mild and no degradation of the CNF occurred. With the incorporation of 0.1 wt% of the CNF-g-PEG in PLA, the ultimate strength and toughness are enhanced by 39% and 70%, respectively.

In another study, Jamaluddin et al., (2019) [22] evaluated the influence of the surface chemistry of cellulose nanofibrils (CNF) on the interaction with the PLA polymer matrix. The authors used the technique of functionalizing CNFs through acetylation to produce ACNFs (acetylated cellulose nanofibrils), as this has been highlighted as an effective method for increasing fibre-polymer adhesion, contributing to increased tensile strength and other mechanical properties of PLA nanocomposites. They report that PLA/ACNF composite film with 1 wt% ACNF showed 25% increment in tensile strength up to 37.6 MPa, while neat PLA exhibited 30.1 MPa, due to better compatibility between CNF and PLA matrix.

Jung et al. (2020) [23] studied CNF/PLA nanocomposites prepared by melt mixing method with freeze-dried CNF and CNF-solvent suspension (eco-friendly plasticizer, named TEC). The widths of CNF were found to be in the range from 15.2 to 66.8 nm (average value: 32.0 nm), and its length was estimated to be several micrometers. The addition of 0.25 wt% CNF in PLA enhanced the tensile strength of CNF/PLA by about 4% (from 71.82 to 74.66 MPa). When the CNF/PLA was plasticized by TEC, the tensile strength of the nanocomposites decreased, while elongation at break increased from 9.50 to 323.62%.

The study carried out by Baheti et al., (2014) [24] discussed in their results that the crystallinity of the treated jute nanofibrils was crucial to understanding how the crystalline structure of the nanofibers influences the interaction with PLA. The crystallinity of the nanofibrils affects the stiffness, strength and mechanical properties of the composites, since a more ordered crystalline structure can promote better load transfer and a more uniform distribution of stresses in the composite material. All the PLA-CNF composite films have higher tensile strength as compared to neat PLA film. The maximum increase was 69.80 MPA (3%CNF+PLA) compared to 25.98 MPA of neat PLA, indicating a better stress transfer across the interphase due to good interfacial bonding between fillers and the polymer matrix.

The study by Cindradewi et al., (2021) [25] evaluated the incorporation of CNFs into polybutylene succinate (PBS), showing improved results in the elastic modulus of the nanocomposites. The authors described that CNFs, when properly sized and well dispersed in the polymer matrix, contribute significantly to increasing the modulus of elasticity, giving the material greater rigidity. The tensile strength of PBS/CNF prepared using the two-step process was increased from 42.9 MPa of neat PBS to 50.8 MPa of PBS/CNF with 5% CNF loading. The elastic modulus was also increased, from 782.7 to 1042.5 MPa. The addition of more than 5% CNF reduced the flexibility of PBS molecular chains, leading to a decrease in the mechanical properties of the composites.

The studies included in this review highlighted the crucial importance the uniform dispersion of CNFs in the polymer matrix, by techniques such as functionalization and the addition of compatibilizers. In addition, the optimization of composite performance is achieved through the appropriate selection of additives and compatibilizers, highlighting the importance of an integrated approach in the formulation of composites with optimized performance. The authors also highlighted that the size of nanocellulose fibrils (CNFs) plays a key role in improving the mechanical properties of polymer composites, increasing the tensile strength, stiffness and other properties of composite materials. However, it was possible to observe a frequent lack of simultaneous reporting of both length and diameter of nanocellulose fibrils in many articles and it may be attributed to measurement complexity and time-consuming techniques used such as atomic force microscopy (AFM). Most of the articles measured only the diameter, which is easier to assess and still provides useful information about the nanocellulose characteristics. However, focusing solely on diameter overlooks the critical influence of fibril length. Both dimensions impact the aspect ratio, fundamental for reinforcement efficiency, and influences dispersion, alignment, and load transfer capacity within the composite. Long fibrils can improve toughness and material strength but may lead to challenges such as agglomeration and difficulties in dispersion within the polymer matrix.

4. CONCLUSIONS

The systematic review evaluated the role of CNFs as reinforcements in polymeric films, highlighting the improvements in the mechanical properties of polymeric matrices through their use. In addition, this study showed that the geometry of the CNFs, including their dimensions and surface charges, plays a crucial role in the properties of composite films and is an important point of analysis. However, the studies highlighted challenges such as the efficient dispersion of the CNFs in the polymer matrix and the promotion of compatibility between the constituent materials. Finally, the incessant search for a homogeneous distribution of CNFs to maximize their potential as mechanical reinforcement of these materials was revealed.

The combined length and diameter of nanocellulose fibrils emerge as critical factors in defining the mechanical properties of polymeric nanocomposites. However, due to the challenges in measurement and the complexity of their interactions within the composite material, many studies concentrate on the more readily measurable and impactful parameters like diameter and surface chemistry. Looking ahead, the potential for future advancements is immense, and it is crucial to delve into both dimensions of CNFs to unlock the full potential of nanocomposite properties, inspiring further research and innovation in the field.

4.1. Declaration of Competing Interest

The authors declare no conflict of interest.

4.2. Acknowledgements

5. REFERENCES

[1] X. Yang et al. "Eco-friendly cellulose nanofibrils designed by nature: effects from preserving native state." *ACS nano* 14.1 (2019): 724-735. DOI: 10.1021/acsnano.9b07659.

[2] L. G. A. Nair and P. Verma. "An overview of sustainable approaches for bioenergy production from agro-industrial wastes." *Energy Nexus* 6 (2022): 100086. DOI : 10.1016/j.nexus.2022.100086.

[3] I. Leppänen,et al. "Hybrid films from cellulose nanomaterials—properties and defined optical patterns." *Cellulose* 29.16 (2022): 8551-8567. DOI:10.1007/s10570-022-04795-0.

[4] M. F. S. Zhao and T. Saito. "Counterion-Dependent Material Properties of Phosphorylated Nanocellulose." *Biomacromolecules* 24.4 (2023): 1881-1887. DOI: 10.1021/acs.biomac.3c00066.

[5] S. Siljander. "Nanoarchitectonics of Nanocellulose-Carbon Nanotube Composites: From Dispersion to Functional Structures." (2022). https://urn.fi/URN:ISBN:978-952-03-2617-3.

[6] E. R. A Aigaje, and H. Baykara. "Processing, properties, modifications, and environmental impact of nanocellulose/biopolymer composites: a review." *Polymers* 15.5 (2023): 1219. DOI : 10.3390/polym15051219.

[7] J. L. Sanchez-Salvador et al. "Nanocellulose from a colloidal material perspective." *Frontiers in Materials* 10 (2023): 1231404. DOI:10.3389/fmats.2023.1231404.

[8] M. N. F. Norrrahim et al. "Performance evaluation of cellulose nanofiber reinforced polymer composites." *Functional Composites and Structures* 3.2 (2021): 024001. DOI: 10.1088/2631-6331/abeef6

[9] N. Vidakis et al. "Biomedical resin reinforced with Cellulose Nanofibers in VAT photopolymerization Additive Manufacturing: The effect of filler loading and process control parameters on Critical Quality Indicators." *Journal of Manufacturing Processes* 101 (2023): 755-769. DOI:10.1016/j.jmapro.2023.06.018.

[10] H. Wei et al. "Direct 3D printing of hybrid nanofiber-based nanocomposites for highly conductive and shape memory applications." *ACS applied materials & interfaces* 11.27 (2019): 24523-24532. DOI: 10.1021/acsami.9b04245.

[11] B. M. Tyson et al. "Carbon nanotubes and carbon nanofibers for enhancing the mechanical properties of nanocomposite cementitious materials." *Journal of Materials in Civil Engineering* 23.7 (2011): 1028-1035. DOI:10.1061/(ASCE)MT.1943-5533.0000266.

[12] J. Goncalves et al. Turbidity-based measurement of bleeding in fresh cement paste as affected by cellulose nanofibres. Cement and Concrete Composites. 123 (2021): 104197. DOI: 10.1016/j.cemconcomp.2021.104197.

[13] L. Shamseer et al. "Preferred reporting items for systematic review and meta-analysis protocols (PRISMA-P) 2015: elaboration and explanation." *Bmj* 349 (2015). DOI: 10.1136/bmj.g7647.

[14] Z. Shi et al. "Carboxylated nanocellulose/poly (ethylene oxide) composite films as solid–solid phase-change materials for thermal energy storage." *Carbohydrate polymers* 225 (2019): 115215. DOI: 10.1016/j.carbpol.2019.115215.

[15] A. Abdulkhani et al. "Preparation and characterization of modified cellulose nanofibers reinforced polylactic acid nanocomposite." *Polymer testing* 35 (2014): 73-79. DOI: 10.1016/j.polymertesting.2014.03.002

[16] Q. Wang et al. "Structure and properties of polylactic acid biocomposite films reinforced with cellulose nanofibrils." *Molecules* 25.14 (2020): 3306. DOI: 10.3390/molecules25143306

[17] Y. Qing et al. "Facile preparation of optically transparent and hydrophobic cellulose nanofibril composite films." *Industrial Crops and Products* 77 (2015): 13-20. https://doi.org/10.1016/j.indcrop.2015.08.016.

[18] O.A.T. Dias et al. "Clean manufacturing of nanocellulose-reinforced hydrophobic flexible substrates." *Journal of Cleaner Production* 293 (2021): 126141. DOI:10.1016/j.jclepro.2021.126141.

[19] Z. Cui et al. "Lightweight MXene/cellulose nanofiber composite film for electromagnetic interference shielding." *Journal of Electronic Materials* 50 (2021): 2101-2110. DOI:10.1007/s11664-020-08718-2.

[20] L. Lai et al. "Mechanically reinforced biodegradable poly (butylene adipate-co-terephthalate) with interactive nanoinclusions." *Polymer* 197 (2020): 122518. DOI : 10.1016/j.polymer.2020.122518.

[21] S. Geng et al. "High-strength, high-toughness aligned polymer-based nanocomposite reinforced with ultralow weight fraction of functionalized nanocellulose." *Biomacromolecules* 19.10 (2018): 4075-4083. DOI : 10.1021/acs.biomac.8b01086

[22] N. Jamaluddin et al. "Surface modification of cellulose nanofiber using acid anhydride for poly (lactic acid) reinforcement." *Materials Today Communications* 21 (2019): 100587. DOI: 10.1016/j.mtcomm.2019.100587.

[23] B. N. Jung et al. "The fabrication of flexible and oxygen barrier cellulose nanofiber/polylactic acid nanocomposites using cosolvent system." *Journal of Applied Polymer Science* 137.47 (2020): 49536. DOI:10.1002/app.49536.

[24] V. Baheti et al. "Influence of noncellulosic contents on nano scale refinement of waste jute fibers for reinforcement in polylactic acid films." *Fibers and Polymers* 15 (2014): 1500-1506. DOI:10.1007/s12221-014-1500-5.

[25] A. W. Cindradewi, et al. "Preparation and characterization of polybutylene succinate reinforced with pure cellulose nanofibril and lignocellulose nanofibril using two-step process." *Polymers* 13.22 (2021): 3945. DOI: 10.3390/polym13223945

[26] H. Soeta et al. "Low-birefringent and highly tough nanocellulose-reinforced cellulose triacetate." *ACS Applied Materials & Interfaces* 7.20 (2015): 11041-11046. DOI: 10.1021/acsami.5b02863.

[27] W Yang et al. "Strong and highly conductive graphene composite film based on the nanocellulose-assisted dispersion of expanded graphite and incorporation of poly (ethylene oxide)." *ACS sustainable chemistry & engineering* 7.5 (2019): 5045-5056. DOI: 10.1021/acssuschemeng.8b05850.

[28] F. Shuji et al. "Superior reinforcement effect of TEMPO-oxidized cellulose nanofibrils in polystyrene matrix: optical, thermal, and mechanical studies." Biomacromolecules 13.7 (2012): 2188-2194. DOI: 10.1021/bm300609c.

[29] E. Barnes, et al. "Effect of cellulose nanofibrils and TEMPO-mediated oxidized cellulose nanofibrils on the physical and mechanical properties of poly (vinylidene fluoride)/cellulose nanofibril composites." *Polymers* 11.7 (2019): 1091. DOI: 10.3390/polym11071091.

3D-PRINTING OF GRAPHENE-BASED COMPOSITES: A SYSTEMATIC REVIEW ON PROCESSING METHODS

Vinícius P. Oliveira[(a)][*]; Débora A.N. Leal[(b)]; João H. L. Moura[(c)]; Eduardo F. Kerche[(d)]; Katielly V. Polkowski[(e)]; Paulo R. C. Correia[(f)] Rodrigo D. O. Polkowski[(g)]

(a) 0009-0004-9172-4692 (TRL9 Tech – Research and Development, Salvador, BA, Brazil)
(b) 0000-0001-7359-2762 (TRL9 Tech – Research and Development, Salvador, BA, Brazil)
(c) 0000-0002-7889-6113(TRL9 Tech – Research and Development, Salvador, BA, Brazil)
(d) 0000-0003-1361-0708 (TRL9 Tech – Research and Development, Salvador, BA, Brazil)
(e) 0009-0003-2554-3677 (TRL9 Tech – Research and Development, Salvador, BA, Brazil)
(f) 0000-0002-3666-8980 (TRL9 Tech – Research and Development, Salvador, BA, Brazil)
(g) 0000-0002-9417-0953 (TRL9 Tech – Research and Development, Salvador, BA, Brazil)
*Corresponding author: vinicius.oliveira@trl9.tech

CODE: BCCM7-197

Abstract: The 3D printing process has been an alternative to traditional methods for processing polymers and composites, but it is necessary to enhance the final properties of these parts. Graphene is a 2D nanomaterial that presents exceptional properties and, consequently, can improve the properties of composites even in small quantities. The intercalation by solution technique is the most commonly used method to achieve a good dispersion of graphene nanoparticles however, frequently, no eco-friendly solvents are used. Seeking to develop composites with greater sustainability, this review aims to explore solvent-free methods, such as extrusion, for producing polymer-based composites loaded with graphene. Therefore, a study was carried out following the Preferred Reporting Items for Systematic Reviews and Meta-Analyses (PRISMA) protocol. This research was restricted to the most common polymers used in 3D printing, namely, Acrylonitrile butadiene styrene (ABS), Polypropylene (PP), Polylactic Acid (PLA) and polyethylene terephthalate (glycol) (PET/PETG). For extrusion, single-screw and twin-screw methods were reported, and the effect of the lateral size of graphene on the final properties of the composites was analyzed. It is expected that this review will inspire new solutions for graphene-based polymeric composites using solvent-free methods.

1. INTRODUCTION

Additive manufacturing and, particularly, the process via fusion deposition modeling (FDM) has become an accessible alternative to injection and extrusion processes for rapid prototyping due to the lower initial machinery cost and ability to print complex geometries as discussed by Prasong *et al.* (2021) [1]. The printing process is versatile and can be used with several polymers already used in the industry, such as polylactic acid (PLA), acrylonitrile butadiene styrene (ABS), polypropylene (PP) and polyethylene terephthalate (glycol) (PETG). However, the implementation printed materials is currently hampered due to the low strength of the final part, which is dependent on numerous parameters, such as printing orientation and speed, type of infill and temperature [1]. Due to the deposition of material in already partially cooled layers, adhesion and consequent mechanical resistance are impaired, creating anisotropy. Furthermore, the 3D printing process generates structural voids and stress concentrations in rounded corners that can serve as locations of mechanical failure [2].

Graphene is a nanomaterial with a 2D structure, and presents excellent properties, such as high tensile strength and low density, which makes it a promising material for addition to polymeric matrices to produce nanocomposites. The structure of graphene is based on an atomic thick sheet composed of carbon atoms with sp^2 hybridization and organized in a hexagonal network structure in a honeycomb form, where a carbon atom is arranged at each vertex of the hexagon [3]. The π bonds throughout the graphene sheet are responsible for its extraordinary mechanical properties. Although its current production cost makes a high production volume unfeasible, the use of graphene for various applications has been growing in recent years, since research indicates improvements in the final properties of polymeric composites when used in concentrations as low as 0.2 wt.%. With the use of graphene, it is possible to obtain a composite with a higher fluidity index, better thermal conductivity, a lower processing temperature, and greater crystallization levels (improving mechanical resistance). Thus, the addition of graphene to nanocomposites makes it possible to develop parts and products with greater durability, greater strength, and lower weight [3]. Incorporating graphene into 3D print filaments to create nanocomposites significantly improves the mechanical strength of the final 3D printed parts, crucially benefiting the 3D printing sector. Enhanced mechanical properties mean printed parts are more resilient, durable, and suitable for a wide range of applications, expanding the possibilities and reliability of 3D printing technology across industries [2].

The nanocomposite preparation method must guarantee a uniform distribution of graphene nanoparticles in the polymeric matrix and good interface adhesion between both components, thus allowing the composite to present better properties than the pure polymer. The method of Melt intercalation consists of mixing graphene nanoparticles with the polymeric matrix in the molten state, with the aid of shear forces. This procedure demands high shear forces and depends on mixing equipment (extruder, intensive mixer, roller mill, etc.) to generate homogeneous mixtures. The Melt Intercalation method is the most environmentally friendly compared with other commonly used methods such as Solution Intercalation and *In-Situ* Polymerization, as it does not require the use of toxic organic solvents and does not generate waste [4]. This method also has the advantage of high scalability, as it is more economical and faster compared to the other two methods. Despite this, according to related literature, the solution intercalation method is still the most widely used, mainly because it requires simple and cheap machinery and provides good homogenization of nanoparticles in polymeric matrices.

Studying and controlling the lateral size of graphene in 3D printing can enhance mechanical, thermal, and electrical properties. Smaller graphene sheets offer higher surface area for interfacial bonding, improving strength, while larger graphene sheets form an interconnected network, improving conductivity [5]. Precise sizing ensures uniform dispersion, optimizing material integrity and functionality in printed parts.

Therefore, this review article aims to answer the following research questions: (I) How to process polymeric composites with graphene without the use of organic solvents? (II) How to ensure good dispersion of graphene in the polymeric matrices? And (III) How does incorporating graphene change the composite printability? Thereby, this systematic review explored solvent-free methods, such as extrusion, for producing polymer-based composites loaded with graphene.

2. LITERATURE REVIEW METHODOLOGY

The systematic review followed PRISMA protocol with the following search string: "Graphene" AND "Extrusion" AND "Composite" in abstract, keywords and title fields, using Scopus (www.scopus.com), Web of Science (www.webofknowledge.com), and MDPI (www.mdpi.com) articles' databases. Articles in English published between 2018 and 2024 were filtered, while conference articles, review articles, book chapters, and duplicated records were removed (Figure 1). The search was carried out on March, 2024.

To restrict the search to the use of polymeric matrices with graphene, articles that developed metallic composites were excluded, as well as those that focused on development and study of electromagnetic shielding and interference. To obtain eco-friendly processing methods, articles that reported the use of organic solvents were removed, and with the aim of understanding development in more common scenarios and with the polymeric materials most used today in 3D printing, the research was restricted only to ABS, PP, PLA and PET/PETG polymeric matrices.
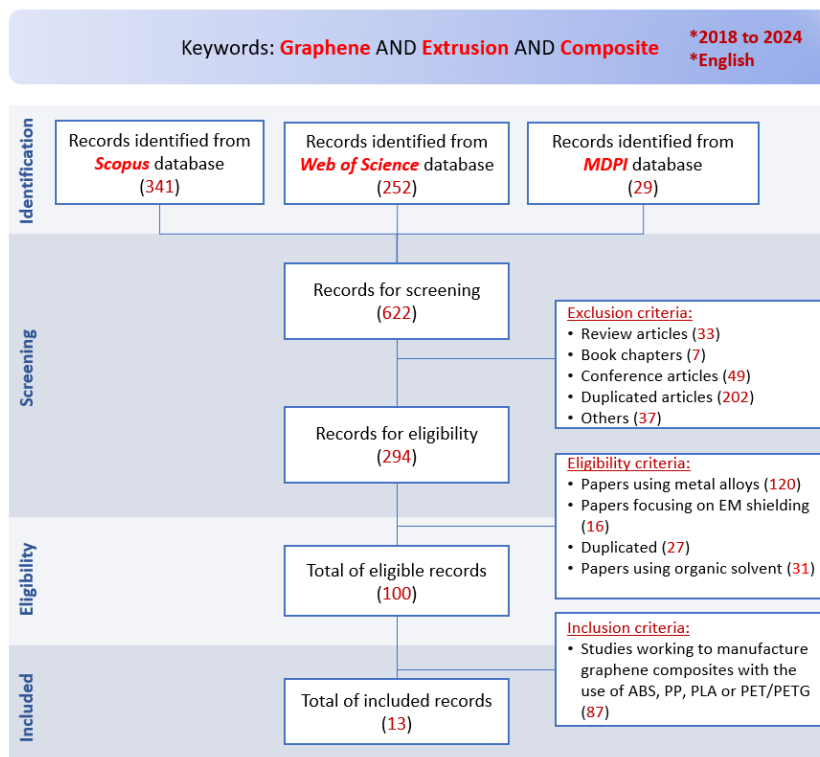
Figure 1. Systematic review flowchart, following PRISMA protocol.

3. RESULTS AND DISCUSSION

From reading the 13 selected articles, it was possible to obtain the type and the wt.% of graphene used to produce the composites, which are available in Table 1.

Table 1. Graphene type and polymers used to produce the nanocomposites.

ARTICLE REFERENCE	GRAPHENE TYPE	BASE MATERIAL	wt.%
[6]	Not specified	PLA	1
[7]	Graphene	PP+HDPE	-
[8]	Multi-layer Graphene	PLA	1.5-9
[9]	Multi-layer Graphene	PLA	3-12
[10]	Graphene oxide	PET	0.1-1
[11]	Graphene	PLA	1-5
[12]	Multi-layer Graphene	PC-ABS	0.2-0.8
[13]	Graphene	PP	0.1-0.5
[14]	Graphene	ABS	1-2
[15]	Graphene, Multi-layer Graphene	PP	6-12
[16]	Not specified	ABS	0.5-10
[17]	Graphene oxide	PP	1-7
[18]	Graphene oxide	Recycled PP and PE	1-10

It was possible to observe that 57% of research focused on the use of graphene with up to 10 nm of thickness, while 36% used multilayer graphene. Furthermore, it was not possible to determine whether graphene was used in its oxide form or in reduced form in two papers, as it was not described. Figure 2 shows the types of polymeric matrices used, being PLA (31%) the most used polymer, followed by PP (23%) and polycarbonate (PC) ABS (15%).
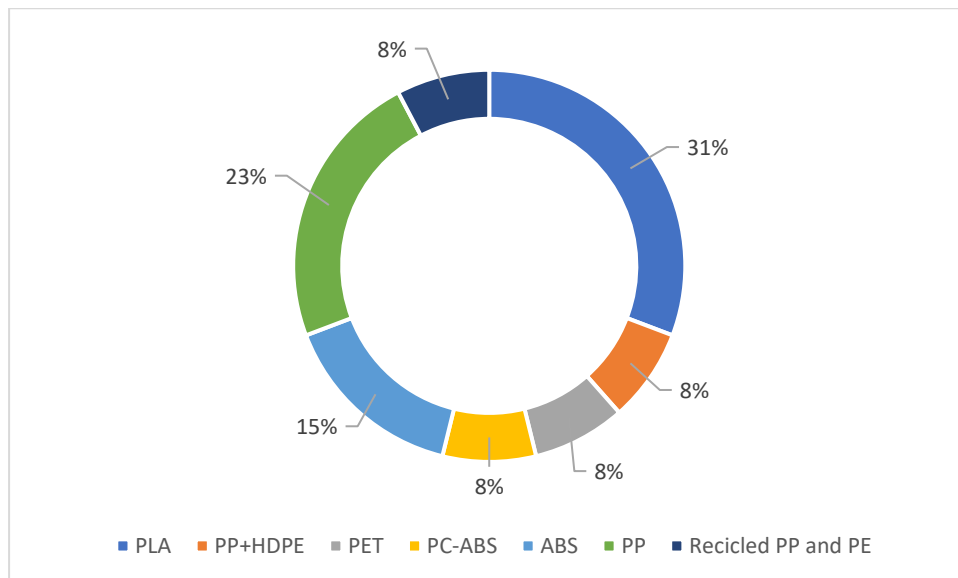
Figure 2. Types and percentage of polymeric matrices used in the nanocomposites, accordingly with the selected articles.

3.1. Processing methods

The Figure 3 represents the extrusion process utilized. Tyagi *et al.* (2024) [14] mixed the graphene nanoparticles mechanically and used a melt indexer machine, while Liang *et al.* (2018) [13] used a compounding machine to ensure good dispersion before extrusion. Yu *et al.* (2020) [10], Rajpurohit *et al.* (2019) [11], Tambrallimath *et al.* (2021) [12] and Liang *et al.* (2018) [13] reported that humidity is an important factor to be controlled during the process, and due to that, the powders and polymer pellets were dried between 4 and 24 hours at temperatures of 80 °C to 120 °C, with Yu. *et al.* (2020) [10] using the vacuum-drying process.
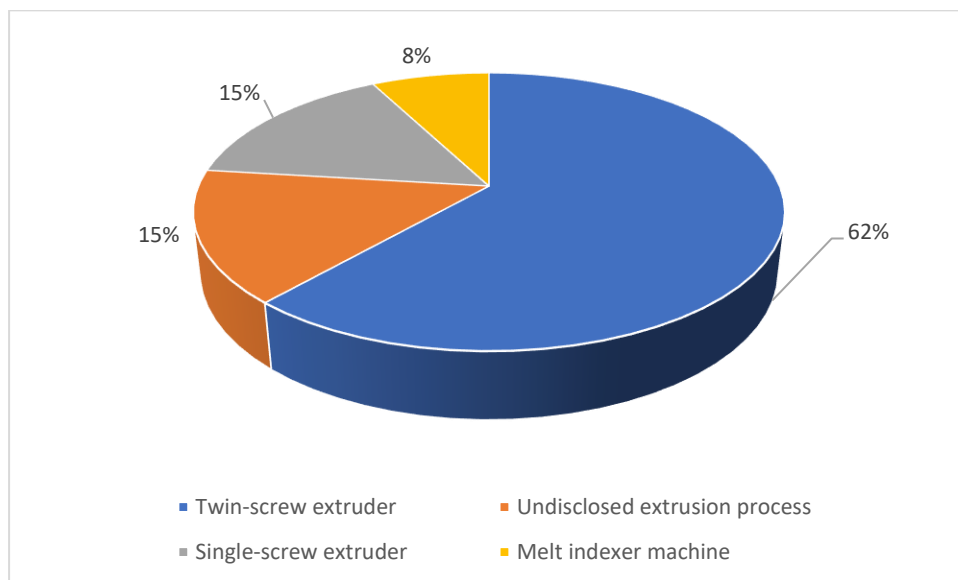
Figure 3. Extrusion methods utilized, accordingly with the selected articles.

Yu *et al.* (2020) [10] described the process of breaking large lateral size of graphene oxide (LGO) to obtain medium (MGO) and small (SGO) lateral size graphene oxide, using different times of the ultrasonication process, with subsequent centrifugation to separate the supernatant and pulverizing through a grinder for creating the powder. The importance of studying graphene lateral size and its impact on the mechanical properties of the composites will be discussed in Section 3.2.

Graphene nanoparticles have high surface energy and tend to agglomerate when processed at high temperatures, which can compromise the final mechanical strength of the composite. The zeta potential can indicate the dispersion's tendency to agglomerate over time and has a reference absolute value of 20 mV for

stability. Ivanova *et al.* (2020) [8] studied the zeta potential in graphene composites and reported an average of -26 mV for pure PLA and -17.5 mV when adding 6 wt.% of graphene nanoparticles, indicating a significant drop in long-term stability with a tendency to agglomerate. This phenomenon is known to cause clogging during the printing process due to the small diameter (usually 0.4 mm) and high temperature of the nozzle. The presence of agglomerates and poor dispersion can also result in an irregular flow of the material being printed, causing defects and a lower final strength of the composite.

3.2. Influence of graphene lateral size in the composite mechanical properties

Yu *et al.* (2020) [10] defined 3 types of graphene oxide (GO) based on its lateral size, GO in its original size and without any type of process, which can be considered large graphene oxide (LGO) with average lateral size of 12 µm. When broken down through ultrasonic baths and separated through centrifugation, it is reduced in size to medium graphene oxide (MGO) and small graphene oxide (SGO), which have an average lateral size of 5 µm and 0.7 µm, respectively. Each lateral size is suitable for different and specific applications. LGO promotes greater thermal conductivity due to the creation of thermal paths, but due to its lower dispersion and higher agglomeration, it usually generates a composite with lower mechanical resistance [5]. While MGO and SGO present better dispersion even without the use of organic solvents and can act as nucleating agents improving crystallization and due to their higher thermal conductivity also acts in preventing crystal growth, which may lead to better mechanical properties [10].

To better understanding the dimensional characteristics of the graphene used, the thickness and diameter were collected using the same dimensional criteria for the classification as Yu *et al.* (2020) [10] between LG (Large) and MG (Medium) Graphene (Table 2).

Table 2. Dimensions of graphene utilized by the literature.

ARTICLE REFERENCE	GRAPHENE THICKNESS (nm)	GRAPHENE DIAMETER (µm)	LATERAL SIZE
[6]	-	90	LG
[7]	-	-	-
[8]	4-20	5-10	MG
[9]	<30	5-7	MG
[10]	<5 atomic layers	10-15	LG
[11]	2-4	5-10	LG
[12]	-	-	-
[13]	1-6 atomic layers	<10	LG
[14]	2-10	-	LG
[15]	100, 30, <5	100, 40, 8	LG
[16]	5	<5	MG
[17]	8-15	>2	MG
[18]	6-10 atomic layers	Primary particles: 1-2, Secondary particles: 30 µm.	MG

Although few articles have described lateral size as a factor to be considered, it is possible to verify that 62% of articles used graphene in LG form, while 23% used MG. Yu. *et al.* (2020) [10] reported that a composite formulation with 0.1 wt.% of SGO had an increase in the tensile strength in 32%, while formulations using MGO and LGO in the same concentration obtained only 11% of increase in the tensile strength. Other papers also reported improvements in the final strength of the composite [6, 13, 16, 18], but only Vidakis *et al.* (2019) [16] and Sultana *et al.* (2023) [18] described the type of graphene used (MG).

Rajpurohit *et al.* (2019) [11] obtained composites with lower mechanical resistance than the pure polymer using graphene in LG form, which showed poor dispersion and large graphene aggregates. On the other hand, Sultana *et al.* (2023) [18] found that the addition of graphene in concentrations lower than 10 wt.% produced composites with lower impact resistance than the neat polymer, although at 10 wt.% of graphene the impact resistance of the composite was superior to the reference polymer. These results are consistent with a study carried out by Jun *et al.* (2018) [5], when using graphene with an ultra-large lateral size of 150 µm, resulted in a reduction in tensile and flexural strength of the composite, with a significant increase in its thermal conductivity. Furthermore, Batakliev *et al.* (2021) [9] and Liang *et al.* (2018) [13] reported ultimate tensile strength of the graphene composites equivalent to reference polymers.

3.3. 3D printing limitations

Some attention should be given during the production of parts from graphene composites using 3D printing. Jun *et al.* (2018) [5] reported an increase in the thermal conductivity of the material, which can lead to defects and clogging during the printing process, possibly due to the plasticization of the material inside the nozzle assembly as it reaches glass transition temperature. Sarturato *et al.* (2023) [17] observed that in composites with PP and talc, the addition of graphene considerably reduced the fluidity index, while Sultana *et al.* (2023) [18] reported no significant change in the fluidity of PP and recycled polyethylene loaded with graphene nanoparticles. Rajpurohit *et al.* (2019) [11] reported a low interaction between the printed layers and low dispersion of graphene, which can be attributed to the use of a single-screw extruder to manufacture the filaments or to the use of LG, as seen in the study of Yu *et al.* (2020) [10]. The decrease in fluidity index can sometimes be overcome by adjusting the printing temperature, but the fine-tuning is a time-consuming process that is required for each composition.

For 3D printing process, the use of composites with SG/SGO is optimal, however the use of MG/MGO also showed improved properties. On the other hand, the use of the LG/LGO form is not ideal as it can cause irregular flow due to agglomerates, which can compromise interlayer and plate adhesion. The study and observation of flow is an important property since the resistance between printed layers is significantly lower than the resistance of the composite material due to the anisotropy generated and the presence of structural voids in printed objects.

4. CONCLUSIONS

The production of polymeric composites with graphene by solvent-free methods is still scarce in literature, and some papers reported decrease in mechanical properties, poor dispersion of the nanoparticles and agglomeration tendency. Conversely, it was reported that graphene with reduced lateral size presents better dispersion in the polymeric matrix compared to large sizes, less tendency to agglomerate during processing and can generate a product with better mechanical properties. In addition, some papers reported no significant decrease in fluidity, while other reported a significant decrease, a characteristic that must be studied and compensated appropriately during the printing process to avoid impairing the final mechanical properties of the printed parts. In summary, this short review presented some studies with the main solvent-free processes reported in literature to obtain polymeric composites loaded with graphene for manufacture parts by 3D printing, as well as parameters and variables that can affect the final properties of the obtained printed composites. Further studies are still needed to understand how the change in the thermal conductivity affects the printability of the composite and the printing parameters and, consequently, the final composite properties.

4.1. Declaration of Competing Interest

The authors declare no conflict of interest.

4.2. Acknowledgements

5. REFERENCES

[1] W. Prasong, A. Ishigami, S. Thumsorn *et al.* Improvement of Interlayer Adhesion and Heat Resistance of Biodegradable Ternary Blend Composite 3D Printing. *Polymers.* Vol. 13. 2021. (doi.org/10.3390/polym13050740).

[2] B. Rankouhi, S. Javadpour, F. Delfanian *et al.* Failure Analysis and Mechanical Characterization of 3D Printed ABS With Respect to Layer Thickness and Orientation. *Journal of Failure Analysis and Prevention.* Vol. 16. 2016. (doi.org/10.1007/s11668-016-0113-2).

[3] Z. Zhen, H. Zhu. Structure and Properties of Graphene. In: *Graphene: Fabrication, Characterizations, Properties and Applications.* (H. Zhu, Z. Xu, D. Xie, Y. Fang), 1st Edition, 2018. Elsevier. (doi.org/10.1016/B978-0-12-812651-6.00001-X).

[4] A. C. C Esteves, A. Barros-Timmons, T. Trindade. Nanocompósitos de matriz polimérica: Estratégias de síntese de materiais híbridos. *Quimica Nova*, Vol. 27. 2004. (doi.org/10.1590/S0100-40422004000500020).

[5]   Y-S. Jun, J. G. Um, G. Jiang *et al.* Ultra-large sized graphene nano-platelets (GnPs) incorporated polypropylene (PP)/GnPs composites engineered by melt compounding and its thermal, mechanical, and electrical properties. *Composites Part B.* Vol. 133. 2018. (doi.org/10.1016/j.compositesb.2017.09.028)

[6]   E.P.M. Basheer, K. Marimuthu. Carbon fibre-graphene composite polylactic acid (PLA) material for COVID shield frame. Materials Science and Engineering Technology, Vol. 53, 2022. (doi.org/10.1002/mawe.202100154).

[7]   W. Wu, X. Li. Composite Polypropylene Fibers Modified with High Density Polyethylene and Graphene. Journal of Macromolecular Science, Part B. 2021. (doi.org/10.1080/00222348.2020.1849160)

[8]   R. Ivanova, R. Kotsilkova, E. Ivanov *et al.* Composition dependence in surface properties of poly(lactic acid)/ graphene/carbon nanotube composites. *Materials Chemistry and Physic.* Vol. 249. 2020. (doi.org/10.1016/j.matchemphys.2020.122702)

[9]   T. Batakliev. Evaluation of the macromechanical properties of pla-based nanocomposites by means of three-point bending method. Journal of Theoretical and Applied Mechanics. Vol. 51. 2021. (. http://jtambg.eu/issues.php?year=2021&vol=51&issue=1)

[10] W. Yu, X. Zhang, H. Liu, X. Zhang. Fabrication of high-strength PET fibers modified with graphene oxide of varying lateral size. *Composites & nanocomposites.* Vol. 55. 2020. (doi.org/10.1007/s10853-020-04652-0)

[11] S. R. Rajpurohit, H. K. Dave. Fused deposition modeling using graphene/PLA nanocomposite filament. I*nternational Journal of Modern Manufacturing Technologies.* Vol. 11. 2019. (https://ijmmt.ro/international-journal-ijmmt/vol11no22019)

[12] V. Tambrallimath, R. Keshavamurthy, S. Bavan *et al.* Mechanical Properties of PC-ABS-Based Graphene-Reinforced Polymer Nanocomposites Fabricated by FDM Process. Polymers. Vol. 13. 2021. (doi.org/10.3390/polym13172951)

[13] J. Z. Liang, Q. Du. Melt Flow and Flexural Properties of Polypropylene Composites Reinforced with Graphene Nano-Platelets. *International Polymer Processing.* Vol. 33. 2018. (doi.org/10.3139/217.3335)

[14] R. Tyagi, A. Tripathi, R. Kumar. On FFF-based 3D printing of wear resistive ABS-Graphene nanocomposites for rapid tooling in wet condition. *Diamond & Related Materials.* Vol. 142. 2024. (doi.org/10.1016/j.diamond.2024.110794)

[15] Z. Xu, S. He, J. Zhang *et al.* Relationship between the structure and thermal properties of polypropylene/graphene nanoplatelets composites for different plateletsizes. *Composites Science and Technology.* Vol. 183. 2019. (doi.org/10.1016/j.compscitech.2019.107826)

[16] N. Vidakis, A. Maniadi, M. Petousis *et al.* Mechanical and Electrical Properties Investigation of 3D-Printed Acrylonitrile–Butadiene–Styrene Graphene and Carbon Nanocomposites. *Journal of Materials Engineering and Performance.* Vol. 29. 2019. (doi.org/10.1007/s11665-020-04689-x)

[17] A. C. P. Sarturato, E. G. R. Dos anjos, J. Marini. Polypropylene/talc/graphene nanoplates (GNP) hybrid composites: Effect of GNP content on the thermal, rheological, mechanical, and electrical properties. Journal of Applied Polymer Science. Vol. 140. 2023. (doi.org/10.1002/app.53657)

[18] S. M. N. Sultana, E. Helal, G. Gutiérrez. Effect of Few-Layer Graphene on the Properties of Mixed Polyolefin Waste Stream. *Advanced Technologies in Graphene-Based Materials.* Vol. 13. 2023. (doi.org/10.3390/cryst13020358)
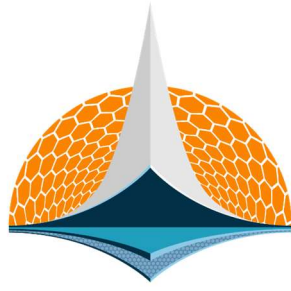
18 Natural fiber composites

Organized and edited by

Sandra Maria da Luz
&
Carla Tatiana Mota Anflor

EVALUATION OF THE MECHANICAL PROPERTIES OF 3D PRINTED COMPOSITES REINFORCED WITH CONTINUOUS JUTE FIBERS AT TWO TEMPERATURE TESTS

Natalia V. dos Santos[a], K. Sales de Oliveira [b], Vitor F. de Botton[c], Daniel C. T. Cardoso[d], T. Doca [e] *

(a) 🔘 0000-0001-5212-9306 (Pontifical Catholic University of Rio de Janeiro – Brazil)
(b) 🔘 0000-0002-0509-9842 (University of Brasília – Brazil)
(c) 🔘 0009-0004-5526-5599 (Pontifical Catholic University of Rio de Janeiro – Brazil)
(d) 🔘 0000-0002-8171-7956 (Pontifical Catholic University of Rio de Janeiro – Brazil)
(e) 🔘 0000-0001-5376-5590 (University of Brasília – Brazil)
* Corresponding author: doca@unb.br

Abstract: The use of natural fibers presents significant potential for the fabrication of high-performance composites in an environmentally sustainable manner, contributing to a reduced ecological footprint. Integrating natural fibers into 3D printing processes offers a unique opportunity to combine their eco-friendly characteristics with the creation of optimized structures. Considering the enhanced mechanical properties of printed composites with continuous fibers, a comprehensive investigation into the effects on composites manufactured using vegetable yarns is imperative. As temperature is a critical factor influencing the properties of thermoplastics, an in-depth analysis is crucial to discern the most favourable printing temperature for achieving optimal mechanical performance when the continuous fiber is added. This study seeks to elucidate the intricate relation between continuous vegetable fibers and their application as reinforcement in the Fused Filament Fabrication (FFF), focusing on the resulting tensile properties of different layer configurations and at different temperatures. Therefore, this research includes an assessment of the influence of two testing temperatures (24 °C and 30 °C) in the tensile behaviour of four different types of specimens: Neat PLA with parallel layers (0°/0°), alternating crossed layers (0°/90°) and Jute Fiber Reinforcement Polymer (JFRP) with 0°/0° layers and 0°/90° layers.

1. INTRODUCTION

The utilization of natural fibers holds immense promise for the development of high-performance composites in an environmentally responsible manner, thereby mitigating ecological impact due to degradability, origin from renewable sources and low carbon footprint. Additionally, natural fibers present an important social factor. In the case of the jute fiber used in this study, its production constituted the main source of income for hundreds of rural communities in Amazonas between 1960 and 1980, and today it is an alternative economic production for these populations [1].

Incorporating natural fibers into 3D printing processes presents a distinctive opportunity to amalgamate their eco-conscious attributes with the creation of structurally optimized designs. Given the superior mechanical characteristics observed in printed composites reinforced with continuous vegetable fibers [2–5] compared to discontinuous vegetable fibers and natural fillers [6–8], a thorough investigation into the effects on composites crafted using vegetable yarns is imperative. As temperature plays a pivotal role in influencing the properties of thermoplastics, a meticulous analysis is essential to identify the effects of temperature for mechanical performance with the addition of continuous fiber.

This study endeavours to unravel the intricate relationship between continuous vegetable fibers and their application as reinforcement in Fused Filament Fabrication (FFF), with a specific focus on the resulting tensile properties across different layer configurations and test temperatures. Accordingly, the research encompasses an evaluation of the impact of two testing temperatures (24 °C and 30 °C) on the tensile behaviour of four distinct types of specimens: Neat PLA with parallel layers (0°/0°), Neat PLA with alternating crossed layers (0°/90°), Jute Fiber Reinforcement Polymer (JFRP) in 0°/0° layers, and JFRP in 0°/90° layers. The findings contribute to a deeper understanding of sustainable printed composites, laying the groundwork for optimizing the design and production of eco-friendly composites endowed with enhanced mechanical properties. Thus, this research advances the cause of sustainable engineering practices.

2. METHODOLOGY

2.1. Materials

The materials used in this work consisted in jute yarns provided by SISALSUL (São Paulo, Brazil) as the reinforcement, and the polylactic acid filament (PLA) with a diameter of 1.75 mm provided by 3DLAB (Minas Gerais, Brazil) used for the matrix.

2.2. Printing process

PLA-jute composites were manufactured by Fused Filament Fabrication (FFF) using an Ender 3 V2 printer adapted for the simultaneous printing of polymer and continuous vegetable fiber yarns through in-nozzle impregnation method [9]. Figure 1 shows the printing process and the layer disposition of the samples. The specimens were prepared under the conditions described in Table 1, stored at room temperature and subjected to 24 and 30 °C during the tensile test as described in section 2.3.

| (a) | (b) |
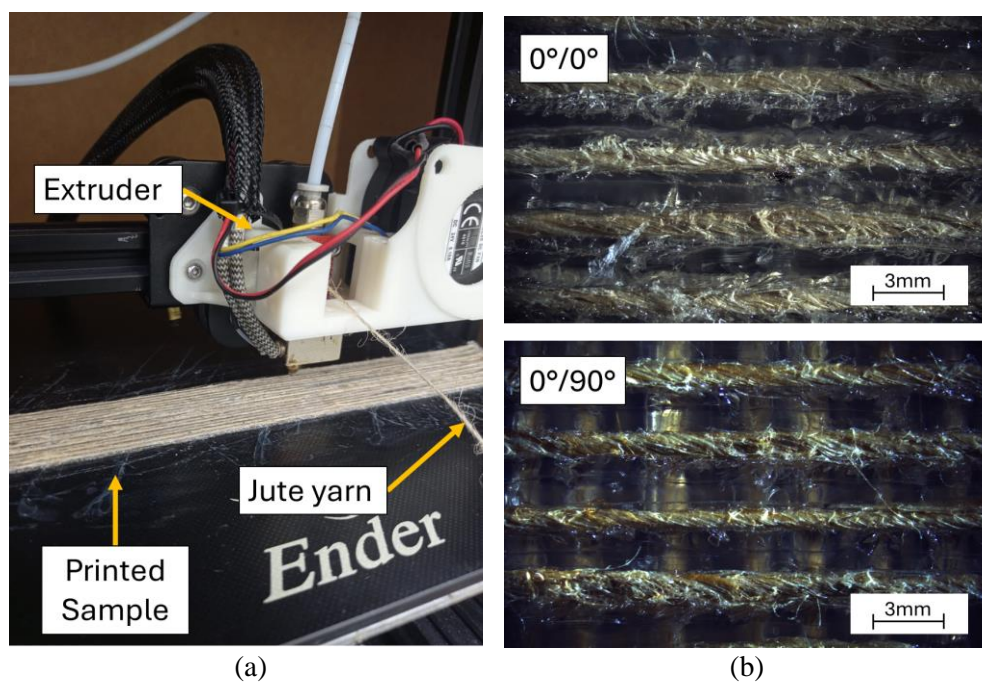
Figure 1. 3D continuous natural yarn printing: (a) printing process and (b) printed samples.

Table 1. Printing parameters.

Parameter	Value
Nozzle diameter	2.1 mm
Printing speed	3.75 mm/s
Extruder temperature	200 °C
Bed temperature	60 °C
Layer height	1.5 mm
Layer width	3.0 mm

2.3. Methods

The tensile tests were performed using a servo-hydraulic system (MTS 810 Landmark, load-cell capacity of 5 kN) available in the Mechanical Engineering Department (UnB, Brasilia, Brazil) (Figure 2). The testing protocol followed the recommendations of ASTM D3039 [10]. The specimens are mounted in a flat clamp system embossed with diamond-shaped grooves for optimal restraining. The contact pressure is set to 1 MPa and the distance between clamps is controlled at 120 mm in all tests. Two test temperatures were evaluated: 24 ± 2 °C and 30 ± 2 °C, the different temperatures being set by the air conditioning system and monitored using a digital thermometer (Instrutherm HT-600, depicted in Fig. 2 a). One test sequence was performed for each temperature. The tests were carried out with a displacement control of 1 mm/min using a clip gauge extensometer until failure. The specimens have a geometry of 200×18×3 mm. Table 2 shows the composition and geometry of the composite.
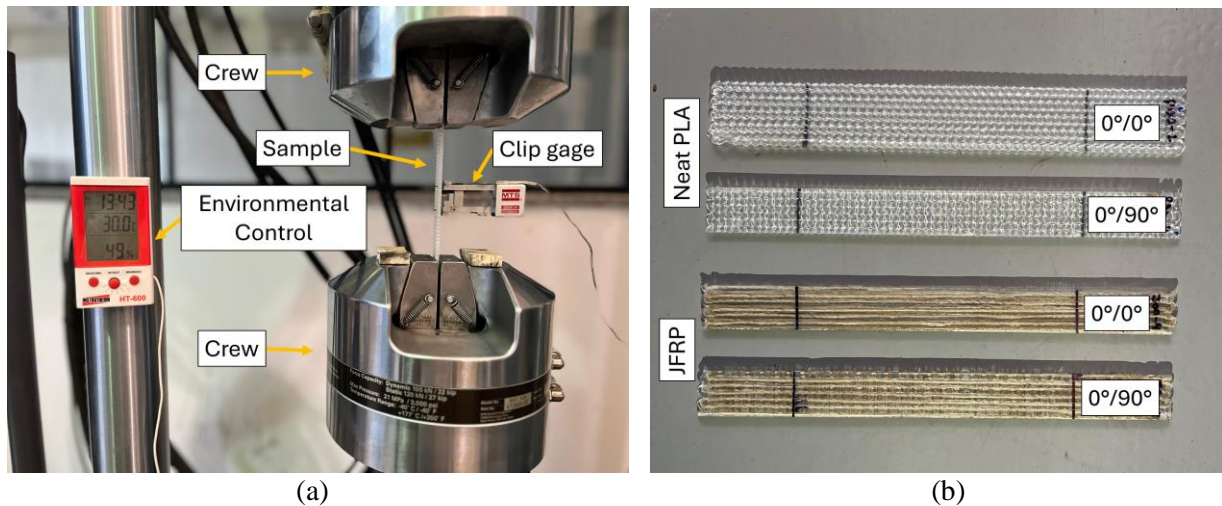
Figure 2. Tensile test: (a) test setup and (b) printed samples.

Table 2. Composite's disposition and geometry.

Type	Description	Disposition
PLA00	Neat PLA with 2 layers printed in longitudinal direction (0°)	0° - 0°
PLA90	Neat PLA with 2 layers printed in longitudinal direction (0°) and transversal direction (90°)	0° - 90°
J00	JFRP with 2 layers printed in longitudinal direction (0°)	0° - 0°
J90	JFRP with 2 layers printed in longitudinal direction (0°) and transversal direction (90°)	0° - 90°

3. RESULTS AND DISCUSSION

Figure 3 shows the representative stress-strain curves for each configuration. This evaluation tested one specimen per condition. More additional tests for each condition are in progress. These have been included in the paper to clarify this issue. For PLA, there were no significant changes in ultimate tensile strength for both 0°/0° and 0/90° orientations. However, there was a notable contrast in the case of samples reinforced unidirectionally with jute yarns. In these cases, the increase in test temperature resulted in a reduction from 53.9 MPa to 32.2 MPa.

This phenomenon can be elucidated by the attenuation of interfacial bonds between the yarn and the matrix, culminating in resistance loss. These interfaces, as noted by Tao et al. [11], are characterized by the brief contact time between the fiber and matrix during the printing process via In-nozzle impregnation, rendering impregnation of the yarn challenging and resulting in a fragile interface between the materials. Consequently, at elevated temperatures, the polymer deforms with reduced load transfer to the yarns, induced by distinct thermal expansion of fibres and matrix, leading to a reduction in the composite's ultimate load capacity.

(a)

(b)

(c)

(d)

(e)

(f)
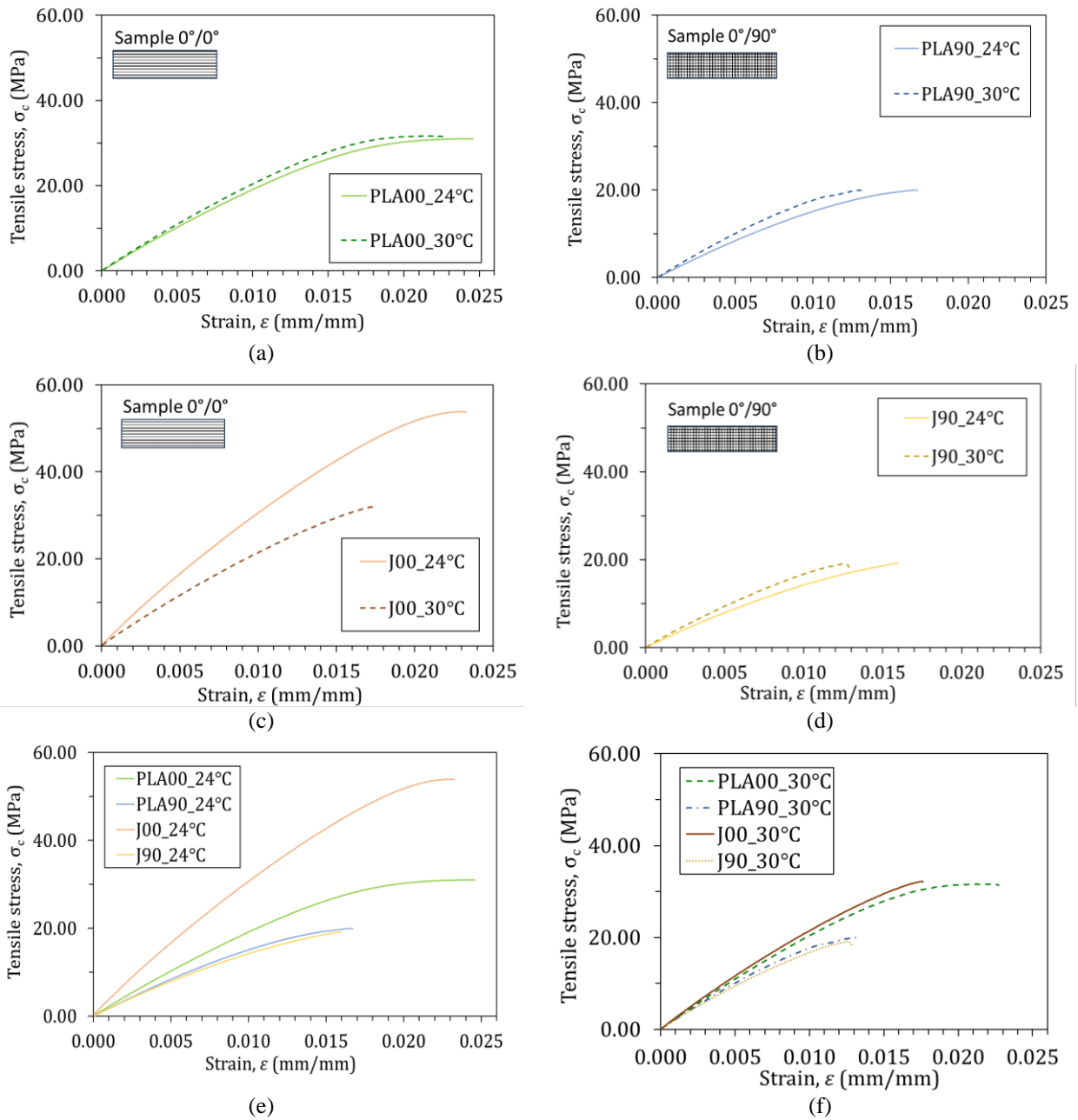
Figure 3. Representative stress x strain curves.

Figure 4 illustrates the representative failure modes observed in the tested tensile specimens. All specimens experienced brittle fracture within the matrix, initiated by crack propagation across the transverse section. As observed by Santos et al. [3], despite the failure of the matrix, the continuous vegetable fibers remain intact, connecting the parts of the sample like charging transmission bridges.

(a)   (b)
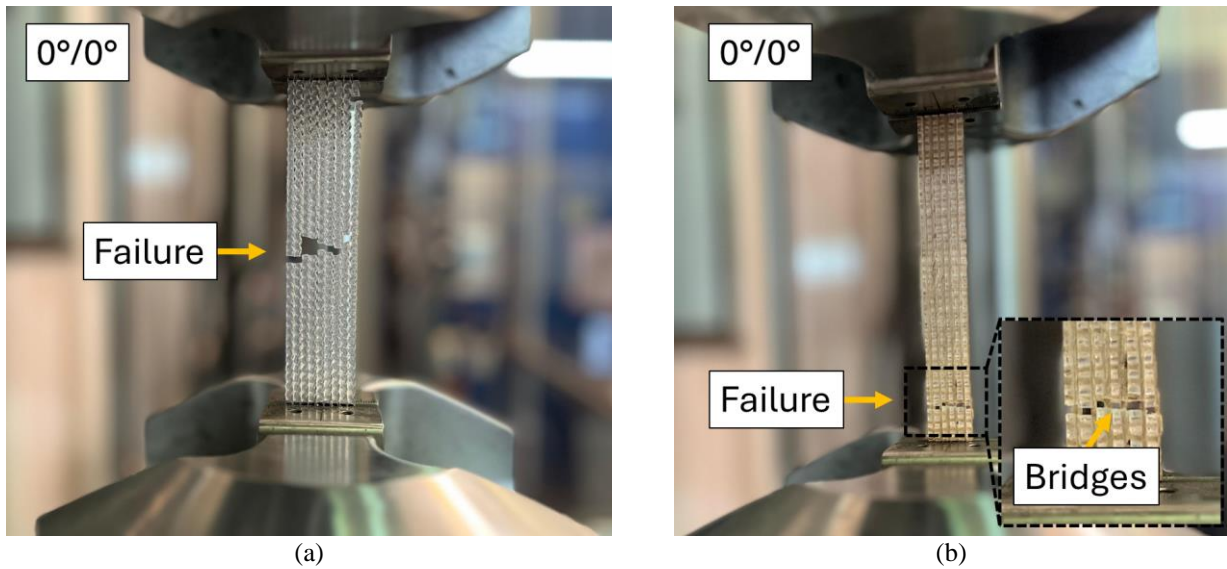
Figure 3. Representative failure mode: (a) PLA00 and (b) J00.

Table 3. Measured properties of PLA-jute composites.

	Measured properties			
	Young Modulus, E [GPa]	Yield stress, σy [MPa]	Ultimate tensile stress, σu [MPa]	Elongation at break, δu [%]
PLA00_24 °C	3.8	43.3	30.9	2.4
PLA00_30 °C	3.4	39.4	31.6	2.3
PLA90_24 °C	1.6	17.9	19.9	1.6
PLA90_30 °C	1.9	17.9	19.9	1.3
J00_24 °C	2.8	33.1	53.9	2.3
J00_30 °C	2.5	29.8	32.2	1.7
J90_24 °C	1.7	18.6	19.1	1.6
J90_30 °C	1.9	19.3	19.1	1.5

The incorporation of jute as a reinforcement in PLA, as seen in Table 3 showed a significant contribution to the improvement of the mechanical properties, providing several benefits compared to conventional PLA properties, such as a percentage increase in tensile strength of 74.5%. As mentioned above, the presence of jute results in a significant increase in the tensile strength and stiffness of the material, which translates into improved load capacity and a more resilient response to different temperature conditions.

4. CONCLUSIONS

The present study evaluated the effects of test temperature on printed composites reinforced with continuous jute vegetable fibers. This way, it is possible to evaluate how ambient temperature influences the reinforcement potential of vegetable yarns. Among the main conclusions it is possible to highlight:

• Composites reinforced unidirectionally with jute yarn exhibited notable changes in resistance as temperature increased, highlighting the impact of temperature on the interfacial resistance of the materials.

• Neat PLA in both configurations displayed insignificant variations in results under varying temperatures, suggesting that the matrix remains intact when exposed to temperatures below its softening point.

As suggestions for future work, the authors emphasize the necessity for a more comprehensive investigation into the effects of temperature on the mechanical properties of JFRP, as well as an in-depth study of methods to enhance yarn impregnation.

4.1. Declaration of Competing Interest

The authors declare no conflict of interest.

4.2. Fundings

4.3. Acknowledgements

5. REFERENCES

[1] Jesus T De, Fraxe P. Nova técnica para extração de fibras de juta e malva em processo a seco no Estado do Amazonas: o resgate da utopia. Inclusão Social 2018;12:161–71.

[2] Cheng P, Wang K, Chen X, Wang J, Peng Y, Ahzi S, et al. Interfacial and mechanical properties of continuous ramie fiber reinforced biocomposites fabricated by in-situ impregnated 3D printing. Ind Crops Prod 2021;170:113760. https://doi.org/10.1016/j.indcrop.2021.113760.

[3] Santos N V., Cardoso DCT. 3D printing of vegetable yarn-reinforced polymer components. J Clean Prod 2023;415. https://doi.org/10.1016/j.jclepro.2023.137870.

[4] Ginoux G, Wu X, Laqraa C, Soulat D, Paux J, Ferreira M, et al. Continuous additive manufacturing of hemp yarn-reinforced biocomposites with improved impregnation method. Compos Sci Technol 2024;251:110561. https://doi.org/10.1016/j.compscitech.2024.110561.

[5] Le Duigou A, Barbé A, Guillou E, Castro M. 3D printing of continuous flax fibre reinforced biocomposites for structural applications. Mater Des 2019;180:107884. https://doi.org/10.1016/j.matdes.2019.107884.

[6] Figueroa-Velarde V, Diaz-Vidal T, Cisneros-López EO, Robledo-Ortiz JR, López-Naranjo EJ, Ortega-Gudiño P, et al. Mechanical and physicochemical properties of 3d-printed agave fibers/poly(Lactic) acid biocomposites. Materials 2021;14. https://doi.org/10.3390/ma14113111.

[7] Shahar FS, Hameed Sultan MT, Safri SNA, Jawaid M, Abu Talib AR, Basri AA, et al. Physical, thermal and tensile behaviour of 3D printed kenaf/PLA to suggest its usability for ankle–foot orthosis – a preliminary study. Rapid Prototyp J 2022;28:1573–88. https://doi.org/10.1108/RPJ-08-2021-0207.

[8] Haryati A, Razali N, Petrů M, Taha M, Muhammad N, Ilyas RA. Effect of chemically treated kenaf fibre on mechanical and thermal properties of PLA composites prepared through fused deposition modeling (FDM). Polymers (Basel) 2021;13. https://doi.org/10.3390/polym13193299.

[9] Santos N V., Cardoso DCT. 3D printing of vegetable yarn-reinforced polymer components. J Clean Prod 2023;415. https://doi.org/10.1016/j.jclepro.2023.137870.

[10] ASTM. ASTM D3039 / D3039M - Standard Test Method for Tensile Properties of Polymer Matrix Composite Materials. Annual Book of ASTM Standards n.d.;15.03. https://doi.org/10.1520/D3039_D3039M-17.

[11] Tao Y, Li P, Zhang J, Wang S, Shi SQ, Kong F. A review of fused filament fabrication of continuous natural fiber reinforced thermoplastic composites: Techniques and materials. Polym Compos 2023;44:8200–22. https://doi.org/10.1002/pc.27477.

SPECIFIC MECHANICAL PROPERTIES OF COMPOSITES REINFORCED WITH JUTE FIBRES

Paulo V. Assis[(a), *], Márcio E. Silveira[(b)], Túlio H. Panzera[(c)], Antônio C. Ancelotti Junior[(d)]

(a) 0000-0002-1983-9979 (Federal University of Itajubá – Brazil)
(b) 0000-0001-9805-5277 (Federal University of São João del-Rei – Brazil)
(c) 0000-0001-7091-456X (Federal University of São João del-Rei – Brazil)
(d) 0000-0003-2031-419X (Federal University of Itajubá – Brazil)
* Corresponding author: paulovictordeassis.eng@gmail.com

Abstract: Composite materials can have excellent mechanical properties, as the combination of materials and fibre orientation can produce optimized and specific structures for each application. When considering factors such as low cost, low density and the search for biodegradable materials, natural fibres and resins obtained from renewable sources have gained relevance in the production of composite structures. Thus, the present work aims to investigate, through a complete 2^2 factorial design, the effect of the matrix phase, epoxy resin or castor oil, and the reinforcement stage arrangement, unidirectional jute yarns or bidirectional fabrics, on the specific mechanical performance of polymer composites reinforced with jute fibres in a volumetric fraction of 30% of fibres. The composite materials were characterized by tensile and 3-point bending tests. The experimental study indicated that the use of castor oil as a matrix phase did not affect the specific tensile strength and specific tensile modulus of the composite materials. The analysis of variance indicated no significance for the specific tensile properties for the main factor matrix phase. However, the matrix phase of castor oil provided a decrease in the properties of specific flexural strength and specific flexural modulus of the composites despite the lower density for the composites manufactured in castor oil. The alteration of phase reinforcement in materials from bidirectional fabric to unidirectional jute yarns caused an expressive increase in all specific mechanical properties of the composites. The manufactured composite materials proved to be a sustainable and economical alternative for engineering applications, mainly those manufactured with unidirectional jute yarns, which exhibited satisfactory mechanical properties.

1. INTRODUCTION

The development and progress in composite materials engineering have provided a growing increase in applications in structural projects, being present in the most diverse industrial sectors, such as aerospace, aeronautical, naval, automotive, civil construction and sporting goods [1]. By replacing metallic materials in some of their applications, composites provide weight reduction in structures, in addition to moderate values of strength and rigidity combined with good fatigue resistance and resistance to corrosion [2].

Laminated composites reinforced with synthetic fibres, such as glass, carbon and kevlar, stand out for their application in structural components, due to their high mechanical properties. On the other hand, natural fibres, such as jute, sisal and linen, attract great interest because they derive from renewable sources, are biodegradable and involve lower energy consumption for manufacturing. Furthermore, composites reinforced with natural fibres, despite having lower properties mechanical, tend to provide cost and density reduction in relation to composites reinforced by synthetic fibres [3].

Synthetic resins, such as epoxy, are the most used in the manufacture of composite materials. However, these resins may pose a risk to the health of workers, as well as causing the emission of pollutants during the

life of the material composite. Given these peculiarities, the search for resins that are biodegradable, do not emit pollutants and come from renewable raw materials [4].

An example of a resin obtained from renewable sources is that produced from castor oil, coming from the plant called Ricinus communis. Your bush is popular in tropical regions and used to obtain the polymer polyurethane. The resin polyurethane obtained has a biodegradable character, which mitigates the problem of degradation extremely long term of plastics in nature. Castor oil polyurethane has attracted recognition for its compatibility with living tissues, which has led to its introduction into medicine for the manufacture of prostheses [5].

The use of natural fibres provides both the expansion and replacement of traditional materials in the manufacture of laminated composites. Consequently, this study seeks to evaluate the specific mechanical properties for a full factorial design for composites manufactured in epoxy resin and castor oil reinforced with jute yarns in unidirectional and fabric.

2. METHODOLOGY

2.1. Materials

The matrices used in the composites were epoxy resin and castor oil. The epoxy resin was obtained by mixing Renlam M and HY956 hardener in a 5:1 (wt/wt) ratio. Castor oil (AGT 1315) was supplied by Imperveg (Brazil). This biopolymer is a two-component adhesive, which consists of a pre-polymer (component A) and a polyol (component B) that were mixed in a ratio of 1:1.2 (wt/wt).

The jute fibre yarns used as reinforcement in the composites were obtained from a jute fibre fabric. This original fabric had a large spacing between the yarns, which required reprocessing of the yarns to create a bidirectional fabric with yarns more closed. Jute fibres were used *in natura* to manufacture the composites.

2.2. Design of experiments

A full factorial design (2^2) was applied to investigate the effect of matrix phase (epoxy resin/castor oil) and reinforcement phase (unidirectional fabric/bidirectional fabric) on the specific mechanical properties of jute fibres composites. The factorial design resulted in 4 experimental conditions, as shown in Table 1. The manufacturing parameters that were kept constant during the experiments were the number of fibre layers per composite plate (2 layers), the uniaxial pressure (654 kPa), the cold-pressing time (22 hours) and the curing time (14 days).

Table 1. Full factorial design.

Experimental condition	Factors	Levels
1	Epoxy resin	Unidirectional yarns
2	Epoxy resin	Bidirecional fabric
3	Castor oil	Unidirectional yarns
4	Castor oil	Bidirecional fabric

The goal of the experiments was to investigate the variables responses of specific tensile and flexural strength, and the specific tensile and flexural modulus. Five specimens were fabricated for each test (tensile and 3-point bending tests), which resulted in ten specimens for each experimental condition. As two replicates were carried out, a total of 80 specimens were manufactured and tested.

The Design of Experiments (DoE) and Analysis of Variance (ANOVA) techniques were performed using the statistical software Minitab 21. In the fabrication of samples and experimental tests were adopted randomization procedure to avoid effects arising from uncontrolled factors on the responses.

2.4. Manufacturing process

The composite materials were fabricated via hand lay-up technique. The metallic mould used to compact the samples had dimensions of 220 x 220 mm. An aluminum plate was placed in the mold and covered with a thin layer of wax as release agent to provide a good surface finish. Each matrix (epoxy resin and castor oil) was prepared by hand-mixing for 5 min at room temperature. The epoxy matrix was prepared by mixing

the resin Renlam M and the hardener HY956 with a 5:1 (wt/wt) proportion. The castor oil was prepared by mixing the pre-polymer and the polyol with a 1:1.2 (wt/wt) proportion. Two fabrics (unidirectional or bidirectional) were added inside the mould (Fig. 1a) and the matrix (epoxy resin or castor oil) was spread over the fibres. The pressure of 654 kPa was used to compact the composite plates (Fig. 1b). The materials were removed from the mould after 22 h under pressure (Fig. 1c). Compaction and curing of the composites were carried out in an environment with controlled conditions (temperature of 23ºC and relative humidity of 55%). Finally, the composite plates were cut using a laser cutting machine according to ASTM standards recommendations (Figs. 1d and 1e) and then tested.

(a) (b) (c)

(d) (e)
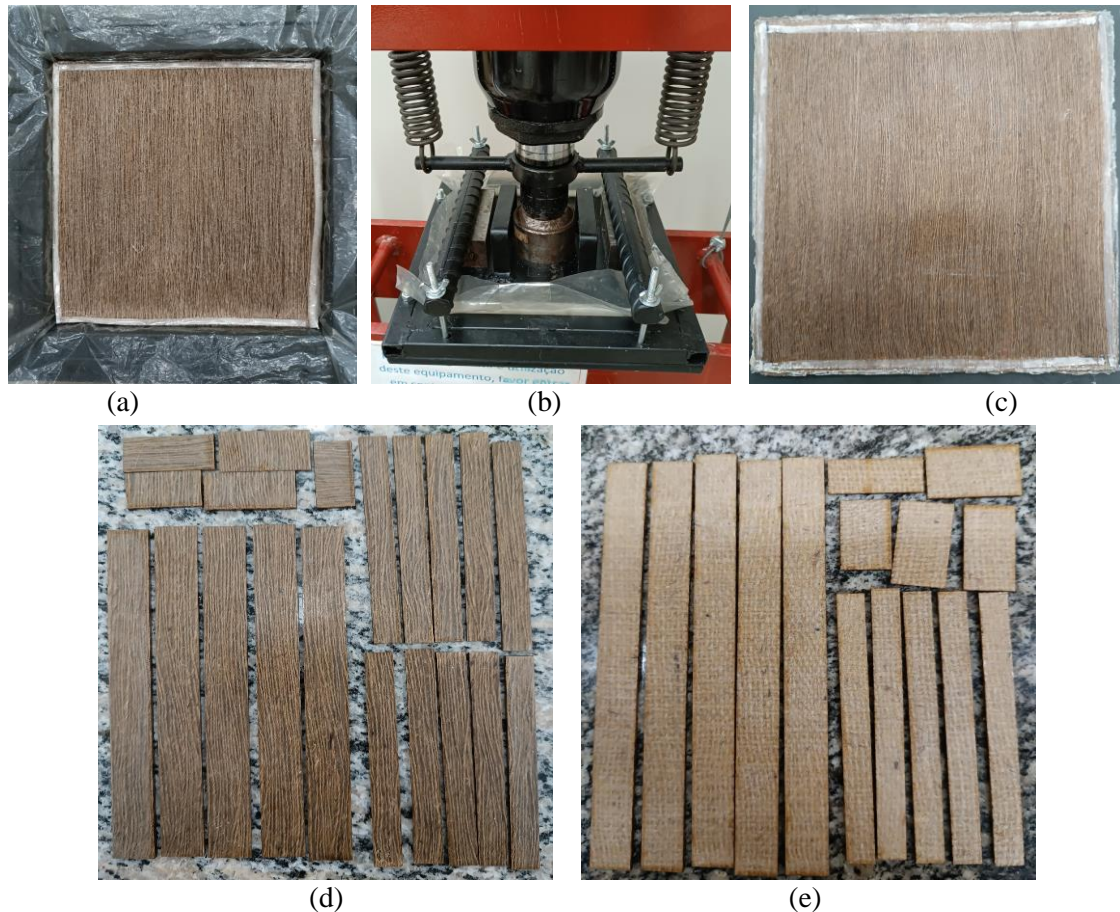
Figure 1. Lamination process (a). Compaction of the material (b). Composite plate after demolding (c). Composite specimens of epoxy resin and unidirectional fibres (d). Composite specimens of castor oil and bidirectional fabric (e).

2.6. Mechanical characterization

Tensile tests in the composite materials were carried out following the recommendations of ASTM D3039-14 [6] and 3-point bending tests were carried out according to ASTM D790-17 [7]. The tensile tests were performed in a Shimadzu AG-XPlus testing machine at a crosshead speed of 2 mm/min and equipped with a 100 kN load cell. The flexural tests were performed in a Instron EMIC 23-100 testing machine equipped with a 1 kN load cell and at a crosshead speed of 2 mm/min. Specific properties were calculated by dividing each mechanical property by its density. The density were obtained by the Archimedes principle.

3. RESULTS AND DISCUSSION

3.1. Statistical results

Table 2 diplays the ANOVA results for the composite materials. P-values less than 0.05 are underlined in the Table 2 and are considered significant in the analysis of variance realized.

Table 2. Analysis of variance (ANOVA).

Experimental Factors		Specific Tensile Strength (MPa)/(g/cm³)	Specific Tensile Modulus (GPa)/(g/cm³)	Specific Flexural Strength (MPa)/(g/cm³)	Specific Flexural Modulus (GPa)/(g/cm³)
Main Factors	Matrix Phase (MF)	0.739	0.252	**0.011**	**0.047**
	Reinforcement Phase (RF)	**0.000**	**0.000**	**0.002**	**0.000**
Interactions	MF x RF	0.368	0.074	0.831	0.188
R2-adj		96.34%	97.81%	91.35%	96.36%

3.4. Specific tensile strength

The main factor arrangement of the jute yarns was significant in specific tensile strength, presenting a null p-value. The main factor matrix phase and the interaction between the matrix phase and arrangement of the jute yarns did not affect the specific tensile strength. Fig. 2 shows the behaviour of the specific tensile strength for the factors matrix phase and arrangement of jute yarns. The bold letters for the experimental conditions indicate the Tukey's groups, in which experimental conditions with similar letters correspond to equivalent means. As evidenced, the main factor matrix phase does not have a significant influence on the response variable of specific tensile strength. The Tukey test groupings confirm that for the same reinforcement phase, the means of specific tensile strength are statistically similar for composites manufactured with epoxy resin or castor oil. This result was achieved due to the combination of satisfactory mechanical performance in tensile and the low density obtained for the composites manufactured from castor oil.

By varying the reinforcement phase of the composite materials from bidirectional fabric to unidirectional yarns, an increase of 116.19% is achieved in the average of specific tensile strength. This result is caused because of the twice number of fibres aligned in the direction of the load for composites manufactured with unidirectional yarns. This result is similar to that obtained for absolute tensile strength, given that the density was similar for composites manufactured in unidirectional jute or bidirectional fabric when fabricated in same matrix phase.
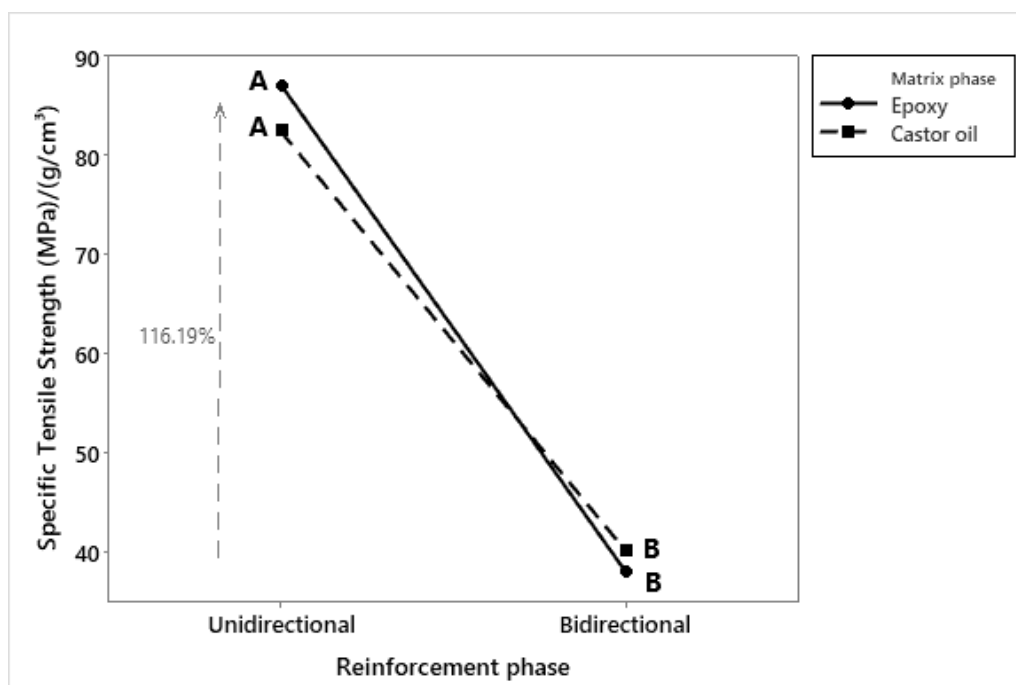
Figure 2. Effect on the average specific tensile strength response.

3.5. Specific tensile modulus

The main factor arrangement of the jute yarns was significant regarding the specific tensile modulus, how indicated by the null p-value. The main factor matrix phase and the interaction between the matrix phase and arrangement of the jute yarns did not affect the response variable for a confiatibility level of 95%. Fig. 3

shows the behaviour of the specific tensile modulus as a function of the factors matrix phase and arrangement of the jute yarns. As shown in the plot, the main matrix phase factor does not influence the response variable. The Tukey test groupings confirm that the means of the specific tensile modulus, for composites manufactured with epoxy resin or castor oil resin, do not present significant differences. By varying the reinforcement phase of the composite materials, from bidirectional fabric to longitudinal yarns, an increase of 92.76% is achieved in the average specific tensile modulus.

The results of statistical equality between the averages of specific tensile modulus of epoxy resin and castor oil composites corroborate those obtained for specific tensile strength. The main reason is the combination between satisfactory mechanical tensile performance and the low density values of composites manufactured with castor oil. Furthermore, materials manufactured with a greater number of fibres aligned to the tensile loading direction resulted in composites with a higher specific tensile modulus.
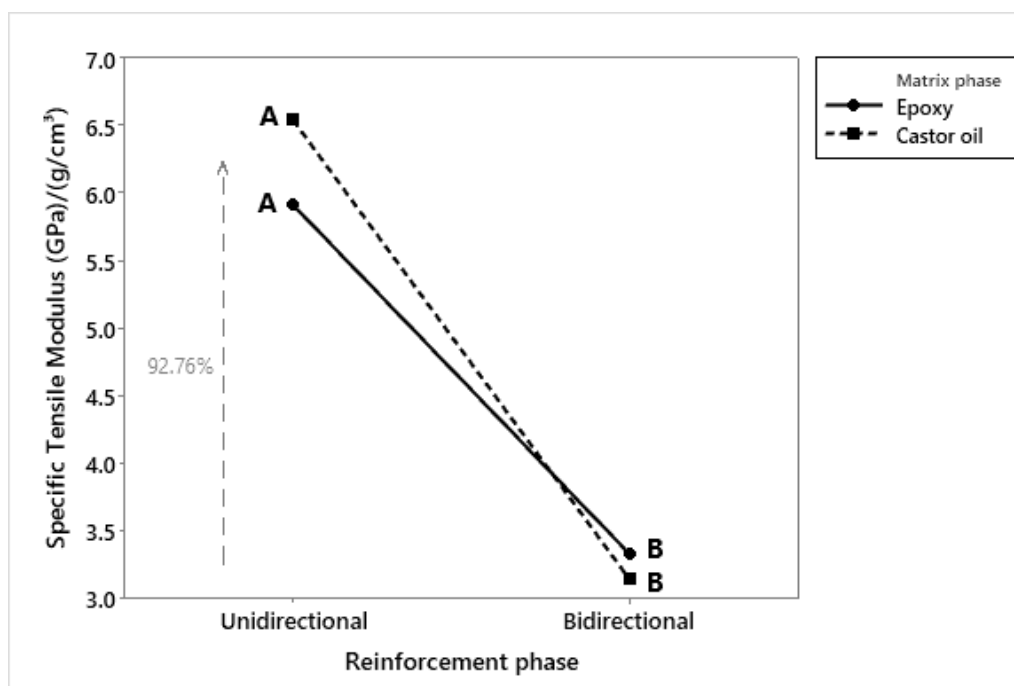
Figure 3. Effect on the average specific tensile modulus of the composites.

3.6. Specific flexural strength

The main factors, matrix phase and arrangement of jute yarns, showed significance on specific flexural strength, as observed by p-values lower than 0.05. The interaction between the matrix phase and the arrangement of the jute yarns did not affect the specific flexural strength, because the p-value obtained was greater than 0.05. Therefore, only the main effects on the response variable of specific flexural strength will be analyzed.

The specific flexural strength for epoxy resin composites is 40.58% higher than the castor oil composites, as shown in Figure 4a. Despite the lower density of castor resin composites, the mechanical flexural performance of epoxy resin composites means that their specific flexural strength is still higher. The average specific flexural strength for composites with yarns aligned in the longitudinal direction was 79.54% higher than for specimens manufactured with bidirectional fabric (Fig. 4b). The result follows the pattern found for absolute flexural strength, since the arrangement of jute yarns did not generate difference on the apparent density of the composite materials.
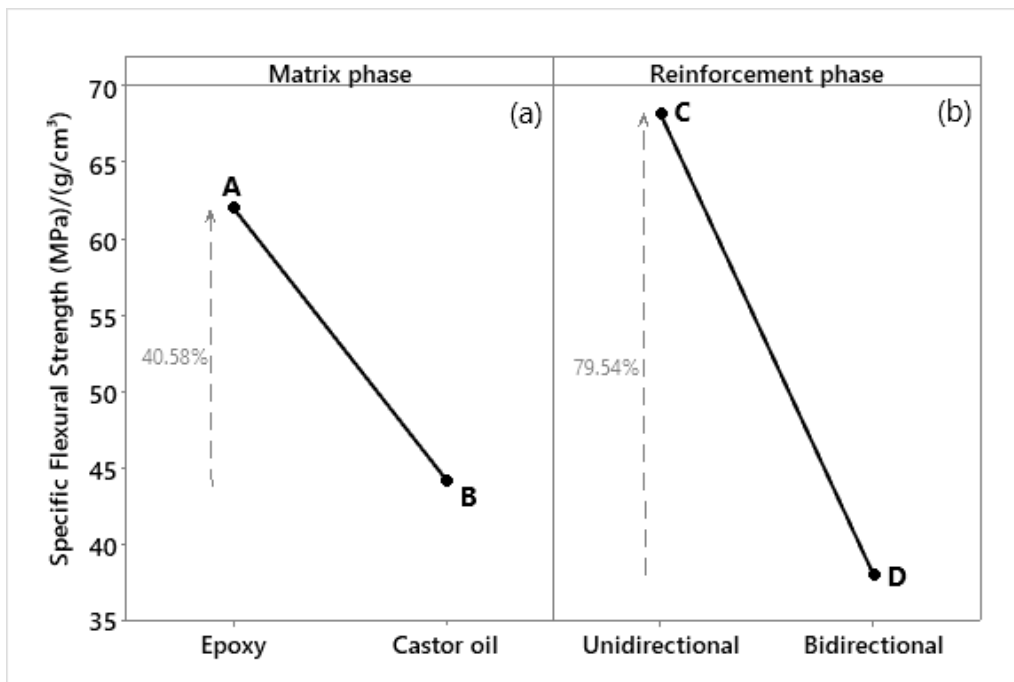
Figure 4. Effect of the main factor matrix phase (a) and the main factor arrangement of jute yarns (b) on the specific flexural strength of the composites.

3.7. Specific flexural modulus

The main factors matrix phase and arrangement of jute yarns showed significance on the specific flexural modulus, as observed by p-values lower than 0.05. The interaction between the matrix phase and the arrangement of the jute yarns did not affect the specific flexural modulus, with a p-value greater than 0.05. Therefore, only the main effects on the response variable will be analyzed. The average specific flexural modulus for epoxy resin composites is 18.86% higher than that for castor oil-based resin composites (Fig. 7a). By varying the reinforcement phase in composite materials from bidirectional fabric to unidirectional yarns, an increase of 136.92% in the specific flexural modulus was obtained (Figure 7b). The composite materials manufactured with unidirectional yarns, with the matrix phase in epoxy resin or castor oil, resulted in specific flexural modulus values in intersecting bands.
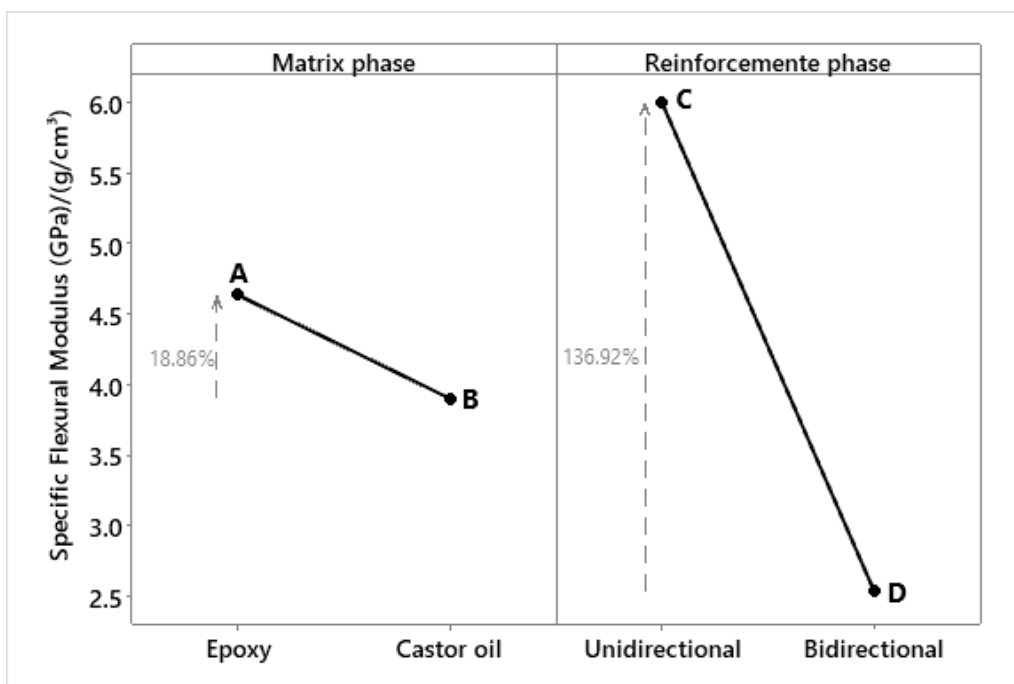
Figure 5. Effect of the main factor matrix phase (a) and the main factor arrangement of jute yarns (b) on the specific flexural modulus response.

4. CONCLUSIONS

In the present work, unidirectional jute fibre yarns and bidirectional fabrics were used as reinforcement phases in epoxy resin and castor oil composites. Statistical design was used to evaluate the effect of the matrix phase and reinforcement phase on the responses of specific tensile strength and tensile modulus as well as specific flexural strength and modulus. The interaction between the matrix phase and the reinforcement phase no generated significance in the response variables. The experimental study indicated that the use of castor oil as a matrix phase did not affect the specific tensile strength and specific tensile modulus of the composite materials. The analysis of variance indicated no significance for the specific tensile properties for the main factor matrix phase. However, the matrix phase of castor oil provided a decrease in the properties of specific flexural strength and specific flexural modulus of the composites despite the lower density for the composites manufactured in castor oil. The alteration of phase reinforcement in materials from bidirectional fabric to unidirectional jute yarns caused an expressive increase in all specific mechanical properties of the composites. The composite materials manufactured demonstrated to be a sustainable and economical alternative to engineering applications, especially those manufactured with unidirectional jute fibres, which exhibited satisfactory mechanical properties.

Declaration of Competing Interest

The authors declare no conflict of interest.

REFERENCES

[1] S. Wicaksono, G.B. Chai. A review of advances in fatigue and life prediction of fibre reinforced composites. *Journal of Materials: Design and Applications*, Volume 227, 2012. ( )

[2] X. Wei et al. New advances in fibre-reinforced composite honeycomb materials. *Science China Technological Sciences*, Volume 63, 2020. ( )

[3] B.T. Ferreira et al. Sisal-glass hybrid composites reinforced with silica microparticles. *Polymer Testing*, Volume 74, 2019. ( )

[4] D. A. L. E. Silva A. Life cycle assessment of wood-based composites: state-of-art and opportunities for reducing enviromental impacts. *Non-conventional Building Materials based on agro-industrial wastes*, 2015. ( )

[5] V. Mussi-Dias et al. Degradação de poliuretano por fungos: perspectivas para preservação ambiental. *Perspectivas Online: Biológicas e Saúde*, Volume 7, 2017. ( )

[6] ASTM D3039-14, Standard Test Method for Tensile Properties of Polymer Matrix Composite Materials. ASTM International, 2014. (www.astm.org).

[7] ASTM D790-17, Standard Test Methods for Flexural Properties of Unreinforced and Reinforced Plastics and Electrical Insulating Materials. ASTM International, 2017. (www.astm.org).

MECHANICAL PROPERTIES OF CASTOR-OIL POLYURETHANE BIOCOMPOSITE REINFORCED WITH BANANA FIBRES

Leandro J. Silva(a) *, Alexandre Z. Silva (b), Júlio C. Santos (c), Rodrigo T. S. Freire (d), Túlio H. Panzera (e)

(a) 0000-0002-4606-3483 (Federal University of São João del Rei – Brazil)
(b) 0009-0008-6116-9375 (Federal University of São João del Rei – Brazil)
(c) 0000-0002-7485-491X (Federal University of São João del Rei – Brazil)
(d) 0000-0001-5206-5639 (Federal University of São João del Rei – Brazil)
(e) 000-0001-7091-456X (Federal University of São João del Rei – Brazil)

* Corresponding author: leandro.silva@ufsj.edu.br

CODE: BCCM7-30

Abstract: The study aims to evaluate the mechanical properties of a castor-oil polyurethane biocomposite reinforced with banana fibres extracted from the pseudo-stem of the banana plant (*Musa balbisiana*) using *Bacillus megaterium* bacteria. Four fibre arrangements are assessed: (i) random continuous fibres, (ii) unidirectional continuous fibres, (iii) random discontinuous fibres with a length of less than 30 mm, and (iv) random milled fibres. The composites undergo 24 hours of cold pressing with a fibre volume fraction of 20%. Tensile, flexural, and impact (Charpy) samples are obtained using a laser-cutting machine. It is found that composites manufactured with unidirectional continuous fibres outperform other arrangements in terms of tensile and flexural modulus, tensile strength, and impact strength. The flexural strength of composites made with continuous fibres (random or unidirectional) achieves close values. Although unidirectional composites demonstrate superior performance, the manufacturing process of these composites is more complex due to the previous manufacture of the unidirectional fibre fabric. In this sense, composites with unidirectional fibres may only be viable for applications directly related to tensile properties.

1. INTRODUCTION

Banana plants are well-suited for cultivation in tropical countries like Brazil, which ranks among the top five largest worldwide producers of the fruit[1]. Banana crops, however, produce a substantial amount of waste after harvesting, and the high humidity in plantations can lead to the proliferation of fungi, posing challenges for treatment control. Consequently, repurposing the banana pseudo-stem is an ecologically sound alternative and a significant contribution to banana production since there is no need for additional plantation areas [2]. The exploration and research of this resource present a significant opportunity in Brazil, adding value to the banana crop by discovering new applications or processing methods that enable the further use of waste as recycled or reused material [3]. This endeavour boosts employment opportunities and enhances families' income in crop regions. Although most banana waste in Brazil is currently used for handicrafts, this represents only 2% of the total banana biomass produced [4, 5]. Notably, significant developments have been made in the fashion market with the production of fabric from Brazilian banana fibres [6]. Moreover, banana fibres have potential applications in various industrial sectors such as furniture, automotive, and civil construction. These fibres exhibit high mechanical properties compared to other natural fibres, making them a promising material for reinforcing composites, particularly polymeric composites [3, 7, 8].

The extraction of banana fibres can be accomplished through various methods: manual extraction with knives and brushes, mechanical extraction by specialised devices, chemical extraction using alkalis, light acids, hypochlorite, and hydrogen peroxide, or biological extraction, which traditionally employs

bacteria or fungi present in the environment to remove the non-cellulosic components of the leaf sheath. The latter method is particularly appealing as the waste generated does not call for additional treatment for disposal, rendering the process environmentally friendlier than the chemical approach despite the longer treatment time required. Additionally, this method yields more resilient fibres with greater stretching capacity compared to the mechanised process [9].

In recent times, there has been a noteworthy surge in interest from scientists and researchers worldwide in polymeric composites based on natural fibres and matrices derived from renewable resources, such as vegetable oils [10]. The inherent characteristics of biobased resins, including their biodegradability in the soil through the action of microorganisms, resulting in a reduction of industrial waste, and the ability to be disposed of after their service life without harming the environment, present them as a potential alternative to the use of synthetic composites, which lack these environmentally friendly traits [11]. The applications of biocomposites, whether involving biopolymers or not, extend to industries such as furniture and packaging and serve as secondary structural components, particularly in the automotive, aerospace, and construction sectors. This growing interest underscores the potential for significant advancements in sustainable material technologies.

One particularly noteworthy option among bio-natural polymers is castor-oil polyurethane. Castor oil is derived from the seeds of the *Ricinus communis* plant, abundant in tropical and subtropical regions, notably in Brazil [12]. The Centre for Innovation and Technology in Composites (CIT^{e}C) at the Federal University of São João del Rei (UFSJ) has undertaken studies involving the manufacturing and characterisation of composites based on castor-oil polyurethane (IMPERVEG® AGT 1315) reinforced with a range of natural fibres, including coconut [13], grass [14], bamboo [15], and banana fibres [16], as well as synthetic fibres [17]. These research efforts signify substantial progress in the exploration of castor oil-based polymers and their potential applications in composite materials.

This study employs a statistical design to analyse the effects of four fibre arrangements in castor-oil polyurethane biocomposites reinforced with banana fibres on various responses, including bulk density (ρ), tensile strength ($\sigma_{tensile}$), flexural strength ($\sigma_{flexural}$), tensile modulus ($E_{tensile}$), flexural modulus ($E_{flexural}$) and Charpy impact energy absorption.

2. METHODOLOGY

Polymeric composites based on castor-oil polyurethane and banana fibres are studied in this work. The two-component castor-oil polyurethane IMPERVEG® AGT 1315, kindly donated by Imperveg (Brazil), is used. The pre-polymer (component A) and polyol (component B) are thoroughly hand-mixed at the proportion 1:1.2 (A:B) by weight. Banana fibres are extracted from the pseudo-stem of the banana plant (*Musa balbisiana*), after fruit harvesting. Figure 1 illustrates the fibre extraction steps. The outermost layer of the leaf sheaths (which possess higher strength) is stripped and immersed for 60 days in an aqueous solution prepared with 2 ml of *Bacillus megaterium* DC48 (Bioaction Mega from Agrisoluções – Brazil) for 100 l of water (Figure 1c). The strips are then combed, water-cleansed (Figure 1d), and, finally, dried in the sun.

(a) (b) (c) (d)

Figure 1. Pseudo-stem of the banana plant (a); detached leaf sheaths (b); strips removed from leaf sheaths and immersed in the Bacillus aqueous solution (c); combing and water cleansing of strips (d).

The extracted fibres are used in pristine conditions as reinforcement to manufacture castor-oil polyurethane composites. Four fibre arrangements (Figure 2) are evaluated as follows: unidirectional continuous fibres (C1), random continuous fibres (C2), random discontinuous fibres with controlled length

(up to 30 mm) (C3), and random discontinuous milled fibres with uncontrolled length (C4). The unidirectional arrangement is created using a fibre-bundle fabric (Figure 2b) manufactured in a handmade weaving loom. Additionally, fibres are scissor-cut and milled in a rotary knife mill (Tecnal TE - 651/2) to allow for the discontinuous arrangements shown in Figure 2c and Figure 2d, respectively.

| (a) | (b) | (c) | (d) |

Figure 2. Random continuous fibres (C2, a), unidirectional continuous fibres (C1, b), random discontinuous fibres (C3, c) and random milled fibres (C4, d).

Composites are manufactured (Figure 3) by cold uniaxial pressing using 300 x 300 mm^2 metallic moulds, considering a fibre volume fraction of 20%. After 24 hours, the samples are demoulded and post-cured for 15 days. Tensile, flexural, impact (Charpy), and bulk density samples are obtained by laser cutting in a 500 W Robotech Machine and tested according to the respective standard [18-21].

| (a) | (b) | (c) | (d) |

Figure 3. Castor-oil polyurethane composites manufactured with unidirectional continuous fibres – C1 (a), random continuous fibres – C2 (b), random discontinuous fibres – C3 (c), random milled fibres – C4 (d).

Analysis of Variance (ANOVA) is used to investigate the effect of the four fibre arrangements considered on the tensile and flexural elastic modulus and strength, as well as impact strength. Two replicates of 5 samples (for each test) are fabricated for this purpose. Main effect plots are obtained according to a 5% significance level. The Anderson-Darling test is performed to assess the normality of the data and validate ANOVA. The adjusted R^2 (R_{adj}^2) is computed to quantify the variance amount explained by the arrangement of fibres. Tukey´s test is used to compare means, classifying different means by groups of letters (A, B, C, etc.), which are presented directly within the effect plots. ANOVA one-way analysis is performed using the Minitab software.

3. RESULTS AND DISCUSSION

Table 1 displays the mean values obtained for the response variables for replicates 1 and 2, respectively. The mean values for each response variable are subjected to the Analysis of Variance procedure, whose results are presented in Table 2. If the P-value is less than or equal to 0.05 (5%), the experimental factor significantly affects the response (underlined p-values in Table 2). The normality test (Anderson-Darling test), based on the residuals, is also conducted to validate the ANOVA model. In this context, the p-value must be higher than 0.05, indicating that the data is normally distributed. As observed in

Table 2, all the response variables have presented p-values higher than 0.05 and are considered to follow a normal distribution. R^2_{adj} values above 83% (for affected responses) strongly indicate that the model can predict the results within a reasonable margin of error. Therefore, the ANOVA one-way model used is considered robust.

Table 1. Mean values for response variables analysed.

Exp. condition	Replicate	ρ (g/cm³)	$\sigma_{tensile}$ (MPa)	$E_{tensile}$ (GPa)	$\sigma_{flexural}$ (MPa)	$E_{flexural}$ (GPa)	I (kJ)
C1	1	0.89	78.60	2.91	57.23	5.34	29.75
	2	0.86	93.62	4.09	60.75	5.49	24.03
C2	1	0.93	21.87	1.55	40.22	1.37	13.59
	2	0.96	16.38	1.32	47.03	1.58	14.15
C3	1	0.92	12.98	1.42	30.51	1.52	12.91
	2	0.93	12.31	1.46	26.40	1.25	16.29
C4	1	1.03	13.45	1.00	30.83	1.80	17.02
	2	0.94	15.56	0.99	27.58	1.73	17.36

Table 2. Analysis of variance.

Response variables	ρ	$\sigma_{tensile}$	$E_{tensile}$	$\sigma_{flexural}$	$E_{flexural}$	I
P-value (fibres arrangement)	0.141	*0.001*	*0.014*	*0.002*	*0.000*	*0.016*
P-value (Anderson-Darling normality test)	0.761	0.626	0.054	0.173	0.639	0.704
R² (%)	-	97.03	84.62	94.15	99.44	83.66

Figure 4 depicts the significant effect plots for the mechanical responses evaluated. Bulk density, which varied from 0.77 to 1.05 g/cm³, is not affected by the fibre arrangements, as revealed by a p-value higher than 0.05 (Table 2). This behaviour can be attributed to the same proportion of fibres and matrix (in volume) used for manufacturing all the composites.

Figure 4a illustrates the effect of the fibre arrangement on the mean tensile strength (8.48 – 119.93 MPa) of the composites. As expected, the continuous and unidirectional fibres (C1 condition) promoted the highest tensile strength. The other conditions achieved equivalent tensile strength, as demonstrated by the results from Tukey's test. A large amount of unaligned fibres with the load direction is embedded in the composite with a random arrangement of fibres, which contributes to a decrease in tensile strength (and modulus, as presented below) in relation to unidirectional-fibre reinforced composites.

Figure 4b illustrates the effect of fibre arrangement on the mean values of Young's modulus (0.60 – 5.35 GPa). The most rigid composite is manufactured with unidirectional banana fibres, a similar behaviour observed for tensile strength. Also, random fibres in the matrix (continuous and discontinuous) present a similar tensile modulus of elasticity, as revealed by the Tukey test comparison method.

The effect plot of fibre arrangement on the flexural strength (13.83 – 69.03 GPa) is presented in Figure 4c. As can be seen, composites manufactured with unidirectional fibres exhibited higher (approximately 102%) flexural strengths than those manufactured with discontinuous fibres. A reasonable explanation for this behaviour is the continuous (longer) fibres on the stress direction during bending. In addition, composites manufactured with continuous fibres (random and unidirectional) present different flexural strength (Tukey test), but they differ only on 35%. This result is quite interesting, considering that, in general, the procedure to fabricate composites with the random fibres is simpler. Tukey's test reveals that both discontinuous banana fibres reinforcing composites, i.e., both cut and milled fibres produced the same flexural strength for the composites.

The flexural moduli vary from 0.76 to 6.11 GPa. Figure 4d depicts the effect of fibre arrangement on mean values for this response. Similar behaviour of tensile strength and Young's modulus is observed for flexural modulus, the most rigid composite is that manufactured with continuous and unidirectional fibres, even than this composite was much thinner than others (more than 50%), which can affect the global flexural stiffness of the composite beams. According to the tukey test, the random fibre arrangements studied in this work (continuous and discontinuous) did not affect the flexural modulus of the banana fibre-reinforced composites. The interface condition plays an important role in flexural properties. In future work, microstructure analysis will be performed to better understand the flexural results.

The fibre arrangement affects the energy absorption (9.98 – 36.78 kJ) during the Charpy impact test, as shown in Figure 4e. Similar behaviour to the tensile properties is observed. Composites manufactured with continuous and unidirectional banana fibres absorbed more energy (~94%) than others. As revealed by Tukey's test, similar energy is absorbed by these randomly reinforced composites.
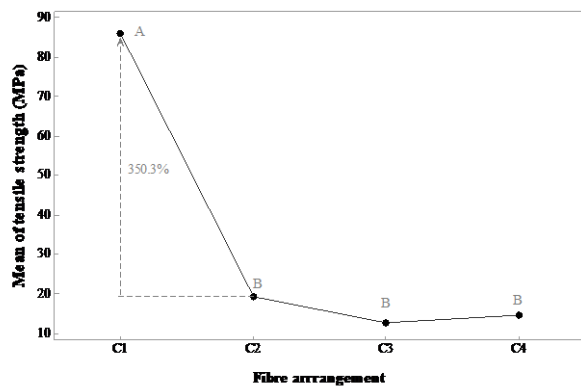
(a)
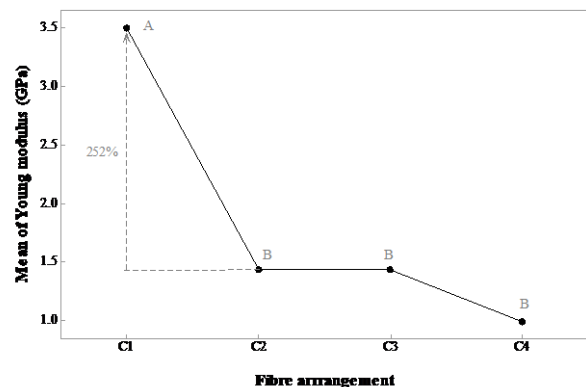
(b)
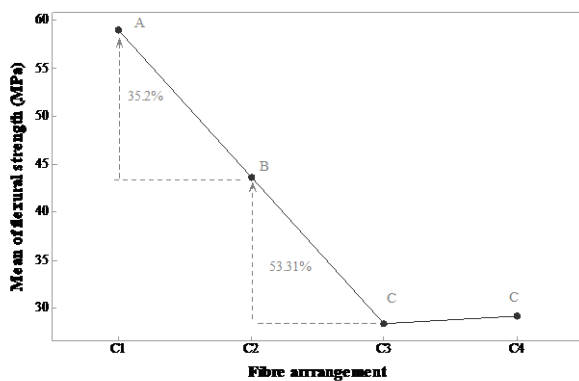
(c)
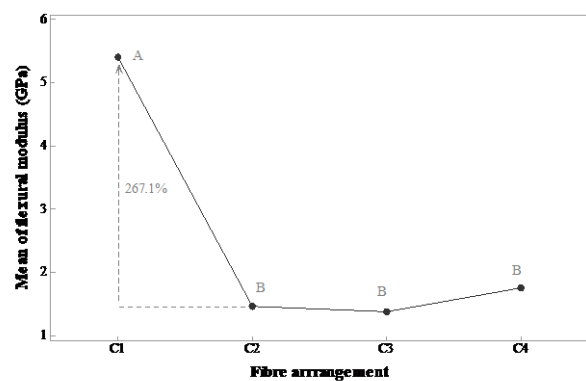
(d)
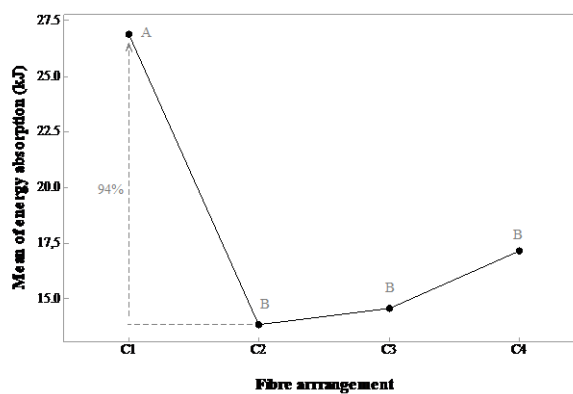
(e)

Figure 4. Significant effects on tensile strength (a), Young modulus (b), flexural strength (c), flexural modulus (d) and energy absorption (e).

4. CONCLUSIONS

In this study, the physical and mechanical properties of polyurethane biocomposites, derived from castor-oil polyurethane and banana fibres, were analysed. The effect of fibre arrangement was examined in relation to bulk density, Charpy impact energy absorption, tensile and flexural strength and modulus. The Analysis of Variance procedure and Tukey's (multiple comparison) test applied to the results revealed the

superior mechanical properties of the composites manufactured with unidirectional continuous banana fibre fabric, except for bulk density (same volume fraction of fibres). Additionally, both arrangements involving continuous fibres produce responses for flexural strength close each other. The results also indicate similar properties for the composites manufactured with random fibres (continuous and discontinuous), which is quite interesting, the use of milled fibres can offer benefits in terms of better repurposing the banana pseudo-stem. In conclusion, although unidirectional composites demonstrate superior performance, the manufacturing process of these composites is more complex due to the manufacture of the unidirectional fibre fabric. In this sense, composites manufactured with randomly banana fibres show promise for applications that are not directly related to tensile efforts.

Declaration of Competing Interest
The authors declare no conflict of interest.

5. REFERENCES

[1] IBGE - Instituto Brasileiro de Geografia e Estatística. *Produção de banana*. 2023 (http://www.ibge.gov.br/explica/producao-agropecuaria/banana/br), acessed 12 March 2024.

[2] P. S. Balzer *et al.* Estudo das Propriedades Mecânicas de um Composto de PVC Modificado com Fibras de Bananeira. *Polímeros: Ciência e Tecnologia*, Volume 17, 2007. (https://doi.org/10.1590/S0104-14282007000100004).

[3] R. R. R. Cecci *et al.* Banana pseudostem fibers characterization and comparison with reported data on jute and sisal fibers. *SN Applied Science*, Volume 2, 2020. (https://doi.org/10.1007/s42452-019-1790-8).

[4] L. F. Pinheiro *et al.* Fibra de bananeira (Musa SP): Produção e Potencial de Aplicações no Brasil. *In: 6º Congresso científico Têxtil e Moda*, 2018.

[5] L. F. Pinheiro. Banana fiber (Musa sp.): extraction process, processing and its applicability in textile products. *Dissertation (Master of Science)* – School of Arts, Sciences and Humanities, University of São Paulo. São Paulo, 2021. (https://doi.org/10.11606/D.100.2021.tde-04052021-193527).

[6] Jornal Nacional. *Pesquisadores desenvolvem fios para roupas a partir da fibra do caule da bananeira*. 2023. (https://g1.globo.com/jornal-nacional/noticia/2023/05/19/pesquisadores-desenvolvem-fios-para-roupas-a-partir-da-fibra-do-caule-da-bananeira.ghtml), Acessed 13 March 2024.

[7] N. G. Jústiz-Smith *et al*. Potential of Jamaican banana, coconut coir and bagasse fibres as composite materials. *Materials characterization*, Volume 59, 2008. (https://doi.org/10.1016/j.matchar.2007.10.011).

[8] S. Mukhopadhyay *et al.* Variability of Tensile Properties of Fibers from Pseudostem of Banana Plant. *Textile Research Journal*, Volume 79, 2009. (https://doi.org/10.1177/0040517508090479).

[9] S. Balda *et al.* Banana fibre: a natural and sustainable bioresource for eco-friendly applications. *Clean Technologies and Environmental Policy*, Volume 23, 2021. (https://doi.org/10.1007/s10098-021-02041-y).

[10] P. FOWLER *et al.* Biocomposites: technology, environmental credentials and market forces. *Journal of the Science of Food and Agriculture*, 2006. (https://doi.org/10.1002/jsfa.2558).

[11] J. J. Andrew and H. N. Dhakal. Sustainable biobased composites for advanced applications: recent trends and future opportunities – A critical review. Composites Part C: Open Access, Volume 7, 2022. (https://doi.org/10.1016/j.jcomc.2021.100220).

[12] R. V. SILVA, Compósito de resina poliuretano derivada de óleo de mamona e fibras vegetais. *Tese de Doutorado*. Universidade de São Paulo, 2003. (https://doi.org/10.11606/T.88.2003.tde-29082003-105440).

[13] E. G. Assis *et al.* Water aging effects on the flexural properties of fully biobased coir fiber composites. *Polymer Engineering and Science*, p. 1-12, 2023. (https://doi.org/10.1002/pen.26479).

[14] G. G. Braga *et al.* Fully Biobased Composite And Fiber-Metal Laminates Reinforced With Cynodon Spp. Fibers. *Polymer Composites*, P. 1-12, 2022. (https://doi.org/10.1002/pc.27109).

[15] F. Napolitano *et al.* Sandwich Panels Made Of Aluminium Skins And Gapped-Bamboo Ring Core. *Journal of the Brazilian Society of Mechanical Sciences and Engineering*, Volume 45, 2023. (https://doi.org/10.1007/s40430-023-04140-x).

[16] L. M. Fonseca *et al.* Natural composites produced with castor oil resin and banana fibres: effects of fibre length and fibre grammage on tensile and flexural properties. *In: Proceedings of 6th Brazilian Conference on Composite Materials,* Volume 01, p. 1-6, 2022. (DOI: https://doi.org/10.29327/566492).

[17] E.D. Vial *et al.* Glass and Aramid Fibre-reinforced Bio-based Polymer Composites Manufactured by Vacuum Infusion: A Statistical Approach to Their Physical and Mechanical Properties. *Applied Composite Materials,* Volume 30, 2023. (https://doi.org/10.1007/s10443-023-10142-8).

[18] ASTM D3039, Standard Test Method for Tensile Properties of Polymer Matrix Composite Materials. ASTM International, 1995.

[19] ASTM D790-15, Standard Test Methods for Flexural Properties of Unreinforced and Reinforced Plastics and Electrical Insulating Materials. ASTM International, 2015.

[20] ISO 179-1, Plastics: Determination of Charpy impact properties: Part 1: Non-instrumented impact test, 2023. (https://www.iso.org/obp/ui/en/#iso:std:iso:179:-1:ed-3:v1:en)

[21] ISO 10545-3, Ceramic Tiles - Part 3: Determination of water absorption, apparent porosity, apparent relative density and bulk density. 1997. (https://www.iso.org/obp/ui/#iso:std:iso:10545:-3:ed-2:v1:en)

PERCOLATION THRESHOLD IN PARTICULATE/SHORT FIBER COMPOSITES – EXPERIMENTAL ASSESSMENT AND ENVIRONMENTAL IMPLICATIONS IN BIOCOMPOSITES

Giovanni Filippone

(a) ● 0000-0002-4382-3686 (Università di Napoli Federico II – Italy)
* Corresponding author: gfilippo@gmail.com

CODE: BCCM7-51

Abstract: Identifying the percolation threshold (Φ_c) in particulate/short fiber composites is crucial in Composites Science. Besides affecting mechanical and transport properties and durability of composites, exceeding Φ_c can be of utmost importance in biocomposites based on hydrolizable matrices, as percolating filler networks allow external water and degradation-promoting species to penetrate, thus accelerating biodegradation. Unfortunately, neither the theoretical approach nor the experimental methods based on the electrical conductivity of the filler can be used in biocomposites. For this materials, a possible approach is exploiting the hygroscopic feature of natural fibers to infer Φ_c from dielectric measurements, but the simplicity and effectiveness of such an indirect method are questionable. The present study explores the potential of rheological analysis for the estimate of Φ_c. In more detail, a linear viscoelastic "two-phase model", originally defined to assess Φ_c in polymer nanocomposites, is extended to particulate (bio)composites and validated to poly(lactic acid) composites with hemp and kenaf fibers. Despite the substantial difference between Brownian nanoparticles and non-Brownian micro-fibers, the predictive feature of the two-phase model keeps working and the values of Φ_c assessed through a single set of linear viscoelastic measurements are perfectly agree with those obtained through more complex and time-consuming dielectric spectroscopy analyses.

1. INTRODUCTION

Biodegradable polymer-based composites reinforced with natural fibers, known as "green composites", have gained interest due to their eco-friendly nature. These composites are non-toxic and fully biodegradable, but their biodegradation should not occur too quickly to ensure a sufficient lifespan. Biodegradation is influenced by the chemical environment and typically involves the hydrolysis of ester groups in bio-polyesters. Natural fibers, being hygroscopic, introduce water into green composites, accelerating biodegradation, especially with poor fiber-matrix adhesion [1-3]. Key factors in biodegradation kinetics include fiber composition (lignin, cellulose, hemicellulose), geometry, and volume fraction (Φ). The pro-degradative effect increases when the percolation threshold (Φ_c) is exceeded, allowing water and degradative species to penetrate the composite. Accurate identification of Φ_c is crucial due to its impact on properties like conductivity, strength, and permeability to water and other species with pro-degradative action [4-6]. However, theoretical approaches requiring uniformity assumptions often mismatch real values. Experimental methods are more reliable, but the non-conductivity and inherent variability of natural fibers severely limit effective techniques. Dielectric spectroscopy and rheological analysis are effective for assessing Φ_c [7-10]. Dielectric spectroscopy measures changes in complex permittivity due to fiber-contained water, while rheological methods detect the transition from liquid- to solid-like behavior as fibers network. Staring from recent results from our group [11], this study applies compares the efficacy of such methods applying them to poly(lactic acid) samples with hemp or kenaf fibers. In particular, an innovative rheological approach, originally derived for polymer nanocomposites [12], is exploited to accurately identified Φ_c, showing excellent agreement with

dielectric spectroscopy, which is slower due to water diffusion times. The rheological method proved preferable for its rapidity and accuracy.

2. METHODOLOGY

2.1. Raw Materials

PLA pellets (Luminy® LX175, density: 1.24 g/cm³, MFI: 6g/10min at 210°C/2.16kg) were supplied by Corbion. Hemp shives and kenaf bast fibers were provided by Equilibrium S.r.l. and Kenaf Eco Fibers Italia, respectively. Fiber compositions are listed in Table 1. The fibers were ground using a Retsch cutting mill with a 0.25 mm grid. Water absorption capacity was determined by thermogravimetric analysis (TGA, mod. Q500 by TA Instruments) after immersing the fibers in water for 7 days and drying them at 110°C under nitrogen flow until a constant weight was achieved.

Table 1. Fiber composition.

Fiber	Cellulose [%]	Hemicellulose [%]	Lignin [%]	Others [%]
Hemp (shives)	44.3	27.2	22	6.2
Kenaf (bast)	31-39	21.5	15-19	-

2.2. Melt Compounding and Specimen Preparation

Fibers were compounded with PLA using a Brabender Pantograph EC batch mixer at fiber volume fractions of 5, 10, 15, 20, 25, 30, and 35%. The PLA was dried overnight at 85°C under vacuum, and the fibers were conditioned at 25°C and 80% RH. Compounding occurred at 180°C and 60 rpm for 6 minutes. The composites were cut into small pieces and hot-pressed into rectangular panels using a hydraulic press pre-heated to 180°C, applying ~150 bar pressure for 4 minutes, then cooled to 40°C under constant pressure before removing the solid panels from the mold.

2.3. Characterization

Fiber size and aspect ratio were measured via optical micrographs using an Olympus BX53M microscope, with about 100 particles measured per fiber type. Rheological tests were performed with a stress-controlled rotational rheometer (AR-G2 by TA Instruments) in parallel plate geometry at 180°C. The elastic (G') and viscous (G'') shear moduli were recorded as a function of frequency from 6×10^2 to 6×10^{-2} rad/s in a nitrogen atmosphere Samples were 1 mm thick disks, dried at 85°C overnight under vacuum. Dielectric spectroscopy was conducted using a rotational rheometer (ARES, Rheometric Scientific) with a dielectric thermal analysis tool. Rectangular specimens (25×12.5×3 mm³) were soaked in tap water at 30°C for 3 weeks to achieve constant weight. Tests were performed at room temperature with a constant compressive force of ~100 gram-force, recording dielectric permittivity across frequencies from 20 to 60,000 Hz, focusing on the imaginary part of the complex permittivity (ε''), which correlates to the real part of the complex conductivity (σ') through $\sigma' = \varepsilon_0 \varepsilon'' f$ (ε_0=8.85 × 10^{-12} Fm^{-1}, permittivity of free space).

3. RESULTS AND DISCUSSION

3.1. Theoretical assessment of Φ_c

For non-spherical particles, the theory of the excluded volume predicts that Φ_c depends on their aspect ratio (AR) and orientation. The analytic expression for Φ_c is given by:

$$\Phi_c(AR) = \frac{\langle V_{ex}\rangle}{\frac{4\pi}{3}+2\pi AR+\frac{\pi}{2}(AR)^2} \left(\frac{\pi}{6}+\frac{\pi}{4}AR\right) \tag{1}$$

where $\langle V_{ex}\rangle$ is the average excluded volume over the orientation distribution function. $\langle V_{ex}\rangle$ varies between values corresponding to perpendicular and parallel arrangements of the particles. In our composites, the ground fibers are similar to short, capped cylinders. Hemp fibers are shorter (207 ± 122 μm) than kenaf fibers (330 ± 183 μm). For capped cylinders, $\langle V_{ex}\rangle$ ranges between 0.7 (perpendicular) and 2.8 (parallel), with

1.4 representing random orientation. Estimating Φ_c using Equation 1 requires knowledge of fiber orientation, which is difficult to predict due to the complex flows during processing. Random orientation is likely due to chaotic flow during melt compounding, though some alignment may occur during compression molding near the specimen surfaces. Given the difficulty in predicting fiber orientation, we refer to the curves of Φ_c as a function of AR for the limiting case of parallel, perpendicular, and random orientations Average AR values are 3.3 ± 1.9 for hemp and 4.7 ± 2.7 for kenaf fibers. Using these values in Equation 1 gives the theoretical Φ_c values in Table 2.

Table 2. Theoretical predictions of Φ_c based on Equation (1).

$\langle V_{ex} \rangle$ (fiber orientation)	Φ_c hemp [%]	Φ_c kenaf [%]
0.7 (perpendicular)	5.2 (4.1–7.1)	4.3 (3.2–6.4)
1.4 (random)	10.4 (8.1–14.1)	8.6 (6.5–12.7)
2.8 (parallel)	20.8 (16.3–28.3)	17.2 (13.0–25.5)

The wide range of possible Φ_c values, due to AR variability, indicates that theoretical calculations only provide broad estimates in real composites. Hence, experimental methods such as rheology and dielectric spectroscopy, which do not require assumptions about fiber morphology and arrangement, are necessary to accurately identify percolating fiber networks.

3.2. Estimating Φc through linear viscoelastic analysis and dielectric spectroscopy

The results of the linear viscoelastic analyses and dielectric spectroscopy measurements are reported in Figure 1.
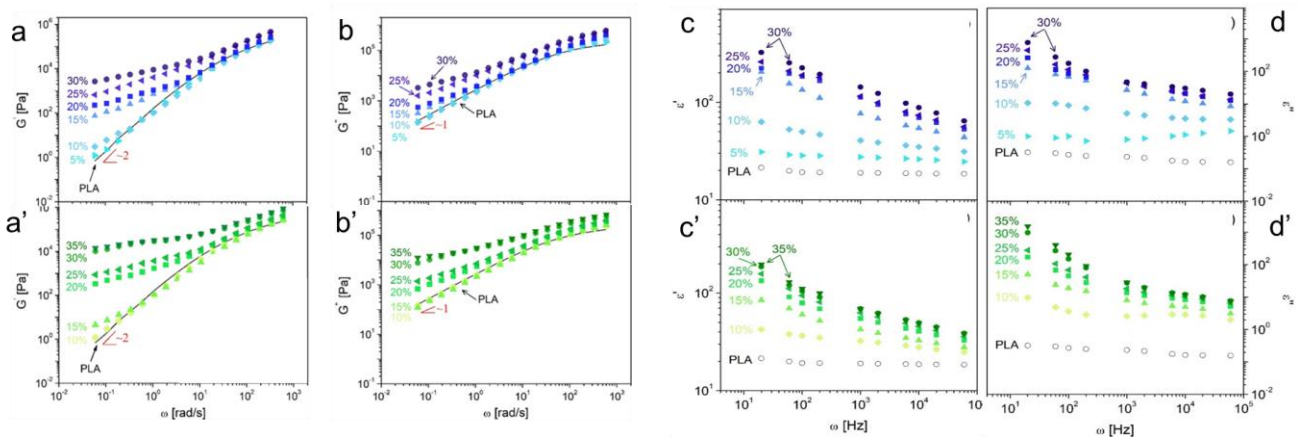
Figure 1. Linear viscoelastic moduli (elastic modulus: a, a'; viscous modulus: b, b') and real (c, c') and imaginary /(d, d') part of the complex permittivity. a-d (blue points): hemp-based composites; a'-d' (green points): kenaf-based composites. Images readapted from [11].

First of all, we consider the rheological analyses. We focus on the elastic modulus (Fig. 1.a, a'), which contains more information than the viscous one, at high oscillation frequency ($\omega > 10^1$ rad s^{-1}) G' increases without changing their frequency dependence significantly. This is due to the dynamics of polymer chains which are minimally affected by fibers. The apparent increase in rheological properties is explained by the concept of shear stress-equivalent inner shear rate, where the actual deformation experienced by the polymer between fibers is higher than the externally imposed deformation. At low oscillation frequency ($\omega < 10^1$ rad s^{-1}), the effect of fibers becomes evident. At low fiber content the modulus slightly increases compared to the neat matrix and shows reduced frequency dependence. At high Φ, the modulus shows clear flattening, indicating a significant slowdown in relaxation dynamics. A plateau in G', indicating frequency-independent behavior, is expected above Φ_c, but it was not clearly observed in our samples within the frequency range tested. Exploring lower frequencies is challenging due to increasing experimental times. To overcome this limitation, we invoke a two-phase model originally conceived for polymer nanocomposites [12], but whose basic assumptions are still invokable for micro-composites. The ability of the model to capture the viscoelastic behavior of the samples investigated here is demonstrated by the possibility to deterministically scale the G'

values of samples at different $\Phi \geq \Phi_c$ onto a single master curve using only two scaling factors with a precise physical meaning. This is shown in Figure 2.a, b. Since the curve of samples below Φ_c are not scalable, we can exclude these samples from the analysis and infer the precise value of the percolation threshold by invoking the percolation theory, according to which the elasticity of samples above Φ_c must scale in a critical fashion with filler content:

$$G_0' \sim (\Phi - \Phi_c)^\nu \tag{2}$$

In Eq. (2), ν is a critical exponent that depends on the stress bearing mechanism and G_0' is the vertical shift factors for the building of the master curves. Plotting G_0' as a function of the reduced fiber content, $\Phi - \Phi_c$, and fitting Equation (2) for different values of Φ_c allows us to precisely identify Φ_c as the value that returns the maximum coefficient of determination R^2. The power-law scaling of the network elasticity is shown in Figure 2.c for the computed values of Φ_c, which were found to be 10.1% for the hemp-based composites and 19.5% for the kenaf-based ones.
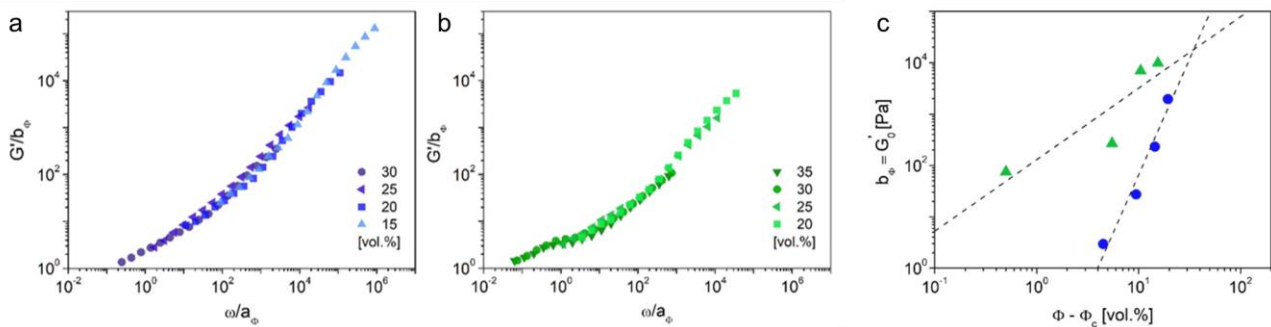
Figure 2. Mastercurves of G' of the hemp- (a) and kenaf-based samples (b), and critical scaling of the fiber network elasticity with reduced fiber content (c): hemp- (circles) and kenaf-based (triangles) composites. The values of Φ_c in (c) are 10.1% for the hemp-based composites, and 19.5% for the kenaf-based ones. Images readapted from [12].

The computed value of Φ_c of the hemp-based composites is much lower than that of the kenaf fibers. This reflects the different aspect ratio of the two fibers, which in turn causes a different degree of orientation in the host PLA matrix. Details on this point are reported in the original publication [12]. To corroborate this finding, now we consider the results of dielectric measurements (Fig. 1.c, c', d, d'). In particular, we focus on the imaginary part of the complex permittivity, ε'', which correlates to the real part of the complex conductivity through the alternated current universal law, $\sigma' = \varepsilon_0 \varepsilon'' f$. Its low frequency value, σ_0', is a good estimate of the sample electrical conductivity, which is expected to exhibit power-law dependence on fiber content above Φ_c:

$$\sigma_0' \sim (\Phi - \Phi_c)^\nu \tag{3}$$

This time, ν is a coefficient that depend on the conductive mechanism. Plotting σ' as a function of the electrical field f and fitting the equation $\sigma'(f) = \sigma_0' + A f^u$ (with A and u as fitting parameters) to the experimental data (Figure 3.a, b), we obtain good estimates of σ_0'. These data were hence plotted against the reduced fiber content, and fitting Equation (3) for different values of Φ_c looking for the maximum coefficient of determination results in the most reliable estimate of Φ_c (Figure 3.c). The
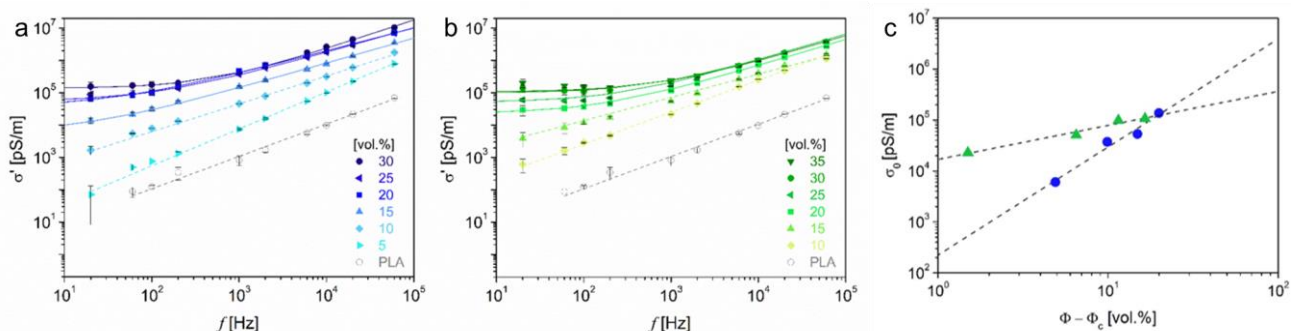
Figure 3. a, b) Real part of the complex conductivity for hemp- (a) and kenaf-based (b) composites at different fiber content. The samples were equilibrated in tap water for ~3 weeks. Lines are the fitting of the alternated current universal law, $\sigma' = \varepsilon_0 \varepsilon'' f$, to the data. c) Critical scaling of the real part of the complex conductivity for the hemp- (circles) and kenaf-based (triangles) composites. The values of Φ_c in (c) are 10.5% for the hemp-based composites, and 18.5% for the kenaf-based ones. Images readapted from [12].

The observed difference in percolation thresholds between the two fiber types, initially evident from rheological analysis, underscores the challenge of theoretically estimating percolation thresholds in natural fiber-based composites. Crucially, the (di)electrically computed Φ_c values closely align with those derived from rheological analysis. However, it's noteworthy that dielectric measurements necessitated an arduous procedure, involving the samples' absorption of equilibrium water content. This process required continuous monitoring of sample weight and dielectric parameters over lengthy experimental durations, approximately three weeks, dictated by the characteristic diffusion time of water in the fibers. In contrast, a sole set of straightforward linear viscoelastic measurements, analyzed within the framework of the two-phase model, suffices to yield equivalent results with the same precision.

4. CONCLUSIONS

The percolation threshold of PLA-based green composites reinforced with short hemp shives or kenaf bast fibers (average length <500 μm) was evaluated using theoretical calculations based on percolation theory, linear viscoelastic analyses in the melt state, and dielectric spectroscopy. A comparison of the three methods' effectiveness was conducted. Theoretical calculations necessitate precise knowledge of fiber geometry (size, shape, aspect ratio), which is challenging to obtain in practical scenarios, resulting in a wide range of possible Φ_c values for short fiber green composites. In our study, this theoretical approach yielded similar ranges of Φ_c (5.2–20.8% for hemp-based and 4.3–17.2% for kenaf-based composites). Extending a viscoelastic model for polymer nanocomposites to our systems allowed us to narrow the Φ-intervals for Φ_c estimation, validated by constructing a master curve of the elastic modulus. Subsequent computation of Φ_c using percolation theory resulted in values of approximately 10.1% for hemp-based and 19.5% for kenaf-based composites. These values, contrary to theoretical predictions for kenaf fibers, were confirmed via dielectric spectroscopy analyses, which required a more laborious and time-consuming sample conditioning procedure before measurements.

5. FUNDINGS

6. REFERENCES

Z.N. Azwa, B.F. Yousif, A.C. Manalo, W. Karunasena, A review on the degradability of polymeric composites based on natural fibres, *Mater. Des.* 47 (2013) 424-442.

[1] M. Bredu, Environmental degradation of plastic composites with natural fillers - A Review, *Polymers* 12 (1) (2020) 166-188.

[2] R. Gunti, A.V. Ratna Prasad, A. Gupta, Mechanical and degradation properties of natural fiber-reinforced PLA composites: Jute, sisal, and elephant grass, *Polym. Compos.* 39 (4) (2018) 1125-1136.

[3] I. Bozyel, D. Gokcen, Determining electrical percolation threshold of randomly distributed conductor materials in polymer composites via pathfinding algorithms, *Compos. Sci. Technol.* (2022) 109404.

[4] W. Wang, M. Sain, P.A. Cooper, Study of moisture absorption in natural fiber plastic composites, *Compos. Sci. Technol.* 66 (3-4) (2006) 379-386.

[5] M.P.M Dicker, P.F. Duckworth, A.B. Baker, G. Francois, M.K. Hazzard, P.M. Weaver, Green composites: A review of material attributes and complementary applications, *Compos. Part A Appl. Sci. Manuf.* 56 (2014) 280-289.

[6]   E. Jayamani, S. Hamdan, M.R. Rahman, M.K.B. Bakri, Comparative study of dielectric properties of hybrid natural fiber composites, *Procedia Eng.* (97) (2014) 536-544.

[7]   W. Wang, M. Sain, P.A. Cooper, Study of moisture absorption in natural fiber plastic composites, *Compos. Sci. Technol.* 66 (3-4) (2006) 379-386.

[8]   K.E. Borchani, C. Carrot, M. Jaziri, Rheological behavior of short Alfa fibers reinforced Mater-Bi® biocomposites, *Polym. Test.* 77 (2019) 105895.

[9]   Z. Stary, J. Kruckel, C. Weck, D.W. Schubert, Rheology and conductivity of carbon fibre composites with defined fibre lengths, *Compos. Sci. Technol.* 85 (2013) 58-64.

[10] L. Vitiello, M. Salzano de Luna, V. Ambrogi, G. Filippone (2024). A simple rheological method for the experimental assessment of the fiber percolation threshold in short fiber biocomposites. *Compos. Sci. Technol.* 245, (2024)110345.

[11] G. Filippone, M. Salzano de Luna, A unifying approach for the linear viscoelasticity of polymer nanocomposites, *Macromolecules* 45 (21) (2012) 8853-8860.

EVALUATION OF THE USE OF LIGNOCELLULOSIC WASTE AS BIOAGGREGATES FOR THE PRODUCTION OF BIOCONCRETE

Selton Thiago Nunes Souza[(a)]*, Diogo Antonio Correa Gomes[(b)], Eduardo Hélio de Novais Miranda[(c)], Cayo Chileno de Nahum Gamaleya[(d)], Saulo Rocha Ferreira[(e)]

(a) 0009-0008-9809-4493 (Federal University of Lavras – Brazil)
(b) 0000-0003-3967-4574 (Federal University of Lavras – Brazil)
(c) 0000-0002-3156-658X (Federal University of Lavras – Brazil)
(d) 0000-0003-4350-1174 (Federal University of Lavras – Brazil)
(e) 0000-0002-4048-907X (Federal University of Lavras – Brazil)
* Corresponding author: selton.souza@estudante.ufla.br

Abstract: The intense rock extraction process for concrete production reduces material availability and environmental impact. Bioaggregate, mainly composed of lignin, homocellulose, and cellulose, can replace conventional aggregates in bioconcrete production. Currently, this waste is either incinerated or sent to landfills, but reusing it could minimize environmental impacts in agroindustry and construction. Suitable characteristics for using lignocellulosic waste in civil construction include low density, water absorption capacity, and low thermal conductivity. This study aims to evaluate replacing crushed stone with various percentages of bioaggregates from *Jacarandá cuspidifolia* in bioconcrete production. Jacarandá biomass, collected at the Federal University of Lavras (UFLA) in Lavras, MG, Brazil, underwent cleaning and chemical characterization. Compression tests after 28 days showed 25% replacement resulted in 25 MPa resistance, with a 6.9% density reduction compared to the reference. With 75% replacement, compressive strength was 15.8 MPa, with a 20.7% density reduction compared to the reference.

1. INTRODUCTION

Growing environmental concerns have changed global guidelines, especially on waste from agroforestry industries. According to Law 12.305/30, industries must dispose of waste correctly to avoid fines. Proper disposal can be expensive and, with inconsistent inspections, many owners risk improper disposal, damaging the environment according to reference [1]. Lignocellulosic materials, such as wood, are often underused and end up being burned or going to landfill, causing environmental problems [2]. In 2009, 91% of the 30 million tons of wood waste came from the timber industry, 3% from construction and 8% from urban areas [3]. In 2016, the agroforestry sector generated 47.8 million tons of waste, with 70.5% from forestry and 29.5% from industry [4]. Approximately 63 million tons of solid waste are generated annually in Brazil. Civil construction, which consumes 60% of the materials extracted, accounts for 40% of this global extraction [5]. In 2014, global consumption of aggregates was 45,370 million tons, with 740 million tons in Brazil [6]. The high extraction of aggregates such as granite gravel, gneiss, limestone and basalt for concrete causes a shortage of these raw materials, damage to the landscape and ecosystems.

To mitigate these impacts, bioconcrete, made with vegetable aggregates and mineral binders, has been proposed. Bio-aggregates, which come from biomass such as wood and coconut shells, can replace conventional gravel, as they are natural and renewable. The construction industry can contribute to the sustainable management of these resources. Using lignocellulosic waste in the manufacture of cementitious

materials reduces the use of conventional aggregates, but studies are needed to guarantee their adequate characteristics [1]. Previous studies have shown promise in replacing gravel with bioaggregates in concrete, with a focus on mechanical and physical properties [7][8][9][10]. Bio-aggregates, such as *Jacaranda cuspidifolia*, have a low density and are advantageous for special properties in lightweight concrete, such as thermal insulation and sound absorption [8]. However, it is crucial to ensure the compatibility of the bioaggregate with the cementitious matrix, requiring treatment to remove unwanted substances and improve its durability [11]. This work aims to evaluate different treatments for bioparticles, proportions of bioaggregates and their effect on the mechanical properties of concrete.

2. METHODOLOGY

2.1. Preparation and characterization of Jacaranda fruit

The experiment was conducted in the laboratory of the Experimental Wood Panel Production Unit (UEPAM) at the Federal University of Lavras (UFLA). The *Jacaranda cuspidifolia* biomass was harvested inside the UFLA campus, located in the city of Lavras - MG, Brazil, latitude 21°13'32.73"S and longitude 44°58'37.46"O. Figure 1 shows the jacaranda tree with fruit and the external and internal surface of the biomass. The aggregates were cleaned in running water and brushed manually to remove any residues so that they would not affect the cement hydration process, crushed in a hammer mill, sieved respecting the grain size limits of gravel 0 (size 4.8 to 9.5 mm), according to the procedure in Figure 1.

JACARANDÁ FRUITS (*in natura*)   BIOAGGREGATE BRITA 0

CROSS SURFACE

Figure 1. Jacaranda fruit in natura / Jacaranda bioaggregate.

2.1.1   Physical and chemical properties

To determine the water absorption capacity of the jacaranda fruit, it was dried in an oven for 24 hours at 103 ± 2 °C, then submerged in water (room temperature). At intervals, the sample was removed from the water and its mass measured over a 24-hour period. For desorption analysis, the sample was kept at room temperature, between 23.3 ± 2 °C, and the mass was measured at certain time intervals for a period of 24 hours.

To determine basic density, the biomass was ground and dried in an oven for 24 hours at 103 ± 2 °C. It was then placed in a container of known volume and weighed to determine its mass, thus calculating Eq. (1).

$$\text{Basic density} \left(\frac{\text{g}}{\text{cm}^3}\right) = \frac{\text{mass (g)}}{\text{volume (cm}^3)} \tag{1}$$

Volumetric variation was also carried out; however, this test followed adaptations to the procedure in [12]. In this context, the jacaranda samples were first submerged in water until saturation and dried in an oven until they reached a constant mass. To check the dimensional variation, micrographs of the saturated and dried specimens were taken using a Motic BA310 trinocular microscope, and the ratios between wet diameters and dry diameters were obtained using the ImageJ software version bundled with 64-bit Java 8. Instructions.

The following chemical properties were obtained: extractive content [13], lignin [14], ash [15] and holocellulose of the biomass according to Eq. (2).

$$\text{Holocellulose (\%)} = 100 - (\text{Total extractives} + \text{Lignin} + \text{Ash}) \tag{2}$$

2.1.2   Calorimetry test

The semi-adiabatic calorimetry test was carried out in a thermal box that was kept in an air-conditioned room (22°C, 90% RH) for 24 hours on pastes with a water/cement ratio of 0.4 and levels of addition of jacaranda fruit particles in relation to the mass of cement of 0 and 10%. The jacaranda fruits analyzed were

crushed to the size of gravel 0 without treatment or treated in hot water (temperature 46 ºC) for 2 hours, cold water (temperature 26 ºC) for 24 hours, ice water (temperature -0.2 ºC) for 1 hour, a 1% NaOH solution (temperature 26 ºC) for 2 hours and a 1% CaOH solution (temperature 26 ºC) for 2 hours [16]. From this procedure, the most suitable treatment for jacaranda fruits in cement matrices was chosen. The temperature curves were obtained using the TC-08 Data Logger and analyzed with the corresponding PicoLog software to investigate the effect of adding jacaranda fruit on cement hydration reactions. For each test, a thermocouple K (32 24 AWG) was placed in the geometric center of the sample.

2.2. Composites made from Jacaranda fruit

2.2.1 Treatment of bioaggregates

In the heat treatment, the jacaranda fruit was washed with water at -0.2 ºC for 1 hour at a particle/water ratio of 100g/l to remove the water-soluble extractives. After this process, the bioparticles were dried in an oven. In order to completely remove the extractives, there were several washing cycles, observing the color of the water in each cycle, resulting in an extractive content of the water.

2.2.2 Bioconcrete production

Portland cement (CPII F40), quartz river sand with particles of up to 840 µm and water were used to produce the cement paste. Water at a temperature of -0.2 ºC was used for the alkaline treatment of the jacaranda biomass, at a ratio of 0.100g/100ml.

The bioconcrete was produced under temperature conditions of 24 ± 4°C and relative humidity of 55 ± 5% in accordance with the standards [17]. To make the composites, mortars with a water to cement ratio (w/c) of 0.6 were made with replacement rates of 25%, 50%, 75% and 100% of the coarse aggregate (gravel 0) with bio-aggregate from the jacaranda fruit with the same granulometry, 1:2.6:2.7 (cement, sand and gravel, respectively), using the bio-aggregates with the best treatment, according to the results of the semi-adiabatic calorimetry analysis.

2.2.3 Compression test

Compression tests of cylindrical specimens were carried out on an electromechanical testing machine developed by AROTEC Time Group Inc., manufactured in Beijing, People's Republic of China, with a 20 kN load cell, at a speed of 0.3 MPa/s according to the standard [18].

3. RESULTS AND DISCUSSION

3.1. Composites made from Jacaranda fruit

3.1.1 Treatment of bioaggregates

Table 1 shows the characterization tests on jacaranda fruit.

Table 1. Waste characterization results.

Material	Basic density (g/cm³)	Humidity (%)	Volumetric Variation (%)	Extractives (%)	Lignin (%)	Ashes (%)	Holocellulose (%)
jacarandá Not treated	0,73	9,38	31,13	8,67	66	1,49	23,85
jacarandá treated				2,77	50,33	0,68	46,22

A The basic density found in the lignocellulosic material was 0.73 g/cm³. This value is considered moderately heavy (0.5-0.8 g/cm³) according to [19], is close to that found for the density of vine waste (0.62 g/m³) [20] and higher than that found for bean waste (0.24 g/cm³) [21]. As the density of conventional aggregates ranges from 2.4 to 2.9 g/cm3, replacing them with jacaranda fruit results in lighter composites, which is positive, as there is a gain in the logistics process [22]. The basic density presented shows that

jacaranda biomass has a low density compared to conventional aggregates, such as limestone gravel 1.6 g/cm³ and/or basalt gravel 1.7 g/cm³ [23].

With regard to extractives and lignin, low molecular weight hydrophobic compounds, the untreated jacaranda fruit showed respective values of 8.67 % and 66.00 %. The values found for lignin were higher than those obtained for soy waste (22.04 %) [16] and coffee waste (29.28 %) [24]. On the other hand, the extractive data was lower than that obtained for sugar cane bagasse (19.59 %) [25] and soybean waste (13.69 %) [16] and, therefore, this component of jacaranda in natura would not have a significant impact on cement matrices. In addition, pre-treatments for its removal are unnecessary, as the value found was below 10% [23].

The ash content of the material was 1.49 %, a value similar to that found for coffee parchment (0.57 %) [26], lower than that found for cocoa residue (3.17 %) [27] and higher than that found for bamboo fibers (0.22 %) [28]. This variation between lignocellulosic materials is to be expected due to the different growing conditions and climate of the regions where they are found. However, ash has no proven impact on the hydration of cementitious matrices [23].

The holocellulose content was 23.85 %, lower than that found in corn cobs (76.70 %) [29] and bean waste (56.55 %) [21]. Lignocellulosic materials are highly hydrophilic due to the hydroxyl groups (OH) present in holocellulose. This can make it difficult to use these materials in various applications due to their negative impact on the physical properties of water and moisture absorption [30]. In this case, low levels of holocellulose, as found in jacaranda fruit, are favorable. However, one of the components of holocellulose is cellulose, which provides good mechanical properties for the material it is applied to. Thus, low levels of this material can mean a loss of mechanical properties in the resulting composites [23].

It can be seen that the water absorption in Figure 2 increases linearly in relation to the test time. The range of values is 24.6 % at 10 minutes of testing to 48.5 % at 24 hours of testing, higher than conventional aggregates (0.2 to 3.0 %) and other lightweight aggregates (10 to 20 %) [31]. This tendency is described in the literature as a negative interference of fibers in cement matrices because, as they are hybrid and porous materials, they have a greater tendency to absorb water and impact on cement hydration processes [32].

The values obtained in this test were, however, lower than those obtained in the work by [21], in which the authors, even after a washing procedure, found water absorption values of over 300 % for pine (Pinus taeda), bamboo (Bambusa vulgaris) and cactus (Cereus jamacaru) particles. This may be related to the greater amount of holocellulose found in all these particles compared to the jacaranda fruit particles, 64.77, 70.85 and 51.21 % respectively, with the exception of the cactus particles.

Even so, the high water absorption values found for jacaranda fruit may be related to the high volumetric variation (31.13 %), which is greater than the volumetric variation of other common bioaggregates, such as wood particles (10 %) and coffee husks (23 %); aggregates with high absorption levels tend to have high drying shrinkage, especially lightweight aggregates [33].
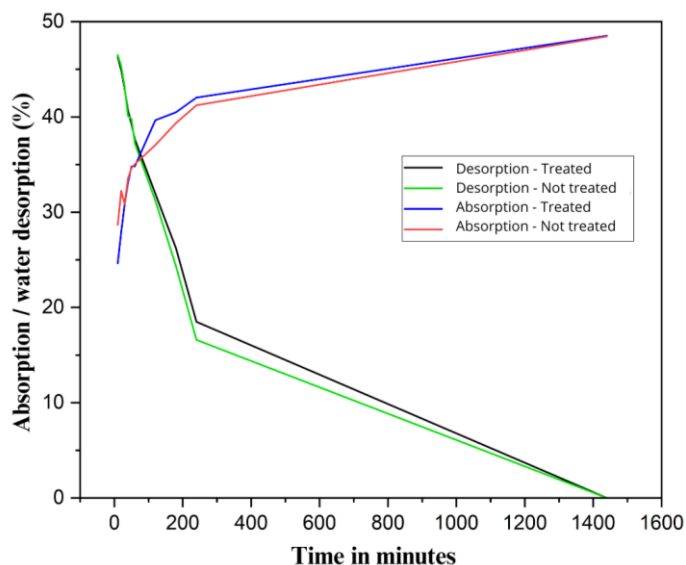
Figure 2. Water absorption / desorption test.

3.1.2 Semi-adiabatic calorimetry

According to the reference [34], cement hydration can be divided into initial reactions up to 2.5 hours, an induction period between 2.5 and 5.0 hours, an acceleration phase between 5.0 and 15.0 hours and a

deceleration phase after 15.0 hours. Figure 3 shows the temperature curves from the semi-adiabatic calorimetry test of 6 cement pastes produced with jacaranda fruit particles, added 10% by mass in relation to the cement mass, and 1 cement paste representing the reference. Initially, it is not clear that the treatment influenced the hydration dynamics of the cement pastes containing the lignocellulosic materials. However, compared to the reference paste, there is a delay in the hydration of the pastes, as indicated by the shifting of the peaks to longer times. This trend is widely documented in the literature, as some chemical components present in lignocellulosic materials, such as extractives, cellulose, hemicellulose and lignin, have the effect of delaying the initial cement hydration reaction [35]. To this end, the treatment used on the bioaggregates to make the test specimens was treatment with cold water.
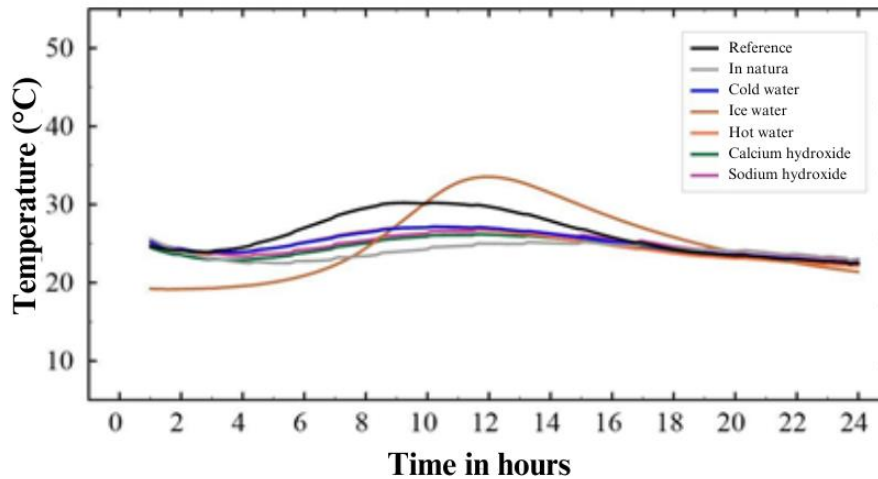
Figure 3. Calorimetry test.

3.2. Composites made from Jacaranda fruit

3.2.1 Composite properties

From the results obtained in Figure 4, it can be concluded that as the percentage of conventional gravel replaced by jacaranda gravel increases, there is a linear decrease in the density of the composites. This is because the density of the bioaggregate is lower than that of conventional aggregate. It can be seen that the composite treated with 25% replacement of conventional gravel with bioaggregate has a density around 6.9% lower than the reference composite. Comparing the 75% treatment composite with the reference, its density is 20.7% lighter.
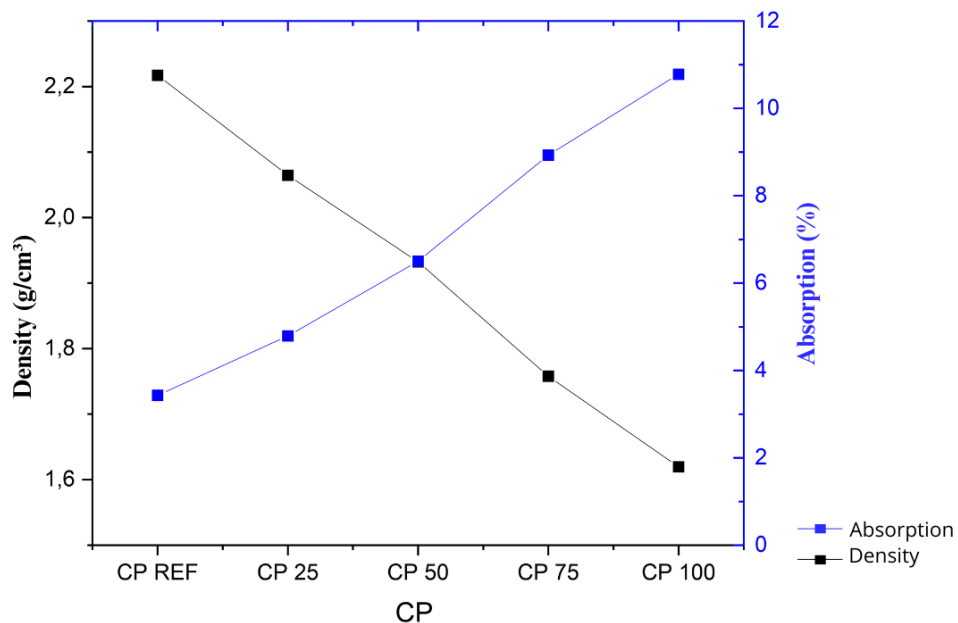
Figure 4. Density and water absorption of the composite.

It is clear that the greater the replacement of conventional aggregate with bioaggregate, the greater the water absorption capacity of this composite. The biomass water absorption test in Figure 2 reinforces the finding that the component responsible for water retention in the constituent materials of bioconcrete is the bioaggregate.

3.2.2 Mechanical properties

Figure 5 shows the average compressive strength of the concrete (at 28 days) of the reference specimens and those with levels of replacement of gravel by 25, 50, 75 and 100% of *Jacaranda cuspidifolia* bio-aggregates. As expected, there is a reduction in compressive strength when greater replacement of conventional aggregate by bio-aggregate is used.
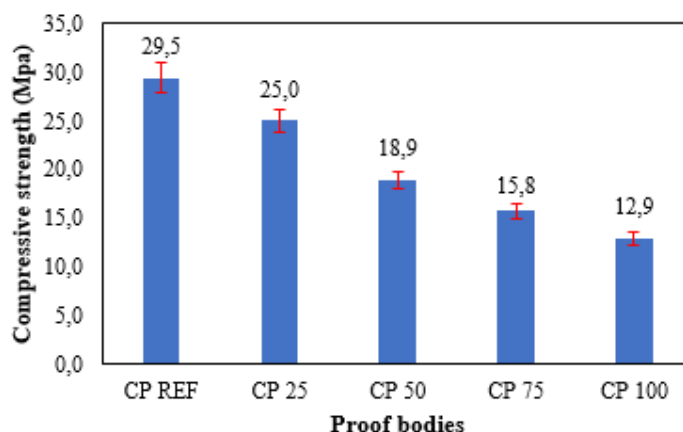
Figure 5. Compressive strength.

Using the ANOVA statistical methodology, it can be concluded that there is a significant difference in compressive strength between the quantities of materials replaced, p-value = 4.57794E-05 $< \alpha$ (0.05). Table 2 shows the results of the Tukey test for the REF, 25, 50, 75 and 100% treatments. It can be concluded that there were no differences in the results for the 25% concrete replacement treatment. That is, p=0.57915888 $> \alpha$ (0.05). On the other hand, the other treatments 50, 75 and 100% show a significant difference in compressive strength. Based on the results, we can conclude that with an increase in the percentage of bioaggregate in concrete, as a substitute for conventional gravel from rocks, there is a reduction in mechanical resistance to compression.

Table 2. Tukey test results for compressive strength.

group 1	group 2	mean	p-value	difference
Ref	Con_25%	4,438	0,57915888	NO SIGNIFICANCE
Ref	Con_50%	10,547	0,0127143	IT HAS SIGNIFICANCE
Ref	Con_75%	13,71	0,00092176	IT HAS SIGNIFICANCE
Ref	Con_100%	16,523	8,4243E-05	IT HAS SIGNIFICANCE

4. CONCLUSIONS

In order to obtain better mechanical performance, it is necessary to evaluate different percentages of jacaranda bio-aggregate. In this investigation, 25% jacaranda substitution provides a concrete that can be used for a structural element, since according to [36], for reinforced concrete structures, i.e. concrete with passive reinforcement, the minimum class is C20.

However, higher substitution levels of bio-aggregates other than those evaluated could have a positive and significant impact on compressive strength. Based on the results, we can conclude that increasing the percentage of bioaggregate in the concrete, as a substitute for conventional gravel from rocks, reduces the mechanical resistance to compression and consequently the density of the bioconcrete.

4.1. Declaration of Competing Interest

The authors declare the following financial interests/personal relationships that could be considered as potential competing interests: Selton Thiago Nunes Souza reports that financial support was provided by the Federal University of Lavras-MG.

5. REFERENCES

[1] SILVA, Maria Fernanda Felippe; ARAUJO, Camilla Kawane Ceciliano de Carvalho; PRATES, Glaucia Aparecida. Aplicação de ferramentas da qualidade para minimizar a porcentagem de defeitos em compósitos cimento-madeira. Revista Principia - Divulgação Científica e Tecnológica do IFPB, João Pessoa, mai. 2024. ISSN 2447-9187. Disponível em: <https://periodicos.ifpb.edu.br/index.php/principia/article/view/7424>. Acesso em: 03 Maio. 2024. (http://dx.doi.org/10.18265/2447-9187a2022id7424).

[2] KARADE, S. R. Cement-bonded composites from lignocellulosic wastes. Construction and building materials, v. 24, n. 8, p. 1323-1330, 2010. (https://doi.org/10.1016/j.conbuildmat.2010.02.003).

[3] TUOTO, M. Levantamento sobre a geração de resíduos provenientes da atividade madeireira e proposição de diretrizes para políticas, normas e condutas técnicas para promover o seu uso adequado. [s.d.]. (https://doi.org/10.5902/1980509835341).

[4] Indústria Brasileira de Árvores. (2017). IBA_RelatorioAnual2017. IBÁ.

[5] ZABALZA BRIBIÁN, I.; VALERO CAPILLA, A.; ARANDA USÓN, A. Life cycle assessment of building materials: Comparative analysis of energy and environmental impacts and evaluation of the eco-efficiency improvement potential. **Building and Environment**, v. 46, n. 5, p. 1133–1140, 1 maio 2011. (https://doi.org/10.1016/j.buildenv.2010.12.002).

[6] MERCADO: Perspectivas para o Setor de Agregados. In: ANEPAC (Brasil, São Paulo, São Paulo). Mercado: Perspectivas para o Setor de Agregados. São Paulo: Anepac, 2022. Disponível em: https://www.anepac.org.br/publicacoes/revista-areia-e-brita. Acesso em: 3 maio 2022.[7] PICANDET, V. Characterization of Plant-Based Aggregates. Em: **Bio-aggregate-based Building Materials**. [s.l.] John Wiley & Sons, Ltd, 2013. p. 27–74. (DOI:10.1002/9781118576809).

[8] Wu, Fan & Yu, Qingliang & Liu, Changwu. (2021). Durability of thermal insulating bio-based lightweight concrete: Understanding of heat treatment on bio-aggregates. Construction and Building Materials. 269. 121800. (DOI: 10.1016/j.conbuildmat.2020.121800).

[9] FREITAS, A. Á. D. et al. Bioconcreto: Uma revisão de sua aplicação na construção civil. **Research, Society and Development**,v.10,n.4,p.e37210414270, 14abr.2021.(https://doi.org/10.33448/rsd-v10i4.14270).

[10] Melo, G., & Andrade, D. E. (2021). *UTILIZAÇÃO DO ENDOCARPO DA MACAÚBA COMO AGREGADO GRAÚDO ALTERNATIVO PARA A PRODUÇÃO DE BIO-CONCRETO.*

[11] M'hamed Yassim Rajiv da Gloria. (2015). *DESENVOLVIMENTO E CARACTERIZAÇÃO DE PAIŃEIS SANDUÍCHES DECONCRETO COM N´UCLEO LEVE E FACES EM LEVE E FACES EM LAMINADOS REFORC̨ADOS COM FIBRAS LONGAS DE SISAL.*

[12] FERREIRA, S. R. et al. Influência de ciclos molhagem-secagem em fibras de sisal sobre a aderência com matrizes de cimento Portland. **Matéria (Rio de Janeiro)**, v. 17, n. 2, p. 1024–1034, 2012. (https://doi.org/10.1590/S1517-70762012000200008).

[13] ASSOCIAÇÃO BRASILEIRA DE NORMAS TÉCNICAS. **ABNT NBR 14853**: Madeira - Determinação do material solúvel em etanol-tolueno e em diclorometano e em acetona. Rio de Janeiro: ABNT,2010.

[14] ASSOCIAÇÃO BRASILEIRA DE NORMAS TÉCNICAS. **ABNT NBR 7989**: Pasta celulósica e madeira - Determinação de lignina insolúvel em ácido. Rio de Janeiro: ABNT,2010.

[15] ASSOCIAÇÃO BRASILEIRA DE NORMAS TÉCNICAS. **ABNT NBR 13999**: Papel, cartão, pastas celulósicas e madeira - Determinação do resíduo (cinza) após a incineração a 525 °C. Rio de Janeiro: ABNT,2017.

[16] BORGES, I. O. et al. Potencial de utilização de resíduos da cultura de soja tratados com água e hidróxido de sódio para produção de painéis aglomerados. **Research, Society and Development**, v. 11, n. 2, p.

e29511225762–e29511225762, 25 jan. 2022. (https://doi.org/10.33448/rsd-v11i2.25762).

[17] ASSOCIAÇÃO BRASILEIRA DE NORMAS TÉCNICAS. **ABNT NBR 7215**: Cimento Portland - Determinação da resistência à compressão de corpos de prova cilíndricos. Rio de Janeiro: ABNT,2019.

[18] ASSOCIAÇÃO BRASILEIRA DE NORMAS TÉCNICAS. **ABNT NBR 5739**: Concreto – Ensaio de compressão de corpos de prova cilíndricos. Rio de Janeiro: ABNT,2018.

[19] WONG, T. M.; LIM, S. C. **A dictionary of Malaysian timbers**. 2. ed ed. Kuala Lumpur: Forest Research Inst. Malaysia, 2002.

[20] WONG, M. C. et al. Grapevine waste in sustainable hybrid particleboard production. **Waste Management**, v. 118, p. 501–509, 1 dez. 2020. (https://doi.org/10.1016/j.wasman.2020.09.007).

[21] MIRANDA, E. H. Evaluation of the influence of the addition of bean residue in gypsum matrices. Clean Technologies and Environmental Policy 2022, [S. l.], v.1, p.1–11,2022. (DOI: 10.1007/S10098-022-02389-9).

[22] IWAKIRI, S.; TRIANOSKI, R. Painéis de madeira reconstituída. [s.l.]:Ajir Gráfica e Editora Ltda., 2020.

[23] LACERDA, M. DENSIDADE DOS MATERIAIS, 2024. (https://operaction.com.br/densidade-dos-materiais/). Acesso em: 04 dezembro de 2023.

[24] SANTOS, C. A. DOS et al. Utilização da madeira de Pinus oocarpa e Coffea arábica para a produção de painéis de partículas orientadas (OSB). Research, Society and Development, v. 11, n. 3, p. e40611326795–e40611326795, 9 mar. 2022. (http://dx.doi.org/10.33448/rsd-v11i3.26795).

[25] SOARES, S. et al. Valorização do bagaço de cana-de-açúcar na produção de painéis aglomerados de baixa densidade. Revista Ciência da Madeira - RCM, v. 8, p. 64–73, 5 maio 2017.(DOI: 10.12953/2177-6830/rcm.v8n2p64-73).

[26] SCATOLINO, M. V. et al. Eucalyptus wood and coffee parchment for particleboard production: Physical and mechanical properties. Ciência e Agrotecnologia, v. 41, p. 139–146, abr. 2017. (https://doi.org/10.1590/1413-70542017412038616).

[27] DE ARAÚJO VELOSO, M. C. R. et al. Sustainable valorization of recycled low-density polyethylene and cocoa biomass for composite production. Environmental Science and Pollution Research, v. 28, n. 25, p. 32810–32822, 1 jul. 2021. (DOI: 10.1007/S11356-021-13061-Y/FIGURES/6).

[28] GOMES, D. A. C. et al. VIABILIDADE DE COMPÓSITOS POLIMÉRICOS DE POLIPROPILENO REFORÇADOS COM FIBRA DE BAMBU. Revista Brasileira de Engenharia de Biossistemas, v. 15, n. 4, p. 511–522, 29 nov. 2021. (http://dx.doi.org/10.18011/bioeng2021v15n4p511-522).

[29] SCATOLINO, M. V. et al. Use of maize cob for production of particleboard. Ciência e Agrotecnologia, v. 37, p. 330–337, ago. 2013. (DOI: 10.1590/S1413-70542013000400006).

[30] JUNIOR, J. B. G. et al. Inclusão de resíduo da cultura de sorgo em painéis aglomerados de eucalipto. Pesquisa Florestal Brasileira, v. 36, n. 88, p. 435–442, 30 dez. 2016. (https://doi.org/10.4336/2016.pfb.36.88.1036).

[31] KIM, Y.-H. et al. Quantitative Measurement of Water Absorption of Coarse Lightweight Aggregates in Freshly-Mixed Concrete. International Journal of Concrete Structures and Materials, v. 14, n. 1, p. 34, 14 jul. 2020. (https://doi.org/10.1186/s40069-020-00408-x).

[32] SUPIAN, A. B. M. et al. Mechanical and physical performance of date palm/bamboo fibre reinforced epoxy hybrid composites. Journal of Materials Research and Technology, v. 15, p. 1330–1341, 1 nov. 2021. (https://doi.org/10.1016/j.jmrt.2021.08.115).

[33] CANGUSSU, L. et al. Chemical Characterization of Coffee Husks, a By-Product of Coffea arabica Production. Foods, v. 10, p. 3125, 16 dez. 2021. (DOI:10.3390/foods10123125).[34] BELL, G. M. M. et al. Study of calcium silicate hydrates by solid state high resolution 29Si nuclear magnetic resonance. Advances in Cement Research, v. 3, n. 9, p. 23–27, jan. 1990. (https://doi.org/10.1680/adcr.1990.3.9.23).

[35] MIRANDA, E. H. DE N. et al. Efeito de diferentes espécies de madeira e bambu na hidratação de matrizes à base de cimento Portland. Matéria (Rio de Janeiro), v. 27, p. e20220194, 4 nov. 2022. (https://doi.org/10.1590/1517-7076-RMAT-2022-0194).

[36] ASSOCIAÇÃO BRASILEIRA DE NORMAS TÉCNICAS. **ABNT NBR 6118**: Projeto de estruturas de concreto – Procedimento. Rio de Janeiro: ABNT,2023.

INFLUENCE OF PLY STACKING SEQUENCE ON MECHANICAL PROPERTIES OF HYBRID NATURAL FIBRE/EPOXY COMPOSITE LAMINATES

R. A. A. Junior[a], H.F.M. de Queiroz[b], M.D. Banea[c]*

(a) 0009-0003-7750-2930 (Federal Center for Technological Education Celso Suckow da Fonseca – Brazil)
(b) 0000-0003-1726-2659 (Federal Center for Technological Education Celso Suckow da Fonseca - Brazil)
(c) 0000-0002-8378-2292 (Federal Center for Technological Education Celso Suckow da Fonseca – Brazil)
* Corresponding author: mdbanea@gmail.com

CODE: BCCM7-87

Keywords: Natural fibres, flax fibre, hybrid composites, mechanical properties.

Abstract: This study investigated the impact of fiber hybridization on the mechanical performance of Natural Fiber Reinforced Composites (NFRCs). Bidirectional jute, unidirectional flax (UD) and flax twill fabrics were used. The NFRCs were manufactured by compression molding with a two-component epoxy resin serving as the matrix. Flax fabric (UD or twill) formed the outer layer in hybrid composites, while the core was formed by bidirectional jute. Nine types of composite architectures were manufactured and tested: neat jute, neat UD flax, neat flax twill, six hybrid cases each with a core of 5 layers of bidirectional jute wrapped symmetrically by 1, 2 and 3 layers of UD flax and flax twill. The study examined the effect of hybridization by increasing the number of outer layers in the composites through uniaxial tensile tests. The results revealed that the addition of external layers in hybrid jute and flax twill composites resulted in slight improvement in the mechanical properties of the composite. Furthermore, hybrid composites with UD flax outer layers exhibited the highest tensile strength and Young's modulus, which was due to the superior properties of UD flax fibers.

1. INTRODUCTION

In several industrial sectors the demand for more environmentally sustainable materials with reduced carbon footprint and more recyclability has grown increased interest over the last decades. In this context, studies on natural fibre-reinforced composites (NFRCs) have been the focus of recent research, showing promising outcomes as greener alternatives that mitigate the carbon footprint and present commendable mechanical properties. Furthermore, NFRCs have also been the focus of several industrial sectors, such as automotive, sport and others [1-3].

Natural fibres, such palm, kenaf, hemp, flax, ramie, sisal, curauá, jute, and others have several advantages including abundance, commercial availability in various types, lower production costs in general, biodegradability, recyclability, and low specific weight and as reinforcement of polymeric-based composite, they can show interesting specific mechanical properties. However, compared to synthetic fibres (e.g., glass, carbon, Kevlar, etc.), natural fibres have some drawbacks such as high susceptibility to moisture and degradation, lower temperature resistance, and variation in mechanical properties [4]. Thus, this limits the large-scale industrial application and applications such as structures. Researchers have employed various techniques as a way to overcome these drawbacks and reach natural fibre-reinforced composites with specific mechanical properties suitable for the project, such as: surface treatments of natural fibers and hybridization technique [5-7].

The hybridization technique consists of using one or more types of reinforcement fiber (synthetic and/or natural) in different configurations (i.e., interlaminar and/or intralaminar). Among the techniques, hybridization, both intralaminar and interlaminar, has shown to be the most promising and effective with the

aim of improving mechanical properties in composites in different configurations (i.e., natural/natural and natural/synthetic). As a result, extensive research efforts are focused on developing hybrid composites by stacking different natural fibers with different properties, resulting in a material with increased mechanical performance [7-9].

Among natural fibres, flax has been gaining prominence in the global market due to properties such as high mechanical strength and stiffness, modulus of elasticity, industrial production ensuring fibre quality, and industrial scalability [10, 11]. These attributes make flax a promising reinforcement in hybrid composites. Additionally, jute emerges as a feasible alternative due to its wide availability, good cost-effectiveness, and adequate mechanical properties [12]. Based on this, many researchers have studied the influence of hybridization on the mechanical performance of hybrid composites with flax fibers and other natural fibers. Several researchers investigated the mechanical properties of hybrid composites by varying several parameters such as the lamination sequence [13, 14] fabric and fiber types [15, 16], fiber treatments [17], manufacturing method [18, 19], among others. For instance, Vincenzo and Luigi [13] studied the quasi-static and dynamic response of epoxy-based composites reinforced with flax and jute. The stacking sequence of pure fabric composites (i.e. pure jute and pure flax) and hybrid composites of the two fibers was evaluated. A surface treatment of the fibers with sodium bicarbonate solution was also carried out in order to improve the fiber-matrix interface. It was found that the hybridization made it possible to achieve mechanical properties intermediate between those of monolithic composites. In addition, they found that the surface treatment had little beneficial effect on the mechanical properties of the composites [13]. Amal, Vishnu and Manesh [14] evaluated the effect of stacking sequence order and hybridization on the mechanical and water properties of woven flax/bamboo composites using epoxy as matrix. The stacking sequence is varied as follows: B/F/F/B, F/B/B/F, F/B/F/B, F/F/B/B. The authors concluded that the optimal stacking order with maximum performance is obtained for B/F/F/B. The increase in tensile, flexion, impact and ILSS values is observed by 8.3%, 25%, 4.4% and 14.6%, respectively. Furthermore, a numerical model for interlaminar shear strength was developed to assist in critical stress analyses.

Mohsin Ejaz et al studied jute and flax fiber composites using PLA as a matrix. The hot compression molding manufacturing method was used to manufacture pure jute and flax composites, and hybrid flax/jute composites. Tensile and impact tests were carried out on the composites, and it was observed that maximum tensile values were obtained for 40% fiber weight. The tensile strength of PLA/flax composites was higher than that of PLA/jute composites and hybrid composites. The hybrid composites also exhibited better interfacial properties. Finally, hybrid composites can absorb more impact energy due to the higher coefficient of friction between different fibers and improved interfaces. The weight loss of the composites as a result of burial in the soil shows that the composites are biodegradable [20].

Although there are several studies on hybrid composites of flax fiber with other natural fibers, there is still a need for further investigations involving hybrid flax/jute composites in different manufacturing configurations, with different fabrics and different applied stresses. Therefore, the primary objective of this study was to experimentally investigate the mechanical behavior of hybrid polymer composites reinforced with flax and jute natural fibers. Mechanical characterization of 11 layers composites of unidirectional flax, twill flax, and jute composites was performed. In addition, the mechanical characterization of hybrid composites was carried out maintaining a jute fabric core with 5 layers and using outer skin layers of high-strength unidirectional or twill flax. The effect of number of layers was studied by testing the composite specimens through tensile tests according to ASTM D3039/D3039M standard.

2. METHODOLOGY

2.1. Materials

Unidirectional flax fabric, 2/2 twill flax fabric and bidirectional jute fabric were used as reinforcements. The unidirectional flax fabrics (300g/m²) and twill 2/2 (200g/m²) were supplied by BComp (Fribourg, Switzerland), and the jute fabric (T10, 248g/m²) was supplied by SisalSul (São Paulo, Brazil). For the manufacture of the composites, a two-component epoxy resin system, HEX 135 SLOW, supplied by Barracuda Advanced Composites (Rio de Janeiro, Brazil), was used as matrix. The mechanical properties of the resin used are described in Table 1.

Table 1. Mechanical properties of the resin used [21].

Polymer	Tensile Strength (MPa)	Young's modulus (GPa)	Tensile Strain (%)
HEX 135 SLOW	60.92 ± 1.42	3.25 ± 0.01	3.20 ± 0.20

2.2. Manufacturing of composites

The composite plates were fabricated via compression molding. Curing was done for 8 hours at 75°C according to the resin manufacturer's recommendations and was performed in a heated plate hydraulic press, Solab SL-20 (São Paulo, Brazil). The HEX 135 SLOW was used in a 100/33 resin/hardener weight ratio. Fig. 1 illustrates the steps of manufacturing. Step I show the fiber fabrics used cut to dimensions of 220 x 150 mm² (length x width). Subsequently, in step II, hand lay-up was carried out, where the layer of fiber fabric was placed on a metallic mold and the resin was smooth applied and spread using a roller. This procedure was repeated until all fabrics layers were embedded in resin. Metal spacers, silicone and adhesive tape were used to control the thickness and avoid the formation of bubbles inside the plates. Then, as can be seen in step III, the metallic mold, with the layers of laminated fibers, was placed in the heated hydraulic press. To cure the resin, a pressure of approximately 30 MPa was used for 8 hours at a temperature of 75°C. After the curing process, the composite plates were allowed to cool under pressure. Lastly, after the curing process, the finished composite plates were removed from the press and marked for subsequent cutting of the specimens, as can be seen in step IV.
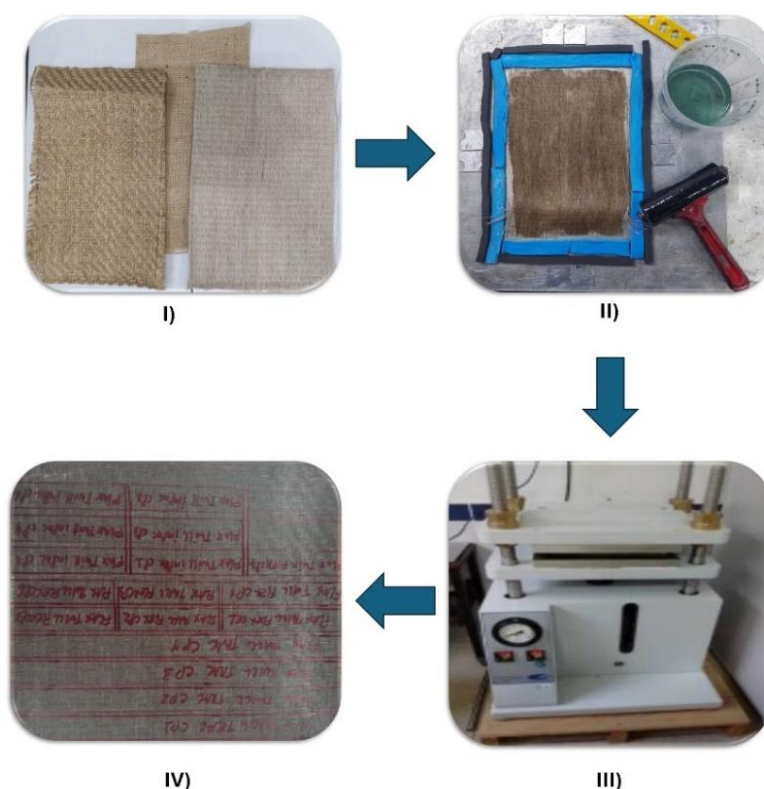
Figure 1. Steps of manufacturing composites plates.

Nine different types of composite plates were manufactured. All the hybrid composites were fabricated with a core of 5 layers of jute bidirectional fabrics and the flax fiber layers were placed symmetrically on the outer skin surfaces with 1, 2 and 3 layers. The neat composites were fabricated with 11 layers of jute bidirectional fabric (J), unidirectional flax fabric (UD) and 2/2 twill fabric (T). For more details about composite names, number of layers, lamination sequence, total fiber-weight fraction, and thickness of each plate see Table 2. The subscript number accompanying each type of fiber (i.e., J, UD, and T) in the stacking sequence column represents the number of layers of that same fabric.

Table 2. Details of the composites.

Composite Name	Stack sequence1	Total fiber-weight fraction (%)	Thickness (mm)
Neat Jute	J_{11}	50.6	5.4
Neat Flax UD	UD_{11}	62	3.1
F-UD1	$UD_1 - J_5 - UD_1$	48	3.5
F-UD2	$UD_2 - J_5 - UD_2$	54	3.7
F-UD3	$UD_3 - J_5 - UD_3$	55	4.0
Neat Flax Twill	T_{11}	58	2.8
F-Twill1	$T_1 - J_5 - T_1$	50	3.1
F-Twill2	$T_2 - J_5 - T_2$	50	3.5
F-Twill3	$T_3 - J_5 - T_3$	52	3.9

[1]J = jute fabric; UD = unidirectional flax fiber fabric; T = 2/2 twill flax fiber fabric.

After manufacturing the composite plates, the specimens were cut using a mini circular saw. The geometry of the specimens followed the ASTM D3039 standard for tensile tests.

2.3. Measurements and characterization

Tensile tests were carried out in accordance with the ASTM D3039 standard, using a 10kN load cell and a crosshead speed of 1 mm/min, on an Instron®5966 universal testing machine (Norwood, MA, USA), located in the LADES/CEFET-RJ laboratory. Fig. 2 illustrates the configuration used to carry out the tensile tests. At least four specimens from each plate were tested, and the average values of the results were used in the calculations of properties and plotting of graphs. All tests were carried out at room temperature (25°C).

Figure 2. Tensile tests set-up.

3. RESULTS AND DISCUSSION

The representative tensile stress-strain curves for all specimens as a function of layers number for the composites reinforced with UD (unidirectional) and 2/2 twill flax fibers fabrics are illustrated in Fig. 3. It can be seen that the specimens generally present brittle behavior. The deformation until failure varied little when comparing the neat and hybrid composites.
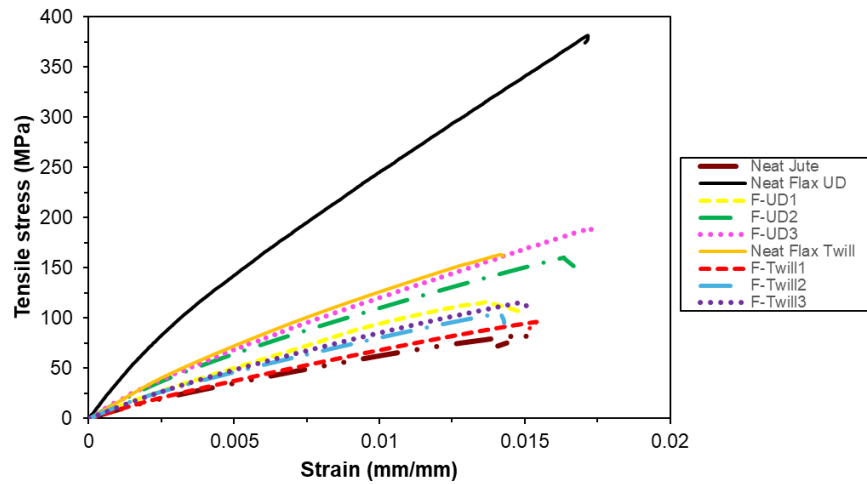
Figure 3. Representative tensile stress-strain curves as a function of composite architecture.

(a)

(b)
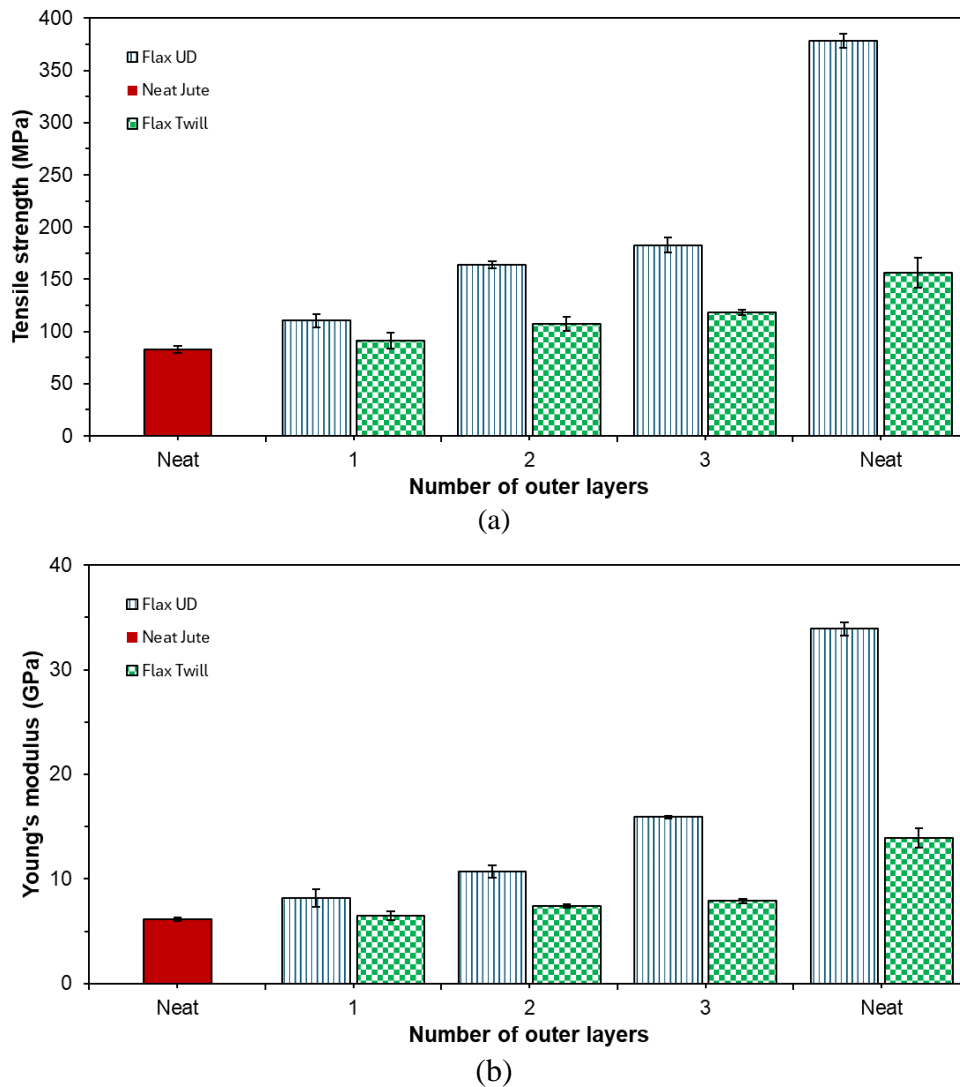
Figure 4. Tensile strength (a) and modulus (b) as a function of number of outer layers.

The tensile data is shows in Fig. 4 (a) and (b) and Table 3. It's possible to observe that the Neat Flax UD presents the highest tensile strength value among all cases (i.e., neat and hybrids) [22]. When comparing the UD flax hybrid composites with the Neat Jute composite, there is a trend of improvement with the increase in the number of layers of UD flax. For instance, for the cases F-UD1, F-UD2, and F-UD3, there were

improvements of approximately 25%, 49%, and 55% in tensile strength, respectively. Meanwhile, for the cases F-Twill1, F-Twill2, and F-Twill3, it is noticeable that the increase in the number of layers of flax twill resulted in a slightly lower improvement in tensile strength, with approximate values of 9%, 23%, and 30%, respectively. The tensile strength values obtained for the Neat UD flax composite specimens are consistent with the literature [10, 23-25]. It is evident that the hybrid UD flax composites with 2 and 3 layers exhibit superior tensile strength compared to the pure flax twill. This behavior becomes interesting as a design factor for structures composed of these fibers.

Fig. 4 (b) presents the stiffness of the composites. Using the pure jute composite as a reference, it becomes clear that increasing the number of layers of UD flax in the hybrid composites provided a greater increase in stiffness compared to the cases of twill flax hybrid composites. For example, for the best UD flax composite, F-UD3, the increase was approximately 61%, while the best twill flax case, F-Twill3, showed an increase of only about 22%. Another important point is that adding 1 layer of flax twill to a jute core does not present a significant improvement. Furthermore, the increase in stiffness provided by 2 outer layers of twill flax is similar to that of 3 layers, this data should be taken into account in structural projects that may use this lamination configuration.

Finally, from Table 3, it can be observed that the strain at rupture of the specimens did not show significant variation depending on the hybridization or number of layers. This is because the core material, jute fiber, is more brittle than the outer layers (flax), and it controls the deformation until failure [26].

Table 3. Tensile test data as function of composite architecture and number of outer layers.

Composite type	Tensile strength (MPa)	Young's modulus (GPa)	Strain (mm/mm)
Neat Jute	82.56 ± 3.58	6.12 ± 0.16	0.017 ± 0.005
F-UD1	110.39 ± 6.50	8.15 ± 0.85	0.015 ± 0.001
F-UD2	163.65 ± 3.45	10.69 ± 0.61	0.017 ± 0.001
F-UD3	182.48 ± 7.13	15.91 ± 0.15	0.016 ± 0.001
Neat Flax UD	378.43 ± 6.48	33.89 ± 0.62	0.017 ± 0.001
F-Twill	91.34 ± 7.86	6.47 ± 0.41	0.015 ± 0.003
F-Twill2	107.13 ± 6.73	7.42 ± 0.18	0.015 ± 0.001
F-Twill3	117.98 ± 2.66	7.88 ± 0.20	0.016 ± 0.001
Neat Flax Twill	156.42 ± 14.38	13.92 ± 0.96	0.017 ± 0.001

4. CONCLUSIONS

This study investigated the influence of fiber hybridization on the mechanical properties of NFRCs. Bidirectional jute, unidirectional (UD) flax, and twill flax fabrics were used as reinforcements, and a two-component epoxy resin was used as the matrix to fabricate the neat and hybrid composites. After testing, it was revealed that the addition of external layers to hybrid composites resulted in varying impacts on mechanical properties. Notably, hybrid composites with UD flax outer layers exhibited superior tensile strength and Young's modulus compared to those with twill flax outer layers. For example, samples reinforced with 3 layers of flax, i.e. F-UD3 and F-Twill3, achieved tensile strengths of 182.48 MPa and 117.98 MPa, respectively. This represents an improvement, compared to the pure jute composite sample, of 61% and 22%, respectively. The results revealed that hybridization with unidirectional flax outer layers resulted in a greater improvement in the mechanical properties of the hybrid composite compared to twill flax, and this is due to the high mechanical properties of UD flax fibers.

4.1. Declaration of Competing Interest

The authors declare no conflict of interest.

4.2. Fundings

5. REFERENCES

[1] JJ Andrew and Dhakal HN. Sustainable biobased composites for advanced applications: recent trends and future opportunities – A critical review. *Composites Part C: Open Access,* 7, 2022. (https://doi.org/10.1016/j.jcomc.2021.100220).

[2] P Jagadeesh, et al. Recent developments and challenges in natural fiber composites: A review. *Polymer Composites,* 43, 2022. (https://doi.org/10.1002/pc.26619).

[3] M Li, et al. Recent advancements of plant-based natural fiber–reinforced composites and their applications. *Composites Part B: Engineering,* 200, 2020. (https://doi.org/10.1016/j.compositesb.2020.108254).

[4] J Neto, et al. A Review of Recent Advances in Hybrid Natural Fiber Reinforced Polymer Composites. *Journal of Renewable Materials,* 10, 2022. (https://doi.org/10.32604/jrm.2022.017434).

[5] JSS Neto, et al. Effect of chemical treatment on the thermal properties of hybrid natural fiber-reinforced composites. *Journal of Applied Polymer Science,* 136, 2019. (https://doi.org/10.1002/app.47154).

[6] MD Banea, Neto JSS, and Cavalcanti DKK. Recent Trends in Surface Modification of Natural Fibres for Their Use in Green Composites. In: Green Composites (Thomas S. and Balakrishnan P.), 1st Edition, 2021. Springer Singapore. (https://doi.org/10.1007/978-981-15-9643-8_12)

[7] DKK Cavalcanti, et al. Mechanical characterization of intralaminar natural fibre-reinforced hybrid composites. *Composites Part B: Engineering,* 175, 2019. (https://doi.org/10.1016/j.compositesb.2019.107149).

[8] AL Pereira, Banea MD, and Pereira AB. Effect of intralaminar hybridization on mode I fracture toughness of natural fiber-reinforced composites. *Journal of the Brazilian Society of Mechanical Sciences and Engineering,* 42, 2020. (https://doi.org/10.1007/s40430-020-02525-w).

[9] H Fernandes Medeiros de Queiroz, et al. The effect of multiscale hybridization on the mechanical properties of natural fiber-reinforced composites. *Journal of Applied Polymer Science,* 138, 2021. (https://doi.org/10.1002/app.51213).

[10] MZ Rahman. Mechanical and damping performances of flax fibre composites – A review. *Composites Part C: Open Access,* 4, 2021. (https://doi.org/10.1016/j.jcomc.2020.100081).

[11] Z Mahboob, et al. Tensile and compressive damaged response in Flax fibre reinforced epoxy composites. *Composites Part A: Applied Science and Manufacturing,* 92, 2017. (https://doi.org/10.1016/j.compositesa.2016.11.007).

[12] MA Ashraf, et al. Jute Based Bio and Hybrid Composites and Their Applications. *Fibers,* 7, 2019. (https://doi.org/10.3390/fib7090077).

[13] V Fiore and Calabrese L. Effect of Stacking Sequence and Sodium Bicarbonate Treatment on Quasi-Static and Dynamic Mechanical Properties of Flax/Jute Epoxy-Based Composites. *Materials,* 12, 2019. (https://doi.org/10.3390/ma12091363).

[14] A Alliyankal Vijayakumar, Prasad V, andKailathuvalappil Kochunny M. Investigation on the effect of stacking order and hybridization on mechanical and water absorption properties of woven flax/bamboo composites. *Polymer Composites,* 43, 2022. (https://doi.org/10.1002/pc.26808).

[15] S Aldroubi, et al. Multi-scale investigation of morphological, physical and tensile properties of flax single fiber, yarn and unidirectional fabric. *Composites Part B: Engineering,* 259, 2023. (https://doi.org/10.1016/j.compositesb.2023.110732).

[16] F Omrani, et al. Mechanical properties of flax-fibre-reinforced preforms and composites: Influence of the type of yarns on multi-scale characterisations. *Composites Part A: Applied Science and Manufacturing,* 93, 2017. (https://doi.org/10.1016/j.compositesa.2016.11.013).

[17] I Van de Weyenberg, et al. Influence of processing and chemical treatment of flax fibres on their composites. *Composites Science and Technology,* 63, 2003. (https://doi.org/10.1016/S0266-3538(03)00093-9).

[18] M Shamsuyeva, Hansen O, andEndres H-J. Review on Hybrid Carbon/Flax Composites and Their Properties. *International Journal of Polymer Science,* 2019, 2019. (https://doi.org/10.1155/2019/9624670).

[19] B Karaçor, Özcanlı M, and Serin H. The influence of hybridization and different manufacturing methods on the mechanical properties of the composites reinforced with basalt, jute, and flax fibers. *Iranian Polymer Journal,* 33, 2024. (https://doi.org/10.1007/s13726-023-01255-9).

[20] M Ejaz, et al. Mechanical and Biodegradable Properties of Jute/Flax Reinforced PLA Composites. *Fibers and Polymers,* 21, 2020.(https://doi.org/10 .1007/s12221-020-1370-y).

[21] J Neto, et al. Analysis of mechanical and thermal properties of epoxy multiwalled carbon nanocomposites. *Journal of Composite Materials,* 54, 2020. (https://doi.org/10.1177/00219983209392).

[22] A Alipour and Jayaraman K. Performance of Flax/Epoxy Composites Made from Fabrics of Different Structures. *Fibers,* 12, 2024. (https://doi.org/10.3390/fib12040034).

[23] A Monti, et al. Mechanical behaviour and damage mechanisms analysis of a flax-fibre reinforced composite by acoustic emission. *Composites Part A: Applied Science and Manufacturing,* 90, 2016. (https://doi.org/10.1016/j.compositesa.2016.07.002).

[24] G Coroller, et al. Effect of flax fibres individualisation on tensile failure of flax/epoxy unidirectional composite. *Composites Part A: Applied Science and Manufacturing,* 51, 2013. (https://doi.org/10.1016/j.compositesa.2013.03.018).

[25] A Moudood, et al. Environmental effects on the durability and the mechanical performance of flax fiber/bio-epoxy composites. *Composites Part B: Engineering,* 171, 2019. (https://doi.org/10.1016/j.compositesb.2019.05.032).

[26] H de Queiroz, Banea M, and Cavalcanti D. Experimental analysis of adhesively bonded joints in synthetic- and natural fibre-reinforced polymer composites. *Journal of Composite Materials,* 54, 2020. (10.1177/0021998319876979).

ACCELERATED CARBONATION IN ADOBE BRICKS MADE WITH PULP AND PAPER MILL SLUDGE AND PIASSAVA FIBERS

Cristian C. Gomes [a], Gustavo L. Calegaro [b], Gabriel L. Insaurriaga [c], Rafael A. Delucis [d], *

(a) 0000-0002-5808-7861 (Federal University of Pelotas – Brazil)
(b) 0009-0004-7050-3129 (Federal University of Pelotas – Brazil)
(c) 0009-0009-7622-0812 (Federal University of Pelotas – Brazil)
(d) 0000-0002-3657-9216 (Federal University of Pelotas – Brazil)
* Corresponding author: rafael.delucis@ufpel.edu.br

Abstract: The utilization of pulp and paper mill sludge contributes significantly to environmental sustainability by effectively reducing waste and offers substantial economic benefits through the repurposing of a by-product that would otherwise necessitate disposal. Adobe bricks are increasingly gaining traction in academia and are poised to be more widely utilized, especially in countries like Brazil, where there exists a significant housing deficit. This study investigates the accelerated carbonation process in adobe bricks by incorporating pulp and paper mill sludge as a partial replacement for clay. Two different carbonation durations (8 and 24 hours) were tested, while the piassava fiber content was kept constant at 3% and acted as a reinforcement. The study demonstrates gains in mechanical properties (compression and bending) due to the incorporation of sludge and subsequent carbonation. Results indicated that there was no range of apparent density values among the studied adobe bricks, even for those bricks subjected to carbonation. These findings highlight the potential of utilizing pulp and paper mill sludge in adobe brick production to enhance properties through accelerated carbonation, offering sustainable solutions for construction materials.

1. INTRODUCTION

In the contemporary construction landscape, the quest for sustainable building materials has gained significant attention, driven by a heightened awareness of the environmental impacts associated with traditional practices. Particularly, the construction industry's substantial carbon dioxide emissions have prompted a reevaluation of conventional materials like concrete and fired clay bricks, leading to a renewed interest in ancient construction techniques such as adobe brick production.

Adobe bricks, composed of a blend of clay matrix, water, coarse sand, and plant fibers, have emerged as a frontrunner in sustainable construction due to their low environmental footprint. Unlike conventional bricks, adobes achieve desired performance parameters like compression strength and water absorption without requiring energy-intensive thermal treatments. Additionally, their proven durability has solidified their status as a viable and eco-conscious choice in contemporary architecture.

However, despite their advantages, adobe bricks often exhibit limitations in mechanical properties such as high water affinity, brittle behavior, and relatively low compressive and tensile strengths. To address these challenges and bolster the overall quality and durability of adobe bricks, researchers have proposed various strategies.

Studies have explored the incorporation of alternative aggregates and additives sourced from renewable resources and waste materials. Joshi et al. [1] and Trang et al. [2] investigated the use of construction and demolition waste, as well as sludge from industrial processes, to enhance adobe brick characteristics. Similarly, Babé et al. [3] and Muñoz et al. [4] explored the benefits of incorporating agricultural waste and

softwood pulp fibers, respectively, in improving adobe brick performance. Furthermore, Ashour et al. [5] demonstrated the positive impact of wheat and barley straw fibers on the thermal properties of adobe bricks. These studies collectively underscore the potential of leveraging natural and waste-derived materials to augment the mechanical integrity of adobe bricks, thereby advancing their suitability as sustainable construction materials.

One promising avenue for enhancing adobe brick properties is accelerated carbonation, a technique widely employed in the treatment of concrete. By subjecting adobe bricks to accelerated carbonation, chemical reactions occur between clay minerals and calcium-containing compounds, resulting in the formation of calcium carbonate within the material. This process effectively fills pores and cracks, leading to improvements in mechanical strength and durability.

In line with these advancements, the present study aims to further enhance the mechanical properties of piassava fiber-reinforced adobe bricks by incorporating lime sludge and hydrated lime. Through accelerated carbonation tests conducted over varying exposure durations, the research seeks to evaluate the efficacy of these modifications in enhancing mechanical strength and durability. By contributing to the ongoing development of sustainable building materials with superior mechanical performance, this study aligns with the imperative to adopt eco-friendly construction solutions in the modern urban environment.

2. METHODOLOGY

2.1. Materials

The piassava fibers utilized in this study were obtained from a vendor in Ilhéus, Brazil, and stored in controlled conditions until reaching stable moisture levels. These fibers, with an average diameter of 400 μm, were trimmed to a length of 3 cm for effective blending with clay and sand components, following established guidelines from previous research. Natural clay sourced from a ceramics workshop in Pelotas, Brazil, underwent drying and milling processes before being sifted through a mesh #2 sieve. The milled clay particles passing through this sieve were selected for further use. Quartz-based sand from a local quarry in Pelotas, Brazil, underwent drying and sieving, with the portion passing through a mesh #4.8 sieve selected for experimentation. Lime sludge, sourced from CMPC Celulose Rio-Grandense, a company in southern Brazil, is a by-product of the causticizing stage in pulp production. After undergoing separation and purification processes, this residue is repurposed as a soil acidity corrector. The procedure for handling the lime sludge upon arrival mirrored that for the clay.

2.2. Manufacture of the adobe bricks Characterization of the adobe bricks

The adobe bricks were produced according to the optimal chemical composition recommended by Vasić et al. [6], maintaining a balanced weight ratio of sand to clay at 4:6. In some instances, clay was substituted with lime sludge or hydrated lime, comprising 20% of the clay's weight. Piassava fibers and water were uniformly incorporated at 3% and 20% by weight, respectively. For manufacturing, natural fibers underwent a soaking process until reaching a stabilized weight gain of approximately 120%. These saturated fibers were then introduced into the material mixture, with the absorbed water deducted from the overall water content. Subsequently, the raw materials were thoroughly mixed using a laboratory mortar mixer and poured into wooden molds. To ensure a dense structure and prevent the formation of internal voids, the molds were subjected to two cycles of dynamic vibration, each lasting 30 seconds. To mitigate water loss during molding, the internal surfaces of the molds were pre-coated with dampened sand. Following molding, certain specimens underwent accelerated carbonation for durations of 8 hours and 24 hours. This process occurred within a controlled environment with saturated carbon dioxide (CO_2), maintained at a temperature of 20 °C and a humidity level of 75% RH. This methodology was adapted from Tonoli et al. [7].

2.3. Characterization of the adobe bricks

For each experimental group, three rectangular adobe bricks measuring 50 mm in length were subjected to compressive strength analysis. To determine the apparent density of these bricks, a digital caliper and precision scale were employed. To ensure accurate load and displacement measurements while minimizing surface irregularities' influence, both the top and bottom surfaces were coated with a 3 mm layer of cement paste. The compression testing procedure commenced with a pre-load of 1 kN, followed by a gradual application of load at a cross-head speed of 0.01 mm/s until failure occurred. Additionally, each group included three prismatic specimens sized at 50 mm × 50 mm × 200 mm, which underwent three-point bending tests

with a span of 150 mm and a test speed of 0.01 mm/s. Mechanical testing was conducted using an Emic DL-30000 universal testing machine.

3. RESULTS AND DISCUSSION

The apparent density values of the adobe bricks, ranging from 1,500 to 2,100 kg/m³, indicated consistent characteristics across various formulations and carbonation durations. While minor fluctuations were observed, particularly with the control bricks exhibiting slightly higher densities, these variations were not deemed significant. Such nuances in apparent density may stem from intricate interactions within the brick matrix during the manufacturing process, influenced by factors like the reaction kinetics of lime-based compounds with water and the evaporation of moisture during accelerated carbonation processes [4].
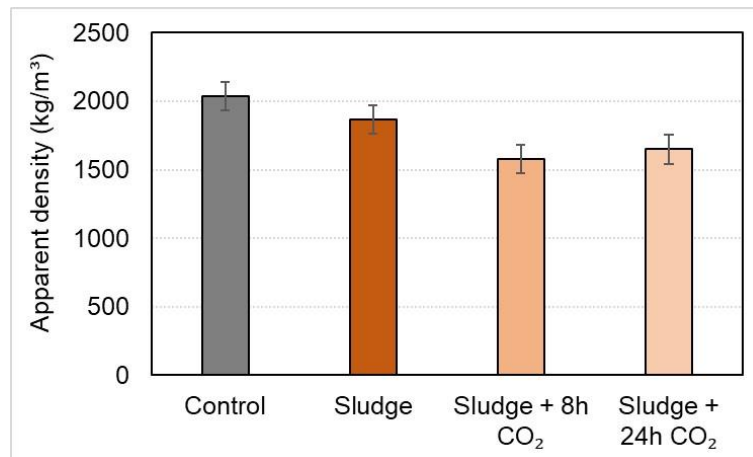
Figure 1. Apparent density of adobe bricks.

Compression testing unveiled standard behaviors, including elastic deformation, peak stress points, and eventual rupture, aligning with patterns observed in analogous studies focusing on natural fiber-reinforced earth-based composites [8]. Incorporating lime sludge resulted in marginal reductions in compressive strength, attributed to impurities like silica and iron oxides within the sludge composition [1]. Intriguingly, bricks subjected to carbonation following lime sludge integration displayed noteworthy strength enhancements, reaching up to 180%, regardless of the duration of carbonation. However, similar improvements were not evident in bricks incorporating hydrated lime [2].
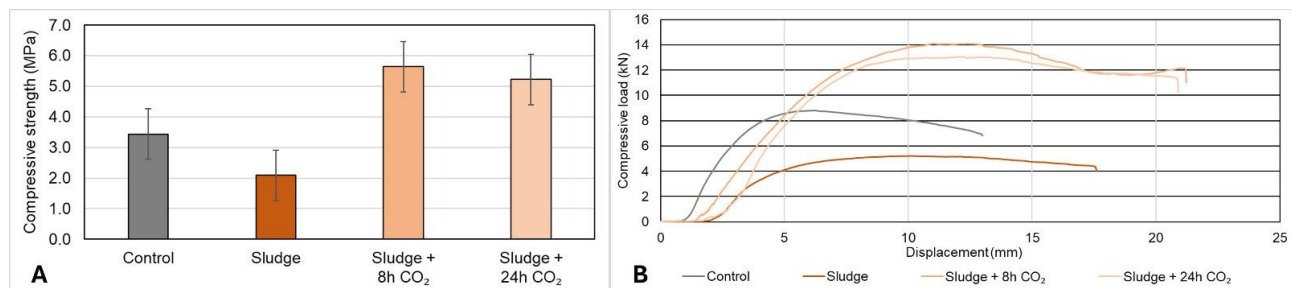
Figure 2. Compressive strength (A) and representative bending curves (B) of adobe bricks.

Bending tests offered insights into the mechanical behavior of the bricks, showcasing substantial strength gains ranging from 250% to 350% for bricks incorporating lime sludge and undergoing carbonation [3,5]. Notably, bricks carbonated for 24 hours exhibited superior strength compared to those carbonated for 8 hours, underscoring the time-dependent aspect of the carbonation process. Moreover, these carbonated bricks demonstrated increased displacement before failure, indicative of enhanced ductility. These enhancements were attributed to chemical reactions between ions present in lime sludge and CO_2 during carbonation, leading to the formation of stable compounds such as metakaolin and calcium silicates.
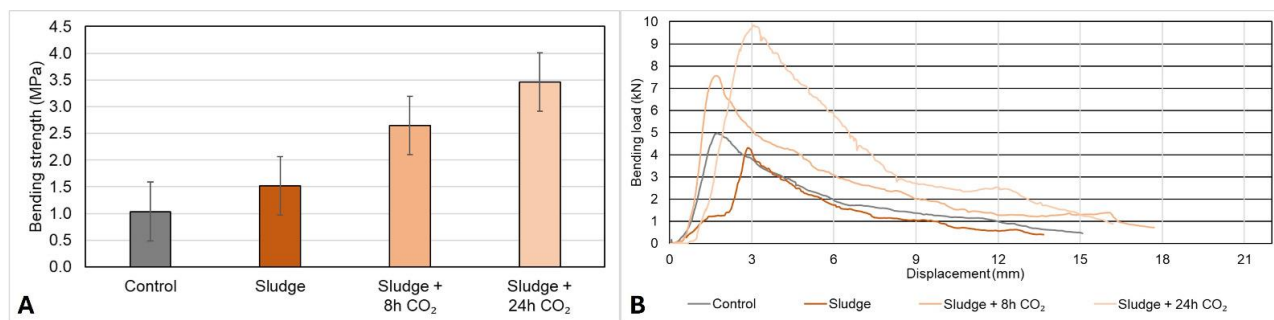
Figure 3. Bending strength (A) and representative bending curves (B) of adobe bricks.

Conversely, bricks incorporating hydrated lime did not exhibit significant changes in compressive strength post-carbonation. However, they displayed augmented bending strength even without carbonation, potentially attributed to impurities acting as binding agents. Interestingly, this improvement in flexural strength was not mirrored in compression tests, suggesting nuanced material behaviors influenced by compositional variations [9].

4. CONCLUSIONS

The current investigation explored the impact of accelerated carbonation on the mechanical properties of adobe bricks incorporating lime sludge. Visual assessments indicated no dominant pink coloration in the carbonated adobe bricks, suggesting that relying solely on this method may not suffice for accurately gauging carbonation extent. Concerning mechanical properties, lime sludge-containing bricks exhibited a significant increase in compressive strength post-carbonation, contrasting with the control group, which showed minimal changes. The carbonation process notably enhanced lime sludge-containing bricks' compressive strength, with improvements of up to 180%. Impurities in lime sludge potentially acted as binding agents, positively impacting adobe bricks' cohesion and mechanical properties. This was evident in flexural strength tests, where lime sludge-containing bricks, even without carbonation, demonstrated increased strength, with improvements reaching up to 350%. Despite compositional and mechanical property variations, the apparent density of adobe bricks remained largely consistent across samples. Minor fluctuations were observed but were not significantly influenced by substitution type or carbonation. Overall, carbonation proved beneficial for lime sludge-containing bricks, enhancing their mechanical properties.

4.1. Declaration of Competing Interest

The authors declare no conflict of interest.

4.2. Fundings

4.3. Acknowledgements

5. REFERENCES

[1] Joshi, A.M., et al. Performance of stabilized adobe blocks prepared using construction and demolition waste. *Journal of Building Pathology and Rehabilitation*, Volume 4 (2019). (https://doi.org/10.1007/s41024-019-0052-x)

[2] Minh Trang, N.T., et al. Reuse of waste sludge from water treatment plants and fly ash for manufacturing of adobe bricks. *Chemosphere*, Volume 284 (2021). (https://doi.org/10.1016/j.chemosphere.2021.131367)

[3] Babé, C., et al. Thermomechanical characterization and durability of adobes reinforced with millet waste fibers (sorghum bicolor). *Case Studies in Construction Materials*, Volume 13 (2020). (https://doi.org/10.1016/j.cscm.2020.e00422)

[4] Muñoz, P., et al. Adobe bricks reinforced with paper & pulp wastes improving thermal and mechanical properties. *Construction and Building Materials*, Volume 254 (2020). (https://doi.org/10.1016/j.conbuildmat.2020.119314)

[5] Ashour, T., et al. Thermal conductivity of unfired earth bricks reinforced by agricultural wastes with cement and gypsum. *Energy and Buildings*, Volume 104 (2015). (https://doi.org/10.1016/j.enbuild.2015.07.016)

[6] Vasić, M.V., et al. Optimization of adobe clay bricks based on the raw material properties (mathematical analysis). *Construction and Building Materials*, Volume 244 (2020). (https://doi.org/10.1016/j.conbuildmat.2020.118342)

[7] Tonoli, G.H.D., et al. Effect of accelerated carbonation on cementitious roofing tiles reinforced with lignocellulosic fibre. *Construction and Building Materials*, Volume 24 (2010). (https://doi.org/10.1016/j.conbuildmat.2007.11.018)

[8] Giaretton, M., et al. Material characterisation of heavy-weight and lightweight adobe brick walls and in-plane strengthening techniques. *Construction and Building Materials*, Volume 310 (2021). (https://doi.org/10.1016/j.conbuildmat.2021.125309)

[9] Vashistha, P., et al. Valorization of paper mill lime sludge via application in building construction materials: A review. *Construction and Building Materials*, Volume 211 (2019). (https://doi.org/10.1016/j.conbuildmat.2019.03.085)

EFFECT OF DIFFERENT CURING CONDITIONS ON THE THERMAL PROPERTIES OF SISAL/EPOXY COMPOSITES

Linconl A. Teixeira [(a)*] and Sandra M. Luz [(b),]

(a) 0000-0002-2922-3027 Engineering Materials Integrity Graduate Program (University of Brasília – Brazil)
(b) 0000-0002-2223-0021 Engineering Materials Integrity Graduate Program (University of Brasília – Brazil)
* Corresponding author: linconl_araujo@hotmail.com

Abstract: The main objective of this work is to study the effect that different curing conditions can have on the thermal properties of sisal/epoxy composites. All the specimens were prepared by mixing epoxy resin and hardener in a proportion of 100:38. Regarding the onset temperatures (T_{onset}), which mark the beginning of sample weight loss, indicating the initial degradation of the material, it was observed that the sisal/epoxy composite cured with an accelerator exhibited a higher temperature (309 °C), compared to the sisal/epoxy composite cured at room temperature with post-cure (259 °C) and the sisal/epoxy composite cured at 100°C/4h in an oven (265 °C). The DSC analysis showed that the sisal/epoxy composite cured at room temperature and post-cured achieved the highest degree of cure among all the composites (~66.25%). In conclusion, the 3rd Cure Condition revealed the best condition for cure, despite the resin manufacturing guide (cure 100: 38 at room temperature without post-cure).

1. INTRODUCTION

Due to their high stiffness and specific strength, epoxy resin-based polymer composites reinforced with fibers are widely used as structural elements. Although polymer matrix composites have been successfully applied in various fields of industry and engineering as semi-structural and structural materials, there is still a need to study the effect that different curing conditions can have on the mechanical performance of these materials.

Thus, the curing process plays a fundamental role in producing epoxy composites. Curing refers to the chemical reaction that occurs between the epoxy resin and the hardener, resulting in the formation of a rigid and resistant three-dimensional network. This network gives the composite its mechanical and thermal properties [1].

An ideal curing cycle for a composite will result in a material with good mechanical strength properties. Both temperature and curing time are critical factors in this process. Generally, lower temperatures require longer curing times to ensure complete curing of the material, which can result in less rigid composites. On the other hand, higher temperatures and shorter curing times can lead to the development of a stiffer composite. However, it is important to be cautious when increasing the curing temperature, as this can affect the final quality of the laminate. Moreover, excessively high temperatures can cause resin degradation, bubble formation, or composite distortion [2].

Reducing curing time is an important consideration, and this can be achieved by adjusting the resin formulation, using multi-component curing systems, or using special additives that accelerate the chemical reaction. Additionally, applying external energy such as heat, light, or radiation can help speed up the curing process, reducing the time required to achieve the desired cure. While accelerators can effectively minimize

curing time, their use also presents challenges that must be considered. Chemical compatibility is one of the main challenges in using accelerators in epoxy resin curing. Chemical incompatibility can lead to unwanted reactions, viscosity changes, and reduced mechanical properties [3].

In summary, properly selecting curing conditions is an essential part of balancing the desired benefits and mitigating the potential disadvantages each curing condition may offer, thereby ensuring a high-quality and high-performance composite. The main objective of this work is to evaluate the effect that different curing conditions have on the thermal properties of sisal/epoxy composites.

2. METHODOLOGY

2.1. Materials and Manufacturing

SisalSul from Brazil supplied the sisal fibers. Before the chemical treatment, the sisal fibers (average length 60 cm) were cut to 20 cm. Then, the sisal fibers were treated with a sodium hydroxide (NaOH) 5% (w/v) solution, and the fibers were mercerized at a ratio of 10:1 (solution: fiber) at 70 °C for 2 h under manual stirring. After the chemical treatment, the fibers were washed with distilled water until they had a neutral pH and dried at room temperature for 120 h.

For the sisal, 50 % (v/v) composites are manufactured with fibers (4 layers). The polymeric matrix was prepared by mixing proper quantities of epoxy resin Araldite LY 5052 and a specific hardener Aradur 5052 in a proportion of 100:38 phr (parts per hundred), both from HUNTSMAN. The composites were developed with three different curing conditions: First - the sisal/epoxy (1st Cure Condition) was cured at room temperature for 24 h with a post-cure at 120 °C for 1h; Second - the sisal/epoxy (2nd Cure Condition) was cured in an oven at 100 °C for 4 h; and the Third - the sample was prepared by mixing epoxy resin, hardener, and accelerator (DY 062) in a proportion 100:38:1 phr, cured at room temperature without post-cure, (3rd Cure Condition).

2.2. Thermogravimetric analysis (TGA) and differential scanning calorimetry (DSC)

The samples were analyzed from 25 to 600 °C at a heating rate of 5°C/min in a simultaneous (TGA-DSC) thermal analyzer (Q600 SDT, TA Instruments, USA) under a nitrogen atmosphere at a 50 mL/min flow rate. Samples weighing 10 ± 0.5 mg were deposited on an aluminum pan. The degree of cure of the epoxy matrix and composites was determined using Equation (1):

$$\alpha_{cura} = 1 - \frac{\Delta H_{res}}{\Delta H_{dyn}} \tag{1}$$

where ΔH_{res} is the residual heat of the reaction measured from the sample, and ΔH_{dyn} is the heat of the reaction measured by an analysis of an unreacted sample of the same material.

3. RESULTS AND DISCUSSION

Fig. 1 shows the TG/DTG curves of the composites with different curing conditions. It is noticeable that the different curing conditions were able to affect the thermal behavior of the composites (see Table 1). According to the data obtained, it is evident that among the composites, the thermal stability of the sisal/epoxy composite [0°] cured with accelerator increased by about 14% and 16% compared to the sisal/epoxy composite [0°] cured at 100°C/4h in an oven and sisal/epoxy composite [0°] cured at room temperature and post-cured, respectively.

Furthermore, concerning the onset temperatures (T_{onset}), which mark the beginning of the mass loss of the samples, in other words, the start of material degradation under analysis, it is noticed that the sisal/epoxy composite [0°] cured with accelerator exhibited a higher temperature (309 °C), compared to the sisal/epoxy composite [0°] cured at room temperature and post-cured (259 °C) and sisal/epoxy composite [0°] cured at 100°C/4h in an oven (265 °C).

Studies indicate [4] and [5] that this gain in thermal properties for the sisal/epoxy composites [0°] cured with an accelerator is related to the epoxy resin curing process. During the curing process, amino-based accelerators initiate the opening of epoxy rings in the resin through a direct reaction with the amine, promoting the homopolymerization of the epoxy resin. This, upon contact with the hydroxyl groups present in the natural fibers, fosters a complex amine/hydroxyl interaction, thus forming a stronger molecular interaction.
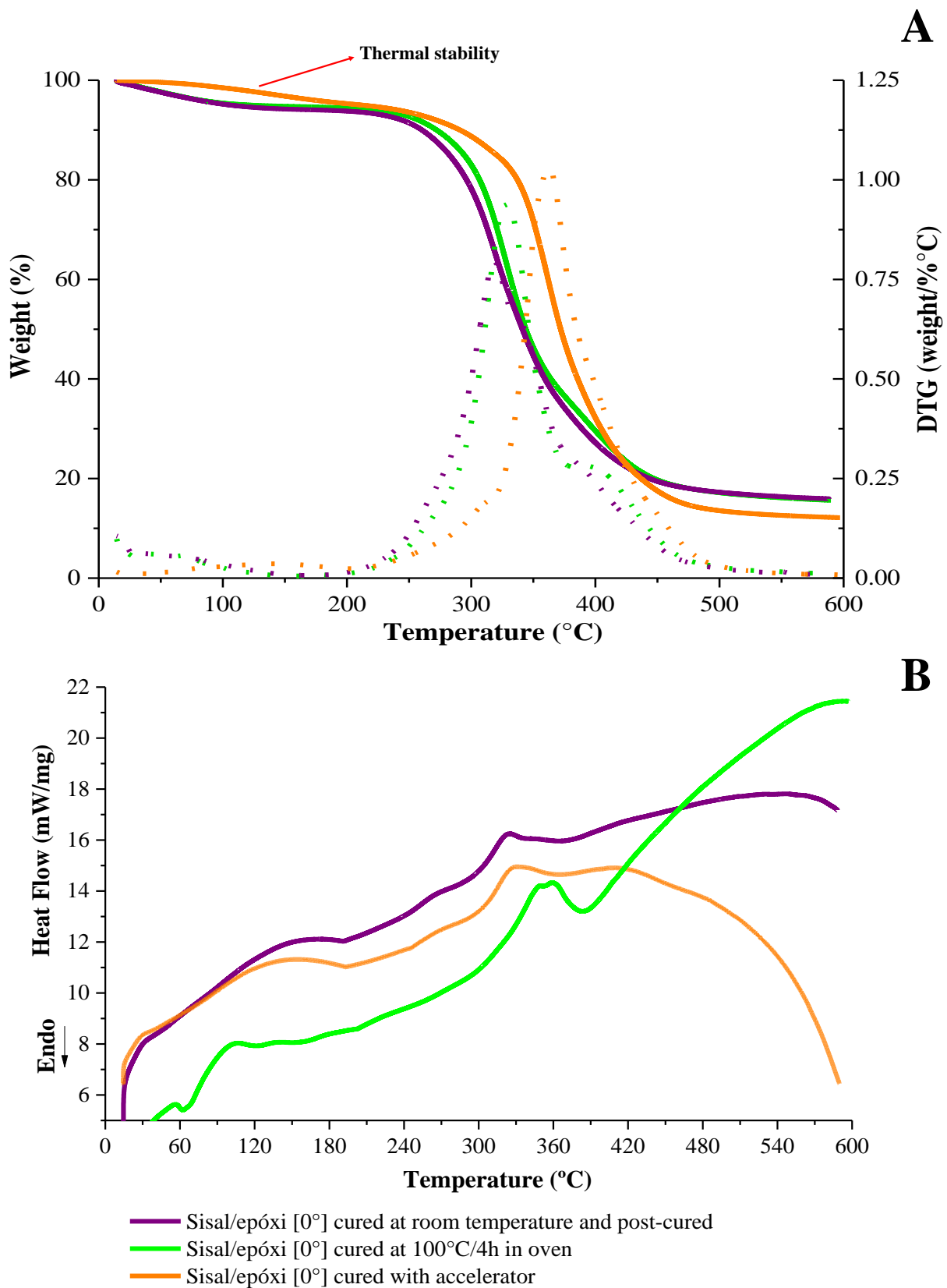
Figure 1. TG/DTG curves (A) and DSC curves (B) of sisal/epoxy composites with different curing conditions.

It is also noted that all composites exhibited three degradation stages (see Figure 1A). The first stage, occurring with a slight mass loss in the range of 90 - 110 °C, is attributed to the release of moisture retained in the natural fiber [6]; the second stage, occurring between 300 - 330 °C, corresponds to the breaking of cross-links and the degradation of the resin itself [170]; the last stage, manifesting at approximately 340 - 450 °C, is related to cellulose degradation [7]. Similar peaks were observed at 341 °C, 358 °C, 348 °C, and 359 °C for composites reinforced with bamboo, hemp, jute, and kenaf fibers, respectively [8].

The DSC curves of the sisal/epoxy [0°] composites are shown in Figure 1B. A similar behavior is observed in the curves of the analyzed samples. Table 1 presents the main parameters obtained from Figure 1B. It is possible to observe that the pure epoxy resin samples (see Figure 1B) exhibited two thermal peaks, while the sisal/epoxy [0°] composites showed three thermal peaks. The first peak, observed in all samples in the temperature range of 106 to 127 °C, is attributed to the polymeric matrix's glass transition temperature (T_g). The second peak, found in the temperature range between 273 and 279 °C, is not as pronounced as the other peaks and is observed only in the composites, being associated with the thermal degradation of sisal fibers. The third peak, located in the temperature range of 329 to 355 °C, corresponds to the degradation of the epoxy resin [9].

Table 1. Thermal properties TGA/DTG and DSC of sisal/epoxy composites.

Samples/properties		Curing at room temperature and with post-cure	Curing at 100°C/4h in an oven	Curing with accelerator
Thermal stability (°C)		132	137	177
T_{onset} **(°C)**		259	265	309
Residue up to 600 °C (%)		15	18	12
1° Stages	T_{peak} **(°C)**	89	93	109
2° Stages	T_{peak} **(°C)**	330	337	302
3° Stages	T_{peak} **(°C)**	350	347	361
T_g **(°C)**		106	107	127
T_{peak} **(°C)**		273	276	279
ΔH(J/g)		16.88	16.07	17.56
T_{peak} **(°C)**		329	338	352
ΔH (J/g)		6.57	6.78	7.02
α_{cure} **(%)**		66.25	61.79	65.47

The T_g of the sisal/epoxy [0°] composite cured with accelerator (127 °C) was higher among the composites. This increase in T_g is associated with greater molecular interaction between sisal and epoxy caused by the use of the accelerator, which provided greater molecular anchoring between the OH group of the fibers and the aromatic ring of the resin, allowing a subsequent reaction with the amine group of the accelerator, thus forming a more complex and harder-to-degrade molecular interaction, resulting in a higher T_g][10], [11].

The degree of cure for the composites suggests that the insertion of fibers into the composites restricted the number of cross-links, contributing to a lower degree of cure, as the fibers can act as physical barriers, hindering resin impregnation inside the composite during the curing process, limiting the interaction between the polymeric matrix and the curing agent, reducing the efficiency of the curing process and leading to a lower degree of cross-linking [12].

4. CONCLUSIONS

The thermal analysis revealed that the sisal/epoxy composite cured with an accelerator presented the highest thermal stability, demonstrating its effectiveness in promoting greater thermal stability for sisal/epoxy composites cured with this condition. Moreover, the accelerator curing method differs from that proposed by the company, which recommends curing at room temperature with postcuring. Also, the accelerator curing method can reduce curing time becomes a promising approach to accelerate the curing process and save processing cycles.

In turn, the DSC analysis showed that the sisal/epoxy composite cured at room temperature and with post-curing achieved the highest degree of curing among all composites (~66.25%).

4.1. Declaration of Competing Interest

The authors declare no conflict of interest.

4.2. Acknowledgments

5. REFERENCES

[1]   Pattanaik A, Mukherjee M, Mishra SB. Influence of curing condition on thermo-mechanical properties of fly ash reinforced epoxy composite. Compos Part B Eng 2019;176:107301. https://doi.org/10.1016/j.compositesb.2019.107301.

[2]   Gholipour-Mahmoudalilou M, Roghani-Mamaqani H, Azimi R, Abdollahi A. Preparation of hyperbranched poly (amidoamine)-grafted graphene nanolayers as a composite and curing agent for epoxy resin. Appl Surf Sci 2018;428:1061–9. https://doi.org/10.1016/j.apsusc.2017.09.237.

[3]   Yousefi N, Evans AD, Harper LT, Maples HA, James T, Bismarck A. Solid epoxy resin systems for automated composite manufacturing. Compos Part A Appl Sci Manuf 2021;142:106205. https://doi.org/10.1016/j.compositesa.2020.106205.

[4]   Gou H, Zhao Y, Zhou Y, Wei W, Fei X, Li X, et al. Effects of different imidazole accelerators on curing behavior and cross-linked network of epoxy resin/phenolic resin/benzoxazine ternary system. Polym Adv Technol 2022;33:610–26. https://doi.org/10.1002/pat.5543.

[5]   Chen F, Liu F, Du X. Molecular dynamics simulation of crosslinking process and mechanical properties of epoxy under the accelerator. J Appl Polym Sci 2023;140:e53302. https://doi.org/10.1002/app.53302.

[6]   Neto JSS, Lima RAA, Cavalcanti DKK, Souza JPB, Aguiar RAA, Banea MD. Effect of chemical treatment on the thermal properties of hybrid natural fiber-reinforced composites. J Appl Polym Sci 2019;136:47154. https://doi.org/10.1002/app.47154.

[7]   Shravanabelagola Nagaraja Setty VK, Goud G, Peramanahalli Chikkegowda S, Mavinkere Rangappa S, Siengchin S. Characterization of Chemically Treated Limonia Acidissima (Wood Apple) Shell Powder: Physicochemical, Thermal, and Morphological Properties. J Nat Fibers 2022;19:4093–104. https://doi.org/10.1080/15440478.2020.1853925.

[8]   Mittal V, Saini R, Sinha S. Natural fiber-mediated epoxy composites – A review. Compos Part B Eng 2016;99:425–35. https://doi.org/10.1016/j.compositesb.2016.06.051.

[9]   Dayo AQ, Gao B, Wang J, Liu W, Derradji M, Shah AH, et al. Natural hemp fiber reinforced polybenzoxazine composites: Curing behavior, mechanical and thermal properties. Compos Sci Technol 2017;144:114–24. https://doi.org/10.1016/j.compscitech.2017.03.024.

[10]   Ignatenko VY, Ilyin SO, Kostyuk A V., Bondarenko GN, Antonov S V. Acceleration of epoxy resin curing by using a combination of aliphatic and aromatic amines. Polym Bull 2020;77:1519–40. https://doi.org/10.1007/s00289-019-02815-x.

[11]   Hayaty M, Honarkar H, Beheshty MH. Curing behavior of dicyandiamide/epoxy resin system using different accelerators. Iran Polym J 2013;22:591–8. https://doi.org/10.1007/s13726-013-0158-y.

[12]   Bang KG, Kwon JW, Lee DG, Lee JW. Measurement of the degree of cure of glass fiber–epoxy composites using dielectrometry. J Mater Process Technol 2001;113:209–14. https://doi.org/10.1016/S0924-0136(01)00657-4.

EVALUATION OF THE FLEXURAL STRENGTH AND MASS LOSS OF BIOCOMPOSITES PRODUCED WITH LIGNOCELLULOSIC PARTICLES

Felipe G. S. Araújo[a]*, Paulo R. C. Marcelino[b], Roseméri B. S. Silva[c], Mateus U. Nascimento[d], Gabriel M. Valane[e], Michel P. Oliveira[f]

(a) 0009-0000-7069-5408 (Federal University of Espirito Santo – Brazil)
(b) 0000-0001-8594-0920 (Federal University of Espirito Santo – Brazil)
(c) 0009-0004-6432-591X (Federal University of Espirito Santo – Brazil)
(d) 0009-0008-3032-8134 (Federal University of Espirito Santo – Brazil)
(e) 0000-0002-2736-4440 (Federal University of Espirito Santo – Brazil)
(f) 0000-0001-9241-0194 (Federal University of Espirito Santo – Brazil)
* Corresponding author: felipe.gabriel.araujo@gmail.com

Abstract: The increasing need to address the issue of waste disposal from agribusiness, such as coffee husks, has been driving research into new applications, exemplified by composites reinforced with lignocellulosic fibers and particles. Therefore, the aim of this study was to evaluate the flexural strength and mass loss of lignocellulosic panels produced using coffee husk particles (CHP) and epoxy resin. The panels were manufactured through a cold pressing process with the addition of 0%, 40%, 50%, and 60% CHP. For mechanical characterization, flexural tests were performed, and thermogravimetric analysis was conducted to observe the mass loss behavior of the material. The results indicate that the increase in CHP content in the composite led to a reduction in maximum flexural strength and an increase in the modulus of elasticity. Regarding mass loss, it was observed that thermal stability decreased with the addition of CHP. In summary, the addition of coffee husk particles resulted in a product with up to 50% less polymer, exhibiting notable thermal and mechanical properties, with particular emphasis on increased rigidity.

1. INTRODUCTION

The agricultural industry is responsible for generating a significant amount of waste [1], and the way these materials are disposed of can result in negative impacts on the environment, such as soil degradation and the proliferation of vectors [2]. Therefore, the reuse of these wastes as raw materials in other productive areas emerges as an excellent alternative to mitigate the environmental impacts resulting from their improper disposal while also creating opportunities for the creation of new products, thus enabling income generation [3].

In the context of new materials, application in composites becomes a promising alternative, and several studies mention the use of plant materials as reinforcing fillers in biocomposites, such as fibers from pineapple leaves, banana stems, sugarcane bagasse, and coffee husks [4-7]. Generally, composites consist of a dispersed reinforcement phase, such as particles or fibers, in a continuous component, the matrix, responsible for transmitting loads to the dispersed phase [8].

The use of coffee husk and coffee grounds waste in the synthesis of biocomposites has been investigated in recent years and confirms the potential application of this resource in composite materials as an alternative for the utilization of these by-products [9-12].

In light of this, it is observed that the wide availability of lignocellulosic fibers, along with the need for renewable sources for the production of polymeric composites, enables technological advances that add value to agro-industrial waste [13]. Thus, the objective of the study was to evaluate the flexural strength and mass loss of biocomposites manufactured with coffee husk particles (CHP) in an epoxy matrix.

2. METHODOLOGY

The coffee husk residues were ground to obtain particles within the particle size range of 0.25 to 0.43 mm and subsequently dried in a circulating oven for 24 hours at 103 °C. For the matrix phase composition, epoxy resin 2004 and hardener 3154 were used, obtained from a reputable company in the state of Espírito Santo. The panels were produced through cold pressing where the particulate material was added to the resin-catalyst mixture (2:1 ratio) in mass fractions of 40%, 50%, and 60%. The composites were subjected to a pressure of 4.6 MPa for 24 hours, then removed from the mold for a post-curing process lasting 3 days.

The treatments consist of epoxy resin panels without particle inclusion (RE), with 40% particles (CHP40), 50% particles (CHP50), and 60% particles (CHP60). Five specimens were selected, fabricated according to ASTM D790 standard [14], from the pressed panels. The flexural test was performed on an Oswaldo Filizola AME-2kN universal testing machine, and morphological analysis was conducted by scanning electron microscopy (SEM) on the fracture region using a JEOL JSMIT200 microscope. The thermal stability behavior was observed by thermogravimetric analysis (TGA), obtained using a Setaran LabSys Evo thermogravimetric analyzer.

The results were subjected to Analysis of Variance and tests for normality and homogeneity. As the prerequisites for parametric analysis were met, Tukey's mean comparison statistics at a significance level of 5% were applied. The data were analyzed using the *agricolae* package in the RStudio statistical software version 4.3.0 [15].

3. RESULTS AND DISCUSSION

The results indicate a trend for a decrease in maximum flexural strength with an increase in the particle fraction in the matrix (Figure 1A). The biocomposites fabricated with 40% CHP recorded the highest average strength value, representing a difference of 16.76% compared to specimens with a higher particle fraction (CHP60). These results may indicate that the use of loads above 30%, by weight, affects different mechanical properties due to increased interactions between the dispersed phase and the insufficient matrix coating of the particles, resulting in low transfer of mechanical stresses, as observed in other studies [16, 17]. Another factor may be the influence of stress concentration points in the matrix due to the high density of particles, leading to early crack propagation until failure [18]. In general, the increase in particles in composites may result in a decrease in mechanical properties, especially when there is low interaction between the particles and the matrix [12].
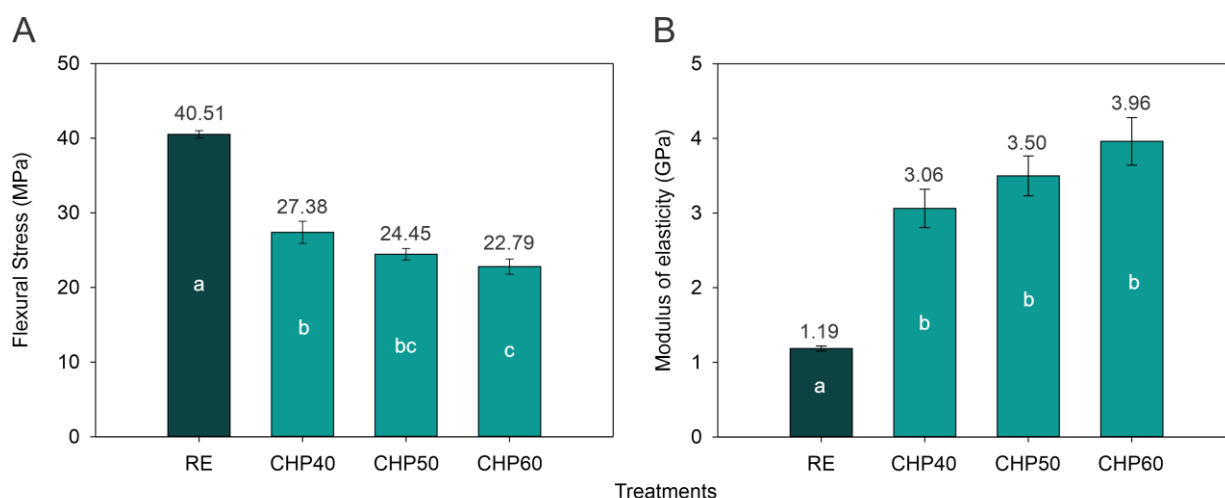
Treatments with different letters indicate statistically significant differences at a confidence level of 0.05 according to Tukey's test.

Figure 1. Flexural stress and modulus of elasticity of epoxy resin and biocomposites.

Regarding the modulus of elasticity (MOE) of the biocomposites, it can be observed that there is a direct relationship between the increase in MOE and the amount of particles in the panels (Figure 1B). This

occurs due to the incorporation of the load, which are rigid components, into the viscoelastic matrix that ultimately reduces the mobility of the polymeric chains, especially when dealing with lignin, which is responsible for part of the rigidity in biocomposites reinforced with plant materials [18-21].

The degradation temperature of biocomposites with PCC addition regularly occurs between the decomposition temperature of the reinforcement and that of the polymeric matrix [22]. Pure epoxy has an initial decomposition temperature of approximately 300 °C, which is higher than that observed for the biocomposites (Figure 2). The initial phase of mass loss of the biocomposites is recorded between 50 and 200 °C and can be attributed to the presence of residual water that is progressively released with increasing temperature in the system [23, 24]. The subsequent phase recorded above 200 °C, for the biocomposites, is related to the decomposition of the structural components of the coffee husk such as hemicellulose, cellulose, and lignin.
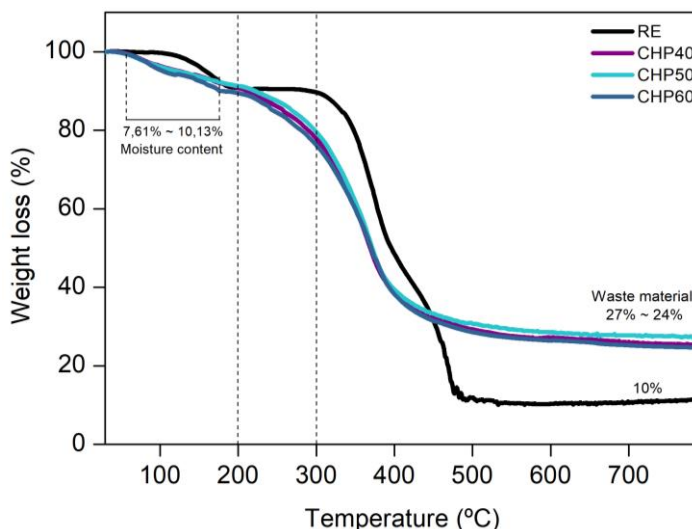
Figure 2. Thermal stability of epoxy resin and biocomposites.

Due to being an amorphous material with a lower degree of polymerization and organization, hemicelluloses decompose first between 250 and 350 °C, followed by cellulose between 275 and approximately 450 °C, and lastly lignin, which has the highest thermal stability due to the absence of aromatic branching in its structure, starting the process around 250 °C and extending up to 900 °C [25-27].

Overall, thermal stability decreased similarly regardless of the particle fraction incorporated into the matrix, and all analyzed biocomposites exhibited a residue level higher than pure resin (RE) at the end of the analysis, due to the fact that they contain constituents that do not undergo thermal decomposition until the temperature reaches 700 °C.

The fracture surfaces of the biocomposites were analyzed by SEM micrographs to visualize the interface between the reinforcement and the polymeric matrix (Figure 3).
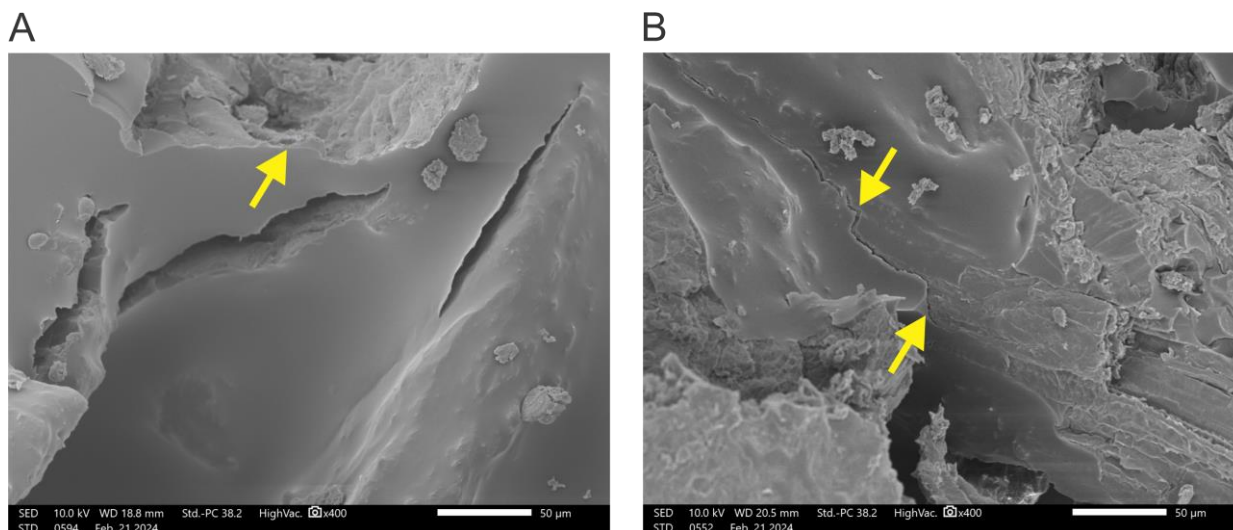
Figure 3. SEM micrographs of the fracture surface of biocomposites with 40% (A) and 60% (B)

It is not possible to discuss chemical adhesion; however, it is observed that there is good physical adhesion since some load particles ended up anchored in the continuous phase, likely due to their roughness, and it is possible to observe that in some cases the texture of the particulate material was molded into the matrix. The interface is responsible for the transfer of mechanical load between the matrix and the reinforcement and can be influenced by various factors such as chemical affinity between the phases, mechanical anchoring, and even the manufacturing process [28].

4. CONCLUSIONS

The production of biocomposites using CHP as reinforcement has shown promise, primarily due to the substantial utilization of residual material, up to 60%, and reduced reliance on the polymeric matrix. Concerning mechanical properties, a significant increase in stiffness is observed with the increasing proportion of CHP in the polymeric matrix. Thermal properties were minimally affected by the addition of particles; however, it is noteworthy that the produced biocomposites exhibit thermal stability up to temperatures close to 300°C, thereby expanding their potential applications. The SEM observation of the interface between the matrix and the particles demonstrated the presence of a consolidated physical bond.

4.1. Declaration of Competing Interest

The authors declare no conflict of interest.

5. REFERENCES

[1]   M. M. Tashima et al. Reaproveitamento da cinza de casca de arroz na construção civil. *Holos Environment*, vol. 11, no. 1, p. 81, Jan. 2011. (doi: 10.14295/holos.v11i1.5435).

[2]   P. R. Jacobi and G. R. Besen. Gestão de resíduos sólidos em São Paulo: desafios da sustentabilidade. *Estudos Avançados*, vol. 25, no. 71, pp. 135–158, Apr. 2011. (doi: 10.1590/S0103-40142011000100010).

[3]   N. K. Cordeiro et al. Gestão de resíduos agrícolas como forma de redução dos impactos ambientais. *Revista de Ciências Ambientais*, vol. 14, no. 2, p. 23, Aug. 2020. (doi: 10.18316/rca.v14i2.5593).

[4]   F. da Luz et al. Graphene-Incorporated Natural Fiber Polymer Composites: A First Overview. *Polymers (Basel)*, vol. 12, no. 7, p. 1601, Jul. 2020. (doi: 10.3390/polym12071601).

[5]   Z. Zhang *et al.* High performances of plant fiber reinforced composites—A new insight from hierarchical microstructures. *Compos Sci Technol*, vol. 194, p. 108151, Jul. 2020. (doi: 10.1016/j.compscitech.2020.108151).

[6]   M. Sood and G. Dwivedi. Effect of fiber treatment on flexural properties of natural fiber reinforced composites: A review. *Egyptian Journal of Petroleum*, vol. 27, no. 4, pp. 775–783, Dec. 2018. (doi: 10.1016/j.ejpe.2017.11.005).

[7]   T. H. Mokhothu and M. J. John. Review on hygroscopic aging of cellulose fibres and their biocomposites. *Carbohydr Polym*, vol. 131, pp. 337–354, Oct. 2015. (doi: 10.1016/j.carbpol.2015.06.027).

[8]   M. Y. M. Zaghloul, M. M. Y. Zaghloul, and M. M. Y. Zaghloul. Developments in polyester composite materials – An in-depth review on natural fibres and nano fillers. *Compos Struct*, vol. 278, p. 114698, Dec. 2021. (doi: 10.1016/j.compstruct.2021.114698).

[9]   A. S. C. de Bomfim et al. Effect of Spent Coffee Grounds on the Crystallinity and Viscoelastic Behavior of Polylactic Acid Composites. *Polymers (Basel)*, vol. 15, no. 12, p. 2719, Jun. 2023. (doi: 10.3390/polym15122719).

[10]   L. H. Mei and N. Oliveira. Caracterização de um compósito polimérico biodegradável utilizando Poli (ε-caprolactona) e borra de café. *Polímeros*, vol. 27, no. spe, pp. 99–109, Jan. 2017. (doi: 10.1590/0104-1428.2139).

[11]   W. M. Cavalcanti et al. Viabilidade de produção de painéis lignocelulósicos a base de resíduos de casca de café e resinas epóxi de óleos vegetais. In: XI Congresso Brasileiro de Gestão Ambiental Vitória/ES. 2020.

[12]   B. Gonçalves et al. Surface Treatments of Coffee Husk Fiber Waste for Effective Incorporation into Polymer Biocomposites. *Polymers (Basel)*, vol. 13, no. 19, p. 3428, Oct. 2021. (doi: 10.3390/polym13193428).

[13]   R. Silva et al. Aplicações de fibras lignocelulósicas na química de polímeros e em compósitos. *Quim Nova*, vol. 32, no. 3, pp. 661–671, 2009. (doi: 10.1590/S0100-40422009000300010).

[14]   ASTM D790-17, Standard Test Methods for Flexural Properties of Unreinforced and Reinforced Plastics and Electrical Insulating Materials. ASTM International, 2017. (www.astm.org).

[15]   R Core Team. R: A Language and Environment for Statistical Computing. Vienna, Austria, Apr. 21, 2023. Accessed: Jun. 21, 2023. [Online]. (https://www.R-project.org/)

[16]   T. G. Y. Gowda et al. Polymer matrix-natural fiber composites: An overview. *Cogent Eng*, vol. 5, no. 1, p. 1446667, Jan. 2018. (doi: 10.1080/23311916.2018.1446667).

[17]   L. G. Furlan, U. L. Duarte, and R. S. Mauler. Avaliação das propriedades de compósitos de polipropileno reforçados com casca de aveia. *Quim Nova*, vol. 35, no. 8, pp. 1499–1501, 2012. (doi: 10.1590/S0100-40422012000800002).

[18]   B. Ahmad et al. Fabrication and characterization of an eco-friendly biodegradable epoxy/chitosan composites. *American Journal of Materials Science*, vol. 7, pp. 166–169, 2017.

[20]   J. A. Méndez et al. Evaluation of the reinforcing effect of ground wood pulp in the preparation of polypropylene-based composites coupled with maleic anhydride grafted polypropylene. *J Appl Polym Sci*, vol. 105, no. 6, pp. 3588–3596, Sep. 2007. (doi: 10.1002/app.26426).

[21]   N. Sultana et al. Short Jute Fiber Preform Reinforced Polypropylene Thermoplastic Composite: Experimental Investigation and Its Theoretical Stiffness Prediction. *ACS Omega*, vol. 8, no. 27, pp. 24311–24322, Jul. 2023. (doi: 10.1021/acsomega.3c01533).

[22]   V. K. Thakur, M. K. Thakur, and R. K. Gupta. Review: Raw Natural Fiber–Based Polymer Composites. *International Journal of Polymer Analysis and Characterization*, vol. 19, no. 3, pp. 256–271, Apr. 2014. (doi: 10.1080/1023666X.2014.880016).

[23]   H. Essabir et al. Structural, mechanical and thermal properties of bio-based hybrid composites from waste coir residues: Fibers and shell particles. *Mechanics of Materials*, vol. 93, pp. 134–144, Feb. 2016, (doi: 10.1016/j.mechmat.2015.10.018).

[24]   S. N. Monteiro, V. Calado, R. J. S. Rodriguez, and F. M. Margem. Thermogravimetric behavior of natural fibers reinforced polymer composites—An overview. *Materials Science and Engineering: A*, vol. 557, pp. 17–28, Nov. 2012. (doi: 10.1016/j.msea.2012.05.109).

[25]   M. H. Zin, K. Abdan, and M. N. Norizan. The effect of different fiber loading on flexural and thermal properties of banana/pineapple leaf (PALF)/glass hybrid composite. in *Structural Health Monitoring of Biocomposites, Fibre-Reinforced Composites and Hybrid Composites*, Elsevier, 2019, pp. 1–17. (doi: 10.1016/B978-0-08-102291-7.00001-0).

[26]   M. Benítez-Guerrero, J. López-Beceiro, P. E. Sánchez-Jiménez, and J. Pascual-Cosp. Comparison of thermal behavior of natural and hot-washed sisal fibers based on their main components: Cellulose, xylan and lignin. TG-FTIR analysis of volatile products. *Thermochim Acta*, vol. 581, pp. 70–86, Apr. 2014. (doi: 10.1016/j.tca.2014.02.013).

[27]   C. Setter et al. Slow pyrolysis of coffee husk briquettes: Characterization of the solid and liquid fractions. *Fuel*, vol. 261, p. 116420, Feb. 2020. (doi: 10.1016/j.fuel.2019.116420).

[28]   F. L. Neto & L. C. Pardini. Compósitos estruturais: ciência e tecnologia. Editora Blucher, 2016.

INFLUENCE OF LIGNOCELLULOSE PARTICLE SIZE ON THE FLEXURAL STRENGTH OF BIOCOMPOSITES

Felipe G. S. Araújo[a]*, Paulo R. C. Marcelino[b], Gabriel M. Valane[c], Mateus U. Nascimento[d], Roseméri B. S. Silva[e], Michel P. Oliveira[f]

(a) 0009-0000-7069-5408 (Federal University of Espirito Santo – Brazil)
(b) 0000-0001-8594-0920 (Federal University of Espirito Santo – Brazil)
(c) 0000-0002-2736-4440 (Federal University of Espirito Santo – Brazil)
(d) 0009-0008-3032-8134 (Federal University of Espirito Santo – Brazil)
(e) 0009-0004-6432-591X (Federal University of Espirito Santo – Brazil)
(f) 0000-0001-9241-0194 (Federal University of Espirito Santo – Brazil)
* Corresponding author: felipe.gabriel.araujo@gmail.com

Abstract: The characteristics attributed to a biocomposite are said to be a function of the combined action of the properties of the matrix-load in proportion, interaction, and size of the dispersed phase. Thus, the aim of the study was to identify the influence of filler particle size on the flexural strength of epoxy matrix biocomposites made with coffee husk particles (CHP). The treatments consist of specimens without particle inclusion, particles up to 0.43mm, particles up to 0.25mm, and fines (<0.25mm), manufactured by cold pressing with the addition of 40% waste. According to the results, reducing the particle size from 0.43mm to fines resulted in a 21.69% increase in maximum flexural strength and a 9.69% increase in the modulus of elasticity. Micrographs show that the addition of CHP to the matrix increased the ductility of the material, and analysis of the phase interfaces revealed low matrix-load interaction, possibly due to the mucilage present on the particle surface, as the material did not undergo any prior treatment. Within the parameters of the research, it is concluded that the biocomposites exhibited promising mechanical behavior, suggesting the fine particle size range as the most effective reinforcement filler.

1. INTRODUCTION

The quality of the particle-matrix interface plays a crucial role in the mechanical properties of composite materials, as it is through it that the transfer of load from the matrix to the particle occurs [1]. In order to optimize the interface, many methods of physical and chemical treatments are often used to alter biomass characteristics, intensifying the adhesion between phases [2, 3]; however, such processing often involves complex and expensive procedures [4].

The use of milling as an alternative method to reduce the size of lignocellulosic particles and promote morphological changes represents an economical and sustainable alternative when compared to other treatment processes [5-10]. According to Castro and Pandolfelli [11], particle size distribution is of fundamental importance in the mixing process of a material, as porosity is influenced by the uniformity of particle distribution, ensuring better compaction and filling of the voids existing between the grains.

Considering that the characteristics of the material resulting from the fabrication of biocomposites are attributed to the product as a function of the combined action of the properties of the load-matrix in proportion, interaction, size, and degree of orientation of the dispersed phase, the work proposes the study of the influence of filler particle size on the flexural strength of epoxy matrix biocomposites made with lignocellulosic particles obtained from coffee husk.

2. METHODOLOGY

Prior to the fabrication of the composites, coffee husk residues were ground, separated by particle size, and dried in an oven at 103°C for 24 hours. Subsequently, the coffee husk particles (CHP) were added to the resin-catalyst mixture in a 2:1 ratio, according to the manufacturer's instructions for epoxy resin 2004, with the addition of 40% CHP in mass fraction calculated from the mold volume. The method used was cold pressing, with the material being kept under a pressure of 4.6 MPa for 24 hours and 3 days under ambient conditions to complete the polymerization process.

After the curing period, the plates were laminated following the guidelines of ASTM D790, and 10 specimens were selected for the three-point bending test. The treatments consisted of epoxy resin composites without particle inclusion (RE), with particles up to 0.43mm (CHP-43), with particles up to 0.25mm (CHP-25), and specimens with particles smaller than 0.25mm (FINES). The tests were conducted on an Oswaldo Filizola AME-2kN universal testing machine, and morphological analysis was performed using a JEOL JSMIT200 scanning electron microscope (SEM).

Analysis of Variance indicated statistical differences among the treatments, and upon verifying the normality and homoscedasticity of the data, Tukey's mean comparison test was applied at a significance level of 5%. All statistical analyses were performed using RStudio software version 4.3.0.

3. RESULTS AND DISCUSSION

The reduction in particle size from CHP-43 to FINES resulted in a 21.69% increase in the maximum flexural strength of the biocomposites (Figure 1). For the same weight fraction, the smaller particle size likely provided a larger surface area, enabling better load transfer between the CHP and the polymeric matrix. Additionally, larger particles may function as stress agents, creating favorable points for crack initiation, resulting in increased brittleness of the biocomposite [12].

Treatments with different letters indicate statistically significant differences at a confidence level of 0.05 according to Tukey's test.
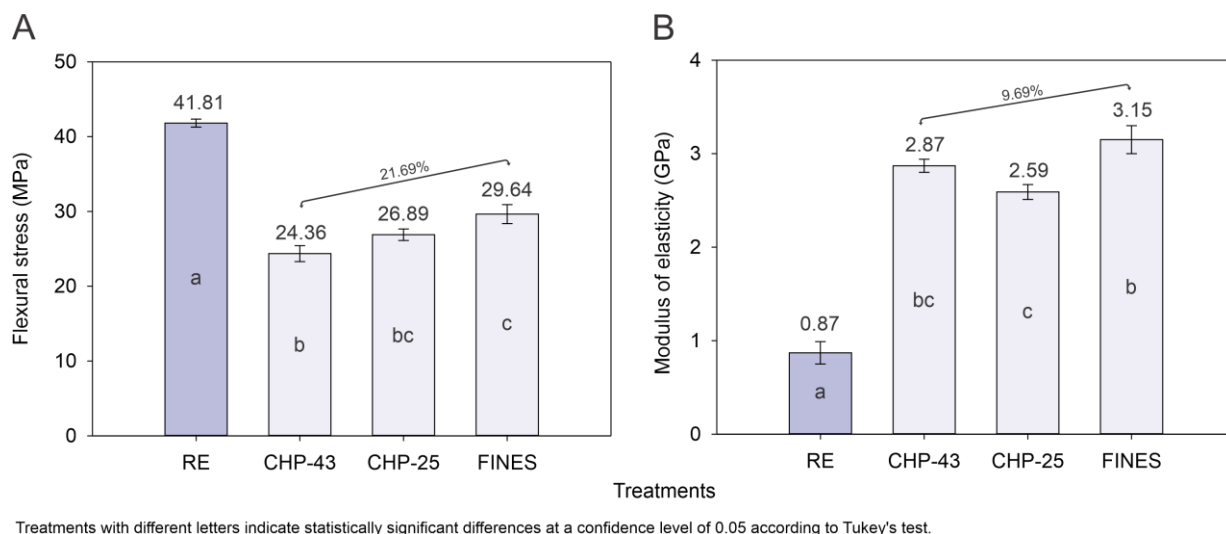
Figure 1. Flexural stress and modulus of elasticity of epoxy resin and biocomposites

The smaller the size of the lignocellulosic particles, the greater their dispersion in the continuous phase, resulting in good matrix-particle compatibility [13], a fact observed by Cui et al. [14], Hemmasi et al. [15], and Febrianto et al. [16], who identified a better contact surface using finer particle sizes, resulting in greater uniformity and consequently higher flexural strength and modulus of elasticity. It is worth noting that the adhesion force is also considered stronger than the cohesion force, which can lead to an increase in the composite's strength [17].

Regarding the micrographs of the fracture surface shown in Figure 2, for the pure epoxy resin, a fracture surface without roughness and with the occurrence of mirrored regions was observed (Figure 2a), which are typical characteristics of thermosetting polymers due to their rigidity, brittleness, and low ductility [18]. With the addition of CHP to the matrix, there is a change in the nature of the failure, from brittle to slightly ductile (Figure 2b), because the presence of lignocellulosic particles helps to form a barrier to crack propagation on the fragile surface of the polymeric matrix [19].
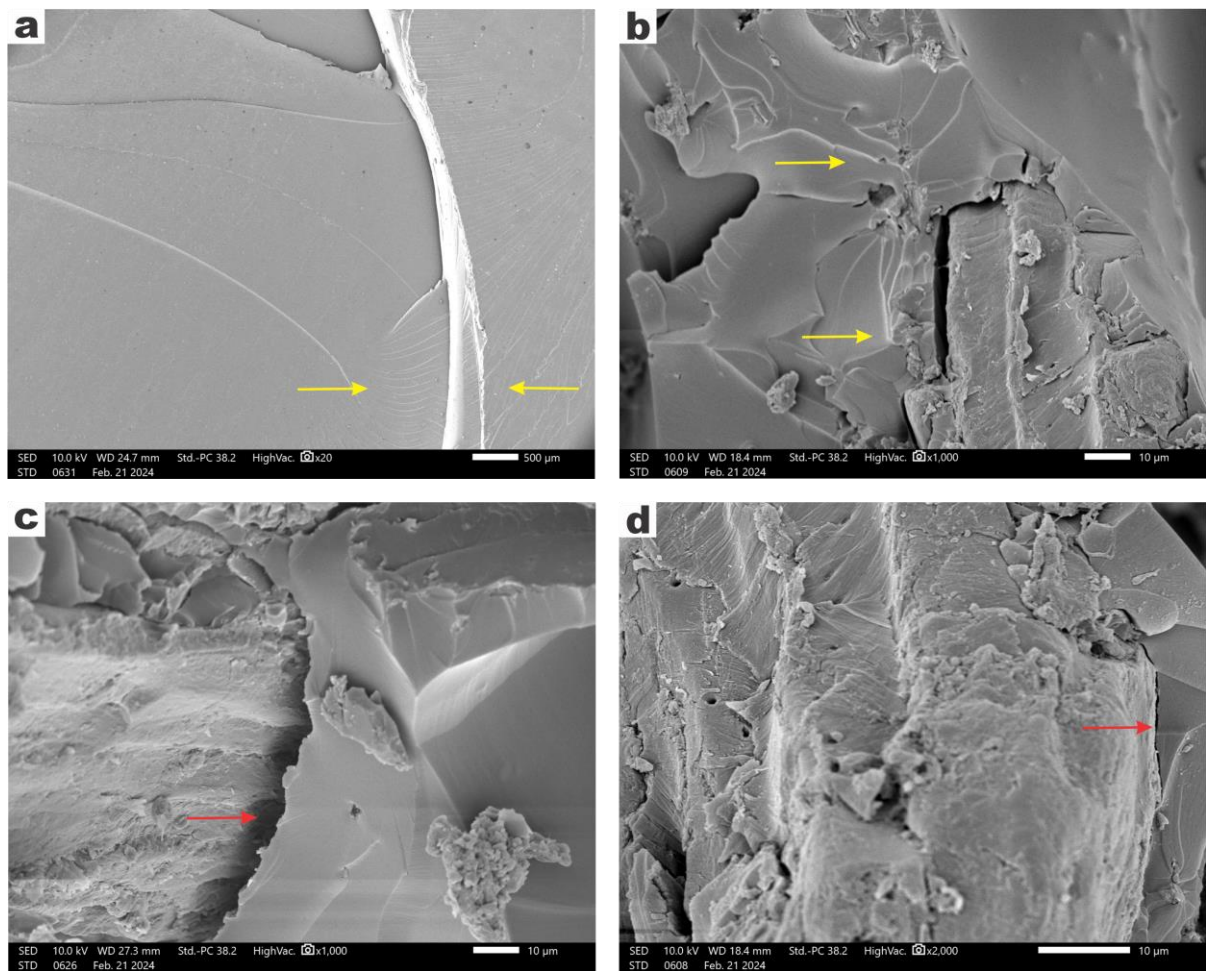
Figure 2. SEM micrographs of the fracture surface of epoxy resin (a), biocomposites CHP-25 (b), CHP-43 (c) and CHP-25 (d)

When examining the interface between the two phases (Figure 2b, c), the disconnection between the matrix and the coffee husk particles becomes evident, as indicated by the red arrows, regardless of the CHP particle size. This fact can possibly be attributed to the mucilage layer present on the particle surface [20], as the material did not undergo any prior treatment.

4. CONCLUSIONS

The different dimensions of the coffee husk particles directly influenced the maximum flexural strength and modulus of elasticity of the material, suggesting the fine particle size range (<0.25mm) as the most effective reinforcement filler. The SEM images confirmed the influence of the particles in increasing the ductility of the biocomposite.

4.1. Declaration of Competing Interest

The authors declare no conflict of interest.

4.2. Fundings

4.3. Acknowledgements

5. REFERENCES

[1]   K. L. Pickering, M. G. A. Efendy, and T. M. Le. A review of recent developments in natural fibre composites and their mechanical performance. *Compos Part A Appl Sci Manuf*, vol. 83, pp. 98–112, Apr. 2016. (doi: 10.1016/j.compositesa.2015.08.038).

[2]   S. Agustin-Salazar, P. Cerruti, and G. Scarinzi. Biobased structural additives for polymers. in *Sustainability of Polymeric Materials*, De Gruyter, 2020, pp. 193–234. (doi: 10.1515/9783110590586-009).

[3]   M. Y. Mahmoud Zaghloul, M. M. Yousry Zaghloul, and M. M. Yousry Zaghloul. Developments in polyester composite materials – An in-depth review on natural fibres and nano fillers. *Compos Struct*, vol. 278, p. 114698, Dec. 2021. (doi: 10.1016/j.compstruct.2021.114698).

[4]   F. Delogu, G. Gorrasi, and A. Sorrentino. Fabrication of polymer nanocomposites via ball milling: Present status and future perspectives. *Prog Mater Sci*, vol. 86, pp. 75–126, May 2017. (doi: 10.1016/j.pmatsci.2017.01.003).

[5]   T. Huber, M. Misra, and A. K. Mohanty. The effect of particle size on the rheological properties of polyamide 6/biochar composites. 2015, p. 150004. (doi: 10.1063/1.4918500).

[6]   Y. Zheng, Z. Fu, D. Li, and M. Wu. Effects of Ball Milling Processes on the Microstructure and Rheological Properties of Microcrystalline Cellulose as a Sustainable Polymer Additive. *Materials*, vol. 11, no. 7, p. 1057, Jun. 2018. (doi: 10.3390/ma11071057).

[7]   A. Isa *et al.* The Influence of Dry-Milled Wood Flour on The Physical Properties of Wood Flour/Polypropylene Composites. *Journal of Wood Chemistry and Technology*, vol. 36, no. 2, pp. 105–113, Mar. 2016. (doi: 10.1080/02773813.2015.1083583).

[8]   N. Suaduang, S. Ross, G. M. Ross, S. Pratumshat, and S. Mahasaranon. Effect of spent coffee grounds filler on the physical and mechanical properties of poly(lactic acid) bio-composite films. *Mater Today Proc*, vol. 17, pp. 2104–2110, 2019. (doi: 10.1016/j.matpr.2019.06.260).

[9]   L. W. Gallagher and A. G. McDonald. The effect of micron sized wood fibers in wood plastic composites. *Maderas. Ciencia y tecnología*, no. ahead, pp. 0–0, 2013. (doi: 10.4067/S0718-221X2013005000028).

[10] S. Agustin-Salazar, M. Ricciulli, V. Ambrogi, P. Cerruti, and G. Scarinzi. Effect of thermal annealing and filler ball-milling on the properties of highly filled polylactic acid/pecan nutshell biocomposites. *Int J Biol Macromol*, vol. 200, pp. 350–361, Mar. 2022. (doi: 10.1016/J.IJBIOMAC.2021.12.101).

[11] A. L. de Castro and V. C. Pandolfelli. Revisão: conceitos de dispersão e empacotamento de partículas para a produção de concretos especiais aplicados na construção civil. *Cerâmica*, vol. 55, no. 333, pp. 18–32, Mar. 2009. (doi: 10.1590/S0366-69132009000100003).

[12] M. E. Golmakani, T. Wiczenbach, M. Malikan, R. Aliakbari, and V. A. Eremeyev. Investigation of Wood Flour Size, Aspect Ratios, and Injection Molding Temperature on Mechanical Properties of Wood Flour/Polyethylene Composites. *Materials*, vol. 14, no. 12, p. 3406, Jun. 2021. (doi: 10.3390/ma14123406).

[13] Z. Dominkovics, L. Dányádi, and B. Pukánszky. Surface modification of wood flour and its effect on the properties of PP/wood composites. *Compos Part A Appl Sci Manuf*, vol. 38, no. 8, pp. 1893–1901, Aug. 2007. (doi: 10.1016/j.compositesa.2007.04.001).

[14] Y. Cui, S. Lee, B. Noruziaan, M. Cheung, and J. Tao. Fabrication and interfacial modification of wood/recycled plastic composite materials. *Compos Part A Appl Sci Manuf*, vol. 39, no. 4, pp. 655–661, Apr. 2008. (doi: 10.1016/j.compositesa.2007.10.017).

[15] A. H. Hemmasi, I. Ghasemi, B. Bazyar, and A. Samariha. Studying the effect of size of bagasse and nanoclay particles on mechanical properties and morphology of bagasse flour/recycled polyethylene composites. *Bioresources*, vol. 8, pp. 3791–3801, 2013.

[16] F. Febrianto, D. Setyawati, M. Karina, E. S. Bakar, and Y. S. Hadi. Influence of Wood Flour and Modifier Contents on the Physical and Mechanical Properties of Wood Flour-Recycle Polypropylene Composites. *Journal of Biological Sciences*, vol. 6, no. 2, pp. 337–343, Feb. 2006. (doi: 10.3923/jbs.2006.337.343).

[17] E. G. Kim, J. K. Park, and S. H. Jo. A study on fiber orientation during the injection molding of fiber-reinforced polymeric composites. *J Mater Process Technol*, vol. 111, no. 1–3, pp. 225–232, Apr. 2001. (doi: 10.1016/S0924-0136(01)00521-0).

[18] E. C. Ramires. Biocompósitos a partir de matrizes poliméricas baseadas em lignina, tanino e glioxal reforçadas com fibras naturais. São Carlos : Instituto de Química de São Carlos, Universidade de São Paulo, 2010. Tese de Doutorado em Físico-Química. (doi: 10.11606/T.75.2010.tde-06042010-165002).

[19] Z. Khan, B. F. Yousif, and M. Islam. Fracture behaviour of bamboo fiber reinforced epoxy composites. *Compos B Eng*, vol. 116, pp. 186–199, May 2017. (doi: 10.1016/j.compositesb.2017.02.015).

[20] A. Shalwan and B. F. Yousif. Investigation on interfacial adhesion of date palm/epoxy using fragmentation technique. *Mater Des*, vol. 53, pp. 928–937, Jan. 2014. (doi: 10.1016/j.matdes.2013.07.083).

IMPACT OF LIGNIN ON VEGETABLE POLYURETHANE COMPOSITES WITH BANANA FIBERS: FOCUS ON THE INTERFACE

Paulo Roberto Correia Marcelino[a] *, Felipe Gabriel Santos Araújo[b], Roseméri Barbosa dos Santos da Silva[c], Gabriel Mendonça Valane[d], Mateus Urbano do Nascimento[e], Michel Picanço Oliveira[f]

(a) 0000-0001-8594-0920 (Federal University of Espírito Santo - Brazil)*
(b) 009-0000-7069-5408 (Federal University of Espírito Santo - Brazil)
(c) 0009-0004-6432-519X (Federal University of Espírito Santo - Brazil)
(d) 0000-0002-2736-4440 (Federal University of Espírito Santo - Brazil)
(e) 0009-0008-3032-8134 (Federal University of Espírito Santo - Brazil)
(f) 0000-0001-9241-0194 (Federal University of Espírito Santo - Brazil)

* Corresponding author: paulocrm02@gmail.com

CODE: BCCM7-115

Keywords: Sustainability, Lignocellulosic fibers, Lignin.

Abstract: The increasing utilization of non-degradable polymers poses a considerable challenge from a sustainability perspective, driving the need to explore renewable sources in the production of these materials. In this context, studies aim to create polymeric composites from plant sources, highlighting natural fibers as sustainable alternatives as additives, such as banana fibers, which are abundant in tropical and subtropical regions, offering biodegradability and renewability to reduce environmental impact. Lignin, found in natural fibers, is valued in various industrial applications, especially in composite material production, due to its adhesive capacity that provides strength and stability to the final products, also being suitable for humid environments due to its hydrophobic nature. In this context, the present work aimed at the development of vegetable polyurethane (PUV) composites reinforced with banana fibers, incorporating lignin into its composition, in order to investigate the effects of lignin on the adhesion between fiber and matrix, and to monitor the influences on the material properties. Composites with different proportions of lignin were produced, and blends with the incorporation of lignin together with banana fibers were prepared. The applied lignin was oven-dried for 24 hours before its utilization, and its application was through dispersion in the matrix during polymerization. The banana fibers were oven-dried at 70°C for 24 hours before their application in the composite, which was manually performed by aligning the fibers in the longitudinal direction of the composite. After the curing time and subjected to tests and analyses, relevant results were observed, where the incorporation of 1% lignin led to an approximately 230% increase in Charpy impact toughness when evaluated. This result was also found when 1% lignin was applied together with 10% fibers. Morphologically, lignin improved the interface between the fiber and the matrix, justifying the elevated mechanical gains. The behavior of lignin in the matrix was observable, where optimal interaction between the matrix and lignin was noted, with more failures in the lignin structure compared to adhesion. When applied together with banana fibers, it provided a better interface, with visually fewer defects. This may indicate that lignin improved the fiber-matrix adhesion, but these are still underestimated results.

1. INTRODUCTION

In recent years, there has been a continuous rise in the utilization of natural/vegetal fibers as additives in polymeric composites, aimed at generating cost-effective engineering materials. The substantial consumer demand and environmental regulations have spurred diverse sectors, including civil engineering, packaging,

and automotive industries, to pursue natural alternatives to conventional non-renewable materials. This impetus has catalyzed the development of novel materials endowed with sustainable attributes, prioritizing products that fulfill industrial requisites while mitigating environmental impac [1]–[3]. Consequently, several studies highlight polyurethanes (PU) as versatile polymers for such applications, further underscoring castor oil, a natural triglyceride, in the synthesis of vegetable-based polyurethanes (GPU). This is primarily due to its abundance in nature and low cost. [4], [5].

As a means of enhancing the mechanical characteristics of composites, vegetable fibers or lignocellulosic particles can be incorporated into them. These materials contain cellulose in their composition, a semi-crystalline polymer known for its remarkable mechanical strength and elasticity modulus, and this could lead to a significant improvement in the performance of the material under study. [6], [7]. Cellulose has already been utilized as an additive in composite materials across various industrial sectors, including paper production, pharmaceuticals, cosmetics, among others. [8]. In addition to cellulose, another compound present in the chemical composition of wood and lignocellulosic materials is lignin, which acts as a natural adhesive in plants. Lignin has also been the subject of numerous research efforts aiming to utilize it in the development of new materials, primarily due to its characteristics such as antioxidant capacity, chemical stability, and potential as a fuel source. [9], [10].

In this context, this study aimed to develop composites with GPU matrix reinforced with lignin particles and banana fibers. The objective was to assess the influence of these materials on the Charpy impact toughness of the composite and to conduct a study on the influence of lignin on the performance of the fiber-matrix interface using scanning electron microscopy.

2. METHODOLOGY

In this study, composite materials produced by incorporating banana fibers and kraft lignin into the vegetable polyurethane resin (GPU) will be evaluated. The polyurethane resin used is sourced from Imperverg Polímeros e Indústria LTDA, specified as a two-component waterproofing agent with a density of 1.0 g/cm³ and thermal stability up to 120°C. Component A is a pre-polymer synthesized using castor oil-derived polyol and diphenylmethane diisocyanate (MDI), while component B consists of pure polyol. The manufacturer recommends a 46% usage of component A to 54% of component B in the GPU formation reaction.

The kraft lignin used in this study was obtained from Klabin S/A, while the banana fibers were manually extracted from a banana pseudostem sourced from Jerônimo Monteiro – ES

2.1. Composite production

The composite specimens were prepared according to the specifications of ASTM D6110-18 for impact testing. Thirty specimens were produced and divided into two groups. The first group contained varying percentages of lignin (0%, 1%, 2%, and 5%), while the second group contained a fixed percentage of 1% lignin with variations in the percentage of banana fibers (0%, 5%, and 10%). The production process involved the polymerization of the polyurethane resin components along with lignin, followed by molding into silicone molds with and without banana fibers. Subsequently, the specimens were placed in a compressed air reactor under a pressure of 90 kPa for 72 hours. After leaving the reactor, they were left to rest at room temperature for 15 days to complete their curing cycle before proceeding to Charpy impact testing. Figure 1 depicts the complete scheme of production and characterization of the studied composites.
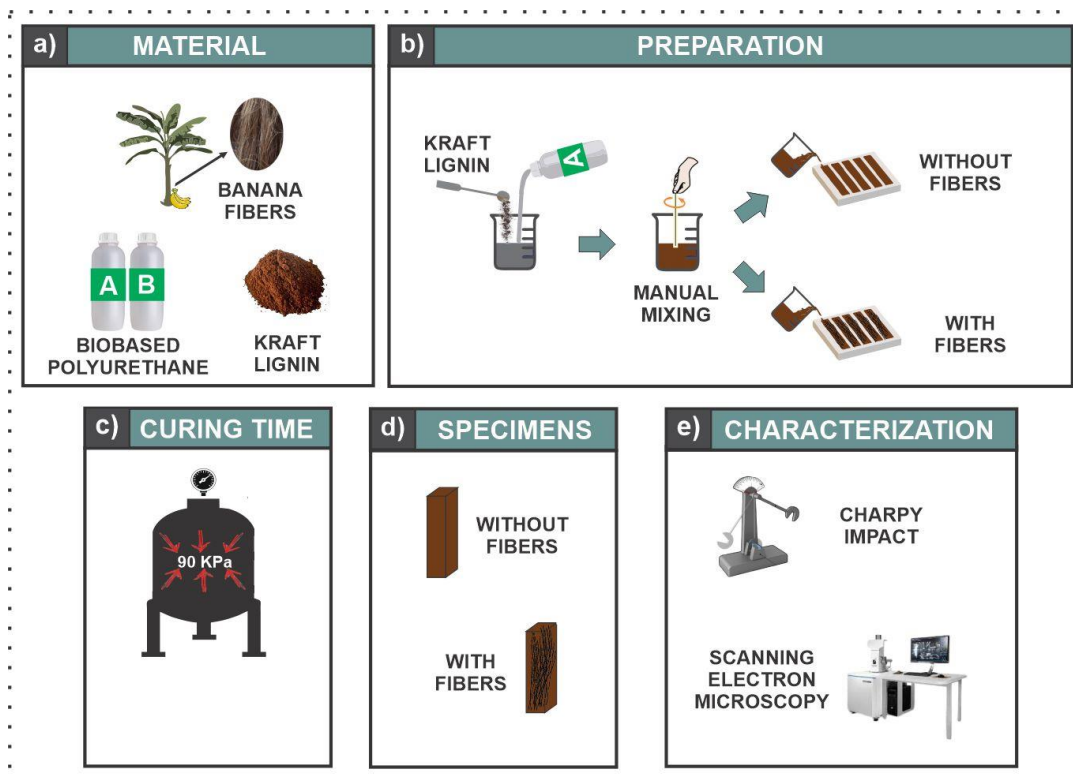
Figure 1: Scheme of production and characterization of the studied composites.

2.2. Statistical analysis

The PAST software was utilized to perform the comparison and distribution of the sample groups through analysis of variance (ANOVA) and Tukey's test for mean comparison to verify the occurrence of significant differences between the treatments.

3. RESULTS AND DISCUSSION

In Figure 2, the data concerning the Charpy impact toughness of the materials developed solely with lignin are depicted. It is noteworthy that the addition of lignin positively influenced this characteristic of the composites. It is evident that there was an increase in Charpy impact toughness for all proportions, with the group containing 1% lignin standing out, showing the best result with an approximately 270% increase compared to the matrix without additives. The groups with 2% and 5% lignin showed increases of approximately 200% and 170%, respectively. These improvements in toughness of the composites compared to the matrix without additives, as well as the better performance of the 1% lignin group, were confirmed through analysis of variance (ANOVA) and Tukey's test for mean comparison. Although the literature does not present many reports on the influence of lignin on the mechanical character of composite materials in general, these results validate the various advantages that lignin can provide when used, as concluded by Gaspar and Fardim (2023) [11] In their study investigating the utilization of lignin-based materials for advanced applications, various materials are being developed using lignin for emerging applications, offering high added value and substantial potential for substituting petroleum-derived materials in diverse sectors.
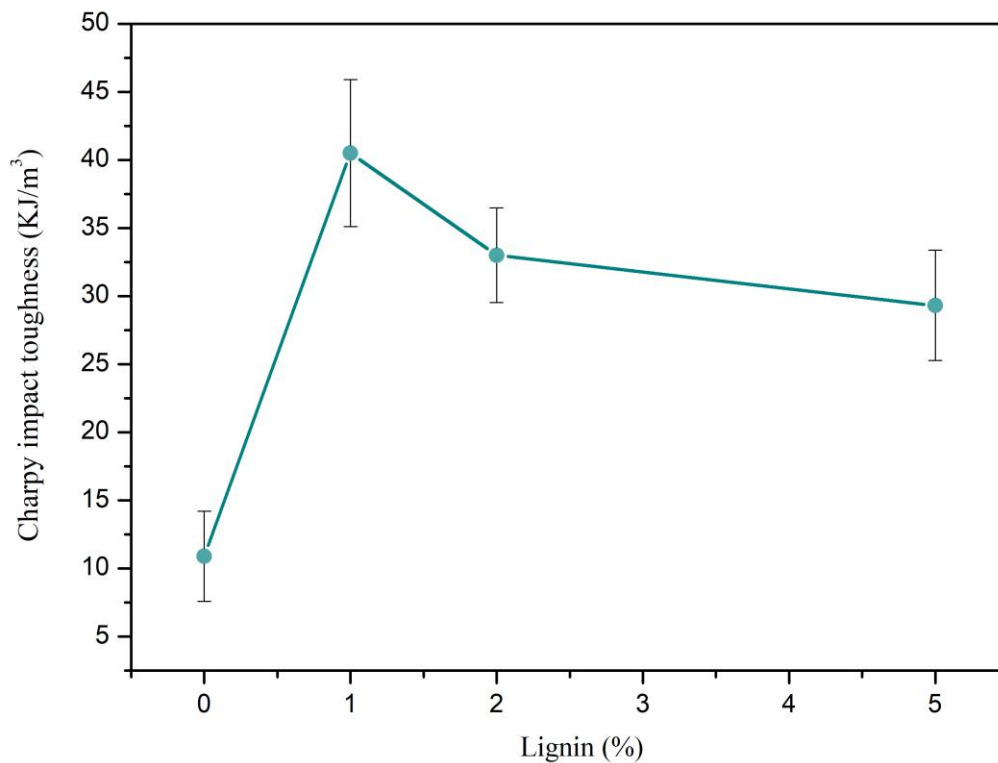
Figure 2: Relationship between increase in Charpy impact toughness and lignin addition.

In Figure 3, the data highlight the influence of banana fibers on the vegetable polyurethane matrix. As observed previously, the addition of 1% lignin resulted in the best performance in this matrix; thus, this value was established in conjunction with the fibers to promote a better fiber-matrix interface. There was an increase in Charpy impact toughness for the proportions of 5% and 10% of applied fibers, with gains of approximately 100% and 290%, respectively, demonstrating the efficiency of these fibers as polymer reinforcement. These gains observed in the toughness of the composites were confirmed through analysis of variance (ANOVA) and Tukey's test for mean comparison. Some studies confirm the efficiency of banana fibers as polymer reinforcement, as noted by Komal et al., (2018) [12] observed improvements in mechanical properties with the addition of banana fibers in their study on the effects of chemical treatment on the mechanical behavior of banana fiber-reinforced composites. Merlini et al., (2011) [13] They conducted a study on the influence of surface treatment of banana fibers on the physicochemical properties of composites with a matrix of vegetable polyurethane. They concluded that banana fibers can be highly effective in enhancing the tensile strength of composites with a polyurethane matrix derived from castor oil, especially when subjected to surface treatment.
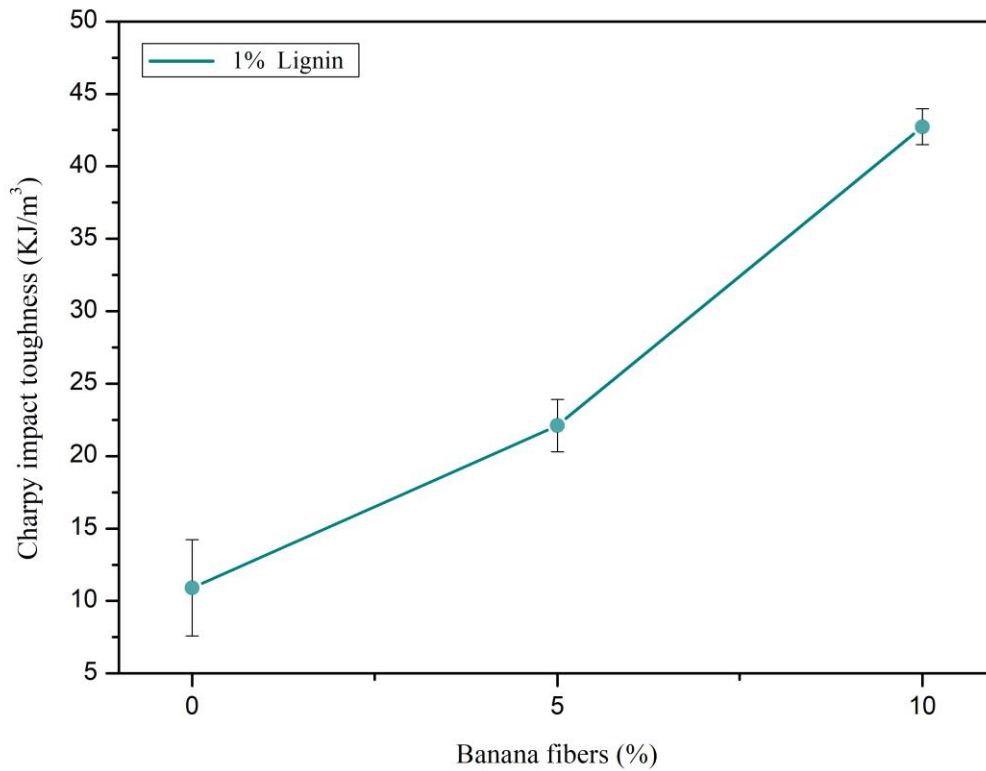
Figure 3: Relationship between increase in Charpy impact toughness and addition of banana fibers.

The good results in the toughness of the produced materials are directly linked to the interface between the matrix and the additives. Through scanning electron microscopy, it was possible to observe the favorable interface of lignin with the matrix, which consequently influenced better compatibility between the matrix and the banana fibers. A well-defined interface directly affects the mechanical characteristics of the material, as it generates a more efficient stress transfer between the fiber and the matrix and reduces stress concentrators [14]. Figure 4 emphasizes the excellent interaction between lignin particles and the vegetable polyurethane matrix, which undoubtedly contributed to the gain in material toughness.
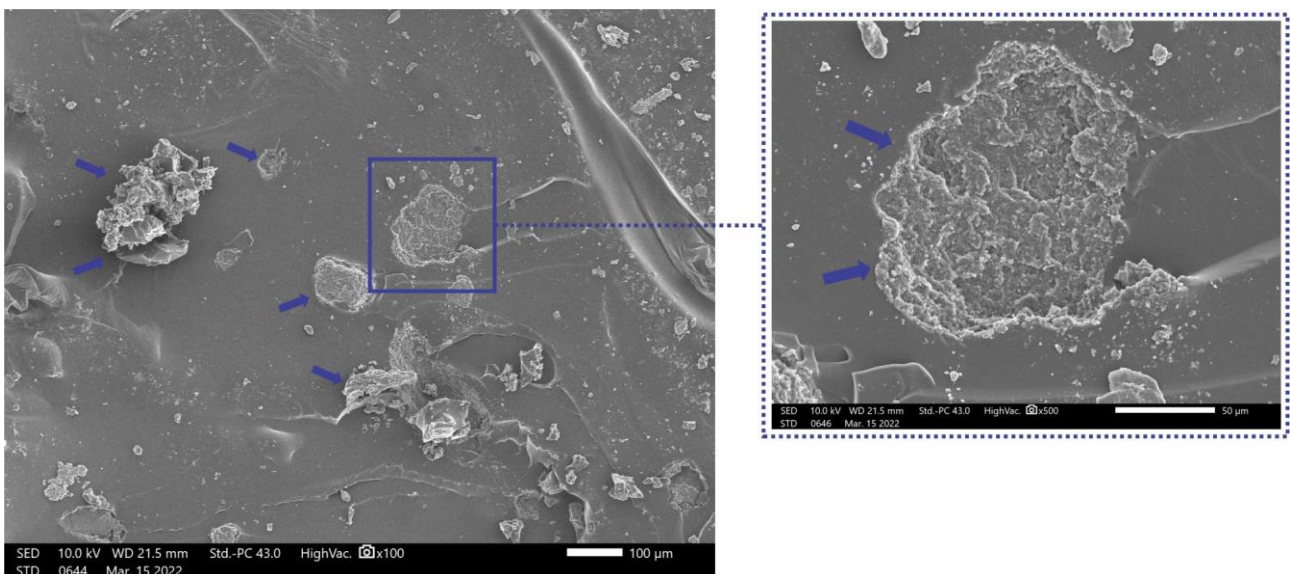
Figure 4: Micrographs highlighting the interface between lignin and the matrix.

Figure 5 displays comparative micrographs of the fiber-matrix interface with and without the presence of lignin. It is noticeable that banana fibers exhibit characteristics common to lignocellulosic materials, such as irregular and highly rough surfaces [15], [16]. The images demonstrate that the material without the presence of lignin lacks a good interface, as indicated by the arrows, showing poor adhesion between the matrix and the fibers. These adhesion failures are also reported by Melo et al., (2022) [15] which states that this signifies poor compatibility between fiber and matrix. In contrast, the micrographs of the material with the presence of lignin already show extremely strong adhesion with few failures, allowing us to conclude that lignin increased the compatibility between fiber and matrix, improving their adhesion and positively influencing the mechanical character of the material.
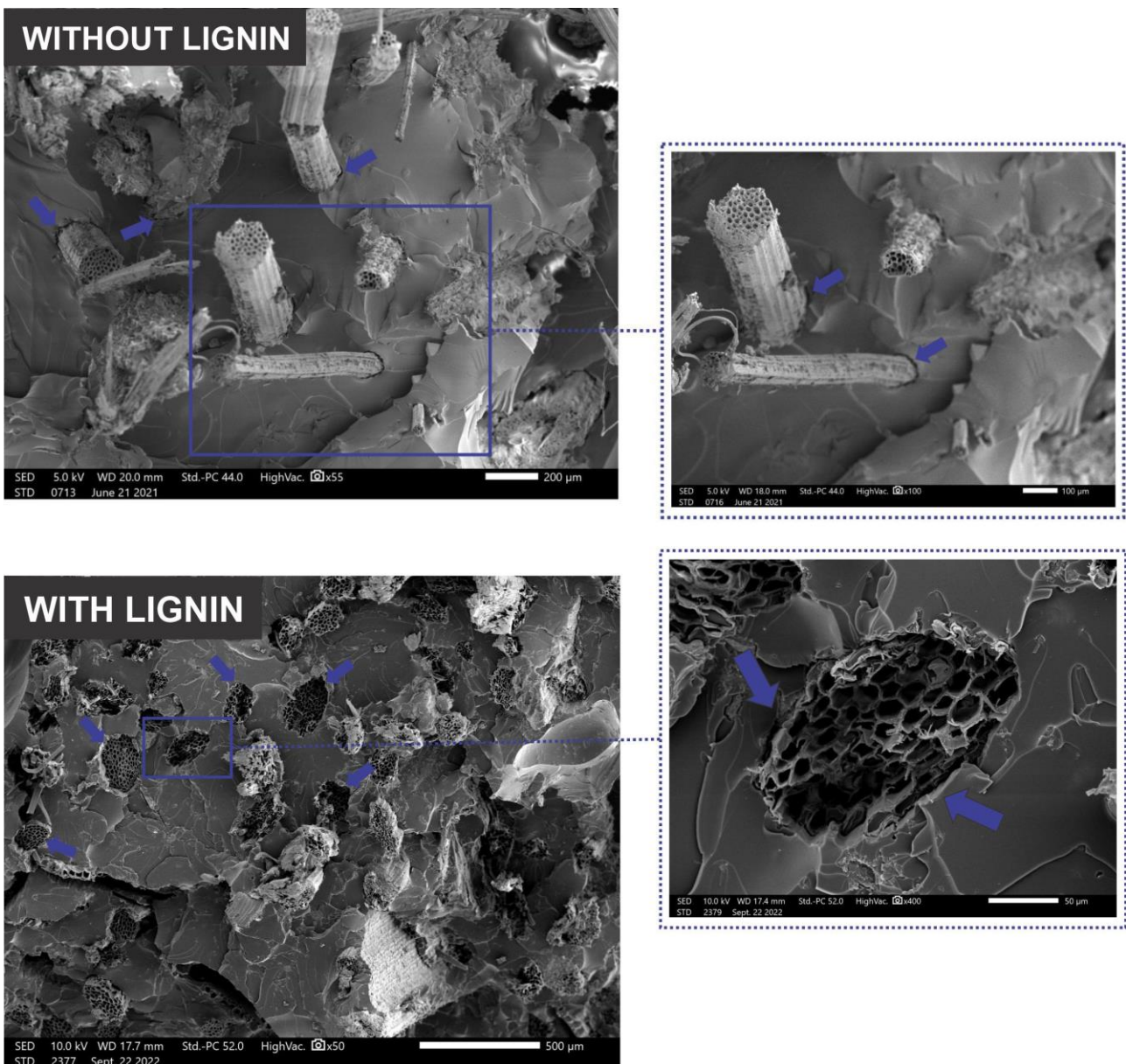
Figure 5: Comparative micrographs of the fiber-matrix interface with and without the presence of lignin.

4. CONCLUSIONS

The incorporation of lignin and banana fibers into vegetable polyurethane matrix composites demonstrated a significant contribution to Charpy impact toughness. The results indicate that the presence of lignin improved adhesion and compatibility between the matrix and fibers, resulting in a reduction of adhesion failures. These findings not only highlight the effectiveness of lignin but also help justify the gains observed

in toughness, emphasizing the potential of banana fibers and lignin as sustainable and effective alternatives in the development of new materials based on sustainability.

4.1. Declaration of Competing Interest

The authors declare no conflict of interest.

4.2. Fundings

5. REFERENCES

[1]   G. S. Rao, K. Debnath, and R. N. Mahapatra, "Degradation characteristics of the pineapple leaf fibre reinforced green composite developed by injection moulding under different environmental conditions," *Ind. Crops Prod.*, vol. 214, no. January, p. 118429, 2024, doi: 10.1016/j.indcrop.2024.118429.

[2]   J. Müssig, Ed., "Front Matter," in *Industrial Applications of Natural Fibres*, Chichester, UK: John Wiley & Sons, Ltd, 2010, pp. i–xxiii.

[3]   O. Das *et al.*, "Natural and industrial wastes for sustainable and renewable polymer composites," *Renew. Sustain. Energy Rev.*, vol. 158, no. December 2021, p. 112054, Apr. 2022, doi: 10.1016/j.rser.2021.112054.

[4]   P. M. Paraskar, M. S. Prabhudesai, V. M. Hatkar, and R. D. Kulkarni, "Vegetable oil based polyurethane coatings – A sustainable approach: A review," *Prog. Org. Coatings*, vol. 156, no. April, p. 106267, Jul. 2021, doi: 10.1016/j.porgcoat.2021.106267.

[5]   A. Kausar, "Polyurethane Composite Foams in High-Performance Applications: A Review," *Polym. Plast. Technol. Eng.*, vol. 57, no. 4, pp. 346–369, Mar. 2018, doi: 10.1080/03602559.2017.1329433.

[6]   V. K. Balla, K. H. Kate, J. Satyavolu, P. Singh, and J. G. D. Tadimeti, "Additive manufacturing of natural fiber reinforced polymer composites: Processing and prospects," *Compos. Part B Eng.*, vol. 174, no. March, p. 106956, 2019, doi: 10.1016/j.compositesb.2019.106956.

[7]   F. Sarasini *et al.*, "Recycling coffee silverskin in sustainable composites based on a poly(butylene adipate-co-terephthalate)/poly(3-hydroxybutyrate-co-3-hydroxyvalerate) matrix," *Ind. Crops Prod.*, vol. 118, no. March, pp. 311–320, Aug. 2018, doi: 10.1016/j.indcrop.2018.03.070.

[8]   K. Solin, "Nanocellulose interactions with protein and water in advanced sensing systems," in *Bioproducts ans Biosystems*, 2022.

[9]   B. Abraham *et al.*, "Lignin-based nanomaterials for food and pharmaceutical applications: Recent trends and future outlook," *Sci. Total Environ.*, vol. 881, no. March, p. 163316, Jul. 2023, doi: 10.1016/j.scitotenv.2023.163316.

[10]   A. M. Braga, A. Cristina, M. Caramez, T. Dâmaso, and E. L. Schultz, "O POTENCIAL DA LIGNINA NO CONTEXTO BRASILEIRO : UM DIAGNOSTICO DE ESPECIALISTAS BRASILEIROS SOBRE TECNOLOGIAS E TENDENCIAS PARA 2030," vol. 84, no. July, pp. 87–97, 2023.

[11]   R. Gaspar and P. Fardim, "Lignin-based materials for emerging advanced applications," *Curr. Opin. Green Sustain. Chem.*, vol. 41, p. 100834, Jun. 2023, doi: 10.1016/j.cogsc.2023.100834.

[12]   U. K. Komal, V. Verma, T. Aswani, N. Verma, and I. Singh, "Effect of chemical treatment on mechanical behavior of banana fiber reinforced polymer composites," *Mater. Today Proc.*, vol. 5, no. 9, pp. 16983–16989, 2018, doi: 10.1016/j.matpr.2018.04.102.

[13]   C. Merlini, V. Soldi, and G. M. O. Barra, "Influence of fiber surface treatment and length on physico-chemical properties of short random banana fiber-reinforced castor oil polyurethane composites," *Polym. Test.*, vol. 30, no. 8, pp. 833–840, Dec. 2011, doi: 10.1016/j.polymertesting.2011.08.008.

[14]   A. Godara *et al.*, "Interfacial shear strength of a glass fiber/epoxy bonding in composites modified with carbon nanotubes," *Compos. Sci. Technol.*, vol. 70, no. 9, pp. 1346–1352, Sep. 2010, doi: 10.1016/j.compscitech.2010.04.010.

[15]   E. C. R. de Melo *et al.*, "Influence of Silanization Treatment of Sponge Gourd (Luffa cylindrica) Fibers on the Reinforcement of Polyester Composites: A Brief Report," *Polymers (Basel).*, vol. 14, no. 16, p. 3311, Aug. 2022, doi: 10.3390/polym14163311.

[16] A. Oushabi, "The pull-out behavior of chemically treated lignocellulosic fibers/polymeric matrix interface (LF/PM): A review," *Compos. Part B Eng.*, vol. 174, p. 107059, Oct. 2019, doi: 10.1016/j.compositesb.2019.107059.

EFFECT OF BANANA FIBER ADDITION ON WATER ABSORPTION OF BIOBASED POLYURETHANE COMPOSITE

Paulo Roberto Correia Marcelino[a] *, Felipe Gabriel Santos Araújo[b], Roseméri Barbosa dos Santos da Silva[c], Gabriel Mendonça Valane[d],Mateus Urbano do Nascimento[e], Michel Picanço Oliveira[f]

(a) 0000-0001-8594-0920 (Federal University of Espírito Santo - Brazil)*
(b) 009-0000-7069-5408 (Federal University of Espírito Santo - Brazil)
(c) 0009-0004-6432-519X (Federal University of Espírito Santo - Brazil)
(d) 0000-0002-2736-4440 (Federal University of Espírito Santo - Brazil)
(e) 0009-0008-3032-8134 (Federal University of Espírito Santo - Brazil)
(f) 0000-0001-9241-0194 (Federal University of Espírito Santo – Brazil)

* Corresponding author: paulocrm02@gmail.com

CODE: BCCM7-116

Keywords: Polymeric composites, Water absorption, Banana fiber.

Abstract: Currently, polymeric composites are widely used in engineering due to the balance between mechanical strength and weight. However, environmental issues associated with synthetic plastics, such as non-biodegradability, raise concerns. Bio-based polyurethane (BPU) emerges as a promising alternative due to its low toxicity and affordable cost. The interaction between the hydrophobic resin and hydrophilic natural fibers may compromise the material in humid environments, therefore evaluating water absorption in composites is essential, as the presence of water can affect structural integrity and accelerate degradation, especially in composites with natural fibers. This study evaluates the influence of banana fibers on water absorption. Samples with different proportions of banana fibers in the BPU matrix were analyzed by electron microscopy and water absorption tests. It was observed that water absorption increases proportionally with the amount of fibers, due to the high porosity of the fibers.

1. INTRODUCTION

Lately, there has been a significant interest in the development of composite materials due to their capability to offer a wide range of properties, particularly in the case of lignocellulosic fiber-reinforced polymer matrix composites, which are materials characterized by good availability, accessibility, low density, and renewable nature. [1]. Despite their favorable characteristics, lignocellulosic fibers exhibit hydrophilic behavior, which can compromise the properties of the material due to water absorption and low compatibility with the polymer matrices, which are generally hydrophobic, and this interaction results in fiber swelling within the composite, causing dimensional instability and potentially significant damage to the material. [2]–[4].

This characteristic of fibers arises from their richness in cellulose and hemicelluloses, which are highly hydrophilic and strongly polar materials, causing significant water absorption by natural fibers that compromises their interaction with the matrix and consequently affects the mechanical strength of the composite depending on the duration and nature of exposure to moisture, thereby also affecting the load transfer between fiber and matrix. [5]–[8].

In this context, this study aims to evaluate the variation in water absorption in biobased polyurethanecomposites as a function of the quantity of banana fibers used in their composition, in order to understand the material's characteristics concerning moisture.

2. METHODOLOGY

This study will assess water absorption in composite materials produced by applying banana fibers in biobased polyurethaneresin (BPU). The polyurethane resin used is sourced from Imperverg Polímeros e Indústria LTDA, specified as a two-component waterproofing agent with a density of 1.0 g/cm3 and thermal stability up to 120°C. Component A is a pre-polymer synthesized from castor oil-derived polyol and diphenylmethane diisocyanate (MDI), while Component B consists of pure polyol. The manufacturer recommends a 46% usage of Component A to 54% of B in the BPU formation reaction.

2.1. Produção dos compósitos

The composites used are part of a separate study where their tensile strength was analyzed. After fracture, they were subjected to water absorption and scanning electron microscopy, which are the topics addressed in this work.

Twenty samples were used, divided into four groups, each containing a variation of banana fiber percentage: 0, 10, 20, and 30%, respectively. The material from the tensile test was submerged in distilled water following ASTM D570 (2018) standards, with five samples for each group. Each sample was initially weighed on a four-digit precision analytical balance and then immersed in distilled water. They remained immersed for two weeks, and water absorption was inferred by the percentage change in mass, with weighing performed weekly. Figure 1 illustrates the methodological scheme of the study.
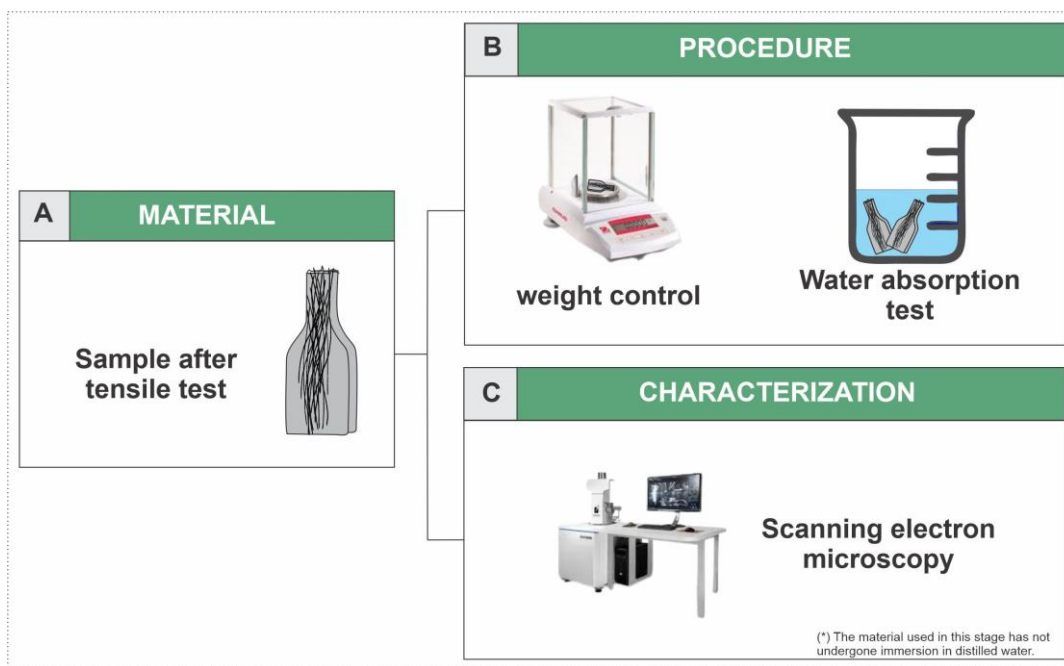
Figure 1: Scheme of production and characterization of the composites under study.

3. RESULTS AND DISCUSSION

The advantages of lignocellulosic fibers for composite materials applications are evident, however, their hydrophilic characteristic poses a limiting factor when exposed to moisture, then the interaction between fiber and matrix is significantly compromised. The absorption of water affects the bond between fiber and polymer, resulting in a decrease in the mechanical properties of the material under study. [5]–[7].

In figure 2, the water absorption curves of composites with biobased polyurethane(BPU) matrix and different proportions of banana fibers are depicted, namely 0, 10, 20, 30%, respectively. It is clear the increase in the percentage of absorption with the increase in the fiber proportion, where the matrix without additives showed a much lower variation compared to the others, with approximately 0.8% average variation. The material with 30% banana fiber content exhibited the highest absorption rate, with values close to 4%. The composites with 20% and 30% showed approximate values of 2% and 3.5%, respectively. Thus, it is evident that a greater quantity of fibers results in higher water absorption. This increasing trend in water absorption is similar to those found by [9], [10], Both studies utilized banana fibers in their research..
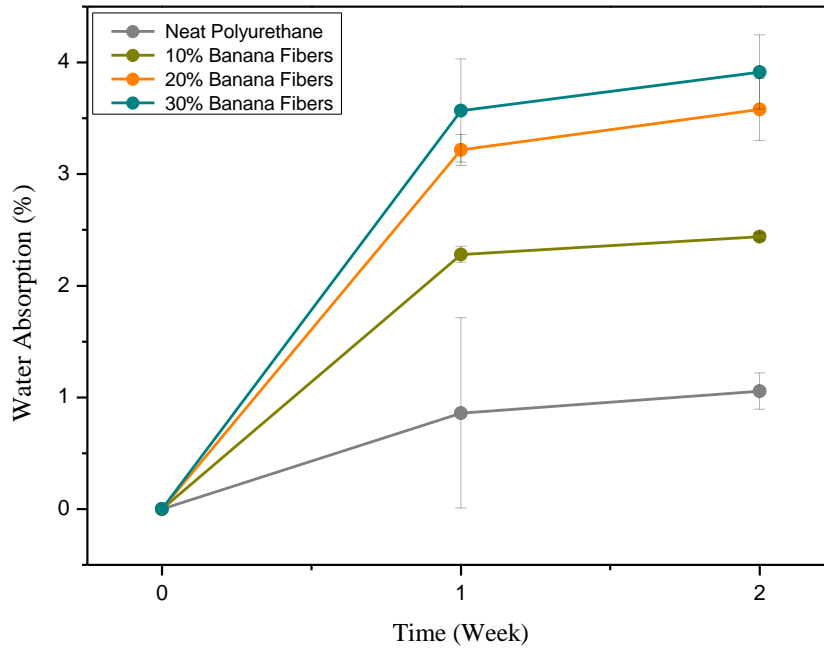
Figure 2: Water absorption of the composites as a function of time and fiber quantity.

The increase in absorption due to the addition of fibers may be a factor justifying the poor interaction between fiber and matrix, as demonstrated by the yellow arrows in figure 3. Moisture absorption can indeed affect the interaction and compatibility of the fiber with the matrix [5]. This hydrophilic characteristic may result from the high porosity of the banana fibers, as highlighted in the squares in figure 3. Additionally, the chemical composition of the fibers contributes to this characteristic, with the presence of cellulose and hemicelluloses, which are hydrophilic sources.
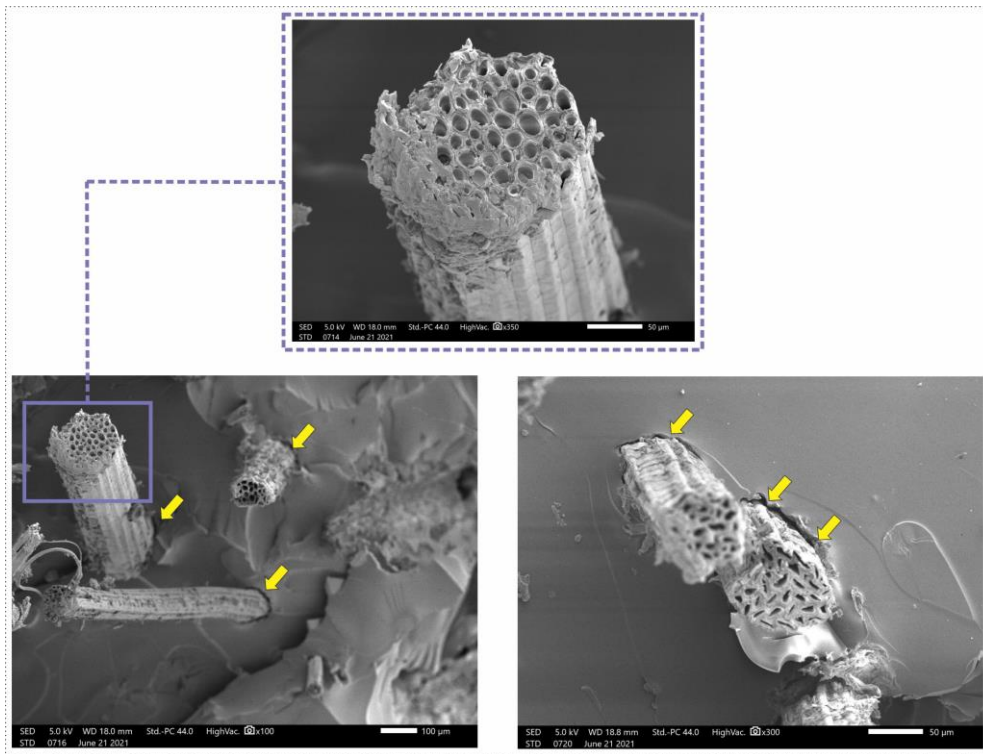
Figure 3: Scanning electron microscopy of the produced composites.

4. CONCLUSIONS

Banana fibers had a significant impact on the water absorption of the materials studied. This result can be attributed to the porosity of the fibers, which leads to their hydrophilicity, where a greater quantity of fibers resulted in greater water absorption. Using SEM micrographs, it can be concluded that the water absorption of banana fibers may be a factor that affects the interaction of materials and their compatibility with polymer matrices.

4.1. Declaration of Competing Interest

The authors declare no conflict of interest.

4.2. Fundings

5. REFERENCES

[1]   S. S. Shifa *et al.*, "Influence of heat treatment and water absorption on mechanical properties of cotton-glass fiber reinforced epoxy hybrid composites: An eco-friendly approach for industrial materials," *Hybrid Adv.*, vol. 5, p. 100181, Apr. 2024, doi: 10.1016/j.hybadv.2024.100181.

[2]   V. K. Balla, K. H. Kate, J. Satyavolu, P. Singh, and J. G. D. Tadimeti, "Additive manufacturing of natural fiber reinforced polymer composites: Processing and prospects," *Compos. Part B Eng.*, vol. 174, no. March, p. 106956, 2019, doi: 10.1016/j.compositesb.2019.106956.

[3]   F. Sarasini *et al.*, "Recycling coffee silverskin in sustainable composites based on a poly(butylene adipate-co-terephthalate)/poly(3-hydroxybutyrate-co-3-hydroxyvalerate) matrix," *Ind. Crops Prod.*, vol. 118, no. March, pp. 311–320, Aug. 2018, doi: 10.1016/j.indcrop.2018.03.070.

[4]   T. Väisänen, O. Das, and L. Tomppo, "A review on new bio-based constituents for natural fiber-

polymer composites," *J. Clean. Prod.*, vol. 149, pp. 582–596, Apr. 2017, doi: 10.1016/j.jclepro.2017.02.132.

[5]   M. K. Singh, R. Tewari, S. Zafar, S. M R, and S. Siengchin, "A Comprehensive Review of Various Factors for Application Feasibility of Natural Fiber-Reinforced Polymer Composites," *SSRN Electron. J.*, pp. 1–25, 2022, doi: 10.2139/ssrn.4226491.

[6]   M. A. Azka, S. M. Sapuan, H. Abral, E. S. Zainudin, and F. A. Aziz, "An examination of recent research of water absorption behavior of natural fiber reinforced polylactic acid (PLA) composites: A review," *Int. J. Biol. Macromol.*, vol. 268, p. 131845, May 2024, doi: 10.1016/j.ijbiomac.2024.131845.

[7]   T. Srinivasan, G. Suresh, P. Ramu, V. Gokul Ram, M. Giresh, and K. Arjun, "Effect of water absorption of the mechanical behavior of banana fiber reinforced IPN natural composites," *Mater. Today Proc.*, vol. 45, pp. 1334–1337, 2021, doi: 10.1016/j.matpr.2020.06.024.

[8]   A. Shalwan and B. F. Yousif, "In State of Art: Mechanical and tribological behaviour of polymeric composites based on natural fibres," *Mater. Des.*, vol. 48, pp. 14–24, Jun. 2013, doi: 10.1016/j.matdes.2012.07.014.

[9]   R. Karthick *et al.*, "Influence of glass fiber hybridization on flexural and water absorption behaviour of banana fiber reinforced epoxy composites," *Mater. Today Proc.*, Aug. 2023, doi: 10.1016/j.matpr.2023.07.355.

[10]   O. Joseph Gbadeyan, T. P. Mohan, and K. Kanny, "Effect of loading nano-clay on banana fibers infused epoxy composite wear rate thermal property and water absorption properties," *Mater. Today Proc.*, vol. 87, pp. 252–256, 2023, doi: 10.1016/j.matpr.2023.05.352.

Evaluation of fracture energy in mode II in hybrid composites with natural fibers

Bernardo Silveira Arantes Mendes[(a)], Bernardo Lopes Rieke Borges[(a)], Ranulfo Martins Carneiro Neto[(b)]*, Eduardo Martins Sampaio[(c)], Mariana Banea[(d)]

(a) Federal University of Rio de Janeiro – Brazil

(b) 0000-0001-8260-960X (Federal University of Rio de Janeiro – Brazil / Programa de Pós-Graduação em Engenharia Mecânica e Tecnologia de Materiais - Federal Center for Technological Education Celso Suckow da Fonseca)

(c) 0000-0002-0339-0716 (University of State of Rio de Janeiro – Brazil)

(d) 0000-0002-8378-2292 (Programa de Pós-Graduação em Engenharia Mecânica e Tecnologia de Materiais - Federal Center for Technological Education Celso Suckow da Fonseca)

* Corresponding author: ranulfoufrj@gmail.com

CODE: BCCM7-130

Keywords: Natural fibers; hybrid composites; mode II; shear fracture energy.

Abstract: Natural fibers reinforced composites represent a rapidly growing family of composites in the market due to their lightness, economic efficiency, and positive sustainable characteristics when compared to other popular materials. However, despite the significant benefits, vegetable fibers present enormous challenges, with a notable emphasis on their high moisture absorption due to their highly hydrophilic composition, resulting in reduced interfacial strength. To overcome this limitation, hybridization emerges as an interesting approach, involving the combination of distinct materials to form a unique composite. Synthetic fibers, recognized for their high moisture resistance, when laminated together with natural fibers, promise to significantly enhance mechanical properties, beneficially altering the energy required for material fracture. Finally, hybridization will benefit from the ecological aspects of natural fibers and the crucial strength of synthetic fibers. In this work, the critical fracture energy in mode II (G_{IIC}) of natural fiber and hybrid composites was determined, as well as the maximum load of the end-notched flexure (ENF) test. Two distinct configurations were tested: i) A laminated structure with four layers of reinforcement, all utilizing natural fibers, ii) A laminated structure consisting of six layers, with the first and last layers reinforced with fiberglass and the four inner layers reinforced with natural fibers. It was found that the joints with reinforcement of fiberglass had much higher values of G_{IIC}. The results may contribute to expanding the application of natural fibers in hybrid composite joints for other engineering areas, especially in pipe repairs, where a good resistance to moisture is required.

1. INTRODUCTION

The technologies developed in recent years, especially those related to the aerospace, maritime, and terrestrial industries, demand a constant evolution of materials with distinct properties, which cannot be found solely with metallic alloys or ceramics. Thus, laminated composites with different fibers have significant potential for expansion in several engineering areas [1]. This is because they consist of materials with different purposes in their composition: Fibers that serve to resist the applied forces in the structure and a matrix aimed at binding the reinforcements and transferring the forces.

The use of fiber-reinforced composites in structures is increasingly on the rise due to gains in cost and structural weight [2]. Carbon and glass fibers are part of the synthetic fiber group and are currently more

popular. However, laminated composites with natural fibers already have applicability in human daily life and have been continuously explored due to their lower environmental impact.

At the present time, a large portion of automobile manufacturers, including renowned brands such as Audi, Volkswagen, Toyota, Daimler-Benz, Volvo, and Ford, are adopting the use of natural fiber-reinforced composites (Table 1). This choice aims to obtain components with a lower environmental impact and lighter weight, resulting in vehicles that are more fuel-efficient. Based on this, vehicles will drive more vigorously the growth of the automotive market for plant-based fibers [3].

Table 1 - Natural fibres used in automotive components [4].

Manufacturer	Model	Applications	Natural fibre
Daimler benz	A, C, E, and S class	Door panels, floor panels, trunk panels, dashboards, pillar cover panels, seat back rests, insulation	Flax, sisal, coir, wood, banana, cotton
BMW	3, 5, and 7 series	Door panels, boot linings, seat backs, headliner panels, noise insulation panels	Flax, sisal, cotton, wood, hemp
Audi	A2, A3, A4, A6, A8, A4 avant, coupe, roadster	Seat backs, back door panels, side door panels, boot liners, spare tire liners	Flax, sisal
Volkswagen	Golf, passat, bora, A4	Seat backs, door panels, boot liners, boot lid finish panels	Flax, sisal
Ford	Mondeo, focus	Door panels, boot liners, floor trays, door inserts	Kenaf, wheat straw, castor, tomato, rice hulls
Toyota	Raum, brevis, harrier, celsior	Floor mats, spare tire covers, door panels and seat backs, luggage compartments	Kenaf, sugarcane, bamboo
General motors	Cadillac DeVille, chevy trailblazer, chevy impala, GMC envoy	Seat backs, cargo area floor mats, noise insulation, door panels, trim, rear bumper	Cotton, flax, wood, kenaf, hemp
Opel	Vectra, astra, zafira	Door panels, head liner panels, instrumental panels	Flax, kenaf
Mitsubishi	Space star, colt	Cargo area floor, door panels, instrumental panels	-
Lotus	Eco elise	Body panels, interior mats, seats, spoilers	Hemp, sisal, kenaf
Fiat	Punto, brava, alfa romeo 146, 156, 159	Door panels	Hemp, sisal
Peugeot	406	Front and rear door panels, seat backs, packaging trays	Hemp, sisal
Volvo	V70, C70	Seat cushions, cargo floor mats	Hemp, sisal, jute, rapeseed
Citroen	C5	Interior door paneling	—

Plant-based fibers not only have benefits but also exhibit one of their main disadvantages, which is their high moisture absorption due to their highly hydrophilic composition, resulting in lower interfacial strength [5]. The most recommended technique in the literature to reduce water absorption is hybridization, which involves using two or more different materials as reinforcements for composites [6]. Synthetic hybridization in Jute and Sisal fibers, employing glass fiber, has a significant impact on material properties and the strength of the bonded joint [7].

Natural fiber reinforcements benefit from ecology, resulting in lower cost and weight, while synthetic reinforcements such as glass fibers exhibit higher strength and lower moisture absorption [8]. For example, the work developed by Wang et al. [9], entitled 'A review on the tensile properties of natural fibers reinforced polymer composites,' which mixed approximately 25% glass fiber with the remaining jute fiber and observed benefits in strength and toughness properties.

Jute fiber exhibits greater stiffness than other popular natural fibers, such as sisal fiber [10]. However, the density of jute is approximately 50% of that of glass fiber, meaning that for every 1.3 units of glass fiber, 2.5 units of jute are required, making the substitution of synthetic fiber with natural fiber viable, with the benefit of lower weight and good stiffness [11]. Upon deeper comparison of materials, it can be observed that the stiffness of jute fibers is almost 80% that of glass fibers [11] and that the cost per unit weight of jute is up to 89% cheaper when compared to glass fibers. In order to highlight the positive aspects and further popularize the use of jute fibers, mechanical and thermal studies are increasingly being promoted [12].

This work is focused in compare the behaviour of composite adhesive joints with two different configurations: i) A laminated structure with four layers of reinforcement, all utilizing natural fibers (juta), ii) A laminated structure consisting of six layers, with the first and last layers reinforced with fiberglass and the four inner layers reinforced with natural fibers (juta). At first tensile tests were performed aiming to access the mechanical properties of both configurations. Then ENF tests were performed and the maximum load and G_{IIC} were obtained and compared.

2. METHODOLOGY

The jute-type natural fibers underwent a drying process in an oven for 15 minutes at a temperature of 100°C, aiming to remove all moisture present in the fiber. After this stage, the jute fiber reinforcement had a thickness of 1 millimeter (Figure 1). To facilitate handling, both the glass fiber and jute vegetable fiber were cut into pieces measuring 30 centimeters in width by 50 centimeters in length. Prior to starting the lamination process, the MDF plates were thoroughly cleaned to prevent any interference with the matrix during the resin drying period.

Figure 1 – Jute fiber without humidity.

In the lamination process, a Peel Ply was employed to facilitate the removal of the matrix after complete drying. For the lamination of the two arrangements with different compositions (Table 2), a brush, roller, and square were used. The brush was employed to spread the resin over the fibers, while the roller was used on each layer of applied fiber to eliminate air bubbles formed during the bonding process. The square was employed to ensure the correct positioning of all fibers during the process.

Table 2 – Joint's configurations.

Group	Layers
Group J0 - Natural fiber JUTA	4 layers of natural fibers
Group J1 - Natural fiber JUTA in the inner layers and one layer fiberglass in the outer layers;	4 layers of natural fibers + 2 layers of fiberglass (1 at the top and 1 at the bottom)

After laminating the arrangements, the matrix composed of reinforcement fibers and resin, responsible for bonding the fibers, was left to air dry completely (Figure 2). After drying, the laminate was cut to the dimensions of the test specimens, which were then subjected to mechanical tests.

Figure 2 – Specimens manufactured with peel ply in the ends.

3. RESULTS AND DISCUSSION

Hereafter the joints from the group J0 and J1 will be called as J0 joints and J1 joints, respectively.

Typical curves obtained from tensile tests are presented in Figure 3. As expected, the addition of layers of fiberglass leads to higher values of both maximum load and stiffness.
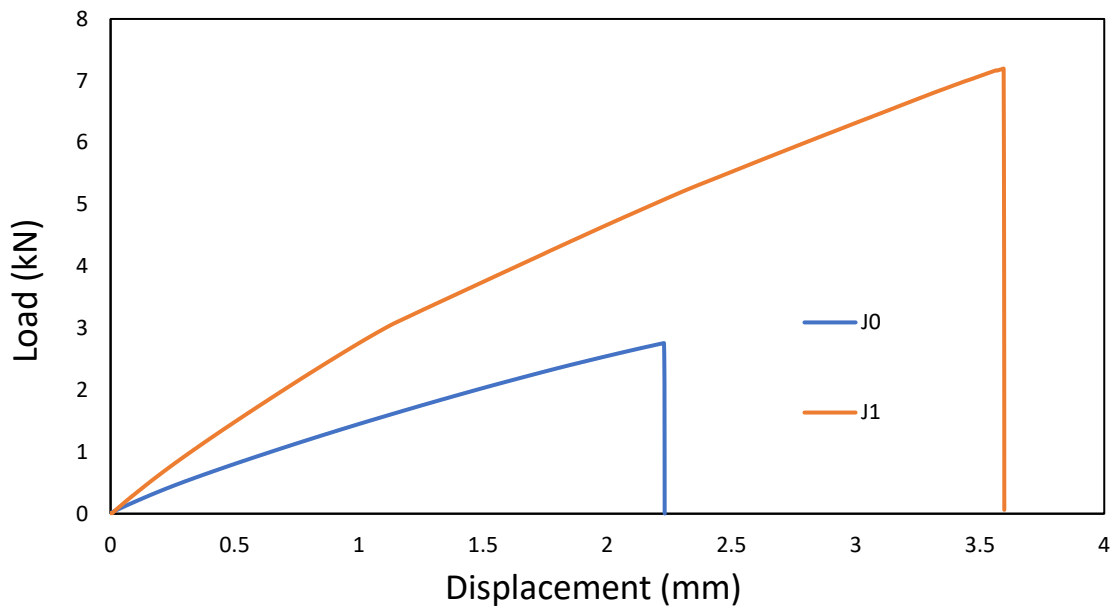
Figure 3 – Typical curves obtained in the tensile tests for both configurations investigated.

Table 3 shows the values of Young's modulus and tensile strength. The data had good repeatability, which is confirmed by the low values of standard deviations.

Table 3 – Mechanical properties obtained in the tensile tests.

Group	Young modulus (GPa)	Tensile strength (MPa)
J0	4.18 ± 0.34	37.45 ± 5.10
J1	7.9 ± 0.64	98.18 ± 8.52

The addition of layers of fiberglass increases both the maximum load and the critical fracture energy in mode II (G_{IIC}) of adhesive joints in ENF tests, as expected. The results are presented in Table 4. From the joint J0 to J1, the average value of the maximum load almost tripled, while the average value of G_{IIC} increased 2.5 times. These results demonstrate the great potential of hybrid composite joints for engineering aplications.

Table 4 – Maximum load and G_{IIC} obtained in the ENF tests.

Group	Maximum load (N)	G_{IIC} (N/mm)
J0	400.97 ± 23.27	1.01 ± 0.29
J1	1164.17 ± 97.07	2.50 ± 0.22

Figures 4 and 5 present typical load vs. displacement curves and R-curves, respectively, for both groups (J0 and J1) tested. The difference between the behavior of J0 and J1 joints is evident in Figure 4, where great changes in maximum load and stiffness can be visualized. However, it should be noted that J0 joint had higher final displacement, which means that a more ductile behavior is observed for this joint when compared to J1. Regarding the R-curves (see Figure 5), the values of fracture energies were obtained by the plateaus observed in the graphs, which was more evident for the J1 joint. For J0 joint a plateau was also observed, however it did not occur over a long crack length. Anyway, the difference between G_{IIC} for J0 and J1 joints is very pronounced, demonstrating that a simple addition of synthetic fibers can lead to significant improvements in the mechanical performance of the adhesive joint.
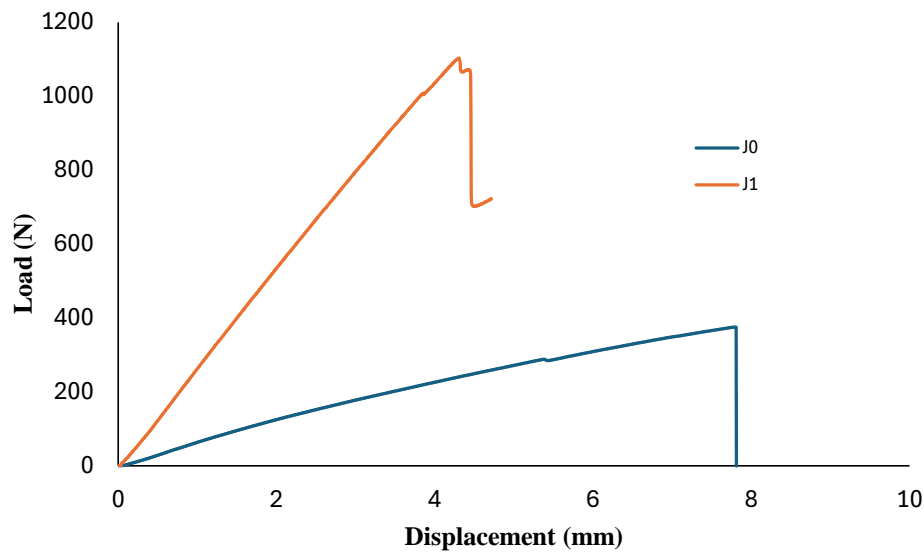
Figure 4 – Typical load vs. displacement curves obtained from the ENF tests for both configurations tested.
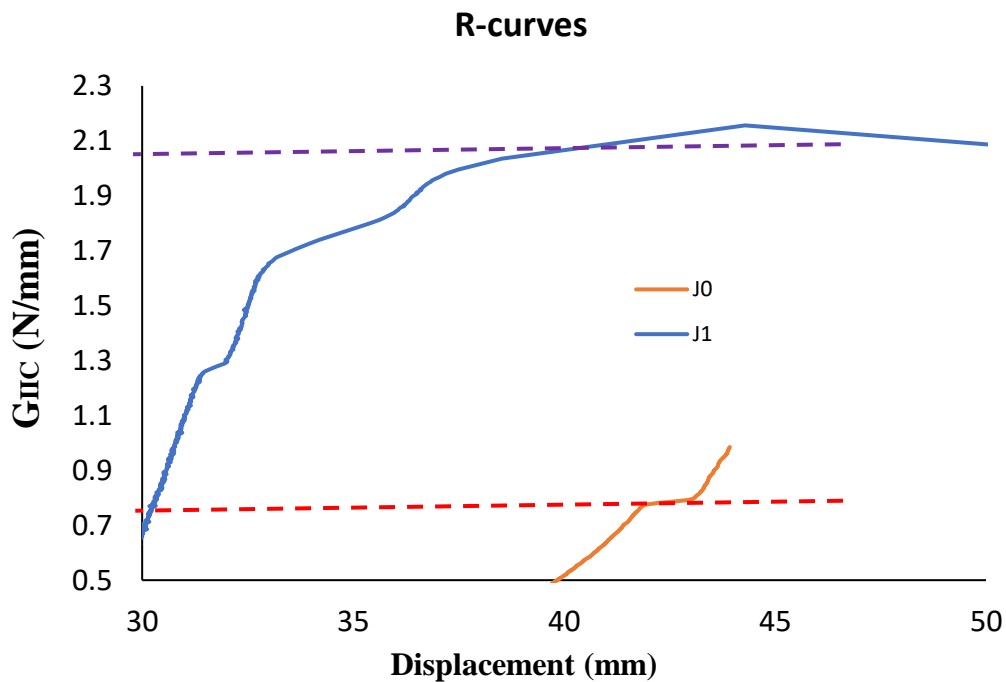
Figure 5 – Typical R-curves obtained from the ENF tests for both configurations tested.

4. CONCLUSIONS

In this work tensile tests were performed in hybrid composites. Additionally, ENF tests were performed in hybrid adhesive joints. The hybridization aimed to avoid moisture absorption and increase the mechanical properties of the adhesive joints.

The tensile tests showed considerable changes in both Young's modulus and tensile strength. As expected J1 group had higher values of J0. For the ENF tests, both maximum load and shear fracture energy were higher for the hybrid joints.

The findings underscore the potential of hybrid composite joints as a viable solution for modern engineering challenges, where both mechanical excellence and environmental responsibility are paramount. Future research should focus on optimizing the processing techniques and investigating the long-term behavior of these hybrid joints to further enhance their applicability and performance in various industrial sectors.

4.1. Declaration of Competing Interest

The authors declare no conflict of interest.

4.2. Fundings

4.3. Acknowledgements

5. REFERENCES

[1] Neto J, Queiroz H, Aguiar R, et al. A review of recent advances in hybrid natural fiber reinforced polymer composites. J Renew Mater 2022; 10: 561–589.

[2] Budhe S, Banea MD, de Barros S. Bonded repair of composite structures in aerospace application: a review on environmental issues. Appl Adhes Sci. 2018;6(1):3.

[3] Li M, Pu Y, Thomas VM, et al. Recent advancements of plant-based natural fiber–reinforced composites and their applications. Compos B: Eng 2020; 200: 108254.

[4] De Queiroz HFM, Banea MD and Cavalcanti DKK. Adhesively bonded joints of jute, glass and hybrid jute/glass fibre-reinforced polymer composites for automotive industry. Appl Adhes Sci 2021; 9: 2.

[5] Rohit K, Dixit S. A review-future aspect of natural fber reinforced composite. Polym Renew Res. 2016;7(2):43–59.

[6] Cavalcanti D, Banea M, Neto J, Lima R, da Silva L, Carbas R. Mechanical characterization of intralaminar natural fiber reinforced hybrid composites. Compos B Eng. 2019;175:107149.

[7] Melese KG, Singh I. Joining behavior of jute/sisal fbers based epoxy laminates using diferent joint confgurations. J Nat Fibers. 2020.

[8] Jawaid M, Abdul Khalil HPS. Cellulosic/synthetic fbre reinforced polymer hybrid composites: a review. Carbohyd Polym. 2011;86(1):1–18.

[9] Ku H, Wang H, Pattarachaiyakoop N, Trada M. A review on the tensile properties of natural fber reinforced polymer composites. Compos B Eng. 2011;42(4):856–73.

[10] Sinha AK, Narang HK, Bhattacharya S. Mechanical properties of hybrid polymer composites: a review. J Braz Soc Mech Sci Eng. 2020;42(8):431.

[11] Roe P, Ansell MP. Jute-reinforced polyester composites. J Mater Sci. 1985;20(11):4015–20.

[12] De Araujo Alves Lima R, Kawasaki Cavalcanti D, de Souza e Silva Neto J, da Meneses Costa H, Banea MD. Efect of surface treatments on interfacial properties of natural intralaminar hybrid composites. Polym Compos. 2020;41(1):314–25.

MECHANICAL BEHAVIOR OF COTTON-REINFORCED POLYURETHANE COMPOSITE

Gustavo Zucco[a]*, Kelvin M. K. Iwasaki[b], Daniela Becker[c], Ricardo De Medeiros[d]

(a) 0009-0005-7742-1078 (Santa Catarina State University – Brazil)
(b) 0000-0001-5751-0085 (Santa Catarina State University – Brazil)
(c) 0000-0003-3250-576X (Santa Catarina State University – Brazil)
(d) 0000-0002-8055-3275 (Santa Catarina State University – Brazil)
* Corresponding author: gustavo.zucco@edu.udesc.com

Abstract: Recently, industries and universities have been researching alternatives to replace conventional materials with eco-friendly options due environmental concerns and the scarcity of raw materials. In this context, natural fiber-reinforced composites have gained attention over synthetic fiber composites. Natural fibers, such as plant fibers, are being studied as substitutes for synthetic fiber-reinforced composites like fiberglass. One key advantage of natural fibers is their abundance in nature, biodegradability, recyclability, and lack of CO2 emissions during manufacturing. Cotton fiber, which has been researched for its application in composite, is the predominant natural fiber used in the Brazilian industry, constituting 95% of its category, alongside fibers such as flax, silk, jute, sisal, wool. Considering this scenario, this study aims to characterize the tensile mechanical properties of cotton fiber when combined with a polyurethane (PU) based resin and analyze the fractography using Scanning Electron Microscopy (SEM). The PU resin, derived from castor oil (a vegetable source) and free from heavy metals or solvents, is a cost-effective biocomponent. The composite laminated were manufactured using the Vacuum Assisted Resin Transfer Molding (VARTM) method following ASTM standard D3039 to obtain specimens for mechanical testing. The tensile mechanical characterization was conducted through a tensile test to determine the material properties. Additionally, SEM analysis of fractured regions was performed to evaluate the morphology of the fiber/matrix interface, revealing microbubbles attributed to the reaction of isocyanate with water molecules, producing carbon dioxide. Finally, it is discussed the potentialities and limitations of using this bio-composite as material in secondary structures.

1. INTRODUCTION

Currently, a wide range of natural fibers is under research and commercial application, including jute, hemp, sisal, flax, curaua, and cotton [1]. Natural fibers are increasingly recognized as sustainable alternatives to synthetic counterparts due to their advantageous characteristics. These include low cost, low density, mechanical properties similar to synthetic fibers, abundant availability in nature, biodegradability, renewability, and minimal energy consumption during acquisition [2]. Moreover, they exhibit high tensile strength, good fiber-matrix interaction, and provide effective protection against external agents [3].

According to Balatinecz and Woodhams [4], the utilization of lignocellulosic fibers in automotive interior components has the potential to reduce the consumption of petroleum-derived materials in thermoplastic plastics by up to 50%. Leão and Tavares [5] also highlight the high potential of fibers sourced from the Amazon region and other tropical forests due to their mechanical characteristics, exemplified by carauá, jute, banana, and cotton. Silva [6] conducted a study on the mechanical behavior of polyurethane resin plates derived from castor oil and reinforced with coconut and sisal fibers. The results indicated that composites reinforced with sisal exhibited better properties compared to those reinforced with coconut fiber. Increasing the volumetric

fraction of fibers led to higher tensile strength and stiffness, as well as increased water absorption, albeit at the cost of reduced flexural strength.

In another study, Liu et al. [7] investigated the impact of altering the linear density of fabric threads (textile weft arrangement) on the fracture behavior of composites. Their findings concluded that incorporating fabric improves the fracture toughness of the materials. Boopalan et al. [8] conducted a comparison of the mechanical properties of banana-jute hybrid composite and pure jute-reinforced composites. The results revealed that the incorporation of banana fiber increased tensile strength by 17%, flexural strength by 4.3%, and impact strength by 35.5% when compared to jute-reinforced composites. Sathishkumar et al. [9] aimed to investigated the mechanical properties of polyester-based composites reinforced with a hybrid sisal-cotton fabric. They found that increasing the number of fabric layers correspondingly enhances the mechanical properties of the composite. Da Costa et al. [10] conducted a series of static tests to evaluate the mechanical and thermal properties of epoxy/polyurethane composites reinforced with fiberglass/cotton, alongside dynamic tests to determine the natural frequencies and damping of the materials. For the polyurethane/cotton composite oriented at 0º, the maximum tensile stress and modulus of elasticity were 61.47 MPa and 2.50 GPa, respectively. At 90º orientation, the maximum tensile stress was 8.64 MPa, with a modulus of elasticity of 0.61 GPa. When oriented at ±45º, the maximum tensile stress and modulus of elasticity were determined to 27.91 MPa and 1.21 GPa, respectively. In terms of bending behavior, the maximum stress at 0° reached 88.00 MPa, with a flexural modulus of 5.38 GPa.

Therefore, the current article aims to study the tensile mechanical characterization of polyurethane matrix composites reinforced with cotton fiber at 0º and 90°. In the fracture regions, a Scanning Electron Microscope (SEM) analysis was performed to investigate the morphology of the fiber-matrix interface and possible microbubbles generated from the reaction of isocyanate with water molecules (air humidity), producing carbon dioxide, which is present in the matrix, generating voids [11-12]. The development of the fabrication process and the mechanical characterization of this composite material are crucial for its structural and functional applications, showcasing significant potential within the automotive and aerospace industry.

2. METHODOLOGY

The materials comprising the manufactured composites are cotton fiber (provided by the textile company Döhler - Brazil) and polyurethane resin KDG (1909), supplied by Kehl Polímeros - Brazil. The resin consists of a mixture with a 1:2 mass ratio of isocyanate to polyol. To eliminate any potential moisture in the fibers, the cotton was dried in an oven at 60°C for about 1 hour. The polyurethane resin was mixed for approximately 5 minutes, as recommended by the manufacturer, before being poured into the mold.

Polyurethane composites reinforced with cotton were obtained through the Vacuum Assisted Resin Transfer Molding (VARTM) method, using a vacuum pump at a pressure of approximately -600 mmHg. The mold is prepared with carnauba wax and tacky tape to delimit the operation region. After preparing the mold, the pre-mixed resin was poured along the lamination area (on top of the peel ply). The fibers were laid in layers above the matrix. After that, a layer of peel ply and flow media is placed, followed by the vacuum bag. The composite plates during fabrication are illustrated in Figure 1.

Figure 1. Experimental setup of the composite plates.

The composite remains in the lamination process for six hours, after which the vacuum pump is turned off. The polyurethane resin, according to the supplier, required a curing time of five days. Consequently, all

manufactured plates were left to cure for a minimum of five days post-production. Using the afore mentioned manufacturing methods, plates were manufactured to characterize fibers with stacking sequence of $[0°]2$ and $[90°]4$, in accordance with the American Society for Testing and Materials (ASTM) standard. Specifically, ASTM D3039 covers the 0° and 90° orientations. For the 0° orientation, two layers of cotton fiber were used, while for the 90° orientation, four layers were used. All manufactures plates have the dimensions of 300×300 mm. Within each plate, five specimens were cut for each orientation, with their dimensions detailed in Table 1 and Table 2.

Table 1. Dimensions of 0º body tests.

	Width (mm)	**Thickness (mm)**
CDP0$_{01}$	14.87	0.55
CDP0$_{02}$	14.97	0.73
CDP0$_{03}$	15.10	0.58
CDP0$_{04}$	14.83	0.60
CDP0$_{05}$	14.50	0.68
Mean	14.85	0.63
Standard Deviation	0.22	0.08

Table 2. Dimensions of 90º body tests.

	Width (mm)	**Thickness (mm)**
CDP90$_{01}$	24.97	1.55
CDP90$_{02}$	24.47	1.60
CDP90$_{03}$	24.73	1.63
CDP90$_{04}$	25.30	1.65
CDP90$_{05}$	25.28	1.65
Mean	24.95	1.62
Standard Deviation	0.36	0.04

The test specimens were cut according to ASTM standards. Tensile tests were carried out on an Instron EMIC 23-100 Universal Testing Machine, following ASTM D3039 (0° and 90°) standard, with a testing speed of 2 mm/min in both cases. Strains are measured within the linear region of the graph using an extensometer that deforms by 1%. The extensometer was removed during the test, and the specimen was subjected to force until fracture occurred. Finally, fractography analysis of a test specimen (oriented at 90º) was performed using a Scanning Electron Microscope (SEM).

3. RESULTS AND DISCUSSION

Properties such as maximum stress (σ_{max}), longitudinal elastic modulus (E_1), transversal elastic modulus (E_2), and maximum strain (ε_{max}) were determined from the tensile test using equations specified in the standards for each orientation. The results for the 0º orientation are presented in Table 3, while those for the 90º orientation are showed in Table 4. Additionally, the mean properties and standard deviation of the calculated values are provided.

Considering the stacking sequence at 0º, the mean and standard deviation of each property were calculated. The average values are 1.58 GPa for E_1, 68.89 MPa for σ_{max}, and 20.38% for ε_{max}. These values are aligned with the properties identified by Da Costa *et al.* [10], who reported 2.50 GPa for longitudinal elastic modulus and 61.47 MPa for maximum stress. The stress-strain graph of the specimens oriented at 0º is shown in Figure 2.

Table 3. Properties obtained for the stacking sequence at $[0°]_2$.

	E_1 (GPa)	σ_{max} (MPa)	ε_{max} (%)
CDP0$_{01}$	1.83	74.71	19.69
CDP0$_{02}$	1.41	55.66	19.69
CDP0$_{03}$	1.71	69.35	19.69
CDP0$_{04}$	1.52	70.51	21.41
CDP0$_{05}$	1.43	74.20	21.41
Mean	1.58	68.89	20.38
Standard Deviation	0.18	7.74	0.94
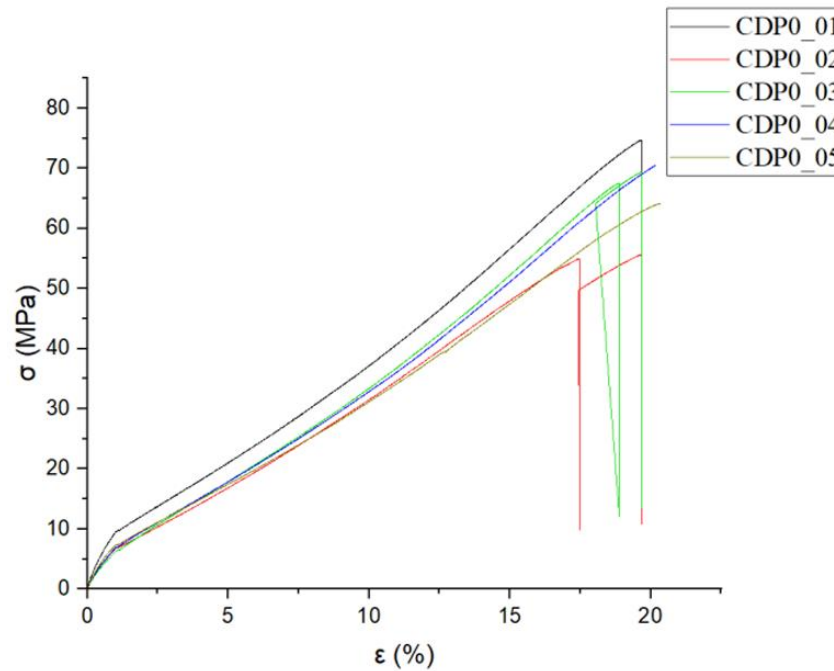
Figure 2. Stress-strain of 0º specimens.

Table 4. Properties obtained for the stacking sequence at $[90°]_4$.

	E_2 (GPa)	σ_{max} (MPa)	ε_{max} (%)
CDP90$_{01}$	0.96	30.61	12.17
CDP90$_{02}$	0.72	25.87	10.71
CDP90$_{03}$	0.97	29.54	12.18
CDP90$_{04}$	1.19	25.85	10.71
CDP90$_{05}$	1.13	28.94	12.49
Mean	0.99	28.16	11.65
Standard Deviation	0.18	2.18	0.87

The mean and standard deviation were also calculated for the 90° orientation. In this case, E_2 is 0.99 GPa, σ_{max} is 28.16 MPa, and ε_{max} is 11.65%. Comparing these results with studies by Da Costa *et al*. [10], the authors reported a maximum stress of 8.64 MPa and transverse elastic modulus of 0.61 GPa. The stress-strain graph of the specimens oriented at 90º is shown in Figure 3.
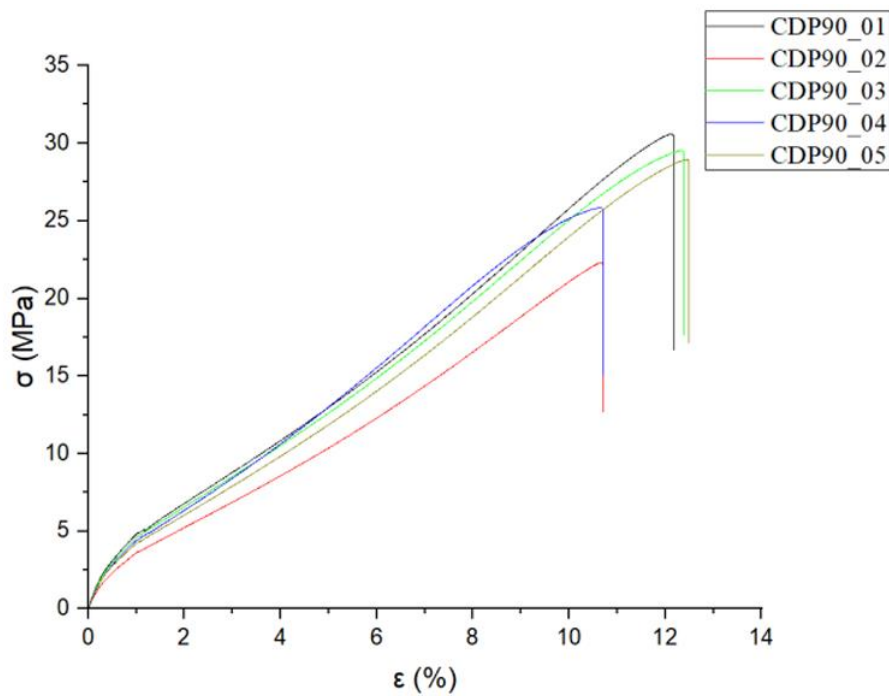
Figure 3. Stress-strain of 90º specimens.

Therefore, it is observed that there is a good agreement in the tensile curves for both stacking sequences (0º and 90º), as confirmed by Table 3 and Table 4. The variation in reported property values can be attributed to the different fibers studied, even though they are made of the same material, manufacturing method vary, as do resin treatment approaches. Different ratios of isocyanate to polyol lead to varying mechanical properties in the polymer. For example, if the ratio were 1:1 (currently it is 1:2), the material would exhibit more brittle behavior and break with less strain. Hence, alternating manufacturing patterns of polyurethane matrix composites reinforced with cotton fiber result in a diverse range of final mechanical properties. Fractography of the cotton fiber-reinforced polyurethane composite was carried out using a Scanning Electron Microscope (SEM) to analyze the matrix/fiber interface at the failure region. The JEOL JCM 7000 NeoScope, available at the University of the State of Santa Catarina, was employed. Photographs were taken at 50x magnification, as shown in Figure 4. The test specimen was stacking sequence equal to 90°.

Figure 4. Fractography of the specimen at 90°.

Upon analysis, it is clear that despite the presence of voids in the composite, the fibers maintain the orientation. The protruding fibers indicate failures in the matrix region, as expected for a specimen oriented at 90°. The lamination process contributed to these voids, highlighting the need for optimizing composite manufacturing method.
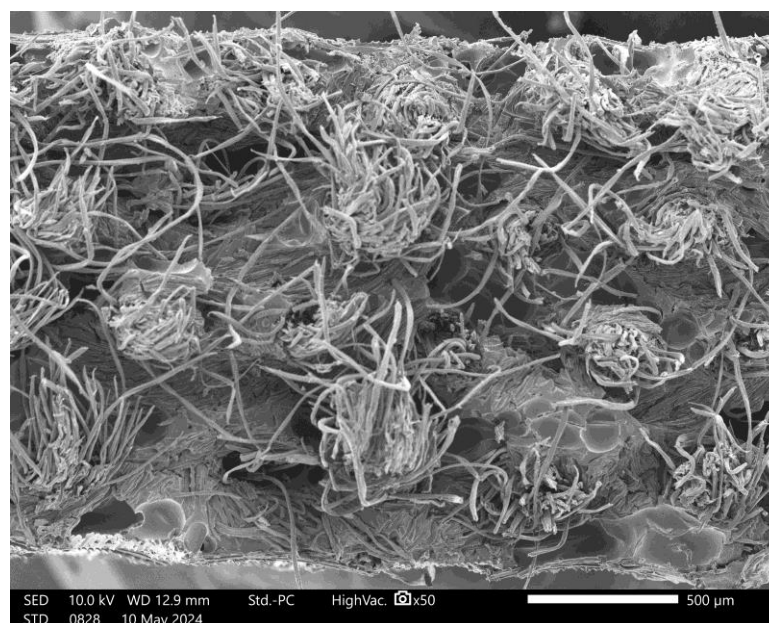
4. CONCLUSIONS

Static tests were conducted to characterize the sustainable composite of a polyurethane matrix reinforced with cotton fiber in the 0º and 90º orientations. The tensile properties were obtained and compared with another study using similar fiber and resin from different suppliers. The polyurethane matrix composite reinforced with cotton fiber exhibited expected behavior, showcasing brittle fractures and mechanical properties close to those reported in the literature. Test specimens at 0º showed fiber failure, while at 90º, the failure occurred in the matrix aligning with material expectations. Another aspect is the composite's high deformability, making it suitable for applications requiring material flexibility based on the stress requirements.

Regarding fractographic analysis, there was noted insufficient interaction between the fiber and matrix in the cotton fiber-reinforced polyurethane composite. SEM micrography revealed voids from the manufacturing process, although notable fiber alignment along the failure region was observed. Finally, this work presents a preliminary study on a sustainable and biodegradable structural composite with exhibit interesting properties within the field of natural materials. While it may not possess the same strength as conventional materials or synthetic fibers, natural reinforcement offers significant potential for application in mobility industries, such as aeronautics, naval, and automotive sectors. the feasibility of using and substituting environmentally harmful materials is tangible and should be investigated.

4.1. Declaration of Competing Interest

The authors declare no conflict of interest.

4.2. Acknowledgements

5. REFERENCES

[1] ARAÚJO, C. R. **Compósitos Elastoméricos de Poliuretanos com Fibras Naturais**. 1998. Tese de Doutorado. Tese de Mestrado, Escola de Química, Universidade Federal do Rio de Janeiro, Brasil.

[2] HARGITAI, Hajnalka; RÁCZ, Ilona; ANANDJIWALA, Rajesh D. **Development of hemp fiber reinforced polypropylene composites**. Journal of Thermoplastic Composite Materials, v. 21, n. 2, p. 165-174, 2008.

[3] FORNARI JR, C. C. M. **Fibras vegetais para compósitos poliméricos**. Ilhéus: Editus, 2017.

[4] BALATINECZ, John J.; WOODHAMS, Raymond T. Wood-plastic composites: Doing more with less. **Journal of Forestry**, v. 91, n. 11, p. 22-26, 1993.

[5] LEAO, Alcides L.; ROWELL, Roger; TAVARES, Nilton. Applications of natural fibers in automotive industry in Brazil—thermoforming process. In: **Science and Technology of Polymers and Advanced Materials: Emerging Technologies and Business Opportunities**. Boston, MA: Springer US, 1998. p. 755-761.

[6] SILVA, R. V. **Composite based on polyurethane resin derived from castor oil and vegetable fibers**. 2003. Tese de Doutorado. Tese]. São Carlos: University of São Paulo.

[7] LIU, Qiang; HUGHES, M. The fracture behaviour and toughness of woven flax fibre reinforced epoxy composites. **Composites Part A: Applied Science and Manufacturing**, v. 39, n. 10, p. 1644-1652, 2008.

[8] BOOPALAN, M.; NIRANJANAA, M.; UMAPATHY, M. J. Study on the mechanical properties and thermal properties of jute and banana fiber reinforced epoxy hybrid composites. **Composites Part B: Engineering**, v. 51, p. 54-57, 2013.

[9] SATHISHKUMAR, T.P. et al. Characterization of sisal/cotton fibre woven mat reinforced polymer hybrid composites. **Journal of Industrial Textiles**, v. 47, n. 4, p. 429-452, 2017.

[10] DA COSTA, Romeu RC et al. Polyurethane derived from castor oil reinforced with long cotton fibers: Static and dynamic testing of a novel eco-friendly composite material. Journal of Composite Materials, v. 54, n. 22, p. 3125-3142, 2020.

[11] SHARMIN, Eram; ZAFAR, Fahmina. Polyurethane: an introduction. **Polyurethane**, v. 1, p. 3-16, 2012.

[12] SANTOS, J.C.d., et al., Sandwich structures of aluminium skins and egg-box-shaped cores made with biobased foam and composites. **Journal of Building Engineering**, 2024. 88: p. 109099.

EVALUATION OF SANDWICH COMPOSITES WITH SISAL FIBER FACE SHEETS AND HONEYCOMB CORE MADE OF DIFFERENT 3D PRINTED MATERIALS

SD Garcia [(a)*], A Bezazi[(b)], H Boumediri[(c)], AC Kieling[(d)], JCM Neto[(e)], AR Torres[(f)], MD dos Santos[(g)], G Garcia del Pino [(h)], TH Panzera[(i)]

(a) 0000-0002-8316-0012 (Federal University of São João del-Rei – Brazil)
(b) 0000-0002-4461-6689 (Universty of Guelma - Algeria)
(c) 0000-0002-9578-0948 (Universty of Guelma - Algeria)
(d) 0000-0002-0552-954X (State University of Amazonas - Brazil)
(e) 0000-0003-1155-0027 (State University of Amazonas - Brazil)
(f) 0000-0001-5138-2932 (State University of Amazonas - Brazil)
(g) 0000-0002-4356-491X (State University of Amazonas - Brazil)
(h) 0000-0003-0754-2390 (State University of Amazonas - Brazil)
(i) 0000-0001-7091-456X (Federal University of São João del-Rei – Brazil)
* Corresponding author: gpino@uea.edu.br

Abstract: The studies of new structural composites with renewable materials and additive manufacturing, allows a better development of high performance for various sectors. In this project, sandwich composites were fabricated and the flexural properties were analysed. The core was manufactured using 3D printing given it´s complex honeycomb geometry, and the faces were built with epoxy resin with and without unidirectional sisal fibers. The epoxy resin (with and without sisal fibers) were fabricated using a mold under cold compression, the sisal fiber is a natural fiber that can be produced in different conditions, and it is very known and planted around the world. The honeycomb core was manufactured in a 3D printer using fused deposition manufacturing, one of the most approachable methods. A total amount of six honeycombs were manufactured for each composite with the 3 most common materials for this type of method, they are PLA, PETG and ABS. The objective of the work was to determine the best combination of material for application to the internal part of a vessel's hull. The composites were tested using the three - point flexural test, where the maximum load, the bending stress at maximum load, the percentage of deformation and the modulus of elasticity of each composite were analysed. Regarding the maximum load and maximum bending stress the PETG - SISAL structure had the best outcome, with 3458 N and 9.72 MPa, respectively. ABS - EPOXY RESIN composite had a poor performance when compared to others, with 1217.31 N of maximum load and 3.42 MPa of bending stress. Regarding the flexural deformation, ABS - SISAL presented the highest percentage with 12.75 % against the PLA - EPOXY RESIN with the lowest result of 3.86 %. The best outcome in the modulus of elasticity parameter was exhibited by the PLA - EPOXY RESIN composite with 0.45 GPa in opposition to ABS - EPOXY RESIN structure with the undermost result of 0.14 GPa.

1. INTRODUCTION

The materials developed for everyday use marked different periods in the progress of civilizations. Composites originate from the first agricultural societies and were somewhat forgotten for centuries. The true re-emergence of these materials began with the use of lightweight composite structures for many technical

solutions during the second half of the 20th century. In the 1980s and 1990s, the use of composites became common to improve the performance of space vehicles and military aircraft. [1]

Vegetable fibers are increasingly explored as promising reinforcements in the composition of composite materials. This awakening of interest is attributed to their low environmental impact, affordable cost, wide availability, versatile applications (construction, packaging, furniture, transportation), low energy consumption and minimal health risks. [2,3] Furthermore, the biodegradability of these fibers presents a solution to mitigate environmental pollution. [4-6]. Among the wide variety of natural fibers, sisal fibers are increasingly cultivated around the world, minimizing their transportation needs and, ultimately, carbon dioxide gas emissions. Furthermore, sisal fibers are considered a viable source of natural fiber due to their high strength and biodegradability [7]. Sisal fiber is adapted for better abrasion and fungus resistance, high strength, better thermal stability and economical and biodegradable reasons [8, 9].

The sisal plant belongs to the *Agave sisalama* family and the fiber is extracted from the leaves and can reach up to 2 m in length. The number of fiber bundles per leaf depends on the age and origin of the plant, with length varying from 60 to 120 mm. A sisal fiber has a density of 1.45 g/cm3 resulting in a porosity of around 17%. This fiber is hydrophilic and can absorb up to 11% moisture in an environment where relative humidity reaches 65%. The chemical composition mainly includes cellulose (50–78%), hemicellulose (10–20%), lignin (8–12%) and waxes (about 2%). In terms of mechanical properties, the tensile strength varies from 300 to 430 MPa, the Young's modulus varies from 5 to 15 GPa and the elongation at break varies from 5 to 14%. [5, 10, 11]

The problem in polymer composites with vegetable fibers is the incompatibility between the vegetable fibers and the polymer matrix due to the fact that the fibers are hydrophilic in nature and the polymer matrix is hydrophobic. As direct consequences of this fact, there is a weak interfacial adhesion between the polar and hydrophilic fiber and the non-polar and hydrophobic matrix and mixing difficulties due to the low wettability of the fiber by the matrix, which leads to a weak interface of these composites, reducing the mechanical resistance of the composite [12]. Therefore, the fibers must be appropriately modified through physical or chemical treatments with the aim of improving adhesion between them and thus improving the mechanical resistance of the composite, one of the most used being treatment with sodium hydroxide (NaOH). [13, 14]

Sandwich panels are types of structural composites whose core is made of a less dense material than the faces. They are designed to be low-weight beams with high rigidity. It consists of 2 faces joined to a core using an adhesive. [15, 16]. One of the most used cores is with a Honeycomb structure. Honeycombs are part of the class of cellular materials, formed by "voids" separated by solid walls, which stand out for having a low relative density. [17]. One of the processes that can be used to manufacture honeycombs is additive manufacturing through FDM (Fused Deposition Modeling) 3D printing.

PLA (Polylactic Acid), PETG (Polyethylene Terephthalate Glycol) and ABS (acrylonitrile, butadiene and styrene) are the 3 most used thermoplastics and popularized as raw materials in 3D printers using FDM, due to their affordable cost, their extrusion viability as they do not require high melting temperatures, in addition to being thermoplastics they can be recycled, and the PLA and PETG are of plant origin making them renewable resources which attracts more interest in these materials.[18]

In this work, the flexural properties of sandwich composites with a 3D printed core by FDM of 3 different types of materials were compared and analyzed: PLA, PETG and ABS, and the external structures, called faces, were plates manufactured through manual lamination using a compression mold, the plates are made up of a composite of unidirectional sisal fibers together with an epoxy resin matrix, and also, plates were manufactured with only resin for comparison purposes, in total 6 sandwich composites were compared and tested using the 3-point bending test.

2. METHODOLOGY

The sandwich panel's face sheets are fabricated with unidirectional sisal fibers supplied by the Company FIBRAEX located in Conceição do Coité, in the state of Bahia, Brazil. Sisal fibers are processed by eliminating impurities, washed in running water and dried at room temperature for 24 hours. For chemical treatment, fiber remains immersed in a solution for 4 hours with 10% by weight of sodium hydroxide, supplied by the Chemistry Laboratory of the Higher School of Technology (UEA/EST). After finishing the immersion time, the fibers are washed several times in running water and then in distilled water to stabilize the pH and left to dry at room temperature for 24 hours and then in an oven at 60°C for 8 hours.

To manufacture the specimens, composite plates made in a metallic mold as shown in Figure 1a, with internal dimensions of 250 mm x 155 mm x 3 mm, a metal sheet with 1 mm thick is placed in the mold cavity to obtain a 2 mm thick composite sheet. Before preparing the composites in the mold, they were placed in an

oven at a temperature of 100 °C for one hour to eliminate moisture. Release wax is applied to the internal surface of the mold (Tec Glaze-N) supplied by the company REDELEASE [19] to facilitate the extraction of the composite from the mold.

The polymer used is Redelease Transparent Epoxy Resin 2001 (0.670 kg) with Redelease Hardener 3154 (0.330 kg), supplied by the company REDELEASE (São Paulo, SP, Brazil) [19], a 4% of anti-bubble additive (Siladit 53) supplied by the company REDELEASE [18]. The test specimens were manufactured by mixing the resin and 4% of the anti-bubble agent in a Becker according to the manufacturer's recommendation, shaking manually for 15 minutes. Then a first part of the resin is placed in the mold, the fibers and finally the rest of the resin content, as seen in Figure 1c. Before closing the mold with the lid, isopropyl alcohol was sprayed on the surface to help eliminate possible bubbles [19]. The fibers are uniformly distributed in the mold area and finally, the mold is closed (Figure 1b) and pressure is applied to the upper lid, using cold pressure.

The mold was closed under pressure for 24 hours in a first curing process, then the composite sheet was removed from the mold with the help of the extractor screws and placed in the oven for 8 hours at temperature of 80 °C, to complete the curing process and increase the strength of the composite. All specimens had the same amount of fiber (20% by weight).
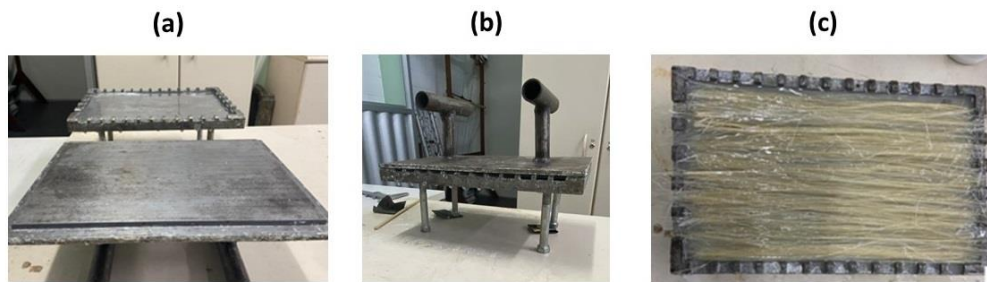
Figure 1: (a) Mold open, (b) mold closed, (c) fibers and resin in the mold.

Cores are made in a honeycomb structure using a 3D printer. Honeycomb cores are the most conventional type of geometry used in the manufacture of sandwich panels. They are non-homogeneous nuclei, with open cells in the transverse direction of the laminate, providing bidirectional support. [20]. The wall thickness was 1 mm ± 0.05mm, considering the horizontal expansion of the filament. The maximum honeycomb measurements were defined according to the mold size of 156 x 250 mm and the honeycomb measurements, so that the largest number of 21 mm hexagons could fit, as can be seen in Figure 2.

The height of the Honeycomb used was taking into account its weight, considering the weight of the resin plate of 110g, and the sandwich composite contains 2 plates, it is assumed that it will have at least 220g, a calculation was carried out based on other bibliographies of 20% of this value, so the honeycomb must be 44 g. For this weight, the density of PLA was considered as it is the highest, the height found was 12 mm (Figure 3). The slicing software was Simplify3D. Due to the type of filament, some parameters were modified, but for comparison purposes, as many parameters as possible were kept the same. These parameters were defined by indication of the filament manufacturer and by bibliographic references
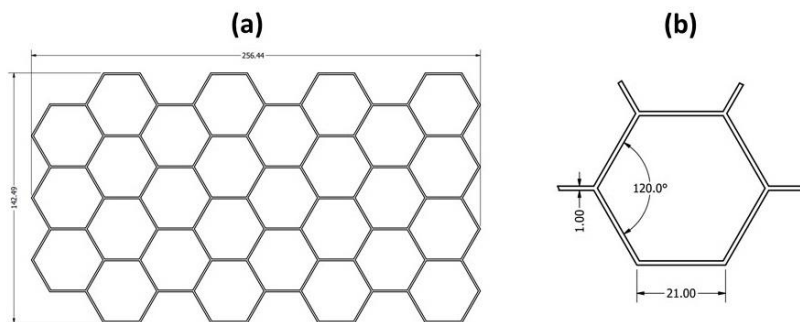
Figure 2: Honeycomb dimensions (a) honeycomb and (b) honeycomb unit cell.
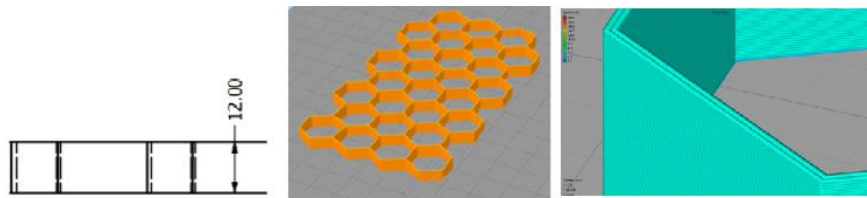
Figure 3: Honeycomb Height

For the honeycomb, 3 types of filaments were used in the manufacture of 6 honeycombs, 2 of each filament, which are PLA, ABS and PETG, they were chosen because they are the most common and easily accessible filaments. The Honeycomb cores were then glued to the composite faces with a resin matrix. After pouring the resin over the faces, the cores were placed centrally (Figure 4) and then a weight was placed on the cores. The process was repeated after 48 hours, to glue the upper face [20]. Subsequently, bending tests were carried out at three points of the sandwich composites.
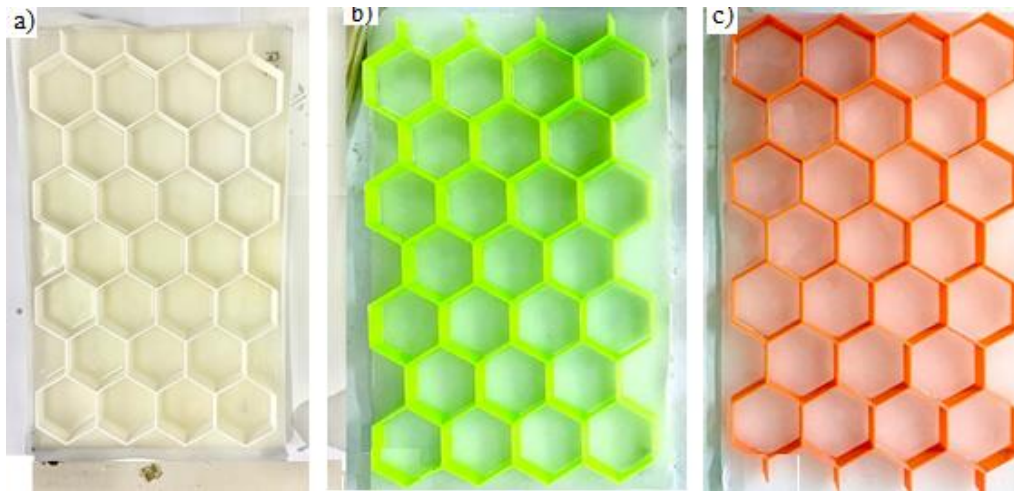
Figure 4: Manufacture and gluing of honeycomb. (a) Honeycomb PLA, (b) Honeycomb ABS, (c) Honeycomb PETG

The tests were carried out on the INSTRON 5984 model machine from EST/UEA, in the P&D Materials laboratory. The tests followed the ASTM standard [21-24] for 3-point bending test, the test speed was 2mm/min. The distance between lower points was 100 mm, as shown in Figure 5.
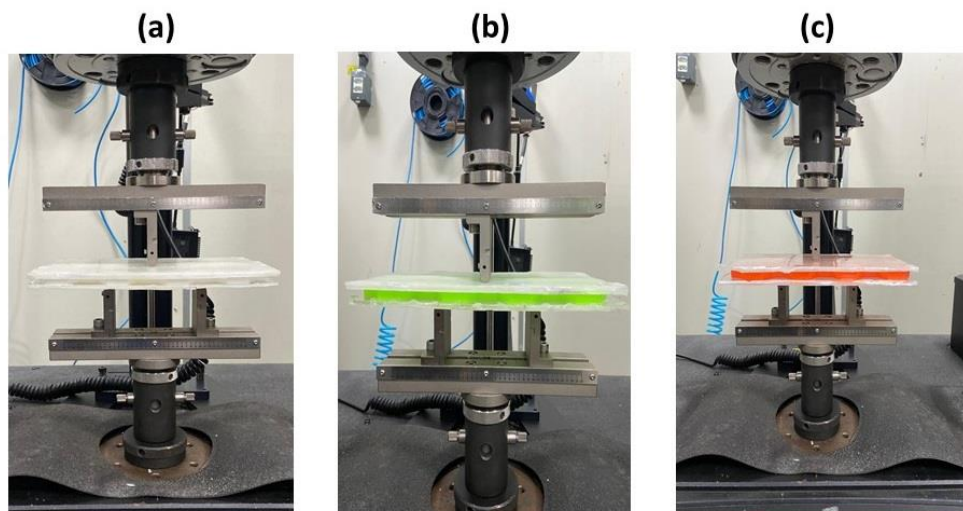
Figure 5: Three - point bending testing: a) Honeycomb PLA, b) Honeycomb ABS, c) Honeycomb PETG

3. RESULTS AND DISCUSSION

The results of the 3-point bending test on the sandwich panels, are presented in table 1 and Figure 6. With the results obtained from the tests, it was possible to analyze and compare the tension and deformation of the test specimens. In all tests, PETG was more resistant, generally 21% to 32% more resistant. Sandwich composites with sisal fiber faces resisted greater maximum load and greater bending stress than those with pure epoxy resin faces. The results were similar to other previous works in the bibliography. [22]

Table 1: Results of three-point bending tests for all specimens

Test body	Core Material	Face Material	Maximum load [N]	Flexural Stress at Maximum Load [MPa]	Flexural Deformation [%]	Modulus of elasticity [Gpa]
1	PLA	Epoxy	1604.13	4.02	3.86	0.45
2	ABS	Epoxy	1717.32	4.42	9.46	0.18
3	PETG	Epoxy	2032.1	5.42	12.13	0.14
4	PLA	Sisal	1973.91	5.55	11.81	0.240
5	ABS	Sisal	2080.78	5.85	12.75	0.16
6	PETG	Sisal	3458.62	9.72	6.3	0.35
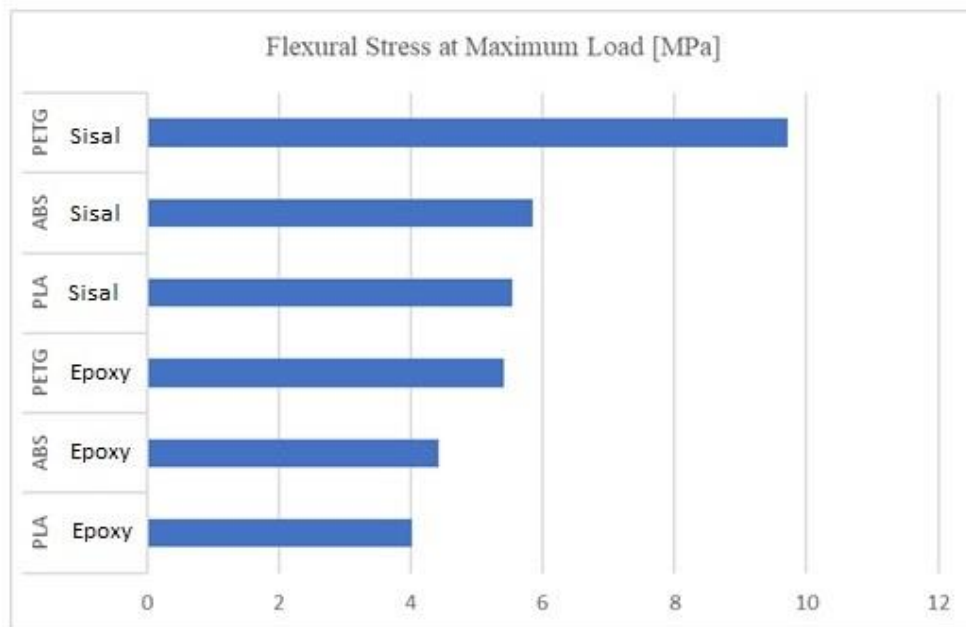
Figure 6: Influence of honeycomb material and the faces materials

4. CONCLUSIONS

The main objective of the work was to create a sandwich composite with a honeycomb core made using a 3D printer, with PLA, ABS and PETG. Sisal fibers contribute to the income of small producers, research related to plant fibers helps the technological growth of composite materials, even enabling their use in industry. Sandwich composites with sisal fiber faces resisted greater maximum load and greater bending stress than those with pure epoxy resin faces.

The materials used in the cores were chosen for their ease of printing and for PLA having ecological origins, it is biodegradable and compostable, can be manufactured using corn, beetroot and cassava, as they are rich in starch. PETG can be obtained through recycling PET bottles, reducing the impacts caused by pollution and ABS was used in order to compare the results related to the other two filaments.

In all tests, PETG was more resistant, than PLA and ABS. Honeycomb proved to be a very resistant, low-density structural arrangement, occupying only 5.4% of the available volume between the faces, which allows it to be used in applications that may require the passage of other internal materials, such as pipes and cables. Furthermore, they can be used in applications that require low density, such as the aeronautical and naval industries.

4.1. Declaration of Competing Interest

The authors declare no conflict of interest.

5. REFERENCES

[1] F M Ventura, Os Compósitos e a sua aplicação na Reabilitação de Estruturas metálicas, Ciência & Tecnologia dos Materiais**, 21(3-4):10-19, 2009**

[2] Achille Désiré Betené Omgba et al. Effect of extension speed on the mechanical performance of sisal and coir fiber bundles. International Journal of Polymer Analysis and Characterization, 2024, doi:10.1080/1023666X.2024.2316966.

[3] Garcia del Pino, G.; DIAZ, F. R. V.; RIVERA, J. L.; KIELING, A. C.; TORRES, A. R. Evaluation of composite materials with fiber of curauá pineaple (*Ananas Erectifolius*). Review of Research. v.4, n1, p.1-7, 2015.

[4] Garcia del Pino, G. et al. Optimal tensile properties of biocomposites made of treated Amazonian curauá fibres using Taguchi Method. Materials Research, v.24, 2021. doi.org/10.1590/1980-5373-MR-2021-0326

[5] Zwane, P. E., T. Ndlovu, T. T. Mkhonta, M. T. Masarirambi, and J. M. Thwala. 2019. Effects of enzymatic treatment of sisal fibres on tensile strength and morphology. Sci. Afr. 6: e00136. doi:10.1016/j.sciaf.2019.e00136.

[6] Kandemir, A.; Longana; Garcia del Pino, G.; *et al*. Natural Fibres as a Sustainable Reinforcement Constituent in Aligned Discontinuous Polymer Composites produced by the HiPerDiF Method. Materials , v. 14, p. 1-17, 2021. doi.org/10.3390/ma14081885

[7] Kumar MD, Jayasrinivasan S, Ashwin S (2021) Study on static and dynamic behavior of jute/sisal fiber reinforced epoxy composites. Mater Today Proceed 46(19):9425–9428

[8] Kumar SS, Raja VM, Chakravarthy CN, Muthalagu R (2021) Determination of mechanical properties and characterization of alkali-treated sugarcane bagasse, pineapple leaf and sisal fibers reinforced hybrid polyester composites for various applications. Fiber Polym 22:1675–1683

[9] Venkatesh R, Raguvaran R, Murugan A et al (2023) Evaluation of thermal adsorption and mechanical behaviour of intralaminar jute/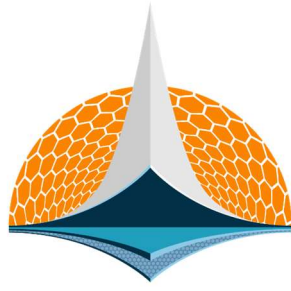sisal/e-glass fibre-bonded epoxy hybrid composite as an insulator. Adsorp Sci Technol 2023. https:// doi.o rg/ 10.1 155/2023/9 2225 62

[10] Sreenivasan, V.S.; Ravindran, D; Manikanda, V.; Narayanasamy, R. Influence of fiber treatments on mechanical properties pf short Sansevieria cylindrica / polyester composites. Materials & Design, v.37, p111–21, 2012

[11] Veigas, M. G., M. Najimi, and B. Shafei. 2022. Cementitious composites made with natural fibers: investigation of uncoated and coated sisal fibers. Case Stud. Constr. Mater. 16:e00788. doi:10.1016/j.cscm.2021.e00788.

[12] Nagappan S, Subramani SP, Palaniappan SK, Mylsamy B (2022) Impact of alkali treatment and fiber length on mechanical properties of new agro waste *Lagenaria siceraria* fiber reinforced epoxy composites. J Natural Fibers 19(13):6853–7664

[13] BRAGA, G. G; ASSUNÇÃO ROSA, FÁBIO ; DOS SANTOS, J C.. ; DEL PINO, GILBERTO GARCIA ; PANZERA, TULIO HALLAK ; SCARPA, FABRIZIO . Fully biobased composite and fiber-metal laminates reinforced with Cynodon spp. fibers. POLYMER COMPOSITES , v. 1, p. 1-12, 2022

[14] Pandey, J.K.; Ahn,S.H.; Lee, C.S.; Mohanty, A.K.; Misra, M. Recent Advances in the Application of Natural Fiber Based Composites. Macromolecular Materials and Engineering, v295, n.11, p.975–89, 2010.

[15] Callister JR., W.D. Ciência E Engenharia De Materiais: Uma Introdução, 7 ª edição. Rio de Janeiro, 2008.

[16] Oliveira PR, Silva LJ, Panzera TH, Garcia del Pino G. and F Scarpa, Transverse fastening reinforcement of sandwich panels with upcycled bottle caps core, Journal of Composite Materials 0(0) 1–9, 2020, DOI: 10.1177/0021998320960522

[17]   YAMASHITA, M.; GOTOH, M. Impact Behavior Of Honeycomb Structures With Various Cell Specifications—Numerical Simulation And Experiment. International Journal of Impact Engineering, v. 32, n. 1, p. 618–630, 2005.

[18]   Giordano, C. M.; Zancul, E. S.; Rodrigues, V. P. Análise Dos Custos Da Produção Por Manufatura Aditiva Em Comparação A Métodos Convencionais. Revista Produção Online. v. 16, n. 2, p. 499–523, 2016.

[19]   REDELEASE. Resina Epóxi Transparente com endurecedor 01 kg. 2024. Disponível em https://www.redelease.com.br/resina–epoxi–transparente–com–endurecedor–01–kg.html.html. Acesso em: 20 de janeiro de 2024.

[20]   E–COMPOSITES. Núcleo Honeycomb de Aramida. 2023. Disponível em: https://www.e–composites.com.br/honeycomb_aramida/p. Acesso em: 15 de fevereiro de 2023.

[21]   ASTM D638-14. Standard test method for tensile properties of plastics. West Conshohocken, PA: ASTM International, 2014.

[22]   Almeida, M. I. Comportamento estrutural de painéis sanduíche compósitos para aplicações na indústria da construção. Instituto Superior Técnico, 2009.

[23]   ASTM INTERNATIONAL. Standard Test Method for Flexural Properties of Polymer Matrix Composite Materials. 2016

[24]   ASTM INTERNATIONAL. Standard Test Method for Flexural Properties of Sandwich Constructions. 2016

19 Non-destructive inspection techniques for composite materials and structures

Organized and edited by

Sandra Maria da Luz
&
Carla Tatiana Mota Anflor

DAMAGE MONITORING OF COMPOSITE STRUCTURES USING A NOVEL BATTERY AS A SENSOR

Mateus Carpena Neto[(a)]*, Denys Eduardo Marques[(b)], Bruno G. Christoff[(c)], João Paulo do Carmo[(d)], Maria Helena Braga[(e)], Marcílio Alves[(f)], Volnei Tita[(g)]

(a) 0009-0008-0769-7142 (University of São Paulo – Brazil)
(b) 0000-0001-5864-0017 (CEFET/RJ – Brazil, and University of São Paulo – Brazil)
(c) 0000-0003-2148-4596 (University of São Paulo – Brazil, and University of Porto – Portugal)
(d) 0000-0001-7955-7503 (University of São Paulo – Brazil)
(e) 0000-0003-4577-2154 (University of Porto – Portugal)
(f) 0000-0002-0285-8276 (University of São Paulo – Brazil)
(g) 0000-0002-8199-1162 (University of São Paulo – Brazil, and University of Porto – Portugal)
* Corresponding author: carpenaneto@usp.br

CODE: BCCM7-88

Abstract: Structural Health Monitoring (SHM) has become a relevant tool for tracking the degradation of structures over time. In addition to advances in SHM research, it is also noteworthy the development of multifunctional elements capable of performing the functions of energy storage and mechanical vibration sensing. In this context, a potential type of sensor for application in SHM techniques are solid-state batteries. This work reports the application of a multifunctional single-element solid-state battery with deformation detection capabilities in vibrational tests to assess its use in monitoring the integrity of structures. The objective of this work is to evaluate the battery's performance in damage detection, using damage metrics on data obtained by the battery in vibration tests. The experiment was conducted using a shaker responsible for vibrating the structure made of composite material with accelerometers and the battery. From the dynamic response of the structure measured by the accelerometers and the battery, it was possible to obtain the system's Frequency Response Function (FRF) under various conditions and consequently characterize its natural frequencies. To simulate damage to the structure, material degradation levels was applied to a region of the beam's composite material. These different levels of damage severity were evaluated using damage metrics found in the literature. Finally, damage metrics are applied to the data collected by the battery in FEM to compare the applicability of batteries in detecting damage in structures. The experimental analyses conducted on the batteries revealed promising results. Despite the limitation in battery sensitivity, which restricted the analysis to low frequencies, it was possible to detect and monitor the increasing damage inflicted on the system. This performance demonstrates that the battery used emerges as a promising element in the context of damage monitoring sensors.

1. INTRODUCTION

Structures in composite materials have played an increasingly important role in industry, particularly in aeronautical engineering. The growing demand for efficiency, performance, and sustainability has driven the adoption of these innovative materials in various applications of composite materials in aeronautical structures.

According to reference [1], to ensure the reliability of aeronautical structures made of composite materials, the Structural Health Monitoring (SHM) technique has proven to be essential. SHM involves the

use of non-destructive techniques capable of evaluating and determining the presence of damage in a structure, thus ensuring its safety and longevity.

One of the most widely used techniques is the method based on the vibrational response of the structure using piezoelectric sensors. As per reference [2], this method uses the analysis of the Frequency Response Function (FRF) of data measured on the structure using piezoelectric sensors, which allows the detection of changes in the dynamic properties of the structure that may indicate the presence of damage.

Despite significant advances in using piezoelectric sensors, research in this area faces several challenges. Sensors are extremely effective at detecting damage, however, the amount of energy absorbed is often limited and may not meet the power demands of electronic components and associated data processing systems.

The objective of this paper is to evaluate the battery's performance in detecting damage by utilizing damage metrics on data gathered from vibration tests.

The present work contributes to the application of novel multifunctional solid-state batteries in the context of damage detection in structures. This novel battery can store energy as well as act as a damage sensor to the structure due to its piezoelectric properties.

2. METHODOLOGY

To develop the work, the properties of materials used in other experiments conducted by GEA (Group of Aeronautical Structures - USP) were utilized. This sensor used during the test is a novel all-solid-state structural battery developed by the research group at the University of Porto. The battery is composed of a sodium-ion-based ferroelectric electrolyte, and the pair of electrodes used are Zinc (−) and Copper (+). Mechanical tests on these batteries were carried out in the study by reference [3] where it was possible to verify that the application of the batteries as sensors was possible, as it can detect the excitation frequencies of the dynamic system in vibratory tests as can be seen in Fig. 1.
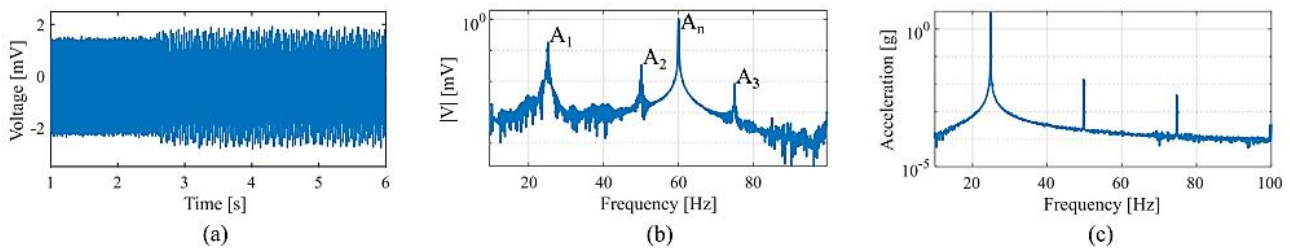
Figure 1. Signal analyses of the test under a base excitation of 25 Hz: (a) raw battery signal on the time domain; (b) raw battery signal on the frequency domain; (c) accelerometer signal on the frequency domain. Available and adapted at [3, p. 5].

According to reference [4], one way to detect damage to structures is to evaluate changes in the modal parameters of the structure, such as natural frequencies, vibration modes, and damping. These modal parameters are directly related to the structure's properties, such as mass and stiffness.

To calculate the modal parameters of the structure, the Finite Element Method (FEM) tool is widely used. The finite element model for this work was developed using Abaqus software. To ensure compatibility with the battery that will be used as a sensor, a representative model of the experiment was created to verify the applicability of the battery as a sensor.

The composite material used consists of a polymeric matrix of polyphenylene sulphide (PPS) with carbon fiber reinforcement composed of a stack of seven bidirectional layers [0°/90°/0°/90°/0°/90°/0°] of 0.31 mm each. The beam has dimensions of 190x30 mm, with 40 mm reserved for fitting the beam into the support. The implementation of the battery was modelled as a concentrated mass at the position where it senses the beam.

The finite element model can be seen in Fig. 2. In this image, obtained from the model developed in the Abaqus software, it is possible to verify the region of application of the boundary conditions. This region is the initial 40 mm of the beam, where it was attached to the support of the shaker. Additionally, the image shows the created elements and the node highlighted in red, which is the position where the battery would sense the dynamic system.
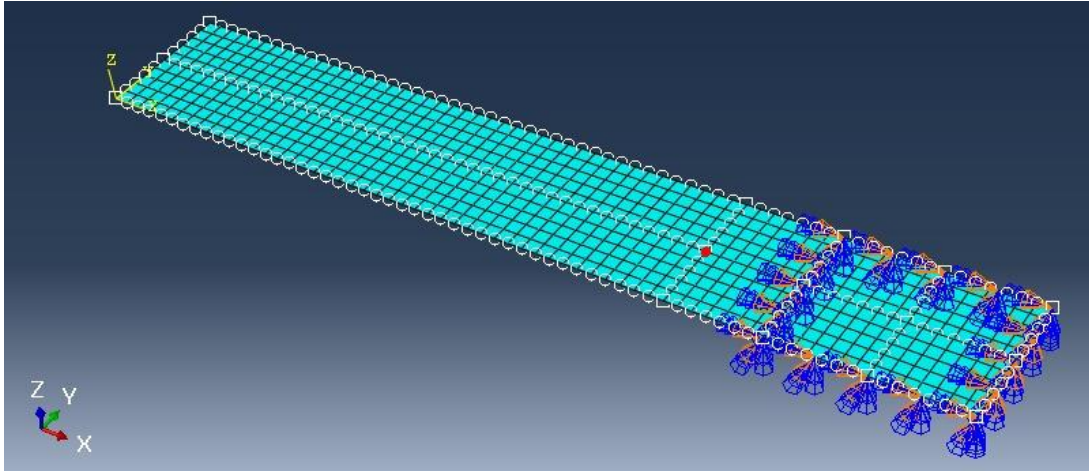
Figure 2. Numerical finite element model.

The cantilever beam is excited from $0 – 1000$ Hz so that the FRF of the undamaged structure can be calculated, that is, without damage, and the natural frequencies of the developed model can be verified with the natural frequencies of the experiment.

Therefore, a degradation of 20% and 40% in the mechanical properties of the composite material was implemented in this work. Material degradation was attributed to the first 60 mm of the beam, including the region reserved for the support. Table 1 shows the values attributed to the composite material in the undamaged condition and the two damaged conditions.

Table 1. Properties of the composite material under different structural integrity conditions.

	Undamaged	**Damaged (20%)**	**Damaged (40%)**
$E_1 \, [GPa]$	59.8	47.84	35.88
$E_2 \, [GPa]$	56.8	45.44	34.08
$G_{12} \, [GPa]$	3.4	2.72	2.04
$G_{13} \, [GPa]$	3.4	2.72	2.04
$G_{23} \, [GPa]$	3.4	2.72	2.04
$\nu_{12} \, [-]$	0.06	0.06	0.06
$\rho \, [Kg/m^3]$	1557	1557	1557

To assess the structural health of a system, it is possible to calculate damage measurements that allow, for example, quantifying the damage to a structure. The damage metric uses nodal information about the dynamic response of a structure when it was intact, that is, without the presence of damage, and after it was damaged. This allows you to quantify variation information from a damage metric calculation.

According to reference [5] carried out an experimental and numerical analysis of the structural integrity of a plate using damage metrics from data obtained by the vibration-based method for detecting damage in composite material plates.

The two damage metrics used in this work is shown in Eq. (1) and Eq. (2). They were chosen based on the magnitude of the FRFs of the structure (undamaged and damaged), considering a frequency range, as per reference [6].

$$Metric \; 1: \frac{f_s}{f_c - f_0} \sum_{i=1}^{n} \left| \frac{H_D(f_i) - H_I(f_i)}{H_I(f_i)} \right| \tag{1}$$

$$Metric \; 2: \frac{\sum_{i=1}^{n} |H_D(f_i) - H_I(f_i)|}{\sum_{i=1}^{n} |H_I(f_i)|} \tag{2}$$

For those metrics, f_0 is the lower frequency, f_c is the upper frequency of the range of interest, f_s is the frequency increment, $H_D(f_i)$ magnitude of the amplitude for damaged structure of the FRF and $H_i(f_i)$ magnitude of the amplitude for undamaged structure of the FRF.

3. RESULTS AND DISCUSSION

In this section, the results obtained will be presented and discussed in three main parts. Firstly, the representativeness of the finite element model applied to the case study will be analyzed. Next, an assessment of the Frequency Response Functions (FRF) of the structure will be carried out, both in the intact state and in the presence of damage, comparing the differences observed. Finally, an analysis of the calculation of damage metrics will be conducted for the two simulated cases in which the material is degraded.

3.1. Results from the finite element model.

To verify whether the model developed using finite elements was representative of the dynamic system of the experiment, a comparison was made between the FRF obtained by the computational test with the structure intact and by the FFT (Fast Fourier Transform) of the experimental data collected by the battery on the cantilever beam, this comparison can be seen in Fig. 3. Thus, it would be possible to compare the values of natural frequencies found in both tests.
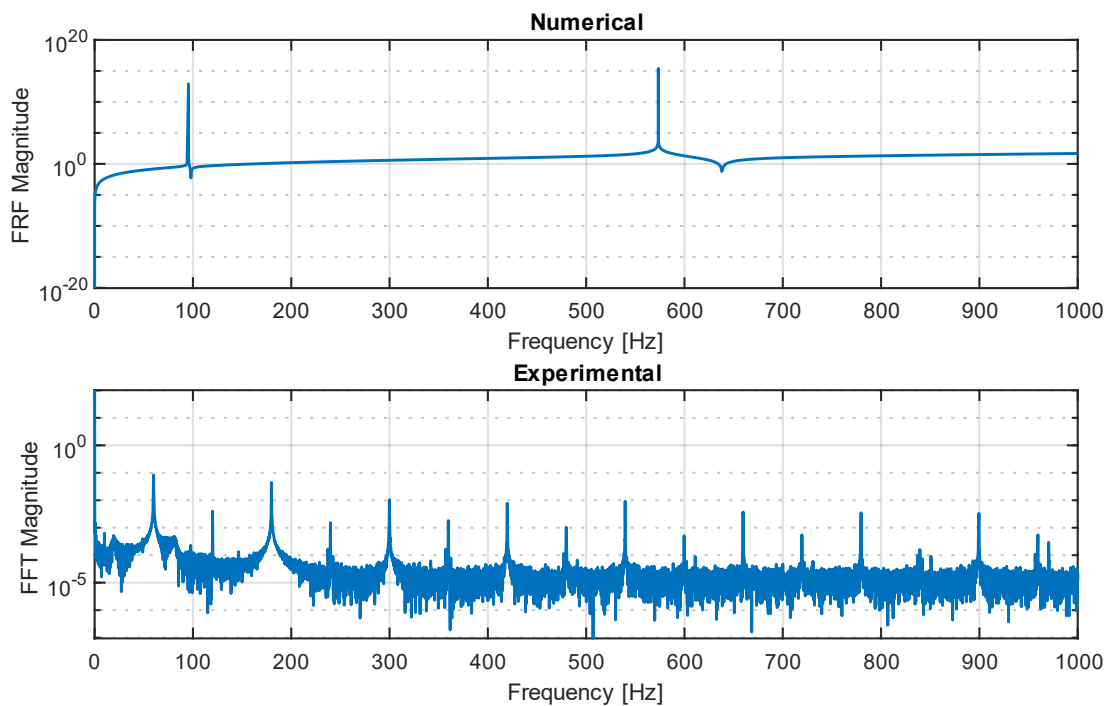
Figure 3. FRF obtained computationally and FFT obtained experimentally using the battery in the structure.

It was verified that there was interference in the data obtained by the battery due to the electrical current that fed the data acquisition system. This interference was notable at the frequency of 60 Hz and its respective harmonics. A filter was applied for the frequency of 60Hz (and its harmonics) using the data acquisition board, however, even applying this filter, peaks due to electrical interference remained   affecting the results.

Even so, it was possible to verify peaks in the response in the frequency domain for the first two normal modes of the structure, which were also observed in the computational response in the frequency domain. Table 2 displays the values of the natural frequencies of these first two normal modes and calculates their percentage difference.

Table 2. Natural frequencies of the first two normal modes obtained from experimental and numerical data.

	Experimental	Numerical	Difference
Mode 1	97.67	95.48	-2.24 %
Mode 2	588.53	573.40	-2.57 %

As the difference between the natural frequency values was low, around 2%, it can be stated that the model developed was satisfactorily representative of the experiment in this study.

3.2. Results of intact and damaged structure.

Using the representative finite element model, the simulations were carried out with the structure intact and with the condition of two damages applied to the degradation of the material in the region close to the fixation of the cantilever beam with the support. The FRF calculated for these simulations is shown in Fig. 4. These FRFs were calculated from the data obtained by the finite element software for the node where the battery was implemented in the cantilever beam, thus being the expected result for the FRF that would be obtained by the batteries in experiments.
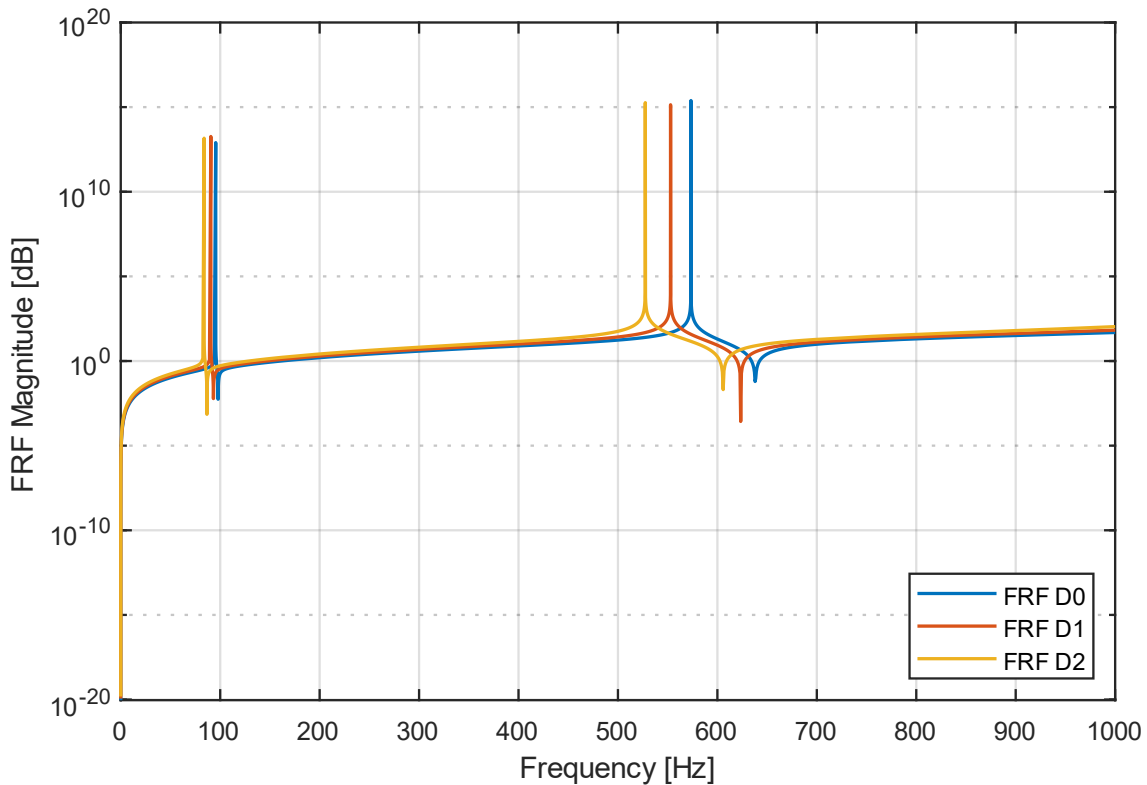
Figure 4. FRF for different conditions of beam structural integrity in the computational analysis.

It is possible to observe that, due to the damage applied to the composite material through the manipulation of its properties, the natural frequencies of the vibration modes were shifted in the graphs and decreased in value, which was expected because damage in the structure caused the reduction of its stiffness, and affected the natural frequencies, as well as vibration modes.. Table 3 displays the natural frequency values of these first two normal modes for each condition defined in the simulation.

Table 3. Natural frequency values of the first two normal modes for each structural integrity condition.

	FRF D0	FRF D1	FRF D2
Mode 1	95.48	90.57	83.81
Mode 2	573.40	552.92	527.486

With the results obtained through the FRF of the system and the changes in the modal parameters of the structure caused by damages, damage metrics can therefore be applied to the experiment.

3.3. Results of calculating damage metrics.

From the FRFs of the experiments, damage analyses were calculated according to previous equations. Although the calculation of the damage metric is generally related to the calculation of a value for the metric, an analysis of the progress of the damage metrics about frequency was made as can be seen in Fig. 5 and Fig. 6.
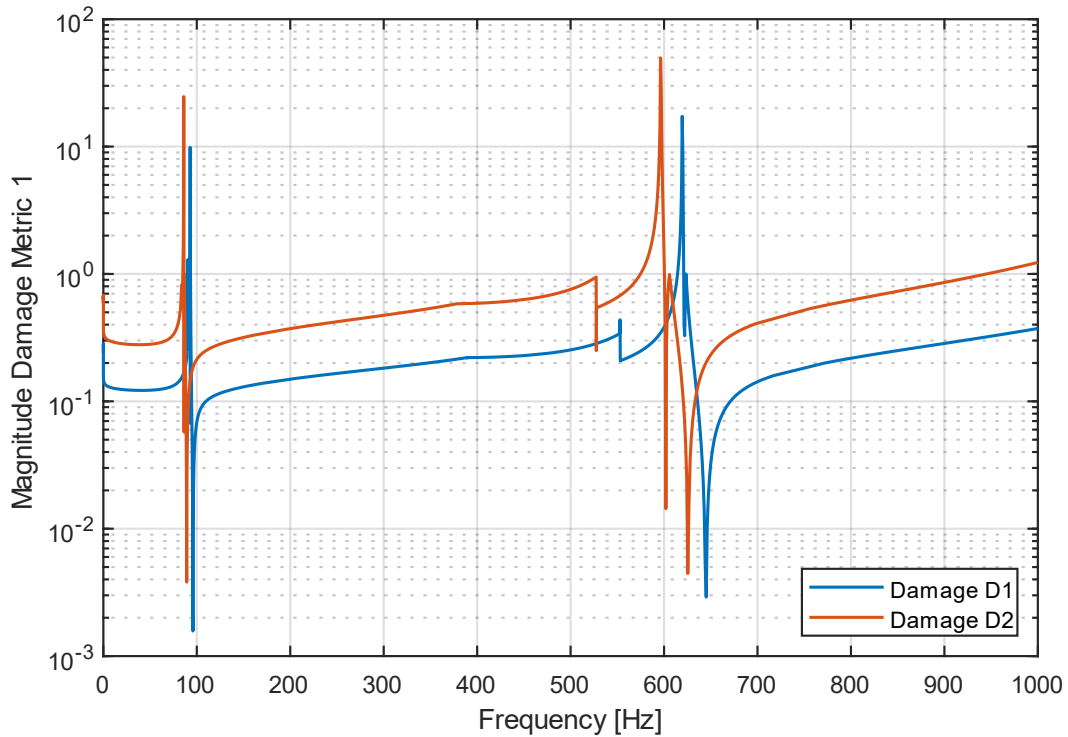
Figure 5. Numerical analysis based on amplitude - damage metric 1.
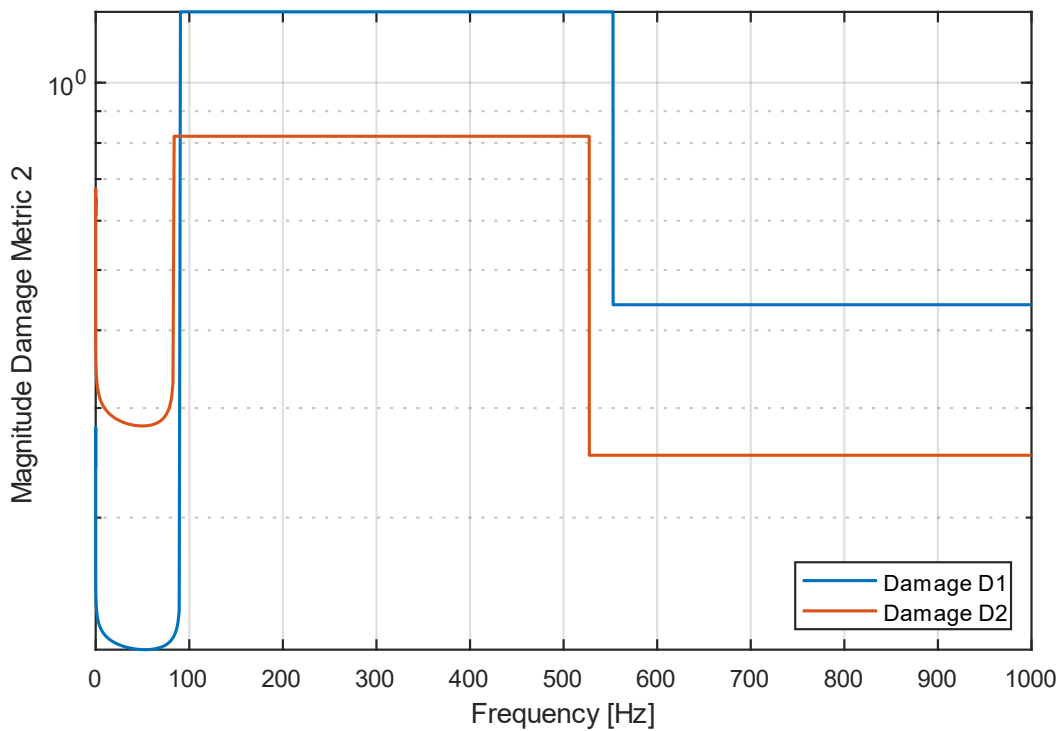
Figure 6. Numerical analysis based on amplitude - damage metric 2.

It is possible to notice that the biggest differences in the calculation of the damage metric occur after the frequency at which the damage affects natural frequencies. Furthermore, it is possible to notice that the progress of the damage metrics follows a similar profile because of the structure and the fact that the damage imposed is of the same type, but at different intensities. Finally, Table 4 shows the calculation of the two damage metrics in this study.

Table 4. Comparison of damage metrics 1 and damage metric 2 for the two damage conditions.

	Metric 1	Metric 2
Damage 1	0.3732	0.4397
Damage 2	1.2317	0.2519

It is possible to notice that metric 1 had an increase in value with greater damage, while metric 2 had this value decrease. It is worth highlighting, therefore, that the behavior of the damage metric depends on the intensity and type of damage that is applied, in addition to being able to analyze the metrics for different frequency bands.

This result therefore demonstrates that batteries used as sensors present promising results in the context of detecting and monitoring damage in composite material using damage metrics.

4. CONCLUSIONS

In this work, a damage metric methodology was presented to evaluate the applicability of a novel multifunctional single-element solid-state battery for detecting and monitoring damage in composite material structures. For this purpose, a finite element model representative of the experiment was developed to acquire the Frequency Response Functions (FRF) of both the intact and damaged structures.

The results obtained through the system's FRFs allowed for the identification of changes in the modal parameters of the structure caused by damage, thereby demonstrating that the damage metrics could be effectively applied. It was observed that the behavior of the damage metric depends on the intensity of the damage, as well as allowing for the analysis of the metrics for different modes of vibration.

Therefore, although the batteries were not used to monitor the damage of the composite structure, the numerical results demonstrated the potential of the novel batteries to be used as sensors, indicating that they could become a valuable tool for predictive maintenance and structural integrity in composite materials, mainly with the reduction of the electrical interference in its signal.

4.1. Declaration of Competing Interest

The authors declare no conflict of interest.

4.2. Fundings

4.3. Acknowledgements

5. REFERENCES

[1] De Medeiros R, Sartorato M, Ribeiro ML, Vandepitte D, Tita V. Numerical and experimental analyses about SHM metrics using piezoelectric materials. International Conference on Noise and Vibration Engineering (ISMA2012), Leuven, Belgium, 2012.

[2] Marques DET, Vandepitte D, Tita V. Damage detection and fatigue life estimation under random loads: A new structural health monitoring methodology in the frequency domain. Fatigue Fract Eng Mater Struct 2021;44:1622–36.

[3] Christoff BG, Marques D, Carmo JP, Braga MH, Tita V. On the strain-sensing capabilities of a novel all-solid-state sodium-based-electrolyte battery under vibration loads. Mech Syst Signal Process 2024;215:111390.

[4] Doebling SW, Farrar CR, Prime MB, Shevitz DW. Damage identification and health monitoring of structural and mechanical systems from changes in their vibration characteristics: a literature review 1996.

[5] De Medeiros R, Sartorato M, Vandepitte D, Tita V. A comparative assessment of different frequency based damage detection in unidirectional composite plates using MFC sensors. J Sound Vib 2016;383:171–90.

[6] Sartorato M, De Medeiros R, Vandepitte D, Tita V. Computational model for supporting SHM systems design: Damage identification via numerical analyses. Mech Syst Signal Process 2017;84:445–61.

NONDESTRUCTIVE INSPECTION OF COMPRESSION MOLDED CARBON FIBER PANELS USING PHASED ARRAY ULTRASOUND AND ACTIVE THERMOGRAPHY

Mario H.F. Batalha[(a)]*, Luis F. P. Santos[(b)], Wellington L. N. de Mello[(c)], Raphael B. C. de Lima[(d)],
Luciano A. L. Ribeiro[(e)], José J. R. Faria[(f)]

(a) 0000-0003-0053-2667 (Instituto de Pesquisas Tecnológicas do Estado de São Paulo – Brazil)
(b) 0000-0002-5089-1089 (Instituto de Pesquisas Tecnológicas do Estado de São Paulo – Brazil)
(c) 0009-0006-1749-0511 (Instituto de Pesquisas Tecnológicas do Estado de São Paulo – Brazil)
(d) 0009-0002-3487-7196 (Maxion Structural Components – Brazil)
(e) 0009-0000-9906-4386 (Maxion Structural Components – Brazil)
(f) 0000-0003-0155-8308 (Subiter Tecnologia – Brazil)
* Corresponding author: mariobatalha@ipt.br

Abstract: The evolution of transport vehicles generates significant challenges for car manufacturers and their suppliers. One of the biggest challenges is the reduction of fuel consumption, in which researchers and engineers have achieved great advances with electric vehicles. New solutions for these topics are related with high-performance materials such as composites. Despite their numerous advantages, quality requirements for composite structures are more complex and stringent when compared to metals, with a strong emphasis on quality control and final part inspection using Nondestructive Testing. The objective of the present study is to qualitatively compare the capabilities of phased array ultrasound and active thermography for the inspection of thick carbon fiber composite components. Two representative panels were produced via compression molding in a hot press, using a snap cure carbon fiber fabric pre-impregnated with epoxy resin composite material. One panel was manufactured considering Flat-Bottom holes, and the other one incorporating internal PTFE (polytetrafluoroethylene) inserts. Results are compared using defect contrast on the inspection images and other aspects, such as inspection time. The results showed that ultrasound presents good sensitivity to different induced patterns. However, potential improvement points for the sensitivity of thermography inspection can be done.

1. INTRODUCTION

The evolution process of transport vehicles generates great challenges for OEMs and their suppliers. One of the biggest challenges is the reduction of fuel consumption, which has been driven by international requirements regarding the reduction of CO_2 emissions. For example, the European Union stipulated, in 2014, that by 2020 the average amount of CO_2 released by the fleet of all new cars was in the order of 95 g CO_2/km, which corresponds to an average autonomy of 24.4 km/L for gasoline and 27.8 km/L for diesel engines [1]. In the past, this problem was easily solved by replacing the metallic material grid with a superior alloy, thus reducing the thickness of the components. There were cases where component thickness reduction limit has already been reached, requiring studies for new materials and applications.

A chassis frame might present different material configurations on its side rails, cross members and supports, according to the main project need, defined at the beginning of the development. An example is the chassis frame presented in Figure 1, developed by the Innovation and Advanced Engineering department of Maxion Structural Components, whose main objective was mass reduction. The chassis was built with

aluminum side rails, and aluminum and composite cross members (carbon fiber, glass fiber and hybrid), with a total mass reduction of 45% of its original weight. The secret for success is the balance of materials within the proper scope of the product, bringing innovation and evolution to the structural components market. The differential in the market today is the ability to find the right match to support the demands in the development of innovative products and processes, applying the right material in the right place.

Figure 1. Chassis frame developed by the Innovation and Advanced Engineering department of Maxion Structural Components.

The use of composites is increasing throughout the whole industry, with a demand of 141.5 kt worldwide in 2019 and an estimated growth up to 197.0 kt in 2023 [2]. Carbon Fiber-Reinforced Polymers (CFRPs) are widely used in high-tech applications, where high strength-to-weight ratio and stiffness are important requirements. In the European market, the total amount of CFRP components used in car-manufacturing grew from 25.5 kt in 2016 to 37.1 kt in 2018 [3,4]. A growth from 69.7 billion to 99.3 billion euros is expected for the global automotive light materials market in 2025 [5].

Despite the numerous advantages, challenges exist regarding the use of composite materials. One of the unique characteristics of composites is the degree of attention required in the material procurement specification and manufacturing [6]. As a consequence, quality requirements for composite structures are more complex and stringent when compared to metals, with a strong emphasis on material qualification methodology and criteria, as well as in-process quality control and final part inspection, using Nondestructive Testing (NDT) [7].

Ultrasonic testing can be considered the most extensively used NDT method for damage detection and characterization of composite structures. Despite the recent advancements, ultrasonic methods suffer from reduced inspection rate (inspected area per unit time), require contact with the part, considerable surface preparation, and experienced personnel for accurate data interpretation and equipment setup [8]. Due to this, many new NDT techniques have been researched in recent years, with a strong trend in non-contact methods, targeting superior inspection rates. Among these, active thermography shows great potential for widespread use in field applications.

To show the capability of each technology, it was used a methodology commonly applied in the aeronautic sector to validate NDT inspections setup for composite components [9,10]. It is based in inspections of representative samples with induced defects. The samples are prepared with the same layer configuration and manufacturing process as the real composite parts, with induced defects that have the purpose of generating signals similar to real defects. The variation in defect geometry and size allows us to understand possible limitations on the capability to detect defects. Thus, the study of these samples has a good representation of defects to be observed in a real part. The use of this methodology contributes to the reliability of the technique when adopted by the automotive sector to validate composite components. Therefore, this is an innovation for a sector that is adapting to a new technology.

Bearing this in mind, the objective of the present study is to compare the capabilities of phased array ultrasound and active thermography, aiming applications in the automotive sector.

1.1. Ultrasonic Testing (UT)

In general terms, an ultrasonic testing system is composed of a transmitter and receiver circuit, a transducer (emits and detects the ultrasonic waves) and a display. Among the different UT methods, the Pulse Echo UT (PE-UT) is the most widely used [11]. More advanced methods have also been developed, namely

the Phased Array UT (PA-UT). Conventional UT transducers generally consist of a single active element that generates and receives ultrasound waves (high-frequency sound waves). On the other hand, PA-UT probes employ several small elements (usually 16-256 units), capable of sweeping a sound beam through a range of angular or linear paths, increasing flexibility and capability of inspection [12].

1.2. Infrared Thermography (IRT)

Infrared Thermography (IRT) can be considered one of the most promising NDT methods for the inspection of composite structures, mainly due to its high inspection rate, non-contact nature, and easy data interpretation [13]. IRT for NDT applications can be classified as passive or active, depending on the available control of the thermal radiation source. In passive mode, the object under analysis is naturally at a temperature higher or lower than the environment, creating a measurable thermal contrast on its surface. On the other hand, in active mode, the object is thermally excited by an external source and its thermal response is analysed [14]. Stimulation sources include optical radiation, ultrasonic wave propagation, eddy current and others [13].

The thermal energy propagates by conduction inside the structure while the infrared camera monitors the temperature variation across the surface. For a uniform surface heating and homogeneous material, the temperature distribution over time is uniform. However, the presence of a subsurface anomaly interferes with the heat flow, due to a localized variation of thermal properties, causing local surface temperature variations. Generally, a shallow defect becomes visible earlier than a deep one and a larger defect produces a more pronounced temperature difference (contrast). Moreover, there are two configurations of thermal camera positioning in relation to the excitation source, named transmission mode and reflection mode. In transmission mode, the thermal camera and the stimulus are on opposite sides of the inspected material, while in the reflection mode, both are located on the same side. Often, in practical applications, accessibility to both sides of a structure is difficult (e.g., aircraft fuselage), making the reflection mode more attractive.

2. METHODOLOGY

Two representative samples were designed using different routes of manufacturing to evaluate the capabilities of phased array ultrasound and active thermography for composites inspection. Each sample generates a different profile of signals, and allow to search possible limitations. The first panel was manufactured considering blind holes, and the second one containing internal PTFE (polytetrafluoroethylene) inserts, as illustrated in Figure 2. The composite material used was a twill 2x2 carbon fiber fabric pre-impregnated with epoxy resin. The lay-up was constructed via hand lay-up, followed by compression molding using a hot press with 25 tons of compression force and a mold temperature of 150 °C.
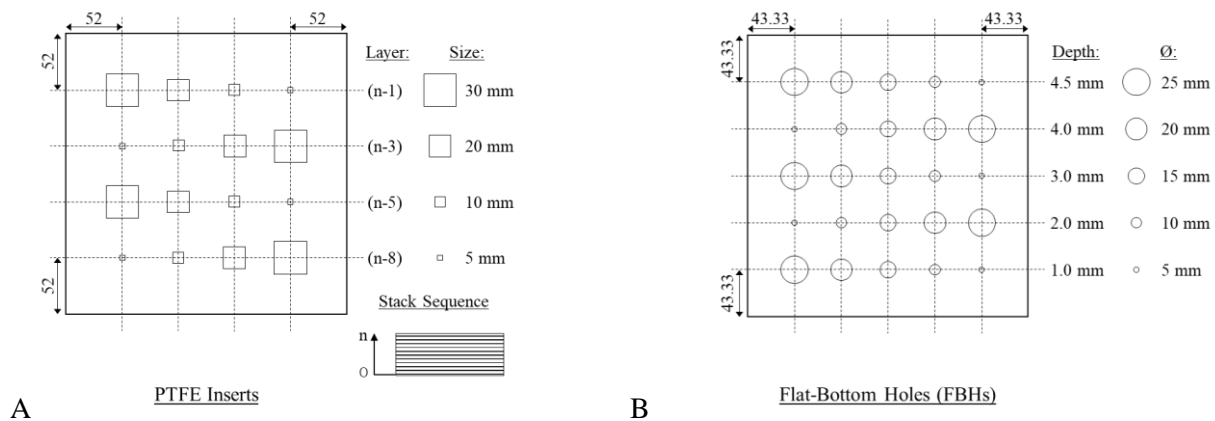
Figure 2. Design of the composite panels: a 16-ply panel with square PTFE inserts (A); and a 15-ply panel with circular FBHs (B), including defects sizes, positions and depths.

The first panel was processed using 15 prepreg layers, oriented at 0°/90°, resulting in a final thickness of approximately 5 mm, without any internal defects. After panel manufacturing via compression molding, it was accurately milled on a CNC machining centre, in order to create 25 circular Flat-Bottom Holes (FBHs), with diameters ranging from 5 to 25 mm, at depths between 1 and 4.5 mm. Each hole represents a different reduction of thickness on the sample. The second panel design was processed using 16 prepreg layers, oriented at 0°/90°, resulting in a final thickness of approximately 5.6 mm, and considering internal defects. During the hand lay-up process, 16 PTFE inserts were positioned between different layers in a similar disposition as the FBH

specimen, and then the laminate was processed via compression molding. The panels have outer dimensions of 250 x 250 mm. Figure 3 exhibits circular FBHs and PTFE inserts.

A   B
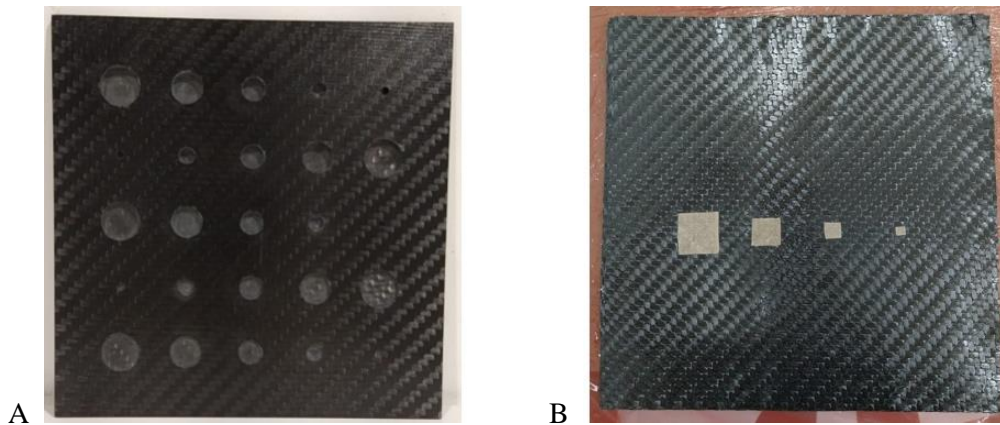
Figure 3. Carbon fiber composite panels: a 15-ply panel containing machined FBHs (A); intermediate ply with PTFE inserts (B).

After fabrication, the specimens were inspected using ultrasound and active thermography techniques. The ultrasound equipment used was an Olympus Omniscan SX. The setup used was a phased array inspection by pulse-echo mode, adjusted for a sound velocity of 3147.1 m/s and signal frequency of 5 MHz. The inspection probe applied contained 64 elements, with 64 mm length, 7 mm of elevation and a pitch of 1 mm, for a 0° angle inspection (linear). For the milled panel, the inspection was conducted in the flat side (without blind holes) to allow the operator to freely move the device, as shown in Figure 4 (A). For the active thermography inspection, an IRT system developed by the Subiter company was used. The system consists of an infrared imager with resolution of 640 x 480 pixels and halogen light sources with a total power of 2 kW. The specimens were inspected in reflection mode, with a 40-second heating time, followed by 20 seconds of transient cooling, as shown in Figure 4 (B). The image sequences were acquired and post-processed using a proprietary software, at an acquisition rate of 30 Hz. Detection capacity of both techniques was carried out by visual analysis of generated color maps. The results are represented by a pixel map, in which its color varies depending on the strength of the signal received after interacting with the part. Defects were located when a minimum contrast defined by the operator was reached. For ultrasound, a 50% drop in signal intensity was considered (represented by colors between blue and white). For thermography, it was done in a similar way, but working with the result in a gray scale.

A   B
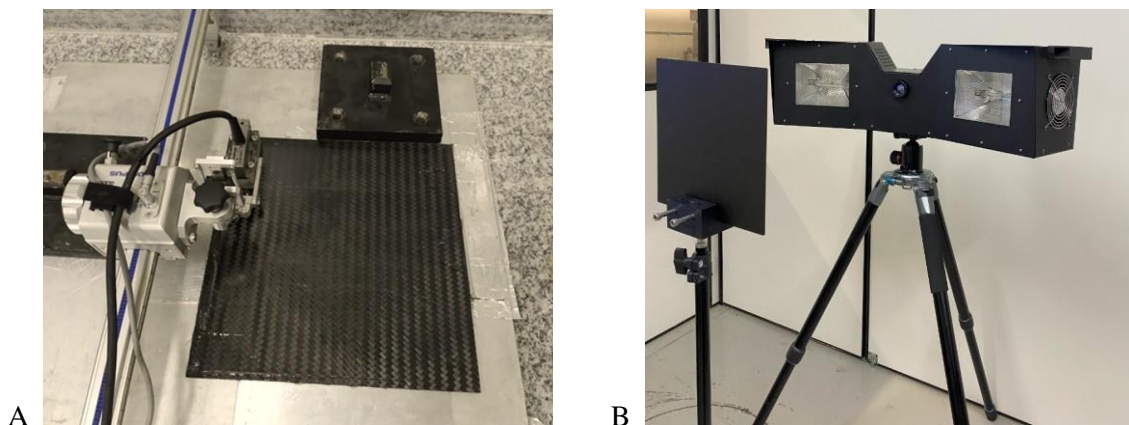
Figure 4. Composite panel inspection by phased-array ultrasound (A); infrared thermography system from Subiter (B).

3. RESULTS AND DISCUSSION

The results of capability using ultrasound are shown in Table 1, by comparison of the number of defects detected in each line. Each insert has 3 categories of detectable behavior: 0 - no detection; 5 - partial detection and 10 - total detection. Ultrasound allow the detection of all induced defects, totalizing 25 circles and 16 squares. According to these results, ultrasound inspection of the samples with similar manufacturing route as

used in Maxion's chassis frame, allowed the detection of defects with a minimum size of 5 mm wide and up to 2.8 mm deep by the signal pattern produced by PTFE inserts. The sample with machined FBH showed a detection resolution with a minimum size of 5 mm wide and a minimum thickness reduction of 1 mm.

Table 1. Results of detection capacity for ultrasound inspection in Carbon fiber composite representative panels.

Ultrasound		PTFE inserts wide [mm]				
		30	**20**	**10**	**5**	
Insert deep [mm]	**0.35**	10	10	10	10	
	1.05	10	10	10	10	
	1.75	10	10	10	10	
	2.80	10	10	10	10	
Ultrasound		Hole wide [mm]				
		25	**20**	**15**	**10**	**5**
Variation of thickness [mm]	**4.50**	10	10	10	10	10
	4.00	10	10	10	10	10
	3.00	10	10	10	10	10
	2.00	10	10	10	10	10
	1.00	10	10	10	10	10

Ultrasound inspections identify potential concern areas through variation in the intensity of the received signal by the equipment, which can also be interpreted using the dB (Decibels) scale. To facilitate the identification, these variations can be represented in a color scale (C-Scan image), as illustrated in Figure 5. White and blue colors indicate considerable signal reduction, which means that the signal had difficulty propagating due to the presence of discontinuities in the material, in the present study, due to the induced defects. When observing the formed patterns, it is possible to notice that the ultrasound had a good capacity to identify the induced defects, regardless of size or depth.

A   B
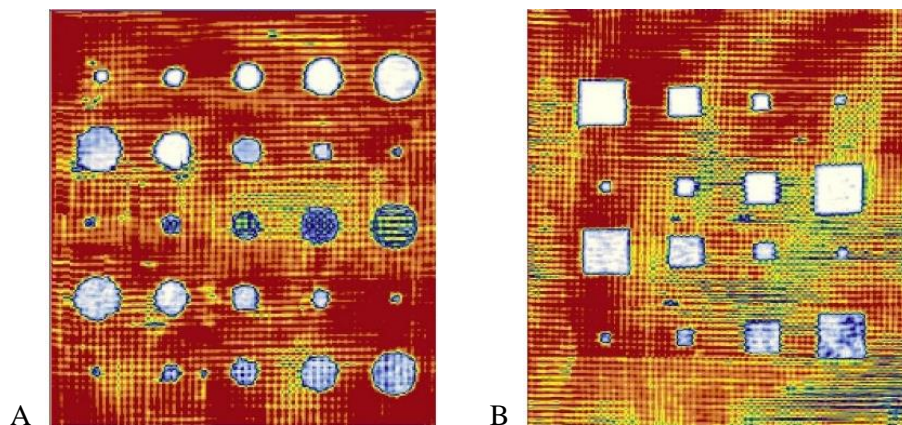
Figure 5. C-Scan images obtained with via ultrasonic testing: 15-ply panel containing machined FBHs (A); 16-ply panel containing PTFE inserts (B).

For the ultrasound inspections, 2 minutes were necessary to collect the top view images, because these samples were not large when compared to the probe used. The greatest amount of time was spent on equipment setup, in which the signal parameters were adjusted and couplant agent (ultrasound gel) applied. Since the technique depends on contact with the part, it is necessary to access part of the surface and ensure that there is no air gap at interface with the probe. The need for contact and adjustment time are still factors that limit the application of this technique to evaluate larger structures, but it is a well-established technique in industry, and widely adopted in various sectors that work with composite technologies.

When thermography technology was applied, the presence of some detection variations was noted, as shown in Table 2. In the sample with PTFE inserts, detection was possible with a minimum defect size of 10 mm wide and up to 0.35 mm deep. The sample with machined FBH showed a detection resolution with a minimum size of 15 mm wide and a minimum thickness reduction of 3 mm.

Table 2. Results of detection capacity for thermography inspection in Carbon fiber composite representative panels.

Thermography		PTFE inserts wide [mm]				
		30	20	10	5	
Insert deep [mm]	**0.35**	5	10	5	0	
	1.05	0	0	0	0	
	1.75	0	0	0	0	
	2.80	0	0	0	0	
Thermography		Hole wide [mm]				
		25	20	15	10	5
Variation of thickness [mm]	**4.50**	10	10	5	0	0
	4.00	10	10	5	0	0
	3.00	5	5	5	0	0
	2.00	0	0	0	0	0
	1.00	0	0	0	0	0

The active thermography inspection was conducted in approximately 1 minute and 15 seconds, considering heating, data acquisition and processing. The active thermography results are processed in the form of high contrast images, easing data analysis. It can be seen from Figure 6 that the IRT system detected a good portion of the FBHs; however, it had difficulties detecting the PTFE inserts. This can be partially explained by the fact that PTFE has a thermal conductivity similar to the carbon fiber laminate (in the transverse direction). Considering the small thickness of the PTFE film, compared to the thickness of the ply, detection by means of thermal propagation becomes a challenge. Better results may be achieved by conducting the IRT test in transmission mode or adjusting acquisition parameters, such as heating time.

A   B
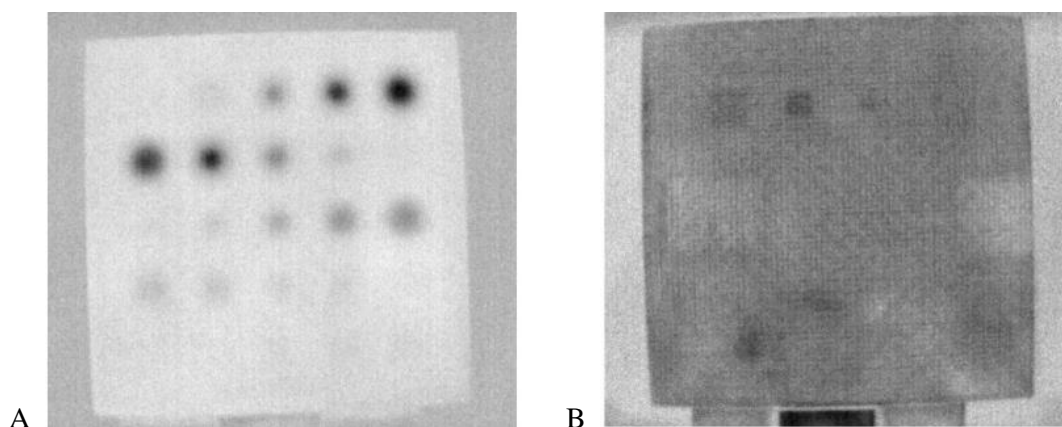
Figure 6. C-Scan images obtained via thermography testing: 15-ply panel containing machined FBHs (A); 16-ply panel containing PTFE inserts (B).

4. CONCLUSIONS

Results revealed that UT was capable of accurately identifying the simulated defects in high thickness CFRP components, with good resolution, despite the defect type, size, and depth. Although accurate results were achieved, UT suffers from low inspection rates, which can be a challenge for high volume production lines. In contrast, active thermography presented defect detection limitations, especially for the test sample with PTFE inclusions. On the other hand, the technique presents advantages with regards to inspection rate and ease of automation. Bearing this in mind, further research is necessary to leverage the application of active thermography for the inspection of thick carbon-fiber composites. Variations of the technique, such as lock-in thermography, in combination with more advanced image processing techniques, may be effective in enhancing defect detection and characterization.

4.1. Declaration of Competing Interest

The authors declare no conflict of interest.

4.2. Acknowledgements

5. REFERENCES

[1] EU Monitor. *Regulation 2014/333 - Amendment of Regulation (EC) No 443/2009 to define the modalities for reaching the 2020 target to reduce CO_2 emissions from new passenger cars*, 2014. (https://www.eumonitor.eu/9353000/1/j9vvik7m1c3gyxp/vjit4jpim3wv), accessed 11 March 2024.

[2] M. Sauer. The Global CF and CC Market - Market developments, trends, outlooks and challenges, *Carbon Composites*, 2019.

[3] M. Sauer. The Global CF and CC Market - Market developments, trends, outlooks and challenges, *Carbon Composites*, 2016.

[4] M. Sauer. The Global CF and CC Market - Market developments, trends, outlooks and challenges, *Carbon Composites*, 2018.

[5] Research and Markets. Automotive Lightweight Material Market by Material (Metal, Composite, Plastic, Elastomer), Application & Component (Frame, Engine, Exhaust, Transmission, Closure, Interior), Vehicle Type (ICE, Electric & Hybrid) and Region – Global Forecast to 2025, *Markets and Markets*, 2020.

[6] E. Bafekrpour, E. Advanced Composite Materials: Properties and Applications, *De Gruyter Open Poland*, 2017. (doi:10.1515/9783110574432).

[7] Z. Fawaz. Quality Control and Testing Methods for Advanced Composite Materials in Aerospace Engineering, *Advanced Composite Materials for Aerospace Engineering*, 2016, p. 429-451, (doi:10.1016/B978-0-08-100037-3.00015-8).

[8] W. H. Sproat and W. H. Lewis. Barely Visible Impact Damage (BVID) Detection in Aircraft Composites, *2nd Aerospace Maintenance Conference 1986*, p. 21-23, 1986. (doi:10.2514/6.1986-1142).

[9] L. S. Charbonneau et al. L. S. Automated defect detection for ultrasonic inspection of CFRP aircraft components, *Ndt & e International 122*, 2021.

[10] N. Yadav et al. In-line and off-line NDT defect monitoring for thermoplastic automated tape layup, *Ndt & e International 137*, 2023.

[11] A. Katunin, K. Dragan and M. Dziendzikowski. Damage Identification in Aircraft Composite Structures: A Case Study Using Various Non-Destructive Testing Techniques, *Composite Structures 12,* p. 1-9, 2015. (doi:10.1016/j.compstruct.2015.02.080).

[12] D. P. Roach and T. M. Rice. A Quantitative Assessment of Advanced Nondestructive Inspection Techniques for Detecting Flaws in Composite Laminate Aircraft Structures, *Federal Aviation Administration*, 2016.

[13] F. Ciampa et al. Recent Advances in Active Infrared Thermography for Non-Destructive Testing of Aerospace Components, *Sensors 18*, p. 609, 2018. (doi:10.3390/s18020609).

[14] X. Maldague and S. Marinetti. Pulse Phase Infrared Thermography, *Journal of Applied Physics 79*, p. 2694-2698, 1996. (doi:10.1063/1.362662).

20 Porous and cellular materials

Organized and edited by

Sandra Maria da Luz

&

Carla Tatiana Mota Anflor

Assessment of Vibration and Cold Pressure Manufacturing Techniques for Silicon Carbide-Reinforced Cementitious Composites as Air Porous Restrictors

Pabllo M. M. Pires[(a)] *, Leandro J. Silva [(b)], Fábio A. Rosa [(c)], Túlio H. Panzera [(d)],

(a) ⓘ 0000-0003-0592-3587 (Federal University of São João del Rei – Brazil)
(b) ⓘ 0000-0002-4606-3483 (Federal University of São João del Rei – Brazil)
(c) ⓘ 0000-0003-3324-7643 (Federal University of São João del Rei – Brazil)
(d) ⓘ 000-0001-7091-456X (Federal University of São João del Rei – Brazil)

Abstract: A wide variety of ceramic materials have been designed for use as porous restrictors in aerostatic bearings. These materials need to possess characteristics such as stiffness, strength, and permeability to support the air pressures and ensure proper airflow distribution. Cementitious composites have emerged as an alternative to sintered ceramics in this regard. To enhance the mechanical performance of cementitious composites, this study proposes incorporating mono-sized silicon carbide (SiC) into compacted or vibrated Portland cementitious composites, along with a superplasticizer (SIKA 100HE). A statistical design is conducted to assess the effects of uniaxial pressure (15 and 30 MPa) and the amount of silicon carbide (30 and 40 wt%) in experiment 1. Additionally, the effects of vibration manufacturing with superplasticizer admixtures (0.6 and 1.0 wt%) combined with two water-to-cement ratios (30 and 35 wt%) are examined in Experiment 2. It is found that a higher amount of SiC (40 wt%) resulted in a more porous material, which shows promise for use as a porous restrictor. Furthermore, the inclusion of superplasticizer and vibration manufacturing lead to a substantial increase in compressive strength, while also reducing porosity levels. However, the impact of these factors should be further assessed through bench testing of porous bearings during operation, which will be the focus of future investigations.

1. INTRODUCTION

Aerostatic bearing operates on the principle of supporting a mechanical load on a thin film of high-pressure air that continuously flows from the bearing into the atmosphere [1]. The high-pressure air flows through the bearing restrictor, which can be made by orifices (single or multiple) or grooves machined in the bearing surface, or using porous and permeable media as restrictors (forcing air through millions of sub-micron pores evenly distributed across the porous face) [2,3]. The porous restrictor requires a uniform pore structure (volume, size and distribution) formed especially by open and connected pores, to achieve a proper and predictable flow characteristic (permeability coefficient) [4]. In this way, a pressure distribution in the bearing gap with high uniformity is created, such enhances the load-carrying capacity, stiffness and damping of the bearing [5]. However, the production of a material with such characteristics is not trivial [6].

Centre for Innovation and Technology in Composite Materials (CITᵉC) group [5, 7-11] has assessed a set of cement-based composites as a low-cost and easy-to-manufacture material, to be applied as a porous restrictor for porous aerostatic thrust bearing. These cementitious composites are reinforced with rigid particles (silica and silicon carbide) and carbon nanotubes. Uniaxial cold compaction or vibration manufacturing processes are used to manufacture cementitious composites. Experimental parameters such as particle amount, size and geometry, levels of compaction, water-to-cement and admixture-to-cement ratios were investigated to obtain suitable porosity and stiffness/strength levels for air-porous bearing. A porogenic

agent is not needed, controlling these dispersive phases and manufacturing factors is sufficient to produce composites with acceptable levels of porosity.

Recently, Yenfei *et al.* [12] carried out a study in which they introduced 20 to 60 wt% SiC into cement to prepare carbide/cement-based composites with better thermal conductivity characteristics. Using a water-to-cement ratio of 0.30, the composites were produced without pressing, employing a superplasticizing additive that allowed the rheological conditions necessary for moulding the wet mortar without compaction. The authors demonstrated that SiC also has a positive effect on mechanical properties, in addition to thermal ones. The compressive strength showed a gradual increase along with the amount of reinforcing particles, reaching the maximum compressive strength when 60 wt% of SiC was added.

In this work, silicon carbide powder and Portland cement are used to produce a porous material, by cold pressing and vibration manufacturing process. Statistical designs identify the effects of SiC amount, compacting pressure, water-to-cement ratio and superplasticizer (admixture)-to-cement ratio on the compressive strength and stiffness of the composites. In addition, density and apparent porosity data are analysed to investigate the ability of the SiC/cement-based composite to be used as a porous restrictor for aerostatic bearings.

2. METHODOLOGY

2.1. Materials

The cementitious composites are produced using Portland cement (CPV-ARI/ASTM Type III) provided by Holcim (Brazil), with silicon carbide (SiC) powder (~10.2µm) from FIVEN NORGE AS and supplied by Fiven Company (Brazil) serving as the reinforcement phase. The vibration manufacturing of the composites is evaluated using the superplasticizer admixture Sika ViscoCrete® 100 HE, supplied by Sika Brasil®.

2.2. Design of experiment

Two experiments are designed to explore SiC-based cementitious composites. The first experiment employs a 2^2 full factorial design to examine the impact of compacting pressure (15 and 30 MPa) and silicon carbide content (30 and 40 wt.%) on apparent porosity, bulk density, compressive strength, and dynamic modulus of elasticity. Additionally, a second experiment, also utilizing a 2^2 full factorial design, is carried out to study the influence, on the same response variables, of superplasticizer-to-cement ratio (sp/c) at 0.6 wt.% and 1.0 wt.%, and water-to-cement ratio (w/c) at 0.30 and 0.35 by weight, for vibrated composites. Tables 1 and 2 present the experimental conditions, along with their respective factors and levels for experiments 1 and 2, respectively.

Table 1. Experiment 1 – 2^2 Full factorial design.

Conditions	Compacting pressure (MPa)	Silicon carbide particles (wt.%)
C1	15	30
C2	15	40
C3	30	30
C4	30	40

Table 2. Experiment 2 - 2^2 Full factorial design.

Conditions	Superplasticizer-to-cement ratio (%)	Water-to-cement ratio
C5	0.6	0.30
C6	1.0	0.30
C7	0.6	0.35
C8	1.0	0.35

2.3. Manufacturing process

Initially, a dry mixture of Portland cement and SiC particles is manually prepared for 2 minutes, following the conditions outlined in Tables 1 and 2. Subsequently, water is introduced and mixed for 5 minutes. In experiment 1, a constant water-to-cement ratio (w/c) of 0.25 (by weight) is maintained. In experiment 2, the weight fraction of SiC remains constant at 40 wt%, while various w/c ratios are utilized

(refer to Table 2). In the latter case, the superplasticizer admixture is blended with water and then added to the SiC/cement mixture.

A metal mould, as depicted in Figure 1, is utilized for fabricating the compacted composites. To aid in sample removal post-compaction (Figure 1b), a PVC pipe is inserted into the cylindrical mould. A thin layer of release agent is applied to the inner and outer surfaces of the metal matrix and PVC pipe, respectively. Following the mixing process, the wet mass is placed in the mould and uniaxially compacted for 1 minute in accordance with the pressure levels specified in Table 1. In the case of vibrated composites (experiment 2), the wet mass is directly placed in PVC pipes affixed to a glass plate and then subjected to continuous vibration on a vibrating table for 10 minutes (Figure 2). After the compaction or vibration procedures, the sample is sealed with plastic film to prevent moisture for up to 28 days at room temperature. Upon completion of the curing period, the sample is extracted from the pipe and machined to achieve parallelism and attain a height twice the diameter, as recommended for the compressive test.
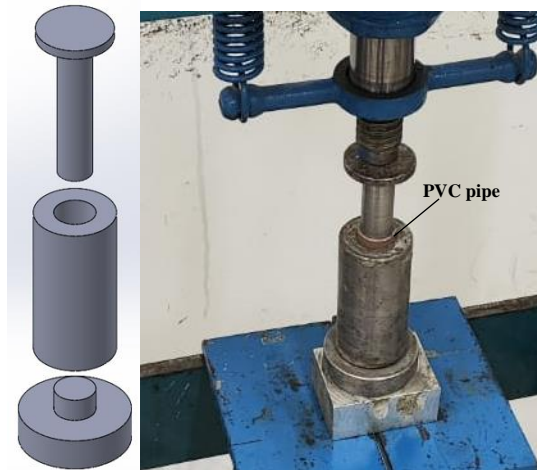
Figure 1 - (a) Scheme of metal of mould and (b) its respective manufacturing process.

Figure 2 - Manufacturing process based on vibrating machine.

3. RESULTS AND DISCUSSION

Table 2 presents the physical and mechanical properties of the SiC/cement-based composite assessed in this study. Conditions C1 to C4 correspond to the composites produced by cold pressing in experiment 1, while conditions C5 to C8 pertain to those evaluated in experiment 2 utilizing vibration manufacturing. Mean values for Replicates 1 and 2 (blocks) are presented in Table 2.

A 2^2 full factorial design is conducted in Minitab® software considering the replicates constructed in two blocks. A blocking analysis has been considered for the two batches of SiC particles in replicates 1 and 2, especially in experiment 2.

Table 2. Physical and mechanical properties for SiC-based cementitious composites. Experiments 1 and 2

Experimental condition	Replicate	Apparent porosity (%)	Bulk density (g/cm^3)	Compressive strength (MPa)	Dynamic modulus (GPa)
C1	1	14.20 (± 1.21)	1.96 (± 0.02)	30.88 (± 1.26)	14.14 (± 0.66)
	2	15.10 (± 1.12)	1.91 (± 0.02)	26.05 (± 3.89)	14.69 (± 1.31)
C2	1	17.32 (± 1.18)	1.93 (± 0.03)	25.46 (± 1.86)	14.28 (± 0.50)
	2	18.14 (± 1.22)	1.92 (± 0.04)	37.25 (± 4.88)	16.43 (± 1.20)
C3	1	7.68 (± 3.45)	2.10 (± 0.04)	43,67 (± 5,94)	14.32 (± 0.24)
	2	7.46 (± 0.79)	2.08 (± 0.02)	55.57 (± 8.48)	12.10 (± 1.04)
C4	1	12.32 (± 1.17)	2.04 (± 0.02)	35.31 (± 7.55)	14.13 (± 0.61)
	2	13.00 (± 0.82)	2.03 (± 0.02)	47.92 (± 3.59)	10.46 (± 0.21)
C5	1	1,34 (± 0.30)	2.28 (± 0.01)	65.06 (± 3.64)	11.09 (± 0.95)
	2	2.19 (± 0.15)	2.26 (± 0.02)	58.97 (± 5.78)	10.03 (± 0.61)
C6	1	1.69 (± 0.36)	2.19 (± 0.03)	76.26 (± 0.83)	11.01 (± 0.68)
	2	2.67 (± 0.16)	2.16 (± 0.02)	44.50 (± 10.62)	10.75 (± 0.28)
C7	1	1.42 (± 0.43)	2.20 (± 0.01)	66.86 (± 3.55)	11.48 (± 0.54)
	2	2.67 (± 0.23)	2.17 (± 0.01)	38.34 (± 11.82)	12.63 (± 1.45)
C8	1	1.76 (± 0.36)	2.19 (± 0.01)	76.48 (± 2.72)	10.58 (± 0.04)
	2	2.34 (± 0.15)	2.18 (± 0.01)	44.38 (± 11.85)	11.07 (± 1.08)

Table 3 shows the results (p-value) from the ANOVA for Experiment 1. Additionally, it includes the p-values for the Anderson-Darling normality test and the coefficient of determination (R^2 adjusted) for all response variables. Significant effects of individual or interaction factors on the response variables are underlined in Table 3 (p-value < 0.05) [17]. Furthermore, all response variables demonstrate a tendency to follow a normal probability distribution based on the Anderson-Darling test (p-value > 0.05), validating the ANOVA model used.

Table 1. Results from ANOVA model for experiment 1.

	Response variables			
	P_{ap}	ρ_v	σ_C	E_d
Individual or interaction factors	*p-values ≤ 0.05*			
Blocks (replication)	0.126	0.080	0.160	0.587
Compacting pressing (CP)	<u>0.000</u>	<u>0.001</u>	<u>0.034</u>	0.204
Silicon carbide particles (SiC)	<u>0.001</u>	0.052	0.589	0.993
CP * SiC interaction	<u>0.030</u>	0.128	0.289	0.532
Normality test (Anderson-Darling) – (*p-values≥0.05)*	0.949	0.584	0.441	0.221
Coefficient of determination (R^2 - adjusted) (%)	99.15	96.64	68.47	00.00

According to the ANOVA, the replications (blocks) in experiment 1 resulted on similar responses (p-values>0.05). Figures 3 and 4 display the mean values and standard deviations for both replications in Experiment 1. Figure 3a indicates that mechanical pressing leads to improvements in compressive strength, especially for composites manufactured with 30 wt% of SiC (Figure 3a), while no discernible effect is observed on the dynamic modulus of elasticity (Figure 3b). Additionally, the increase in the SiC amount from 30 to 40 wt% does not impact the compressive strength and dynamic modulus.

(a)   (b)
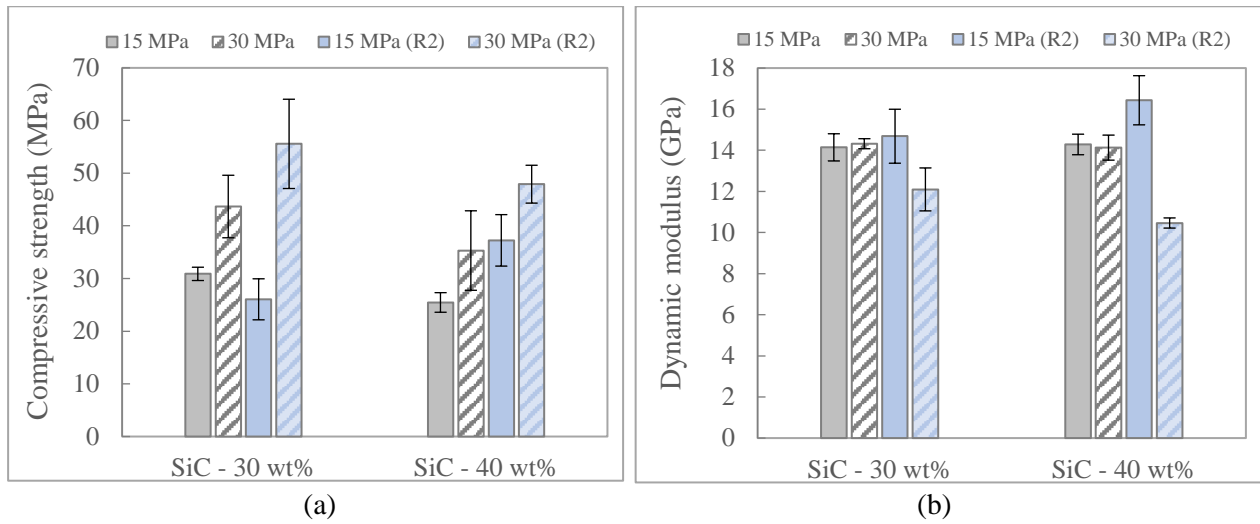
Figure 3 – Compressive strength (a) and dynamic modulus of elasticity (b) for compacted composites - Experiment 1.

Figure 4 shows the physical properties of the compacted composites from experiment 1. As expected, the increase in mechanical compaction raises the bulk density and notably diminishes the apparent porosity. In contrast, the increase in the SiC amount from 30 to 40 wt% only impacts the apparent porosity, leading to an increase in the overall volume of open pores, but not in the same range in both compacting pressure levels.

(a)   (b)
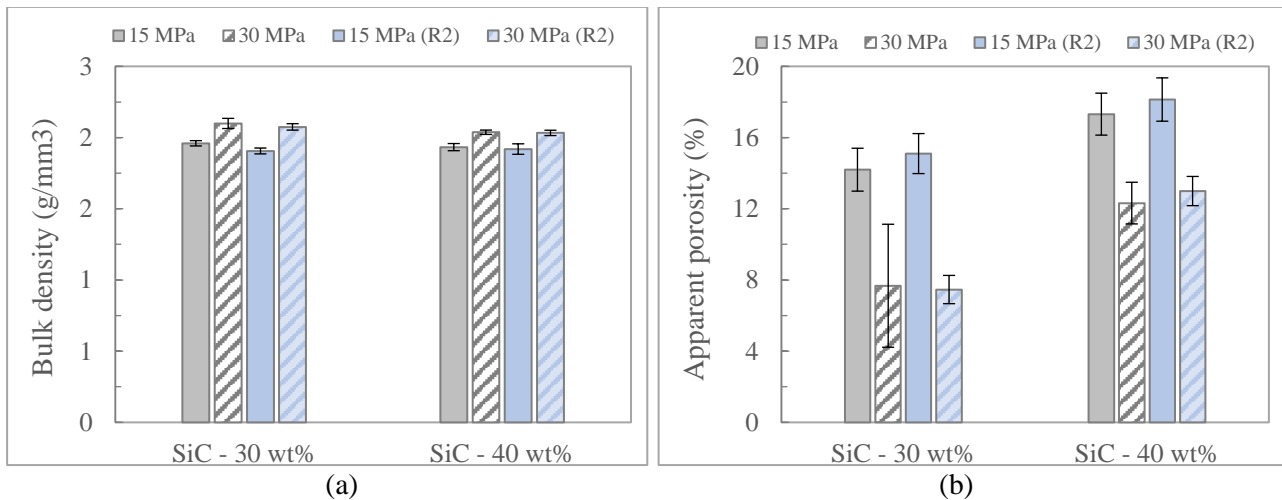
Figure 4 – Bulk density (a) and apparent porosity (b) for compacted composites – Experiment 1.

Table 4 shows the results (p-value) from the ANOVA for the investigated experimental factors in Experiment 2. Significant factors or interactions are underlined (P-value ≤ 0.05). The use of SiC particles from a new batch resulted in different responses in experiment 2, except for dynamic modulus.

Table 4. Results from ANOVA model for experiment 2.

	Response variables			
	P_{ap}	ρ_v	σ_C	E_d
Individual or interaction factors	*p-values ≤ 0.05*			
Blocks (replication)	0.007	0.018	0.028	0.877
Water-to-cement ratio (W/C)	0.628	0.004	0.598	0.228
Superplasticizer-to-cement ratio (Sp/C)	0.229	0.002	0.511	0.410
W/C * Sp/C interaction	0.238	0.002	0.381	0.203
Normality test (Anderson-Darling) – (*p-values≥0.05*)	0.371	0.584	0.935	0.529
Coefficient of determination (R² - adjusted) (%)	86.24	97,53	66.59	21.00

The mechanical and physical properties obtained from Experiment 2 are depicted in Figures 5 and 6, respectively, for both replications. In Figure 5a, it is observed that the increase in water-to-cement ratio (w/c) and superplasticizer-to-cement ratio (sp/c) levels leads to a minor rise in compressive strength. However, due to the high variability of the data, such variation is not statistically significant (see results from ANOVA in Table 4). Similarly, these factors do not significantly affect the dynamic modulus (Figure 5b), although a slightly increasing trend is noticeable when the w/c level rises from 0.30 to 0.35, particularly at sp/c 0.6. Furthermore, a slight increment is observed between 0.6 to 1.0 sp/c% when 0.3 w/c is set, and a contrasting behaviour is noted when considering 0.35 w/c.
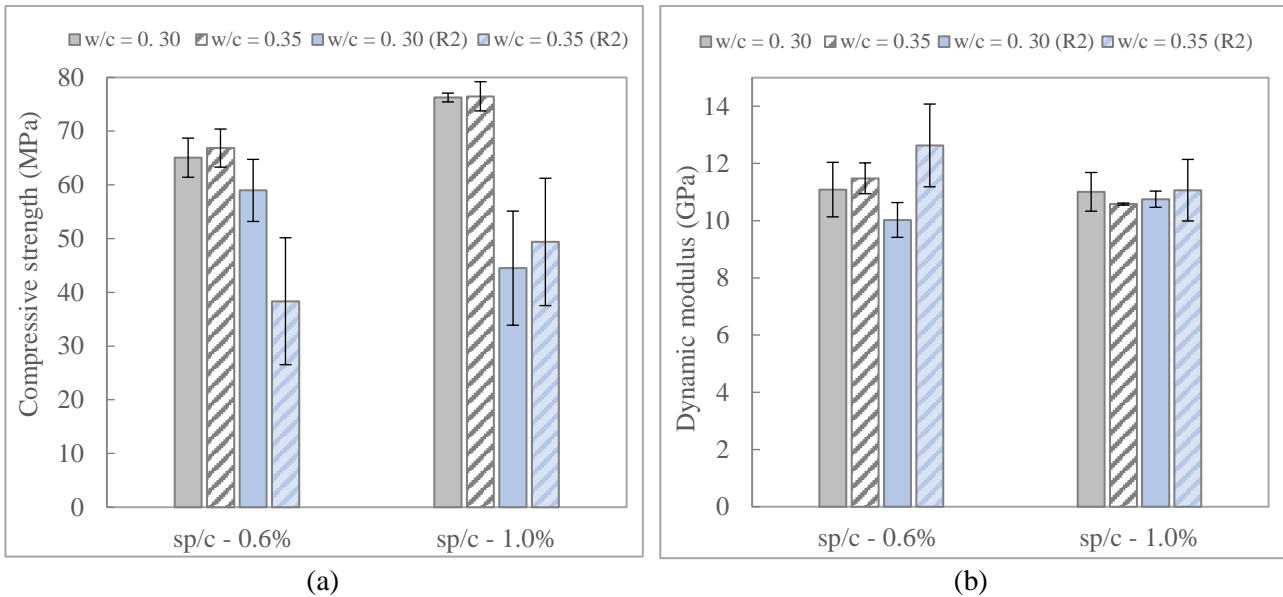
Figure 5 – Compressive strength (a) and dynamic modulus of elasticity (b) for composites manufactured by vibration – Experiment 2.

A slight reduction in bulk density is achieved when sp/c levels increase (Fig. 6a). Although a large variation is noted in the apparent porosity response, the data show an increased porosity trend with the rise in w/c ratio (Fig. 6b). No notable changes are observed between sp/c levels.
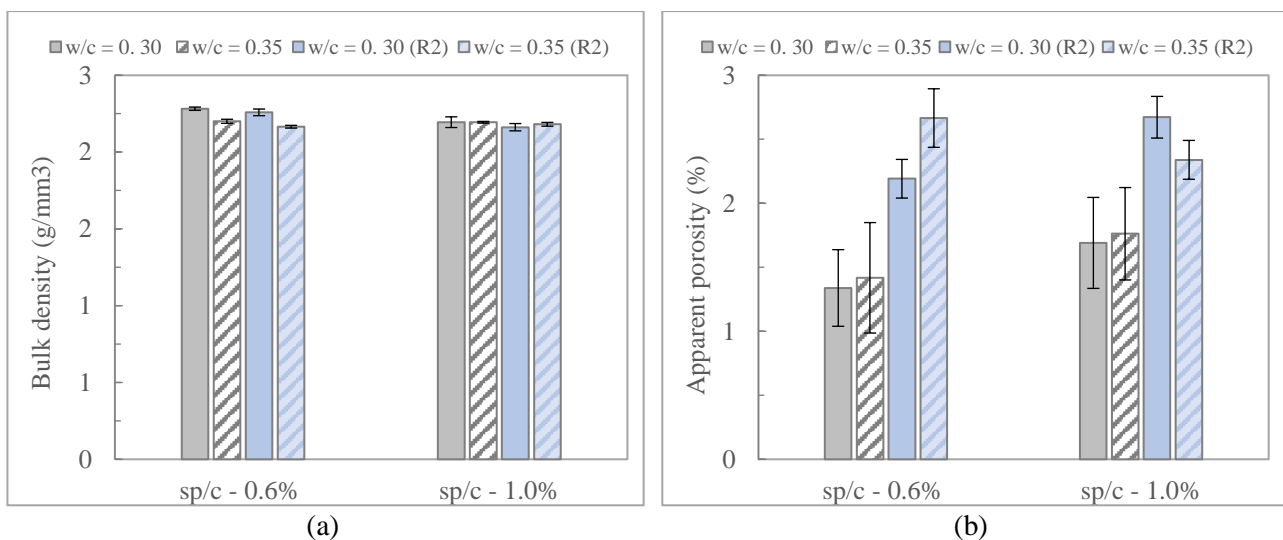
Figure 6 – Bulk density (a) and apparent porosity (b) for vibrated composites – Experiment 2.

The comparison between the results from experiments 1 and 2 reveals that vibration manufacturing, coupled with the use of superplasticizer admixtures, yields composites with higher compressive strength. However, this increase in compressive strength is accompanied by a significant reduction in apparent porosity, rendering these composites unsuitable for application as porous media in aerostatic bearings. Further investigation will be carried out to examine additional responses, especially permeability and

microstructure analysis, and conducting experimental evaluations through bench testing of the porous bearing during operation.

4. CONCLUSIONS

Mono-sized silicon carbide (SiC) was integrated into compacted and vibrated Portland cementitious composites in conjunction with a superplasticizer. Statistical designs were employed to evaluate the impacts of uniaxial pressure, SiC quantity, superplasticizer admixtures, and water-to-cement ratio across 2 experiments. It was observed that a higher SiC amount (40 wt.%) resulted in a more porous material, showing potential for use as a porous restrictor. The increase in w/c ratio led to increased porosity levels. Additionally, the incorporation of superplasticizer and vibrational manufacturing led to a significant increase in compressive strength but reduced porosity levels, rendering them unsuitable as porous restrictors. Subsequent investigations will encompass the assessment of permeability and microstructure, alongside testing as a porous restrictor in a bench test for aerostatic thrust bearings.

4.1. Declaration of Competing Interest

The authors declare no conflict of interest.

4.2. Acknowledgements

5. REFERENCES

[1] A.H. Slocum. Precision machine design. Society of Manufacturing Engineers, Prentice Hall, New Jersey, 1992.

[2] F. Wardle. *Aerostatic bearings. Ultra-precision bearings*. s.l. : Elsevier, 2015. (https://doi.org/10.1533/9780857092182.227).

[3] X. Xiao *et al.* Study on static characteristics of aerostatic bearing based on porous SiC ceramic membranes. Membranes. 2022, 12 (898):1-14. (https://doi.org/10.3390/membranes12090898).

[4] Y. B. P. Kwan and J. Corbett. Porous aerostatic bearings - an update review. *Wear,* Volume 222, 1998. (https://doi.org/10.1016/S0043-1648(98)00285-3).

[5] L. J. Silva *et al.* Cementitious porous material applied to precision aerostatics bearings. *International Journal of Precision Engineering and Manufacturing.* Volume 19, 2018. (https://doi.org/10.1007/s12541-018-0027-x).

[6] P. S. Rao and S. Agarwal. Effect of permeability and different slip velocities at both the porous interface using couple stress fluids on the slider bearing load carrying mechanism. *Proceedings of the Institution of Mechanical Engineers, Part J: Journal of Engineering Tribology*. Volume 230, 2016. (https://doi.org/10.1177/1350650115595054).

[7] L. J. Silva *et al.* Carbon nanotubes and superplasticizer reinforcing cementitious composite for aerostatic porous bearings. *Proceedings of the Institution of Mechanical Engineers, Part J: Journal of Engineering Tribology.Volume 231,* 2017. (https://doi.org/10.1177/1350650117696388).

[8] T. H. Panzera *et al.* Microstructural design of materials for aerostatic bearings. *Cement and Concrete Composites.* Volume 30, 2008. (https://doi.org/10.1016/j.cemconcomp.2007.08.013).

[9] T. H. Panzera *et al.* Physical properties of cement composites designed for aerostatic bearings. *Materials and Structures.* Volume 42, 2009. (https://doi.org/10.1617/s11527-008-9407-5).

[10] T. H. Panzera *et al.* Evaluation of compacted cementitious composites for porous bearings. *International Journal of Applied Ceramic Technology*. Volume 10, 2013. (https://doi.org/10.1111/j.1744-7402.2012.02751.x).

[11] Z. M. V. Missagia *et al*. Assessment of compacted-cementitious composites as porous restrictors for aerostatic bearings. *Proceedings of the Institution of Mechanical Engineers, E Part L: Journal of Materials: Design and applications*. Volume 234, 2020. (https://doi.org/10.1177/1464420719874434).

[12] D. YINFEI *et al.* Using silicon carbide to increase thermal conductivity of cement composite for improving heating efficiency of floor heating system. *Construction and Building Materials,* Volume 325, 2022. (https://doi.org/10.1016/j.conbuildmat.2022.126707).

CHITOSAN-BASED (NANO)COMPOSITE AEROGELS FOR CO_2 ADSORPTION

Martina Salzano de Luna [a],[*], Veronica Ambrogi [b], Giovanni Filippone [c], Mariano Sirignano [d]

(a) 0000-0003-0600-3133 (University of Naples Federico II – Italy)
(b) 0000-0002-5701-3625 (University of Naples Federico II – Italy)
(c) 0000-0002-4382-3686 (University of Naples Federico II – Italy)
(d) 0000-0003-4363-7194 (University of Naples Federico II – Italy)
* Corresponding author: martina.salzanodeluna@unina.it

Abstract: Ensuring optimal indoor and outdoor air quality is nowadays crucial. Among others, new technologies, such as heterogeneous photocatalysis (HP), show promise in addressing such environmental issues. HP aims to completely break down relevant organic air pollutants into less harmful by-products, mainly water and CO_2. CO_2 production itself may raise further environmental concerns, and hence complementary strategies for managing anthropogenic carbon dioxide are needed. Adsorption stands out as a promising method due to its energy efficiency and high capacity. Current research is focusing on developing new materials for CO_2 adsorption, often by combining different functional materials to create high-performance systems. However, this process is complex, as the preparation and composition significantly affect the adsorbent properties. Our research mainly focuses on utilizing chitosan and zeolite micro-particles to create composite aerogels through freeze-drying, eventually optimizing the process to enhance CO_2 adsorption efficiency of the resulting materials. Additionally, other materials (such as soot) were also investigated as active adsorbent phase in the composites.

1. INTRODUCTION

Nowadays, ensuring good air quality indoors and outdoors is a pressing necessity. Sustainable and environmentally friendly methods like heterogeneous photocatalysis offer effective solutions to address this challenge [1]. It allows the mineralization of prevalent organic air pollutants such as volatile organic compounds (VOCs), polycyclic aromatic hydrocarbons (PAH), and BTX (benzene, toluene, and xylene isomers) into less harmful substances, such as water and CO_2. Nevertheless, the production of CO_2 could represent itself an environmental issue. For this reason, CO_2 capture and storage is needed as complementary strategy for managing the resulting carbon dioxide emissions [2]. Among the array of technologies available for capturing CO_2, adsorption is particularly promising due to its low energy requirements and the potential for achieving significant loading capacities [3].

In the wide panorama of established "active" materials for CO_2 adsorption, most of the highest performing materials are in the powdery form, and are characterized by a high surface area. This aspect represent a main technological drawback, since monolithic adsorbents such as pellets and beads are preferred for large-scale applications. Among the possible strategies to obtain coherent monolithic adsorbents, a feasible approach is based on the development of composite structures in which a binding agent is exploited to "glue together" adsorbent powders. In doing this, the main challenge is preserving the porosity of the powdery adsorbent material, thus without compromising its CO_2 capture ability. Accordingly, composite aerogels for

CO_2 adsorption are generally prepared by considering two main constituents: an active adsorbent phase and a binder phase, whose main role is to provide stability and structural integrity to the final aerogel material.

In our work, zeolite 13 X (ZX) was first exploited as active material, using chitosan (CS) as binder. In the second part of the work, other active materials were explored, mainly focusing on soot. Soot is a well-known combustion by-product, and it is an air pollutant itself. On the other hand, in a perspective of reuse of wastes, and thanks to its peculiar chemical-physical features, soot has been recently investigated for the development of new advanced materials [4]. In particular, soot particles have been also already exploited in the field of environmental remediation [5,6]. Overall, we optimized the preparation process in order to maximize the adsorption performances of the developed composite aerogels.

2. METHODOLOGY

2.1. Preparation of composite aerogel beads

Composite aerogel beads made of zeolite and chitosan were prepared according to the protocol by Luzzi et al [7]. Briefly, an aqueous dispersion of CS and ZX was obtained in a 2 vol % solution of acetic acid in distilled water under stirring at room temperature. The CS/ZX ratio was varied from 50 to 90% of zeolite powder. The dispersion was added drop by drop with a syringe to an alkaline bath to get hydrogel beads, which were then frozen by immersion in hexane at −25 °C and finally freeze-dried to obtain porous CS-ZX aerogel beads.

The preparation of chitosan/soot composite was carried out in the same way. Moreover, to further improve chemical and mechanical stability of the prepared composite beads, the polymeric binder was also chemically crosslinked. For this purpose, glutaraldehyde was used as reference crosslinker. In addition, other more sustainable compounds were investigated as crosslinkers, namely polyethylene glycol diglycidyl ether or citric acid.

2.2. Characterization of composite aerogel beads

The microstructure of composite aerogel beads was investigated by scanning electron microscopy (SEM). To investigate the mechanical resistance of the beads in their working conditions, confined uniaxial compression tests were carried out on a fixed volume beads column. The CO_2 capture ability was evaluated by performing adsorption isotherms at 25 °C with a custom gravimetric apparatus based on a McBain-type balance [8].

3. RESULTS AND DISCUSSION

The visual appearance of the composite beads is given by the picture in Figure 1.

Figure 1. Representative SEM images showing the inner microstructure of aerogel beads: pristine chitosan (left) and composite chitosan/zeolite 10/90 wt.%/wt.% (right).

The preparation protocol followed for composite aerogels preparation resulted in rather homogenous spherical beads, whose average size is slightly more than 2 mm in diameter. As shown in Figure 1, this size allows good packing of the beads that is a useful aspect for what concerns the actual applicability of developed adsorbent materials in beads column. More detailed information about the morphology of the aerogel beads can be gained looking at the representative SEM images reported in Figure 2.
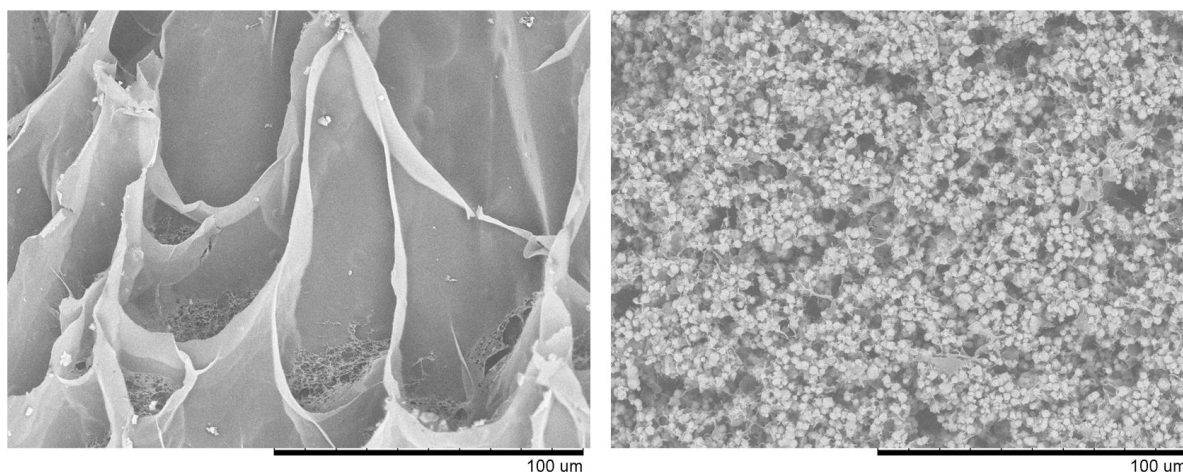
Figure 2. Representative SEM images showing the inner microstructure of aerogel beads: pristine chitosan (left) and composite chitosan/zeolite 10/90 wt.%/wt.% (right).

The inner morphology of the beads significantly changes upon addition of zeolite particles. Pristine CS aerogel shows the honeycomb-like structure that is typical of freeze-dried materials (because of the voids left by sublimation of ice crystals formed during the freezing step). In the composite aerogel, the chitosan skeleton cannot be recognized, while homogeneously dispersed ZX micro-particles glued together by thin polymeric filaments can be clearly distinguished. This suggests that the surface area of the adsorbent particles is likely preserved in the composite structure, with beneficial effect on the adsorption performance of the developed composite adsorbents. To prove this, CO_2 adsorption isotherms were measured for CS/ZX samples at different composition. The output is shown in Figure 3, in which the weight normalized adsorbed amount of CO_2 (q_e) is reported as function of the CO_2 pressure in the testing chamber.
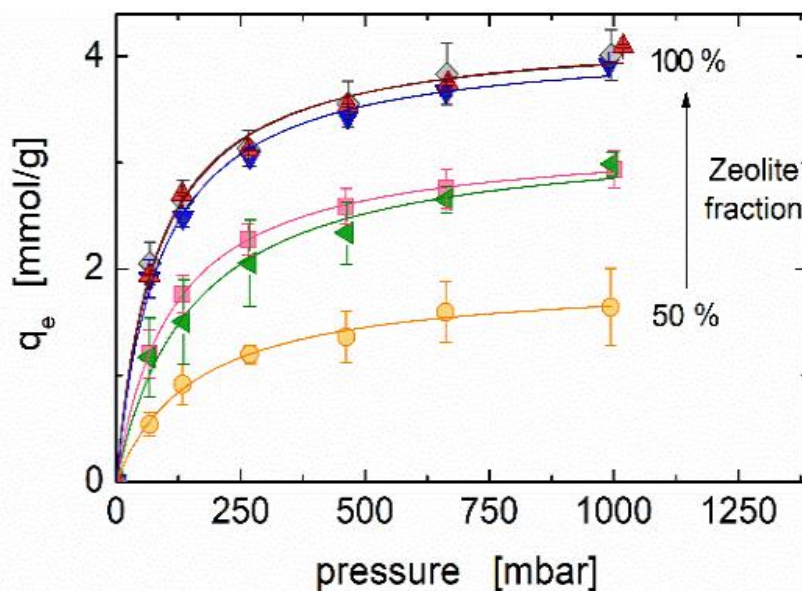
Figure 3. CO_2 adsorption isotherms at 25°C of chitosan-zeolite aerogels at different composition. Data of pristine zeolite powder is also reported as reference (red triangles). Readapted from [7].

Evidently, the adsorption capacity of the aerogels increases as the zeolite content increases. The most relevant result is that the composites aerogels at the highest zeolite contents (i.e. 86% and 90%, inverted triangles and diamonds in Figure 3, respectively) exhibited a CO_2 adsorption behaviour that is comparable to that of pristine zeolite particles. This suggest not only that the presence of the chitosan binder does not act detrimentally on the available surface area of the zeolite particles, but also that it plays an active role in the adsorption process, at least when its content is low. This has been ascribed to the peculiar structure of the

polymeric phase in the composites at the highest particle loadings: when in the form of thin filamenst, indeed, the amino groups of chitosan are more likely to be exposed and thus actively work in the adsorption process by interacting with carbon dioxide molecules. Targeted measurements are currently ongoing to support such a hypothesis.

On the other hand, starting from these encouraging results, other kinds of composite beads are currently under investigation, with the aim of (i) exploiting byproducts as active adsorbent phase (chitosan/soot composite aerogel beads) and (ii) chemically crosslink the polymeric binder phase so as to improve mechanical resistance and stability of the aerogels and their performance also in humid conditions.

4. CONCLUSIONS

The present work aims at the development of composite aerogels to be used for CO_2 adsorption. Besides serving themselves for carbon dioxide removal from air, the developed materials are also intended to work in a two-step air purification system, which allows the mineralization of different (organic) air pollutants and the subsequent removal of the produced CO_2. To do so, composite aerogels were produced in the form of beads by using a phase-inversion technique followed by freeze-drying. Zeolite 13X powder was selected as active adsorbent material and chitosan as binder. The beads demonstrated remarkable CO_2 adsorption capacity due to the well-dispersed zeolite powder, which maintained its inherent specific surface area even at high loadings (up to 90 wt.%). In addition to offering structural integrity, chitosan likely played an active role in CO_2 capture, particularly when it is present at lower concentrations. Starting from such promising results, other materials (such as soot) were also investigated as active adsorbent phase in the composites.

4.1. Declaration of Competing Interest

4.2. Fundings

4.3. Acknowledgements

5. REFERENCES

[1] S. Kim, S. Kim, H. J. Park, et al. Practical scale evaluation of a photocatalytic air purifier equipped with a Titania-zeolite composite bead filter for VOC removal and viral inactivation. *Environmental research*, Volume 204, 2022 (https://doi.org/10.1016/j.envres.2021.112036)

[2] H. C. Lau, S. Ramakrishna, K. Zhang, et al. The role of carbon capture and storage in the energy transition. *Energy & Fuels*, Volume 35(9), 2021 (https://doi.org/10.1021/acs.energyfuels.1c00032).

[3] T. Wilberforce, A. G. Olabi, E. T. Sayed, et al. Progress in carbon capture technologies. *Science of The Total Environment*, Volume 761, 2021 (https://doi.org/10.1016/j.scitotenv.2020.143203).

[4] M. R. Mulay, A. Chauhan, S. Patel, et al.. Candle soot: Journey from a pollutant to a functional material. *Carbon*, Volume 144, 2019 (https://doi.org/10.1016/j.carbon.2018.12.083).

[5] R. Gusain, N. Kumar, S. S. Ray, Recent advances in carbon nanomaterial-based adsorbents for water purification. *Coordination Chemistry Reviews*, Volume 405, 2020 (https://doi.org/10.1016/j.ccr.2019.213111).

[6] M. Salzano de Luna, M. Sirignano, Upcycling soot particles into chitosan-based aerogels for water purification from organic pollutants. *Journal of Hazardous Materials Letters*, Volume 2, 2021 (https://doi.org/10.1016/j.hazl.2021.100019).

[7] E. Luzzi, P. Aprea, M. Salzano de Luna et al. Mechanically coherent zeolite 13X/chitosan aerogel beads for effective CO_2 capture. *ACS Applied Materials & Interfaces*, Volume 13(17), 2021 (https://doi.org/10.1021/acsami.1c04064).

[8] N. Gargiulo, A. Peluso, P. Aprea et al. Use of a metal organic framework for the adsorptive removal of gaseous HCl: a new approach for a challenging task. *ACS applied materials & interfaces*, Volume 10(17), 2018 (https://doi.org/10.1021/acsami.8b03007).

FABRICATION OF OLEOGELS VIA OIL ABSORPTION IN AEROGEL TEMPLATES OF CELLULOSE AND STARCH

Laiane Carvalho [(a)], Larissa Andreani Carvalho [(b)], Sandra Maria da Luz[(c)], Simone Monteiro e Silva [(d)], Leonardo Fonseca Valadares [(e)*]

(a) 0009-0003-6110-2721 (University of Goiás – Brazil)
(b) 0000-0002-6567-5725 (Embrapa Agroenergia – Brazil)
(c) 0000-0002-2223-0021 (University of Brasília – Brazil)
(d) 0000-0002-2774-1656 (University of Brasília – Brazil)
(e)* 0000-0002-4190-8598 (Embrapa Agroenergia - Brazil)

CODE: BCCM7-150

Abstract: The oleogelation technique is one innovative method applied for oil structuring and producing the so-called oleogels, which have the potential for various applications, such as reduce trans and saturated fats in foods and drug delivery. Several methods and/or combinations of them can be used to promote oleogelation and are usually divided into direct dispersion and indirect methods, such as emulsion, solvent exchange, and porous solid materials, such as foams and aerogels. Aerogels are solid materials with high specific surface area, high porosity, and very low density, which is suitable for oil sorption. In this work, pure and composites aerogels of potato starch and microfibrillated cotton cellulose were prepared via freeze-drying and tested as templates for oleogel. The increase in starch concentration increases the density and reduces the porosity of the aerogel as consequence of the higher solids content in the aqueous dispersions. The composites showed the morphology of conglutinates and planar aggregates, but superior mechanical properties compared to pure biopolymers, with improvement in elastic modulus and plasticity, as well as greater thermal stability. The higher oil absorption capacity was observed on pure cellulose aerogel (179.42 g/g). Although the addition of starch reduced the absorption capacity of the composites, they have excellent absorption capacities, ranging from 18.95 to 55.59 g/g and an oil holding capacity of up to 81.54%. These results show that cellulose and starch aerogels, hydrophilic polysaccharides, can be used to structure oil and produce oleogel indirectly by the oil sorption mechanism, having potential for oil absorption and delivery.

1. INTRODUCTION

The oleogelation is particularly a technique with potential for structuring fats, transforming edible liquid oil into a solid gel using structuring agents, forming the so-called oleogels. Oleogels are defined as semi-solid systems resulting from the trapping of liquid oil in a three-dimensional lattice without modifying the chemical characteristics of the oil [1]. Typically, oleogels are induced by structuring agents or oleogelators that can be low molecular weight, such as wax, lecithin, esters, and ceramides, and high molecular weight, such as proteins and polysaccharides [2]. Oleogels combine the nutritional profile of liquid oils and the functionality of solidified fats without using high levels of saturated fatty acids. In addition to food nutrition, these materials have been studied in various processes such as delivery of active compounds and oil treatment [3,4].

Several methodologies can be employed for the preparation of oleogels, which include the use of foams or aerogels as templates to trap the oil. Aerogels are solid materials produced by supercritical drying of CO_2 or by freeze-drying, with characteristics such as high porosity and low density, which is suitable for oil

sorption. Among the various sources, polysaccharide aerogels (e.g., cellulose, chitosan, alginate, starch, agar etc.) have received the most attention. In this sense, cellulose and starch stand out for being the most abundant biopolymers and are mostly GRAS (Generally Recognized As Safe). However, the aerogels of pure cellulose ou pure starch have some disadvantages: cellulose, despite having bending properties, have a soft structure and deforms easily, while pure starch aerogel has inferior mechanical properties and high hydrophilicity [5]. Therefore, although the study on cellulose and starch composite aerogels is incipient, some studies suggest that the production of aerogels from the mixture of these two biopolymers can modulate the properties of the final material.

Thus, the objective of this work was to study the properties of aerogels based on starch and microfibrillated cellulose (MFC) and oleogels produced by them indirectly from oil absorption.

2. METHODOLOGY

Commercial hydrophilic cotton was obtained from Farol (Minas Gerais, Brazil). Potato starch (product reference: S2004) was purchased from Sigma Aldrich (Bangalore, India). The soybean oil was purchased in a local market. Distilled water was used to prepare the hydrocolloids. The other reagents used in the experiments were of analytical grade.

Initially, the precursor materials of the aerogel were prepared: microfibrillated cellulose and gelatinized starch. An aqueous dispersion of cellulose of approximately 0.25 % (w/w) was produced by shearing cotton in a blender (Britannia, BLQ1280, 1150W) with a filter attached. After all the cotton had been dispersed, the shearing of the cellulose proceeded in an Ultra-turrax homogenizer (IKA, T25 D S32) in 10 cycles of 5 min at the speed of 18,000 rpm. Gelatinized starch was produced by mixing soluble potato starch in distilled water at the proportion of 4% (w/w). Then, the mixture was kept at 70 °C with constant stirring in a water bath for 30 minutes.

The aerogels were produced with the following cellulose/starch compositions: 100/0, 80/20, 50/50, 20/80 and 0/100. To form the composites, the two polymers were mixed in those proportions with the Ultra-turrax at the speed of 15,000 rpm for 1 minute, to homogenize the mixture. Then, the hydrogels were added in Petri dishes and Falcon tubes for molding into the shape of monoliths, and frozen in a -18 °C freezer for 24 hours and for a further four hours in the freezer at -80 °C. Finally, the material was dried in a freeze dryer (LIOTOP, K120) for 96 hours at -93 ºC and 300 µHg. The oleogels were obtained by immersing the aerogel monoliths in soybean oil for 5 minutes, which ensured their saturation.

The aerogels were characterized for their apparent density (ρ_a), porosity (P) and volumetric shrinkage (VS), according to the following equations:

$$\rho_a = \frac{m}{V} \tag{1}$$

$$VS = \frac{V_d - V}{V_d} \tag{2}$$

$$P = 1 - \frac{\rho_a}{\rho_b} \quad \Rightarrow \quad P = 1 - \rho_a \times \left(\frac{w_{celulose}}{\rho_{celulose}} - \frac{w_{starch}}{\rho_{starch}} \right) \tag{3}$$

where m is the mass and V is the volume of the aerogel, V_d is the volume of the dispersion, $w_{cellulose}$ and w_{starch} is the mass fraction of the cellulose and starch in the aerogel, respectively, $\rho_{cellulose}$ is the density of the cellulose and ρ_{starch} is the density of the starch. According to the literature, the cellulose density of cotton fiber is 1.50 g.cm^{-1} and the density of potato starch is equal to 1.45 g.cm^{-1} [6].

The aerogels were characterized as for the morphology (JEOL, JSM 7001F), crystallinity (Bruker, D8 FOCUS), chemical interaction (Shimadzu, Affinity-1), mechanical properties (Arotec, WDW-20E) and thermal properties (TA Instruments, SDT Q600).

3. RESULTS AND DISCUSSION

3.1. Physical properties of the aerogels

The values of bulk density, porosity and volumetric shrinkage of pure and composite aerogels can be seen in Table 1.

Table 1. The physical characteristics of the aerogels.

Sample	Solid content (%)	ρ_0 (g.cm^{-3})	P (%)	VS (%)
S0C100	0.25	0.003 ± 0.000^a	99.8 ± 0.2^a	30.5 ± 0.5^a
S20C80	1.00	0.013 ± 0.000^b	99.1 ± 0.3^b	31.2 ± 1.5^a
S50C50	2.13	0.030 ± 0.001^c	$98,0 \pm 0.5^c$	33.1 ± 1.5^a
S80C20	3.25	0.047 ± 0.000^d	96.8 ± 0.2^d	$33,7 \pm 0.4^a$
S100C0	4.00	0.056 ± 0.002^e	96.2 ± 0.2^e	33.0 ± 1.9^a

ρ_0 = bulk density, P = porosity and VS = volumetric shrinkage.

Results are expressed as mean values ± standard deviation of triplicate. Different superscript letters within the same column represent significant difference (p < 0.05).

The apparent density of the aerogels was in the range of 0.003 and 0.056 g·cm^{-3}, and the porosity between 96.2 and 99.8%. As expected, a lower solids content in the aqueous dispersion used to produce the aerogels resulted in a less dense and more porous structure. This inverse ratio between solids content and porosity can be explained by the increase in bonds with increased solids content between starch and cellulose in the same volume [7]. In the production of aerogels, it is also common to observe a decrease in volume after freeze-drying. This is due to several factors, such as the removal of the solvent (water), the composition and the degree of gelling of the precursor material [8]. Thus, the volumetric shrinkage (VS) can be used as a macroscopic indicative of the polymeric matrix stability during aerogel production [9]. The volumetric shrinkage of all aerogels was relatively close, ranging from 30.5% to 33,0%. In addition, it is possible to verify in the aerogels with higher levels of cellulose a lower volumetric reduction, which can be explained by the greater distance between the fibers in the aqueous matrix, leading to the formation of more open interconnected networks. A representative set of SEM images of the aerogels is shown in Fig. 1.
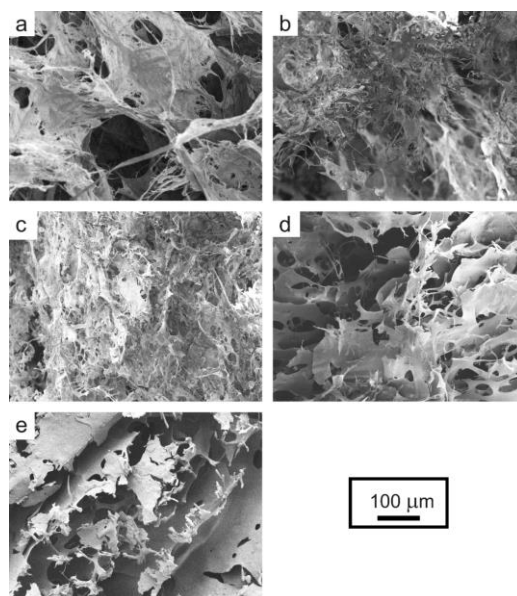
Figure. 1. Scanning electron microscopy images of the aerogels a) S0C100, b) S20C80, c) S50C50, d) S80C20 and e) S100C0.

It is observed from pure cellulose aerogel variations in the diameters of the fibrils, which is due to both the raw material (mechanically produced MFC) and the production process (freeze-drying). Some cracks are evident due to the cellulose preparation process. Moreover, pure cellulose aerogel has the shape of three-

dimensional networks formed by web-like structures, which is justified by the action of capillary forces and hydrogen bonds between hydroxyl groups during freezing and freeze-drying [10]. In aerogels with low and intermediate starch concentrations (Figs 1b and c), conglutinated structures are observed with fibrils embedded within the starch matrix and this possibly allowed the cellulose fibers to be coated and protected from capillary forces during freezing and drying. On the other hand, with a higher concentration of starch (Figs 1d and e), there are more compact and dense structures, in the shape of leaves. The leaf-like structures are usually attributed to the slow growth of water crystals that compress the gel lattice into planar aggregates [11]. The microstructure of aerogels is related to the viscosity of the gel, so that less viscous gels have less resistance to the formation of ice crystals, allowing the formation of lamellar ice layers [12].

Fig. 2 shows the X-ray diffraction (XRD) patterns of the aerogels and some differences with respect to crystallinity are observed. As expected, the pure cellulose material presents diffraction peaks referring to the presence of a crystalline structure at $2\theta \approx 22.9°$ due to the crystalline plane (200), and the overlapping peaks $11\bar{0}$ and 110 (14.8° and 16.7°, respectively), characteristic of cellulose polymorph I [13]. It is verified that these peaks decrease with the addition of starch, not being observed in the S100C0 sample, which indicates that the starch in the aerogels is amorphous, due to the rupture of the granules during the gelatinization process.

Despite small differences between them, the FTIR spectra of the aerogels show the general characteristic spectrum of cellulose and starch (Fig 2.). Characteristic bands were detected at 3400 cm^{-1} and 2900 cm^{-1}, and were attributed to O–H and C–H stretching vibrations, respectively [14]. A peak at 1732 cm^{-1} was observed in the pure cellulose spectrum, which is attributed to the vibration of C=O [15]. The peak at 1640 cm^{-1} was related to the flexural vibrations of the adsorbed water [16]. The band at 1429 cm^{-1} is attributed to CH$_2$ deformation vibration which is a type of the "crystallinity band" of cellulose [14]. In addition, the sharp peak at 1371 cm^{-1} reflects asymmetric C−H deformations. The band at 1159 cm^{-1} corresponds to the C-O-C stretch of the β-1,4-glycosidic bond. A sharp and strong band at 1059 cm^{-1} has been assigned to C−O stretch in cellulose, hemicellulose, and lignin or C−O−C stretch in cellulose and hemicellulose [15]. C-H vibration of cellulose which corresponds to the β-glycosidic linkage occurs at 895–901 cm^{-1} [16].
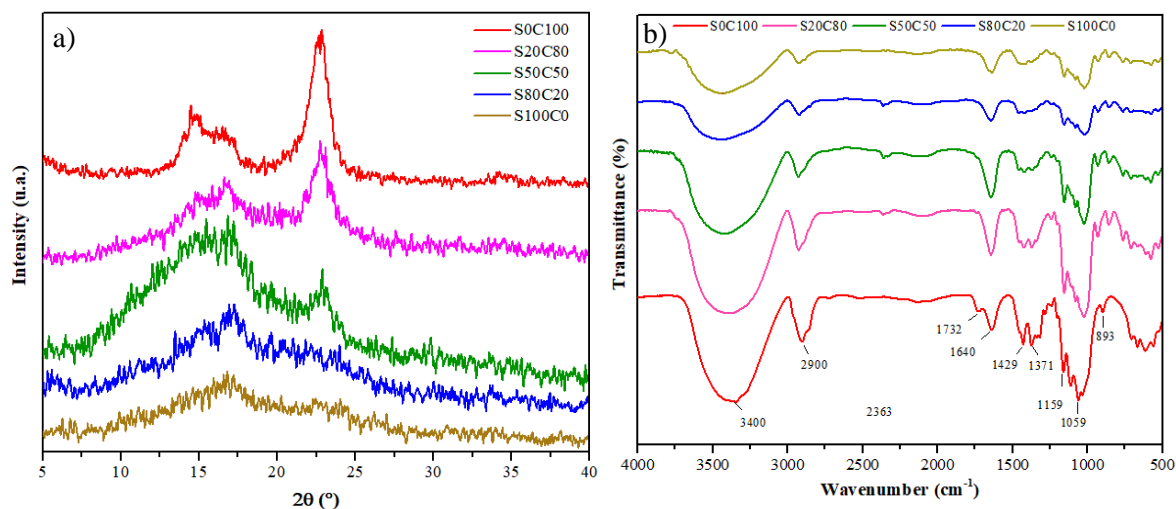
Figure 2. a) X-ray diffraction (XRD) and b) FTIR spectra of the pure and composites aerogels.

Fig. 3a shows the stress-strain curves of the aerogels with characteristic behavior of porous material, with the presence of the three regions normally found for biopolymer-based aerogels: elastic region, plastic region and densification region [17]. The increase in the solids content and, therefore, in the density of the aerogels correlated with the modulus of elasticity and tensile strength. Nonetheless, the pure starch aerogel (S100C0) exhibited low mechanical properties. The addition of microfibrillated cellulose (MFC) produced better flexural properties, acting as a reinforcement to the starch aerogel. This finding was probably due to good dispersion and the micron size of cellulose that allowed an effective contact area with the starch matrix [14].

Specifically, the S80C20 aerogel curve presents the highest inclination in all regions (elastic, plastic and densification), presenting the highest elastic modulus and the highest yield stress compared to the other pure and composite aerogels, indicating the more elastic characteristic. On the other hand, the aerogel containing the same proportions of cellulose and starch (S50C50) was less elastic and more plastic, with a greater extension of the plateau region. These two aerogels suggest that, while the addition of starch gives

elasticity to the aerogel, cellulose adds plasticity and in small amounts is already sufficient to act as a reinforcement for the aerogel predominantly composed of starch.

The compressive modulus (E) generally depends on density according to the simple scaling law $E \sim \rho^{\alpha}$ for aerogel materials (Fig. 3b), where the scaling exponent α typically ranges from 1 to 4, depending on the network material and structure [18]. The exponent α reflects the microstructures typically observed for each system. As can be seen in Fig. 3, $\alpha = 1.748$ for the aerogels produced in this work. This value is consistent with that reported by other work for cellulose nanofiber aerogels, in which $\alpha = 1.8$. The exponent around 2 has also been reported for other polysaccharide-based aerogels (1.6 for chitosan and 1.9 for xanthan) [19]. These values are attributed to the predominantly foam-like structures, i.e., regular open cell structure, observed in most cellulose aerogels [18].
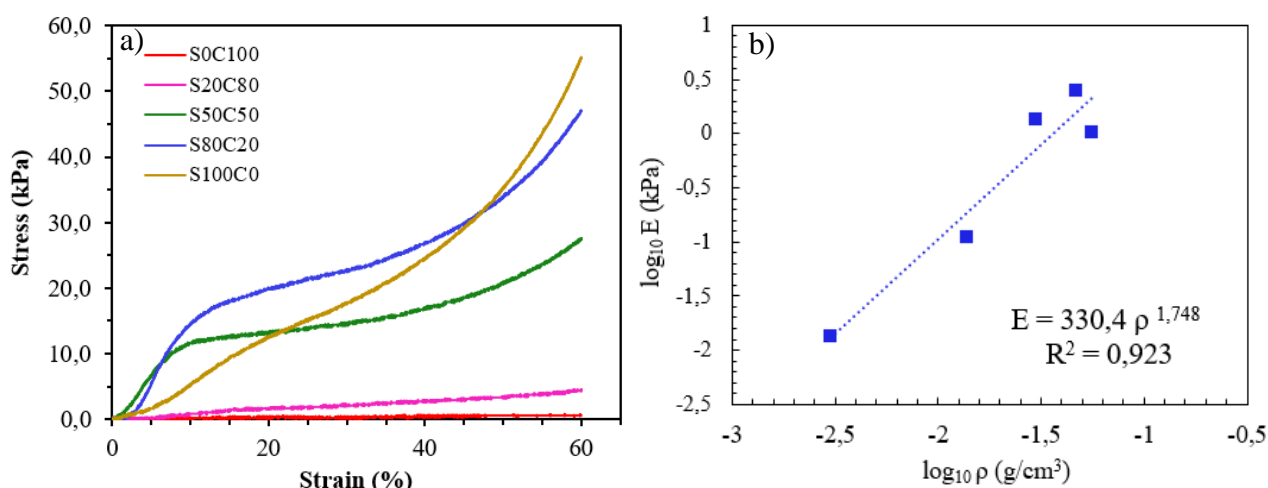
Figure. 3. a) Stress vs strain curves and b) Young's Modulus (E) as a function of bulk density (ρ) of the aerogels.

The thermogravimetric curves (TGA and DTG) and DSC of the samples of pure microfibrillated cellulose, pure starch and cellulose/starch composites are shown in Fig. 4. Starch aerogels and their composites exhibited higher water loss at the initial stages of the process compared to the pure cellulose aerogel. This outcome aligns with expectations, considering the inherently hydrophilic nature of starch. The onset temperature of all aerogels was lower than the of pure cellulose aerogel, indicating that the addition of starch contributes to reduce thermal stability. Nevertheless, during the heating of the samples from 20 to 600 °C under a nitrogen atmosphere, S0C100 and S100C0 exhibited residual weights of 11.09% and 19.68%, respectively. This difference can be attributed to the increased condensation in the starch aerogel, enhancing its resistance to degradation. In contrast, the cellulose aerogel, being more porous and featuring an expanded contact surface due to the microfibrillation process, was more susceptible to thermal degradation [20]. Particularly, the residue of S80C20 surpassed all other aerogels, signifying that this blend of cellulose and starch offers enhanced thermal stability. This observation can be attributed to the improved structural and spatial arrangement facilitated by the interaction between fibers and starch in this specific composition.

In the DTG curves, four mass loss stages were identified, with peaks of varying intensities among the aerogels. The first stage occurs at low temperatures (less than 100 °C) and is attributed to the evaporation of water adsorbed on the material. The second stage was identified only in the samples with the highest starch contents (S80C20 and S100C0) in the range of 230-250 °C, which indicates starch degradation. The third stage of mass loss can be clearly observed in the DTG curves in the range of 250-310 °C, which is due to starch degradation and burning, and in the range of 250-390 °C due to cellulose degradation. The curves of the aerogels show a single endothermic peak, indicating a good interaction between the cellulose fibers and the starch matrix. Composite aerogels showed higher T_m value (65.39-70.68 °C) than pure aerogels (51.59-54.68 °C), suggesting a significant improvement in thermal stability. This can be attributed to the interactions between starch and cellulose, resulting in a decrease in the mobility of macromolecules. In addition, the enthalpy of degradation (14.64-75.53 J/g) increases with the addition of starch, with the opposite effect for cellulose, probably due to the reduction of crystallinity, increasing thermal resistance and, consequently, requiring more energy for degradation.
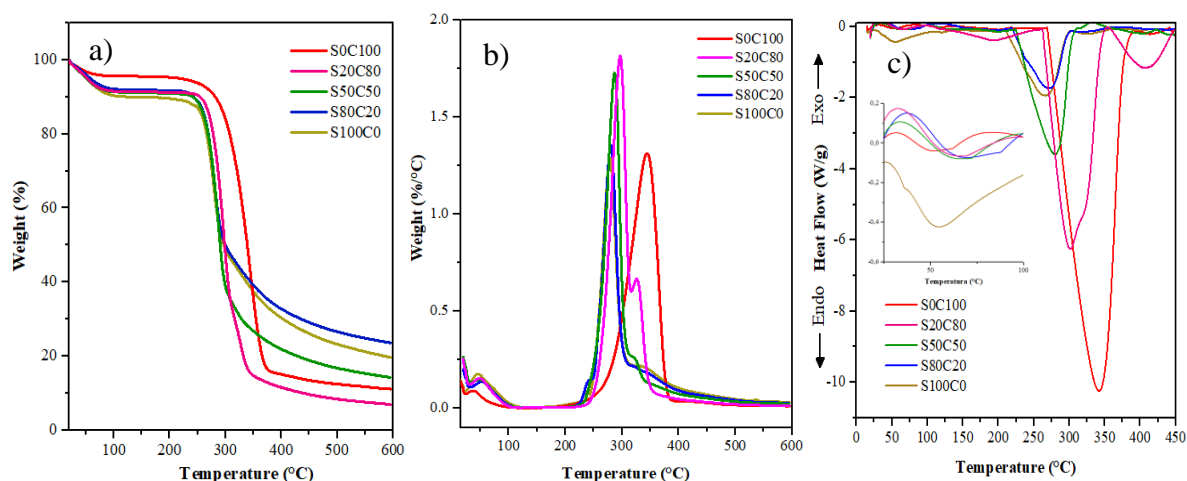
Figure 4. (a) TGA, b) DTG and c) DSC curves of the aerogels.

3.2. Oleogel characterizations

Oleogels are mainly characterized by the oil absorption and oil holding capacity, hardness, rheological and thermal properties. As shown in Table 2, all aerogels showed a good absorption capacity. The addition of starch to cellulose reduced the oil absorption capacity, being higher for pure cellulose aerogel (S0C100) with 179.42 g/g and lower for pure starch aerogel (S100C0) with 14.76 g/g. This significant difference between the aerogels was possibly because the oil-trapping ability of the aerogels was affected not only by the properties of the biopolymer, since cellulose is amphiphilic, but also by the organization of the polymer network and its internal architecture [1].

The Fig 5. presents the digital photographs of the aerogels and oleogels. In aerogels with higher starch concentrations, density increases, resulting in fewer pores and, consequently, reduced ability to trap oil. However, the addition of starch significantly influenced the structuring of the oil, with aerogels having the highest starch content exhibiting the highest oil retention. The oil holding capacity of the S0C100 oleogel was very poor because the network strength of the S0C100 aerogel was too weak due to the lowest hardness, and the network structure of the S0C100 oleogel would be most likely to be destroyed with the external force, resulting in a large amount of the oil leakage in the oleogel (Fig. 5).
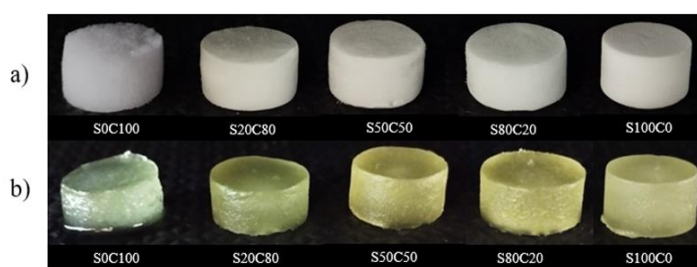
Figure 5. Digital photographs of the aerogels (a) before and (b) after absorbing oil.

The Table 2 presents the oil adsorption and oil holding capacity and the hardness of the oleogels. The combination of starch and cellulose fibers appears to have an optimal point where the upper structural arrangement retains more oil, exemplified by S50C50 (81.54%). The higher oil retention observed may be related to the greater plasticity of the aerogel, as observed in the stress *vs* strain curve of both the aerogel and the oleogel (Fig. 3a and Fig 6), since the plasticity allows the oleogel to adapt to different conditions, such as temperature and pressure. Thus, it can be inferred that this combination of biopolymers, in particular, results in a more synergistic oleogelator system. Predominantly, the hardness of oleogels is assessed by penetration/compression measurements. The values obtained from the compression of the oleogels indicate that the hardness is directly related to the increase in the solids content, as expected. This may explain the higher oil-holding capacity for aerogels with higher starch concentrations, as the structure becomes more enclosed and able to trap more oil.

Table 2. Oil adsorption capacity and oil holding capacity of the aerogels and hardness of oleogel.

Sample	Oil absorption capacity (g/g)	Oil holding capacity (%)	Hardness of oleogel (N)
S0C100	179.42 ± 2.59^a	56.55 ± 4.59^d	0.22 ± 0.08^d
S20C80	55.59 ± 1.76^b	66.78 ± 5.36^b	0.96 ± 0.34^c
S50C50	29.74 ± 1.30^c	81.54 ± 1.29^a	5.00 ± 0.46^b
S80C20	18.95 ± 0.66^d	74.94 ± 2.36^{ab}	13.28 ± 4.63^a
S100C0	14.76 ± 0.62^e	79.55 ± 2.05^a	15.28 ± 2.98^a

Results are expressed as mean values $\pm$ standard deviation of triplicate. Different superscript letters within the same column represent significant difference ($p < 0.05$).

The stress *vs* strain curves obtained in the oleogel compression test are shown in Fig. 6. It is observed that the hardness or compressive strength of oleogels is proportional to the solids content (i.e., the addition of starch content). In addition, with the increment of starch, the oleogel presents an increase in the elastic region, with an inverse relationship for cellulose, which, in this turn, confers greater plasticity to the oleogel. This result is consistent with the work of Gravelle (2017), who showed an improvement in the plasticity of the oleogel with the addition of ethyl cellulose (Fig. 6).
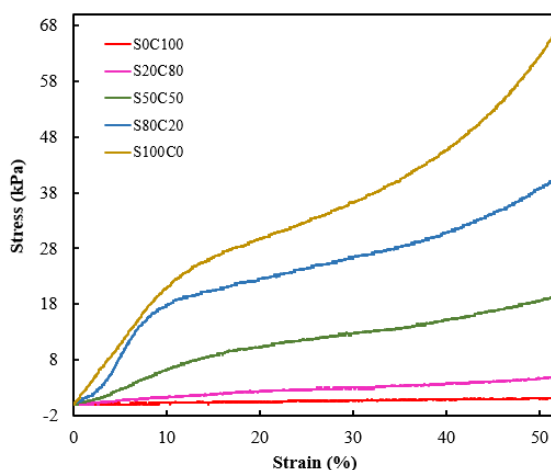
Figure 6. Stress *vs* strain curves of the oleogels obtained from the compression tests.

4. CONCLUSIONS

In this work, aerogels from pure cellulose and starch and its composites were prepared from microfibrillated cellulose from cotton and potato starch and were transformed into oleogels via oil sorption. Compared to pure biopolymer aerogels, composite aerogels showed good mechanical properties and thermal stability. These aerogels are able to absorb considerable amounts of oil with high oil-holding capacity in the form of oleogels. In addition, the starch concentration significantly influenced the mechanical strength and the holding capacity of the oil, while the cellulose added mechanical flexural properties, such as plasticity, acting as a reinforcement to the aerogel. In summary, this work presented a simple approach to the production of oleogels, without the use of chemical reactions and temperature, only by immersing the aerogels in oil. These results suggest that cellulose and starch-based aerogels can be used to absorb lipophilic molecules, suggesting promising applications, including the control oil spills. Meanwhile, oleogels can be employed in various areas such as food and pharmaceuticals, as all material used are GRAS.

4.1. Declaration of Competing Interest

The authors declare no conflict of interest.

4.2. Fundings

5. REFERENCES

[1] Manzocco L, Valoppi F, Calligaris S, Andreatta F, Spilimbergo S, Nicoli MC. Exploitation of κ-carrageenan aerogels as template for edible oleogel preparation. Food Hydrocoll 2017;71:68–75. https://doi.org/10.1016/j.foodhyd.2017.04.021.

[2] Li J, Zhang C, Li Y, Zhang H. Fabrication of aerogel-templated oleogels from alginate-gelatin conjugates for in vitro digestion. Carbohydr Polym 2022;291. https://doi.org/10.1016/j.carbpol.2022.119603.

[3] Abdullah, Zou YC, Farooq S, Walayat N, Zhang H, Faieta M, et al. Bio-aerogels: Fabrication, properties and food applications. Crit Rev Food Sci Nutr 2022;0:1–23. https://doi.org/10.1080/10408398.2022.2037504.

[4] Yang WJ, Yuen ACY, Li A, Lin B, Chen TBY, Yang W, et al. Recent progress in bio-based aerogel absorbents for oil/water separation. Cellulose 2019;26:6449–76. https://doi.org/10.1007/s10570-019-02559-x.

[5] Ago M, Ferrer A, Rojas OJ. Starch-Based Biofoams Reinforced with Lignocellulose Nanofibrils from Residual Palm Empty Fruit Bunches: Water Sorption and Mechanical Strength. ACS Sustain Chem Eng 2016;4:5546–52. https://doi.org/10.1021/acssuschemeng.6b01279.

[6] Paulauskiene T, Teresiute A, Uebe J, Tadzijevas A. Sustainable Cross-Linkers for the Synthesis of Cellulose-Based Aerogels: Research and Application. J Mar Sci Eng 2022;10. https://doi.org/10.3390/jmse10040491.

[7] Yildirim N, Shaler SM, Gardner DJ, Rice R, Bousfield DW. Cellulose nanofibril (CNF) reinforced starch insulating foams. Cellulose 2014;21:4337–47. https://doi.org/10.1007/s10570-014-0450-9.

[8] Payanda Konuk O, Alsuhile AAAM, Yousefzadeh H, Ulker Z, Bozbag SE, García-González CA, et al. The effect of synthesis conditions and process parameters on aerogel properties. Front Chem 2023;11:1–26. https://doi.org/10.3389/fchem.2023.1294520.

[9] Mehling T, Smirnova I, Guenther U, Neubert RHH. Polysaccharide-based aerogels as drug carriers. J Non Cryst Solids 2009;355:2472–9. https://doi.org/10.1016/j.jnoncrysol.2009.08.038.

[10] Chen W, Yu H, Li Q, Liu Y, Li J. Ultralight and highly flexible aerogels with long cellulose i nanofibers. Soft Matter 2011;7:10360–8. https://doi.org/10.1039/c1sm06179h.

[11] Baudron V, Gurikov P, Smirnova I, Whitehouse S. Porous starch materials via supercritical-and freeze-drying. Gels 2019;5:9–13. https://doi.org/10.3390/gels5010012.

[12] Chen W, Abe K, Uetani K, Yu H, Liu Y, Yano H. Individual cotton cellulose nanofibers: Pretreatment and fibrillation technique. Cellulose 2014;21:1517–28. https://doi.org/10.1007/s10570-014-0172-z.

[13] Nindiyasari F, Griesshaber E, Zimmermann T, Manian AP, Randow C, Zehbe R, et al. Characterization and mechanical properties investigation of the cellulose/gypsum composite. J Compos Mater 2015;50:657–72. https://doi.org/10.1177/0021998315580826.

[14] Nordin N, Othman SH, Kadir Basha R, Abdul Rashid S. Mechanical and thermal properties of starch films reinforced with microcellulose fibres. Food Res 2018;2:555–63. https://doi.org/10.26656/fr.2017.2(6).110.

[15] Li D, Zhu FZ, Li JY, Na P, Wang N. Preparation and characterization of cellulose fibers from corn straw as natural oil sorbents. Ind Eng Chem Res 2013;52:516–24. https://doi.org/10.1021/ie302288k.

[16] Abidi N, Cabrales L, Haigler CH. Changes in the cell wall and cellulose content of developing cotton fibers investigated by FTIR spectroscopy. Carbohydr Polym 2014;100:9–16. https://doi.org/10.1016/j.carbpol.2013.01.074.

[17] Wang Y, Wu K, Xiao M, Riffat SB, Su Y, Jiang F. Thermal conductivity, structure and mechanical properties of konjac glucomannan/starch based aerogel strengthened by wheat straw. Carbohydr Polym 2018;197:284–91. https://doi.org/10.1016/j.carbpol.2018.06.009.

[18] Zhao S, Malfait WJ, Guerrero-Alburquerque N, Koebel MM, Nyström G. Biopolymer Aerogels and Foams: Chemistry, Properties, and Applications. Angew Chemie - Int Ed 2018;57:7580–608. https://doi.org/10.1002/anie.201709014.

[19] Buchtová N, Pradille C, Bouvard JL, Budtova T. Mechanical properties of cellulose aerogels and cryogels. Soft Matter 2019;15:7901–8. https://doi.org/10.1039/c9sm01028a.

[20] Teles VC, Roldi M, Luz SM, Santos WR, Andreani L, Valadares LF. Obtaining Plasticized Starch and Microfibrillated Cellulose from Oil Palm Empty Fruit Bunches: Preparation and Properties of the Pure Materials and Their Composites 2021:3746–59.

BACTERIAL CELLULOSE AEROGELS WITH HYDROXYAPATITE INCORPORATION CYCLES FOR TISSUE REPAIR

Garcia, G.D. [a]*, Aguiar, A. C. [b], Magnago, R. F. [c], Lona, L. M. F. [d]

(a) 0000-0003-0438-0736 (University of Campinas – Brazil)
(b) 0000-0003-4552-1881 (University of Campinas – Brazil)
(c) 0000-0001-7306-7984 (Universidade Federal de Santa Catarina – Brazil)
(d) 0000-0001-5304-9025 (University of Campinas – Brazil)
* Corresponding author: guigarcia0000@hotmail.com

Abstract: Tissue engineering is fundamental for improving people's health and quality of life. However, creating biomaterials for this purpose remains a significant challenge due to the complexity of their fabrication, high costs, and difficulty in large-scale production. Fortunately, biofabrication using bacterial cellulose (BC) and its modification through the impregnation of suspended particles have emerged as a promising and advantageous technique for scaffold production due to its simplicity, low cost, and scalability. However, it is essential to direct efforts towards improving fundamental properties such as mechanical strength and cell adhesion capacity. This work aims to develop a new biomaterial for potential use as scaffolds for bone regeneration through the preparation and evaluation of BC aerogels. The process begins with preparing BC hydrogels in cubic and cylindrical formats, followed by surface phosphorylation and impregnation with hydroxyapatite (HAp) particles. Initially, process parameters such as volume and incubation time were investigated for cubic hydrogels, along with the influence of lyophilization on the structure of cubic BC hydrogels. Simultaneously, cylindrical BC aerogels were developed using static fermentation techniques and phosphorylation, followed by HAp incorporation and lyophilization. Preliminary results indicate that HAp incorporation resulted in aerogels with different characteristics compared to the original hydrogels. A significant reduction in moisture and an increase in porosity were observed after HAp incorporation, indicating a change in the aerogel structure. The interaction between BC and HAp limited water absorption after rehydration. The swelling ratio (SR) showed interesting behavior, with a general downward trend as the number of HAp incorporation cycles increased. However, cycle 4 showed a notable increase in SR, suggesting a significant influence of surface area on aerogel swelling capacity. Porosity increased progressively with the increasing number of HAp incorporation cycles, indicating a more porous structure and, therefore, more conducive to nutrient diffusion and cell proliferation. These preliminary results provide an essential basis for future research aimed at improving the manufacturing and modification methods of BC aerogels.

1. INTRODUCTION

Tumors, infections, traumas, degenerative diseases, and congenital conditions are among the leading causes of bone defects. Moreover, in 2017, approximately 22 million orthopedic surgeries were performed, with 70% of them requiring some type of implant for bone repair [1]. Bone diseases can lead to tissue disorders and limitations, making healing difficult or impossible, and in many cases, bone grafting is necessary to aid in the regeneration process [2]. Biomaterial scaffolds can provide structural support for cell migration, proliferation, and fixation [3], [4]. The choice of biomaterial for scaffold production is crucial, as it should have non-toxic characteristics, aid in the integration and replacement of the region for bone regeneration, and

contain a network of interconnected pores that allow nutrient transport to cells. These scaffolds can be obtained through the drying of hydrogels, for example, bacterial cellulose [6].

Bacterial cellulose (BC) is a natural polymer biosynthesized by bacteria (*e.g.*, *Gluconacetobacter xylinus*, *Acetobacter G-xylinus* e *Azotobacter*) that has high chemical purity (*i.e.*, no lignin and hemicellulose) [9]. It stands out in this field for its three-dimensional nanofiber structure (*i.e.*, porous presence), biocompatibility, biodegradability, high surface area, good mechanical performance, and versatility for surface modifications [10], [11].

BC can have its properties adapted during the biosynthesis process. In this context, it is feasible to employ physical and/or chemical treatments to modify, enhance, and add specific and desirable characteristics to the cellulose material [12]. An example of this is the phosphorylation process, a chemical treatment that replaces the -OH groups of BC inducing the formation of calcium phosphates (CaP), making the material suitable for biomedical applications [2].

Ceramics, such as hydroxyapatite (HAp), are already used as bone substitutes in the dental field, presenting osteoconductive and osteoinductive properties [14], [15]. HAp is part of calcium phosphates and is a natural component of hard tissues, such as bones and teeth, playing a fundamental role in bone structure and supporting their growth and development [16]. Calcium phosphates are recognized for their osteoinductive and osteoconductive properties, stemming from their ability to interact with cells and trigger specific cellular responses like adhesion, proliferation, and bone formation [17].

The use of HAp in the biomedical industry has garnered significant attention due to its unique physicochemical Properties [18]. However, as an alternative material for bone defect repair, HAp faces some limitations such as fragility and low dispersion in aqueous environments. Therefore, combining HAp with a polymeric matrix, such as CB, can be a desirable approach to optimize its characteristics and enhance mechanical performance, aiming to mimic the natural bone structure more efficiently [19], [20]. Thus, this work aims to develop aerogels using a combination of phosphorylated BC hydrogels, with the incorporation of HAp cycles to produce biomaterials for bone tissue repair.

2. METHODOLOGY

2.1. Aerogel preparation

2.2. Preparation of Modified Hestrin-Schramm (HS) Culture Medium

The culture medium used was the Modified Hestrin-Schramm (HS) medium [21], composed of 50 gL^{-1} of glucose ($C_6H_{12}O_6$), 0,73 gL^{-1} of magnesium sulfate heptahydrate ($MgSO_4.7H_2O$), 0,2 gL^{-1} of magnesium sulfate heptahydrate (KH_2PO_4) and 4 gL^{-1} of yeast extract. The reagents were dissolved in 980 mL of distilled water and autoclaved at 121 °C for 15 minutes. At the end of the autoclaving process, 20 mL of 99.8% ethyl alcohol (C_2H_6O). was added. Cultivation was carried out in a 250 mL glass bottle containing 80% of the culture medium and 20% (v/v) of inoculum (*K. xylinus* bacteria).

2.3. Preparation of bacterial cellulose hydrogels

The production of BC hydrogels was tested in two conformities: cylindrical (**Fig. 1a**) and cubic (**Fig. 1b**). Cubic hydrogels were obtained through the hydrophobization of molds (*e.g.* polystyrene - PS). In this case, acetone was used to partially dissolve the internal structure of the mold, followed by the addition of Teflon particles throughout the internal region. This mold hydrophobization allowed air access between the mold and the culture medium. Incubation occurred at a temperature of 30°C, with saturated humidity, and the incubation days were studied using an experimental design (ranging from 4 to 24 days). For cylindrical hydrogels, 5 mL of culture medium containing bacteria (with a 20% v/v inoculum proportion of bacteria to 80% v/v modified HS medium) were used, which were placed in a cylindrical container (*e.g.* Falcon tube). Subsequently, they were incubated in an oven at 30°C for 14 days. Both produced hydrogels were purified with a 0.1 M sodium hydroxide (NaOH) solution for 24 hours to remove the culture medium and bacteria. Finally, the BC hydrogels were washed several times with ultrapure water and stored refrigerated at approximately 9 ± 1°C for future use.
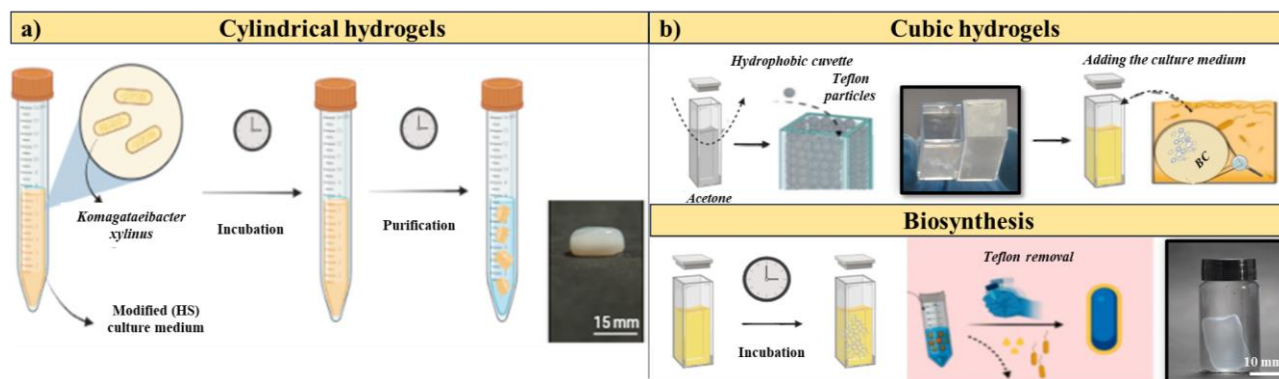
Figure 1. Biofabrication process of BC hydrogels in cylindrical **(a)** and cubic **(b)** shapes.

2.4. Surface modification

To stimulate the formation and adhesion of hydroxyapatite onto BC, a surface modification will be performed through the phosphorylation of BC hydrogels. The procedure will be like that described by Wan *et al.* [22]. Briefly, the BC hydrogels will be placed in a round-bottom flask equipped with a condenser and a nitrogen gas inlet. Dimethylformamide (DMF) and urea will be added to the flask; this mixture will be heated to 110°C, and a solution of phosphoric acid (H_3PO_4) will be added. Subsequently, the temperature will be raised to approximately 140°C and kept at reflux for 1 hour. After this process, the BC hydrogels will be washed multiple times with ultrapure water to remove excess phosphoric acid and stored refrigerated at approximately 9 ± 1°C for future use.

2.5. Formation and incorporation of hydroxyapatite

After the phosphorylation process, the formation of hydroxyapatite will occur through alternating immersion cycles, like the method described by Saska *et al.* [23]. A cycle consists of immersion in $CaCl_2$ followed by immersion in Na_2HPO_4. In summary, the BC hydrogels will be added to a 0,1 M $CaCl_2$ solution (pH 4,80) for 30 minutes in an ultrasonic bath. Then, the BC hydrogels will be washed with ultrapure water and placed in a 0.06 M Na_2HPO_4 solution (pH 8,30) for another 30 minutes in an ultrasonic bath. An experimental design will be developed to assess the number of cycles required for hydroxyapatite formation.

2.6. Physico-chemical characterizations

To evaluate moisture absorption at 25°C, BC aerogels were subjected to a drying process using a moisture balance (MOC63c, Shimadzu Corporation). This procedure was repeated after 24 and 48 hours. The drying temperature was maintained constant at 105°C until the process was completed. **Eq. 1** describes the calculation to determine the percentage of moisture in the aerogels.

$$\text{Moisture (\%)} = \left[\frac{\text{Moist sample (g)} - \text{Dry sample (g)}}{\text{Moist sample (g)}} \right] * 100 \tag{1}$$

The swelling ratio of the aerogels was determined using a method like that of Torgbo *et al.*[10]. The swelling ratio (SR) was calculated by weighing the dry aerogels (Wd). The aerogels were immersed in phosphate-buffered saline (PBS) solution at pH 7.4 and 37°C. After 24 hours, the aerogels were removed and dried to remove excess absorbed buffer, and the wet weight (Ww) was recorded. **Eq. 2** presents the swelling ratio.

$$\text{SR (\%)} = \left[\frac{\text{Ww} - \text{Wd}}{\text{Wd}} \right] * 100 \tag{2}$$

The porosity of the samples was determined using the liquid displacement method, like the method described by Torgbo *et al.*[10]. In summary, the aerogels were placed in a graduated glassware with 30 mL of distilled water (V1) at 37°C for 48 hours. The total volume of water after immersing the sample is recorded as (V2), and the remaining volume of water in the graduated glassware after removing the sample is denoted as (V3). The percentage porosity (%) is determined by **Eq. 3**.

$$\text{Porosity (\%)} = \left[\frac{(V1 - V3)}{(V2 - V3)} \right] * 100 \tag{3}$$

3. RESULTS AND DISCUSSION

CB hydrogels of two shapes were developed to determine the ideal conditions for the aerogel biofabrication process. In addition, the surface was modified using the phosphorylation technique, followed by the incorporation of four cycles of HAp into the modified CB.

3.1. Biofabrication of CB aerogels

To improve the biofabrication of cubic hydrogels, two process variables were explored, namely volume and time, to identify the best parameter. The incubation volume varied from 0.40 to 1.30 mL, and the incubation time ranged from 6 to 24 days. To characterize the hydrogels, the thickness of the hydrogels was measured after freeze-drying. **Fig. 2a** shows the appearance of the hydrogels after their biosynthesis and **Fig. 2b** shows the thickness surface graph.
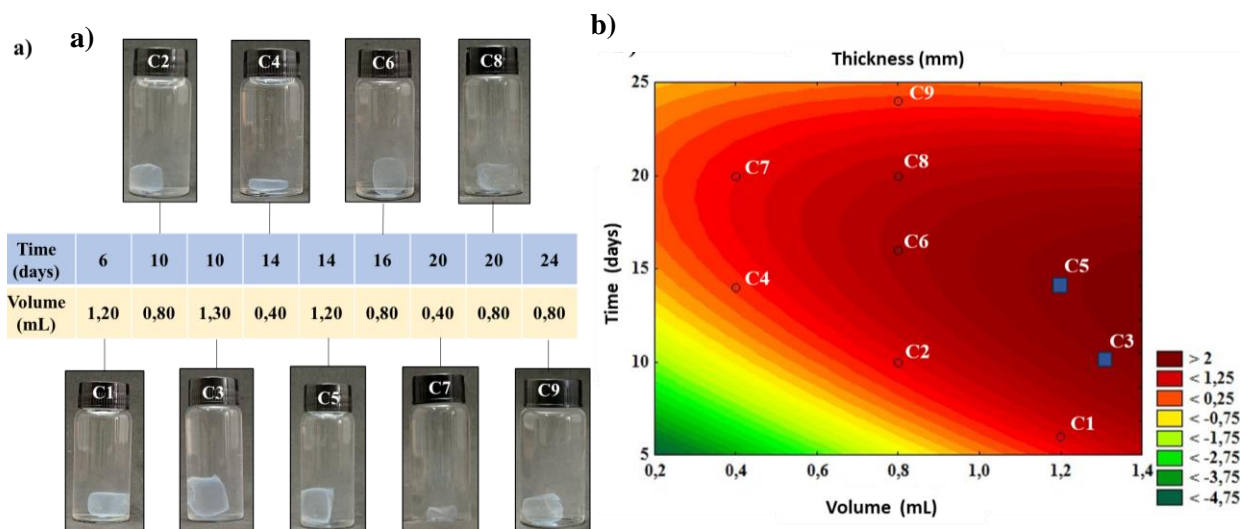
Figure 2. Hydrogels under different conditions **(a)**; Experimental design for the variables **(b)**.

Analyzing **Fig. 2a**, it is noticeable that samples C3, C5, C8, and C9 exhibited perforations. This likely occurs because cubic hydrogels tend to break when removed from the mold, according to Greca *et al.* [24], increasing the incubation volume results in a longer path for oxygen to penetrate the mold, hindering oxygenation of the culture medium during incubation, thus leading to a less resistant structure with perforations. Additionally, as the number of days of incubation increases, the material's maximum support capacity also increases [24]. Furthermore, it can be observed that samples C1, C2, C4, C6, and C7 had a similar appearance to each other, varying only in size, which is related to the incubated volume. Analyzing the thickness surface after the lyophilization process in **Fig. 2b**, the blue squares represent optimal manufacturing process conditions (*e.g.* C3 e C5). However, when subjecting the cubic hydrogels to the lyophilization process, a change in their shape was observed.

According to Greca *et al.* [24] these characteristics arise due to the lyophilization technique employed, in which hydrogels are formed through an air-water interface via hydrophobic microparticles, allowing air permeability in the mold. However, this peculiarity results in a predominantly liquid composition inside, as bacterial cellulose formation occurs from the outside in, forming a biofilm layer that, after lyophilization, leads to the loss of mold appearance. Following this alteration, it becomes evident that this approach may not be feasible for application as aerogels in bone regeneration.

Simultaneously, the production of cylindrical CB aerogels began with the development of hydrogels that were incubated for 14 days, as the literature indicates this timeframe is ideal for achieving maximum yield [25]. **Fig. 3** presents the BC hydrogels in their front view (**Fig. 3a**) and top view (**Fig. 3b**).
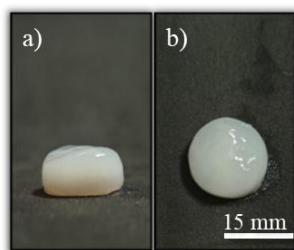
Figure 3 CB hydrogels front view **(a)** and top view **(b)**.

Analyzing **Fig 3a**, one can observe the surface of the hydrogels, displaying a whitish coloration characteristic of purified CB. However, it is noticeable that the hydrogel exhibits a rough upper surface. This is because the upper part is in contact with oxygen, being the first region to form, resulting in a denser region. On the other hand, the lower part is in contact with the culture medium, where CB formation would be occurring, making it a less dense and clearer region. Additionally, **Fig. 3b** resents the hydrogels in cylindrical shapes, with a diameter of 15 mm. After the phosphorylation step, the cylindrical CB hydrogels were subjected to four cycles of HAp incorporation, followed by the lyophilization process.

3.2. Moisture (%)

The results are divided between the humidity immediately after lyophilization and the values obtained after 24 and 48 hours. **Fig. 4** presents the humidity analysis for different samples of BC aerogels.
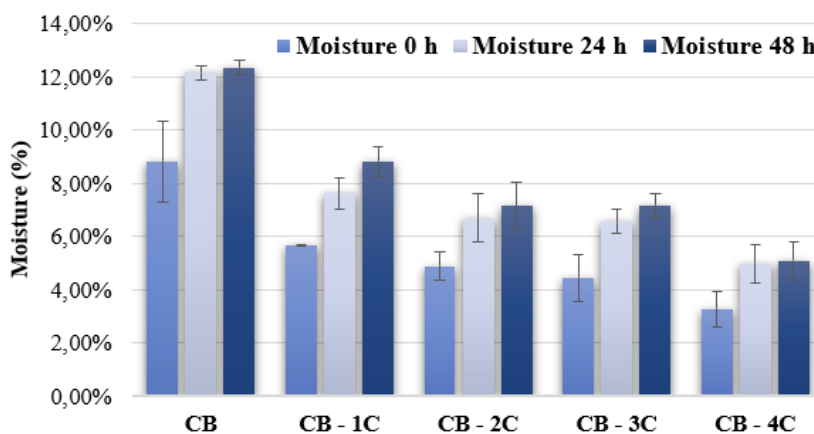
Figure 4. Moisture values for CB aerogels after freeze-drying with HAp incorporation cycles.

A trend of decreasing moisture levels with increasing cycles of HAp incorporation can be observed. The CB sample used as a control exhibited an initial moisture content of $8.83 \pm 1.52\%$. Upon phosphorylation and subsequent HAp incorporation cycles, the modified samples (*e.g.* CB - 1C, CB - 2C, CB - 3C e CB - 4C) showed a reduction in moisture levels, reaching $3.29 \pm 0.67\%$ in the CB - 4C sample. Statistical analysis revealed that the moisture content values among the HAp incorporation cycles did not differ significantly from each other but were all statistically different from the control sample.

Regarding rehydration after 24 hours, an increase in moisture can be observed in all samples, indicating that aerogels tend to absorb water from the environment. However, even after rehydration, the samples with HAp maintained lower moisture levels than the CB sample. The decrease in rehydration in samples with more cycles of HAp incorporation can be explained by the interaction between HAp and modified CB. As more incorporation cycles are performed, HAp deposits more efficiently on the surface of CB, creating a denser barrier resistant to water penetration. This reduces rehydration capacity as water finds it more challenging to penetrate and disperse within the material's structure.

3.3. Swelling ratio (SR)

The results regarding the swelling ratio (SR) are presented in **Tab. 1**. In various applications, such as in biomaterials for tissue engineering, swelling can be desirable as it allows the material to adapt to the biological environment and interact more effectively with surrounding tissues[27]. It can be observed that the control sample exhibited the highest degree of swelling, at $3433.33 \pm 339.69\%$. After the incorporation of HAp

cycles, the samples showed a significant reduction in swelling ratio compared to the control, ranging from $1395.85 \pm 45.45\%$ to $1846.06 \pm 57.25\%$.

Table 1. Swelling ratio (RI) for aerogels incorporating HAp cycles

Samples	RI 24 h (%)	RI 48 h (%)
CB	$3433,33 \pm 339,69^a$	$3740,38 \pm 443,41^a$
CB – 1C	$1707,56 \pm 182,84^{bc}$	$1875,26 \pm 168,79^{bc}$
CB – 2C	$1681,96 \pm 62,19^{bc}$	$1780,67 \pm 50,96^{bc}$
CB – 3C	$1395,85 \pm 45,45^b$	$1451,00 \pm 91,02^b$
CB – 4C	$1846,06 \pm 57,25^c$	$1962,56 \pm 117,57^c$

Averages followed by the same letter in the rows have no statistically significant difference between them using the Tukey test at 5% probability.

When analyzing the relationship between the number of cycles and swelling, the SR decreases with an increase in the number of HAp incorporation cycles. Additionally, Torgbo *et. al.* [27] conducted swelling studies on CB/magnetite/HAp biomaterials and showed a significant decrease in swelling capacity with the incorporation of HAp and magnetite particles while maintaining a high degree of porosity. Athukorala *et al.* [28] they also reported that CB/HAp biomaterials exhibited slightly lower SR compared to their control.

The abundance of hydroxyl groups impacts CB, resulting in its absorption capacity; however, the crosslinking of calcium phosphate (CaP) with hydroxyl groups led to a reduction in swelling capacity due to the hydrophobic nature of HAp [26]. There were no statistical differences between samples CB-1C, CB-2C, and CB-3C, as well as between CB-1C, CB-2C, and CB-4C. This could be attributed to the less uniform or efficient formation of the HAp layer in the initial cycles. Additionally, Portela *et. al.* [29] reported that SR is related to the available pore volume and surface area, thus requiring additional analyses of morphology and porosity for confirmation. Among these, it can be observed that at the 48-hour SR, the aerogels continued to absorb water and swell over the period, suggesting a good water retention capacity.

3.4. Porosity

Porosity is an essential characteristic in biomaterials as it directly influences nutrient diffusion and cell proliferation. More porous aerogels provide a larger surface area and internal volume, which facilitates substance exchange and promotes more effective interaction with surrounding cells. [10]. **Fig. 8** illustrates the results regarding the porosity of CB aerogels after the incorporation of HAp in different cycles.
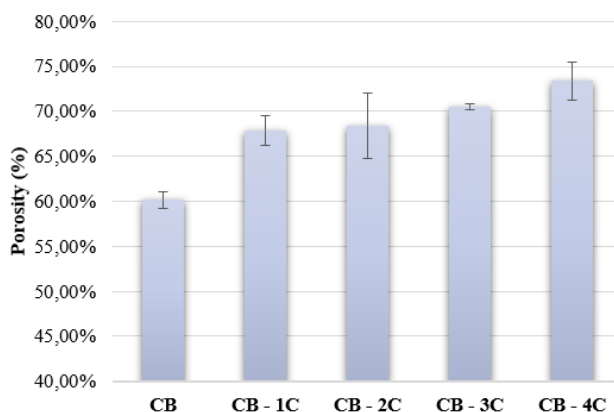
Figure 8. Study of the porosity of CB aerogels with the incorporation of HAp cycles.

A progressive increase in porosity is observed as the number of cycles increases, ranging from $60.17 \pm 0.96\%$ for the CB sample to $73.41 \pm 2.14\%$ for the CB - 4C sample. This indicates that the incorporation of HAp results in more porous aerogels. However, upon analyzing the standard deviations, it is noted that the CB - 1C, CB - 2C, CB - 3C, and CB - 4C samples do not show statistical differences among themselves, but all differ statistically from the control sample (CB). This additional porosity can be attributed to the opening of glucopyranose rings and the disorder in the ordered packing of CB, caused by the oscillation effect of ultrasonic radiation and the ionic interaction among various components, resulting in the formation of more pores in the aerogels [10]. Greater porosity will stimulate cell growth and the uniform distribution of cells, aiding in the vascularization of the matrix structure [30].

4. CONCLUSIONS

The results of this study provided insights into biofabrication. Parameter variations in the biofabrication of cubic hydrogels demonstrated a significant impact on their structure and resistance. It is important to note that the lyophilization step for cubic hydrogels proved critical due to their hollow nature, resulting in changes in the shape of the hydrogels that may limit their application as aerogels for bone regeneration. In the case of cylindrical aerogel production, the incorporation of HAp and lyophilization resulted in aerogels with distinct moisture levels, swelling ratios, and porosity compared to CB aerogels without incorporation. Moisture analysis showed a significant reduction in moisture levels after the incorporation of HAp cycles, indicating a modification in their structure. Furthermore, the swelling ratio (RI) exhibited an interesting behavior, with a general reduction trend as the number of HAp incorporation cycles increased. As for porosity, there was a progressive increase as the number of cycles increased, which is a highly desirable characteristic in biomaterials as it facilitates the diffusion of nutrients and cellular interaction.

4.1. Declaration of Competing Interest

4.2. Fundings

4.3. Acknowledgements

5. REFERENCES

[1]   Research and Markets, 'Orthopedic Surgery - Global Trends & Opportunities', 2018.

[2]   Z. Y. Qiu, Y. Cui, and X. M. Wang, 'Natural Bone Tissue and It's Biomimetic', *Mineralized Collagen Bone Graft Substitutes*, pp. 1–22, Jan. 2019, doi 10.1016/B978-0-08-102717-2.00001-1.

[3]   G. Turnbull *et al.*, '3D bioactive composite scaffolds for bone tissue engineering', *Bioact Mater*, vol. 3, no. 3, pp. 278–314, Sep. 2018, doi: 10.1016/j.bioactmat.2017.10.001.

[4]   D. Hatch, 'Bone Grafting - Basic Science', Orthobullets.

[5]   G. Tang *et al.*, 'Recent Trends in the Development of Bone Regenerative Biomaterials', *Front Cell Dev Biol*, vol. 9, May 2021, doi: 10.3389/fcell.2021.665813.

[6]   M. H. Salehi *et al.*, 'Electrically conductive biocompatible composite aerogel based on nanofibrillated template of bacterial cellulose/polyaniline/nano-clay', *Int J Biol Macromol*, vol. 173, pp. 467–480, Mar. 2021, doi 10.1016/J.IJBIOMAC.2021.01.121.

[7]   M. T. Maia *et al.*, 'Advances in Bacterial Cellulose/Strontium Apatite Composites for Bone Applications', *Polymer Reviews*, vol. 61, no. 4, pp. 736–764, Oct. 2021, doi 10.1080/15583724.2021.1896543.

[8]   A. Rastogi and R. Banerjee, 'Statistical optimization of bacterial cellulose production by Leifsonia soli and its physico-chemical characterization', *Process Biochemistry*, vol. 91, pp. 297–302, Apr. 2020, doi: 10.1016/j.procbio.2019.12.021.

[9]   N. Eslahi, A. Mahmoodi, N. Mahmoudi, N. Zandi, and A. Simchi, 'Processing and Properties of Nanofibrous Bacterial Cellulose-Containing Polymer Composites: A Review of Recent Advances for Biomedical Applications', *Polymer Reviews*, vol. 60, no. 1, pp. 144–170, Jan. 2020, doi: 10.1080/15583724.2019.1663210.

[10]   S. Torgbo and P. Sukyai, 'Fabrication of microporous bacterial cellulose embedded with magnetite and hydroxyapatite nanocomposite scaffold for bone tissue engineering', *Mater Chem Phys*, vol. 237, p. 121868, Nov. 2019, doi 10.1016/j.matchemphys.2019.121868.

[11] S. Torgbo and P. Sukyai, 'Bacterial cellulose-based scaffold materials for bone tissue engineering', *Appl Mater Today*, vol. 11, pp. 34–49, Jun. 2018, doi: 10.1016/j.apmt.2018.01.004.

[12] I. Karadagli, B. Schulz, M. Schestakow, B. Milow, T. Gries, and L. Ratke, 'Production of porous cellulose aerogel fibers by an extrusion process', *J Supercrit Fluids*, vol. 106, pp. 105–114, Nov. 2015, doi: 10.1016/j.supflu.2015.06.011.

[13] T. A. Esquivel-Castro, M. C. Ibarra-Alonso, J. Oliva, and A. Martínez-Luévanos, 'Porous aerogel and core/shell nanoparticles for controlled drug delivery: A review', *Materials Science and Engineering: C*, vol. 96, pp. 915–940, Mar. 2019, doi 10.1016/j.msec.2018.11.067.

[14] R. Zhao, R. Yang, P. R. Cooper, Z. Khurshid, A. Shavandi, and J. Ratnayake, 'Bone Grafts and Substitutes in Dentistry: A Review of Current Trends and Developments', *Molecules*, vol. 26, no. 10, p. 3007, May 2021, doi: 10.3390/molecules26103007.

[15] A.-G. Niculescu and A. M. Grumezescu, 'An Up-to-Date Review of Biomaterials Application in Wound Management', *Polymers (Basel)*, vol. 14, no. 3, p. 421, Jan. 2022, doi 10.3390/polym14030421.

[16] A. Mathew, R. Augustine, N. Kalarikal, and S. Thomas, 'Tissue Engineering: Principles, Recent Trends and the Future', in *Nanomedicine and Tissue Engineering*, Apple Academic Press, 2016, pp. 31–82. doi: 10.1201/b19867-3.

[17] J. Jeong, J. H. Kim, J. H. Shim, N. S. Hwang, and C. Y. Heo, 'Bioactive calcium phosphate materials and applications in bone regeneration', *Biomater Res*, vol. 23, no. 1, p. 4, Dec. 2019, doi 10.1186/s40824-018-0149-3.

[18] M. Farokhi *et al.*, 'Silk fibroin/hydroxyapatite composites for bone tissue engineering', *Biotechnol Adv*, vol. 36, no. 1, pp. 68–91, Jan. 2018, doi: 10.1016/j.biotechadv.2017.10.001.

[19] M. Azadi, A. Teimouri, and G. Mehranzadeh, 'Preparation, characterization and biocompatible properties of β-chitin/silk fibroin/nanohydroxyapatite composite scaffolds prepared using a freeze-drying method', *RSC Adv*, vol. 6, no. 9, pp. 7048–7060, 2016, doi: 10.1039/C5RA22987A.

[20] J. Gleeson, N. Plunkett, and F. O'Brien, 'Addition of hydroxyapatite improves stiffness, interconnectivity and osteogenic potential of a highly porous collagen-based scaffold for bone tissue regeneration', *Eur Cell Mater*, vol. 20, pp. 218–230, Oct. 2010, doi: 10.22203/eCM.v020a18.

[21] R. T. A. Machado *et al.*, 'Komagataeibacter rhaeticus grown in sugarcane molasses-supplemented culture medium as a strategy for enhancing bacterial cellulose production', *Ind Crops Prod*, vol. 122, pp. 637–646, Oct. 2018, doi: 10.1016/j.indcrop.2018.06.048.

[22] Y. WAN *et al.*, 'Synthesis and characterization of hydroxyapatite–bacterial cellulose nanocomposites', *Compos Sci Technol*, vol. 66, no. 11–12, pp. 1825–1832, Sep. 2006, doi: 10.1016/j.compscitech.2005.11.027.

[23] S. Saska, H. S. Barud, A. M. M. Gaspar, R. Marchetto, S. J. L. Ribeiro, and Y. Messaddeq, 'Bacterial Cellulose-Hydroxyapatite Nanocomposites for Bone Regeneration', *Int J Biomater*, vol. 2011, pp. 1–8, 2011, doi: 10.1155/2011/175362.

[24] L. G. Greca, J. Lehtonen, B. L. Tardy, J. Guo, and O. J. Rojas, 'Biofabrication of multifunctional nanocellulosic 3D structures: a facile and customizable route', *Mater Horiz*, vol. 5, no. 3, pp. 408–415, 2018, doi: 10.1039/C7MH01139C.

[25] D. Lahiri *et al.*, 'Bacterial Cellulose: Production, Characterization, and Application as Antimicrobial Agent', *Int J Mol Sci*, vol. 22, no. 23, p. 12984, Nov. 2021, doi: 10.3390/ijms222312984.

[26] V. Andree *et al.*, 'Influence of drying methods on the physical properties of bacterial nanocellulose', *Mater Res Express*, vol. 8, no. 2, p. 025402, Feb. 2021, doi: 10.1088/2053-1591/abe016.

[27] P. A. Shiekh, A. Singh, and A. Kumar, 'Oxygen-Releasing Antioxidant Cryogel Scaffolds with Sustained Oxygen Delivery for Tissue Engineering Applications', *ACS Appl Mater Interfaces*, vol. 10, no. 22, pp. 18458–18469, Jun. 2018, doi: 10.1021/acsami.8b01736.

[28] S. S. Athukorala, C. J. Liyanage, and A. C. A. Jayasundera, 'Hydroxyapatite incorporated bacterial cellulose hydrogels as a cost-effective 3D cell culture platform', *Soft Mater*, vol. 20, no. 2, pp. 183–192, Apr. 2022, doi: 10.1080/1539445X.2021.1944208.

[29] R. Portela, C. R. Leal, P. L. Almeida, and R. G. Sobral, 'Bacterial cellulose: a versatile biopolymer for wound dressing applications', *Microb Biotechnol*, vol. 12, no. 4, pp. 586–610, Jul. 2019, doi 10.1111/1751-7915.13392.

[30] N. Xue *et al.*, 'Bone Tissue Engineering in the Treatment of Bone Defects', *Pharmaceuticals*, vol. 15, no. 7, p. 879, Jul. 2022, doi 10.3390/ph15070879.

21 Recycling and reuse of composites

Organized and edited by

Sandra Maria da Luz
&
Carla Tatiana Mota Anflor

FULL USE OF RECYCLED CARTON PACKAGING TO OBTAIN ALUMINUM OXIDE

Renata de O. Gomes [(a)*], Maria Del P.H. Falla [(b)]

(a) 0000-0002-6371-9587 (University of Brasília – Brazil)
(b) 0000-0003-1623-9510 (University of Brasília – Brazil)
* Corresponding author: engenheirarenatagomes@gmail.com

Abstract: The aluminum deposits found in landfills represent a significant source of solid waste. Although various approaches have been implemented to mitigate these residues, they often result in adverse environmental effects. This study aims to present a more sustainable recycling approach, seeking benefits for society in terms of health and economy through the development of materials for energy storage. The focus of this research is on the recovery of aluminum from long-life carton packaging, with an emphasis on the synthesis and characterization of aluminum oxide nanoparticle derived from these waste materials. Aluminum oxide nanoparticles were produced through co-precipitation of aluminum leaf waste, using a constant annealing process at room temperature, followed by mortar grinding to achieve the desired size range. Subsequently, the particles were thoroughly characterized, encompassing analyses of size and phases through X-ray diffraction, identification of functional groups through infrared spectroscopy, and morphological observation through scanning electron microscopy (SEM) and transmission electron microscopy (TEM). Predominantly, the particles revealed α-Al_2O_3 and γ-Al_2O_3 phases, with an average size of 2 nm, respectively. Additionally, several OH groups associated with Al-O bonds were identified. This study contributes to advancing the understanding and application of sustainable aluminum waste recycling techniques, promoting both environmental and technological benefits.

1. INTRODUCTION

Food packaging and other common uses make aluminum foil a significant source of waste, often disposed of in landfills. Although recycling is the most common approach to deal with these wastes [1], existing methods face challenges and contribute to pollution due to the use of heavy machinery, often powered by fossil fuels such as coal, resulting in harmful emissions to air quality. Additionally, the aluminum melting process during recycling can pose serious health risks, including liver damage, skin problems, cancer, and compromised immune system [2]. Given these limitations and negative impacts, it is crucial to develop more efficient and environmentally sustainable recycling approaches.

Carton packaging is widely used in the food and beverage industry, consisting of six distinct layers that act as protective barriers [3]. These layers consist of Low-Density Polyethylene (LDPE), constituting 20%, which acts as a barrier against moisture, air, and fats; aluminum (Al), with a percentage of 5%, aiming to protect against the entry of oxygen, light, and air; and paperboard, constituting 75%, providing rigidity and protection against impacts. These layers ensure the integrity of the contents during the transportation and storage of the packaged products [4].

Current recycling techniques can be broadly categorized into three main types: energy recycling, chemical recycling, and mechanical recycling. In energy recycling, the focus is on recovering energy from waste through controlled incineration. Chemical recycling involves chemical processes such as pyrolysis and hydrolysis to transform waste into value-added products. Meanwhile, mechanical recycling entails the separation of recyclable materials based on physical characteristics to produce new products [5]. For the

recycling of carton packaging, the industry commonly employs the hydropulping process, which relies on mechanical methods to separate the layers of cardboard and optimize the recovery of recyclable materials, aiming at the production of new packaging and other products. Through this process, it is possible to remove the cardboard and the aluminum foil with LDPE [6].

Several studies have investigated methods for extracting Al- LDPE using solvents, aiming to separate Al- LDPE from post-consumer carton packaging. In these methods, LDPE is dissolved in an organic solvent and subsequently separated from the undissolved Al, a process referred to as Selective Dissolution-Precipitation (SDP) [6,7]. According to Falla (2018) [8], another method for the separation of Al-LDPE can be implemented since the components have distinct volatilities concerning temperature [8].

Aluminum oxide (γ-Al$_2$O$_3$), known as alumina, stands out as an extremely versatile material, finding broad applications in the field of micro and nanoelectronics [2]. Widely used in sectors such as microelectronics, catalysis, refractories, abrasives, rubber, dielectric windows, and structures, alumina has various phases (γ, η, δ, θ, κ, χ, ρ), with the 'γ' phase particularly employed in industrial catalysis due to its surface area optimized surface area, oxygen sublattice in octahedral sites, and remarkable structural stability. Additionally, γ-Al$_2$O$_3$ exhibits features such as increased hardness, strength, chemical resistance, and Young's modulus.

The aluminum oxide has various applications, being used in the manufacturing of cement, ceramics, ion batteries, among others. Its versatility and useful properties make it a chemically significant compound in several industries [2,9,10]. In this work, the synthesis of aluminum oxide (Al$_2$O$_3$) nanoparticles was realized from aluminum waste using the green process of residual aluminum foil as in Nduni et. al. (2018) [2]. [2,9,10]. In light of this, we recovered and recycled aluminum foil from accumulated and environmentally polluting residual carton packaging in landfills. Subsequently, it was converted into aluminum oxide nanoparticles.

2. METHODOLOGY

2.1. Sample preparation

To obtain the raw material, post-consumer carton packaging was collected from residential and commercial waste. The recycling process of carton packaging occurs through two different methods: the first process is carried out through hydropulping, and the second process involves manual material separation. Figure 1 illustrates the two methods for separating paperboard from aluminum with LDPE.

In the first method used, hydropulping helped to separate the cardboard from the aluminum laminate with LDPE [6]. Strips measuring 1 cm by 8 cm were cut, and three of them were placed in each 14 mL tube filled with distilled water. The mixture was agitated in a centrifuge at 400 rpm for 2 hours at room temperature, resulting in the swelling and separation of the paper into outer layers of card-board and aluminum with LDPE. In the second method, separation was carried out manually after immersing the packaging in water for a few days, which facilitated the separation of the cardboard. Both methods were effective, but the manual method was chosen due to its simplicity and efficiency in material separation.

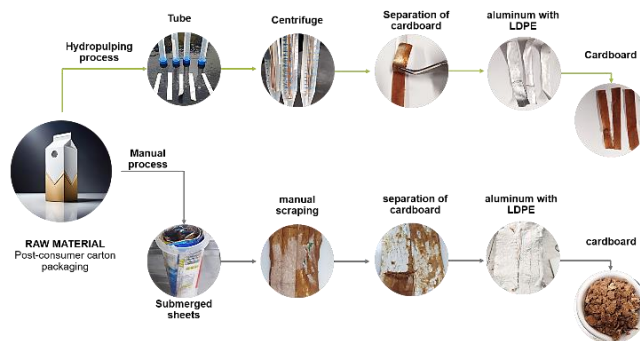**Figure 1.** Presents the two methods for separating the cardboard from the aluminum with LDPE.

2.2. Separation of Aluminum from LDPE

The methodology followed in the previous study, which involved distinct volatilities concerning temperature [8], was applied. The experiment was conducted using a modified simple distillation system for the separation of aluminum foil from LDPE, with five repetitions adopted.

This adapted system consists of a distillation flask containing aluminum foil and LDPE, a condenser for cooling and condensing vapours, and a collection container to receive the distilled liquid. The system allows the separation of components in the mixture based on their different volatilities, thereby enabling the separation of LDPE from the aluminum foil. This method is widely used due to its simplicity and efficiency in substance separation. Figure 2 illustrates the process used for the separation of the two elements, Al and LDPE.
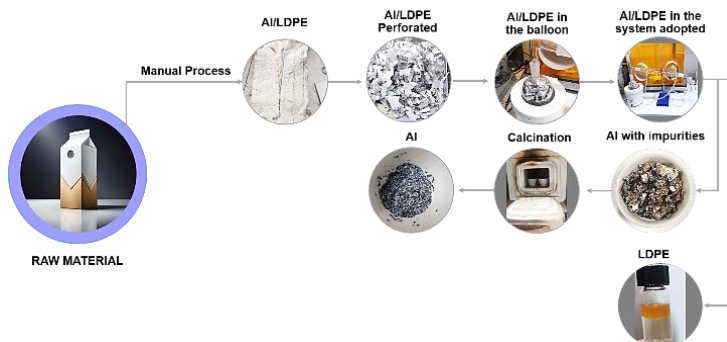
Figure 2. Summary of the Al and LDPE separation process.

The assay was conducted using a manual process for cardboard paper removal, resulting in only aluminum foil with LDPE. Subsequently, the aluminum sheets were randomly cut into small pieces, and 15 g of the sample was weighed using a Shimadzu balance, model AUY220, with a maximum capacity of 220 g and a precision of 0.1 mg.

In a 500 mL round-bottom flask with a 24/40 joint, the cut sheets were placed, and then the system was assembled using a 500 mL simple distillation apparatus with a complete heating mantle. The interchangeable glassware used in the assay included a 500 mL round-bottom flask with a 24/40 joint, an adapter joint with an outlet for a thermometer distillation head, a Liebig condenser with 2 joints and a 300 mm glass olive, a 105º angle tube with a vacuum outlet and 2 joints, a 500 mL flat-bottom flask with a 24/40 joint, a 45 cm base with a rod, a 3-finger clamp with a 60 mm opening rotary clamp, a 14x8 mm silicone hose measuring 2 meters, a rubber stopper for connecting the glassware, a 500 mL heating mantle with temperature regulator, and a digital thermometer MT-450A type "K".

The procedure began with temperature control, adjusting every 10 minutes on the heating mantle until reaching 150 ºC, maintaining this temperature constant for 1 hour. This was done with the aid of the digital thermometer MT-450A, using a "K" type thermocouple. The procedure lasted a total of 2 hours.

The aluminum sheets were added to the ceramic crucible, which was placed in a muffle furnace at room temperature. A heating rate of approximately 30 ºC/min was used to reach the working temperature of 700 ºC, which was maintained for 50 hours, followed by cooling. Finally, the sample was macerated for 5 minutes in a mortar, allowing for the obtainment of aluminum.

2.3. Synthesis of Aluminum Oxide

The methodological approach used in this experiment follows the same path as presented in a previous study [2] which demonstrated the production of aluminum oxide from aluminum sheets. The technique employed involved the application of chemical processes to obtain aluminum oxide (Al_2O_3). Figure 3 shows the chemical process used in the production of Al_2O_3.
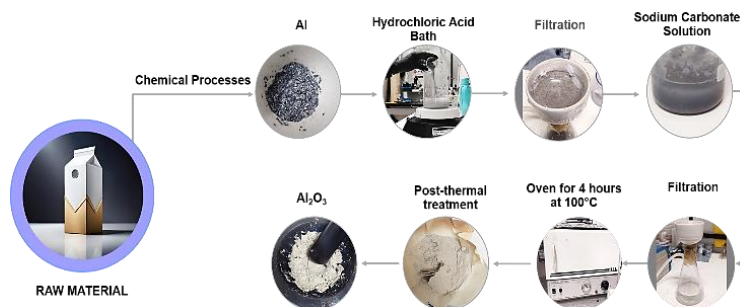
Figure 3. Chemical processes for obtaining aluminum oxide.

The assay was carried out using the recovered Al from the raw material. The acid bath was prepared with a solution of hydrochloric acid (HCl) diluted in 60 mL of a 500 mL beaker and 60 mL of distilled water. This mixture was stirred, and 10.0 g of Al was gradually added until all effervescence ceased, which took approximately 15 minutes.

Subsequently, the sample was removed from the acid bath, filtered to remove impurities, cooled, and washed. Then, the filtered material underwent the second process by slowly adding a solution of sodium carbonate, 10 g (Na_2CO_3), diluted in 100 mL of distilled water, to precipitate the aluminum oxide, ensuring that all aluminum chloride had been converted to Al_2O_3, and allowing it to stand for 1 hour.

The clear solution was separated by decantation, and then an additional amount of water was added. The material was allowed to settle before conducting a second decantation (to wash the sodium chloride). The solution was subsequently filtered to isolate the aluminum oxide, which underwent a drying process in an oven at 100°C for a duration of 4 hours to remove residual water. Finally, a mortar grinding technique was used to complete the procedure.

2.4. Characterizations X-Ray Diffraction

At X-ray Diffractometry Laboratory Institute of Geosciences (IG), we performed X-ray diffraction using an XRD-6000 diffractometer, which swept the range from $2\theta = 5°$ to $60°$ at a sweep rate of $0.5°/min$, operating with a voltage of 40 kV/30 mA and using radiation from a Cu-Kα lamp (1.5406 Å).

This equation provided a percentage measure of the amount of crystalline structure in relation to the amorphous structure of the material, serving as a valuable indicator of the properties and crystalline purity of the polymer in question.

The estimated average crystallite sizes (D, nm) of the prepared alumina Al_2O_3 nanoparticles were determined using the Debye-Sherrer formula, which was then calculated using the following equation 1.

$$D = 0{,}9\lambda/((\beta * cos(\theta B)) \tag{1}$$

Where D represents the average size of crystallites (or grains) in a material, measured in nanometers (nm), 0.9 is an empirical fitting constant used in the Debye-Scherrer formula, λ is the wavelength of the radiation used in X-ray diffraction ($\lambda = 1.5406$ Å), β is the full width at half-maximum (FWHM) of the diffraction peak, measured in radians. The calculation was performed using XRD software (Origin Pro 8, version 2018) by the diffraction peaks, and $cos(\theta B)$ is the cosine of the Bragg diffraction angle (θB), which is the angle at which diffraction occurs, measured in radians.

2.5. Fourier Transform Infrared Spectroscopy (FTIR)

FTIR spectra of Al and Al_2O_3 samples were performed using a Fourier Transform Infrared spectrometer (NICOLET IS10 from Thermo Scientific), with the aid of a diffuser reflectance accessory (DRIFT). The spectra were recorded in the range of 4,000 to 400 cm^{-1}, with a resolution of 4 cm^{-1} and 64 scans.

2.6. Scanning Electron Microscopy (SEM)

A scanning electron microscope, model JEOL JSM-7001F, with power of 15 kW, was used at the Laboratory of Microscopy and Microanalysis (LMM) of the Institute of Biology (IB) of University of Brasilia (UnB), to analyze the morphology of samples Al and Al_2O_3. SEM is a widely used technique to observe nanomaterials with high resolution and magnification, providing nanometric details.

2.7. Transmission Electron Microscopy (TEM)

In the LMM of the IB at UnB, a TEM was used to examine the structure of samples Al and Al_2O_3. The samples were deposited on a carbon microgrid (300 mesh) and let it dry. So, the grid was stained with a 1% uranyl acetate solution and dried at room temperature. Images were captured using a model of a transmission electron microscope JEOL JEM 1011, operating at 80 kV. To establish particle measurements, they were randomly selected from different images to determine its average diameter using Image J software.

2.8. Thermogravimetric Analysis (TGA)

The Al and Al_2O_3 samples were submitted for thermogravimetric analysis using a thermal device analyzer model SDT Q600 (TA Instruments). An approximate amount of 12 mg of each sample was used and

placed in an alumina crucible. The analysis was conducted in a nitrogen atmosphere, with a gas flow of 100 mL/min and a heating rate of 10 °C/min, ranging from room temperature to 700 °C.

3. RESULTS AND DISCUSSION

3.1. X-ray diffraction pattern (XRD)

The diffractorgrams in Figure 4. show X-ray diffraction and the peak angles (15.3°, 28.5°, 32°, 38.5° and 44.7°), revealed the presence of crystalline phases of nanoparticles. Al_2O_3 in the α and γ forms, in addition to some small amounts of elemental Al.
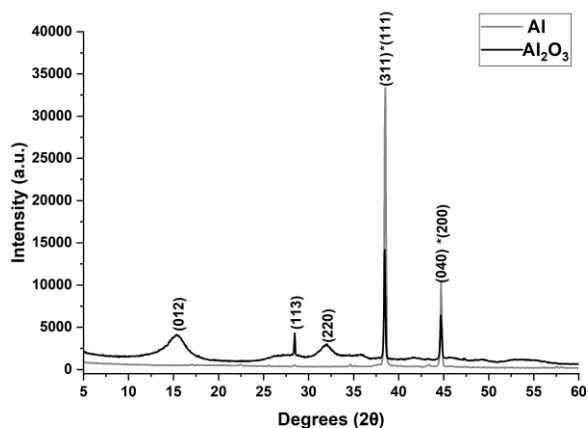
Figure 4. X-ray diffraction patterns: Al - Aluminum and Al2O3 – Aluminum Oxide.

In Figure 4, the diffractogram referring to aluminum is shown. Table 1 summarizes the X-ray diffraction peaks, corresponding hkl indices, interplanar distances (d), and polymorphic phases associated with Al-specific diffraction angles.

Table 1. Experimental results to show contaminated

Peak (Diffraction Angle 2θ)	D-spacing (Å)	Phase	Peak (Diffraction Angle 2θ)
38,5°	2,33	Aluminum	*(1 1 1)
44,7°	2,03	Aluminum	*(2 0 0)

The two main peaks approximately at 38° and 45° can be associated with the planes of an aluminum crystal *(111) and *(200) as mentioned in the literature [11,12].

Alumina nanoparticles are associated with four main polymorphs, namely α, θ, γ and κ. The polymorphic phase change is linked to variations in critical parameters of the crystal lattice, such as particle diameter and density [2]. Table 2 revealed the presence of crystalline phases of Al_2O_3 nanoparticles in summary.

Table 2. Summary of X-ray diffraction peaks of Al_2O_3.

Peak (Diffraction Angle 2θ)	D-spacing (Å)	Phase	Peak (Diffraction Angle 2θ)
15,3°	5,78Å	α-Al_2O_3	(012)
28,5°	3,13 Å	γ-Al_2O_3	(113)
32,0°	2,79 Å	γ-Al_2O_3	(220)
38,5°	2,33 Å	γ-Al2O3	(311)
44,7°	2,03 Å	γ-Al_2O_3	(040)
15,3°	5,78Å	α-Al_2O_3	(012)

The first peak was identified as α-Al$_2$O$_3$ (alpha-Alumina), revealing diffraction angles of approximately 2θ= 15.3°. These diffraction angles correspond to the crystalline planes (012), some studies affirm the presence of nanoparticles, according to the literature [2]. In the second peak approximately at 2θ = 28.5 we associate this diffraction with the (113) planes of γ-Al$_2$O$_3$ (gamma-alumina), as indicated by previous studies [13]. Two peaks approximately at 2θ= 32.0° and 38.5° correspond to the (220) and (311) planes, typical of crystals formed by γ-Al$_2$O$_3$ (gamma-alumina) nanoparticles, according to the literature, including the JPCDS card number: 10-0425 [14]. Last peak approximately at 2θ = 44.7°, is compatible with the (040) planes of γ-Al$_2$O$_3$ (gamma-alumina), as reported in previous studies [13].

No other diffraction peaks indicating other impurities or other alumina phases were identified. The estimated average crystallite sizes (D, nm) of the prepared alumina nanoparticles were determined using the Debye-Sherrer formula in Eq. 1. reported. The average individual particle size was approximately 5 nm. Some X-ray diffraction (XRD) studies of Alumina Al$_2$O$_3$ nanoparticles revealed average diameter at 2.524 nm [13] 66.5144 nm [2].

3.2. FTIR Spectroscopy Analysis

Figure 5. shows the spectrograms of samples (a) Al, Laminated, and (b) Al$_2$O$_3$, in the frequency range between 4000 and 500 cm^{-1}.
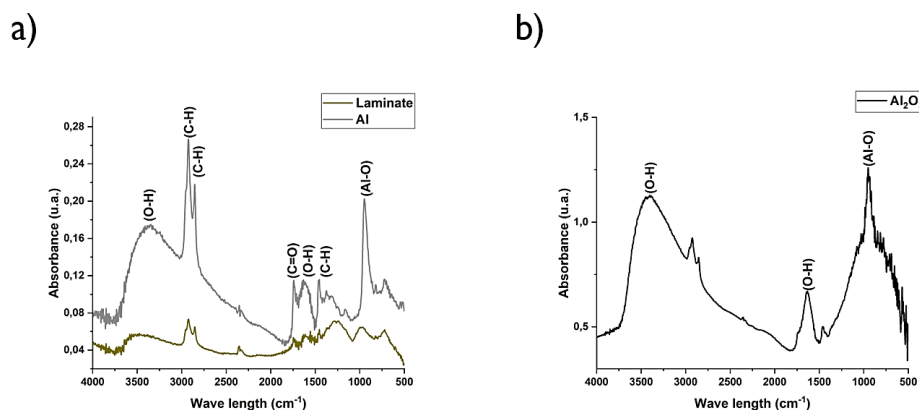
Figure 5. FTIR spectra: (a) removal of aluminum (Al) and aluminum laminate and (b) Al$_2$O$_3$.

In the spectra of aluminum (Al) and aluminum foil extraction, the presence of the absorption band at 3362 cm^{-1} and 1629 cm^{-1}, these bands indicate the presence of axial vibration and angular deformation of the O-H bond. These results suggest the presence of water absorbed on the surface of the sample.

Other relevant bands were found at frequencies of 2937 cm^{-1}, 2854 cm^{-1} and 1453 cm^{-1}, which correspond to the axial and angular vibrations of the C-H bond. Indicating the presence of methylene groups (CH$_2$) in the sample. The presence of this band suggests the possibility of organic residues, as shown in the spectrum of the laminate, there was already the presence of (C-H).

Band at 1744 cm^{-1}, is related to the carbon and oxygen C=O bond. Indicates the presence of carbonyl groups present in organic residues from the extracted material.

Finally, a band was observed at 951 cm^{-1}, associated with the Al-O bond of the AlO$_4$ group. Its presence indicates the presence of bonds between aluminum (Al) and oxygen (O) in the sample. This occurs due to the formation of aluminum oxide on the surface of Al exposed to air, as expected.

The results obtained in the analysis of the commercial aluminum foil used in the work [2] demonstrate similarities with the results mentioned in the absorption spectra. Furthermore, the identification of the band at 951 cm^{-1} related to the Al-O bond in commercial aluminum foil indicates the possible formation of aluminum oxide on its surface, as observed in previous results.

The results presented in Table 3, summary of Al and Lamindo's results, are in line with the findings documented in the scientific literature. The temperatures recorded for the corresponding spectra were 140°C, 240°C, 376°C, 404°C, 440°C, 540°C and 740°C [14].

Table 3. FTIR spectra: (a) Al sample and Al film.

Wave Number (cm^{-1})	Functional Groups	Vibration Type
3362	O-H (Hydroxyl)	Axial vibration of the O-H bond

2937	CH₂ (Methylene)	Axial vibration of the C-H bond
2854	CH₂ (Methylene)	Angular deformation of the C-H bond
1744	C=O (Carbonyl)	Vibration of the carbon-oxygen bond (C=O)
1629	O-H (Hydroxyl)	Angular deformation of the O-H bond
1453	CH₂ (Methylene)	Angular vibration of the C-H bond
951	Al-O (AlO₄ group)	Vibration of the Al-O bond (AlO₄ group)
3362	O-H (Hydroxyl)	Axial vibration of the O-H bond
2937	CH₂ (Methylene)	Axial vibration of the C-H bond

Figure 5. (b) shows spectra of Al_2O_3, absorption bands were identified at 3399 cm^{-1} and 1636 cm^{-1}, associated with vibrations of the O-H bond, suggesting the presence of hydroxyl groups (OH). Furthermore, a band was observed at 950 cm^{-1}, indicating the presence of bond vibration (Al-O), characteristic of aluminum oxide. The spectra of the synthesized and standard aluminum oxide particles show similarities, with several peaks comparing to other studies as expected [2]. These results are summarized in Table 4 below.

Table 4. FTIR spectra: (b) Al_2O_3

Wave Number (cm⁻¹)	Functional Groups	Vibration Type
3399	O-H (Hydroxyl)	Axial vibration O-H
1636	O-H (Hydroxyl)	Angular deformation O-H
950	Al-O (Aluminum-Oxygen)	Vibration of the Al-O bond

3.3. SEM and TEM Analyses

Figure 6 presents the SEM micrographs for the analyzed samples, highlighting the surface of the sample (a) referring to Al and the sample (b) referring to Al_2O_3.
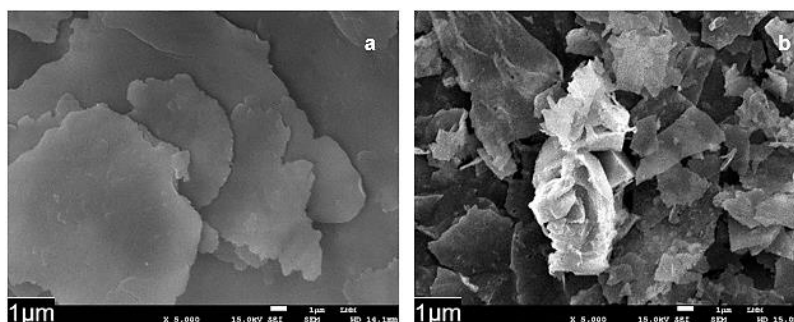
Figure 6. FTIR spectra: (a) removal of aluminum (Al) and aluminum laminate and (b) Al_2O_3.

The micrograph of aluminum in Figure 6 (a) shows aluminum removed from post-consumer carton packaging, at 5000X mag-nification. The images reveal non-homogeneous, smooth sufarces, with the presence of blades of different sizes, with no identification of residues or different materials other than aluminum.

In Figure 6 (b), when magnifying the Al_2O_3 by 5000X, the surface demonstrates a lack of uniformity, with sheets of different sizes distributed irregularly. This observation is in line with the literature, which describes Al_2O_3 particles as having lamellar morphology[15].

This comparison of the two samples (a) and (b) highlights the similarities in the non-homogeneous texture and the lamellae overlapping each other disorderly and parallel to each other, and in relation to this surface, (as if they were sheets, one on top of the other).

Figure 7 shows the micrographs obtained by Transmission Electron Microscopy (TEM), for the analyzed samples Al and Al_2O_3.
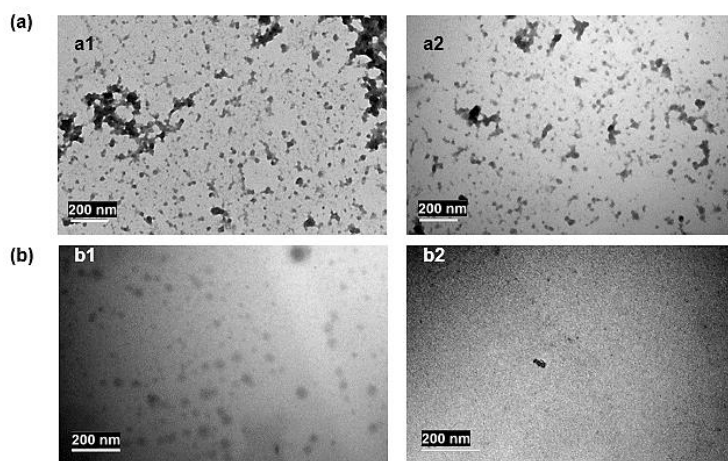
Figure 7. TEM images: (a) Al – Aluminum, (b) Al$_2$O$_3$ – Aluminum oxide; with 15000X magnification for (a1 and a2).

In Figure 7 (a1 and a2), analyzes of the Al sample were carried out at a magnification of 15,000X. The results revealed an average diameter of approximately 5 nanometers (nm). In previous studies, the average size of aluminum nanoparticles ranged from 40 to 110 nm, and these particles are spherical and have an amorphous oxide passivation layer, with a thickness that varies between 2 and 3 nm [16]. Another study described the microstructure of nanocrystalline aluminum, revealing an average grain size of 4.5 nm [17].

In Figure 7 a (b1 and b2), in the Al$_2$O$_3$ sample, it was observed that the average diameter of the nanoparticles is 2 nm. It was evident that the sample has particles of different sizes. According to the literature, Al$_2$O$_3$ generally has a thickness varying between 3-4 nanometers (nm) [18], are also reports of particles from the α-Al$_2$O$_3$ and γ-Al$_2$O$_3$ phases with an average size of 63.763 nm and 66.5144 nm [2], and particle diameter of the γ-Al$_2$O$_3$ phases approximately 2.5 ± 1 nm [13].

4. CONCLUSIONS

The recovery of recycled aluminum foil from carton packaging has proven to be an accessible recovery process. Aluminum oxide nanoparticles were successfully synthesized and characterized from recovered aluminum foil waste. Functional groups, crystallinity, particle size, and phases were characterized to resemble standard aluminum oxide nanoparticles. Presenting promising results as a cost-effective alternative for aluminum recovery, this study proposes a new alternative path, highlighting aluminum oxide as a value-added material.

4.1. Declaration of Competing Interest

The authors declare no conflict of interest.

4.2. Fundings

This field is optional. Indicate fundings, if there is any.

4.3. Acknowledgements

5. REFERENCES

[1]   Yusuf NK, Lajis MA, Ahmad A. Multiresponse optimization and environmental analysis in direct recycling hot press forging of aluminum AA6061. Materials 2019;12. https://doi.org/10.3390/ma12121918.

[2]   Nduni MN, Osano AM, Chaka B. Synthesis and characterization of aluminium oxide nanoparticles from waste aluminium foil and potential application in aluminium-ion cell. Clean Eng Technol 2021;3. https://doi.org/10.1016/j.clet.2021.100108.

[3]   TETRA PAK INTERNATIONAL. A anatomia de embalagens cartonadas da Tetra Pak®. The Anatomy of Tetra Pak® Carton Packaging 2023.

[4]   Geueke B, Groh K, Muncke J. Food packaging in the circular economy: Overview of chemical safety aspects for commonly used materials. J Clean Prod 2018;193:491–505. https://doi.org/10.1016/j.jclepro.2018.05.005.

[5]   Torres, Lange LC. Technological routes, challenges and potential for municipal solid waste energetic valorization by coprocessing in Brazil. Engenharia Sanitaria e Ambiental 2022;27:25–30. https://doi.org/10.1590/S1413-415220210221.

[6]   Georgiopoulou I, Pappa GD, Vouyiouka SN, Magoulas K. Recycling of post-consumer multilayer Tetra Pak® packaging with the Selective Dissolution-Precipitation process. Resour Conserv Recycl 2021;165. https://doi.org/10.1016/j.resconrec.2020.105268.

[7]   Hao Y, Ma H, Wang Q, Ge L, Yang Y, Zhu C. Refractory DOM in industrial wastewater: Formation and selective oxidation of AOPs. Chemical Engineering Journal 2021;406. https://doi.org/10.1016/j.cej.2020.126857.

[8]   Falla MDPH, Lee J, Bertoldi AE de M, Shynkarenko O, Henrique L. . Obtaining and Characterization of biopropellants doped with metal nanoparticles for applications in hybrid propulsion. Advanced Materials World Congress 2018, Singapoure: 2018.

[9]   Brial V, Tran H, Sorelli L, Conciatori D, Ouellet-Plamondon CM. Evaluation of the reactivity of treated spent pot lining from primary aluminum production as cementitious materials. Resour Conserv Recycl 2021;170. https://doi.org/10.1016/j.resconrec.2021.105584.

[10]   Zawadiak J. Tetra Pak Recycling – Current Trends and New Developments. American Journal of Chemical Engineering 2017;5:37. https://doi.org/10.11648/j.ajche.20170503.12.

[11]   González-Castaño M, Cancellieri C, Maeder X, Hack E, Schmutz P. Enhancing the insulating and dielectric properties of barrier anodic Al2O3 on high purity aluminum. Appl Surf Sci 2020;505. https://doi.org/10.1016/j.apsusc.2019.144522.

[12]   Koroleva E V., Thompson GE, Skeldon P, Noble B. Crystallographic dissolution of high purity aluminium. Proceedings of the Royal Society A: Mathematical, Physical and Engineering Sciences 2007;463:1729–48. https://doi.org/10.1098/rspa.2007.1846.

[13]   Wahab R, Alam M. Highly efficient and fast electrochemical sensor based on aluminium oxide (Al2O3) nanoparticle for the detection of organosulfur compounds. Sens Actuators A Phys 2022;347. https://doi.org/10.1016/j.sna.2022.113967.

[14]   Al Mahmood A, Hossain R, Sahajwalla V. Microrecycling of the metal–polymer-laminated packaging materials via thermal disengagement technology. SN Appl Sci 2019;1. https://doi.org/10.1007/s42452-019-1099-7.

[15]   Saleh AK, Shaban AS, Diab MA, Debarnot D, Elzaref AS. Green synthesis and characterization of aluminum oxide nanoparticles using Phoenix dactylifera seed extract along with antimicrobial activity, phytotoxicity, and cytological effects on Vicia faba seeds. Biomass Convers Biorefin 2023. https://doi.org/10.1007/s13399-023-04800-x.

[16]   Kim K. High energy pulsed plasma arc synthesis and material characteristics of nanosized aluminum powder. Metals and Materials International 2008;14:707–11. https://doi.org/10.3365/met.mat.2008.12.707.

[17]   Guan X, Liang A, Branicio PS. High pressure shear induced microstructural evolution in nanocrystalline aluminum. Comput Mater Sci 2022;203. https://doi.org/10.1016/j.commatsci.2021.111105.

[18]   Mafra Mendes Freitas Santos LF, Chen Abrego F, Franklin Albertin Torres K, Scodeler Raimundo D. Inducing aluminum oxide growth at room temperature and atmospheric pressure through low dose gamma-ray irradiation. Radiation Physics and Chemistry 2023;204. https://doi.org/10.1016/j.radphyschem.2022.110666.

ANALYSIS OF SHEAR STRENGTH IN EPOXY MATRIX COMPOSITES INCORPORATING RED CERAMIC WASTE AND COCONUT SHELL

David C.R. Velasco[a], Mayara T. Campos [b], Felipe P.D. Lopes [c], Carlos M.F. Vieira [d]

(a) 0000-0001-9800-9764 (Darcy Ribeiro North Fluminense State University – Brazil)
(b) 0009-0003-9881-9961 (Darcy Ribeiro North Fluminense State University – Brazil)
(c) 0000-0003-1867-6722 (Darcy Ribeiro North Fluminense State University – Brazil)
(d) 0000-0003-2012-1769 (Darcy Ribeiro North Fluminense State University – Brazil)
* Corresponding author: david.velasco@iff.edu.br

Abstract: The development of new materials plays a fundamental role in the search for more efficient materials with a lower socio-environmental impact. Among the characteristics that can be optimized, the shear resistance stands out, which is fundamental for various applications, such as structural repairs and use as adhesives. In this context, this work aims to characterize the performance of epoxy formulations previously developed for pipe coatings in terms of their shear resistance. These formulations were developed by incorporating particulate waste from red ceramics (chamote) and/or from the extraction of coconut shell fiber (coconut shell powder) into an epoxy matrix. The epoxy system used was Bisphenol A diglycidyl ether/Diethylenetriamine (DGEBA/DETA), in a proportion of 16 phr. The following formulations were evaluated: without particulates; only with ceramic particles (20% vol. chamotte); only with lignocellulosic particles (2.5% vol. of coconut shell powder) and hybrids (17.5% chamotte and 2.5% coconut shell powder). These composites were manufactured in silicone molds and, after curing at room temperature, they underwent a post-curing process at 70°C for 3 hours. The shear test carried out was of the Iosipescu type, according to ASTM D5379/D5379M, at a speed of 0.5 mm/min. The results of this study made it possible to characterize the shear strength and shear modulus of the formulations evaluated, in addition to investigating the effect of incorporating residues on the behavior of the epoxy system.

1. INTRODUCTION

The use of polymer matrix composites has been presenting new solutions to the demands of various industrial sectors, enabling the creation of materials with high mechanical resistance while having the advantage of having a low density, becoming attractive for various applications [1-2].

Epoxy systems are commonly used in the repair and reinforcement of concrete structures, aerospace, marine, chemical, and electrical. Its use as a base matrix is due to its exceptional characteristics mechanical, electrical, and thermal strength, as well as their accessibility and structural strength [3-4]. It should also be added that the use of fibers and particulates can present improvements in thermal, electrical and mechanical properties [5-6].

The concept of developing environmentally friendly materials has sparked interest in both the industrial community and academics [2]. In this sense, there was a growing interest in the use of natural fibers from renewable resources in the production of Natural Fiber Reinforced Composites (NFRC) [7-8]. These natural fibres offer several superior environmental advantages compared to synthetic fibres, such as:a) lower energy consumption during manufacturing, b) biodegradability, c) renewability, d) lower weight, e) reasonable cost, and f) sustainable supply [9-11].

Incorporating natural plant fibers into fiber-reinforced polymer composites can help industries reduce their reliance on non-renewable resources, mitigate environmental impact and comply with stricter regulations related to greenhouse gas emissions [12].

Coconut fiber is one of the most widely used natural fibers today as an alternative in the development of technologies with less environmental impact. When compared to other natural fibers, coconut fiber stands out for having a higher lignin content in its composition, a component that gives greater rigidity and strength to the fiber. Due to the presence of a high content of hydroxyl groups in its structure and non-cellulosic components on its surface, it can be combined with different physical and chemical methods to improve its adhesion to the polymer. [13-15].

During the processing of the coconut shell, a residue is produced in the form of powder, the coconut shell powder. The powder produced is considered an agricultural waste, which was initially used as an agricultural substrate due to being a biological material, but new research has revealed the potential use of this material in the development of composite materials [16-17].

In recent years, due to urban development and increasing activity in the real estate sector, There has been an increase in the demand for building materials. This phenomenon can be closely linked to environmental issues, since intensive industrial production can lead to significant impacts resulting from the extraction of raw materials, atmospheric emissions, and eventual waste generation. In this context, waste management becomes one of the primary challenges faced today [18-19].

Chamote, crushed red ceramic waste, has been incorporated into different matrices due to its advantages of abundance, low energy consumption and low cost [15,18-19].

One of the sectors with the largest production of pieces in Brazil is the red ceramics sector. It is estimated that 13.7 million m² of parts are produced annually worldwide [18]. According to the National Association of the Ceramic Industry (ANICER), Brazil produces more than 8 billion pieces per year [20], Of this amount 10% of the production is lost, due to defects, damage during transport, etc [19].

Thus, the present work aims to analyze the influence of the incorporation of red ceramic and coconut shell residues on the shear strength of epoxy matrix composites.

2. METHODOLOGY

In the present study, the epoxy system Bisphenol A diglycidyl ether/diethylenetriamine (DGEBA/DETA) was adopted, in a proportion of 16 parts of hardener to 100 parts of resin. This system is supplied by AVIPOL and produced by SILAEX, identified under codes SQ2050/SQ3131. The chamotte used was obtained from defective pieces from Três Estrelas ceramics, located in Campos dos Goytacazes/RJ. Coconut shell powder was obtained as a by-product of the coconut fiber extraction process by a local producer in Salvador/BA.

Both residues were crushed in a ball mill for 24 hours and sieved using a mesh with an opening of 150 microns. The material used is shown in Figure 1.

Figure 1. Waste used in this work after processing.

The formulations used in this work are presented in Table 1, which comes from previous analysis. To remove moisture, the waste was left in an oven for 24 hours at 60 °C, before its immediate use.

Table 1. Evaluated formulations.

ID	Epoxy	Chamotte	Coconut Powder
EP	100 %	-	-
CH	80 %	20 %	-
CP	97.5 %	-	2.5 %
HB	80 %	15 %	5 %

Five samples were produced for each formulation in open silicone molds, at room temperature, with standard dimensions as shown in Figure 2 [21]. Once curing at room temperature was complete (5 days at around 25°C), the specimens underwent a post-curing process at 70°C for 3 hours.
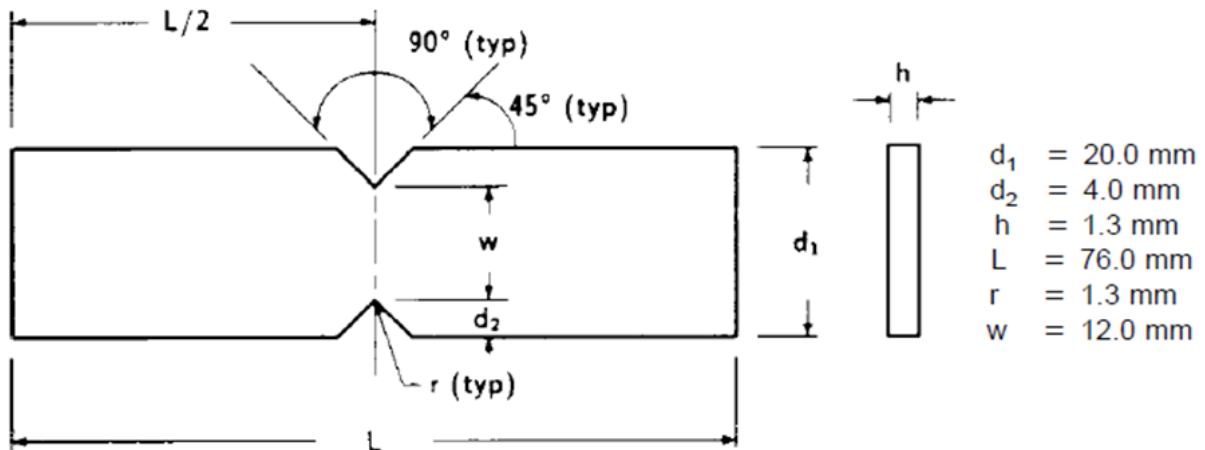
Figure 2. Test body used in this test [21].

The test was carried out on the INSTRON universal testing machine, model 5582, located in the LAMAV/UENF advanced materials laboratory. The test speed was 0.5 mm/min, and the results were validated using a strain gage, according ASTM [21], as shown in Figure 3.
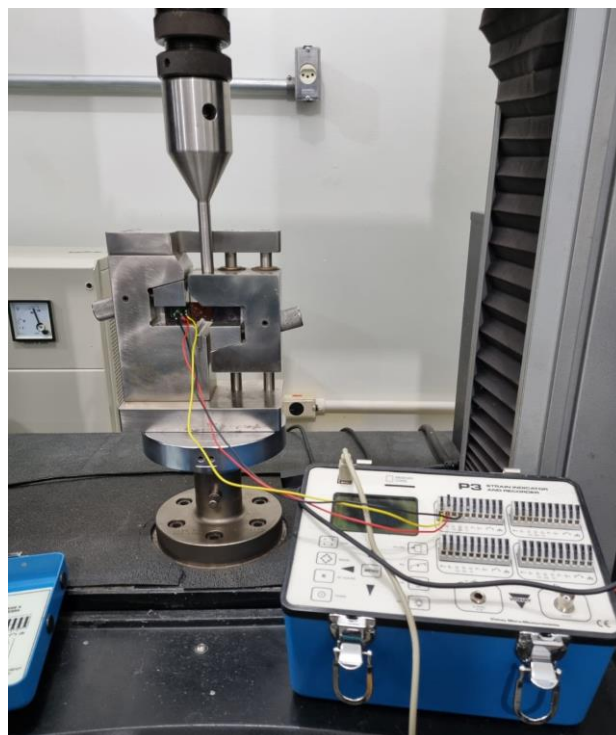
Figure 3. Test validation using strain gage.

Aiming to verify the existence of significant variations, the results of this work were evaluated using analysis of variance and Tukey test, [22], using 10% as the significance level.

3. RESULTS AND DISCUSSION

The results of the test executed in this work are available in Figure 4.
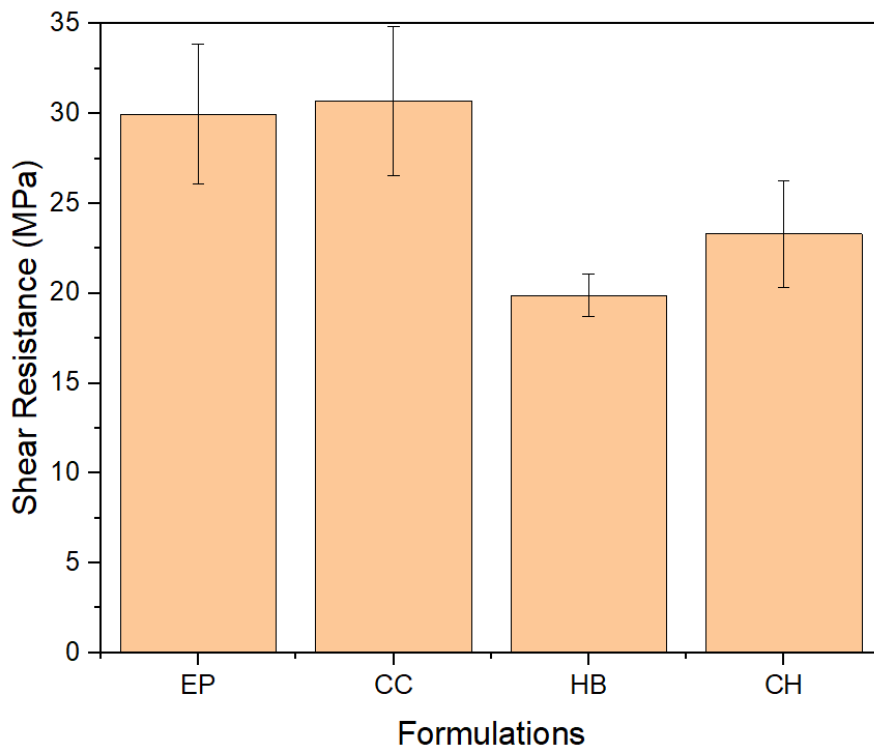
Figure 4. Shear resistance of evaluated formulation.

From the statistical analysis of the results of the EP and CC formulation in this work, it can be observed that the shear strength did not vary significantly when adding few coconut shell particulates. However, when comparing formulations with more particulates, CH and HB, significant strength losses can be observed, from 24 and 35% respectively.

The inclusion of particulates such as chamotte tends to increase young modulus and resistance, which is observed not only in theoretical models, but also in experimental analyses on addition of similar wastes. However, there are studies where the opposite behavior is also observed, which is attributed to the agglomeration of particulates and their worse wettability [23-25]. This is proven when it is observed that when replacing part of the ceramic particles with lignocellulosic particles, the shear resistance was significantly reduced, this being apparent in Figure 4 and confirmed in the statistical analyses carried out. Thus, the CC formulation performs better than other formulations with residues, not because coconut shell powder is a more promising residue than chamotte, but because it uses smaller amounts of particulates and therefore facilitates them to have better wettability. and dispersion.

When examining the shear resistance properties alongside other parameters assessed within the same formulations, as detailed in Table 2, It is observed that the shear strength reflects the trends observed in other static tests carried out in literature.

Table 2. Evaluated formulations.

ID	Shear Resistance (MPa)	Compression Resistance (MPa)[26]	Flexural Resistance (MPa) [27]
EP	29.96 ± 3.90	90.33 ± 3.05	87.15 ± 9.16
CH	23.30 ± 2.97	66.26 ± 4.54	36.47 ± 5.03
CP	30.69 ± 4.16	94.22 ± 1.57	71.93 ± 4.68
HB	19.90 ± 1.18	68.28 ± 1.90	33.27 ± 4.08

4. CONCLUSIONS

The present research demonstrates that the incorporation of evaluated residues, in reduced quantities, allows for the preservation of shear strength. However, formulations containing a higher proportion of particulates (20% by volume) showed significant losses in this characteristic, aligning with other properties evaluated in previous studies.

4.1. Declaration of Competing Interest

The authors declare no conflict of interest.

4.2. Acknowledgements

5. REFERENCES

[1] G. Golakiya, D. Cree. Valorization of purified agricultural brown eggshell by-product as filler in bio-epoxy composites. Waste Management Bulletin, Volume 2, 2024. DOI : 10.1016/j.wmb.2024.02.006.

[2] A. H. Birniwa, S. S. Abdullahi, M. Ali, R.E.A. Mohammad. A. H. Jagaba, M. Amran, S. Avudaiappan, N. Maureira-Carsalade, E. I. S. Flores. Recent trends in treatment and fabrication of plant-based fiber-reinforced epoxy composite: a review. Journal of Composites Science. 2023. DOI: 10.3390/jcs7030120.

[3] A. D. Watpade., et al. "Comparative analysis of machine learning models for predicting dielectric properties in MoS2 nanofiller-reinforced epoxy composites." Ain Shams Engineering Journal, 2024. DOI: 10.1016/j.asej.2024.102754.

[4] S, Poonam, et al. Compositional influence of synthesized magnetic nanoparticles on epoxy composites: dielectric, magnetic, and optical characteristics. Journal of Macromolecular Science, Part B, 2024. DOI: 10.1080/00222348.2023.2263293.

[5] W Zhi, et al. Mechanical and anticorrosion properties of furan/epoxy-based basalt fiber-reinforced composites. Journal of Applied Polymer Science, 2017. DOI: 10.1002/app.44799.

[6] A.R, Ravindran, R.B. Ladani, S. Wu, A. J. Kinloch, C.H. Wang, A. P. Mouritz. The electric field alignment of short carbon fibres to enhance the toughness of epoxy composites. Composites Part A: Applied Science and Manufacturing, 2018. DOI: 10.1016/j.compositesa.2017.12.006.

[7] V.S. Hiremath, D. M. Reddy, R. R. Mutra, A. Sajeev, T. Dhilipkumar, J. Naveen. Thermal degradation and fire retardant behaviour of natural fibre reinforced polymeric composites-A Comprehensive Review. Journal of Materials Research and Technology. 2018. DOI: 10.1016/j.jmrt.2024.04.085.

[8] H. Bisheh, J. Jelovica. Analytical assessment of wave dynamics for natural fibre-reinforced composite plates. European Journal of Mechanics - A/Solids, Volume 106, 2024. DOI: 10.1016/j.euromechsol.2024.105280.

[9]   H. Bisheh. Design and analysis of hybrid natural/synthetic fibre-reinforced composite automotive drive shafts. Structures, Volume 61, 2024, 106057, ISSN 2352-0124. DOI: 10.1016/j.istruc.2024.106057.

[10]   O. A. Dickens, Park, Giseok, J. W. Kim, J. Kim. Biobased natural fiber-reinforced composites derived from lignin-based resin and mercerized jute fibers, Materials Letters. Volume 360, 2024. DOI: 10.1016/j.matlet.2024.136055.

[11]   S. Gowtham, T. Jeevanantham, J. Emelda, J. Edric, Investigation on effect of fibre orientation on mechanical behaviour of polymer matrix natural fibre reinforced composite material, Materials Today: Proceedings, 2024. DOI: 10.1016/j.matpr.2024.04.022.

[12]   P. Thangapandian, S. Seenivasan, P. Raj Kumar, S. Kailasavalli, S. Paulsingarayar, Effects of chemical treatment on natural (rice straw/neem saw dust) fiber morphology and mechanical properties of its composite material. Materials Letters, Volume 364, 2024, 136288, ISSN 0167-577X. DOI: 10.1016/j.matlet.2024.136288.

[13]   Y. N. Wearn, L. S. Montagna, F. R. Passador. Compósitos de fibra de coco/LDPE: efeito do tratamento superficial das fibras de coco em compósitos verdes. Matéria (Rio de Janeiro), 2020.

[14]   C. Demirdağ, M. Nodehi, A. Bideci, O. S. Bideci, M. Tuncer, O. Gencel, T. Ozbakkaloglu. The use of natural (coconut) and artificial (glass) fibers in cement – polymer composites: An experimental study. Construction and Building Materials, Volume 412, 2024. DOI: 10.1016/j.conbuildmat.2024.134895.

[15]   D. C. R. Velasco, F. P. D. Lopes, N. T. Simonassi, C. M. F. Vieira. Influência da incorporação de resíduos na permeabilidade ao vapor de água de compósitos de matriz epoxídica/Influence of the incorporation of waste on the water vapor permeability of epoxide matrix composites. Brazilian Journal of Development, 2022. DOI: 10.34117/bjdv8n4-101.

[16]   Sundarababu J, Anandan SS, Griskevicius P. Evaluation of mechanical properties of biodegradable coconut shell/rice husk Powder polymer composites for light weight applications. Mater Today Proc 2021;39:1241–7. DOI: 10.1016/j.matpr.2020.04.095.

[17]   Ishizaki, M. H., Visconte, L. L., Furtado, C. R., & Leblanc, J. L. (2009). Efeito do Teor e da Granulometria da Fibra de Coco Verde nas Propriedades Mecânicas de Compósitos com Polipropileno. Revista Souza Marques, 10(21), 50-55.

[18]   M. Samadi, G. F. Huseien, H. Mohammadhosseini, H.S. Lee, N. H. A. S. Lim, M. M. Tahir, R. Alyousef. Waste ceramic as low cost and eco-friendly materials in the production of sustainable mortars. Journal of Cleaner Production, 2022. DOI: 10.1016/j.jclepro.2020.121825.

[19]   Associação Nacional da Industria Cerâmica. *Dados do Setor*. Anicer, 2023. Disponível em: <https://www.anicer.com.br/anicer/setor/>. Acesso em: 21 de Abr de 2024.

[20]   M. G. P. Cherene, G. C. Xavier, L. S. Barroso, J. S. M. Oliveira, A. R. G. Azevedo, C. M. Vieira, J. Alexandre, S. N. Monteiro. Technological and microstructural perspective of the use of ceramic waste in cement-based mortars, *Construction and Building Materials*, Volume 367, 2023. DOI: 10.1016/j.conbuildmat.2022.130256.

[21]   D30 Committee. ASTM D5379: Test Method for Shear Properties of Composite Materials by the V-Notched Beam Method. DOI: 10.1520/D5379_D5379M-19E01.

[22]   M. D Copenhaver; B Holland. Computation of the distribution of the maximum studentized range statistic with application to multiple significance testing of simple effects. Journal of Statistical Computation and Simulation, v. 30, n. 1, p. 1-15, 1988. DOI: 10.1080/00949658808811082.

[23]   REDDY, J. R. S. Size Effect of Clay Filler Particles on Mechanical Properties of Pultruded Polymer Composites Under Shear Loading. 2017. Doctoral thesis. Minnesota State University, Mankato.

[24]   Khashaba U, Othman R, Najjar IM. Development and characterization of structural adhesives for aerospace industry with alumina nanoparticles under shear and thermo-mechanical impact loads. *under shear and thermo-mechanical impact loads. Proceedings of the Institution of Mechanical Engineers, Part G:Journal of Aerospace Engineering*. 2020. DOI: 10.1177/095441001987555.

[25]   Nayak SK, Satapathy A, Mantry S. Processing and wear response study of glass-polyester composites with waste marble dust as particulate filler. *Polymer Composites.* Volume: 41, 2020. DOI: 10.1002/pc.25537.

[26] D.C.R, Velasco; R.R.R. Junior; Lopes, F. P. D, Lopes; N. T, Simonassi; CMF.Vieira; Monteiro, S.M Neves. Efeito da variação da proporção resina/endurecedor no comportamento à compressão compósitos poliméricos particulados, p. 2171-2184. In: 76º Congresso Anual da ABM - Internacional, São Paulo, 2023. ISSN: 2594-5327. DOI 10.5151/2594-5327-40278.

[27] D.C.R, Velasco; R.R.R. Junior; Lopes, F. P. D, Lopes; N. T, Simonassi; CMF.Vieira; Monteiro, S.M Neves.; Vieira, Carlos Maurício Fontes. Influência da variação da estequiometria entre resina epóxi e endurecedor na resistência à flexão de compósitos particulados, p. 2080-2093. In: 76º Congresso Anual da ABM - Internacional, São Paulo, 2023.ISSN: 2594-5327. DOI 10.5151/2594-5327-40118.

INVESTIGATION ON THE COMPRESSIVE BEHAVIOR OF EPOXY COMPOSITES REINFORCED WITH SEALING BLOCK`S WASTE

David C.R. Velasco[(a)], Darcy L.R. Oliveira [(b)], Felipe P.D. Lopes [(c)], Carlos M.F. Vieira [(d)]

(a) 0000-0001-9800-9764 (Darcy Ribeiro North Fluminense State University – Brazil)
(b) 0009-0005-6757-8856 (Darcy Ribeiro North Fluminense State University – Brazil)
(c) 0000-0003-1867-6722 (Darcy Ribeiro North Fluminense State University – Brazil)
(d) 0000-0003-2012-1769 (Darcy Ribeiro North Fluminense State University – Brazil)
* Corresponding author: davidc.r.v2014@gmail.com

CODE: BCCM7-171

Keywords: Sustainability, Composite, Compression Resistance

Abstract: The growing demand for more sustainable actions, both in industry and academia, results in the urgent need to seek more sustainable materials to face contemporary challenges, such as the excessive use of raw materials and the massive production of industrial waste. In this context, this study aims to evaluate the effects of adding 10%, 20% and 40% chamotte (sealing block waste) in powder form to a DGEBA/DETA epoxy system, using a stoichiometric ratio of 16phr. In this study, the compressive strength was evaluated, according to ASTM D695, to highlight the influence of adding ceramic waste to the resin. By understanding these aspects, it is possible to contribute to the development of more sustainable and ecologically responsible materials.

1. INTRODUCTION

Sustainability has become a subject of extreme focus today. This is due to the major environmental problems that can be observed today [1]. Deforestation, emissions of polluting gases, improper disposal of products and various other problems plague the contemporary world [2], thus generating enormous problems for biodiversity and life on the planet [3].

Various researchers from different fields have come together to try to create and manage processes that are more sustainable [4], both in the production of materials and in their disposal. One aspect that has been studied and improved is the so-called circular economy [5], which has the main objective of generating a reuse of products, seeking to maximize profits and the well-being of nature [6].

With a focus on producing more sustainable products, several industries and countries are seeking to innovate and provide a greater quantity of "Green" products in their production [7]. In an effort to generate greater efficiency in the production of this type of material, several countries have created and implemented laws that encourage greener production.

One possible solution to produce eco-friendly materials is the use of waste, seeking to increase the strength of the final material, or just reduce the amount of non-reusable material used on certain occasions [8], One industry that produces waste in extensive quantities is the construction industry [9]. Its numbers are estimated at 1.8 billion tons generated annually in China alone [10], thus denoting the impact that this industry generates.

In contrast to the construction industry, the production of products from red ceramics in Brazil stands out among the others in the sector, with more than 5,500 ceramics and pottery factories in Brazil, producing more than 8 billion blocks and tiles [11]. The importance of using this waste for application in a product and/or service is clear, due to the large quantity of products produced, which consequently generate huge amounts of waste.

To achieve the goal of generating a cheaper and less environmentally damaging material, several researchers use waste in the production of polymer composites [12]. One of the advantages of putting an end to the chamotte (ceramic waste) mentioned above is to generate a larger area for planting and consequently a greater increase in capital, this is since much of the chamotte is disposed of in landfills, reducing the productive quality of the soil [13].

Figure 1. Ceramic Waste Pile [14].

Some examples of work using chamotte as a dispersed phase in a polymer composite were those by Júnior *et al.*[15] and Velasco *et al.*[16]. In the first article cited, the author observed an increase in mechanical strength as the amount of chamotte applied to the composite increased. The second study showed that applying a greater amount of chamotte, around 20% in relation to the volume, resulted in lower water vapor permeability, an important property for applications that require impermeable materials.

Looking at the results above, the residue has been researched with satisfactory results, thus generating greater safety in relation to the material applied. The aim of this work is to apply chamotte to a polymeric matrix, epoxy, and to evaluate the compressive strength of the composites manufactured, to increase the strength of the composites manufactured and reduce the amount of resin used, which is not recyclable.

2. METHODOLOGY

This article was produced using a two-component polymer resin: Diglycidyl Ether Bisphenol A (DGEBA) resin and Triethylenetetramine (TETA) hardener. This epoxy system is sold by the company AVIPOL, under the respective trade names: SQ2050 and SQ3131. The reinforcement used in the epoxy matrix was chamotte particulate, sieved using a 0.15mm (100 mesh) sieve. The diagram below, in Fig. 2, shows the process of synthesizing chamotte for use.

Figure 2. Material and equipment used for particulate preparation

The diagram above shows all the stages and equipment used to complete Chamote. Figure 2.1 shows the material as it was initially obtained. After obtaining the material, it was passed through a jaw mill (Fig. 2.2) to turn the pieces into chips (Fig. 2.3). Subsequently, it passed through a ball mill (Fig. 2.4) for 24 hours, aiming to obtain the particulates in small particle formats (Fig. 2.5). After this, it was sieved using a 100-mesh sieve, and the material was placed in an oven for around 24 hours at 70ºC to remove the moisture.

In this work, four formulations were evaluated, which are presented in Table 1. All the specimens were manufactured and cured at room temperature using an open silicone mold, which was then sanded to obtain a better finish and support for the tests. The dimensions of the specimens were on average 12 x 12 x 5 mm, following the ASTM D695-15 standard [17].

Table 1. Compositions of the Specimens

ID	EPOXY	CHAMOTTE
EP	100%	-
10CH	90%	10%
20CH	80%	20%
40CH	60%	40%

After initial curing at room temperature, a subsequent post-curing step was conducted at 70°C for a duration of 3 hours. Following this stage, the specimens underwent testing using an Instron universal testing machine, model 5582, located at UENF's LAMAV. The speed adopted for the tests was 1.3 mm/min at room temperature (25°C).

3. RESULTS AND DISCUSSION

Figure 3 shows the modulus of elasticity obtained through the compression test. Therefore, it can be observed that the addition of chamotte residues progressively increases the rigidity of the epoxy system, in line with what was observed in other works [18]. This can be attributed to the addition of a more rigid material that not only tends to increase the rigidity of the composite because of partial replacement of a less rigid material (epoxy) by a more rigid one (ceramic), but also because its presence decreases the mobility of remaining polymer chains [19].
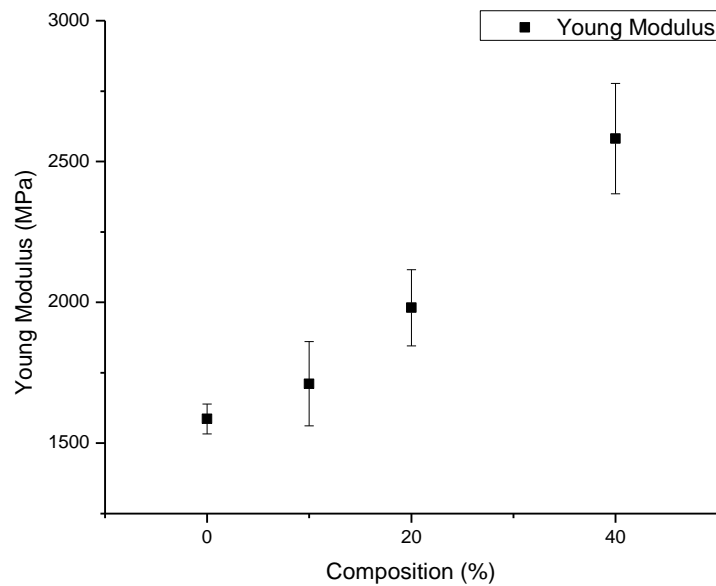
Figure 3. Graph of Young Modulus with standard deviation

The compression resistance of the test specimens can be seen below in Figure 4. This result shows that the addition of chamotte residue was not only beneficial from an environmental point of view, but also from a technological point of view, and could result in gains in mechanical resistance of up to 10%.
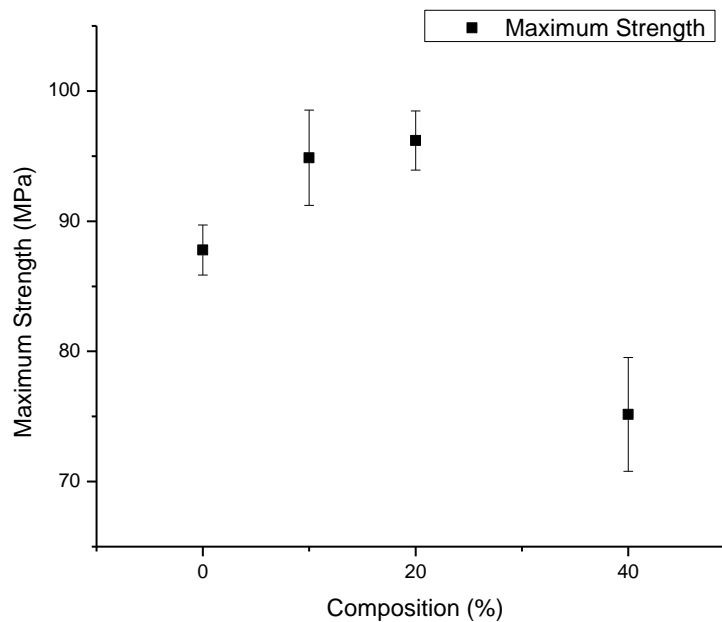
Figure 4. Graph of Maximum Strength with standard deviation

It can be seen in the graph above that the compressive strength of the specimens increased with the addition of a certain amount of particulate up to 20% vol. However, with the addition of 40% particulates, a significant reduction in resistance was observed. This phenomenon can be attributed to the heightened viscosity of the resin induced by the increased particle content that dificults the escape of bubbles and leading to the formation of regions where the particulate remains unwetted by the resin [20; 21].

Despite the formulation containing 40% particulates exhibiting a 15 to 20% lower resistance compared to the others, it remains potentially viable for applications with less demanding technical specifications. This viability is particularly noteworthy due to the potential cost savings achieved through the substitution of resin with waste.

4. CONCLUSIONS

Through this work, it is possible to verify the technological feasibility of using chamotte in epoxy resins, which can increase the mechanical resistance and modulus of elasticity of the composites by up to 10% and 63% respectively. The addition of particulates increased the modulus of elasticity progressively up to 40% (maximum amount of particulates evaluated), while the resistance of the composites was only increased up to 20%, this being the formulation with the greatest resistance to compression.

4.1. Declaration of Competing Interest

The authors declare no conflict of interest.

4.2. Acknowledgements

5. REFERENCES

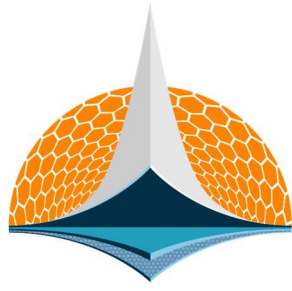[1] Y Jiang et al. Do renewable energy, environmental regulations and green innovation matter for China's zero carbon transition: Evidence from green total factor productivity. Journal of Environmental Management. Volume 352, 2024 (https://doi.org/10.1016/j.jenvman.2024.120030).

[2] P.K Yadav, R Sachan, D.K Dwivedi. Ecological Consequences: Understanding the effects of agricultural pollution on ecosystem, wildfire, and biodiversity. In: A comprehensive exploration of soil, water & air pollution in agriculture (A Kumar et al), 1st Edition, 2024. BFC Publications. (ISBM – 978-93-5992-493-9).

[3] W.E Rees. The Human Ecology of Overshoot: Why a Major "Population Correction" Is Inevitable. World. Volume 4, 2023 (https://doi.org/10.3390/world4030032).

[4] H Wu et al. Constructed Wetlands for Pollution Control. Nature Reviews Earth & Environment. Volume 4, 2023 (https://doi.org/10.1038/s43017-023-00395-z).

[5] M Lieder, A Rashid. Towards circular economy implementation: a comprehensive review in context of manufacturing industry. Journal of Cleaner Production. Volume 115, 2016 (https://doi.org/10.1016/j.jclepro.2015.12.042).

[6] M.C Simoens. Unpacking pathways to a circular economy: A study of packaging innovations in Germany. Sustainable Production and Consumption. Volume 1, 2024. (https://doi.org/10.1016/j.spc.2024.04.008).

[7] J Kim et al. Energy, material, and resource efficiency for industrial decarbonisation: A systematic review of sociotechnical systems, technological innovations, and policy options. Energy Research & Social Science. Volume 112, 2024 (https://doi.org/10.1016/j.erss.2024.103521).

[8] M Muhammadi et al. Recent progress in natural fiber reinforced composite as sound absorber material. Journal of Building Engineering. Volume 84, 2024 (https://doi.org/10.1016/j.jobe.2024.108514).

[9] S Gupta, K.N Jha, G Vyas. Construction and demolition waste causative factors in building projects: survey of the Indian construction industry experiences. Volume 24, 2022 (https://doi.org/10.1080/15623599.2022.2111962).

[10] C.Q Wang et al. Utilization of all components of waste concrete: Recycled aggregate strengthening, recycled fine powder activity, composite recycled concrete and life cycle assessment. Journal of Building Enginnering. Volume 82, 2024 (https://doi.org/10.1016/j.jobe.2023.108255).

[11] ANICER. Associação Nacional da Indústria Cerâmica, 2021. (https://www.anicer.com.br/anicer/setor/). Acessed 05 April 2024

[12] R Taurino, F Bondioli, M messori. Use of different kinds of waste in the construction of new polymer composites: review. Materials Today Sustainability. Volume 21, 2023 (https://doi.org/10.1016/j.mtsust.2022.100298).

[13] A.G Díaz et al. Investigation of waste clay brick (chamotte) addition and activator modulus in the properties of alkaline activation cements based on construction and demolition waste. Journal of Building Engineering. Volume 84, 2024 (https://doi.org/10.1016/j.jobe.2024.108568).

[14] C. M. F Vieira, S. N Monteiro. Incorporation of solid wastes in red ceramics: an updated review. Matéria. Volume 14, 2009 (https://doi.org/10.1590/S1517-70762009000300002).

[15] J.N.O Júnior et al. Evaluation of hot pressing processing by physical properties of ecofriendly composites reinforced by Eucalyptus sawdust and chamotte residues. Polymers. Volume 15, 2023. (https://doi.org/10.3390/polym15081931).

[16] D.C.R Velasco et al. Influence of the Use of Anti-bubble Additives on the Permeability and Porosity of Anticorrosive Coatings. In: Composite Materials : Sustainable and Eco-Friendly Materials and Application (Brian Wisner et al.), 1st Edition, 2024. Springer. (https://doi.org/10.1007/978-3-031-50180-7_10).

[17] ASTM D695-15, Standard Test for Compressive properties of Rigid Plastics. ASTM International, 2015. (www.astm.org).

[18] A. S Jose, A Athijayamani, S. P Jani. A review on the mechanical properties of bio waste particulate reinforced polymer composites. Materials Today proceedings. Volume 37, 2020. (https://doi.org/10.1016/j.matpr.2020.07.360).

[19] S li et al. The development of a W-shaped channel extrusion for fabricating magnesium alloy shells by combining high amplitude shear strain with a shorter process. Journal of Materials Research and Technology. Volume 25, 2023. (https://doi.org/10.1016/j.jmrt.2023.06.085).

[20] D. C. R Velasco et al. Evaluation of Composites Reinforce by Processed and Unprocessed Coconut Husk Powder. Polymers. Volume 15, 2023. (https://doi.org/10.3390/polym15051195).

[21] M. M Rueda et al. Rheology and applications of highly filled polymers: A review of current understanding. Progress in Polymer Science. Volume 66, 2017. (https://doi.org/10.1016/j.progpolymsci.2016.12.007).

22 Smart composites

Organized and edited by

Sandra Maria da Luz
&
Carla Tatiana Mota Anflor

INVESTIGATION OF SELF-HEALING ON GLASS-FIBER-EPOXY COMPOSITES WITH IMPACT DAMAGE

Joao Felipe B. Pontes, Evans P. da Costa Ferreira [a], Raimundo C. S. Freire Jr. [b], José Daniel D. Melo[c], Ana Paula C. Barbosa[d] *

(a) 0000-0002-4078-0537 (Federal University of Rio Grande do Norte – Brazil)
(b) 0000-0003-0920-7916 (Federal University of Rio Grande do Norte – Brazil)
(c) 0000-0002-3696-5133 (Federal University of Rio Grande do Norte – Brazil)
(d) 0000-0002-9510-4851 (Federal University of Rio Grande do Norte – Brazil)
* Corresponding author: ana.cysne@ufrn.br

Abstract: The damage of composite structures caused by impact during service time is a critical issue, as it reduces stiffness and strength of the composite material. Materials with self-healing ability offer great potential for new scientific and technological developments. This is a research area with great possibilities for advances in the field of materials science and engineering. In this sense, the present work aims at the manufacture and characterization of a composite material, additivated with a thermoplastic healing agent, where the ability to heal localized damage and delamination was evaluated. This healing agent is activated via heat supply, through an external source, which promotes increased mobility of the thermoplastic agent, poly (ethylene-co-acid-methacrylic) (EMAA). The specimens were divided into 4 study groups, and a total of 20 specimens meeting the following conditions were evaluated: 0% EMAA without damage (reference material), 0% EMAA with damage, 10% EMAA with damage, 10% EMAA with damage and healed. The damage was conducted on the specimens in a controlled manner, via impact machine by free fall, thus being characterized as low speed impact. Visual inspection was employed to evaluate affected areas, to compare the behavior of specimens under the influence of impact energy and EMAA effect, in relation to the filling of cracks and energy absorption. Results indicate the potential of self-healing in reducing the area of impact damage in the laminates.

1. INTRODUCTION

Many materials, with their various chemical compositions, microstructures e fabrication processes, are susceptible to damage induced during their service life. Damage can be caused by impact, creep, corrosion and aging; and reduce strength and service life, as well as reliability and safety of structural components.

The use of composite materials has been intensified in the last decades. Corrosion resistance and the attractive combination of properties (high stiffness / strength) with low density can be obtained with composites and are required for many applications [1, 2]. One example is observed in aeronautic industry, where there are airplanes built with approximately 50 wt.% of composite material [3].

Nevertheless, composite materials are susceptible to microcracks and delamination, which can evolve to severe damage and catastrophic failure during service. Therefore, studies involving damage and possibilities of reducing or delaying damage in composite materials are of great importance, as this problem reduces reliability and safety of these materials [4].

In this context, smart materials stand out as an attractive alternative from the technological point of view. One possibility is that of a self-healing material, where the ability to restore properties may promote an extension of its service life. Many studies were developed in the last years involving self-healing composite

materials. One of these alternatives involves the use of thermoplastic healing agents, like poly(ethylene-co-methacrylic acid), as in [5, 6, 7, 8].

The aim of this study is to evaluate the behaviour of glass-fiber epoxy composites with a thermoplastic healing agent when subjected to low-velocity impact damage and evaluate potential of the healing agent in reducing damage in the composite material.

2. METHODOLOGY

The prepreg material used in this work is Hexply® M9.6F/32%/UD1600+V50/G+F from Hexcel. This unidirectional prepreg has mass fraction of 32% epoxy, reinforced with glass fiber UD1600+V50 (E-glass) with 2.56 g/cm^3 density. The thickness of prepreg lamina is 1.0 mm.

The thermoplastic employed in this work was the copolymer poly(ethylene-co-methacrylic acid) (EMAA) from Sigma-Aldrich, with 15% of methacrylic acid and 85% of ethylene. Before adding it to the composite, the thermoplastic was cryogenically milled and particles were sieved to 250-125 µm range. 10 wt.% of thermoplastic, regarding the mass of epoxy matrix in the lamina. In this way, 3.2 wt.% of thermoplastic was added to the composite.

4 laminae were used for the preparation of each plate with configuration 0°/90°/90°/0°. Composite plates were prepared by uniaxial pressing at 120°C for 40 minutes, according to supplier instructions. A steel mould with 30 x 30 cm was used for this purpose. Plates with and without thermoplastic material were fabricated, so that unmodified and modified composites were prepared.

The laminates were cut with dimensions 10 x 15 cm and 5 samples were prepared for each investigated condition. In this way, 20 samples were prepared and 4 conditions were investigated: 0% EMAA no damage (V6 to V10), 0% EMAA damaged (VD1 to VD5), 10% EMAA damaged (E6 to E10), 10% EMAA damaged and healed (EH1 to EH5).

The healing cycle employed in this work was 150°C for 30 minutes.

The samples were tested according to ASTM D7136 for measurement of damage resistance to a drop-weight impact event. The composite plates were subjected to an out-of-plane, concentrated impact using a drop-weight device with a hemispherical impactor striker tip, which has 16 mm diameter and 58 HC hardness. The potential energy of the drop-weight, as defined by the mass and drop height of the impactor, was specified prior to the tests. The height was calculated according to Eq. 1:

$$H = \frac{E}{m_d \cdot g} \qquad \text{(Eq. 1)}$$

where:
H = drop-height of impactor, m,
md = mass of impactor for drop height calculation, kg, and
g = acceleration due to gravity, 9.81 m/s^2

In this way, 3 kg drop-weight was employed at various heights, so that 3 different energy levels (15 J, 31 J and 62 J) were employed for preliminary tests on unmodified laminates. After preliminary tests, unmodified and modified laminates were tested at 15 J. The damage resistance is quantified in terms of the resulting size and type of damage in the specimen.

Geometric dimensions for the detected damage were measured and recorded, using a calliper. Locations of points relative to the center of the specimen were recorded, along with the damage width, damage length, and maximum damage diameter. In this way, the damaged area was calculated using the damage length and damage width.

3. RESULTS AND DISCUSSION

Preliminary tests were carried out in order to determine the level of energy to be employed in this study. The free fall device employed in this work was developed according to ASTM D7136 and 3 different energy levels (15 J, 31 J and 62 J) on unmodified laminates were employed for the preliminary tests. The results are shown in Figure 1. 15 J was chosen as the energy level in this work, as higher energy levels produced damage that are too extensive to be repaired with self-healing techniques.
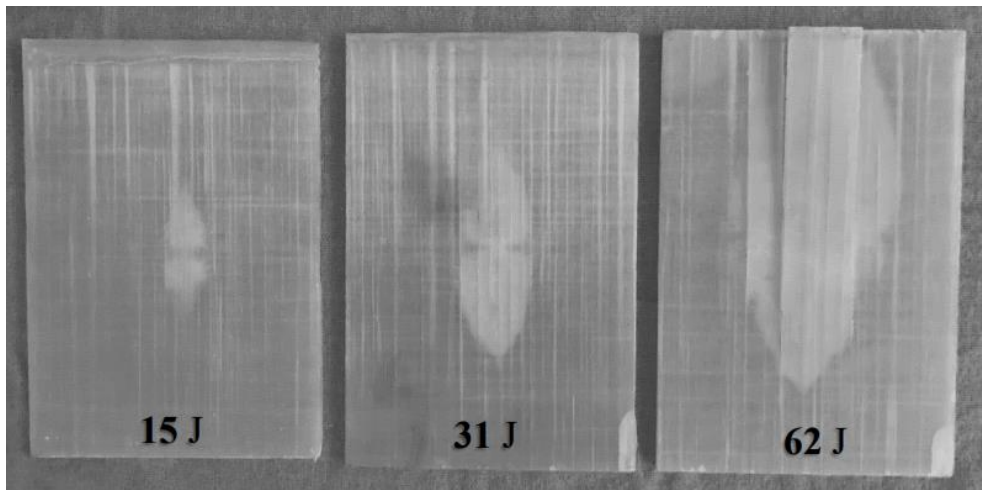
Figure 1: Samples with impact damage produced with 3 different energy levels (15 J, 31 J and 62 J).

The following figure (Figure 2) shows the results of impact tests on all samples investigated in this work:
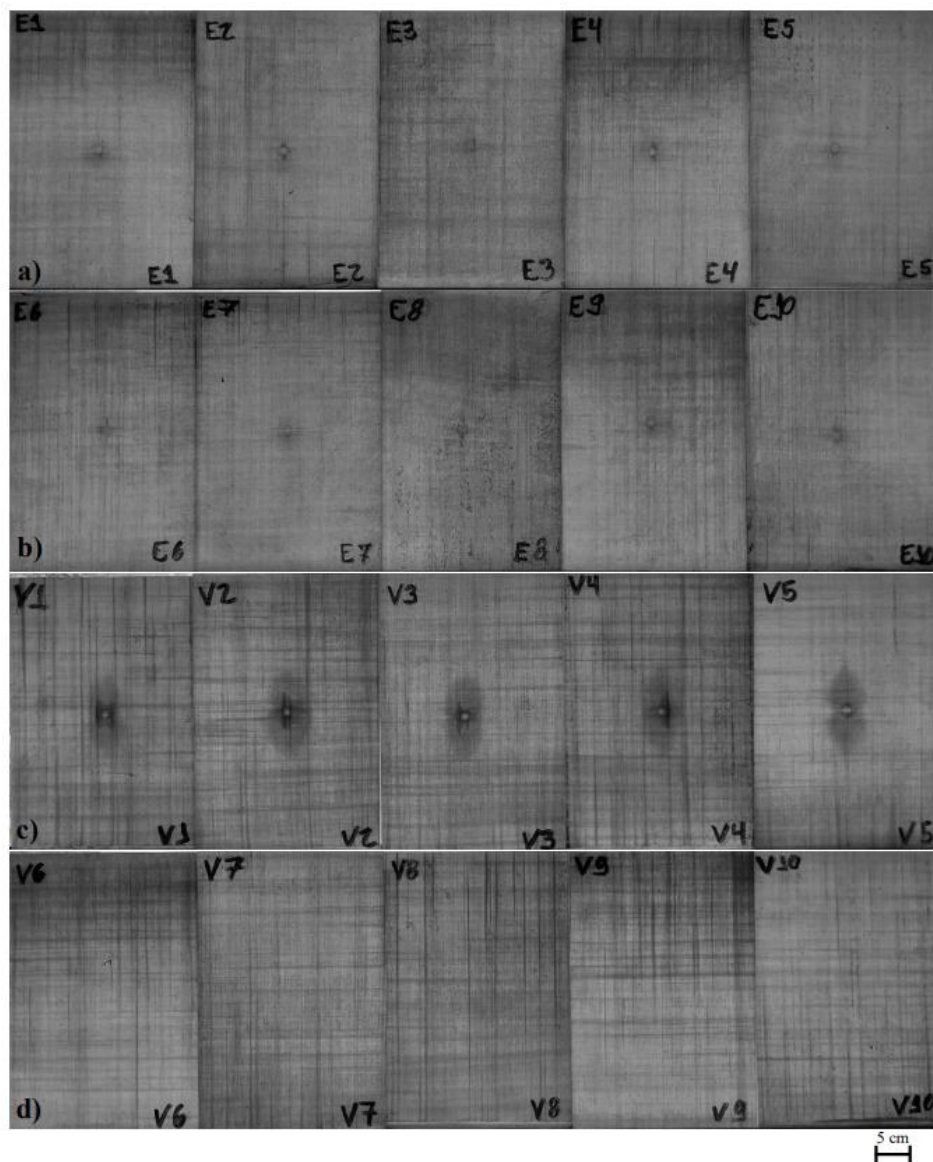

Figure 2: Samples investigated in this work: a) group EH; b) group E; c) group VD; group V.

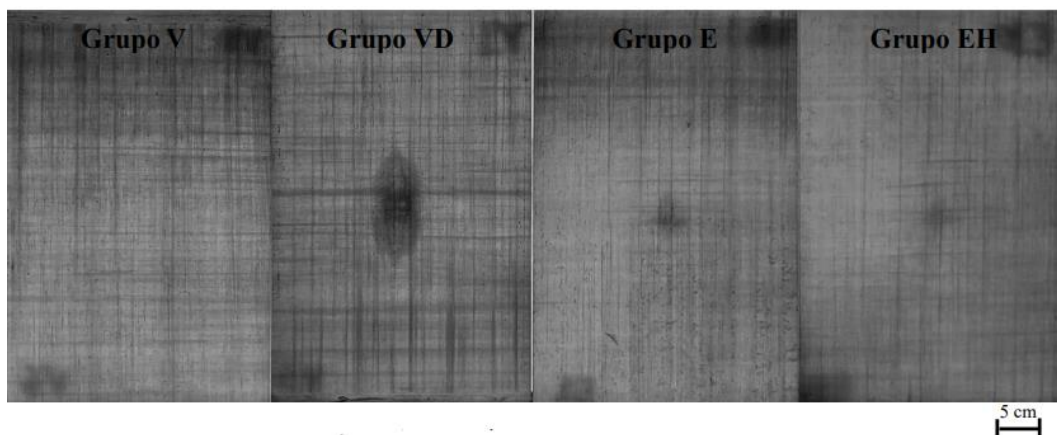The following figure (Figure 3) shows just one sample of each group, for better visualization of results:

Figure 3: Representative samples of each group investigated in this work.

Table 1 and Figure 4 show the results obtained as damaged area for the investigated groups.

Table 1: Damaged area (cm^2) of samples for groups EH, E and VD.

Group	Area sample 1	Area sample 2	Area sample 3	Area sample 4	Area sample 5	Average
EH	0.30	0.20	0.28	0.28	0.40	0.29
E	1.00	0.80	1.40	0.80	0.60	0.92
VD	7.65	7.20	8.10	9.31	6.75	7.80
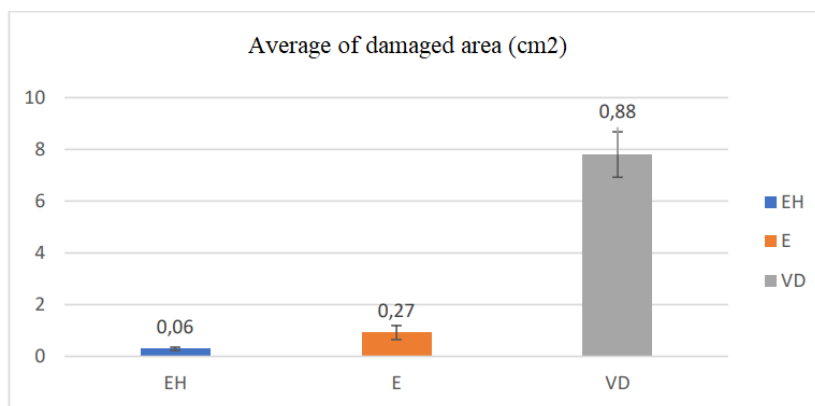
Figure 4: Average of damaged area (cm^2) for studied groups EH, E and VD.

Results suggest that the unmodified damaged composite (group VD) has a much larger damaged area if compared to the groups where the thermoplastic EMAA was added. This suggests that the thermoplastic acted as a toughening agent, as expected, dissipating energy during impact. Interleaving, which is a technique in which an additional layer, such as a nonwoven polymer veil, or thermoplastic film is added between the laminae of reinforcing fibres within a composite [9], can reduce delamination through the bridging of cracks that occur along the matrix-rich interlaminar regions and by creating a more tortuous path for any crack to follow, dissipating more energy in the process [10]. The good adhesion of EMAA to epoxy, which was already observed in the literature [6, 11], may have contributed to an efficient toughening of the laminate.

It is noteworthy that the area of samples with EMAA with healing cycle (EH group) is smaller than the area of samples with EMAA without healing cycle (E group). This suggests that the delaminated area was partially healed by the healing agent. In previous studies [12] with EMAA as healing agent in carbon-epoxy laminates, where damage was carried out by interlaminar shear strength (ILSS) tests, the thermoplastic showed

strong adhesion to the carbon-epoxy composite even preventing visible delamination to develop at the specimen mid-plane. Thermoplastic ligaments which bridge fiber and epoxy resins were observed in samples after healing confirmed the healing efficiency suggested in ILSS tests [12]. In this work, the same mechanism of formation of ligaments of thermoplastic after healing may have contributed to the reduction of damaged area of healed samples, as compared to the damaged area of samples without healing cycle.

4. CONCLUSIONS

The objective of this work was to evaluate the potential of the thermoplastic EMAA as a healing agent for laminates with impact damage. For the conditions investigated in this work, results suggest that the thermoplastic material has the ability to heal damaged areas, as the damaged area of samples with EMAA with healing cycle (EH group) is smaller than the area of samples with EMAA without healing cycle (E group). It seems that the thermoplastic was able to flow to damaged areas and partially fill in delaminations in the composite and thermoplastic ligaments may have contributed to the healing process. Moreover, as expected, results suggest that the thermoplastic acted as a toughening agent, as the damaged area of modified laminates was much smaller than the area in unmodified laminates (without thermoplastic), as the toughening agent can reduce delamination and create a more tortuous path for cracks, dissipating more energy. Overall, results suggest the potential of the healing agent in restoring delaminated areas in composites with impact damage. Future investigations are focused on the modification of mechanical properties of the laminates with addition of the thermoplastic.

4.1. Declaration of Competing Interest

The authors declare no conflict of interest.

4.2. Fundings

4.3. Acknowledgements

.

5. REFERENCES

[1] Krishan K. Chawla, Composite Materials: Science and Engineering, 2019, Springer. (https://doi.org/10.1007/978-3-030-28983-6).

[2] Clyne, T. W., & Hull, D. (2019). An Introduction to Composite Materials (3rd ed.), 2019, Cambridge: Cambridge University Press. (https://doi.org/10.1017/9781139050586)

[3] A. F. Padilha, Materiais de Engenharia: Microestrutura e Propriedades, pp. 271–287, 2000, Hemus.

[4] C. Fortes, "Mecânica da Fratura," Mater. Construção Civ. e Princípios Ciência e Eng. Mater., no. 51, pp. 241–280, 2010.

[5] S. Meure, R. J. Varley, D. Y. Wu, S. Mayo, K. Nairn, and S. Furman, "Confirmation of the healing mechanism in a mendable EMAA-epoxy resin," European Polymer Journal, vol. 48, no. 3. pp. 524–531, 2012.

[6] S. Meure, D. Y. Wu, and S. Furman, "Polyethylene-co-methacrylic acid healing agents for mendable epoxy resins," Acta Mater., vol. 57, no. 14, pp. 4312–4320, Aug. 2009.

[7] K. Pingkarawat, C. H. Wang, R. J. Varley, and A. P. Mouritz, "Healing of fatigue delamination cracks in carbon–epoxy composite using mendable polymer stitching," J. Intell. Mater. Syst. Struct., vol. 25, no. 1, pp. 75–86, Jan. 2014.

[8] Pingkarawat, C. Dell'Olio, R. J. Varley, and A. P. Mouritz, "Poly(ethylene-comethacrylic acid) (EMAA) as an efficient healing agent for high performance epoxy networks using diglycidyl ether of bisphenol A (DGEBA)," Polymer, vol. 92. pp. 153– 163, 2016

[9] Vallack, N., Sampson, W.W. Materials systems for interleave toughening in polymer composites. J Mater Sci 57, 6129–6156 (2022). https://doi.org/10.1007/s10853-022-06988-1

[10] Tsotsis TK (2009) Interlayer toughening of composite materials. Polym Compos 30:70– 86. https://doi.org/10.1002/pc.20535

[11] Dell'Olio C, Yuan Q, Varley RJ. Epoxy/Poly(ethylene-co-methacrylic acid) blends as thermally activated healing agents in an epoxy/amine network. Macromol Mater Eng 2015;300:70–9.

[12] Allana Azevedo do Nascimento, Fernando Fernandez, Fábio S. da Silva, Evans P.C. Ferreira, José Daniel D. Melo, Ana P. Cysne Barbosa, Addition of poly (ethylene-co-methacrylic acid) (EMAA) as self-healing agent to carbon-epoxy composites, Composites Part A: Applied Science and Manufacturing, Volume 137, 2020, https://doi.org/10.1016/j.compositesa.2020.106016.

23 Structural health monitoring in composite structures thermal problems on composite structures

Organized and edited by

Sandra Maria da Luz
&
Carla Tatiana Mota Anflor

STRUCTURAL MONITORING OF COMPOSITE CFRP PLATE UNDER TEMPERATURE VARIATION USING THE MACHINE LEARNING-PYMLDA CODE

Amanda Aryda Silva Rodrigues de Sousa [a]*, Marcela Rodrigues Machado[b], Rafael de O. Teloli[c], Jefferson da Silva Coelho[d]

(a) 0000-0002-0907-2989 (Department of Mechanical Engineering, University of Brasilia, Brasília, 70910-900, Brazil)
(b) 0000-0002-7488-7201 (Department of Mechanical Engineering, University of Brasilia, Brasília, 70910-900, Brazil)
(b) 0000-0002-7658-5514 (Supmicrotech-ENSMM, CNRS, FEMTO-ST, Departement Mecanique Appliquee, UBFC - Universite de Bourgogne Franche-Comte, Besancon, France)
(d) 0000-0002-6524-5282 (Department of Mechanical Engineering, University of Brasilia, Brasília, 70910-900, Brazil)
* Corresponding author: eng.amandaaryda@gmail.com

CODE: BCCM7-107

Abstract: Composite materials have been employed in many engineering structures, such as airplanes, wind turbines, and aerospace structures, among others. Those materials are well-recognized for their resistance combined with lightweight. Such structures are subjected to substantial mechanical loads and extreme environmental conditions during operation, leading to increased failure frequency and maintenance costs. To mitigate costs and enhance operational efficiency, employing a reliable Structural Health Monitoring (SHM) methodology capable of detecting structural defects is crucial. The successful integration of Machine Learning (ML) techniques with SHM in various applications has allowed for the development of precise and automated procedures. Among the available techniques, systems based on vibration analysis demonstrate significant potential for structural monitoring and fault diagnosis. This study aims to conduct the integrity monitoring of a composite structure under temperature variation using SHM-ML through the machine learning for damage assessment-PyMLDA code. The input signal measured from the CFRP plate is ultrasonic-guided elastic waves. The PyMLDA code can detect, categorize, recognize pattern, and quantify damage using as input the temporal or frequency responses of the structure providing accurate and on-demand structural monitoring. The practical application of this approach can make a substantial contribution to reducing operational costs and increasing the lifespan of composite structures, thereby fortifying the sustainability and economic viability of composite systems.

1. INTRODUCTION

Composite materials have been employed in many engineering structures, such as airplanes, wind turbines, aerospace structures, among others. These materials are renowned for their superior rigidity, corrosion resistance, fatigue endurance, and wear resistance, as well as their enhanced thermal properties and reduced weight. Additionally, they enable the fabrication of complex geometries [1, 2]. Despite their advantages, composite structures are often subjected to mechanical loads and extreme environmental conditions during operation, which can lead to increased failure rates and maintenance costs. Common issues include delamination, matrix cracking, fiber debonding, interlayer air entrapment, non-uniform epoxy resin distribution, and insufficient consolidation pressure [3, 4, 5, 6]. Among these, delamination is the most critical defect, severely compromising structural integrity and potentially resulting in catastrophic failures [7].

To mitigate costs and enhance operational efficiency, employing a reliable SHM methodology capable of detecting structural defects is crucial. The successful integration of ML techniques with SHM in various applications has allowed for the development of precise and automated procedures. Among the available techniques, systems based on vibration analysis demonstrate significant potential for structural monitoring and fault diagnosis.

Liu et al. [8] and Jakkamputi et al. [9] investigated the performance of several ML models in identifying damage, highlighting the effectiveness of gradient-boosted decision Trees (GBDT) and Decision Trees (DT). Additionally, Ferreira et al. [10] explored autonomous defect detection in thermoplastic composites using a Support Vector Machine (SVM) with autoregressive features, demonstrating a significant increase in accuracy. Furthermore, studies by Pashmforoush et al. [11], Hamdi et al. [12], and Diaz-Escobar et al. [13] applied techniques such as K-means and K-Nearest Neighbors (KNN) to evaluate delamination and classify damage in composites, showing robustness across different contexts and types of data delamination and classify damage in composites, showing robustness in different contexts and types of data. These results indicate not only the variety of ML approaches available for SHM but also their ability to offer accuracy and effectiveness in damage detection and classification in composite structures.

This study aims to conduct the integrity monitoring of a composite structure under temperature variation using SHM-ML through the machine learning for damage assessment-PyMLDA code, developed by Coelho et al. [14]. The input signal measured from the carbon fiber reinforced polymer (CFRP) plate is ultrasonic-guided elastic waves. The PyMLDA code, can detect, categorize, recognize pattern, and quantify damage using as input the temporal or frequency responses of the structure providing accurate and on-demand structural monitoring. The practical application of this approach can make a substantial contribution to reducing operational costs and increasing the lifespan of composite structures, thereby fortifying the sustainability and economic viability of composite systems.

2. METHODOLOGY DAMAGE DETECTION

The study conducted by Sousa et al. [15] and Coelho et al. [16] provides valuable insights into optimizing the hyperparameters of algorithms used in damage assessment, emphasizing the significance of PyMLDA as a comprehensive tool for structural monitoring. PyMLDA is instrumental in all stages of the process, from the acquisition of input data to pre-processing and feature selection, followed by the training and validation of the ML model, and the evaluation of results using appropriate metrics. In this work, the experimental data, collected from a CFRP plate, and consisting of ultrasound-guided elastic waves, is processed, and analysed by PyMLDA to predict structural patterns and assess the damage. Figure 1 visualizes the stages of this integrated process.
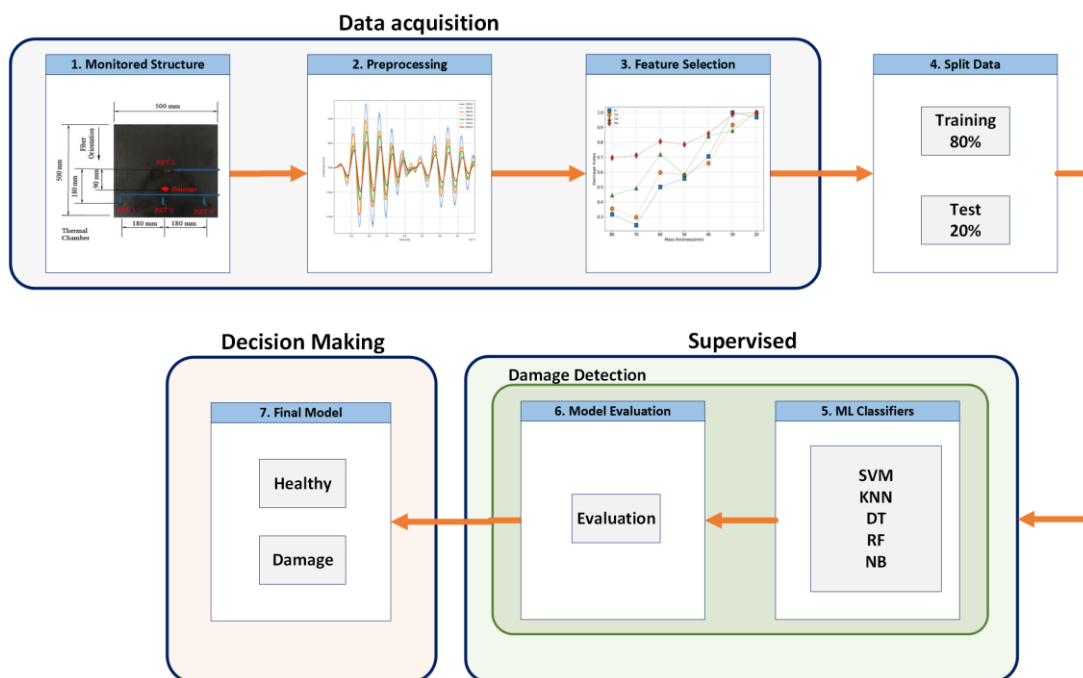

Figure 1. PyMLDA integrated process steps for this work.

The PyMLDA analysis covers the KNN, Random Forest (RF), Decision Tree (DT), Naive Bayes (NB), and SVM algorithms, providing a comprehensive understanding of the performance of each in the classification task. This thorough evaluation of different machine learning models helps identify which ones are most effective in generalizing to independent datasets, aiding in the selection of the most suitable algorithm for specific data analysis and the implementation of strategies for maintaining structural integrity.

The PyMLDA excels in structural damage detection due to its flexibility in receiving damage indices as input. This feature simplifies the decision-making process in structural monitoring while enhancing the identification, classification, and quantification of damage levels. Consequently, PyMLDA provides a comprehensive damage assessment, including graphical visualizations of the results obtained through classification models. The workflow starts with extracting patterns and characteristics from the data using specific damage indices, followed by applying classification techniques to categorize the state of the damage. This enables the differentiation between intact structures and various damage levels. In this study, PyMLDA will be employed to classify the data, using damage indices to normalize time series, as detailed below.

2.1. Damage Index

The Damage Index (DI) is a crucial component designed to compare reference signals with those obtained in the presence of discontinuity or structural damage, providing essential information about structural health [17]. Within this scope, the covariance damage index, represented by Equation (1), is particularly relevant. Using time series data, the DI allows for continuous and precise analysis of structural integrity, facilitating the detection, localization, and assessment of damage severity. This method enhances preventive maintenance and the safety of monitored structures.

$$DI := COV = \frac{1}{N-1} \sum_{i=1}^{N} (y_i - \bar{y})(x_i - \bar{x}). \tag{1}$$

Here, x_i denotes the values of reference signals, y_i signifies the values of signals amidst damage presence, $\bar{x}$ represents the mean of reference signals, and $\bar{y}$ embodies the mean of damaged signals.

This statistical measure, crucial in discerning inter-signal relationships, encapsulates deviations relative to their respective means, thus offering a comprehensive insight into their covariance. Such insights, essential in time series analysis, underpin vital applications, including but not limited to pattern detection. This process facilitates a thorough analysis of spectra comparison between undamaged and damaged structures, with covariance serving as a DI that accurately illustrates this relationship [18]. The normalization of the DIs is imperative to ensure precise comparison, where normalized values between zero and one denote the absence or presence of damage, respectively, according to equation (2):

$$COV_{normalized} = \frac{1}{maxCOV} COV. \tag{2}$$

3. RESULTS AND DISCUSSION

The experimental setup entails a CFRP polymer plate, as illustrated in Figure 2, featuring dimensions of 500 x 500 x 2 mm and comprising 10 layers of single-weave fibers aligned along the edges. To monitor the plate's behavior, four SMART layers of PbZrTi (PZT) with a 6.35 mm diameter are affixed using epoxy resin, with PZT 1 serving as an actuator and the others (PZT 2, PZT 3, and PZT 4) as sensors. An excitation signal comprising a 5-cycle sine wave with a 35V amplitude, and a 250 kHz frequency is employed, recorded within a 100 μs window utilizing suitable acquisition equipment. Data acquisition is conducted across varied controlled temperatures (0°C, 10°C, 30°C, and 60°C) employing a Thermotron-manufactured thermal chamber. The dataset undergoes statistical characterization via 100 repeated tests at each temperature, and the entirety of the dataset is publicly accessible on the GitHub Repository CONCEPT: CarbON-epoxy CompositE PlacaTe47 [19].
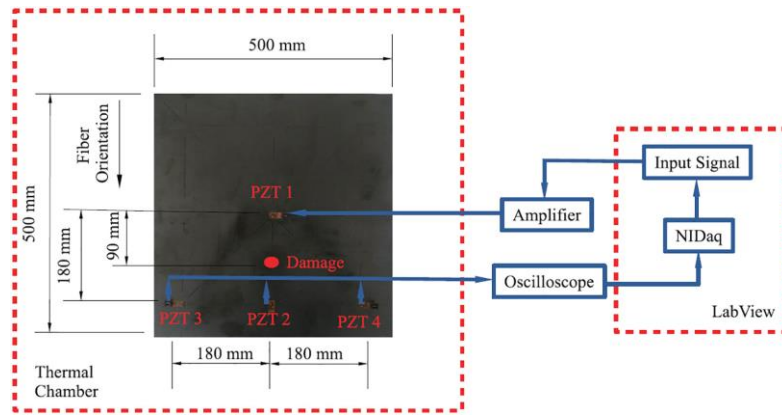
Figure 2. Experimental configuration.

Damage simulation entails progressively increasing the mass applied to the plate, varying the diameter from 20 to 80 mm in 10 mm increments. The measurements acquired for each temperature and mass diameter facilitate a detailed analysis of the damage effects on the recorded signals. As depicted in Figures 3a to 3d, the primary effect of damage manifests as a reduction in waveform amplitude, with this reduction contingent upon temperature, exhibiting greater prominence at lower temperatures compared to higher temperatures. The challenge with this issue lies in quantifying the damage extent, attributed to temperature's influence on signal attenuation related to the damage.

(a)

(b)

(c)

(d)
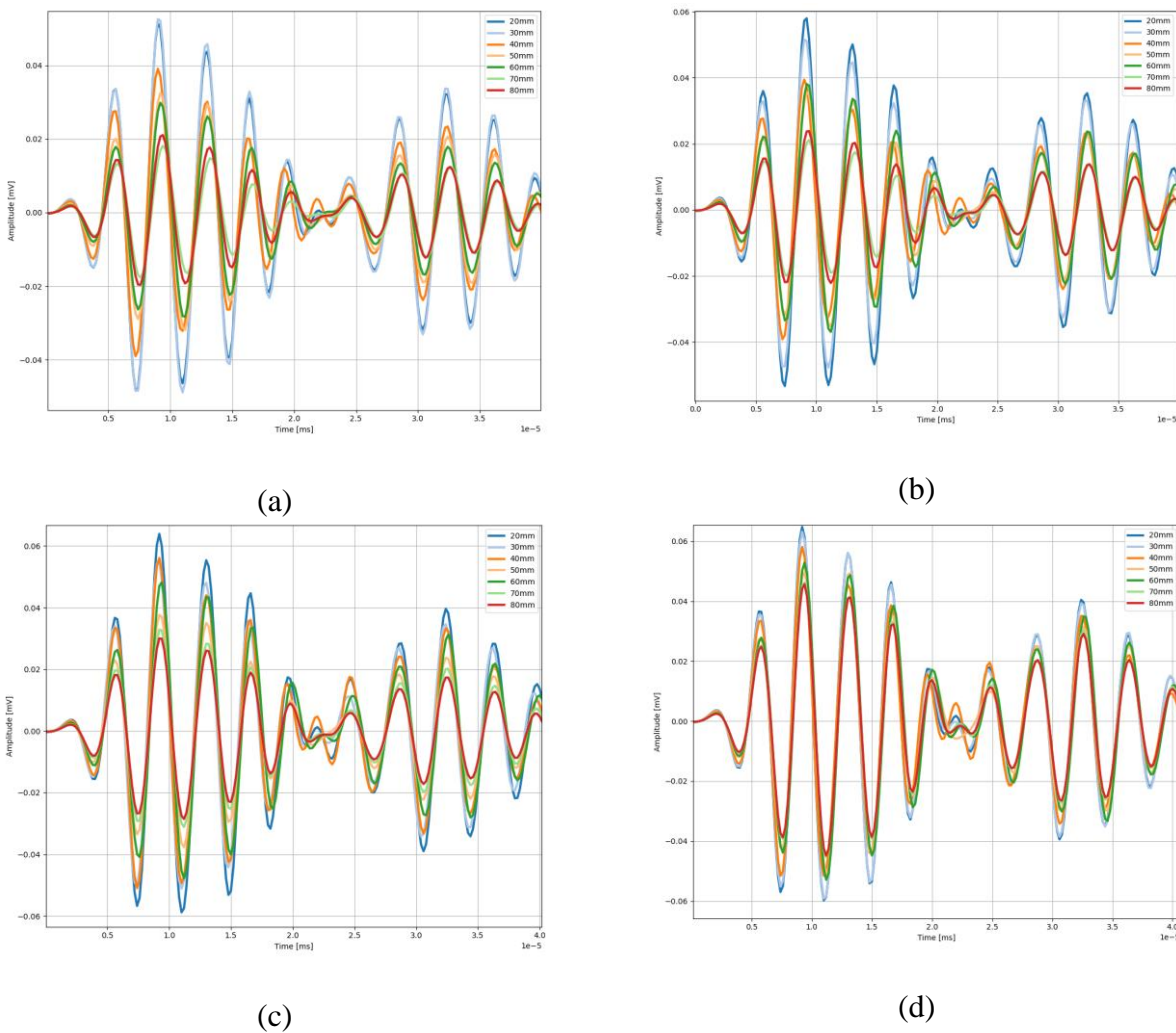
Figure 3. Results for progressive damaged conditions from 20 mm to 80 mm at (b) 0∘C; (c) 10∘C; (d) 30∘C; and (e) 60∘C.

Damage detection poses challenges due to the influence of temperature on signal attenuation related to the damage. In this context, the proposed work exclusively utilizes the temporal signals from PZT 2 due to its proximity to damaged areas, where the damage signal is stronger. The damaged temporal signals are then compared with reference signals under healthy conditions. The resulting data from these measurements are normalized using the COV damage index, previously mentioned, and employed as input in ML algorithms, enabling the identification and quantification of damage through pattern recognition. This integrated approach provides a deeper understanding of structural behavior, considering variables such as temperature, applied mass, and structural condition effects. Thus, the DI ranges from zero to one, where a value close to one indicates no damage, while lower values approaching zero indicate the presence of damage. This study utilizes the DI as structural information in the training and testing datasets of the ML multiclass algorithms.
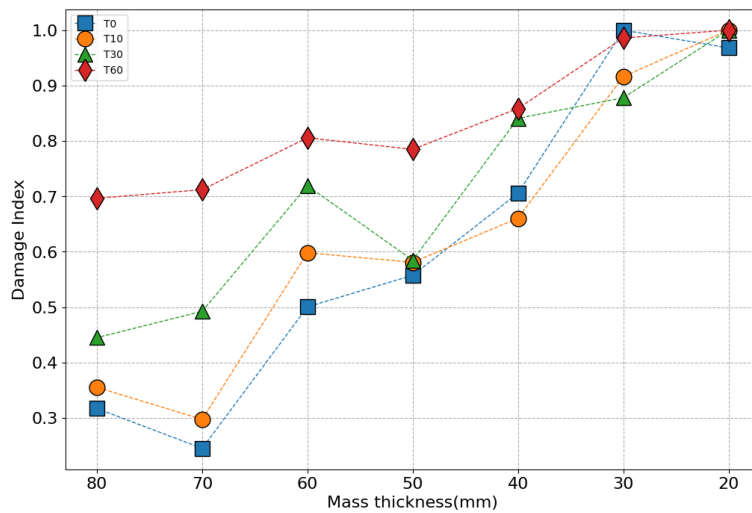

Figure 4. Relationships among mass thickness, damage index, and various temperatures.

Figure 4 provides a detailed insight into the relationships among mass thickness, damage index, and various temperatures. It is observed that variations in mass thickness impact the damage index, with this influence being more pronounced under different temperature conditions. For instance, while the line corresponding to 0°C exhibits a more pronounced initial increase in the damage index for intermediate mass thicknesses, the line associated with 60°C shows a distinct decreasing trend after peaking at specific thicknesses. These observations suggest a complex interaction between temperature, mass thickness, and the damage index.

Based on defined criteria, which classify a damage factor from 1 to 0.98 as healthy and a damage factor from 0.97 to 0.3 as damaged, we can analyze the data points on the graph. For example, for a mass thickness of 30 mm and a temperature of 10°C, it is observed that the data point is clearly below 0.98, indicating that it falls within the range classified as damaged. This analysis allows us to identify and categorize the state of each data point relative to the established criteria, providing valuable insights into structural integrity under different temperature and mass thickness conditions.

3.1. PyMLDA Evaluation

By incorporating these damage indices as inputs into the PyMLDA code, it is possible to analyze the data and identify 23 distinct classes in damage categorization. The quantification of damage, through temporal damage indices, while varying mass and temperature, encompassed conditions of both integrity and damage in the plate, with damages ranging from 30 to 80 mass units and temperatures of 10°C, 30°C, and 60°C.

Moreover, to ensure the robustness and reliability of the model, cross-validation was performed during algorithm training. This procedure divides the dataset into smaller subsets, called "folds", where the model is trained on one part of the data and validated on another. This process is repeated multiple times with different combinations of training and validation, ensuring that the model is comprehensively evaluated across the entire dataset.

The resulting classification from the algorithm, applied to the test data, is then assessed using rigorous metrics, including Accuracy, Precision, Recall, and F1-score, as presented in Table 1. These metrics provide insights into the model's performance, where Accuracy evaluates the proportion of correct predictions for all positive class classifications, Recall assesses the proportion of correct predictions made relative to all positive

examples in the dataset, and F1-score is a harmonic mean between Precision and Recall, providing an overall measure of the model's performance. Cross-validation ensures that these metrics are reliable and representative of the true performance of the model on unseen data.

Table 1. Classification resulting from the PyMLDA.

Performance Metrics	SVM (%)	KNN (%)	NB (%)	RF (%)	DT (%)
Cross-validation	96,43	99,93	99,71	99,93	99,78
Accuracy	99,64	99,64	98,93	99,64	99,64
Precision	96,00	96,00	96,00	96,00	96,00
Recall	96,00	96,00	95,00	96,00	96,00
F1-Score	96,00	96,00	95,00	96,00	96,00

Table 1 presents the classification results from PyMLDA, offering a comparative analysis of five machine learning models, revealing a set of crucial metrics for assessing their performance. Cross-validation, highlights KNN and RF as the most effective in generalizing to independent datasets, both achieving a score of 99.93%. However, the SVM exhibits a notably lower score at 96.43%, suggesting lesser generalization capability.

Regarding accuracy, precision, recall, and F1-score, all models, except NB, demonstrate consistent results, with an accuracy of 99.64%, precision of 96.00%, recall of 96.00%, and an F1-score of 96.00%. NB, on the other hand, shows slightly lower accuracy at 98.93% and slightly inferior recall at 95.00%, resulting in an F1-score of 95.00%. However, despite minor differences in performance metrics, it's important to note that both KNN and RF stand out for their ability to avoid overfitting and maintain consistent performance on unseen data. Therefore, relying solely on these metrics may not provide sufficient information to diagnose potential errors associated with the algorithms' estimations. Hence, the confusion matrix is also utilized to track the dataset classification. In this case, the confusion matrix of one of the algorithms considered most robust in the study, KNN, is shown.

In the confusion matrix, the vertical and horizontal axes represent, respectively, the actual classes and the classes predicted by the model, while the cells of the matrix show the number of instances classified into each class. The main diagonal displays instances correctly classified, while values off this diagonal indicate misclassifications. Figure 5, the confusion matrix of the KNN algorithm is presented, where a good performance of the model is observed, evidenced by the predominance of values on the main diagonal. However, a single instance was misclassified, indicating overall high but not perfect accuracy. Classes like healthy stand out for having a substantially larger number of instances, while other classes have a more modest number, with the damage class with mass 80 and temperature 10 registering the lowest number of correctly classified instances. These analyses highlight the model's accuracy despite some discrepancies, providing valuable insights into the distribution and classification of instances across different classes.
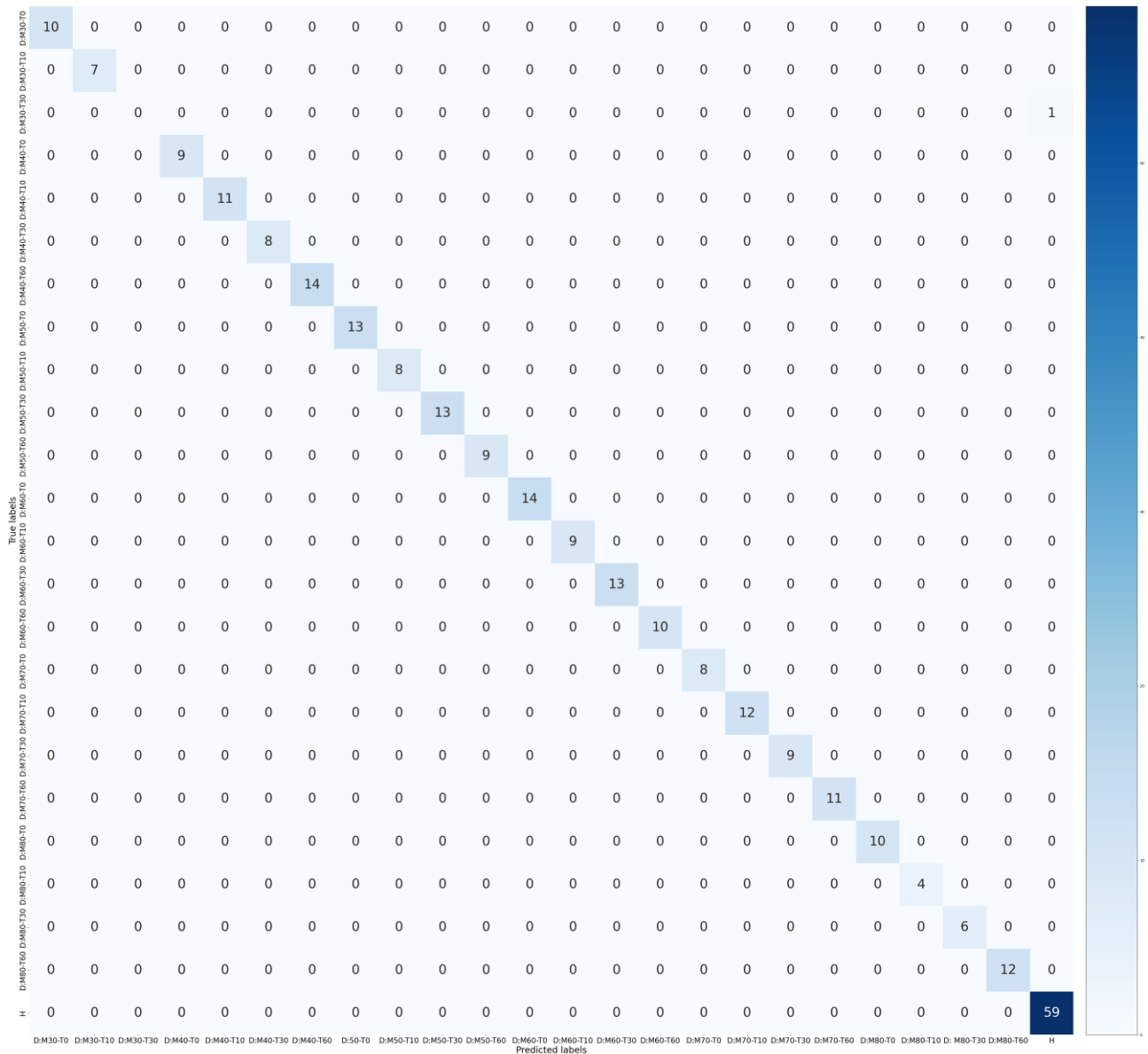
Figure 5. Confusion matrix of the KNN algorithm.

4. CONCLUSIONS

The analysis of the relationships between mass thickness, damage index, and various temperatures in CFRP plate, using the PyMLDA code, reveals the complexity of the factors that influence structural integrity. Note that variation in mass thickness has a significant impact on the damage index, with this influence being even more pronounced under different temperature conditions. Observations such as the pronounced initial increase in the damage index for intermediate mass thicknesses at lower temperatures, and the distinct downward trend at higher temperatures after a peak at specific thicknesses, suggest a complex interaction between temperature, mass thickness, and damage index. Based on the criteria established to classify the state of damage, analysis of the data points reveals valuable insights into structural integrity under different environmental conditions. The quantification of damage, using time-series damage indices over a broad spectrum of conditions, provides a solid basis for the identification and categorization of damage, covering 23 distinct classes. The comparative analysis of five machine learning models highlights KNN and RF as the most effective in generalizing to independent data sets. Thus, this comprehensive analysis provides a solid basis for implementing effective strategies to prevent and maintain structural healthy.
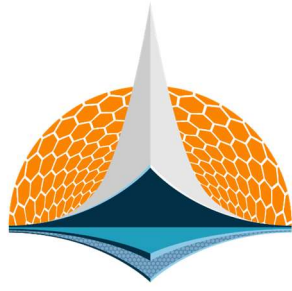
4.1. Acknowledgements

5. REFERENCES

[1] Ghrib M, Berthe L, Mechbal N, et al. (2017) Generation of controlled delaminations in composites using symmetrical laser shock configuration. Composite Structures 171: (https://doi.org/286–297. 10.1016/j.compstruct.2017.03.039).

[2] Hassani, S., Mousavi, M., Gandomi, A.H.: Structural health monitoring in composite structures: a comprehensive review. Sensors 22(1), 153 (2021). (https://doi.org/10.3390/s22010153).

[3] Mei, H.; Giurgiutiu, V. Guided wave excitation and propagation in damped composite plates. *Struct. Health Monit.* **2019**, *18*, 690–714. (https://doi.org/10.1177/147592171876595).

[4] Talreja, R. Manufacturing defects in composites and their effects on performance. In *Polymer Composites in the Aerospace Industry*; Irving, P., Ed.; Woodhead Publishing: Cambridge, UK, 2020; pp. 83–97. (https://doi.org/10.1016/B978-0-08-102679-3.00004-6)

[5] Shi, Y.; Swait, T.; Soutis, C. Modelling damage evolution in composite laminates subjected to low velocity impact. *Composite Struct.* **2012**, *94*, 2902–2913. (https://doi.org/10.1016/j.compstruct.2012.03.039).

[6] Khan, A.; Kim, H.S.; Youn, B.D. Modeling and assessment of partially debonded piezoelectric sensor in smart composite laminates. *Int. J. Mech. Sci.* **2017**, *131–132*, 26–36. (https://doi.org/10.1016/j.ijmecsci.2017.06.031).

[7] Khan A, Kim HS. A brief overview of delamination localization in laminated composites. Multiscale Sci Eng. 2022;4(3):102–110. (https://doi.org/10.1007/s42493-022-00085-w).

[8] Liu P, Xu D, Li J, et al. Damage mode identification of composite wind turbine blade under accelerated fatigue loads using acoustic emission and machine learning. Struct Heal Monit. 2020;19(4):1092–1103. (https://doi.org/10.1177/1475921719878259).

[9] Jakkamputi L, Devaraj S, Marikkannan S, et al. Experimental and computational vibration analysis for diagnosing the defects in high performance composite structures using machine learning approach. Appl Sci. 2022;12(23):12100. (https://doi.org/10.3390/app122312100).

[10] Viotti ID, Gomes GF. Delamination identification in sandwich composite structures using machine learning techniques. Comput Struct. 2023;280:106990 (https://doi.org/10.1016/j.compstruc.2023.106990)

[11] Pashmforoush F, Khamedi R, Fotouhi M, et al. Damage classification of sandwich composites using acoustic emission technique and k-means genetic algorithm. J Nondestruct Eval. 2014;33(4):481–492. (https://doi.org/10.1007/s10921-014-0243-y)

[12] Hamdi K, Moreau G, Aboura Z. Digital image correlation, acoustic emission and in-situ microscopy in order to understand composite compression damage behavior. Compos Struct. 2021;258:113424. (https://doi.org/10.1016/j.compstruct.2020.113424)

[13] Diaz-Escobar J, Díaz-Montiel P, Venkataraman S, et al. Classification and characterization of damage in composite laminates using electrical resistance tomography and supervised machine learning. Struct Control Heal Monit. 2023;2023:1–19. (https://doi.org/10.1155/2023/1675867).

[14] Coelho, Jefferson S. ; Machado, Marcela R. Sousa, A. A. S. R., PyMLDA: A Python open-source code for Machine Learning Damage Assessment, Software Impacts, Volume 19, 100628. (https://doi.org/10.1016/j.simpa.2024.10062).

[15] Sousa, A. A. S. R.; Coelho, J. S. ; Machado, M.R. ; Dutkiewicz, M. . Multiclass Supervised Machine Learning Algorithms Applied to Damage and Assessment Using Beam Dynamic Response. Journal of Vibration Engineering & Technologies, p. 1-20, 2023. (https://doi.org/10.1007/s42417-023-01072-7).

[16]   Coelho, Jefferson S. ; Machado, Marcela R. ; Dutkiewicz, Maciej ; O. Teloli, Rafael . Data-driven machine learning for pattern recognition and detection of loosening torque in bolted joints. Journal of the Brazilian Society of Mechanical Sciences and Engineering, v. 46, p. 75, 2024. (https://doi.org/10.1007/s40430-023-04628-6).

[17]   Barreto, Lucas S. et al. Damage indices evaluation for one-dimensional guided wave-based structural health monitoring.Latin American Journal of Solids and Structures, Rio de Janeiro, v. 18, n. 2, e354, 2021. (https://doi.org/10.1590/1679-78256292).

[18]   Giurgiutiu, V. (2014), Structural health monitoring with piezoelectric wafer active sensors, Elsevier Inc, Academic Press, 2nd edition.(https://doi.org/10.13111/2066-8201.2010.2.3.4)

[19]   Silva S and Paixão J. Unesp-concept: Carbon-epoxy composite plate, 2020. (https://doi.org/10.13140/RG.2.2.35767.34722).

24 Sustainability of composite material

Organized and edited by

Sandra Maria da Luz
&
Carla Tatiana Mota Anflor

ENVIRONMENTAL ANALYSIS OF CONDUCTIVE REGENERATED CELLULOSE NANOCOMPOSITE FILMS

Lays F. de M. S. Kataoka [(a)*], Maria del P. H. Falla [(b)], Sandra M. da Luz [(c)]

(a) 0000-0003-1766-7509 (University of Brasília – Brazil)
(b) 0000-0003-1623-9510 (University of Brasília – Brazil)
(c) 0000-0002-2223-0021 (University of Brasília – Brazil)
* Corresponding author: lays.furtado94@gmail.com

Abstract: The demand for synthetic polymers has contributed to a growing environmental impact. In this context, conductive regenerated cellulose films are a promising alternative for applications in electronic devices. Despite cellulose being of renewable origin, it is essential to emphasize the need to assess the environmental impacts of its extraction and derived materials production, which involves the intensive use of various chemical reagents and energy. Therefore, this study aims to evaluate a conductive nanocomposite film of regenerated cellulose containing silver nanoparticles (RCF-AgNP) environmentally. Bleached cellulose extracted from jute fiber was used for film production. Cellulose dissolution occurred in an aqueous solution of NaOH, and the films were regenerated in water. The silver nanoparticles incorporated into the nanocomposites were also synthesized from sodium borohydride and silver nitrate. To environmentally evaluate the production process of the nanocomposite film, a Life Cycle Assessment (LCA) from cradle to gate was developed to produce 1 kg of film, considering impact categories such as global warming, acidification and eutrophication potential, water usage, and energy demand. The jute production scenario was based on cultivation in Brazil, using secondary data from the literature. For cellulose and nanocomposite film production, primary data were experimentally collected. The results demonstrate environmental benefits associated with jute production through cultivation. Jute contributes to preserving the ozone layer by absorbing CO_2 and cleaning the air by emitting O_2. The highest global warming potential impact is in the cellulose extraction and bleaching stages, as well as water and energy usage. The results indicated the environmental advantages of RCF-AgNP production for future electronic device applications.

1. INTRODUCTION

Due to environmental concerns, the increasing production of plastic and plastic pollution are considered significant global issues. Addressing this problem could be the substitution of fossil-based plastics with natural materials such as cellulose, which is abundant, renewable, naturally occurring, and can be obtained from natural fibers [1]. Among cellulose sources, jute (*Corchorus capsularis*) stands out as an abundant and inexpensive natural fiber, noted for being one of the richest sources of cellulose [2].

The application of various cellulose products has recently gained increasing attention due to their desirable properties, such as biodegradability and sustainability [1]. Cellulose biopolymers can be conductors in electronic devices, potentially mitigating environmental impacts at the end of their life cycle [3,4]. Besides, they provide attractive properties such as nontoxicity, compostability, biocompatibility, and film-forming capacity [5,6].

Regenerated cellulose films can produce conductive films in sensors, transistors, solar cells, supercapacitors, electromagnetic shielding, and other electronic elements [6]. Developing nanocomposites represents a valid method to enhance biodegradable polymers' physical properties, such as conductivity [7]. Silver nanoparticles can be inserted during the cellulose regeneration, producing excellent conductive

nanocomposites. Previous work has shown promising results in extracting cellulose from jute to produce conductive films [8].

These conductive regenerated cellulose films can be recognized as a more sustainable choice than petrochemical polymers due to the use of renewable raw materials in their manufacturing and biodegradability. However, it is essential to understand that agricultural practices employed for cultivating these raw materials, energy demand, and using chemicals for processing and film production may have environmental impacts similar to synthetic polymers [9,10]. Therefore, it is crucial to acknowledge that using renewable resources requires careful balance [3,4].

In this environmental sphere, it is not enough to merely develop a new product of renewable origin and claim it is environmentally sustainable. This hypothesis must be subjected to study through scientifically recognized methods. It is important to identify chemicals and evaluate energy input throughout the entire life cycle of a biologically based product to propose safer alternatives and remediation solutions [10]. In this context, environmental assessment through Life Cycle Assessment (LCA) methodology can be employed to evaluate the conductive regenerated cellulose films throughout their life cycle [11].

To demonstrate environmental impact, a Life Cycle Assessment (LCA) study was performed from cradle to gate to produce regenerated cellulose nanocomposite films from jute fiber containing silver nanoparticles (AgNPs), using 1 kg of nanocomposite as the functional unit. The literature regarding the LCA of this type of material lacks data. Therefore, implementing LCA in this context can contribute to data production and enrich the foundations of LCA and existing literature on the subject.

2. METHODOLOGY

2.1. Life Cycle Assessment (LCA)

The study used ISO 14040 and 14044, international regulatory standards encompassing Life Cycle Assessment (LCA) principles, structure, guidelines, and requirements. Process modeling was performed using the Gabi Professional software from Sphera and its database.

2.1.1. Description of the production process

The RCF- AgNPs nanocomposite film was produced from cellulose obtained from jute fibers. The jute fibers are cultivated in Brazil and obtained from Sisalsul LTDA. The processes for obtaining bleached cellulose from jute were described by [8]. Two alkaline treatments with KOH and NaOH are performed, followed by acetylation with acetic acid and nitric acid, and fiber bleaching with sodium chlorite and acetic acid. In the alkaline treatment with KOH, cellulose recovery is possible through chemical methods; however, this process will not be considered within this scope. Electricity and water were employed in all stages.

The methodology of [6] described the processes for synthesizing AgNPs and producing regenerated cellulose films. AgNPs were produced from silver nitrate and sodium borohydride solutions, then stabilized with carboxymethyl cellulose. The reagents were quantified for environmental analysis. However, the environmental burdens of producing these reagents were not included at this stage, thus considering only electricity and water.

From bleached cellulose and silver nanoparticles, it is possible to produce the nanocomposite film RCF - AgNPs, which has properties for application as a conductive material. The processes for obtaining the RCF - AgNPs film were described by [8]. The bleached cellulose undergoes a milling process, then is dissolved in a solution of AgNPs and pre-frozen sodium hydroxide, followed by centrifugation, where the liquid part is poured into a Petri dish for subsequent coagulation in water and drying in ambient conditions.

2.1.2. Goal and scope of the LCA

This study aims to assess the environmental impacts of obtaining regenerated cellulose film with silver nanoparticles (RCF—AgNP) from jute. It study justifies itself by demonstrating a greater understanding of the impacts of jute production and RCF—AgNP nanocomposite production by compiling an inventory of inputs and outputs, including chemical use and energy demand.

The functional unit adopted was 1 kg of RCF - AgNP. The system's function under study obtained RCF - AgNP for application as a conductive material in electronic devices/sensors.

2.1.3. System boundaries

The system boundaries were defined from cradle to gate, considering raw material extraction and processing up to RCF - AgNP nanocomposite (Figure 1). The reference flow was delimited so that all primary and secondary data relate to measuring components and operations necessary to meet the system's function and functional unit.

As seen in Figure 1, the main production processes of cellulose RCF - AgNP can be divided into: 1) jute fiber production; 2) obtaining jute cellulose through alkaline treatments with KOH, NaOH, acetylation with acetic and nitric acids, and bleaching with sodium chlorite; 3) AgNP synthesis; 4) nanocomposite production. It also illustrates the processes where primary and secondary data are quantified, non-LCA considered stages, and flows of inputs, wastes, and products.
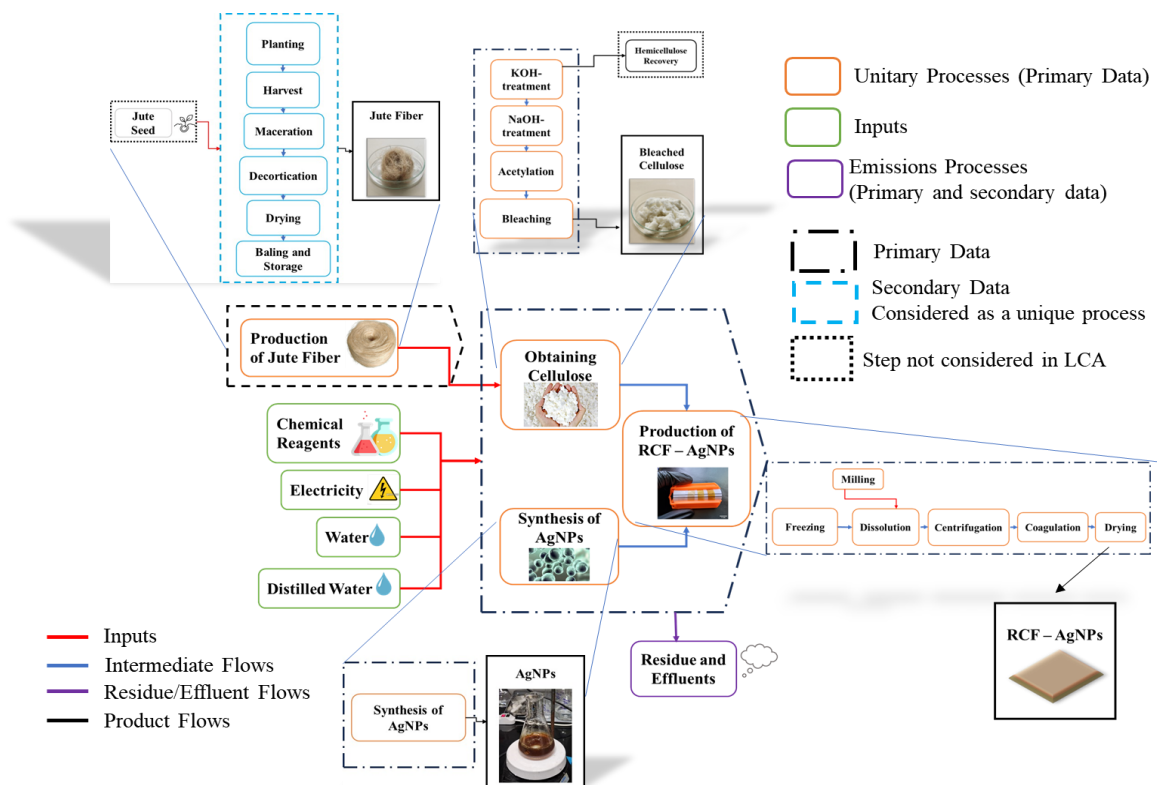

Figure 1. System boundaries of RCF - AgNP nanocomposite production.

2.2. Life Cycle Inventory (LCI)

The LCA study was performed based on primary data from film production in the laboratory and on secondary data, either from a review of existing literature in this domain or from LCA software databases when primary data were insufficient to complete the study. Secondary data was used for the following processes: jute production, production of inputs (reagents, water, distilled water, electricity), extraction processes (water, energy, and chemicals), and emissions, effluents, and waste. Table 1 shows the inputs of LCI.

Jute fibers are commonly cultivated and used in India, Bangladesh, China, Nepal, Thailand, and Brazil. The process of planting jute fibers in Brazil differs from those in these countries. In Brazil, jute cultivation up to plant refining is carried out through manual labor in communities of small farmers in the Amazon River region [3]. The jute cultivation methods adopted in the Amazon region were used in this study. In this region, jute plants are fast-growing shrubs, varying in height from 2 to 4 meters on average, with a vegetative cycle of approximately 6 months. The average fiber yield considered is 1500 kg/ha [12].

According to producers, jute fields do not require irrigation if the annual precipitation exceeds 2200 mm, a condition assumed in the present LCA. The soil does not need preparation, as the river helps enrich all nutrients for the plants during its overflow [3].

During retting, the fibrous bundles are separated from the bark tissues by anaerobic fermentation, where the fiber bundles are submerged in water, and logs are placed on top to prevent the stem bundles from floating. Retting in the river lasts about 8 to 10 days due to the region's hot climate, which promotes easy fermentation of the stems and subsequent fiber extraction. The decortication and washing of the fibers are done manually. The stems are dipped and agitated several times in water to remove the dark bark in the decortication process.

Then, the fibers are separated and taken for drying, and then spread out on racks near the retting site. Finally, the fibers are baled and stored [13].

Table 1. Inputs of LCA of RCF-AgNPs nanocomposite.

Inputs	Quantity	Unit	Inputs	Quantity	Unit
Production of Jute Fiber			**Production of RCF-AgNPs**		
Carbon dioxide	19.01	kg	*Milling*		
Jute seeds	0.01	kg	Electricity	30.42	MJ
Synthesis of AgNPs			Jute Cellulose	1.55	kg
Electricity	0.04	MJ	*Freezing*		
Distilled water	31.81	kg	AgNP solution	31.87	kg
Water	9.65	kg	Electricity	739.73	MJ
Carboxymethylcellulose	0.04	kg	Distilled water	38.55	kg
Silver Nitrate	0.01	kg	Sodium hydroxide	5.85	kg
Sodium borohydrate	0.02	kg	*Dissolution*		
Obtaining Cellulose			Electricity	2	1.76
KOH treatment			Dissolving solution to RCF	76	kg
Electricity	1.12	MJ	Jute cellulose milled	1.55	kg
Distilled water	25.75	kg	*Centrifugation*		
Jute Fiber	2.57	kg	Electricity	22.53	MJ
Potassium hydroxide	30.30	kg	RCF Solution	77.82	kg
Water	207.81	kg	*Coagulation*		
NaOH treatment			RCF solution centrifuged	57.4	kg
Electricity	949.74	MJ	Water	5633.80	kg
Distilled water	41.57	kg	*Drying*		
KOH treated jute fiber	2.08	kg	RCF gel films	53	kg
Sodium hydroxide	3.21	kg			
Water	343.81	kg			
Acetylation					
Acetic acid	41.03	kg			
Electricity	260.23	MJ			
NaOH treated fiber	1.96	kg			
Nitric acid (60%)	8.92	kg			
Water	323.33	kg			
Bleaching					
Acetic acid	0.37	kg			
Acetylated fiber	1.78	kg			
Electricity	74.08	MJ			
Distilled water	35.67	kg			
Sodium hypochlorite	0.45	kg			
Water	251.40	kg			

Cultivation, harvesting, drying, and fiber storage were assigned without impacts. The stage of retting and decortication of the fiber emits some impacts related to this process, and considering the database literature, Brazilian information is scarce. Therefore, in the fiber retting and decortication process, secondary data from National Jute Board through PricewaterhouseCoopers [14] in India were used, only for these processes, as the others differ due to water usage, pesticides, and others.

The impacts of the retting process from this source were obtained in stagnant water retting tanks. In Brazil, this process is carried out in the flowing water of the river, reducing anaerobic activity emissions and, therefore, suggesting lower impacts. However, considering this scenario, the data were used for this study.

Additionally, the capture of CO_2 from plants was considered in the cultivation process inputs, according to the photosynthesis process.

Cellulose was extracted from jute fibers for application as a nanocomposite film. In the laboratory stages of cellulose production and RCF—AgNP production, data related to water consumption, energy, reagents, and waste will be accounted for each subprocess using primary data from the experiments. In processes for the synthesis of AgNPs, the reagents were quantified. Still, the environmental burdens of producing these reagents were not included at this stage, thus considering only electricity and water.

The Gabi Professional software from Sphera database was utilized to assess the environmental impacts associated with the production and synthesis of ancillary chemicals (sodium hydroxide, potassium hydroxide, acetic acid, nitric acid). Additionally, it was used to evaluate the impacts associated with the production and supply of electricity, water, and wastewater treatment.

Electricity consumption was estimated for each unit process, considering the equipment power (kW), usage time (h), and the capacity used in mass (kg) or volume (L). That is, the total electrical consumption of each piece of equipment was considered based on its volume or mass without accounting for its maximum capacity.

2.3. Life Cycle Impact Assessment (LCIA)

The LCI stage results allowed for quantification of the environmental impacts, considering the Global Warming Potential (GWP 100 years) [kg CO_2 eq.], Eutrophication Potential (EP) [kg Phosphate eq.], and Global Warming Potential (GWP 100 years) [kg CO_2 eq.] categories and Energy Demand by the CML 2001 method [15].

3. RESULTS AND DISCUSSION

Figure 2 shows the Global Warming Potential in kg CO_2 eq. The cellulose production process consumes much water, energy, and inputs. Thus, this process exhibited the highest global warming potential, accounting for approximately 71% of kg CO_2 eq. emissions, followed by nanocomposite production at around 29%.

In cellulose production, treatments with NaOH and acetylation are the major contributors to impact in this category. In contrast, the solution's freezing is the contributing factor in the nanocomposite production process. Among the factors that have the greatest influence in this emission category is energy consumption, which is the major contributor, followed by the consumption of distilled water, which also demands high energy values. Katakojwala et al. [16] show values between 146.6 to 261.35 kg CO_2 eq. for microcrystalline cellulose extraction, which is compatible with this study's impact values.

The global warming potential of jute fiber production was negative due to CO_2 capture by plants during the cultivation stage, which contributed positively to the final balance of impacts in this category, as also seen in Guest et al. [17].
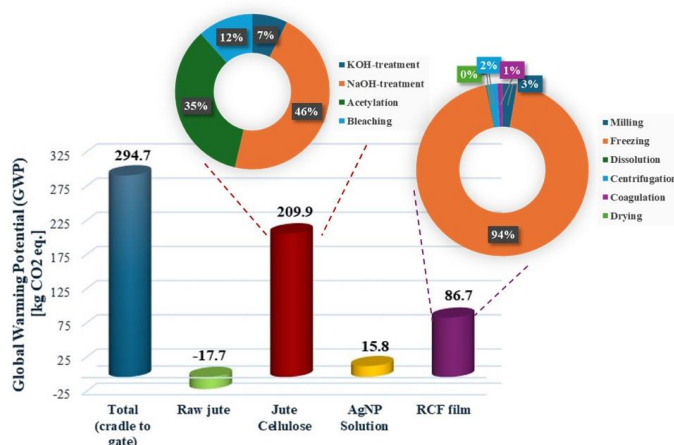
Figure 2. Global Warning Potential for 1 kg of RCF - AgNPs nanocomposite.

Figure 3 displays the values of Eutrophication Potential, given in kg Phosphate eq., with cellulose production contributing most to this impact category, at around 56.5%, due to the significant amount of organic and inorganic matter in the water from fiber degradation products and the high demand for electric energy. Additionally, there is a contribution of about 10% in the fiber-obtaining stage due to the maceration and retting processes that release organic matter into the river.

Katakojwala et al. [16] show values between 0.06 to 0.12 kg phosphate eq. for microcrystalline cellulose extraction, which is compatible with this study's impact values. According to Figueirêdo et al. [18], the production and distribution of electricity are primarily responsible for impacts on climate change and eutrophication in cellulose derivative production systems, as is the case in this study, evident in the processes of cellulose obtaining, nanocomposite film production, and silver nanoparticle synthesis.

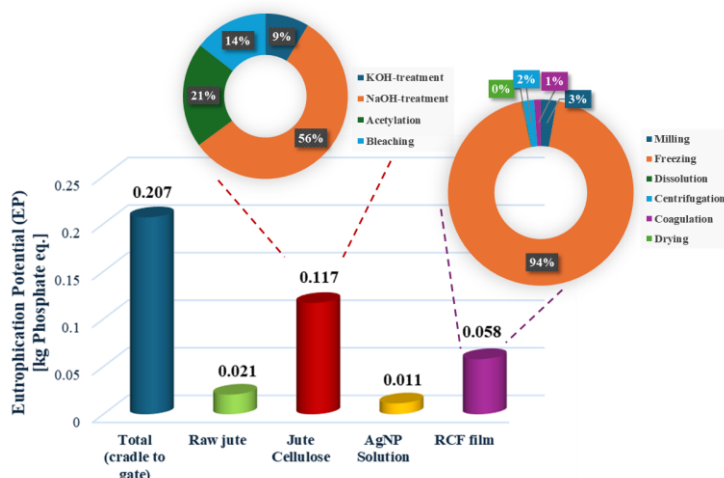**Figure 3.** Eutrophication Potential for 1 kg of RCF - AgNPs nanocomposite.

Figure 4 shows the Acidification Potential, given in kg SO_2 eq. It is observed that the cellulose obtaining stage has a higher contribution in this category due to the use of reagents and distilled water, in addition to the use of electricity, such as in the case of freezing in the nanocomposite production stage. The process with the highest burden generated in the NaOH treatment subprocess also shows the impact of removing part of the lignin from the fibers. Katakojwala et al. [16] show values between 0.53 to 0.94 kg SO_2 eq. for microcrystalline cellulose extraction, which is compatible with this study's impact values.
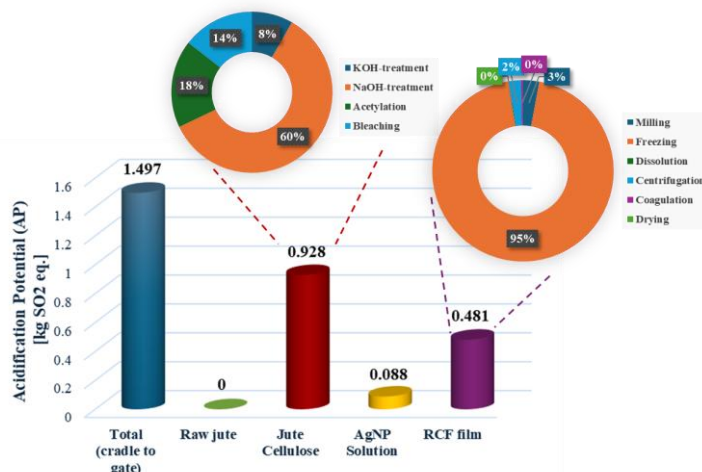

Figure 4. Acidification Potential for 1 kg of RCF - AgNPs nanocomposite.

Analyzing the energy consumption results in Figure 5, it was found that obtaining jute cellulose (around 5847MJ) was responsible for the highest energy consumption, with the alkaline treatment process with NaOH being the largest responsible for this consumption, with around 2690 MJ, followed by the acetylation treatment, with around 2046 MJ. These values are due to the use of the water bath in the process of obtaining cellulose, where in the case of treatment with NaOH, the reaction time was high.

The nanocomposite production process required the most energy, around 2387 MJ, and the freezing process of the solution used to dissolve the cellulose was primarily responsible for this consumption. The jute planting process does not require any equipment and is carried out manually, meaning there is no energy consumption. In the nanoparticle synthesis process, around 5% of the total energy used to produce 1 kg of RCF-AgNPs was used.

For Leão et al. [15], the energy consumption accounted for in their study to produce cellulose nanocrystals was between 756 and 1.14×10^5 MJ/kg in different production processes analyzed, which is compatible with this study.

Due to the high energy use of the equipment, the cellulose production route could be changed to reduce the energy use of this process. This route carried out in this study allows the recovery of hemicellulose; therefore, it would be important to evaluate routes that also will enable this reuse of material with added value.
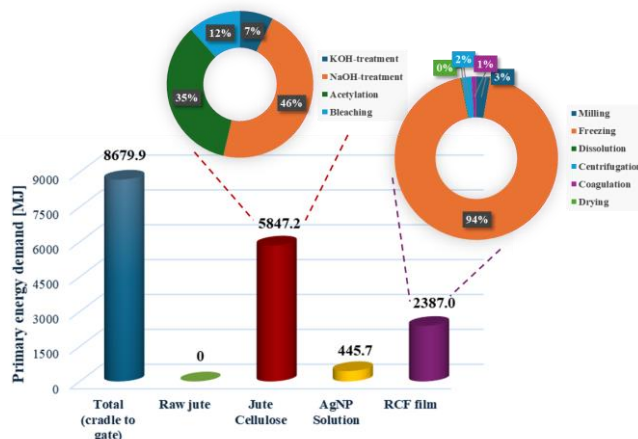

Figure 5. Electrical energy consumption in MJ/kg for 1 kg of RCF - AgNPs nanocomposite.

Electricity contributes most of the load to all impact categories analyzed in this study. Electricity consumption is a critical environmental point in the life cycle of RCF-AgNPs nanocomposite. Reducing impacts by using renewable sources of electrical energy on site in the RCF-AgNPs production process is an option. Optimizing the cellulose production process, such as recovering excess solvents and using by-products as inputs for other processes, is important to making it a low-carbon material.

A limitation of a comparative analysis of this study is the absence of LCAs from regenerated cellulose films, in addition to the potential variation of raw materials using different cellulose dissolution methods. Future studies could also expand the scope of LCA to include a more comprehensive analysis of the life cycle of conductive regenerated cellulose nanocomposite films. This would involve considering additional phases, such as the use phase and end-of-life scenarios, to understand environmental performance better.

4. CONCLUSIONS

Cellulose-derived products are commonly considered more sustainable; however, the high energy inputs that their production still requires, along with the use of chemicals or heat in some pre-treatments, require a critical view. The LCA provided valuable information on the environmental performance of the production of RCF-AgNPs nanocomposite, showing where the processes and subprocesses make the greatest contribution to the studied impact categories and energy use.

Future optimization of the production process to reduce electricity consumption was seen as important. This was the largest contributor to the impact categories studied and can guide the main interested parties in improving the environmental sustainability of the production of conductive regenerated cellulose nanocomposite films for application in electronic devices.

4.1. Declaration of Competing Interest

The authors declare no conflict of interest.

4.2. Acknowledgments

5. REFERENCES

[1] Foroughi F, Ghomi ER, Dehaghi FM, Borayek R, Ramakrishna S. A review on the life cycle assessment of cellulose: From properties to the potential of making it a low carbon material. Materials 2021;14:1–23. https://doi.org/10.3390/ma14040714.

[2] Erdoğan UH, Seki Y, Aydoğdu G, Kutlu B, Akşit A. Effect of Different Surface Treatments on the Properties of Jute. Journal of Natural Fibers 2016;13:158–71. https://doi.org/10.1080/15440478.2014.1002149.

[3] Alves C, Ferrão PMC, Silva AJ, Reis LG, Freitas M, Rodrigues LB, et al. Ecodesign of automotive components making use of natural jute fiber composites. J Clean Prod 2010;18:313–27. https://doi.org/10.1016/j.jclepro.2009.10.022.

[4] Leao AL, Rowell ; Roger, Tavares N. Applications of Natural Fibers in Automotive Industry in Brazil — Thermoforming Process. Science and Technology of Polymers and Advanced MateriJJ/s 1998:755–61. https://doi.org/doi:10.1007/978-1-4899-0112-5_66.

[5] Van Vlierberghe S, Dubruel P, Schacht E. Biopolymer-based hydrogels as scaffolds for tissue engineering applications: A review. Biomacromolecules 2011;12:1387–408. https://doi.org/10.1021/bm200083n.

[6] Liu X, Xiao W, Ma X, Huang L, Ni Y, Chen L, et al. Conductive Regenerated Cellulose Film and Its Electronic Devices – A Review. Carbohydr Polym 2020;250:1–16. https://doi.org/10.1016/j.carbpol.2020.116969.

[7] Petrucci R, Fortunati E, Puglia D, Luzi F, Kenny JM, Torre L. Life Cycle Analysis of Extruded Films Based on Poly(lactic acid)/Cellulose Nanocrystal/Limonene: A Comparative Study with ATBC Plasticized PLA/OMMT Systems. J Polym Environ 2018;26:1891–902. https://doi.org/10.1007/s10924-017-1085-3.

[8] Kataoka LF de MS, Leão RM, Gontijo AB, Falla M del PH, Luz SM. Regenerated cellulose films from jute fibers applied in conductive nanocomposites. Mater Today Commun 2022;33. https://doi.org/10.1016/j.mtcomm.2022.104645.

[9] Yates MR, Barlow CY. Life cycle assessments of biodegradable, commercial biopolymers - A critical review. Resour Conserv Recycl 2013;78:54–66. https://doi.org/10.1016/j.resconrec.2013.06.010.

[10] Ponnusamy PG, Mani S. Life cycle assessment of manufacturing cellulose nanofibril-reinforced chitosan composite films for packaging applications. International Journal of Life Cycle Assessment 2022;27:380–94. https://doi.org/10.1007/s11367-022-02035-y.

[11] Santos GZB dos, Caldas LR, Melo Filho J de A, Monteiro NBR, Rafael SIM, Marques da Silva N. Circular alternatives in the construction industry: An environmental performance assessment of sisal fiber-reinforced composites. Journal of Building Engineering 2022;54. https://doi.org/10.1016/j.jobe.2022.104603.

[12] Dias MC, Jackson Bacelar J, Xavier N, Ferdinando Barreto J. Recomendação Técnica para Juta Produção de sementes de juta n.d.

[13] EMBRAPA, Silva JF da. Recomendações Básica: Unidade de Execução de Pesquisa de Ambito Estadual de Belém - JUTA. 1989.

[14] PricewaterhouseCoopers. JUTE ECOLABEL: ANNEXURES TO LIFE CYCLE ASSESSMENT STUDY. 2006.

[15] Leão RM, Miléo PC, Maia JMLL, Luz SM. Environmental and technical feasibility of cellulose nanocrystal manufacturing from sugarcane bagasse. Carbohydr Polym 2017;175:518–29. https://doi.org/10.1016/j.carbpol.2017.07.087.

[16] Katakojwala R, Mohan SV. Microcrystalline cellulose production from sugarcane bagasse: Sustainable process development and life cycle assessment. J Clean Prod 2020;249. https://doi.org/10.1016/j.jclepro.2019.119342.

[17] Guest G, Bright RM, Cherubini F, Strømman AH. Consistent quantification of climate impacts due to biogenic carbon storage across a range of bio-product systems. Environ Impact Assess Rev 2013;43:21–30. https://doi.org/10.1016/j.eiar.2013.05.002.

[18] De Figueirêdo MCB, De Freitas Rosa M, Lie Ugaya CM, De Souza Filho MDSM, Da Silva Braid ACC, De Melo LFL. Life cycle assessment of cellulose nanowhiskers. J Clean Prod 2012;35:130–9. https://doi.org/10.1016/j.jclepro.2012.05.033.

INNOVATIVE SUSTAINABLE SANDWICH PANELS COMPOSED OF BOTTLE CAPS, STEEL AND BIOBASED POLYMER

Gabriel Bernardo de Magalhães Santos[a], Pedro Henrique Franco Ferreira[b], Eli Henrichs[c], Rovin Thomas[d], Túlio Hallak Panzera[e]

(a) 0000-0002-8971-3319 Gabriel Bernardo de Magalhães Santos, gabriel.biernardo@gmail.com, Centre for Innovation and Technology in Composite Materials – CIT^{e}C, Department of Mechanical and Production Engineering, Federal University of São João del Rei – UFSJ, 36307- 352, Brazil
(b) 0009-0002-6554-0246 Pedro Henrique Franco Ferreira, PedroHFranco03@outlook.com, Federal University of São João del Rei – UFSJ, 36307- 352, Brazil
(c) Eli Henrichs, eli.henrichs@gmail.com, Iowa State University, United States of America.
(d) Rovin Thomas, Nanyang Technological University, 50 Nanyang Ave, Singapore 639798 rovin.thomas@outlook.com
(e) 0000-0001-7091-456X (Federal University of São João del-Rei – Brazil), panzera@ufsj.edu.br

Abstract: This study describes the characterisation of sandwich panels consisting of galvanised steel skins and a core composed of reused bottle caps, bonded together using a bioadhesive derived from castor oil polyurethane. Two different castor oil polymers are subjected to three-point bending tests and statistically compared with a synthetic epoxy-based adhesive system to evaluate their maximum load capacities. The sandwich panels demonstrate a load capacity of up to 1500 N when using the synthetic epoxy-based adhesive. One configuration employing the alternative castor oil biobased adhesive achieves a comparable maximum load of approximately 1250 N (83% of the synthetic adhesive's capacity), displaying significant potential for continued deformation beyond the maximum load, thereby absorbing substantial energy. These results suggest that a sustainable biobased adhesive has the potential to replace a synthetic one while maintaining suitable mechanical performance.

1. INTRODUCTION

Sandwich panels are structural components formed by combining two rigid, thin sheets, known as skins or facesheets, with a lighter and relatively thicker core [1]. This class of structure is known for its high bending stiffness and strength, coupled with lightweight characteristics [2]. A wide range of materials can be used as the skin of the panel, with ceramic, composite laminates, and metal being the most common choices [3]. Galvanised steel, in particular, is extensively utilized in the automotive industry, prized for its reliable mechanical properties and corrosion resistance [4]. As for the core, polymeric foams and wood are common components, although geometrically efficient approaches such as honeycomb structures are widely used due to their lower density and impressive mechanical properties [5]. The adhesion between the skins and core typically occurs through the injection of resin or polymeric adhesive at the skin-core interface [6]. Sandwich panels find applications in various fields, including sports, aeronautics, automotive, and aerospace industries [7].

Polypropylene (PP) bottle caps are not typically recycled alongside polyethylene terephthalate (PET) plastic bottles, leading to a significant gap in the recycling rate of these materials [8]. In Brazil, 54.4% of recycled polymers consist of PET, while 20.3% are composed of PP [9]. Repurposing PP bottle caps as a

tubular honeycomb core in sandwich panels demonstrates remarkable resistance without substantially increasing the weight [10]. Similar to bottle caps, tubular honeycombs can serve as a core for sandwich panels in various applications, including fuel storage and transport [8]. Oruganti and Ghosh [11] illustrated that circular cells can enhance panel stiffness when compared to hexagonal cells in honeycombs. Additionally, according to Hu et al. [12], adopting hexagonal packing of tubular cells increases the energy absorption capacity by 23% compared to cubic packing.

Yi-Chun Chen and Wei Tai concluded that the abundance of -OH groups in the chemical composition of castor oil makes it an excellent alternative for producing Polyurethane (PU) resins [1]. In the pursuit of using green materials, a biobased castor oil resin brings us closer to an environmentally friendly product. Consequently, the present study focuses on assessing the feasibility of employing a castor oil polymer system as the adhesive for the skin-core interface in composite sandwich panels, constructed with galvanised steel skins and a core of reused bottle caps. Two different compositions of the castor oil resin undergo testing under three-point loading and are statistically compared with a synthetic epoxy-based adhesive system to evaluate their maximum load capacity.

2. METHODOLOGY

2.1. Materials

The skins of the sandwich panels consist of galvanised steel sheets, while the core is composed of reused bottle caps and is bonded to the skins using either synthetic or biobased polymers. The core utilises Coca Cola® bottle caps arranged in a hexagonal pattern, with the orientation of the caps alternating. As demonstrated in prior studies, the use of alternated bottle caps results in a 20% increase in strength compared to single-aligned caps [13]. The caps undergo cleaning with isopropyl alcohol to eliminate impurities, and each panel, with in-plane dimensions of 245 x 85 mm^2, incorporates 23 bottle caps. Three different polymeric resins are chosen for skin-to-core adhesion. The first is a synthetic adhesive (epoxy), while the others are two biobased castor oil polymers. The adhesive systems are as follows: (i) Epoxy (EPX) – Huntsman, consisting of a combination of epoxy resin (Type M) and hardener agent (HY 951) in a mass ratio of 5:1; (ii) Castor Oil 1 (CAS1), comprising two components named AGT 1315 A and AGT 1315 B in a mass ratio of 1:1.5; and (iii) Castor Oil 2 (CAS2), created by mixing the components ADA and ADB in a mass ratio of 1:1. The two castor oil polymers are supplied by Imperveg® (a Brazilian company) as eco-friendly alternatives for adhesive agents.

2.2. Sandwich panels manufacturing and testing

The sandwich panels are fabricated using a manual process. In Figure 1a, the manual mixing of the two-component polymer is exhibited. Initially, the first skin of each sample, after undergoing a sanding process to enhance adhesiveness (Figure 1b), is placed inside a mould. Subsequently, the adhesive is deposited, and the bottle caps are arranged in a hexagonal pattern with alternating orientations (Figure 1c). A wooden plate and 3.5 kPa weights are then placed over each sample, which is allowed to rest for 24 hours before the opposite skins are applied following the same process. Subsequently, the panels are left to cure for 14 days in a controlled environment at a temperature of 20±1°C and a relative humidity of 57±2%. Eight panels are produced for each type of polymeric resin (EPX, CAS1, and CAS2), totalling 24 samples. The final in-plane dimensions of the panels are 245 x 85 mm2, with a total thickness of approximately 14 mm. Three-point bending tests are conducted following ASTM C393 [16], using a Shimadzu test machine equipped with a 100 kN load cell, a support span of 170 mm, and a cross-head speed of 2.5 mm/min, as shown in Figure 1d.

Figure 1. a) Castor oil resin, b) sanded skin, c) panel assembly (first skin), and d) three-point bending test.

3. RESULTS AND DISCUSSION

Figure 2 provides the typical force-displacement curves obtained across the three-point bending tests for all three proposed panels with different adhesive systems. It is possible to notice a tendency of hierarchical order for the maximum load as EPX > CAS2 > CAS1. Table 1 presents the descriptive statistics for the evaluated maximum load, alongside the One-Way ANOVA analysis results performed in Minitab® statistical software. The low values of standard deviation (StDev) and coefficient of variation (CoefVar) indicate that the data are statistically reliable and closely clustered around the mean values. The P-value greater than 0.05 from the Anderson-Darling test suggests that all data follow a normal distribution. The P-value lower than 0.05 from Bartlett's test indicates a non-homogeneity of variances across different conditions for the target property. Therefore, the Welch P-value is used for assessing possible mean differences, and the reported value lower than 0.05 indicates that there is at least one mean that is different from the others. The Games-Howell test is used for multiple comparisons, and the different letters attributed to each condition (A, B, C) indicate that the three sets of data are statistically different from each other. It can be noted that the panels with CAS2 castor oil-based adhesive have a maximum load close to that of the ones made with the epoxy adhesive (approximately 83%, i.e., 1243 N compared to 1484 N). Additionally, CAS2 panels show significant potential to continue deforming after reaching the maximum load, absorbing significant rates of energy. CAS1 demonstrates an inferior load capacity of 504 N, which is equivalent to 34% and 41% of the load capacity of EPX and CAS2 panels, respectively.
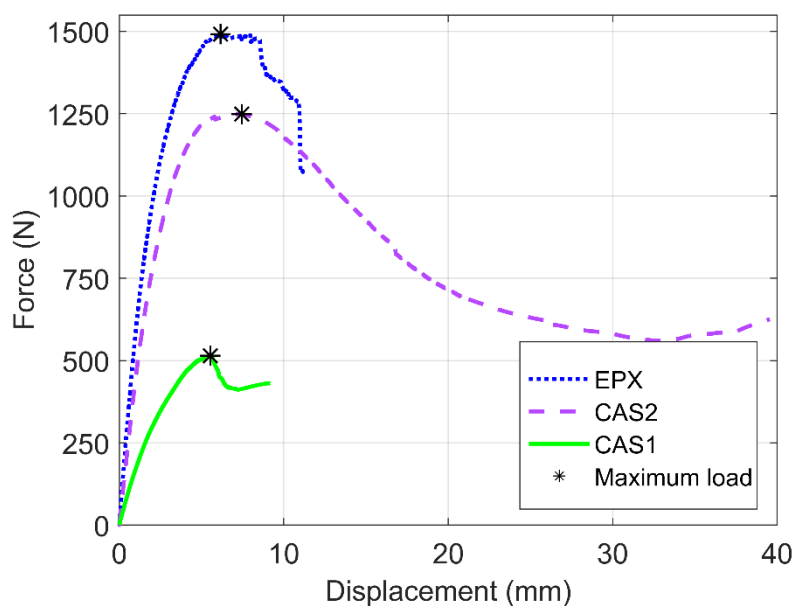

Figure 2. Typical force-displacement curves.

Table 1. Statistical assessment of maximum load.

Condition		Maximum load (N)		
		EPX	CAS2	CAS1
Mean		1484	1243	504
StDev		± 144	± 111	± 35
CoefVar		10%	9%	7%
P-value	Anderson-Darling	0.411	0.702	0.394
	Bartlett		0.006	
	Welch		0.000	
Games-Howell		A	B	C

4. CONCLUSIONS

Sandwich panels, comprising galvanised steel skins and a core of reused bottle caps, exhibit a flexural load capacity of up to 1500 N when utilising a synthetic epoxy-based adhesive system. One of the studied configurations, employing an alternative castor oil biobased adhesive, achieves a comparable maximum load of approximately 1250 N (83%) and demonstrates significant potential for continued deformation after reaching the maximum load, effectively absorbing substantial amounts of energy. These findings highlight the potential for a biobased adhesive of sustainable origin to replace a synthetic one while maintaining suitable mechanical performance. Subsequent research will focus on examining the failure modes across the three proposed panels and a wider range of properties beyond the maximum load. These properties include flexural modulus, flexural strength, resilience, core shear modulus, core shear stress, and facing stress. Furthermore, forthcoming formulations will incorporate the RJS Method for the mechanical evaluation of sandwich structures [17, 18].

Declaration of Competing Interest

The authors declare no conflict of interest.

Acknowledgements

REFERENCES

[1] Yi-Chun Chen, Wei Tai. Castor Oil-Based Polyurethane Resin for Low-Density Composites with Bamboo Charcoal. Polymers, Volume 10, 2018. (https://doi.org/10.3390/polym10101100)

[2] J.M. Davies, Lightweight Sandwich Construction, 1st Edition, 2008, John Wiley & Sons. (ISBN 0-632-04027-0).

[3] P.R. Oliveira et al. Improved sustainable sandwich panels based on bottle caps core. Composites Part B: Engineering, Volume 199, 2020. (https://doi.org/10.1016/j.compositesb.2020.108165)

[4] Górka, J. Assessment of the Corrosion Resistance, Properties and the Structure of Tig Braze Welded Galvanised Steel Sheets. Archives of Metallurgy and Materials, Volume 65, 2020. (10.24425/amm.2019.131095)

[5] Gibson LJ, Ashby MF. Cellular solids. MRS Bulletin, Volume 28, 1997. (https://doi.org/10.1557/mrs2003.79)

[6] T. Bitzer, Honeycomb Technology: materials, design, manufacturing, applications and testing, Springer, Netherlands 1997

[7] L.B.L. Gato et al. Sandwich Structures Made of Discarded Bottle Caps Core and Hybrid Glass Fibre Composite Skins. Applied Composite Materials, Volume 28, 2021. (https://doi.org/10.1007/s10443-021-09922-x)

[8] P.R. Oliveira et al. Transverse fastening reinforcement of sandwich panels with upcycled bottle caps core. Journal of Composite Materials, Volume 55, 2020. (https://doi-org.ez32.periodicos.capes.gov.br/10.1177/0021998320960522)

[9] ABIBLAST. Perfil 2022. https://www.abiplast.org.br/publicacoes/perfil-2022abiplast/

[10] P.R. Oliveira et al. A novel recycling route for polyethylene bottle caps as circular honeycomb core. In: 4th Brazilian Conference on Composite Materials BCCM4, 2018. (https://doi.org/10.21452/bccm4.2018.14.02)

[11] Oruganti R and Ghosh A. FEM analysis of transverse creep in honeycomb structures. Acta Mater 2008; 56: 726–735

[12] Allen HG. Analysis and design of structural sandwich panels. Oxford: Pergamon Press, 1969.

[13] P.R. Oliveira et al. Sustainable sandwich structures made from bottle caps core and aluminium skins: A statistical approach. Thin-Walled Structures, Volume 130, 2018. (https://doi.org/10.1016/j.tws.2018.06.003)

[16] ASTM C393, "Test Method for Core Shear Properties of Sandwich Constructions by Beam Flexure," doi: https://doi.org/10.1520/c0393_c0393m-20.

[17] R. J. da Silva et al., "A core rigidity classifier method and a novel approach to account for geometric effects on the elastic properties of sandwich structures," Composite Structures, vol. 282, p. 115075, Feb. 2022, doi: https://doi.org/10.1016/j.compstruct.2021.115075.

[18] R. J. da Silva et al., "Enhanced core rigidity classifier method (RJS 2.0): a comprehensive approach to properly measure elastic properties of sandwich structures," Composite Structures, pp. 117981–117981, Feb. 2024, doi: https://doi.org/10.1016/j.compstruct.2024.117981.

Preliminary assessment on the effects of Na2SO4 as an alkaline activator for Hybrid Alkali-Activated Cement (HAAC)

Helena B.Farias [(a), *], Rafaela K.R. Silva [(b)], Paulo H.R. Borges [(c)]

(a) 0000-0001-5467-368X (Federal Centre for Technological Education of Minas Gerais – Brazil)
(b) 0009-0008-9359-1271 (Federal Centre for Technological Education of Minas Gerais – Brazil)
(c) 0000-0002-4072-6557 (Federal Centre for Technological Education of Minas Gerais – Brazil)

* Corresponding author: farias.helenabranjao@gmail.com

Abstract: [Até 200 palavras] In the current global panorama, society faces an urgent and complex problem: climate change. The cement industry is the second largest emitter of CO_2. The direct emission of carbon dioxide, about half of which is emitted during cement production, is due to the chemical process that occurs in the manufacture of clinker. The production of clinker involves calcining limestone ($CaCO_3$) which will transform into calcium oxide (CaO) and release CO_2 into the atmosphere. The substitution of clinker for Supplementary Cementitious Materials (SCMs) has been widely performed to produce low-carbon binders. However, the substitution of clinker by SCMs alters some significant technical points. When comparing a cement produced with a high proportion of clinker with a blended cement, differences in setting time, hydration heat, and strength at early ages become evident. Hybrid Alkali-Activated Cements (HAACs) are binders composed of ordinary Portland cement (OPC) and SCMs activated by an alkali. This system is expected to present characteristics like cement with a high clinker content. This research studied the development of a hybrid system in which different levels of Na2SO4 were tested to obtain an optimal percentage and analyze whether the system exhibits characteristics of a cement with a high clinker content.

1. INTRODUCTION

The Hybrid Systems (HSs) are binders composed of OPC and SCMs activated by an alkali [1], [2]. This type of binder has been researched worldwide, as it is seen as a transition on the usage of alternative types of cement with a low carbon footprint [3].

Regarding the terminology, there is not an agreement in literature, which difficult finding the papers in scientific bases. Usually, it is used "HACs" (Hybrid Alkaline Cements), or "HAACs" (Hybrid Alkali-Activated Cements) to indicate that the HS has OPC content of less than 30% and SCMs content of less than 70% (references). In the works of Park, the material is called Hybrid Alkaline Cement Composite (HACC) when the SH has a high calcium content (references). Moreover, there are several papers with no clear definition of the name of the material and the system is named according to the sample (references).

The SCMs are not reactive enough to be activated by the small amount of OPC in the mixes for strength development at early ages, hence it is necessary to add an alkali source to favor the reaction, but still in lower quantities than the dosage for alkali-activated materials (AAM) [1], [4], [5], [6], [7] . The HAACs present advantages of both systems (OPC and AAM), solving common issues presented by each one when done separately.

The AAM – especially with low calcium - usually require thermal curing to set the system. The OPC specimens present setting at ambient conditions (25 ºC), only requiring humidity control to avoid cracks, due to the exothermic reactions in the first 24 hours of setting. As the OPC releases heat during the curing process,

it has this advantage over the geopolymer, and so the SH can take advantage of this feature to cure the AAM present in the system (references).

The corrosive nature of the most usual activators used to manufacture the AAM is an obstacle to the production of alkali-activated cement on a large scale in the industry. On the other hand, the HAACs can be produced with smaller quantities of alkalis, when compared to the AAM, considering the alkalinity provided by the OPC itself which helps to upscale the activation of the SCMs in the mix [1], [2], [8].

The synthesis of HAACs commonly applies activators like sodium silicate (water glass, Na2SiO3) and/or sodium hydroxide (NaOH) to provide enough alkalis to the activation of the SCMs. This can enhance the mechanical properties of the cement in the early ages, but the acceleration of the reaction also leads to the reduction of workability and to flash setting, which limits the usage of this cement [1], [6], [7], [9], [10].

The usage of sodium sulfate (Na2SO4) as the activator for the HAACs has been studied to enhance workability, the setting time, and the strength at early age. The Na2SO4 is an alkaline activator soluble in water, with pH lower than the usual activators for AAM. Consequently, it does not accelerate the reaction to cause flash setting, then it may lead to lower mechanical strength values at an early age [11], [12].

2. METHODOLOGY

The cement used in this work was Pozzolanic Portland Cement (CPIV) produced by LIZ as a composite cement according to the Brazilian standard ABNT NBR 16697 [13], which permits the amount of clinker from 45 up to 85%, the pozzolan content from 15 to 50%, and the calcium sulfates from 0 to 10%. The anhydrous sodium sulfate (SS, Na2SO4) was provided by Sulfal Quimica. This activator was applied in two ways: as a powder and in solution, and both routes as 3% (wt) of the cement. The aggregate used was the standardized sand supplied by IPT.

The chemical composition of the CP IV was assessed by the X-ray Fluorescence (XRF) spectroscopy. The setting time was assessed via the Vicat needle test, following the Brazilian standard NBR 16607 [15].

The compressive strength test was performed according to the ABNT NBR 7215 [14]. A total of ten cylindric samples with dimensions of 5 cm x 10 cm were molded for each composition. The samples were demolded after 24 hours and sealed in plastic bags until the test date to avoid humidity exchange with the environment. Four samples were tested at 1 day of curing, three at 7 days, and 3 at 28 days of curing. The compositions are listed in Table 1.

Table 1 – Compositions of the HAACs tested.

Code	CP IV	SS (wt% of CP IV)	Dosage (b/a)	Water (c/w)
CP IV 0%	100%	-	1:3	0,48
CP IV 3%p	100%	3% (powder)	1:3	0,48
CP IV 3%s	100%	3% (solution)	1:3	0,48

The setting time was assessed via the Vicat test, following the Brazilian standard NBR 16607 [15].

3. RESULTS AND DISCUSSION

The result of XRF is show in the Table 2.

Table 2 – XRF result

Content	Amount (%)
CaO	69,813
SiO2	16,956
Al2O3	4,274
Fe2O3	2,978
SO3	2,221
K2O	1,135
MgO	1,039
MnO	0,611
SrO	0,503
TiO2	0,447
ZnO	0,023

The setting time presented by the composite cement mortars are shown in Table 3.

Table 3 – Setting time results.

Code	Setting time (h)
CP IV 0%	03:30
CP IV 3%p	02:30
CP IV 3%s	02:20

Analysing the data provided by Table 2, it is noticeable that there is a tendency to decrease the setting time with the addition of the SS, whether in powder or solution.

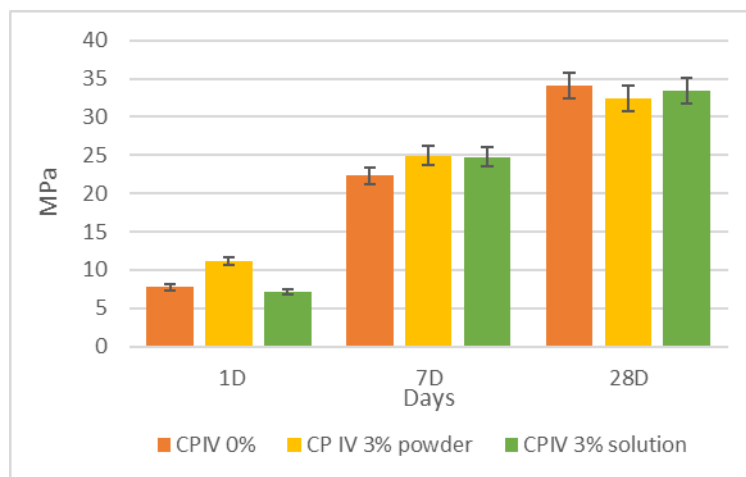The compressive strength results are shown in Figure 1.

Figure 1. Compressive strength of the mixes.

The compressive strength results were analysed by the ANOVA test. This indicates that the samples at early age present significative statistical differences when comparing the CPIV activated with the sulfate powder (CODE) with the reference (CPIV 3%) and with the addition of solution. Therefore, it is possible to note that there is an increase of 44% in the compressive strength after 1 by adding 3% of Na_2SiO_4 powder.

Regarding the results for 7 and 28 days, the results do not show significant statistical differences, so there is no further effect from the addition of the sulfate in powder or in solution.

Further studies are needed to analyse the material with other percentages of SS and its effect on other properties, like setting time, at later ages.

4. CONCLUSIONS

The preliminary results indicate that there is a tendency to obtain shorter setting time and higher compressive strength values in early ages with the addition of SS. The form of addition of SS – in powder or solution – did not lead to a significant difference in these properties. However further research is needed to evaluate the effect with percentages of SS addition other than 3%, specially to observe if there is negative effect at later ages.

4.1. Declaration of Competing Interest

The authors declare no conflict of interest.

4.2. Fundings

5. REFERENCES

[1] A. K. Mohapatra and B. Pradhan, "Hybrid alkali activated cements (HAACs) system: A state-of-the-art review on fresh, mechanical, and durability behaviour," *Constr Build Mater*, vol. 361, Dec. 2022, doi: 10.1016/J.CONBUILDMAT.2022.129636.

[2] A. Palomo, P. Monteiro, P. Martauz, V. Bilek, and A. Fernandez-Jimenez, "Hybrid binders: A journey from the past to a sustainable future (opus caementicium futurum)," *Cem Concr Res*, vol. 124, 2019, doi: 10.1016/j.cemconres.2019.105829.

[3] J. M. Etcheverry, Y. A. Villagran-Zaccardi, P. Van den Heede, V. Hallet, and N. De Belie, "Effect of sodium sulfate activation on the early age behaviour and microstructure development of hybrid cementitious systems containing Portland cement, and blast furnace slag," *Cem Concr Compos*, vol. 141, Aug. 2023, doi: 10.1016/j.cemconcomp.2023.105101.

[4] W. Al-Kutti, M. Nasir, M. A. Megat Johari, A. B. M. S. Islam, A. A. Manda, and N. I. Blaisi, "An overview and experimental study on hybrid binders containing date palm ash, fly ash, OPC and activator composites," *Constr Build Mater*, vol. 159, pp. 567–577, Jan. 2018, doi: 10.1016/j.conbuildmat.2017.11.017.

[5] E. Batuecas, I. Ramon-Alvaraez, S. Sanchez-Delgado, M. Torres-Carrasco, and Z. Leng, "Carbon footprint and water use of alkali-activated and hybrid cement mortars," *J Clean Prod*, vol. 319, 2021, doi: 10.1016/j.jclepro.2021.128653.

[6] S. Joseph, R. Snellings, and Ö. Cizer, "Activation of Portland cement blended with high volume of fly ash using Na2SO4," *Cem Concr Compos*, vol. 104, Nov. 2019, doi: 10.1016/j.cemconcomp.2019.103417.

[7] L. L. Xue, Z. H. Zhang, and H. Wang, "Hydration mechanisms and durability of hybrid alkaline cements (HACs): A review," *Constr Build Mater*, vol. 266, Jan. 2021, doi: 10.1016/j.conbuildmat.2020.121039.

[8] M. Askarian, Z. Tao, G. Adam, and B. Samali, "Mechanical properties of ambient cured one-part hybrid OPC-geopolymer concrete," *Constr Build Mater*, vol. 186, pp. 330–337, Oct. 2018, doi: 10.1016/J.CONBUILDMAT.2018.07.160.

[9] A. K. Mohapatra and B. Pradhan, "A study on early age properties of hybrid alkali activated mortars cured under ambient condition," *Mater Today Proc*, vol. 65, pp. 954–960, Jan. 2022, doi: 10.1016/j.matpr.2022.03.530.

[10] L. Xue, Z. Zhang, and H. Wang, "Early hydration kinetics and microstructure development of hybrid alkali activated cements (HAACs) at room temperature," *Cem Concr Compos*, vol. 123, Oct. 2021, doi: 10.1016/J.CEMCONCOMP.2021.104200.

[11] X. Dai, S. Aydin, M. Yucel Yardimci, and G. De Schutter, "Fresh and hardened state properties, reaction kinetics and microstructure of sodium sulfate/sodium hydroxide – Activated slag mixtures," *Constr Build Mater*, vol. 401, p. 132943, Oct. 2023, doi: 10.1016/j.conbuildmat.2023.132943.

[12] G. Yang, T. Wu, C. Fu, and H. Ye, "Effects of activator dosage and silica fume on the properties of Na2SO4-activated high-volume fly ash," *Constr Build Mater*, vol. 278, Apr. 2021, doi: 10.1016/j.conbuildmat.2021.122346.

[13] ABNT, "NBR 16697: Cimento Portland — Requisitos." Rio de Janeiro, 2018.

[14] ABNT, "NBR 7215: Cimento Portland - Determinação da resistência à compressão de corpos de prova cilíndricos." Rio de Janeiro, 2019.

[15] ABNT, "NBR 16607: Cimento Portland - Determinação dos tempos de pega." Rio de Janeiro, 2018.